MEDICAL RADIOLOGY

Diagnostic Imaging

A. L. Baert
K. Sartor

Imaging of Orbital and Visual Pathway Pathology

W. S. Müller-Forell
Editor

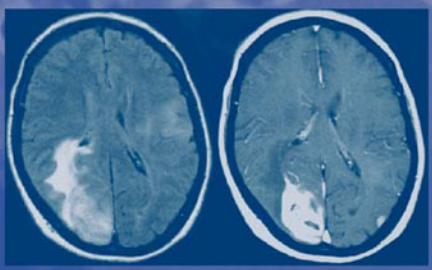

Springer

MEDICAL RADIOLOGY
Diagnostic Imaging

Softcover Edition

Editors:
A. L. Baert, Leuven
K. Sartor, Heidelberg

W. S. Müller-Forell (Ed.)

Imaging of Orbital and Visual Pathway Pathology

With Contributions by

E. Boltshauser · S. Kollias · W. Lieb · E. Martin · W. S. Müller-Forell · S. Pitz
U. Schwarz · W. Wichmann

Foreword by
K. Sartor

Preface by
N. Pfeiffer

With 433 Figures in 1368 Separate Illustrations, 66 in Color

Springer

PD Wibke S. Müller-Forell, MD
Institute of Neuroradiology
Medical School University of Mainz
Langenbeckstrasse 1
55101 Mainz
Germany

Medical Radiology · Diagnostic Imaging and Radiation Oncology
Series Editors: A. L. Baert · L. W. Brady · H.-P. Heilmann · F. Molls · K. Sartor

Continuation of
Handbuch der medizinischen Radiologie
Encyclopedia of Medical Radiology

ISBN 3-540-27988-1 Springer-Verlag Berlin Heidelberg New York
ISBN 978 3-540-27988-4 Springer-Verlag Berlin Heidelberg New York

Library of Congress Cataloging-in-Publication Data

Imaging of orbital and visual pathway pathology / W. S. Müller-Forell (ed.) ; with contributions by E. Boltshauser ... [et al.] ; foreword by A. L. Baert.
p. ; cm. – (Medical radiology)
Includes bibliographical references and index.
ISBN 3540633022 (hardcover; alk. paper) ISBN 3540279881 (softcover; alk. paper)
1. Eye--Imaging. 2. Visual pathways--Imaging. I. Müller-Forell, W. S. (Wibke S.), 1949- II. Series.
[DNLM: 1. Orbital Diseases--pathology. 2. Diagnostic Imaging. 3. Orbit--pathology. 4. Orbital Diseases--diagnosis. 5. Orbital Diseases--radiography. 6. Visual Pathways--pathology. WW 202 I31 2002]
RE79.I42 I534 2002
617.7'0754--dc21 2001049328

Springer-Verlag Berlin Heidelberg New York
a member of BertelsmannSpringer Science+Business Media GmbH

http//www. springeronline.com

Printed in Germany

Cover-Design and Typesetting: Verlagsservice Teichmann, 69256 Mauer

Printed on acid-free paper - 21/3151xq – 5 4 3 2 1

Dedicated to

Professor Dr. Sigurd Wende
1924–1991

An extraordinary neuroradiologist,
a challenging teacher
and a wonderful paternal friend.

Foreword

Most information about the external world enters the human mind via the visual system; when seeing and looking are impaired, important aspects of life may elude us or the world becomes disturbingly distorted. While the globe may be likened to a camera, it is the brain that constructs an image of the world. It does this by making sense of the signals it receives from the retina, in which it is helped by data stored in memory as well as data gathered through other modes of perception. The retinal signals, induced by photons hitting photoreceptor cells, travel first by way of the optic nerves, optic chiasm and optic tracts to relay stations, the lateral geniculate bodies, then via the optic radiations to the back of the occipital lobes; some signals, however, are shunted from the lateral geniculate bodies to the brainstem. The primary visual cortex needs the adjacent "association" cortex to provide a first rendition of the image of the world. Further input from other cortical and subcortical areas completes the image, for example, by adding an affective quality to it. Most „images" are finally elevated to the level of consciousness but some remain subconscious, although not necessarily without important consequences. This (parallel) processing of visual signals is accompanied by and related to neural mechanisms that precisely coordinate eye (and head/body) movement. A system this complex may become impaired in many different places and almost invariably will become impaired sooner or later. Pathologies that impair the system's anatomy and function may be intrinsic, that is, confined to the optic pathways, or extrinsic, i.e., arising in neighboring structures. Since the visual system extends from the anterior circumference of the globe to the tip of the occipital pole, there is a tremendous potential for intrinsic and extrinsic pathologies.

There was a time when the term "monograph" frequently indicated not only that the book thus classified dealt with just one subject but also that it was written by just one person; being an expert on a certain subject was synonymous with knowing everything there was to know about this subject. Today, because of the literally exponential growth of knowledge in almost all areas of medicine, it generally takes several or many experts to cover even "small" subjects. Furthermore, it is no longer considered sufficient to deal with a subject from one – let us say the radiologist's – point of view alone. How can one satisfactorily write on modern imaging of the visual system without asking the neuro-ophthalmologist – who best understands the system's function and who also uses some imaging – or the clinical scientist experienced in the pertinent pathology to participate? Even with regard to radiologic imaging the (neuro-)radiologist would be ill advised to focus on morphology alone, ignoring the tremendous progress that clinically practicable fMRI has made in recent years.

Consequently, Dr. Müller-Forell, a neuroradiologist, has teamed up with several internationally renowned experts from related clinical fields to realize her ambitious project, a comprehensive treatise on imaging of the visual system "front to back". As there is

nothing of similar scope on the market, this represents a most welcome and timely endeavor. The resulting book, thoroughly organized and an admirable feat, conveys invaluable information on methodology, normal anatomy, and orbital and intracranial pathology, as well as on normal and abnormal function. I am convinced that the book's superior quality will ensure its warm reception by all clinicians interested in this important topic, including radiologists, ophthalmologists, neurologists, neurosurgeons, and otorhinologists.

Heidelberg — Klaus Sartor

Preface

As an ophthalmologist, I feel greatly honored to have been asked to write a preface for this book. Orbital and visual pathway pathology is a field comprising a multitude of medical disorders that overlap the fields of ophthalmology, otorhinolaryngology, neurosurgery, general medicine and, of course, the diagnostic disciplines, especially neuroradiology. Diagnosis of many of these disorders is highly challenging. Fortunately, with the development and refinement of imaging techniques, especially CT and MRI, tremendous advances have been accomplished. Yet even with these new methods at hand diagnosis is usually far from being straightforward. This book, edited by Wibke Müller-Forell with contributions from herself, E. Boltshauser, S. Kollias, W. Lieb, E. Martin, S. Pitz, U. Schwarz and W. Wichmann, will greatly facilitate this task.

The general part not only describes ophthalmologic imaging techniques in a detailed, state-of-the-art way but also displays the anatomy of the visual pathway from the outer orbit to the visual cortex. The images are of extremely high quality, and many will find anatomical details that they have not discovered previously. Much and successful effort was also put into the summary of the relevant neuro-ophthalmology, and this will prove to be helpful for many readers. The same is even more true for the chapter on functional magnetic resonance imaging. This relatively new technique needs to be understood so that it can be used to its full extent.

The special part with its display of orbital and intracranial pathology of the optic pathway is exhaustive. I found it difficult to finish this preface, because even when proofreading the book it turned out to be a compulsive page-turner. It is richly illustrated throughout with real cases, often comprising a photo of the patient, a case history, and a display of the adequate imaging methods, accompanied by the description of the treatment and histological results. While it is a systematic book, the material is arranged in such a way that the cases can even be read as a quiz. I found many cases similar to those I have seen in my practice, but I also found cases that taught me what I perhaps should have diagnosed, but did not, in the past. Especially helpful is the chapter on optic pathway pathology in children. It is, I believe, unique and will be extremely helpful for those who see children with neuro-ophthalmological problems.

The reader will soon discover that this book is based upon a tremendous amount of clinical experience and knowledge of real cases of the kind that arise daily from the interdisciplinary approach and co-operation between neuroradiologists and other clinicians as mentioned above. Few – if any – have such a fundus of clinical experience at their fingertips. I am sure that this book will enormously help everybody who is entrusted with the clinical problem of difficult-to-diagnose diseases of the orbit and visual pathway. I wish the book well, and I am sure it will be received with great enthusiasm.

Mainz

Norbert Pfeiffer

Introduction

Imaging of the pathology of the entire visual system has thus far been given room for only a limited discussion in a small number of comprehensive neuroradiological textbooks. This is the first textbook and atlas dealing with the diseases of the entire visual pathway. The title of this book emphasizes that the subject is not restricted to the orbit, but is extended to the pathologies which may affect the visual pathway from the lens to the striate cortex of the occipital lobe. The book provides a context for the history and/or clinical symptomatology of individually involved parts of the visual system and the corresponding pathological findings, to ensure that all physicians involved in the treatment of disorders of the visual system, regardless of whether they are neuroradiologists, ophthalmologists, oto-/rhinolaryngologists, neurosurgeons or neurologists will find this textbook an invaluable source of practical and theoretical knowledge.

In the first section of the book particular attention is given to the most important current imaging methods, including ultrasound, computer tomography and magnetic resonance imaging, although here the focus is less on the physical aspects dealt with in greater depth in purely neuroradiological textbooks (for interested readers the respective radiological textbooks are indicated in the reference section). Even though the purpose of this book is to assist referring physicians in their decision as to which method is best suited to provide the most specific information to their questions, we are not offering any ready-made "cooking recipes", because each individual patient requires an individual examination protocol. Another chapter of this book is devoted to the detailed discussion of imaging CT- and MR-anatomy of the orbit and the intracranial/intracerebral visual pathway. The chapter on neuroophthalmology is designed to provide comprehensive knowledge of this complex field and the great variety of related diagnostic criteria. The following chapter discusses the most current developments in functional MR-imaging (fMRI) of the visual system, as well as indications for applications of the method, and results obtained in its use.

In the first chapter of the special part an overview of the complexity of visual impairment in newborns and children is presented, a field which is generally discussed only in special pediatric or neuroradiological textbooks. The focus of this special part of the book is the on the presentation of individual patient histories, symptoms and imaging (-in some cases- histological) findings. Equal importance is given to both the discussion of the accurate diagnosis and the illustration of various imaging modalities. CTs in relevant windows (soft tissue, bone) and different, multiple MR-sequences are presented to demonstrate different diagnostic criteria in different patients with similar clinical symptoms, their relevance and results. The anatomy of the visual pathway is meticulously characterized in the presentation of the course of the pathology from the orbit, the prechiasmatic and postchiasmatic intracranial regions, to the occipital lobe, though the occurrence of redundant histological diagnoses is inevitable. Since the patients chosen

for presentations are from our own patient population, on the other hand, some histologies may be missing. The reason for this is that especially in the intracranial space there is no exclusivity of all possible pathologies.

I feel deeply indebted to a large number of people for their support, on a personal as well as on a practical level. First and foremost I wish to thank Prof. Dr. Fritz Heuck for his patience and constant support over the past few years, and for his firm conviction that this work was to come to successful completion. My dear friend Dr. Renate Gustorf-Aeckerle merits many, many thanks for her active role the initiation of the book and for her continued encouragement all through this project. It gives me great pleasure to thank all my co-authors for their substantial efforts and contributions. In particular the wonderful active cooperation of Dr. Susanne Pitz deserves special thanks, as does the prolonged daily cooperation with Prof. Dr. Wolfgang Lieb. I am very pleased and indeed proud that the extended period of time I was given the opportunity to spend at the Institute of Neuroradiology of the University Hospital of Zurich (USZ) resulted in the fruitful cooperation with the following well-known and respected specialists: Prof. Dr. Boltshauser and Prof. Dr. Martin-Fiori of the Children's University Hospital, Prof. Dr. Wichmann of the Department of Neuroradiology at the Klinik im Park, Priv. Doz. Dr. Spyros Kollias, Institute of Neuroradiology, and Priv. Doz. Dr. Urs Schwarz from the Clinic of Neurology of the USZ, who all contributed in such a wonderful way to the present tome.

There are many individuals without whose contributions to the realisation of this atlas would not have been possible: Special thanks are in order for both the excellent work and the remarkably friendly cooperation of Mrs. Keuchel and her colleagues Mrs. Soldevilla and Mrs. Nessler from the photographic laboratory of the Clinic of Radiology, University of Mainz. The expert realization of a consistent lay-out for the diagrams by Mr. Stefan Kindel, graphic artist at the Clinic of Neurosurgery of the University of Mainz, was of immense help. I would not have wanted to miss his prompt initiative, and his constructive, positive and always friendly cooperation. Special thanks are also due to Mrs. Gisela Rumsey, who corrected the manuscript in an admirable effort. The help of Mrs. Ursula Davis from Springer Verlag was overwhelming, especially since her support was not only needed, but provided in a particularly sympathetic and amicable manner that I will never forget.

Last but not least, I would like to offer grateful thanks to my beloved husband, Dr. Hans-Joachim Forell, for his constant, loving and patient support, and for his tacit consent that this work was to be dedicated not to him, but to a common fatherly friend. His silent contribution is invaluable, especially since he had to spend many, many evenings and weekends alone, accompanied only by Felix (our cat).

Mainz Wibke S. Müller-Forell

Contents

General Part

The requested page could not be found.

1 Ophthalmologic Imaging Methods

Wolfgang E. Lieb, Wibke S. Müller-Forell, Werner Wichmann

CONTENTS

W. Lieb, MD, PhD
Professor, Eye Clinic, University of Würzburg, Julius Maximilians University, Josef-Schneider-Strasse 11, 97080 Würzburg, Germany
PD W. S. Müller-Forell, MD
Institute of Neuroradiology, Medical School, University of Mainz, Langenbeckstrasse 1, 55101 Mainz, Germany
W. Wichmann, MD, PhD
Professor, Institute of Neuroradiology and Radiology, Klinik im Park AG, Seestrasse 220, 8027 Zurich, Switzerland

1.1 Color Doppler Ultrasonography of the Eye and Orbit

Wolfgang E. Lieb

Color Doppler imaging is the significant development of the last decade in ultrasonography that allows for simultaneous two-dimensional structural imaging in the Doppler evaluation of blood flow. With this technique, it has become possible for the first time to display indirectly the fine orbital vessels such as the ophthalmic artery and its branches, the central retinal artery, the posterior ciliary artery, and the lacrimal artery. On the other hand, also the display of venous structures such as the superior ophthalmic vein, the vortex veins, and the central retinal vein is possible. In addition to this qualitative display, it also enables quantitative assessment of the hemodynamics in those vessels by looking at the Doppler spectrum and determining flow velocities during various periods of the cardiac cycle.

This technique is now being used in ophthalmology to evaluate orbital tumors and vascular lesions, intraocular tumors, carotid cavernous sinus fistulas, and hemodynamic changes in patients with retinal vascular disease such as central retinal artery occlusion, central retinal vein occlusion, and diabetic retinopathy. Several studies have even been made to study drug effects on the hemodynamics.

1.1.1 Introduction

Real time A-mode and B-mode ultrasonography has been used for the diagnostic evaluation of ophthalmic disorders since the early 1960s. Modern digital high-resolution equipment has improved diagnostic imaging and made it an essential part of certain ophthalmologic evaluations. Doppler ultrasound detects

changes in the frequency of sound reflected from flowing blood, allowing estimation of the flow velocity. Doppler ultrasonography of the carotid arteries and the periorbital vessels is frequently employed in patients with ischemic ocular disease. The technology of Duplex scanning allows for simultaneous B-mode imaging and Doppler spectral analysis. Since the diameters of the vessels in the eye and orbit are too small to be imaged with conventional Duplex scans, Doppler spectra are obtained without precise localization and without knowledge of the Doppler angle. The latest technological change in the character of diagnostic ultrasound is color Doppler imaging. To facilitate localization of vascular structures, the two-dimensional flow information in color Doppler imaging (CDI) is encoded in color and superimposed on the gray scale structural image. Since the sensitivity of detecting Doppler shifts is not limited by the resolution of the gray scale image, Doppler shifts in very small vessels can be detected, depicting the course of the vessels (Grant et al. 1989, 1992; Merritt 1987; Mitchell 1990; Mitchell et al. 1988, 1989; Powis 1988; Pozniak et al. 1992; Ranke et al. 1992).

The introduction of the so called "power Doppler", which represents the summation of the square from the spectral amplitudes of the Doppler signal, was an important new step in CDI technology. Hereby the coding for direction is neglected in order to improve sensitivity for very small vessels or vessels with low blood flow (Adler et al. 1995; Allard et al. 1999; Babcock et al. 1996; Bascom and Cobbold 1996; Griewing et al. 1996a,b; Hamper et al. 1997; Martinoli et al. 1998; Murphy and Rubin 1997; Pugh et al. 1996; Rubin et al. 1994; Winsberg 1995; Wu et al. 1998). Modern broad band transducers with frequencies up to 15 MHz have greatly improved orbital gray-scale and color Doppler imaging.

The three major areas of application of CDI and its new modifications of signal processing such as power Doppler, tissue harmonic imaging, 3-dimensional CDI, as well as the use of contrast agents can be described as primarily:

1. Vascular evaluation
   Application of CDI includes the detection and measurement of arterial stenosis and flow-restricting or flow-disturbing abnormalities. This can be performed for the large abdominal vessels, the aorta, iliac, femoral, and popliteal artery, and other peripheral arteries, and of course, for large vessels of the head and neck, the carotid bifurcation, and the vertebral arteries (Allard and Cloutier 1999; Bazzocchi et al. 1998; Bendick et al. 1998; Carroll 1996; Erickson et al. 1989b, Erickson et al. 1989c; Ferrara and DeAngelis 1997; Foley et al. 1989; Grant et al. 1990, 1992; Landwehr and Lackner 1990; Landwehr et al. 1989, 1990, 1991; Merritt 1987, 1989; Whelan et al. 1992)
2. Organ perfusion
   CDI can be utilized to visualize the perfusion of the liver, kidneys, spleen, placenta, and brain. It can be used as a guide to obtain selective Doppler information which allows better assessment of the hemodynamics in those organs. The major indications of this category is the assessment of perfusion in kidney transplants (Bazzocchi et al. 1998; Becker and Cooperberg 1988; Deane et al. 1992; Fleischer and Kepple 1992; Lerner et al. 1990; Levine et al. 1997; Lewis and James 1989; Middleton et al. 1989; Rifkin et al. 1993; Seibert et al. 1998; Wilson and Thurston 1992; Winkler 1998; Winters 1996).
3. Tumor neovascularity
   CDI adds a new dimension to the ultrasound evaluation of mass lesions (Maresca et al. 1991; Orr and Taylor 1990; Taylor et al. 1991). This technique is already being successfully used to differentiate some benign from malignant tumors of the liver (Goldberg et al. 1990), tumors of the female breast, the testicles, as well as tumors of the eye and orbit (Falco et al. 1992; Guthoff et al. 1989, 1991a; Jain et al. 1992; Lieb 1998; Lieb et al. 1990b; Wolff-Kormann et al. 1992a,b).

1.1.2 Ophthalmic Examination Technique

The ultrasound transducer is applied to the closed eyelids using sterile ophthalmic methylcellulose as a coupling gel . During the examination, the patient lies in a supine position, and care is taken not to apply pressure to the eye to avoid artifacts. Horizontal and vertical scans through the eye and orbit are performed. Depending on the direction of flow with respect to the transducer, the blood flow data displayed are either in red or blue. The colors can be arbitrarily assigned, but in this study flow toward the transducer is depicted as red and away from the transducer as blue. The color saturation in the image represents the average frequency (first moment average) from a spectral analysis performed at each sample site. These frequencies can be turned into velocities by solving the Doppler equation for velocity.

When examining the eye and orbit through the eyelids, the ultrasound beam is essentially parallel to the orbital and ocular vessels, and thus most arterial flow is depicted in red. Arteries can usually be distinguished from veins by noting the pulsatility of the former. Pulsed Doppler spectral analysis also helps to distinguish between pulsatile arterial and the usually more continuous or minimally pulsatile venous flow, and allows for the quantification of data. When the ultrasound beam is at an angle of 90 deg to a vascular structure or if a vessel contains only stagnant blood, no Doppler flow information is obtained, and the structure is shown in gray scale display only.

All examinations are performed in a "low" or "medium" flow setting to allow for optimal detection of low to medium Doppler frequency shifts of the slow-flowing blood in the small orbital vessels. For the ophthalmic artery, medium to high flow settings are applied, since flow in this vessel is faster. Color threshold levels are adjusted to minimize artifacts by lid and involuntary eye movements. To obtain Doppler spectra, a sample volume of approximately 0.2×0.2 mm is chosen within the vessel . The proximal and distal portions of the vessel are imaged to facilitate determination of the Doppler flow angle for estimation of velocity. The scan images can be recorded on videotape and later reviewed with the benefit of cine-loop and frame by frame analysis of selected segments. Images can be photographed during cine-loop replay by using a 35 mm camera that photographs directly from an isolated on-board color monitor. The duration of the examination ranges from 20 to 30 min for both (Belden et al. 1995; Guthoff 1988; Guthoff et al. 1991a; Lieb 1993, 1998; Lieb et al. 1991; Williamson and Harris 1996).

1.1.3 Safety Considerations

As in any diagnostic test, there may be some risk in diagnostic ultrasound. Therefore, the sonographer and physician need to know something about this risk.

The American Institute of Ultrasound in Medicine (AIUM) has reviewed reports of bioeffects in ultrasound and has issued a statement in respect of ultrasound bioeffects on in vivo mammalian tissue.

According to the AIUM, there is in the low MHz frequency (0.5–10.0 MHz) no independently confirmed significant biological effect in mammalian tissue exposed in vivo to unfocussed ultrasound with intensities below 100 mW/cm^2 or focussed ultrasound with intensities of 1000 mW/cm^2 (Lizzi and Mortimer 1988; Lizzi et al. 1981).

Currently, in the USA, the Food and Drug Administration (FDA) has established guidelines of ultrasound intensity limits for various clinical applications. The basis for these limits was linked to the measured output level of machines sold for ophthalmic and other particular applications prior to the enactment of the 1976 Medical Device Amendment. These parameters have not been based upon the assessment of risks published today.

For the instrument used in our studies (QAD 1 and QAD 2000, Siemens-Quantum, Issaquah, Wash., USA), the estimated in situ peak temporal average intensity (SPTA) in the color imaging mode is 2–3 mW/cm^2 for the 7.5 MHz transducer. During spectral analysis, the in situ peak temporal average intensity is approximately 50–100 mW/cm^2, exceeding the currently approved FDA upper guidelines of 17 mW/cm^2. The Spatial Peak Average Intensity (SPAI) is the highest intensity within the ultrasound field average over an entire scan frame period.

Depending on the device settings for commercially available color Doppler units, the acoustic intensity values given in the AIUM bioeffect statements and in the FDA guidelines may be exceeded, especially during pulsed Doppler spectrum analysis. However, the SPTA intensities of 100 mW/cm^2 should not be treated as a magic number. According to studies by Lizzi et al. (1981; Lizzi and Mortimer 1988) and Coleman et al. (1986), who did intensive experiments on ultrasound bioeffects to ocular tissues, the intensities used for diagnostic imaging are significantly lower than those which would be expected to cause unwanted ocular side-effects, especially chorio-retinal lesions and cataract formation.

1.1.4 Vascular Topography of the Normal Eye and Orbit

Horizontal and vertical sections of the globe and normal orbit at the level of the optic nerve display Doppler signals along the course of the central retinal artery (CRA) and the central retinal vein (CRV) (Fig. 1.1a).

The CRA and the accompanying vein can be depicted within the anterior 2 mm of the optic nerve shadow. In some instances, they can be traced up to the point of entering into the optic nerve. The CRV usually runs next to the CRA and can be differenti-

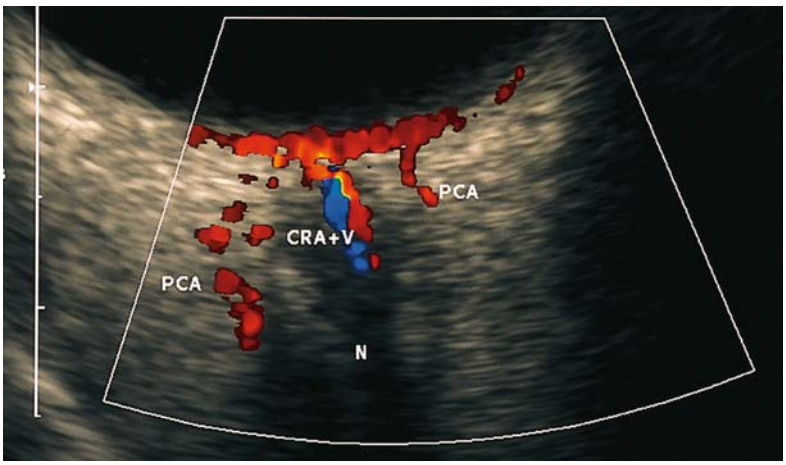

a

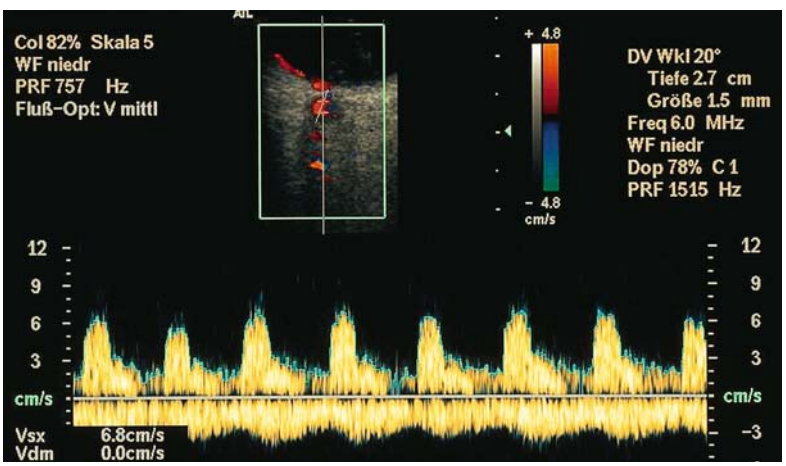

b

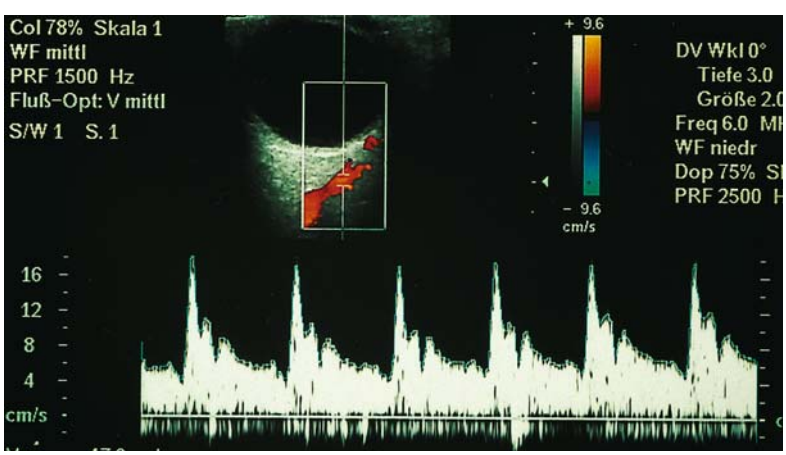

c

Fig. 1.1.a Horizontal section through the globe at the level of the optic nerve. Displayed are the central retinal artery (*CRA*), the central retinal vein (*CRV*), and the temporal short posterior ciliary artery (*PCA*). **b** Analysis of the Doppler spectrum. A cursor is placed on the vessel, and the angle is corrected according to the vessel's course. The spectrum of the CRA shows usually venous overlap caused by the CRV running close to the CRA. **c** Doppler spectrum and course of the ophthalmic artery

ated from it by the color coding and also by its Doppler characteristics and its continuous flow in systole and diastole. The spectrum of the CRA shows usually a venous overlap from the CRV (Fig. 1.1b). On either side of the optic nerve, slightly posterior to the CRA, the short and long posterior ciliary arteries can be identified. Several groups have published their experiences and normal values (Table 1.1) with good overall reproducibility (Aburn and Sergott 1993a,b; Belden et al. 1995; Erickson et al. 1989a; Gillies et al. 1999; Giovagnorio et al. 1993; Greenfield et al. 1995; Guthoff et al. 1991b; Lieb et al. 1991; Niwa et al. 1998; Senn et al. 1996; Williamson et al. 1995). The Doppler spectrum of the posterior ciliary arte-

Table 1.1. Blood flow velocities in orbital vessels: data from 222 normal eyes (Lieb and Schenk 1998)

	Mean (STD) peak systolic (cm/s)	Mean (STD) end-diastolic (cm/s)
Central retinal artery (CRA)	9.6±(1.4)	2.4±(0.8)
Central retinal vein (CRV)	–4.2±(0.8)	
Ophthalmic artery (OA)	37.7±(7.0)	8.8±(2.8)
Posterior ciliary artery (PCA)	11.3±(2.2)	3.6±(1.2)
Superior ophthalmic vein (SOV)	–7.6±(1.8)	
Vortex veins (Vv)	–8.5±(2.2)	

ries shows velocity time spectra which are similar to those of the CRA. The end-diastolic flow in the posterior ciliary arteries (PCA) is higher, however, reflecting the low resistance vascular channels of the choroid (Lieb et al. 1992a,b). Further posterior in the posterior orbit, segments of the main ophthalmic artery can be seen. The ophthalmic artery can be traced temporally to the optic nerve to the point where it usually crosses over the optic nerve towards the medial orbit. In Hayreh's series, the crossing of the ophthalmic artery over the optic nerve in the mid-orbit was a common finding in 80% of cases studied (Hayreh 1963a,b; Lang and Kageyama 1990).

The flow velocity wave form of the ophthalmic artery (OA) is similar to that of the internal carotid artery, showing a high maximum peak systolic flow and low diastolic flow velocity. Sometimes the superior orbital artery and the lacrimal artery can be identified (Fig. 1.1c). Of the venous structures, flow in the vortex veins can be demonstrated in all four quadrants, the superior ophthalmic vein can be identified at the posterior aspect of the globe and in the superior nasal orbit (Fig. 1.2). The superior ophthalmic vein (SOV) can be traced posteriorly until it crosses over

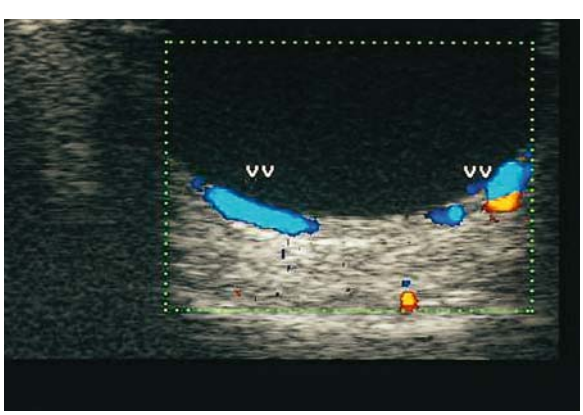

Fig. 1.2. Section of the superior hemisphere of the globe displaying the nasal and temporal vortex veins

the optic nerve (Berges 1992; Erickson et al. 1989; Lieb et al. 1991; Williamson and Harris 1996). The spectrum with the continuous, nonpulsatile flow pattern together with the color coding in blue is characteristic of venous flow.

1.1.5 Retinal and Retinal Vascular Disease of the Eye

Few reports have dealt with CDI in the evaluation of retinal disorders. Wells et al. and others (Verbruggen et al. 1999; Wells et al. 1991) have used CDI to depict a patent hyaloid artery in a case of persistent hyperplastic primary vitreous (PHPV). Wong et al. (1991) used the vascularity in the retinal vessels of retinal detachments as an additional criterion to distinguish a detached retina from dense vitreous strands (Fig. 1.3). In a study comparing the flow velocities of the CRA and OA in patients with arterial

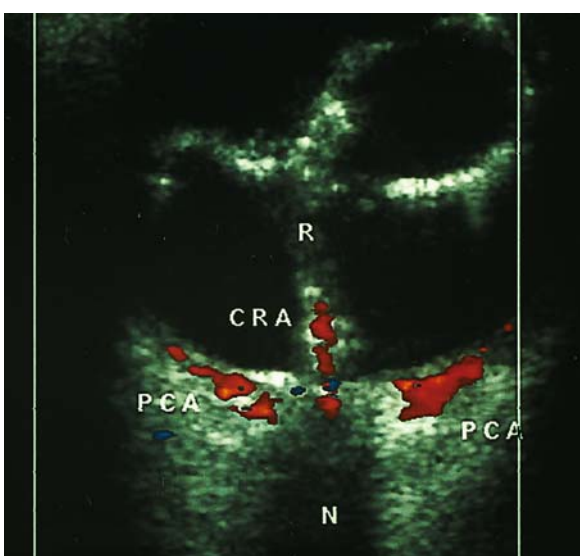

Fig. 1.3. Total funnel-shaped retinal detachment inserting at the optic nerve (*N*) with a membrane behind the lens . There is blood flow visible in the detached retina (*R*), the central retinal (*cra*), and the posterior ciliary arteries (*pca*)

hypertension and carotid artery disease, Cesarone et al. found significantly reduced systolic and end-diastolic flow velocities compared with a normal control group (Cesarone et al. 1992). We found a group of patients with proliferative diabetic retinopathy who showed a significant decrease of the peak systolic and end-diastolic flow velocity of the CRA. The blood flow velocities in the PCA and OA were unchanged com-

pared to age-matched controls (Göbel et al. 1993; Goebel et al. 1995). The pharmacological influence on flow parameters has been investigated by Belfort (1992) and Baxter et al. (1992) using CDI. In the first study, Belfort was able to detect a significant reduction in pulsatility and Pourcelot's index of the CRA and PCA in a group of pre-eclamptic women who were treated with magnesium sulfate. The study by Baxter evaluated the effect of posture and topical ß-blockers on the hemodynamics of the orbital vessels. They found no effect of posture but a fall in Pourcelot's index. Since the identification of the orbital vessels is difficult to reproduce in their study, caution should be used when interpreting this information as an indication that CDI is capable of demonstrating subtle pharmacologic effects on orbital hemodynamics. Ho et al. (1992) published the first study to use CDI in the diagnosis and investigation of ocular ischemic syndrome (OIS). It demonstrated reduced ocular blood flow in one of the ophthalmic artery, PCA, or CRA in eyes with OIS. Furthermore, in some eyes with OIS, CDI demonstrated nondetectable or reversal of blood flow velocities in corresponding posterior ciliary or ophthalmic arteries (Ward et al. 1995; Wolf et al. 1987; Wong et al. 1998). In general, lower flow values represent compromised blood flow proximal to the point of sampling by CDI or increased resistance distal to the sampling point (Costa et al. 1999; Geroulakos et al. 1996; Hu et al. 1995; Lee and Fu 1997; Mawn et al. 1997).

1.1.6 Intraocular Tumors

Effective vasculature is essential for all tumor growth. It is formed by newly sprouted, ingrowing vessels and by incorporation of existing host vessels into the tumor mass. Other than the qualitative information provided by intravenous fluorescein angiography, to date no technique is available to assess the tumor-associated blood flow in the eye and orbit.

Recently, several groups reported their results using conventional Duplex scanning and CDI on intraocular tumors (Guthoff et al. 1989, 1991a; Hirai et al. 1998; Lieb et al. 1990b; Pineda et al. 1998; Wolff-Kormann et al. 1992a,b). They were able to demonstrate flow within the intraocular tumors and noted a decrease in Doppler shift after therapy. Abnormal Doppler signals have been reported for many tumors (Shimamoto et al. 1987) such as breast carcinomas (Cosgrove et al. 1990; Raza and Baum 1997), hepatomas (Bartolozzi et al. 1997; Goldberg et al. 1993; Hosten et al. 1999; Imamura et al. 1998; Ishiguchi et al. 1996), and renal tumors (Chen et al. 1998; Lewis and James 1989; Polascik et al. 1999; Ramos et al. 1988) and are helpful in their differential diagnosis. Histopathologically, tumor vessels are often primitive vascular channels lacking smooth muscle, consisting only of an endothelial layer and connective tissue (Paweletz and Knierim 1989). Low resistance to flow is expected, since in most neoplasms the vessels lack normal arteriolar smooth muscle, the recognized site of peripheral vascular resistance.

High sensitivity in detecting even minimal flow is necessary to allow detection of fine tumor vascularity (Fig. 1.4a,b). Lesions that can simulate uveal melano-

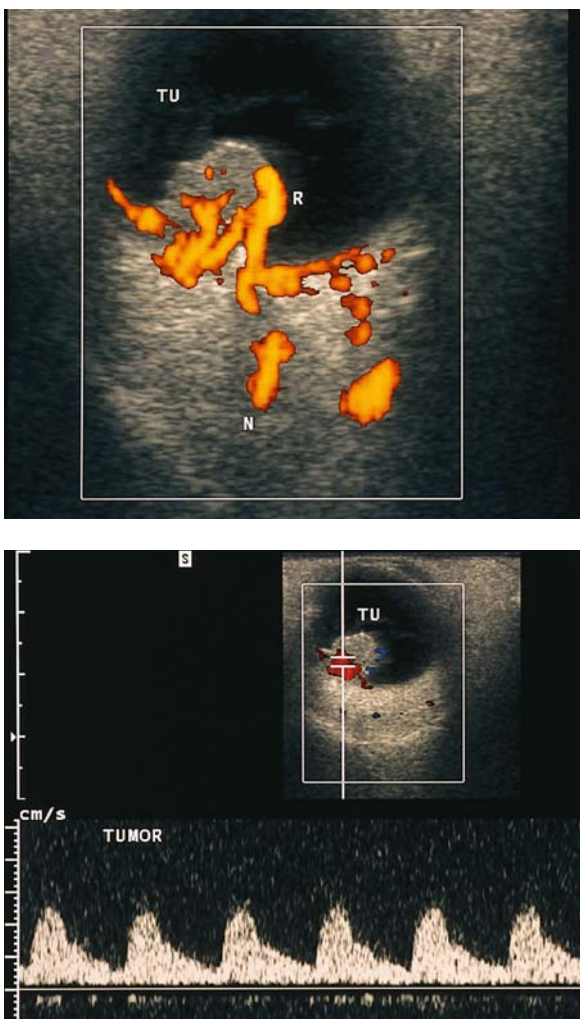

a b

Fig. 1.4.a Power spectrum display of a large choroidal melanoma with fan-shaped vasculature throughout the tumor (*TU*). *R*, retina; *N*, optic nerve. **b** Spectrum analysis of tumor vessels demonstrating neoplastic vasculature with low resistance flow characteristics

mas, such as large subretinal hemorrhages, usually do not have a distinctive blood supply. Therefore, they can be differentiated from melanomas on the basis of the absence of Doppler flow. Further improvement in the detection of low blood flow in neoplasms was achieved with ultrasound contrast agents such as Levovist (Albrecht et al. 1998; Bauer et al. 1999; Bogers et al. 1999; Brown et al. 1998; Cennamo et al. 1994; Kim et al. 1998; Pugh et al. 1996; Rizzatto et al. 1997; Schlief 1991; Uggowitzer et al. 1999) and the power Doppler mode (Kurjak et al. 1998; Silverman et al. 1999).

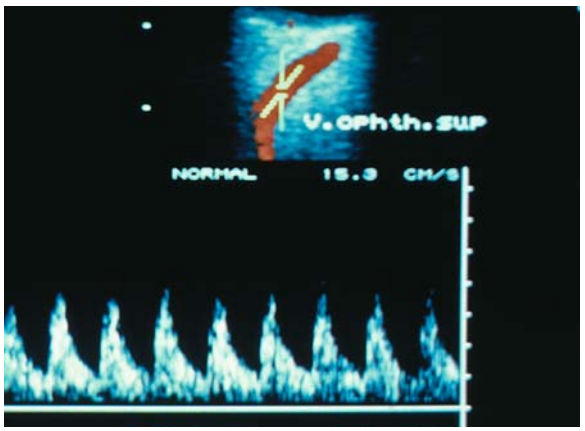

a

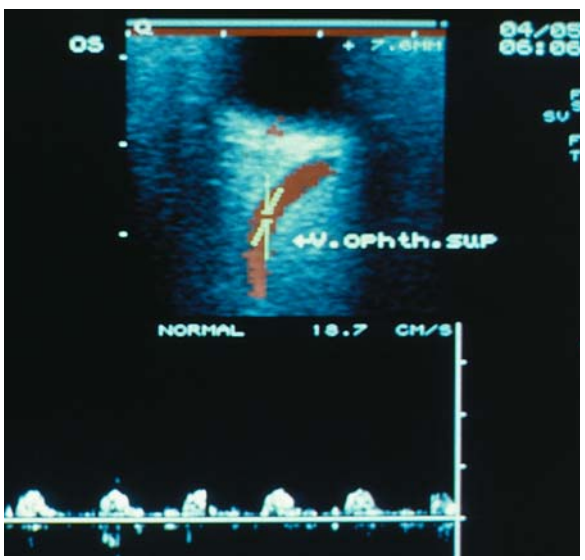

b

Fig. 1.5.a High flow carotid cavernous sinus fistula. The flow in the dilated superior ophthalmic vein (SOV) is reversed and therefore displayed in *red*, and the spectrum shows a characteristic high flow shunt pattern with high end-diastolic flow velocities. **b** After spontaneous partial thrombosis of the SOV, there is a blunted spectrum within the vessel as a sign of less flow

1.1.7 Orbital Disorders

In the orbit CDI has been used to study orbital vascular lesions such as orbital varices, carotid cavernous sinus fistulas (CCF), as well as orbital mass lesions. Flaharty et al. (1991) as well as Kotval et al. (1990) have reported their experience with CDI in the diagnosis and monitoring of carotid cavernous sinus fistulas. In all cases of CCF studied, CDI was able to demonstrate the dilated, arterialized SOV with high velocity blood flow towards the transducer (Fig. 1.5a,b). CDI further depicted the dilated preseptal high blood flow shunts and the secondary extraocular enlargement of muscles characteristic of this entity (Aung et al. 1996; Costa et al. 1997; Martin et al. 1995; Nagy et al. 1995). The recent report from Soulier-Sotto et al. (1992) confirmed the findings and stressed the point that this technique can be also used to monitor CCF noninvasively to assess their spontaneous course or effects of embolization or balloon occlusion. In contrast to CCSF, orbital varices, when studied with CDI, demonstrate relatively low blood flow velocities, and the dynamic evaluation depicts venous inflow and outflow into the varix during inspiration and Valsalva maneuvers (Kawaguchi et al. 1997; Lieb et al. 1990; Wildenhain et al. 1991). When studying orbital mass lesions, CDI adds a new dimension to their evaluation.

Whereas computed tomography (CT) scanning and magnetic resonance imaging (MRI) give a good topographic display of those lesions and some indications of their vascularity, when studying contrast enhancement or signal intensities, CDI directly displays active flow in those lesions (Fig. 1.6). Several tumors have been studied by Jain et al. (1992), but in their report they were unable to attribute specific vascularity patterns to individual tumors. We found that cavernous hemangiomas of the orbit usually show only very little to almost no flow and extremely low venous flow velocities throughout the lesion. In contrast to this, lymphomas and metastatic lesions contain large arterial and venous vessels supplying the tumor (Lieb et al. 1992a). Compression of the CRA has been shown in a case of amaurosis caused by a cavernous hemangioma. The authors (Knapp et al. 1992) demonstrated clearly that CDI is able to substantiate hemodynamic changes caused by the tumor, which in their case caused intermittent amaurosis by vascular compression of the central retinal vessels. Several groups have found the information obtained by CDI quite helpful and supplementary to CT and MRI in planning the surgical approach to a tumor (Ivekovic et al. 2000; Zuravleff and Johnson

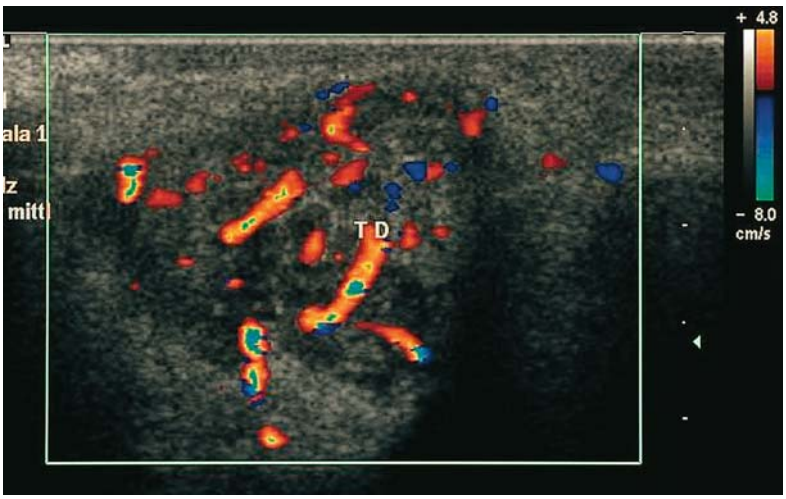

Fig. 1.6. Well-circumscribed tumor (*TD*) in the anterior orbit with significant vascularity. Histologically shown to be a hemangiopericytoma

1997) and in patients with thyroid ophthalmopathy (Benning et al. 1994; Nakase et al. 1994).

In our opinion, CDI provides useful information in the orbit:

1. for the evaluation of the normal orbital and ocular vasculature,
2. for the evaluation of other orbital vessels displaced by a mass lesion or tumor
3. for the primary evaluation and follow-up of orbital vascular lesions as varices, arteriovenous malformations, and CCFs
4. for the assessment of the vascularity pattern of orbital or intraocular mass lesions,
5. for the differentiation of intraocular tumors from hemorrhage, and vitreous bands from retinal detachment.

Studies evaluating the role of CDI investigating hemodynamic changes of orbital vessels indicate that this technique provides additional useful information in CRV occlusions, diabetic retinopathy, arterial occlusions, and perhaps in glaucoma (Chiou et al. 1999; Evans et al. 1999a,b; Harris et al. 1995; Sergott et al. 1994).

References

Aburn NS, Sergott RC (1993a) Color Doppler imaging of the ocular and orbital blood vessels. Curr Opin Ophthalmol 4:3–6

Aburn NS, Sergott RC (1993b) Orbital colour Doppler imaging. Eye 7:639–647

Adler RS, Rubin JM, Fowlkes JB, Carson PL, Pallister JE (1995) Ultrasonic estimation of tissue perfusion: a stochastic approach. Ultrasound Med Biol 21:493–500

Albrecht T, Patel N, Cosgrove DO, Jayaram V, Blomley MJ, Eckersley R (1998) Enhancement of power Doppler signals from breast lesions with the ultrasound contrast agent EchoGen emulsion: subjective and quantitative assessment. Acad Radiol 5 [Suppl 1]: 15–21

Allard L, Cloutier G. (1999) Power Doppler ultrasound scan imaging of the level of red blood cell aggregation: an in vitro study. J Vasc Surg, 30:157–168

Allard L, Cloutier G, Guo Z, Durand LG. (1999) Review of the assessment of single level and multilevel arterial occlusive disease in lower limbs by duplex ultrasound. Ultrasound Med Biol 25:495–502

Aung T, Oen FT, Fu ER (1996) Orbital colour Doppler imaging in carotid-cavernous sinus fistula. Aust NZ J Ophthalmol 24:121–126

Babcock DS, Patriquin H, LaFortune M, Dauzat M (1996) Power doppler sonography: basic principles and clinical applications in children. Pediatr Radiol 26:109–115

Bartolozzi C, Lencioni R, Paolicchi A, Moretti M, Armillotta N, Pinto F (1997) Differentiation of hepatocellular adenoma and focal nodular hyperplasia of the liver: comparison of power Doppler imaging and conventional color Doppler sonography. Eur Radiol 7:1410–1415

Bascom PA, Cobbold RS (1996) Origin of the Doppler ultrasound spectrum from blood. IEEE Trans Biomed Eng 43:562–571

Bauer A, Hauff P, Lazenby J, von Behren P, Zomack M, Reinhardt M, Schlief R. (1999) Wideband harmonic imaging: a novel contrast ultrasound imaging technique. Eur Radiol 9 [Suppl 3]: S364–S367

Baxter GM, Williamson TH, McKillop G, Dutton GN (1992) Color Doppler Ultrasound of orbital and optic nerve blood flow: effects of posture and Timolol 0.5%. Invest Ophthalmol Vis Sci 33:604–610

Bazzocchi M, Quaia E, Zuiani C, Moroldo M (1998) Transcranial Doppler: state of the art. Eur J Radiol 27 [Suppl 2]: S131–S148

Becker CD, Cooperberg PL (1988) Sonography of the hepatic vascular system. AJR 150:999–1005

Belden CJ, Abbitt PL, Beadles KA (1995) Color Doppler US of the orbit. Radiographics 15:589–608

Belfort MA (1992) The effect of magnesium sulphate on blood flow velocity in the maternal retina in mild pre-eclampsia: a preliminary colour flow Doppler study. Br J Obstet Gynaecol 99:641–645

Bendick PJ, Brown OW, Hernandez D, Glover JL, Bove PG

(1998) Three-dimensional vascular imaging using Doppler ultrasound. Am J Surg 176:183–187
Benning H, Lieb W, Kahaly G, Grehn F. (1994) Farbkodierte Duplexsonographie bei Patienten mit endokriner Orbitopathie. Ophthalmologe 91:20–25
Berges O (1992) Écho-Doppler couleur (ECD) en ophtalmologie. Aspect des vaisseaux orbitaires normaux. Apport diagnostique de l'EDC à l'étude des tumeurs oculaires, de la pathologie vasculaire orbitaire et des tumeurs de l'orbite. JEMU 13:264–274
Bogers HA, Sedelaar JP, Beerlage HP, de lRJ, Debruyne FM, Wijkstra H, Aarnink RG. (1999) Contrast-enhanced three-dimensional power Doppler angiography of the human prostate: correlation with biopsy outcome. Urology 54:97–104
Brown JM, Quedens CC, Alderman JL, Greener Y, Taylor KJ (1998) Contrast-enhanced sonography of tumor neovascularity in a rabbit model. Ultrasound Med Biol 24:495–501
Carroll BA (1996) Carotid ultrasound. Neuroimaging Clin North Am 6:875–897
Cennamo G, Rosa N, Vallone GF, Smaltino F (1994) First experience with a new echographic contrast agent. Br J Ophthalmol 78:823–826
Cesarone MR, Laurora G, Steigerwalt R, Belcaro G (1992) Retinal Duplex scanning in cerebrovascular disease and hypertension. Vasa 21:163–166
Chen P, Maklad N, Redwine M (1998) Color and power Doppler imaging of the kidneys. World J Urol 16:41–45
Chiou HJ, Chou YH, Liu CJ, Hsu CC, Tiu CM, Teng MM, Chang CY (1999) Evaluation of ocular arterial changes in glaucoma with color Doppler ultrasonography. J Ultrasound Med 18:295–302
Coleman DJ, Lizzi FL, Silverman RH, Dennis PH, Driller J, Rosada A, Iwamoto T (1986) Therapeutic ultrasound. Ultrasound in Med & Biol
Cosgrove D, Bamber J, Davey J, McKinna J, Sinnett H (1990) Color Doppler signals from breast tumors. Radiology 176:175–180
Costa VP, Molnar LJ, Cerri GG (1997) Diagnosing and monitoring carotid cavernous fistulas with color Doppler imaging. J Clin Ultrasound 25:448–452
Costa VP, Kuzniec S, Molnar LJ, Cerri GG, Puech LP, Carvalho. CA(1999) The effects of carotid endarterectomy on the retrobulbar circulation of patients with severe occlusive carotid artery disease. An investigation by color Doppler imaging. Ophthalmology 106:306–310
Deane C, Cowan N, Giles J, Walters H, Rifkin I, Severn A, Parsons V (1992) Arteriovenous fistulas in renal transplants: color Doppler ultrasound observations. Urol Radiol 13:211–217
Erickson SJ, Hendrix LE, Massaro BM, Harris GJ, Lewandowski MF, Foley WD, Lawson TL (1989a) Color Doppler flow imaging of the normal and abnormal orbit. Radiology 173:511–516
Erickson SJ, Mewissen MW, Foley WD, Lawson TL, Middleton WD, Lipchik EO, Quiroz FA, Macrander SJ (1989b) Color Doppler evaluation of arterial stenoses and occlusions involving the neck and thoracic inlet. Radiographics 9:389–406
Erickson SJ, Mewissen MW, Foley WD, Lawson TL, Middleton WD, Quiroz FA, Macrander SJ, Lipchik EO (1989c) Stenosis of the internal carotid artery: assessment using color Doppler imaging compared with angiography. AJR 152:1299–1305
Evans DW, Harris A, Cantor LB (1999) Primary open-angle glaucoma patients characterized by ocular vasospasm demonstrate a different ocular vascular response to timolol versus betaxolol. J Ocul Pharmacol Ther 15:479–487
Evans DW, Harris A, Chung HS, Cantor LB, Garzozi HJ (1999) Effects of long-term hypotensive therapy with nonselective beta-blockers on ocular hemodynamics in primary open-angle glaucoma. J Glaucoma 8:12–17
Falco L, Esente S, Fantani S, Pasarelli N, Utari S (1992) Our experience in the diagnosis of intraocular tumors by a B-scan system and angiodynography (Doppler). Preliminary results. Acta Ophthalmol Suppl 204:76–80
Ferrara K, DeAngelis G (1997) Color flow mapping. Ultrasound Med Biol 23:321–345
Flaharty PM, Lieb WE, Sergott RC, Bosley TM, Savino PJ (1991) Color Doppler imaging. A new noninvasive technique to diagnose and monitor carotid cavernous sinus fistulas. Arch Ophthalmol 109:522–526
Fleischer AC, Kepple DM (1992) Transvaginal color duplex sonography: clinical potentials and limitations. Semin Ultrasound Ct Mr 13:69–80
Foley WD, Middleton WD, Lawson TL, Erickson S, Quiroz FA, Macrander S (1989) Color Doppler ultrasound imaging of lower-extremity venous disease. AJR 152:371–376
Geroulakos G, Botchway LT, Pai V, Wilkinson AR, Galloway JM. (1996) Effect of carotid endarterectomy on the ocular circulation and on ocular symptoms unrelated to emboli. Eur J Vasc Endovasc Surg 11:359–363
Gillies WE, Brooks AM, Scott M, Ryan L (1999) Comparison of colour Doppler imaging of orbital vessels in elderly compared with young adult patients. Aust NZ J Ophthalmol 27:173–175
Giovagnorio F, Quaranta L, Bucci MG (1993) Color Doppler assessment of normal ocular blood flow. J Ultrasound Med 12:473–477
Göbel W, Lieb W, Ho A, Sergott R, Farhoumand R, Grehn F (1993) Die Farb-Duplex Sonographie als neues Verfahren zur Untersuchung der orbitalen Gefäße bei Retinopathia diabetica. Ophthalmologe 91: 26–30
Goebel W, Lieb WE, Ho A, Sergott RC, Farhoumand R, Grehn F (1995) Color Doppler imaging: a new technique to assess orbital blood flow in patients with diabetic retinopathy. Invest Ophthalmol Vis Sci 36:864–870
Goldberg BB, Hilpert PL, Burns PN, Liu JB, Newman LM, Merton DA, Witlin LA (1990) Hepatic tumors: signal enhancement at Doppler US after intravenous injection of a contrast agent. Radiology 177:713–717
Goldberg BB, Liu JB, Burns PN, Merton DA, Forsberg F (1993) Galactose-based intravenous sonographic contrast agent: experimental studies. J Ultrasound Med 12:463–470
Grant E, Tessler F, Perrella R (1989) Clinical Doppler imaging. AJR 152:707–717
Grant EG, Tessler FN, Gomes AS, Holmes CL, Perrella RR, Duerinckx AJ, Busuttil RW (1990) Color Doppler imaging of portosystemic shunts. AJR 154:393–397
Grant EG, Schiller VL, Millener P, Tessler FN, Perrella RR, Ragavendra N, Busuttil R (1992) Color Doppler imaging of the hepatic vasculature. AJR 159:943–950
Greenfield DS, Heggerick PA, Hedges T (1995) Color Doppler imaging of normal orbital vasculature (see comments). Ophthalmology 102:1598–1605
Griewing B, Doherty C, Kessler C (1996) Power Doppler ultra-

sound examination of the intracerebral and extracerebral vasculature. J Neuroimaging 6:32–35
Griewing B, Doherty C, Zeller JA, Kallwellis G, Walker ML, Kessler C (1996) Power Doppler – a new tool for transcranial duplex assessment of intracranial vasculature. Bildgebung 63:35–38
Guthoff R (1988) Ultraschall in der ophthalmologischen Diagnostik. Ein Leitfaden für die Praxis. Enke, Stuttgart
Guthoff R, Berger RW, Helmke K, Winckler B (1989) Doppler sonographische Befunde bei intraokularen Tumoren. Fortschr Ophthalmol 86:239–241
Guthoff RF, Berger RW, Winkler P, Helmke K, Chumbley LC. (1991a) Doppler ultrasonography of malignant melanomas of the uvea. Arch Ophthalmol 109:537–541
Guthoff RF, Berger RW, Winkler P, Helmke K, Chumbley LC (1991b) Doppler ultrasonography of the ophthalmic and central retinal vessels. Arch Ophthalmol 109:532–536
Hamper UM, DeJong MR, Caskey CI, Sheth S (1997) Power Doppler imaging: clinical experience and correlation with color Doppler US and other imaging modalities. Radiographics 17:499–513
Harris A, Spaeth GL, Sergott RC, Katz LJ, Cantor LB, Martin BJ (1995) Retrobulbar arterial hemodynamic effects of betaxolol and timolol in normal-tension glaucoma. Am J Ophthalmol 120:168–175
Hayreh SS (1963a) Arteries of the orbit in the human being. Br J Surg 50:938–953
Hayreh SS (1963b) The cilio-retinal arteries. Br J Ophthalmol 47:71–79
Hirai T, Ohishi H, Yamada R, Yoshimura H, Hirohashi S, Uchida H, Hashimoto H, Jibiki T, Takeuchi Y (1998) Three-dimensional power Doppler sonography of tumor vascularity. Radiat Med 16:353–357
Ho AC, Lieb WE, Flaharty PM, Sergott RC, Brown GC, Bosley TM, Savino PJ (1992) Color Doppler Imaging of the ocular ischemic syndrome. Ophthalmology 99:1453–1462
Hosten N, Puls R, Bechstein WO, Felix R (1999) Focal liver lesions: Doppler ultrasound. Eur Radiol 9:428–435
Hu HH, Luo CL, Sheng WY, Teng MM, Wong WJ, Luk YO (1995) Transorbital color Doppler flow imaging of the carotid siphon and major arteries at the base of the brain. AJNR Am J Neuroradiol 16:591–598
Imamura M, Shiratori Y, Shiina S, Sato S, Obi S, Okudaira T, Teratani T, Kato N, Akahane M, Ohtomo K, Minami M, Omata M (1998) Power Doppler sonography for hepatocellular carcinoma: factors affecting the power Doppler signals of the tumors. Liver 18:427–433
Ishiguchi T, Shimamoto K, Fukatsu H, Yamakawa K, Ishigaki T. (1996) Radiologic diagnosis of hepatocellular carcinoma. Semin Surg Oncol 12:164–169
Ivekovic R, Lovrencic HA, Novak LK, Demarin V (2000) Value of color-Doppler imaging in diagnosis of intrabulbar and intraorbital tumors. Coll Antropol 24:205–210
Jain R, Sawhney S, Berry M (1992) Real-time sonography of orbital tumours. Colour Doppler characterization; initial experience. Acta Ophthalmol Suppl 204:46–49
Kawaguchi S, Nakase H, Noguchi H, Yonezawa T, Morimoto T, Sakaki T (1997) Orbital varix diagnosed by color Doppler flow imaging – case report. Neurol Med Chir Tokyo 37:616–619
Kim AY, Choi BI, Kim TK, JK Han, Yun EJ, Lee KY, Han MC (1998) Hepatocellular carcinoma: power Doppler US with a contrast agent – preliminary results. Radiology 209:135–140
Knapp ME, Flaharty PM, Sergott RC, Savino PJ, Mazzoli RA, Flanagan JC (1992) Gaze-induced amaurosis from central retinal artery compression. Ophthalmology 99:238–240
Kotval PS, Weitzner IJ, Tenner MS (1990) Diagnosis of carotid-cavernous fistula by periorbital color Doppler imaging and pulsed Doppler volume flow analysis. J Ultrasound Med 9:101–106
Kurjak A, Kupesic S, Breyer B, Sparac V, Jukic S (1998) The assessment of ovarian tumor angiogenesis: what does three-dimensional power Doppler add? Ultrasound Obstet Gynecol 12:136–146
Landwehr P, Lackner K (1990) Farbkodierte Duplexsonographie vor und nach PTA der Arterien der unteren Extremität. Fortschr Röntgenstr 152:35–41
Landwehr P, Dölken W, Lackner K (1989) In-vitro-Messung des intravasalen Blutflusses mit der Farb-Doppler-Sonographie. Fortschr Röntgenstr 150:192–197
Landwehr P, Tschammler A, Hohmann M (1990) Gefäßdiagnostik mit der farbkodierten Duplexsonographie. Dtsch Med Wochenschr 115:343–351
Landwehr P, Schindler R, Heinrich U, Dölken W, Krahe T, Lackner K (1991) Quantification of vascular stenosis with color Doppler flow imaging: in vitro investigations. Radiology 178:701–704
Lang J, Kageyama I (1990) The anatomy of the ophthalmic artery and its branches. Verh Anat Ges 83:315–316
Lee HM, Fu ER (1997) Orbital colour Doppler imaging in chronic ocular ischaemic syndrome. Aust NZ J Ophthalmol 25:157–163
Lerner RM, Mevorach RA, Hulbert WC, Rabinowitz R (1990) Color Doppler US in the evaluation of acute scrotal disease. Radiology 176 :355–358
Levine D, Hulka CA, Ludmir J, Li W, Edelman RR (1997) Placenta accreta: evaluation with color Doppler US, power Doppler US, and MR imaging. Radiology 205:773–776
Lewis BD, James EM (1989) Current applications of duplex and color Doppler ultrasound imaging: abdomen. Mayo Clin Proc 64:1158–1169
Lieb WE (1993) Color Doppler ultrasonography of the eye and orbit. Curr Opin Ophthalmol 4:68–75
Lieb WE (1998) Color Doppler imaging of the eye and orbit. Radiol Clin North Am 36:1059–1071
Lieb WE, Merton D, Shields J, Cohen S, Mitchell D, Goldberg B. (1990a) Color Doppler imaging in the demonstration of an orbital varix. Br J Ophthalmology 74:305–308
Lieb WE, Shields JA, Cohen SM, Merton DA, Mitchell DG, Shields CL, Goldberg BB (1990b) Color Doppler imaging in the management of intraocular tumors. Ophthalmology 97:1660–1664
Lieb WE, Cohen SM, Merton DA, Shields JA, Mitchell DG, Goldberg BB (1991) Color Doppler imaging of the eye and orbit. Technique and normal vascular anatomy. Arch Ophthalmol 109:527–531
Lieb WE, Flaharty PM, Ho A, Sergott RC (1992a) Color Doppler imaging of the eye and orbit. A synopsis of a 400 case experience. Acta Ophthalmol Suppl 204:50–54
Lieb WE, Flaharty P, Göbel W, Ho A, Sergott R, Richard G, Grehn F (1992b) Color Doppler imaging – a technique to study the hemodynamics of ocular and orbital veins. Invest Ophthalmol Vis Sci (abstract) 33:1047
Lizzi F, Mortimer A (1988) Bioeffects considerations for the safety of diagnostic ultrasound. J Ultrasound Med 7:1–38
Lizzi F, Coleman D, Driller J, Franzen L, Leopold M (1981)

Effects of pulsed ultrasound on ocular tissue. Ultrasound Med Biol 7:245–252
Maresca G, Danza FM, Vecchioli A (1991) Tissue characterization by color-Doppler. Rays 16:346–360
Martin TJ, Troost BT, Ginsberg LE, Tegeler CH, Weaver RG (1995) Left dural to right cavernous sinus fistula. A case report. J Neuroophthalmol 15:31–35
Martinoli C, Derchi LE, Rizzatto G, Solbiati L (1998) Power Doppler sonography: general principles, clinical applications, and future prospects. Eur Radiol 8:1224–1235
Mawn LA, Hedges T, Rand W, Heggerick PA (1997) Orbital color Doppler imaging in carotid occlusive disease. Arch Ophthalmol 115:492–496
Merritt C (1987) Doppler color-flow Imaging. J Clin Ultrasound 15:591–597
Merritt CRB (1989) Ultrasound safety: what are the Issues? Radiology 173:304–306
Middleton W, Thorne D, Melson G (1989) Color Doppler ultrasound of the normal testis. AJR 152:293–297
Mitchell DG (1990) Color Doppler imaging: principles, limitations, and artifacts. Radiology 177:1–10
Mitchell DG, Merton D, Needleman L, Kurtz AB, Goldberg BB, Levy D, Rifkin MD, Pennell RG, Vilaro M, Baltarowich O et al (1988) Neonatal brain: color Doppler imaging, part I. Technique and vascular anatomy. Radiology 167:303–306
Mitchell DG, Merton DA, Mirsky PJ, Needleman L (1989) Circle of Willis in newborns: color Doppler imaging of 53 healthy full-term infants. Radiology 172:201–205
Murphy KJ, Rubin JM (1997) Power Doppler: it's a good thing. Semin Ultrasound Ct Mr 18:13–21
Nagy ZZ, Nemeth J, Suveges I, Lanyi F (1995 A case of paradoxical worsening of dural-sinus arteriovenous malformation syndrome after neurosurgery. Eur J Ophthalmol 5:265–270
Nakase YOT, Yoshikawa K, Inoue Y (1994) Color doppler imaging of orbital venous flow in dysthyroid optic neuropathy. Jpn J Ophthalmol 38:80–86
Niwa Y, Yamamoto T, Kawakami H, Kitazawa Y (1998) Reproducibility of color Doppler imaging for orbital arteries in Japanese patients with normal-tension glaucoma. Jpn J Ophthalmol 42:389–392
Orr NM, Taylor KJW (1990) Doppler detection of tumor vascularity. Clin Diagnostic Ultrasound 26:149–163
Paweletz N, Knierim M (1989) Tumor related angiogenesis. Crit Rev Oncol Hematol 9:197–242
Pineda R, Theodossiadis PG, Gonzalez VH, Hu LK, Hart LJ, Gragoudas ES, Young LH (1998) Establishment of a rabbit model of extrascleral extension of ocular melanoma. Retina 18:368–372
Polascik TJ, Hamper U, Lee BR, Dai Y, Hilton J, Magee CA, Crone JK, Shue MJ, Ferrell M, Trapanotto V, Adiletta M, Partin AW (1999) Ablation of renal tumors in a rabbit model with interstitial saline-augmented radiofrequency energy: preliminary report of a new technology. Urology 53:465–472
Powis R (1988) Color flow imaging. Understanding its science and technology. J Diagn Med Sonogr 4:234–245
Pozniak MA, Zagzebski JA, Scanlan KA (1992) Spectral and color Doppler artifacts. Radiographics 12: 35–44
Pugh CR, Arger PH, Sehgal CM (1996) Power, spectral, and color flow Doppler enhancement by a new ultrasonographic contrast agent. J Ultrasound Med 15:843–852
Ramos I, Taylor K, Kier R, Burns P, Snower D, Carter D (1988) Tumor vascular signals in renal masses: detection with Doppler ultrasound. Radiology 168:633–637
Ranke C, Hendrickx P, Roth U (1992) Color and conventional image-directed Doppler ultrasonography: accuracy and sources of error in quantitative blood flow measurements. J Clin Ultrasound 20:187–193
Raza S, Baum JK (1997) Solid breast lesions: evaluation with power Doppler US. Radiology 203:164–168
Rifkin M, Sudakoff G, Alexander A (1993) Prostate: techniques, results, and potential applications of Color Doppler US scanning. Radiology 186:509–513
Rizzatto G, Chersevani R, Abbona M, Lombardo VL, Macorig D (1997) High-resolution sonography of breast carcinoma. Eur J Radiol 24:11–19
Rubin JM, Bude RO, Carson PL, Bree RL, Adler RS (1994) Power Doppler US: a potentially useful alternative to mean frequency-based color Doppler US. Radiology 190:853–856
Schlief R (1991) Ultrasound contrast agents. Curr Opin Radiol 3:198–207
Seibert JJ, Avva R, Hronas TN, Mocharla R, Vanderzalm T, Cox K, Kinder D, Lidzy B, Knight KL (1998) Use of power Doppler in pediatric neurosonography: a pictorial essay. Radiographics 18:879–890
Senn BC, Kaiser HJ, Schotzau A, Flammer J (1996) Reproducibility of color Doppler imaging in orbital vessels. Ger J Ophthalmol 5:386–391
Sergott RC, Aburn NS, Trible JR, Costa VP, Lieb WJ, Flaharty PM. (1994) Color Doppler imaging: methodology and preliminary results in glaucoma (published erratum appears in Surv Ophthalmol 1994, 39:165). Surv Ophthalmol 38 [Suppl]: S65–S70
Shimamoto K, Sakuma S, Ishigaki T, Makino N (1987) Intratumoral blood flow: evaluation with color Doppler echography. Radiology 165:683–685
Silverman RH, Kruse DE, Coleman DJ, Ferrara KW (1999) High-resolution ultrasonic imaging of blood flow in the anterior segment of the eye. Invest Ophthalmol Vis Sci 40:1373–1381
Soulier-Sotto V, Beaufrere L, Laroche JP, Dauzat M, Bourbotte G, Bourgeois JM, Janbon C, Arnaud B (1992) Diagnostic par écho-Doppler-couleur d'une fistule durale de la loge caverneuse à révélation ophthalmologique. J Fr Ophthalmol 15:38–42
Taylor GA, Perlman EJ, Scherer LR, Gearhart JP, Leventhal BG, Wiley J (1991) Vascularity of tumors in children: evaluation with color Doppler imaging. AJR 157:1267–1271
Uggowitzer MM, Kugler C, Riccabona M, Klein GE, Leber K, Simbrunner J, Quehenberger F (1999) Cerebral arteriovenous malformations: diagnostic value of echo-enhanced transcranial Doppler sonography compared with angiography. Am J Neuroradiol 20:101–106
Verbruggen AM, Boroffka SA, Boeve MH, Stades FC (1999) Persistent hyperplastic tunica vasculosa lentis and persistent hyaloid artery in a 2-year-old basset hound. Vet Q 21:63–65
Ward JB, Hedges T, Heggerick PA (1995) Reversible abnormalities in the ophthalmic arteries detected by color Doppler imaging. Ophthalmology 102:1606–1610
Wells RG, Miro P, Brummond R (1991) Color-flow Doppler sonography of persistent hyperplastic primary vitreous. J Ultrasound Med 10:405–407
Whelan JF, Barry MH, Moir JD (1992) Color flow Doppler ultrasonography: comparison with peripheral arteriogra-

phy for the investigation of peripheral vascular disease. J Clin Ultrasound 20:369–374

Wildenhain P, Lehar S, Dastur K, Dodd G III (1991) Orbital varix: color flow imaging correlated with CT and MR studies. J Comput Assist Tomogr 15:171–173

Williamson TH, Harris A (1996) Color Doppler ultrasound imaging of the eye and orbit. Surv Ophthalmol 40:255–267

Williamson TH, Lowe GD, Baxter GM (1995) Influence of age, systemic blood pressure, smoking, and blood viscosity on orbital blood velocities. Br J Ophthalmol 79:17–22

Wilson SR, Thurston WA (1992) Gastrointestinal sonography. Curr Opin Radiol 4:69–77

Winkler P (1998) Advances in paediatric CNS ultrasound. Eur J Radiol 26:109–120

Winsberg F (1995) Power Doppler US (letter). Radiology 195: 873

Winters WD (1996) Power Doppler sonographic evaluation of acute pyelonephritis in children. J Ultrasound Med 15:91–96

Wolf S, Körper N, Reim M, Ringelstein EB (1987) Ocular blood supply in internal carotid obstructions. In: Ben Ezra D, Ryan SJ, Glaser BM, Murphy R (eds) Ocular circulation and neovascularization. Dr W Junk Publ, Dordrecht/Boston/Lancaster, pp 37–42

Wolff-Kormann PG, Kormann B, Hasenfratz GC, Spengel FA (1992a) Duplex and color Doppler ultrasound in the differential diagnosis of choroidal tumors. Acta Ophthalmol Suppl 204:66–67

Wolff-Kormann PG, Kormann B, Riedel KG, Hasenfratz GC, Stefani FH, Spengel FA, Lund O-E (1992b) Quantitative Color Doppler imaging in untreated and irradiated choroidal melanoma. Invest Ophthalmol Vis Sci 33:1928–1933

Wong AD, Cooperberg PL, Ross WH, Araki DN (1991) Differentiation of detached retina and vitreous membrane with color flow Doppler. Radiology 178:429–431

Wong YM, Clark JB, Faris IB, Styles CB, Kiss JA (1998) The effects of carotid endarterectomy on ocular haemodynamics. Eye 12: 89–94

Wu SJ, Shung KK, Brasseur JG (1998) In situ measurements of Doppler power vs. flow turbulence intensity in red cell suspensions. Ultrasound Med Biol 24:1009–1021

Zuravleff JJ, Johnson MH (1997) An ophthalmic surgeon's view of orbital imaging techniques. Semin Ultrasound CT MR 18:395–402

1.2 Computed Tomography

Wibke S. Müller-Forell

1.2.1 Technical Principles

Computed tomography (CT) was the first modern imaging technique which was able to distinguish different soft tissues by measurement of their different densities, a revolutionary method especially for the intracranial brain structures. The basis of this technique is the measurement of different absorption values after exposure to X-rays. In the slice of interest, the absorption values of parts of a defined matrix (so-called voxels) are transformed to gray-scale units by specific algorithms, the reconstruction is shown on a display, and all data are sampled in a digital manner.

The absorption value is named after its inventor as the Hounsfield unit (HU) (Hounsfield 1973). It varies linearly in proportion to the absorption coefficient and is defined arbitrarily: thus, water is defined at 0 HU, air may have –1000 HU and less, and in bone, values of more than +1000 HU are measured. The mean values of fat range from –70 to –100 HU, cerebrospinal fluid (CSF) shows about 4–10 HU, and brain parenchyma normally presents as 35 HU (white matter) to 45 HU (gray matter). In routine examinations, the absolute absorption values are not as important as the relative density of the adjacent tissue. Isodense tissue is defined for tissue with a density of normal brain parenchyma, whereas tissue of high absorption of X-rays (e.g., bone or a fresh hemorrhage) is called hyperdense, appearing bright. Tissue of high water content (e.g., edema or necrosis) looks hypodense, appearing gray to black.

An important disadvantage of CT is the presence of beam-hardening artifacts (Hounsfield artifacts), making the differential diagnosis of small pathologies difficult or even impossible. They are caused by the enormous density differences between bone and parenchyma apparent in some regions of the endocranium, e.g., the posterior fossa or the optic canal. The so-called partial volume effect is to be mentioned also: in borderlines of different absorption values, a false hyperdensity may be seen, when different tissues overlap in adjacent voxels. In those cases, experience and knowledge of anatomical details are needed in order to differentiate normal from pathological structures.

CT, in concert with MRI and ultrasound (for orbital pathologies), is one of the so-called noninvasive imaging modalities. It remains the method of choice for intracranial emergency screening, also for suspected fractures, and when an analysis of possible bony changes, e.g., a calcification is helpful or essential for the decision of the differential diagnosis. The distinctly different X-ray absorption of bone, fat, muscles, vitreous body, and lens represents a very good natural intrinsic contrast of the different orbital tissues.

1.2.2 Radiation Burden

The lens is the organ most sensitive to radiation exposure, as an irradiation with a dose between 0.5 and 2 Gy can cause detectable opacities (Maclennan and Hadley 1995). The dependence of slice thickness, number of slices, axis of intersection, and mAs-product per slice is known, as the higher the number and the thinner the slices, the higher the effective radiation dosage at the interesting organ (lens) (Trommer et al. 1997). However, in orbital imaging, an axis parallel to the infraorbitomeatal line is mandatory in axial view, in order to view the optic nerve and lens in one single slice.

The development of modern CT equipment with spiral (helical) technique, in which a defined volume is exposed to continuous radiation, acquired by a rotating X-ray tube and detector system, has completely changed the original method, where the acquisition was done slice by slice. With conventional CT of a biplane (axial and coronal) protocol, the radiation dose is about 75 mGy, but only 35 mGy for single-slice helical CT (Lakits et al. 2000). The newest generation of multislice spiral (helical) technique (MS-spiral-CT) represents the development of the single-slice

technique. Along with the advantage of a quick data acquisition of a large volume and a high resolution (Ohnesorge et al. 1999), the increased radiation burden of a factor 1.5 compared with the single-slice technique in examinations of petrous bone (somewhat comparable to orbital imaging) has to be taken into consideration, although a "normal" brain scanning showed the lowest irradiation (Giacomuzzi et al. 2001). One might speculate that a single MS-spiral-CT examination would utilize the same radiation dose, but with the advantage of a short acquisition time, reducing motion artifacts, and the ability of multidirectional reconstruction, any question can be answered. In addition to multiplanar reconstructions, postprocessing today allows the generation of three-dimensional volume-rendering images of the bone and of the basal arteries including the circle of Willis. Sophisticated reformations require a stack of very thin sectioned scans, and the new multidetector-row helical CT offers the possibility to sample these data in a few seconds (Hu et al. 2000).

1.2.3 Contrast Medium

In normal extracranial parenchymal tissue (e.g., the lacrimal gland) the effect of diffusion of iodized contrast material out of the lumen of capillary vessel into the extracellular space is seen as increased density (>10 HU). As a result of the sum of all contrast medium-filled capillaries with an intact blood-brain barrier (BBB), the contrast enhancement of normal brain parenchyma is only 3–5 HU. The BBB represents a property of the pial vessel, where the tight junction of their capillary endothelium prevents a passive diffusion of macromolecules, such as water-soluble contrast medium (Sage and Wilson 1994). In case of a breakdown of the BBB, whether caused by a tumor or an infection, the continuous endothelial tight junctions are destroyed, and the extravasation of contrast medium into the pathologic process leads to a contrast enhancement (>5 HU).

In CT examination of the orbit, the indication of IV contrast is limited to suspected vascular lesions, as differential diagnosis is mainly led by morphological changes. If indicated, two main contraindications should be considered:

1. a distinct renal impairment may lead to renal failure. The risk of contrast agent-induced renal failure is high in dehydrated patients, in those with a known renal or cardiovascular insufficiency, and in those suffering from plasmocytoma, hypertonus, and hyperuricemia (Katzberg 1997). Especially in patients with diabetes mellitus and an additional renal insufficiency, the risk of contrast-induced renal failure is about 9% (Parfrey et al. 1989). Although no absolute limiting value can be defined, the serum creatinine should not exceed >1.5 mg/dl, and the use of nonionic contrast agent should be standard (Schwab et al. 1989; Uder 1998).
2. in case of a manifest or known history of hyperthyreosis, an application of iodized contrast material should be avoided. If imperatively necessary, it should be applied only after blockage of the thyroid, in order to avoid a thyrotoxic crisis, still a life-threatening disease (Kahaly and Beyer 1989). It is recommended to start prophylactic medication at least 2–4 h before the application and continue it for 14 days, at a dosage of 900 mg perchlorate per day. In patients at risk, a facultative medication with 20 mg Thiamazol per day can be administered additionally (Rendl and Saller 2001).

A known allergic reaction to iodine represents a relative contraindication, as short-term medication with H1- and H2-blockers immediately before the exposure to iodized contrast medium can prevent this complication (Wangemann et al. 1988).

1.2.4 Imaging Protocol

As already mentioned, CT imaging of the brain is mainly restricted to emergency and/or screening situations. CT examination of the orbit may be indicated in other cases, especially because of its lower cost and its better and quicker availability than MRI equipment, while the image quality for a definite diagnosis is comparable. Depending on the local environment, in Europe the indication of whether CT or MRI is applied for a special orbital diagnosis differs widely, possibly because of the lower availability of MRI equipment in some countries (Weetman and Wiersinga 1998). The axial intersection should be acquired parallel to the infraorbitomeatal line (Fig. 1.7), in order to ensure a view parallel to the orbital axis, and thus visualization of the optic nerve and the medial and lateral rectus muscle in one image. Depending on the scanner equipment available, a slice thickness of 2–3 mm

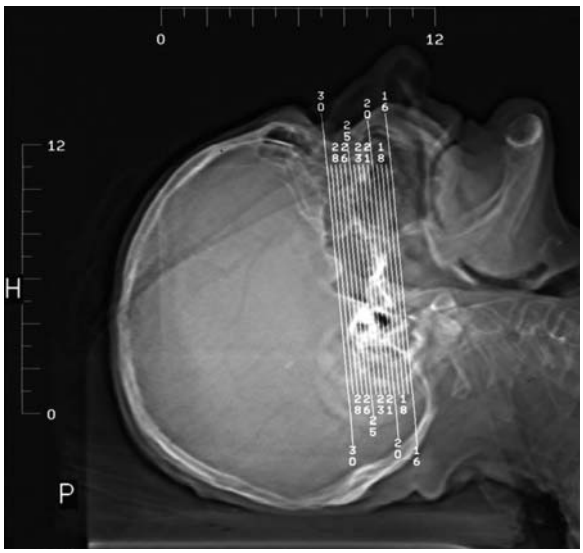

Fig. 1.7. Scout view of an axial imaging protocol, demonstrating the slice position parallel to the infraorbitomeatal line

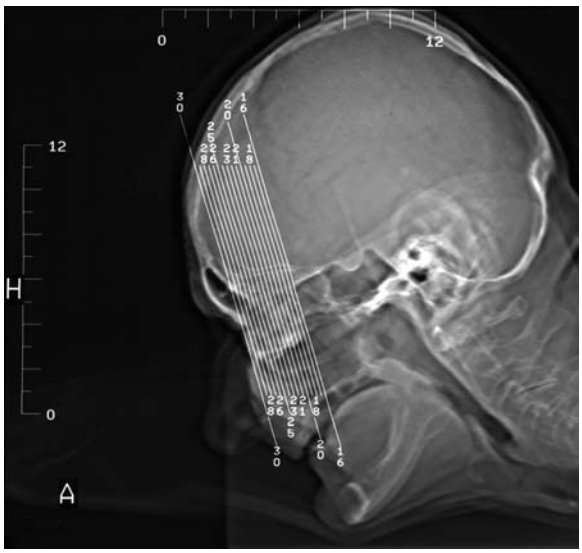

Fig. 1.8. Coronal scout view

should be used; in most cases, an additional coronal view is necessary. This should be planned perpendicular to the axis of the orbit or the skull base (Fig. 1.8). For questions demanding a high-resolution imaging of the optic canal, a small volume of 1 mm slices, parallel to a line from the posterior foramen magnum to the hard palatine proved to be useful. The window should be adapted to the specific orbital tissue, thus a width of 350–400 HU and a level of 80–100 HU is to be chosen. For the detection of bony changes, a so-called bone window with a window width of >1000 HU is mandatory.

1.3
Magnetic Resonance Imaging (MRI)

W. Wichmann

1.3.1
Basic Physical and Technical Principles of MRI

Magnetic resonance imaging (MRI) is a method to generate cross-sectional images from the interior of the body based on the physical phenomena of nuclear magnetic resonance without using ionizing radiation. Atomic nuclei such as those of ^{1}H, ^{13}C, ^{14}Na, ^{19}F, ^{23}N, and ^{31}P with an odd number of protons and/or neutrons have a magnetic dipole moment. Hydrogen nuclei are abundant in biological tissue, as in the hydrogen atoms of water molecules. This is the reason for the use of hydrogen nuclei in medical MRI. Without the influence of an external magnetic field, the directions of the innumerable single dipoles are randomly arranged such that they cancel each other out, resulting in no macroscopic magnetic dipole moment. However, in the presence of an external static magnetic field, the small nuclear magnetic dipoles tend to align in the direction of the field, like a compass needle to the magnetic field of the earth. The nuclear magnetic dipoles are not aligned statically, rather they are staggering around the direction of the external static magnetic field. This phenomenon can be compared with the tumbling of a top around the direction of the gravitational force. This movement is called precession. The number of revolutions of this precession, designated Larmor frequency, depends on the magnetic moment of the nucleus and the strength of the external magnetic field applied. In case of a 1.5-T MRI scanner, the Larmor frequency of the hydrogen nuclei is 63.87 MHz. This characteristic allows the transfer of energy from an external radiofrequency pulse to the nuclei provided that the frequency is precisely the same. This means that there is a resonance between the transmitter and the macroscopic oscillating magnetic moment, which acts as the receiver. During energy absorption, the precessing nuclear spin axes circumscribe a cone that becomes increasingly flat. This can be illustrated as an exciting nucleus that opens its umbrella. The Brownian motion of molecules leads to a continuous rearrangement of the dipoles, such that statistically only one per million (5 ppm: parts per million) of the hydrogen nuclei are aligned with the direction of an external 1.5-T field at room temperature. After the termination of the applied radiofrequency pulse, the macroscopic magnetic field returns to its prior state by emitting simultaneously decreasing electromagnetic waves with the precessional frequency. These waves emitted during the relaxation are measurable and represent values which are attributed to the brightness of the individual pixels (picture elements) of which the images are composed by the application of sophisticated mathematical reconstruction algorithms.

1.3.1.1
Relaxation, Special Sequences

There are two types of relaxation. One is the signal decay of the sum vector parallel to the strong external magnetic field, which is termed the longitudinal relaxation or the T1 relaxation. During the T1 relaxation (spin-lattice relaxation), the excess energy is transferred from the nuclei to the environment (the term lattice is derived from crystalline solids and is used here in a broader meaning). The other relaxation is the signal decay of the sum signal vector perpendicular to the strong magnetic field and is designated the transverse or T2 relaxation. In T2 relaxation, there is a dispersion of the primarily synchronized precessional rotation of the spins. One can imagine the spins as an ensemble of ballet dancers, who initially obey the instructions of the maestro and start all in the same position (they are in phase). After this moment, they show a lack of discipline, and each ballet dancer turns a little faster or slower than the others (loss of coherence), resulting in a random distribution of the positions (out of phase). If we return to the spinning direction, at the beginning of this process we can record the net sum vector of all synchronized (in phase) individual spins, with a rapid decay as they go off phase. The loss of coherence is caused by minute local magnetic inhomogeneities around the macromolecules. As

the adjacent spins also exchange excitation energy with each other, T2 relaxation is termed spin-spin relaxation. Signals registered from the biological tissue depend on the water or proton concentration that can be excited and on the relaxation characteristics. Pure or so-called free water would show a high concentration of excitable protons and a slow relaxation caused by only slightly restricted tumbling of small molecules. On the other hand, protons bound to macromolecules would show a fast relaxation by dissipating their energy to the environment and a loss of coherence. The MRI characteristics of tissue are defined by the composition of these components, represented in this paper in a simplified manner. Manipulation of the MRI examination parameters enables us to enhance the differences between the local tissues, resulting in a better inherent contrast. The terms T1-weighted (T1w), proton density-weighted (PDw) or T2-weighted (T2w) characterize MRI sequences or images and define the more pronounced biophysical effect of the specific image information. Proton density (PD)-weighted images are similar to T2-weighted images, but have a shorter echo of 10–50 ms and are less dependent on the relation than on the concentration of protons, i.e., water concentration in the tissue (Bösiger 1985). The fluid-attenuated inversion recovery (FLAIR) sequence combines T2-weighting and suppression of the so-called free, not tissue-bound water.

After intravenous administration of a MRI-specific contrast medium, such as gadopentate dimeglumine (biologically inert as complexly bounded gadolinium, i.e., GD-DTPA® or GD-DOTA®), a different take-up by tissues is seen, analogous to the iodized contrast medium used in CT. The use of contrast medium (in T1-weighted sequences) can further improve the contrast between anatomical details and also between normal and pathological tissues because of its different signal enhancement. If these contrast-enhancing structures are embedded in primarily hyperintense tissue (such as the extraocular muscles, or potential lesions within the retro-orbital fat) the signals will interfere, resulting in a loss of tissue contrast between the anatomical components. This problem can be solved using a pulse sequence that suppresses the high signal of the native hyperintense tissue. In the case of fat, the sequence is designed to be fat-suppressed (FS). Special MRI protocols enable a differentiation of flowing blood from nonmoving tissue (so-called stationary tissue), the basis for MR angiography. In MR angiography, the signal of stationary tissue is suppressed and the signal of flowing blood is enhanced, without any application of contrast material.

The so-called diffusion-weighted MRI (DWI) is able to image molecular diffusion. Tissue-bound water has a restricted molecular diffusion compared with free water, due to frequent collisions with macromolecules, in particular proteins. Therefore, tissues with a different viscosity and a different ratio of intra- and extracellular spaces show different diffusion properties. For this reason, diffusion-weighted MRI discriminates reliably an arachnoid cyst filled with free water and an epidermoid tumor of solid tissue (Fig. 6.129c, 7.66), whereas in conventional sequences, liquor and epidermoid tumor can both give the same signal intensity (Laing et al. 1999; Gizewski 2001). The so-called anisotropic diffusion of water molecules in the fiber pathways, which is much more restricted across the fibers than along them, can also be imaged in different planes (Hajnal et al. 1991). Diffusion-weighted MRI can disclose an acute infarction at a very early stage, and in the case of elderly patients with multiple chronic infarctions, it helps to uncover additional new lesions (Schaefer 2001). It also seems that diffusion-weighted sequences image a cystic tumor different to the central colliquation of an abscess, so offering an additional tool in the differential diagnosis (Kim et al. 1998).

Along with a strong and very homogeneous main magnetic field and all devices (antennas or coils) to excite the protons by a radiofrequency pulse and to receive the electromagnetic waves emitted from them, there is a need for a space-encoding system. Temporary, superimposed, magnetic gradient fields cause changes of the Larmor frequency and the phase of spin populations in small volumes (voxels), with a precise local attribution. Where the magnetic field is stronger, the precessional frequency is higher, and where the magnetic field is weaker, the frequency is lower. It is possible to identify the location of signal-generating spin pools by small space-encoded differences of the frequencies, like distinguishing radio stations. Additional space-encoded different phases of precessing spin pools are used.

For more superficially located structures, such as the orbits, the image resolution can be optimized by using phased-array surface coils instead of the conventional head coil. Surface coils are specially designed antennas, which can be applied near the region of interest and fades out disturbing signals from the environment. In case of an examination of the orbit, they are placed obliquely over both orbits, in order to lighten the orbital apex. It should be

emphasized that a relatively small unilateral surface coil (with a diameter of about 4 cm) applied anteriorly over one orbit is only suitable for imaging the ipsilateral globe and does not provide a more posterior "illumination".

1.3.1.2 Restrictions

1.3.1.2.1 Ferromagnetic Material, Pacemaker, Neurostimulator, Ventricular Shunts with magnetically adjustable valves

When approaching the temperature of absolute zero, no electrical resistance as e.g., in the coil of the electric magnet is found. For this reason, the most frequently used modern high-field MRI scanners (0.5–1.5 T) today are based on a superconducting coil of the main magnet, a system with a liquid helium-cooled main coil.

This strong main magnetic field necessitates a few precautions. Patients with ferromagnetic implants, e.g., older aneurysm or other vessel clips, pacemakers, neurostimulators, and traumatically incorporated metallic-ferromagnetic foreign bodies (e.g. debris arising from working with metal, or old shell splinters), should not be exposed to high-field MRI. In addition to the image quality disturbance caused by the so-called susceptibility artifacts of the ferromagnetic material (Lüdeke et al. 1985) (Fig. 1.9), this can endanger the patient (Kanal and Shellock 1993). Whereas metal devices fixed on bone do not present a danger if exposed to MR, ferromagnetic foreign bodies, or clips in the lung, abdomen, eye, and adjacent to vessels can twist due to the strong main magnetic field and lead to a life-threatening complication. Ventricular shunts with transcutaneous magnetically pressure-adjustable valves (MEDOS and SOPHY valves) can be maladjusted in MRI, and therefore the systems have to be checked radiologically after MRI (Miwa et al. 2001; Ortler et al. 1997). As new magnet-compatible devices (Wichmann et al. 1997) have only been developed in the last decade, MRI is still unavailable to most patients with an implanted pacemaker or neurostimulator. The problems are not only caused because of the fact that these devices are usually magnetically programmable, there is an additional risk from the electrodes, which can act as antennas and interact with the changing electromagnetic fields. One must be always absolutely certain about the individual patient's magnet compatibility, probably with the result of a rejection of the patient for MRI if there remains any doubt.

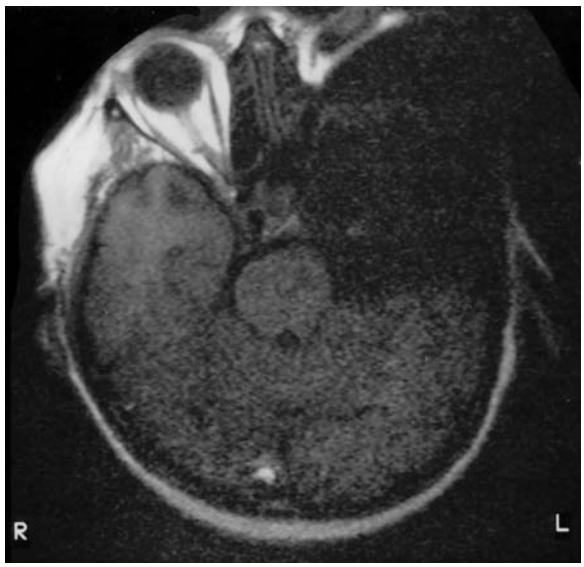

Fig. 1.9. Axial localizer of MRI, demonstrating the deformed loss of signal at the left orbit, caused by a fixed shell splinter in the left maxillary bone

1.3.1.2.2 Claustrophobia, Sedation, Surveillance

To perform a MRI examination, it is necessary to bring the entire patient into the narrow shaft of the equipment, as the optimal homogeneity of the magnetic field is in the center of the magnet. Even for an examination of only the head or the orbit, the patient has to be placed deep inside the MRI. This is mainly a problem for claustrophobic patients, and thus they need sedation before the MRI examination. However, a sedated patient placed in this narrow tunnel is not accessible. In case of deep sedation, special magnet-compatible monitoring devices are needed for surveillance, including at least essential peripheral pulse oximetry. In MRI, the acquired data are not separately sampled sections, as for CT, but the data sampling is simultaneous for all sections of one sequence and the acquisition time depends on the examination parameters, e.g., the repetition time chosen. Therefore, one MRI sequence may last only a few minutes or even more than 10 min. If the patient moves during this time, a loss of image quality of all sections results. During MRI of the orbit, the patient should keep the eyes open and try to maintain a midline resting position. Consequently, in the case of uncooperative patients, who are not able to remain motionless, the quality of the images will be impaired.

1.3.2 General Considerations of MRI Imaging Protocols

As MRI is only able to image tissue with mobile protons (see chapter 1.3.1 Physical and technical principles), the trace of mobile protons within pure bone is not sufficient to generate a perceptible MR signal, resulting in a hypointense appearance of compact bone; in other words, it looks black on MR images. Air, surrounding the head and filling the paranasal sinuses, does not contain any protons, and thus also appears black. This is the reason that those interfaces between compact bone and air cannot be displayed on MR, although they are seen on CT. Not only in the cranial region is bone normally surrounded by MR signal-generating structures, it normally contains fatty marrow, well seen on MRI. For example, an indirect definition of the bony contours is made by the mucosa of a paranasal sinus. The domain of MRI is soft tissue; its MR contrast is superior to that of CT. This excellent natural intrinsic contrast of MR, differentiating bone, fat, muscles, nerves, glands, components of the globe, and the intracranial nervous tissue (Table 1.2), is not restricted by artifacts from surrounding bone. Another advantage of MRI is the capability of real multiplanar high resolution imaging without additional impairment of the patient. To optimize image resolution in orbital MRI, one should use phased-array surface coils (Breslau et al. 1995).

Although most diseases require the same examination protocol, every individual patient suffers from an individual disease, which explains why universally valid "recipes" may be right in one patient and inadequate in another. In general, two different planes (axial and coronal) at least should be done as a minimum; especially in the orbit, a third (or fourth, individually planned) may improve the examination result.

As a rule, in our institutions every MRI examination of the head includes a T2-weighted overview of the entire brain, whether the orbit or the pituitary is the target of interest, as, e.g., in optic nerve neuritis the main underlying disease may be multiple sclerosis. The different axis of orbital imaging can be planned directly according to the individual patient's anatomy, and thus the external landmarks, known from CT are not necessary. A T1-weighted axial sequence without contrast is essential for orbital MRI examination. The orbital T2-weighted scans should be combined with fat suppression. Alternatively, a

Table 1.2. Overview of signal intensities of specific orbital tissue and brain parenchyma in standard sequences

	T1-weighted	T1-weighted (fat suppressed)	PDw (proton density-weighted)	T2-weighted
Fat	↑↑	↓↓	↓	↗ to →
Globe (vitreous body)	↓	↓	→	↑
External rectus muscles	↓	↑↑(after contrast medium)	↗	↘
Bone (cortex)	0	0	0	0
Bone (marrow)	↑	↓	↑	↘
Gray matter	↓	↓	→	↗ to ↑
White matter	↗	↗	→	↓
CSF	↓	↓	→	↑ to ↑↑
Vessels	0	0	0	0

→ intermediate signal (gray)
↗ moderately hyperintense (light gray)
↑ hyperintense (bright, white)
↘ moderately hypointense (indifferent gray)
↓ hypointense (dark gray)
0 no signal (black)
(with permission of Müller-Forell and Lieb 1995)

short-tau inversion-recovery (STIR) sequence or a combined fat- and water-suppression sequence can be used to prevent the confusing signal elevation of normal fat caused by the so-called J-coupling effect (Henkelman et al. 1992) of the fast (turbo) spin-echo sequences. This undesirable high signal of fat in a T2-weighted sequence also covers discrete changes in the water content of the fat as, e.g., in the case of inflammation. The T1-weighted imaging after i.v. administration of gadolinium also has to be combined with a fat signal suppression to avoid the contrast canceling interference of contrast-enhanced structures and the naturally high signal of healthy fat. One possibility for examination of the orbit with MRI is to use a 3D volume acquisition scan and later post-scan processing, i.e., multiplanar and curved (along the optic nerves) reformations, and also an equalization of primary nonsymmetrical patient positioning. However, one should realize that sequences used for 3D acquisition mostly have disadvantages, such as reduced internal contrast (fast spin-echo with long echo train) or susceptibility artifacts (gradient-echo sequences).

So-called proton density-weighted sequences (PD), which have a short TE (echo time) and a long TR (time repetition), are more sensitive to internal structural alterations such as demyelinization or edema than T2-weighted images, especially in turbo spin-echo with a long echo train. The T2-weighted turbo, or fast spin-echo sequence, allows an early or first echo to be generated in addition to the late T2-weighted echo. This first echo is described as proton density weighted, but it is a mixture of most commonly the first four echoes of a longer echo train and, therefore, should be correctly designated as pseudo-echo. Despite disadvantages compared with a conventional proton density spin-echo, this is more sensitive to changes in myelinization or tissue hydration than the T2-weighted images. On the one hand, strong T2-weighted sequences are able to display the interfaces of nervous tissue to cerebrospinal fluid (CSF)-filled spaces with high resolution, but on the other hand, a T2-weighted sequence is not suitable for demonstrating small T2-hyperintense lesions bordering on these interfaces. This diagnostic restriction of T2-weighted images is caused by the fact that a hyperintense lesion would merge with the abutting, similarly hyperintense CSF-filled space and therefore can easily be overlooked. The fluid-attenuated inversion recovery (FLAIR) sequence resolves this problem by suppressing the signal of free water and in this way improving the detectability of hyperintense lesions bordering on CSF-filled spaces such as a ventricle or subarachnoid space. The classic example of this problem is to demonstrate small subependymally located plaques of multiple sclerosis. However, it should be mentioned that the FLAIR sequence does not produce as good spatial resolution as, e.g., a T2-weighted TSE sequence and is liable to produce artifacts (Bakshi et al. 2000).

One of the quality limiting factors in orbital MRI is the acquisition time. The longer this time, the higher the risk of image artifacts caused by eye movements. To image the optic nerves, the scan plane should be orientated along the infraorbitomeatal line (Tamraz 1994). This orientation offers the highest probability of displaying almost the entire optic nerve path in one of the cuts. There is no guarantee, however, because the nerves often follow a slightly undulating course, making an image in a noncurved plane impossible. The slice thickness is best chosen between 2 and 3.5 mm with a minimal interslice gap. Thinner slices usually have a too low signal-to-noise ratio, thus looking less definite. The coronal planes can be adjusted orthogonal to the infraorbitomeatal line, or orthogonal to each long axis of the orbits. In special cases, two different scans are needed for this latter purpose, one for each orbit. Additional sagittal scans precisely along the long axis of each orbit can be performed. One should be aware that in parallel MRI scans along the extension of the optic nerves, a small inaccuracy in the symmetry of the scan plane, relative to the course of the optic nerves, results in a large deviation on the MRI, complicating a correct assessment and comparison of both sides. On the other hand, a smaller inaccuracy, in fact slightly more orthogonally oriented to the course of the nerves, will not cause a strong distortion. For coronal scans, a thickness of about 3 mm is sufficient.

The extension of the chiasm, adjoining prechiasmal optic nerves, and optic tracts are best seen on scans parallel to the plane along the chiasm and the posterior commissure (Tamraz 1994). Of course, coronally oriented scans also need to be performed.

For the region of the optic pathway from the lateral geniculate nucleus to the visual cortex, the scans should be adjusted along the canthomeatal plane, and should be orientated in the coronal and if possibly also in the sagittal direction. For structures embedded in nervous tissue such as the lateral geniculate nucleus and the optic radiation, it is worthwhile trying a high-resolution T1-weighted inversion recovery (IR) sequence that offers an excellent contrast between gray and white matter but needs a longer acquisition time (see Figs. 2.44, 2.47, 2.48, 6.3, 6.9, 6.11, 6.83, 6.179, 7.63).

For suspected vascular lesions, the protocols described above should be supplemented with MR angiography (see Figs. 6.61, 6.62, 6.186, 6.197, 7.53).

In special cases, diffusion-weighted MRI helps to distinguish reliably between liquor-isointense epidermoid and arachnoid cyst (Laing et al. 1999; Gizewski 2001) (see Fig. 7.65). Diffusion-weighted MRI also indicates an acute infarction very early on, just a few hours after onset (Schaefer 2001) (see Figs. 3.27, 7.73, 7.77, 7.78). Diffusion-weighted MRI might be able to discriminate cystic tumor and abscess (Kim et al 1998).

References

Bakshi R, Caruthers SD, Janardhan V, Wasay M (2000) Intraventricular CSF pulsation artifact on fast fluid-attenuated inversion-recovery MR images: analysis of 100 consecutive normal studies. AJNR Am J Neuroradiol 21:503–508

Bösiger P (1985) Kernspin-Tomographie für medizinische Diagnostik. Teubner, Stuttgart

Breslau J, Dalley RW, Tsuruda JS, Hayes CE, Maravilla KR (1995) Phased-array surface coil MR of the orbits and optic nerves. AJNR Am J Neuroradiol 16:1247–1251

Giacomuzzi SM, Torbica P, Rieger M, Lottersberger C, Peer S, Peer R, Perkmann R, Buchberger W, Bale R, Mallouhi A, Jaschke W (2001) Untersuchungen zur Strahlenexposition bei der Einzelschicht- und Mehrschicht Spiral-CT (eine Phantom-Studie). Fortschr Röntgenstr 173:643–649

Gizewski ER (2001) Epidermoid oder Arachnoidalzyste: CISS, FLAIR und Diffusionsbilder als Ausweg aus dem diagnostischen Dilemma. Fortschr Röntgenstr 173:77–78

Hajnal JV, Doran M, Hall AS, Collins AG, Oatridge A, Pennock JM, Young IR, Bydder GM (1991) MR imaging of anisotropically restricted diffusion of water in the nervous system: technical, anatomic, and pathologic considerations. J Comput Assist Tomogr 15:1–18

Henkelman RM, Hardy PA, Bishop JE, Poon CS, Plewes DB (1992) Why fat is bright in RARE and fast spin-echo imaging. J Magn Reson Imaging 2:533–540

Hounsfield G (1973) Computerized transverse axial scanning (tomography), part 1. Description of the system. Br J Radiol 46:1016–1022

Hu H, He HD, Foley WD, Fox SH (2000) Four multidetector-row helical CT: image quality and volume coverage speed. Radiology 215:55–62

Kahaly G, Beyer J (1989) Notfälle bei Patenten mit endokrinen Erkrankungen und Stoffwechselstörungen: Thyreotoxische Krise. In: Schuster HP (ed) Notfallmedizin, vol 3. Urban and Schwarzenberg, Munich, pp 285–291

Kanal E, Shellock FG (1993) MR imaging of patients with intracranial aneurysm clips. Radiology 187:612–614

Katzberg RW (1997) Urography into the 21st century: new contrast media, renal handling, imaging characteristics, and nephrotoxicity. Radiology 204:297–312

Kim YJ, Chang KH, Song IC, Kim HD, Seong SO, Kim YH, Han MH (1998) Brain abscess and necrotic or cystic brain tumor: discrimination with signal intensity on diffusion-weighted MR imaging. AJR 171:1487–1490

Laing AD, Mitchell PJ, Wallace D (1999) Diffusion-weighted magnetic resonance imaging of intracranial epidermoid tumours. Aust Radiol 43:16–19

Lakits A, Prokesch R, Scholda Ch, Nowotny R, Kaider A, Bankier A (2000) Helical and conventional CT in the imaging of metallic foreign bodies in the orbit. Acta Ophthalmol Scand 78:79–83

Lüdeke KM, Roschmann P, Tischler R (1985) Susceptibility artefacts in NMR imaging. Magn Reson Imaging 3:329–343

Maclennan AC, Hadley DM (1995) Radiation dose to the lens from computed tomography scanning in a neuroradiology department. Br J Radiol 68:19–22

Miwa K, Kondo H, Sakai N (2001) Pressure changes observed in Codman-Medos programmable valves following magnetic exposure and filliping. Childs Nerv Syst 17:150–153

Müller-Forell W, Lieb W (1995) Neuroradiologie in der Ophthalmologie. Ophthalmologe 92:595–614

Ohnesorge B, Flohr T, Schaller S, Klingenbeck-Regn K, Becker C, Schöpf UJ, Brüning R, Reiser MF (1999) Technische Grundlagen und Anwendung der Mehrschicht-CT. Radiologe 11:923–931

Ortler M, Kostron H, Felber S (1997) Transcutaneous pressure-adjustable valves and magnetic resonance imaging: an ex vivo examination of the Codman-Medos programmable valve and the Sophy adjustable pressure valve. Neurosurgery 40:1050–1057

Parfrey PS, Griffiths SM, Barrett BJ, Paul MD, Genge M, Withers J, McManamon PJ (1989) Contrast material-induced renal failure in patients with diabetes mellitus, renal insufficiency, or both. A prospective controlled study. N Engl J Med 10:395–397

Rendl J, Saller B (2001) Schilddrüse und Röntgen-kontrastmittel. Pathophysiologie, Häufigkeit und Prophylaxe der jodinduzierten Hyperthyreose. Dt Ärztebl 98:B339–B343

Sage MR, Wilson AJ (1994) The blood-brain-barrier: an important concept in neuroimaging. AJNR Am J Neuroradiol 15:601–622

Schaefer PW (2001) Applications of DWI in clinical neurology. J Neurol Sci 186 [Suppl 1]:25–35

Schwab SJ, Hlatky MA, Pieper KS, Davidson CJ, Moris KG, Skelton TN, Bashore TM (1989) Contrast nephrotoxicity: a randomized controlled trial of a nonionic and an ionic radiographic contrast agent. N Engl J Med 320:149–153

Tamraz J (1994) Neuroradiologic investigation of the visual system using magnetic resonance imaging. J Clin Neurophysiol 11:500–518

Trommer G, Koesling S, Nerkelun S, Gosch D, Kloppel R (1997) Darstellbarkeit von Orbita-Fremdkörpern in der CT. Ist die Fremdkörperübersicht noch sinnvoll? Fortschr Röntgenstr 166:487–492

Uder M (1998) Nierenschädigung durch jodhaltige Röntgenkontrastmittel. Urologe 37:530–531

Wangemann BU, Jantzen JP, Dick W (1988) Anaesthesiologische Aspekte allergischer Reaktionen am Beispiel des „Kontrastmittelzwischenfalls". Anaesthesiol Intensivmed 29:205–214

Weetman AP, Wiersinga WM (1998) Current management of thyroid-associated ophthalmopathy. Results of an international study. Clin Endocrinol (Oxf) 49:21–28

Wichmann W, von Ammon K, Fink U, Weik T, Yasargil GM (1997) Aneurysm clips made of titanium: magnetic characteristics and artifacts in MR. AJNR Am J Neuroradiol 18:939–944

The requested page could not be found.

2 Anatomy

Werner Wichmann, Wibke S. Müller-Forell

CONTENTS

In this chapter, *Gray's Anatomy* (Williams 1995) serves as the basis for most of the anatomical descriptions made; if not, the references are given in full.

W. Wichmann, MD, PhD
Professor, Institute of Neuroradiology and Radiology, Klinik im Park AG, Seestrasse 220, 8027 Zürich, Switzerland
PD W. S. Müller-Forell, MD
Institute of Neuroradiology, Medical School, University of Mainz, Langenbeckstrasse 1, 55101 Mainz, Germany

2.1 Bony Orbit and Optic Canal

(Figs. 2.1c–2.6c, 2.9c–2.13c)

The orbits are bilateral bony cavities composed of multiple bones (frontal, temporal, zygomatic, lacrimal, sphenoidal, ethmoidal, maxillary, and palatinal bones) containing and protecting the eyeballs, extraocular muscles, lacrimal apparatus, fascial sheaths, nerves, ciliary ganglion, vessels, and the fat in which all is embedded. The orbits have a quasi-pyramidal shape with the base opening forward. As all walls converge to the apex, the medial walls are essentially parallel (Casper et al. 1993), although the long axes of the orbit diverge anterolaterally at an angle of about 45°. The orbits directly border on the paranasal sinuses, only separated by bony plates, and thus the osseous walls of the orbits are shared with the sinuses.

The floor of the orbit is also the roof of the maxillary sinus. This bony plate is notched by a small infraorbital groove, which runs from posterior to anterior, becoming a small canal, leading anteriorly to the infraorbital foramen and containing the infraorbital nerve (Figs. 2.12d, 6.167). This is the site where an inferior blow-out fracture can occur.

A very thin bony plate separates the orbit medially from the ethmoid air cells. This translucent paper-thin osseous plate (lamina papyracea) presents another weak point of the orbital walls. Not only can a medial blow-out fracture occur with resulting orbital emphysema, but the walls can be distorted and displaced medially by massively enlarged medial rectus muscles in Grave's disease (Casper et al. 1993).

The anterior roof of the orbit is the floor of the frontal sinus, while the posterior orbital roof forms a part of the floor of the anterior cranial fossa. Anterolaterally of the superior orbital wall is a shallow groove for the lacrimal gland. The lateral orbital wall is relatively thick, the posteromedial region of the lateral orbital wall directly abuts the middle cranial fossa, and the anterolateral region of the lat-

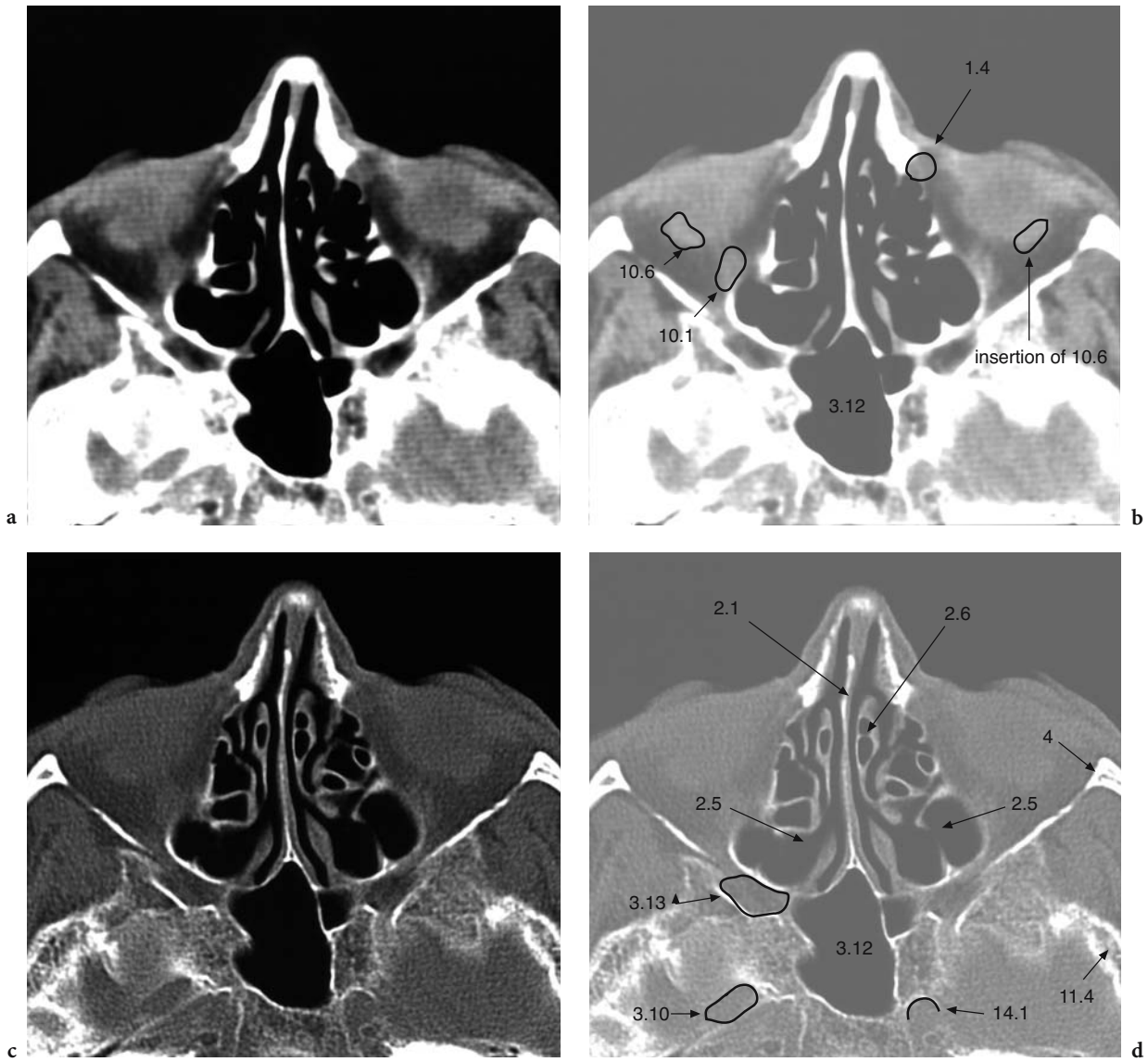

Fig. 2.1.a Axial CT of the inferior orbit. **b** Corresponding diagram: 1.4 = lacrimal sac/fossa, 3.12 = sphenoid sinus, 10.1 = inferior rectus muscle, 10.6 = insertion of inferior oblique muscle. **c** Corresponding bone window, **d** corresponding diagram: 2.1 = nasal septum, 2.5 = ethmoid sinus, 2.6 = middle turbinate (concha), 4 = zygomatic bone, 3.10 = oval foramen (foramen ovale), 3.12 = sphenoid sinus, 3.13 = pterygo-palatine fossa, 11.4 = temporal bone, 14.1 = carotid canal

eral wall adjoins the temporal fossa (Daniels et al. 1995).

The optic canal (or the optic foramen) in the posterior region of the superior orbital plate connects the superomedial corner of the orbital apex to the middle cranial fossa (Figs. 2.4c, 2.8c, 2.9c). The optic canal forms an angle of about 45° with the sagittal plane, carrying the optic nerve and the ophthalmic artery.

The gap between the posterior lateral and superior wall of the orbit is called the superior orbital fissure (Figs. 2.3b,d, 2.9b,d, 2.10b,d). This opening between the small and great wing of the sphenoid bone also communicates with the middle cranial fossa. The superior and the inferior ophthalmic veins, the oculomotor, trochlear, abducent nerves, branches of the ophthalmic division of the trigeminal nerve, and the carotid sympathetic plexus pass through the superior

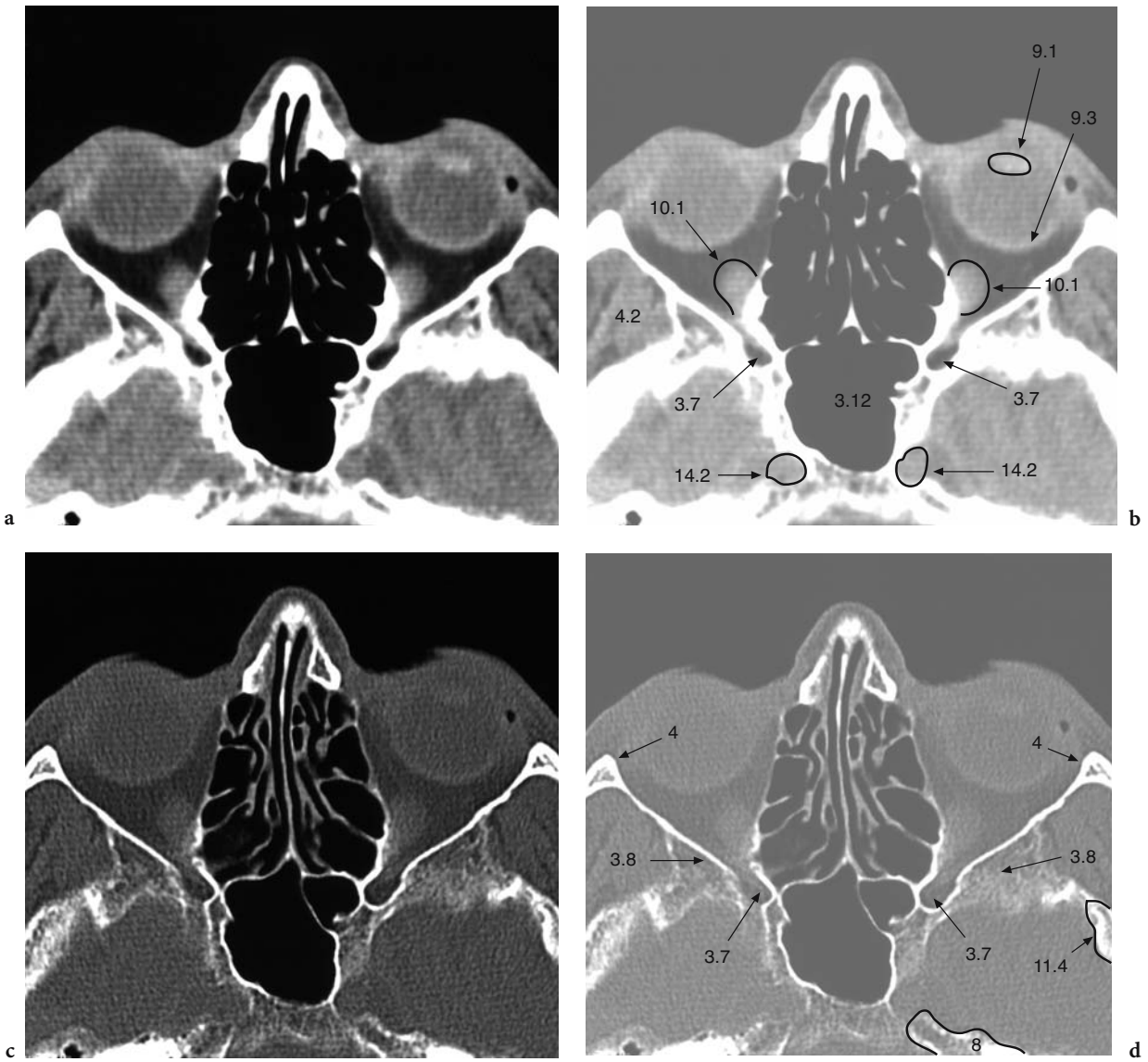

Fig. 2.2.a Axial CT at the inferior region of the orbit. **b** Corresponding diagram: 3.7 = inferior orbital fissure, 3.12 = sphenoid sinus, 4.2 = temporal fossa, 9.1 = lens, 9.3 = sclera, 10.1 = inferior rectus muscle, 14.2 = internal carotid artery (ICA). **c** Corresponding bone window. **d** Corresponding diagram: 3.7 = inferior orbital fissure, 3.8 = great wing of the sphenoid bone, 4 = zygomatic bone, 8 = petrous bone, 11.4 = temporal bone

orbital fissure. Posterior to the slightly widened inferomedial region of the superior orbital fissure lies the cavernous sinus. The superior orbital fissure is separated from the optic canal by a bony bridge, called the optic strut (Rhoton and Natori 1996; Daniels et al. 1995).

The inferior orbital fissure is located in the posterior orbital floor, posteromedially and inferiorly in communication with the pterygopalatine fossa, anterolaterally with the infratemporal fossa (Figs. 2.2.b,d, 2.8–2.10). Small venous connections from the inferior ophthalmic vein are transmitted through the inferior orbital fissure to the pterygoid plexus, but it also contains branches of the internal maxillary artery, the zygomatic and infraorbital nerves. A thin layer of smooth muscle borders the superior region of the inferior orbital fissure.

(Text continues on p. 38)

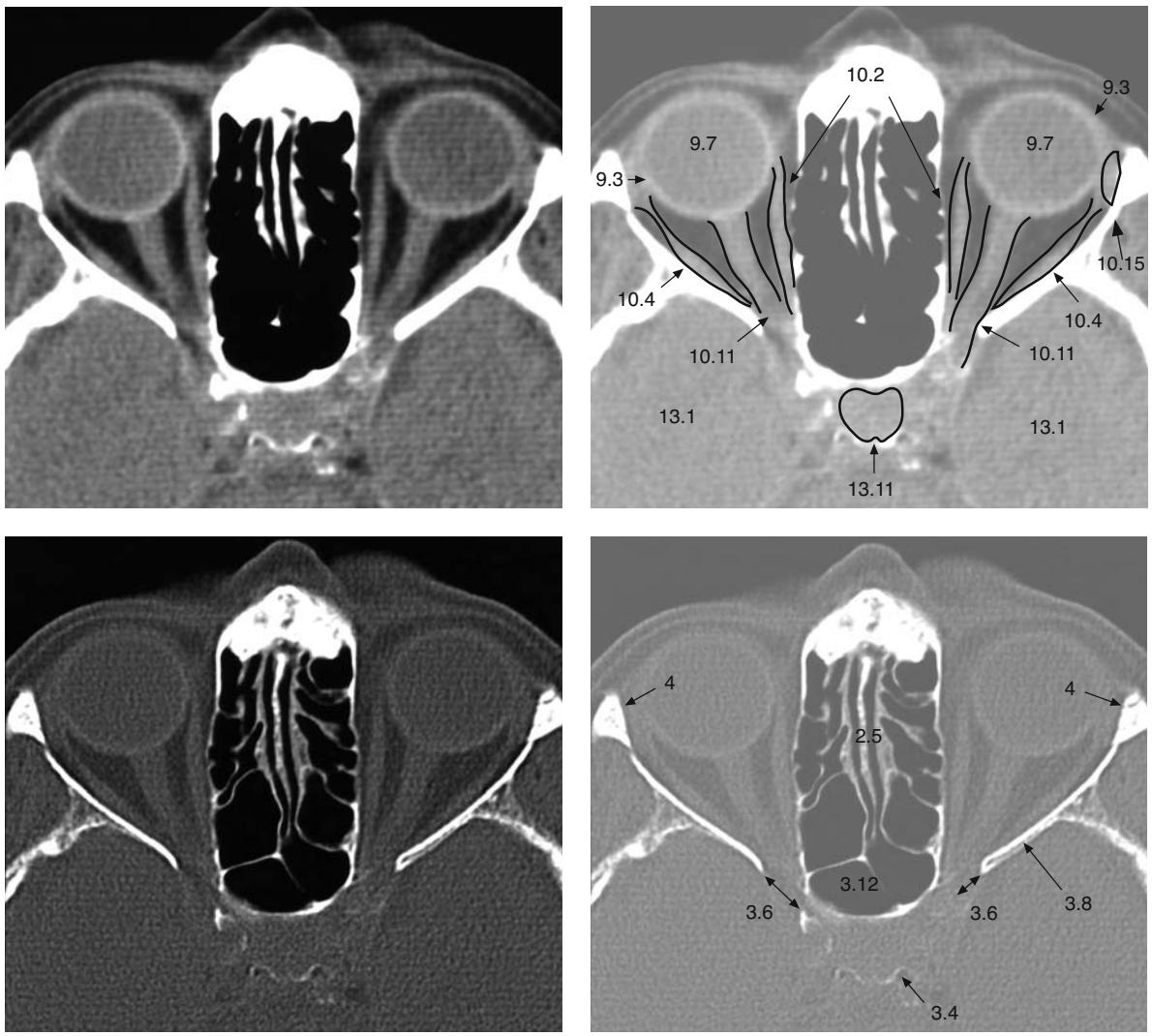

Fig. 2.3.a Axial midorbital CT. **b** Corresponding diagram: 9.3 = sclera, 9.7 = vitreous body, 10.2 = medial rectus muscle, 10.4 = lateral rectus muscle, 10.11 = optic nerve, 10.15 = lacrimal gland, 13.1 = temporal lobe, 13.11 = pituitary gland. **c** Corresponding bone window, **d** corresponding diagram: 3.4 =dorsum sellae, 3.6 = superior orbital fissure, 3.8 = great wing, 3.12 = sphenoid sinus, 4 = zygomatic bone

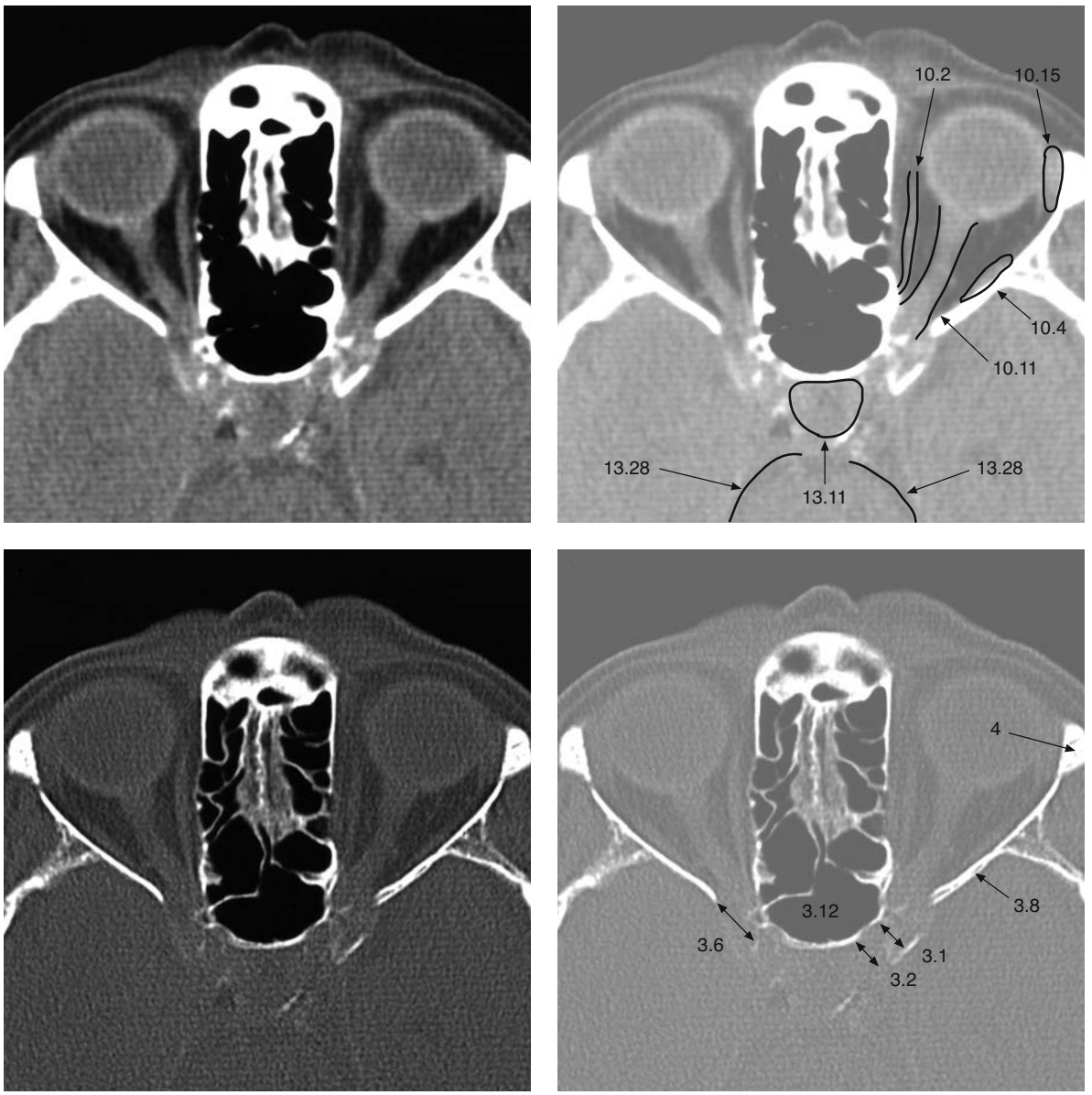

Fig. 2.4.a Axial CT at the level of the optic nerve. **b** Corresponding diagram: 10.2 = medial rectus muscle, 10.4 = lateral rectus muscle, 10.11 = optic nerve, 10.15 =lacrimal gland, 13.11 = pituitary gland, 13.28 = mesencephalic (ambient) cistern. **c** Corresponding bone window, **d** corresponding diagram: 3.1 = anterior clinoid process, 3.2 = optic canal, 3.6 = superior orbital fissure, 3.8 = great wing of the sphenoid bone, 3.12= sphenoid sinus, 4 = zygomatic bone

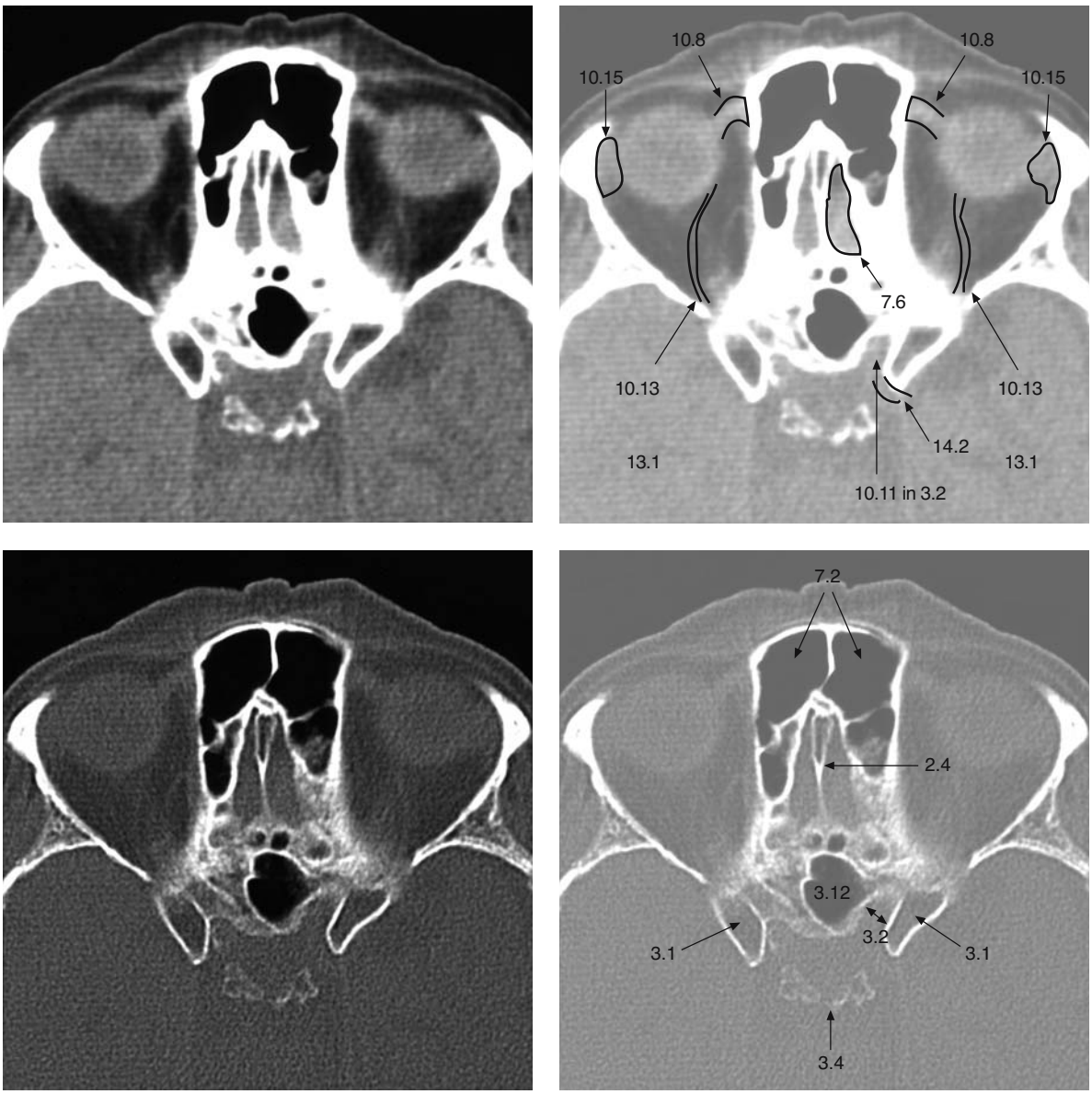

Fig. 2.5.a Axial CT of the superior region of the orbit. **b** Corresponding diagram: 7.6 = olfactory groove, 10.8 = trochlea, 10.11 = optic nerve (in 3.2 = optic canal), 10.13 = superior ophthalmic vein, 10.15 = lacrimal gland, 13.1 = temporal lobe, 14.2 = ICA (internal carotid artery). **c** Corresponding bone window. **d** Corresponding diagram: 2.4 = crista galli, 3.1 = anterior clinoid process, 3.2 = optic canal, 3.4 = dorsum sellae, 3.12 = sphenoid sinus, 7.2 = frontal sinus

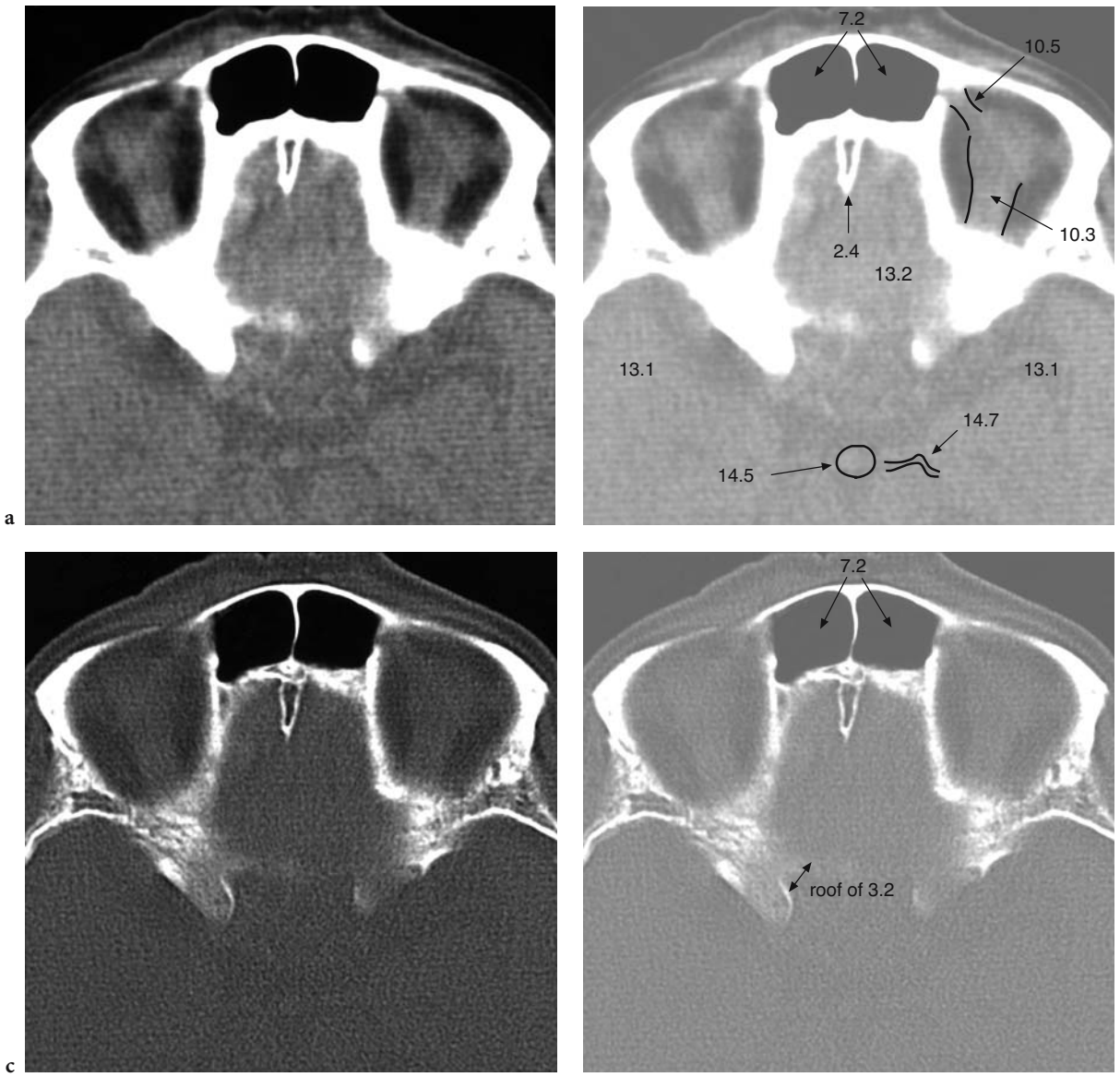

Fig. 2.6.a Axial CT of the superior orbit. **b** Corresponding diagram: 2.4 = crista galli, 7.2 = frontal sinus, 10.3 = superior rectus muscle, 10.5 = superior oblique muscle, 13.1 = temporal lobe, 13.2 = frontal lobe (gyrus rectus), 14.5 = (top of the) basilar artery, 14.7 = (p1 segment of the) posterior cerebral artery (PCA). **c** Corresponding bone window. **d** Corresponding diagram: 3.2 = optic canal, 7.2 = frontal sinus

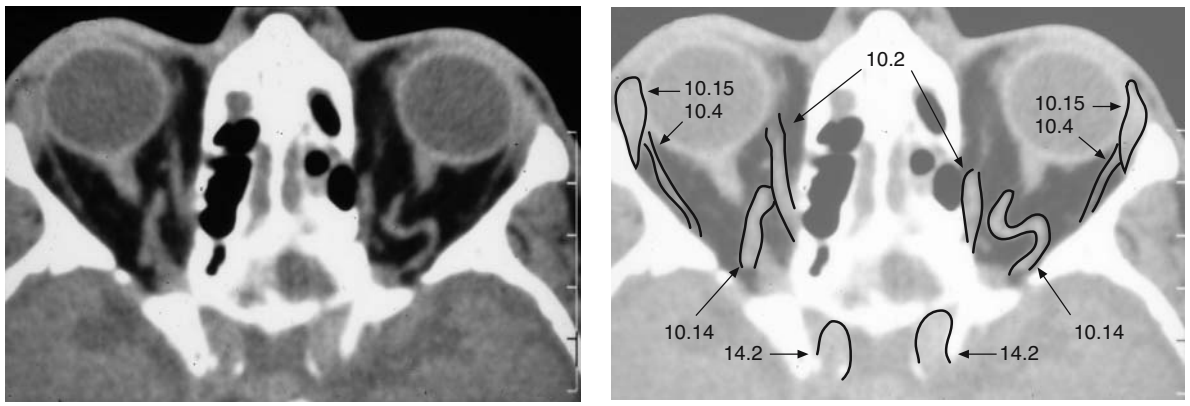

Fig. 2.7.a Axial CT of the infraoptic region. **b** Corresponding diagram: 10.2 = medial rectus muscle,10.4 = lateral rectus muscle, 10.14 = ophthalmic artery, 10.15 = lacrimal gland, 14.2 = ICA

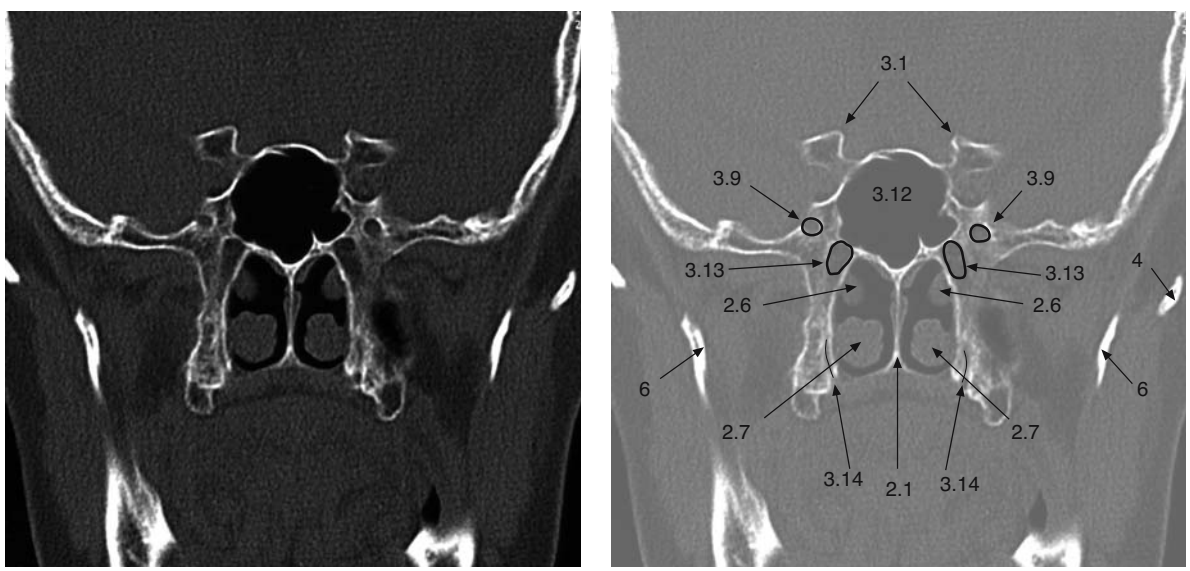

Fig. 2.8.a Coronal CT (bone window) at the dorsal opening of the optic canal. **b** Corresponding diagram: 2.1 = nasal septum, 2.6 = middle turbinate, 2.7 = inferior turbinate, 3.1 = anterior clinoid process, 3.9 = round foramen, 3.12 = sphenoid sinus, 3.13 = pterygopalatine fossa, 3.14 = pterygopalatine canal, 4 = zygomatic bone, 6 = mandibular bone

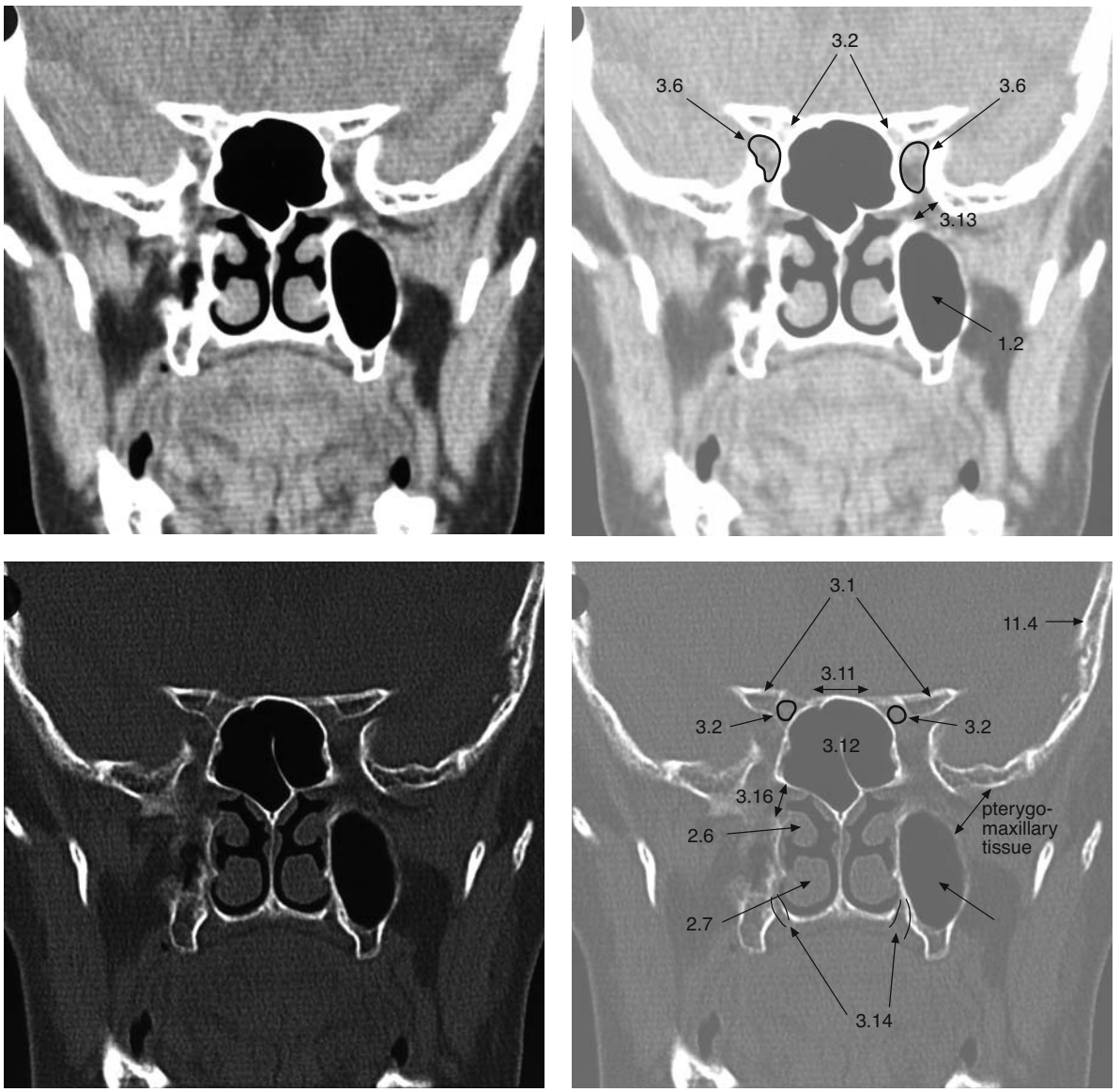

Fig. 2.9.a Coronal CT at the level of the optic canal. **b** Corresponding diagram: 1.2 = maxillary sinus, 3.2 = optic canal with optic nerve, 3.6 = superior orbital fissure, 3.13 = pterygopalatine fossa. **c** Corresponding bone window. **d** Corresponding diagram: 1.2 = maxillary sinus, 2.6 = middle turbinate, 2.7 = inferior turbinate, 3.1 = anterior clinoid process, 3.2 = optic canal, 3.11 = sphenoid plane, 3.12 = sphenoid sinus, 3.14 = pterigopalatine canal, 3.16 = sphenopalatine foramen, 11.4 = temporal bone

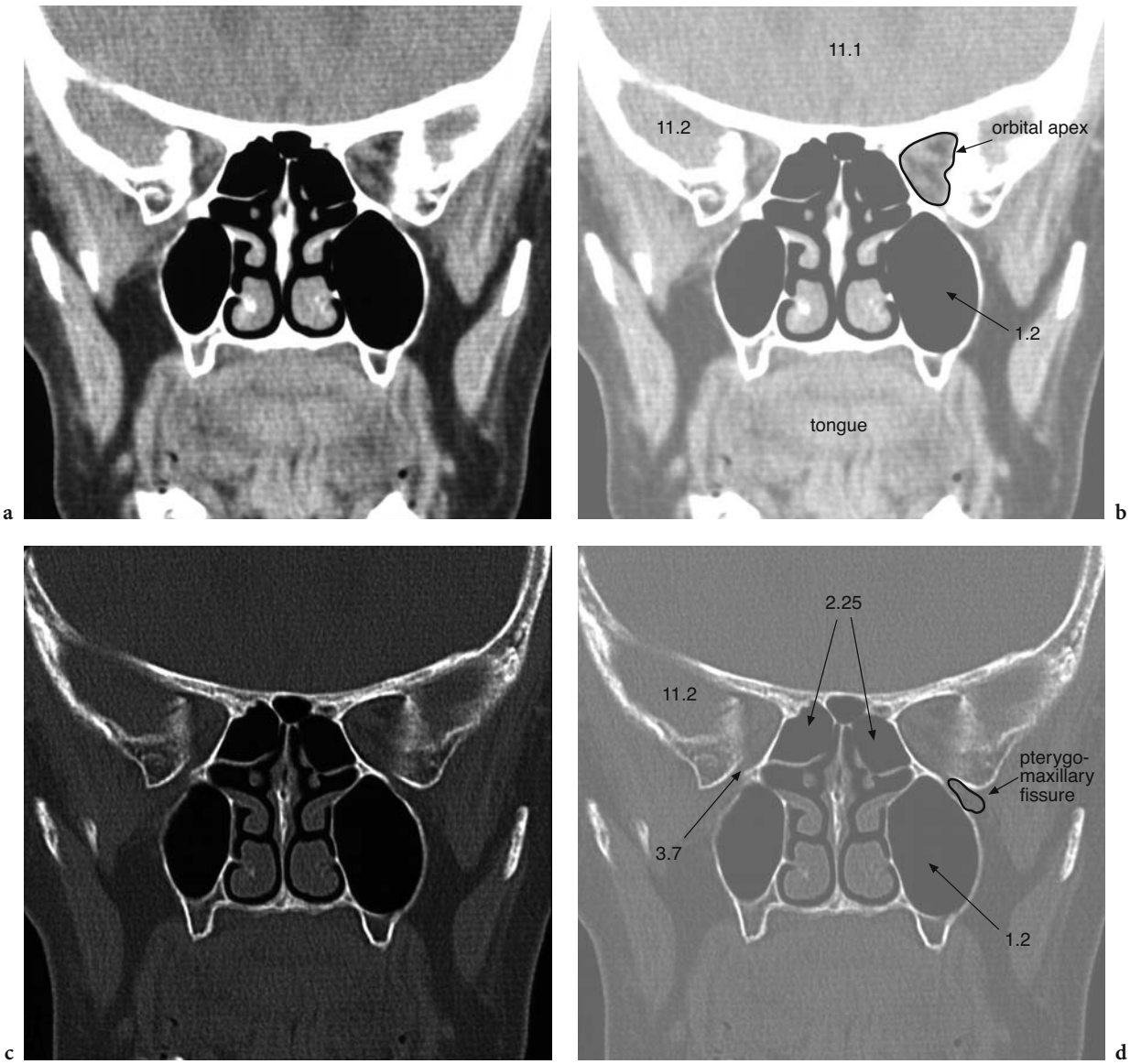

Fig. 2.10.a Coronal CT at the orbital apex. **b** Corresponding diagram: 1.2 = maxillary sinus, 11.1 = anterior cranial fossa, 11.2 = middle cranial fossa. **c** Corresponding bone window. **d** Corresponding diagram: 1.2 = maxillary sinus, 2.5 = ethmoid sinus, 3.7 = inferior orbital fissure, 11.2 = temporal lobe

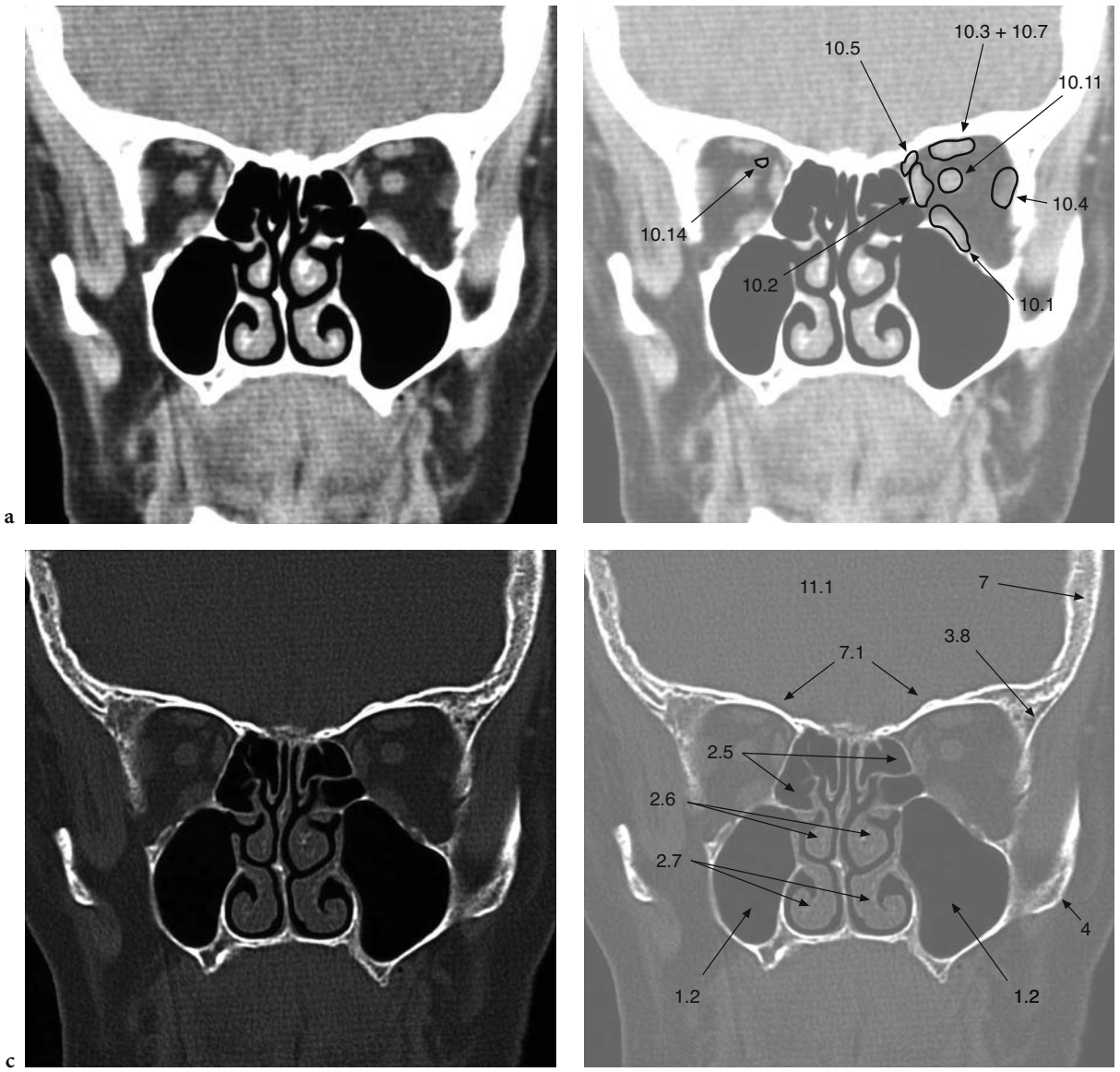

Fig. 2.11.a Coronal CT at the midorbital region. **b** Corresponding diagram: 10.1 = inferior rectus muscle, 10.2 = medial rectus muscle, 10.3 = superior rectus muscle, 10.4 = lateral rectus muscle, 10.5 = superior oblique muscle, 10.7 = levator palpebrae muscle, 10.11 = optic nerve, 10.14 = ophthalmic artery. **c** Corresponding bone window. **d** Corresponding diagram: 1.2 = maxillary sinus, 2.5 = ethmoid sinus, 2.6 = middle turbinate, 2.7 = inferior turbinate, 3.8 = great wing of the sphenoid sinus, 4 = zygomatic bone, 7 = frontal bone, 7.1 = orbital roof, 11.1 = anterior cranial fossa

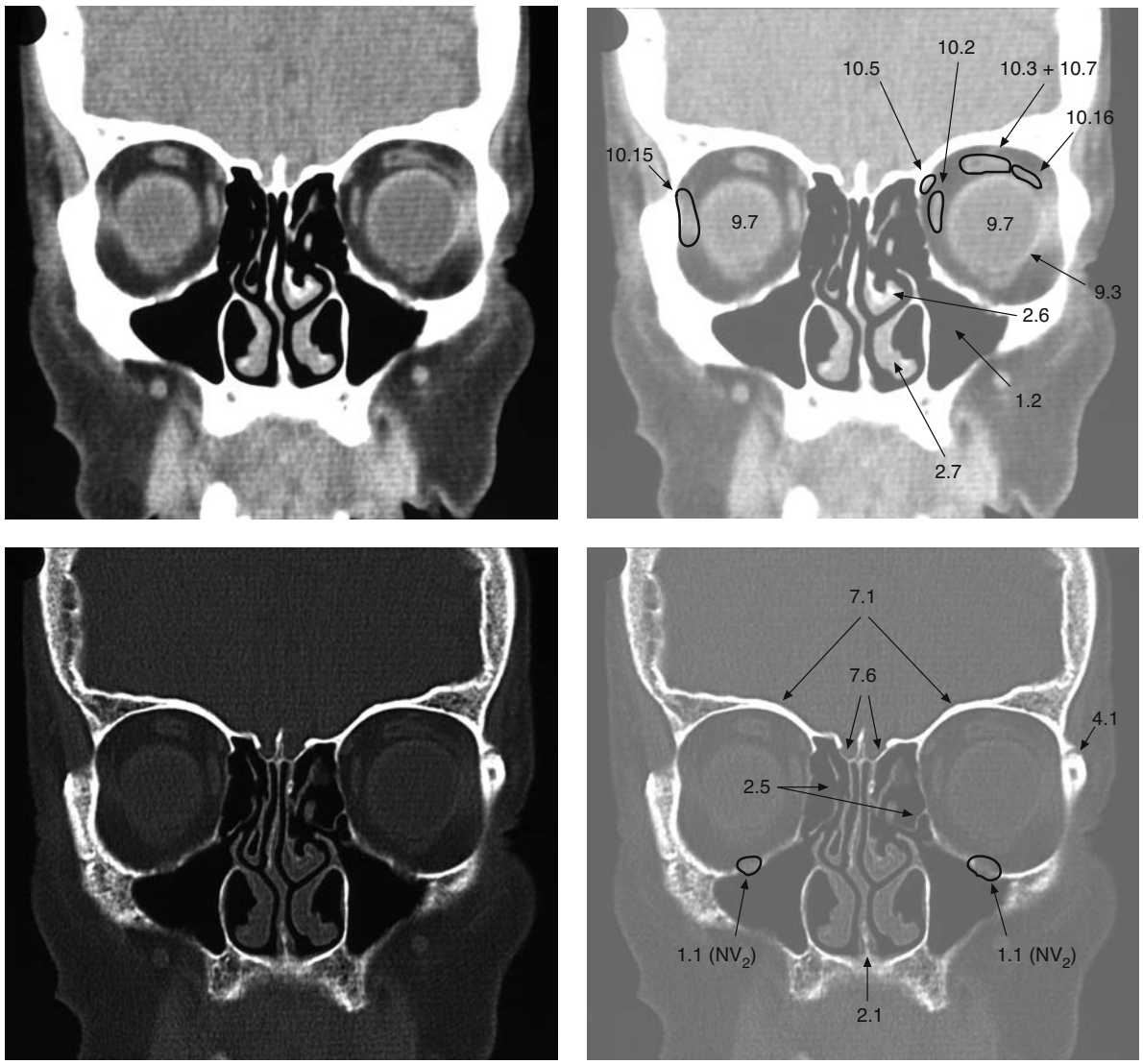

Fig. 2.12.a Coronal CT at the level of the posterior globe. **b** Corresponding diagram: 1.2 = maxillary sinus, 2.6 = middle turbinate, 2.7 = inferior turbinate, 9.3 = sclera, 9.7 = vitreous body, 10.2 = medial rectus muscle, 10.3 = superior rectus muscle, 10.5 = superior oblique muscle, 10.7 = levator palpebrae muscle, 10.15 = lacrimal gland, 10.16 = intermuscular septum. **c** Corresponding bone window. **d** Corresponding diagram: 1.1 = infraorbital foramen (NV_2), 2.1 = nasal septum, 2.5 = ethmoid sinus, 4.1 = fronto-zygomatic suture, 7.1 = orbital roof, 7.6 = olfactory groove

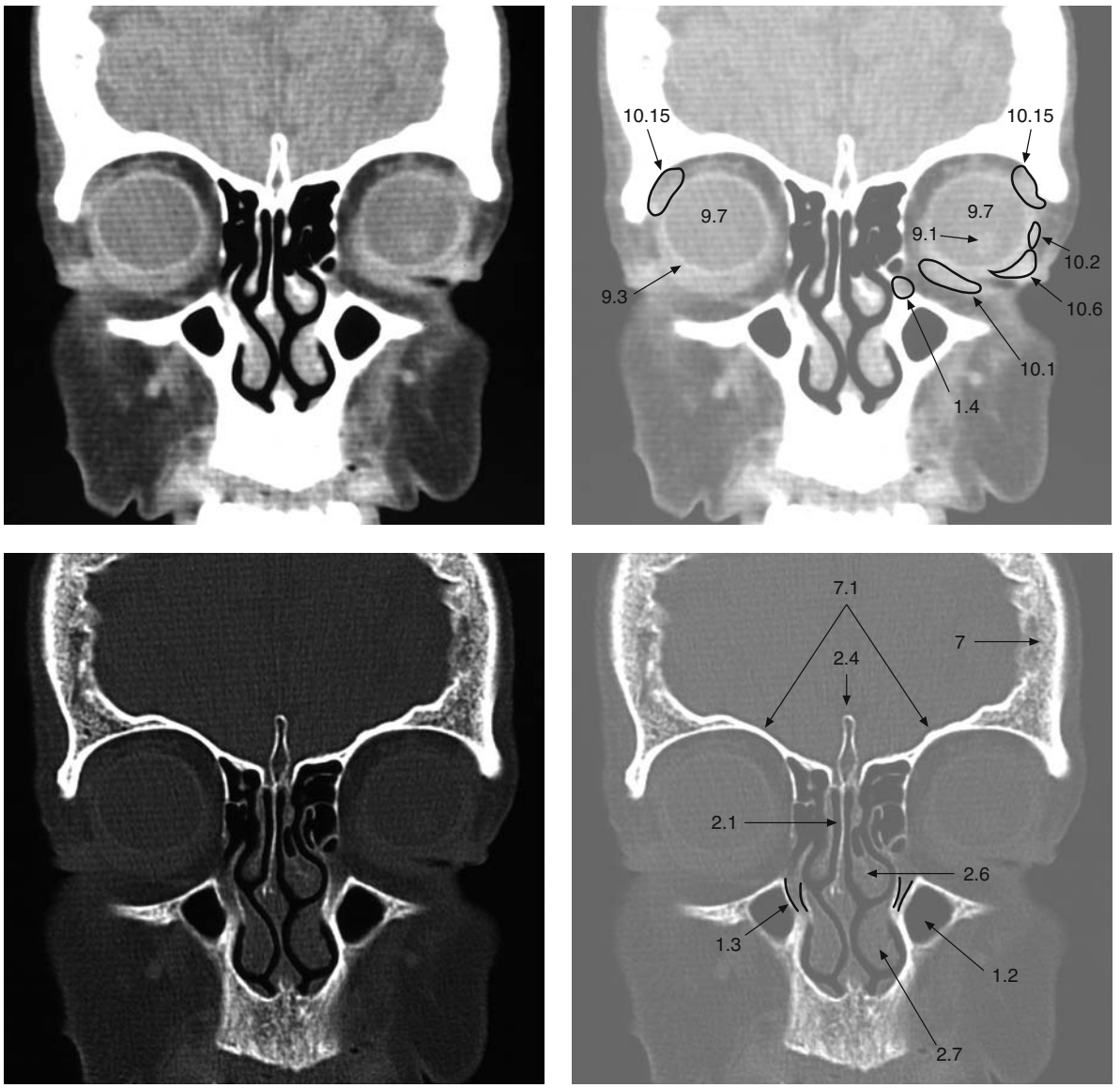

Fig. 2.13.a Coronal CT at the region anterior orbit. **b** Corresponding diagram: 1.4 = lacrimal sac/fossa, 9.1 = lens (partial volume), 9.3 = sclera, 9.7 = vitreous body, 10.1 = inferior rectus muscle, 10.2 = (tendon of the) medial rectus muscle, 10.6 = inferior oblique muscle, 10.15 = lacrimal gland. **c** Corresponding bone window. **d** Corresponding diagram: 1.2 = maxillary sinus, 1.3 = nasolacrimal duct, 2.4 = crista galli, 2.6 = middle turbinate, 2.7 = inferior turbinate, 7 = frontal bone, 7.1 = orbital roof

2.2 Optic Nerve Sheath and Fasciae

(Figs. 2.3, 2.4, 2.11, 2.17, 2.25–2.27)

The orbit is lined by a periosteal layer, the so-called periorbita, which is loosely adherent to the bone. Anteriorly, the periorbita blends with the periosteum of the orbital margin and to the orbital septum, while in the posterior region it fuses with the dural sheath of the optic nerve to form a unique sheet, the dura of the optic canal, which is tightly adherent to the bone. The orbital septum (Fig. 2.15b) is a thin fibrous membrane, becoming thicker laterally, with attachment to, although not exactly following, the orbital margin. The septum, directly in contact with the orbital fat and separating it from the lacrimal glands, borders the orbits anteriorly. The orbital septum separates the extra-orbital preseptal space from the postseptal orbital space. In this way, the orbital septum represents an important neuroradiological landmark which indicates whether a superficial lesion involves the orbit or not (Hoffmann et al. 1998).

The globe is enveloped by a thin membranous socket, termed Tenon's capsule, that separates it from the retro-orbital fat. Tenon's capsule is perforated posterolaterally, in order to allow the passage of the optic nerve, the ciliary vessels and nerves, as well as the tendons of the four recti muscles. The fibers of the capsule fuse with the optic sheath and the tubular muscular fasciae. Directly posterior to Tenon's capsule, the muscular sheath of the four recti muscles form a short fascial ring, called the intermuscular septum, best seen on coronal view (Figs. 2.27, 2.28). This ring encloses the anterior aspect of the so-called intraconal space, and the more posterior region of the intraconal space is defined incompletely by the four rectus muscles.

The subdivision of the orbital space into four compartments is a reliable, proven help in the differential diagnosis of the various space-occupying, vascular, inflammatory or infiltrative lesions that may involve the orbit. The four rectus muscles and their fasciae form an incomplete cone including the muscles themselves. Using this cone, the retro-orbital space can be subdivided into an intraconal and extraconal space; pathologic processes of the nasal and paranasal area, the temporal fossa, and the intracranial region may invade the latter because of the close neighborhood (Fig. 2.29) (chapters 2.4, 6.2, 6.3). To facilitate the differential diagnosis of retro-orbital lesions, the first step of image analysis should attribute the discovered lesion to one of these spaces. The other orbital compartments are the globe (chapters 2.3, 6.1) and the optic nerve (chapters 2.5, 6.4).

2.3 Globe

Although CT is able to differentiate the lens and its ciliary bodies from the fluid of the anterior chamber and of the vitreous, respectively, MRI is able to acquire high resolution images of the cornea, the fluid of the anterior and posterior chambers, the iris, the lens with the lens capsule, the vitreous body, and components of the uveal tract (Breslau et al. 1995). After i.v. administration of gadolinium, the vascular tunic (choroid, ciliary body, and iris) and in particular the macula are depicted as a strongly contrast-enhancing structure (Figs. 2.16, 2.17). The different histological composition of these tissues, especially their different water content, explains the biophysical characteristics responsible for the soft-tissue contrast on MRI. Although there is analogous contrast enhancement of the vascular tunic on CT after i.v. application of iodinate contrast medium, in contrast to MRI it cannot be differentiated exactly from the sclera.

(Text continues on p. 47)

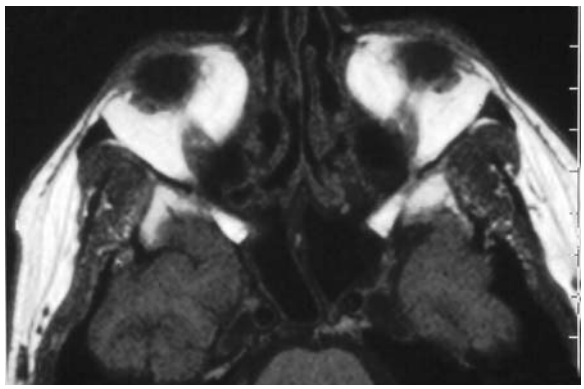

a

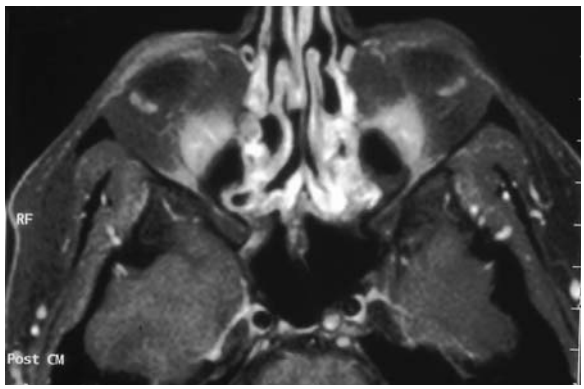

b

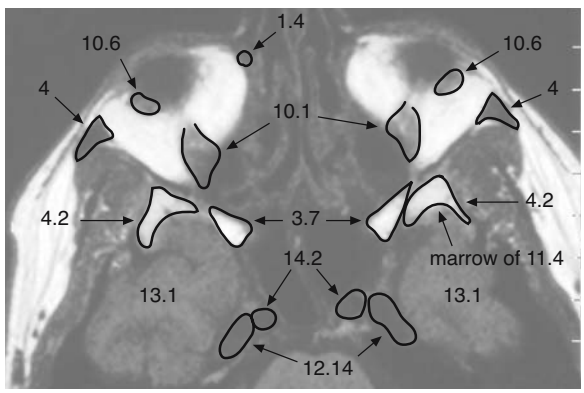

c

Fig. 2.14.a Axial T1-weighted native MRI at the inferior orbit. **b** Corresponding contrast-enhanced (FS) view. **c** Corresponding diagram: 1.4 = lacrimal sac/fossa, 3.7 = (fat in the) inferior orbital fissure, 4 = zygomatic bone, 4.2 = (muscles in the) temporal fossa, 10.1 = inferior rectus muscle, 10.6 = (tendon of the) inferior oblique muscle, 11.4 = (fatty marrow of the) temporal bone, 12.14 = trigeminal (Gasserian) ganglion, 13.1 = temporal lobe, 14.2 = ICA

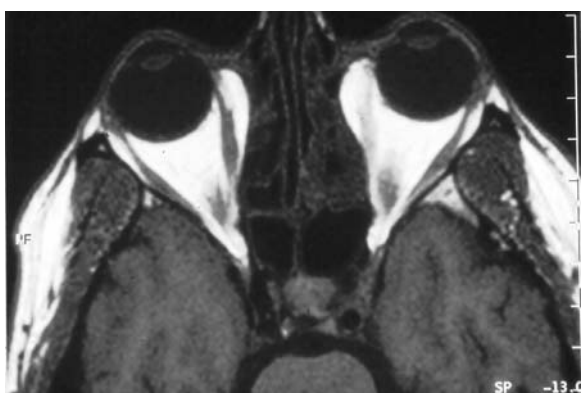

a

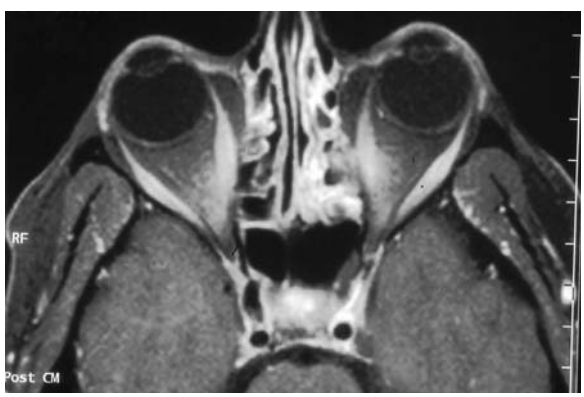

b

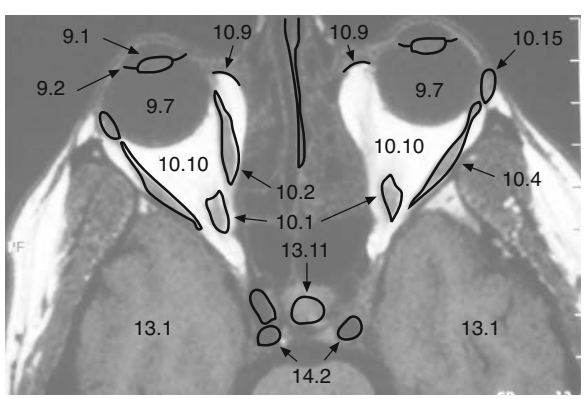

c

Fig. 2.15.a Axial T1-weighted native MRI at the inferior orbital region. **b** Corresponding contrast-enhanced (FS) view. **c** Corresponding diagram: 9.1 = lens, 9.2 = ciliary body, 9.7 = vitreous body, 10.1 = inferior rectus muscle, 10.2 = medial rectus muscle, 10.4 = lateral rectus muscle, 10.9 = orbital septum, 10.10 = orbital fat, 10.15 = lacrimal gland, 13.1 = temporal lobe, 13.11 = pituitary gland, 14.2 = ICA

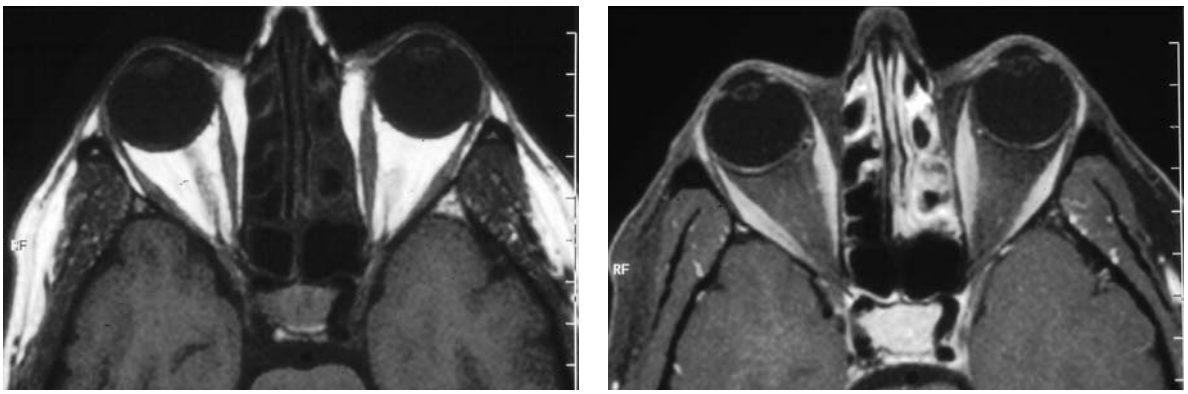

a b

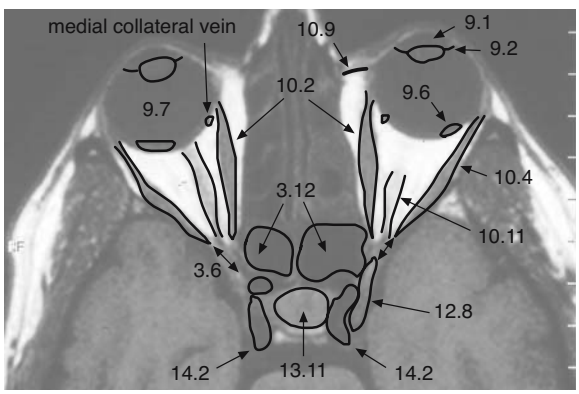

c

Fig. 2.16.a Axial T1-weighted native MRI at the midorbital region. **b** Corresponding contrast-enhanced (FS) view. **c** Corresponding diagram: 3.6 = superior orbital fissure, 3.12 = sphenoid sinus, 9.1 = lens, 9.2 = ciliary body, 9.6 = macula, 9.7 = vitreous body, 10.2 = medial rectus muscle, 10.4 = lateral rectus muscle, 10.9 = orbital septum, 10.11 = optic nerve, 12.8 = oculomotor nerve, 13.11 = pituitary gland, 14.2 = ICA

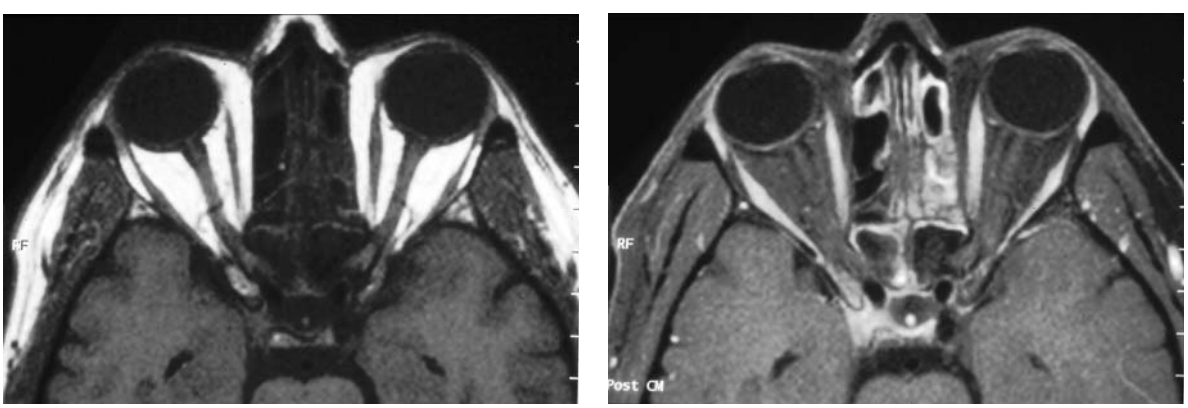

a b

Fig. 217. a Axial T1-weighted native MRI of the orbit at the level of the optic canal. **b** Corresponding contrast-enhanced (FS) view. **c** Corresponding diagram: 3.2 = optic canal, 3.4 = dorsum sellae, 3.12 = sphenoid sinus, 9.6 = macula, 9.7 = vitreous body, 10.2 = medial rectus muscle, 10.4 = lateral rectus muscle, 10.11 = optic nerve, 10.14 = ophthalmic artery, 10.15 = lacrimal gland, 13.1 = temporal lobe, 13.12 = pituitary stalk, 14.2 = ICA. **d** Corresponding proton density-weighted (PDw) (FS) view. **e** Corresponding T2-weighted (FS) view (note the mucous inflammation of both ethmoid sinuses, left>right)

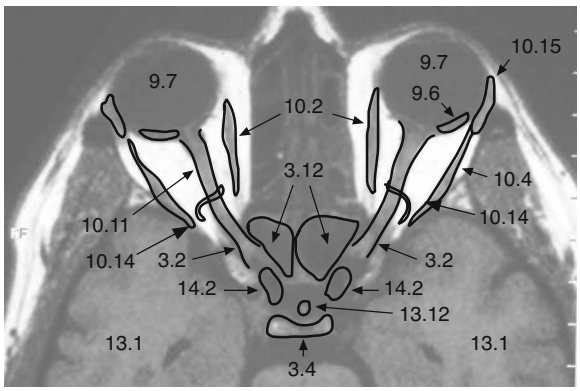

c

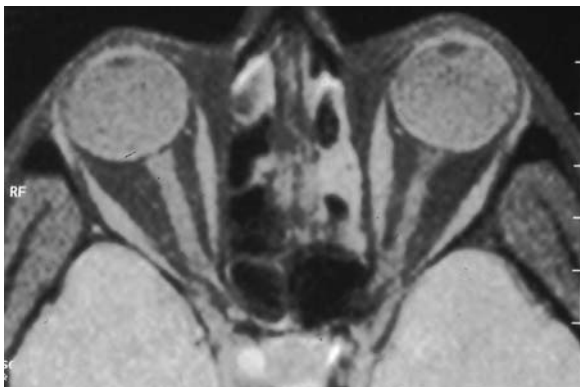

d

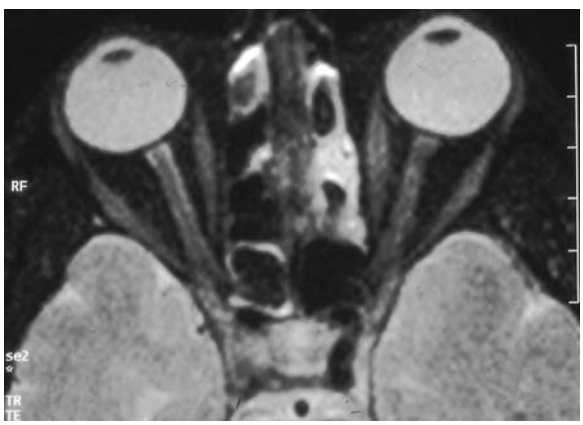

e

Fig. 2.17c–e

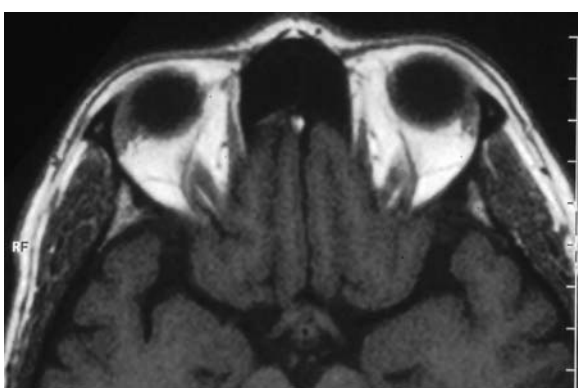

a

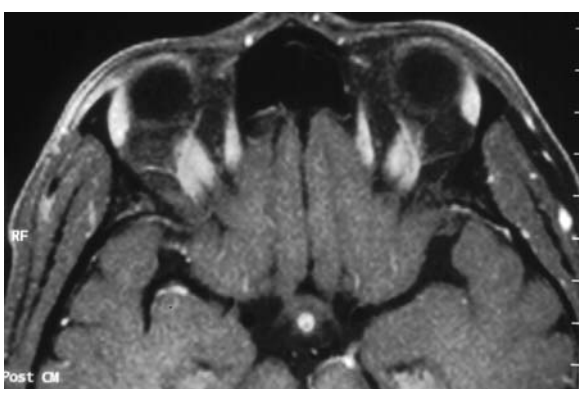

b

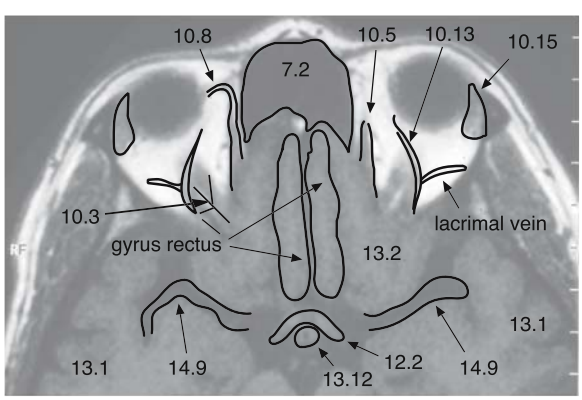

c

Fig. 2.18.a Axial T1-weighted native MRI of the superior orbital region. **b** Corresponding contrast-enhanced (FS) view. **c** Corresponding diagram: 7.2 = frontal sinus, 10.3 = superior rectus muscle, 10.5 = superior oblique muscle, 10.8 = trochlea of superior oblique muscle, 10.13 = superior ophthalmic vein, 10.15 = lacrimal gland, 12.2 = chiasm, 13.1 = temporal lobe, 13.2 = frontal lobe, 13.12 = pituitary stalk, 14.9 = middle cerebral artery (MCA)

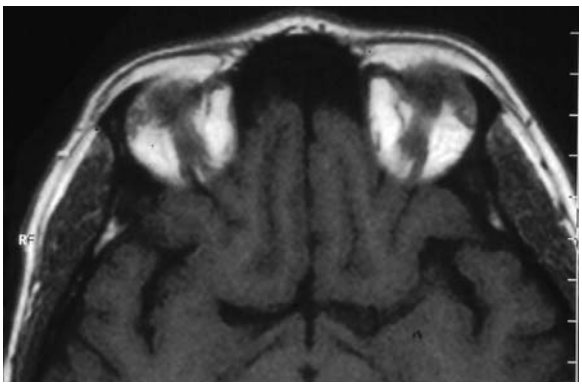

a

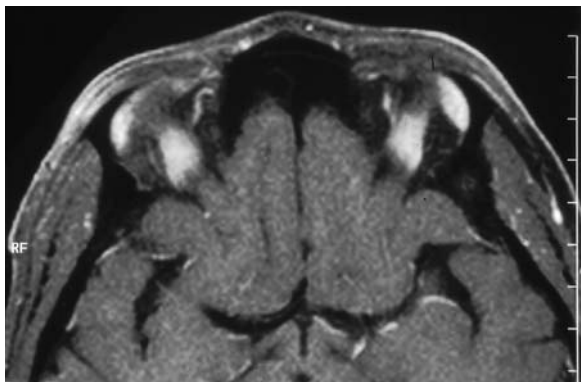

b

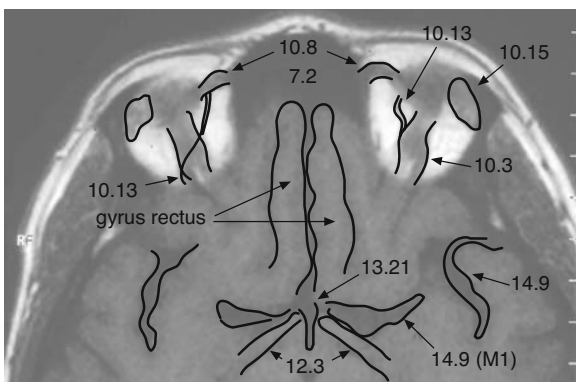

c

Fig. 2.19.a Axial T1-weighted native MRI of the region of the orbital roof. **b** Corresponding contrast-enhanced view. **c** Corresponding diagram: 7.2 = frontal sinus, 10.3 = superior rectus muscle, 10.8 = trochlea of the superior oblique muscle, 10.13 = superior ophthalmic vein, 10.15 = lacrimal gland, 12.3 = optic tract, 13.21 = third ventricle, 14.9 = MCA

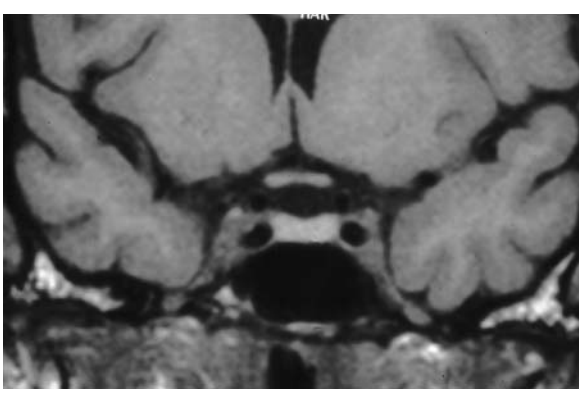

a

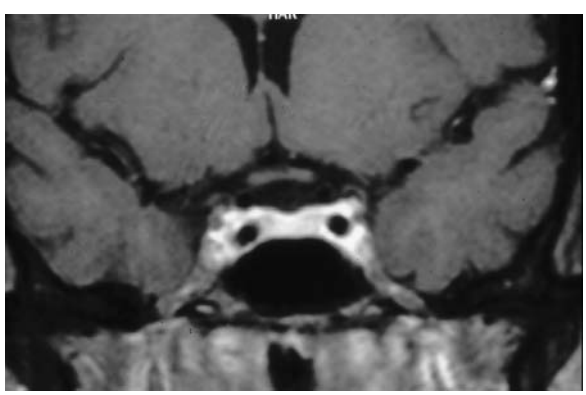

b

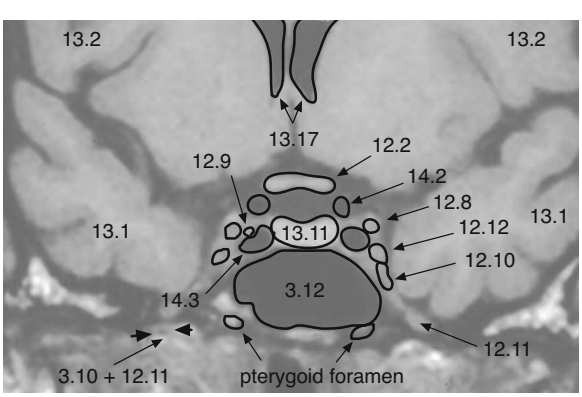

c

Fig. 2.20.a Coronal T1-weighted native MRI of the region of the cavernous sinus. **b** Corresponding contrast-enhanced view. **c** Corresponding diagram: 3.10 = oval foramen, 3.12 = sphenoid sinus, 12.2 = chiasm, 12.8 = oculomotor nerve (N III), 12.9 = abducent nerve (N VI), 12.10 = maxillary nerve (N V_2), 12.11 = mandibular nerve (N V3), 12.12 = ophthalmic nerve (N V_1), 13.1 = temporal lobe, 13.2 = frontal lobe, 13.11 = pituitary gland, 13.17 = ventricle, 14.2 = ICA, 14.3 = siphon of ICA

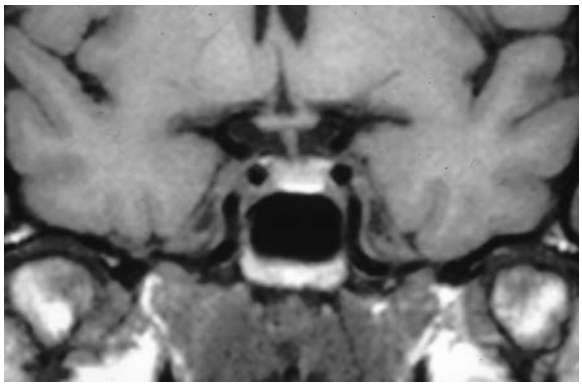

a

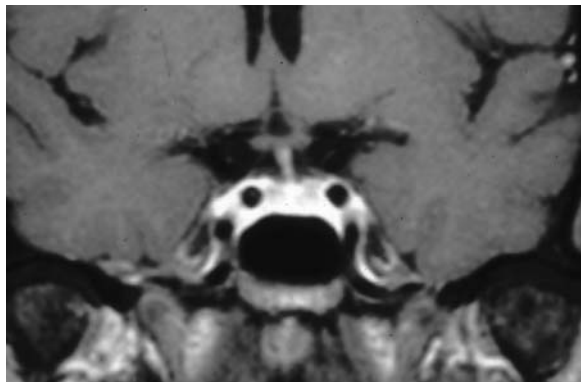

b

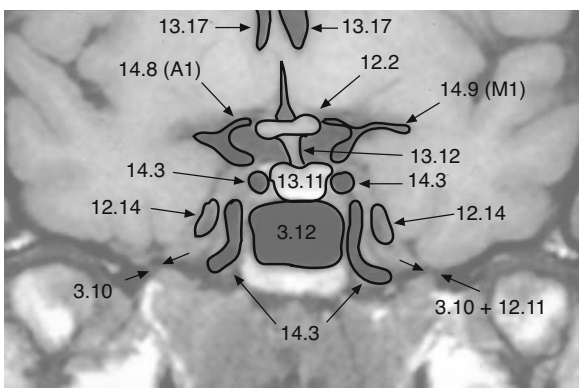

c

Fig. 2.21.a Coronal T1-weighted native MRI of the region of the pituitary stalk. **b** Corresponding contrast-enhanced view. **c** Corresponding diagram: 3.10 = oval foramen, 3.12 = sphenoid sinus, 12.2 = chiasm, 12.11 = mandibular nerve ($N V_3$), 12.14 = trigeminal (Gasserian) ganglion, 13.11 = pituitary gland, 13.12 = pituitary stalk, 13.17 = ventricle, 14.3 = siphon of ICA, 14.8 = anterior cerebral artery (ACA), 14.9 = MCA

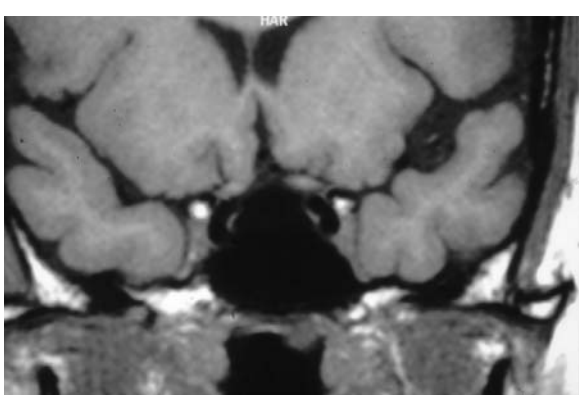

a

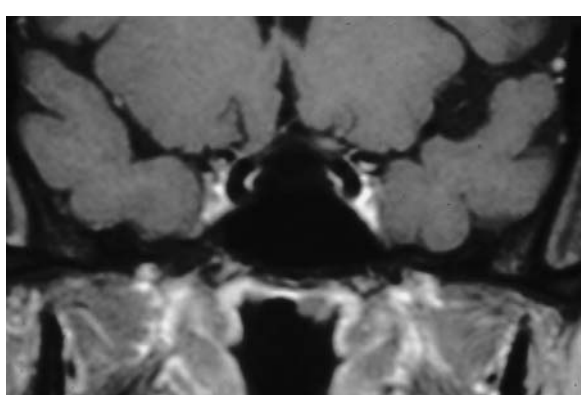

b

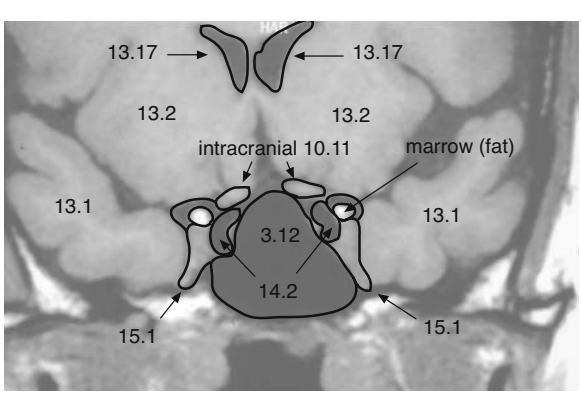

c

Fig. 2.22.a Coronal T1-weighted native MRI at the level of the prechiasmatic intracranial optic nerves. **b** Corresponding contrast-enhanced view. **c** Corresponding diagram: 3.12 = sphenoid sinus, 10.11 = optic nerve (prechiasmatic intracranial portion), 13.1 = temporal lobe, 13.2 = frontal lobe, 13.17 = ventricles, 14.2 = ICA ("knee" of the siphon), 15.1 = cavernous sinus

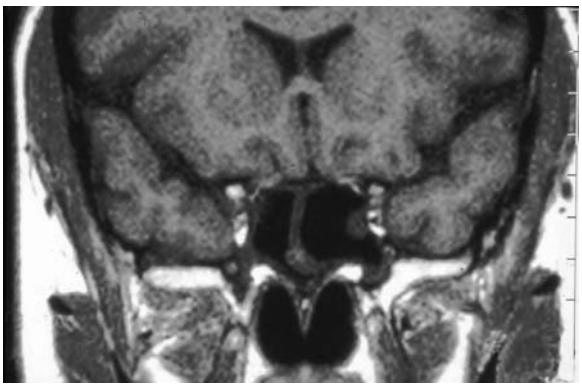

a

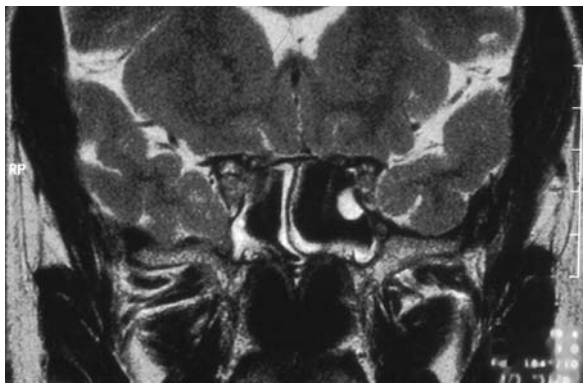

b

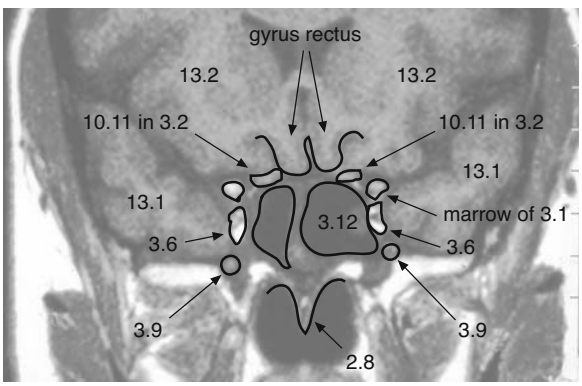

c

Fig. 2.23.a Coronal T1-weighted native MRI at the posterior level of the optic canal. **b** Corresponding T2-weighted view. **c** Corresponding diagram: 2.8 = vomer, 3.1 = anterior clinoid process, 3.2 = optic canal, 3.6 = superior orbital fissure, 3.9 = round foramen, 3.12 = sphenoid sinus, 10.11 = optic nerve, 13.1 = temporal lobe, 13.2 = frontal lobe (note the marginal soft tissue in the sphenoid sinus, hypointense on T1-weighted, hyperintense on T2-weighted image, corresponding to mucosal inflammation)

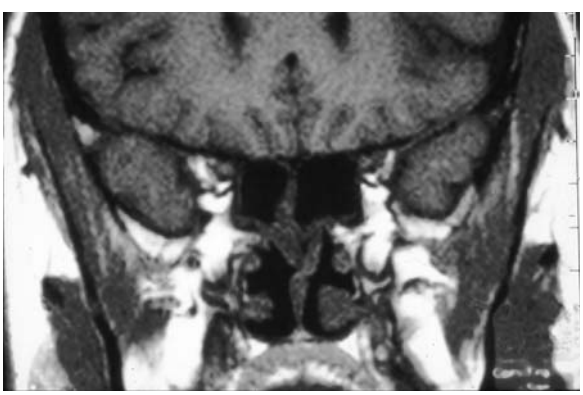

a

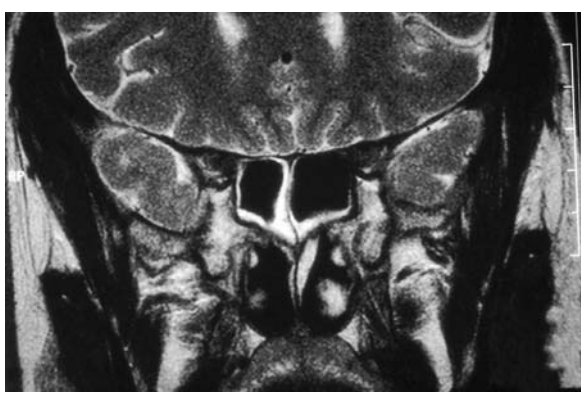

b

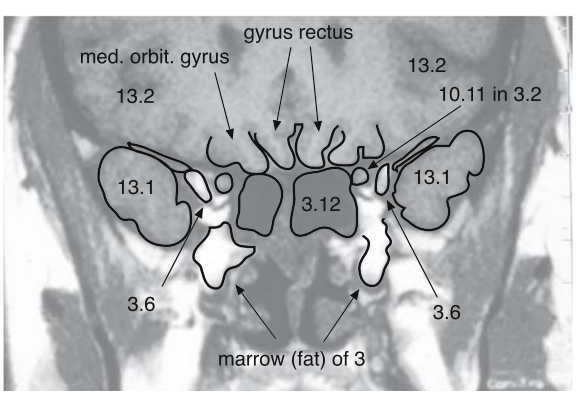

c

Fig. 2.24.a Coronal T1-weighted MRI at the middle of the optic canal. **b** Corresponding T2-weighted view. **c** Corresponding diagram: 3 = sphenoid bone, 3.2 = optic canal, 3.6 = superior orbital fissure, 3.12 = sphenoid sinus, 10.11 = optic nerve, 13.1 = temporal lobe, 13.2 = frontal lobe

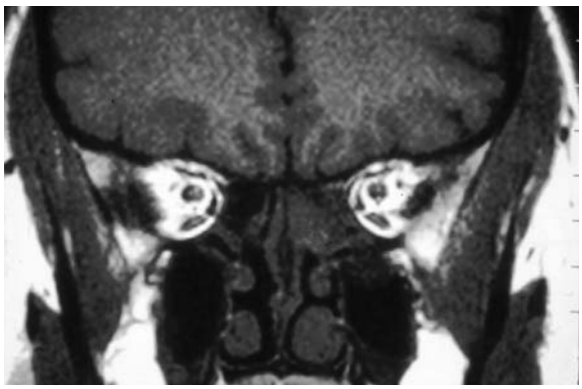

a

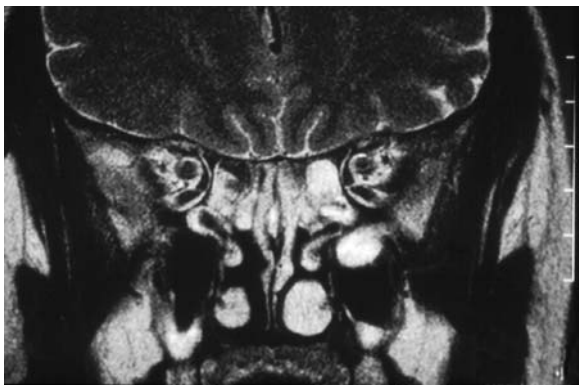

b

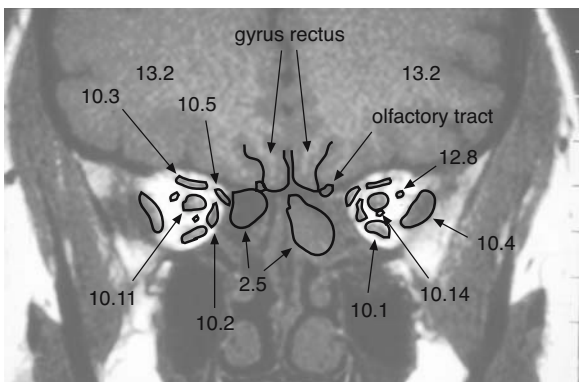

c

Fig. 2.25.a Coronal T1-weighted MRI at the region of the orbital apex. **b** Corresponding T2-weighted view. **c** Corresponding diagram: 2.5 = ethmoid sinus, 10.1 = inferior rectus muscle, 10.2 = medial rectus muscle, 10.3 = superior rectus muscle, 10.4 = lateral rectus muscle, 10.5 = superior oblique muscle, 10.11 = optic nerve, 10.14 = ophthalmic artery, 12.8 = oculomotor nerve, 13.2 = frontal lobe

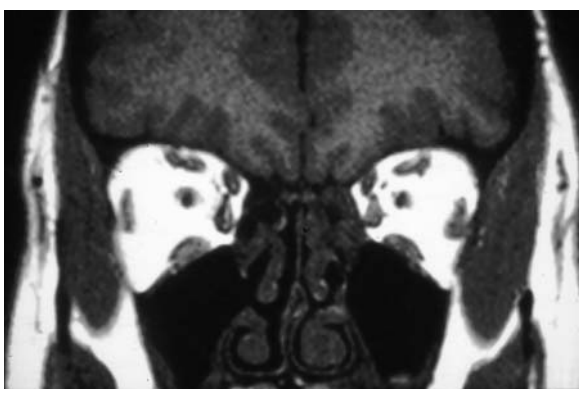

a

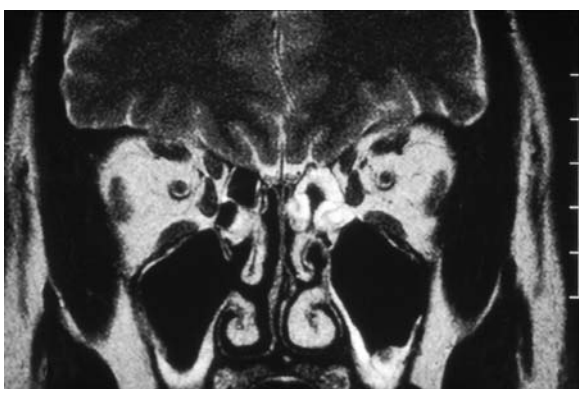

b

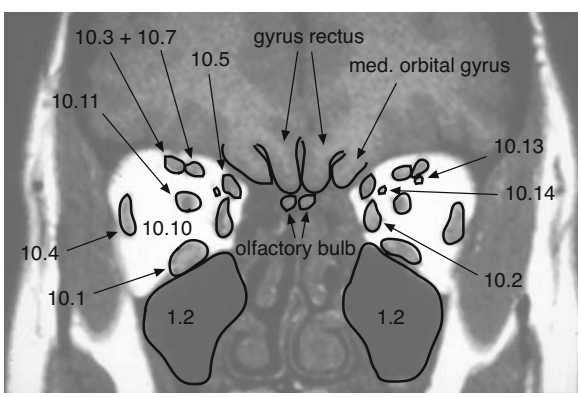

c

Fig. 2.26.a Coronal T1-weighted MRI of the midorbital region. **b** Corresponding T2-weighted view. **c** Corresponding diagram: 1.2 = maxillary sinus, 10.1 = inferior rectus muscle, 10.2 = medial rectus muscle, 10.3 = superior rectus muscle, 10.4 = lateral rectus muscle, 10.5 = superior oblique muscle, 10.7 = levator palpebrae muscle, 10.10 = orbital fat, 10.11 = optic nerve, 10.13 = superior ophthalmic vein, 10.14 = ophthalmic artery (note again the mucoid inflammation of the ethmoid and maxillary sinus)

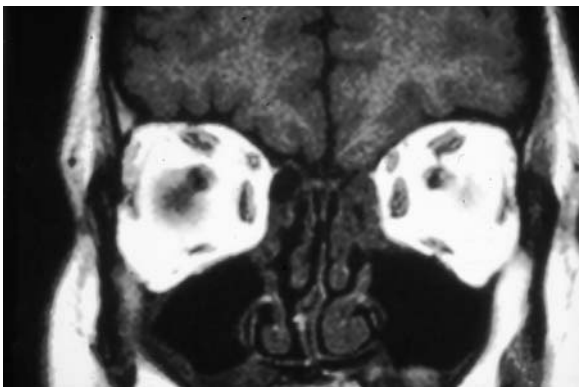

a

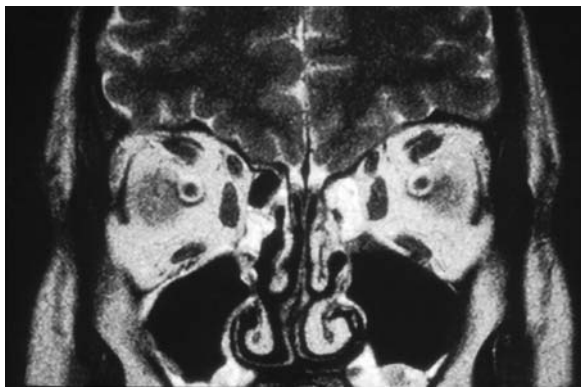

b

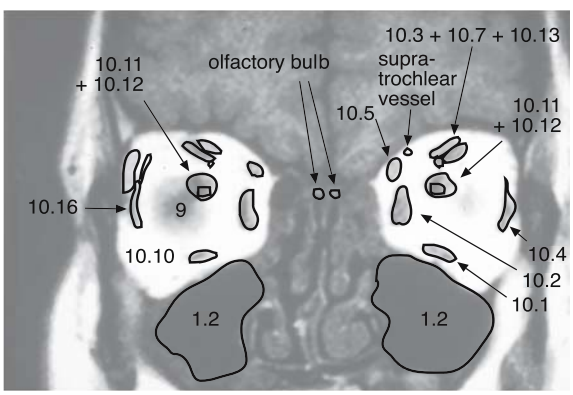

c

Fig. 2.27.a Coronal T1-weighted MRI at the region of the posterior globe. **b** Corresponding T2-weighted view. **c** Corresponding diagram: 1.2 = maxillary sinus, 9 = globe (partial volume), 10.1 = inferior rectus muscle, 10.2 = medial rectus muscle, 10.3 = superior rectus muscle, 10.4 = lateral rectus muscle, 10.5 = superior oblique muscle, 10.7 = levator palpebrae muscle, 10.10 = orbital fat, 10.11 = optic nerve, 10.12 = optic nerve sheath, 10.13 = superior ophthalmic vein, 10.15 = lacrimal gland (partial volume), 10.16 = intermuscular septum

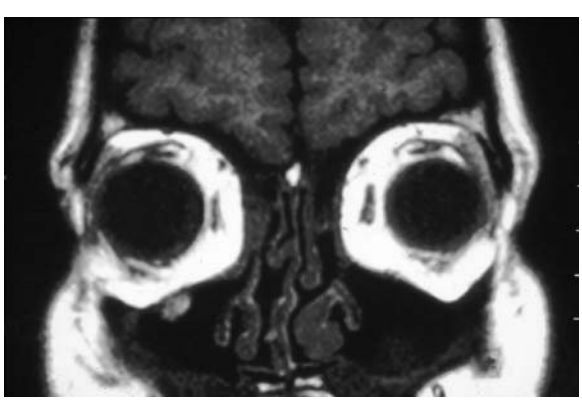

a

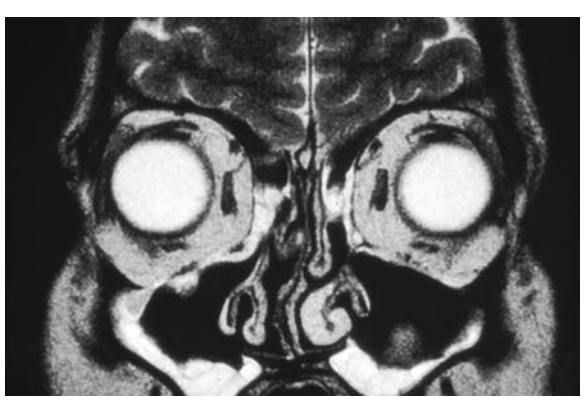

b

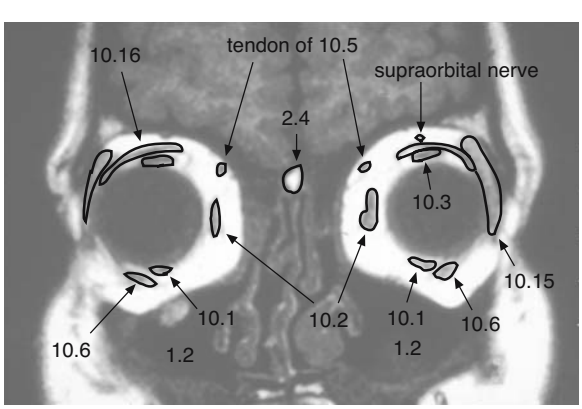

c

Fig. 2.28.a Coronal T1-weighted MRI at the middle of the globe. **b** Corresponding T2-weighted view. **c** Corresponding diagram: 1.2 = maxillary sinus, 2.4 = crista galli, 10.1 = inferior rectus muscle, 10.2 = medial rectus muscle, 10.3 = superior rectus muscle, 10.5 = superior oblique muscle, 10.6 = inferior oblique muscle, 10.15 = lacrimal gland, 10.16 = intermuscular septum (note the different hyperintensities of orbital fat and mucoid inflammation in the ethmoid sinus (bilateral), separated by the small hypointensity of the medial orbital wall on the T2-weighted view)

2.4 The Extraocular Muscles, Intra- and Extraconal Space (Figs. 2.30, 2.31)

The four rectus muscles and the superior oblique muscle are long, stretched, fusiform muscles with a slightly thickened middle region. Together with the levator palpebrae muscle, they originate from a common annular tendon, Zinn's ligamentous ring, attached to the bone of the orbital apex (Fig. 2.10a). Anterior to the orbital opening of the optic canal, this annular tendon encircles the optic nerve with its dural sheath and the ophthalmic artery eccentrically. Furthermore, the annular tendon crosses the inferomedial region of the inferior orbital fissure, where the distal oculomotor and abducent nerves enter the annular tendon. The superior and inferior ophthalmic veins pass the superior and the inferior orbital fissure, respectively, outside the annular tendon. The superior ophthalmic vein then passes in a stretched S-like course directly below the anterior region of the superior rectus muscle from posterolateral to medioanterior (Figs. 2.5, 2.18). Usually it collects the blood from the face via the angular vein with an antegrade flow direction to the cavernous sinus. However, in anatomic variations there can be reversed flow, if the middle cerebral and uncal veins both drain into the cavernous sinus (Servo 1982). The four rectus muscles insert on the globe posterior to the corneoscleral border. The superior oblique muscles course forward superomedially of the medial rectus muscle, forming a small, round tendon anteriorly which is deflected posterolaterally by a pulley, the trochlea (Figs. 2.5, 2.18, 2.19), and is then attached to the sclera posterior of the equator. The thin and broad inferior oblique muscle originates from the medial orbital floor and passes posterolaterally to insert into the inferolateral sclera (Figs. 2.1, 2.13, 2.14, 2.28, 2.33). The levator palpebrae muscle runs above the globe and terminates anteriorly in an aponeurosis (Figs. 2.12, 2.27, 2.28). Some of these tendinous fibers are attached to the tarsus, while the remnant fibers radiate directly to the skin of the upper eyelid.

2.4.1 Lacrimal Gland

The lacrimal gland and system represent a functional subunit of the orbit, located in the extraconal space. The lacrimal gland consists of two parts, incompletely separated by the aponeurosis of the levator palpebrae muscle: a superior larger orbital and an inferior smaller palpebral lobe, connected only at the lateral edge of the aponeurosis (Fig. 2.33). The orbital part is nestled to the lacrimal fossa in the anterior aspect of the superolateral orbital wall (Figs. 2.5, 2.13, 2.28). The structure of the lacrimal gland resembles the salivary glands with secretory cells (acini), granules, and ducts (Bron et al. 1997). The lacrimal ducts open into the superior conjunctival fornix. At the medial end of the lid, two lacrimal puncta, one superior and one inferior, open to short (2 mm), primary vertical, then horizontal superior and inferior lacrimal canaliculi, which join to the membranous lacrimal sac, the widest portion of the drainage system (Fig. 2.34). The lacrimal sac (Fig. 2.1) lies in the lacrimal fossa, a bony hollow formed by the lacrimal bone and the superior and anterior maxillary processes. Normally 10–12 mm in length, it has a downward continuation into the lacrimal duct, which lies in the osseous nasolacrimal canal with a length of about 10–15 mm, formed by the maxillary bone (Figs. 2.13, 2.34). As the posterolateral direction is the exit into the inferior concha, the valve of Hasner marks the endpoint of the excretory lacrimal system (Bron et al. 1997) (Fig. 2.34).

(Text continues on p. 50)

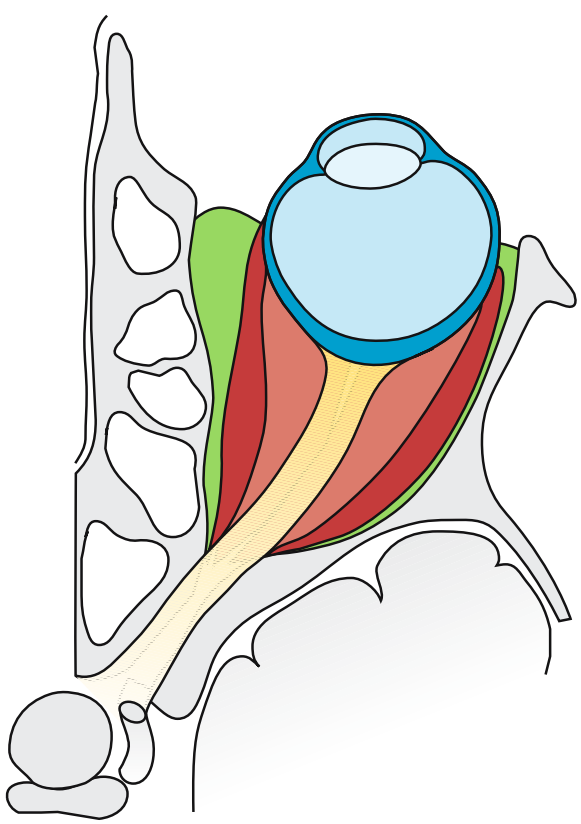

Fig. 2.29. Diagram of the four compartments of the orbital space

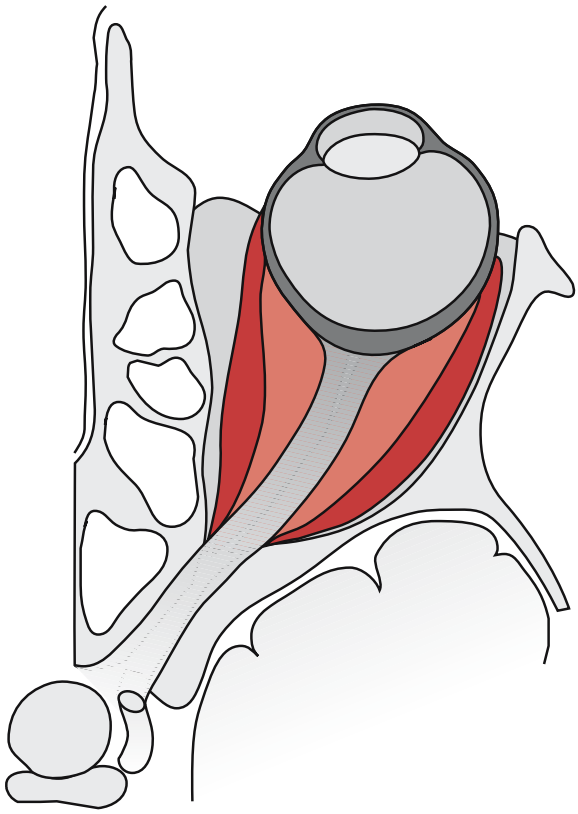

Fig. 2.30. Diagram of the intraconal space

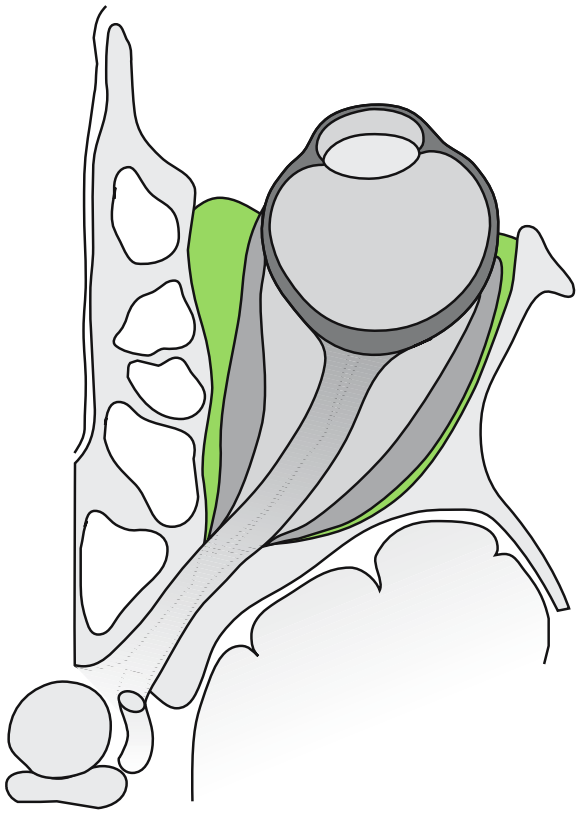

Fig. 2.31. Diagram of the extraconal space

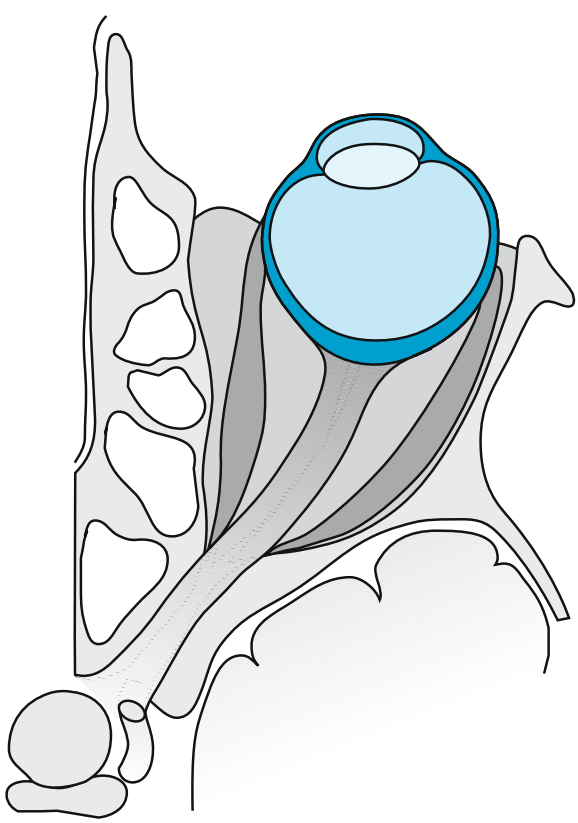

Fig. 2.32. Diagram of the orbital compartment globe

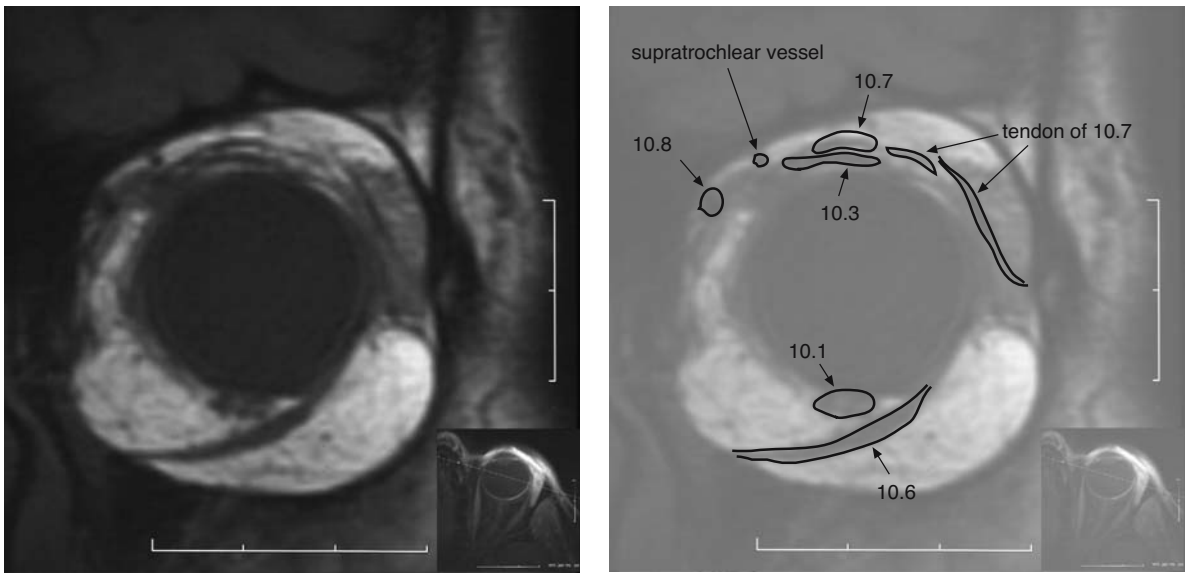

a b

Fig. 2.33.a Coronal T1-weighted high resolution MRI of the left globe (see *insert*) with demonstration of the two different parts of the lacrimal gland. **b** Corresponding diagram: 10.1 = inferior rectus muscle, 10.3 = superior rectus muscle, 10.6 = inferior oblique muscle, 10.7 = tendon of levator palpebrae muscle, dividing the lacrimal gland into a superior orbital and an inferior palpebral portion, 10.8 = trochlea

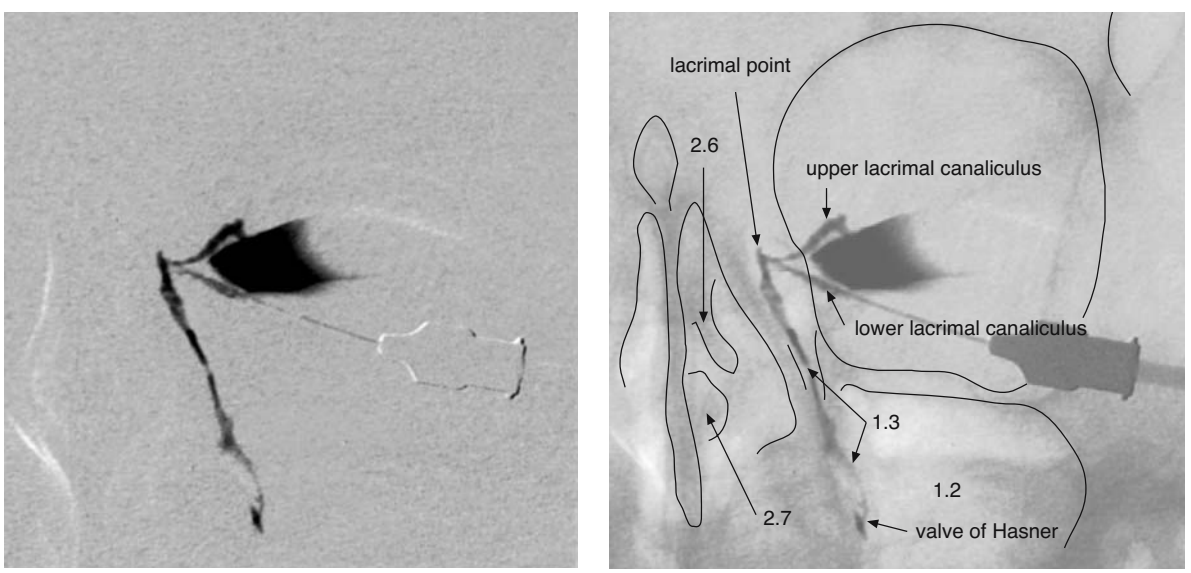

a b

Fig. 2.34.a Frontal view of the lacrimal drainage system (DSA, puncture of the inferior lacrimal point). **b** Corresponding diagram (not subtracted): 1.2 = maxillary sinus, 1.3 = lacrimal sac/duct, 2.6 = middle turbinate, 2.7 = inferior turbinate

2.5 Optic Nerve (Fig. 2.35)

The optic nerve can be divided into an intraocular, an intraorbital, a canalicular, and an intracranial segment. Although the optic nerves are part of the cranial nerves, their structure differs from that of the other cranial nerves (to simplify matters, in the rest of this article the optic nerves are cited in the singular). Phylogenetically, the optic nerve and the retina represent an evagination of the brain. Therefore, the optic nerve contains the same tissue components as the brain, and thus meningiomas or optic gliomas can develop in the optic nerves, analogous to intracranial tumors, whereas schwannomas or neurofibromas develop from the other cranial nerves. About 4 mm nasal to the central part of the posterior pole of the globe, the superficial nerve fiber layers converge, exit, and pierce the outer retina, the choroid, and the lamina cribrosa, forming the optic nerve head and intraorbital optic nerve. As it traverses the annular tendon near the optic foramen, the attachments of the superior and medial rectus muscles are adherent to its dural sheath, explaining the characteristic orbital pain in retrobulbar neuritis (Bron et al. 1997).

As part of the brain, the entire intraorbital optic nerve is embedded in meningeal and arachnoidal sheaths in continuation with the respective intracranial layers. As already mentioned, the outermost sheath corresponds to the dura mater, tightly adherent to the bone within the optic canal. In the orbit, this sheath divides into two layers, one of which remains the outer sheath, blending with the sclera of the eyeball, the other becoming the orbital periosteum (periorbita) (Bron et al. 1997). The intermediate arachnoid layer is attached inside, while the inner arachnoid layer is attached to the pia mater that envelops the nerve and also the branches of the central retinal vessels.

The central retinal artery is the most important branch of the ophthalmic artery and pierces the optic nerve inferomedially, approximately 10 mm behind the globe, then running to the globe centrally inside of the nerve. The path of the central retinal vein also runs through the center of the optic nerve, but it exits the nerve 1–2 mm dorsal of the entry point of the central retinal artery, then running dorsally below the optic nerve. It may join the superior ophthalmic vein and can drain either into this, into another orbital vein, or directly into the cavernous sinus. It is assumed that inside the bulb no functionally sufficient venous collateralization to the central retinal vein exists, explaining the retinal bleeding and secondary glaucoma in case of a venous occlusion (Lang 1981).

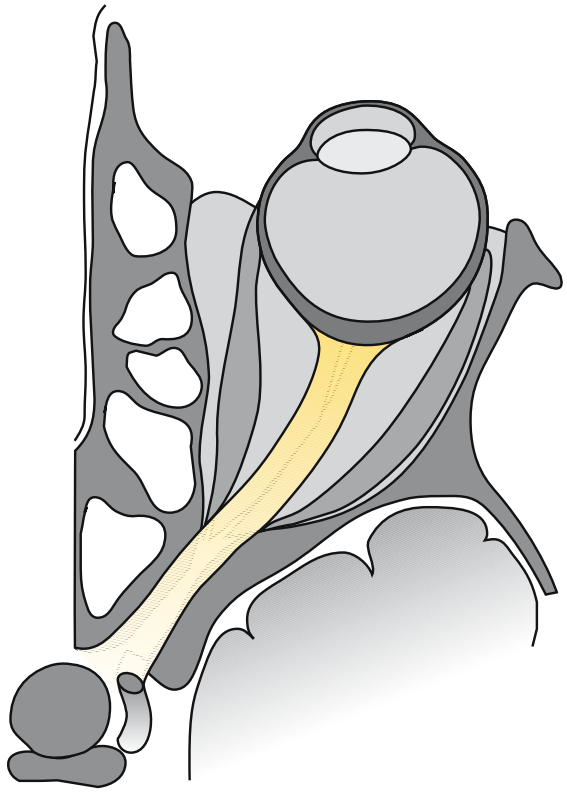

Fig. 2.35. Diagram of the orbital compartment optic nerve

A tube-shaped subarachnoid space extending between the intermediate and the inner arachnoid layer communicates with the intracranial subarachnoid space. A slight or pronounced bulbous widening of the arachnoid sheath of the proximal optic nerve is a normal appearance (Fig. 2.36) and should not be misinterpreted as some form of optic nerve CSF disturbance, although according to histologic studies on this segment, one expects the most dural bulging in the case of intracranial hypertension at the optic nerve head (Helmke and Hansen 1996) (Figs. 6.185, 6.186).

The intraorbital optic nerve has a length of about 4–4.5 cm, and its course is slightly tortuous (Fig. 2.37). It runs posteromedially through the muscle cone of the four rectus muscles to the orbital apex and enters the optic canal. Passing the optic canal, the tube-shaped subarachnoid space surrounding the optic nerve shows a remarkable narrowing, which explains why no perioptic CSF is visible intracanalicularly on T2-weighted coronal MRI (Figs. 2.24, 2.36).

2.5.1 Intracanalicular Optic Nerve, Prechiasmal Area

(Fig. 2.36)

The length of the optic canal is about 5 mm, its width about 3–4 mm, and the course of the intracranial prechiasmatic optic nerve has an extension of about 10 mm (Fig. 2.38). The internal carotid artery lies laterally and below it, giving rise to the ophthalmic artery at the anteromedial wall of the upper carotid siphon (Figs. 6.196, 7.30, 7.46, 7.47, 7.51). At the intracranial end of the optic canal, the ophthalmic artery is located inferolaterally to the optic nerve inside the subarachnoid space. Within the orbital end of the optic canal, the ophthalmic artery exits the dura laterally (Rhoton and Natori 1996). The intradural segment of the internal carotid artery starts a little more proximally than the origin of the ophthalmic artery (Oikawa et al. 1998). The A1 segment of the anterior cerebral artery crosses above the prechiasmatic optic nerve (Fig. 2.39). The relation of the vessels of the circle of Willis is shown by two different views of the vascular anatomy, demonstrated with MRA (Figs. 2.40, 2.41).

2.6 Chiasm, Postchiasmal Area

(Figs. 2.36, 2.38, 2.39, 2.42)

The intracranial optic nerves then run posteromedially to the midline, where they merge together to form the caudocranially flat X-shaped optic chiasm. The posteromedial chiasm, containing the posterior part of the decussating fibers, partially forms the anterior floor of the third ventricle (Fig. 2.42). The optic recess of the third ventricle is bordered inferoposteriorly by the superoposterior aspect of the chiasm and anteriorly by the inferior lamina terminalis, which merges inferiorly with the chiasm. Posterior to the chiasm, the tuber cinereum and the pituitary stalk extend inferiorly. The bone below the chiasm forms a groove between the optic canals, the chiasmatic sulcus, which opens anterolaterally into the optic canals and is limited posteriorly at the midline by a ridge of the tuberculum sellae. Dorsal to this, the diaphragm of the sella covers the pituitary fossa. The localization of the chiasm varies between the position in the chiasmatic sulcus and more posteriorly near the sellar diaphragm (prefixed, postfixed chiasm) (Renn and Rhoton 1975).

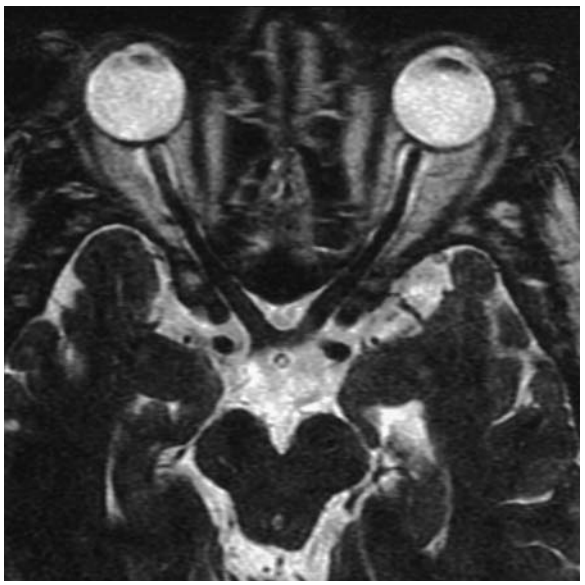
a

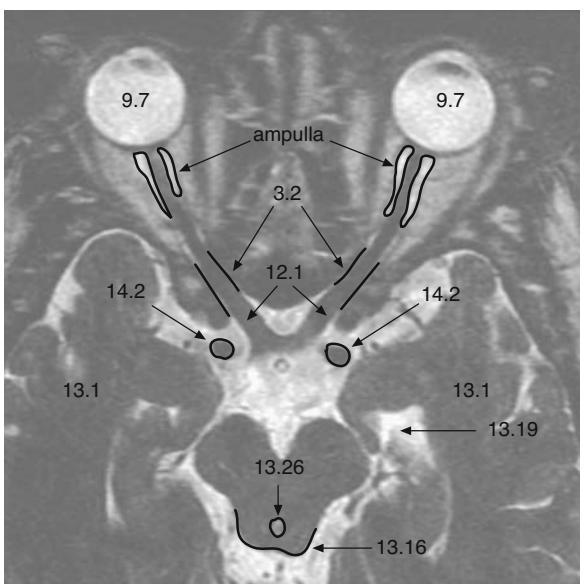

b

Fig. 2.36.a Axial T2-weighted MRI of the orbit and neighboring brain area, demonstrating the (normal finding of a) widening of the proximal optic nerve sheath (ampulla). **b** Corresponding diagram: 3.2 = optic canal, 9.7 = vitreous body, 12.1 = prechiasmatic optic nerve, 13.1= temporal lobe, 13.16 = (inferior colliculi of the) quadrigeminal plate, 13.19 = temporal horn, 13.26 = aqueduct, 14.2 = ICA

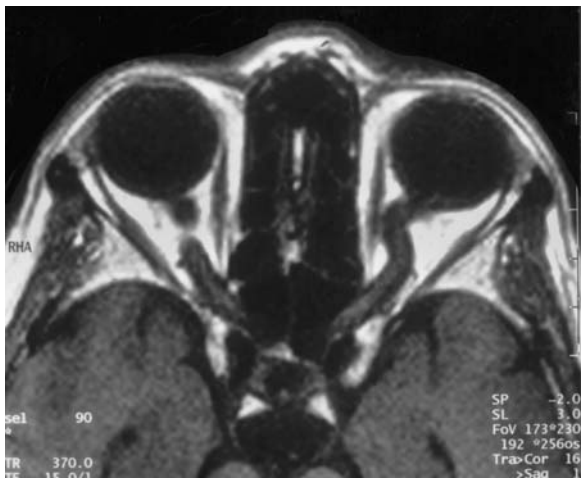

Fig. 2.37. Axial T1-weighted MRI of the optic nerve, demonstrating the tortuous course of the left as a normal variant

2.7 Intracranial Visual Pathway

2.7.1 Optic Tract (Figs. 2.38, 2.39)

Dorsolaterally of the chiasm, the optic visual pathway continues backwards, forming the optic tracts. They cross posterior to the anterior perforated substance and anterior to the lateral tuber cinereum and the lateral perforated substance, respectively (Duvernoy 1998). More dorsolaterally, the optic tracts lie above the uncus and surround the crus cerebri. The main part of the tracts ends in the lateral geniculate nuclei (Figs. 2.43, 2.44). Small divisions of the tracts terminate in the superior colliculus, in the pretectal area, in nuclei of the accessory optic tract, and in the hypothalamic suprachiasmatic nucleus (Nieuwenhuys et al. 1988). The brachium colliculi superiores, which courses below the lateral pulvinar of the thalamus between the lateral geniculate nucleus and the colliculus superior, also contains others fibers that connect the lateral geniculate nucleus with the colliculus superior. On high resolution MRI, the lateral geniculate nucleus and the brachium colliculi superioris (Fig. 2.44) can be depicted (Nieuwenhuys et al. 1988; Horton et al. 1990; Duvernoy 1998).

(Text continues on p. 55)

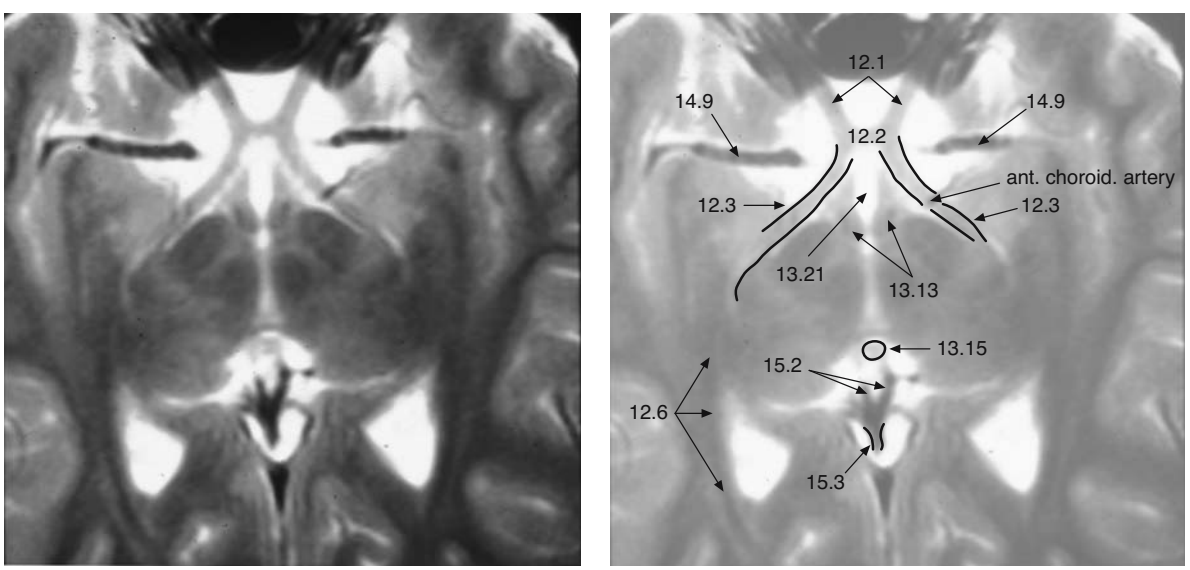

a b

Fig. 2.38.a Axial T2-weighted MRI of the chiasmatic region. **b** Corresponding diagram: 12.1 = prechiasmatic optic nerve, 12.2 = chiasm, 12.3 = optic tract, 12.6 = optic radiation, 13.13 = mammillary body, 13.15 = pineal gland, 13.21 = third ventricle, 14.9 = MCA (M1), 15.2 = (distal portion of the) internal cerebral veins (draining into the), 15.3 = (proximal) vein of Galen (note the wide prechiasmatic cistern (as an individual, normal variant), especially in comparison with Fig. 2.39)

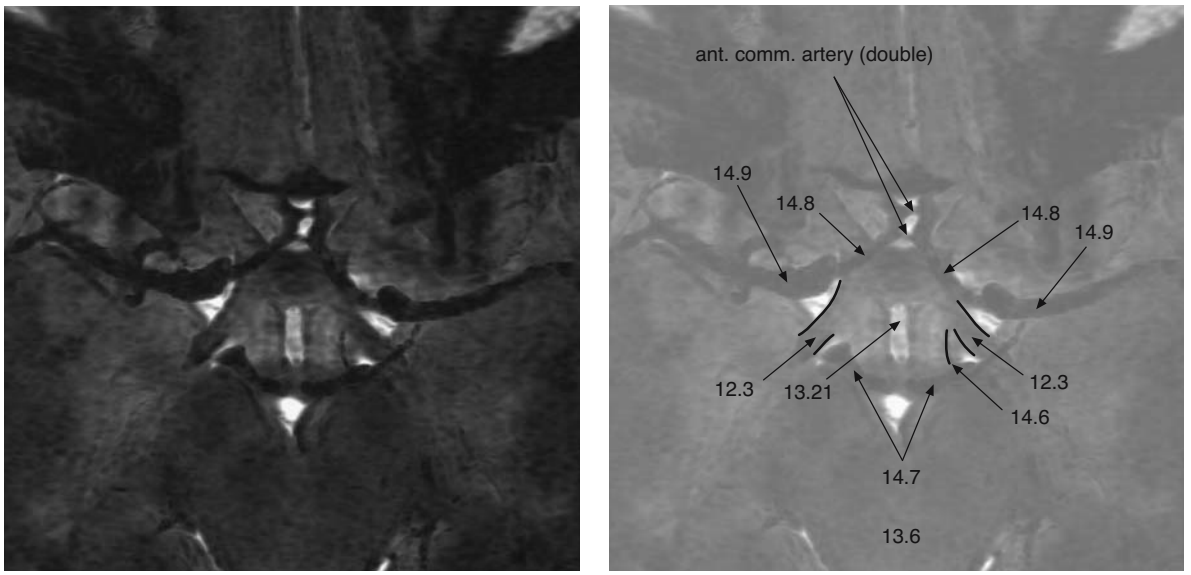

Fig. 2.39.a Axial T2-weighted (MIN) view of the chiasmatic region. **b** Corresponding diagram: 12.3 = optic tract, 13.6 = pons, 13.21 = third ventricle, 14.6 = posterior communicating artery (Pcomm), 14.7 = PCA (P1), 14.8 = ACA (A1, A2), 14.9 = MCA (M1)

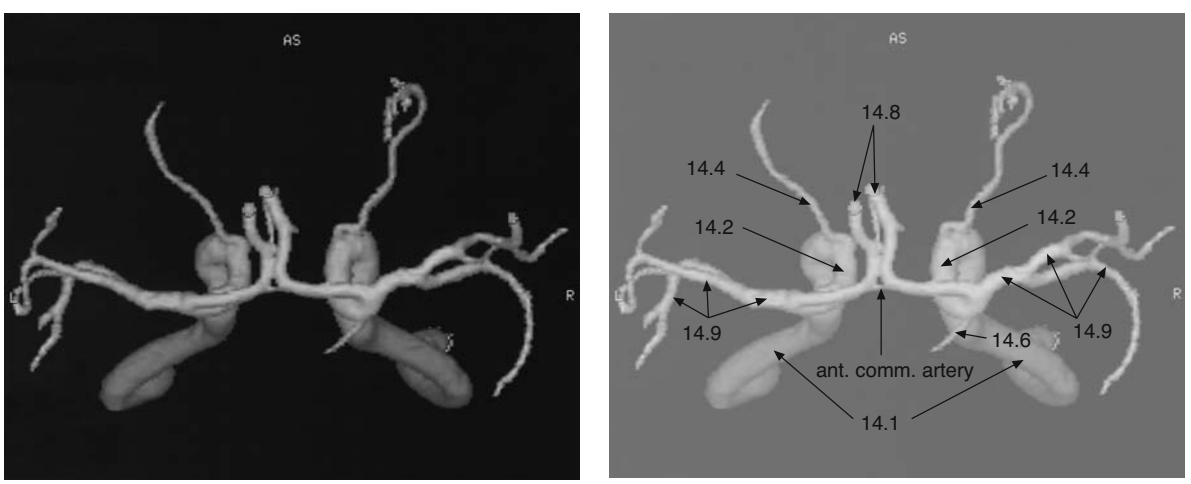

Fig. 2.40.a Axial view of 3D-MRA of the anterior part of the circle of Willis. **b** Corresponding diagram: 14.1 = (ICA in the) carotid canal, 14.2 = ICA, 14.4 = ophthalmic artery, 14.6 = Pcomm, 14.8 = ACA (A1, A2), 14.9 = MCA (M1–M3)

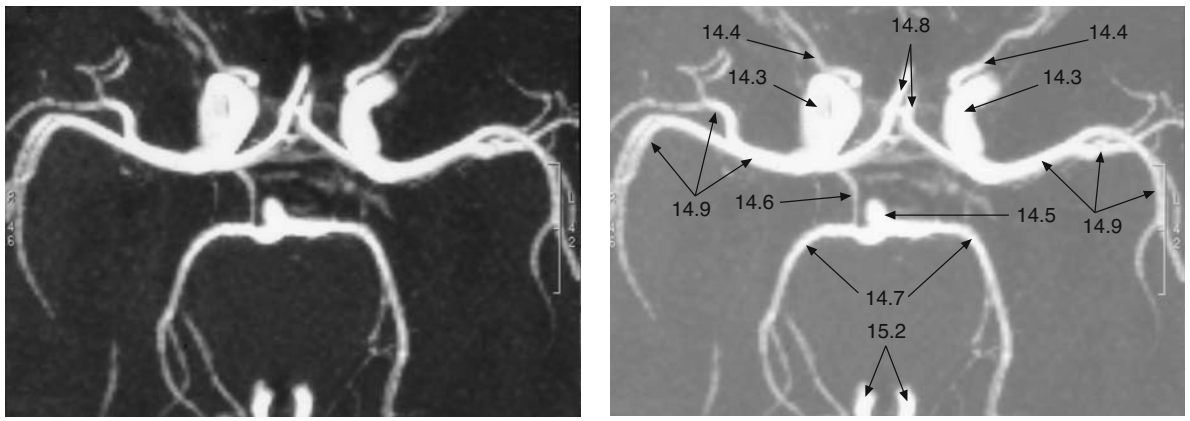

a b

Fig. 2.41.a 2D-MRA of the circle of Willis. **b** Corresponding diagram: 14.3 = siphon of ICA, 14.4 = ophthalmic artery, 14.5 = (top of the) basilar artery, 14.6 = Pcomm, 14.7 = PCA, 14.8 = ACA (A1, A2), 14.9 = MCA (M1–M3), 15.2 = (distal portion of the) internal cerebral vein

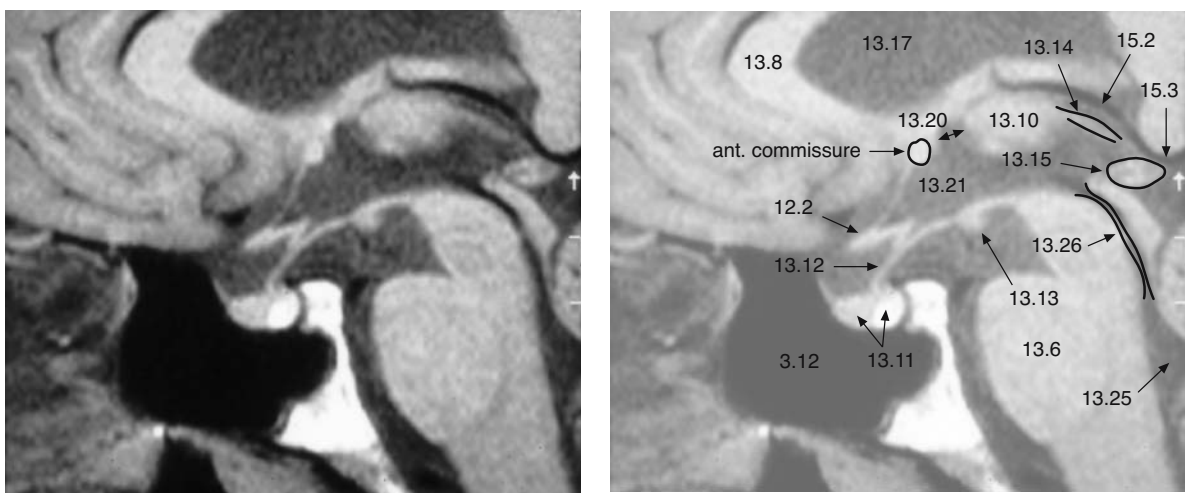

a b

Fig. 2.42.a Midsagittal T1-weighted MRI of the sellar region. **b** Corresponding diagram: 3.12 = sphenoid sinus, 12.2 = chiasm, 13.6 = pons, 13.8 = rostrum (of the corpus callosum), 13.10 = thalamus, 13.11 = pituitary gland [anterior pituitary (adenohypophysis): isointense, posterior pituitary (neurohypophysis): hyperintense], 13.12 = pituitary stalk, 13.13 = mammillary body, 13.14 = fornix, 13.15 = pineal gland, 13.17 = ventricle, 13.20 = foramen of Monro, 13.21 = third ventricle, 13.25 = fourth ventricle, 13.26 = aqueduct, 15.2 = internal cerebral vein, 15.3 = vein of Galen

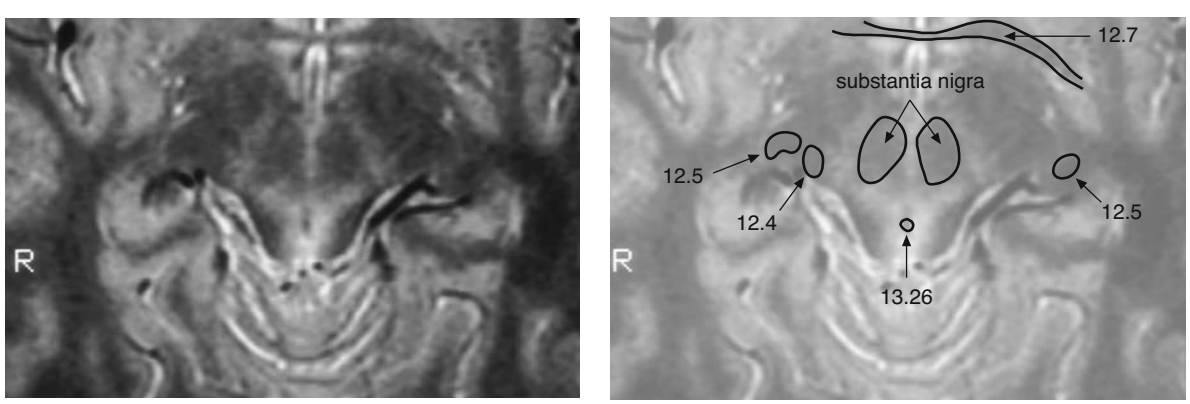

a b

Fig. 2.43.a Axial PD-weighted MRI of the mesencephalic region (sector) at the level of the anterior commissure. **b** Corresponding diagram: 12.4 = medial geniculate nucleus, 12.5 = lateral geniculate nucleus, 12.7 = anterior commissure, 13.26 = aqueduct

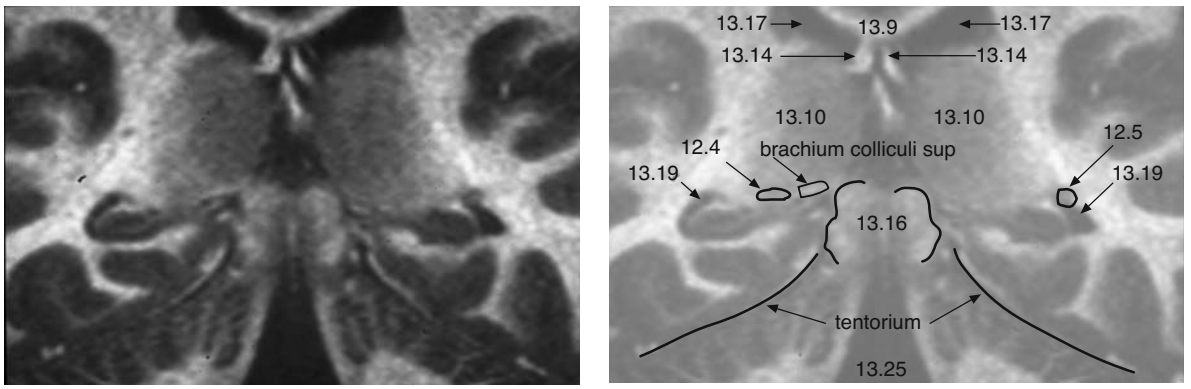

a b

Fig. 2.44.a Coronal T1-weighted (IR) view of the midthalamic region. **b** Corresponding diagram: 12.4 = medial geniculate nucleus, 12.5 = lateral geniculate nucleus13.9 = body (of the corpus callosum), 13.10 = thalamus, 13.14 = fornix, 13.16 = quadrigeminal plate, 13.17 = ventricle, 13.19 = temporal horn of the ventricle, 13.25 = fourth ventricle

2.7.2 Optic Radiation (Figs. 2.45, 2.46)

About half of the fibers that originate in the lateral geniculate nucleus and project to the occipital visual cortex run directly backward lateral to the more superior aspect of the lateral ventricle within the inferior parietal lobe. The other half of the fibers describes a large forward directed loop (Meyer's loop) within the temporal lobe above and lateral to the anterior temporal horn of the lateral ventricle. Then the fibers curve backward lateral to the temporal and occipital horn of the lateral ventricle. The fibers of the optic radiation are separated by the interposed tapetum from the lateral wall of the ventricle. The tapetum is a thin layer composed of fibers from the forceps major of the callosal radiation. Tapetum and optic radiation together form a thin caudo-cranially directed plate of fibers, termed the sagittal stratum. On T2-weighted MRI, it is possible to identify and trace systems of parallel coursing, compact, myelinated fibers as the optic radiation, which are embedded in more loosely arranged white matter (Curnes et al. 1988). On MRI in most cases, it is not possible to subdivide the sagittal stratum and differentiate the optic radiation and the tapetum. Only under special conditions, if there is edema or a gliosis, can they be separated on T2-weighted MRI (Kitajima et al. 1996). Behind the sagittal stratum, the myelinated fibers of the optic radiation bend medially to project on the visual cortical field and diverge in a fan-like manner, no longer depicted on MRI as the fibers are looser than the optic radiation.

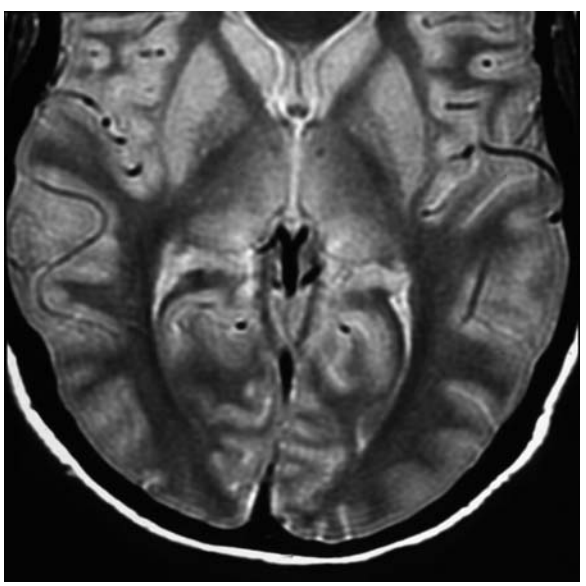

a

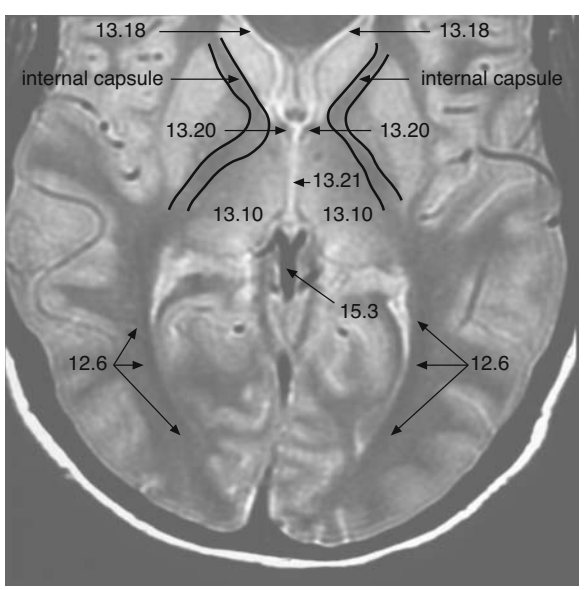

b

Fig. 2.45.a Axial T2-weighted view of the brain at the level of the internal capsule. **b** Corresponding diagram: 12.6 = optic radiation, 13.10 = thalamus, 13.18 = frontal horns of the ventricles, 13.20 = foramen of Monro, 13.21 = third ventricle, 15.3 = vein of Galen

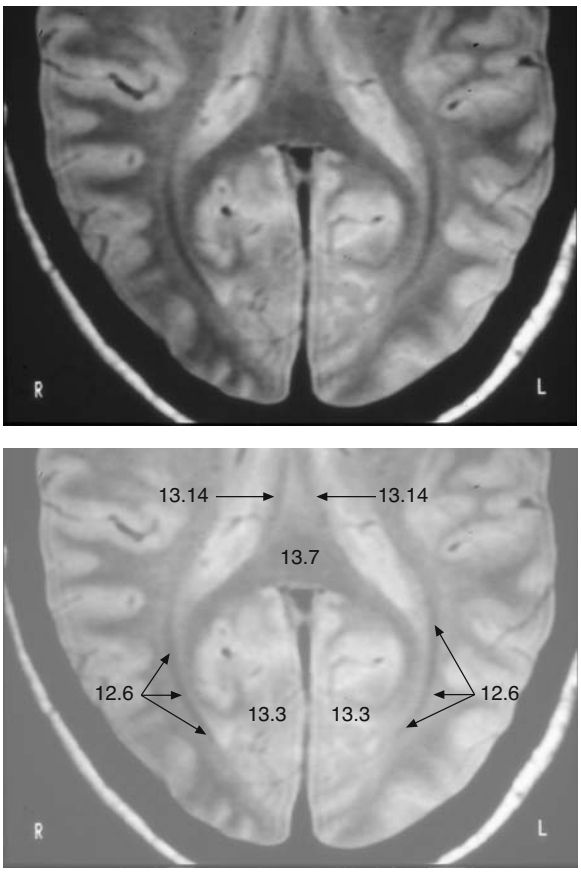

Fig. 2.46.a Axial PD-weighted view of the optic radiation some millimeters above Fig. 2.45. **b** Corresponding diagram: 12.6 = optic radiation, 13.3 = occipital lobe, 13.7 = (posterior knee of the) corpus callosum, 13.14 = fornix

2.7.3
Striate Cortex (Figs. 2.47–2.50)

The primary visual cortex, the striate cortex, is located in the wall along the calcarine fissures, seen on the medial surface of the occipital lobe (Figs. 2.47, 2.48). It should be emphasized that the striate cortex wraps around the occipital pole to the posterolateral aspect of the occipital lobe. In other words, one can imagine folding back the calcarine fissure laterally and smoothing out the normally gyrated striate cortex, leading to an artificially flattened ellipsoid map of the visual cortex that is about 80–40 mm (Horton and Hoyt 1991b). The folding along the calcarine fissure indicates the horizontal meridian. The lower contralateral visual field is represented above the horizontal meridian, whereas the upper contralateral visual field shows its representation below the horizontal meridian. The peripheral visual field is projected to the anterior part of this ellipsoid map where the calcarine fissure joins the parieto-occipital fissure. The striate cortex around and lateral to the occipital pole contains the representation of the central visual field, especially of the fovea. An expanded area of the visual cortex is attributed to the central visual field, and a relatively small part is occupied by the peripheral visual field representation. This anatomic arrangement is called cortical magnification of the central vision (Holmes 1945). Correlative studies of the past few years, since functional MRI has been able to localize occipital lesions with attributed visual field defects in an anatomical way, have led to a postulated refinement of the classic retinotopic Holmes map. It seems that the above-mentioned so-called cortical magnification of the central visual field was underestimated by Holmes (Horton and Hoyt 1991b; Wong and Shape 1999). A revised map of the retinotopic representation of the human visual striate cortex is shown in Figs. 2.49, 2.50 (Horton and Hoyt 1991a). According to the literature, high resolution MRI is able to identify in vivo the specific intracortical myeloarchitecture of the striate cortex that differs from the extrastriate cortex (Clark et al. 1992). This can be demonstrated by comparison of the striate and precentral cortex obtained from specimens (Fig. 2.51), where the myeloarchitecture shows a more distinct visibility than on in vivo MRI.

2.7.4
Extrastriate Visual Association Cortex

Except anteriorly, the primary visual cortex (V1 or area 17) is surrounded by the secondary visual area V2 (area 18), which in turn is surrounded by the tertiary visual area V3 (area 19 corresponds partially to V3). These areas are designated the circumstriatal visual association cortex. Whereas the upper and lower quadrants of the primary visual cortex are in continuation within the depth of the calcarine fissure, the extrastriate cortex is divided into separate upper and lower quadrants flanking above and below the intervening primary visual cortex. Each quadrant of the bisected secondary visual cortex runs on both sides of the primary visual cortex along the upper and lower vertical meridians which are shared by the primary and secondary cortex. On the outer border of the secondary cortex, the quadrants of the bisected tertiary cortex are arranged along the horizontal

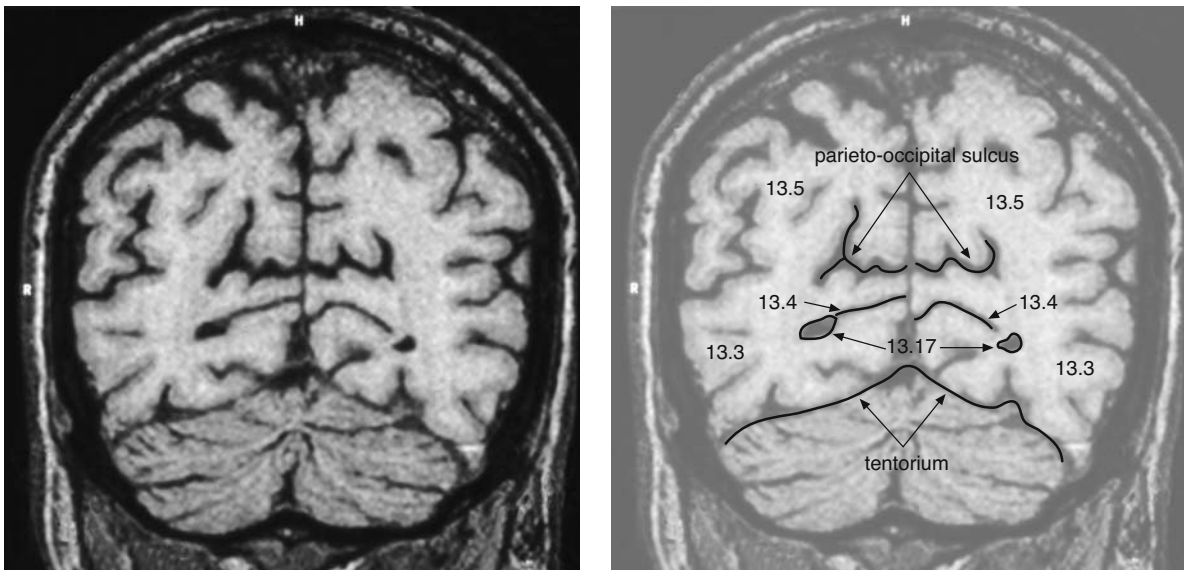

a b

Fig. 2.47.a Coronal T1-weighted view (reconstruction of a 3D data set) of the region of the calcarine sulcus. **b** Corresponding diagram: 13.3 = occipital lobe, 13.4 = calcarine sulcus, 13.5 = parietal lobe, 13.17 = (most posterior parts of the inferior horns of the) ventricles

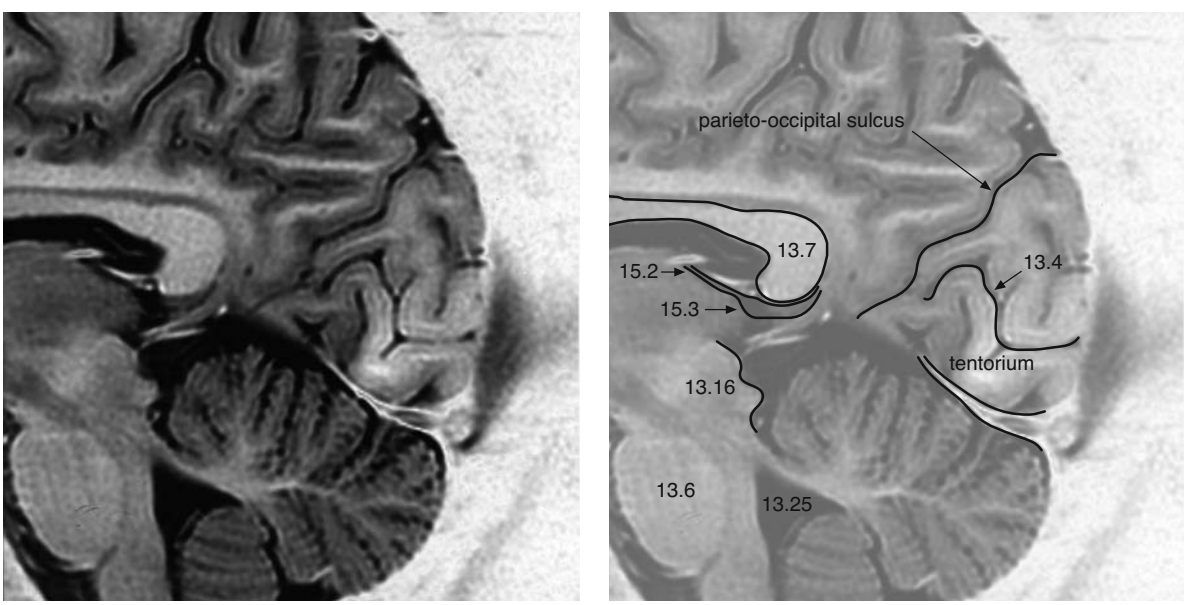

c d

Fig. 2.48.a Sagittal paramedian T1-weighted (IR) view of the parieto-occipital region with striate cortex. **b** Corresponding diagram: 13.4 = calcarine sulcus, 13.6 = pons, 13.7 = corpus callosum, 13.16 = quadrigeminal plate, 13.25 = fourth ventricle, 15.2 = internal cerebral vein, 15.3 = vein of Galen

meridian that is shared by the adjoining secondary and tertiary cortex (Fig. 2.52). This explains why a lesion of the extrastriate cortex that crosses the horizontal meridian between areas V2 and V3 will respect the horizontal meridian and result in a perfect quadrantanopia. In this described condition, a precise anatomical location or extension of the lesion is not required. In the case of a quadrantanopia, this does not necessarily imply that a lesion lies within the extrastriate cortex; it can also be caused indirectly by compression by a bordering tumor (Van Essen et al. 1986; Horton and Hoyt 1991a).

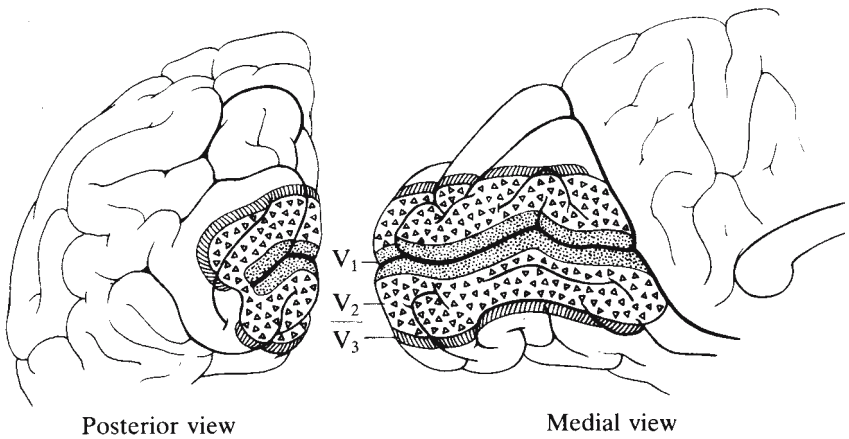

Fig. 2.49. Schematic diagram showing arrangement of V1, V2, and V3 along the medial and posterior occipital surface. Most of V1 is buried within the calcarine fissure. Considerable variation occurs among individuals in the relative position and size of different cortical visual areas. (With permission of Horton and Hoyt 1991a)

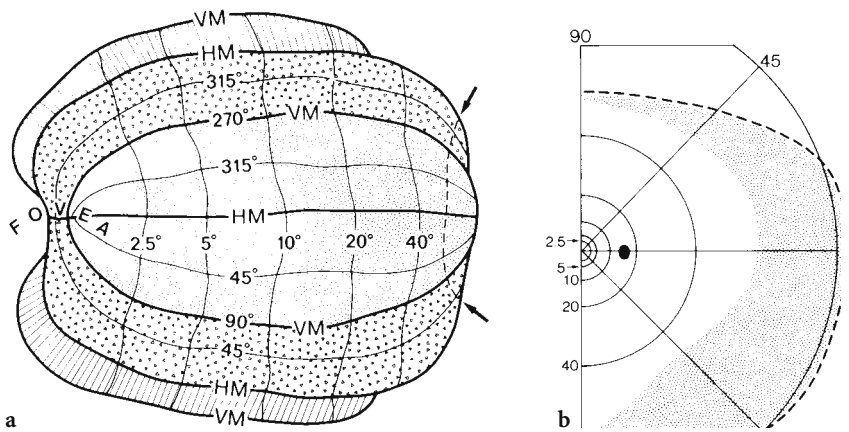

Fig. 2.50.a Artificially flattened map showing the retinotopic organization of V1 (*stippled area*), V2 (*small triangles*), and V3 (*striped*) in the left occipital lobe. **b** Right visual field coordinates corresponding to map in **a**. The monocular temporal crescent (*stippled area*) is represented within a small area at the rostral end of striate cortex (border between binocular and monocular field runs between *arrows* in **a**). V2 and V3 are split along the representation of the horizontal meridian into separate dorsal and ventral halves. More than half of the visual cortex is devoted to processing the central 10° of vision. (With permission of Horton and Hoyt 1991a)

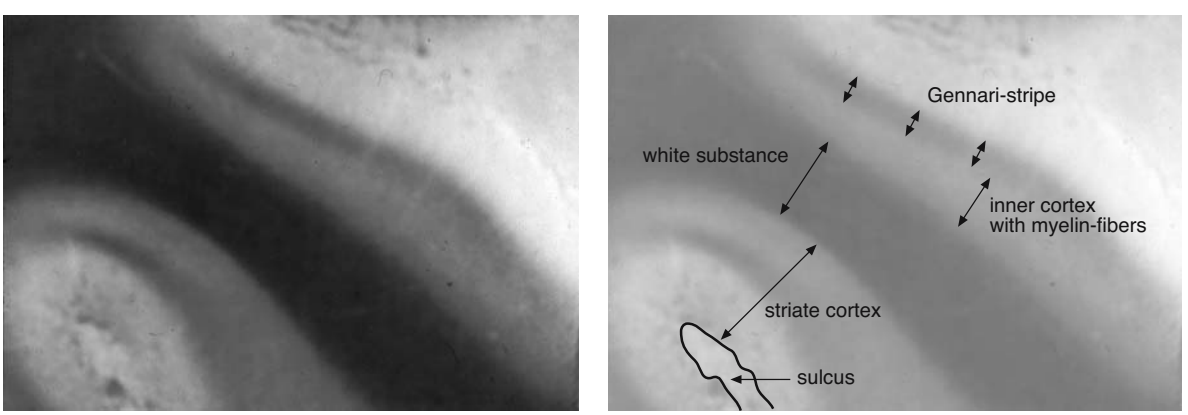

Fig. 2.51.a PD-weighted high resolution MRI (3.8 T) of a human specimen (1.5 mm thickness) of the striate cortex. **b** Corresponding diagram (the compartments are shown lateral to the white substance)

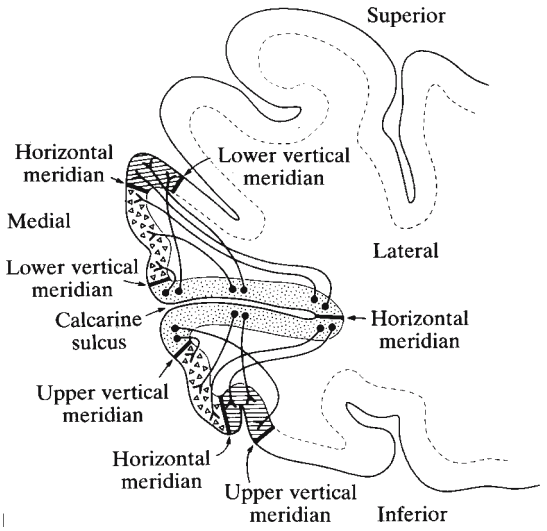

Fig. 2.52. Schematic coronal section through right occipital lobe showing connections from V1 (*stippled area*) to V2/V3 (*small triangles* and *striped*, respectively). Projections pass between common retinotopic coordinates. In V1, the horizontal meridian is represented along the base of the calcarine sulcus. Fibers coursing in the white matter of the upper and lower calcarine banks serve the lower and upper visual quadrants, respectively. For simplicity, feedback pathways from V2/V3 to V1 and projections between V2 and V3 are omitted. The ventral V1 and V3 pathway is doubtful (Van Essen et al. 1986). (With permission of Horton and Hoyt 1991a)

References

Breslau J, Dalley RW, Tsuruda JS, Hayes CE, Maravilla KR (1995) Phased-array surface coil MR of the orbits and optic nerves. Am J Neuroradiol 16:1247–1251

Bron AJ, Tripathi RC, Tripathi BJ (1997) Wolff's anatomy of the eye and orbit, 8th edn. Chapman and Hall, London

Casper DS, Chi TL, Trokel SL (1993) Orbital disease. Imaging and analysis. Thieme, New York

Clark VP, Courchesne E, Grafe M (1992) In vivo myeloarchitectonic analysis of human striate and extrastriate cortex using magnetic resonance imaging. Cereb Cortex 2:417–424

Curnes JT, Burger PC, Djang WT, Boyko OB (1988) MR imaging of compact white matter pathways. AJNR Am J Neuroradiol 9:1061–1068

Daniels DL, Leighton PM, Mafee MF et al (1995) Anatomic moment. osseous anatomy of the orbital apex. AJNR Am J Neuroradiol 16:1929–1935

Duvernoy HM (1998) The human hippocampus, 2nd edn. Springer, Berlin Heidelberg New York

Helmke K, Hansen HC (1996) Fundamentals of transorbital sonographic evaluation of optic nerve sheath expansion under intracranial hypertension. I. Experimental study. Pediatr Radiol 26:701–705

Hoffmann KT, Hosten N, Lemke AJ, Sander B, Zwicker C, Felix R (1998) Septum orbitale: high-resolution MR in orbital anatomy. AJNR Am J Neuroradiol 19:91–94

Holmes G (1945) The organization of the visual cortex in man. Proc R Soc Lond B 132:348–361

Horton JC, Hoyt WF (1991a) Quadrantic visual field defects. Brain 114:1703–1718

Horton JC, Hoyt WF (1991b) The representation of the visual field in human striate cortex. A revision of the classical Holmes map. Arch Ophthalmol 109:816–824

Horton JC, Landau K, Maeder P, Hoyt WF (1990) Magnetic resonance imaging of the human lateral geniculate body. Arch Neurol 47:1201–1206

Kitajima M, Korogi Y, Takahashi M, Eto K (1996) MR signal intensity of the optic radiation. AJNR Am J Neuroradiol 17:1379–1383

Lang J (1981) Klinische Anatomie des Kopfes. Springer, Berlin Heidelberg New York, p 92

Nieuwenhuys R, Voogd J, van Huijzen C (1988) The human central nervous system, 3rd edn. Springer, Berlin Heidelberg New York, pp 20, 92, 107, 182, 183

Oikawa S, Kyoshima K, Kobayashi S (1998) Surgical anatomy of the juxta-dural ring area. J Neurosurg 89:250–254

Renn WH, Rhoton AL Jr (1975) Microsurgical anatomy of the sellar region. J Neurosurg 43:288–298

Rhoton AL, Natori Y (1996) The orbit and sellar region: microsurgical anatomy and operative approaches. Thieme, New York

Servo A (1982) Visualization of the superior ophthalmic vein on carotid angiography. Neuroradiology 23:141–146

Van Essen DC, Newsome WT, Maunsell JHR, Bixby JL (1986) The projections from striate cortex (V1) to areas V2 and V3 in the macaque monkey: asymmetries, areal boundaries, and patchy connections. J Comp Neurol 244:451–480

Williams PL (1995) Gray's anatomy, 38th edn. Churchill Livingstone, New York

Wong AM, Shape JA (1999) Representation of the visual field in the human occipital cortex: a magnetic imaging and perimetric correlation. Arch Ophthalmol 117:208–217

The requested page could not be found.

3 Neuro-ophthalmology: A Short Primer

Urs Schwarz

CONTENTS

3.1 Introduction

The spectacular symbiosis between the visual system, the vestibular system, and the optomotor system, each of which is a miracle on its own, is able to solve an abundant array of amazing tasks (Fig. 3.1). In particular, the connection between vision and the optomotor control is most intriguing, as the eye performs both the input and the output simultaneously. Altogether, it is not surprising that the implementation of these intricate neural networks encompasses almost every part of the brain (Fig. 3.2). Moreover, these systems are probably amongst the best investigated so far; and enormous knowledge has been amassed over the past few decades employing a variety of techniques from single cell recordings, optical imaging, eye movement recordings, functional magnetic resonance imaging, to neuropsychological examinations. In addition, this research has clarified many fundamental principles of neural and neuronal processing, which subsequently have enriched other fields of brain research as well as computational neuroscience.

The optomotor system provides a magnificent window into the nervous system for clinicians, as people suffering from even the smallest disruption soon are unable to pursue their regular routines. Armed with thorough neuroanatomical and neurophysiological knowledge of this system's workings, a clinician will be able to diagnose and localize many conditions right at the bedside.

A systematic review bearing on the whole spectrum of normal and pathological visual, vestibular, and optomotor neural processing would be more than one's lifetime work. Hence, this improperly short primer is very selective, fractional, and undeniably biased. An attempt was made to seduce the reader to dive further into this fascinating realm of neuro-ophthalmology by presenting a basic framework of functional neuroanatomy. The basic neuroscientist will find plenty in the works of Carpenter (1988), Zeki (1993), Milner and Goodale (1995), Wandell (1995), Zigmond et al. (1999), Kandel et al. (2000); the clinician, on the other hand, will find more answers in the seminal oeuvres (Baloh and Honrubia 1990; Grüsser and Landis 1991; Miller and Newman 1997; Huber and Kömpf 1998; Leigh and Zee 1999).

3.2 Vision and Visual Perception

Light entering the eye is projected onto the retina, where it is converted into an electrical signal by the

U. Schwarz, MD
Priv.-Doz., Department of Neurology, University Hospital (USZ), Frauenklinikstrasse 26, 8091 Zürich, Switzerland

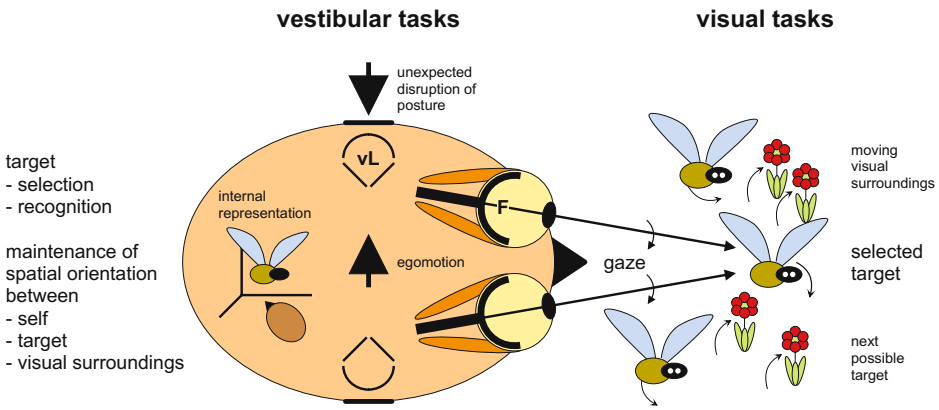

Fig. 3.1. Optomotor tasks. The visuo-, vestibulo-, and proprioceptive-optomotor systems ensure maintenance of orientation in space as well as target selection and recognition despite a host of sensory conflicts and adversary disturbances. Its main goals are to keep the target of interest on the fovea (stabilization of gaze) and to produce an accurate internal representation of spatial relations between the visual surroundings, the target, and the self. *vL*, vestibular labyrinth

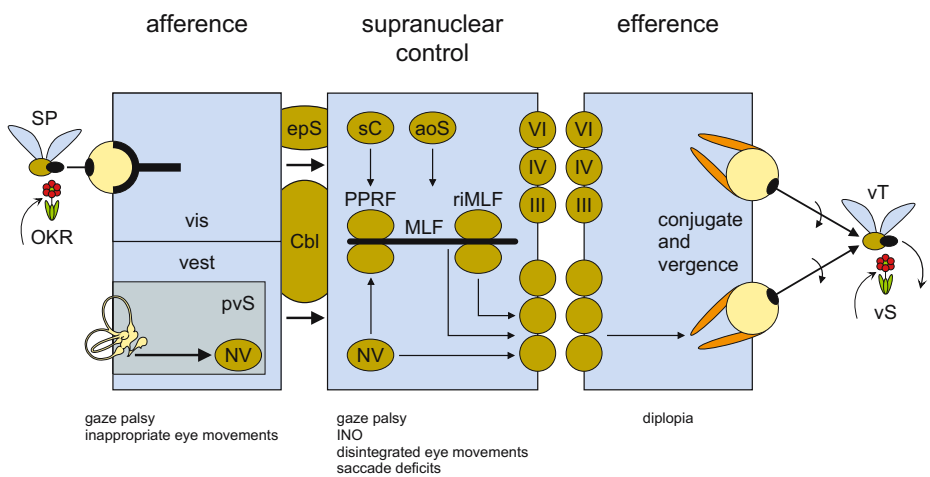

Fig. 3.2. Synopsis of the optomotor system (modified after Schwarz et al. 2000). Multisensory, visual, vestibular, and proprioceptive (not shown) signals (afference) are cortically and subcortically integrated and guided to the supranuclear optomotor control system, which computes appropriate conjugate and vergence signals for each eye muscle and distributes them via the medial longitudinal fasciculus (*MLF*) to the individual oculomotor nuclei (efference). Therefore, the supranuclear control implements the final common pathway for any mechanism that requests eye movements. Typical eye movement patterns due to lesions of the afferences, supranuclear control, and efferences are shown at the *bottom*. The exemplary scene shows the complexity of the visual computation: While smoothly following a moving visual target (*vT*) with the eyes, the visual surroundings (*vS*) is shifted in the opposite direction (evoking full field stimulation) and, hence, elicits an optokinetic response (*OKR*). Sensory integration must solve the problem of these counteracting demands and generate appropriate signals to the supranuclear control for smooth pursuit eye movements (*SP*) only. *pvS*, peripheral vestibular system; *epS*, extrapyramidal system; *aoS*, accessory optic system; *Cbl*, cerebellum; *NV*, vestibular nucleus; *PPRF*, paramedian pontine reticular formation; *riMLF*, rostral interstitial nucleus of the MLF; *III*, oculomotor nucleus; *IV*, trochlear nucleus; *VI*, abducens nucleus; *INO*, internuclear ophthalmoplegia

photoreceptors. A geometrically well-defined array of these highly specialized cells connects via an intrinsic local network to one single ganglion cell, thus implementing the first receptive field of the visual system. Consecutively, signals of the retinal ganglion cells are transmitted through their axons, which together form the optic nerve, to the optic chiasm in front of the pituitary stalk, where half of them are cross routed: Axons from the temporal half of one retina join axons from the nasal part of the other retina in the optic tract. Axons from the temporal retina remain ipsilateral. Hence, visual objects in one hemifield, which are projected nasally onto the ipsilateral retina and temporally onto the contralateral retina, are processed in contralateral central visual centers with information coming from both retinae.

The optic tract projects to three major subcortical structures:

- The pretectum controls the pupillary reflex.
- The superior colliculus controls saccadic eye movements.
- The lateral geniculate nucleus is the major relay for input to the visual cortex.

Signals for each geniculate cell are sampled from a distinct ensemble of ganglion cell axons, which establishes the next layer of receptive fields. Finally, axons emerging from the geniculate nuclei are projected onto layer 4 of the striate (primary) visual cortex (Brodmann area 17), which is located at the pole of the occipital lobe (Fig. 3.3). Here, visual information – already partially segregated into simple graphical categories – is analyzed further (Marr 1982; Livingstone and Hubel 1988; Hubel 1988). In parallel, even more specialized receptive fields sample primitive graphical properties – such as color, form and size, position, orientation, speed, and depth and disparity – of visual objects, which, in turn, are transmitted to various dedicated areas in the extrastriate visual cortex (Brodmann areas 18, 19, and 37) (Brodmann 1909; Zeki 1993; Wandell 1995; Zilles and Clarke 1997). Each of these many regions reconstructs a purpose-filtered map of the visual world or attended parts of it. Connected to other cortical areas, this information will be used to solve such complex tasks as face recognition, target selection, processing of target motion and optic flow patterns, computation of the direction of motion, generation of eye and limb movements, and many more. In particular, L. Ungerleider and M. Mishkin

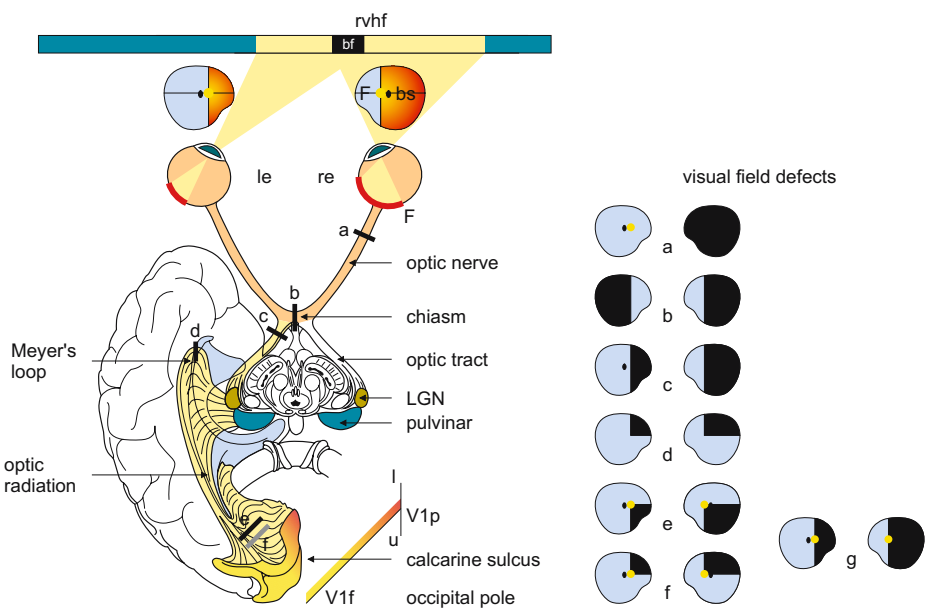

Fig. 3.3. Anatomy of the retino-geniculo-cortical system and typical visual field defects. *Left panel.* The right visual hemifield (*rvhf*) projects to the nasal portion of the right and the temporal portion of the left retina. Retinal ganglion cell axons form the optic nerve. Fibers from the nasal retinal half cross the midline in the optic chiasm and join those from the temporal retinal half of the other eye, which remain ipsilateral, in the optic tract and synapse in the superior colliculus and tectum (both not enhanced) as well as in the lateral geniculate nucleus (*LGN*). Axons emerging from the LGN arc around the inferior horn of the lateral ventricle, forming the optic radiation with its lowermost part called Meyer's loop. They end at the striate visual cortex (*V1*). Note the overrepresentation (magnification) of the foveal part (shown by the *shadings* in the visual hemifield and *V1*). Moreover, the visual hemifield is divided by the calcarine sulcus. The lower part projects above the sulcus, the upper part below it. The pulvinar of the thalamus receives its input directly from V1 (layer 5, Fig. 3.12). *Right panel.* Visual defects (shown as *black areas*) are produced by distinct lesions in the retino-geniculo-cortical pathway. *a* Total loss of vision due to a lesion in the optic nerve. *b* Bitemporal hemianopsia due to a lesion in the center of the optic chiasm. *c* Contralateral homonymous hemianopsia to the right including the fovea due to a lesion along the optic tract *d* Anopsia in the upper right quadrant of the visual field including the fovea due to a lesion in Meyer's loop. *e/f* Partial deficits, including narrow scotomas (not shown), result from lesions close to the striate cortex. *e* A deficit resulting from a lesion in the upper part of the optic radiation. *f* A deficit after a lesion in the lower part. *g* Due to the large representation of the fovea and the fact that the occipital pole receives its blood supply from two main arterial systems, the fovea is often spared in lesions close to the striate cortex. le, left eye; re, right eye; *bf*, binocularly seen part of the *rvhf; F*, fovea; *V1f*, foveal representation in visual area 1; *V1p*, peripheral representation in visual area 1; *d*, projection of lower visual hemifield; *u*, projection of upper visual hemifield

defined two anatomically distinct major pathways (Ungerleider and Mishkin 1982) (Fig. 3.4):

- Occipito-parietal regions form the ventral or 'where' pathway, which subserves spatial vision. These regions are also referred to as the 'how' pathway, which subserves all visually guided action by implementing visuomotor transformation (Milner and Goodale 1995).
- Occipito-temporal regions form the dorsal or 'what' pathway, which subserves object vision.

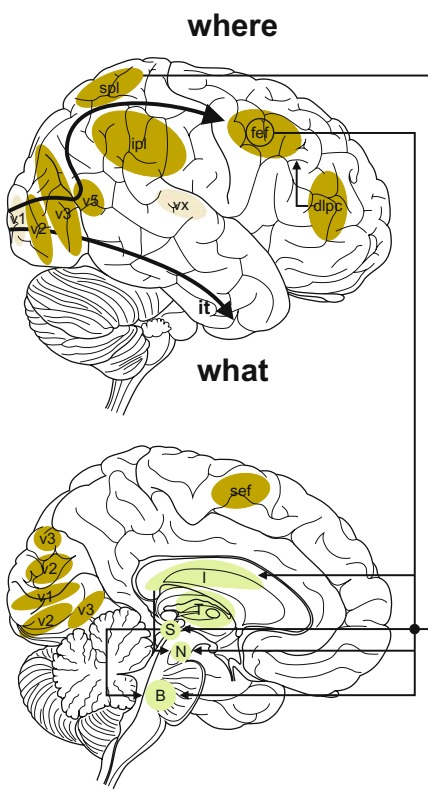

Fig. 3.4. Cortical and subcortical control of visually induced or volitional eye movements (modified after Schwarz et al. 2000). Note: Due to considerable variability, cortical areas are shown patchy and approximately. After primordial analysis of the visual scene in the striate cortex (*v1*, BA 17) and the first relay in the extrastriate cortex (*v2*, BA 18), signals are forwarded in two distinctly different pathways: The ventral *what* stream transmits object properties, such as shape and color, to the inferior temporal cortex (*it*). The dorsal *where* stream routes position and velocity signals via the polysensory posterior parietal cortex (*spl*, *ipl*), which adds additional information, in particular, from the primary vestibular cortex (*vx*, BA 41, BA 42), and projects to the frontal eye fields (*fef*, BA 6 in humans), supplementary eye fields (*sef*, BA 6), and dorsolateral prefrontal cortex (*dlpc*, BA 46) where cortical eye movement commands are generated. The frontal eye field activates the brain stem optomotor centers, directly or indirectly via the superior colliculus (*S*). In addition, signals are routed to the substantia nigra (*N*), which projects back to the striatum (*I*) via the thalamus (*T*). Therefore, each eye movement also activates the extrapyramidal system (see Fig. 3.39). *BA*, Brodmann area; *v1*, primary visual cortex; *v2–v5*, extrastriate visual areas; *spl*, superior parietal lobule BA 5, BA 7); *ipl*, inferior parietal lobule (BA 39, BA 40); *B*, brain stem optomotor centers

In summary, it is important to realize that the visual system first splits the contents of the visual world into various simple graphical categories in order to then reconstruct many filtered versions of it that are used in parallel to solve a variety of cognitive and motor tasks. Moreover, it implies that no single region of the brain represents the visual world the way we psychologically perceive it: as a whole entity. Rather, there are many representations of it throughout the brain, which explains at once the variety of clinically distinct signs and symptoms in connection with different focal cortical lesions (Grüsser and Landis 1991).

3.2.1 Receptive Fields

Receptive fields are the fundamental neuronal tools of neural information processing networks. In essence, they establish a computational rule by which a specific spatial and/or temporal input pattern to the cell is converted into a temporal discharge profile (Fig. 3.5). In particular, in visual physiology where the expression was first coined by Hartline, receptive fields are simply defined as the region of the retina that must be illuminated to obtain a response (Hartline 1938).

The receptive field of a visual neuron is mapped electrophysiologically by observing its response to an array of stationary and moving visual stimuli of different sizes, orientations, shapes, and colors (Fig. 3.6). Over the past few decades, a host of receptive fields has been defined at almost every stage of visual processing: From retinal ganglion cells (Kuffler 1953), simple and complex cells of the primary visual cortex (Figs. 3.7, 3.8) (Hubel and Wiesel 1959), to even more elaborate computers such as velocity tuned cells in motion-processing areas, neurons at progressively higher levels in visual processing have progressively larger and more complex receptive fields (Livingstone et al. 2001).

From an engineering point of view, receptive fields are linear or nonlinear filters. Not surprisingly, attempts were soon made to fit the response curves to mathematical models and express the receptive field as a filter's pulse response. Successful examples comprise difference-of-Gaussians (DOG) filters for simple center-surround profiles (Rodieck 1965), and the more complex Gabor filters (Gabor 1946) for simple cells, which were documented experimentally (Jones et al. 1987; Jones and Palmer 1987a,b) based on theoretical considerations (Daugman 1985) (Fig. 3.9).

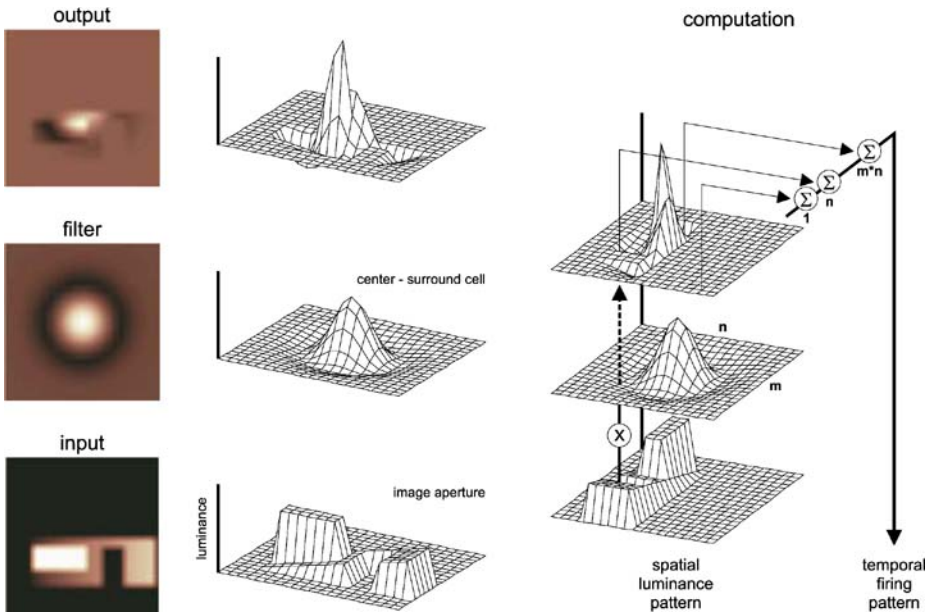

Fig. 3.5. Receptive fields are filters. The physical image is depicted as a landscape of luminance. The exemplary simple center-surround cell picks up the overall luminance change in its aperture (receptive field) by folding (×) the input with its transfer function (receptive field property). The *left panel* shows pseudo-colored 2D representations of the image, the pulse response of the cell (difference-of-Gaussians, DOG), and the folded image. The *middle panel* shows 3D representations of the former, where the signal intensity is shown on the z-axis. The *right panel* depicts the transformation from spatial input to temporal output by convolution (shown for three image elements only). The sum of all spatial elements (m^*n) will determine the firing frequency. Note that the output of this simple filter is not unambiguous, as the same firing pattern will be obtained after rotation of the image

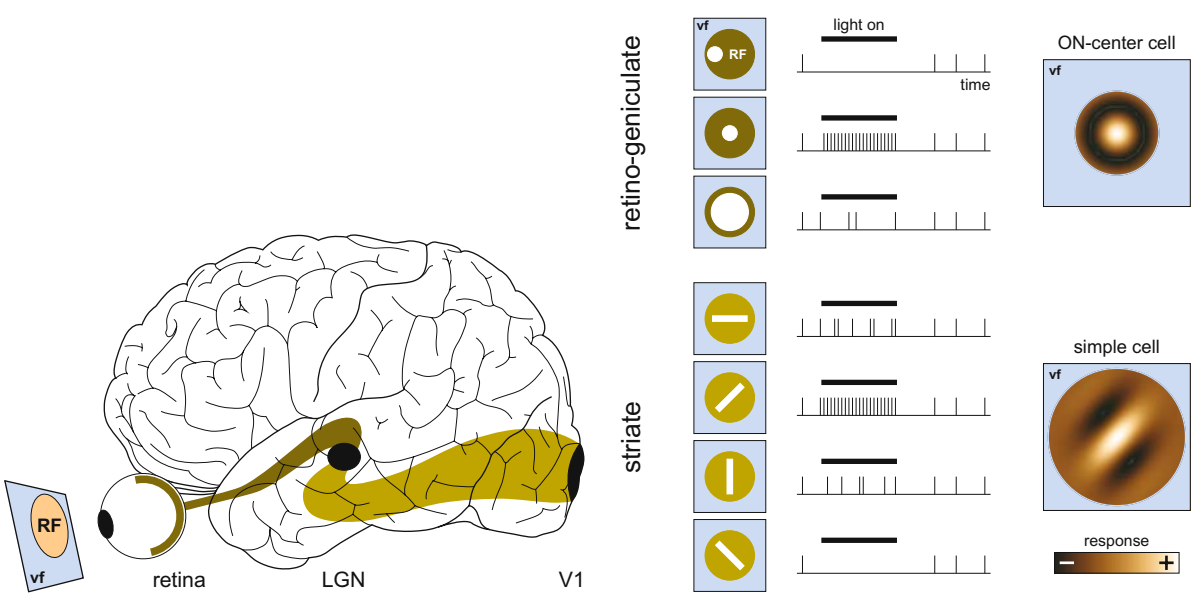

Fig. 3.6. The properties of receptive fields are obtained by single cell recording in animals (after Hubel and Wiesel 1959; Wurtz and Kandel 2000). *Left panel*. Single neurons are recorded in the retina, the lateral geniculate nucleus (*LGN*), and the striate visual cortex (*V1*). Their receptive fields (*RF*) are mapped with various visual stimuli. *Right top panel*. Single cells in the retina and the LGN discharge differently to small light spots at various positions in their receptive field (*bold bar* indicating illumination). In the exemplary cell, mapping would reveal an ON-center organization of the receptive field (simulated by a difference-of-Gaussian filter). *Right bottom panel*. Simple cells in V1 respond best to light bars at a certain position and, in particular, a certain orientation within its receptive field. A versatile Gabor filter is used to simulate the full extent of this hypothetical cell's receptive field. *vf*, visual field

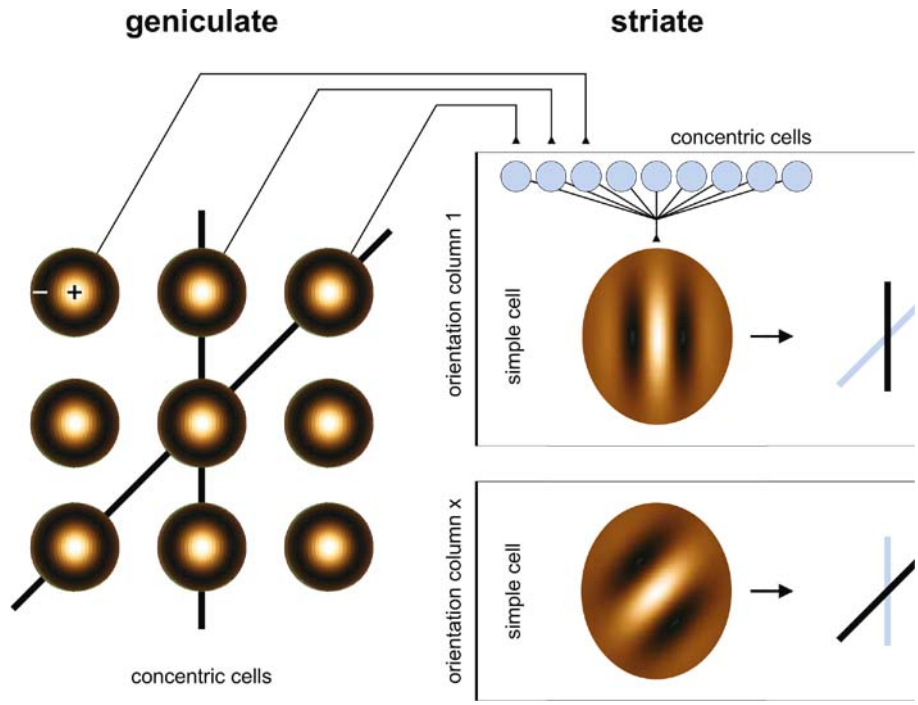

Fig. 3.7. Simple receptive fields in the striate visual cortex (*V1*) (after Hubel and Wiesel 1962; Wurtz and Kandel 2000). A small cluster of exemplary concentric genicular ON-center cells project to concentric cells in layer 4C of V1 (shown are three connections only), which, in turn, connect to simple cells that are located in a different orientation column. According to the layout of its receptive field (modeled by a set of Gabor filters), each of the simple cells will respond best to a certain orientation of a bar, hence, implementing the next step in feature extraction

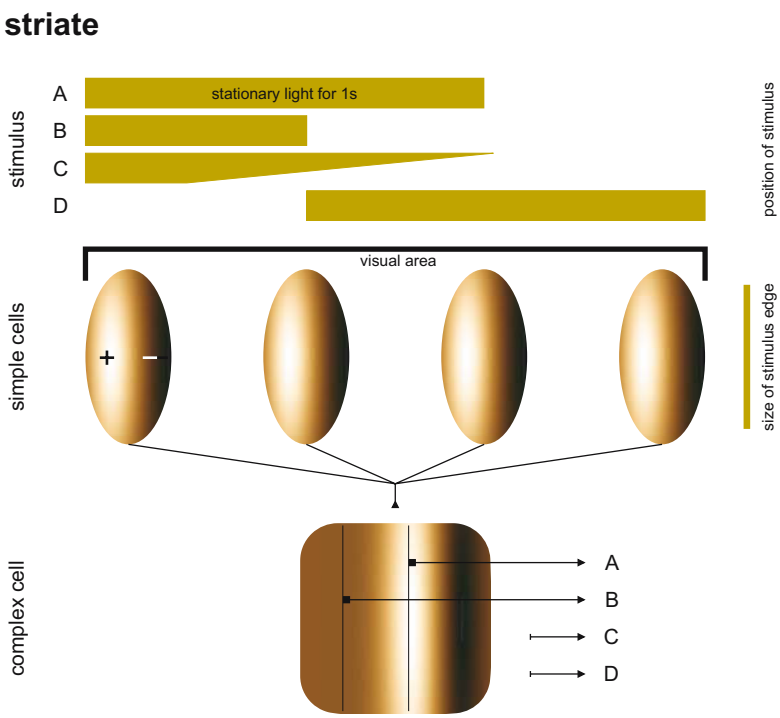

Fig. 3.8. Complex receptive fields in the striate visual cortex (*V1*) (after Hubel and Wiesel 1962; Wurtz and Kandel 2000). Simple cells (modeled by a set of Gabor filters), each of which monitors a small space in the visual field, connect to a complex cell. The cell responds best to a bar of light at a certain position and orientation of its edge with respect to the cluster of simple cells. A hypothetical complex receptive field property is shown at the *bottom*. In this case, *stimulus A* elicits the maximal response while *stimulus B* elicits a smaller response. *Stimuli C* and *D* will not yield any response

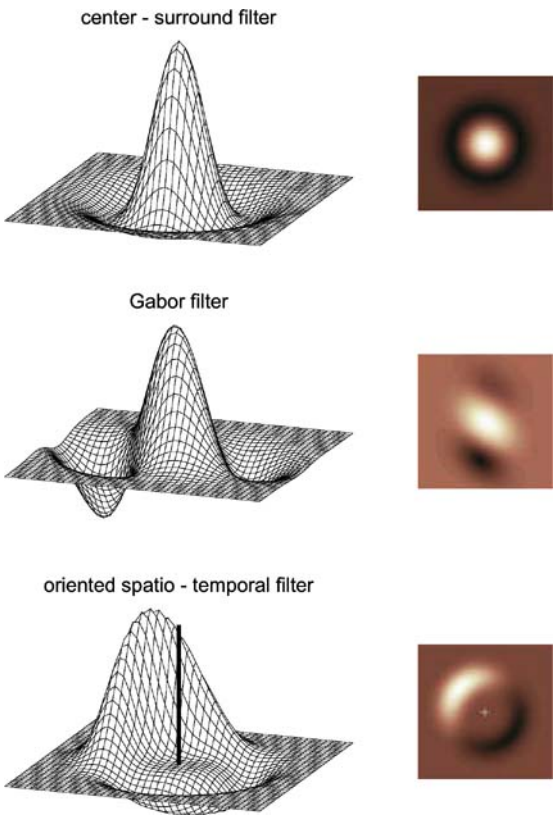

Fig. 3.9. Filter cascade of the visual system. Shown are 3D and pseudo-colored 2D pulse responses of a typical simple center-surround filter (*LGN*), a Gabor filter (*striate cortex*) (Daugman 1985; Jones et al. 1987; Jones and Palmer 1987a,b), and a hypothetical, oriented spatiotemporal filter (*V5*, *MT/MST*)

3.2.2 The Retino-geniculo-cortical Pathway

3.2.2.1 The Retina

Light is focused by the cornea and lens before it reaches the layer of photoreceptors in the retina with its two distinct regions: The fovea, where vision is most acute due to the arrangements of the receptors, and the optic disc, which contains no receptors and constitutes the blind spot. The human retina contains two kinds of receptors that absorb light and transduce it into electrical signals (Reid 1999):

- Cones, concentrated in the fovea and specialized for day vision, are most sensitive for direct rays and mediate color vision since they discriminate between different parts of the visible light spectrum. Losing their function renders people legally blind. Several inherited defects of color vision are known. The most common form is found in trichromats with one or more anomalous cone pigments. In more severe forms, a single cone type is missing entirely (dichromats), which results in the disability to distinguish certain color-combinations: protanopia (red-blindness), deuteranopia (green-blindness), and tritanopia (blue-blindness). However, only monochromats (one cone type only) are truly color-blind.
- Rods, not present in the fovea and specialized for night vision, are most sensitive to scattered light and achromatic.

The output of these light receptors is transmitted via a complex local network of horizontal, bipolar, and amacrine interneurons to the retinal ganglion cells, whose axons travel to the optic disc where they become myelinated and establish the optic nerve.

The input to the ganglion cells comes from receptors within a circumscribed area and implements the first receptive field within the visual system. These fields are circular in shape, of varying size, and with a distinct center-and-surround layout. Two classes can be distinguished: On-center ganglion cells are excited by light directed to their center, whereas off-center ganglion cells are inhibited by light to that region of their receptive field (Fig. 3.7). Since both classes are present in roughly the same number, and each photoreceptor sends its output to both types of ganglion cells, they form two parallel input streams for higher-order visual processing (Mansilla et al. 1995; Lee 1996).

The response of ganglion cells is optimized for the detection of contrast, rather than the intensity of the image, and for fast changes in the visual scene. Moreover, ganglion cells can be divided into two groups, both of which include on-center and off-center cells (Schein 1987; Livingstone and Hubel 1988; Shapley et al. 1991; Croner and Kaplan 1995; Benardete and Kaplan 1997a,b):

- M-cells with large receptive fields respond best to large objects and rapid changes in the stimulus. They form the magnocellular pathway, which establishes the first step in motion processing.
- P-cells, on the other hand, with small receptive fields that respond to color constitute the parvocellular pathway that establishes the first step in object processing.

3.2.2.2 The Lateral Geniculate Nucleus

The majority of retinal ganglion cells (~90%) synapse in the lateral geniculate nucleus (LGN) of the

thalamus, which carries visual information to the cerebral cortex. The projection preserves the retinotopic representation of the contralateral visual hemifield, although the fovea is represented much larger (~50% of the lateral geniculate nucleus) than the retinal periphery. This disproportionate representation is commonly expressed by a magnification factor: The ratio of the area in the lateral geniculate nucleus that maps a 1° area in the retina.

The lateral geniculate nucleus consists of six layers. Ganglion cells from the ipsilateral and the contralateral retina end at different layers. Axons of the ganglionic M-cells project to the ventral layers 1 (contralateral retina) and 2 (ipsilateral retina), while those of the P-cells project to layers 3 and 5 (ipsilateral retina) and 4 and 6 (contralateral retina) (Wurtz and Kandel 2000). In addition, a third class of retinal ganglion cells projects to the intercalated layer between the M- and P-layers. This koniocellular pathway, which is not yet well understood, seems to perform fast visual motion processing as well as color processing (Martin et al. 1997; Morand et al. 2000; Hendry and Reid 2000).

Receptive fields in the lateral geniculate nucleus are similar to those of the retinal ganglion cells, with a small concentric on-center or off-center layout (Fig. 3.7). They respond best to small spots of light, whereas diffuse light scatter produces only weak responses. Altogether, they advance segregation of the visual image into the main categories of spatial and object vision (Wiesel and Hubel 1966; Pettigrew and Dreher 1987; Shou and Leventhal 1989; Gawne et al. 1991; McClurkin et al. 1991a,b; DeAngelis et al. 1995; Funke et al. 1996; Alonso et al. 1996; Cai et al. 1997; Benardete and Kaplan 1997a,b, 1999; Wolfe and Palmer 1998; Usrey et al. 1999; Ruksenas et al. 2000).

Without this important relay, the ability for visual perception is lost, although some limited visual capacity to detect visual elements and their motion coarsely (blindsight) is preserved by direct pathways passing through the superior colliculus (Fig. 3.10) (Weiskrantz 1990; Williams et al. 1995).

3.2.2.3 The Primary Visual Cortex

The primary visual cortex (visual area 1: V1, Brodmann area 17) is located at the pole of the occipital lobe extending along its medial surface, which is divided by the calcarine fissure, to the parieto-occipital sulcus (Fig. 3.11). Because of a conspicuous white stripe, which is caused by myelinated axons in layer 4 (stria of Gennari), it is also called the striate cortex. The input to the striate cortex comes from both eyes, yet exclusively from the contralateral visual hemifield. Projections from the retina remain strictly retinotopic, with a large overrepresentation of the fovea (~50%, magnification factor), which begins at the occipital pole. The upper part of the visual hemifield is projected onto cells below the calcarine fissure, the lower part to cells above it.

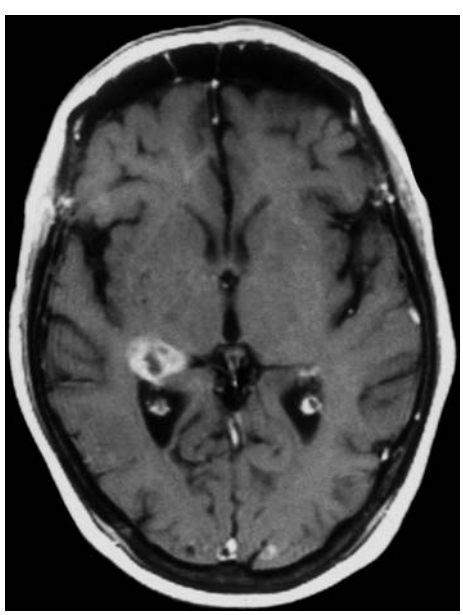

a

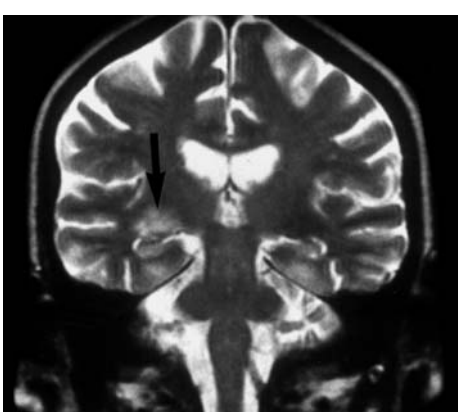

b

Fig. 3.10a,b. A 63-year-old woman with acute vision impairment and known breast carcinoma. Diagnosis: metastasis at the right lateral geniculate nucleus. MR: **a** Axial T1-weighted contrast-enhanced image showing a central necrotic tumor in the region of the right thalamic pulvinar. **b** Coronal T2-weighted view with infiltration of right optic tract (*arrow*) and the lateral geniculate nucleus. (With permission of Dr. R. Gustorf-Aeckerle, Katharinenhospital, Stuttgart)

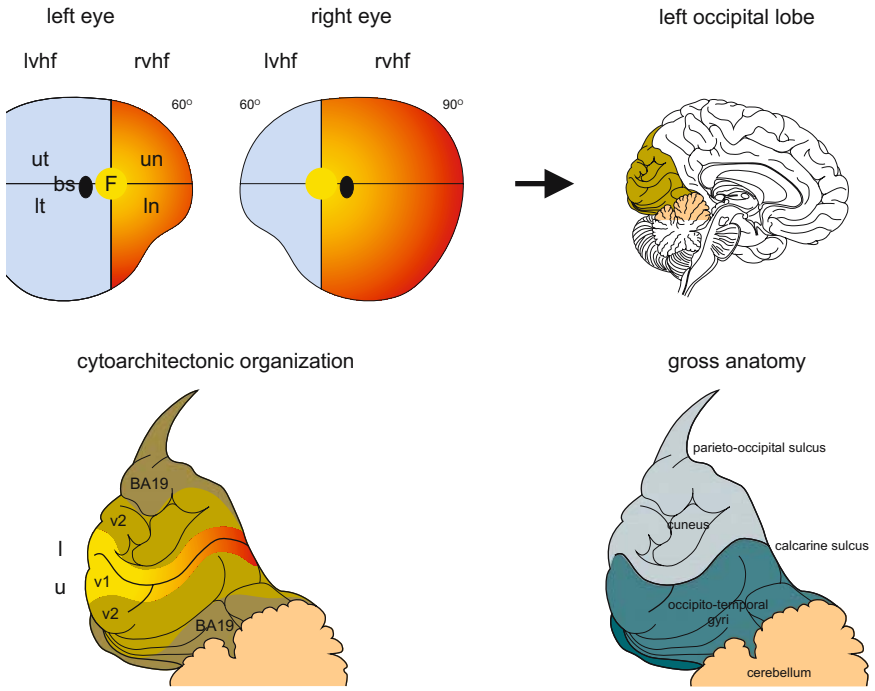

Fig. 3.11. Representation of the visual field in the primary visual cortex (after Figs. 5b and 12 of Nieuwenhuys et al. 1988). *Top left panel*. The right visual hemifield is represented retinotopically in v1 of the left occipital lobe, which is shown in the *top right panel*. *Bottom left panel*. Cytoarchitectonic organization of the medial aspect of the occipital lobe according to Brodmann (1909) showing layouts of *v1, v2,* and *BA19*, which contains many extrastriate visual areas. Note that this organization does not adhere to gross anatomical features. Different color gradients in the visual hemifield and along *v1* indicate the magnification of the fovea (*yellow*) that is located at the occipital pole with respect to the periphery (*red*) that extends to the parieto-occipital sulcus. *Bottom right panel*. Gross anatomy of the left occipital sulcus. *lvhf*, left visual hemifield; *rvhf*, right visual hemifield; *ut*, upper temporal quadrant; *lt*, lower temporal quadrant; *un*, upper nasal quadrant; *ln*, lower nasal quadrant; *l*, lower; *u*, upper; *v1*, striate visual cortex (Brodmann area 17); *v2*, extrastriate visual area (Brodmann area 18); *BA19*, Brodmann area 19

Axons from the lateral geniculate nucleus travel via the optic radiation, which curves around the inferior horn of the lateral ventricle into the temporal lobe (Meyer's loop) for the lower half of the retina. They synapse in two layers of the striate cortex (Fig. 3.12):

- The magnocellular and parvocellular pathways end in different sublaminae of layer 4C.
- The koniocellular pathway ends in layers 2 and 3.

These axons carry input into a complex intrinsic neural engine, which is highly organized into functional modules with respect to retinal topography and visual contents and establishes the most important engine for visual perception (Hubel and Wiesel 1959, 1962; Livingstone and Hubel 1988; Reid 1999; Wurtz and Kandel 2000):

- Ocular dominance columns
  Alternating patches in layer 4 receive input from either the right or left eye via their respective layers in the lateral geniculate nucleus.

They are further subdivided into:

- Orientation columns
  Small vertically grouped ensembles of cells with a concentric receptive field cell in layer 4C and simple cells above and below monitor identical retinal positions and respond to identical axes of orientation. Since the axis of orientation is slightly shifted from one column to the other, a group of adjacent columns smoothly covers the whole cycle of orientation changes. Simple cells of each column project onto a complex cell, which are selective for orientation and direction of visual stimuli within their receptive fields.
- Blobs
  Barrel-shaped ensembles of cells in layers 2 and 3 only that respond to color but not orientation are scattered between orientation columns. They receive their input solely from interneurons that are linked to the parvocellular pathway.

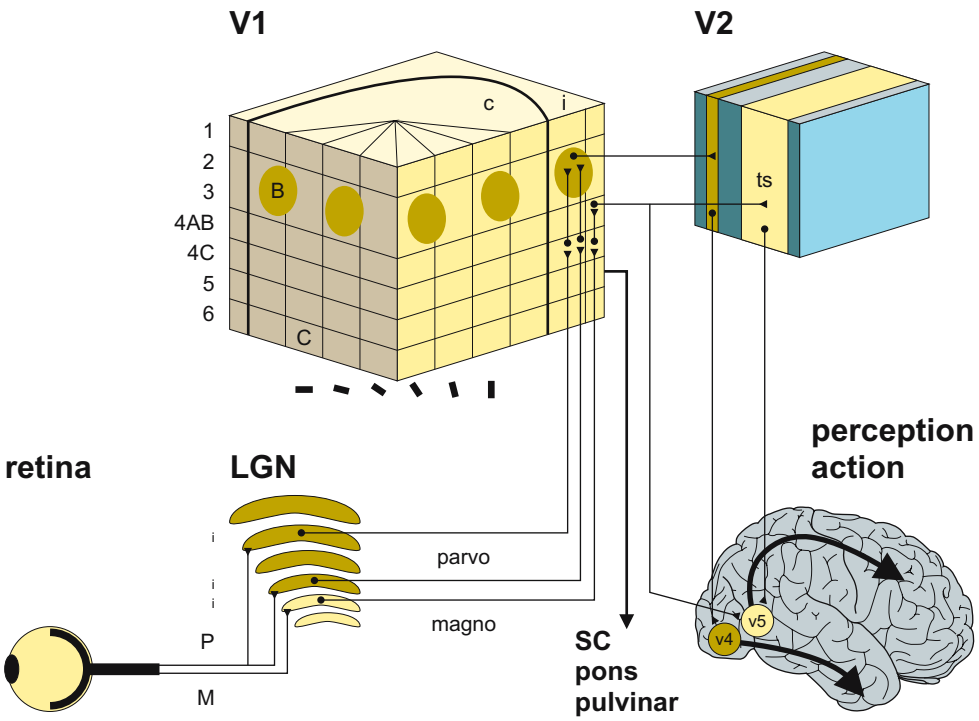

Fig. 3.12. Simplified synopsis of major visual pathways from the retina to higher-order processing units in the cortex (after Wurtz and Kandel 2000). See text for description. Two distinctly different pathways transmit signals for feature extraction (*mustard*) and position processing (*yellow*). The former is implemented first by the retinal P-ganglion cells, which synapse at the outer layers of the lateral geniculate nucleus, continues as the parvocellular (*parvo*) pathway to layer 4C in V1, and finally ends in the blobs (*B*). Blobs project to the thin stripes of V2, where axons emerge travelling via V4 to inferior temporal areas. In contrast, position processing starts with the retinal M-ganglion cells synapsing at the inner layers of the LGN, continues in the magnocellular (*magno*) pathway to layer 4C in V1, and ends in layer 4B within an orientation column. Layer 4A axons carry information to extrastriate area V5, either directly or via the thick stripes (*ts*) in V2, which, in turn, project to area V5. A slab of V1 constitutes a hypercolumn, which processes visual information from a small area of the visual field. It consists of orientation columns, which contain directional sensitive, simple (and complex) cells that form a smooth continuum (*black bars*). In addition, signals from each eye are processed in separate, ipsilateral, and contralateral ocular dominance patches (*bold black line*). *V1*, primary visual cortex; *V2*-*V5*, extrastriate visual areas; *M*, M-ganglion cells; *P*, P-ganglion cells; *c*, contralateral; *i*, ipsilateral; *C*, orientation columns

A complete set of such computational engines, which together respond to lines of all orientations within a certain very small area of the visual field, is referred to as a hypercolumn (Hubel and Wiesel 1979; LeVay et al. 1985). It covers ~1mm^2 of the striate visual cortex and is repeated regularly. Within such hypercolumns, columns that code the same orientation are interconnected horizontally through cells in layers 3 and 5. These additional connections effectively allow integration of visual information that lies outside a cell's receptive field and, thus, may contribute to the fact that a cell's orientation can be influenced by the context of a visual feature (orientation plasticity) (Wurtz and Kandel 2000).

Each set transmits signals to a variety of structures:

- Cells above layer 4C project to cortical structures.
  - Layers 2 and 3 cells connect to extrastriate areas V2, V3, and V4. In addition, axons cross via the corpus callosum to corresponding cortical areas on the other side of the brain.
  - Layer 4B cells connect to the middle temporal area V5.
- Cells below layer 4C project to subcortical structures.
  - Layer 5 cells connect to the pulvinar, the superior colliculus, and the pons.
  - Layer 6 cells connect back to the lateral geniculate nucleus and the claustrum.

3.2.2.4 Lesions in the Retino-geniculo-cortical Pathway

Solitary small lesions in the retino-geniculo-cortical pathway produce typical, localizing gaps in the visual field. These deficits are summarized in Fig. 3.3. Note that removal of binocular input, in particular, affects the perception of stereopsis. They may be caused by the full scope of known etiologies and typically are accompanied by other neurological signs or symptoms (for review see Miller and Newman 1997):

- Strokes
  Note: The primary visual cortex receives its blood supply mainly from the posterior cerebral artery, which originates in the posterior circulation; all other structures, including a small part of the occipital pole (middle cerebral artery), receive their supply from branches of the internal carotid artery.
  - Ischemic, e.g., thromboembolic event, venous thrombosis, vasculitis, coagulopathy, migraine related.
  - Hemorrhagic, e.g., vascular malformations, amyloid angiopathies.
- Inflammatory processes
  - Acute, e.g., abscess, meningitis, encephalitis, acute disseminated encephalomyelitis.
  - Chronic, e.g., multiple sclerosis, sarcoidosis, syphilis, borreliosis, AIDS, progressive multifocal leukoencephalopathy, early stage of prion disease affecting primarily occipital and parietal areas (Heidenhain's variant).
- Space-occupying processes
  - Tumor
  - Vascular malformation
  - Hydrocephalus

In addition, primary visual processing is often impaired, albeit more diffusely, and accompanied by extrastriate and other cognitive or motor deficits in patients suffering from (heredo-)degenerative disorders, which lead to cortical atrophies (e.g., Alzheimer's disease; Gilmore et al. 1994; Kaskie and Storandt 1995; Lakshminarayanan et al. 1996; Rizzo and Nawrot 1998) or primarily an impairment of subcortical structures (e.g., Parkinson's disease; Bulens et al. 1987; Haug et al. 1994; Lieb et al. 1999).

Moreover, various toxic-metabolic conditions produce global or selective deterioration of the visual performance. In particular, the GABA transaminase-inhibiting antiepileptic drug Vigabatrin is known to cause persistent constrictions of the visual fields by severely damaging signal processing in the retina (Harding et al. 2000; Coupland et al. 2001; Malmgren et al. 2001).

Loss of vision due to ocular pathology or deficits along the retino-geniculo-cortical pathway, in particular after posterior cortical lesions on the right side, may lead to incapacitating positive visual perceptual disorders:

- Hallucinations: perception of objects that do not exist in reality.
  - Hallucinated percepts of true or hallucinated objects:
- Metamorphopsias: morphing distortion or size distortion of visual elements.
  - Micropsia: visual elements are unrealistically small.
  - Macropsia: visual elements are unrealistically large.
  - Prosopometamorphopsia: morphing or mutilating distortion of faces.
- Tessellopsias: regular, lattice-like patterns overlie the visual scene.
- Dendropsias: irregular, tree-like structures overlie the visual scene.
- Hyperchromatopsias: static or exploding shapes or patterns in vivid colors.
- Palinopsias: perseveration of visual elements after removal or across eye movements.

Palinopsias are distinct from the physiologic afterimage. They may be spatial or temporal. Spatial palinopsias are subdivided into illusory visual spread and polyopia (Critchley 1951). Temporal palinopsias, on the other hand, are subdivided into immediate perseverations, short-latency palinopsias and long-latency palinopsias, in which the false percept may reoccur month or years later (Kölmel 1982) (Table 3.1). Many more subtle forms may exist

Table 3.1. Classes of palinopsias (Critchley 1951; Kölmel 1982; ffytche and Howard 1999)

Spatial:	
Illusory visual spread	A visual pattern extends beyond its true boundaries and covers neighboring objects
Polyopia	A visual object becomes multiplied and the repeated copies form rows, columns, or matrices
Temporal:	
Perseveration	A stationary visual object remains in the center of vision after an eye movement or follows it during an eye movement
Short-latency palinopsia	Reappearance of a previous visual object after a few seconds or minutes
Long-latency palinopsia	Reappearance of a previous visual object after months or years

besides these currently eight distinct types of positive visual phenomena. They are not yet fully understood. However, one common feature is increased activity in specialized visual cortical areas after deafferentation (FFYTCHE et al. 1998; FFYTCHE and HOWARD 1999; SANTHOUSE et al. 2000).

After eye diseases, similar complex visual hallucinations may occur, as in the Charles Bonnet syndrome (DE MORSIER 1936). Nowadays, however, this eponym is more generally defined as complex hallucinations in the psychologically normal, i.e., with preserved insight (DE MORSIER 1967). Other pathological conditions and diseases may cause disturbing visual hallucinations with or without loss of normal insight: drugs, metabolic disorders, Parkinson's disease, Alzheimer's disease, dementia with Lewy bodies, schizophrenia and other psychiatric disorders, acute brain syndromes, peduncular hallucinosis, epileptic seizures, and migraine (MANFORD and ANDERMANN 1998). Seizures and migraine attacks often cannot be distinguished easily, although the development and contents of the hallucination differ considerably (PANAYIOTOPOULOS 1999).

Hallucinations have nothing in common with another group of visual disturbances, namely, the agnosias. In the latter, extrastriate visual modules are damaged directly, leading to loss of the respective visual map, e.g., face recognition or color.

3.2.3 The Extrastriate Visual Cortex

After the preliminary analysis of the visual scene by the retino-geniculo-cortical system, which only extracts its coarsest features to produce a primal sketch (MARR 1982), the magnocellular and parvocellular pathways feed into two anatomically and functionally distinct different extrastriate cortical pathways (UNGERLEIDER and MISHKIN 1982): the dorsal and the ventral pathways (Fig. 3.4).

The extrastriate visual area V2 (Brodmann area 18), which surrounds the striate visual cortex on the mesial and lateral surface of the occipital lobe (ZILLES and CLARKE 1997), is the common relay for both types of information and probably the first stage in complex, real, and illusory contour processing as well as other analyses categorized as intermediate level vision, including the ability to identify objects after various transformations, when they are partially occluded, or when they change in size and perspective (Fig. 3.13). Moreover, objects are put into categories and selected by looking at them or reaching for them, and new objects that are repeatedly encountered are recognized (HUBEL and WIESEL 1962; KANIZSA 1976; BRADLEY and PETRY 1977; ZEKI et al. 1991; FELLEMAN and VAN ESSEN 1991; MENDOLA et al. 1999; WURTZ and KANDEL 2000; Ts'o et al. 2001). However, there are still some compelling visual effects that have not yet been explained (Fig. 3.14).

Lesions in either pathway cause characteristic clinical entities (Table 3.2).

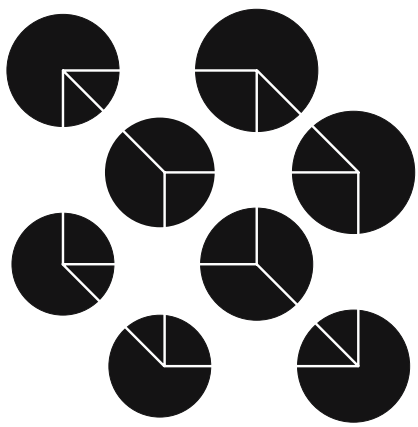

Fig. 3.13. Illusory contours. A few inducers (*black circles with white lines*) form a cube-shaped object (a modified Kanizsa figure) to the observer, even though there are no corresponding changes in luminance (illusory contours). Cells in extrastriate visual V2 already respond to such stimuli (intermediate visual processing)

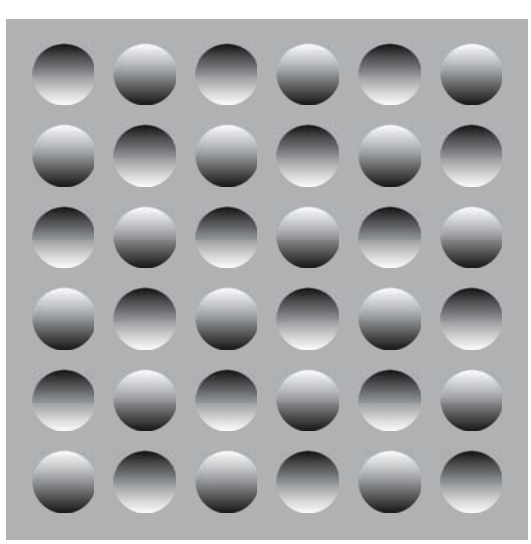

Fig. 3.14. Shape-from-shading. Shades are important depth cues. Here, they produce an overwhelming sensation of 3-dimensional, filled and empty holes in a board. So far, nothing is known about the neural mechanisms which help produce this compelling visual experience

Table 3.2. Classes of visual agnosias after Kandel and Wurtz (2000). *BA*, Brodmann area

Class	Probable site of lesion	Deficit
Motion/depth:		
Visuospatial agnosia	BA 18, 37 on right	Stereoscopic vision
Motion agnosia	V5 bilaterally	Detecting target motion Detecting optic flow
Form/pattern:		
Object agnosia	BA 18, 20, 21 on left or corpus callosum	Naming Using real objects Recognizing
Drawing agnosia	BA 18, 20, 21 on right	Recognizing drawn objects
Prosopagnosia	BA 20, 21 bilaterally	Recognizing faces
Color:		
Color agnosia	BA 18 on right	Associating colors with objects
Color anomia	BA 18, 37 pathways to speech areas or language areas	Naming colors
Achromatopsia	BA 18, 37	Distinguishing hues

3.2.3.1 The Dorsal Pathway

From layer 4B of the primary visual cortex, magnocellular information is transmitted to cells in the thick stripes of V2 as well as to cells in V5, which is located in the monkey-homologue areas of the middle temporal (MT) and the medial superior temporal area (MST) at the intersection of Brodmann areas 19, 37, and 39. In addition, the thick stripes of V2 project onto V5 as well (Figs. 3.4, 3.12). These pathways and regions establish the first step of higher-order cortical processing of target motion in three-dimensional space (depth) and extraction of optic flow as well as heading of ego-motion in the dorsal pathway (Lisberger et al. 1987; Richer et al. 1991; Watson et al. 1993; Morrone et al. 1995; Cheng et al. 1995; Hotson and Anand 1999; Previc et al. 2000; Kourtzi and Kanwisher 2000; Malmgren et al. 2001). Together with information from V4 via the posterior inferior temporal area (PIT) and lateral intraparietal area (LIP), the output is routed to the parietal lobe, in particular the superior parietal lobule (Brodmann areas 5 and 7) (Merigan and Maunsell 1993). These parietal regions compute the visuo-motor transformation, which is necessary to change the retinotopic frame of reference used by the visual areas into a suitable frame of reference for motor commands (Goldberg et al. 1990; Barash et al. 1991a,b; Duhamel et al. 1992; Andersen et al. 1992, 1993, 1998; Colby et al. 1993; Jeannerod et al. 1995; Andersen 1995, 1997; Caminiti et al. 1996; Rushworth et al. 1998; Duhamel et al. 1998; Burnod et al. 1999; Colby and Goldberg 1999; Kusunoki et al. 2000; Xing and Andersen 2000; Snyder et al. 2000). Finally, these signals are projected onto premotor and motor cortical areas. In particular, signals to the frontal eye fields (FEF, Brodmann area 6 in humans; Petit et al. 1997), the supplementary eye fields (SEF, Brodmann area 6) and the dorsolateral prefrontal cortex (DLPC, Brodmann area 46) are used to generate gaze-shifting eye movements (see below) (Fig. 3.15).

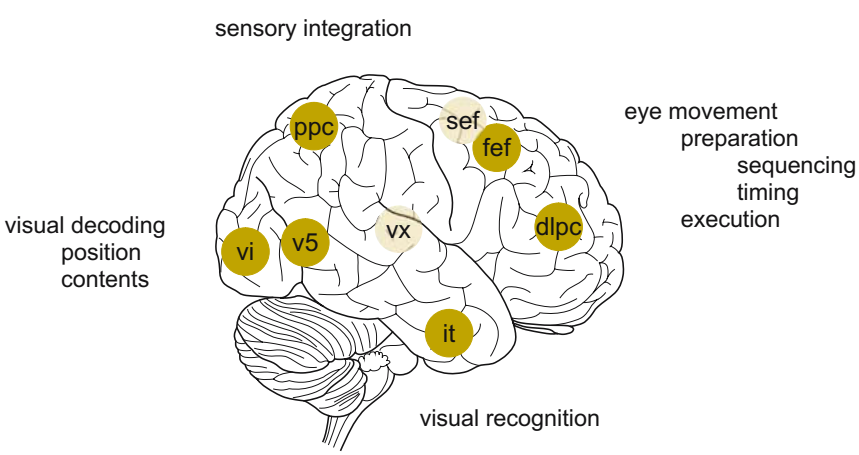

Fig. 3.15. Contributions of important cortical areas to the generation of visually guided reflexive and volitional saccades and smooth pursuit eye movements. *vi*, striate and extrastriate visual cortex; *v5*, motion processing part of the extrastriate visual cortex (junction of Brodmann areas 19, 37, and 39, including middle temporal area *MT* and medial superior temporal area *MST*); *it*, inferior temporal areas; *ppc*, posterior parietal cortex; *vx*, primary vestibular cortex (Brodmann areas 41 and 42); *fef*, frontal eye field (Brodmann area 6 in humans); *sef*, supplementary eye field (Brodmann area 6); *dlpc*, dorsolateral prefrontal cortex (Brodmann area 46)

3.2.3.2 The Ventral Pathway

From blobs and interblob regions, parvocellular information is transmitted to V2 cells in the thin stripes and interstripe regions, respectively (Fig. 3.12). This pathway establishes the first step in higher-order cortical processing of object features such as form and color. In particular, many cells respond to both actual and illusory contours, indicating that they carry out the next step in the increasing abstraction from simple line elements to meaningful objects (Figs. 3.13, 3.14) (von der Heydt et al. 1984; Peterhans and von der Heydt 1993). Subsequently, signals pass via V4 to the inferior temporal cortex (IT), which executes such complex tasks as recognition of faces and other complex and colored objects (Desimone et al. 1985; Desimone and Schein 1987; Hasselmo et al. 1989; Rolls 1992; Allison et al. 1994; Kapur et al. 1995; Sams et al. 1997; Gauthier et al. 1997; Faillenot et al. 1997, 1999; Dolan et al. 1997; Watanabe et al. 1999; Bar and Biederman 1999; Shen et al. 1999).

3.2.4 The Accessory Optic System

The accessory optic system is located in the midbrain rostral to the superior colliculus and receives visual input directly from the retinal ganglion cells as well as from cortical areas V1, V2, and V5 (Telkes et al. 2000; Distler and Hoffmann 2001). For the most part, this phylogenetically old system subserves the optokinetic reflex (see below).

3.3 Eye Movements

The paramount goal of the optomotor system is to keep the fovea, the most sensitive part of the retina, on the selected target of interest despite various possible visual and vestibular disturbances (Fig. 3.1). Six distinctly different control systems have emerged to accomplish the chore. They employ two principal classes of gaze control mechanisms (Glimcher 1999; Goldberg 2000):

- Reflex gaze-stabilization mechanisms
  - Vestibulo-ocular eye movements counteract brief head movements (acceleration domain) and are driven by the vestibular system (vestibulo-ocular reflex, VOR).
  - Optokinetic-ocular eye movements counteract sustained head movements (velocity domain) and are driven by the visual system (optokinetic reflex, OKR).
- Intentional gaze-shifting mechanisms
  - Saccadic eye movements rapidly shift the fovea from one object to another across the visual background.
  - Smooth pursuit eye movements keep the fovea on a moving target along its complex 3-dimensional trajectory through the visual surroundings.
  - Vergence eye movements, which only evolved in binocular vertebrates, add a signal to all other eye movements to differentially move each eye if the point of fixation changes in depth.
  - Fixation freezes the eye at a given position for intent gaze and intense observation and actively suppresses all other eye movements.

Except for vergence, all eye movements are conjugate, i.e., both eyes move the same amount in the same direction. Vergence movements, on the other hand, are disconjugate.

Although each of the six different eye movement systems employs a distinctly different premotor neural circuit for gaze control, they all share a final pathway with a common set of supranuclear structures for synchronizing motor output, motoneurons, and muscles.

A multitude of peripheral and central neurological disorders result in characteristic disturbances of the optomotor system (Miller and Newman 1997; Huber and Kömpf 1998; Leigh and Zee 1999). Careful clinical examination of eye movements (Fig. 3.16) usually reveals the site of the lesion very accurately and often is superior to neuroradiological imaging, as many lesions are localized infratentorial in the mesencephalon, pons, or cerebellum.

3.3.1 The Oculomotor Nuclei and the Extraocular Muscles

Each eye is moved by six extraocular muscles arranged in three antagonistic pairs that rotate it like a globe within the socket of its orbit (Fig. 3.17). The muscles themselves are controlled by three cranial nerves. It is the task of elaborate premotor control circuits within the brainstem and cerebellum to compute the final motor signal for each eye muscle, by weighting and integrating the requests for a change in eye position from all possible visual, vestibular, and

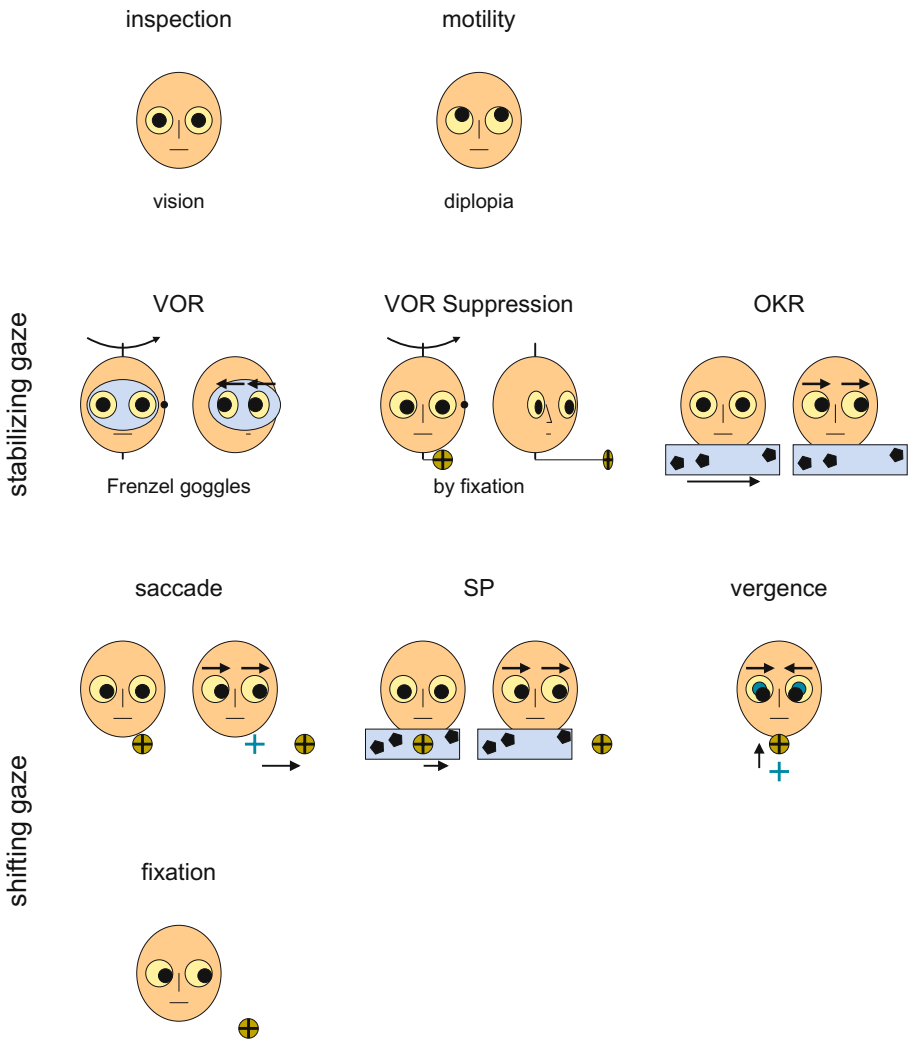

Fig. 3.16. Clinical examination of the optomotor system (modified after Schwarz et al. 2000). The investigation comprises both visually and vestibularly induced eye movements. *Inspection*: reveals misalignment of the eyes and spontaneous nystagmus. Visual acuity must be sufficient and visual fields normal to proceed with examination of visually induced eye movements. *Motility*: eyes should move freely and painlessly in all directions without diplopia. *Gaze-holding mechanisms*. *VOR*: the peripheral vestibular system is examined by rotating the patient while he/she is wearing Frenzel goggles (to remove visual input). A normal physiological vestibulo-ocular nystagmus must appear. *OKR*: a large visual pattern evokes a normal physiological optokinetic nystagmus when quickly moved in front of the patient. Note that this test also engages the smooth pursuit system. Lack of response may be due to a lesion in the cortical and/or the accessory, subcortical visual system. Note that both nystagmus patterns must evoke conjugate reflex eye movements and resetting saccades. These tests are particularly suitable to reveal even a minor unilateral INO due to the continuous generation of saccades. *Gaze-shifting mechanisms*. *Saccade*: the patient must quickly switch gaze from one small eccentric target to another. Note latency, velocity, and precision of the eye movements. A difference in performance between resetting saccades (during nystagmus) and intentional saccades most likely is due to a cortical, extrapyramidal, collicular, or cerebellar lesion and requires further investigations. *SP*: a small target is slowly moved back and forth in front of a stationary visual background (note difference to OKR). Conspicuously jerking movements may be due to lack of cooperation or concentration (catch-up saccades) or to a structural or functional (intoxication) lesion, particularly in the striate or extrastriate visual cortex, the parietal lobe, or the cerebellum. *Vergence*: changing the point of fixation in depth (straight ahead of the patient) examines solely the oculomotor nuclei and nerves. This is of great importance in the diagnosis of an INO (lack of conjugate adduction, preserved adduction during vergence). *Fixation*: the eyes must remain motionless in the resting position and on eccentric targets. Possible pathologies include saccadic intrusions or gaze-evoked nystagmus (quick phase directed away from central position), which is often caused by cerebellar lesions (intoxication). *VOR suppression by fixation*: the patient is asked to fixate a spot that is rotated together with the head (cross on a fingernail). Alternatively, the patient is asked to read out loud a text while walking around. In this test, the VOR must be suppressed by fixation (and probably also by the SP system). Lack of gaze stabilization is mostly due to cerebellar lesions. *VOR*, vestibulo-ocular reflex; *OKR*, optokinetic reflex; *SP*, smooth pursuit

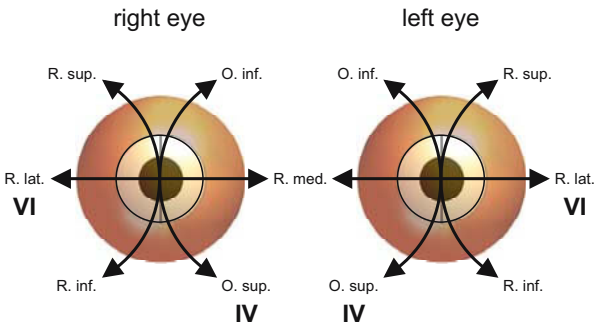

Fig. 3.17. Primary pulling direction of the extraocular muscles. Together, the superior rectus and inferior oblique muscles elevate the eyes from their mid-position, whereas the inferior rectus and superior oblique muscles lower them. In addition, the oblique muscles rotate the eyes in- and outward (torsion). *R*, rectus muscles; *O*, oblique muscles

proprioceptive sources, and distribute them through the medial longitudinal fasciculus to each oculomotor nucleus (Fig. 3.2). Once the signals reach the oculomotor nuclei, the eye movement cannot be stopped. The nuclear motor command signals must comprise both a dynamic and a static component to move and hold the eye in an eccentric position since extraocular muscles act like a system of springs that tend to keep the eyeball in a central position in its socket. Characteristically, each motor signal consists of a brief, transient burst of spikes (pulse), to overcome viscous resistance and accelerate the eye, and a sustained discharge level (step) that is linearly dependent on the eccentricity and maintained as long as the eye is kept in its new position (Fig. 3.18). This continuing neuronal and, consequently, steady muscular activity is necessary to counteract the restoring spring tensions of the eye muscles (Robinson 1964, 1970, 1973; Robinson et al. 1969; Fuchs and Luschei 1970; Robinson and Keller 1972; Skavenski and Robinson 1973; Glimcher 1999).

Three axes of rotation that intersect at the center of the eyeball define the orientation of the eye:

- Horizontal: yaw
- Vertical: pitch
- Torsional: roll

Possible movements are (Fig. 3.17):

- Abduction: rotates the eye away from the nose
- Adduction: rotates the eye toward the nose in the horizontal plane
- Elevation: rotates the eye upward in the vertical plane
- Depression: rotates the eye downward in the vertical plane
- Intorsion (negative torsional according to the right-hand-rule) rotates the top of the eye toward the nose
- Extorsion (positive torsional) rotates the top of the eye away from the nose.

Torsional movements do not change the line of sight and become apparent only in extreme pathological processes (see trochlear nerve palsy below) (Goldberg 2000).

3.3.1.1 Anatomy of the Ocular Motor Nuclei and Nerves

All ocular motor nuclei are located in the midline of the brain stem ventral to the aqueduct of Sylvius and fourth ventricle and close to the medial longitudinal fasciculus and reticular formation. Both the oculomotor (III) and trochlear (IV) nerves lie within the mesencephalon close to the ponto-mesencephalic junction, and the abducens nerve (VI) is situated in the lower pons close to the ponto-medullary junction (Fig. 3.19). For a comprehensive review, see Buttner-Ennever (1988), Leigh and Zee (1999).

3.3.1.1.1 The Oculomotor Nerve (III)

The oculomotor nucleus lies at the ventral border of the periaqueductal gray matter and extends rostrally to the level of the posterior commissure and caudally to the trochlear nucleus (Fig. 3.19). Its efferent fibers innervate the external medial rectus, superior and inferior rectus, the inferior oblique muscle (see Fig. 3.17), and the levator palpebrae superioris (Buttner-Ennever 1988; Leigh and Zee 1999). All projections from the oculomotor nucleus are ipsilateral except for those to the superior rectus muscle, which is completely crossed, and to the levator palpebrae superioris, which are both crossed and uncrossed (Horn et al. 1999, 2000). In addition, the nerve carries parasympathetic fibers to the ciliary muscle and the sphincter pupillae subserving control of lens accommodation, pupillary diameter, and choroidal blood flow. These fibers originate from the single Edinger-Westphal nucleus, which is part of the autonomic nervous system and forms the top of the ocular nucleus (Marinkoviç et al. 1989; Kimura 1991; Gamlin and Reiner 1991; Trimarchi 1992; Klooster and Vrensen 1998; Donzelli et al. 1998). The fascicles of the oculomotor nerve pass ventrally through the medial longitudinal fasciculus, the red nucleus, the substantia

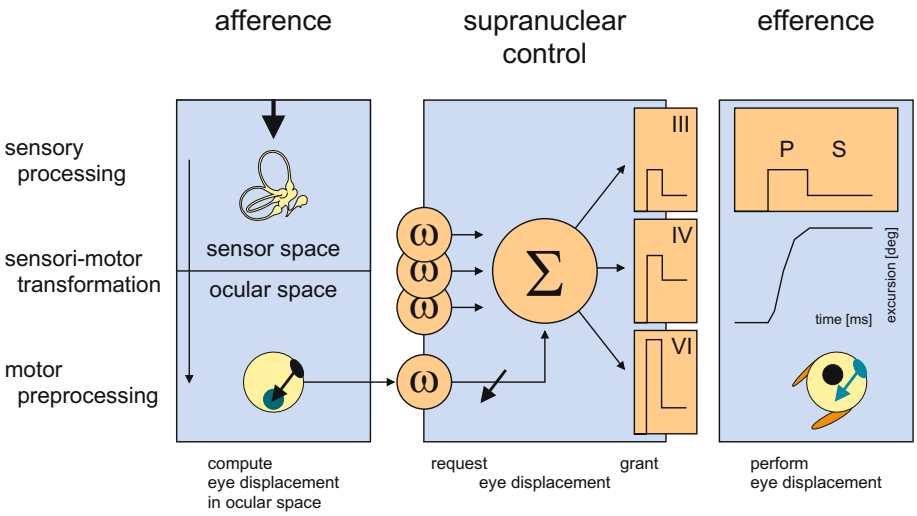

Fig. 3.18. Important computational steps from sensory input to motor action. *Left panel*. Eye movement requests resulting from primary sensory processing, which takes place entirely in its own frame of reference, e.g., a retinal frame of reference within the retino-geniculo-cortical system, first undergo sensorimotor transformation, e.g., into an oculocentric frame of reference, in order to become comparable with those from other sources (*black arrow* indicates desired eye movement). *Middle panel*. The supranuclear optomotor control sums weighted (w), e.g., by attention, request and, finally, generates a solution consisting of a distinctly different pulse/step signal to each oculomotor nucleus. *Right panel*. Supranuclear pulse/step signals are converted by the efference system (ocular plant) into signals that are appropriate for the respective eye muscles. The pulse component moves the eye into a new position, whereas the step component keeps it there. The step is produced by summation of the pulse in the 'neural integrator'. Note the final eye position (position of the pupil) does not fully comply with the requested movement (*gray arrow*) in this example. *P*, pulse; *S*, step; *III*, oculomotor nuclei; *IV*, trochlear nuclei; *VI*, abducens nuclei

nigra, and the medial part of the cerebral peduncle. Recent investigations revealed a topographic organization from lateral to medial in the following order: inferior oblique, superior rectus, medial rectus and levator palpebrae, inferior rectus, and pupil (Castro et al. 1990; Gauntt et al. 1995). The rootlets of the third nerve emerge from the interpeduncular fossa and fuse to a single trunk, which passes through the basal cistern between the posterior cerebral artery and superior cerebellar artery (Marinkoviç and Gibo 1994). It runs lateral to the communicating artery below the uncus of the temporal lobe over the petroclinoid ligament medial to the trochlear nerve and lateral to the posterior clinoid process. The blood supply for the intracranial segment of the oculomotor nerve originates from thalamoperforating branches. As the oculomotor nerve leaves the dura, it lies close to the free edge of the tentorium cerebelli. In the cavernous sinus, it runs above the trochlear nerve and receives sympathetic fibers from the carotid artery (Marinkoviç et al. 2001). Leaving the cavernous sinus, it is crossed superiorly by the trochlear and abducens nerves, and divides into a superior and inferior ramus, which pass through the superior orbital fissure into

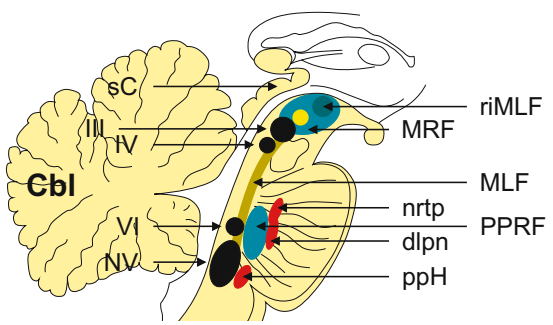

Fig. 3.19. Diagram of important supranuclear and nuclear brainstem structures that control eye movements. Afferent, visual, and vestibular signals from the superior colliculus (*sC*) and the vestibular nuclei (*NV*), respectively, as well as signals from the paramedian pontine reticular formation (*PPRF*) and mesencephalic reticular formation (*MRF*) are distributed via the medial longitudinal fasciculus (*MLF*), which ends in the rostral interstitial nucleus (*riMLF*). Together with portions of the nucleus reticularis tegmenti pontis (*nrtp*), the PPRF generates ipsilateral, horizontal saccades, while the riMLF generates vertical and torsional saccades. In addition, the interstitial nucleus of Cajal (*yellow circle* in the MRF) plays an important role in maintaining the eccentric (vertical) eye position after saccade. Other structures mediate cortical signals for smooth pursuit eye movements to the cerebellum (dorsolateral pontine nucleus, *dlpn*), or are part of the 'neural integrator', in particular, the prepositus hypoglossi nucleus (*ppH*), which provides the step component of the final signal to the oculomotor nuclei. *Cbl*, cerebellum; *III*, oculomotor nucleus; *IV*, trochlear nucleus; *VI*, abducens nucleus

the orbit of the eye (annulus of Zinn) (Natori and Rhoton 1994, 1995). The medial rectus, inferior rectus, and inferior oblique muscles are supplied by the inferior ramus of the oculomotor nerve, which branches in the posterior orbit, whereas the superior oculomotor ramus that runs lateral to the optic nerve and ophthalmic artery supplies the superior rectus and levator palpebrae superioris muscles.

It should be mentioned that the levator palpebrae superioris muscle and the pupil have additional sympathetic innervation, which reaches the eye via a different, clinically important route: Preganglionic fibers originate from nuclei within the intermediolateral column of the upper thoracic spinal cord, leave the cord with the first thoracic root, run to the apex of the pleura to synapse in the superior cervical ganglion. Postganglionic fibers run with the carotid artery and join the ophthalmic branch of the trigeminal nerve at its entrance into the orbit (Goldberg 2000).

3.3.1.1.2 The Trochlear Nerve (IV)

The trochlear nucleus lies at the ventral border of the central, periaqueductal gray matter, dorsal to the medial longitudinal fasciculus, at the level of the inferior colliculus (Leigh and Zee 1999) (Fig. 3.19). Its axons innervate the contralateral superior oblique muscle (see Fig. 3.17). The fibers pass caudally and dorsolaterally around the central gray matter and cross at the roof of the aqueduct. The nerve emerges dorsally from the brainstem caudal to the inferior colliculus and in close proximity to the tentorium cerebelli. It runs laterally around the upper portion of the pons between the superior cerebellar and posterior cerebral arteries into the prepontine cistern. Within the cistern, the trochlear nerve receives its blood supply from branches of the superior cerebellar artery (Marinkoviç et al. 1996). After penetrating the dura at the tentorial attachment, the nerve enters the cavernous sinus where it runs below the oculomotor nerve and above the ophthalmic division of the facial nerve. Crossing over the oculomotor nerve, the trochlear nerve enters the superior orbital fissure above the annulus of Zinn, passes along the medial part of the orbit, and supplies the superior oblique muscle (Natori and Rhoton 1994, 1995).

3.3.1.1.3 The Abducens Nerve (VI)

The abducens nucleus is located in the lower pons in the floor of the fourth ventricle and is covered by the genu of the facial nerve (Leigh and Zee 1999) (Fig. 3.19). It contains motoneurons that supply the lateral rectus muscle (see Fig. 3.17) and internuclear neurons. The axons of these cells cross the midline and pass through the contralateral medial longitudinal fasciculus to supply motoneurons of the medial rectus muscle in the contralateral oculomotor nucleus. The abducens nucleus, therefore, is a part of the ocular plant as well as the supranuclear ocular control and constitutes the primary generator for horizontal conjugate eye movements. Fibers to the lateral rectus muscle pass ventrally, laterally, and caudally through the pontine tegmentum and medial lemniscus to leave at the caudal aspect of the pons close to the anterior inferior cerebellar artery. The nerve runs through the prepontine cistern along the clivus and close to the inferior petrosal sinus. It penetrates the dura at the petrous crest medial to the trigeminal nerve, and passes under the petroclinoid ligament into Dorello's canal (Umansky et al. 1991, 1992). In the cavernous sinus, the abducens nerve lies lateral to the internal carotid artery and medial to the ophthalmic division of the trigeminal nerve (Marinkoviç et al. 1994). Finally, the abducens nerve enters the orbit via the superior orbital fissure, runs through the annulus of Zinn, and supplies the lateral rectus muscle (Natori and Rhoton 1995).

3.3.1.2 Lesions of the Extraocular Nuclei and Nerves

The hallmark of (acute) lesions of the extraocular muscles or their supplying nerves is double vision (diplopia) unless the patient was amblyopic, because the object's image no longer lies on corresponding locations on the retinae. Table 3.3 lists important diseases of the extraocular muscles and neuromuscular junction, which must be excluded carefully due to the therapeutic consequences. Figure 3.20 depicts the main clinical findings for isolated nerve palsies. Table 3.4 lists important etiologies of ocular nerve lesions according to anatomical localizations. However, infratentorial, space-occupying, or ischemic lesions in the brainstem or its proximity rarely cause isolated ocular nerve palsies. Often, they affect multiple cranial nerves and are accompanied by other neurological findings including loss of supranuclear optomotor functions (see below) (Figs. 3.21–3.23). For an extensive review, see Miller and Newman (1997), Huber and Kömpf (1998), Leigh and Zee (1999).

Table 3.3. Important differential diagnosis of extraocular eye muscle paresis (Leigh and Zee 1999; Schwarz et al. 2000)

Strabismus concomitants
Vergence spasm
Brain stem lesions with supranuclear oculomotor involvement:
- internuclear ophthalmoplegia (INO)
- skew deviation

Disorders of the neuromuscular junction:
- myasthenia gravis
- Lambert-Eaton myasthenic syndrome
- botulism

Myopathy:
- chronic progressive external ophthalmoplegia (CPEO)
  - mitochondrial cytopathy
    - Kearns-Sayre syndrome
    - MELAS
      - mitochondrial encephalopathy
      - lactic acidosis
      - stroke
  - myotonic dystrophy
  - oculopharyngeal dystrophy
  - myotubular myopathy
  - inflammation

Endocrine ophthalmoparesis:
- M. Basedow

Congenital aplasia/hypoplasia of extraocular muscles
Restrictive ophthalmopathy
Tumor of the orbit:
- metastasis
- lymphoma
- pseudotumor

Trauma:
- blowout fracture of the orbit

3.3.1.2.1 Oculomotor Palsy

A lesion of the oculomotor nerve results in a loss of adduction (with crossed diplopia) and upward movements, while downward movements are partially intact due to the superior trochlear muscle (trochlear nerve). The eye has a characteristic resting position that is 'down and out' (Leigh and Zee 1999). Furthermore, since eyelid elevation, accommodation, and pupillary constriction are governed by the oculomotor nerve, complete (i.e., internal and external) damage also results in drooping of the eye (ptosis), blurred vision mainly for near objects, and pupillary dilatation (mydriasis) (Fig. 3.20). Incomplete, external lesions, however, are more common (Guy et al. 1985; Trobe 1986; Carlow 1989). In addition, brainstem lesions, e.g., cavernomas, may cause selective loss of oculomotor nerve or nucleus functions (Fig. 3.24).

Important components of the differential diagnosis of the oculomotor palsy include the ophthalmoplegic aneurysm and sequels of the internal carotid, communicans posterior, or posterior cerebral artery (Vukov 1975; Roman and Edwards 1979; Hamer 1982; Guy et al. 1985; Bartleson et al. 1986; Boccardo et al. 1986; Moorthy et al. 1989; Guy and Day 1989; Fujiwara et al. 1989; DiMario and Rorke 1992; Ranganadham et al. 1992; Striph 1993; Varma and Miller 1994; Leng et al. 1994; Dehaene 1994; Keane 1996; Tiffin et al. 1996; Kasner et al.

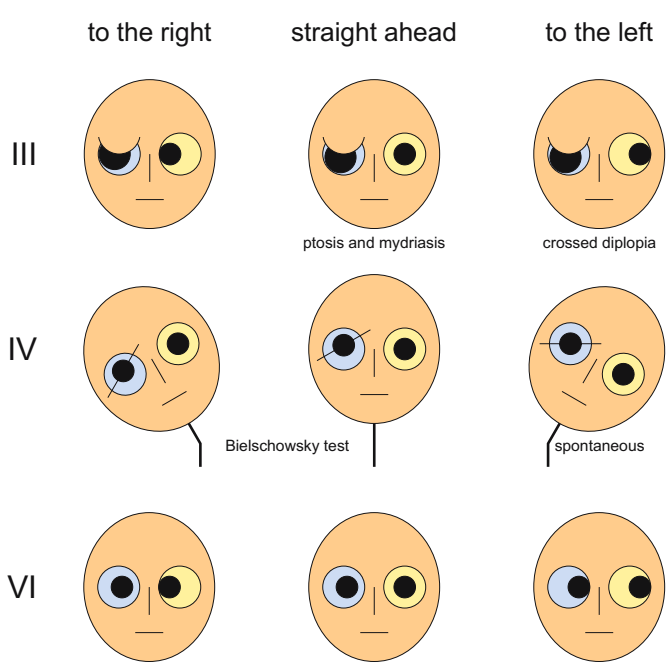

Fig. 3.20. Eye position and direction of diplopia due to isolated palsies of the right oculomotor, trochlear, and abducens nerve (modified after Schwarz et al. 2000). A complete, internal and external palsy of the oculomotor nerve causes additional ptosis and mydriasis. A trochlear palsy causes a conspicuous head tilt towards the unaffected side to compensate for the lack of inversion by the superior oblique muscle. Note the position of the horizontal eye axis shown for each head position. Diplopia is worse after tilting the head in the opposite direction (positive Bielschowsky test). See text for further explanations. *III*, oculomotor nerve; *IV*, trochlear nerve; *VI*, abducens nerve

Table 3.4. Important etiologies of ocular nerve lesions listed by anatomical location (Leigh and Zee 1999; Schwarz et al. 2000). Infarctions of the vasa nervorum of the oculomotor nerve can only be localized clinically in the superior orbital fissure and the cavernous sinus; in all other cases, it remains uncertain. The ophthalmoplegic migraine and immune-mediated neuropathies can affect all ocular nerves along their infranuclear, extracerebral sections. *III*, oculomotor nerve; *IV*, trochlear nerve; *VI*, abducens nerve; *ICA*, internal carotid artery; *AICA*, anterior inferior cerebellar artery; *PICA*, posterior inferior cerebellar artery; *PcoA*, posterior communicating artery; x, typically affects this nerve; + preferentially affects this nerve; = often affects multiple nerves at the same time; [empty] = affects all nerves equally

Localization	III	IV	VI
Uncertain/multifocal:			
ophthalmoplegic migraine			+
infarction (diabetes/hypertension)			
neuropathy (postinfectious/postvaccinal)	=	=	=
Orbital:			
inflammation	=	=	=
bacterial			
fungal			
infiltration	=	=	=
disease of eye muscles			
granuloma			
tumor			
trauma		+	
Superior orbital fissure/cavernous sinus:			
vasculitis (arteritis)	=	=	=
infarction (diabetes/hypertension)	x		
pituitary infarction	+		
cavernous sinus thrombosis	=	=	=
aneurysm/dissection of ICA	=	=	=
direct/dural arteriovenous fistula to ICA	=	=	=
inflammation			
herpes zoster	=	=	=+
sphenoid sinusitis	+		
mucocele	+		
tumor			
pineal gland		+	
ependymoma		+	
pituitary adenoma	+		+
nasopharyngeal carcinoma	+		+
meningioma	=	=	=
metastasis/lymphoma	=	=	=
paraneoplastic syndrome	=	=	=
Tolosa-Hunt syndrome	=	=	=
Tentorial edge:			
increased intracranial pressure	=	=	=
hydrocephalus			
pseudotumor cerebri			+
sinus thrombosis			+
supratentorial/transtentorial herniation			
trauma			

Localization	III	IV	VI
Petrous:			
inferior petrosal sinus thrombosis			x
aneurysm			x
arteriovenous malformation			x
persistent trigeminal artery			x
inflammation			x
mastoiditis			
tip of petrous bone			
foraminal herniation	=	=	=+
trauma			x
following lumbar puncture			+
spinal/epidural anesthesia			
myelography			
ventriculoatrial shunt			+
Subarachnoid:			
hemorrhage			
infarction (diabetes)	x		
aneurysm of PcoA	+		
compression by AICA, PICA, basilar A			x
meningitis infectious/neoplastic	=	=	=
tumor			
Fascicular:			
multiple sclerosis			
hemorrhage			
infarction (diabetes/hypertension)			
neurosurgical complication			
tumor			
Nuclear:			
Wernicke's encephalopathy			+
infarction			
inflammation			
tumor			
trauma			
myokymia		x	
congenital hypoplasia			
Möbius syndrome			x
Duane syndrome			x

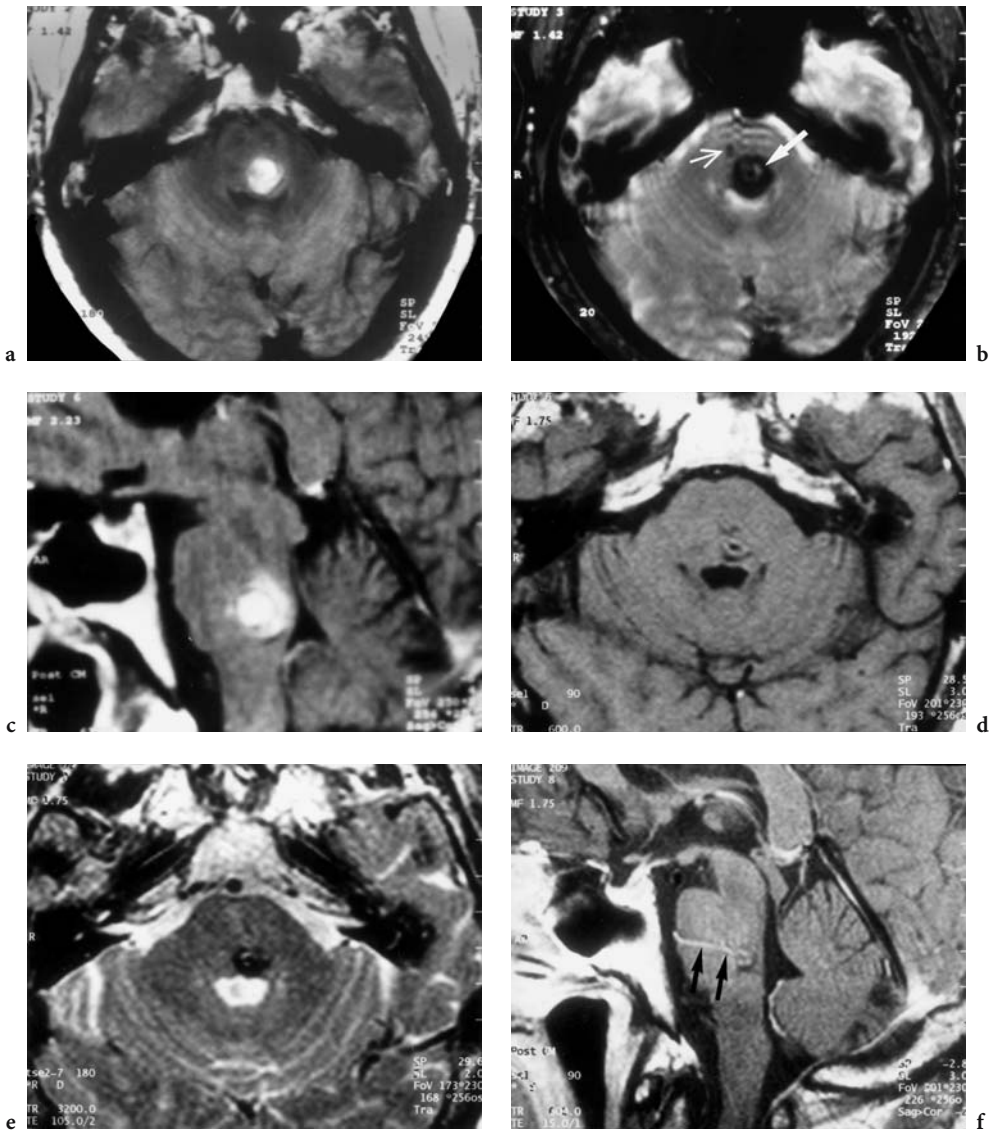

Fig. 3.21a-f. Follow-up of a 63-year-old man with sudden onset of left NV and NVI paresis. Diagnosis: acute brainstem cavernoma hemorrhage with associated DVA (developmental venous anomaly). MRI initial examination: **a** Axial T1-weighted native image showing left paramedian predominantly hyperintense lesion in the rhombencephalon corresponding to the presence of acute to subacute hemorrhage. **b** Corresponding T2-weighted image with hypointense hemorrhage signal but intermediate part (*big white arrow*). The *small white arrow* indicates the draining vein of the DVA. **c** Left paramedian sagittal view demonstrating slight space-occupation by the hemorrhage with expansion to the floor of the fourth ventricle. Corresponding images of a second MRI done 3 months later: **d** Axial T1-weighted native image enabling detection of recurrence of the hemorrhage by a small target-like formation in the parenchyma of the brainstem. Note enlargement of the fourth ventricle diameter (compare with **a**). **e** Axial T2-weighted view with characteristic hypointense hemosiderin deposit (compare with **b**). **f** Midsagittal T1-weighted, contrast-enhanced view, demonstrating the perforating draining vein of the DVA, clearly visualized after i.v. gadolinium. [With permission of Radiologen am Brand, Mainz (**a**–**c**), Dr. Müller-Forell, Institute of Neuroradiology Medical School, Mainz]

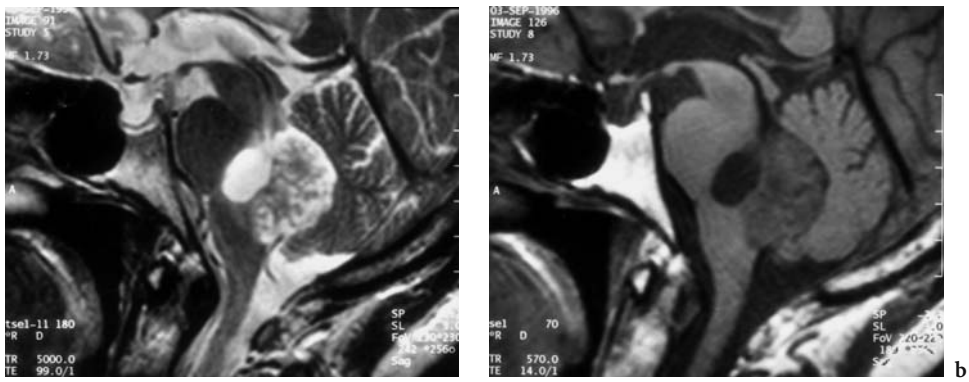

Fig. 3.22a-c. A 51-year-old man with right NIII and bilateral NVI paresis. Diagnosis: plexus papilloma of the fourth ventricle. MRI: **a** Midsagittal T2-weighted image showing a tumor occupying the entire fourth ventricle. The apparently solid tumor part with irregular signal intensity is surrounded by a CSF-equivalent signal, while a ventral cyst depresses and infiltrates the rhombencephalon. Note ventral depression of the cerebellar vermis and the flow void in the aqueduct. **b** Corresponding T1-weighted native image showing the intraventricular location of the solid tumor part. Note widening of the roof of the fourth ventricle with open aqueduct, better seen than in the T2-weighted image. **c** Axial T1-weighted, contrast-enhanced view, demonstrating homogeneous signal enhancement of the solid tumor part. The cyst should not be mistaken for the fourth ventricle of which the remnant is seen posteriorly (*white arrow*). (With permission of Dr. Müller-Forell, Institute of Neuroradiology, Medical School, Mainz)

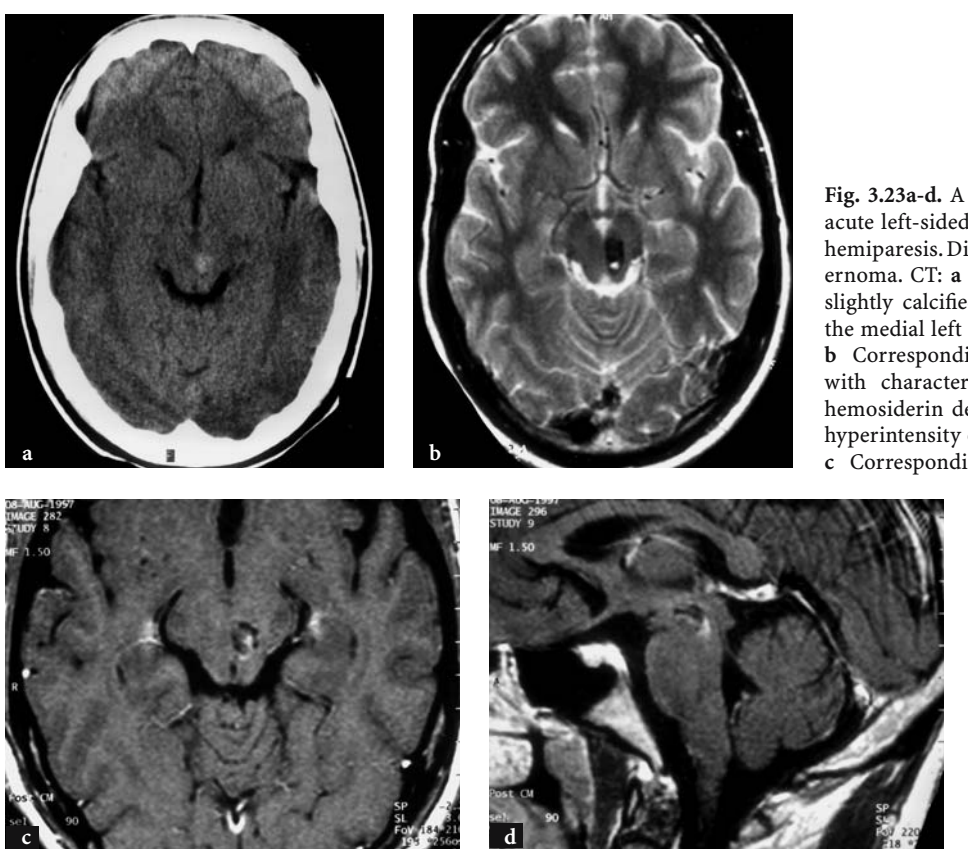

Fig. 3.23a-d. A 20-year-old man with acute left-sided NIII paresis and right hemiparesis. Diagnosis: tegmental cavernoma. CT: **a** Axial native view with slightly calcified hyperdense focus in the medial left cerebral peduncle. MR: **b** Corresponding T2-weighted view with characteristic hypointensity of hemosiderin deposit/calcification and hyperintensity of the cavernous space. **c** Corresponding T1-weighted, contrast-enhanced image with signal enhancement of the venous area. **d** Paramedian sagittal T1-weighted, contrast-enhanced cut, demonstrating localization of the cavernoma in the medial tegmentum. (With permission of Dr. Müller-Forell, Institute of Neuroradiology, Medical School, Mainz)

1997; Cawley et al. 1998; Dayan and Elston 1999; Silva et al. 1999; Birchall et al. 1999), and the (rare) ophthalmoplegic migraine, especially in children (Raymond et al. 1977; Troost 1996).

3.3.1.2.2 Trochlear Palsy

An isolated lesion of the trochlear nerve results in deficits in extorsion and depression, causing hypertropia of the affected eye (Bixenman 1981; Brazis 1993; Leigh and Zee 1999). Due to the deviation, the perception of slant is disturbed, and the patient typically complains that horizontal lines will be slanted with respect to each other (reading, descending stairs) (Sanfilippo 1973; Guyton 1988). Therefore, a common finding is head tilt away from the lesion in order to compensate for the misalignment (Fig. 3.20), and the most reliable clinical test is the head-tilt test (Bielschowsky's test), where the hypertropia and resultant slant misalignment are maximized as the head is tilted toward the side of the lesion. It should be noted that in a patient with skew deviation (as part of a central [vestibular] disorder), the head-tilt test is usually negative (Vanooteghem et al. 1992; Leigh and Zee 1999). Since this nerve is the longest and thinnest of the cranial nerves, it is particularly susceptible to traumatic damage (Sydnor et al. 1982).

3.3.1.2.3 Abducens Palsy

The abducens palsy is the most common ocular motor paralysis (Leigh and Zee 1999). A lesion of this nerve results in loss of abduction beyond the midline

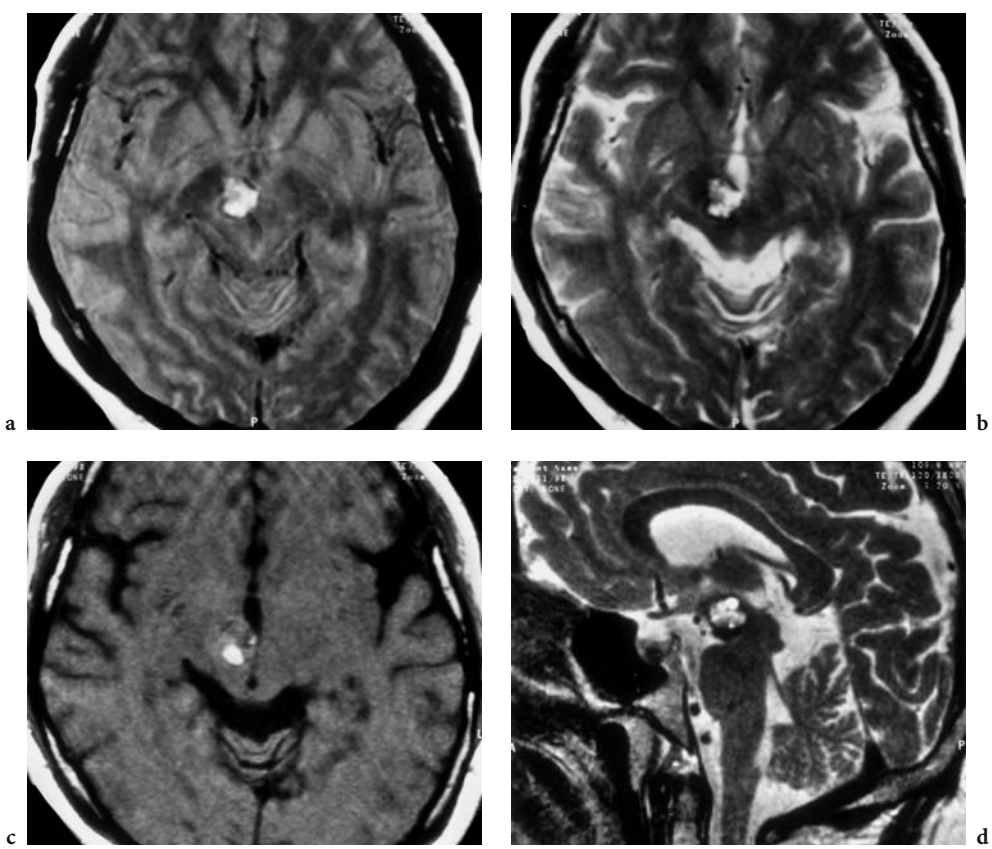

Fig. 3.24a-d. A 22-year-old woman with recurrent diplopia for both lateral views, presenting with acute right NIII paresis that resolved completely after 6 weeks. Diagnosis: mesencephalic cavernoma (history of four hemorrhages). MRI: **a** Axial proton density view, the high signal demonstrating the presence of blood (methemoglobin) in the cavernoma of the right cerebral peduncle. Note the symmetric formation of the substantia nigra. **b** Corresponding T2-weighted image, more clearly demonstrating the hypointense rim of hemosiderin confirming former hemorrhage. Note the slight suppression of the medial part of the third ventricle. **c** Corresponding T1-weighted native image where the hyperintensity represents a small cyst, filled with thrombotic material (hemosiderin), confirming subacute hemorrhage. **d** Right paramedian sagittal T2-weighted view demonstrating the entire width of the lesion. (With permission of Dr. Müller-Forell, Institute of Neuroradiology, Medical School, Mainz)

(with uncrossed diplopia) (Figs. 3.20, 3.25). Typically, patients will have less double vision when looking at a nearby object, because convergence adducts each eye. A nuclear lesion will cause conjugate horizontal gaze palsy, due to the internuclear neurons that run into the medial longitudinal fasciculus (Meienberg and Muri 1992), and very often a peripheral paresis of the facial nerve due to its anatomical proximity.

3.3.2 Supranuclear Synchronization of Eye Movements

In order to attain the appropriate combination of conjugate and vergence eye movements, all six oculomotor nuclei are interconnected via the medial longitudinal fasciculus (MLF) (Figs. 3.2, 3.19). This general-purpose data path travels dorsally in the pons to the rostral interstitial nucleus of the MLF (riMLF), which is located in the mesencephalic reticular formation (MRF), and conveys signals for horizontal, vertical, and torsional gaze (Buttner-Ennever 1988; Buttner-Ennever et al. 1989; Buttner-Ennever and Horn 1997; Leigh and Zee 1999; Horn et al. 1999):

- For horizontal gaze, it carries axons from the abducens internuclear neurons, which mediate conjugate eye movement commands, to the medial rectus motoneurons in the contralateral oculomotor nucleus. The abducens nucleus itself is considered the horizontal gaze center, as it receives

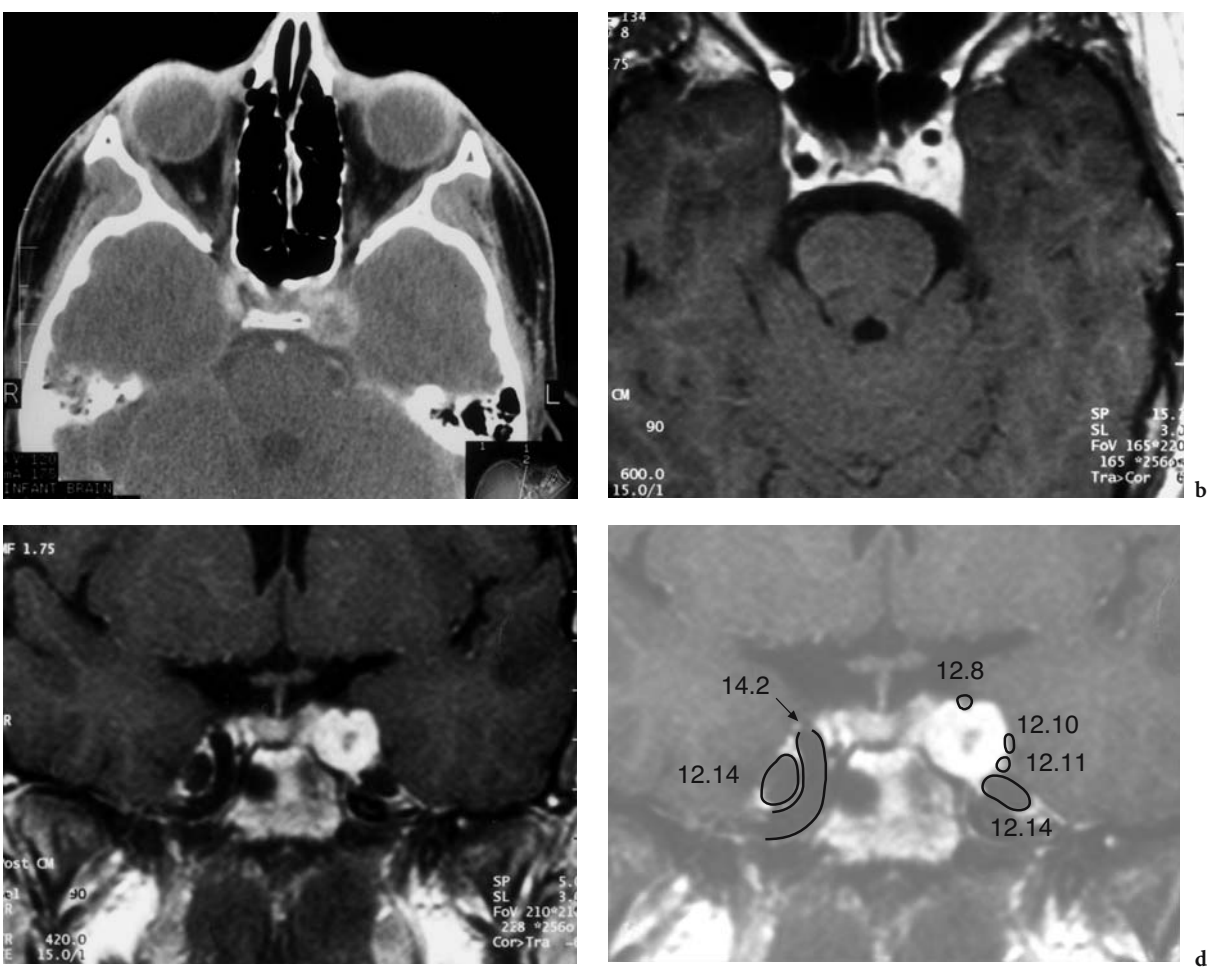

Fig. 3.25a-d. A 13-year-old boy with recurrent double vision associated with left NVI paresis. Diagnosis: suspected NVI schwannoma (no histology). CT: **a** Axial contrast-enhanced image with an inhomogeneous enhancing tumor of the left posterior part of the cavernous sinus. **b** Corresponding T1-weighted, contrast-enhanced MRI. **c** Coronal view showing the growth exclusively in the cavernous wall, and identifying compression of the left trigeminal ganglion. **d** Corresponding diagram (compression of nerves NIII, NV1,and NV2, nerves VI, NIV are too small). 12.8 = oculomotor nerve, 12.10 = N V2 (maxillary nerve), 12.11 = N V3 (mandibular nerve, 12.14 = trigeminal (Gasserian) ganglion, 14.2 = ICA. (With permission of Dr. Müller-Forell, Institute of Neuroradiology, Medical School, Mainz)

commands for slow and fast horizontal eye movements from all sources. Its motor neurons project directly to the ipsilateral lateral rectus muscle.
- For vertical gaze, it carries axons which mediate signals for vestibulo- and otolith-ocular reflexes, smooth pursuit, and gaze holding from the vestibular nuclei to the oculomotor and trochlear nuclei as well as the interstitial nucleus of Cajal (inC).

Lesions of the medial longitudinal fasciculus disconnect the motoneurons projecting to the medial rectus muscle from the horizontal gaze center, which results in the well-known clinical entity of an internuclear ophthalmoplegia (INO):
- Ipsilateral supranuclear paresis during conjugate horizontal adduction
- Normal behavior during vergence-induced adduction
- Contralateral abduction nystagmus in the lateral rectus muscle, which is due to a slight compensatory increase in the activity of its projecting abducens motoneurons.

INOs are most often encountered in patients with multiple sclerosis (Fig. 3.26). Table 3.5 summarizes other important etiologies (Anderson 1992; Al-Din et al. 1994; Najim et al. 1994; Steinlin et al. 1995; Verhagen et al. 1996; Komaba et al. 1997; Galindo et al. 1998; Constantoyannis et al. 1998; Dalmau and Porta-Etessam 2000; Kumar et al. 2000; Eggenberger et al. 2000; Cassidy et al. 2000).

Table 3.5. Important etiologies of internuclear ophthalmoplegia (INO) (Leigh and Zee 1999; Schwarz et al. 2000)

Demyelinization:
multiple sclerosis
postirradiation
Brainstem infarction:
syphilis (vasculitis)
Infection:
meningoencephalitis
syphilis (meningitis)
Space-occupying lesion:
subdural hematoma
hydrocephalus/syringobulbia
Arnold-Chiari malformation
supratentorial arteriovenous malformation
neoplasia
brain stem/fourth ventricle
infiltration
paraneoplastic syndrome
Degenerative disorder:
progressive supranuclear palsy (PSP)
Steele-Richardson-Olszewski syndrome
Nutritional disorder:
Wernicke's encephalopathy
pernicious anemia
Metabolic disorder:
hepatic encephalopathy
Fabry's disease
abetalipoproteinemia
Intoxication (selection):
barbiturate
lithium
phenothiazine
propranolol
tricyclic antidepressants
Trauma:
cervical hyperextension
Pseudo-internuclear ophthalmoplegia:
myasthenia gravis
Miller Fisher syndrome

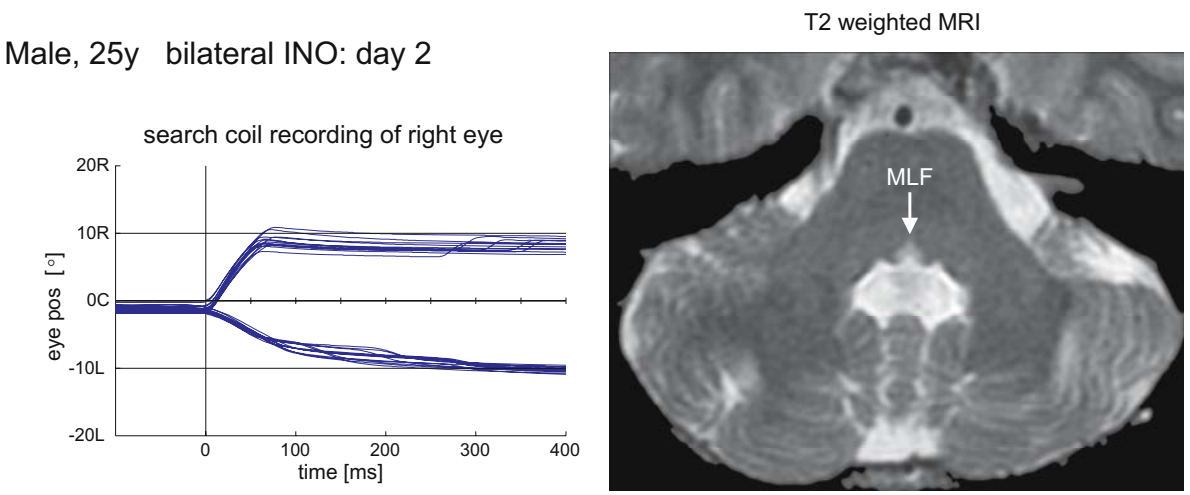

Fig. 3.26. A 25-year-old man with sudden onset of dizziness and double vision 2 days before presenting with a bilateral internuclear ophthalmoplegia (INO). Diagnosis: acute onset of multiple sclerosis. *Left panel.* Eye position recordings of the right eye show individual trials of visually guided saccades 10° to the right (upward deflection) and left (downward deflection), which are aligned with the onset of the saccade. Note the marked slowing of the adducting saccades (to the *left*) and post-saccadic drift of the abducting saccade. *Right panel.* Axial, T2-weighted MRI shows bright signals bilateral in the medial longitudinal fasciculus (*MLF*)

This well understood clinical picture might be complicated, e.g., in one-and-a-half syndrome, if the underlying process affects other structures, e.g., oculomotor nuclei, its nerve rootlets, or brainstem centers for the generation of saccades.

Furthermore, due to the particular arrangement of the blood supply to the cerebellum with the superior cerebellar arteries and the anterior and posterior inferior cerebellar arteries as well as the brainstem with short and long perforating arteries that emerge from the basilar artery, the infratentorial optomotor system is often involved in ischemic strokes (Fig. 3.27). Several unique and easily recognized clinical entities are known (Table 3.6) (Wall et al. 1986; Bogousslavsky and Meienberg 1987; Liu et al. 1992; Bassetti et al. 1996; Johkura et al. 1998).

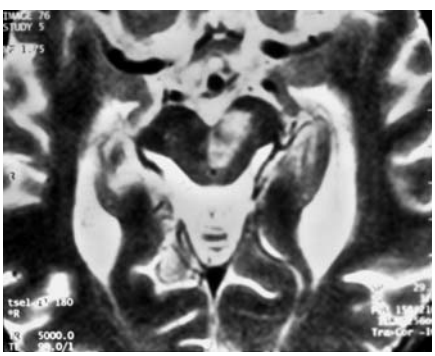

a

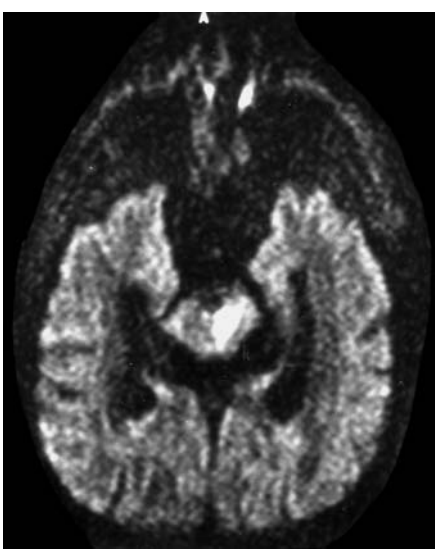

b

Fig. 3.27a,b. A 61-year-old man with sudden onset of double vision; on neurological examination an internuclear ophthalmoplegia (INO) of the right eye was found. Diagnosis: acute infarction of the left brainstem. MRI: **a** Axial T2-weighted (TSE) view with hyperintense area of the left peduncle, reaching the aqueduct. **b** Corresponding DWI image, confirming the diagnosis. (With permission of Dr. Müller-Forell, Institute of Neuroradiology, Medical School, Mainz)

Table 3.6. Important midbrain (Liu et al. 1992; Miller and Newman 1997) and ponto-medullary syndromes that involve optomotor structures. *c*, contralateral; *i*, ipsilateral

Syndrome/localization	Clinical signs
Midbrain	
Weber's syndrome	
oculomotor nerve fascicle	i: oculomotor nerve palsy
cerebral peduncle	c: hemiparesis
Claude's syndrome (1912)	
oculomotor nerve fascicle	i: oculomotor nerve palsy
tegmentum	c: ataxia
red nucleus	c: asynergia
superior cerebellar peduncle	
Benedikt's syndrome (1889)	
oculomotor nerve fascicle	i: oculomotor nerve palsy
tegmentum	c: hemiparesis
red nucleus	c: tremor
substantia nigra	c: involuntary movements
superior cerebellar peduncle	
cerebral peduncle	
Parinaud's syndrome	
dorsal midbrain	Supranuclear vertical gaze-palsy
	Convergence-retraction nystagmus
	Lid retraction
Nothnagel's syndrome (1879)	
+/- oculomotor nerve fascicle	Supranuclear vertical gaze-palsy
dorsal midbrain	Convergence-retraction nystagmus
paramedian midbrain	Lid retraction
	i: +/- oculomotor nerve palsy
	i: ataxia
Pons	
one-and-a-half syndrome	
paramedian pons	i: abducens nucleus palsy
	c: internuclear ophthalmoplegia
Millard-Gubler syndrome	
ventral pons	i: abducens nerve palsy
	i: facial nerve paresis
	c: hemiparesis
Foville's syndrome	
ventral pons	i: abducens nerve palsy
	i: facial nerve paresis
	i: sensory loss (facial)
	i: deafness
	c: hemiparesis
Medulla	
Wallenberg's syndrome	
dorsolateral medulla	Spontaneous nystagmus
	Impairment of saccades
	Impairment of smooth pursuit
	i: hypertropia (skew deviation)
	+/- ocular tilt reaction (toward lesion)
	i: loss of temp/pain sensation (face)
	i: Horner's syndrome
	Dysphagia
	Dysarthria
	Dysphonia
	c: loss of temperature/pain sensation (body)

3.3.3 Gaze Holding Mechanisms

3.3.3.1 The Vestibulo-ocular Reflex

The vestibular system senses head movements and – with a very short latency (<20 ms) – elicits extraordinarily precise, compensatory eye movements in the opposite direction in order to stabilize the gaze: the vestibulo-ocular reflex (VOR). The vestibular labyrinth is composed of several parts that detect both angular and linear motion (Fig. 3.28). Each of the three semicircular canals, that are oriented coarsely at 90° to one other, responds to angular acceleration, while the otolith organs (utricle and saccule) respond to linear acceleration (including gravity).

Rotation of a semicircular canal deflects the cupula due to the inertia of the endolymph, a watery fluid filling the thin membranous tube. The gelatinous cupula is a part of the crista in the ampulla enclosing the hair cells, which consist of several stereocilia and one kinocilium. The hair cells transduce the mechanical shearing into neural impulses (Correia et al. 1996). They react optimally to forces applied in one direction: Deflection of the stereocilia towards the kinocilium causes depolarization, hence, increase in firing frequency of the vestibular nerve, and hyperpolarization otherwise (Leigh and Zee 1999). Linear accelerations of the head, on the other hand, stimulate hair cells of the macula of the utricle (aligned with the horizontal plane) and saccule (aligned with the parasagittal plane). These hair cells are also embedded in a gelatinous mass. However, additional calcium carbonate crystals (otoconia) are attached on top of the membrane. Altogether, the layout of these hair cells with their directional tuning allows accurate representation of any 3-dimensional head movement in the central nervous system as well as the sense of the subjective 'upright'.

The blood supply of the labyrinth derives from the labyrinthine artery that usually arises from the anterior inferior cerebellar artery and rarely directly from the basilar artery (Fig. 3.29) (Mazzoni 1972; Leigh and Zee 1999). At the labyrinth, the labyrinthine artery branches into several smaller arteries (Fig. 3.30). Occlusion may cause selective loss of labyrinthine functions and/or deafness (Grad and Baloh 1989; Oas and Baloh 1992).

Nerves from the cristae and maculae reach Scarpa's ganglion. The vestibular nerve itself is divided into the superior division, which runs with the facial nerve and innervates the anterior and lateral canals and the utricle, and the inferior division, which runs with the cochlear nerve and innervates the posterior canal and the saccule. From Scarpa's ganglion, the vestibular nerve traverses the cerebellopontine angle below the facial nerve and enters the brainstem between the inferior cerebellar peduncle and the spinal portion of the trigeminal tract (Leigh and Zee 1999). Finally, vestibular afferents synapse on neurons in one of the four vestibular nuclei on each side.

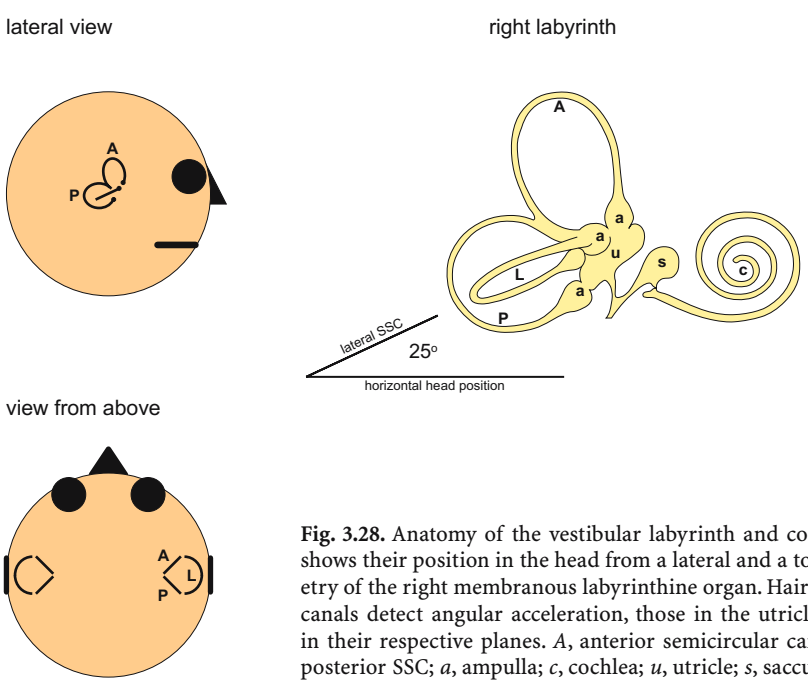

Fig. 3.28. Anatomy of the vestibular labyrinth and cochlea (after Henn 2000). The *left panel* shows their position in the head from a lateral and a top view. The *right panel* shows the geometry of the right membranous labyrinthine organ. Hair cells in the ampullae of the semicircular canals detect angular acceleration, those in the utricle and saccule detect linear acceleration in their respective planes. *A*, anterior semicircular canal (*SSC*); *L*, lateral (horizontal) SSC; *P*, posterior SSC; *a*, ampulla; *c*, cochlea; *u*, utricle; *s*, saccule

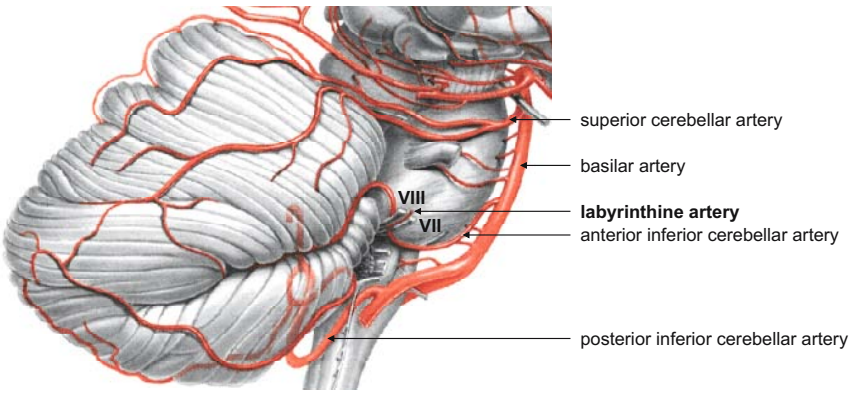

Fig. 3.29. Arterial blood supply of the brainstem and cerebellum (modified after Fig. 3.40; Nieuwenhuys et al. 1988). Only major branches are labeled

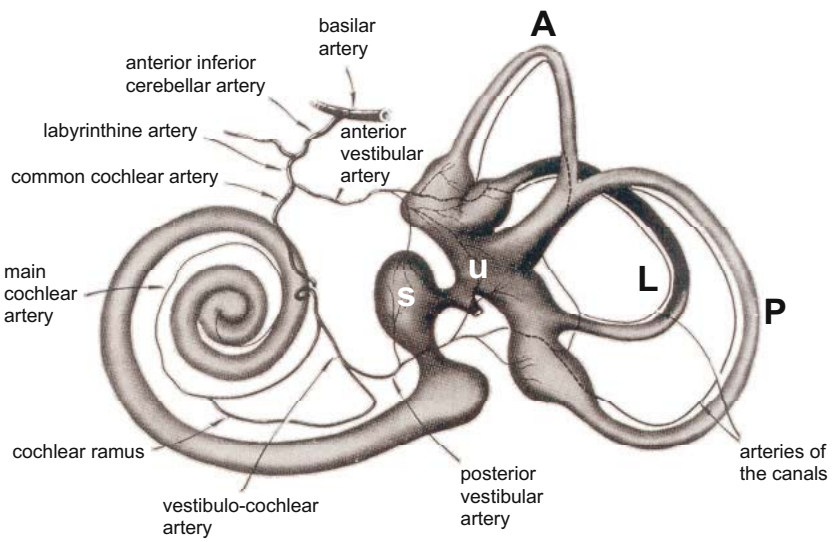

Fig. 3.30. Arterial blood supply of the labyrinth (from Schuknecht 1974). Occlusion of terminal branches may affect single semicircular canals, the utricle, the saccule, and/or the cochlea and cause distinct peripheral vestibular and/or auditory pathologies (see Fig. 3.28 for labels)

Due to their dynamic properties, the canals have already performed a first integration from acceleration to velocity. Hence, in their operational range, the firing frequency of vestibular afferents is roughly proportional to head velocity (Dickman and Correia 1989a,b, 1992; Angelaki et al. 1995; Hullar and Minor 1999; Hess and Angelaki 1999). These velocity signals are transmitted immediately via a so-called direct pathway from the vestibular nuclei to the extraocular muscles, which are aligned in pairs, with corresponding pairs of canals, and most likely account for the dynamic component of the VOR (Scudder and Fuchs 1992). However, in order to maintain eye position after cessation of the head movement, the labyrinthine velocity signal must be integrated once more: A copy of the velocity signal is fed into an additional premotor neural integrator (especially the cerebellum and the prepositus nucleus of the hypoglossal nerve), which adds a position signal to the velocity signal (Raphan et al. 1979; Cannon and Robinson 1987; Anastasio 1991; Hain and Zee 1992).

In addition, the vestibular cerebellum (flocculus, nodulus and uvula, dorsal vermis, fastigial nucleus, and uncinate fasciculus) continuously monitors the performance of the VOR as well as its integration with other eye movement generators (e.g., fixation suppression or smooth pursuit) and is the main source for repair of lesions in the peripheral vestibular system as well as adjustment of the VOR due to changes of the visual input (e.g., wearing new eyeglasses or after eye surgery) (Schwarz 1976; Miles and Lisberger 1981; Waespe and Cohen 1983; Lisberger et al. 1984; Galiana 1986; Suarez et al. 1992; Lewis and Zee 1993; Ito 1993; Solomon and Cohen 1994; Baloh et al. 1997; Belton and McCrea 1999, 2000).

Acute unilateral lesions in the peripheral vestibular system (labyrinth, vestibular nerve, and its brainstem entry zone) (Leigh and Zee 1999) are incapacitating and typically cause (Biedert et al. 1985; Ojala and Palo 1991; Baloh and Jacobson 1996; Hotson and Baloh 1998; Baloh 1998a; Schwarz et al. 2000; Strupp and Arbusow 2001):

- Vertigo: the illusion of movement of self or the environment
- Nausea and vomitus
- Imbalance and falls
- Spontaneous nystagmus (see below)
- Oscillopsia: the illusion of jerky movements of the environment
- Loss of caloric response

and often include otolith signs and symptoms (Figs. 3.31–3.33) (Aoki et al. 1999; Bohmer 1999; Vibert et al. 1999; Vibert and Hausler 2000; Tilikete et al. 2001).

- Ocular tilt reaction: skew deviation, counter rolling of the eyes, head tilt
- Tilt of subjective visual vertical

as well as

- Deafness.

See Table 3.7 for important etiologies. The patient's history together with additional neurological findings supplies the key information to differentiate acute and chronic peripheral and central vestibular disorders (Fig. 3.34) (Brandt and Dieterich 1993, 2000; Dieterich and Brandt 1993; Baloh 1998b).

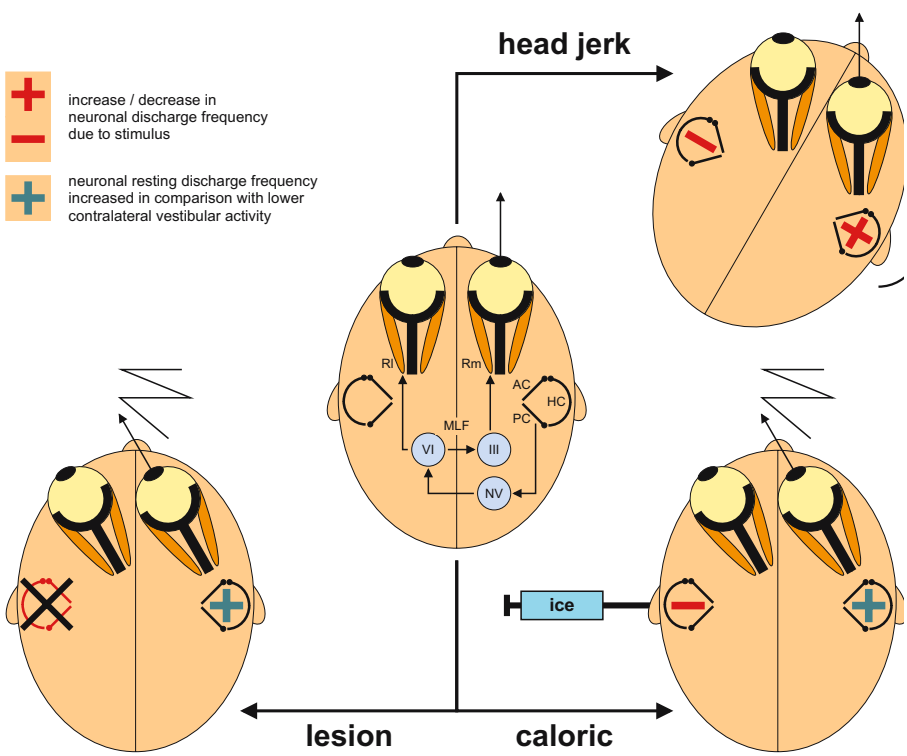

Fig. 3.31. The vestibulo-ocular reflex (*VOR*) is elicited by three different conditions. Important connections between the right labyrinth and the extraocular muscles are depicted schematically in the *center panel*. *Head jerk*. During a physiological, brisk head movement to the right, the right lateral semicircular canal is activated (+) due to the inertia of the endolymph (*curved arrow*) while the left canal is inhibited (-). Signals travel via the vestibular nucleus to the contralateral abducens nucleus, which innervates the ipsilateral lateral rectus muscle and generates supranuclear optomotor commands. These signals, in turn, reach the contralateral oculomotor nucleus, which innervates the medial rectus muscle, via the medial longitudinal fasciculus. Together, these muscles produce an accurate compensatory eye movement in the opposite direction of the head movement to maintain stability of gaze (*straight arrow*). *Caloric stimulation*. Cold water induces flow of the endolymph and inhibits the left labyrinth (-). The apparent activation of the right labyrinth (+) elicits the same response. Since the difference in labyrinthine discharge is maintained over a longer period, the eyes are reset periodically, which leads to a typical vestibular nystagmus (see Fig. 3.35). *Lesion of the left vestibular organ*. Loss (-) of input from the left vestibular organ (or nerve) elicits the same response. Note the optomotor system cannot distinguish between these three entirely different conditions. *AC*, anterior semicircular canal (*SSC*); *HC*, horizontal SSC; *PC*, posterior SSC; *III*, oculomotor nucleus; *VI*, abducens nucleus; *MLF*, medial longitudinal fasciculus; *NV*, vestibular nuclei; *Rl*, lateral rectus muscle; *Rm*, medial rectus muscle

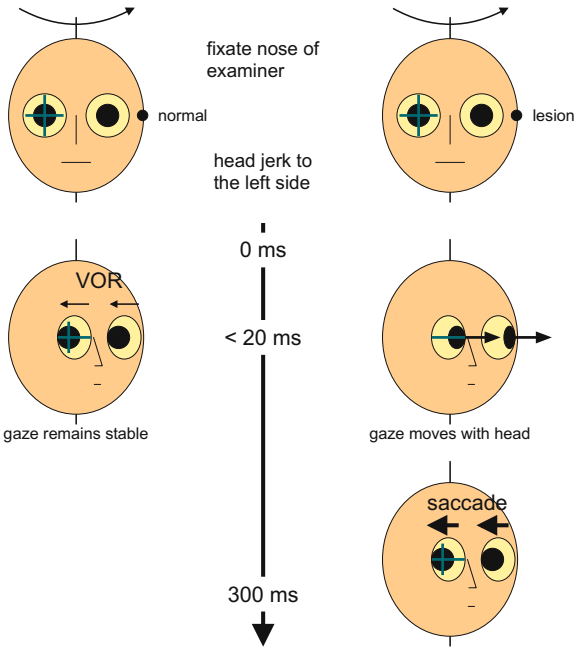

Fig. 3.32. The head impulse test (modified after Schwarz et al. 2000). Unilateral testing of the peripheral vestibular system is performed by the head impulse test. The subject is asked to fixate the nose of the examiner. Under normal circumstances, the VOR counteracts a brief jerk (shown to the left) with a very short latency (<20 ms), which cannot be detected. After loss of the VOR due to a lesion in the vestibular labyrinth or nerve, the eyes initially move together with the head. The patient must elicit a saccade to gaze back to the examiner's nose, which has an easily detectable delay of several hundred milliseconds

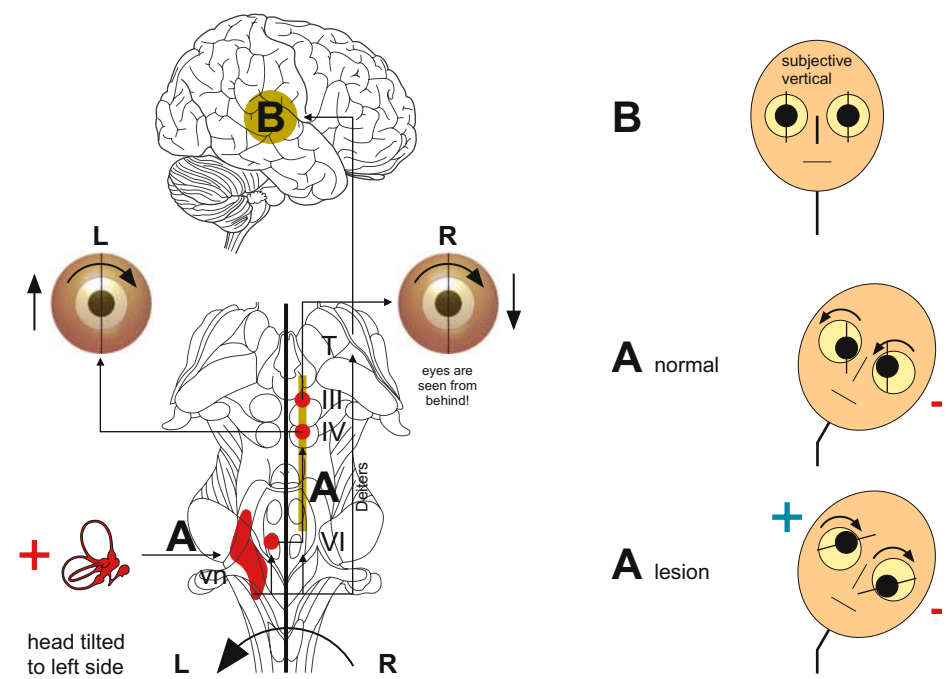

Fig. 3.33. Tonic vestibular pathways cause counter-roll of the eyes and maintain the subjective visual vertical. *Left panel*. Head tilt to the left activates (+) the maculae of the utricle and saccule. Signals, mediated via the vestibular nuclei (*vn*), reach the ipsilateral abducens nucleus (*VI*) and cross the midline to reach the contralateral trochlear nucleus (*IV*) and oculomotor nucleus (*III*) via the medial longitudinal fasciculus (*MLF*). In addition, the abducens nucleus (*VI*) sends supranuclear signals to the contralateral ocular nuclei in the medial longitudinal fasciculus as well. Altogether, the signals cause a counter-roll of both eyes, an elevation of the left eye, and a depression of the right eye (eyes are shown from behind!). Note signals from the trochlear nucleus (*IV*) cross the midline again to reach the contralateral superior oblique muscle. Moreover, vestibular information is sent directly via the Deiters tract to the thalamus (*T*), which, in turn, projects to the primary vestibular cortex. These signals are necessary to maintain the subjective visual vertical. *Upper right panel*. Upright posture and normal subjective visual vertical require normal functioning of all tonic vestibular structures including the final pathway marked *B*. *Middle right panel*. Normal ocular counter-roll reaction after a head tilt to the left. *Bottom right panel*. A lesion along the pathways marked *A* causes apparent head tilt to the right and therefore evokes the ocular counter-roll in the opposite direction, which, in turn, causes a rotation of the subjective visual vertical *to the right*. This is counterbalanced by a final head tilt to the left resulting in a skew deviation of the eyes (hypertropia of the upper eye). Note that the inappropriate eye movements cause a head tilt, whereas under normal circumstances the head tilt causes eye movements.

Table 3.7. Important etiologies of vertigo (Leigh and Zee 1999; Schwarz et al. 2000)

Benign paroxysmal positional vertigo (BPPV)[a,b]

Acute unilateral partial lesion of the vestibular nerve[a]
- labyrinthitis
- vestibular neuritis

Ménière syndrome[a]

Basilar migraine[a]

Multiple sclerosis[a,b]

Epilepsy[a]

Posttraumatic vertigo

Other focal lesions or diseases
- ischemic/hemorrhagic infarct[a]
  - labyrinth/vestibular nerve: anterior inferior cerebellar a. s(AICA)
  - ponto-cerebellar: posterior inferior cerebelli a. (PICA)[b]
    - Wallenberg syndrome
- venous congestion[a]
  - hyperviscosity syndrome
- Valsalva induced[a]
  - Arnold-Chiari malformation[b]
- viraler infect of labyrinth/vestibular nerve
  - herpes zoster
- bacterial infect of labyrinths/vestibular nerve
  - tuberculoses
- spirochetal infect of labyrinths/vestibular nerve
  - syphilis
  - Lyme disease
- tumor
  - vestibular nerve
    - acoustic neurinoma
    - neurofibromatosis II
  - cerebellopontine[b]
  - glomus tumor
- autoimmune disease[a]
  - Cogan syndrome I
  - Susac's syndrome
- degeneration of hair cells
- otosclerosis[a]
- perilymph fistula[a]
- congenital anomaly of labyrinth

Drug-induced vertigo
- anti-vertiginous medication (!)
- antihypertensives
- antidepressants
- sedatives
- antiepileptics

Physiologic vertigo
- motion sickness [a,b]
- height vertigo [a,b]

[a] Recurrent vertigo
[b] Positionally induced or enhanced vertigo

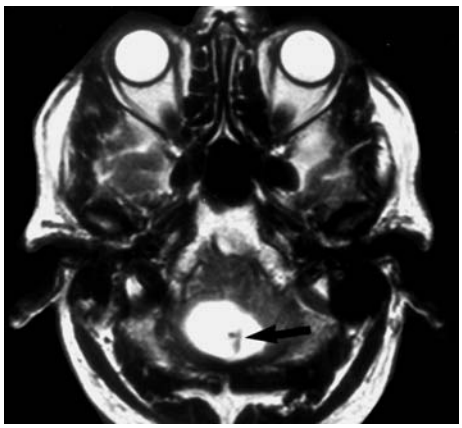
a

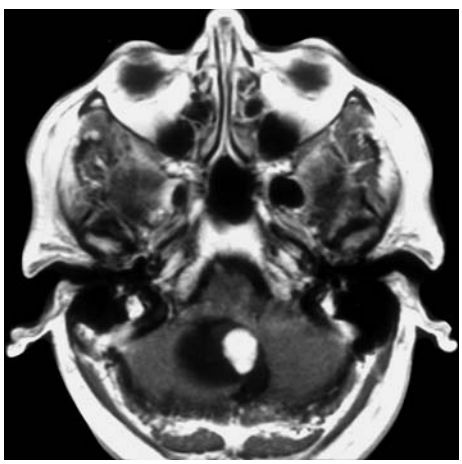
b

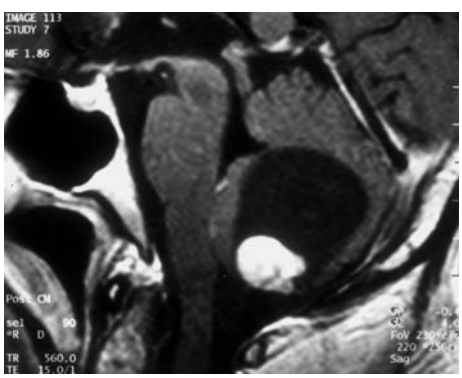

c

Fig. 3.34a-c. A 60-year-old man with unspecific vision disturbances, balance disorder, gaze nystagmus to the left, and chronic headache. Diagnosis: hemangioblastoma. MRI: **a** Axial T2-weighted view at the level of the inferior cerebellum with a primarily cystic formation and a more solid part located at the periphery (*arrow*). **b** Corresponding T1-weighted, contrast-enhanced image showing homogeneous, strong signal enhancement of the solid tumor part. **c** Midsagittal T1-weighted, contrast-enhanced view, demonstrating intraparenchymal location of the tumor in the inferior cerebellar vermis. Although the exit of the fourth ventricle is compressed, CSF circulation continues to be compensated by gentle widening of the aqueduct and third ventricle. (With permission of Dr. Müller-Forell, Institute of Neuroradiology, Medical School, Mainz)

3.3.3.2 The Optokinetic Reflex

For simple geometrical reasons, head and eye movements cause apparent motion of the visual surroundings on the retina (retinal slip) (Schwarz and Ilg 1999), and sustained self-rotation in the light causes a compelling sensation (circularvection) despite the lack of peripheral vestibular stimulation (Leigh and Zee 1999). The optokinetic system extracts this global pattern and generates compensatory eye movements to annihilate the disturbing slip and quickly stabilize the visual world on the retina. Hence, this optokinetic reflex (OKR) – supported by the smooth pursuit system (see below) – acts as a visual counterpart to the VOR and enhances the purely vestibular response substantially in the low-frequency range. Together, the vestibulo-ocular and optokinetic systems attain an almost perfect retinal stabilization across a wide range of head movements.

Visual information subserving the OKR travels from the retina directly to the accessory optic system in the pretectum, a midbrain area located rostral to the superior colliculus (Mai 1978; Fredericks et al. 1988; Hoffmann 1996). Both velocity and direction of the retinal slip are extracted by pretectal neurons (Hoffmann and Distler 1989), which themselves project to the vestibular nuclei via pontine and medullary pathways (Buttner-Ennever 1988; Fuchs and Mustari 1993; Wallman 1993). Furthermore, the convergence of visual and vestibular signals upon central vestibular neurons suggests a common final pathway for gaze-holding eye movements (Henn et al. 1974; Glimcher 1999).

Deterioration of the OKR, especially a reduction in velocity, occurs in a variety of diseases, notably in multiple sclerosis (Todd et al. 2001), and often is accompanied by malfunctioning of the central vestibular system.

3.3.3.3 Nystagmus

Nystagmus denotes a rapid involuntary oscillation of the eyes, which typically consists of a slow phase followed by a quick resetting saccade. Traditionally, the direction of the nystagmus is determined by the quick phase. Both the direction and velocity of the slow component are determined either by a physiological stimulus or the site of the lesion within the oculomotor system. Figure 3.35 shows the generation of a pathological vestibular nystagmus due to a labyrinthine lesion. It should be noted, however, that

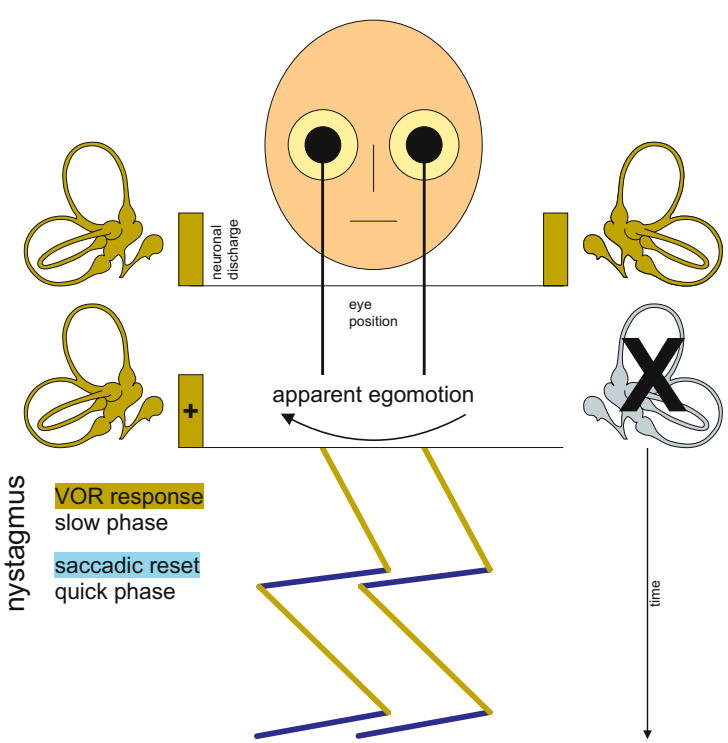

Fig. 3.35. Development of a unidirectional spontaneous nystagmus (modified after Schwarz et al. 2000). Acute loss of the neuronal resting discharge in the left labyrinth (*X*) is equivalent to a head movement to the right (see Fig. 3.31), as the drive of the optomotor system and perception of ego-motion only depends on the difference between the vestibular inputs from both sides. Accordingly, the optomotor system generates an eye movement to the left (*VOR*, *slow phase*), which periodically is interrupted by a resetting saccade (*fast phase*) if the eye position exceeds a certain limit. Altogether, these jerky back-and-forth movements of the eyes constitute a nystagmus. Its direction is defined by the direction of the saccade and is independent of the eye position

- The nystagmus itself is not pathological. Rather, it is the expected consequence of pathological sensory processing.
- The resetting saccade is elicited automatically and entirely independently from the source of the slow component. It is generated in the brain stem as a response to an excessive excursion of the eyeballs to set them back to their mid-position.

Therefore, to obtain a nystagmic eye-movement pattern, the oculomotor system must be able to generate both components.

Physiological nystagmus occurs at the onset and end of a rotation in complete darkness (vestibular nystagmus during acceleration or deceleration) or while observing a very large, moving pattern (optokinetic nystagmus).

There are a variety of well-known pathological nystagmus patterns (Leigh and Zee 1999), two of which are of particular importance:

- Unidirectional spontaneous nystagmus (horizontal, vertical, or mixed, and typically with an additional torsional component) is almost invariably due to pathology within the peripheral or central vestibular system. The slow phase is evoked by a pathological difference in the firing frequency of vestibular signals, which simulates head motion and consequently induces compensating eye movements and activates vestibulospinal reflexes. Finally, conflicting visual and proprioceptive inputs cause the full spectrum of motion sickness.
- Gaze-evoked nystagmus occurs if the eyes slowly drift from any eccentric position toward the midline and are repositioned by a saccade. It is always due to an impaired neural velocity-to-position integrator (see above) and typically is caused by an infratentorial lesion or intoxication (drugs, alcohol).

3.3.4 Gaze Shifting Mechanisms

3.3.4.1 Saccades

Saccades are stereotyped, very quick and precise, machine-like eye movements that bring a novel target of interest onto the fovea and allow exploring the world in a sequence of fixations. They are elicited both reflexively and volitionally in a variety of contexts and tasks (Table 3.8).

The characteristics of the velocity profile are well known and, in particular, show a consistent relationship between the peak velocity and the size of the displacement (see Fig. 3.36) (Becker 1989). This so-called main sequence cannot be changed voluntarily.

The final motor commands for all saccades are generated in the brainstem and consist of a pulse and a step component (see above, Figs. 3.18, 3.37).

Burst cells that lie within the paramedian pontine reticular formation (PPRF) generate the pulse for horizontal saccades, whereas the burst cells for vertical and torsional saccades are located in the rostral interstitial nucleus of the MLF (riMLF) (Fig. 3.19). Oblique saccades are generated by the pontine and mesencephalic centers. Purely vertical saccades require synchronization of both riMLF, which is accomplished by a communication traversing the posterior commissure (Horn et al. 1995; Horn and Buttner-Ennever 1998).

A family of burst cells exists that start firing at various times before the occurrence of a saccade (Hepp and Henn 1983; Henn et al. 1989; Sparks and Mays 1990):

- Medium-lead burst cells activate motoneurons and interneurons in the ipsilateral abducens nucleus
- Long-lead burst cells drive the medium-lead burst cells. They receive activating input from higher-order gaze centers
- Inhibitory burst cells suppress contralateral abducens neurons and are activated by medium-lead burst cells

In contrast, omnipause cells, located in the nucleus of the dorsal raphe close to the PPRF, burst continuously except shortly before and during a saccade. In addition, pulse signals are fed into the neural integrator, which includes cerebellar pathways (see above), to provide the necessary tonic signal for the step component that keeps the eye in its eccentric position.

Table 3.8. Classes of saccadic eye movements

Volitional:	Internally triggered
visually induced	Reading/exploring
acoustically induced	By continuous noise
predictive	Before occurrence of an expected target
remembered	To a former target position
searching	For a new target amongst many
antisaccade	Precisely opposite to actual target
Reflexive:	Externally triggered
visually induced	By a novel target
acoustically induced	By a novel noise
Spontaneous:	
in darkness	
while thinking	
Fast phase of nystagmus	

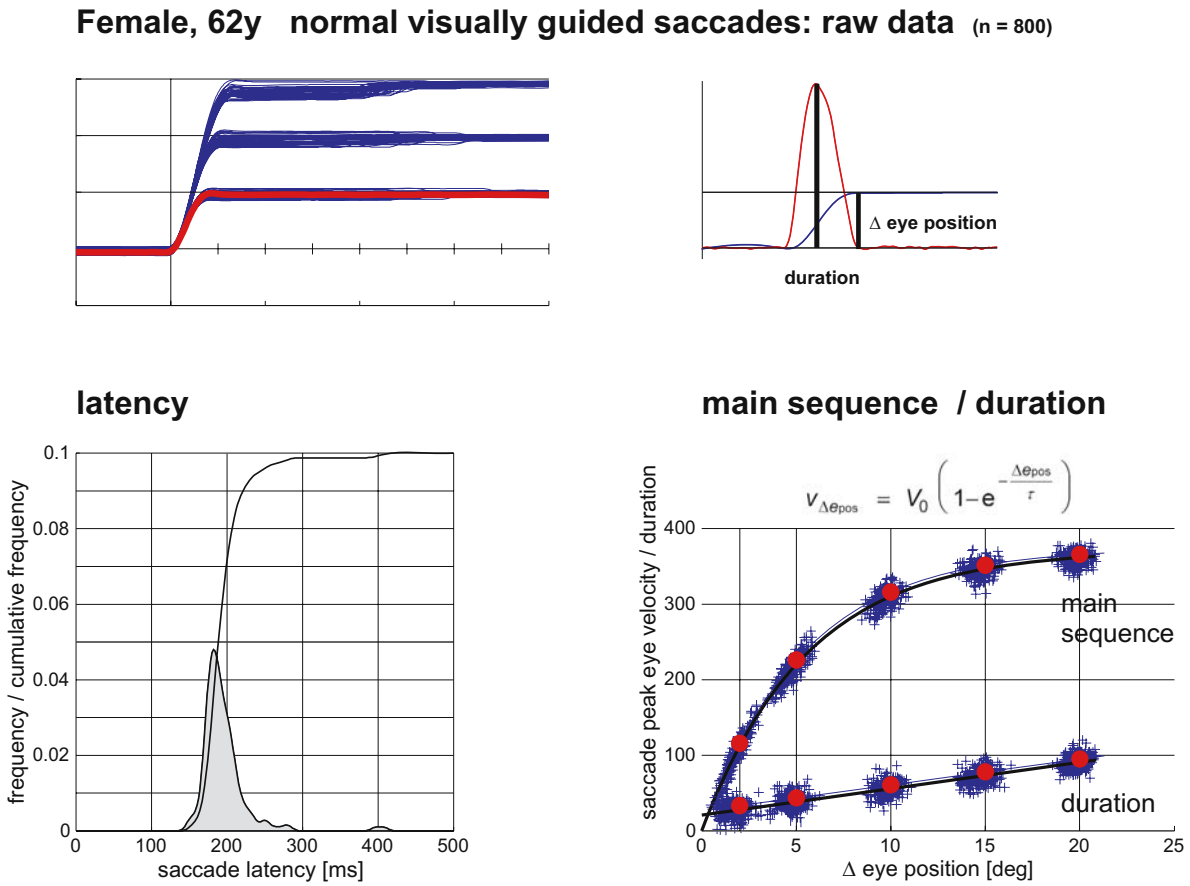

Fig. 3.36. Typical saccade parameters obtained from a 62-year-old healthy woman. *Left upper panel*. Exemplary original eye position traces sampled from visually guided saccades 5°, 10°, and 15° to the right (upward deflection). Saccades are aligned with respect to their onset; hence, the latency distribution will be reflected at negative points on the time axis. Note the machine-like feature of saccade performance. *Right upper panel*. The main sequence is computed from the ratio of the eye excursion and the peak eye velocity from each individual trace (*red trace in upper left panel*). *Lower right panel* shows the main sequence (*black line*) obtained from all eye movements including excursions to 20° to the right (original traces not shown for simplicity) as well as saccade durations for this subject. The main sequence typically is parametrized by an exponential function with two variables (see equation). *Lower left panel*. Latency distribution for the same data. Note the narrow range with a characteristic peak around 200 ms

Any mismatch of pulse and/or step components quickly leads to deterioration of saccadic performance (Fig. 3.37) (saccadic dysmetria and intrusions including opsoclonus and ocular flutter, gaze-evoked nystagmus).

Hence, saccades are spatially triggered by a mutually inhibitory push-pull mechanism of premotor omnipause and burst cells, which are part of the brain stem oculomotor system. However, given the broad range of involvement of saccade-class eye movements in almost all aspects of highly developed oculomotor behavior, it seems obvious that additional layers of input, particularly from the cerebral cortex, which governs cognitive behavior, memory, attention, and decision making, exert control on their execution. Cortical – including extrapyramidal – requests for saccades are mediated by the superior colliculus (SC) (Mohler and Wurtz 1977; Guitton et al. 1985; Schiller et al. 1987; Sparks 1989; Robinson and McClurkin 1989; Goldberg and Segraves 1989; Dominey and Arbib 1992; Segraves and Park 1993; Colby et al. 1995; Lekwuwa and Barnes 1996; Gancarz and Grossberg 1999; Gaymard and Pierrot 1999; Goldberg 2000; Leichnetz 2001; Pare and Wurtz 2001; Sommer and Wurtz 2001; Hanes and Wurtz 2001).

Figure 3.38 shows a simplified synopsis of higher-order saccade processing (Weber et al. 2000): Both omnipause and burst cells receive retinotopically organized input directly from the frontal eye fields (FEF) and the superior colliculi (SC). A complex neuronal network of the different layers of the superior

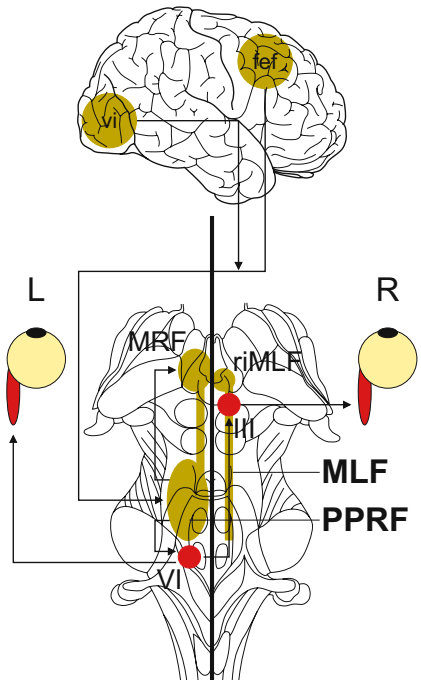

Fig. 3.37. Control of volitional saccades by the paramedian pontine reticular formation (*PPRF*) (after Schwarz et al. 2000). First, signals from the frontal eye field (*fef*), and to a lesser degree from the visual areas (*vi*), reach the contralateral PPRF. The PPRF, in turn, routes fef signals to the mesencephalic reticular formation (*MRF*) for vertical and torsional saccade components. More importantly, it computes the final pulse/step parameters for the horizontal saccadic displacement and sends these requests to the ipsilateral abducens nucleus (*VI*), which innervates the ipsilateral lateral rectus muscle. In addition, it generates supranuclear eye movement commands with travel to the contralateral oculomotor (*III*) and trochlear (not shown) nucleus via the medial longitudinal fasciculus (*MLF*). In this example, the oculomotor nucleus simply innervates the ipsilateral medial rectus muscle, generating a purely horizontal saccade. Lesions of the PPRF or any higher order structure result in a conjugate gaze palsy without diplopia. Lesions of the MLF, on the other hand, result in an internuclear ophthalmoplegia (INO) with a dissociation of conjugate eye movements (see Fig. 3.26). *riMLF*, rostral interstitial nucleus of the MLF

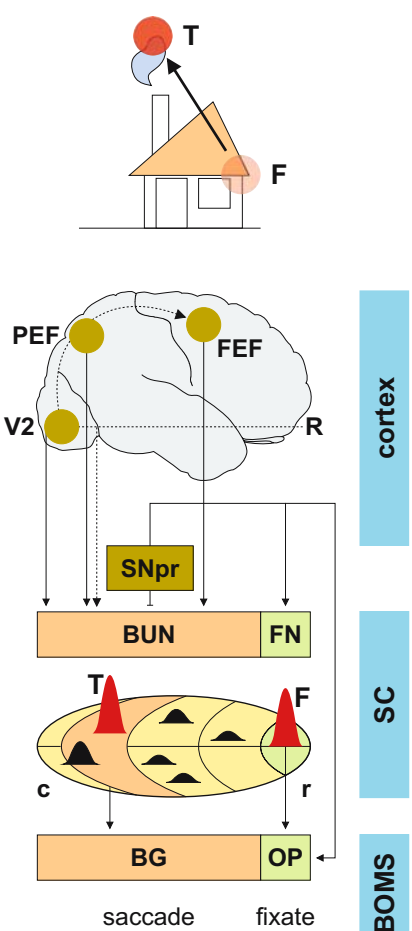

Fig. 3.38. Simplified diagram of oculomotor behavior during an intended saccade, which would result in a gaze shift from the current point of fixation (*F*) to a novel target (*T*) (modified after Weber et al. 2000). See chapter 3.2.4.1 for details. The retinotopic superior colliculus (*SC*) consists of a sensory, intermediate, and motor layer and is an important computational relay between various cortical and subcortical structures that require access to the brainstem saccade generator. It is able to prepare and maintain a map of many possible saccades, one of which may be released, employing a very efficient and elegant push-pull mechanism between its fixation neurons and the corresponding omnipause neurons, which are located in the nucleus raphe interpositus close to the pontine midline, as well as its peripheral buildup neurons and their corresponding burst neurons, which are located in the paramedian pontine reticular formation (PPRF) and mesencephalic reticular formation (MRF) (Figs. 3.19, 3.37). Hence, shifting the focus of attention is either overt and produces a saccade, or it is covert, in which case the saccade is computed but not executed, and fixation is maintained. Furthermore, it indicates that both the network for generating saccades and the network subserving attentional mechanisms at least in part share the same pathways. *PEF*, parietal eye field; *FEF*, frontal eye field; *R*, retinal input; *SNpr*, substantia nigra pars reticulata; *BUN*, build-up neuron; *FN*, fixation neuron; *SC*, superior colliculus (all layers merged); *c*, caudal; *r*, rostral; *BOMS*, brainstem oculomotor system; *BG*, burst-generator neuron; *OP*, omnipause neuron. Heights of Gaussians indicate discharge activity of a cell cluster

colliculus itself integrates direct retinal input (R) and various competing subcortical signals, as well as cortical signals emerging from striate and extrastriate visual areas, e.g., V2 (Brodmann area 18), the parietal eye fields (PEF), and mainly the FEF with its direct as well as (caudally inhibitory) indirect pathway through the substantia nigra pars reticulata (SNpr) (Fig. 3.39) (Keating and Gooley 1988; Hikosaka et al. 2000). At this level, a similar push-pull interaction between the discharge activity of the rostral fixation neurons and more caudal build-up neurons, which are anatomically connected to the omnipause and burst cells, respectively, decides whether and where a saccade should be made. During visual fixation, fixation neurons activate omnipause cells, which prevent burst cells from eliciting an unwanted saccade. After the appearance of a novel visual target (T), retinotopically matching build-up neurons, which activate burst cells, start firing, while fixation neurons and omnipause cells are gradually inhibited (Dorris et al. 1997). Finally, if activity of a confined cluster of build-up neurons overrides the activity of the fixation neurons, the burst cells move the eyes to the spatial location coded by this particular cluster. However, while T conveys the movement signal to a possible new target, and therefore reflects and fully employs premotor computation of the metrics for an appropriate saccade, this process by itself does not guarantee that an eye movement will be triggered, since the neurons in the superior colliculus (fixation neurons and build-up neurons) are functionally not tightly connected with their respective counterparts in the brainstem oculomotor system (omnipause and burst cells) (Everling et al. 1998). Instead, this mechanism ensures that prior to each movement, a target map is generated, and an attention mechanism is engaged (covertly) that is necessary for the selection process by enhancing the response to relevant features (Vanni and Uutela 2000; Beauchamp et al. 2001). Hence, the superior colliculus acts as a complex sensori-motor engine processing command signals for the eye movement in parallel with resolving conflicts in target selection occurring at various cortical levels by competitive inhibition. The occipital cortex contributes with feature maps extracted by pre-attentive segmentation, while the parietal eye field reconstructs an observer-centered frame of reference from various spatial maps (visual, vestibular, and somatosensory) and engages in the selection process by enhancing signals coding seemingly important objects. In addition, the frontal eye field provides signals to the attention system that represent further weighting of relevant location vectors from the parietal eye field in view of the behavioral context composed of a memory trace of previous motor outputs as well as expectancy and intention.

Figures 3.15, 3.40, and 3.41 summarize the influence of cortical areas on saccade performance in normal and pathological conditions (Fox et al. 1985; Nagel et al. 1990; Pierrot et al. 1991, 1995; Pierrot 1994; Sullivan et al. 1995; Heide et al. 1995, 2001; Heide and Kompf 1998; Gaymard et al. 1998; Leigh and Zee 1999).

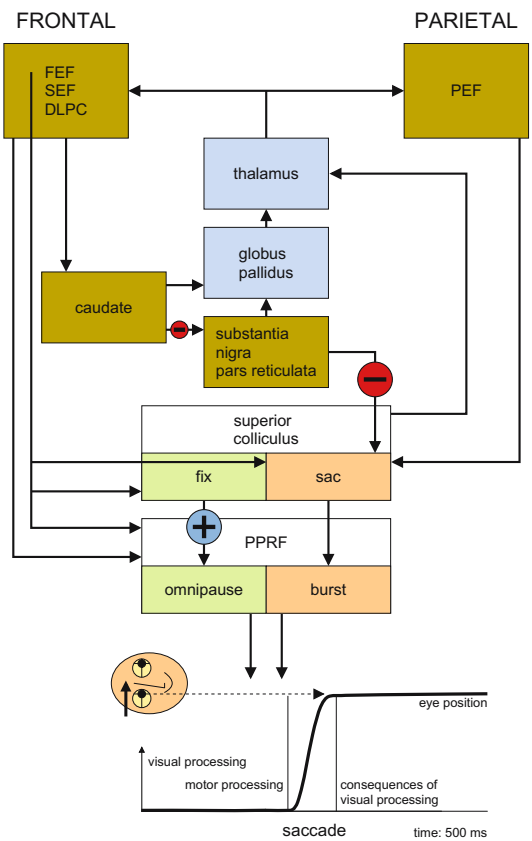

Fig. 3.39. Simplified diagram of the involvement of the extrapyramidal system in the generation of saccadic eye movements (see also Fig. 3.38). *Top panel*. During visual processing and visuo-motor transformation, fixation is maintained by the omnipause neurons, which are directly controlled by fixation neurons (*fix*) in the superior colliculus. In addition, the pars reticulata of the substantia nigra inhibits peripheral build-up neurons (*sac*), albeit not in a very clear way and profoundly influenced by the behavioral context. It is controlled by the frontal cortical eye movement system via the caudate nucleus, which, in turn, inhibits the substantia pars reticulata. Depending on the site of an extrapyramidal lesion, it may cause (a) incapacitating saccadic intrusions as well as (b) the inability to launch a new saccade. *Bottom panel*. Eye position during execution of a saccade. Shown are the various epochs of supranuclear control. Shortly before the eyes are moved into a new position, the omnipause neurons are inhibited. Subsequently, the brainstem burst neurons are activated by the peripheral build-up neurons (*sac*) of the superior colliculus

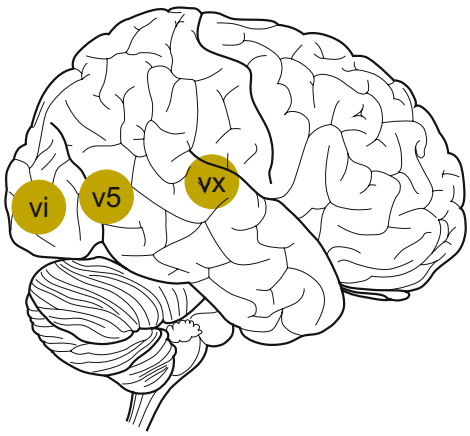

v1
anopsias
defects of perception
acutely: unable to make sac or generate smooth pursuit to visual stimuli presented into the blind field
chronically: strategies develop to scan the environment and place the target into intact field

v5 (MT)
retinotopic defect of motion vision causing sac and smooth pursuit to be impaired when visual stimuli fall into affected visual field

v5 (MST)
directional defect of smooth pursuit for ipsilateral target motion

vx
contralateral tilt of subjective visual vertical
circularvection abolished during optokinetic stimulation

Fig. 3.40. Characteristic deficits of saccades and smooth pursuit eye movements after lesions of various visual cortical areas (see Fig. 3.15 for labels)

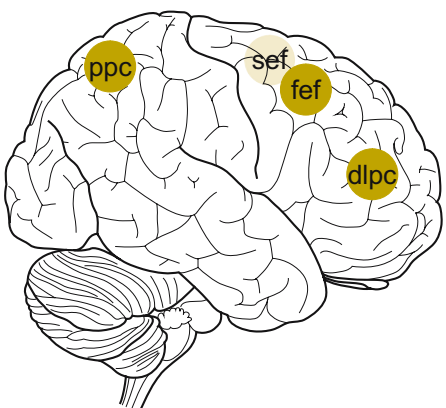

ppc
contralateral inattention
ipsilateral gaze deviation / preference
increased latency for visually guided sac
errors on response to double-step sac
impaired smooth pursuit
if target moves across background

ppc bilateral
Balint's syndrome
peripheral visual inattention (simultanagnosia)
inaccurate arm pointing (optic ataxia)
difficulties in making visually guided sac

sef
does not affect visually guided sac
inaccuracy of memory guided sac
if gaze shifts during memory period
impaired ability to make remembered sequence of sac
especially with left-sided lesions

fef
increase in reaction time of sac
visual target in overlap task
remembered target location
imagined target in antisac task
hypometria of sac
visual / remembered target contralateral
reduced ability to make sac
in anticipation of predictable target stepping contralaterally
impaired ability to inhibit inappropriate sac to novel target
impairment of smooth pursuit and okr moving ipsilaterally

dlpc
inaccuracy of sac made to
remembered target locations contralaterally
defects of
predictive sac
memory guided sac
antisac

Fig. 3.41. Characteristic deficits of saccades and smooth pursuit eye movements after lesions of various parietal and frontal cortical areas (see Fig. 3.15 for labels)

3.3.4.2 Smooth Pursuit Eye Movements

Smooth pursuit eye movements minimize the retinal slip of a target moving through a stationary visual environment (Tychsen and Lisberger 1986). As a geometrical consequence of the ongoing eye movement, the optokinetic system (see above) is engaged in the opposite direction (global motion of the stationary surroundings). It is still a conundrum how the self-induced optokinetic reflex is suppressed or even cancelled (Schwarz and Ilg 1999; Born et al. 2000; Lindner et al. 2001).

Smooth pursuit signals originate in the striate and extrastriate (notably area V5) visual cortex, which implement the cortical motion processing system that computes direction and speed of the target (Figs. 3.4, 3.15) (Barton et al. 1996; Lekwuwa and

Barnes 1996; Greenlee 2000). Transformed target parameters are conveyed to a subregion of the frontal eye field which is not shared by the saccade system (Petit et al. 1997; Petit and Haxby 1999). Motor commands from the frontal eye field as well as target parameters extracted by V5 are transmitted to the dorsolateral pontine nucleus (DLPN), which is the crucial relay in the smooth pursuit system between cortical motion processing and the oculomotor system of the cerebellum and brain stem (Suzuki and Keller 1984; Mustari et al. 1988; Leichnetz 1989; Buttner-Ennever and Buttner 1992; Kawano et al. 1992; Kato et al. 1993). Lesions in this nucleus severely disrupt ipsilateral smooth pursuit (May et al. 1988; Suzuki et al. 1999). The output of the DLPN neurons is transmitted to the vestibular cerebellum (flocculus, paraflocculus, and vermis). Finally, cerebellar pursuit information is passed to the medial vestibular nuclei, the paramedian pontine reticular formation, and the nucleus prepositus hypoglossi.

Any disruption in the smooth pursuit system leads to inadequate eye velocity signals, and the resulting lag must be compensated for by small saccades. Cerebellar and brainstem lesions cause pursuit deficits toward the side of the lesion (Nawrot and Rizzo 1995; Deleu et al. 1997), whereas lesions of the lateral geniculate nucleus as well as cortical lesions cause a variety of deficits (Leigh and Tusa 1985; Dursteler et al. 1987; Thurston et al. 1988; Morrow and Sharpe 1993; Keating 1993; Page et al. 1994; Lekwuwa and Barnes 1996; Heide et al. 1996):

- Parietal lesions may cause
  - directional deficits for targets moving toward the side of the lesion
  - retinotopic deficits for targets moving in the visual hemifield opposite to the lesion
- Frontal eye field lesions cause varying deficits, which depend on the dysfunctional ensemble of neurons that encode a particular direction.

In addition, false perception of motion might occur due to the lack of compensation for self-induced eye movements (Haarmeier et al. 1997).

3.3.4.3 Vergence

Vergence eye movements have developed only with binocular foveal vision in order to converge or diverge the lines of gaze from both eyes onto a target moving in depth (minimizing disparity). Together with accommodation, they are controlled by neurons in the midbrain (Morgan 1968; Toates 1974; Hain and Zee 1989; Averbuch and Leigh 1996; Gamlin et al. 1996; Buttner-Ennever and Horn 1997). Hence, lesions in this region may cause a complete deterioration of vergence, which typically involves vertical eye movements as well. On the other hand, vergence is often preserved in an internuclear ophthalmoplegia with supranuclear paresis of the medial rectus muscle during conjugate horizontal eye movements and, therefore, can be a useful test in differentiating this lesion from a nuclear or infranuclear oculomotor palsy or paresis of the medial rectus muscle (Milder and Billson 1989; Zee 1992; Downey and Leigh 1998).

3.3.4.4 Fixation

A neural system of fixation, which is most likely tightly linked to the saccadic and smooth pursuit system, actively prevents disruptive eye movements. Disorders of this system (e.g., congenital nystagmus or saccadic intrusions) cause seemingly poor vision and poor reading skills.

References

Al-Din, Anderson M, Eeg O, Trontelj JV (1994) Neuro-ophthalmic manifestations of the syndrome of ophthalmoplegia, ataxia and areflexia: a review. Acta Neurol Scand 89:157–163

Allison T, McCarthy G, Nobre A, Puce A, Belger A (1994) Human extrastriate visual cortex and the perception of faces, words, numbers, and colors. Cereb Cortex 4:544–554

Alonso JM, Usrey WM, Reid RC (1996) Precisely correlated firing in cells of the lateral geniculate nucleus. Nature 383:815–819

Anastasio TJ (1991) Neural network models of velocity storage in the horizontal vestibulo-ocular reflex. Biol Cybern 64:187–196

Andersen RA (1995) Encoding of intention and spatial location in the posterior parietal cortex. Cereb Cortex 5:457–469

Andersen RA (1997) Multimodal integration for the representation of space in the posterior parietal cortex. Philos Trans R Soc Lond B Biol Sci 352:1421–1428

Andersen RA, Brotchie PR, Mazzoni P (1992) Evidence for the lateral intraparietal area as the parietal eye field. Curr Opin Neurobiol 2:840–846

Andersen RA, Snyder LH, Li CS, Stricanne B (1993) Coordinate transformations in the representation of spatial information. Curr Opin Neurobiol 3:171–176

Andersen RA, Snyder LH, Batista AP, Buneo CA, Cohen YE (1998) Posterior parietal areas specialized for eye movements (LIP) and reach (PRR) using a common coordinate frame. Novartis Found Symp 218:109–122

Anderson ML (1992) Imaging advances in neuro-ophthalmology. Curr Opin Ophthalmol 3:615–619

Angelaki DE, Hess BJ, Suzuki J (1995) Differential processing

of semicircular canal signals in the vestibulo-ocular reflex. J Neurosci 15:7201–7216
Aoki M, Ito Y, Burchill P, Brookes GB, Gresty MA (1999) Tilted perception of the subjective 'upright' in unilateral loss of vestibular function. Am J Otol 20:741–747
Averbuch H, Leigh RJ (1996) Eye movements. Curr Opin Neurol 9:26–31
Baloh RW (1998a) Dizziness: neurological emergencies. Neurol Clin 16:305–321
Baloh RW (1998b) Vertigo. Lancet 352:1841–1846
Baloh RW, Honrubia V (1990) Clinical neurophysiology of the vestibular system. Davis, Philadelphia
Baloh RW, Jacobson KM (1996) Neurotology. Neurol Clin 14:85–101
Baloh RW, Lopez I, Beykirch K, Ishiyama A, Honrubia V (1997) Clinical-pathologic correlation in a patient with selective loss of hair cells in the vestibular endorgans. Neurology 49:1377–1382
Bar M, Biederman I (1999) Localizing the cortical region mediating visual awareness of object identity. Proc Natl Acad Sci USA 96:1790–1793
Barash S, Bracewell RM, Fogassi L, Gnadt JW, Andersen RA (1991a) Saccade-related activity in the lateral intraparietal area. I. Temporal properties; comparison with area 7a. J Neurophysiol 66:1095–1108
Barash S, Bracewell RM, Fogassi L, Gnadt JW, Andersen RA (1991b) Saccade-related activity in the lateral intraparietal area. II. Spatial properties. J Neurophysiol 66:1109–1124
Bartleson JD, Trautmann JC, Sundt TM (1986) Minimal oculomotor nerve paresis secondary to unruptured intracranial aneurysm. Arch Neurol 43:1015–1020
Barton JJ, Simpson T, Kiriakopoulos E, Stewart C, Crawley A, Guthrie B, Wood M, Mikulis D (1996) Functional MRI of lateral occipitotemporal cortex during pursuit and motion perception. Ann Neurol 40:387–398
Bassetti C, Bogousslavsky J, Barth A, Regli F (1996) Isolated infarcts of the pons. Neurology 46:165–175
Beauchamp MS, Petit L, Ellmore TM, Ingeholm J, Haxby JV (2001) A parametric fMRI study of overt and covert shifts of visuospatial attention. Neuroimage 14:310–321
Becker W (1989) Metrics. In: Wurtz RH, Goldberg ME (eds) The neurobiology of saccadic eye movements. (Reviews of oculomotor research, vol 3) Elsevier, New York, pp 13–39
Belton T, McCrea RA (1999) Contribution of the cerebellar flocculus to gaze control during active head movements. J Neurophysiol 81:3105–3109
Belton T, McCrea RA (2000) Role of the cerebellar flocculus region in the coordination of eye and head movements during gaze pursuit. J Neurophysiol 84:1614–1626
Benardete EA, Kaplan E (1997a) The receptive field of the primate P retinal ganglion cell. I. Linear dynamics. Vis Neurosci 14:169–185
Benardete EA, Kaplan E (1997b) The receptive field of the primate P retinal ganglion cell. II. Nonlinear dynamics. Vis Neurosci 14:187–205
Benardete EA, Kaplan E (1999) Dynamics of primate P retinal ganglion cells: responses to chromatic and achromatic stimuli. J Physiol (Lond) 519(3):775–790
Biedert S, Weidauer H, Reuther R (1985) Differential diagnosis of tinnitus and vertigo. A review. Nervenarzt 56:535–542
Birchall D, Khangure MS, McAuliffe W (1999) Resolution of third nerve paresis after endovascular management of aneurysms of the posterior communicating artery. Am J Neuroradiol 20:411–413
Bixenman WW (1981) Diagnosis of superior oblique palsy. J Clin Neuroophthalmol 1:199–208
Boccardo M, Ruelle A, Banchero MA (1986) Isolated oculomotor palsy caused by aneurysm of the basilar artery bifurcation. J Neurol 233:61–62
Bogousslavsky J, Meienberg O (1987) Eye-movement disorders in brain-stem and cerebellar stroke. Arch Neurol 44:141–148
Bohmer A (1999) The subjective visual vertical as a clinical parameter for acute and chronic vestibular (otolith) disorders. Acta Otolaryngol 119:126–127
Born RT, Groh JM, Zhao R, Lukasewycz SJ (2000) Segregation of object and background motion in visual area MT: effects of microstimulation on eye movements. Neuron 26:725–734
Bradley DR, Petry HM (1977) Organizational determinants of subjective contour: the subjective Necker cube. Am J Psychol 90:253–262
Brandt T, Dieterich M (1993) Skew deviation with ocular torsion: a vestibular brainstem sign of topographic diagnostic value. Ann Neurol 33:528–534
Brandt T, Dieterich M (2000) Perceived vertical and lateropulsion: clinical syndromes, localization, and prognosis. Neurorehabil Neural Repair 14:1–12
Brazis PW (1993) Palsies of the trochlear nerve: diagnosis and localization – recent concepts. Mayo Clin Proc 68:501–509
Brodmann K (1909) Vergleichende Lokalisationslehere der Grosshirnrinde in ihren Prinzipien dargestellt auf Grund des Zellenbaues. Johann Ambrosius Barth, Leipzig
Bulens C, Meerwaldt JD, Van der Wildt GJ, Van Deursen JB (1987) Effect of levodopa treatment on contrast sensitivity in Parkinson's disease. Ann Neurol 22:365–369
Burnod Y, Baraduc P, Battaglia M, Guigon E, Koechlin E, Ferraina S, Lacquaniti F, Caminiti R (1999) Parieto-frontal coding of reaching: an integrated framework. Exp Brain Res 129:325–346
Buttner-Ennever JA (1988) Neuroanatomy of the oculomotor system. (Reviews of oculomotor research, Vol 2) Elsevier, New York
Buttner-Ennever JA, Buttner U (1992) Neuroanatomy of the ocular motor pathways. Baillieres Clin Neurol 1:263–287
Buttner-Ennever JA, Horn AK (1997) Anatomical substrates of oculomotor control. Curr Opin Neurobiol 7:872–879
Buttner-Ennever JA, Horn AK, Schmidtke K (1989) Cell groups of the medial longitudinal fasciculus and paramedian tracts. Rev Neurol (Paris) 145:533–539
Cai D, DeAngelis GC, Freeman RD (1997) Spatiotemporal receptive field organization in the lateral geniculate nucleus of cats and kittens. J Neurophysiol 78:1045–1061
Caminiti R, Ferraina S, Johnson PB (1996) The sources of visual information to the primate frontal lobe: a novel role for the superior parietal lobule. Cereb Cortex 6:319–328
Cannon SC, Robinson DA (1987) Loss of the neural integrator of the oculomotor system from brain stem lesions in monkey. J Neurophysiol 57:1383–1409
Carlow TJ (1989) Paresis of cranial nerves III, IV, and VI: clinical manifestation and differential diagnosis. Bull Soc Belge Ophtalmol 237:285–301
Carpenter RHS (1988) Movements of the eyes. Pion, London
Cassidy L, Taylor D, Harris C (2000) Abnormal supranuclear eye movements in the child: a practical guide to examination and interpretation. Surv Ophthalmol 44:479–506

Castro O, Johnson LN, Mamourian AC (1990) Isolated inferior oblique paresis from brain-stem infarction. Perspective on oculomotor fascicular organization in the ventral midbrain tegmentum. Arch Neurol 47:235–237

Cawley CM, Zipfel GJ, Day AL (1998) Surgical treatment of paraclinoid and ophthalmic aneurysms. Neurosurg Clin North Am 9:765–783

Cheng K, Fujita H, Kanno I, Miura S, Tanaka K (1995) Human cortical regions activated by wide-field visual motion: an H2(15)O PET study. J Neurophysiol 74:413–427

Colby CL, Goldberg ME (1999) Space and attention in parietal cortex. Annu Rev Neurosci 22:319–349

Colby CL, Duhamel JR, Goldberg ME (1993) The analysis of visual space by the lateral intraparietal area of the monkey: the role of extraretinal signals. Prog Brain Res 95:307–316

Colby CL, Duhamel JR, Goldberg ME (1995) Oculocentric spatial representation in parietal cortex. Cereb Cortex 5:470–481

Constantoyannis C, Tzortzidis F, Papadakis N (1998) Internuclear ophthalmoplegia following minor head injury: a case report. Br J Neurosurg 12:377–379

Correia MJ, Ricci AJ, Rennie KJ (1996) Filtering properties of vestibular hair cells: an update. Ann NY Acad Sci 781:138–149

Coupland SG, Zackon DH, Leonard BC, Ross TM (2001) Vigabatrin effect on inner retinal function. Ophthalmology 108:1493–1496

Critchley M (1951) Types of viusal perseveration: 'paliopsia' and 'illusory visual spread'. Brain 74:267–299

Croner LJ, Kaplan E (1995) Receptive fields of P and M ganglion cells across the primate retina. Vision Res 35:7–24

Dalmau J, Porta-Etessam J (2000) Paraneoplastic cerebral syndromes with oto-neuro-ophthalomologic manifestations. Rev Neurol 31:1213–1219

Daugman JG (1985) Uncertainty relation for resolution in space, spatial frequency, and orientation optimized by two-dimensional visual cortical filters. J Opt Soc Am A 2:1160–1169

Dayan MR, Elston JS (1999) Fluctuating oculomotor hyperfunction and hypofunction caused by aneurysmal compression of the third cranial nerve. Br J Ophthalmol 83:1204

de Morsier G (1936) Les automatismes visuels. (Hallucinations visuelles rétrochiasmatiques) Schweiz Med Wochenschr 66:700–703

de Morsier G (1967) Le syndrom de Charles Bonnet: hallucinations visuelles des vieillards sans deficience mentale. Ann Med Psychol 125:702

DeAngelis GC, Ohzawa I, Freeman RD (1995) Receptive-field dynamics in the central visual pathways. Trends Neurosci 18:451–458

Dehaene I (1994) Isolated oculomotor nerve palsy. Acta Neurol Belg 94:5–7

Deleu D, Michotte A, Ebinger G (1997) Impairment of smooth pursuit in pontine lesions: functional topography based on MRI and neuropathologic findings. Acta Neurol Belg 97:28–35

Desimone R, Schein SJ (1987) Visual properties of neurons in area V4 of the macaque: sensitivity to stimulus form. J Neurophysiol 57:835–868

Desimone R, Schein SJ, Moran J, Ungerleider LG (1985) Contour, color and shape analysis beyond the striate cortex. Vision Res 25:441–452

Dickman JD, Correia MJ (1989a) Responses of pigeon horizontal semicircular canal afferent fibers. I. Step, trapezoid, and low-frequency sinusoid mechanical and rotational stimulation. J Neurophysiol 62:1090–1101

Dickman JD, Correia MJ (1989b) Responses of pigeon horizontal semicircular canal afferent fibers. II. High-frequency mechanical stimulation. J Neurophysiol 62:1102–1112

Dickman JD, Correia MJ (1992) Vestibular efferent system in pigeons. Anatomical organization and effect upon semicircular canal afferent responsiveness. Ann NY Acad Sci 656:927–930

Dieterich M, Brandt T (1993) Ocular torsion and tilt of subjective visual vertical are sensitive brainstem signs. Ann Neurol 33:292–299

DiMario FJ, Rorke LB (1992) Transient oculomotor nerve paresis in congenital distal basilar artery aneurysm. Pediatr Neurol 8:303–306

Distler C, Hoffmann KP (2001) Cortical input to the nucleus of the optic tract and dorsal terminal nucleus (NOT-DTN) in macaques: a retrograde tracing study. Cereb Cortex 11:572–580

Dolan RJ, Fink GR, Rolls E, Booth M, Holmes A, Frackowiak RS, Friston KJ (1997) How the brain learns to see objects and faces in an impoverished context. Nature 389:596–599

Dominey PF, Arbib MA (1992) A cortico-subcortical model for generation of spatially accurate sequential saccades. Cereb Cortex 2:153–175

Donzelli R, Marinkovic S, Brigante L, Nikodijevic I, Maiuri F, de Divitis O (1998) The oculomotor nuclear complex in humans. Microanatomy and clinical significance. Surg Radiol Anat 20:7–12

Dorris MC, Pare M, Munoz DP (1997) Neuronal activity in monkey superior colliculus related to the initiation of saccadic eye movements. J Neurosci 17:8566–8579

Downey DL, Leigh RJ (1998) Eye movements: pathophysiology, examination and clinical importance. J Neurosci Nurs 30:15–22

Duhamel JR, Colby CL, Goldberg ME (1992) The updating of the representation of visual space in parietal cortex by intended eye movements. Science 255:90–92

Duhamel JR, Colby CL, Goldberg ME (1998) Ventral intraparietal area of the macaque: congruent visual and somatic response properties. J Neurophysiol 79:126–136

Dursteler MR, Wurtz RH, Newsome WT (1987) Directional pursuit deficits following lesions of the foveal representation within the superior temporal sulcus of the macaque monkey. J Neurophysiol 57:1262–1287

Eggenberger ER, Desai NP, Kaufman DI, Pless M (2000) Internuclear ophthalmoplegia after coronary artery catheterization and percutaneous transluminal coronary balloon angioplasty. J Neuroophthalmol 20:123–126

Everling S, Pare M, Dorris MC, Munoz DP (1998) Comparison of the discharge characteristics of brain stem omnipause neurons and superior colliculus fixation neurons in monkey: implications for control of fixation and saccade behavior. J Neurophysiol 79:511–528

Faillenot I, Toni I, Decety J, Gregoire MC, Jeannerod M (1997) Visual pathways for object-oriented action and object recognition: functional anatomy with PET. Cereb Cortex 7:77–85

Faillenot I, Decety J, Jeannerod M (1999) Human brain activity related to the perception of spatial features of objects. Neuroimage 10:114–124

Felleman DJ, Van Essen DC (1991) Distributed hierarchical processing in the primate cerebral cortex. Cereb Cortex 1:1–47

ffytche DH, Howard RJ (1999) The perceptual consequences of visual loss: 'positive' pathologies of vision. Brain 122:1247–1260

ffytche DH, Howard RJ, Brammer MJ, David A, Woodruff P, Williams S (1998) The anatomy of conscious vision: an fMRI study of visual hallucinations. Nat Neurosci 1:738–742

Fox PT, Fox JM, Raichle ME, Burde RM (1985) The role of cerebral cortex in the generation of voluntary saccades: a positron emission tomographic study. J Neurophysiol 54:348–369

Fredericks CA, Giolli RA, Blanks RH, Sadun AA (1988) The human accessory optic system. Brain Res 454:116–122

Fuchs AF, Luschei ES (1970) Firing patterns of abducens neurons of alert monkeys in relationship to horizontal eye movement. J Neurophysiol 33:382–392

Fuchs AF, Mustari MJ (1993) The optokinetic response in primates and its possible neuronal substrate. Rev Oculomot Res 5:343–369

Fujiwara S, Fujii K, Nishio S, Matsushima T, Fukui M (1989) Oculomotor nerve palsy in patients with cerebral aneurysms. Neurosurg Rev 12:123–132

Funke K, Meller P, Pape HC, Eysel UT (1996) Linear and nonlinear components in the centre-surround response of X- and Y-cells in the cat lateral geniculate nucleus. Brain Res 742:50–62

Gabor D (1946) Theory of communication. J IEE 93:429–459

Galiana HL (1986) A new approach to understanding adaptive visual-vestibular interactions in the central nervous system. J Neurophysiol 55:349–374

Galindo M, Pablos JL, Gomez R (1998) Internuclear ophthalmoplegia in systemic lupus erythematosus. Semin Arthritis Rheum 28:179–186

Gamlin PD, Reiner A (1991) The Edinger-Westphal nucleus: sources of input influencing accommodation, pupilloconstriction, and choroidal blood flow. J Comp Neurol 306:425–438

Gamlin PD, Yoon K, Zhang H (1996) The role of cerebro-pontocerebellar pathways in the control of vergence eye movements. Eye 10(2):167–171

Gancarz G, Grossberg S (1999) A neural model of saccadic eye movement control explains task-specific adaptation. Vision Res 39:3123–3143

Gauntt CD, Kashii S, Nagata I (1995) Monocular elevation paresis caused by an oculomotor fascicular impairment. J Neuroophthalmol 15:11–14

Gauthier I, Anderson AW, Tarr MJ, Skudlarski P, Gore JC (1997) Levels of categorization in visual recognition studied using functional magnetic resonance imaging. Curr Biol 7:645–651

Gawne TJ, McClurkin JW, Richmond BJ, Optican LM (1991) Lateral geniculate neurons in behaving primates. III. Response predictions of a channel model with multiple spatial-to-temporal filters. J Neurophysiol 66:809–823

Gaymard B, Pierrot D (1999) Neurology of saccades and smooth pursuit. Curr Opin Neurol 12:13–19

Gaymard B, Ploner CJ, Rivaud S, Vermersch AI, Pierrot D (1998) Cortical control of saccades. Exp Brain Res 123:159–163

Gilmore GC, Wenk HE, Naylor LA, Koss E (1994) Motion perception and Alzheimer's disease. J Gerontol 49:52–57

Glimcher PW (1999) Eye movements. In: Zigmond MJ, Bloom FE, Landis SC, Roberts JL, Squire LR (eds) Fundamental neuroscience. Academic, San Diego, pp 993–1010

Goldberg ME (2000) The control of gaze. In: Kandel ER, Schwartz JH, Jessell TM (eds) Principles of neural science. McGraw-Hill, New York, pp 782–800

Goldberg ME, Segraves MA (1989) The visual and frontal cortices. Rev Oculomot Res 3:283–313

Goldberg ME, Colby CL, Duhamel JR (1990) Representation of visuomotor space in the parietal lobe of the monkey. Cold Spring Harb Symp Quant Biol 55:729–739

Grad A, Baloh RW (1989) Vertigo of vascular origin. Clinical and electronystagmographic features in 84 cases. Arch Neurol 46:281–284

Greenlee MW (2000) Human cortical areas underlying the perception of optic flow: brain imaging studies. Int Rev Neurobiol 44:269–292

Grüsser O-J, Landis T (1991) Visual agnosias and other disturbances of visual perception and cognition. Macmillan, London

Guitton D, Buchtel HA, Douglas RM (1985) Frontal lobe lesions in man cause difficulties in suppressing reflexive glances and in generating goal-directed saccades. Exp Brain Res 58:455–472

Guy JR, Day AL (1989) Intracranial aneurysms with superior division paresis of the oculomotor nerve. Ophthalmology 96:1071–1076

Guy JR, Savino PJ, Schatz NJ, Cobbs WH, Day AL (1985) Superior division paresis of the oculomotor nerve. Ophthalmology 92:777–784

Guyton DL (1988) Ocular torsion: sensorimotor principles. Graefes Arch Clin Exp Ophthalmol 226:241–245

Haarmeier T, Thier P, Repnow M, Petersen D (1997) False perception of motion in a patient who cannot compensate for eye movements. Nature 389:849–852

Hain TC, Zee DS (1989) Vergence. Bull Soc Belge Ophtalmol 237:145–161

Hain TC, Zee DS (1992) Velocity storage in labyrinthine disorders. Ann NY Acad Sci 656:297–304

Hamer J (1982) Prognosis of oculomotor palsy in patients with aneurysms of the posterior communicating artery. Acta Neurochir (Wien) 66:173–185

Hanes DP, Wurtz RH (2001) Interaction of the frontal eye field and superior colliculus for saccade generation. J Neurophysiol 85:804–815

Harding GF, Wild JM, Robertson KA, Lawden MC, Betts TA, Barber C, Barnes PM (2000) Electro-oculography, electroretinography, visual evoked potentials, and multifocal electroretinography in patients with vigabatrin-attributed visual field constriction. Epilepsia 41:1420–1431

Hartline HK (1938) The response of single optic nerve fibers of the vertebrate eye to illumination of the retina. Am J Physiol 121:400–415

Hasselmo ME, Rolls ET, Baylis GC (1989) The role of expression and identity in the face-selective responses of neurons in the temporal visual cortex of the monkey. Behav Brain Res 32:203–218

Haug BA, Trenkwalder C, Arden GB, Oertel WH, Paulus W (1994) Visual thresholds to low-contrast pattern displacement, color contrast, and luminance contrast stimuli in Parkinson's disease. Mov Disord 9:563–570

Heide W, Kompf D (1998) Combined deficits of saccades and visuo-spatial orientation after cortical lesions. Exp Brain Res 123:164–171

Heide W, Blankenburg M, Zimmermann E, Kompf D (1995)

Cortical control of double-step saccades: implications for spatial orientation. Ann Neurol 38:739–748
Heide W, Kurzidim K, Kompf D (1996) Deficits of smooth pursuit eye movements after frontal and parietal lesions. Brain 119(6):1951–1969
Heide W, Binkofski F, Seitz RJ, Posse S, Nitschke MF, Freund HJ, Kompf D (2001) Activation of frontoparietal cortices during memorized triple-step sequences of saccadic eye movements: an fMRI study. Eur J Neurosci 13:1177–1189
Hendry SH, Reid RC (2000) The koniocellular pathway in primate vision. Annu Rev Neurosci 23:127–153
Henn V (2000) Vertigo. In: Fölsch UR, Kochsiek K, Schmidt RF (eds) Pathophysiologie. Springer, Berlin, Heidelberg, New York, pp 527–538
Henn V, Young LR, Finley C (1974) Vestibular nucleus units in alert monkeys are also influenced by moving visual fields. Brain Res 71:144–149
Henn V, Hepp K, Vilis T (1989) Rapid eye movement generation in the primate. Physiology, pathophysiology, and clinical implications. Rev Neurol (Paris) 145:540–545
Hepp K, Henn V (1983) Spatio-temporal recoding of rapid eye movement signals in the monkey paramedian pontine reticular formation (PPRF). Exp Brain Res 52:105–120
Hess BJ, Angelaki DE (1999) Inertial processing of vestibulo-ocular signals. Ann NY Acad Sci 871:148–161
Hikosaka O, Takikawa Y, Kawagoe R (2000) Role of the basal ganglia in the control of purposive saccadic eye movements. Physiol Rev 80:953–978
Hoffmann KP (1996) Comparative neurobiology of the optokinetic reflex in mammals. Rev Bras Biol 56(1/2):303–314
Hoffmann KP, Distler C (1989) Quantitative analysis of visual receptive fields of neurons in nucleus of the optic tract and dorsal terminal nucleus of the accessory optic tract in macaque monkey. J Neurophysiol 62:416–428
Horn AK, Buttner-Ennever JA (1998) Premotor neurons for vertical eye movements in the rostral mesencephalon of monkey and human: histologic identification by parvalbumin immunostaining. J Comp Neurol 392:413–427
Horn AK, Buttner-Ennever JA, Suzuki Y, Henn V (1995) Histological identification of premotor neurons for horizontal saccades in monkey and man by parvalbumin immunostaining. J Comp Neurol 359:350–363
Horn AK, Buttner U, Buttner-Ennever JA (1999) Brainstem and cerebellar structures for eye movement generation. Adv Otorhinolaryngol 55:1–25
Horn AK, Buttner-Ennever JA, Gayde M, Messoudi A (2000) Neuroanatomical identification of mesencephalic premotor neurons coordinating eyelid with upgaze in the monkey and man. J Comp Neurol 420:19–34
Hotson JR, Anand S (1999) The selectivity and timing of motion processing in human temporo-parieto-occipital and occipital cortex: a transcranial magnetic stimulation study. Neuropsychologia 37:169–179
Hotson JR, Baloh RW (1998) Acute vestibular syndrome. N Engl J Med 339:680–685
Hubel DH (1988) Eye, brain, and vision. Scientific American Library, New York
Hubel DH, Wiesel TN (1959) Receptive fields of single neurones in the cat's visual cortex. J Physiol 148:574–591
Hubel DH, Wiesel TN (1962) Receptive fields, binocular interaction and functional architecture in the cat's visual cortex. J Physiol (Lond) 160:106–154
Hubel DH, Wiesel TN (1979) Brain mechanisms of vision. Sci Am 241:150–162
Huber A, Kömpf D (1998) Klinische Neuroophthalmologie. Thieme, Stuttgart
Hullar TE, Minor LB (1999) High-frequency dynamics of regularly discharging canal afferents provide a linear signal for angular vestibuloocular reflexes. J Neurophysiol 82:2000–2005
Ito M (1993) Neurophysiology of the nodulofloccular system. Rev Neurol (Paris) 149:692–697
Jeannerod M, Arbib MA, Rizzolatti G, Sakata H (1995) Grasping objects: the cortical mechanisms of visuomotor transformation. Trends Neurosci 18:314–320
Johkura K, Matsumoto S, Komiyama A, Hasegawa O, Kuroiwa Y (1998) Unilateral saccadic pursuit in patients with sensory stroke: sign of a pontine tegmentum lesion. Stroke 29:2377–2380
Jones JP, Palmer LA (1987a) An evaluation of the two-dimensional Gabor filter model of simple receptive fields in cat striate cortex. J Neurophysiol 58:1233–1258
Jones JP, Palmer LA (1987b) The two-dimensional spatial structure of simple receptive fields in cat striate cortex. J Neurophysiol 58:1187–1211
Jones JP, Stepnoski A, Palmer LA (1987) The two-dimensional spectral structure of simple receptive fields in cat striate cortex. J Neurophysiol 58:1212–1232
Kandel ER, Wurtz RH (2000) Constructing the visual image. In: Kandel ER, Schwartz JH, Jessell TM (eds) Principles of neural science. McGraw-Hill, New York, pp 492–506
Kandel ER, Schwartz JH, Jessell TM (2000) Principles of neural science. McGraw-Hill, New York
Kanizsa G (1976) Subjective contours. Sci Am 234:48–52
Kapur N, Friston KJ, Young A, Frith CD, Frackowiak RS (1995) Activation of human hippocampal formation during memory for faces: a PET study. Cortex 31:99–108
Kaskie B, Storandt M (1995) Visuospatial deficit in dementia of the Alzheimer type. Arch Neurol 52:422–425
Kasner SE, Liu GT, Galetta SL (1997) Neuro-ophthalmologic aspects of aneurysms. Neuroimaging Clin North Am 7:679–692
Kato I, Sato S, Watanabe S, Nakashima H, Takeyama I, Watanabe Y (1993) Role of the dorsolateral pontine nucleus in two components of optokinetic nystagmus (OKN). Acta Otolaryngol Suppl 504:7–12
Kawano K, Shidara M, Yamane S (1992) Neural activity in dorsolateral pontine nucleus of alert monkey during ocular following responses. J Neurophysiol 67:680–703
Keane JR (1996) Aneurysmal third-nerve palsies presenting with pleocytosis. Neurology 46:1176
Keating EG (1993) Lesions of the frontal eye field impair pursuit eye movements, but preserve the predictions driving them. Behav Brain Res 53:91–104
Keating EG, Gooley SG (1988) Disconnection of parietal and occipital access to the saccadic oculomotor system. Exp Brain Res 70:385–398
Kimura S (1991) The parasympathetic direct pathway from the midbrain to the ciliary muscle in cats and monkeys. Nippon Ganka Gakkai Zasshi 95:1031–1036
Klooster J, Vrensen GF (1998) New indirect pathways subserving the pupillary light reflex: projections of the accessory oculomotor nuclei and the periaqueductal gray to the Edinger-Westphal nucleus and the thoracic spinal cord in rats. Anat Embryol (Berl) 198:123–132

Komaba Y, Nomoto T, Kitamura S, Terashi A (1997) Cavernous angioma with olivary hypertrophy and contralateral cerebellar diaschisis. Intern Med 36:504–507
Kourtzi Z, Kanwisher N (2000) Activation in human MT/MST by static images with implied motion. J Cogn Neurosci 12:48–55
Kölmel HW (1982) Visuelle Perseveration. Nervenarzt 53:560–571
Kuffler SW (1953) Discharge patterns and functional organization of mammalian retina. J Neurophysiol 16:37–68
Kumar PD, Nartsupha C, West BC (2000) Unilateral internuclear ophthalmoplegia and recovery with thiamine in Wernicke syndrome. Am J Med Sci 320:278–280
Kusunoki M, Gottlieb J, Goldberg ME (2000) The lateral intraparietal area as a salience map: the representation of abrupt onset, stimulus motion, and task relevance. Vision Res 40:1459–1468
Lakshminarayanan V, Lagrave J, Kean ML, Dick M, Shankle R (1996) Vision in dementia: contrast effects. Neurol Res 18:9–15
Lee BB (1996) Receptive field structure in the primate retina. Vision Res 36:631–644
Leichnetz GR (1989) Inferior frontal eye field projections to the pursuit-related dorsolateral pontine nucleus and middle temporal area (MT) in the monkey. Vis Neurosci 3:171–180
Leichnetz GR (2001) Connections of the medial posterior parietal cortex (area 7m) in the monkey. Anat Rec 263:215–236
Leigh RJ, Tusa RJ (1985) Disturbance of smooth pursuit caused by infarction of occipitoparietal cortex. Ann Neurol 17:185–187
Leigh RJ, Zee DS (1999) The neurology of eye movements. Oxford University Press, New York
Lekwuwa GU, Barnes GR (1996) Cerebral control of eye movements. I. The relationship between cerebral lesion sites and smooth pursuit deficits. Brain 119(2):473–490
Leng SZ, Lu XQ, Zhao JH (1994) Eye manifestations of basicranial aneurysms. Chung Hua Yen Ko Tsa Chih 30:19–21
LeVay S, Connolly M, Houde J, Van Essen DC (1985) The complete pattern of ocular dominance stripes in the striate cortex and visual field of the macaque monkey. J Neurosci 5:486–501
Lewis RF, Zee DS (1993) Ocular motor disorders associated with cerebellar lesions: pathophysiology and topical localization. Rev Neurol (Paris) 149:665–677
Lieb K, Brucker S, Bach M, Els T, Lucking CH, Greenlee MW (1999) Impairment in preattentive visual processing in patients with Parkinson's disease. Brain 122(2):303–313
Lindner A, Schwarz U, Ilg UJ (2001) Cancellation of self-induced retinal image motion during smooth pursuit eye movements. Vision Res 41:1685–1694
Lisberger SG, Miles FA, Zee DS (1984) Signals used to compute errors in monkey vestibuloocular reflex: possible role of flocculus. J Neurophysiol 52:1140–1153
Lisberger SG, Morris EJ, Tychsen L (1987) Visual motion processing and sensory-motor integration for smooth pursuit eye movements. Annu Rev Neurosci 10:97–129
Liu GT, Crenner CW, Logigian EL, Charness ME, Samuels MA (1992) Midbrain syndromes of Benedikt, Claude, and Nothnagel: setting the record straight. Neurology 42:1820–1822
Livingstone M, Hubel DH (1988) Segregation of form, color, movement, and depth: anatomy, physiology, and perception. Science 240:740–749
Livingstone MS, Pack CC, Born RT (2001) Two-dimensional substructure of MT receptive fields. Neuron 30:781–793
Mai JK (1978) The accessory optic system and the retinohypothalamic system. A review. J Hirnforsch 19:213–288
Malmgren K, Ben-Menachem E, Frisen L (2001) Vigabatrin visual toxicity: evolution and dose dependence. Epilepsia 42:609–615
Manford M, Andermann F (1998) Complex visual hallucinations. Clinical and neurobiological insights. Brain 121(10):1819–1840
Mansilla AO, Barajas HM, Arguero RS, Alba CC (1995) Receptors, photoreception and brain perception. New insights. Arch Med Res 26:1–15
Marinkoviç S, Gibo H (1994) The neurovascular relationships and the blood supply of the oculomotor nerve: the microsurgical anatomy of its cisternal segment. Surg Neurol 42:505–516
Marinkoviç S, Marinkoviç Z, Filipoviç B (1989) The oculomotor nuclear complex in humans. Microanatomy and clinical significance. Neurologija 38:135–146
Marinkoviç SV, Gibo H, Stimec B (1994) The neurovascular relationships and the blood supply of the abducent nerve: surgical anatomy of its cisternal segment. Neurosurgery 34:1017–1026
Marinkoviç S, Gibo H, Zeliç O, Nikodijeviç I (1996) The neurovascular relationships and the blood supply of the trochlear nerve: surgical anatomy of its cisternal segment. Neurosurgery 38:161–169
Marinkoviç S, Gibo H, Vucevic R, Petrovic P (2001) Anatomy of the cavernous sinus region. J Clin Neurosci 8:78–81
Marr D (1982) Vision: a computational investigation into the human representation and processing of visual information. Freeman, San Francisco
Martin PR, White AJ, Goodchild AK, Wilder HD, Sefton AE (1997) Evidence that blue-on cells are part of the third geniculocortical pathway in primates. Eur J Neurosci 9:1536–1541
May JG, Keller EL, Suzuki DA (1988) Smooth-pursuit eye movement deficits with chemical lesions in the dorsolateral pontine nucleus of the monkey. J Neurophysiol 59:952–977
Mazzoni A (1972) Internal auditory artery supply to the petrous bone. Ann Otol Rhinol Laryngol 81:13–21
McClurkin JW, Gawne TJ, Optican LM, Richmond BJ (1991a) Lateral geniculate neurons in behaving primates. II. Encoding of visual information in the temporal shape of the response. J Neurophysiol 66:794–808
McClurkin JW, Gawne TJ, Richmond BJ, Optican LM, Robinson DL (1991b) Lateral geniculate neurons in behaving primates. I. Responses to two-dimensional stimuli. J Neurophysiol 66:777–793
Meienberg O, Muri R (1992) Nuclear and infranuclear disorders. Baillieres Clin Neurol 1:417–434
Mendola JD, Dale AM, Fischl B, Liu AK, Tootell RB (1999) The representation of illusory and real contours in human cortical visual areas revealed by functional magnetic resonance imaging. J Neurosci 19:8560–8572
Merigan WH, Maunsell JH (1993) How parallel are the primate visual pathways? Annu Rev Neurosci 16:369–402
Milder DG, Billson FA (1989) Supranuclear disorders of eye movement. Aust NZ J Ophthalmol 17:15–21
Miles FA, Lisberger SG (1981) Plasticity in the vestibulo-ocular reflex: a new hypothesis. Annu Rev Neurosci 4:273–299

Miller NR, Newman NJ (1997) Walsh and Hoyt's clinical neuro-ophthalmology. Lippincott/Williams and Wilkins, Baltimore
Milner AD, Goodale MA (1995) The visual brain in action. Oxford University Press, Oxford, UK
Mohler CW, Wurtz RH (1977) Role of striate cortex and superior colliculus in visual guidance of saccadic eye movements in monkeys. J Neurophysiol 40:74–94
Moorthy G, Behrens MM, Drachman DB, Kirkham TH, Knox DL, Miller NR, Slamovitz TL, Zinreich SJ (1989) Ocular pseudomyasthenia or ocular myasthenia 'plus': a warning to clinicians. Neurology 39:1150–1154
Morand S, Thut G, de P, Clarke S, Khateb A, Landis T, Michel CM (2000) Electrophysiological evidence for fast visual processing through the human koniocellular pathway when stimuli move. Cereb Cortex 10:817–825
Morgan MW (1968) Accommodation and vergence. Am J Optom Arch Am Acad Optom 45:417–454
Morrone MC, Burr DC, Vaina LM (1995) Two stages of visual processing for radial and circular motion. Nature 376:507–509
Morrow MJ, Sharpe JA (1993) Retinotopic and directional deficits of smooth pursuit initiation after posterior cerebral hemispheric lesions. Neurology 43:595–603
Mustari MJ, Fuchs AF, Wallman J (1988) Response properties of dorsolateral pontine units during smooth pursuit in the rhesus macaque. J Neurophysiol 60:664–686
Nagel L, Buchtel HA, Welch KM (1990) Cerebral control of directed visual attention and orienting saccades. Brain 113(1):237–276
Najim a, Anderson M, Eeg O, Trontelj JV (1994) Neuro-ophthalmic manifestations of the syndrome of ophthalmoplegia, ataxia and areflexia. Observations on 20 patients. Acta Neurol Scand 89:87–94
Natori Y, Rhoton AL (1994) Transcranial approach to the orbit: microsurgical anatomy. J Neurosurg 81:78–86
Natori Y, Rhoton AL (1995) Microsurgical anatomy of the superior orbital fissure. Neurosurgery 36:762–775
Nawrot M, Rizzo M (1995) Motion perception deficits from midline cerebellar lesions in human. Vision Res 35:723–731
Nieuwenhuys R, Voogd J, van Huijzen C (1988) The human central nervous system. Springer, Berlin Heidelberg New York
Oas JG, Baloh RW (1992) Vertigo and the anterior inferior cerebellar artery syndrome. Neurology 42:2274–2279
Ojala M, Palo J (1991) The aetiology of dizziness and how to examine a dizzy patient. Ann Med 23:225–230
Page WK, King WM, Merigan W, Maunsell J (1994) Magnocellular or parvocellular lesions in the lateral geniculate nucleus of monkeys cause minor deficits of smooth pursuit eye movements. Vision Res 34:223–239
Panayiotopoulos CP (1999) Elementary visual hallucinations, blindness, and headache in idiopathic occipital epilepsy: differentiation from migraine. J Neurol Neurosurg Psychiatry 66:536–540
Pare M, Wurtz RH (2001) Progression in neuronal processing for saccadic eye movements from parietal cortex area lip to superior colliculus. J Neurophysiol 85:2545–2562
Peterhans E, von der Heydt R (1993) Functional organization of area V2 in the alert macaque. Eur J Neurosci 5:509–524
Petit L, Haxby JV (1999) Functional anatomy of pursuit eye movements in humans as revealed by fMRI. J Neurophysiol 82:463–471
Petit L, Clark VP, Ingeholm J, Haxby JV (1997) Dissociation of saccade-related and pursuit-related activation in human frontal eye fields as revealed by fMRI. J Neurophysiol 77:3386–3390
Pettigrew JD, Dreher B (1987) Parallel processing of binocular disparity in the cat's retinogeniculocortical pathways. Proc R Soc Lond B Biol Sci 232:297–321
Pierrot D (1994) Saccade and smooth-pursuit impairment after cerebral hemispheric lesions. Eur Neurol 34:121–134
Pierrot D, Rivaud S, Gaymard B, Agid Y (1991) Cortical control of reflexive visually-guided saccades. Brain 114(3):1473–1485
Pierrot D, Rivaud S, Gaymard B, Muri R, Vermersch AI (1995) Cortical control of saccades. Ann Neurol 37:557–567
Previc FH, Liotti M, Blakemore C, Beer J, Fox P (2000) Functional imaging of brain areas involved in the processing of coherent and incoherent wide field-of-view visual motion. Exp Brain Res 131:393–405
Ranganadham P, Dinakar I, Mohandas S, Singh AK (1992) A rare presentation of posterior communicating artery aneurysm. Clin Neurol Neurosurg 94:225–227
Raphan T, Matsuo V, Cohen B (1979) Velocity storage in the vestibulo-ocular reflex arc (VOR). Exp Brain Res 35:229–248
Raymond LA, Tew J, Fogelson MH (1977) Ophthalmoplegic migraine of early onset. J Pediatr 90:1035–1036
Reid RC (1999) Vision. In: Zigmond MJ, Bloom FE, Landis SC, Roberts JL, Squire LR (eds) Fundamental neuroscience. Academic, San Diego, pp 821–851
Richer F, Martinez M, Cohen H, Saint H (1991) Visual motion perception from stimulation of the human medial parieto-occipital cortex. Exp Brain Res 87:649–652
Rizzo M, Nawrot M (1998) Perception of movement and shape in Alzheimer's disease. Brain 121:2259–2270
Robinson DA (1964) The mechanics of human saccadic eye movements. J Physiol (Lond) 174:245–264
Robinson DA (1970) Oculomotor unit behavior in the monkey. J Neurophysiol 33:393–403
Robinson DA (1973) Oculomotor control system. Invest Ophthalmol 12:164–166
Robinson DA, Keller EL (1972) The behavior of eye movement motoneurons in the alert monkey. Bibl Ophthalmol 82:7–16
Robinson DA, O'Meara DM, Scott AB, Collins CC (1969) Mechanical components of human eye movements. J Appl Physiol 26:548–553
Robinson DL, McClurkin JW (1989) The visual superior colliculus and pulvinar. Rev Oculomot Res 3:337–360
Rodieck RW (1965) Quantitative analysis of cat retinal ganglion cell response to visual stimuli. Vision Res 5:583–601
Rolls ET (1992) Neurophysiological mechanisms underlying face processing within and beyond the temporal cortical visual areas. Philos Trans R Soc Lond B Biol Sci 335:11–20
Roman C, Edwards KR (1979) Painful ophthalmoplegia: oculomotor nerve palsy without mydriasis due to compression by aneurysm. Headache 19:43–46
Ruksenas O, Fjeld IT, Heggelund P (2000) Spatial summation and center-surround antagonism in the receptive field of single units in the dorsal lateral geniculate nucleus of cat: comparison with retinal input. Vis Neurosci 17:855–870
Rushworth MF, Johansen B, Young SA (1998) Parietal cortex and spatial-postural transformation during arm movements. J Neurophysiol 79:478–482
Sams M, Hietanen JK, Hari R, Ilmoniemi RJ, Lounasmaa OV (1997) Face-specific responses from the human inferior occipito-temporal cortex. Neuroscience 77:49–55

Sanfilippo S (1973) Investigation of torsional defects. Am Orthop J 23:73–77
Santhouse AM, Howard RJ, ffytche DH (2000) Visual hallucinatory syndromes and the anatomy of the visual brain. Brain 123:2055–2064
Schein SJ, de Monasterio FM (1987) Mapping of retinal and geniculate neurons onto striate cortex of macaque. J Neurosci 7:996–1009
Schiller PH, Sandell JH, Maunsell JH (1987) The effect of frontal eye field and superior colliculus lesions on saccadic latencies in the rhesus monkey. J Neurophysiol 57:1033–1049
Schuknecht HF (1974) Pathology of the ear. Harvard University Press, Cambridge, MA
Schwarz DW (1976) Clinically relevant physiology of the vestibulo-ocular reflex. J Otolaryngol 5:425–436
Schwarz U, Ilg UJ (1999) Asymmetry in visual motion processing. Neuroreport 10:2477–2480
Schwarz U, Steurer J, Candinas R (2000) Schwindel. In: Siegenthaler W (ed) Differentialdiagnose innerer Krankheiten. Thieme, Stuttgart, pp 881–905
Scudder CA, Fuchs AF (1992) Physiological and behavioral identification of vestibular nucleus neurons mediating the horizontal vestibuloocular reflex in trained rhesus monkeys. J Neurophysiol 68:244–264
Segraves MA, Park K (1993) The relationship of monkey frontal eye field activity to saccade dynamics. J Neurophysiol 69:1880–1889
Shapley R, Reid RC, Kaplan E (1991) Receptive fields of P and M cells in the monkey retina and their photoreceptor inputs. Neurosci Res Suppl 15:S199–S211
Shen L, Hu X, Yacoub E, Ugurbil K (1999) Neural correlates of visual form and visual spatial processing. Hum Brain Mapp 8:60–71
Shou TD, Leventhal AG (1989) Organized arrangement of orientation-sensitive relay cells in the cat's dorsal lateral geniculate nucleus. J Neurosci 9:4287–4302
Silva MN, Saeki N, Hirai S, Yamaura A (1999) Unusual cranial nerve palsy caused by cavernous sinus aneurysms. Clinical and anatomical considerations reviewed. Surg Neurol 52:143–148
Skavenski AA, Robinson DA (1973) Role of abducens neurons in vestibuloocular reflex. J Neurophysiol 36:724–738
Snyder LH, Batista AP, Andersen RA (2000) Intention-related activity in the posterior parietal cortex: a review. Vision Res 40:1433–1441
Solomon D, Cohen B (1994) Stimulation of the nodulus and uvula discharges velocity storage in the vestibulo-ocular reflex. Exp Brain Res 102:57–68
Sommer MA, Wurtz RH (2001) Frontal eye field sends delay activity related to movement, memory, and vision to the superior colliculus. J Neurophysiol 85:1673–1685
Sparks DL (1989) The neural encoding of the location of targets for saccadic eye movements. J Exp Biol 146:195–207
Sparks DL, Mays LE (1990) Signal transformations required for the generation of saccadic eye movements. Annu Rev Neurosci 13:309–336
Steinlin MI, Blaser SI, MacGregor DL, Buncic JR (1995) Eye problems in children with multiple sclerosis. Pediatr Neurol 12:207–212
Striph GG (1993) Consecutive oculomotor nerve palsy from a de novo cerebral aneurysm. J Clin Neuroophthalmol 13:181–187
Strupp M, Arbusow V (2001) Acute vestibulopathy. Curr Opin Neurol 14:11–20
Suarez H, Rosales B, Claussen CF (1992) Plastic properties of the vestibulo-ocular reflex in olivo-ponto-cerebellar atrophy. Acta Otolaryngol 112:589–594
Sullivan EP, Jenkins IH, Henderson L, Kennard C, Brooks DJ (1995) The functional anatomy of remembered saccades: a PET study. Neuroreport 6:2141–2144
Suzuki DA, Keller EL (1984) Visual signals in the dorsolateral pontine nucleus of the alert monkey: their relationship to smooth-pursuit eye movements. Exp Brain Res 53:473–478
Suzuki DA, Yamada T, Hoedema R, Yee RD (1999) Smooth-pursuit eye-movement deficits with chemical lesions in macaque nucleus reticularis tegmenti pontis. J Neurophysiol 82:1178–1186
Sydnor CF, Seaber JH, Buckley EG (1982) Traumatic superior oblique palsies. Ophthalmology 89:134–138
Telkes I, Distler C, Hoffmann KP (2000) Retinal ganglion cells projecting to the nucleus of the optic tract and the dorsal terminal nucleus of the accessory optic system in macaque monkeys. Eur J Neurosci 12:2367–2375
Thurston SE, Leigh RJ, Crawford T, Thompson A, Kennard C (1988) Two distinct deficits of visual tracking caused by unilateral lesions of cerebral cortex in humans. Ann Neurol 23:266–273
Tiffin PA, MacEwen CJ, Craig EA, Clayton G (1996) Acquired palsy of the oculomotor, trochlear and abducens nerves. Eye 10:377–384
Tilikete C, Rode G, Nighoghossian N, Boisson D, Vighetto A (2001) Otolith manifestations in Wallenberg syndrome. Rev Neurol (Paris) 157:198–208
Toates FM (1974) Vergence eye movements. Doc Ophthalmol 37:153–214
Todd L, King J, Darlington CL, Smith PF (2001) Optokinetic reflex dysfunction in multiple sclerosis. Neuroreport 12:1399–1402
Trimarchi F (1992) Neuro-ophthalmology. Curr Opin Neurol Neurosurg 5:740–743
Trobe JD (1986) Isolated third nerve palsies. Semin Neurol 6:135–141
Troost BT (1996) Ophthalmoplegic migraine. Biomed Pharmacother 50:49–51
Ts'o DY, Roe AW, Gilbert CD (2001) A hierarchy of the functional organization for color, form and disparity in primate visual area V2. Vision Res 41:1333–1349
Tychsen L, Lisberger SG (1986) Visual motion processing for the initiation of smooth-pursuit eye movements in humans. J Neurophysiol 56:953–968
Umansky F, Elidan J, Valarezo A (1991) Dorello's canal: a microanatomical study. J Neurosurg 75:294–298
Umansky F, Valarezo A, Elidan J (1992) The microsurgical anatomy of the abducens nerve in its intracranial course. Laryngoscope 102:1285–1292
Ungerleider LG, Mishkin M (1982) Two cortical visual systems. In: Ingle DJ, Goodale MA, Mansfield RJW (eds) Analysis of visual behavior. MIT Press, Cambridge, MA, pp 549–586
Usrey WM, Reppas JB, Reid RC (1999) Specificity and strength of retinogeniculate connections. J Neurophysiol 82:3527–3540
Vanni S, Uutela K (2000) Foveal attention modulates responses to peripheral stimuli. J Neurophysiol 83:2443–2452
Vanooteghem P, Dehaene I, Van Z, Casselman J (1992) Com-

bined trochlear nerve palsy and internuclear ophthalmoplegia. Arch Neurol 49:108–109
Varma R, Miller NR (1994) Primary oculomotor nerve synkinesis caused by an extracavernous intradural aneurysm. Am J Ophthalmol 118:83–87
Verhagen WI, Huygen PL, Dalman JE, Schuurmans MM (1996) Whipple's disease and the central nervous system. A case report and a review of the literature. Clin Neurol Neurosurg 98:299–304
Vibert D, Hausler R (2000) Long-term evolution of subjective visual vertical after vestibular neurectomy and labyrinthectomy. Acta Otolaryngol 120:620–622
Vibert D, Hausler R, Safran AB (1999) Subjective visual vertical in peripheral unilateral vestibular diseases. J Vestib Res 9:145–152
von der Heydt R, Peterhans E, Baumgartner G (1984) Illusory contours and cortical neuron responses. Science 224:1260–1262
Vukov JG (1975) Intracavernous aneurysm with isolated 6th nerve palsy. Ann Ophthalmol 7:1071–1074
Waespe W, Cohen B (1983) Flocculectomy and unit activity in the vestibular nuclei during visual-vestibular interactions. Exp Brain Res 51:23–35
Wall M, Slamovits TL, Weisberg LA, Trufant SA (1986) Vertical gaze ophthalmoplegia from infarction in the area of the posterior thalamo-subthalamic paramedian artery. Stroke 17:546–555
Wallman J (1993) Subcortical optokinetic mechanisms. Rev Oculomot Res 5:321–342
Wandell BA (1995) Foundations of vision. Sinauer Associates, Inc, Sunderland, MA
Watanabe S, Kakigi R, Koyama S, Kirino E (1999) It takes longer to recognize the eyes than the whole face in humans. Neuroreport 10:2193–2198
Watson JD, Myers R, Frackowiak RS, Hajnal JV, Woods RP, Mazziotta JC, Shipp S, Zeki S (1993) Area V5 of the human brain: evidence from a combined study using positron emission tomography and magnetic resonance imaging. Cereb Cortex 3:79–94
Weber B, Schwarz U, Kneifel S, Treyer V, Buck A (2000) Hierarchical visual processing is dependent on the oculomotor system. Neuroreport 11:241–247
Weiskrantz L (1990) The Ferrier lecture 1989. Outlooks for blindsight: explicit methodologies for implicit processes. Proc R Soc Lond B Biol Sci 239:247–278
Wiesel TN, Hubel DH (1966) Spatial and chromatic interactions in the lateral geniculate body of the rhesus monkey. J Neurophysiol 29:1115–1156
Williams C, Azzopardi P, Cowey A (1995) Nasal and temporal retinal ganglion cells projecting to the midbrain: implications for "blindsight". Neuroscience 65:577–586
Wolfe J, Palmer LA (1998) Temporal diversity in the lateral geniculate nucleus of cat. Vis Neurosci 15:653–675
Wurtz RH, Kandel ER (2000) Central visual pathways. In: Kandel ER, Schwartz JH, Jessell TM (eds) Principles of neural science. McGraw-Hill, New York, pp 523–547
Xing J, Andersen RA (2000) Models of the posterior parietal cortex which perform multimodal integration and represent space in several coordinate frames. J Cogn Neurosci 12:601–614
Zee DS (1992) Internuclear ophthalmoplegia: pathophysiology and diagnosis. Baillieres Clin Neurol 1:455–470
Zeki S (1993) A vision of the brain. Blackwell Scientific Publications, Oxford
Zeki S, Watson JD, Lueck CJ, Friston KJ, Kennard C, Frackowiak RS (1991) A direct demonstration of functional specialization in human visual cortex. J Neurosci 11:641–649
Zigmond MJ, Bloom FE, Landis SC, Roberts JL, Squire LR (1999) Fundamental neuroscience. Academic Press, San Diego
Zilles K, Clarke S (1997) Architecture, connectivity, and transmitter receptors of human extrastriate visual cortex. In: Rockland KS, Kaas JH, Peters A (eds) Cerebral cortex, Vol 12. Plenum, New York, pp 673–742

4 Functional Magnetic Resonance Imaging of the Human Visual System

Spyros S. Kollias

CONTENTS

4.1 Introduction

Over the past two decades, the neuroscience and medical communities have witnessed a tremendous growth in the field of noninvasive imaging of brain function. Technological advances in both structural and functional neuroimaging techniques have played a key role in understanding the neurobiology of mind processes, and the field of cognitive neuroscience emerged as a very important growth area in neuroscience. At the forefront of this research are the new techniques of functional brain imaging: positron emission tomography (PET), electrical and magnetic source imaging, and more recently functional magnetic resonance imaging (fMRI). Newer-generation PET cameras can now dynamically scan the entire brain with high sensitivity, allowing for the detection of neurotransmitter and receptor uptake and regulation. Electrical and magnetic source imaging have the ability to resolve patterns of brain activation on temporal scales measured in milliseconds, and users of these methods have made great strides in challenging the problem of source localization. Among these techniques, the one that probably created the most excitement in the medical/scientific community is fMRI. The high spatial resolution and lesion detectability provided by conventional structural MRI made the use of acquired brain lesions in the living neurological patient feasible as experimental probes for investigating hypotheses about the relationship between large-scale neural systems and cognitive processes, thus expanding significantly the lesion approach in the field of cognitive neuroscience (Damasio and Frank 1992). Structural MRI has also been used for linking physiological measures obtained by functional brain mapping methods such as positron emission tomography (PET), magnetoencephalography (MEG), and electroencephalography (EEG) to their corresponding anatomical structures for a more complete understanding of the function/structure relation in the nervous system (Aine 1995).

More recent developments in MR data acquisition and hardware/software technology (i.e., new pulse sequences in standard clinical imagers and high-power, rapidly oscillating magnetic field gradients used in echo planar imaging) demonstrated that the MRI signal could be made sensitive to changes in blood flow and blood oxygenation, thus providing important physiological information related to brain function. Different MR strategies have been used to study the various phenomena that accompany changes in neuronal activity (Aine 1995; DeYoe et al. 1994; Kollias et al. 1996b; Kwong 1995 for review). The most widely employed approach has been the one using changing net tissue deoxyhemoglobin content as an endogenous contrast mechanism to detect regions of increased neuronal activity. Combining a PET observation by Fox and Raichle (1986) that during changes in neuronal activity there are local changes in the amount of oxygen in the tissue with a much earlier observation by Pauling and Coryell (1936) that changing the amount of oxygen carried by hemoglobin changes the degree to which hemoglobin disturbs a magnetic field, Ogawa et al. (1990) were able to demonstrate that in vivo changes in blood oxygenation could be detected with MR tech-

PD S. S. Kollias, MD
Institute of Neuroradiology, University Hospital of Zurich, Frauenklinikstrasse 10, 8091 Zurich, Switzerland

nology. The MR signal arising from this combination of brain physiology and nuclear magnetic resonance physics became known as the blood-oxygen-level-dependent (BOLD) signal. Soon after these initial observations, combination of this endogenous contrast mechanism with rapid imaging technology led to several demonstrations of BOLD signal changes in normal humans during sensory motor or cognitive tasks, giving birth to the rapidly developing field of fMRI and advancement of the technique into the functional imaging arena (Bandettini et al. 1992; Blamire et al. 1992; Kwong et al. 1992). Since these early demonstrations, fMRI has become the technology of choice for many functional activation studies in humans because: (a) it provides both anatomic and functional information in a subject at the same session, so the anatomic site of the active regions may be determined accurately; (b) it is noninvasive, thus allowing repeated use with adult and child volunteers and patients without any risks of irradiation hazards; (c) it is widely available in most medical centers operating clinical MRI scanners and therefore financially affordable; and (d) it has better spatial and temporal resolution than other methods using the same hemodynamic phenomena to localize neuronal activity [i.e., PET, single photon emission tomography (SPECT)].

Over the past few years, research has focused on continuing advancement of fMRI techniques and methodological approaches with the following aims: (a) to increase the detectability, reliability, and interpretability of the functionally induced signal changes; (b) to improve understanding of the underlying biophysical mechanisms responsible for these changes; (c) to expand the applications of the technique in basic neuroscience for exploiting functionally specialized areas in virtually every sensory, motor, and cognitive system; and (d) to validate and establish the technique as a useful clinical tool for applications such as presurgical planning and evaluation of organizational changes in the functional anatomy associated with pathologic conditions. To offer comprehensive information about the progress of fMRI methodology over the past few years and its input in understanding visual function in normal and pathologic conditions, the subsequent sections of this chapter summarize progress made in the following areas: (a) recent issues related to fMRI methodology, (b) progress in understanding the organization and functional properties of cortical visual areas in the healthy human, and (c) current applications of fMRI to study changes in brain activity in patients with impaired visual function.

4.2 Recent Progress in fMRI Techniques and Methodology

While the obvious advantages of fMRI generated much enthusiasm about the potential of the technique to evolve into the imaging modality of choice for the functional investigation of the human brain, pertinent limitations and methodological shortcomings were recognized early on in the development of the method (Aine 1995; Kollias et al. 1996b; Moseley and Glover 1995 for review). One immediate limitation of fMRI arises from the fact that the physiological estimates localized by this technique are not direct measures of neural activity but rather hemodynamic correlates of neural currents [i.e., changes in cerebral blood flow (CBF), cerebral blood volume (CBV) and oxygen content]. A typical fMRI experiment measures the correlation between the fMRI response and a stimulus. From this, scientists hope to infer something about neural function. Often it is assumed that there is a simple and direct relationship between neural activity and the fMRI response. Although the link between neuronal function and associated hemodynamic changes has been studied for more than a century (Raichle 1998) and many investigators will agree that local neuronal activity is coupled to cerebrovascular hemodynamic changes in both space and time, the precise relationship between these changes remains incompletely understood. Beyond its obvious physiological interest, understanding of the dynamics of neuronal/vascular coupling is critical for understanding the origin of the fMRI signal and the ultimate limits that the hemodynamic measures pose in the temporal and spatial resolution of the technique. For example, early work (Kwong et al. 1992; Blamire et al. 1992; Bandettini et al. 1993) reported initial changes in the hemodynamic response around 1 s poststimulus with mean rise-time constants at 4–8 s attributed to a local reduction in deoxygenated hemoglobin (Fig. 4.1). More recent studies report subtle, but observable changes in hemodynamic parameters within a few hundred milliseconds after neuronal stimulation. An initial "undershoot" or decrease in the signal intensity occurring 0.5–2 s after stimulus onset has been observed using high field strength MRI systems (Ernst and Hennig 1994; Menon et al. 1995b; Hu et al. 1997) and was attributed to a focal early deoxygenation phase which precedes a more spatially distributed increase in oxygenated hemoglobin. This biphasic-response time course is similar to that observed using intrinsic optical imaging in the physiologically

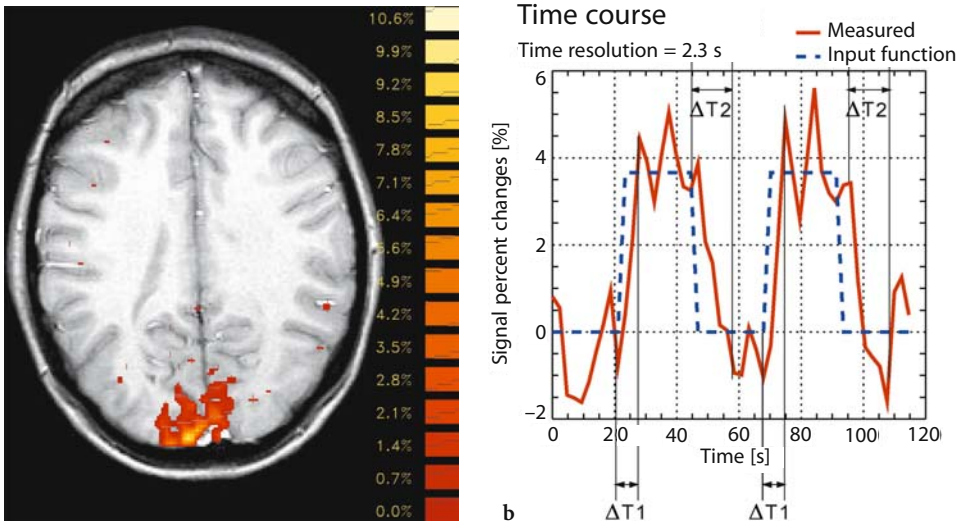

Fig. 4.1. Functional map (**a**) and oxygenation-sensitive time course (**b**) of activated time course in a 26-year-old female volunteer. Stimulation was obtained by using a stroboscopic white-light flashing stimuli at a frequency of 10 Hz. The subject, who was lying supine in the gantry, looked up into an adjustable angled mirror that allowed her to view the stroboscope comfortably in the direction of her feet; it was fixed in the line of sight. The visual angles of the stimulus were 30° horizontal and 27° vertical. The activation protocol consisted of 10 image sets alternating in the "off" and "on" condition every 20 s. During the visual stimulation periods, the subject was instructed to stare at the center of the light-emitting source. During the resting state, the subject was kept in the dark and was instructed to avoid eye movements. Statistically significant ($p<0.001$) changes in the calcarine cortex of less than 5% are superimposed on high resolution anatomical magnetic resonance (MR) image obtained at the same anatomic location as the functional series. Measurements from seven normal volunteers (**b**) have shown that the mean exponential time constant of signal increase (DT1) was 4.8±2.8 s, and the mean exponential time of signal decay (DT2) was 6.1±1.4 s

stimulated visual cortex (Malonek and Grinvald 1996). Using this technique, an almost immediate increase in deoxyhemoglobin concentration is followed, after a brief interval, by an increase in oxyhemoglobin which is greater in magnitude and extends over a much larger area of the cortex than the changes in deoxyhemoglobin. Although the origin of such changes remains controversial, their occurrence created hope that more precise timing and spatial information may be obtained with fMRI by observing this early and spatially confined hemodynamic event (Duong et al. 2000).

The dynamic character of fMRI experiments (changes occur 1–2 s after the neuronal activity onset and evolve over a 10–12 s period) and the opportunity to examine the behavior of the signal over time suggested that more detailed information about the dynamics of underlying physiological changes can be extracted from the fMRI data by inspecting the dynamic evolution of the signal. This advantage of fMRI stimulated a series of studies investigating the relationship between signal changes and underlying neuronal changes and led to the application of new methodological approaches expanding the spectrum of task designs that can be examined with this technique. Several aspects of fMRI signal dynamics have been described, including the time to reach a plateau after stimulus onset and the time to return to baseline after stimulus cessation (Binder and Rao 1994 for review). Measurements in normal volunteers on application of transient visual stimulation demonstrated that local changes in deoxyhemoglobin levels following cerebral activation are highly consistent but delayed (by 4.8 ± 2.8 s) relative to the underlying neuronal activity (Fig. 4.1). Using a high temporal resolution (0.42 s) fMRI sequence, the influence of the interstimulus interval on the fMRI signal magnitude and the areas of recruitment in the primary visual cortex was studied. It was observed that the signal saturates in the activated state when the rest periods are shorter than 10 s, which is a direct consequence of the dynamic equilibrium state reached by repeated stimulation without recovery intervals (Fig. 4.2). The minimum resting time at which a stimulation condition produced statistically significant signal changes was 2 s. The fMRI signal during prolonged steady-state extended duration stimulation has been investigated by several groups (Hathout et al. 1994; Frahm et al. 1996; Bandettini et al. 1997; Kollias et al. 2000) addressing the evolution of hemodynamic and

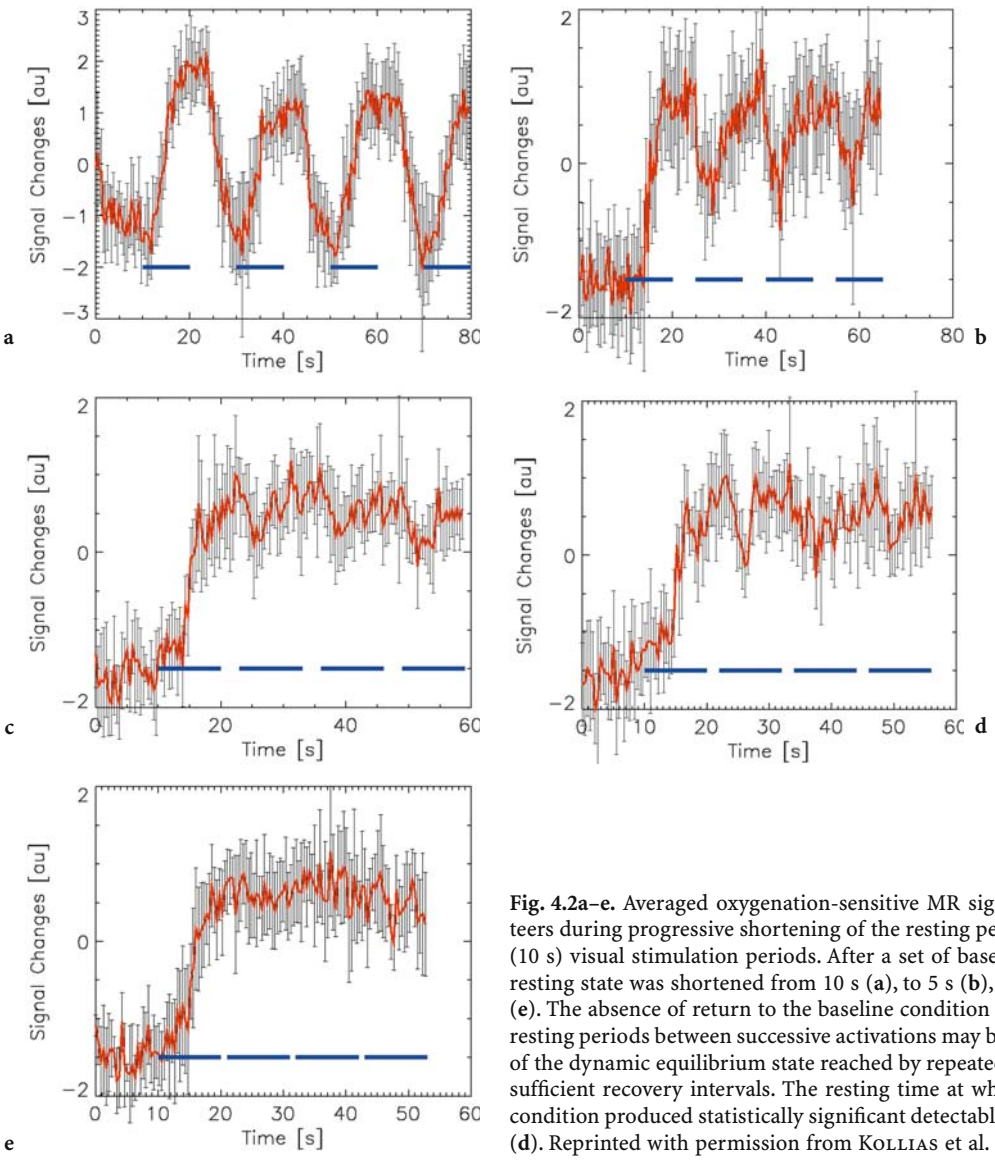

Fig. 4.2a–e. Averaged oxygenation-sensitive MR signal from seven volunteers during progressive shortening of the resting period between constant (10 s) visual stimulation periods. After a set of baseline images (10 s), the resting state was shortened from 10 s (**a**), to 5 s (**b**), 3 s (**c**), 2 s (**d**), and 1 s (**e**). The absence of return to the baseline condition with shortening of the resting periods between successive activations may be a direct consequence of the dynamic equilibrium state reached by repeated stimulations without sufficient recovery intervals. The resting time at which a new stimulation condition produced statistically significant detectable signal change was 2 s (**d**). Reprinted with permission from Kollias et al. (2000)

metabolic responses to neuronal activation. It was demonstrated that both flow rate and oxygenation consumption rate remain elevated during prolonged periods of brain activation provided there is no habituation to the presented stimulus (Fig. 4.3). These initial fMRI studies had significant implications for optimizing stimulation paradigms that would elicit robust activation in the visual cortex using fMRI methodology, but also provided insight into the underlying physiological mechanisms of brain activation.

More recent investigations explored the fMRI signal responses to brief stimulus events, exploring the limitations that the vascular source of the signal places in the temporal resolution of the technique. Small but resolvable signal changes were demonstrated using visual stimulation as brief as 34 ms in duration (Savoy et al. 1995). Another study showed that not only could brief stimulus duration be detected but also that the hemodynamic response summates in a roughly linear fashion over time, demonstrating that fMRI is sensitive to transient phenomena and can provide at least some degree of quantitative information about the underlying neuronal events (Boynton et al. 1996). These last findings, combined with the high temporal resolution afforded by MR technology, suggested that the method might be able to interpret transient signal changes in ways directly analogous to EEG- and MEG-evoked potentials and led to the development of event-related (ER-fMRI)

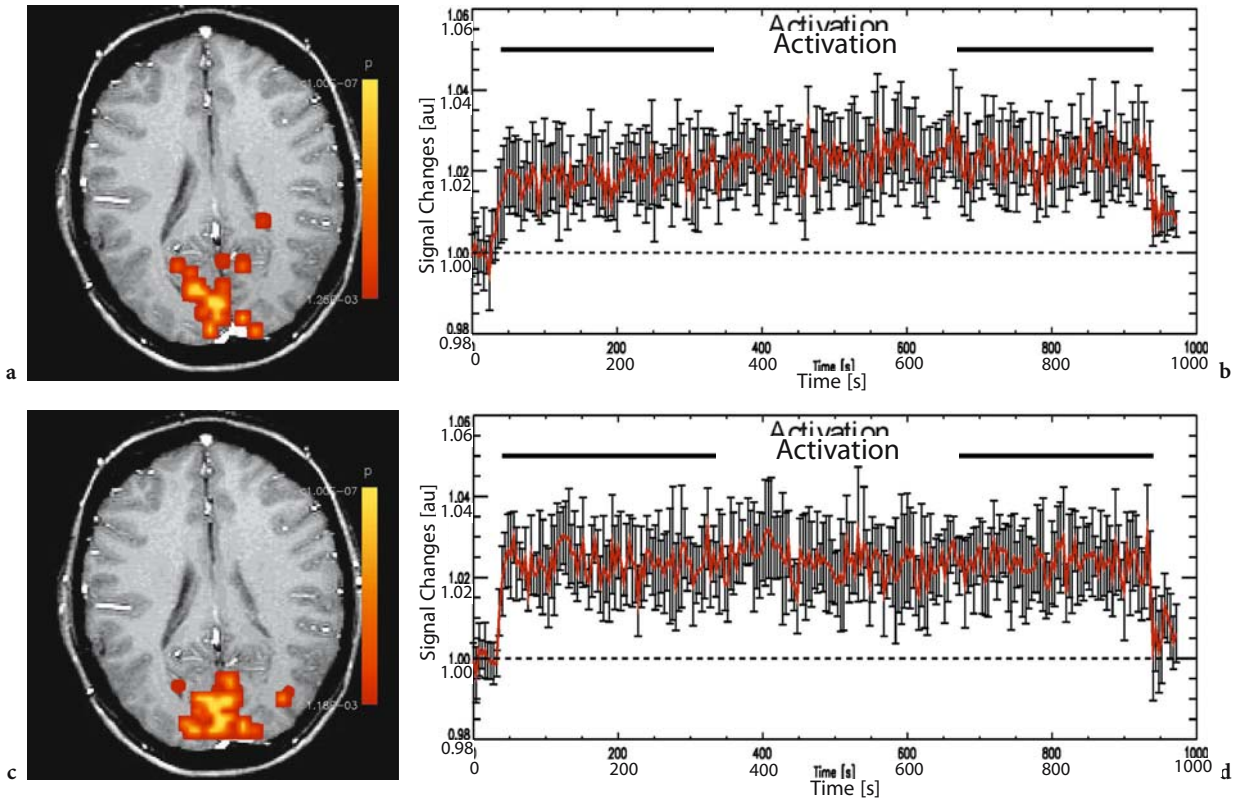

Fig. 4.3. Functional maps (**a**, **c**) from a representative subject and averaged time courses of signal response (**b**, **d**) from seven subjects during sustained visual stimulation with a red and black checkerboard flashing at 8 Hz (**a**, **b**) and white pattern of concentric black circles growing at a rate of 1 Hz (**c**, **d**). No significant decrease in oxygenation-sensitive signal intensity during 12 min of sustained activation is observed, suggesting stable levels of oxidative metabolic rate and oxygen extraction fraction in the visual cortex during extended stimulation times. Reprinted with permission from Kollias et al. (2000)

procedures (Rosen et al. 1998 for review). Several subsequent studies using ER-fMRI paradigms and newly developed methods for data analysis demonstrated convincingly that brain mapping based on single-trial response functions is possible (Buckner et al. 1996, 1998; Dale and Buckner 1997; Friston et al. 1998). In one of these studies (Dale and Buckner 1997), it was shown that visual stimuli lateralized to one hemifield could be detected within intermixed trial paradigms and that when left- or right-hemifield stimuli were randomly presented to the subjects much more rapidly than the hemodynamic response (in this case one stimulus every 2 s), it was still possible to extract out the identical lateralization pattern to that seen with much longer interstimulus intervals. By using analysis methods similar to those applied in evoked response potential research, the trials were averaged to reveal the predicted pattern of contralateral visual cortex activation. These methodological developments allowed fMRI to depart from "block" testing procedures (extended periods of "on" versus "off" activations), permitting greater flexibility in the design of fMRI experiments, and led to a number of new applications in cognitive neuroscience research that could not have been done with conventional blocked task paradigms (Rosen et al. 1998). For example, using a visual working memory paradigm in which the act of encoding a stimulus was temporally separated from the act of maintaining the stimulus, and analysis procedures that separated the within-trial components, it was shown that posterior visual areas contributed proportionately more to perceptual encoding operations and prefrontal areas to maintenance operations (Courtney et al. 1997). Many issues concerning how these studies (particularly single-trial events) should be performed and several fundamental questions concerning underlying physiological mechanisms remain unsolved. For example, the precise limits of the "linear modeling" approach across functionally specialized regions within a sensory modality and across modalities, as well as the source (vascular or neuronal) of nonlinearities which are observed in several instances, remain unclear at present (Rosen et al. 1998). The manner and limits to

how ER-fMRI can be applied are still being explored. As our understanding of the characteristics and limitations of ER-fMRI studies improves, it is anticipated that several applications of human brain mapping will take advantage of this approach in the future.

Parallel to these methodological advances, recent technical progress in MRI data acquisition techniques that are selectively sensitive to hemodynamic perturbations within the microvasculature promise more accurate source localization for the fMRI signal. It has been suggested that using high field MR systems, a significant portion of the BOLD signal arises from the cortical capillary bed (Menon et al. 1995a). However, with the commonly used 1.5 T systems, most of the BOLD contrast comes from changes in blood oxygenation in large draining veins (Lai et al. 1993). This presents a problem for fMRI applications because large vessels drain blood from relatively large regions of cortex, and their oxygenation level only informs us about the average activity over these regions. This is described in the fMRI literature as the brain/vein problem. Several techniques and imaging strategies have been proposed to reduce this problem and improve the spatial accuracy of the method (Kwong 1995 for review). For example, MR perfusion techniques, broadly named arterial spin labeling techniques, that allow for noninvasive measurement of brain tissue perfusion using magnetically tagged arterial water as an endogenous contrast tracer have been developed and applied successfully in functional brain studies (Edelman et al. 1994; Kwong et al. 1995; Kim and Tsekos 1997). These techniques appear to offer higher spatial and temporal resolution than BOLD fMRI by measuring functionally induced changes in perfusion at the level of distal arterioles and capillaries, thus being less sensitive to flow downstream into large draining cortical veins. Several variations of these techniques are presently undergoing development and testing. It is expected that with further optimization (e.g., multislice acquisitions, improvements in the sensitivity), except that of better spatial localization, this alternative approach will lead to further applications in functional brain imaging (i.e., ER-fMRI) by reducing the intrinsic temporal lags, and hence variation, created by imaging flow downstream into draining venous vessels.

Various types of artifacts and noise commonly accompany changes in MR signal obtained during brain activation (Aine 1995; Kollias et al. 1996b; DeYoe et al. 1994; Kwong 1995 for review). The field is continually trying to develop methods for the reduction of motion artifacts (e.g., better head immobilization, image acquisition synchronized to the cardiac rhythm), for postimaging motion correction (e.g., realigning algorithms), and to implement new data analysis models to extract small signal contributions due to blood properties that correlate with neuronal activity (Buckner 1998). Several analysis procedures (e.g., correlation analysis, principal component analysis, statistical parametric mapping, and nonparametric mapping) have been employed in the past to make the responses more visible and improve confidence in the interpretation of the results (Bandettini et al. 1993). Commonly, these analyses make fixed assumptions that the hemodynamic signal change will occur a few seconds after the onset of the experimental manipulation and will decrease a few seconds following the cessation of the manipulation according to the delay in the hemodynamic response relative to the neuronal activity. However, this model does not account for potential deviations from the expected response and makes limited fixed assumptions about the shape of the hemodynamically induced signal. More recently, several analyses have been proposed to allow for variance in the hemodynamic response that make no or minimal assumptions about its shape and timing and thus are sensitive to all forms of signal change (Friston et al. 1997; Zarahn et al. 1997; Golay et al. 1998). An example of this is a correlation based fuzzy logic clustering algorithm which allows identification of activation patterns without prior knowledge of the timing of the paradigm. In a recent study (Golay et al. 1998), comparison of the functional maps obtained with the fuzzy algorithm with those obtained by a standard cross-correlation technique in a series of phasic visual stimulation experiments with known input function showed a good correlation, demonstrating the ability of the fuzzy algorithm to provide functional maps of human brain activity based on BOLD signal changes. Further applications of the fuzzy clustering approach promise exploration of more complex mental activities that are associated with unpredictable spatial and temporal responses (Fig. 4.4). Other analysis approaches have been proposed for exploring single-trial data both when comparing different trial types and when constructing activation maps based on single-trial runs (Dale and Buckner 1997; Buckner et al. 1998; McKeown et al. 1998). Analyzing fMRI data is still an active area of research. It is not obvious whether one method is the best, or if different tools will be required depending upon the nature of the specific question asked about the data.

Another issue gaining attention over the past few years is the ability of fMRI to provide quantitative

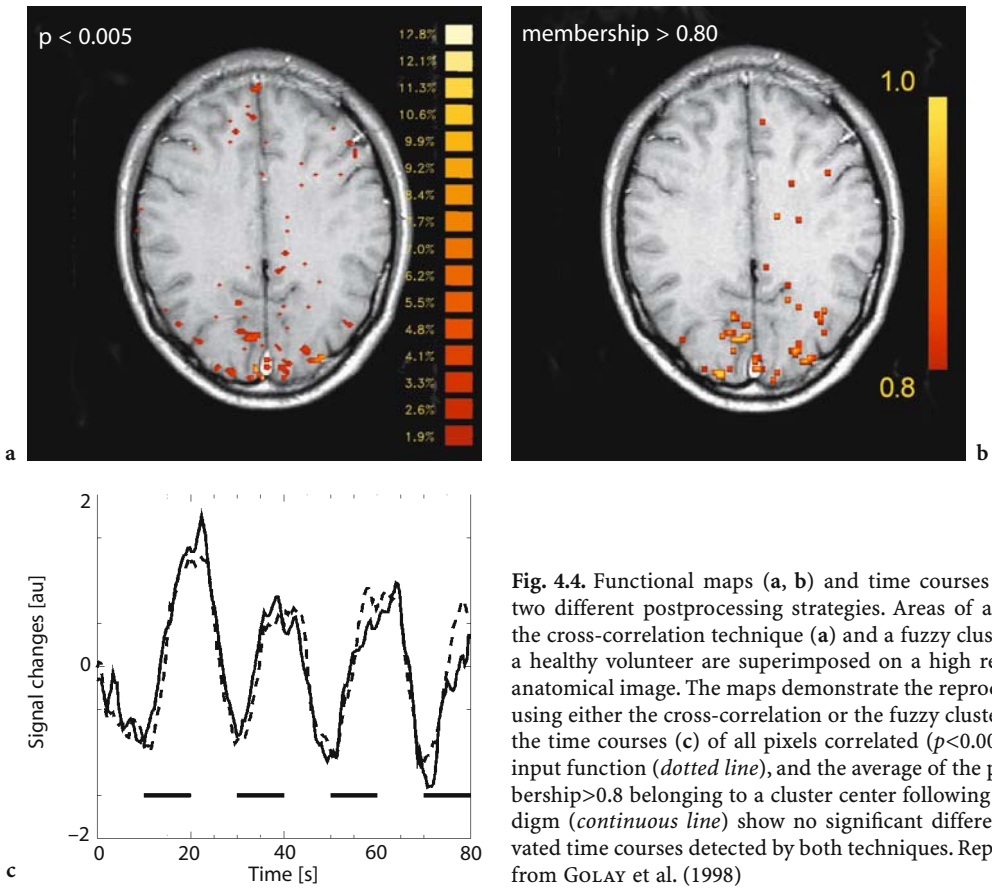

Fig. 4.4. Functional maps (**a**, **b**) and time courses (**c**) obtained by using two different postprocessing strategies. Areas of activation computed by the cross-correlation technique (**a**) and a fuzzy clustering algorithm (**b**) of a healthy volunteer are superimposed on a high resolution, T1-weighted, anatomical image. The maps demonstrate the reproducibility of the results, using either the cross-correlation or the fuzzy clustering technique. Plot of the time courses (**c**) of all pixels correlated (p<0.005) with a box-squared input function (*dotted line*), and the average of the pixels that have a membership>0.8 belonging to a cluster center following the off-on visual paradigm (*continuous line*) show no significant differences between the activated time courses detected by both techniques. Reprinted with permission from Golay et al. (1998)

information. The goal is to turn the signal intensities observed in fMRI data into meaningful magnitude values and if possible to provide absolute quantitative assessment of functionally induced perturbations in hemodynamic parameters. The difficulty in achieving this goal stems from the fact that the response obtained from a typical fMRI experiment is not quantitative in terms of physiologic measurement. It reflects certain signal intensity changes derived from an interaction of the properties of the tissue being measured, the pulse sequence applied, and the local magnetic field, among other aspects (Buckner 1998). Because of these factors, currently applied fMRI is often criticized as a qualitative method that can be used to locate regions of tissue activation approximately. Various strategies for obtaining quantitative information are presently being tested. Several studies have quantified effects by counting the number of voxels within a region that reach a certain statistical threshold, potentially allowing activation maps to be measured in terms of their spatial extent (Kim et al. 1993). Others measure the magnitude of the signal (percentage signal change) in a given voxel or region and follow its changes across different parametric and/or systematic experimental manipulations (Boynton et al. 1996; Dale and Buckner 1997). These data suggest that fMRI can provide some degree of quantitative information about the underlying neuronal behavior. However, these approaches will have to be explored further and validated before they become widely applied. Absolute quantitation of hemodynamic changes (e.g., absolute CBF) cannot be achieved at this time since the mean transit time cannot be calculated accurately. Nonetheless, a more recent experimental study using a high magnetic field scanner (4 T) and spin-echo approach (more sensitive for capillary dimensions than the routinely used gradient-echo approach) shows that high resolution absolute blood volume images can be obtained by using hemoglobin as a natural intravascular contrast agent (Van Zijl et al. 1998). Providing a quantitative model to interpret the observed MR signal changes in terms of flow, volume, and oxygenation levels of blood during neuronal activation, this study promises to extend the interpretation of qualitative patterns of neuronal activation into quantitative measures of distributed neuronal processing.

From the methodological and technical issues discussed above, it is obvious that fMRI is a continuously evolving method. Its ultimate limits in temporal and spatial resolution for mapping brain function are not yet determined. Further technical advances (e.g., new data acquisition algorithms, higher magnetic field scanners, improvements in radio-frequency receiver coil technology) and the development of more sophisticated data analysis and quantitative methods promise further improvements in the spatial and temporal domain and greater flexibility in experimental design for a truly comprehensive understanding of the functional organization of the human brain.

4.3 Applications of fMRI in the Investigation of Human Visual Physiology

Since its early days, fMRI methodology has been applied extensively to visual studies. As with any new technique, most initial experiments were devised to validate the method, and the findings largely confirmed those obtained with PET. Activation of the primary visual cortex (V1) has been easy to demonstrate in simple-to-perform experiments using various stimulation paradigms. However, in the past few years, the enhanced spatial resolution of fMRI and its ability to study activation in individual subjects combined with new and creative ways for obtaining and displaying maps of regional brain activity have significantly advanced our knowledge about the functional organization of the human visual cortex. Thus, methods for measuring cortical activity by correlating the temporal responses of different activity foci with periodic stimuli ("phase encoding") (Engel et al. 1994) and application of new visualization algorithms that emphasize surface representations of the human cortical sheet (Van Essen et al. 1998) allowed several groups to map the retinotopic borders and spatial extent of multiple visual areas in humans with a precision similar to that achieved in nonhuman primates (Schneider et al. 1993; Sereno et al. 1995; DeYoe et al. 1996; Tootell et al. 1996, 1998a,b; Engel et al. 1997). These mappings have demonstrated several homologies in the topological organization between human and monkey early visual areas, but discordances (e.g., the extent of central vision in V1, the width of V3 and VP relative to V1, and the lower and upper field cortical representations of V4) have also been observed (Courtney and Ungerleider 1997 for discussion). Although there were some differences among the various measurements (e.g., concerning the extent of the representation of the central 2° in the human V1 area), it was demonstrated from these studies that the borders of several different, retinotopically organized areas in the posterior occipital lobe can be identified efficiently and with high spatial precision using fMRI (Engel et al. 1997). An example of this precision is the demonstration for the first time in humans using a neuroimaging technique of the paired cortical representations of the monocular "blind spot" (Tootell et al. 1998a). More importantly, the retinotopic establishment of spatial borders was critical for interpreting the results of subsequent studies examining the functional specialization of these areas. A wide range of stimulus properties (e.g., motion, color, luminance contrast, orientation) was used by several groups to identify distinct visual cortical areas on the basis of their selectivity for a particular function (e.g., motion selectivity) or their differences in global functional properties (e.g., low versus high contrast sensitivity). Such stimuli also offered a valuable means for distinguishing cortical areas that are less well retinotopic. One of the first such regions to be identified using fMRI was the presumed human homologue of area MT (V5). In addition to its known motion selectivity, it was demonstrated that V5 is linked with higher contrast sensitivity than V1. Other extrastriate areas such as presumptive V3 also have high contrast sensitivity, but unlike the case in MT, presumptive area V3 shows very little motion bias. This intersection of attributes suggests that the functional isolation of area MT could be greatly enhanced by testing with a moving/stationary stimulus of low contrast (Tootell et al. 1998a). Additionally, the high sensitivity to contrast and motion in MT provided persuasive evidence for magnocellular dominance. This is in accordance with the finding that the input to MT in monkeys derives from cells in the magnocellular layers of the lateral geniculate nucleus which also show higher contrast and motion sensitivity than those in the parvocellular layers. Another fMRI study using three different kinds of motion (i.e. simple motion, optical flow, and biological motion) demonstrated a high degree of functional specialization in the MT area to different subspecializations within the same submodality of visual motion (Howard et al. 1996). The same study found that motion stimuli also activated neighboring, but nonoverlapping regions of auditory cortex that are normally activated by the perception of speech, providing evidence for a link between motion processing and language. Similar to the functional characteriza-

tion of MT, other fMRI studies investigated the cortical representation of other submodalities of vision. For example, an area in the ventral occipitotemporal cortex most often observed in the collateral sulcus and lingual gyrus was selectively activated by the perception of (or attention to) colored stimuli (Sakai et al. 1995; Kleinschmidt et al. 1996), confirming previous results from PET studies (Zeki et al. 1991); however, this still leaves unanswered the question of whether this color-selective area in humans is the homologue of monkey V4 (Courtney and Ungerleider 1997). A form-selective area in the lateral occipitotemporal cortex, termed area LO, has been suggested as the homologue to monkey V4 (Malach et al. 1995). Whereas area LO responds to all objects regardless of object recognition, other areas specialized for the perception of complex object categories such as faces, letter strings, and buildings have been identified within specialized regions of the ventral occipitotemporal extrastriate cortex (Courtney et al. 1997; Puce et al. 1996; Kanwisher et al. 1997; Aguirre et al. 1998). These studies demonstrated that different regions of the visual cortex process different visual stimulus attributes and that a high degree of functional specialization selective for particular classes of behaviorally significant objects may exist (or develop) within the visual system. The sensitivity of fMRI to identify experience- or learning-dependent (noninnate) functions and assess the variability in the locus of the same area across different subjects suggests that the method could be used to measure remodeling of the visual cortical areas over the course of weeks, or even years, as expert knowledge is acquired (Courtney and Ungerleider 1997; Polk and Farah 1998).

Over 30 separate visual areas have been identified in the monkey cortex, covering about one-half of the total cortex (Felleman and Van Essen 1991 for review). These areas are organized into two functionally specialized processing pathways both originating in area V1 and each being composed of multiple areas beyond V1. The occipitotemporal pathway, or ventral stream, processes the physical attributes of stimuli that are crucial for object identification, such as color, shape, and pattern, while the occipitoparietal pathway, or dorsal stream, is crucial for localizing objects in space and for the visual guidance of movements towards these objects. As one progresses from lower level to higher level visual cortical areas, there is a progressive loss in retinotopy and a progressive increase in selectivity, such that more useful representations of the visual input can be seen at each successive stage of processing (Courtney and Ungerleider 1997). Major goals of functional neuroimaging include identifying the regions that participate in various information-processing operations, characterizing the functional role played by each region, and modeling the integrations among regions. Several fMRI studies have provided evidence for a strong correlation between specific cortical locations "upstream" from V1 and higher level visual processing. For example, activation of the area LO by all objects regardless of meaning but lack of its involvement during object recognition provided evidence that this area represents an intermediate link in the chain of processing stages leading to object recognition in the human visual cortex. Other examples of fMRI studies demonstrating "bottom-up" hierarchical processing within visual cortical areas include the consistent activation of regions beyond V1 during the perception of illusory contours produced by Kanizsa figures (Hirsch et al. 1995) and the increased activity in MT area relative to V2 and V3a areas during motion aftereffect, even after correcting for the greater motion selectivity of MT (Tootell et al. 1995). Both dorsal and ventral visual processing pathways have reciprocal connections with regions beyond the modality-specific visual system, which mediate feedback inputs from higher-order processing stations to lower-order ones, thus mediating some "top-down" influences on the visual cortical areas. Several aspects of "top-down" contributions to the processing of visual information have also been demonstrated in fMRI investigations. One example of a simple working memory task for faces showed that posterior occipitotemporal areas in the ventral pathway had mostly transient responses to stimuli, indicating their dominant role in perceptual processing, whereas prefrontal areas demonstrated sustained activity over memory delays, indicating their predominant role in working memory. Interestingly, more anterior occipitotemporal areas demonstrated some sustained activity during memory delays as well, presumably reflecting top-down influences mediated from the prefrontal cortex (Courtney et al. 1997; Ungerleider et al. 1998). Similar findings were reported by using a letter working memory task (Cohen et al. 1997). Activation of visual cortical areas has been demonstrated with other higher cognitive functions such as attention (Corbetta 1998), mental imagery (LeBihan et al. 1993), mental rotation (Cohen et al. 1996), and long-term memory retrieval (Aguirre and D'Esposito 1997). These studies demonstrated convincingly that fMRI is capable of detecting weaker signal responses associated with higher-order cognitive paradigms within indi-

vidual subjects independent of, or even in the absence of, visual stimulus input (Fig. 4.5).

The selected studies cited above confirmed the ability of fMRI in localizing visual cortical areas with high spatial precision, in characterizing the functional role played by each region, in demonstrating dynamic processes within the brain at high spatial and temporal resolution, and even in depicting the cortical representation of cognitive functions.

Several other issues important to human visual physiology have been explored over the past 3 years by various groups using fMRI methodology that were not mentioned in this short review. As discussed in the previous section, the ultimate limits in spatial and temporal resolution of fMRI have not yet been determined. For example, high resolution fMRI at 4 T was used to directly map ocular dominance regions in the human visual cortical layers (Menon et al. 1997), and another one at 3 T demonstrated the functional subnuclear organization of the lateral geniculate nucleus during parvocellular and magnocellular activation (Ugurbil et al. 1999; Chen and Ugurbil 1999). Demonstrating the feasibility for noninvasively mapping the functional organization of small targets in the living human, such as structures within the same nucleus and cortical columns, opens up the possibility of mapping specialized populations of neurons that are not accessible to electrophysiological or other methods of invasive mapping. As the technology and methods for data analysis are being devel-

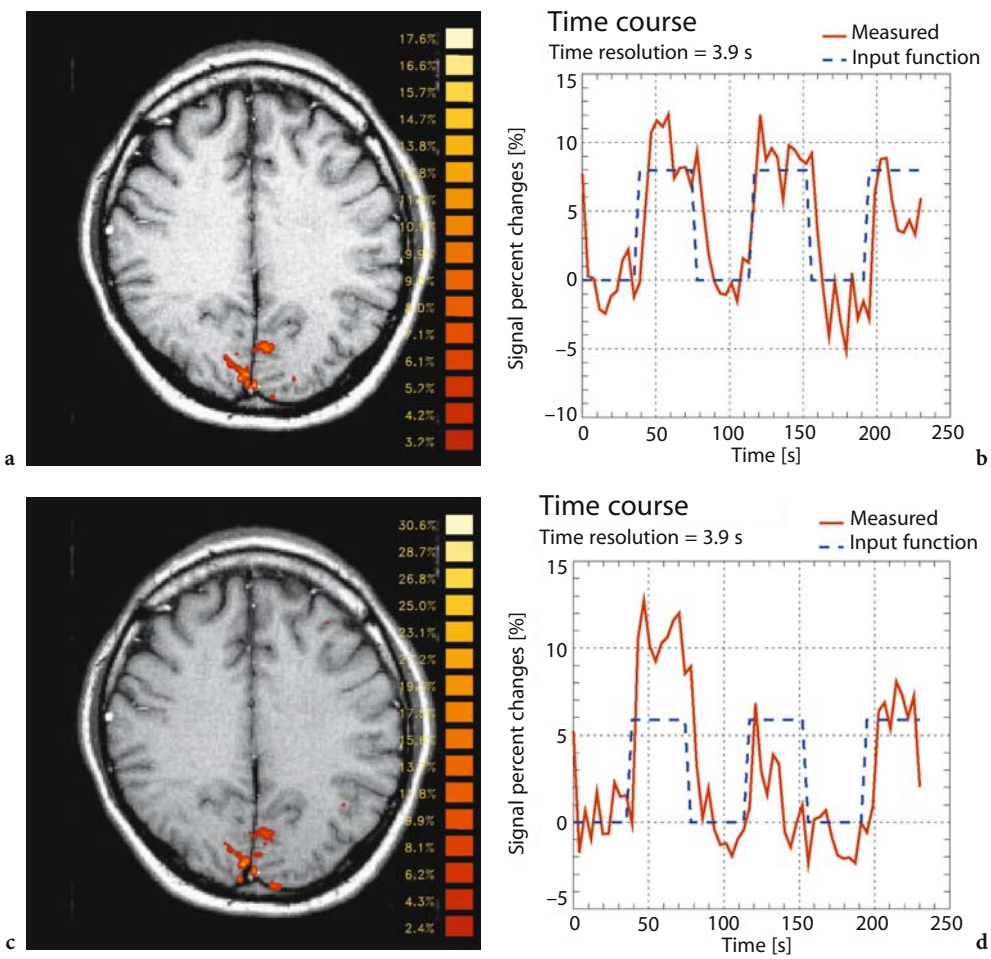

Fig. 4.5. Functional map (**a**) and signal time course (**b**) of a healthy volunteer during an on-off visual stimulation paradigm (stroboscopic white-light flashing at 10 Hz) show statistically significant ($p<0.001$) activation in the primary visual cortex. The signal intensity increases (*red continuous line*) are time-locked to the three periods of stimulus delivery (*blue dotted line*). In a second experiment (**c**, **d**), the middle stimulation period was replaced by a visual imagery task during which the same subject was instructed to mentally recall, while being kept in the dark, a series of colored pictures shown to him before the two experiments. A statistically significant increase of signal intensity is observed during visual recall, although to a lesser degree than during direct visual stimulation

oped, significant progress in our understanding of the functional organization of the visual system in the living human brain is anticipated.

4.4 Applications of fMRI in the Investigation of Visual Pathology in Humans

Early in the development of fMRI, its noninvasiveness, wide availability, and sensitivity to single subject analysis suggested its potential application to clinical problems. Several studies have explored the use of the technique for clinical applications such as the presurgical identification of normal and diseased brain tissue for treatment planning and the exploration of brain mechanisms underlying various disease processes or the recovery from brain insult (Kollias et al. 1996a, 1998a). Apart from its obvious clinical/diagnostic utility, the desire to apply this method to clinical problems is enhanced by the fact that correlation of neurological deficits following specific brain damage with neuroimaging findings has been an important approach for understanding the functional organization of the human brain (Grabowski and Damasio 1996). For example, lesion-deficit correlation in patients with lesions along the visual pathway provided a schema of retinotopic organization of striate and extrastriate cortical areas by relating the anatomical extent of a lesion as detected on a MR or CT scan to the functional perimetric findings (Horton and Hoyt 1991). Moreover, correlation of neuropsychological and psychophysical deficits with the anatomic location of lesions revealed the remarkable segregation of functions in the human visual cortex and the variety of basic and higher visual impairments that can result from its damage (Rizzo and Nawrot 1993; Zeki 1992 for review). The differential visual impairments produced by focal lesions in clinical cases suggested that the human visual cortex might be organized, similar to that of the monkey, into two anatomically distinct and functionally specialized ventral and dorsal processing pathways (Ungerleider and Haxby 1994). Specific syndromes such as visual object agnosia, prosopagnosia, and achromatopsia are produced by occipitotemporal lesions, whereas other syndromes such as optic ataxia, visual neglect, constructional apraxia, gaze apraxia, akinotopsia, and disorders of spatial cognition are produced by occipitoparietal lesions (Ungerleider and Haxby 1994; Farah 1990; Newcombe and Ratcliff 1989). Although lesion studies provided significant insight into understanding the function of the human visual cortex and its disorders, it was easy to recognize the limitations of this approach. Lesions in human patients, unlike those produced in animal models, are hardly ever as confined as one would wish, often involving not only local neurons but also subcortical fiber connections; they rarely allow the subject to be his own control, and they fail to capture the temporal dimension of phenomena (Grabowski and Damasio 1996). Therefore, the lesion approach in humans cannot conclusively demonstrate that the neurons within a specific area are themselves critical to the computational support of an impaired cognitive process. On the other hand, functional neuroimaging is able to demonstrate the differential neural activity of a specific neuroanatomical region, whereas is unable to prove that the observed activity is necessary for a putative isolated cognitive process because one never has perfect control over the cognitive processes in which a subject engages (Felleman and Van Essen 1991). The ability of fMRI to demonstrate the function-structure relationship in both a control state in healthy volunteers and specific to the individual brain-damaged patient makes it possible to overcome these limitations and investigate the organization of the human visual cortex with far greater precision than with lesion studies or functional neuroimaging studies in healthy subjects alone.

Several fMRI studies over the past 3 years, albeit many preliminary, demonstrated that the application of fMRI in patients with visual impairments is feasible. Data from patients with congruous homonymous hemianopia caused by retrochiasmal pathology (Miki et al. 1996a) and patients with visual loss caused by lesions of the optic nerves and chiasm (Miki et al. 1996b) reported good agreement between the findings of fMRI and those of perimetric examination. fMRI examinations in patients harboring space-occupying lesions involving the posterior afferent visual system showed that the activation patterns in the visual cortex identified by fMRI were consistent with the visual field deficits and with the traditional teaching of retinotopic representation. Additionally, it was demonstrated that fMRI can be obtained routinely and successfully in patients with visual abnormalities as part of their conventional neuroradiological evaluation (Kollias et al. 1998b). Visual field defects such as hemianopias (Fig. 4.6), scotomas (Fig. 4.7), and quadranopias (Fig. 4.8) could be reliably detected using fMRI methodology, providing essential information about the function-structure relationship specific to the individual patient with implications

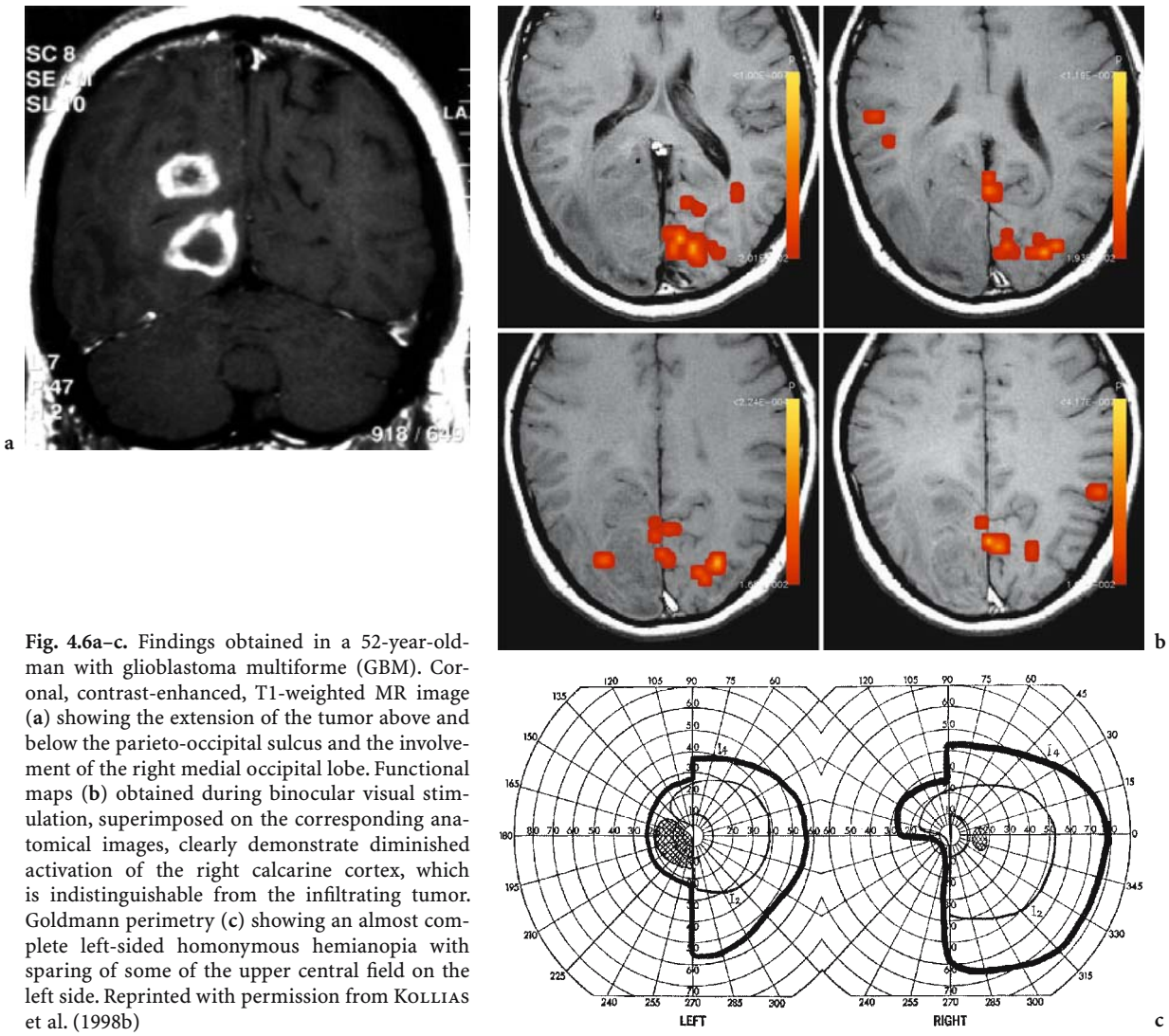

Fig. 4.6a–c. Findings obtained in a 52-year-old-man with glioblastoma multiforme (GBM). Coronal, contrast-enhanced, T1-weighted MR image (**a**) showing the extension of the tumor above and below the parieto-occipital sulcus and the involvement of the right medial occipital lobe. Functional maps (**b**) obtained during binocular visual stimulation, superimposed on the corresponding anatomical images, clearly demonstrate diminished activation of the right calcarine cortex, which is indistinguishable from the infiltrating tumor. Goldmann perimetry (**c**) showing an almost complete left-sided homonymous hemianopia with sparing of some of the upper central field on the left side. Reprinted with permission from Kollias et al. (1998b)

for diagnosis and therapy planning. Another study of three albino subjects showed asymmetric activation of the primary visual cortex during monocular visual stimulation, a finding consistent with the known crossing abnormalities of the visual pathways in albinism, confirming the potential of the technique for evaluation of the visual pathways in pathologic conditions (Hedera et al. 1994). An increased hemodynamic response to photic stimulation has been observed in schizophrenic patients that may reflect diffuse structural brain changes as well as primary or iatrogenic impairment in mitochondrial function or energy metabolism, suggesting that fMRI has the potential to provide insight into the pathophysiology of various disease processes (Reshaw et al. 1994). Insight into the pathophysiology of dyslexia was provided by studying visual motion processing in normal and dyslexic men using fMRI (Eden et al. 1996). It was found that dyslexics, compared with normal controls, have an almost complete lack of activation in area MT (part of the magnocellular visual subsystem) during motion perception while showing normal activation to textured patterns. These results support the idea that the known language deficits in dyslexics reflect a general deficit in the visual processing of the temporal properties of stimuli which may manifest itself as disorders of phonological awareness, rapid naming, rapid visual processing, or motion detection. More recent studies have attempted to elucidate a variety of other pathologies afflicting the visual system. For example, activation in the ipsilateral hemisphere was produced by stimulating the blind hemifield in a patient with a large cortical lesion and unconscious residual visual abilities within their hemianopic visual field ("blindsight"), whereas activation was absent in another patient with a similar

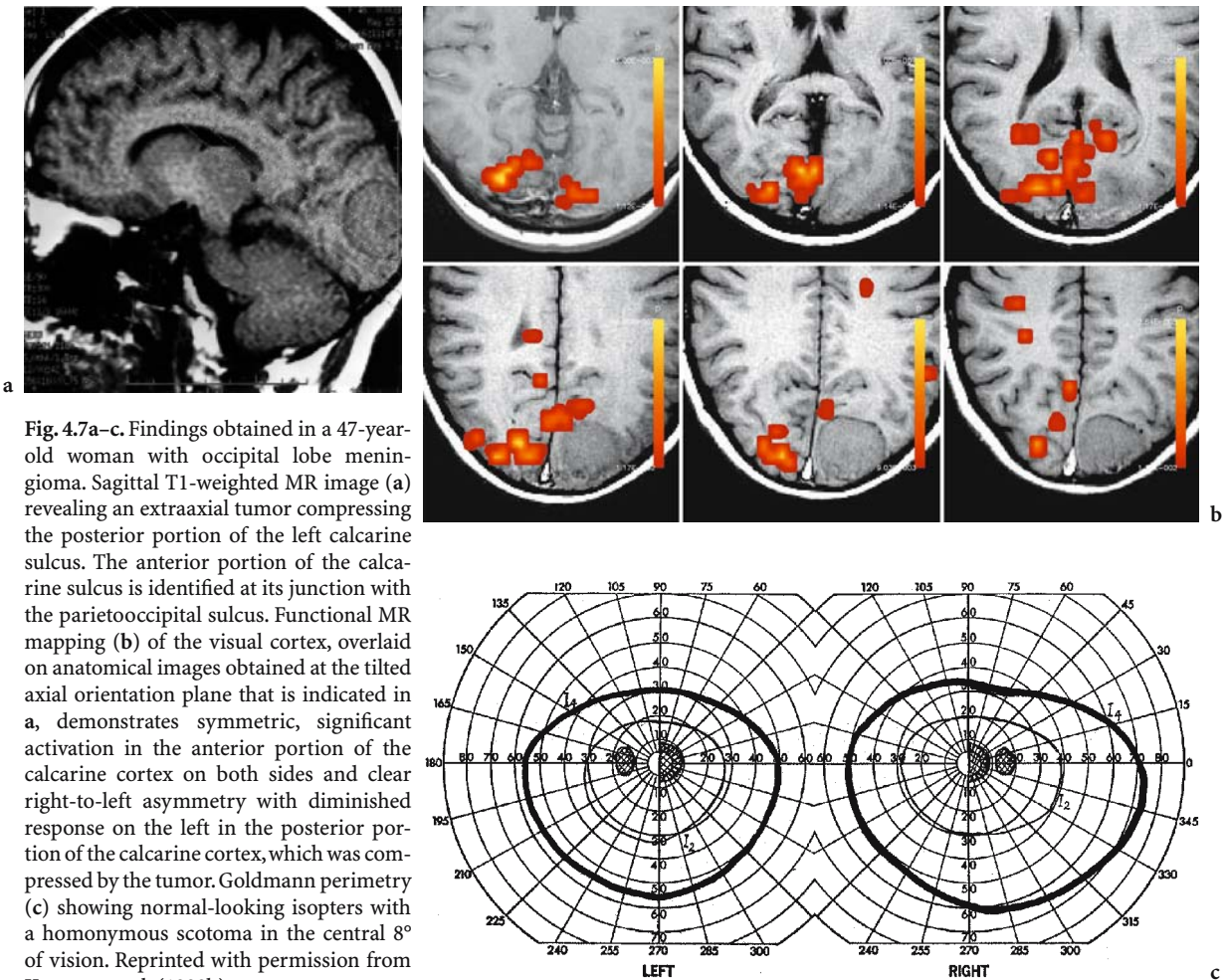

Fig. 4.7a–c. Findings obtained in a 47-year-old woman with occipital lobe meningioma. Sagittal T1-weighted MR image (**a**) revealing an extraaxial tumor compressing the posterior portion of the left calcarine sulcus. The anterior portion of the calcarine sulcus is identified at its junction with the parietooccipital sulcus. Functional MR mapping (**b**) of the visual cortex, overlaid on anatomical images obtained at the tilted axial orientation plane that is indicated in **a**, demonstrates symmetric, significant activation in the anterior portion of the calcarine cortex on both sides and clear right-to-left asymmetry with diminished response on the left in the posterior portion of the calcarine cortex, which was compressed by the tumor. Goldmann perimetry (**c**) showing normal-looking isopters with a homonymous scotoma in the central 8° of vision. Reprinted with permission from Kollias et al. (1998b)

lesion but without "blindsight", suggesting that the contralesional occipital cortex may contribute to the mediation of "blindsight" (Bittar et al. 1999). Using phase-encoded stimuli and displaying their measurements on flattened representations of the visual cortex, another group documented that in the absence of the striate cortex and upon stimulation of the blind field, extrastriate responses are distributed near the lower vertical meridian, suggesting that subcortical projections within the lesioned hemisphere which bypass V1 or transcallosal connections from cortical areas in the intact hemisphere may be responsible for the residual vision (Basele et al. 1999). Investigating the activation patterns of cortical and subcortical sensorimotor interaction during optokinetic stimulation in patients with complete homonymous hemianopia, a lack of activation in the thalamus and lateral geniculate nucleus of the affected side was shown. This finding indicated that activation of these structures relies on the visual input of the ipsilateral hemisphere and bilateral activation of the MT/MST areas, suggesting direct ipsilateral or contralateral transcallosal input in these areas (Brandt et al. 1998). Large-scale reorganization of the visual cortex has been demonstrated with fMRI in a patient with an early cortical lesion (colpocephaly) coexisting with normal gross visual function (Bittar et al. 2000). Analyzing differences of cortical activation between normal and amblyopic eye stimulation, it was found that extrastriate ventral areas show a selective deficit to gratings of higher spatial frequencies, suggesting that the amblyopic deficits may be caused by the inefficient transmission of neuronal signals to V2 and other extrastriate visual areas (Muckli et al. 1998). fMRI was used to examine whether preattentive and attentive visual processing activates the parieto-occipital systems differentially and provided further evidence to delineate the neural substrate for the two distinct modes of visual processing, helping to elucidate the neurophysiological mechanisms underlying

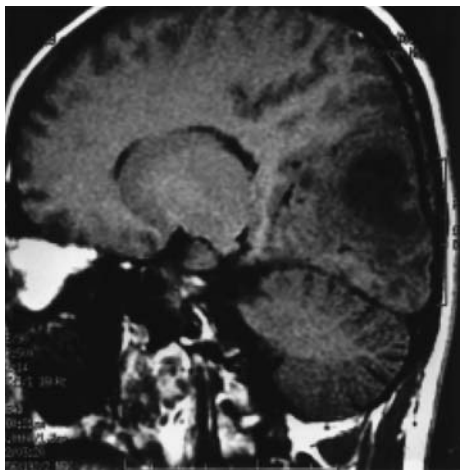

a

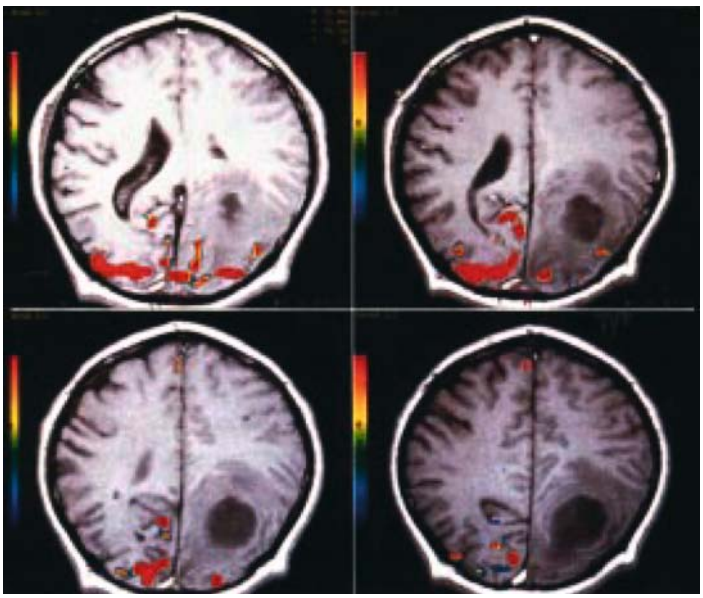

b

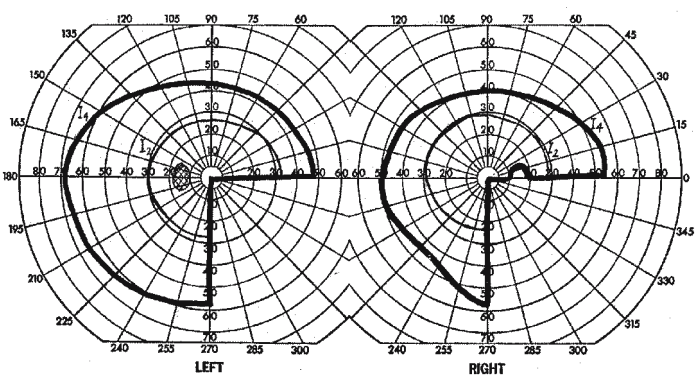

c

Fig. 4.8a–c. Findings obtained in a 44-year-old man with occipital abscess. Sagittal T1-weighted MR image (**a**) demonstrating the abscess with moderate perilesional edema located between the calcarine sulcus inferiorly and the parieto-occipital sulcus superiorly. Functional MR imaging data (**b**) superimposed on the corresponding MR anatomical sections demonstrate significant bilateral activation in the most inferior section through the primary calcarine cortex and diminished activity on the left side in the more superior sections through the supracalcarine V2/V3 cortical areas. Goldmann perimetry (**c**) shows a right-sided, inferior quadrantanopia with perfectly aligned margins along both the horizontal and vertical meridians. Reprinted with permission from Kollias et al. (1998b)

visual attention disorders (Nakamura et al. 2000). Comparing the visual cortical function of patients with intractable occipital lobe epilepsy with that of control subjects, it was demonstrated that patients had abnormal activation patterns concordant with the side of seizure onset, indicating that fMRI is a reliable method for identifying areas of abnormal visual cortical function ipsilateral to the epileptogenic region (Masuoka et al. 2000). In multiple sclerosis patients with unilateral optic neuritis, the area of activation in the primary visual cortex measured by fMRI is dramatically reduced in response to stimulation of the affected eye, indicating that this method has the potential to provide more detailed topographic information relating to functional deficits in multiple sclerosis (Gareau et al. 1999). Increased cerebral activity in the ventral extrastriate visual cortex was found in patients with visual hallucinations which persists between hallucinations, providing insight into the differentiation of neural processes specific to consciousness from unconscious afferent signals (Ffytche et al. 1998).

Human lesion studies using fMRI are able to address questions not only regarding the organization and functional specialization of visual cortical areas but also to make inferences about functional interactions among cortical areas subserving specific cognitive operations. Several questions regarding the organization of human visual cortical areas and their participation in complex cognitive tasks remain to be answered. Much of our present knowledge is strongly influenced by current theories of visual cortex organization in monkeys. However, homologies of cortical areas in the monkey remain tentative, and caution is necessary when using information from macaques to understand cortical organization in humans (Kass 1995). Although fMRI cannot reveal the cortical mechanisms at the level of individual neurons, a combination of well designed studies in healthy volunteers and selected brain-damaged individuals can be

used to test hypotheses generated by work in animals and advance our knowledge about the functional organization of the visual cortex, both at a basic level of visual processing and into areas of cognition that are unique to the human brain.

Acknowledgement. This work was supported by Swiss National Foundation grant no. 31-42180.94.

References

Aguirre GK, D'Esposito M (1997) Environmental knowledge is subserved by separable dorsal/ventral neural areas. J Neurosci 17:2512–2518

Aguirre GK, Zarahn E, D'Esposito M (1998) Neural components of topographical representation. Proc Natl Acad Sci USA 95:839–846

Aine CJ (1995) A conceptual overview and critique of functional neuroimaging techniques in humans. I. MRI/fMRI and PET. Crit Rev Neurobiol 9:229–309

Bandettini PA, Wong EC, Kinks RS et al (1992) Time course EPI of human brain function during task activation. Magn Reson Med 25:390–397

Bandettini PA, Jesmanowicz A, Wong EC et al (1993) Processing strategies of time-course data sets in functional MRI on the human brain. Magn Reson Med 30:161–173

Bandettini PA, Kwong KK, Davis TL et al (1997) Characterization of cerebral blood oxygenation and flow changes during prolonged brain activation. Hum Brain Mapping 5:93–109

Basele HA, Morland AB, Wandell BA (1999) Topographic organization of human visual areas in the absence of input from primary cortex. J Neurosci 19:2619–2627

Binder JR, Rao SM (1994) Human brain mapping with functional magnetic resonance imaging. In: Kertesz A (ed) Localization and neuroimaging in neuropsychology. Academic, San Diego, pp 185–212

Bittar RG, Ptito A, Faubert J, Dumoulin SO, Ptito A (1999) Activation of the remaining hemisphere following stimulation of the blind hemifield in hemispherectomized subjects. Neuroimage 10:339–346

Bittar RG, Ptito A, Dumoulin SO, Andermann F, Reutens DC (2000) Reorganization of the visual cortex in callosal agenesis and colpocephaly. J Clin Neurosci 7:13–15

Blamire AM, Ogawa S, Ugurbil K et al (1992) Dynamic mapping of the human visual cortex by high-speed magnetic resonance imaging. Proc Natl Acad Sci USA 89:11069–11073

Boynton GM, Engel SA, Glover GH et al (1996) Linear systems analysis of functional magnetic resonance imaging in human V1. J Neurosci 16:4207–4221

Brandt T, Bucher SF, Seelos KC, Dietrich M (1998) Bilateral functional MRI activation of the basal ganglia and middle temporal/medial superior temporal motion-sensitive areas: optokinetic stimulation in homonymous hemianopia. Arch Neurol 55:1126–1131

Buckner RL (1998) fMRI data analysis. Syllabus of the 4th international conference on functional mapping of the human brain (brain mapping course), pp 82–92

Buckner RL, Bandettini PA, O'Craven KM et al (1996) Detection of cortical activation during averaged single trials of cognitive task using functional magnetic resonance imaging. Proc Natl Acad Sci USA 93:14878–14883

Buckner RL, Goodman J, Burock et al (1998) Functional-anatomic correlates of object priming in humans revealed by rapid presentation event-related fMRI. Neuron 20:285–296

Chen W, Ugurbil K (1999) High spatial resolution functional magnetic resonance imaging at very-high-magnetic field. Top Magn Reson Imaging 10:63–78

Cohen MS, Kosslyn SM, Breiter HC et al (1996) Changes in cortical activity during mental rotation: a mapping study using functional MRI. Brain 119:89–100

Cohen JD, Perlstein WM, Braver TS et al (1997) Temporal dynamics of brain activation during a working memory task. Nature 386:604–608

Corbetta M (1998) Frontoparietal cortical networks for directing attention and the eye to visual locations: identical, independent, or overlapping neural systems. Proc Natl Acad Sci USA 95:831–838

Courtney SM, Ungerleider LG (1997) What fMRI has taught us about human vision. Curr Opin Neurobiol 7:554–561

Courtney SM, Ungerleider LG, Keil K et al (1997) Transient and sustained activity in a distributed neural system for human working memory. Nature 386:608–611

Dale AM, Buckner RL (1997) Selective averaging of rapidly presented individual trials using fMRI. Hum Brain Mapping 5:329–340

Damasio H, Frank RJ (1992) Three-dimensional in vivo mapping of brain lesions in humans. Arch Neurol 49:137–143

DeYoe EA, Bandettini P, Neitz J et al (1994) Functional magnetic resonance imaging (FMRI) of the human brain. J Neurosci Methods 54:171–187

DeYoe EA, Carman GJ, Bandettini P et al (1996) Mapping striate and extrastriate visual areas in human cerebral cortex Proc Natl Acad Sci USA 93:2382–2386

Duong TQ, Kim DS, Ugurbil K, Kim SG (2000) Spatiotemporal dynamics of the BOLD fMRI signals: towards mapping submillimeter cortical columns using the early negative response. Magn Reson Med 44:231–242

Edelman RP, Siewert B, Daeby DG et al (1994) Qualitative mapping of cerebral blood flow and functional localization with echo-planar MR imaging and signal targeting with alternating radio frequency. Radiology 192:513–520

Eden GF, VanMeter JW, Rumsey JM et al (1996) Abnormal processing of visual motion in dyslexia revealed by functional brain imaging. Nature 382:66–69

Engel SA, Rumelhart DE, Wandell BA et al (1994) MRI of human visual cortex. Nature 369:525

Engel SA, Glover GH, Wandell BA (1997) Retinotopic organization in human visual cortex and the spatial precision of functional MRI. Cereb Cortex 7:181–192

Ernst T, Hennig J (1994) Observation of a fast response in functional MR. Magn Reson Med 32:146–149

Farah MJ (1990) Visual agnosia. MIT Press, Cambridge, MA

Felleman DJ, Van Essen DC (1991) Distributed hierarchical processing in the primate cerebral cortex. Cereb Cortex 1:1–47

Ffytche DH, Howard RJ, Brammer MJ, David A, Woodruff P, Williams S (1998) The anatomy of conscious vision: and fMRI study of visual hallucinations. Nat Neurosci 1:738–742

Fox PT, Raichle ME (1986) Focal physiological uncoupling of cerebral blood flow and oxidative metabolism during somatosensory stimulation in human subjects. Proc Natl Acad Sci USA 83:1140–1144

Frahm J, Kruger G, Merdoldt KD et al (1996) Dynamic uncoupling and recoupling of perfusion and oxidative metabolism during focal activation in man. Magn Reson Med 35:143–148

Friston KJ, Josephs O, Rees G, et al (1997) Nonlinear event-related responses in fMRI. Magn Reson Med 39:41–52

Friston KJ, Fletcher P, Josephs O et al (1998) Event-related fMRI: characterizing differential responses. Neuroimage 7:30–40

Gareau PJ, Gati JS, Menon RS et al (1999) Reduced visual evoked responses in multiple sclerosis patients with optic neuritis: comparison of functional magnetic resonance imaging and visual evoked potentials. Mult Scler 5:161–164

Golay X, Kollias SS, Stoll G et al (1998) A new correlation-based fuzzy logic clustering algorithm for fMRI. Magn Reson Med 40:249–260

Grabowski TJ, Damasio AR (1996) Improving functional imaging techniques: the dream of a single image for a single mental event (commentary). Proc Natl Acad Sci USA 93:14302–14303

Hathout GM, Kirlew KA, So GJK et al (1994) MR imaging signal response to sustained stimulation in human visual cortex. JMRI 4:537–543

Hedera P, Lai S, Haake EM et al (1994) Abnormal connectivity of the visual pathways in human albinos demonstrated by susceptibility-sensitized MRI. Neurology 44:1921–1926

Hirsch J, DeLaPaz RL, Relkin NR et al (1995) Illusory contours activate specific regions in human visual cortex: evidence from functional magnetic resonance imaging. Proc Natl Acad Sci USA 92:6469–6473

Horton JC, Hoyt WF (1991) The representation of the visual field in the human striate cortex: a revision of the classic Holmes map. Arch Ophthalmol 109:816–824

Howard RJ, Brammer M, Wright I et al (1996) A direct demonstration of functional specialization within motion-related visual area and auditory cortex of the human brain. Curr Biol 6:1015–1019

Hu X, Le TH, Ugurbil K (1997) Evaluation of the early response in fMRI in individual subjects using short stimulus duration. Magn Reson Med 37:877–884

Kanwisher N, McDermott J, Chun MM (1997) The fusiform face area: a module in human extrastriate cortex specialized for the perception of faces. J Neurosci 17:4302–4311

Kass JH (1995) Progress and puzzles. Curr Biol 5:1126–1128

Kim SG, Tsekos NV (1997) Perfusion imaging by a flow-sensitive alternating inversion recovery (FAIR) technique: application to functional brain imaging. Magn Reson Med 37:425–435

Kim SG, Ashe J, Hendrich K, Ellermann JM, Merkle H, Ugurbil K, Georgopoulos AP (1993) Functional magnetic resonance imaging of motor cortex: hemispheric asymmetry and handedness. Science 261:615–617

Kleinschmidt A, Lee BB, Requardt M et al (1996) Functional mapping of color processing by magnetic resonance imaging of responses to selective P- and M-pathway stimulation. Exp Brain Res 110:279–288

Kollias SS, Golay X, Valavanis A (1996a) Localization of regional brain activity using functional magnetic resonance imaging: preliminary applications in neurosurgical patients. Crit Rev Neurosurg 6:159–177

Kollias SS, Valavanis A, Golay XG et al (1996b) Functional magnetic resonance imaging of cortical activation. Int J Neuroradiol 2:450–472

Kollias SS, Bernays R, Marugg R, Romanowski B, Yonekawa Y, Valavanis A (1998a) Target definition and trajectory optimization for interactive MR-guided biopsies of brain tumors in an open-configuration MRI system. J Magn Reson Imaging (JMRI) 8:143–159

Kollias SS, Landau K, Khan N et al (1998b) Functional evaluation of the visual cortex in patients with retrochiasmatic lesions using magnetic resonance imaging. J Neurosurg 89:780–790

Kollias SS, Golay X, Boesiger P, Valavanis A (2000) Dynamic characteristics of oxygenation-sensitive MR signal during application of varying temporal protocols for imaging of human brain activity. Neuroradiology 42:591–601

Kwong KK (1995) Functional magnetic resonance imaging with echo planar imaging. Magn Reson Med 11:1–20

Kwong KK, Belliveau JW, Chesler DA et al (1992) Dynamic magnetic resonance imaging of human brain activity during primary sensory stimulation. Proc Natl Acad Sci USA 89:5675–5679

Kwong KK, Chesler DA, Weisskoff RM et al (1995) MR perfusion studies with T1-weighted echo planar imaging. Magn Reson Med 34:878–887

Lai S, Hopkins AL, Haacke EM et al (1993) Identification of vascular structures as a major source of signal contrast in high resolution 2D and 3D functional activation imaging of the motor cortex at 1.5 T: preliminary results. Magn Reson Med 30:387–392

LeBihan D, Turner R, Zeffiro TA et al (1993) Activation of human primary visual cortex during visual recall: a magnetic resonance imaging study. Proc Natl Acad Sci USA 90:11802–11805

Malach R, Reppas JB, Benson RR et al (1995) Object-related activity revealed by functional magnetic resonance imaging in human occipital cortex. Proc Natl Acad Sci USA 92:8135–8139

Malonek D, Grinvald A (1996) Interactions between electrical activity and cortical microcirculation revealed by imaging spectroscopy: implications for functional brain mapping. Science 272:551–554

Masuoka LK, Anderson AW, Gore JC, McCarthy G, Spencer DD, Novotny EJ (2000) Functional magnetic resonance imaging identifies abnormal visual cortical function in patients with occipital lobe epilepsy. Epilepsia 40:1248–1253

McKeown MJ, Jung T-P, Makeig S et al (1998) Spatially independent activity patterns in functional MRI data during the stroop color-naming task. Proc Natl Acad Sci USA 95:803–810

Menon RS, Ogawa S, Strupp JP et al (1995a) BOLD based functional MRI at 4 Tesla includes a capillary bed contribution: echo-planar imaging correlates with previous optical imaging using intrinsic signals. Magn Reson Med 33:453–459

Menon RS, Ogawa S, Ugurbil K (1995b) High-temporal-resolution studies of the human primary visual cortex at 4 T: teasing out the oxygenation contribution in FMRI. Int J Imaging Systems Technol 6:209–215

Menon RS, Ogawa S, Strupp JP et al (1997) Ocular dominance in human V1 demonstrated by functional magnetic resonance imaging. J Neurphysiol 77:2780–2787

Miki A, Nakajima T, Fujita M et al (1996a) Functional magnetic resonance imaging in homonymous hemianopsia. Am J Ophthalmol 121:258–266

Miki A, Nakajima T, Takagi M et al (1996b) Detection of visual dysfunction in optic atrophy by functional magnetic reso-

nance imaging during monocular visual stimulation. Am J Ophthalmol 122:404–415
Moseley EM, Glover HG (1995) Functional MR imaging: capabilities and limitations. Neuroimaging Clin North Am 5:161–191
Muckli L, Tonhausen N, Goebel R et al (1998). Reduced fMRI response to monocular amblyopic eye stimulation in extrastriate visual areas. Proceedings of the 4th international conference on functional mapping of the human brain, p 19
Nakamura K, Honda M, Okada T, Hankawa T, Fukuyama H, Konishi J, Shibasaki H (2000) Attentional modulation of parieto-occipital cortical responses: implications for hemispatial neglect. J Neurol Sci 176:136–143
Newcombe F, Ratcliff G. (1989). Disorders of visuospatial analysis. In: Boller F, Grafman J (eds) Handbook of neuropsychology. Elsevier, Amsterdam, pp 333–356
Ogawa S, Lee TM, Kay AR, Tank DW (1990) Brain magnetic resonance imaging with contrast dependent on blood oxygenation. Proc Natl Acad Sci USA 87:9868–9872
Pauling L, Coryell CD (1936) The magnetic properties and structure of hemoglobin, oxyhemoglobin, and carbonmonoxyhemoglobin. Proc Natl Acad Sci USA 22:210–216
Polk TA, Farah MJ (1998) The neural development and organization of letter recognition: evidence from functional neuroimaging, computational modeling, and behavioral studies. Proc Natl Acad Sci USA 95:847–852
Puce A, Allison T, Asgari M et al (1996) Differential sensitivity of human visual cortex to faces, letterstrings, and textures: a functional magnetic resonance imaging study. J Neurosci 16:1192–5215
Raichle ME (1998) Behind the scenes of functional brain imaging: a historical and physiological perspective. Proc Natl Acad Sci USA 95:765–772
Reshaw PF, Yurgelun-Todd DA, Cohen BM (1994) Greater hemodynamic response to photic stimulation in schizophrenic patients: an echo planar MRI study. Am J Psychiatry 151:1493–1495
Rizzo M, Nawrot M (1993) Human visual cortex and its disorders. Curr Opin Ophthalmol 4:38–47
Rosen BR, Buckner RL, Dale AM (1998) Event-related functional MRI: past, present, and future. Proc Natl Acad Sci 95:773–780
Sakai K, Watanabe E, Onodera Y et al (1995) Functional mapping of the human colour centre with echo-planar magnetic resonance imaging. Proc R Soc Lond [Biol] 261:89–98
Savoy RL, Bandettini PA, O'Kraven KM et al (1995) Pushing the temporal resolution of fMRI: studies of very brief visual stimuli onset variability and asynchrony, and stimulus-correlated changes in noise. Proceedings of the ISMRM 3rd annual meeting Nice, France, p 450
Schneider W, Noll DC, Cohen JD (1993) Functional topographic mapping of the cortical ribbon in human vision with conventional MR scanners. Nature 365:150–153
Sereno MI, Dale AM, Reppas JB et al (1995) Borders of multiple visual areas in humans revealed by functional magnetic resonance imaging Science 268:889–893
Tootell RBH, Reppas JB, Dale AM et al (1995) Visual motion aftereffect in human cortical area MT revealed by functional magnetic resonance imaging. Nature 375:139–141
Tootell RBH, Dale AM, Sereno MI et al (1996) New images form human visual cortex. Trends Neurosci 19:481–498
Tootell RB, Hadjikhani NK, Vanduffel W et al (1998a) Functional analysis of primary visual cortex in humans. Proc Natl Acad Sci USA 95:811–817
Tootell RB, Mendola JD, Hadjikhani NK et al (1998b) The representation of the ipsilateral visual field in human cerebral cortex. Proc Natl Acad Sci 95:818–824
Ugurbil K, Hu X, Chen W, Zhu XH, Kim SG, Georgopoulos A (1999) Functional mapping in the human brain using high magnetic fields. Philos Trans R Soc Lond B Biol Sci 354:1195–1213
Ungerleider LG, Haxby JV (1994) "What" and "where" in the human brain. Curr Opin Biol 4:157–165
Ungerleider LG, Courtney SM, Haxby JV (1998) A neural system for human visual working memory. Proc Natl Acad Sci USA 95:883–890
Van Essen DC, Drury HA, Joshi S et al (1998) Functional and structural mapping of human cerebral cortex: solutions are in the surfaces. Proc Natl Acad Sci USA 95:788–795
Van Zijl PCM, Eleff SM, Ulatowski JA et al (1998) Quantitative assessment of blood flow, blood volume and blood oxygenation effcts in functional magnetic resonance imaging. Nat Med 4:159–167
Zarahn E, Aguirre GK, D'Esposito M (1997) Empirical analyses of BOLD fMRI statistics. I. Spatially unsmoothed data collected under null-hypothesis conditions. Neuroimage 5:179–197
Zeki S (1992) The visual image in mind and brain. Scientific American 267:69–76
Zeki S, Watson JPG, Lueck CJ et al (1991) A direct demonstration of functional specialization in human visual cortex. J Neurosci 11:641–649

The requested page could not be found.

Special Part

The requested page could not be found.

5 Optic Pathway Pathology in Children

Eugen Boltshauser and Ernst Martin

CONTENTS

E. Boltshauser, MD
Professor, Department of Child Neurology
E. Martin, MD
Professor, Department of Neuroradiology and Magnetic Resonance, University Children's Hospital, Steinwiesstrasse 75, 8032 Zürich, Switzerland

5.1 Introduction

5.1.1 General Remarks

The optic pathways can be involved in a large spectrum of congenital as well as acquired conditions in children. In this context, an approach guided by clinical presentations in a pediatric university hospital is preferable over an extensive review. Therefore, we have arbitrarily divided the chapter into:

- congenital pathology/infantile presentations
- acquired optic pathway lesions
- work-up in systemic diseases
- unexpected (incidental) findings

Any neuroimaging procedure should be based on profound clinical (including ophthalmological if appropriate) examination. This should allow the neuroradiologist to formulate specific questions.

We generally refer to standard textbooks for pediatric aspects of neurology (Aicardi 1998), ophthalmology (Brodsky et al. 1995; Nelson et al. 1991), neuroimaging (Barkovich 1995) and for defined syndromes (McKusick 1998).

5.1.2 Normal Myelination of Optic Pathways

Microscopic myelin of the visual system first appears in the optic tract during the 7th month of gestation. It then proceeds both rostrally to the optic chiasm and optic nerves and occipitally along the optic radiation to the occipital lobe. Around term, the intensity of myelin staining in the visual system approaches that of myelin in the mature brain (Yakovlev and Lecours 1967; Gilles et al. 1983; Van Der Knaap and Valk 1995), while the cortical visual system in man is believed to differentiate postnatally (Atkinson 1984). The development of stereopsis and visual topography during infancy is accompanied by changes in visual

evoked potential (VEP) signals and coincides with the most salient phases in the anatomical development of the human visual system (Garey 1984).

On magnetic resonance imaging, myelinated fiber tracts exhibit high signal intensity on short TR/TE and low signal intensity on long TR/TE images (Barkovich 1995; Van Der Knaap and Valk 1995). At birth, the ventrolateral region of the thalamus, the dorsal limb of the internal capsule, the central portion of the centrum semiovale, and the dorsolateral putamen show T1 hyperintense signals, indicating myelinated supratentorial structures. During the first postnatal month, the optic nerve, optic tract and optic radiation appear hyperintense on T1-weighted images, whereas low signal intensity on T2-weighted images is seen in the optic tract by the age of 1 month. During the subsequent 2 or 3 months this T2 hypointensity proceeds posteriorly along the optic radiation, ending in the subcortical white matter of the visual cortex. The occipital white matter of the calcarine area is the earliest subcortical area to be myelinated before the Rolandic area. Increasing signal intensity of the white matter of the primary visual cortex surrounding the calcarine fissure can be observed between 3 and 6 months of life on T1-weighted images and low signal intensity between 4 and 8 months on T2-weighted images.

tagmus can be associated with a number of conditions (such as albinism, aniridia, Leber amaurosis, achromatopsia, congenital dystrophy, stationary night blindness, optic nerve hypoplasia). Ophthalmological assessment often supplemented by electroretinography will assist to delineate most of these conditions.

5.2.2 Microphthalmos/Anophthalmos

Uni- or bilateral microphthalmos/anophthalmos may be seen in various conditions (Albernaz et al. 1997; Nelson et al. 1991). Neuroimaging is performed to assess orbital anatomy, optic chiasm, and posterior visual pathways as well as possible brain malformations. Typical cases are illustrated in Figs. 5.1–5.4. Aicardi syndrome, observed only in girls, is considered to result from an X-linked mutation that is lethal in boys. The relevant triad consists of a typical optic disc appearance with "chorioretinal lacunae", infantile spasms, and agenesis of the corpus callosum (Aicardi 1992; Brodsky et al. 1995). In addition, other central nervous system malformations are always present, in particular migration anomalies (heterotopias, polymicrogyria) and midline arachnoid cysts.

5.2 Congenital Pathology of Optic Pathways: Infantile Presentations

5.2.1 General Remarks

In this section, a number of typical presentations will be discussed.

Depending on the situation, a careful ophthalmological examination has to supplement the general pediatric and neurological examination. A few "rules" may help in guiding further diagnostic steps and indicate where to focus on neuroimaging.

Cortical visual impairment (blindness) is <u>not</u> accompanied by nystagmus. Congenital nystagmus is not present at birth but has its onset at 2–3 months. In general, congenital nystagmus points to retinal or anterior optic pathway pathology. Clinical signs of retinal disease in congenital nystagmus are: photophobia, paradoxical pupillary responses, high myopia, oculodigital reflex. Bilateral nystagmus is only seen if the visual acuity is below 20/70. Congenital nys-

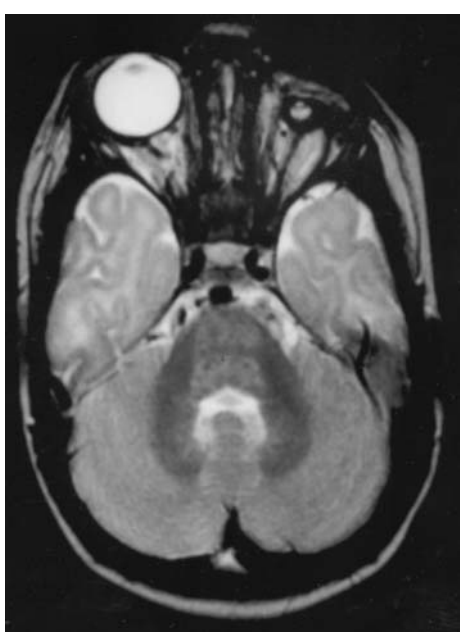

Fig. 5.1. T2/FSE axial magnetic resonance image (MRI) of a 5-month-old girl with unilateral anophthalmos (clinically). MRI shows normal orbital anatomy and normal brain

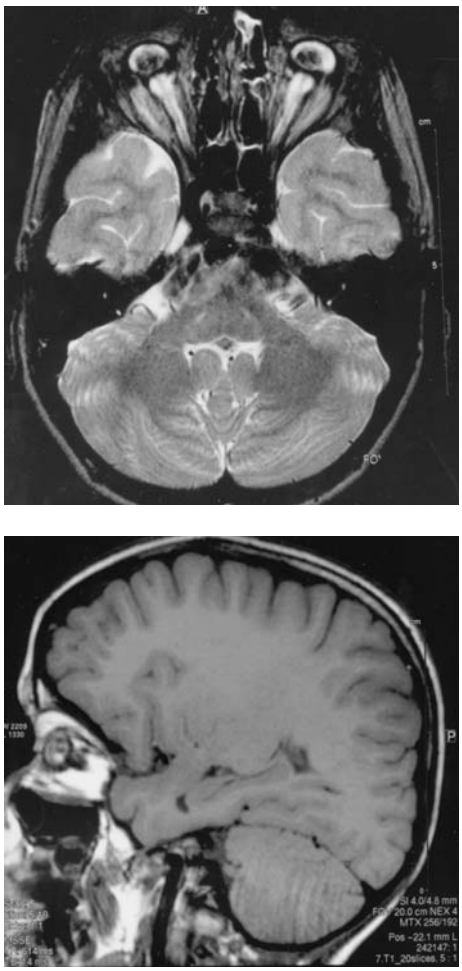

Fig. 5.2. a Axial T2-weighted , **b** parasagittal T1-weighted MRI of a 7-year-old boy with bilateral microphthalmos, marked mental retardation and epilepsy. Normal brain anatomy

Congenital eye malformations including microphthalmos are part of several genetically determined syndromes associated with neuronal migration disorders, such as Fukuyama congenital muscular dystrophy and Walker-Warburg syndrome (Barkovich 1995, 1998; McKusick 1994). Neuroimaging is essential in delineating these disorders.

Waugh et al. (1998) found a large proportion of additional brain pathology in a series of children with congenital disorders of the peripheral visual system.

5.2.3 Macrophthalmos/Buphthalmos

Buphthalmos may be a rare presentation of Sturge-Weber syndrome. In a minority of patients, the typical port-wine trigeminal nevus may be missing. Neuroimaging (in particular T1-weighted MRI with contrast) may assist to demonstrate the leptomeningeal angiomatosis. Macrophthalmos is seen rarely as a presenting symptom of neurofibromatosis type 1.

5.2.4 Ocular Tumors

Retinoblastoma is the most common intraocular tumor in infancy, affecting about 1 in 20,000 infants. The most frequent presenting symptom is leukokoria,

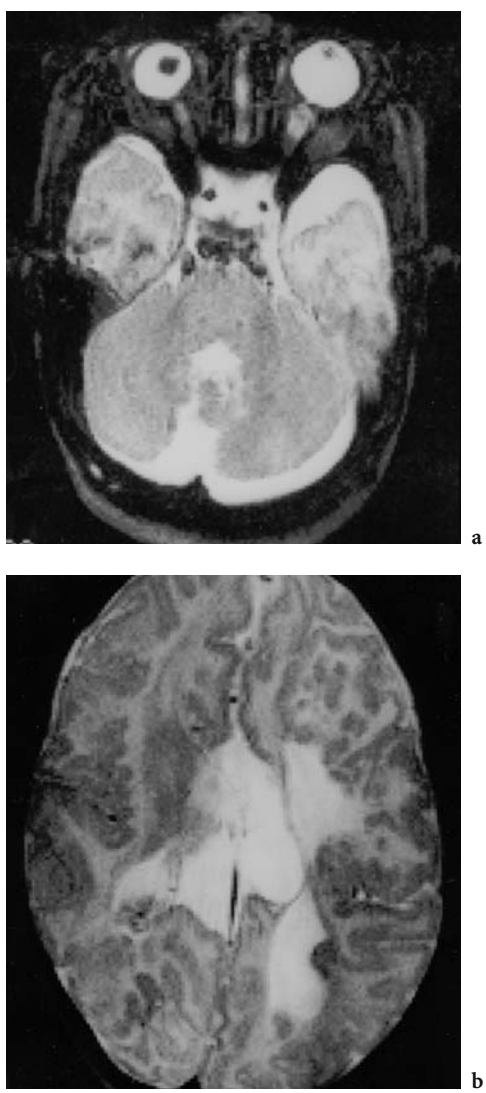

Fig. 5.3a,b. T2 axial MRI of a 3-month-old girl with AICARDI syndrome: bilateral (asymmetric) microphthalmos, vermis hypoplasia, areas of polymicrogyria, multiple gray matter heterotopias, agenesis of corpus callosum and interhemispheric arachnoid cyst. (Reproduced with permission of Ferdinand Enke Verlag: Boltshauser et al. 1992, Fig. 4)

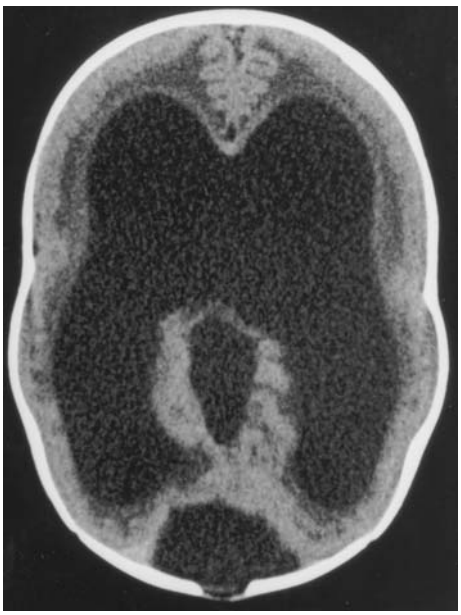

Fig. 5.4. Computed tomography (CT) of newborn with microphthalmos and cataracts: broad communication between lateral ventricles, Dandy-Walker like aspect of posterior fossa (not shown), cortical migration anomalies with polymicrogyria, evident in anterior interhemispheric fissure. Diagnosis: Walker-Warburg syndrome

also called "cat's eye reflex". Leukokoria generally represents an advanced stage of the disease. For detailed ophthalmological presentations, diagnostic work-up, and differential diagnosis, we refer to the standard ophthalmological literature. Computed tomography (CT) displays punctate or more homogeneous areas of calcification in 95% of retinoblastomas (Barkovich 1995). Contrast enhancement of tumor tissue is generally found. Contrast enhancement is also demonstrable with MRI. T1-weighted images reveal the tumor as hyperintense, T2-weighted images usually as a hypointense mass (Fig. 5.5). Proton density images may assist in the demarcation of the tumor. MRI can occasionally provide evidence of distal optic nerve infiltration. A large proportion of retinoblastomas are genetically determined, and about a third occurs bilaterally. When tumorous tissue is also demonstrated in the pineal region by neuroimaging, it is termed trilateral/trilocular retinoblastoma. This may already be present on initial evaluation.

5.2.5 Spasmus Nutans

So-called spasmus nutans typically presents at 6–12 months with disconjugate nystagmus, torticollis, and head titubation. Review of a larger series of patients suggests that the association with optic glioma is extremely low. Neuroimaging of infants initially diagnosed with spasmus nutans may not be immediately necessary (Arnoldi and Trychsen 1995).

5.2.6 Congenital Nystagmus

We refer to 5.2.1 for general remarks about congenital nystagmus.

As outlined above, congenital nystagmus can be due to retinal diseases. Unless a systemic condition affecting both the retina and brain is considered, imaging does not have priority. However, some syndromes with retinal blindness (such as Leber amaurosis and Joubert syndrome) are often associated with cerebellar vermis hypoplasia (see 5.2.8).

5.2.6.1 Pelizaeus-Merzbacher Disease

Congenital nystagmus may be a presenting feature of a dysmyelinating disorder. A prototype is Pelizaeus-Merzbacher disease (PMD), due to mutations (usually duplication) of the proteolipid protein gene at Xq22. PMD typically has its onset in the first half year with (rotatory/irregular pendular) nystagmus, head nodding, and often congenital stridor, followed by cerebellar dysfunction and spasticity. Although an X-linked condition, a few cases with identical characteristic clinical and imaging findings have been seen in girls; an example is shown in Fig. 5.6. The neuroimaging appearance of PMD is that of a "lack" of myelination.

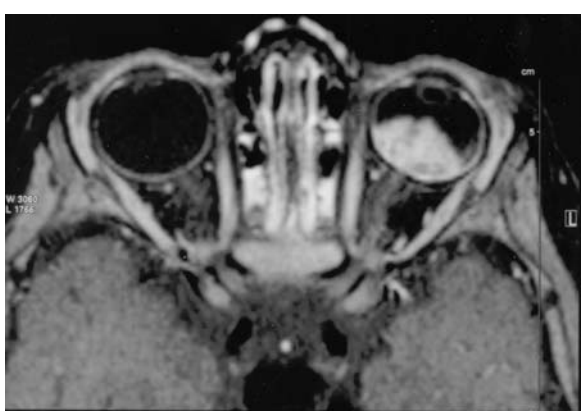

Fig. 5.5. T1/fat suppression axial MRI. Left intraocular tumor corresponding retinoblastoma. CT (not shown) with dense calcification

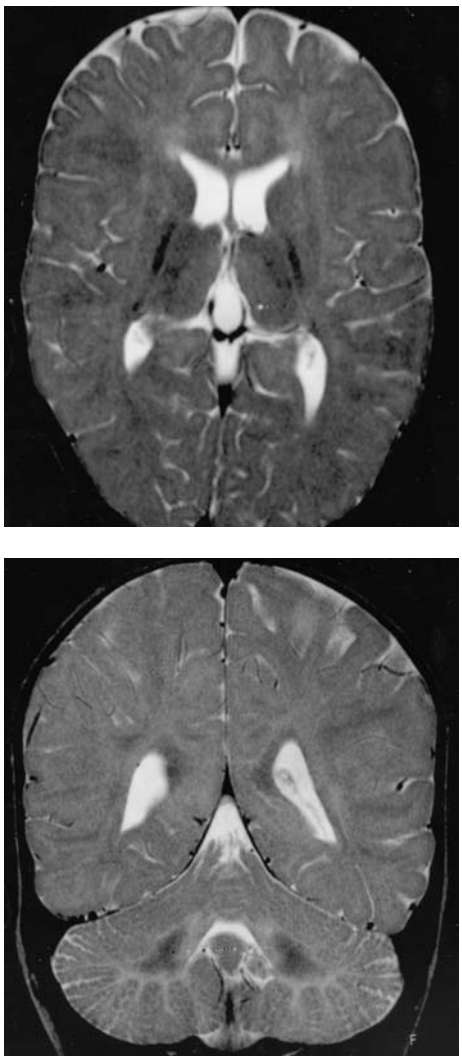

Fig. 5.6. a Axial, **b** coronal T2 MRI of an 18-month-old girl with a clinical constellation compatible with Pelizaeus-Merzbacher disease. Minimal myelination of the posterior limb of the internal capsule and cerebellar white matter, otherwise almost no myelin

5.2.6.2 Other White Matter Disorders

Apart from PMD, other dysmyelinating conditions can present with congenital nystagmus. The exact genetic/biochemical basis of these rare conditions is still unknown. An example of an infant with this presentation is illustrated in Fig. 5.7.

5.2.6.3 Septo-optic Dysplasia

Septo-optic dysplasia (SOD) typically presents as congenital nystagmus. Fundus examination reveals bilateral optic nerve hypoplasia. In addition, the syndrome consists of an absence of the septum pellucidum (Figs. 5.8, 5.9). Hypothalamic-pituitary dysfunction is present in a minority of patients, presenting as neonatal hypoglycemia and/or growth retardation (Sorkin et al. 1996). The prognosis is quite variable, ranging from blindness to useful vision. Affected children may be mentally retarded. In some children, additional CNS malformations can be found, in particular hypoplasia of the corpus callosum and cortical dysplasia (Sener 1996). SOD is unlikely to be a homogeneous entity. Hypoplasia of the optic nerves and absent septum are also seen as part of the holoprosencephaly complex (Barkovich 1995). The septum pellucidum is also mostly missing in rhombencephalosynapsis. It is suggested that SOD is a vascular disruption sequence (Lubinsky 1997).

5.2.6.4 Optic Nerve Hypoplasia

Hypoplasia of the optic nerves may be uni- or bilateral. It is not a clinical or pathogenetic entity. We have seen several children with unilateral optic nerve hypoplasia presenting to the ophthalmologist with "poor vision" or strabismus. The intracranial anterior optic pathways are usually markedly asymmetric, but additional anomalies are exceptional.

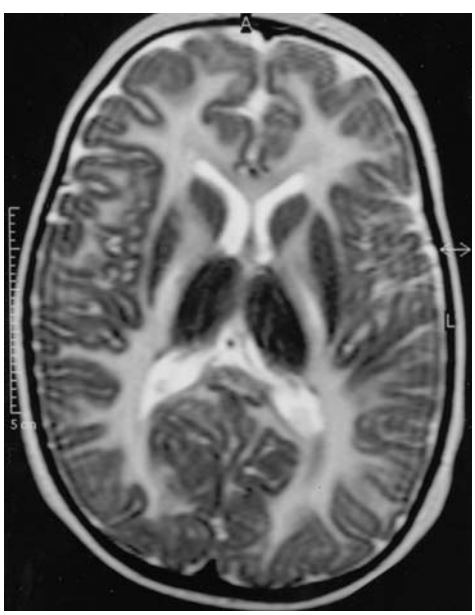

Fig. 5.7. Axial T2 MRI (mod.) of a 7-month-old girl with pendular nystagmus and hypotonia: "lack" of myelination, etiology unknown

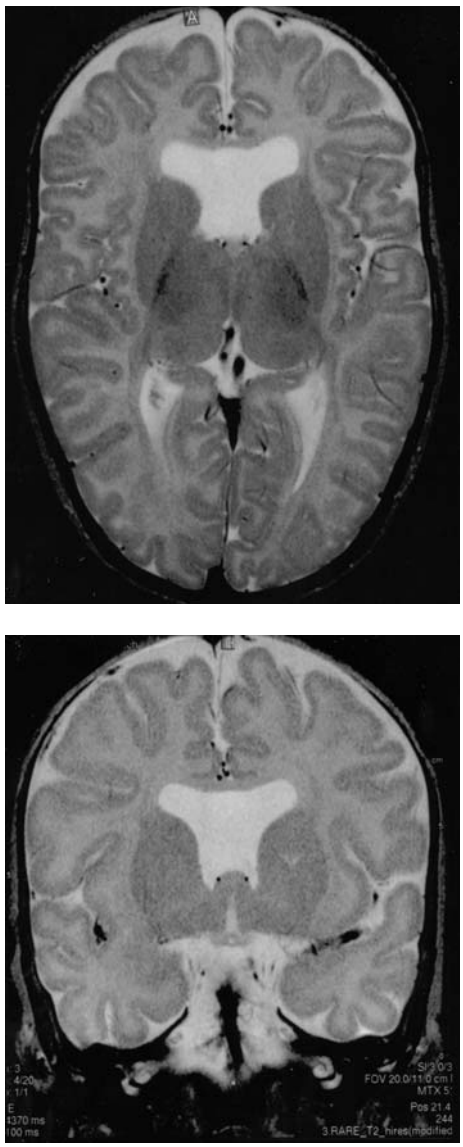

Fig. 5.8. a Axial, **b** coronal T2-/FSE MRI of a 3-month-old-girl without visual fixation. Absent septum pellucidum and almost no identifiable optic nerves. Diagnosis: septo-optic dysplasia. Patient clinically blind at 1 year

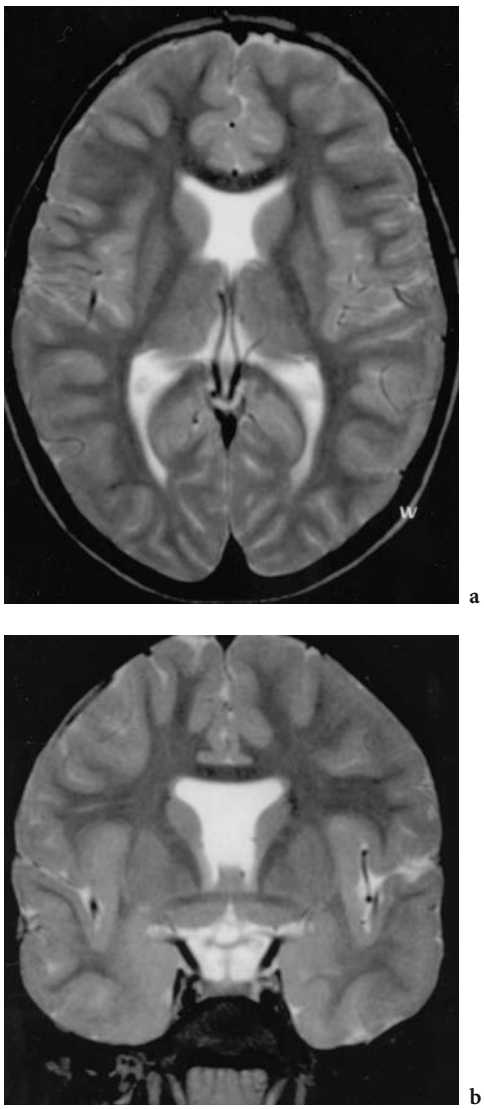

Fig. 5.9. a Axial, **b** coronal T2-/FSE MRI of a 4-year-old boy. Clinically convergent strabismus and bilateral optic nerve hypoplasia. MRI shows absent septum pellucidum. Diagnosis: septo-optic dysplasia. Visual acuity at 6 years: R 1.0, L <0.1

5.2.7 Delayed/Absent Visual Development

5.2.7.1 Periventricular Leukomalacia

Periventricular leukomalacia (PVL) is a well-known complication of prematurity before 34 weeks' gestational age. PVL affects primarily the posterior part of the hemispheric white matter. Clinically, it may go along with spastic diplegia type of cerebral palsy and is often accompanied by delayed visual development (Jacobson et al. 1996; Lanzi et al. 1998; Olsen et al. 1997).

As is evident from Figs. 5.10 and 5.11, MRI allows the detection of specific residual findings: variable reduction of periventricular white matter predominantly involving the posterior aspects, increased size of lateral ventricles, often with an irregular contour (e vacuo). The remaining white matter often shows increased T2 signal, presumably corresponding to gliosis.

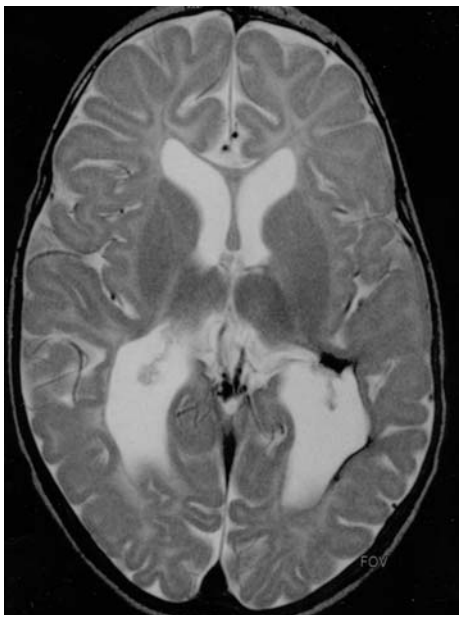

a

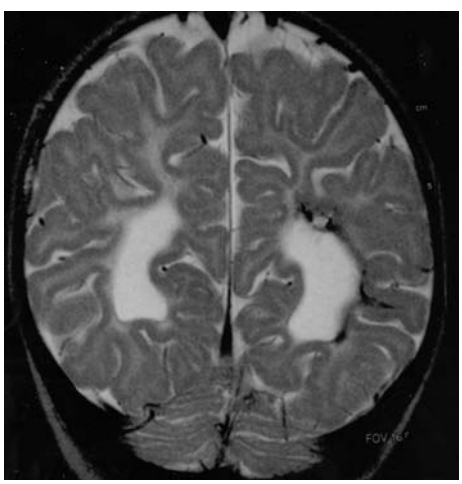

b

Fig. 5.10a,b. **a** Axial, **b** coronal T2-/FSE MRI of an 8-month-old girl who was born prematurely (32 weeks) and subsequently developed tetraspastic cerebral palsy, visual impairment, and infantile spasms. Periventricular leukomalacia is evident: loss of white matter particularly in the posterior parts, irregular ventricular dilatation. There is hemosiderin lateral to the left trigone/posterior horn following periventricular hemorrhage

5.2.7.2 Postanoxic Cortical Visual Impairment

Perinatal hypoxia may lead to several lesion patterns of CNS injury. Occasionally, but exceptionally, predominant damage occurs in term infants in the cortical/subcortical occipital lobe with a clinical correlate of delayed visual development, but often in the context of marked spastic cerebral palsy (Casteels et al. 1997). Typical examples are shown in Figs. 5.12 and 5.13.

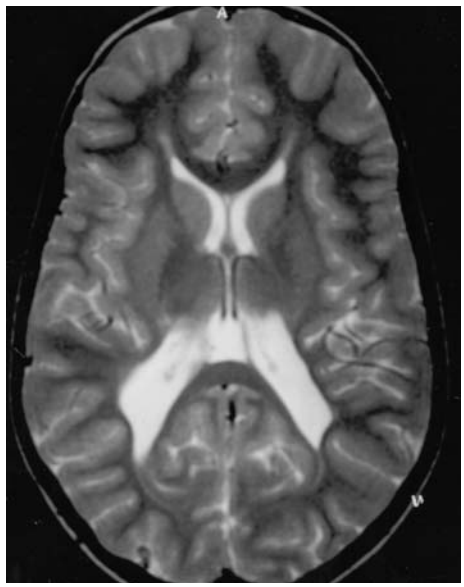

Fig. 5.11. Axial T2-/FSE MRI. Follow-up examination of an 8-year-old girl, born prematurely (28 weeks). Clinically marked tetraspasticity. Periventricular leukomalacia with reduced bulk of white matter, irregular dilatation of posterior lateral ventricles, and T2 hyperintensity of central occipital and frontal white matter

5.2.7.3 Delayed Visual Maturation

Infants with delayed visual maturation (DVM) as an isolated finding also present with a lack of visual awareness in the first few months. No ocular abnormalities can be found; electroretinography, visual evoked potentials, and MRI are normal (Russel-Eggitt et al. 1998). Exceptionally, children with DVM may also have nystagmus (Bianchi et al. 1998). A confident diagnosis of DVM can only be made in retrospect when normal vision has appeared and is maintained.

5.2.8 Retinal Blindness

The prototype of retinal blindness is Leber congenital amaurosis, an autosomal, recessively inherited dystrophy involving rods and cones. It is genetically heterogeneous (Camuzat et al. 1995). It may occasionally go along with cerebellar vermis hypoplasia, but basically the CNS anatomy is normal. Myelination of the optic radiation appears grossly normal, the diagnosis cannot be positively supported by neuroimag-

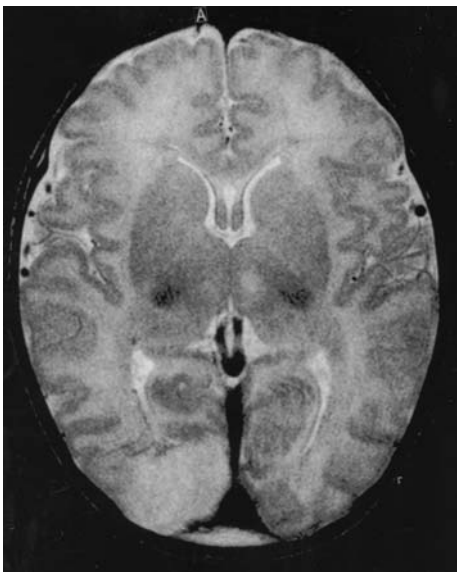

Fig. 5.12. Axial T2-/FSE MRI at 1 day following severe perinatal asphyxia: blurred anatomy of basal ganglia. Localized signal alteration in right occipital lobe (necrosis)

ing (Steinlin et al. 1992). Recently, Breitenseher et al. (1998) confirmed that the posterior visual pathways and occipital cortex appear normal in patients with congenital peripheral blindness. Congenital amaurosis may be an occasional presenting feature of Joubert syndrome and related syndromes. Neuroimaging is a key investigation to confirm this condition. It reveals cerebellar vermis aplasia and a "molar tooth" appearance of the midbrain (Steinlin et al. 1997; Maria et al. 1997).

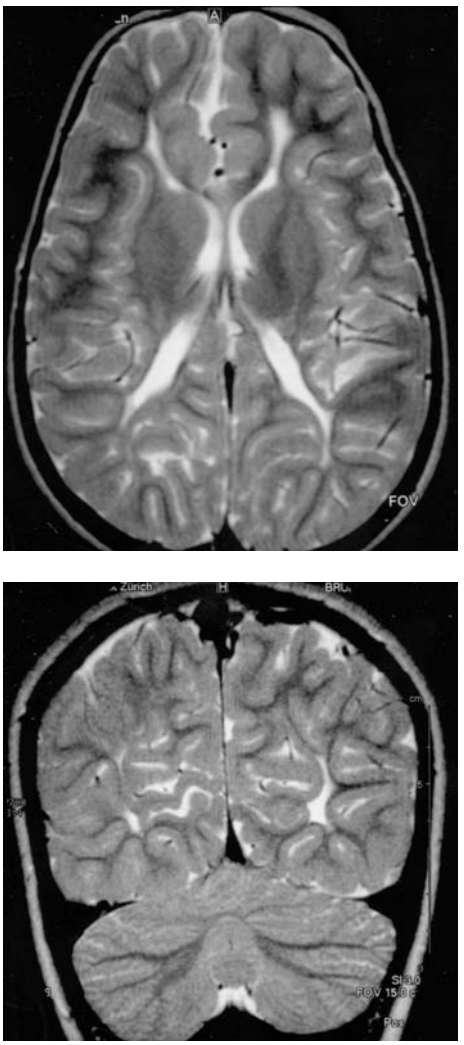

Fig. 5.13. a Axial, **b** coronal T2-/FSE MRI. Follow-up in 4-year-old term infant following severe perinatal asphyxia, with moderate cerebral palsy and visual impairment. There is a marked asymmetrical loss of occipital white matter, but also signal alteration of the periventricular frontal white matter

5.3 Acquired Optic Pathway Lesions

5.3.1 General Remarks

In this section, relevant noncongenital disorders often leading to visual impairment will be mentioned. Depending on the underlying pathology, the child may present with nonspecific findings (such as weakness, impaired consciousness) or complain of symptoms clearly pointing to visual system involvement. However, it is often difficult or impossible to obtain an accurate history of the onset in children. Young children may not notice unilateral visual loss, and bilateral visual loss is often only noticed when it becomes incapacitating.

5.3.2 Optic Neuritis

It is controversial whether autoimmune disorders affecting white matter or anterior optic pathways are fundamentally different in adults and children. They are very rare in the pediatric age group. Isolated pediatric optic neuritis is usually considered post-infectious following a febrile or "flu-like" illness; it can be "idiopathic". Figure 5.14 illustrates a case of isolated pediatric optic neuritis occurring subsequently after an interval of several months and resulting in bilateral blindness. All investigations (including brain imaging, CSF examinations, and mitochondrial muta-

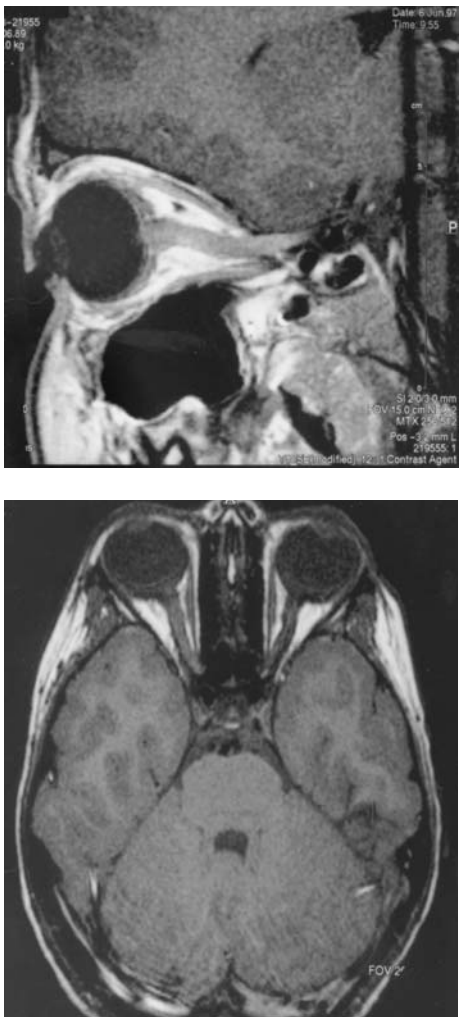

Fig. 5.14. a Oblique orbital, **b** axial T1-weighted, contrast-enhanced MRI of an 8-year-old boy with the clinical diagnosis of unilateral optic neuritis. Contrast enhancement of right optic nerve. Clinically, no recovery

tion screening) were normal. Optic neuritis may accompany other neurological signs (see 5.3.3 and 5.3.4). It is still questioned whether Devic's neuromyelitis optica is a distinctive disorder (O'Riordan et al. 1996; O'Riordan 1997). Reviewing the long-term course of 71 patients with neuromyelitis optica, Wingerchuk et al. (1999) concluded that Devic's syndrome differed in clinical, laboratory, and neuroimaging features from multiple sclerosis.

5.3.3 Multiple Sclerosis

It is estimated that about 2% of patients with multiple sclerosis (MS) present during childhood. Presenting symptoms may be variable such as muscular weakness, gait abnormalities, visual symptoms, and seizures (Ghezzi et al. 1997; Hanefeld 1992). Imaging findings in pediatric MS are not considered to be different from those in adults (Barkovich 1995).

5.3.4 Acute Disseminated Encephalomyelitis

Acute disseminated encephalomyelitis (ADEM) or parainfectious encephalomyelitis is considered an autoimmune response. This hypothesis is supported by the fact that the gross pathologic and histologic manifestations resemble those of experimental allergic encephalitis. ADEM involves primarily white matter but can also affect cortical and deep gray matter. Children typically develop acute focal neurologic signs and/or seizures late in the course of a viral illness or post vaccination. Headache, fever, irritability, and drowsiness maybe found (Tselis and Lisak 1995; O'Riordan et al. 1996). Neuroimaging reveals usually multiple foci of T2 hyperintensities; these may be circumscribed, confluent, or occasionally affect white matter diffusely (Murthy 1998). Various patterns of contrast enhancement may be found in the acute/subacute phase. Differentiation of MS from ADEM is not always possible in the beginning. The prognosis of ADEM is favorable as a rule, leading to complete clinical recovery, both from the clinical and the neuroimaging points of view. Occasionally, sequelae can be found. A severe case of ADEM is illustrated in Fig. 5.15.

5.3.5 Occipital Infarction/Stroke-like Episodes

An extensive list of systemic disorders including vasculopathies and coagulopathies may be associated with stroke in children (Aicardi 1998; Barkovich 1995). These are predominant in the carotid (middle cerebral) artery territory, and visual complaints are not clinically the leading symptoms. We have seen a few children with occipital infarction secondary to compression of the posterior cerebral artery at the tentorial notch related to brain edema or severe hydrocephalus and shunt dysfunction, respectively. An example is illustrated in Fig. 5.16.

Involvement of the occipital lobes in the context of so-called reversible posterior leukoencephalopathy (related to hypertension) has been reported in children (Pavlaks et al. 1997). So-called stroke-

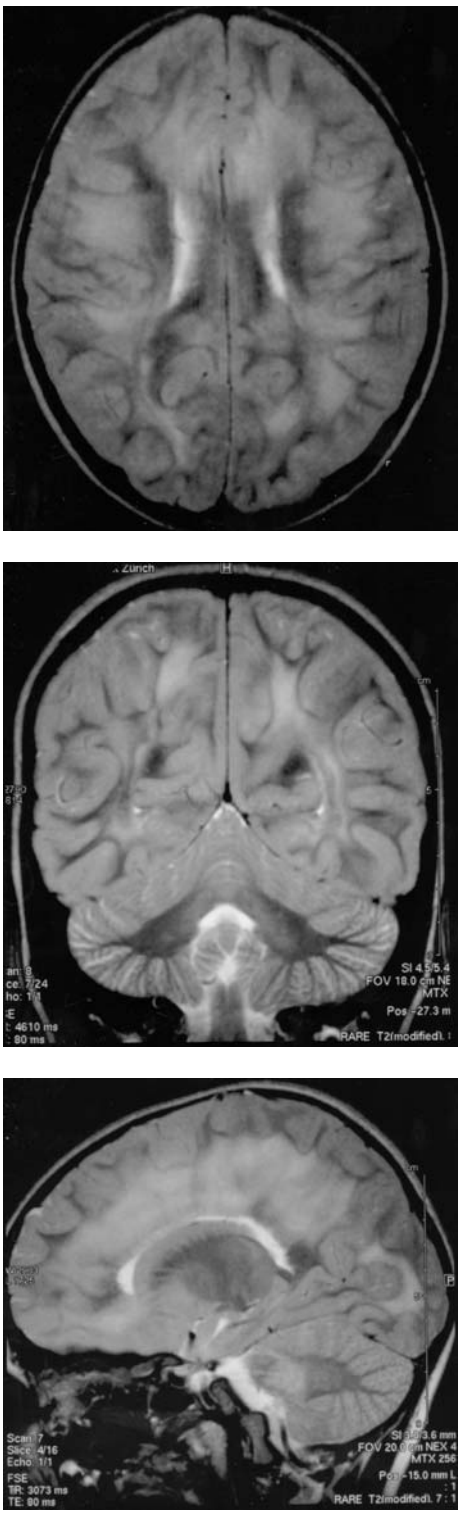

Fig. 5.15. a Axial, **b** coronal, **c** parasagittal T2-/FSE MRI of a 6-year-old boy with drowsiness and reduced vision: extensive confluent T2 signal alteration of supratentorial and cerebellar white matter. Clinical diagnosis: acute disseminated encephalomyelitis (ADEM). Subsequent incomplete recovery with marked bilateral visual impairment

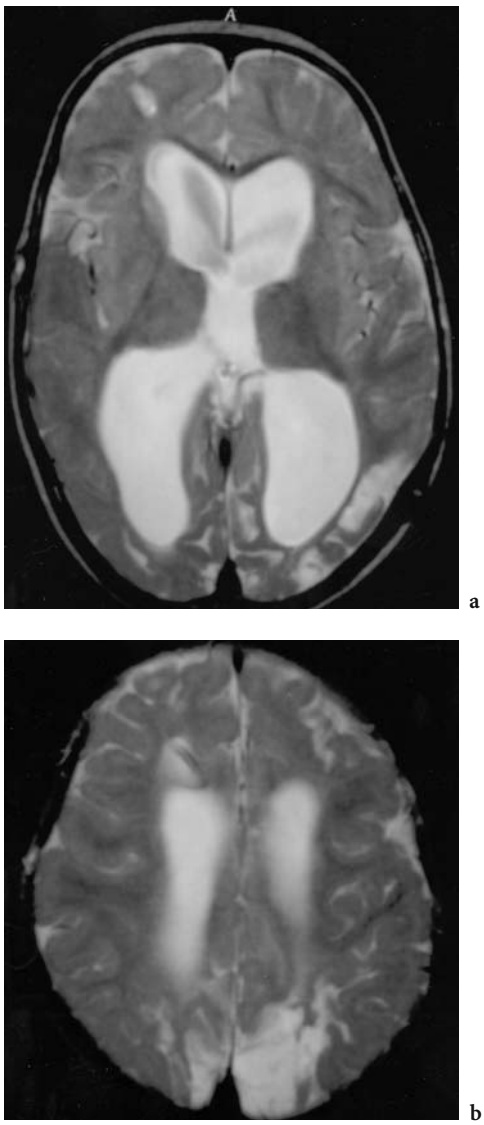

Fig. 5.16a,b. Axial T2-weighted FSE MRI of a 2-year-old boy with hydrocephalus. Shunt in right frontal horn. Bilateral occipital infarction following shunt dysfunction

like episodes involving the occipital lobes are possible presentations of some metabolic conditions (Brodsky et al. 1995; Huemer et al. 1998; Sperl et al. 1997). The prototype is MELAS syndrome (Mitochondrial Encephalopathy, Lactic Acidosis, and Stroke-like episodes) (Ohno et al. 1997). The stroke-like episodes are accompanied by headache, vomiting, vision loss, and hemiparesis, prompted by uni- or bilateral ischemic-like lesions in the occipital brain. Most patients with features of the MELAS phenotype have a A3243G point mutation in the mitochondrial genome, usually detectable in peripheral lymphocytes. Several other pathogenic mtDNA

mutations associated with stroke-like episodes have been identified, indicating that MELAS is a genetically heterogeneous disorder (Hanna et al. 1998). On the other hand, patients with a A3243G mutation can present with a wide range of clinical phenotypes, including Leigh syndrome and progressive external ophthalmoplegia (Koga et al. 2000). The pathogenic mechanism for the stroke-like episodes in MELAS is not clear. Diffusion-weighted MRI points to vasogenic edema (Yoneda et al. 1999). Proton magnetic resonance spectroscopy revealed elevated concentrations of lactate and glucose, and reduced values for N-acetyl aspartate (NAA) and total creatine (Wilichowski et al. 1999).

The occipital lobe is also typically involved in "metabolic crisis" related to OTC (ornithine carbamyl transferase) deficiency (Bajaj et al. 1996).

5.3.6 Intoxications

A number of exogenous toxins can cause demyelination resulting in spongiform leukoencephalopathies. Subcortical U-fibers are typically involved. This may lead to permanent or transient central blindness. We have seen such a situation in an infant with accidental heroin intoxication. Widespread white matter injury may also rarely occur during chemotherapy, particularly following intrathecal methotrexate. Methylmercury poisoning leads to tissue loss in the calcarine and parietal cortex (Davis et al. 1994).

5.3.7 Trauma (Nonaccidental Injury)

Injuries to the optic pathways due to head trauma will not be discussed here. However, we would like to point to so-called nonaccidental injury by shaking infants less than 6 months of age. The typical presentation is impaired consciousness and convulsions, often resulting in status epilepticus. Typically, bilateral retinal hemorrhages are present. Extensive cerebral damage in this condition usually results in permanent neurological sequelae including visual impairment or even cortical blindness (Ewing-Cobbs et al. 1998). The neuroimaging correlate in the acute stage is not spectacular, with evidence of brain swelling and often some interhemispheric blood accumulation. Follow-up neuroimaging as a rule demonstrates extensive cerebral atrophy (Fig. 5.17).

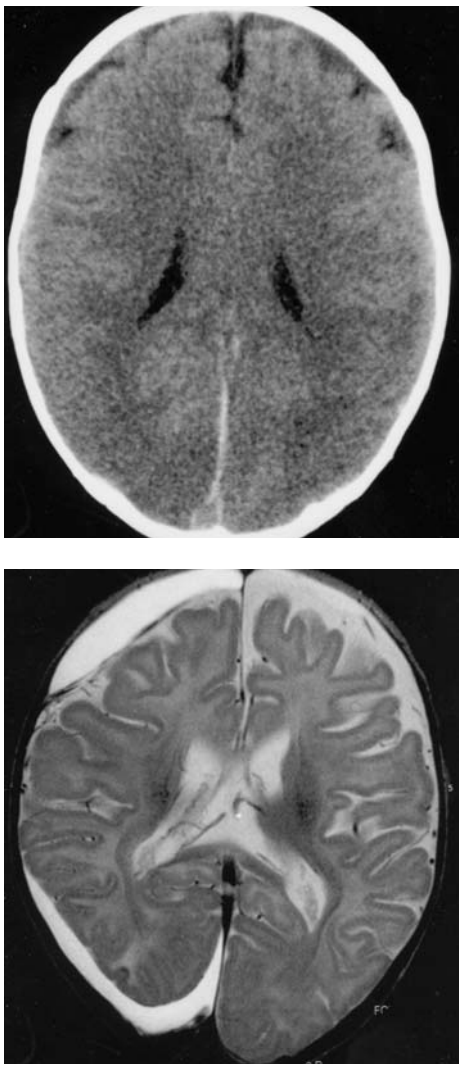

Fig. 5.17a,b. **a** Axial CT, **b** axial MRI of a 4-month-old baby admitted following seizures. Bilateral retinal hemorrhages suggested nonaccidental injury. **a** Brain swelling, minimal blood accumulation in interhemispheric fissure. **b** Three weeks later: marked atrophy and secondary subdural effusions

5.3.8 Proptosis

Children may come to clinical attention due to proptosis evident on inspection or realized by diplopia. Proptosis can result from many conditions including benign or malignant space-occupying lesions of the orbit (Brodsky et al. 1995; Nelson et al. 1991). Neuroimaging is obviously of the utmost importance in the work-up. Illustrative examples are shown in Figs. 5.18, 5.19. For proptosis in the context of neurofibromatosis, see 5.4.

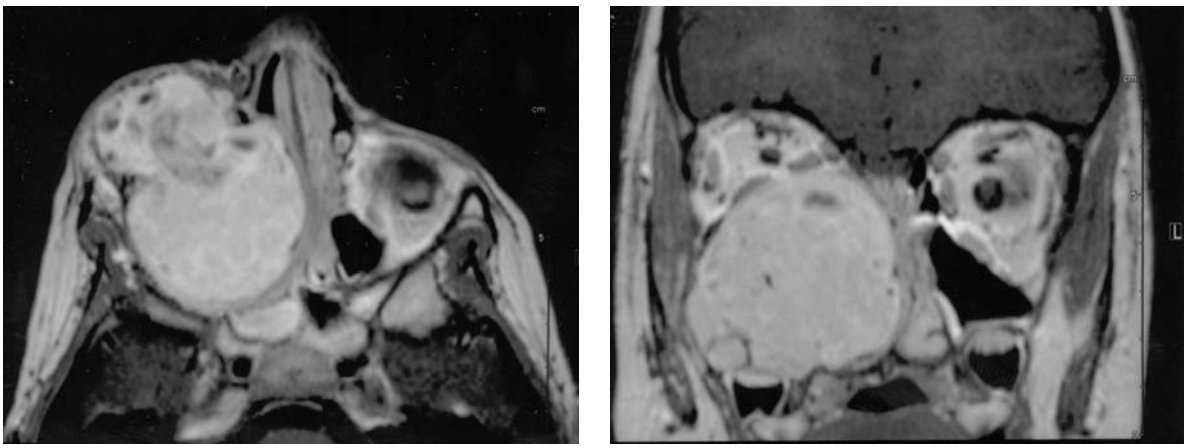

Fig. 5.18. a Axial, **b** coronal T1-weighted, contrast-enhanced MRI of a 2-year-old girl with proptosis since 7 months. Extensive extraconal space-occupying lesion. Histology: hemangioma

5.4 Work-up in Systemic Diseases

In this section, a few conditions will be discussed in which optic pathway involvement is common but not necessarily associated with visual symptoms. Neuroimaging may be fundamental to establishing or supporting the diagnosis. Typical examples are the neurofibromatoses.

5.4.1 Neurofibromatosis Type 1

This topic has been recently reviewed by several authors (Gutmann et al. 1997; Inoue et al. 1997; Pollak and Mulvihill 1997; Upadhyaya and Cooper 1998). Neurofibromatosis type 1 (NF1) is an autosomal dominant disorder due to mutations in the very large NF1 gene at chromosome 17q11. About 50% of patients have new germ-line mutations, i.e. they have no positive family history. The prevalence in most populations is about 1:4000 individuals. As is evident from the listing of diagnostic criteria (Table 5.1), optic pathway glioma (OPG) is such a criterion. OPG are tumors of infancy; in larger series, the mean age at diagnosis is 4–5 years. At least two-thirds of the OPG are clinically silent, while others may present as proptosis, strabismus, or decrease of visual acuity. OPG may be localized anywhere along the visual pathways, but a retrochiasmatic location is less common. "All"

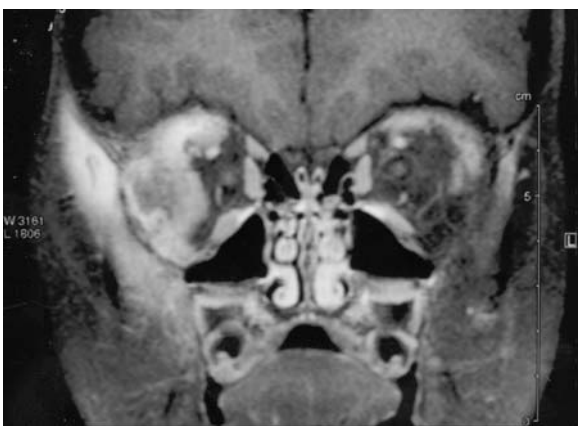

Fig. 5.19. Coronal T1-weighted, fat-suppressed MRI of a 2.5-year-old child with proptosis since 6 months. Lateral extraconal irregular lesion. Histology: Langerhans histiocytosis. Subsequently, multiple additional bony lesions were detected

Table 5.1. Diagnostic criteria for neurofibromatosis type 1

The presence of two or more of the following is diagnostic:

1. Six or more café au lait spots, greater than 5 mm in diameter in prepubertal children and over 15 mm in post-pubertal individuals
2. Two or more neurofibromas of any type, or one plexiform neurofibroma
3. Axillary and/or inguinal freckling
4. Optic nerve glioma
5. A distinctive osseous lesion, such as dysplasia of the sphenoid wing, thinning of long bone cortex, with or without pseudarthrosis
6. A first-degree relative (parent, sibling, or offspring) with NF1 according to the above criteria

OPG are pilocytic astrocytomas. The natural history is variable: An OPG may exceptionally regress spontaneously, a minority is progressive and may lead to additional visual impairment, exceptionally to blindness. The majority remain static for long periods (forever?) (Kuenzle et al. 1994). It is now well documented that OPG in the context of NF are comparatively benign and differ in behavior from OPG not related to NF1 (Listernick et al. 1995; Alshail et al. 1997; Shuper et al. 1997). On imaging, OPG may enhance with contrast. Occasionally, an optic nerve glioma may be mimicked by an optic sheath dural ectasia. In NF1 patients, an increased frequency of tumors outside the optic pathways is observed, particularly in the brainstem (Bilaniuk et al. 1997; Kuenzle et al. 1994). It is important to distinguish astrocytomas from benign lesions commonly encountered in NF1: T2 hyperintensities are often found in the basal ganglia (particularly globus pallidus), brainstem, and cerebellum, not enhancing with contrast and not having space-occupying effects. These lesions have also been called "unidentified bright objects" (UBO). On T1-weighted images, they are isointense with gray matter. In the age range of 4–10 years, they can be found in up to 80% of affected individuals, while in cross-sectional studies in adults, they are rare. Thus, they do not represent true hamartomas or early tumors. Typical examples of OPG and UBO are shown in Figs. 5.20–5.22.

Mild proptosis is not uncommon in NF, even in the absence of an optic nerve glioma. It can be related to sphenoid wing dysplasia, but often no obvious explanation is evident.

5.4.2 Neurofibromatosis Type 2

Neurofibromatosis type 2 (NF2) is an autosomal dominant disorder due to mutations at chromosome 22q12. The prevalence is about 1:40,000 individuals. At least half of all cases are new mutations. The diagnostic criteria for NF2 are given in Table 5.2. For a review of the general clinical and imaging features, we refer the reader to Inoue et al. (1997) and Pollak and Mulvihill (1997). The involvement of the brain structures in NF1 and NF2 are quite different: While NF2 consistently affects the acoustic/vestibular nerve, this is never encountered in NF1. NF2 is not associated with optic pathway gliomas

Table 5.2. Diagnostic criteria for neurofibromatosis type 2

The following are diagnostic:

1. Bilateral vestibular schwannomas; or
2. A first-degree relative with NF2, and either
   - a unilateral vestibular schwannoma or
   - two of the following: meningioma, schwannoma, glioma, neurofibroma, posterior subcapsular lens opacity, or cerebral calcification; or
3. Two of the following:
   - unilateral vestibular schwannoma
   - multiple meningiomas
   - either schwannoma, glioma, neurofibroma, posterior subcapsular lens opacity, or cerebral calcification

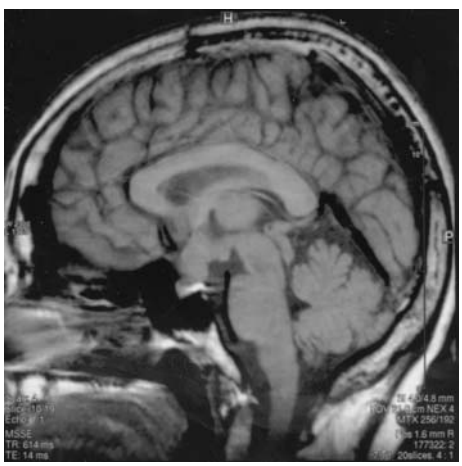

a

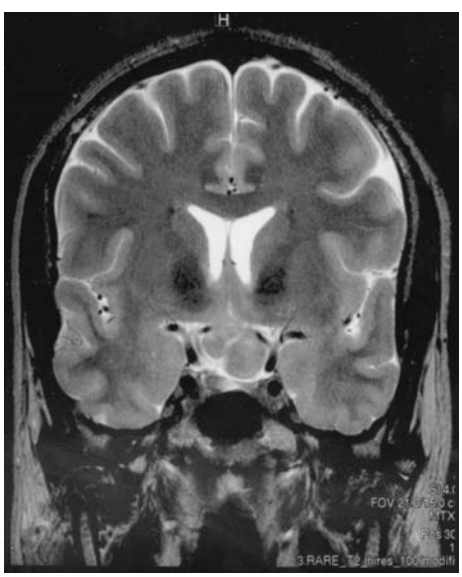

b

Fig. 5.20. a Sagittal T1-weighted, **b** coronal T2-weighted FSE MRI of a 26-year-old patient with NF1. Asymmetrical optic chiasm glioma known for 12 years. Bilateral vision 1.0!

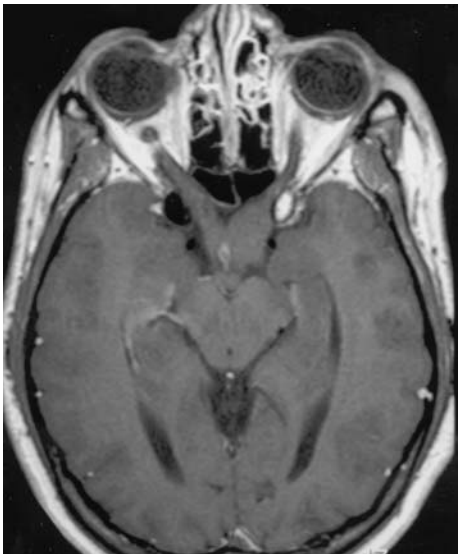

a

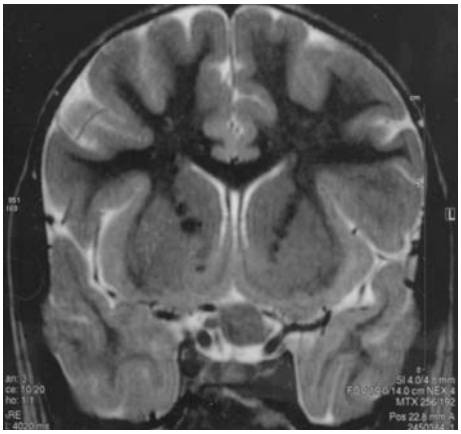

b

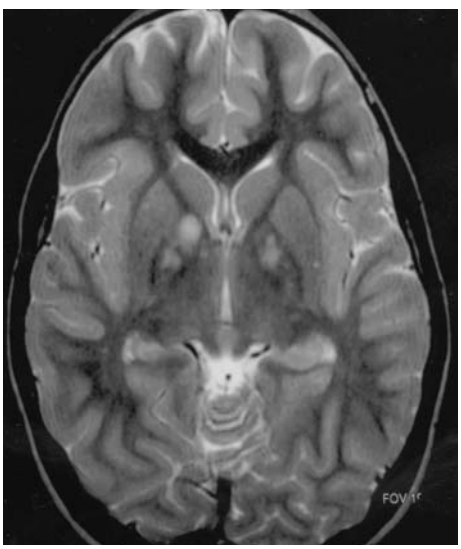

c

Fig. 5.21. **a** Axial-tilted T1-weighted, **b** coronal, **c** axial T2-weighted FSE MRI. **a**, **b** Grossly asymmetric chiasm/left optic nerve glioma in 6-year-old girl. MRI prompted by incidentally recognized unilateral reduced visual acuity. Vision right 1.25, left 0.3. NF1 subsequently diagnosed. **c** Multiple T2 hyperintensities in globus pallidus bilaterally. In the subsequent 2 years, no change in visual acuity

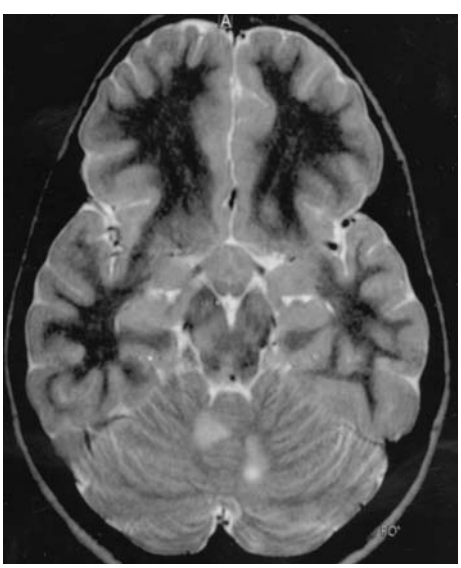

Fig. 5.22. T2-weighted FSE MRI of an 11-year-old girl with precocious puberty and NF1. MRI shows hypothalamic glioma and multiple "UBOs" in brainstem and cerebellum

but may indirectly affect visual pathways by the commonly occurring meningiomas. These may appear in the region of the sphenoid/cavernous sinus and may affect the optic nerve sheaths (Fig. 5.23). Thus, NF2 may occasionally present as proptosis, strabismus (diplopia), or decrease of visual acuity related to optic nerve sheath meningioma. These meningiomas may display calcification (Fig. 5.24). In contrast to NF1 where genotype/phenotype correlations are poor, severe NF2 mutations often have a severer clinical course (Evans et al. 1998; Parry et al. 1996).

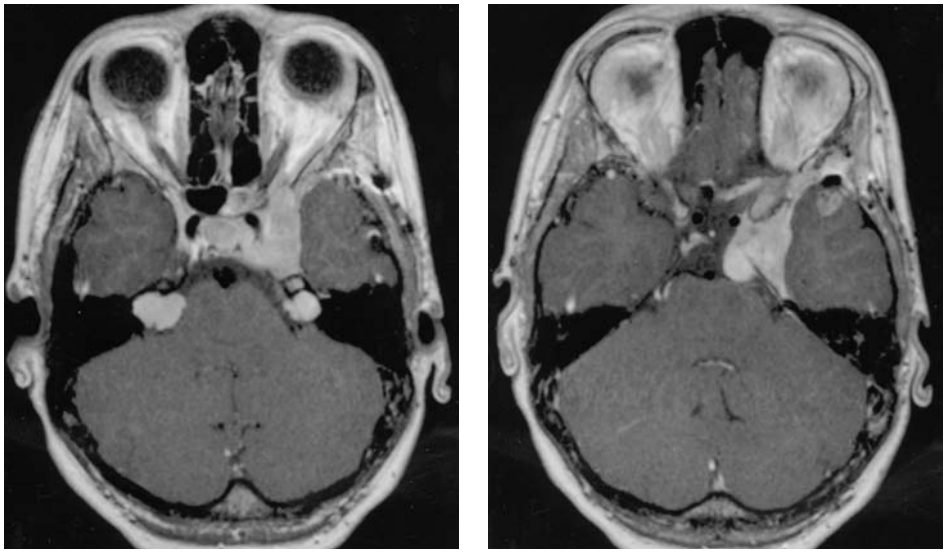

a b

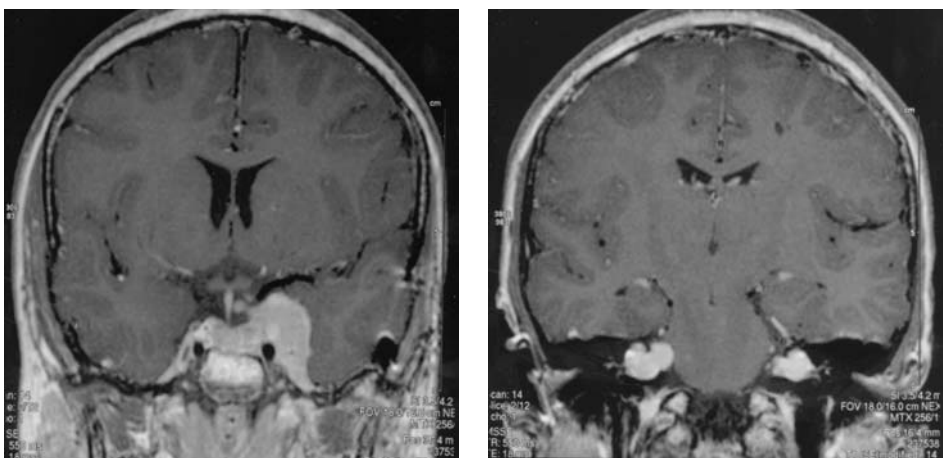

c d

Fig. 5.23a–d. T1-weighted, contrast-enhanced MRI of newly diagnosed NF2 in a 14-year-old girl. MRI shows bilateral acoustic neuromas, meningioma at tip of left temporal lobe, mass (presumably a meningioma) in suprasellar/left parasellar/sphenoid area

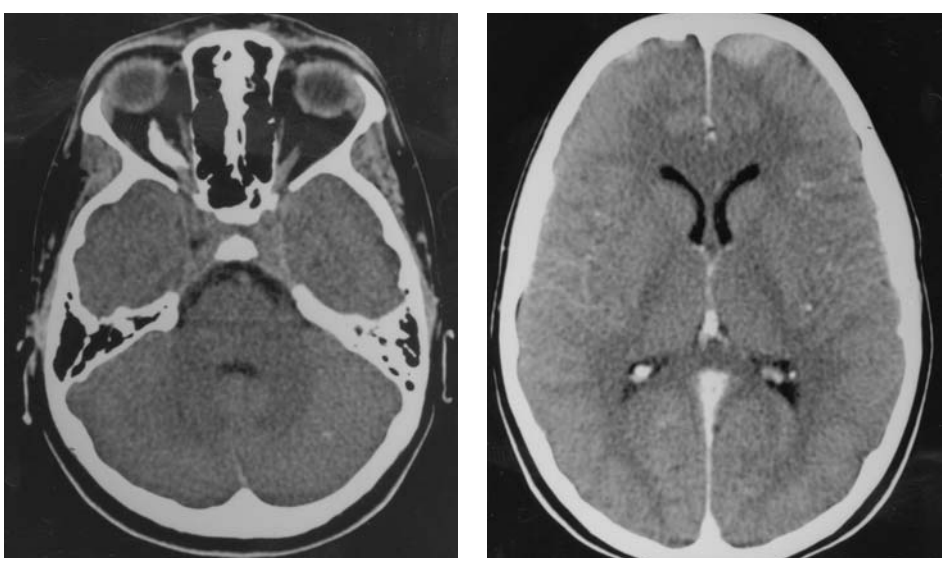

a b

Fig. 5.24. a Axial plain CT, **b** axial CT following administration of contrast medium in a 14-year-old patient prompted by new onset of diplopia. Plain CT reveals calcifying right optic nerve sheath meningioma. Following contrast: left frontal meningioma. Bilateral acoustic neuromas not shown

5.5 Unexpected ("Incidental") Findings

5.5.1 General Remarks

Occasionally, a neuroimaging work-up for nonvisual problems may reveal abnormalities of the optic pathways or their neighboring structures. The most common problems in pediatric neurology are seizure disorders. In the assessment following convulsions, a broad spectrum of brain lesions can be found, which may be localized in the occipital lobe.

5.5.2 Occipital Lobe Lesions Presenting with Epilepsy

The following may be found:

- Parenchymal (cystic) defects: We have seen a few patients with such defects who had no obvious history of an intercurrent event. One has to assume that these lesions occurred either in the prenatal or neonatal period. Even large defects usually have no clinical correlate and may (surprisingly!) not result in detectable visual field defects (Fig. 5.25).
- Altered myelination: We have seen a few children with altered myelination of the occipital lobe detected in the context of a seizure work-up without a corresponding clinical/visual correlate. Since the pathogenesis remains unknown, we can only speculate and assume a residual (pre-/perinatal) event (Fig. 5.26).
- Calcifications: Bilateral subcortical occipital calcification and epilepsy has been reported, mostly associated with clinical or subclinical celiac disease (Hernandez et al. 1998; Nunes et al. 1995).
- Migration anomalies: Abnormal migration involving the occipital lobe has been occasionally found in the evaluation of a seizure disorder (Kuzniecky et al. 1997; Kuzniecky 1998).
- Tumor: Very exceptionally, a tumor in the occipital area results in seizures. One of our pediatric patients with NF2 first presented with a seizure obviously related to a meningioma overlying the occipito-parietal area.

5.5.3 Developmental Delay

In the evaluation of developmental delay, neuroimaging is often performed to assess the brain's anatomy. In this context, anomalies of the posterior normal pathways and/or occipital lobes may be encountered (Fig. 5.27). Due to the patient's young age and/or limited cooperation, it is often not possible to determine whether the visual fields are altered.

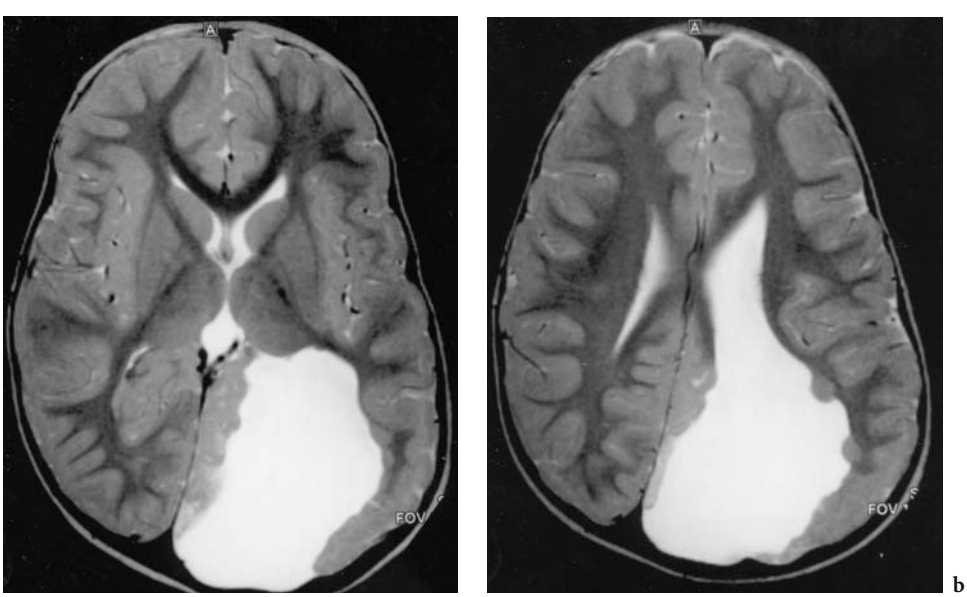

a b

Fig. 5.25a,b. Axial T2-weighted FSE MRI of a 3-year-old boy with delay in motor and speech development and macrocephaly. MRI reveals large occipital parenchymal defect with several nodular heterotopias. No obvious visual field defects detectable, but final evaluation not yet possible at this age. Seizures occurred at 6 years of age

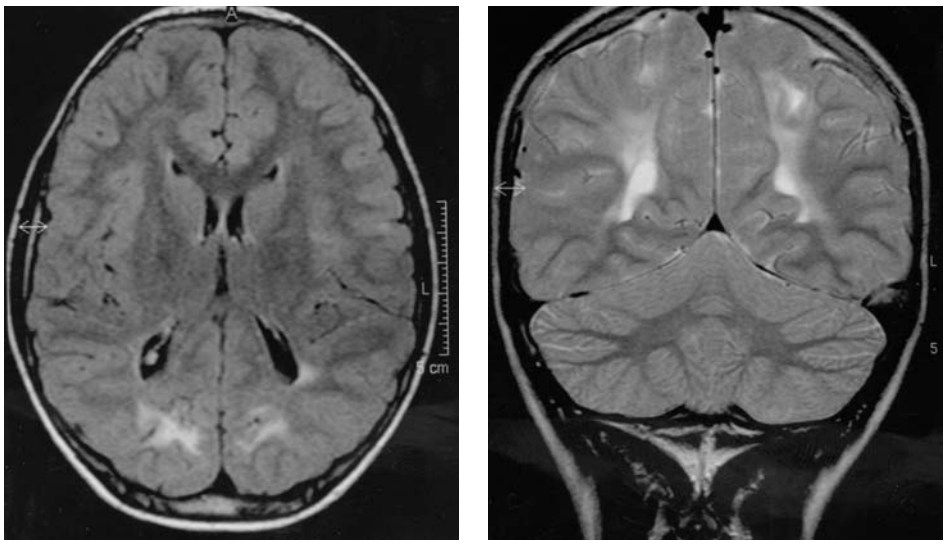

a b

Fig. 5.26. a Axial, **b** coronal T2-weighted FSE MRI (mod.) of a 10-year-old boy with several convulsions of recent onset. T2 hyperintensity of bilateral occipital white matter. No clinical/ophthalmological correlate. Normal mitochondrial and peroxisomal laboratory findings

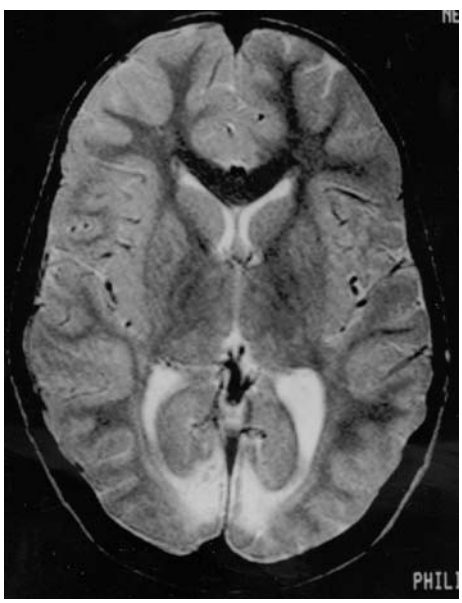

Fig. 5.27. Axial T2-weighted MRI of a 6-year-old girl with moderate mental retardation, spastic cerebral palsy, visual impairment. History of prolonged seizures at 3 months. MRI shows bilateral focal signal alteration in the medial occipital cortical/subcortical areas. The exact pathogenesis remains speculative (seizure related)

References

Aicardi J (1998) Diseases of the nervous system in childhood, 2nd edn. MacKeith, Leeds

Albermaz VS, Castillo M, Hudgins PA, Mukherji SK (1997) Imaging findings in patients with clinical anopththalmos. AJNR Am J Neuroradiol 18:555–561

Alshail E, Rutka JT, Becker LE, Hoffman HJ (1997) Optic chiasmatic-hypothalamic glioma. Brain Pathol 7:799–806

Arnoldi KA, Tychsen L (1995) Prevalence of intracranial lesions in children initially diagnosed with disconjugate nystagmus (spasmus nutans). J Pediatr Ophthalmol Strabismus 32:296–301

Atkinson J (1984) Human visual development over the first 6 months of life. A review and a hypothesis. Hum Neurobiol 3:61–74

Bajaj SK, Kurlemann G, Schuierer G, Peters PE (1996) CT and MRI in a girl with late-onset ornithine transcarbamylase deficiency: case report. Neuroradiology 38:796–799

Barkovich AJ (1995) Pediatric neuroimaging, 2nd edn. Raven, New York

Barkovich AJ (1998) Neuroimaging manifestations and classification of congenital muscular dystrophies. AJNR Am J Neuroradiol 19:1389–1396

Bianchi PE, Salati R, Cavallini A, Fazzi E (1998) Transient nystagmus in delayed visual maturation. Dev Med Child Neurol 40:263–265

Bilaniuk LT, Molloy PT, Zimmermann RA, Philips PC, Vaughan SN, Liu GT, Sutton LN, Needle M (1997) Neurofibromatosis type 1: brain stem tumours. Neuroradiology 39:642–653

Boltshauser E, Steinlin M, Thun-Hohenstein L, Bänziger O, Pezzoli V, Martin E (1992) Bildgebende Untersuchungen des Gehirns bei blinden und sehbehinderten Kleinkindern. Klin Monatsbl Augenheilkd 200: 620–622

Breitenseher M, Uhl F, Prayer Wimberger D, Deecke L, Trattnig S, Kramer J (1998) Morphological dissociation between

visual pathways and cortex: MRI of visually deprived patients with congenital peripheral blindness. Neuroradiology 40:424–427

Brodsky MC, Baker RS, Hamed LM (1995) Pediatric neuroophthalmology. Springer, Berlin Heidelberg New York

Camuzat A, Dollfus H, Rozet JM, Gerber S, Bonneau D, Bonnemaison M, Briard ML, Dufier JL, Ghazi I, Leowski C, Weissenbach J, Frezal J, Munnich A, Kaplan J (1995) A gene for Leber's congenital amaurosis maps to chromosome 17p. Hum Mol Genet 4:1447–1452

Casteels I, Demaerel P, Spileers W, Lagae L, Missotten L, Casaer P (1997) Cortical visual impairment following perinatal hypoxia: clinicoradiologic correlation using magnetic resonance imaging. J Pediatr Ophthalmol Strabismus 34:297–305

Davis LE, Kornfeld M, Mooney HS, Fiedler KJ, Haaland KY, Orrison WW, Cernichiari E, Clarkson TW (1994) Methylmercury poisoning. Long-term clinical, radiological, toxicological, and pathological studies of an affected family. Ann Neurol 35:680–688

Evans DGR, Trueman L, Wallace A, Collins S, Strachan T (1998) Genotype/phenotype correlations in type 2 neurofibromatosis (NF2): evidence for more severe disease associated with truncating mutations. J Med Genet 35:450–455

Ewing-Cobbs L, Kramer L, Prasad M, Canales DN, Louis PT, Fletcher JM, Vollero H, Landry SH, Cheung K (1998) Neuroimaging, physical, and developmental findings after inflicted and noninflicted traumatic brain injury in young children. Pediatrics 102:300–307

Garey L (1984) Structural development of the visual system of man. Hum Neurobiol 3:75–80

Ghezzi A, Deplano V, Faroni J, Grasso MG, Liguori M, Marrosu G, Pozzilli C, Simone IL (1997) Multiple sclerosis in childhood: clinical features of 149 cases. Multiple Sclerosis 3:43–46

Gilles FH, Shankle W, Dooling EC (1983) Myelinated tracts: growth patterns. In: Gilles FH, Leviton A, Doolling EC (eds) The developing human brain. Wright, Boston, pp 117–192

Gutmann DH, Aylsworth A, Carey JC, Korf B, Marks J, Pyeritz RE, Rubenstein A, Viskochil D (1997) The diagnostic evaluation and multidisciplinary mangament of neurofibromatosis 1 and neurofibromatosis 2. JAMA 278:51–57

Hanefeld F (1992) Multiple sclerosis in childhood. Curr Opin Neurol Neurosurg 5:359–363

Hanna MG, Nelson IP, Morgan-Hughes JA, Wood NW (1998) MELAS: a new disease associated mitochondrial DNA mutation and evidence for further genetic heterogeneity. J Neurol Neurosurg Psychiatry 65:512–517

Hernandez MA, Colina G, Ortigosa L (1998) Epilepsy, cerebral calcifications and clinical or subclinical coeliac disease. Course and follow up with gluten-free diet. Seizure 7:49–54

Huemer M, Muehl A, Wandl-Vergesslich K, Strobl W, Wanders RJA, Stoeckler-Ipsiroglu S (1998) Stroke-like encephalopathy in an infant with 3-hydroxy-3-methylglutaryl-coenzyme A lyase deficiency. Eur J Pediatr 157:743–746

Inoue Y, Nemoto Y, Tashiro T, Nakayama K, Nakayama T, Daikokuya H (1997) Neurofibromatosis type 1 and type 2: review of the central nervous system and related structures. Brain Dev 19:1–12

Jacobson L, Ek U, Fernell E, Flodmark O, Broberger U (1996) Visual impairment in preterm children with periventricular leukomalacia – visual, cognitive and neuropaediatric characteristics related to cerebral imaging. Dev Med Child Neurol 38:724–735

Koga A, Akita Y, Takane N, Sato Y, Kato H (2000) Heterogeneous presentation in A3243G mutation in the mitochondrial $tRNA^{Leu(UUR)}$ gene. Arch Dis Child 82:407–411

Kuenzle Ch, Weissert M, Roulet E, Bode H, Schefer S, Huisman T, Landau K, Boltshauser E (1994) Follow-up of optic pathway gliomas in children with neurofibromatosis type 1. Neuropediatrics 25:295–300

Kuzniecky R (1998) Symptomatic occipital lobe epilepsy. Epilepsia 39 [Suppl 4]:524–531

Kuzniecky R, Giliam F, Morawetz R, Faught E, Palmer C, Black L (1997) Occipital lobe developmental malformations and epilepsy: clinical spectrum, treatment, and outcome. Epilepsia 38:175–181

Lanzi G, Fazzi E, Uggetti C, Cavallini A, Danova S, Egitto MG, Ferrari Ginevra O, Salati R, Bianchi PE (1998) Cerebral visual impairment in periventricular leukomalacia. Neuropediatrics 29:145–150

Listernick R, Darling C, Greenwald M, Strauss L, Charrow J (1995) Optic pathway tumors in children: the effect of neurofibromatosis type 1 on clinical manifestations and natural history. J Pediatr 127:718–722

Lubinsky MS (1997) Hypothesis: septo-optic dysplasia is a vascular disruption sequence. Am J Med Genet 69:235–236

Maria BL, Hoang KBN, Tusa RJ, Mancuso AA, Hamed LM, Quisling RG, Hove MT, Fennell EB, Booth-Jones M, Ringdahl DM, Yachnis AT, Creel G, Frerking B (1997) "Joubert syndrome" revisited: key ocular motor signs with magnetic resonance imaging correlation. J Child Neurol 12:423–430

McKusick VA (1998) Mendelian inheritance in man, 12 edn. John Hopkins University Press, Baltimore (online access: http://www.ncbi.nlm.nih.gov/Omim)

Murthy JMK (1998) MRI in acute disseminated encephalomyelitis following Semple antirabies vaccine. Neuroradiology 40:420–423

Nelson LB, Calhoun JH, Harley RD (1991) Pediatric ophthalmology, 3rd edn. Saunders, Philadelphia

Nunes ML, Costa da Costa J, Severini MH (1995) Early onset bilateral calcifications and epilepsy. Pediatr Neurol 13:80–82

Ohno K, Isotani E, Hirakawa (1997) MELAS presenting as migraine complicated by stroke: case report. Neuroradiology 39:781–784

Olsen P, Pääkkö E, Vainionpää, Pyhtinen J, Järvelin MR (1997) Magnetic resonance imaging of periventricular leukomalacia and its clinical correlation in children. Ann Neurol 41:754–761

O'Riordan JI (1997) Central nervous system white matter diseases other than multiple sclerosis. Curr Opin Neurol 10:211–214

O'Riordan JI, Gallagher HL, Thompson AJ, Howard RS, Kingsley DPE, Thompson EJ, McDonald WI, Miller DH (1996) Clinical, CSF, and MRI findings in Devic's neuromyelitis optica. J Neurol Neurosurg Psychiatry 60:382–387

Parry DM, MacCollin MM, Kaiser-Kupfer MI, Pulaski K, Nicholson HS, Bolesta M, Eldridge R, Gusella JF (1996) Germline mutations in the neurofibromatosis 2 gene: correlations with disease severity and retinal abnormalities. Am J Hum Genet 59:529–539

Pavlakis StG, Frank Y, Kalina P, Chandra M, Lu D (1997) Occipital-parietal encephalopathy: a new name for an old syndrome. Pediatr Neurol 16:145–148

Pollack IF, Mulvihill JJ (1997) Neurofibromatosis 1 and 2. Brain Pathol 7:823–836

Russell-Eggitt I, Harris CM, Kriss A (1998) Delayed visual maturation. An update. Dev Med Child Neurol 40:130–136

Sener RN (1996) Septo-optic dysplasia associated with cerebral cortical dysplasia (cortico-septo-optic dysplasia). J Neuroradiol 23:245–247

Shuper A, Horev G, Kornreich L, Michowiz S, Weitz R, Zaizov R, Cohen IJ (1997) Visual pathway glioma. An erratic tumour with therapeutic dilemmas. Arch Dis Child 76:259–263

Sorkin JA, Davis PC, Meacham LR, Parks JS, Drack AV, Lambert SR (1996) Optic nerve hypoplasia: absence of posterior pituitary bright signal on magnetic resonance imaging correlates with diabetes insipidus. Am J Ophthalmol 122:717–723

Sperl W, Felber S, Skladal D, Wermuth B (1997) Metabolic stroke in carbamyl phosphate synthetase deficiency. Neuropediatrics 28: 229–234

Steinlin M, Martin E, Schenker K, Boltshauser E (1992) Myelination of the optic radiation in Leber congenital amaurosis. Brain Dev 14:212–215

Steinlin M, Schmid M, Landau K, Boltshauser E (1997) Follow-up in children with Joubert syndrome. Neuropediatrics 28:204–211

Tselis AC, Lisak RP (1995) Acute disseminated encephalomyelitis and isolated central nervous system demyelinative syndromes. Curr Opin Neurol 8:227–229

Upadhyaya M, Cooper DN (1998) Neurofibromatosis type 1: from genotype to phenotype. Bios Scientific, Oxford

Van der Knaap MS, Valk J (1995) Magnetic resonance of myelin, myelination, and myelin disorders, 2nd edn. Springer, Berlin Heidelberg New York, pp 1–21, 31–49

Waugh MC, Chong WK, Sonksen P (1998) Neuroimaging in children with congenital disorders of the peripheral visual system. Dev Med Child Neurol 40:812–819

Wilichowski E, Pouwels PJW, Frahm J, Hanefeld F (1999) Quantitative proton magnetic resonance spectroscopy of cerebral metabolic disturbances in patients with MELAS. Neuropediatrics 30:256–263

Wingerchuk DM, Hogancamp WF, O'Brien PC, Weinshenker BG (1999) The clinical course of neuromyelitis optica (Devic's syndrome). Neurology 53:1107–1114

Yakovlev PI, Lecours AR (1967) The myelogenic cycles of regional maturation of the brain. In: Minkowski A (ed) Regional development of the brain in early life. Blackwell, Oxford, pp 3–70

Yoneda M, Maeda M, Kimura H, Fujii A, Katayama K, Kuriyama M (1999) Vasogenic edema on MELAS: a serial study with diffusion-weighted MR imaging. Neurology 53:2182–2184

The requested page could not be found.

6 Orbital Pathology

W. Müller-Forell and S. Pitz

CONTENTS

The orbit may be affected by more than 107 different clinical pathologies with a confusing number of symptoms (Rootman 1988). While only a small number of these diseases require diagnostic imaging, the evaluation of clinical signs and symptoms plays a crucial role in determining the appropriate neuroradiological investigation. Inflammatory disease may present with a history of acute progression, generally associated with pain, and a subacute course may lead to the diagnosis of, e.g., Graves disease, while benign tumors are characterized by chronic, painless progression. Concomitant internal diseases, on the other hand, may lead to the initial diagnosis of an orbital manifestation of a systemic condition, like lymphoma or hyperthyroidism. Another important diagnostic factor is the age of the patient: infections, trauma, and various malignant tumors (e.g., rhabdomyosarcoma or neuroblastoma) constitute the most frequent orbital diseases in children, while Graves' disease represents the leading disease in middle life, and the greatest number of neoplasms are observed in the group of elderly patients (Rootman 1988).

The ophthalmologic examination should consist of an assessment of visual acuity, inspection, testing of motility, exophthalmometry, slit lamp findings as well as an evaluation of pupillary function, refraction anomalies, pathologic changes of the fundus, and visual field deficits. The relevant information should be routinely communicated before beginning the neuroradiological examination.

PD W. Müller-Forell, MD
Institute of Neuroradiology, Medical School University of Mainz, Langenbeckstrasse 1, 55101 Mainz, Germany
S. Pitz, MD
Department of Ophthalmology, Medical School University of Mainz, Langenbeckstrasse 1, 55101 Mainz, Germany

6.1 Globe

The majority of diseases of the globe are assessed by ophthalmologic methods, with the ultrasound technique being ideally suited in an ophthalmologic setting. However, in some cases patient-related factors may exert a negative effect on the outcome of the investigation, and magnetic resonance imaging (MRI) may be indicated in children or noncooperative patients. MRI is the method of choice, in particular when leukokoria might prevent the funduscopic evaluation of a process. Yet, even under normal conditions, the high anatomical resolution provided by the most advanced MRI technology does not allow differentiation of the three primary layers of the globe: the sclera, uvea, and retina. Nevertheless, due to the fact that some ocular diseases are accompanied by detachment and/or effusion, the different primarily potential spaces may be visualized.

Symptoms indicating the presence of an intraocular pathology are closely related to the time of manifestation of the disease: Congenital lesions may

present with obvious asymmetry of the eyes, e.g. an apparently microphthalmic eye (see Sect. 5.2.2). Binocular disease with severely impaired visual function may lead to nystagmus. Leukokoria (syn. cat's eye) is a hallmark of intraocular pathology: normally both fundi reflect light (visible as an annoying phenomenon in some photographs). An intraocular cause of the change in color has to be ruled out if the light reflex in one eye appears grayish or white (instead of red, caused by the blood-filled uvea just below the transparent retina). In addition to the congenital cataract, the most common causes of leukokoria are (in order of incidence) retinoblastoma (>50%, see Sect. 6.1.2.1), a persistent hyperplastic primary vitreous (see Sect. 6.1.1.3), Coats disease (see Sect. 6.1.1.4), followed by retinopathy of the premature (ROP), unilateral congenital cataract, and intraocular inflammation (*Toxocara*) (Howard and Ellsworth 1965; Mafee 1996). In these cases, leukokoria is frequently accompanied by strabismus. The direction of the eye deviation serves as a diagnostic indicator in strabismus: while nonorganic strabismus in childhood commonly occurs as a convergent squint, organically induced strabismus primarily presents as an exodeviation (divergent squint) (Elston 1997; Hunter and Ellis 1999). The accurate identification of the cause of leukokoria is essential to ensure prompt identification and appropriate treatment, particularly in the case of retinoblastoma, a highly malignant primary retinal cancer (Mafee 1996).

6.1.1 Congenital Lesions

6.1.1.1 Anophthalmos, Microphthalmos, Orbital Cysts

Congenital anophthalmos represents a rare condition and is characterized by bilateral absence of the globe, due to a developmental defect with growth failure of the primary optic vesicle out of the cerebral vesicle in early embryonic development (De Potter et al. 1995). Microphthalmos is characterized by an unilateral incidence and may be observed as either an isolated disorder or (in about 10%) in association with other craniofacial anomalies (De Potter 1995; Mafee 1996) (see Sect. 5.2.2).

In clinical practice, the term anophthalmos is applied in cases where no eye is visible on inspection. However, there is a broad spectrum of abnormalities extending from the absence of any ocular structure (which can be definitively assessed only by histologic sectioning of the affected orbit) to varying degrees of microphthalmos. In pure anophthalmos, the extraocular muscles may be well developed. In microphthalmos, the eye is small but present, sometimes accompanied by a colobomatous cyst with a primarily inferior location as evidence of the absent closure of the embryonic optic fissure (with the defect extending to the retina, choroid, and sclera). This cyst may be the cause of rapidly increasing swelling, mimicking neoplasia. A variety of bony and soft-tissue deformities is characteristic in all cases of anophthalmos and in most cases of microphthalmos. The mechanism by which the presence of the globe induces growth of the surrounding orbit, facial and adnexal structures is not yet understood, and descriptions of the growth-inducing characteristics have been based on clinical and experimental observations (Casper et al. 1993).

One role of imaging under the described conditions is to rule out associated intracranial abnormalities (see Sect. 5.2.2), the other is to evaluate the orbital content and to identify the presence of extraocular muscles in patients who may undergo surgery for microphthalmos. However, when anophthalmos is suspected, the presence of cryptophthalmos (the eye is covered with a layer of skin), a combined cyst, or retinoblastoma must be ruled out (De Potter et al. 1995). Another important differential diagnostic measure is the exclusion of orbital cephalocele, in order to avoid the choice of an inappropriate surgical approach to the cystic orbital lesion.

6.1.1.2 Optic Nerve Coloboma/Staphyloma

Although there is no actual need for diagnostic imaging in optic nerve coloboma, it may represent an incidental finding in systemic disorders (e.g., Joubert or Warburg syndrome). The characteristic features of optic nerve coloboma should be known because it serves as an important differential diagnostic criterion identifiable as a congenital or acquired notch, gap, hole, or fissure in which tissue or a portion of tissue is lacking (Hopper et al. 1992; Mafee 1996). In clinical ophthalmology, two forms of optic nerve coloboma can be differentiated: (a) isolated from the optic nerve and (b) retinochoroidal coloboma. Congenital coloboma represents an anomaly of the optic head, occurring during organogenesis of the eye (Taylor and Hoyt 1997; Cassier et al. 1986). Coloboma may affect the optic nerve, ranging from small "optic pits" to large optic nerve colobomas comprising the entire disc diameter, the so-called

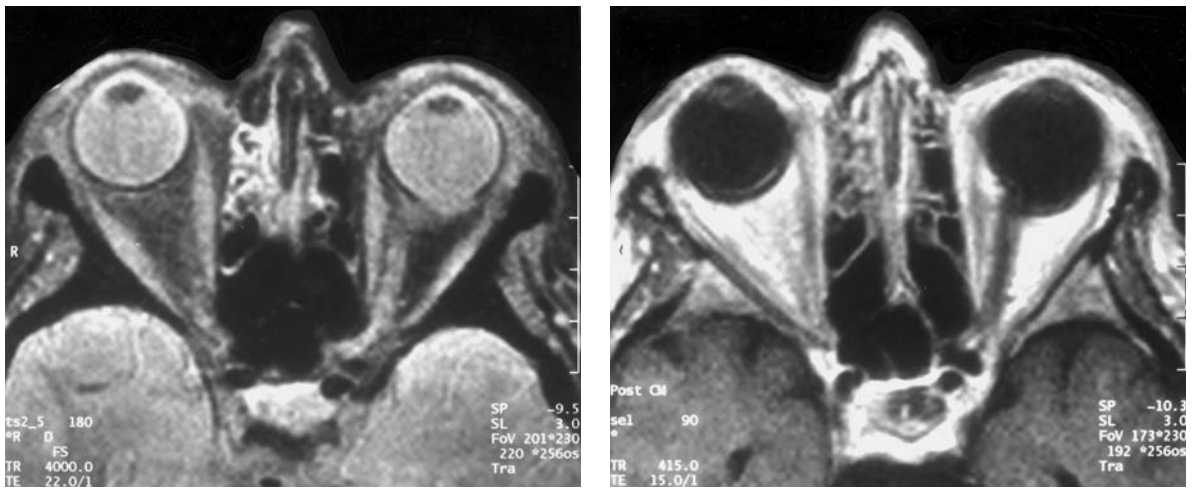

Fig. 6.1a,b. A 71-year-old woman with staphyloma. MRI: **a** Proton-weighted image with a scleral defect of the posterior circumference of the left globe at the level and lateral of the optic nerve. **b** Corresponding T1-weighted view demonstrates a marked deformation of the left globe compared with the right globe

morning-glory papilla, and may involve the retina, the choroid/iris, as well as the lids. The vast majority of these colobomatous tissue defects are typically located in the inferior uveal quadrant, as in this location the closure of the embryonic eye cup is defective (Taylor and Hoyt 1997). The characteristic ophthalmoscopic findings of complete coloboma of the optic nerve disc, a morning glory papilla, include an enlarged, excavated disc with a central core of white tissue, surrounded by an elevated annulus of light and variable pigmented subretinal tissue (Mafee 1996). CT and MRI show a posterior global defect with optic disc excavation (Fig. 6.27a–c). Any cystic retroglobal structure associated with microphthalmos should be suspected as being a colobomatous cyst (Mafee 1996) (see 6.1.1.1). In contrast to coloboma, staphyloma is rarely a congenital condition, and most cases are observed in conjunction with severe myopia as an ectasia of the posterior globe (Fig. 6.1). This condition is caused by an attenuated sclera, due to changes in the composition of proteoglycans in the interfibrillar substance of the ectatic sclera (Gardner et al. 1984; Cassier et al. 1986). Other rare etiologies of staphyloma include postoperative thinning of the sclera following repeated surgery.

6.1.1.3 Persistent Hyperplastic Primary Vitreous

Persistent hyperplastic primary vitreous (PHPV) is a congenital anomaly resulting from the abnormal persistence of the fetal fibrovascular primitive stroma (hyaloid system) of the eye (Manschot 1958; Castillo et al. 1997). This congenital, primarily unilateral anomaly may be present at birth and is the most common lesion closely resembling a retinoblastoma. PHPV can, however, be differentiated on the basis of the history and an ocular examination. Leukokoria may be identified in a microphthalmic eye at birth or during the first weeks of life, and on examination of the anterior segment, the ciliary processes are shown to be drawn into a contracting, retrolental, loose fibrovascular mass attached to a cataractous lens, representing the remnants of the fetal hyaloid artery that should have regressed by the 8th month of gestation (Reese 1955; De Potter et al. 1995).

As both conditions may lack calcification, CT is not always able to differentiate PHPV from retinoblastoma, and MRI is therefore the method of choice in the differential diagnosis (Mafee et al. 1987a; De Potter et al. 1995). The fibrovascular retrolental mass appears hypointense in T1-weighted and T2-weighted images, while the vitreous body appears hyperintense with both modalities. The detached gliotic retinal tissue may have a funnel-like appearance as it arises from the optic disc and extends to the retrolental mass, presenting hypointense with hyperintense subretinal fluid on T1-weighted and T2-weighted images (Fig. 6.2). It may demonstrate none or moderate enhancement after i.v. gadolinium administration. In the presence of hemorrhage into the subretinal space, a gravitational fluid-fluid level may be seen (De Potter et al. 1995; Kueker and Ramaekers 1999).

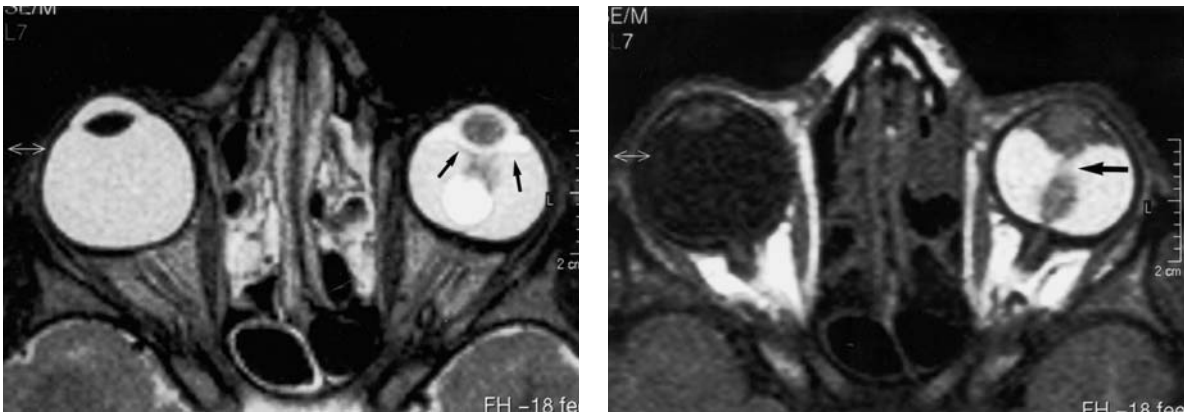

a **b**

Fig. 6.2a,b. An 11-year-old boy with leukokoria and poor vision in the left eye. Diagnosis: persistent hyperplastic primary vitreous. MRI: **a** Axial T2-weighted image, demonstrating a small left eye with distorted lens. The very high signal material in the center might represent the compressed vitreous enveloped by subretinal hematoma. The slight hypodense lines correspond to the displaced retina (*arrows*). **b** Corresponding T1-weighted image with hyperintense signal of the intraocular hemorrhage accompanying retinal detachment. Note the isointense structure, connecting the optic disc with the lens (*arrow*). (With the permission of Kueker and Ramaekers 1999)

6.1.1.4 Coats' Disease

Coats' disease is a unilateral idiopathic retinal vascular disorder in which teleangiectasia and aneurysmatic retinal vessels cause progressive intraretinal exudation and possibly exudative retinal detachment (Coats 1908; Egerer 1974; Silodor et al. 1988; De Potter et al. 1995; Mafee 1996). Although mostly young males aged 6–8 years old are affected, the condition is occasionally encountered in adults. Even though present at birth, the vascular anomaly of Coats' disease does not generally become symptomatic until retinal detachment occurs, which finally leads to central vision loss (Sherman et al. 1983) and to the development of painful neovascular glaucoma, necessitating enucleation of the affected eye (Silodor et al. 1988). The ophthalmoscopic findings vary in accordance with the stage of progression. At the early stages of the disease, the diagnosis is reliably established by ophthalmoscopy, and CT or MRI findings provide little additional information. Therapy with photocoagulation, cryotherapy, or both of these methods reduces or even eliminates dilated and saccular aneurysms, exudates, and retinal detachment (Egerer et al. 1974; De Potter et al. 1995). At more advanced stages, complete secondary exudative retinal detachment with accumulation of cholesterol particles in the subretinal space may develop (De Potter et al. 1995). Diagnostic imaging is helpful at this stage and used in differentiating advanced Coats' disease from exophytic retinoblastoma to prevent enucleation for suspected retinoblastoma (Chang et al. 1984; Silodor et al. 1988).

Although CT can confirm calcification in retinoblastoma, MRI is superior to CT in differentiating Coats' disease from retinoblastoma (De Potter et al. 1995; Mafee et al. 1989; Mafee 1996). The most significant finding in T1-weighted, PD, and T2-weighted images is the identification of homogeneous hyperintensity of the subretinal fluid caused by the high protein content in comparison with the vitreous body of the opposite eye (Fig. 6.3). While the detached V-shaped retina, identified by a low signal on both T1- and T2-weighted images, may show enhancement after i.v. gadolinium, the subretinal fluid does not (Mafee 1996; De Potter et al. 1995). In contrast, MRI is able to highlight the retinoblastoma as an inhomogeneous, moderately hyperintense mass on T1-weighted and PD sequences (but with hypointense areas on T2-weighted images), allowing differentiation from the associated retinal detachment with exudation (Fig. 6.4). After i.v. contrast administration, the tumor mass shows moderate to marked enhancement in retinoblastoma, in contrast to the subretinal fluid in Coats' disease (Mafee et al. 1989; De Potter et al. 1995).

6.1.2 Tumors

Tumors of the globe may arise from different layers, the most common ones being the choroid and the retina. Retinoblastoma in children and malignant

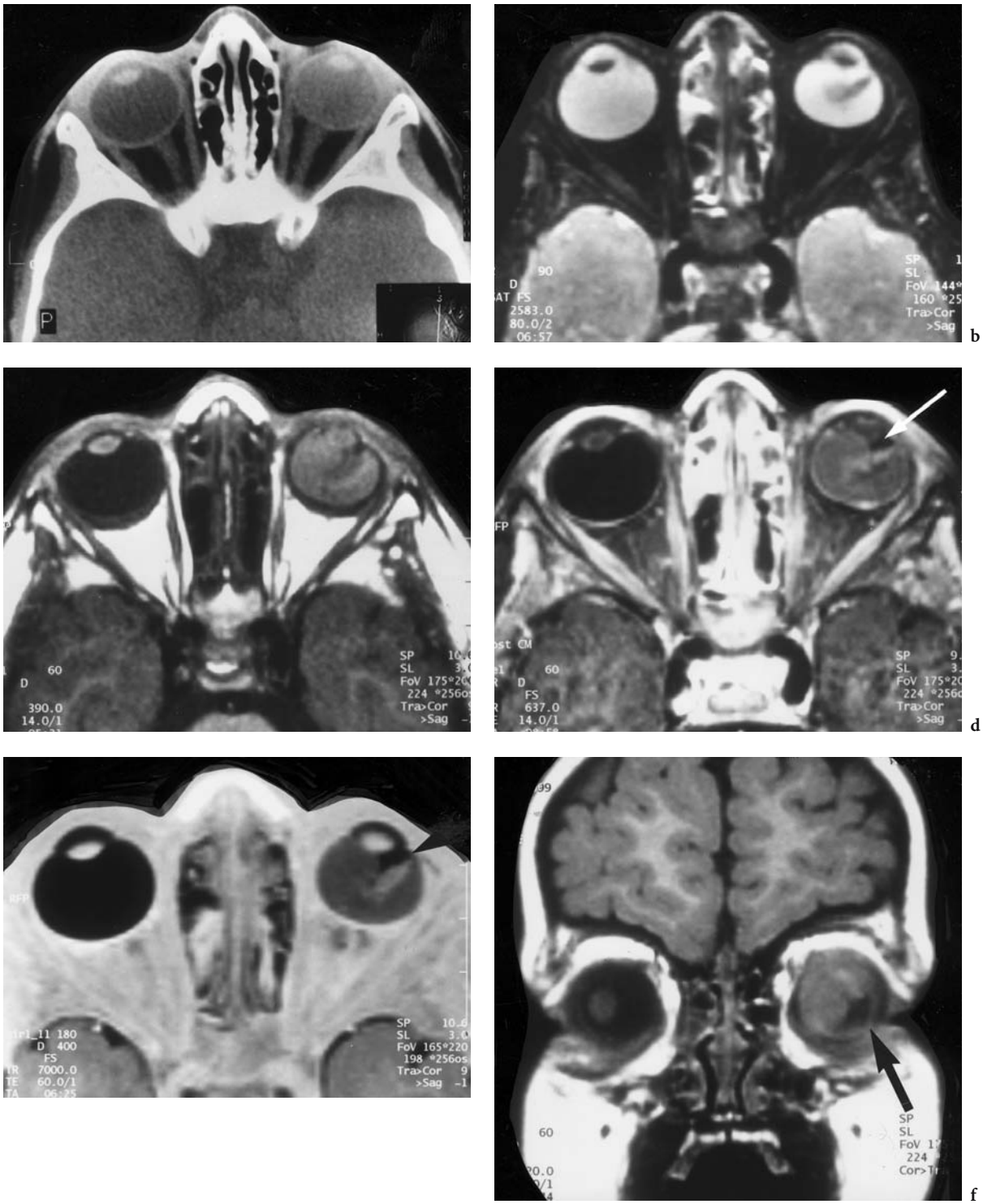

Fig. 6.3a–f. A 2-year-old boy presenting with leukokoria and complete retinal detachment of the left eye. Diagnosis: Coats disease. **a** CT: axial view showing only slight hyperdensity (43 HE) of the left globe; comparison with the right (15 HE). Note diminuation of the left globe. MRI: **b** Axial T2-weighted image presenting the retinal detachment as a clearly defined, bilateral, biconvex, V-shaped hyperintensity in the left globe. The hyperintense region at the point of the angle may be an indication of slight hemorrhage. **c** Corresponding T1-weighted view with a relatively homogeneous signal of the subretinal fluid. **d** Corresponding contrast-enhanced (FS) view with slight signal enhancement of the detached retina. The remaining vitreous body (*white arrow*) is represented by a small area of hypointensity behind the lens. **e** Corresponding IR view yielding the most impressive image of the characteristic V-shaped, bilateral retinal detachment (the *arrowhead* points to the remaining vitreous body). **f** Coronal T1-weighted slice at the level of the remaining vitreous body (*arrow*), demonstrating the V-shaped retinal detachment and the presence of slight hemorrhage in the upper region

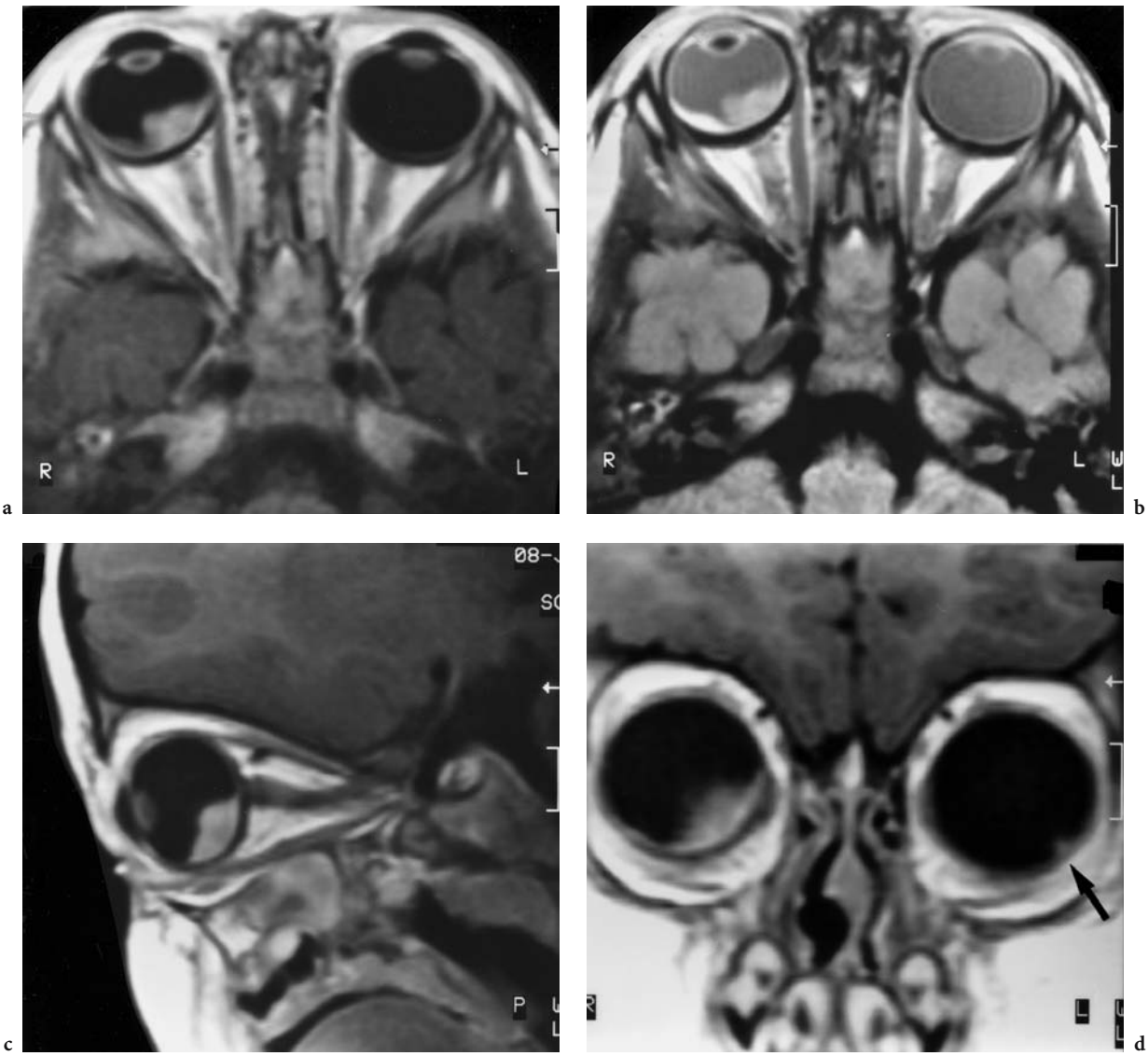

Fig. 6.4a–d. A 1-year-old girl with leukokoria of the right eye. Diagnosis: bilateral retinoblastoma. Triplanar MRI (surface coil over both orbits): **a** Axial T1-weighted, contrast-enhanced image showing the hyperintense tumor crossing the optic nerve in the medial and posterior region of the right globe. The crescent-shaped, less hyperintense lateral pathology corresponds to a retinal detachment, more readily identified as (hyperintense) fluid and differentiated from the solid tumor in **b**, the corresponding proton-weighted image. **c** Sagittal paramedian T1-weighted, contrast-enhanced image confirming an intact optic nerve, even though the tumor has crossed it, an important finding of prognostic and therapeutic value. **d** Coronal T1-weighted, contrast-enhanced view enabling detection of a second tumor in the inferior lateral part of the contralateral globe (*arrow*)

melanoma in adult patients represent the most significant diagnoses.

6.1.2.1 Retinoblastoma

Retinoblastoma is the most common, highly malignant intraocular tumor in childhood (see also Sect. 5.2.4). Over 90% of all diagnoses of retinoblastoma are made in children younger than 5 years of age, with an equal sex distribution (Abramson 1982). Four types of retinoblastoma have been recognized:

1. Non-heritable retinoblastoma presumably caused by postzygotic retinoblast mutation,
2. Retinoblastoma inherited as an autosomal dominant trait,
3. Retinoblastoma associated with the deletion of band 14 of the long arm of chromosome 13 and

4. Bilateral retinoblastoma and pinealoma (trilateral retinoblastoma) (Jakobiec et al. 1977; Abramson et al. 1981; Bader et al. 1982; Mafee 1996).

As the prognosis depends on the stage of tumor growth, an early and thorough ophthalmological and neuroradiological diagnosis is not only a challenge for the attending physicians, but mandatory for the treatment of the young patients. A retinoblastoma is the prototype of a hereditary tumor and occurs in 1:20,000 of all newborns. About 50% of all cases, presenting as multifocal bilateral tumors, are hereditary (Knudson 1978). The latter form of retinoblastoma is inherited as an autosomal dominant trait due to a mutation in both alleles of the RB1-gene at chromosome 13q14 (Cavanee et al. 1986; Bachmann et al. 1998). While the first of these mutations is a germ-cell mutation, the second occurs locally in diverse primitive retinal progenitor cells (either nuclear layer or photoreceptor cells) (Kyritsis et al. 1984), which serves to explain the bilateral and multifocal occurrence (Abramson 1982; Hopper et al. 1992; Bachmann et al. 1998). However, 15% of children presenting with a unilateral retinoblastoma harbor a germinal mutation. The remaining cases of retinoblastoma are sporadic, due to a mutation in both alleles of the RB-gene in one single primitive retinal cell (Zhu et al. 1992; Lohmann et al. 1997). They are unilateral and monofocal and occur in older children.

The small ovoid or round tumor cells comprise scant cytoplasm and relatively large nuclei and may be composed of poorly to well differentiated tumor cells, the latter forming Flexner–Wintersteiner rosettes. Due to rapid growth, retinoblastoma may display extensive necrosis or foci of calcification (Popoff and Ellsworth 1971; Tso 1980).

Retinoma as a nonmalignant manifestation of RB1 mutation (Gallie et al. 1982) develops when the second mutation occurs in a nearly developed retinal cell with reduced potential to acquire mutations, resulting in a benign disordered growth of the retina.

The most common clinical sign of retinoblastoma, found in 60% of the patients, is leukokoria (Fig. 6.5) followed by strabismus (20%). Other clinical signs

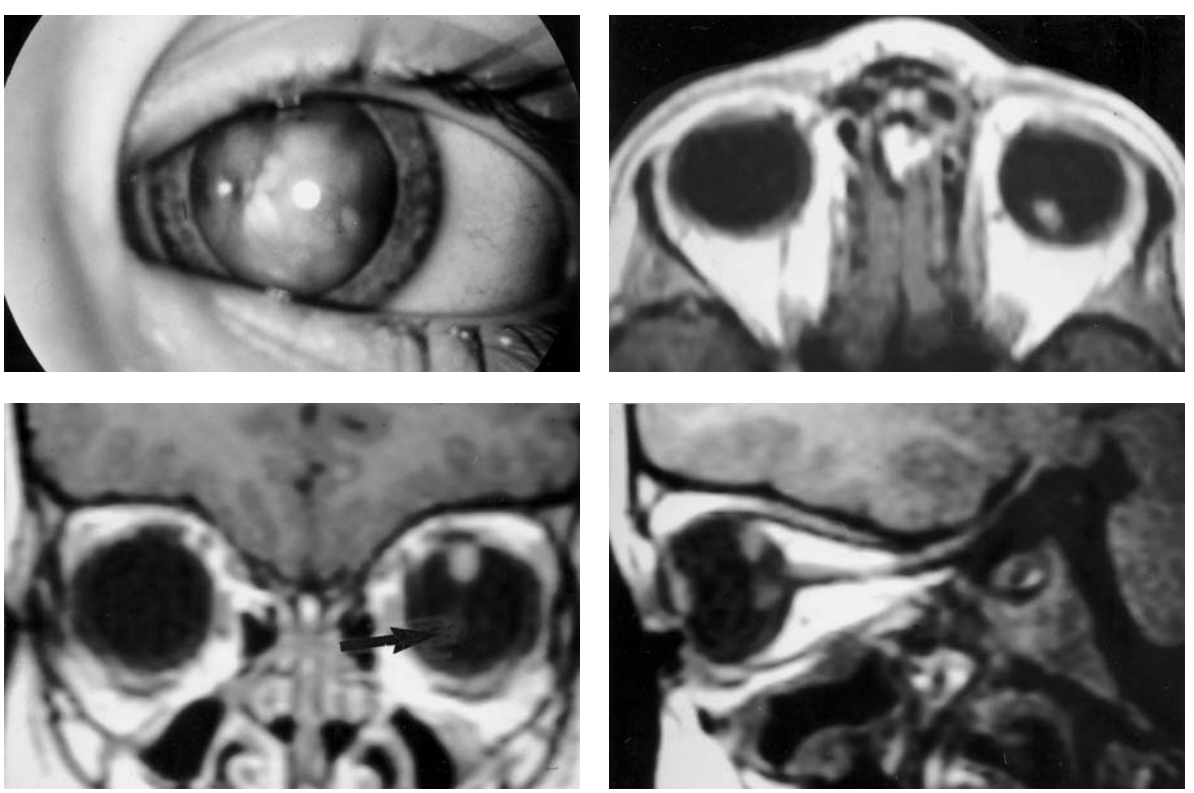

Fig. 6.5a–d. A 4-year-old boy with leukokoria of the left eye. Diagnosis: retinoblastoma. **a** View of the left eye, demonstrating leukokoria. **b** Axial T1-weighted, contrast-enhanced view with a small mass in the superior vitreous body. **c** Coronal T1-weighted, contrast-enhanced view shows the known drop-shaped tumor as well as a shadow at the center of the vitreous body (*arrow*), giving rise to the suspicion of a second lesion. **d** Sagittal paramedian contrast-enhanced, T1-weighted image, depicting two tumors located superior and inferior to the cribriform plate, respectively

like pain caused by secondary glaucoma (Abramson 1982) are considerably rarer. Three different growth patterns are discerned:

1. An endophytic pattern with anterior tumor growth from the retina into the vitreous cavity with vitreous seeds, simulating endophthalmitis.
2. The exophytic pattern: the tumor grows into the subretinal space, producing a secondary retinal detachment and thus simulating Coats' disease (Haik et al. 1985; De Potter et al. 1995).
3. In diffuse retinoblastoma, the tumor grows along the retina, appearing as a placoid mass, simulating inflammatory or hemorrhagic conditions. This rare form presents diagnostic difficulties because of its lack of calcification and its frequent occurrence outside the typical age group (Haik et al. 1985).

Although ophthalmoscopy allows confirmation of retinoblastomas as small as 0.02 mm, imaging techniques should be used in the diagnosis of these tumors. In addition to ultrasonography, CT and MRI are valuable tools in the assessment of tumor extension in the medial, inferior, and lateral aspects of the globe, extraocular extension, intracranial metastasis, and/or a second tumor. Calcification is frequently present in retinoblastoma (>90%), since DNA released from necrotic retinoblastoma tumor cells has a propensity to form a DNA-calcium complex (Mafee 1996). These calcifications may be small or large, single or multiple, punctuate or finely speckled (Char et al. 1984; Mafee and Peyman 1987; Casper et al. 1993). In children younger than 3 years old, intraocular calcification is highly suggestive of retinoblastoma, because only microphthalmos and colobomatous cysts also exhibit calcification. As mentioned above, the diffuse form of retinoblastoma may have no calcification (Mafee and Peyman 1987; Char et al. 1984), and the diagnosis may be difficult. A retinal astrocytoma (ocular hamartoma) may – sometimes prior to any other clinical signs of tuberous sclerosis – likewise present with intraocular calcification (Mafee and Peyman 1987) (Fig. 6.7).

Although the specificity of MRI in detecting calcifications is inferior to CT, it represents the most important imaging method in the pretherapeutic differential diagnosis of retinoblastoma. This is due to its high sensitivity in highlighting pathologic changes in the ocular anatomy, enabling the simultaneous assessment of possible intracerebral infiltration caused by perineural growth along the optic nerve. Retinoblastomas appear slightly hyperintense compared to normal vitreous matter on T1-weighted and proton-weighted images (Fig. 6.4), while on T2-weighted images, they are seen as areas of low signal intensity (Mafee 1996) (Fig. 6.6). Especially fat-suppressed sequences after injection of paramagnetic gadolinium further increase the high sensitivity of MRI due to the fact that retinoblastomas exhibit moderate to marked enhancement (Figs. 6.4–6.6). In case of infiltration of the choroid, no enhancement is seen in this particular region (De Potter et al. 1996; Flanders et al. 1996). MRI technology allows the detection of tumors as small as 2–3 mm, if the patients undergo a thorough examination in all three directions (Figs. 6.4, 6.6). Although retinoblastoma is a bulbar tumor, we consider the use of a surface coil obsolete in the diagnosis of this pathology when performed as a single examination. Despite its excellent sensitivity and high resolution, the limited field of vision (FOV) of the simple surface coil renders the indispensable examination of the optic nerve, chiasm, contralateral globe, and/or cerebrum impossible, in contrast to phase array surface coils (see Chap. 1).

The most common differential diagnoses of retinoblastoma are lesions also presenting with leuko-koria, e.g., PHPV lesions (Fig. 6.2) (see Sect. 6.1.1.3) and Coats' disease (see Sect. 6.1.1.4) (Fig. 6.3). Less frequently observed are retinal detachment, endophthalmitis, toxocariasis, late stages of ROP (retinopathy of the premature), choroidal hemangioma (Fig. 6.16), ciliary body medulloepithelioma, retinal hamartoma, or drusen of the optic nerve head. Drusen of the optic head consists of a primarily autosomal-dominant preliminary mucoprotein matrix deposit with blurred papilla, but only subclinical visual field deficits (Fig. 6.8), a differential diagnosis to papilledema in idiopathic cerebral hypertension (see also Sect. 6.4.1.3.3), and demonstrates calcification of the optic head (Mafee et al. 1995; De Potter et al. 1996). Other rare differential diagnoses of leukokoria are morning glory anomaly or retinal detachment (Mafee 1996; Yan et al. 1998), while choroidal astrocytomas are seen in the course of a tuberous sclerosis (Fig. 6.7). Although case reports exist about rare infections with optic nerve involvement in cysticercosis, intraocular echinococcosis (Fig. 6.9), with a presentation closely resembling leukokoria, is rather unusual (Chandra et al. 2000).

6.1.2.2 Malignant Uveal Melanoma

Malignant melanoma of the ciliary body and the choroid is the most common primary intraocular malignant disease in adults. The incidence of the disease increases with age and ranges from 5.2 to 7.5

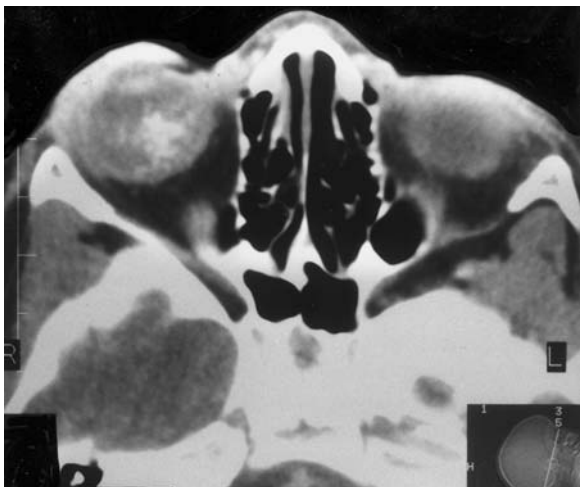

a

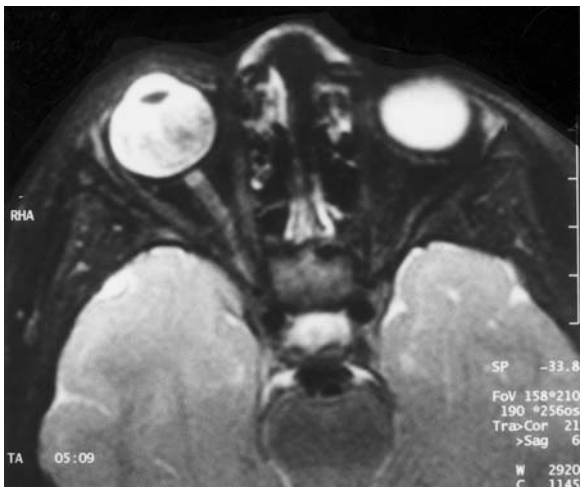

b

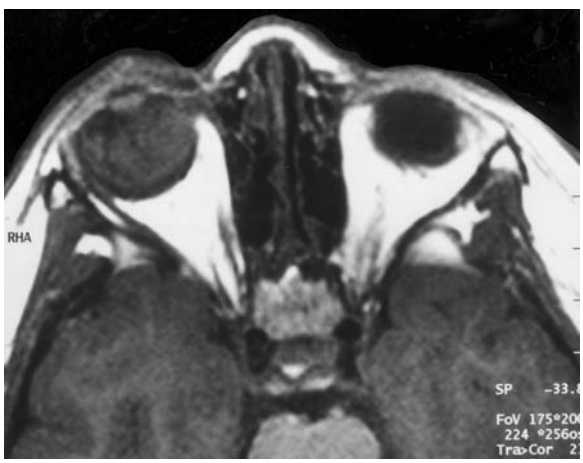

c

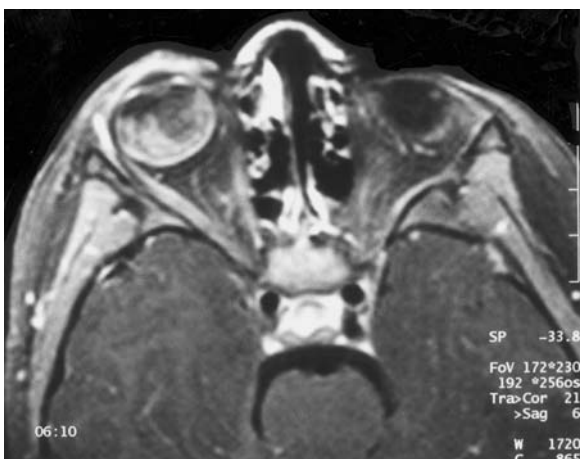

d

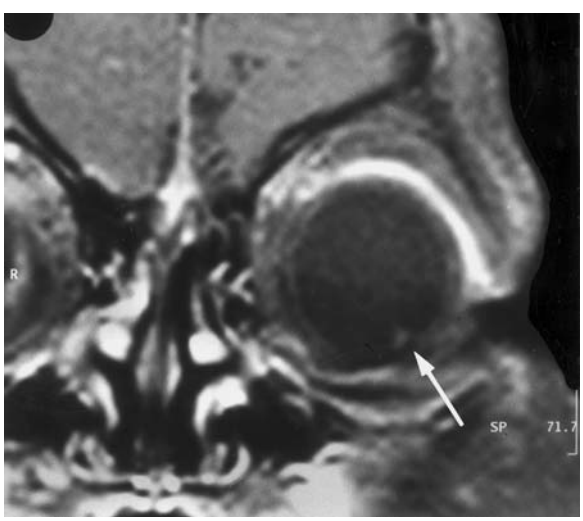

e

Fig. 6.6a–e. A 2 year-old-girl presenting with leukokoria of the right eye. Diagnosis: bilateral retinoblastoma. Axial contrast-enhanced CT: **a** No significant enhancement, but visualization of specific partial calcification of the tumor of the right globe. MRI: **b** Corresponding T2-weighted view with an irregular hypointense mass of the posterior right globe. **c** Corresponding T1-weighted native image with a slightly hyperintense (compared with the vitreous) irregular tumor of the right globe. **d** Corresponding T1-weighted, contrast-enhanced view with extensive marked enhancement of the noncalcified areas. At the inferior part of the contralateral globe, an additional (only 2 mm in diameter) tumor is detected, confirmed both on the coronal image *(white arrow)* (**e**) and on a second ophthalmological examination

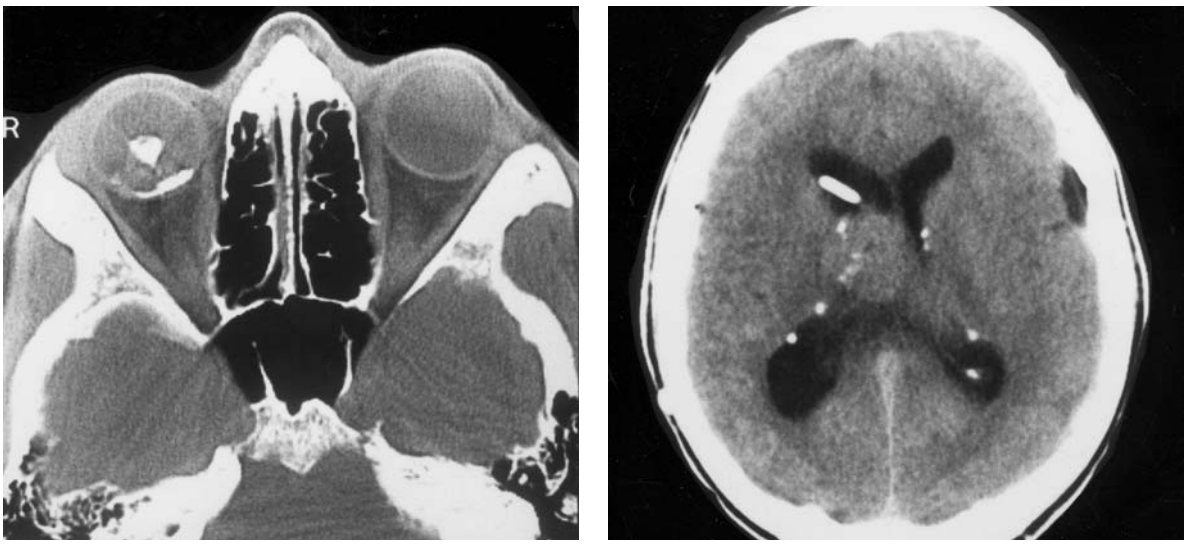

Fig. 6.7a,b. A 21-year-old man with Pringle disease. Diagnosis: phthisis. CT: **a** Axial view with ocular calcification of the globe and posterior sclera. **b** Axial cranial view with ependymal calcification and giant cell astrocytoma, extending into the right lateral ventricle (state after ventricular shunting for occlusive hydrocephalus). (With permission of Dr. R. Gustorf-Aeckerle, Katharinen Hospital, Stuttgart)

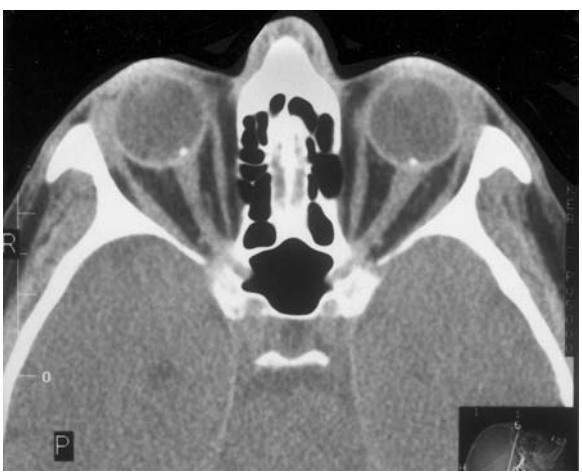

Fig. 6.8. A 59-year-old man with unspecific history. Diagnosis: drusenpapilla. CT: the axial view demonstrates the bilateral calcification of the papilla

cases per million per year at a mean age of 53 years (De Potter et al. 1995; McLean 1996). Malignant melanomas occur predominantly in Caucasians (ratio 15:1 Caucasians and blacks) (Yanoff and Fine 1975; Margo and McLean 1984). The current WHO classification of tumors of the choroid – in contrast to the former Callender classification – only discerns three histological types, i.e. mixed, epithelioid, and necrotic melanomas (Callender 1931; McLean et al. 1978; Campbell and Sobin 1998). The mixed type consists of spindle B and epithelioid cells. Spindle cell A tumors are currently classified as benign choroidal nevi. Spindle cell tumors have a relatively good prognosis in comparison with mixed or purely epithelioid melanomas (McLean 1995; Mafee 1998). Tumor growth is generally nodular, while flat lesions diffusely infiltrating the uvea are rare. A nodular melanoma may exhibit a well-circumscribed, ovoid or dome-shaped appearance. Bruch's membrane may rupture with tumor progression, assuming a characteristic mushroom shape (Fig. 6.10) (De Potter et al. 1995; Mafee 1996). The factors associated with a poor systemic prognosis include: (1) older patients (>60 years), (2) large tumor basal diameter and thickness (>15 mm/3 mm), (3) location of the tumor in the anterior uvea and ciliary body, (4) presence of epithelioid cells, and (5) extraocular extension (Char 1978; De Potter et al. 1995; Damato et al. 1996a,b).

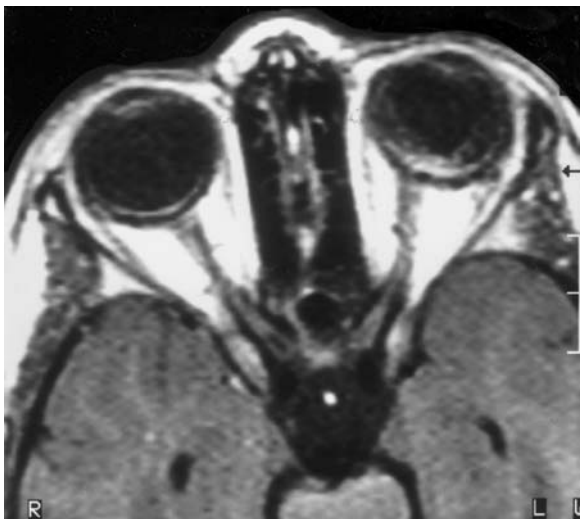

a

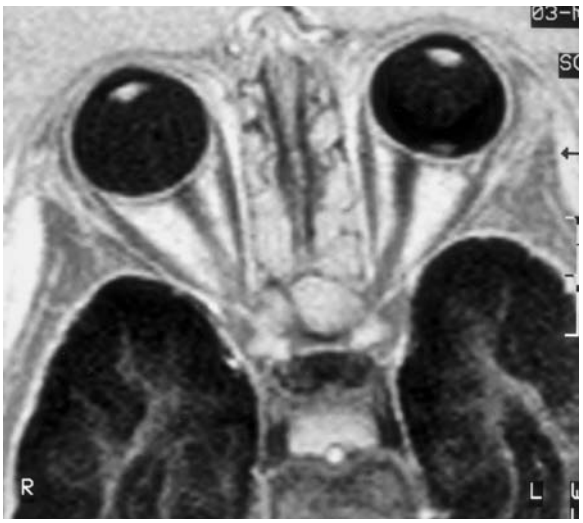

b

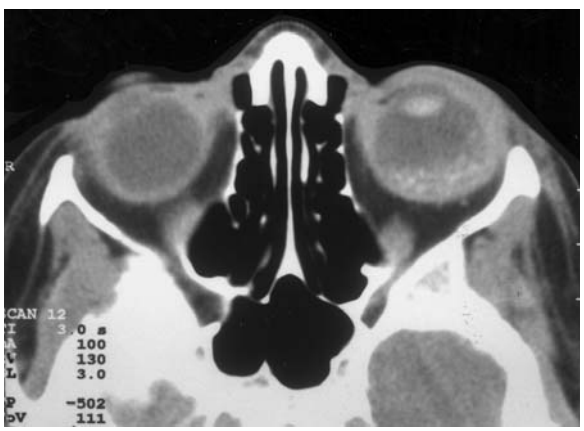

c

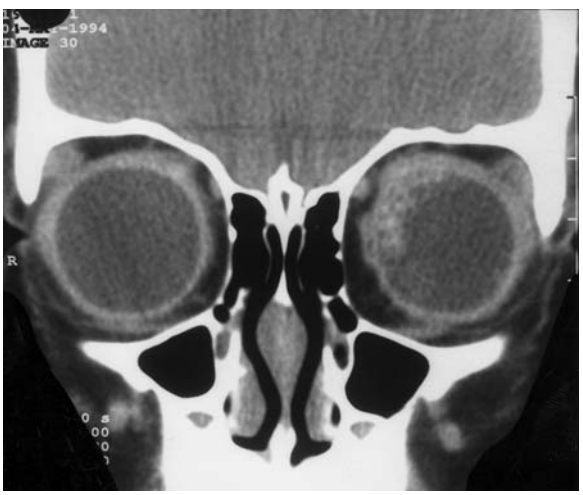

d

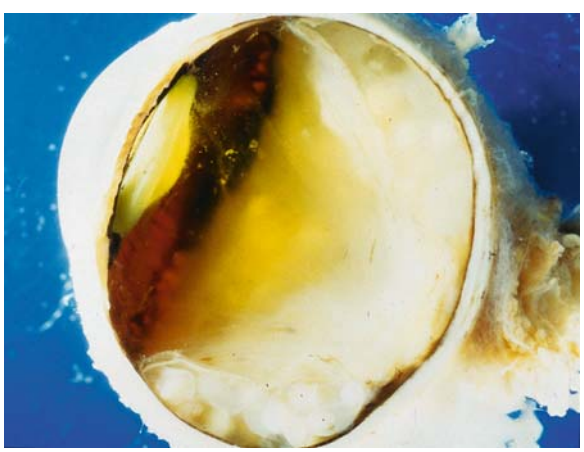

e

f

Fig. 6.9a–f. A 9-year-old girl with leukokoria of the left eye. Diagnosis: echinococcus of the vitreous body. MRI: **a** Axial T1-weighted, contrast-enhanced image with only slight enhancement in the posterior region of the globe, but no typical tumor enhancement. **b** Corresponding IR sequence without definite finding. An additional CT in axial (**c**) and coronal (**d**) views confirmed the suspected diagnosis of retinoblastoma on the basis of widespread calcification. Histology after exenteration of the left globe showed the presence of echinococcus throughout the entire globe. **e** Specimen of the exenterated globe, where the posterior part is filled with the tapeworm. Note the complete retinal detachment of the subretinal mass. **f** Histologic view, demonstrating the scolex (head of the tapeworm)

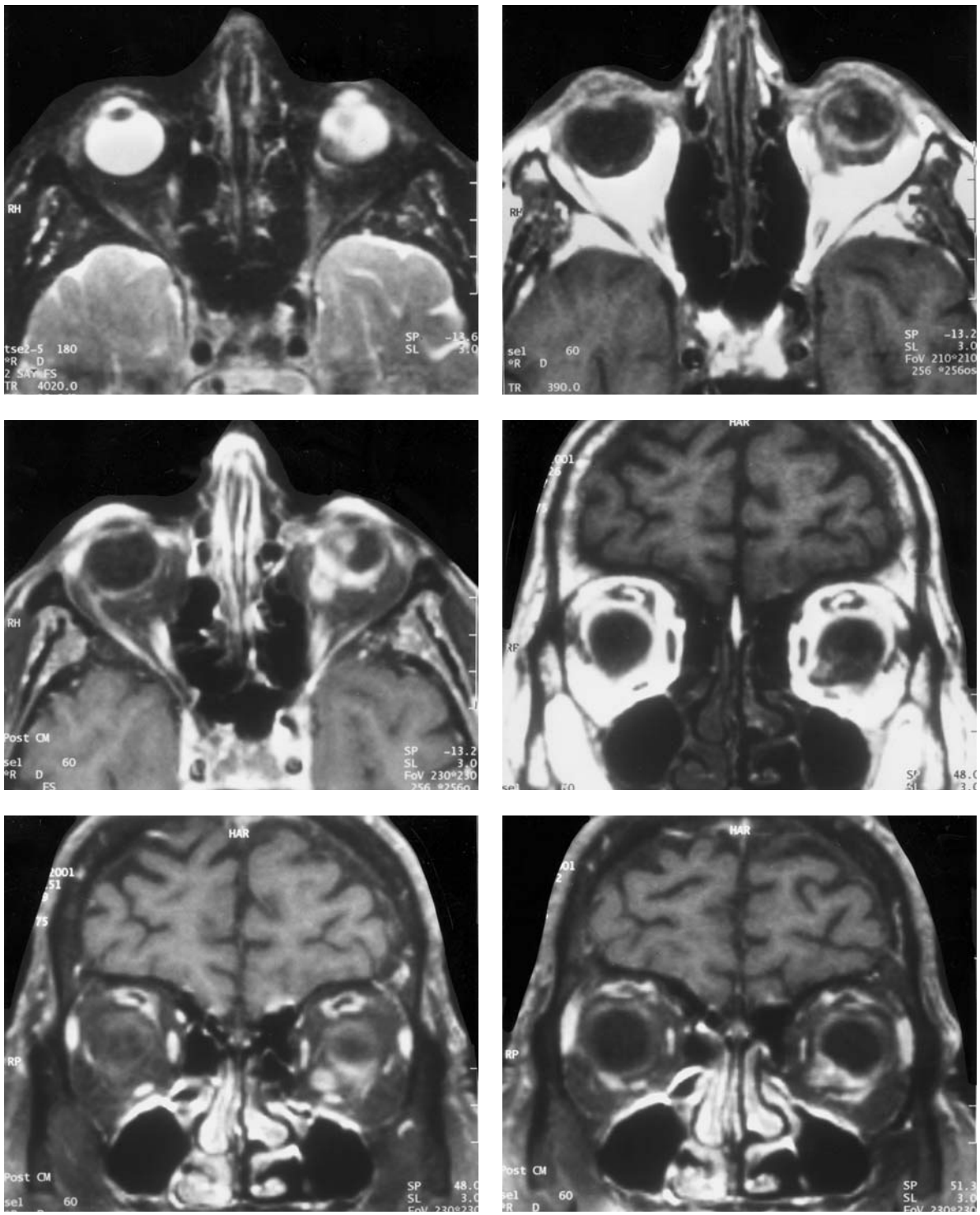

Fig. 6.10a–f. A 73-year-old woman with known malignant melanoma, who had refused therapy for half a year. Diagnosis: malignant melanoma with intraorbital expansion. MRI: **a** Axial T2-weighted (FS) view of the inferior orbit with irregular hypointense mass in the posterior circumference of the left globe and medial extraocular retrobulbar space. **b** Corresponding T1-weighted native view, demonstrating the hyperintense signal of the melanoma, apparently infiltrating the posterior choroid. **c** Corresponding T1-weighted, contrast-enhanced (FS) view with homogeneous enhancement of the tumor, the intraocular mass reaching the inferior ciliary body and lens. Note the similar signal characteristics of the posterior circumference of the globe (representing the infiltrated choroid) and the extraocular tumor. **d** Coronal T1-weighted native view. **e** Corresponding T1-weighted, contrast-enhanced (FS) view, where the extraocular expansion between the inferior and medial rectus muscle is best seen. **f** Coronal T1-weighted, contrast-enhanced (FS) view 3 mm anterior to **e** with demonstration of the site of rupture of Bruch's membrane

The sites of metastasis are liver, lung, bone, kidney, and brain. The question of the most effective therapy is still being controversially discussed, with options ranging from photocoagulation, transpupillary thermotherapy (TTT) to radiation therapy with ruthenium or strontium plaques, local excision, or enucleation (Char 1978; Duffin et al. 1981; Peyman et al. 1984; Osterhuis et al. 1995; Damato et al. 1996a,b; Shields et al. 1998).

Diagnosis of uveal melanoma is usually made by ophthalmoscopy, fluorescein angiography, and ultrasound, with the last-mentioned being indicated especially in lesions smaller than 3 mm (Mafee et al. 1985), although imaging with CT or MRI is required when opaque media preclude direct ophthalmoscopic visualization (Shields and Zimmerman 1973; Zimmerman 1973; Harnsberger 1990; Mafee et al. 1985; De Potter et al. 1995; Mafee 1998).

Although most uveal melanomas are seen on CT as elevated, primarily hyperdense, sharply circumscribed, enhancing tumors, high-resolution MRI has become the imaging technique of choice in the definition of retrobulbar/extraocular tumor extension. Melanin produces stable free radicals which cause a paramagnetic proton relaxation enhancement that shortens both T1 and T2 relaxation times, resulting in a moderately high signal on T1-weighted and proton density-weighted scans and signal reduction with moderately low signal on T2-weighted images (Fig. 6.13). This somewhat unique signal pattern is caused by the binding capacity of natural melanin for paramagnetic metal ions (i.e., iron, copper) (Enochs et al. 1997). Hence the well-defined solid tumors present (in up to 95%) as hyperintense (with respect to the vitreous body) on T1-weighted sequences and hypointense on T2-weighted images (Damadien et al. 1973; Gomori et al. 1986; Haik et al. 1987; Mafee and Peyman 1987) (Figs. 6.11–6.15). Associated retinal detachment as an area of moderate to very high signal intensity on T1-weighted, PD, and T2-weighted images is better visualized with MRI than CT (Mafee 1996). It is important to know that in some cases an isointense signal is seen on T2-weighted images and that the content of melanin is not always in correlation to the brightness of the signal. Gadolinium-enhanced, T1-weighted images are superior to noncontrast T1-weighted images in detecting and delineating malignant melanomas. The additional use of fat-suppressed sequences improves the contrast difference in signal intensity of choroidal melanomas associated with retinal detachment as well as the detection of small melanomas (De Potter et al. 1994, 1996; Flanders et al. 1996). While in most cases the tumor shape is of no specific diagnostic value, the detection of a mushroom or collar-button shaped tumor caused by the growth and rupture through Bruch's membrane on ophthalmoscopic, US, and CT/MRI (Fig. 6.10) is highly suggestive of choroidal melanoma (Mafee 1998).

In addition to retinoblastoma, the differential diagnosis includes choroidal hemangioma (Fig. 6.16) (see Sect. 6.1.2.3.1), choroidal nevi, choroidal detachment (see Sect. 6.1.2.3.5), choroidal cysts, neurofibroma and schwannoma of the uvea, uveal leiomyoma, ciliary body adenoma, as well as retinal detachment, disciform degeneration of the macula, and metastatic tumors (Fig. 6.19) (see Sect. 6.1.2.3.4) (Mafee 1998).

(Text continues on p. 163)

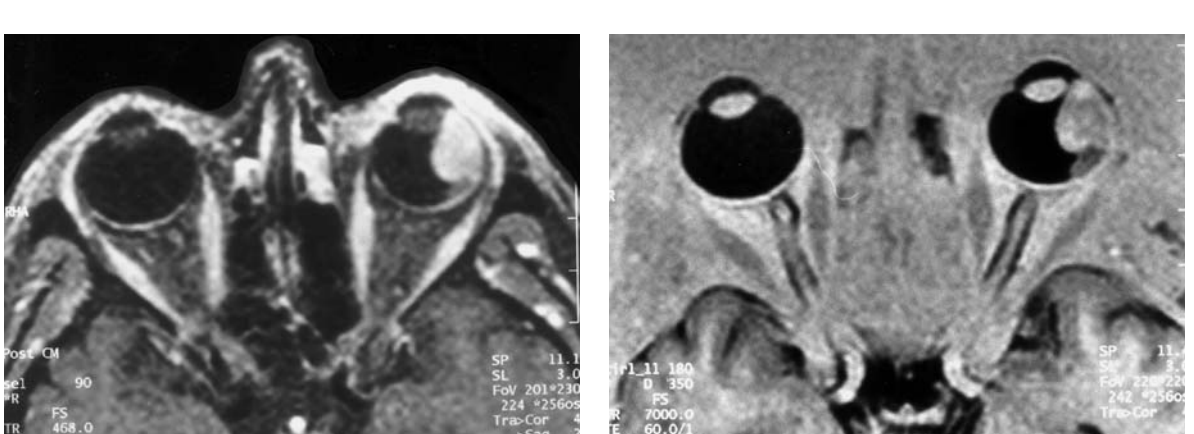

Fig. 6.11a,b. A 59-year-old woman with progressive visual deficit of the left eye. Diagnosis: choroidal melanoma with secondary infiltration of the ciliary body. Axial MRI: **a** T1-weighted, contrast-enhanced view outlining the tumor, which apparently originates in the lateral ciliary body; additional retinal detachment in the posterior part. **b** Corresponding IR image providing a more conclusive delineation of the pathologic process

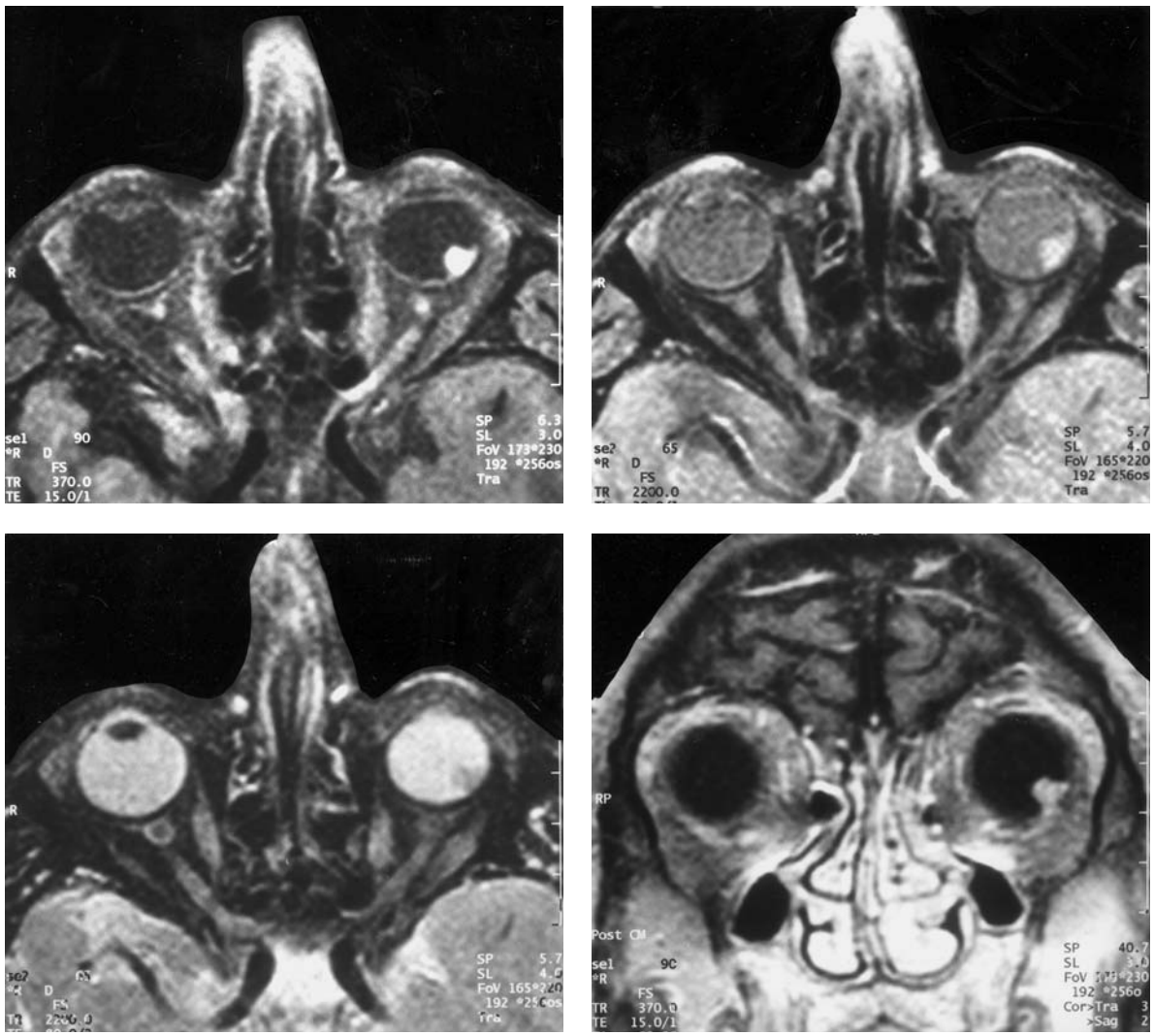

Fig. 6.12a–d. A 73-year-old man with visual deficit of the left eye. Diagnosis: small choroidal melanoma. MRI: **a** Axial T1-weighted, contrast-enhanced (FS) image showing the small, irregular, but extensive choroidal tumor, located lateral to the macula. **b** Corresponding proton density image with hyperintense melanin signal. **c** Corresponding T2-weighted image with signal change to hypointensity. **d** Coronal T1-weighted, contrast-enhanced view

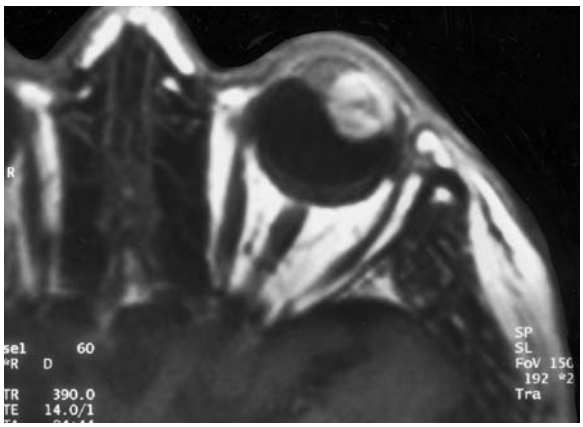

a

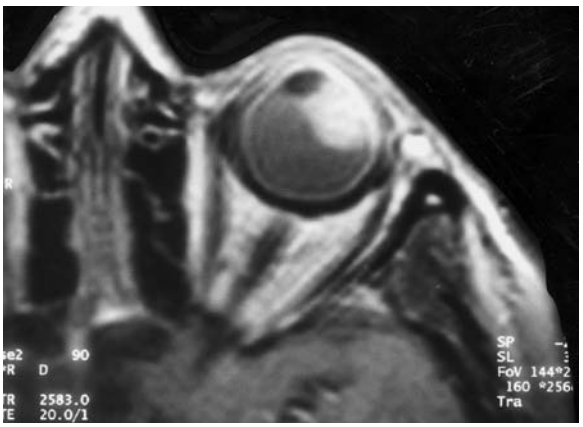

b

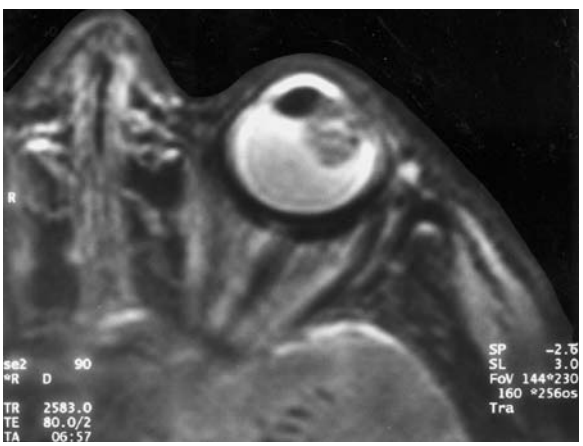

c

Fig. 6.13a–c. A 61-year-old woman with visual deficit. Diagnosis: ciliary body melanoma. Axial MRI: **a** T1-weighted native image showing the hyperintense tumor in the ciliary body; **b** Corresponding proton density image with the tumor appearing as hyperintense with signal changing to hypointensity on the T2-weighted sequence (**c**)

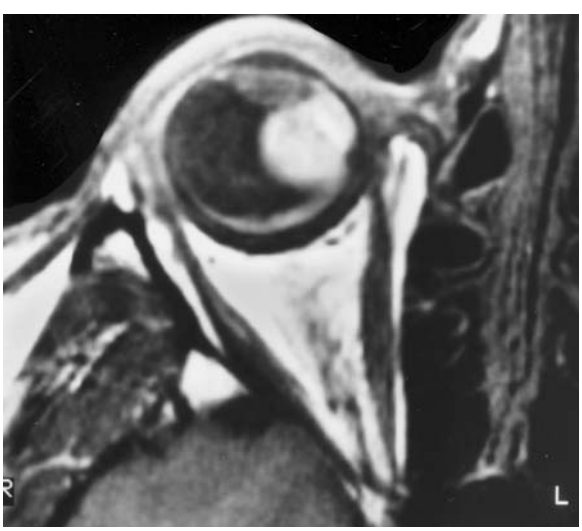

a

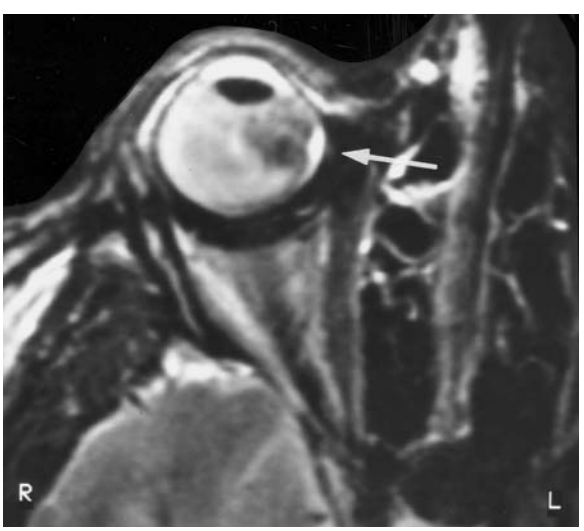

b

Fig. 6.14a,b. A 46-year-old woman with visual loss of the left eye. Diagnosis: choroidal melanoma, extending to the ciliary body of the left globe. MRI: **a** Axial T1-weighted, contrast-enhanced image showing a well-defined, homogeneous lesion at the medial circumference of the right globe, extending to the medial ciliary body, and along the posterior choroid. **b** Corresponding T2-weighted image allowing visualization of the hypointense signal of the melanin (caused by its susceptibility). Note the faint fluid signal corresponding to a slight, associated retinal detachment (*white arrow*) and imposing as a small, hypointense area on the T1-weighted image (**a**)

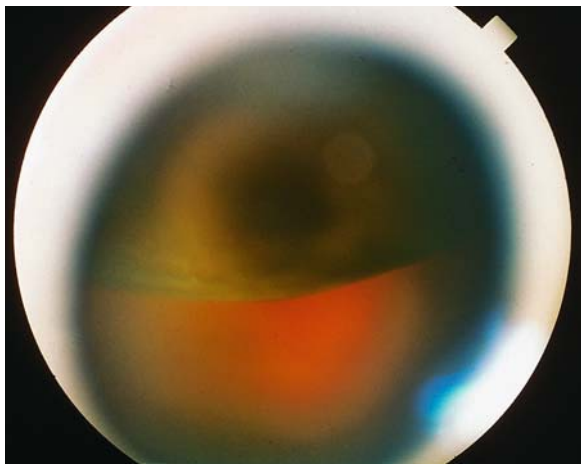
a

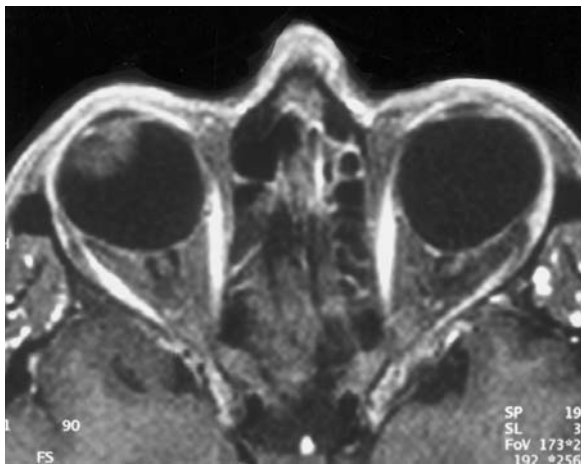

b

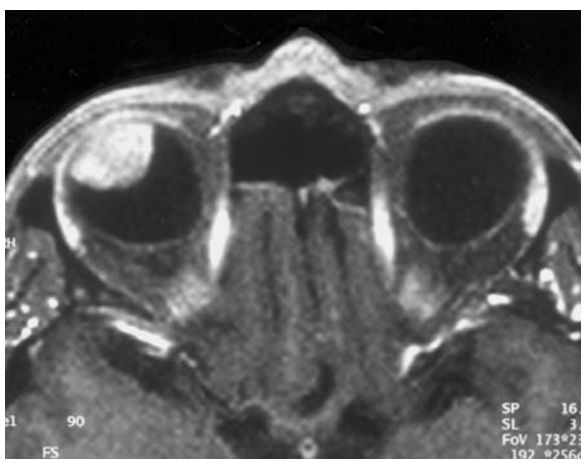

c

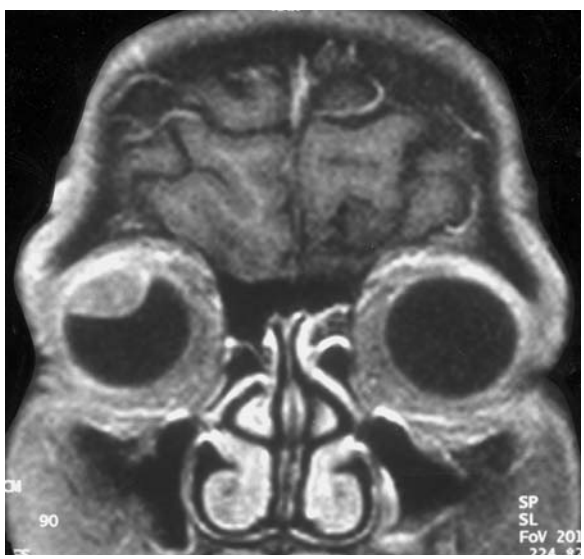

d

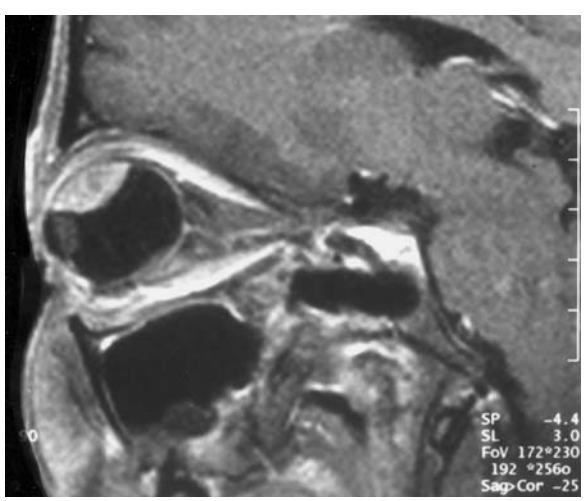

e

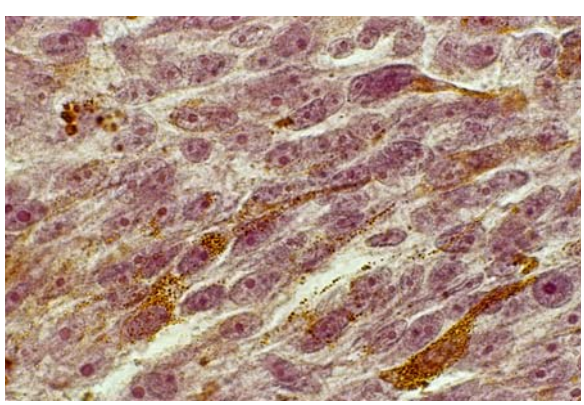
f

Fig. 6.15a–f. A 60-year-old woman with choroidal melanoma, initially thought to arise from the ciliary body. Diagnosis: choroidal melanoma extending to the ciliary body. **a** Funduscopic view of a large, prominent uveal melanoma. MRI: **b** Axial T1-weighted, contrast-enhanced (FS) view at the level of the lens, showing a normal configuration of the ciliary body of the right eye, but a hazy lesion behind the lens becomes clearly apparent. **c** The entire tumor is seen 3 mm cranial of **b**. **d** Coronal view leads to the suspicion that the extended contact of the tumor with the upper circumference of the globe is responsible for the operatively confirmed development at the upper lateral quadrant. **e** Corresponding parasagittal view, confirming the diagnosis. The diagnosis is supported by the normal location of the lens and the lens-shaped configuration of the tumor. **f** Histology: H&E-stained section of a spindle B cell uveal melanoma featuring scattered pigmented tumor cells

6.1.2.3. Miscellaneous Choroidal Lesions (i.e. Choroidal Hemangioma, Choroidal Osteoma, Ocular Hamartoma, Uveal Metastasis, Choroidal Detachment)

Although less than 1% (2 of 413) of enucleated eyes were found to contain choroidal lesions other than malignant melanoma (Collaborative Ocular Melanoma Study, COMS 1998), the differential diagnosis should not fail to also consider other choroidal lesions, as the respective therapeutic regimens differ substantially.

6.1.2.3.1 Choroidal Hemangioma

Choroidal hemangiomas are congenital vascular hamartomas seen in middle-aged to elderly patients with neurocutaneous syndromes. They may present as circumscribed, solitary or diffuse lesions, while histologically three descriptive categories are classified (Mafee 1998): cavernous, capillary, and mixed type lesions.

Uveal hemangiomas occur as circumscribed or diffuse, capillary or cavernous angiomatosis, the latter frequently in association with ipsilateral facial nevus flammeus in Sturge-Weber syndrome (Barkovich 2000; Stroszczynski et al. 1998; Mafee 1998; Yan et al. 1998). While the localized form presents on ophthalmoscopy as a well-defined, reddish-orange lesion of the posterior pole of the globe, diffuse uveal hemangiomas may not be readily discernible.

On CT/MRI, choroidal hemangiomas present as lenticular hyperdense/hyperintense (in both T1- and T2-weighted images) structures in the juxtapapillary or macular region, and on comparison with the vitreous body (Fig. 6.16), they demonstrate marked/intense contrast enhancement (Medlock et al. 1991; De Potter et al. 1995; Mafee 1998).

Retinal hemangioma may occur isolated or in Hippel-Lindau syndrome (Fig. 6.17). This rare, autosomal dominant, familial multisystem disorder, one of the

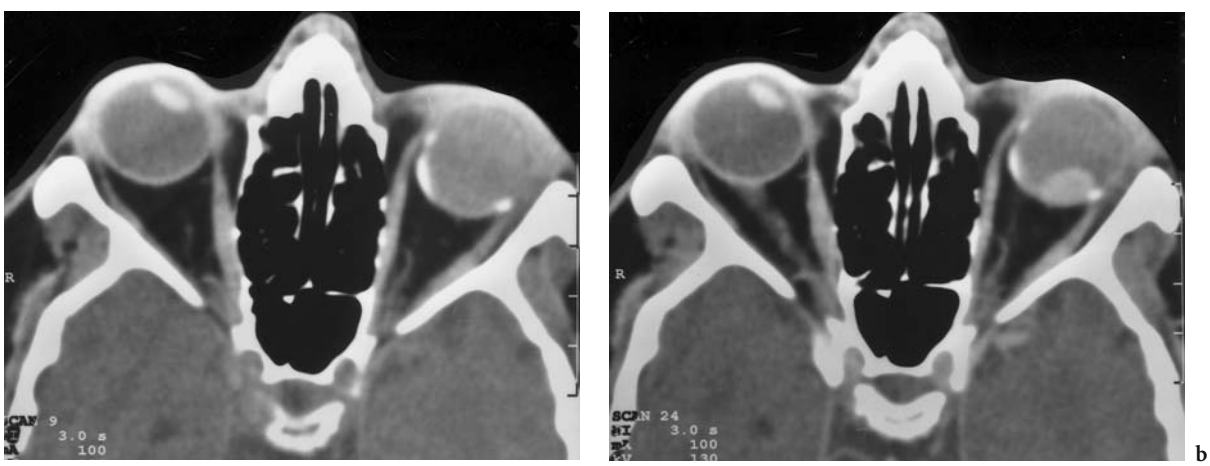

Fig. 6.16a,b. A 30-year-old man with slowly progressing blurred vision. Diagnosis: choroidal hemangioma of the left globe. Axial CT: **a** The native image only shows the silicone circle, performed for recurrent retinal detachment. **b** The biconvex, homogeneous enhancement of this vessel malformation is seen after i.v. contrast

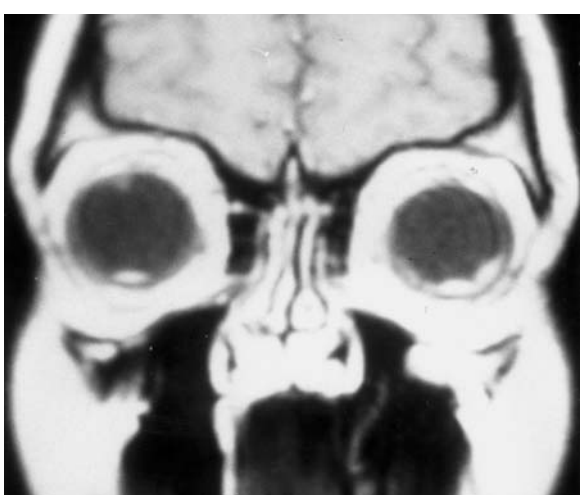

Fig. 6.17. A 20-year-old woman with Hippel–Lindau disease. Diagnosis: bilateral inferior choroidal hemangioma. Coronal T1-weighted MRI. (With permission of Radiologen am Brand, Mainz)

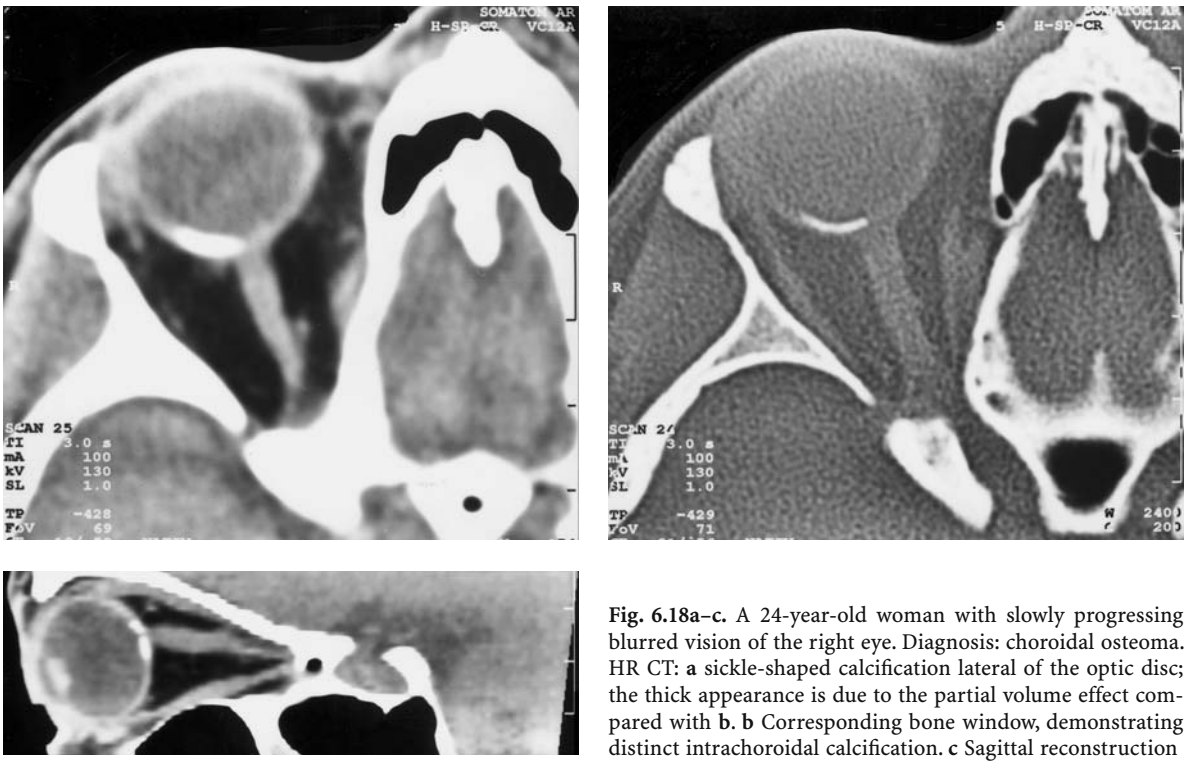

Fig. 6.18a–c. A 24-year-old woman with slowly progressing blurred vision of the right eye. Diagnosis: choroidal osteoma. HR CT: **a** sickle-shaped calcification lateral of the optic disc; the thick appearance is due to the partial volume effect compared with **b**. **b** Corresponding bone window, demonstrating distinct intrachoroidal calcification. **c** Sagittal reconstruction

neurocutaneous syndromes (syn. phakomatosis), is characterized by multiple hemangioblastomas of the central nervous system with a preference for the cerebellum and spinal cord, angiomatosis of the retina, pancreatic and renal cysts, and a relatively high incidence of renal cell carcinoma (Rubinstein 1972; Sartor 1992; Osborn 1994) (see NF 1, Sturge-Weber). A bilateral or multifocal presentation is characteristic for capillary hemangioma in Hippel-Lindau disease, while a differentiation from the isolated form is not possible by clinical or histological presentation of the retinal angiomatosis. It appears as a reddish nodule with a dilated, tortuous feeding artery and vein in the mid-periphery of the retina (De Potter et al. 1996).

On MRI, sufficiently large retinal hemangiomas (Fig. 6.17) may simulate retinoblastomas or melanomas (depending on the age of the patient). As the diagnosis is based on the typical ophthalmoscopic appearance, the major role of imaging consists of ruling out a possible association with cerebellar and/or spinal hemangioblastomas (Sartor 1992; Osborn 1994; De Potter et al. 1996).

6.1.2.3.2 Choroidal Osteoma

The rare choroidal osteoma (Fig. 6.18) is typically seen in young women before completion of the third decade of life. This benign ossifying tumor contains marrow, mast cells, loose fibrovascular elements, and mesenchymal cells. The diagnosis can be made clinically and in combination with characteristic ultrasound findings as the choroidal osteoma presents as a yellow-white or orange-red mass in the macula or juxtapapillary region (Mafee 1998), although it is seen as a sharply demarcated, lentiform calcification on CT. On MRI, it presents with a high signal on nonenhanced T1-weighted and low signal on T2-weighted images, with marked signal enhancement after gadolinium injection, simulating both retinoblastoma and choroidal melanoma. The enhancement corresponds to the central core of the osteoma, consisting of fatty marrow within the intertrabecular spaces (De Potter et al. 1995; Müller-Forell and Lieb 1995a; Mafee 1998; Yan et al. 1998).

6.1.2.3.3 Ocular Hamartoma

Ocular hamartomas (syn. retinal astrocytoma) are rare tumors seen most frequently in patients with tuberous sclerosis (Fig. 6.7) or neurofibromatosis, in whom radiological findings may look similar to early retinoblastoma or present with intraocular calcification (Abramson 1982; Margo et al. 1983; Dotan et al. 1991; Mafee and Peyman 1987).

6.1.2.3.4
Uveal Metastasis

The choroid is the most common site of carcinoma metastasis to the eye, as hematogenous embolic dissemination of malignant cells gain access to the eye with the bloodstream via the short posterior ciliary arteries (Michaelson and Campbell 1940; De Potter et al. 1995; Mafee 1996, 1998; Shields et al. 1997). The most common sources of secondary carcinoma are the breast and lung (Stoffelns and Dick 2000). In contrast to uveal melanoma, uveal metastasis may occur bilaterally or be multifocal and affects both eyes in about one-third of cases (Mafee 1990). Decreased vision, field deficits, and pain (the latter depending on the intraocular location) combined with rapid progressive tumor enlargement enable the clinical differential diagnosis of choroidal metastasis of distant carcinoma, while the imaging presentation may lead to confusion of uveal metastasis with uveal melanoma (Fig. 6.19).

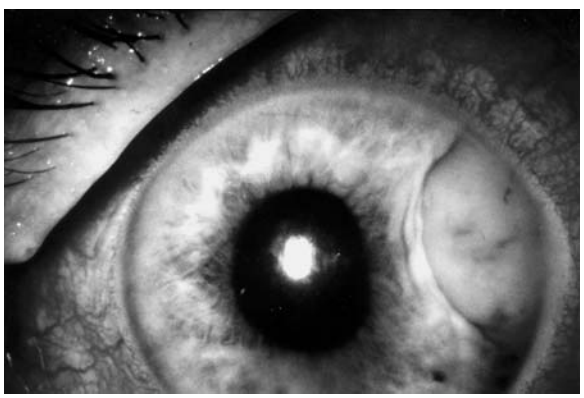

a

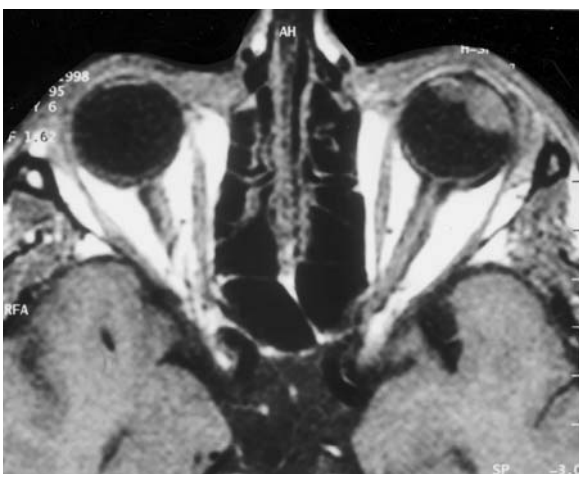

b

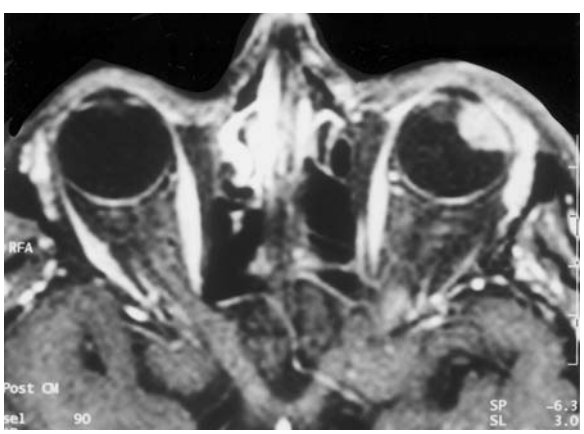

c

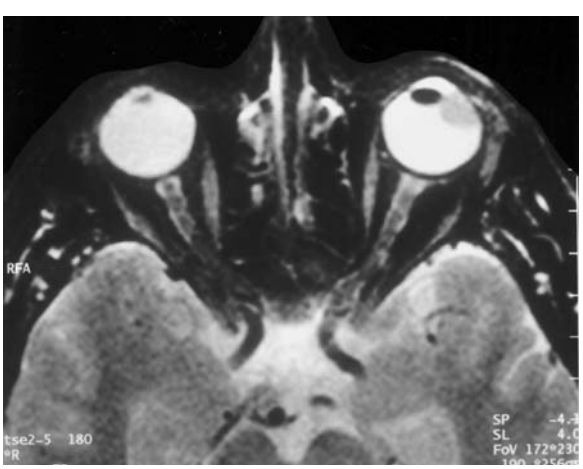

d

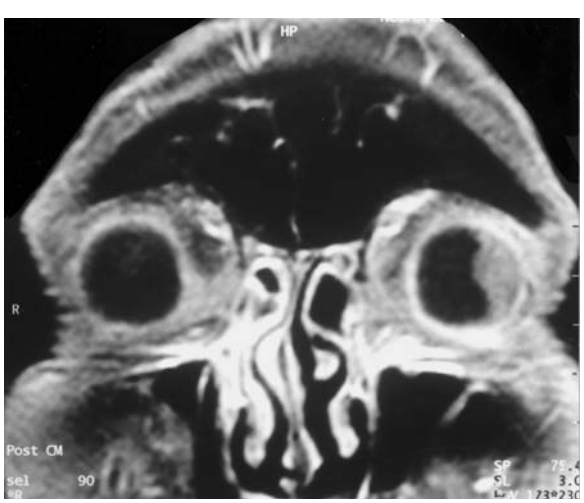

e

Fig. 6.19a–e. A 64-year-old man with suspected choroidal melanoma and a sudden onset of severe pain in the left eye, requiring emergency enucleation. Diagnosis: uveal metastasis from lung cancer. MRI: **a** Macroscopic view of the left eye demonstrating a 10 mm prominent, barely vascularized, whitish mass in the temporal iridocorneal angle. **b** Axial T1-weighted view showing a lesion apparently originating in the anterior lateral choroid, pressing against and dislocating the lens. **c** Corresponding contrast-enhanced image which did not enable exclusion of invasion of the anterior chamber (surgically proven). **d** Corresponding T2-weighted image demonstrating widening of the anterior chamber and hypointensity of the lesion. **e** Coronal T1-weighted, contrast-enhanced view showing irregular growth of the tumor

6.1.2.3.5
Choroidal Detachment

Choroidal hemorrhage and choroidal detachment may be easily mistaken for a choroidal tumor, especially when a rupture of Bruch's lamina has occurred (Mafee 1996). The imaging characteristics of choroidal detachment are discussed in detail in Sect. 6.1.4.

6.1.3
Inflammatory Disorders

6.1.3.1
Primary Inflammation: Scleritis

Even though the sclera is not highly vascularized, it may be affected by diverse inflammatory processes such as metabolic (gout), bacterial, fungal, or viral conditions. It is also one of the predominantly affected structures in one form of local idiopathic orbital inflammation (Mafee 1998). Presentation may be acute or chronic (Watson 1982) and is classified into an anterior and posterior form. The clinical presentation of a slowly progressing, painful thickening and flush of the sclera may be indicative of anterior scleritis, while the posterior form exhibits proptosis and eventually decreased vision, due to thickening of the sclera and choroid with choroidal folds. Posterior scleritis is less common, predominantly affecting women, and sometimes requires imaging. Histologically, it may present as diffuse or localized, nodular, necrotic, or granulomatous inflammation. Due to the inflammatory reaction with leakage of proteinaceous edema fluid into the interstice of the uvea and Tenon's capsule, scleral sequesters and exudative retinal detachment may be seen in the vicinity of the inflammatory process (Flanders et al. 1989; Mafee 1998) (Fig. 6.20).

Depending on the grade of the inflammatory process, CT and MRI of scleritis is characterized by scleral thickening with contrast enhancement (Figs. 6.20–6.22). Subretinal effusion, clearly seen on ultrasound, may also be demonstrated and appear hyperintense on T1-weighted and hyperintense on T2-weighted MR images. Unlike melanoma, no enhancement is found in the nodular form of posterior scleritis (Harnsberger 1990; Mafee 1998).

6.1.3.2
Secondary Inflammation

6.1.3.2.1
Behçet Syndrome

Typical clinical manifestations of Behçet syndrome, first described in 1937 by the Turkish dermatologist H. Behçet, are the triad of recurrent oral ulcers (98%), genital ulcers (88%), and intraorbital inflammation (76%), the latter involving the anterior and/or posterior ocular chambers. The disease is characterized by periods of remission and exacerbation (Banna and El-Ramahi 1991); ocular involvement has been described as an indicator of systemic dis-

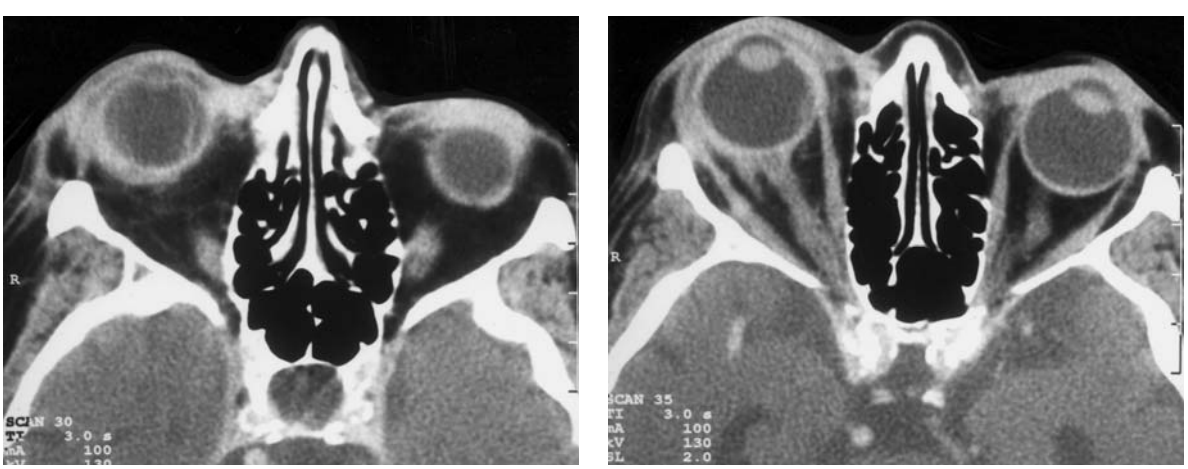

a b

Fig. 6.20a,b. An 83-year-old woman with chronic articular rheumatism, presenting with subacute (onset 4 weeks prior to presentation) painful swelling and protrusion of the right eye. Diagnosis: posterior scleritis and retinal detachment. Axial contrast-enhanced CT: **a** Despite swelling of the posterior part of the sclera, a crescent-shaped bilateral retinal detachment is apparent in the inferior part of the right globe. **b** Paraoptic retrobulbar inflammation as well as some medial retinal detachment are seen at the level of the optic nerve in the protruded right globe

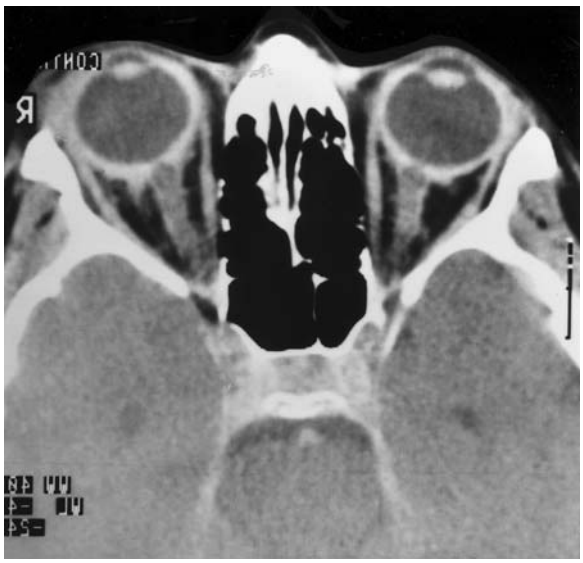

Fig. 6.21. A 63-year-old woman with diabetes, presenting with acute, painful, blurred vision. Diagnosis: bilateral posterior scleritis. Axial contrast-enhanced CT with bilateral scleral thickening; the blurred contour at the posterior part of the globe indicates extension of the inflammatory process into the orbit

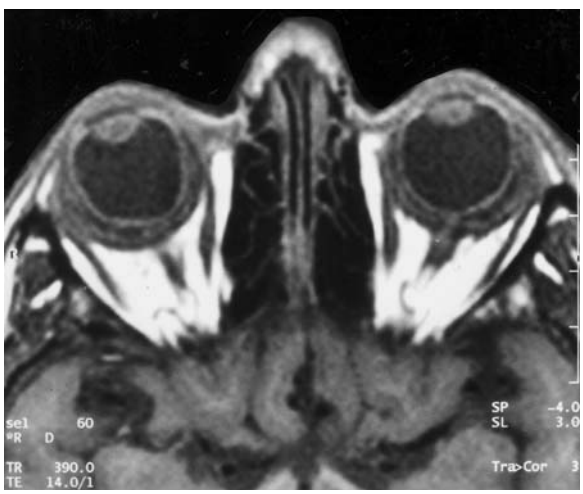

a

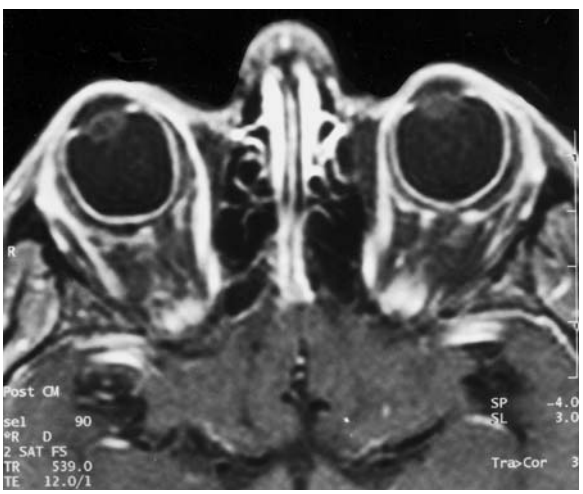

b

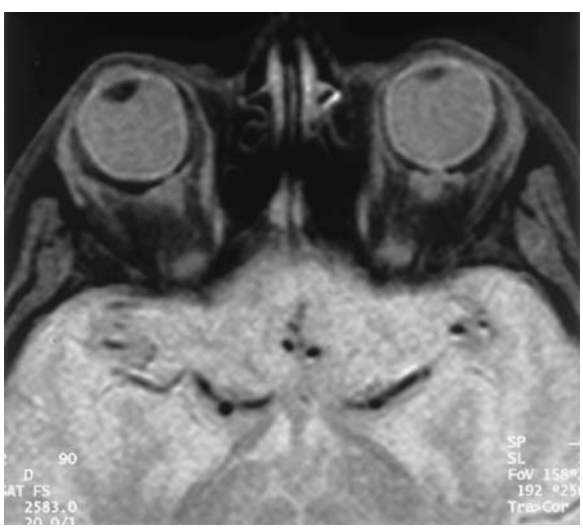

c

Fig. 6.22a–c. A 45-year-old woman with persistent, previously untreated, subacute, bilateral, blurred vision. Diagnosis: chronic posterior scleritis. T1-weighted MRI: **a** Axial view showing deformed scleral circumference of both globes and segmentation of the posterior retrobulbar space: slight crescent-shaped signal loss medial and lateral of the optic nerve; the presence of connective tissue extending from the sclera to the tendinous parts of the external muscles indicates enlargement of Tenon's capsule. **b** Contrast-enhanced (FS) view with demarcation of scleral inflammatory thickening of Tenon's capsule and retrobulbar inflammation. **c** Corresponding T2-weighted proton density image, demonstrating transformation of the fluid in Tenon's capsule, thought to be due to the persistent, untreated inflammatory process

ease (Foster et al. 1991). Although rare, with a prevalence of less than 1 to 10,000, it is over 5 times more common in men than in women (Atmaca et al. 1996); the third decade is the preferred age of onset, and people of the Middle East and Japan have a greater risk of being affected (Foster and Nguyen 2000). By definition, the identification of at least two of the main symptoms enables the diagnosis to be established, while other common symptoms include thrombophlebitis, arthralgia, or arthritis. In rare cases, neurological symptoms may be identified, indicating a secondary involvement of the central nervous system and an aggravation of the disease, (Kupersmith 1993) (see 7.3.2.1.2.1). The main feature of cerebral CNS involvement of this multisystem, immune-related vasculitis is chronic, relapsing, inflammatory cellular infiltration around venules and capillaries, resulting in dural sinus thrombosis, infarctions, or aseptic meningitis (Chajek and Fainaru 1975; Kupersmith 1993; Zierhut et al. 1997; Wechsler et al. 1999).

Ocular and oral lesions most frequently represent the first clinical signs. The classic ophthalmologic finding in approximately one-third of cases is a sterile granulomatous anterior uveitis, presenting with pathognomonic hypopyon iritis, occasionally accompanied by aqueous effusion, and frequently followed by panuveitis. Recurrent iridocyclitis may result in visually significant cataract, as well as in anterior and posterior synechia formation with subsequent glaucoma (Foster and Nguyen 2000). Retinal phlebitis and/or retinal vein thrombosis with exudates and hemorrhages are the classical posterior segment findings (Foster and Nguyen 2000; Kupersmith 1993) (Fig. 6.23). The leading neuro-ophthalmological symptom is uni- or even bilateral optic neuropathy.

Most of the secondary inflammatory ocular processes are not differentiated by modern imaging techniques, although these may help in clarifying the suspected underlying disease. The clinical differential diagnosis includes all causes of retinal microangiopathy, i.e., AIDS-related retinal microvas culopathy with iridocyclitis, systemic lupus erythematosus (SLE), herpes retinitis and encephalovasculitis, infectious vasculitis, and Crohn disease as well as other rather rare diseases (Kupersmith 1993).

Only in rare cases does the first clinical presentation of Behçet disease not include the classical triple symptom complex of recurrent ulcerations of the oral and genital region and ocular inflammation, but involvement of the brain is observed in immune-related vasculitis (Chajek and Fainaru 1975; Banna and El-Ramahi 1991; Wechsler et al. 1999). These patients may present with dural sinus thrombosis or neurologic deficits resulting from brainstem and motor system involvement rather than affection of

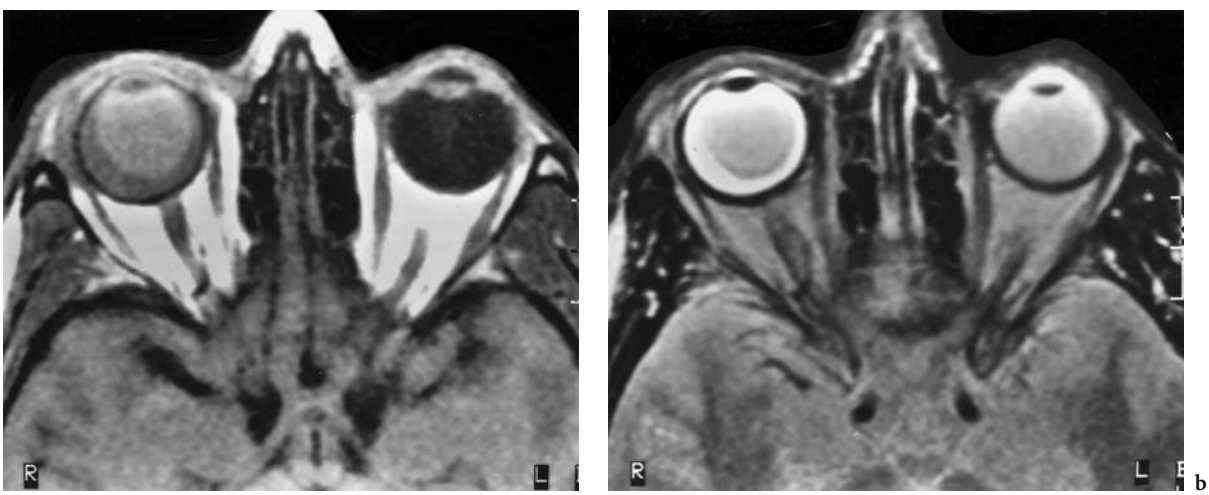

Fig. 6.23a,b. A 35-year-old man with acute visual loss of the right eye associated with known Behçet disease. Diagnosis: spontaneous vitreous body hemorrhage of the right globe and ipsilateral subchoroidal effusion. MRI: **a** Axial T1-weighted native view with subacute hemorrhage of the right vitreous body indicated by slight signal enhancement compared with the left globe. In addition, a comparison with the normal signal of the left globe indicates the presence of effusion characterized by signal diminution at the posterior part of the globe. **b** Corresponding T2-weighted, proton density image with demarcation of the fluid by signal enhancement of the proton-containing fluid (T2-time prolongation). At that time of examination, the signal of the right vitreous body appeared similar to the left one due to the fact that the isointense subacute hemorrhage of the vitreous body did not yet contain methemoglobin. The diagnosis of vitreous hemorrhage can only be made based on a comparison with the T1-weighted image. (From Müller-Forell and Lieb 1995)

the sensory system. The presence of central nervous system dysfunction indicates a severe, unfavorable, long-term course of the disease, even when a remittance and relapse without neurologic symptoms may occur (Kupersmith 1993; Akman-Demir et al. 1999; Wechsler et al. 1999).

Histopathology is characterized by perivascular lymphocytic infiltration and areas of minimal demyelination in the vicinity of the affected vessels, especially the veins, capillaries, and possibly the arterioles (Fukuyama et al. 1987; Numano 2000). They present as infarctions, best demonstrated on T2-weighted MR images, and are often seen in the brainstem (Fig. 7.78). Some authors consider the presence of cerebral venous thrombosis to be the first symptom of neuro-Behçet disease (Huss et al. 1992; Humberclaude et al. 1993; Proebstle et al. 1996; Tohme et al. 1997).

6.1.3.2.2 Sarcoidosis

Sarcoidosis is a chronic, multisystemic, granulomatous disorder of unknown etiology, involving any organic system, with clinical symptoms of central nervous system affection in approximately 10% of patients (Clark et al. 1985; Hayes et al. 1987; Rothova 2000) (see Sect. 7.3.2.2.3). Direct central nervous and ocular involvement may mimic a large number of more common diseases. Most of the central nervous system sarcoidotic granulomas have an affinity for the meningeal layers (Lexa and Grossman 1994); uveitis as a frequent and early feature of sarcoidosis is a common ophthalmoscopic finding (Rothova 2000), but rarely seen on imaging (Fig. 6.24). In the differential diagnosis of optic nerve or optic nerve sheath involvement, the idiopathic orbital inflammation may look very similar (Carmody et al. 1994).

6.1.4 Miscellaneous Lesions

6.1.4.1 Detachment of the Different Layers of the Globe

In rare cases, detachment of different layers of the globe may present as the only or accompanying feature of choroidal and/or retinal pathology. In healthy people, these layers are not separated by spaces, but these may be created in the course of pathologic disorders due to an accumulation of either serous or hemorrhagic fluid (Mafee 1996).

As described in the chapter on anatomy, the ocular globe consists of three primary layers:
1. the sclera,
2. the uvea,
3. the retina.

The sclera represents the outer coat and is composed of collagen-elastic tissue.

The uvea also consists of three components: the choroid, the ciliary body, and the iris. The choroid is located between the sclera and the retina, and both structures are separated by Bruch's membrane, a 5-layer membrane formed by the basal lamina of retinal pigment epithelium (RPE) and the choriocapillaris, respectively.

The retina is histologically composed of seven layers. However, two principal parts may be distinguished from a functional point of view: (1) a thin inner layer, harboring sensory cells (photoreceptors), first and second order neurons, as well as neuroglial elements; (2) the hyaloid membrane of the vitreous body (membrana limitans interna) is located adjacent to the inner layer. The retinal pigment epithelium, the outer layer of the retina, nourishes the retina together with the vessels of the choroid (Mafee 1996; Bron et al. 1997).

Only under pathologic conditions, when an accumulation of fluid or hemorrhage may occur, do possible spaces between these layers become visible and distinguishable by imaging techniques. A thorough knowledge of the anatomic features of the detachment enables the differentiation of three potential spaces, each exhibiting a characteristic configuration on CT and/or MR (see Table 6.1):
1. the posterior hyaloid space. Posterior hyaloid detachment in adults over 50 years of age is caused by physiologic liquefaction of the vitreous body. In myopic individuals, it may generally occur at a younger age. Posterior hyaloid detachment may also occur in infants with (PHPV or in traumatic disease (Fig. 6.25, 6.28). On imaging, it presents as gravitational layering fluid (Goldberg and Mafee 1983; Mafee 1996).
2. the subretinal space. Retinal detachment is characterized by a V-shaped configuration of the detached retinal layers. The apex is characteristically directed towards the optic disc, resulting from the attachment of the retina to the optic nerve centrally and to the pars plana of the ciliary body. This configuration does not extend to the ciliary body, as the retina terminates peripherally at the ora serrata. This is an important differential diagnostic criterion to choroidal detachment (Mafee 1996).

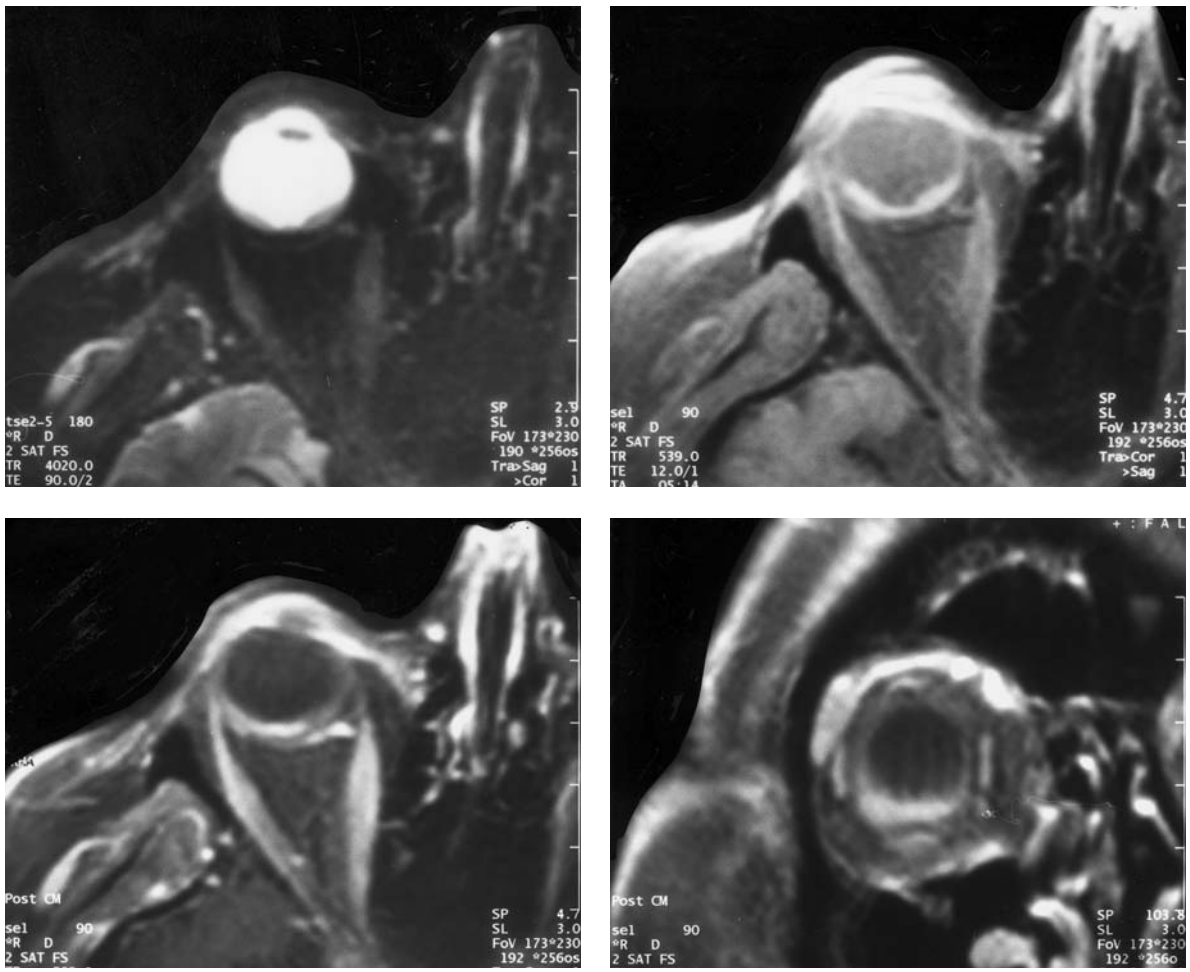

Fig. 6.24a–d. A 47-year-old woman with chronic pulmonary sarcoidosis, presenting with acute uveitis. Diagnosis: uveal and retro-ocular granuloma in sarcoidosis. MRI: **a** Axial T2-weighted (FS) image demonstrating thickening of the choroid bilateral to the optic nerve. **b** Axial T1-weighted native (FS) scan (3 mm below **a**) showing primarily hyperintense infiltration at the same site. **c** After i.v. gadolinium, no enhancement of existing granulomas, but another, apparently new granuloma is visible at the center of the previous infiltration. Additional extra- and retro-ocular granuloma, sparing the sclera, can be identified by enhancement. **d** Coronal T1-weighted, contrast-enhanced (FS) view with confirmation of the granuloma with inferior location

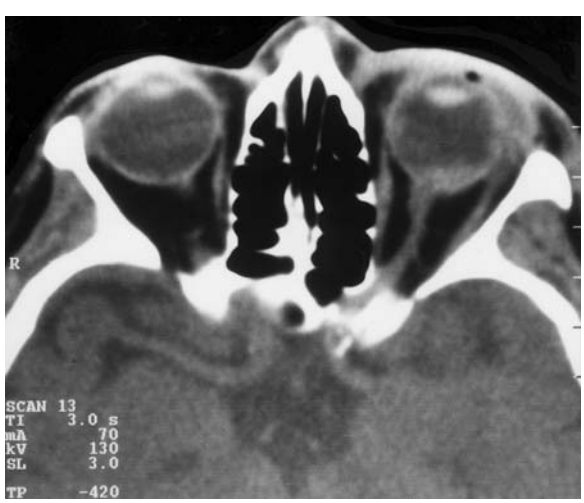

Fig. 6.25. A 73-year-old woman suffering from acute visual loss after a sudden fall. Diagnosis: acute hemorrhage into the posterior hyaloid space. Axial CT: no apparent fracture, but a hyperdense area identified at the posterior left globe was diagnosed as intravitreous hematoma; diagnosis confirmed at surgery

Table 6.1. Imaging characteristics of different detachments of the globe

	disease	imaging	
posterior hyaloid detachment	adults: macular degeneration infants: PHPV	vitreous, retrohyaloid space fluid-fluid level	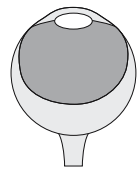
retinal detachment	any choroidal lesion! mass subretinal hemorrhage macular degeneration trauma	v-shaped with apex to optic disc lentiform -folds (best seen on coronal view)	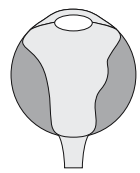
choroidal detachment	after trauma, after intraocular surgery, contusion, choroidal inflammation, (glaucoma-therapy) a) haemorrhagic b) serous caused by ocular hypotony	a) lentiform b) crescent-like, semilunar to ring-shaped	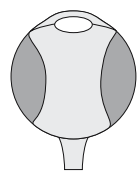 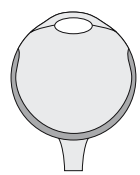

Although very thin and beyond the limits of resolution on CT and/or MRI, the significant contrast difference between subretinal effusion (mostly hyperintense on MRI) and the vitreous cavity outlines the retina. Retinal folds (Fig. 6.27d), mainly seen on coronal/sagittal MRI, represent detached and folded retinal leaves (Mafee 1996). Any choroidal lesion may eventually produce retinal detachment (Figs. 6.26, 6.3), most frequently seen in adults as neoplasms like malignant melanoma and choroidal hemangiomas.

3. the subchoroidal space. Choroidal detachment may occur in two different forms with different imaging characteristics, i.e., serous and hemorrhagic choroidal detachment. Although the etiology of both forms may be similar, as they may occur after intraocular surgery, penetrating ocular injury, or inflammatory disorders (Mafee and Peyman 1984; Mafee et al. 1988; Mafee 1996), hemorrhagic detachment presents as a lens-like configuration, sometimes difficult to differentiate from retinal detachment. Even if large and irregular, it is defined by the more parallel configuration of subchoroid hemorrhage (Fig. 6.27), caused by the fixation of the choroid by the posterior ciliary arteries and veins at the optic disc and macula (Weiter and Ernest 1974; Mafee and Peyman 1987; Mafee 1996).

Serous choroidal detachment is characterized by a crescent or ring-shaped formation, isodense or sometimes hyperdense on CT and hyperintense on T2-weighted MRI (Weiter and Ernest 1974; Mafee and Peyman 1987; Mafee 1996). The underlying cause of serous choroidal detachment is essentially ocular hypotony as a result of inflammatory diseases, or ocular surgery (mainly filtrating glaucoma surgery) (Wing et al. 1982; Mafee and Peyman 1984; Mafee et al. 1988). Increased permeability of the choroidal capillaries caused by ocular hypotony leads to diffuse swelling of the entire choroid followed by choroidal effusion (Fig. 6.23, Fig. 6.29, Fig. 6.6), choroidal edema, and finally fluid accumulation in the potential subchoroidal space, seen as choroidal detachment (Mafee 1996).

(Text continues on p. 174)

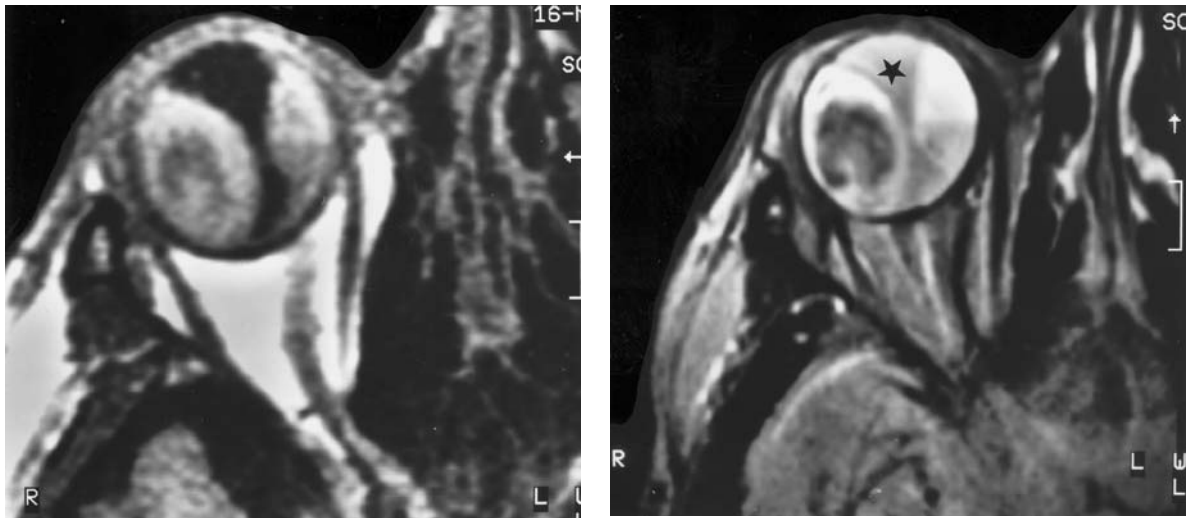

Fig. 6.26a,b. A 36-year-old woman with acute visual loss 1 day after intraocular operation. Diagnosis: subretinal hemorrhage. Axial MRI: **a** T1-weighted native image (head coil and focal magnification) with biconvex configured, medial and lateral subchoroidal hemorrhage. The low signal at the center of the lateral area represents fresh, intracellular hemoglobin, while sedimentation of blood particles is seen in the medial area. **b** Corresponding T2-weighted sequence (surface coil over both orbits and magnification) also demonstrates signal reduction due to the fresh hemorrhage. Note normal signal intensity of the intact vitreous body (*star*) in both acquisitions (T1-weighted: hypointense, T2-weighted: slightly hyperintense)

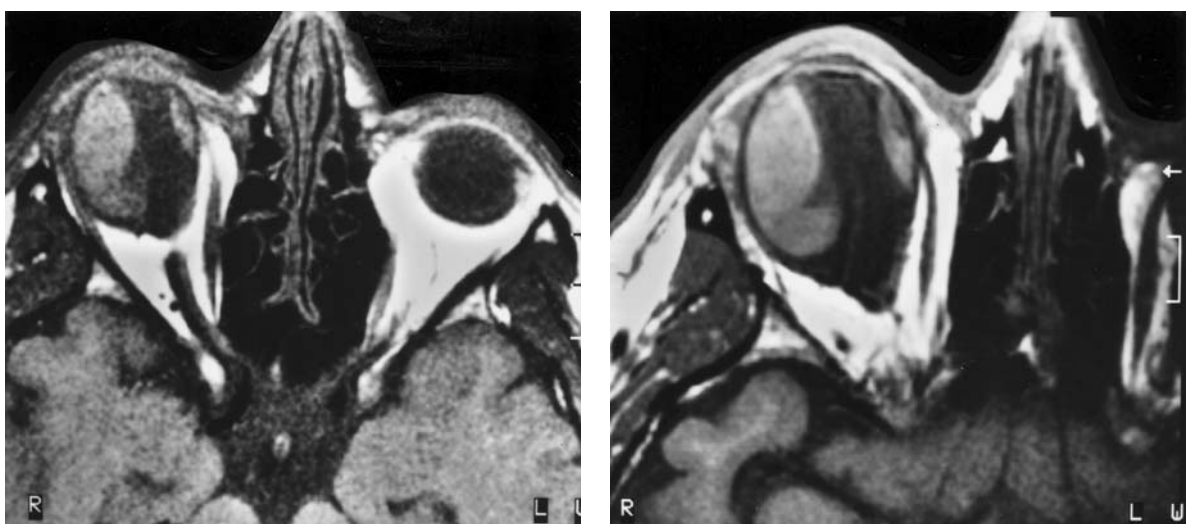

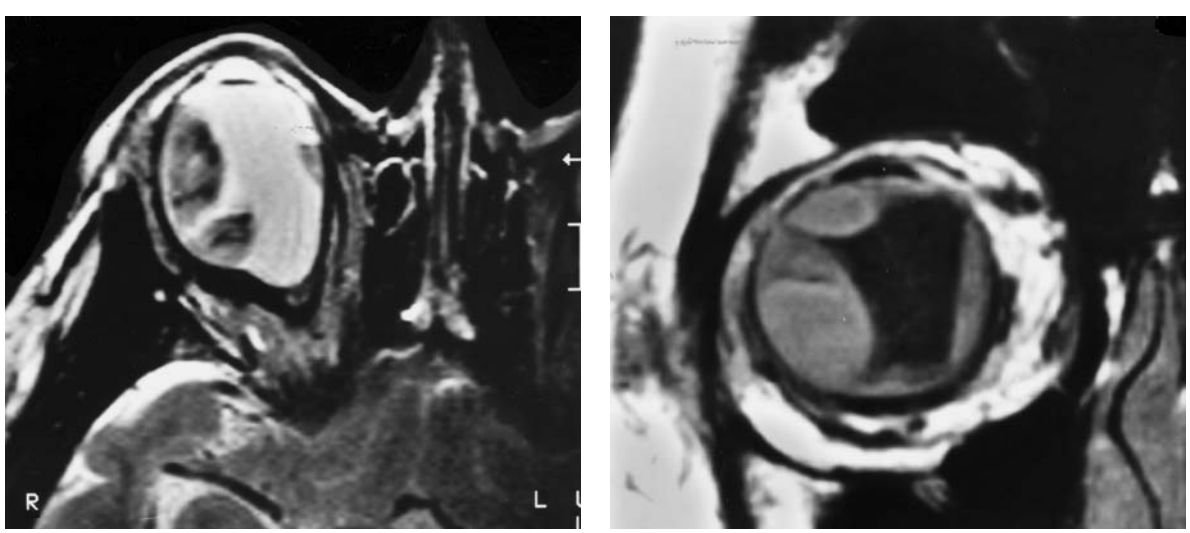

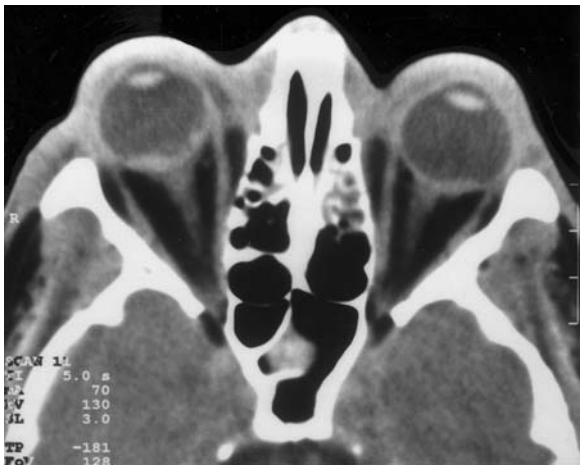

Fig. 6.28. A 19-year-old man with vision loss after a black-powder explosion. Diagnosis: bilateral intravitreous hematoma, with detachment. Axial CT with small, bilateral, hyperdense fluid levels at the posterior circumference of both globes

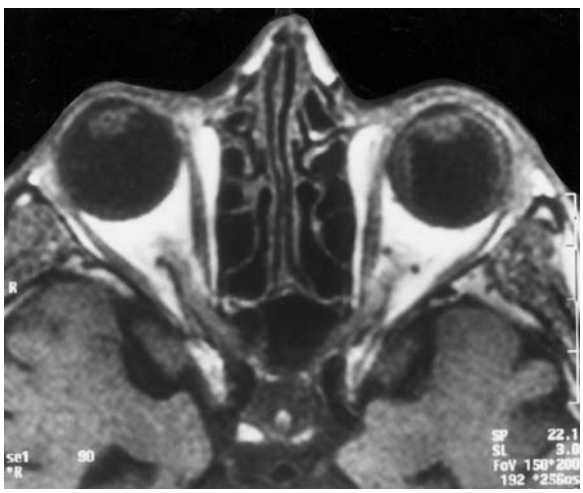

a

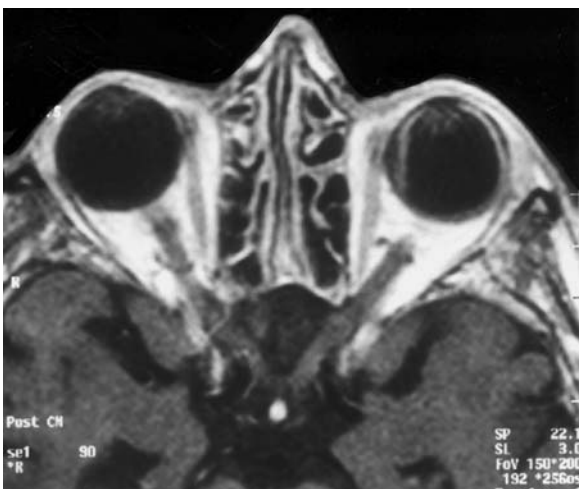

b

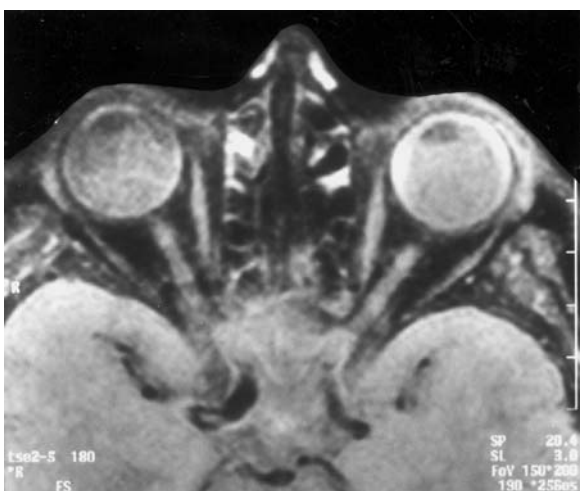

c

Fig. 6.29a–c. A 75-year-old woman with paroxysmal glaucoma. Diagnosis: choroidal detachment of the left globe. MRI: **a** Axial T1-weighted image, showing the bilateral hyperintense layer of the left choroid, enhancing after i.v. gadolinium in (**b**) corresponding contrast-enhanced, T1-weighted view. **c** Corresponding proton density image with typical fluid signal enhancement and characteristic shape

◁ **Fig. 6.27a–d.** A 36-year-old woman with acute pain symptomatology developing 2 days after glaucoma operation. Diagnosis: expulsive hemorrhage arising from the origin of the vortex vein. MRI: **a** Axial T1-weighted native image (head coil) identifying biconvex, subchoroidal fluid with mixed signal intensity and poor SNR compared with **b**. Note the different size of the right (myopic) and left (normal) globes. **b** Corresponding T1-weighted measurement with surface coil, demonstrating superior solution of the intraglobal and intraorbital structures. Iso- to slight hyperintensity of the fresh hemorrhage with fluid-fluid level. **c** Corresponding axial T2-weighted image with hypointense hemorrhage (performed with surface coil as in **b** and **d**). The signal loss of the surface coil towards the left orbit is more apparent here than on the T1-weighted image. **d** Coronal T1-weighted image confirming additional bleeding in the superior globe as well as additional subretinal hemorrhage inferiorly. In addition to expulsive hemorrhage, note the staphyloma, viewed as an protrusion of the globe into the optic nerve in **b** and **c**

6.1.4.2 Traumatic Lesions (Including Foreign Bodies, Penetrating Injuries, and Vitreous Hemorrhage)

Physiologically, the globe (eyeball), its neurovascular structures and muscles are protected by the bony orbit and shock-absorbing retrobulbar fat. Nevertheless, the globe, as the most anterior and therefore most exposed structure of the visual system, is extremely vulnerable. On the other hand, the external integrity of the globe and orbit should never lead to the assumption of intact, unaffected retroglobal orbital structures, since innocuous orbital trauma may produce devastating functional deficits (Fig. 6.30). Injury of the globe may occur as a component of major facial trauma or as an isolated event (Fig. 6.31). Different causes as, e.g., motor vehicle (car/motorcycle) accidents (Fig. 6.32) or sports-related injuries might contribute to the relatively common occurrence of orbital trauma (Johnston 1975). Orbital injuries may be divided into blunt trauma and penetrating injuries. While the former are due to an impact with low velocity forces, the latter are the result of impact at proportionally high energy with penetration of the object (Anderson et al. 1982). While most metallic foreign bodies are well-tolerated, copper and iron may cause purulent inflammation, and by far more disastrous, almost immediate severe toxic damage of the retinal photoreceptors. Iron may induce retinal siderosis, while organic foreign bodies (e.g., wood) are likely to cause microbial endophthalmitis (Grant 1974; Gerkowicz et al. 1985; Ho et al. 1996; Carmody 2000).

The care of these patients requires an interdisciplinary approach by different specialized physicians (general surgeons, neurosurgeons, radiologists, ophthalmologists). CT is the diagnostic method of choice in traumatic lesions involving the orbit. It is readily available and enables both accurate visualization of bony and soft-tissue injuries and exact localization of (mostly ferromagnetic) foreign bodies without the risk of dislocation. In cases of extreme swelling of the lid, where ophthalmoscopy is impossible, CT can visualize the full extent of the injury rapidly and accurately (Fig. 6.33).

There is a great variety of injuries to the globe, ranging from rupture (Fig. 6.34) to dislocation of the lens (Figs. 6.35–6.37), and vitreous (Fig. 6.32), retrohyaloid

(Text continues on p. 177)

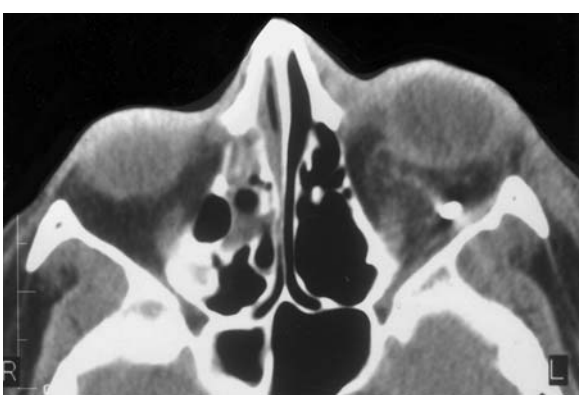

a

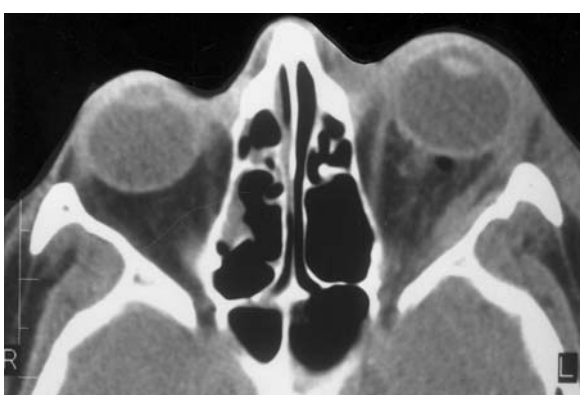

b

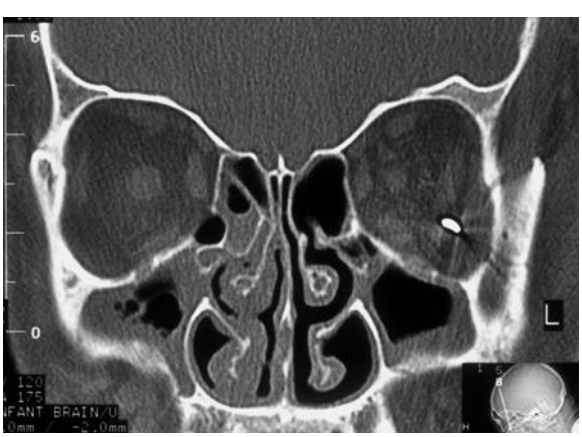

c

Fig. 6.30a–c. A 33-year-old man who suffered an accident with a foreign body. Diagnosis: double perforation of the left globe by metallic foreign body. CT: **a** Axial view of the inferior orbit demonstrates the location of the foreign body as retrobulbar in the intraconal area. **b** Axial view at the level of the inferior part of the optic nerve showing only a retrobulbar air inclusion, which is pathognomonic of a double perforation. **c** Coronal view in bone window with definition of the foreign body in the inferior and lateral intraconal area

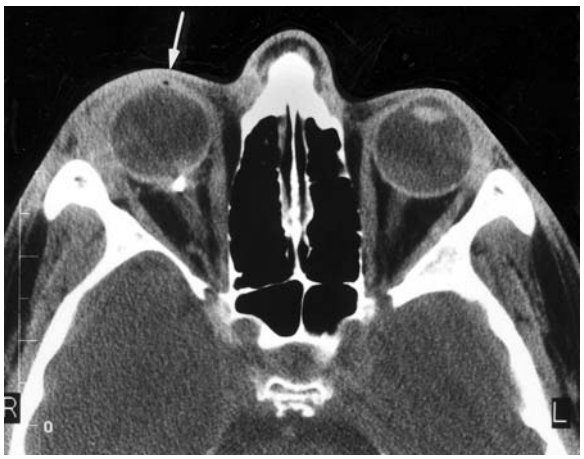

a

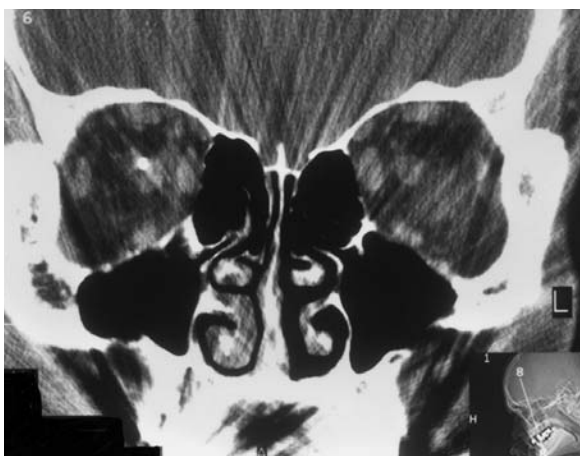

b

Fig. 6.31a,b. A 26-year-old man with complete visual loss after an accident working around the house. Diagnosis: perforation of the globe by a foreign body. HR-CT: **a** Axial view with double perforation of the globe, identified by a small air bubble in the anterior sclera (*white arrow*), dislocation of the lens (comparison with the left side), and localization of a metallic foreign body at the upper level of the cribriform plate. **b** Coronal view showing the location of the foreign body at the origin of the optic nerve. (With permission of Müller-Forell 1998)

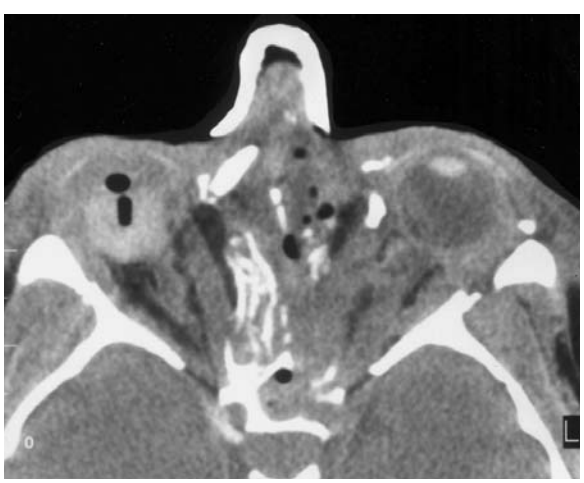

Fig. 6.32. Axial CT of a 20-year-old woman with bilateral vision loss (maximum dilation of the left pupil, no light reaction) 20 h after a frontal car accident (wearing seat belt at time of accident). Diagnosis: right globe rupture with air inclusions, rupture and hematoma of the right optic nerve, fracture of the left optic canal with injury to the left optic nerve. Note the fracture of all middle face bones and bilateral orbital walls, swelling of the medial and lateral rectus muscle, suspicion of intramuscular hematoma (plaster splint of the nasal bones)

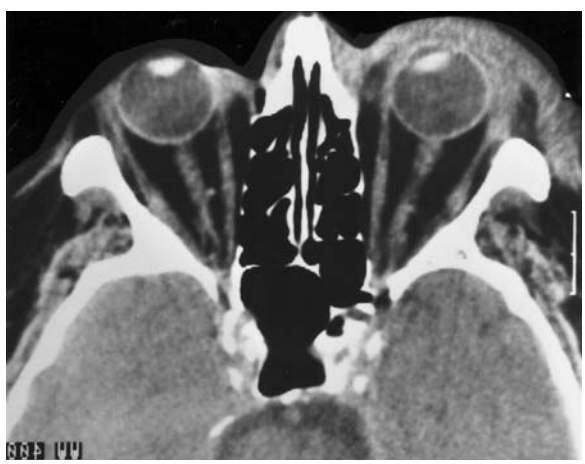

Fig. 6.33. A 69-year-old man with blunt orbital trauma. Ophthalmoscopy was impossible due to the severely swollen lid. Indication for imaging was the exclusion of a retrobulbar hematoma; CT showed a regular orbit in addition to the preseptal conjunctival and lid edema

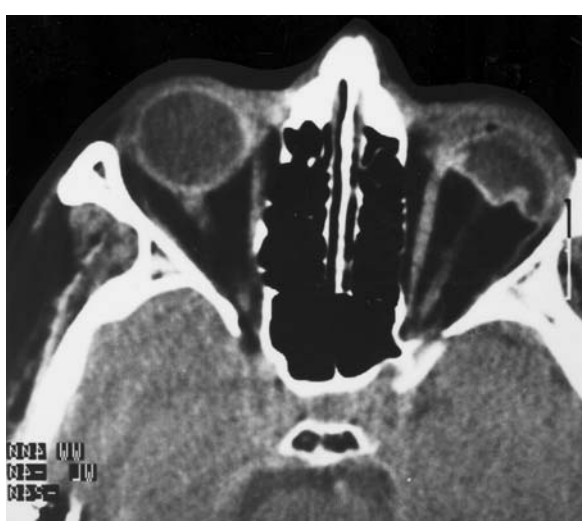

Fig. 6.34. A 43-year-old male car accident victim. Diagnosis: rupture of the left bulb. Axial CT

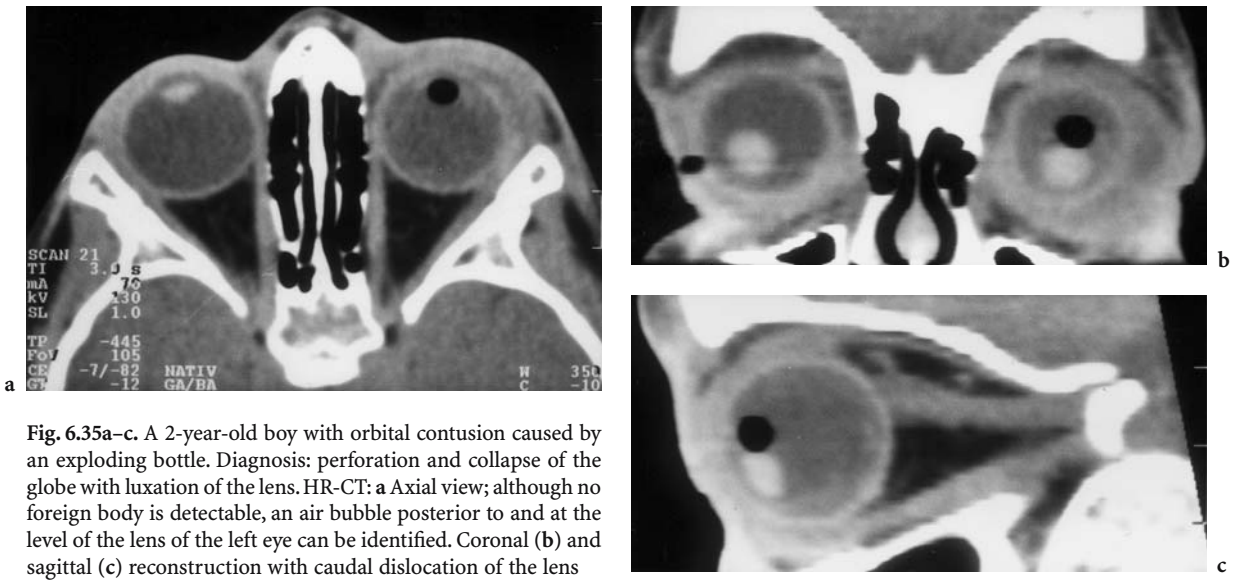

Fig. 6.35a–c. A 2-year-old boy with orbital contusion caused by an exploding bottle. Diagnosis: perforation and collapse of the globe with luxation of the lens. HR-CT: **a** Axial view; although no foreign body is detectable, an air bubble posterior to and at the level of the lens of the left eye can be identified. Coronal (**b**) and sagittal (**c**) reconstruction with caudal dislocation of the lens

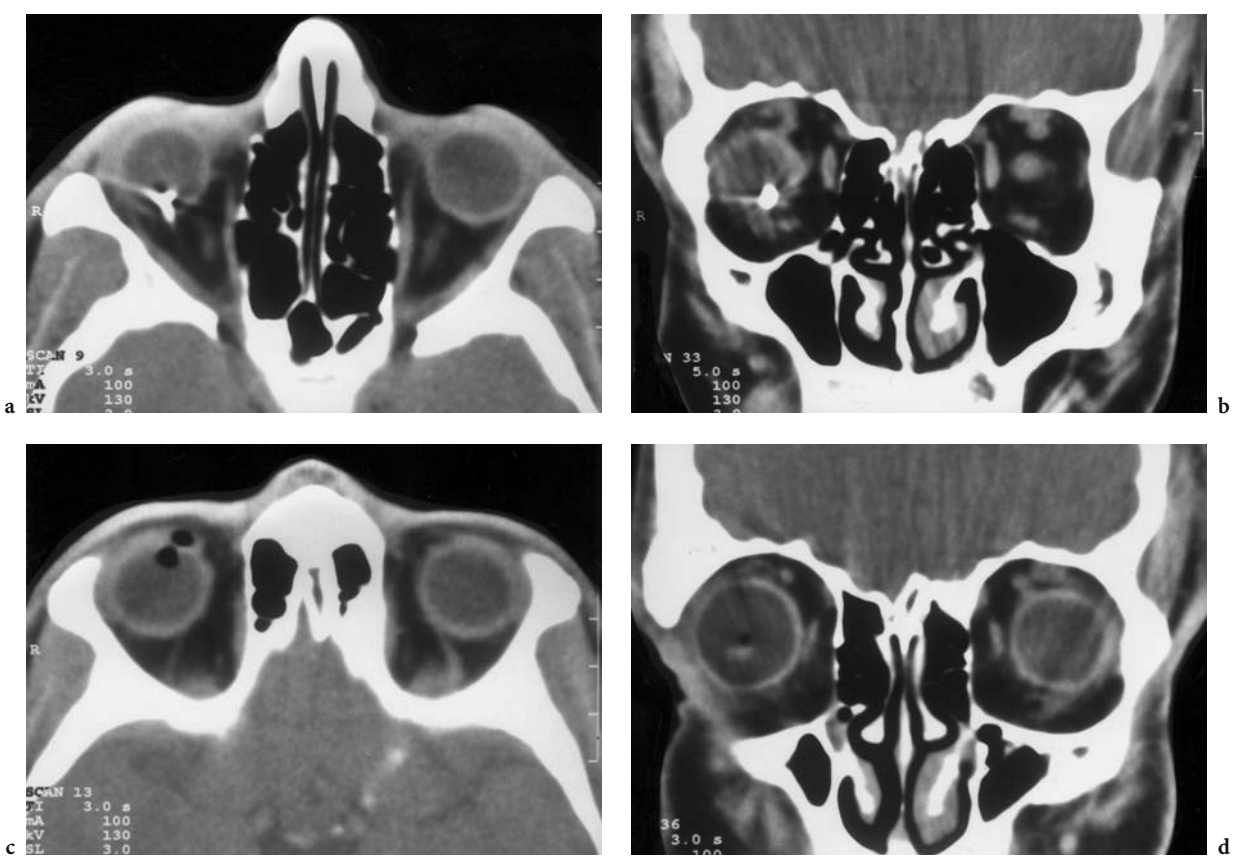

Fig. 6.36a–d. A 22-year-old man with vision loss of the right eye after a hammer-chisel injury. Diagnosis: keratorhexis, lens dislocation, and iris injury due to foreign-body injury. CT: **a** Axial view of the inferior orbit with definition of the metallic foreign body in the posterior region of the right globe. **b** Corresponding coronal view. **c** Axial view of the superior orbit: air inclusion defines the location of the entrance of the foreign body. **d** Corresponding coronal view depicts an additional air inclusion superior to a hyperdense formation, confirmed on vitrectomy as the lens

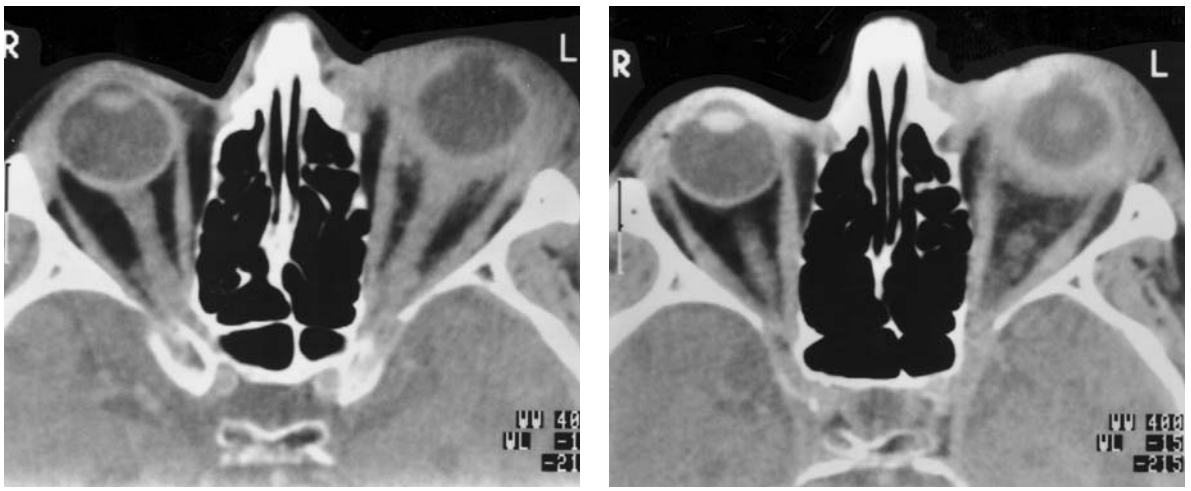

a b

Fig. 6.37a,b. A 48-year-old male car accident victim. Diagnosis: luxation of the lens, episcleral and retrobulbar hematoma. Axial CT: **a** Note the dislocation of the lens into the vitreous body as well as conjunctival hematoma, and in **b** thickening of the sclera due to the presence of an episcleral and retrobulbar hematoma, as well as the asymmetrical width of the globe when compared with the right side

(Figs. 6.25, 6.35), or retro-ocular hematoma (Figs. 6.37). In extensive facial injuries, where imaging is primarily performed to exclude extraconal and/or intracerebral lesions, damage to the globe may also be seen. In case of a suicidal patient with bullet injury in the absence of direct global trauma (Fig. 6.198), rupture of the globe may be caused by the development of shock waves. Subretinal/subchoroidal hemorrhages were found in a young man after an explosion in the course of a black powder experiment (Fig. 6.28). In cases with foreign body injuries, CT can define the exact location of the object in the respective orbital structure (Fig. 6.36). In the case of a young man who was admitted to hospital with an acute, complete visual deficit as a result of an injury suffered doing home repair work, ophthalmoscopy could not identify the location of a metal fragment, which had obviously perforated the globe twice, while CT accurately defined the fragment location at the site of the papilla (Fig. 6.31).

Hemorrhagic choroidal detachment may occur as a complication of intraocular surgery. Although the diagnosis can be made with ultrasound, MRI (especially using a surface coil) is the method of choice in defining the extent and location of the hemorrhage, which is of particular importance with a view to the prognosis for the involved eye (Mafee and Peyman 1984) (Figs. 6.26, 6.27).

Phthisis bulbi referring to a scarred, retracted, shrunken globe may be defined as a type of secondary (developmental) microphthalmos (Harnsberger 1990) (Fig. 6.38). It is generally associated with dystrophic calcification and may be the result of infection, penetrating trauma (Fig. 6.39), repeated orbital surgery, or noninfectious inflammation (Carmody 2000).

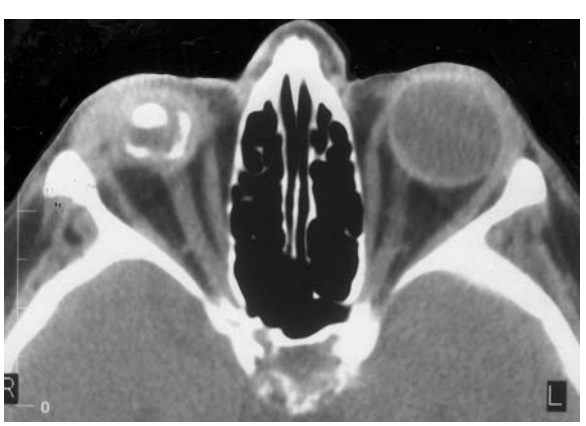

Fig. 6.38. A 66-year-old woman with phthisis bulbi of the right globe. Axial CT: small globe with calcification of the lens and a part of the globe

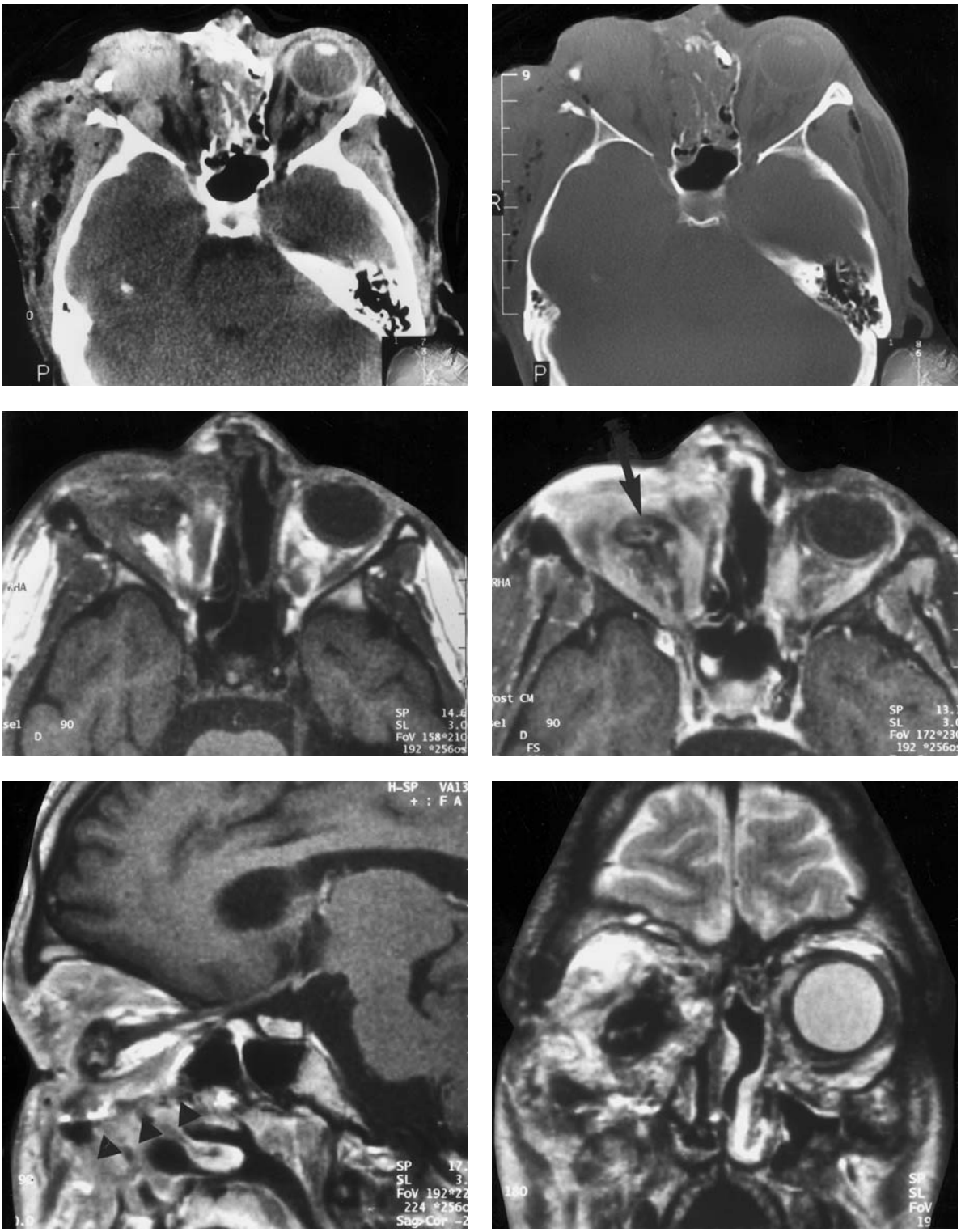

Fig. 6.39a–f. A 19-year-old male car accident victim (no seat belts worn at the time of the accident). At follow-up (6 months after accident), the patient presented with suspicion of endophthalmitis. Diagnosis: right globe rupture with vitreous body hemorrhage, multiple orbital wall fractures, developing posttraumatic phthisis. Axial CT: **a** Multiple fractures of all orbital walls with penetrating fragment into the globe, vitreous hemorrhage, and post-bulbar hematoma. **b** Corresponding bone window. MR (carried out 6 months later): **c** axial T1-weighted view with small, shrunken right bulb in the inferior orbit and dislocation of the medial external muscle into the fractured ethmoidal sinus. **d** Corresponding contrast-enhanced (FS) view with enhancement of fibrous scar tissue as intense as enhancement of the external muscles. Note signal enhancement of the residual choroid (*arrow*). **e** Parasagittal, T1-weighted, contrast-enhanced (FS) view, showing the integrity of the optic nerve, although differentiation of the external muscles from scars in the area is difficult. Note the irregularity of the orbital floor (*arrowheads*). **f** Coronal T2-weighted image, demonstrating posttraumatic enlargement of the entire right orbit and hyperintensity of the scars in the vicinity of the shrunken globe

6.2 Conal/Intraconal Area

6.2.1 Solid Tumors

6.2.1.1 Peripheral Nerve Tumors

The orbit is host to a great number of nerves, including the motor branches of cranial nerves III, IV, VI, sensory branches of cranial nerve V, as well as sympathetic and parasympathetic branches, each of which is a potential starting-point for tumor growth. Peripheral nerve tumors account for about 4% of all orbital neoplasms with a preference for (plexiform) neurofibromas and schwannomas (Henderson 1994). Although their location is discussed in special chapters on these tumors, they may also be located in the intraconal as well as extraconal orbital compartment, depending on their origin in the course of the multiple nerves and their branches.

6.2.1.1.1 Schwannoma

Schwannomas (synonyms: neurinoma, neurilemoma) are benign, slowly progressing, encapsulated tumors (WHO I) composed of differentiated spindle-shaped neoplastic Schwann cells, mostly including solid cells (Antoni A pattern) and loosely textured, often lipidic areas (Antoni B pattern). Although not exclusively, they do have a high incidence in patients with neurofibromatosis type II (NF 2). Orbital schwannomas account for only 1%–8% of all orbital tumors (Housepian et al. 1982; Henderson 1994). They usually originate from sensory branches of the trigeminal nerve (Jakobiec and Font 1986) and present as globoid, encapsulated masses measuring from a few millimeters to centimeters in size (Woodruff et al. 2000). Patients with orbital schwannoma are normally adults and present with a slowly progressing, mostly painless proptosis (Fig. 6.40) (De Potter et al. 1995).

Imaging shows a well-defined, intra- or extraconal, ovoid to elongated mass (Fig. 6.40), suggestive of an expanding peripheral nerve tumor. On MRI, schwannoma may present with a homogeneous or just as well heterogeneous signal, depending on the histologic features of the tumor. On T1-weighted images, they have an iso- to hypointense signal in relation to the orbital fat and demonstrate a varying degree of contrast enhancement (Figs. 6.41, 6.93), with a more intense signal enhancement of the myxoid portions of the tumor (Antoni B) (De Potter et al. 1995; Abe et al. 2000). On T2-weighted images, these tumor portions show greater signal intensity compared with the more cellular parts, which renders the differential diagnosis from cavernous hemangioma, eccentric optic nerve sheath meningioma (Fig. 6.178), neurofibroma (Fig. 6.94), melanoma (Fig. 6.45), fibrous histiocytoma, and hemangiopericytoma (Fig. 6.92) more difficult (De Potter et al. 1995).

As another differential diagnosis, lymphoid hyperplasia, extending along peripheral sensory nerves (Fig. 6.167) or fascial planes and muscles, represents an extremely rare entity (Yeo et al. 1982).

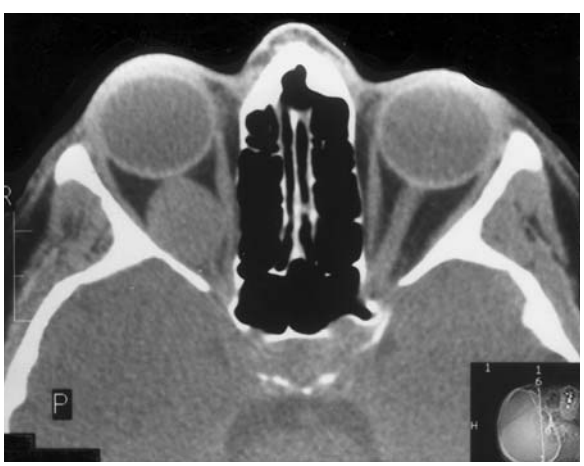

a

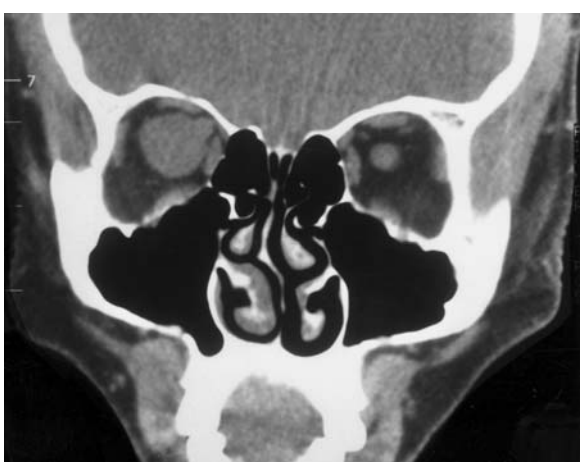

b

Fig. 6.40a,b. A 61-year-old woman with slowly progressing right axial proptosis and a history of painful pressure in the right orbit associated with a slowly progressing visual deficit. Diagnosis: neurinoma. CT: **a** Axial medial orbital view, showing a clearly defined intraconal mass, sparing the apex. **b** Coronal view demonstrates localization inferior and lateral of the dislocated optic nerve

6.2.1.1.2
Neurofibroma

Neurofibromas (WHO I) consist of neoplastic Schwann cells, perineurial-like cells, and fibroblasts in a matrix of collagen fibers and mucosubstances (Woodruff et al. 2000). Plexiform neurofibromas, the most common type affecting the orbit, present as elongated, multinodular, nonencapsulated lesions as they involve multiple trunks or fascicles of a large nerve, sometimes suggesting the image of a "bag of worms" (Woodruff 1996). These highly vascular, poorly defined, and diffusely infiltrating tumors represent an overgrowth of the components of a peripheral nerve (Harkin and Reed 1969). Diffuse neurofibroma, seen in the first decade of life, represents the most frequent manifestation of neurofibromatosis of the orbit, while localized neurofibromas are seen in middle-aged patients (Bilaniuk et al. 1990; De Potter et al. 1995; Carroll et al. 1999).

Neurofibromatosis type 1 (NF1) can be found in patients with multiple neurofibroma, although this tumor may occur as a sporadic, solitary nodule unrelated to any syndrome (Woodruff et al. 2000). Localized, singular neurofibromas present as a slow-growing, painless, well-circumscribed mass leading to axial exophthalmos.

Imaging in isolated neurofibroma depicts a circumscribed, oval to elongated, encapsulated, intra- or extraconal mass with mild contrast enhancement on CT (Fig. 6.42). MRI shows a serpiginous, irregular, often infiltrating mass, which may at times infiltrate the orbital fat with marked contrast enhancement, caused by the high vascular component (Bilaniuk et al. 1990; Carroll et al. 1999). On T1-weighted images, neurofibromas are seen as homogeneous iso-

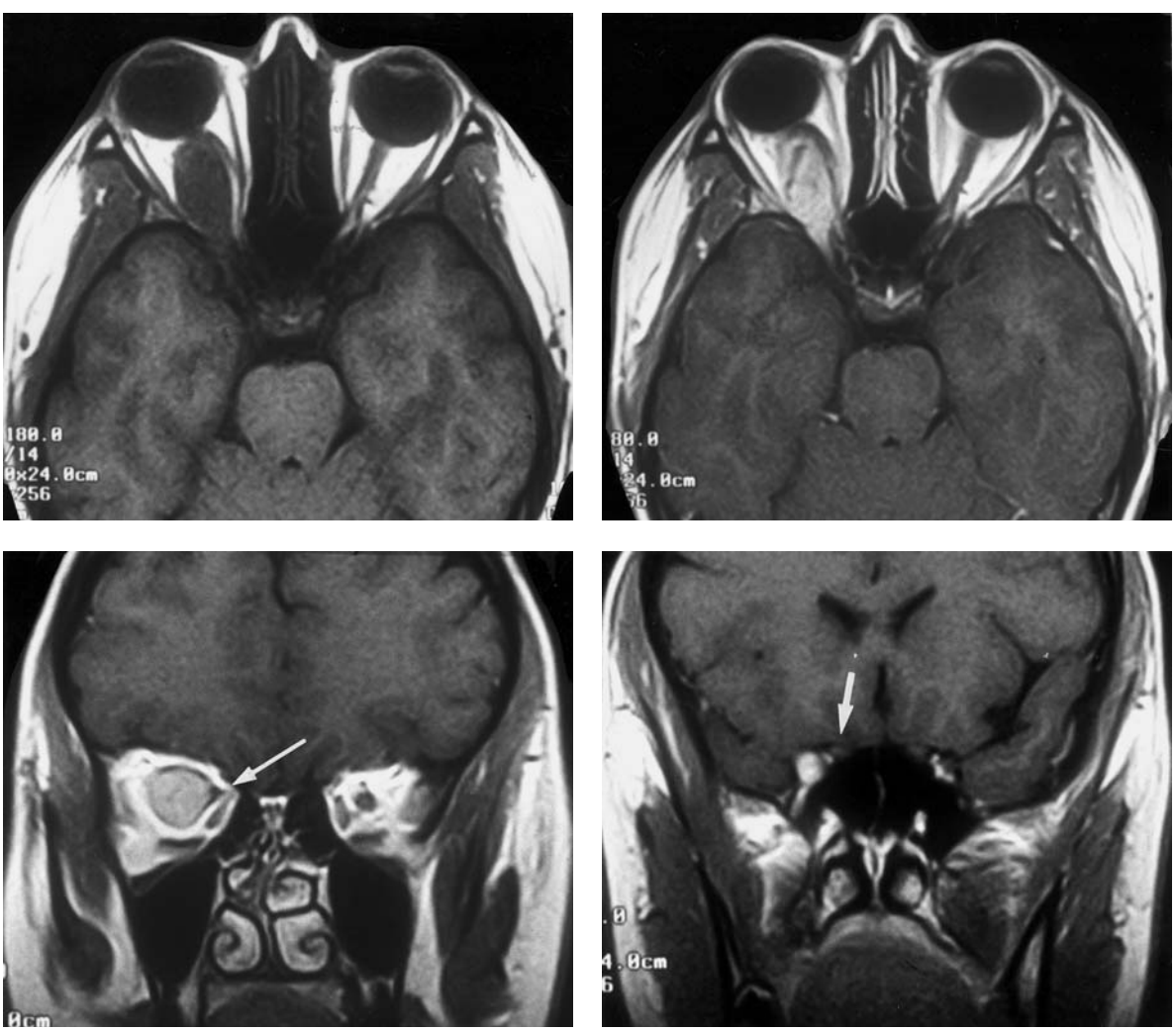

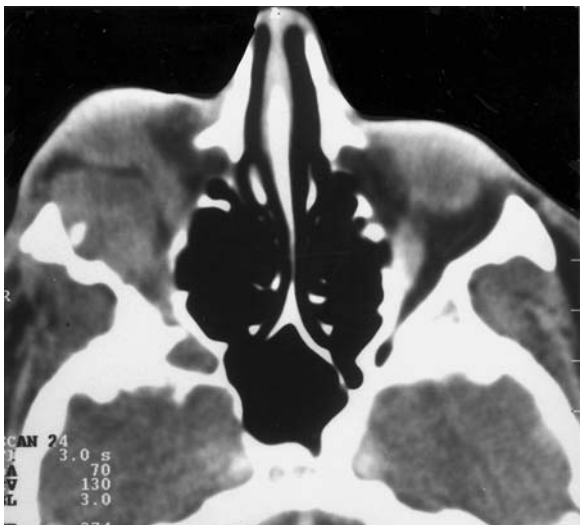

a

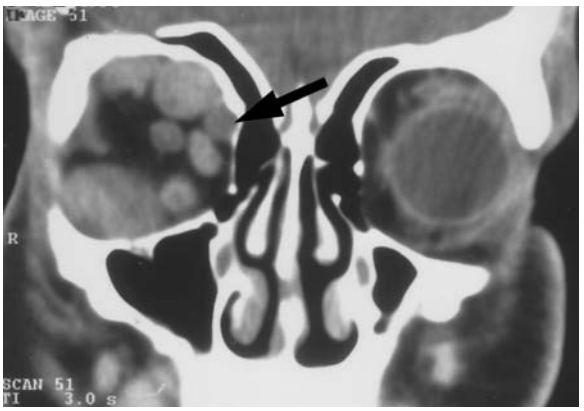

b

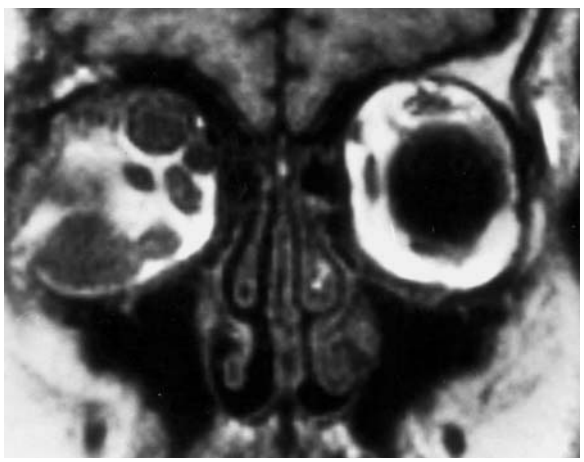

c

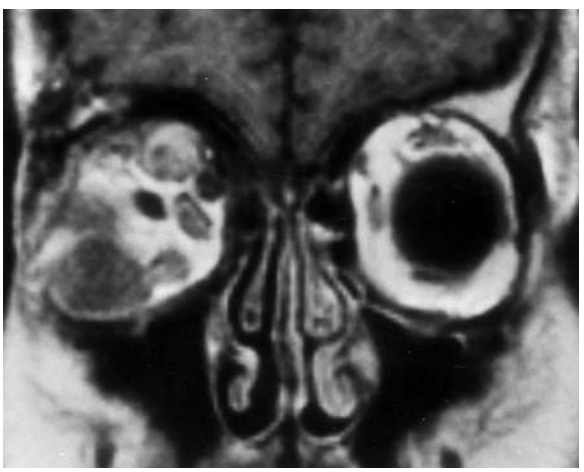

d

e

Fig. 6.42a–e. A 43-year-old man with known NF 1 and slowly progressing exophthalmos of the right side. Diagnosis: recurrent multiple intraorbital neurofibroma. CT: **a** Axial view of the inferior part of the orbit with a lesion lateral to and displacing the inferior rectus muscle. **b** Coronal view showing the tumor between the inferior and lateral rectus muscle. An additional tumor which is sharply differentiated from the surrounding tissue is visualized between the superior rectus and the oblique muscle (*arrow*), the latter with inferior displacement to the level of the medial rectus muscle. A comparison with the contralateral orbit demonstrates enlargement of all muscles. MRI: **c** corresponding coronal native T1-weighted image. **d** Following contrast enhancement, the smaller superior tumor exhibits an increase in signal intensity, compared with the inferior tumor as well as with the rectus muscles. (MR images with permission of Röntgeninstitut Unna.) **e** Histology (×55): dense network of a fibrillary connective tissue in the endoneural space of an enlarged peripheral nerve, surrounded by a thickened perineurium (with permission of Dr. Bohl, Department of Neuropathology, Medical School, University of Mainz)

◁ **Fig. 6.41a–d.** A 22-year-old woman with slowly progressing protrusion and sense of compression of the right eye, which was nearly blind since childhood. Diagnosis: neurinoma. MRI: **a** Axial T1-weighted view with a paraoptic, well defined tumor of the right intraconal area. **b** Corresponding contrast-enhanced view, demonstrating the kinking and medialization of the right optic nerve by the homogeneous enhancing tumor. Note the pointed configuration of the lesion at the orbital apex. **c** Coronal, T1-weighted, contrast-enhanced view in the middle of the orbit, where the compression and narrowing of the optic nerve (*white arrow*) are apparent. **d** Coronal, T1-weighted, contrast-enhanced view at the level of the superior orbital fissure. Apparently, the starting point of the tumor growth is the orbital fissure (most likely the abducent nerve) but not the optic nerve, which is unequivocally seen medially (*white arrow*). (With permission of the colleagues of the Röntgenologische Gemeinschaftspraxis Limburg/Lahn)

to hypointense tumors, while on T2-weighted images, they present with a homogeneous to heterogeneous signal characteristic (Fig. 6.94) (De Potter et al. 1995), sometimes with expansion into the bony walls and/or enlargement of the orbit (Bilaniuk et al. 1990; De Potter et al. 1995). Plexiform neurofibromas present as a poorly defined, irregular mass.

6.2.1.2 Lymphoma

The term lymphoma (syn. lymphoproliferative disorder) describes a heterogeneous group of neoplasms of the lymphoid system with distinct entities defined by clinical, histological, immunological, molecular, and genetic characteristics (Asao et al. 1998; Valvassori et al. 1999). With an increasing incidence, orbital lymphomas account for up to 55% of all malignant orbital tumors (Margo and Mulla 1998), whereas low-grade non-Hodgkin lymphomas (NHL) account for about 10% of all orbital masses (Shields et al. 1984b). Although most lymphoid tumors arise from lymph nodes, orbital lymphoma may represent the only or first manifestation of a generalized lymphoma (Fig. 6.43) or be associated with a generalized systemic disease (Valvassori et al. 1999). Lymphoproliferative disorders include benign, atypical, and malignant lesions. Most of those involving the orbit are B-cell lymphomas (White et al. 1996), although orbital lymphomas primarily belong to low-grade non-Hodgkin variants or extranodal mucosa-associated lymphoid tissue (MALT lymphoma) (De Potter et al. 1995; Polito et al. 1996; Galieni et al. 1997; Valvassori et al. 1999). The classification of leukemias and lymphomas has undergone radical changes as traditional morphologic and cytochemical descriptive classifications were superseded and replaced by molecular biologic, cytogenic, and immunophenotyping molecular genetic analysis. This analysis enables us to distinguish clonal from polyclonal lymphoproliferations, to determine the B- or T-cell identity of malignancies, the genetic lineage of neoplasms lacking surface antigens, and the developmental stage of early B- or T-cell precursors (Kawamoto and Miyanaga 1997; Specht and Laver 2000). MALT lymphomas are composed of cells ranging from small lymphocytes with few atypia to small lymphocytes with slightly irregular nuclei, to monocytoid B-cells, all of which have the potential for invasion of epithelial structures (Specht and Laver 2000). Prognosis and management decisions, regardless of whether this involves radiotherapy alone (with excellent local control in MALT lymphoma), systemic chemotherapy alone or in combination with radiotherapy, are determined by anatomic site, stage, and histological features (Bairey et al. 1994; Polito et al. 1996; Valvassori et al. 1999; Agulnik et al. 2001). Orbital involvement in leukemia, a disease of the bone marrow predominantly occurring in childhood, is not common (Valvassori et al. 1999).

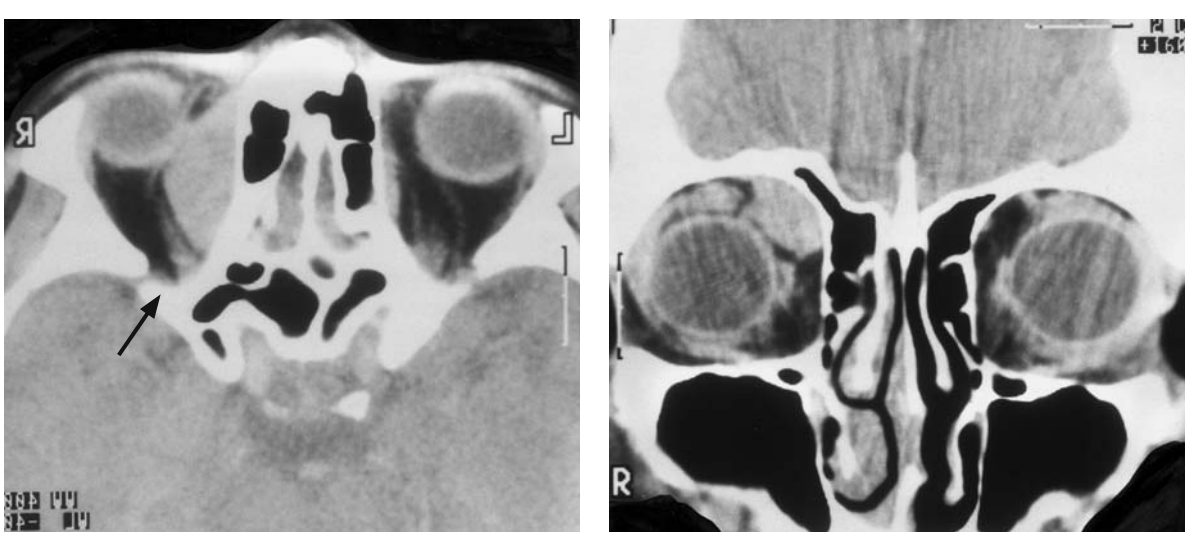

a b

Fig. 6.43a,b. A 32-year-old man with double vision. Diagnosis: lymphoma of the right superior oblique muscle as the first manifestation of generalized lymphoma. CT: **a** Axial view with a sharply defined, tumor-like mass in the right superior medial orbit and slight impression of the proximal part of the superior rectus muscle (*arrow*). Note the small size of the superior ophthalmic vein visualized in both orbits. **b** Coronal view showing additional involvement of the superior oblique muscle. (With permission of Müller-Forell 1998)

Clinical findings in orbital lymphoma include painless, mostly unilateral (in rare cases bilateral; Fig. 6.138) proptosis and motility disturbances in patients (most commonly) older than 50 years. Although any other orbital tissue may be involved (Fig. 6.44), the preferred orbital structure is the lacrimal gland (see Sect. 6.3.4.2.3). The patient presents with extra-axial proptosis, combined with an inferior displacement of the globe and a smooth, palpable mass of pink color in the superior lateral orbit. Even in cases of the rare involvement of extraocular muscles (Fig. 6.43), eye motility is not significantly impaired because of the presence of only a small amount of collagen deposition (Weber et al. 1996b).

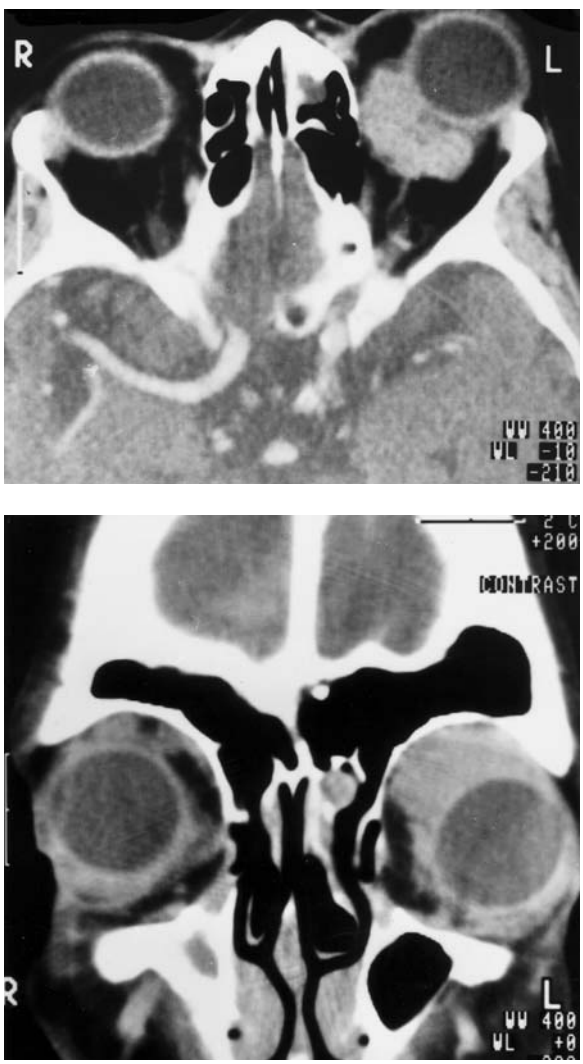

a

b

Fig. 6.44a,b. An 82-year-old woman with slowly progressing, painless, unilateral, extra-axial proptosis of the left eye. Diagnosis: lymphoma. Contrast-enhanced CT: **a** Axial and **b** Coronal view with a clearly defined retro- and suprabulbar located formation with slight enhancement, not separated from the superior rectus muscle, but adapting to the contour of the globe; the latter finding excludes the presence of hemangioma as a specific differential diagnostic criterion. (With permission of Müller-Forell and Lieb 1995)

6.2.1.3 Miscellaneous

Most malignant tumors of the orbit are metastases from peripheral malignancies, but at times they originate in the orbit itself. Primary melanoma of the orbit (Fig. 6.45), although a rare entity, should be included in the differential diagnosis when a solid, irregular mass is seen which exhibits indifferent, but mainly homogeneous signal characteristics and signs of bony destruction.

6.2.2 Vascular Lesions

The question of whether vascular lesions of the orbit, an important and substantial component of orbital abnormalities, should be classified as vascular tumors or vascular malformations is still being controversially discussed (Mullikan and Young 1988; Bilaniuk 1999). Some authors have proposed classifying these lesions according to their hemodynamic properties as arterial, high- or low-flow lesions, or as distensible, nondistensible, or stagnant venous lesions (Rootman et al. 1986). Comparable to the multidisciplinary approach in the management of these lesions, many specialists are involved in the classification process. In view of that fact that there is continuing disagreement as to the most appropriate terminology, we suggest that the compromise solution of combining traditional, familiar nomenclature with pathophysiological terms may be ideally suited to end the current discord and to establish an uniform terminology (Rootman et al. 1992; Bilaniuk 1999). CT and MRI play a crucial role in the management of vascular lesions; they exert a major influence on the choice of therapy, and imaging assists in the definition of the approach if surgery is to be performed (Bilaniuk 1999).

6.2.2.1 Capillary Hemangioma in Childhood

Capillary hemangioma is the most common orbital vascular tumor in childhood. It consists of plump, rapidly dividing endothelial cells with lumina of varying size, pericytes, and multilaminated basement membranes (Mulliken and Glowacki 1982;

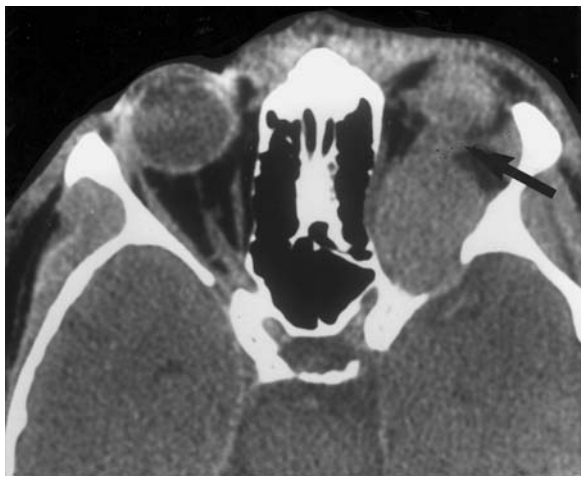

a

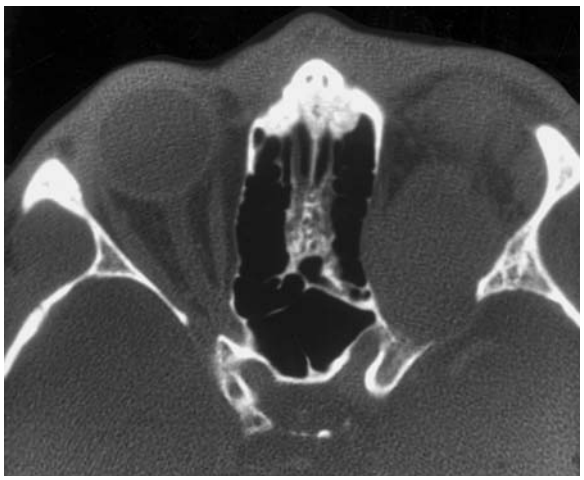

b

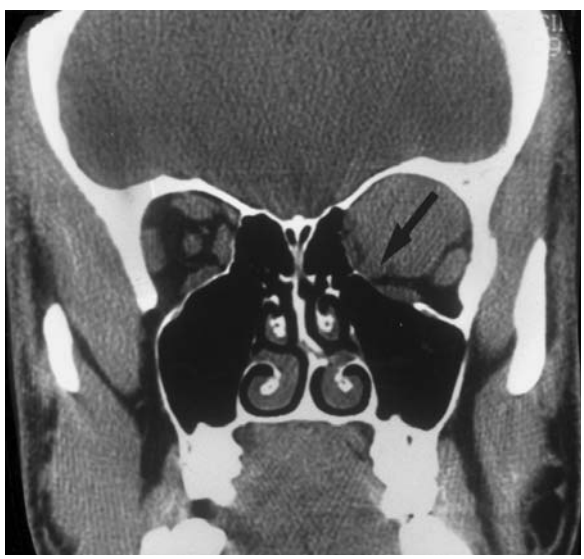

c

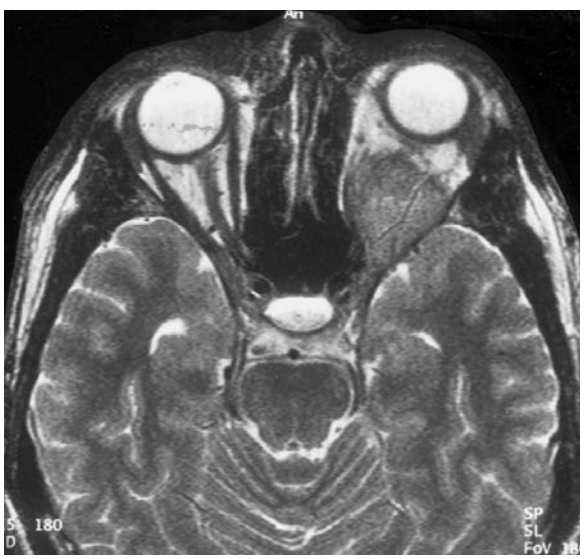

d ▷

Lasjaunias 1997). They may be present at birth or during the first year of life and are more common in girls (Mulliken and Glowacki 1982) (Figs. 6.46, 6.47). They represent an abnormal growth of capillary blood vessels dominated by varying degrees of endothelial proliferation and phases of involution (Teske et al. 1994; De Potter et al. 1995). In the presence of orbital involvement, there is a high risk of visual acuity deficits as well as distortion of extraocular muscles, the cornea, and optic nerve (Deans et al. 1992). Although capillary hemangiomas prefer the superomedial extraconal quadrant of the orbit, expansion may be seen in any orbital compartment (Fig. 6.47). For still unknown reasons (Mullikan and Young 1988), capillary hemangiomas frequently show a tendency towards spontaneous involution in childhood (5–10 years of life), sometimes with complete disappearance (Lasjaunias 1997; Bilaniuk 1999).

On imaging, capillary hemangioma presents as a lobulated, irregularly marginated, septated parenchymal mass, slightly hypodense on CT (Figs. 6.46, 6.47) and iso- to hyperintense on T1-weighted and moderately hyperintense on T2-weighted MR images. As in other intraorbital masses, fat-suppressed, T2-weighted or contrast-enhanced, T1-weighted images provide excellent details and facilitate the differential diagnosis from rhabdomyosarcoma or metastatic neuroblastoma, especially if feeding and draining vessels are seen (Bilaniuk et al. 1990; Bilaniuk and Rapoport 1994; De Potter et al. 1995; Lasjaunias 1997). Some arterial supply may be visible on 2D TOF MR-angiography (De Potter et al. 1995).

Therapy depends on the orbital extent and effect on the visual apparatus and includes laser, cryo- or radiation therapy, surgery, or conservative treatment

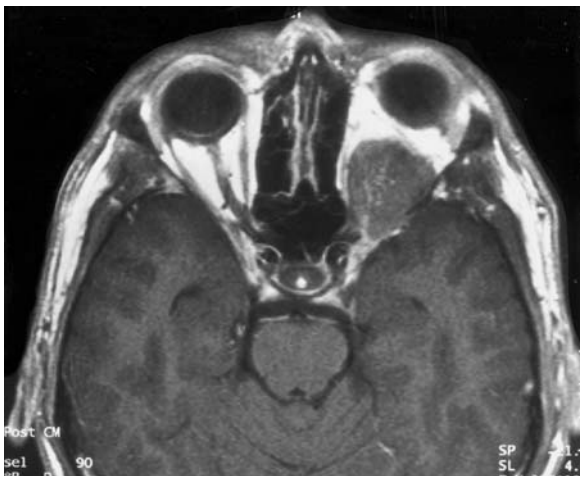

e

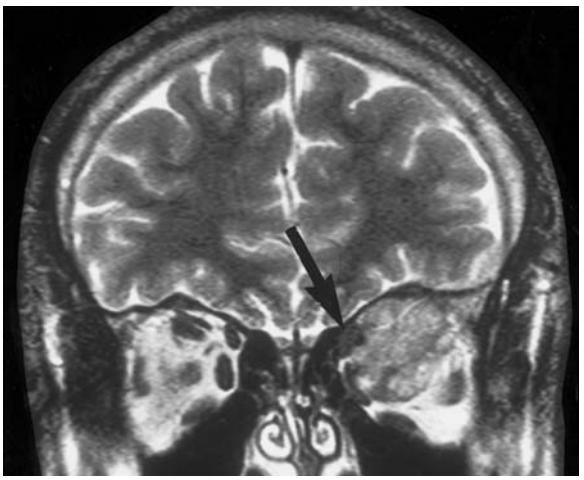

f

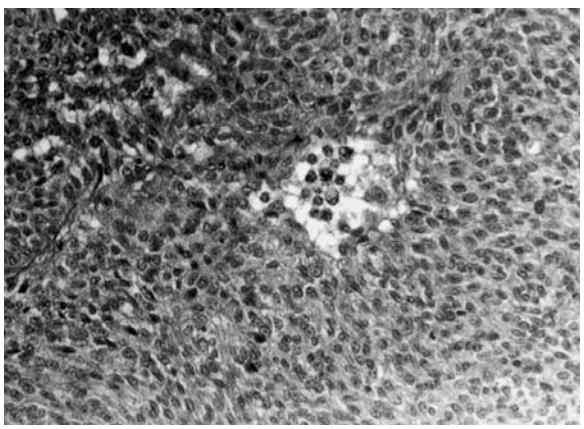

g

Fig. 6.45a–g. A 19-year-old man with slowly progressing, extra-axial left proptosis and inferior globe dislocation. Diagnosis: primary malignant melanoma. CT: **a** Axial view at the level of the optic canal, showing a clearly defined homogeneous tumor widening the left superior orbital fissure, compressing the posterior part of the lamina papyracea and the superior rectus muscle (*arrow*), while the optic canal appears to be unaffected. **b** Corresponding view in bone window. **c** Coronal view showing marked inferior medial dislocation of the optic nerve (*arrow*) between the medial and inferior rectus muscle. MRI (with permission of the staff at RNS Wiesbaden): **d** axial T2-weighted view, corresponding to **a** with isointense to intermediate signal of the tumor. **e** Corresponding T1-weighted, contrast-enhanced image without significant signal enhancement of the tumor. **f** Coronal T2-weighted view demonstrating superior differentiation of the tumor and oblique rectus muscle (*arrow*). **g** Histology (×280): the dense tumor consists of relatively uniform cells with round or oval nuclei and only small cytoplasmic edges. Some round tumor cells in the middle contain grains of a dark brown pigment (melanin) (with permission of Dr. Bohl, Department of Neuropathology, Medical School, University of Mainz)

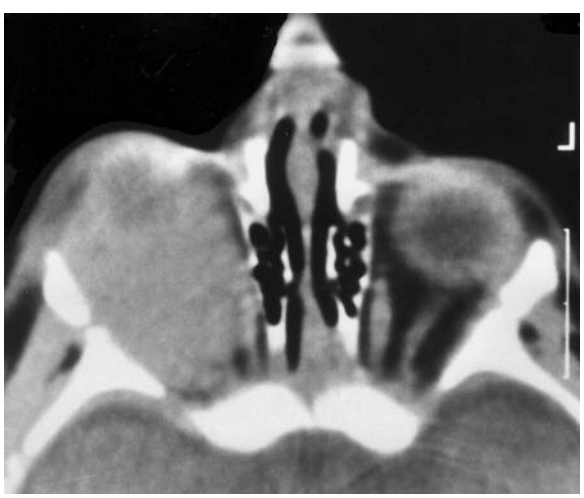

a

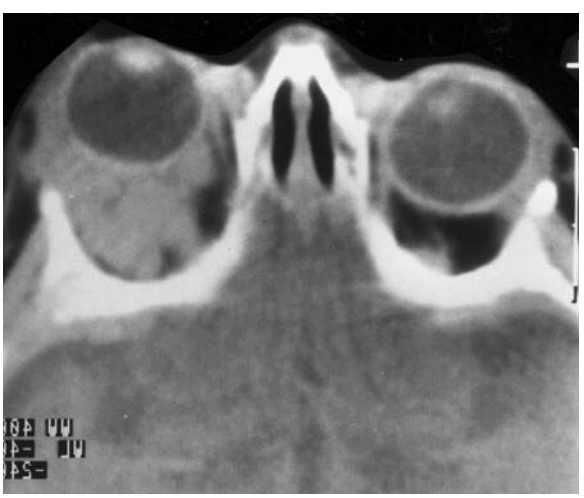

b

Fig. 6.46a,b. A 3-month-old boy with progressive exophthalmos developing in the 2nd and 3rd month of life; accentuated when screaming. Diagnosis: juvenile hemangioma. Axial CT: **a** Homogeneous, irregular mass is seen throughout the entire enlarged right orbit; no differentiation of normal orbital structures except in the apex region, where a well-demarcated small medial rectus muscle can be identified. **b** Showing the apparent protrusion of the globe

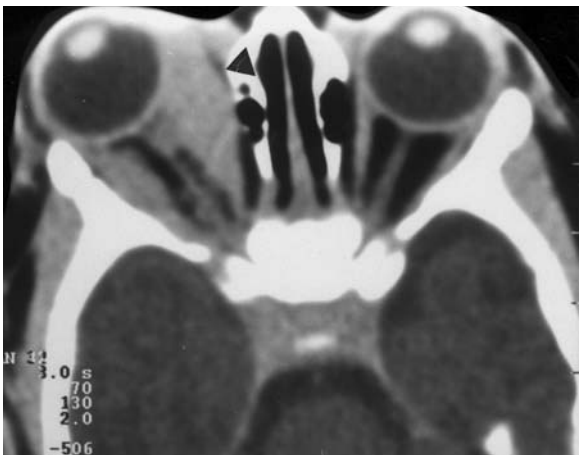

a

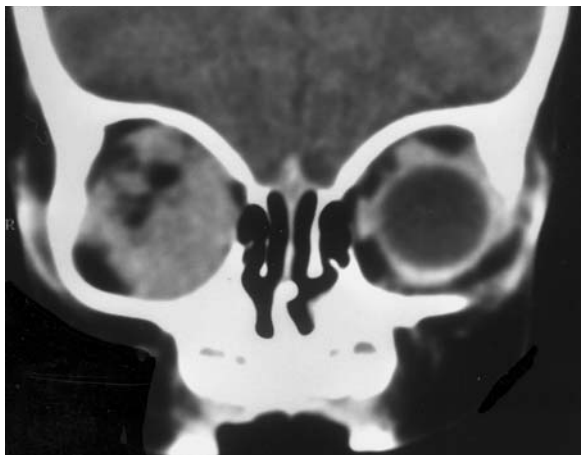

b

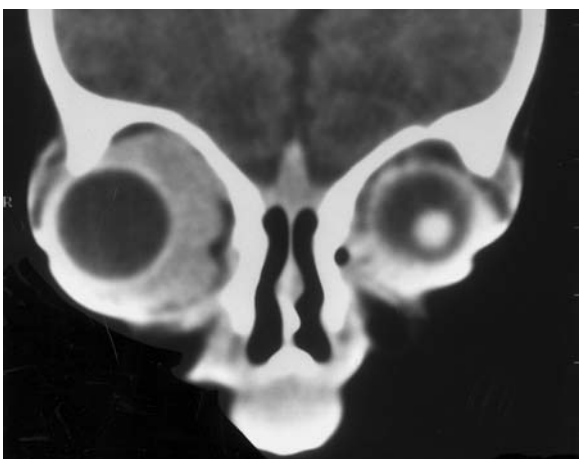

c

Fig. 6.47a–c. A 2-month-old girl with divergent strabismus and progressive proptosis of the right eye. Diagnosis: juvenile capillary hemangioma. CT: **a** Axial contrast-enhanced view, showing proptosis of the right globe, an increase in the diameter of the right orbit, enlargement of the medial rectus muscle, and an additional formation medial to the lateral rectus muscle. Note the medial, extraconal, postseptal, intraorbital hypodensity of the fatty tissue (*arrowhead*). **b** Coronal view of the retroglobal orbit; the muscles cannot be differentiated from the lesion. **c** A further coronal, more frontal view showing the hemangioma "embracing" the posterior region of the globe

with corticosteroids or interferon (Teske et al. 1994; Lasjaunias 1997; Achauer and Vander Kam 1989; Bilaniuk 1999).

6.2.2.2 Cavernous Hemangioma

The term cavernous hemangioma is still being controversially discussed, as there is no cellular proliferation but slow enlargement over a period of time (Bilaniuk 1999). Cavernous hemangiomas consist of large ectatic (cavernous) spaces lined by flattened endothelial cells and surrounded by a capsule of fibrous tissue (Jakobiec et al. 1974; Garner 1988). They are thought to arise from pre-existent vascular malformations, the vessels of which are initially collapsed, but become patent and dilated with time due to alterations in arterial or venous pressure changes (Hood 1970; Bilaniuk 1999). Cavernous hemangiomas do not have a prominent arterial supply or show infiltrative expansion, in contrast to capillary hemangiomas of childhood (Atlas and Galetta 1996), an entirely different lesion. Cavernous hemangiomas are isolated from the orbital vascular system and thus from the systemic circulation (Harris and Jakobiec 1979).

Cavernous hemangioma of the adult type occurs predominantly in the 4th and 5th decade of life and represents an orbital lesion, consisting of large (cavernous) spaces surrounded by a capsule (Hood 1970; Garner 1988). They account for 5%–7% of all orbital tumors and occur predominantly in women. The leading clinical symptom is a slowly progressing, painless, axial exophthalmos (Figs. 6.48, 6.49), occasionally with a mild visual deficit or visual obscurations due to optic nerve compression or extension by stretching (Fig. 6.49). Some 25% of patients have choroidal folds or papilledema. Single and unilateral, multiple tumors may occasionally be observed and are primarily located in the intraconal space. In rare cases, they may be found in the extraconal space (Fig. 6.162) or in the lacrimal gland or even intraosseously (Ruchman and Flanagan 1983; Dyer and Atkinson 1985; Shields et al. 1987a; Ohbayashi et al. 1988; Leatherbarrow et al. 1989; McNab and Wright 1989;

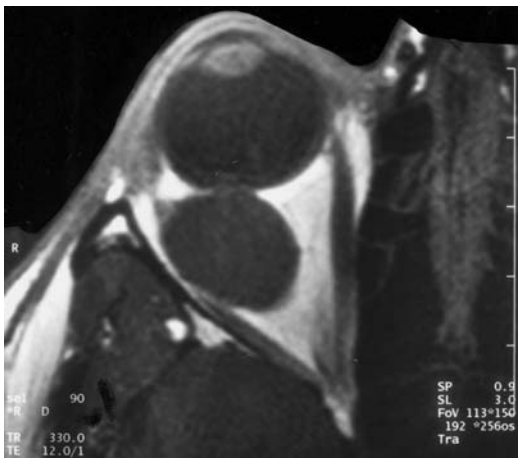

a

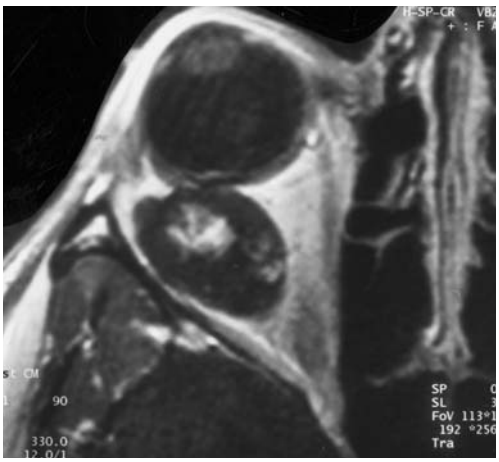

b

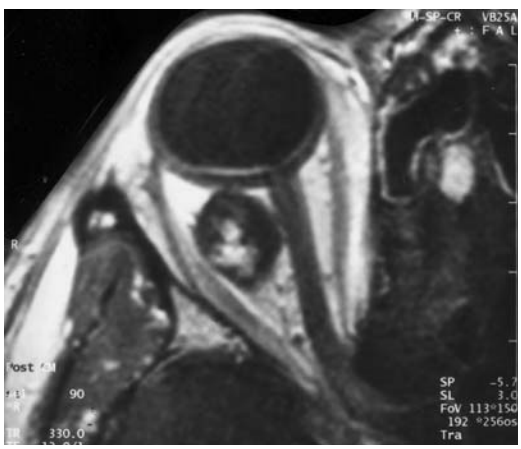

c

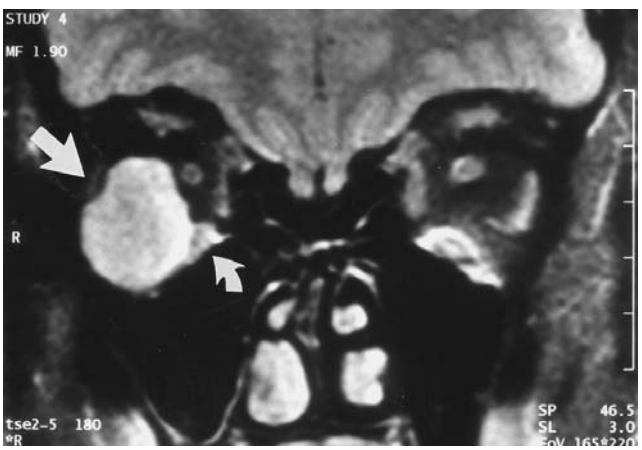

d

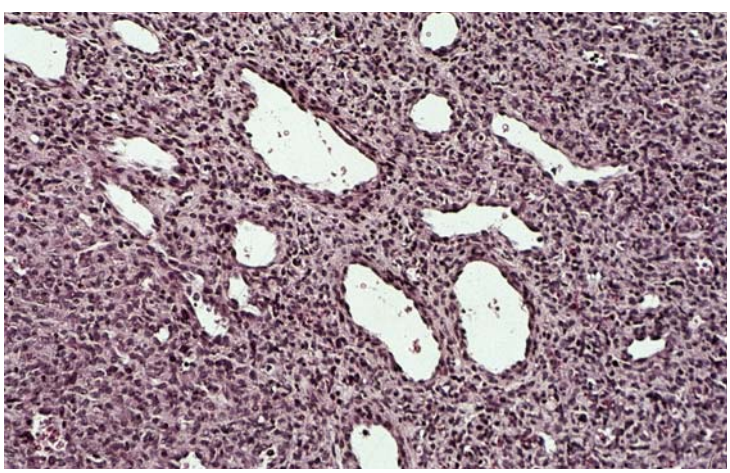

e

Fig. 6.48a–e. A 46-year-old man with slowly progressing hyperopia and discrete exophthalmos of the right eye. Diagnosis: cavernous hemangioma. MRI: **a** Axial T1-weighted native view, showing a well-encapsulated, sharply defined intraconal tumor, pressing on the posterior lateral part of the globe. **b** Corresponding contrast-enhanced image with signal enhancement in the central area only. **c** Axial, T1-weighted, contrast-enhanced view at the level of the optic nerve with more clearly defined intraconal localization lateral to the optic nerve. **d** Coronal proton density-weighted (FS) view depicting the entire volume of the tumor displacing the inferior (*curved arrow*) and lateral (*arrow*) muscles and enlarging the muscle cone. **e** Histology (H&E section) demonstrating multiple vascular channels lined by a single layer of endothelial cells. Note scattered erythrocytes within the lumen of the vascular channels. (With permission of Müller-Forell 1998)

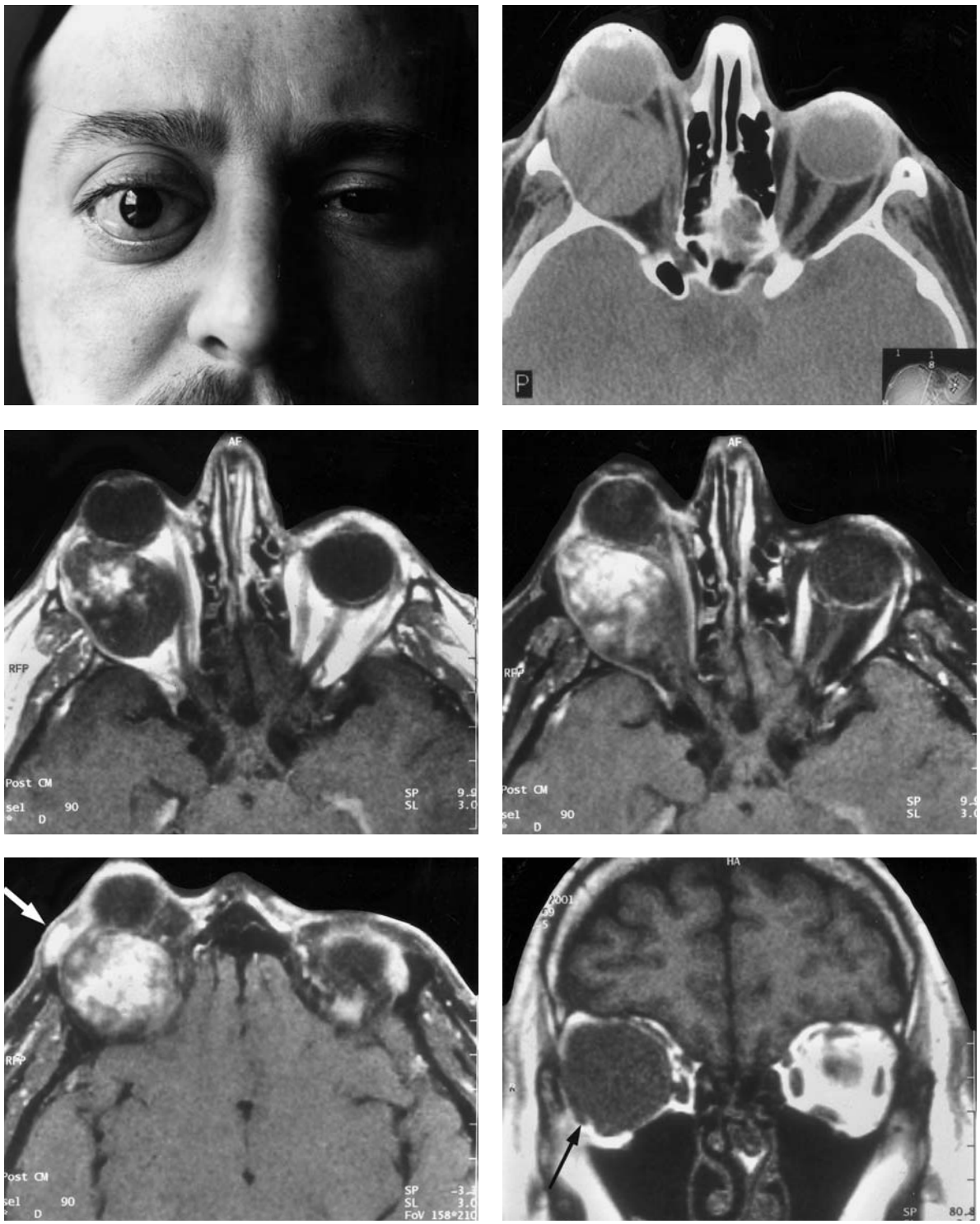

Fig. 6.49a–f. A 32-year-old man with extreme proptosis of the right eye for more than 15 years, who presented with the complaint of progressive visual deficit. Diagnosis: cavernous hemangioma. **a** Portrait of the patient with extreme protrusion of the right eye. CT: **b** Axial view with exophthalmos measurement of 33 mm. Sharply defined, encapsulated, intraconal tumor lateral of the optic nerve with medial dislocation and slight compression of the medial rectus muscle. Note the medial dislocation of the optic nerve at the entrance to the optic canal. The resulting hypomochlion may be accountable for the visual impairment. MRI: **c** Corresponding axial T1-weighted native view with apparent impression of the globe. **d** Corresponding T1-weighted, contrast-enhanced (FS) view. **d** Axial, T1-weighted, contrast-enhanced (FS) view of the upper orbit, showing the extraorbital dislocation of the lacrimal gland (*white arrow*). **f** Coronal T1-weighted native view. The entire orbit is occupied by the cavernoma. Note the close vicinity of the optic nerve to the medial rectus muscle and flattening of the other external muscle with inferior dislocation of the lateral muscle (*arrow*)

Orcutt et al. 1991; Sullivan et al. 1992a; D'Hermies et al. 1993; Guenalp and Guenduez 1995; Atlas and Galetta 1996; Sweet et al. 1997). Histologically, this tumor has a thin capsule and consists of large vascular channels that are outlined by endothelium. Venous thrombosis is common due to the stagnant circulation, while lymph follicles and inflammatory signs are rare (Figs. 6.48, 5.50).

On imaging, cavernomas demonstrate characteristic features, presenting as a sharply outlined tumor with medium reflectivity on ultrasound A-scan. On B-scan, the tumor is seen as a round to oval lesion with a smooth surface and regular internal structure (Coleman et al. 1972; Bellone et al. 1974; Bettelheim and Till 1975; Ossoinig et al. 1975; Byrne and Glaser 1983; Cappaert et al. 1983). The major task of CT, and in particular of MRI, apart from showing the characteristic morphology of a well-defined, round or oval, mainly intraconal (occasionally extraconal) mass that usually, but not always (Fig. 6.50), spares the

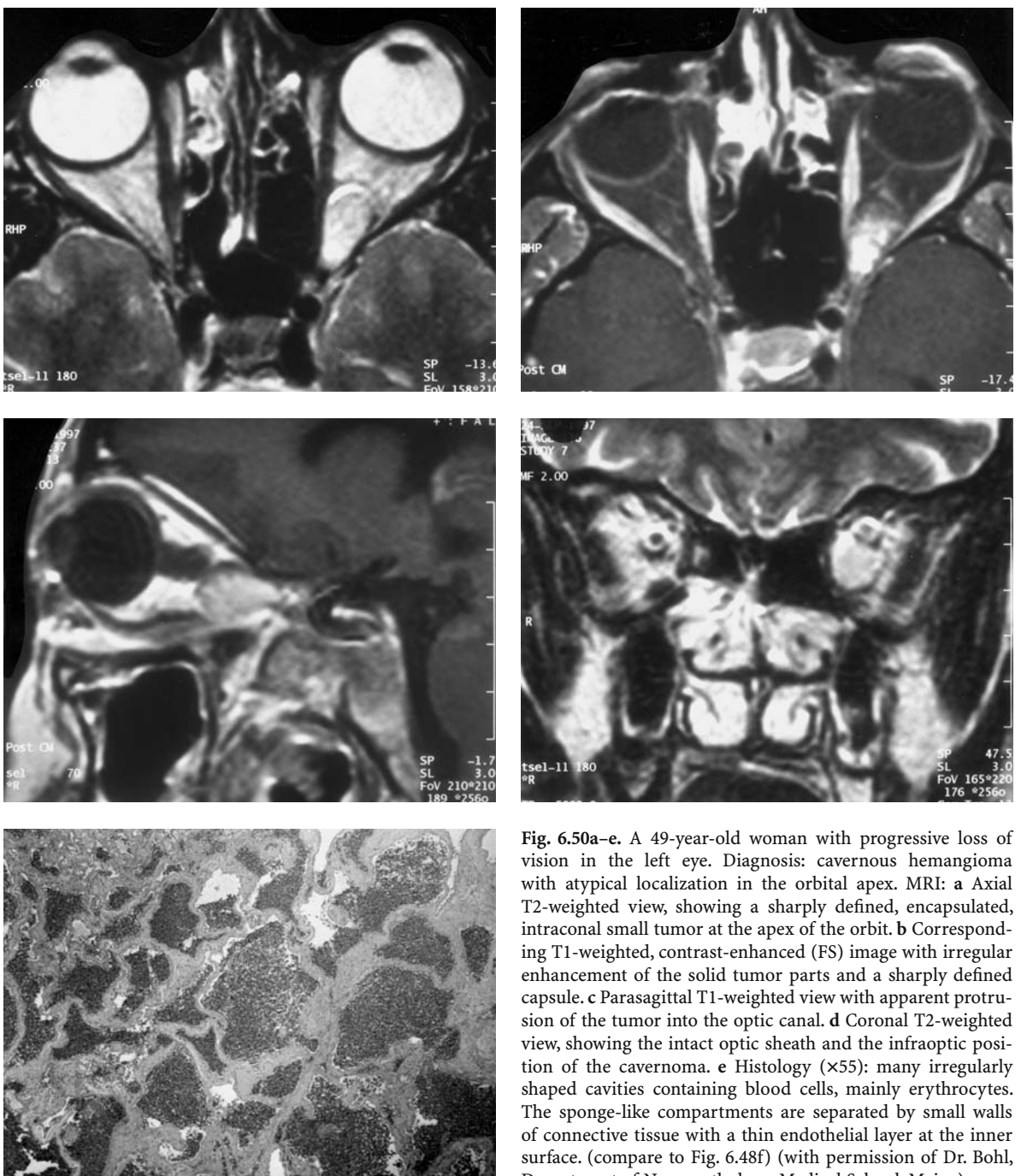

Fig. 6.50a–e. A 49-year-old woman with progressive loss of vision in the left eye. Diagnosis: cavernous hemangioma with atypical localization in the orbital apex. MRI: **a** Axial T2-weighted view, showing a sharply defined, encapsulated, intraconal small tumor at the apex of the orbit. **b** Corresponding T1-weighted, contrast-enhanced (FS) image with irregular enhancement of the solid tumor parts and a sharply defined capsule. **c** Parasagittal T1-weighted view with apparent protrusion of the tumor into the optic canal. **d** Coronal T2-weighted view, showing the intact optic sheath and the infraoptic position of the cavernoma. **e** Histology (×55): many irregularly shaped cavities containing blood cells, mainly erythrocytes. The sponge-like compartments are separated by small walls of connective tissue with a thin endothelial layer at the inner surface. (compare to Fig. 6.48f) (with permission of Dr. Bohl, Department of Neuropathology, Medical School, Mainz)

orbital apex, consists of the accurate anatomic delineation and definition of the relationship of the mass to the optic nerve and muscle cone (Figs. 6.48, 6.49, 6.51, 6.52). Calcifications correspond to phleboliths, which may be regarded as a pathognomonic sign. Although no deformation of the globe may be seen even in the presence of large tumors, because of the soft consistency of these masses, in the case of rather large lesions a slight expansion of the bony orbit may be apparent (Fig. 6.49) (Jacobs and Kinkel 1976; Gyldenstedt et al. 1977; Davis et al. 1980; Wende et al. 1977; Savoiardo et al. 1983; Sood et al. 1992; Weber 1992; Atlas and Galetta 1996). Compared with the MRI presentation of orbital fat and muscles, cavernous hemangiomas normally give an iso- to hypointense signal in T1-weighted images (Figs. 6.48, 6.51), and some hyperintense areas may be visible in the presence of thrombosis. While contrast enhancement is generally extensive, early images are characterized by an inhomogeneous, heterogeneous signal because of internal septations. In late images, lesion enhancement is homogeneous (Mafee et al. 1987b; Bilaniuk 1999). On T2-weighted images, the lesions exhibit a hyperintense, mostly homogeneous, at times irregular signal.

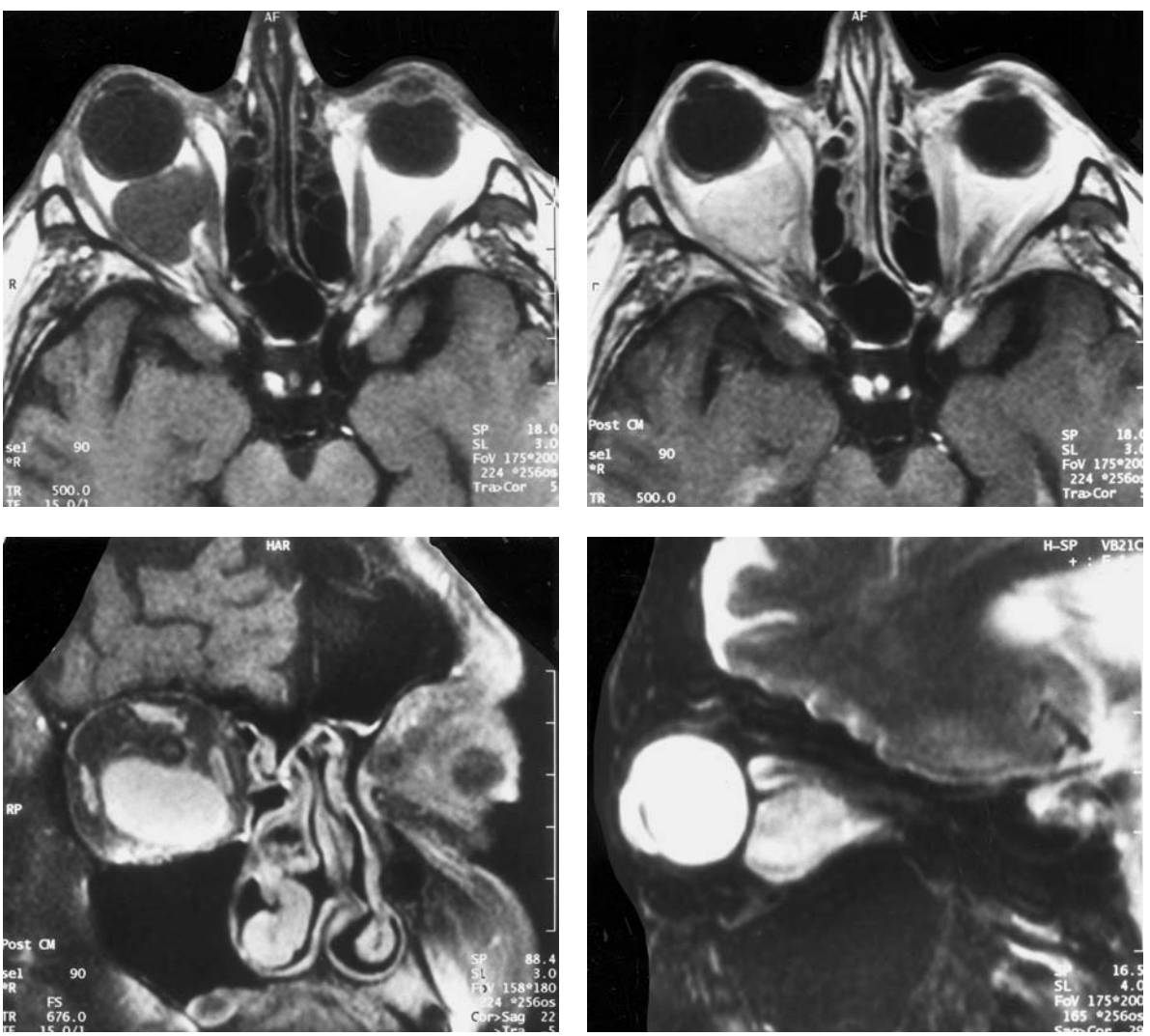

Fig. 6.51a–d. A 68-year-old man with exophthalmos of the right eye. Diagnosis: cavernous hemangioma. MRI: **a** Axial T1-weighted native image with a sharply outlined, lobulated, retro-orbital, intraconal tumor and slight protrusion of the right bulb. **b** Corresponding, contrast-enhanced view with homogeneous enhancement. **c** Coronal, T1-weighted, contrast-enhanced (FS) cut at a right angle to the optic nerve demonstrating the infraoptic location and entire width of the tumor (coronal angle perpendicular to the optic nerve). **d** Parasagittal T2-weighted view with inferior impression and compression of the optic nerve together with a widening of the anterior subarachnoid space of the optic nerve sheath

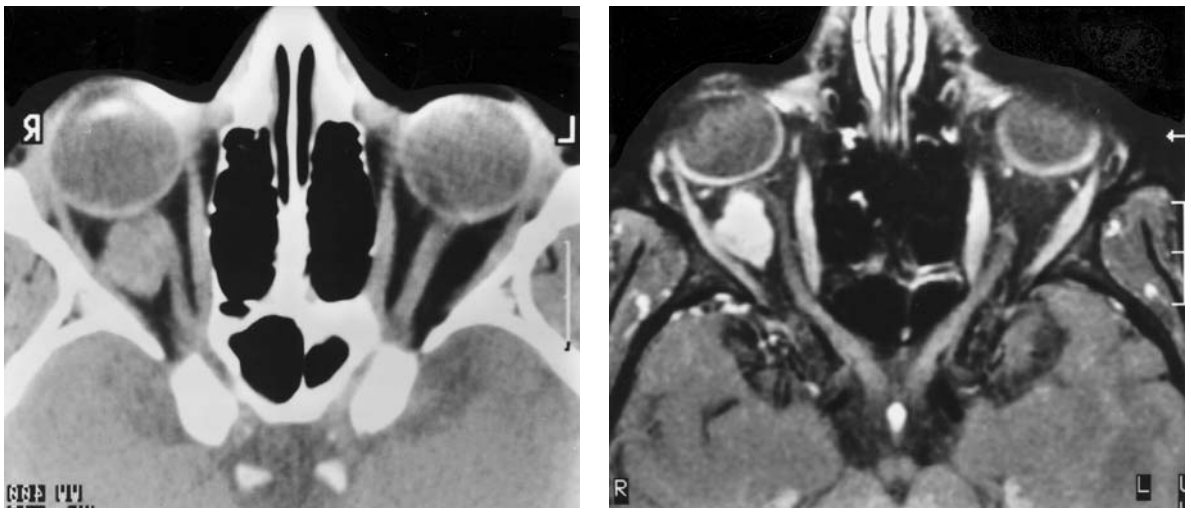

a b

Fig. 6.52a,b. A 14-year-old boy with visual deficit and papilledema of the right eye. Diagnosis: cavernous hemangioma. CT: **a** Axial, native view with a sharply delineated intraconal lesion, lateral of the medially displaced optic nerve. MRI: **b** Corresponding T1-weighted, contrast-enhanced (FS) image with superior tumor differentiation lateral of the dislocated optic nerve. (With permission of Müller-Forell and Lieb 1995b)

The most important differential diagnosis is an orbital varix, which may also demonstrate a well-delineated mass, but should be considered if intralesional flow or intermittent exophthalmos is seen on Valsalva maneuver.

The differential diagnosis should further include hemangiopericytoma (Fig. 6.92), fibrous histiocytoma, and neurinoma (Fig. 6.40) (Tan et al. 1987; Atlas et al. 1988; Weber 1992; Bilaniuk and Rappoport 1994; Mukherji et al. 1994; Zhu et al. 1995; Atlas and Galetta 1996; Thorn et al. 1999).

The treatment of choice is periodic observation in cases where no symptoms are present and the tumor was detected incidentally (Fig. 6.53), while complete surgical removal through an anterior medial, lateral orbitotomy, or a transconjunctival approach is indicated when the patient is symptomatic, or the lesion is growing. Shrinkage of the tumor by selective coagulation or aspiration may facilitate removal. The visual prognosis is excellent in most cases; malignant transformation or local recurrence has not been demonstrated.

6.2.2.3 Venous Lymphatic Malformation (Lymphangioma)

The term lymphangioma, which has been used until very recently, should be replaced by venous lymphatic malformation, as it describes a vascular anomaly (Bilaniuk 1999). Occurring in the head and neck, predominantly in children and young adults, this vascular malformation of unknown origin is considered to represent a vascular anomaly with abortive vessels, which spread among normal structures (Harris et al. 1990; Bilaniuk 1999). Venous lymphatic malformation presents as an unencapsulated mass that consists primarily of thin-walled, endothelial-lined, bloodless, vascular and lymph channels, containing numerous cystic spaces of different sizes. They may clinically resemble capillary hemangiomas with the difference of diffuse growth in the absence of spontaneous regression (Graeb et al. 1990; De Potter et al. 1995; Kaufman et al. 1998). The tendency towards spontaneous hemorrhage results in the sudden onset of proptosis combined with periorbital swelling and reduced eye motility, at times leading to optic nerve compression (Katz et al. 1998; Carmody 2000).

On imaging, venous lymphatic malformation presents primarily as an extraconal, although in some instances intraconal, infiltrative, multilobular mass with indistinct borders and poor encapsulation (Figs. 6.54, 6.55, 6.165). Since venous lymphatic malformations are slowly growing lesions, an asymmetric enlargement of the orbit may be seen in young individuals (Fig. 6.54). Calcification may be present on CT (Fig. 6.55), while MRI shows an isointense (relative to the brain) mass in T1-weighted series, but a hyperintense signal in proton density or T2-weighted images that corresponds to the presence of a large number of fluid channels. As thrombosis and hemorrhages are known to occur, MRI may show an inhomogeneous signal (Kazim et al. 1992), giving rise to its description as a "chocolate-

(Text continues on p. 195)

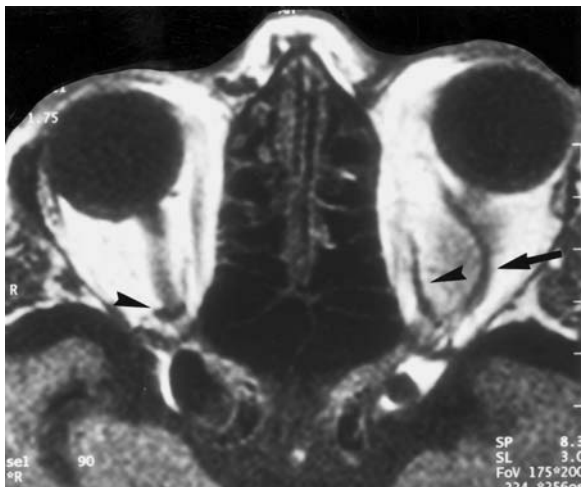
R
sel 90
*R

a

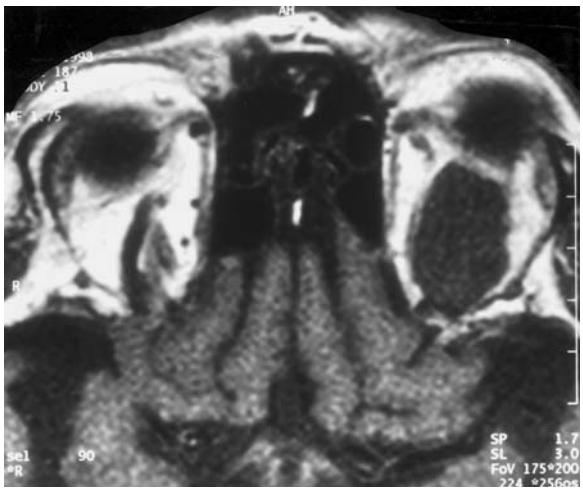
R
sel 90
*R

b

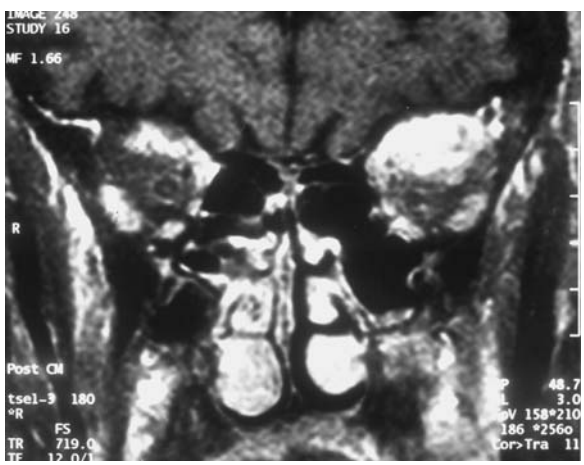
STUDY 16
MF 1.66
R
Post CM
tsel-3 180
*R
FS
TR 719.0

c

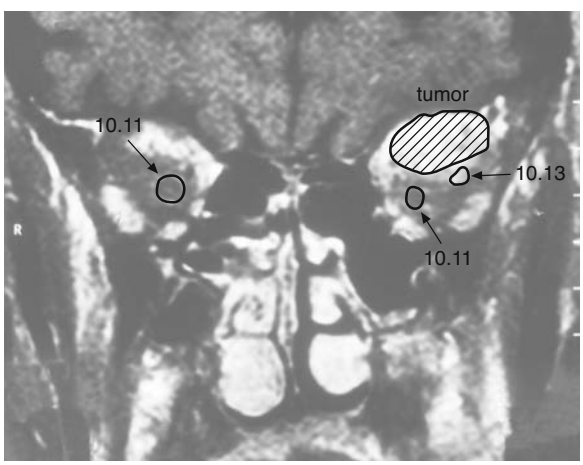
tumor
10.11
10.13
10.11
R

d

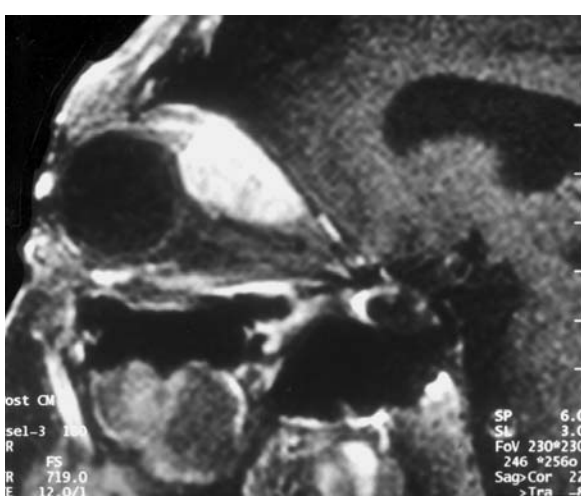
R
FS
R 719.0

e

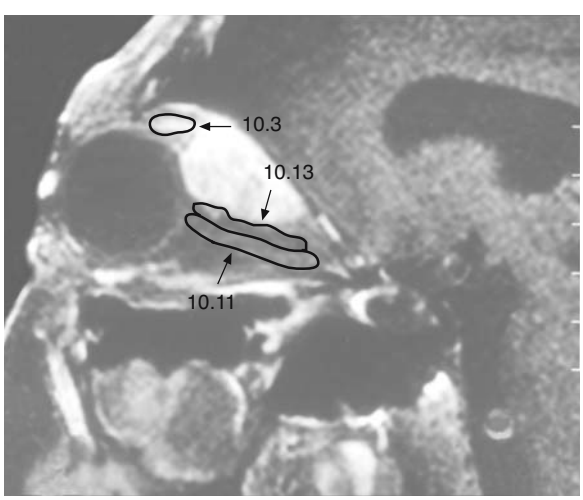
10.3
10.13
10.11

f

Fig. 6.53a–f. A 72-year-old man with double vision and extra-axial proptosis of the left eye persisting for 18 months. Diagnosis: suspected cavernous hemangioma (no surgery). MRI: **a** Axial T1-weighted native view at the level of the optic canal, demonstrating the inferior depression of the superior ophthalmic vein (*arrow*). Note the dilated ophthalmic arteries (*arrowheads*). **b** Axial T1-weighted view with an isointense, well-defined lesion of the upper right orbital region. Note the contralateral superior ophthalmic vein. **c** Coronal, T1-weighted, contrast-enhanced (FS) view with extension of the mass above the superior ophthalmic vein. **d** Corresponding diagram. 10.11 = optic nerve, 10.13 = superior ophthalmic vein. **e** Parasagittal, T1-weighted, contrast-enhanced (FS) image showing the supraoptic localization of the mass, sparing of the orbital apex. Note signal void of the enlarged, caudally dislocated, right superior ophthalmic vein, located between the hemangioma and the optic nerve. **f** Corresponding diagram. 10.3 = superior rectus muscle, 10.11 = optic nerve, 10.13 = superior ophthalmic vein

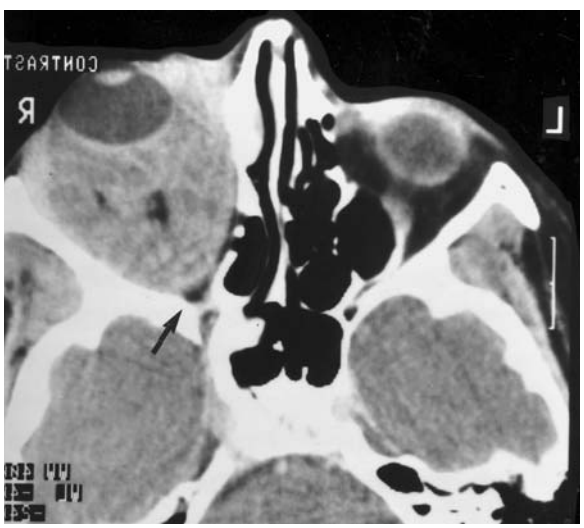

a

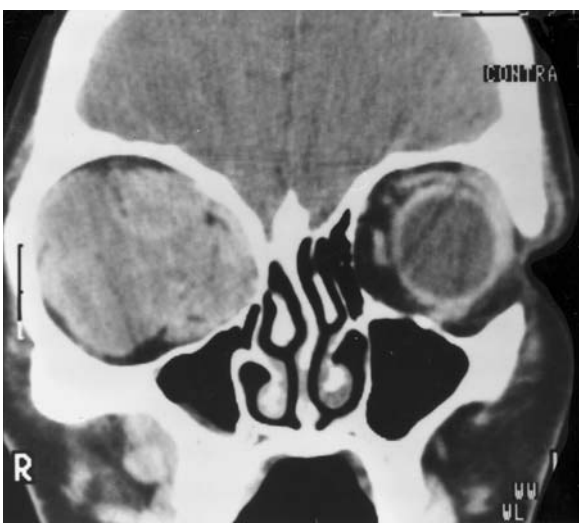

b

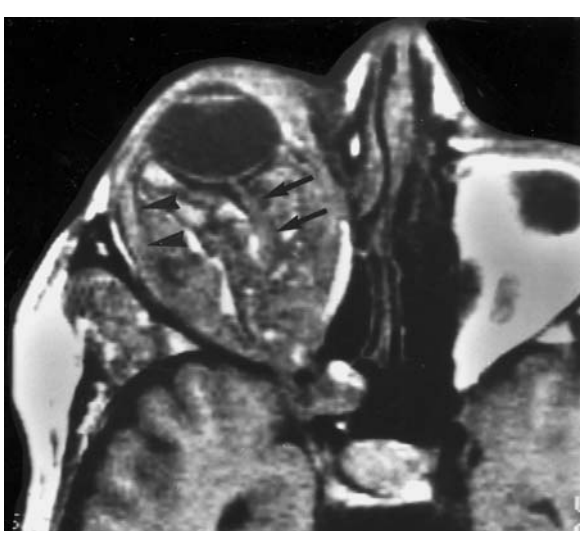

c

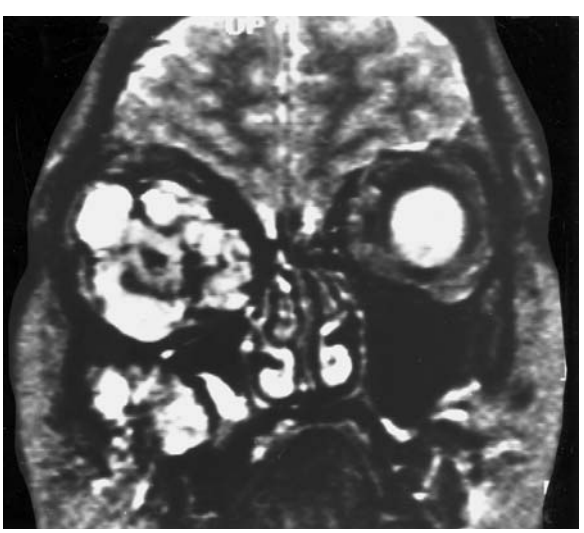

d

Fig. 6.54a–d. A 20-year-old woman with unilateral exophthalmos of the right eye since childhood. Diagnosis: venous lymphatic malformation. CT: **a** Axial contrast-enhanced view showing an enhancing, space-occupying lesion filling the entire, significantly enlarged right orbit. Note lack of identification of the rectus muscles, the still spared orbital apex, and smooth contact with the apparently normal globe. **b** Coronal contrast-enhanced view demonstrating severe dilation of the orbital circumference, leading to the diagnosis of a benign lesion with slow, dislocating growth. MRI: **c** axial T1-weighted native image, corresponding to **a**, showing a remnant of orbital fat as a hyperintense formation. The suspected intraconal location of the tumor is confirmed by the differentiation of the lateral rectus muscle (*arrowheads*) and the medially dislocated optic nerve (*arrows*). **d** Coronal T2-weighted view, corresponding to **b**, demonstrating a venous lymphatic malformation characterized by large, septated, liquid-filled caverns, presenting with a high signal. Note the central hypointensity, corresponding to the optic nerve not identified on CT. (With permission of Müller-Forell and Lieb 1995b)

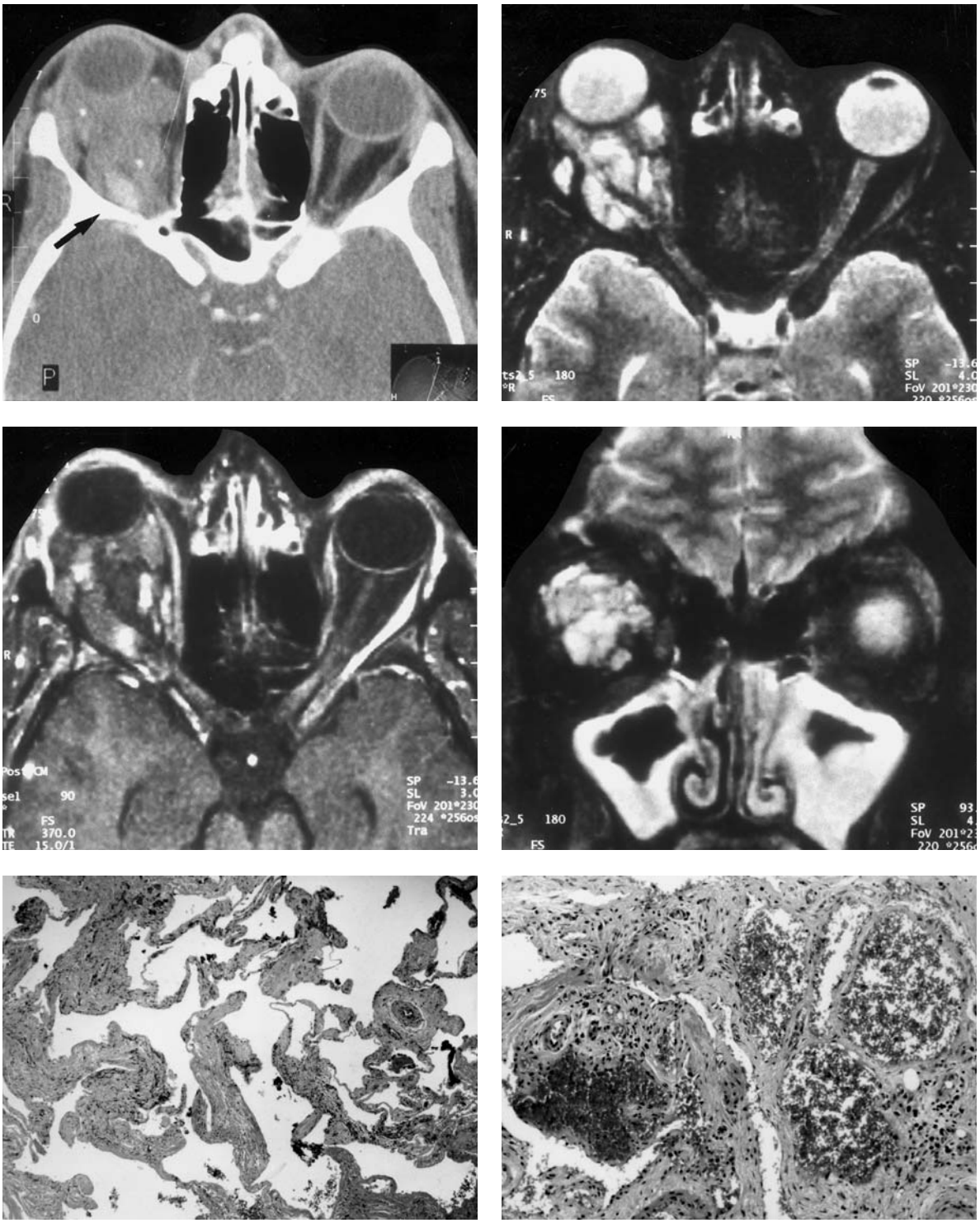

Fig. 6.55a–f. A 34-year-old man presenting with persistent proptosis of the right eye, and recently increasing afference deficit. Diagnosis: venous lymphatic malformation. CT: **a** Axial contrast-enhanced view of the medial orbital region, demonstrating protrusion and apparently inferior dislocation of the globe. Only slight enhancement (*arrow*) of a posterior part of the lobulated, mainly (but not exclusively) intraconal lesion is seen; the optic nerve cannot be identified. Note some punctuated calcifications. MRI: **b** Corresponding T2-weighted view with better demonstration of the lobular architecture of the lesion and different signal intensities where bright signal areas represent cystic/colloidal areas. **c** Corresponding T1-weighted, contrast-enhanced (FS) image. Note the lack of signal enhancement of the entire lesion, except for a small area in the lateral posterior orbit, corresponding to CT in **a**. **d** Coronal T2-weighted view of the retrobulbar region where the lobular character of the lesion is best visualized (note thickening of the maxillary sinus mucosa, caused by chronic sinusitis). Histology (×55): **e** Irregularly shaped, empty vessels with only small walls surrounded by fat containing connective tissue and in some areas by ocular muscle tissue. **f** (×140) Other areas of the tumor have a sponge-like structure with the cavities containing blood and thrombotic material. (With permission of Dr. Bohl, Department of Neuropathology, Medical School, Mainz)

cyst", as well as causing difficulties in its differentiation from a cavernous hemangioma on both imaging and histology. Apart from morphologic characteristics, which in some cases include a bony expansion (Katz et al. 1998), the most important differential diagnostic criterion from idiopathic orbital inflammation and/or hemangiomas is the absence of contrast enhancement (Fig. 6.55) (Kaufman et al. 1998).

6.2.2.4 Orbital Venous Anomaly (syn. "orbital varix")

The classical definition of a primary orbital varix is that of a venous malformation with abnormal uni- and bilateral dilation of one or more orbital veins. Symptoms consist of variable proptosis, associated with an increase in systemic venous pressure (Lloyd et al. 1971; Rootman and Graeb 1988). However, the nomenclature of orbital varix is discussed controversially: Wright et al. (1997) postulate the same underlying abnormality as in venous lymphatic malformations (see Sect. 6.2.2.3) and propose the term "orbital venous anomaly". As orbital veins do not have valves, systemic venous pressure changes occur during coughing, forced expiration, and bending forward, and the Valsalva maneuver may cause intermittent proptosis (Cohen et al. 1995). Hemorrhage or thrombosis may lead to acute, painful exophthalmos, sometimes with decreased orbital motility (De Potter et al. 1995; Bilaniuk 1999).

On CT, an intraconal, well-defined, elongated mass is seen, generally in the course of the superior ophthalmic vein, which is sometimes marked by calcification, corresponding to small phleboliths. In cases of a primarily occult lesion, Valsalva maneuver or a prone position may be helpful in demonstrating the lesion, due to an increase in orbital pressure (Shields et al. 1984a; De Potter et al. 1995, Bilaniuk 1999). The dilated veins show highly intensive homogeneous contrast enhancement (Fig. 6.56).

In MRI studies, the morphology of orbital varices manifests as a triangular configuration tapering toward the apex and the convex anterior margin (Fig. 6.58). After gadolinium administration, the optimum delineation of signal enhancement in orbital varices is achieved in fat-suppressed series (Fig. 6.57c–e). Gradient-echo sequences may be used to evaluate the blood flow and to perform the Valsalva maneuver (De Potter et al. 1995).

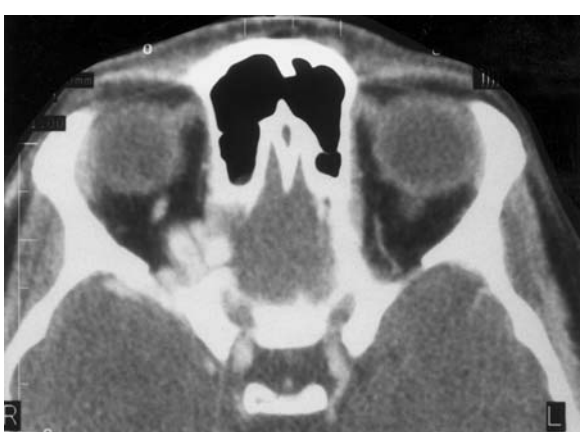

a

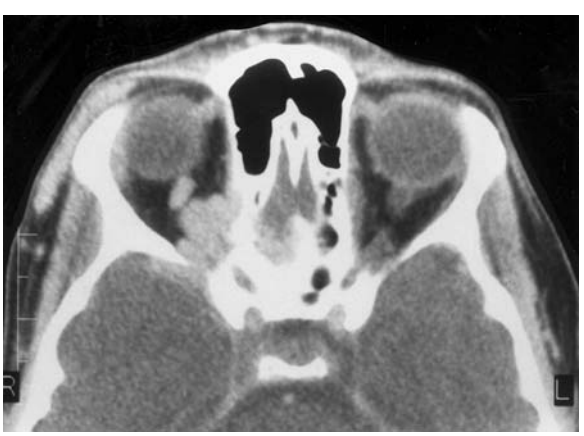

b

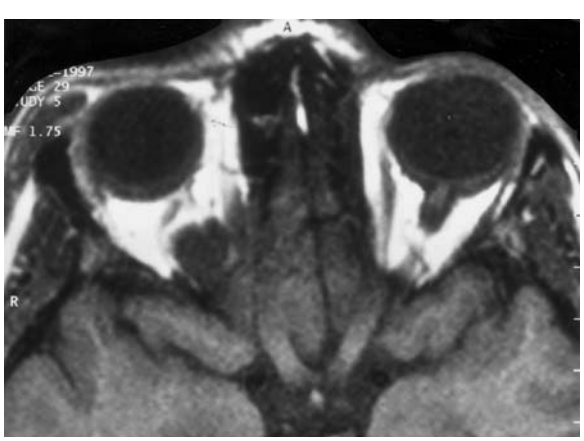

c

Fig. 6.56a–c. A 33-year-old woman with recurrent right orbital protrusion, occurring particularly on physical exertion. Diagnosis: orbital varices. CT: **a** Axial contrast-enhanced view showing several small, enhancing lesions at the superior apex of the right orbit. **b** Corresponding view after Valsalva maneuver, demonstrating enlargement of the varices. MRI: **c** corresponding T1-weighted view without increased intraorbital pressure

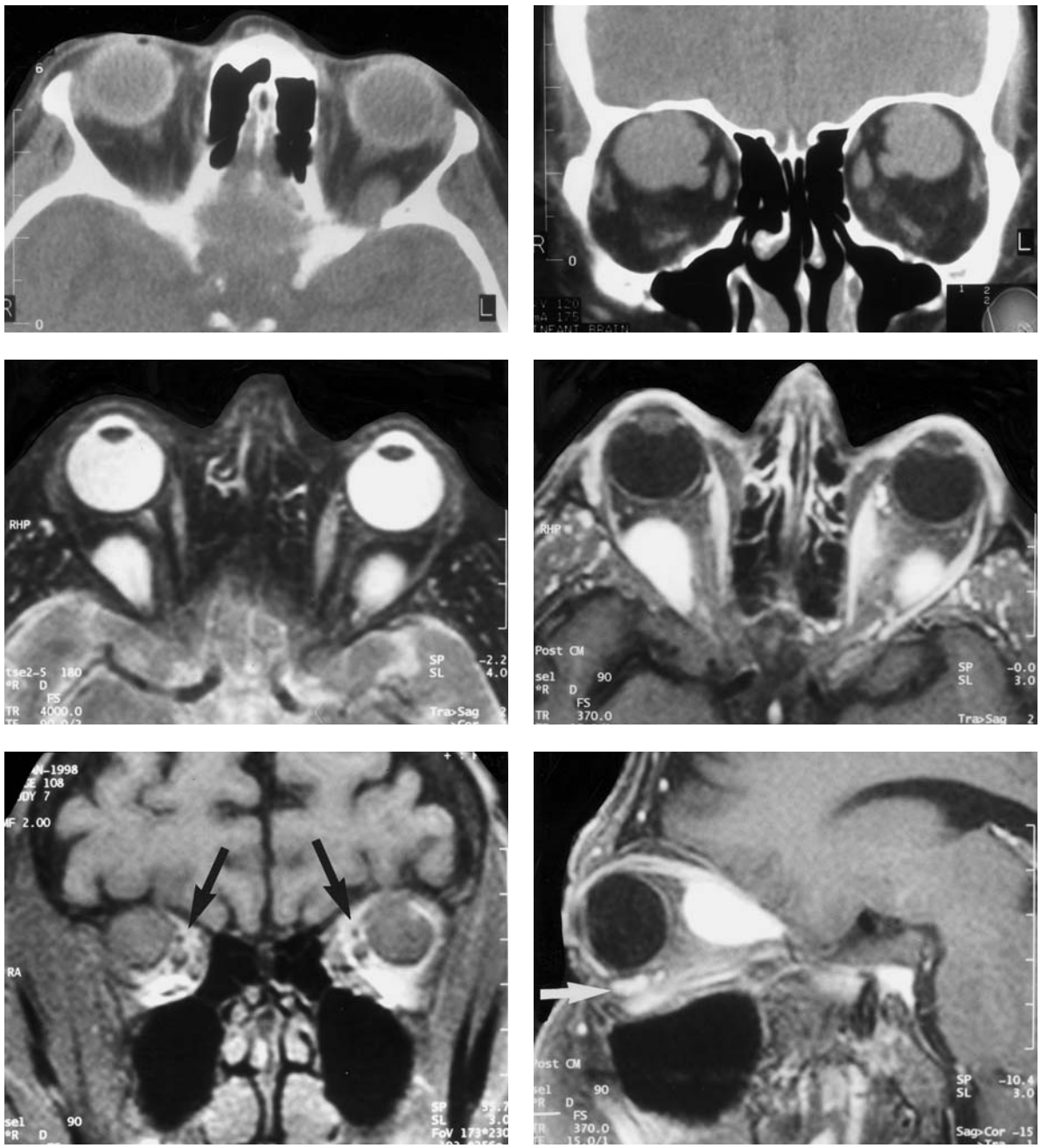

Fig. 6.57a–f. A 67-year-old woman with recurrent, painless, bilateral orbital protrusion, which is more pronounced on bending down. Diagnosis: orbital venous anomaly. CT: **a** Axial view of the upper orbit showing a sharply defined, oval formation in the left superior orbit adjacent to the orbital apex. **b** Coronal view demonstrating clearly defined lesions of different sizes in the lateral muscle cone between the lateral rectus and the superior oblique muscle in close vicinity to the medially dislocated optic nerve. The different sizes result from the prone position of the patient with consecutive increase of intraorbital pressure. MRI: **c** Axial T2-weighted view, corresponding to a with hyperintense, bilateral, intraconal lesions lateral of the optic nerve. **d** Corresponding axial, T1-weighted, contrast-enhanced (FS) image where the enlarged veins exhibit a homogeneous signal enhancement. **e** Coronal T1-weighted native view corresponding to **b**, demarcating the well-defined vascular formation with medial and inferior dislocation of the optic nerve. Note the normal diameter of both medially dislocated superior ophthalmic veins (*arrows*). **f** Sagittal, T1-weighted, contrast-enhanced (FS) view with homogeneous signal enhancement of the orbital varices, reaching and molding the orbital apex. Note another small varix in the inferior extraconal area (*white arrow*)

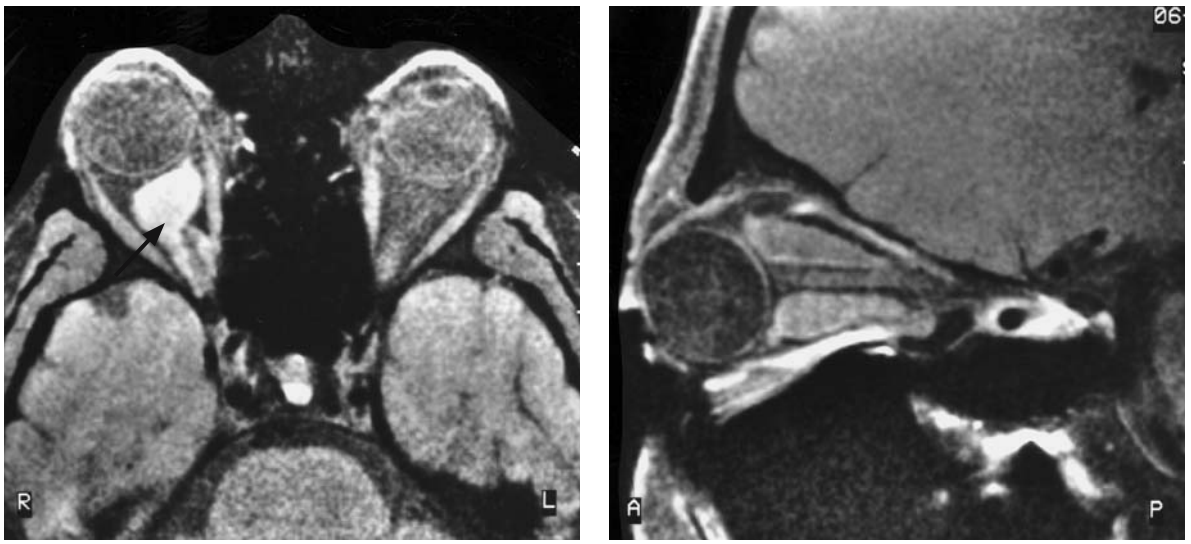

a b

Fig. 6.58a,b. A 42-year-old man with recurrent exophthalmos. Diagnosis: orbital venous anomaly. Contrast-enhanced MRI: **a** Axial view with an intraconal, lobulated but sharply defined, hyperintense formation with extension into the apex of the orbit, where the optic nerve demarcates as a hypointense structure (*arrow*). **b** Parasagittal view demonstrating the infra- and supraoptic sections of the varices as well as expansion towards the orbital apex and optic canal. (With permission of Müller-Forell and Lieb 1995b)

6.2.2.5 Thrombosis of Orbital Veins

Orbital vein thrombosis, whether in varicoid veins or secondary to different primary diseases, is characterized by an intravasal mass in the dilated superior ophthalmic vein. Depending on the imaging technique used, a primarily hyperdense, dilated superior ophthalmic vein without enhancement after administration of iodinated contrast is seen on CT (Fig. 6.59). On MRI, the appearance depends on the age of the thrombosis and the paramagnetic hemoglobin properties. The absence of the signal void within a dilated superior ophthalmic vein suggests the diagnosis, which is confirmed by a hypointense signal on T1-weighted and T2-weighted images in the presence of deoxyhemoglobin, both of which increase in the presence of methemoglobin (De Potter et al. 1995).

6.2.2.6 Carotid-Cavernous Fistula (CCF)

The carotid-cavernous fistula represents an arteriovenous shunt of the internal carotid artery in its cavernous compartment, leading to arterialization of the superior ophthalmic vein. The resulting venous congestion of the orbit causes hypervolemia of the globe and orbit, clinically manifesting as pulsatile exophthalmos (identified on auscultation), combined with dilated episcleral vessels, chemosis, secondary glaucoma, eventually also featuring papilledema, ocular pain, and ophthalmoplegia (Flanagan 1979). The described pathologic mechanisms may lead to vision loss as a result of increased intraorbital pressure.

Color-coded ultrasound can definitively demonstrate reversal of blood flow (Fig. 6.60b). On imaging, proptosis combined with enlargement of extraocular muscles and widening of the superior ophthalmic vein is indicative of CCF. It is seen on CT with contrast enhancement after iodinated contrast medium (Fig. 6.60a), and on MRI due to the signal void of the arterialized flow in the superior ophthalmic vein. Although on both CT- and MR-angiography a diagnosis of CCF can be done (Figs. 6.61, 6.62) (De Potter et al. 1995; Coskun et al. 2000), imaging techniques give only insufficient information concerning the flow dynamics in terms of differentiating precise flow characteristics. The etiology of CCF may be traumatic (Fig. 6.61) or spontaneous (Fig. 6.62), with the latter occurring primarily in diabetic older

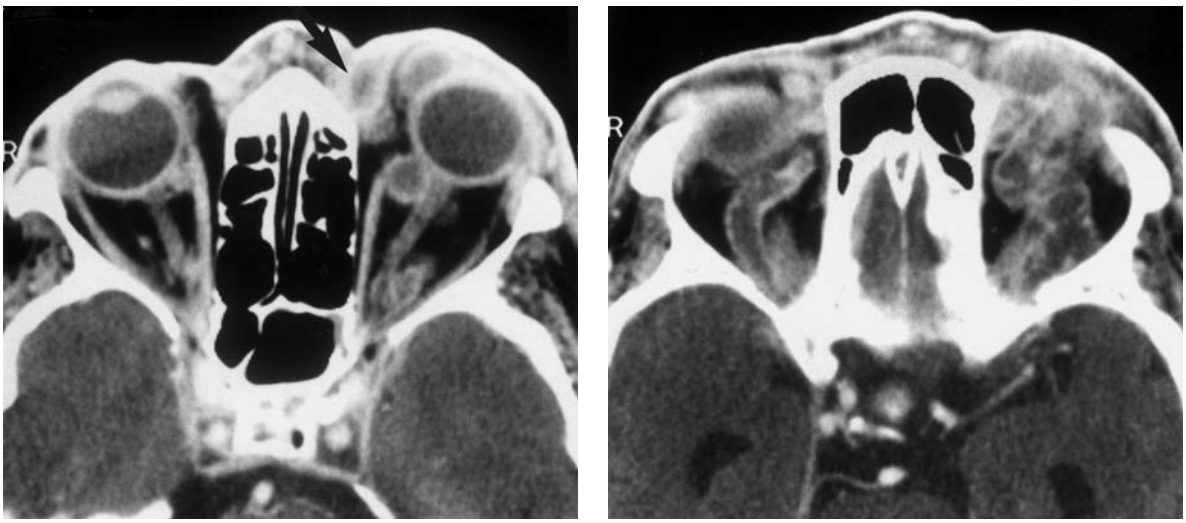

Fig. 6.59a,b. A 43-year-old woman with tongue and oropharynx carcinoma presenting in a febrile state with acute N III paresis and left-sided protrusion. Diagnosis: extensive thrombosis of the cavernous sinus and intraorbital veins. Axial contrast-enhanced CT: **a** Enlarged, sharply defined structures with central low density at the level of the optic nerve. The lesions are intraconal, extraconal, as well as preseptal (enlarged angular vein [*arrow*]). Note enhancement of both ICA in the hypodense, nonenhancing, but thrombosed cavernous sinus. **b** Involvement of both superior ophthalmic veins in the superior part of the orbit, the thrombi sparing the normal intravascular contrast (rubber phenomenon). (With permission of Dr. R. Gustorf-Aeckerle, Katharinen Hospital, Stuttgart)

women (Fig. 6.63). The therapeutic regimen does not depend on the etiology but on the flow characteristics, whether the symptoms are caused by a so-called high-flow or low-flow fistula.

Digital subtraction angiography (DSA) is the examination of choice in defining the CCF type. Pathophysiological classification of CCF into high-flow (type A) (Figs. 6.60–6.62) and low-flow (type B) fistula (Fig. 6.63) is crucial in determining the definite therapy (Debrun 1993). In high-flow fistula, interventional neuroradiological procedures with balloon and/or coil embolization, used to occlude the site of the ICA injury (Figs. 6.61, 6.62), will protect against or even reverse the threat of vision loss. In some cases, therapy for low-flow fistula may be unnecessary, since these frequently close spontaneously (Debrun 1993).

The differential diagnosis of a dilated superior ophthalmic vein should include not only CCF, but also consider cerebral arteriovenous malformation (AVM) with atypical venous drainage (e.g., AVM of the vein of Galen, type II) (Berenstein and Lasjaunias 1992).

(Text continues on p. 205)

Fig. 6.60a–d. A 48-year-old woman with slowly progressing, bilateral proptosis associated with bruit. Diagnosis: spontaneous carotid-cavernosus fistula (CCF, type A) of the left ICA. CT: **a** Axial contrast-enhanced image with bilateral dilation of the superior ophthalmic vein with emphasis to the left, suggesting the presence of free flow in the intercavernous sinus. **b** Color duplex sonography demonstrating a severely dilated superior ophthalmic vein (*red*) with reversal of flow direction and arterial pulsatile Doppler spectrum. Assessment of the flow velocity enables the differentiation between a high-flow and low-flow fistula. **c** DSA of the left ICA (*arrowheads*) in lateral view: The origin of the arteriovenous fistula (*large arrow*) of the ICA is identified in the cavernous sinus. As a result of the large shunt volume, not only are the cavernous sinus and the superior ophthalmic vein (*star*) filled, but also the pterygoid venous plexus, the superior petrosal sinus, and the internal jugular vein (*small arrows*); however, there is no evidence of filling of the intracranial vessels. **d** Corresponding anteroposterior (AP) view with identification of the site of the fistula (*large arrow*), ipsilateral ophthalmic superior vein (*large star*), superior petrosal sinus (*small star*), and intercavernous sinus (*small arrow*). (With permission of Müller-Forell and Lieb 1995b)

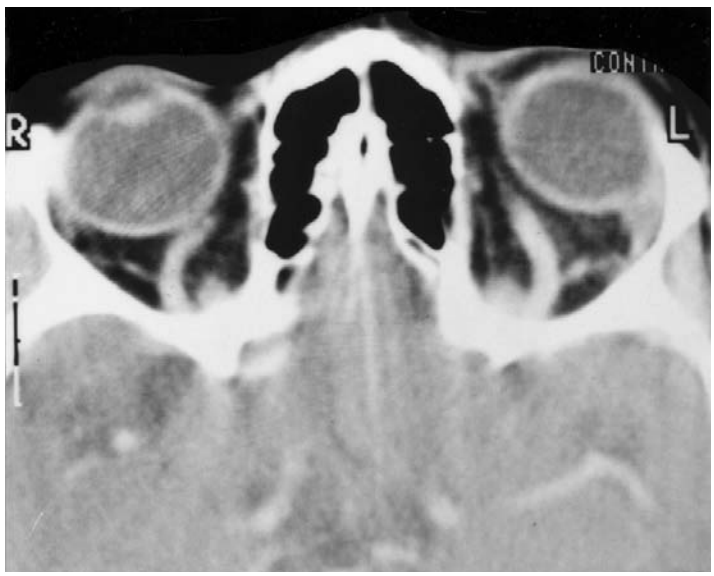
R
L

a

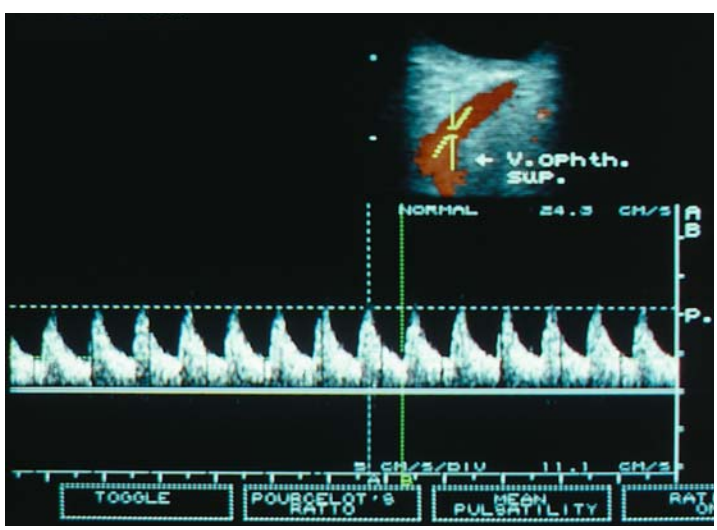
← V. Ophth. sup.
NORMAL
TOGGLE
POURCELOT'S RATIO
MEAN PULSATILITY

b

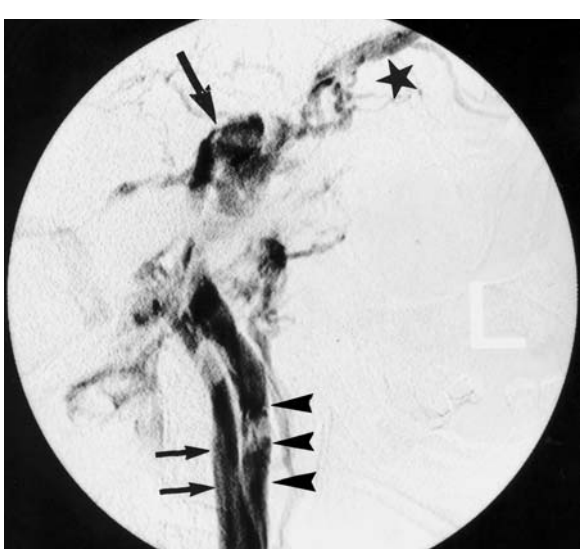

c

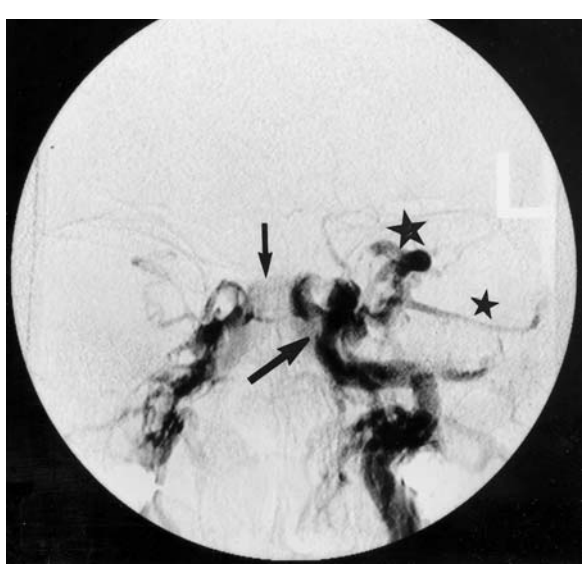

d

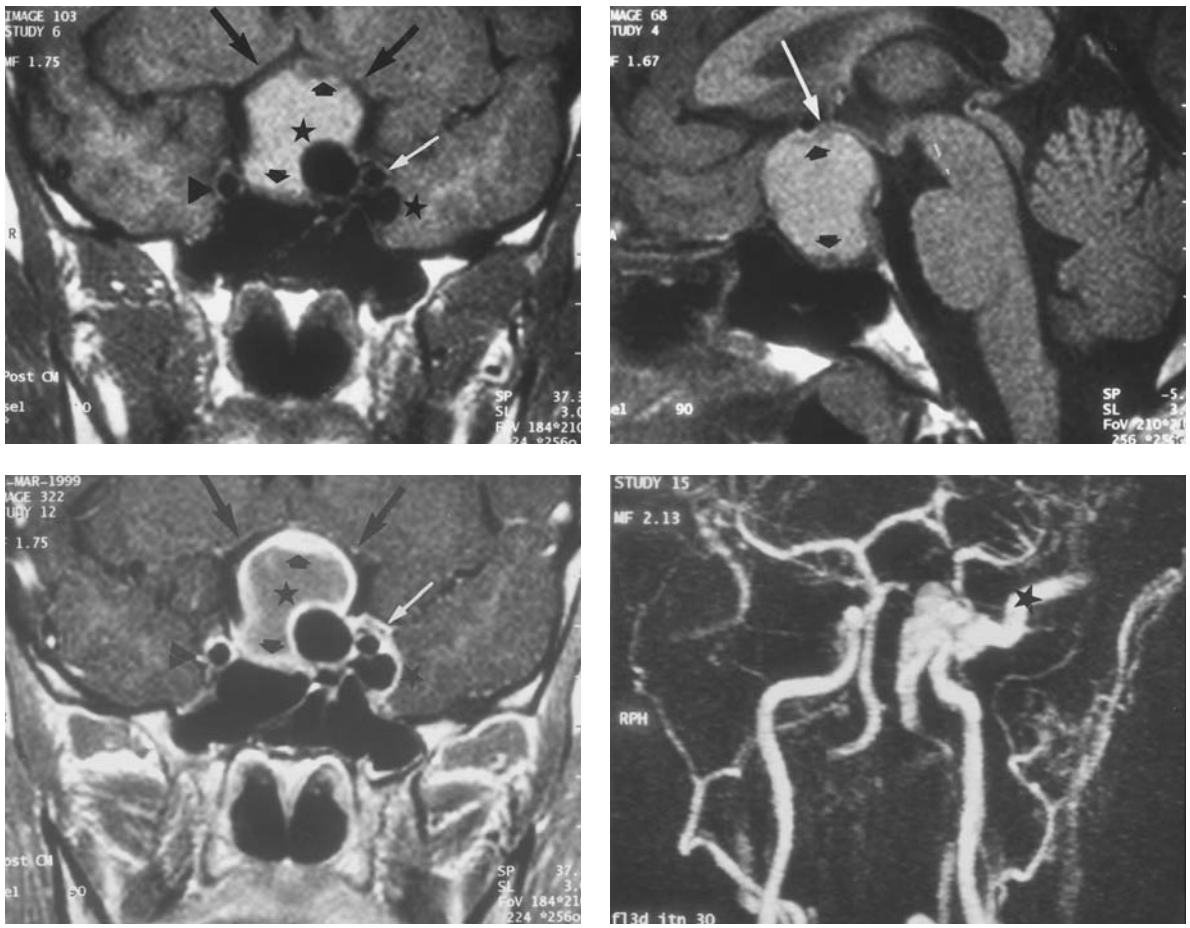

Fig. 6.61a–k. A 25-year-old woman after sellar surgery (external) by transsphenoidal approach for pituitary adenoma 6 months previously. The patient developed proptosis and chemosis of the left eye with pulsatile bruit postoperatively, but ignored the presence of symptoms. Diagnosis: iatrogenic high-flow CCF of the left ICA after transsphenoidal biopsy for intra- and suprasellar pituitary adenoma. MRI: **a** Coronal T1-weighted native view demonstrating substantial suprasellar extension of the pituitary adenoma with compression and apicalization of both A1 segments (*arrows*). Note the spherical signal void (*stars*) medial and lateral of the cavernous segment of the left ICA (*white arrow*, right ICA: *triangle*) as well as the small, isointense pituitary gland remnant at the sellar floor and at the upper border of the tumor (*short arrows*). **b** Midsagittal T1-weighted native view demonstrating a (neuro-ophthalmologically silent) compression of the chiasm (*white arrow*) (*short arrows*: remnants of normal pituitary gland). **c** Coronal, T1-weighted, contrast-enhanced view (corresponding to **a**), demonstrating the cystic nature of the tumor and signal enhancement of the pituitary gland remnants. **d** Coronal contrast-enhanced MR-angiography (3D-TOF) with demonstration of carotid leakage into the ipsilateral cavernous sinus and filling of the superior ophthalmic vein (*star*). DSA: **e** AP view of an early phase of left ICA, showing only slight distal filling, but immediate opacification of the cavernous sinus and basal plexus (*arrowhead*), compare with **a**, **c**, **d**. **f** Corresponding lateral view with slight opacification of the superior ophthalmic vein (*star*) and basal plexus (*arrowhead*), but intense contrast of the cavernous sinus. **g** Oblique view of the right ICA with contralateral carotid compression, demonstrating the intact Willis' circle and collateral circulation of the left hemisphere, as well retrograde filling of the cavernous sinus fistula. Note the extension of the elevated anterior cerebral arteries (caused by the pituitary mass). **h** Lateral view of the left vertebral artery with confirmation of the blood supply to the left hemisphere by Pcom. **i** AP view of the left ICA after balloon occlusion of the fistula, demonstrating antegrade flow in the left ICA. Continued elevation of the A1 segment due to the presence of the tumor (compare with **a**, **c**, **d**). **k** Corresponding lateral view. A slight contrast loss in the carotid siphon is due to overprojection of the inflated balloon

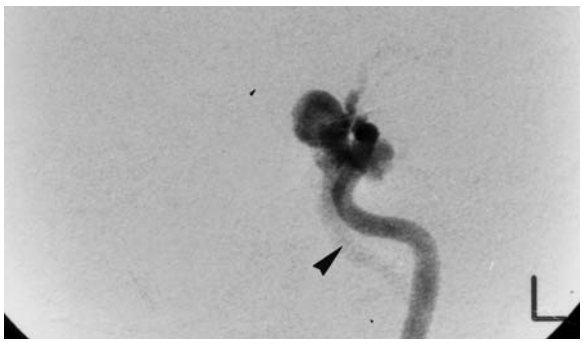

e

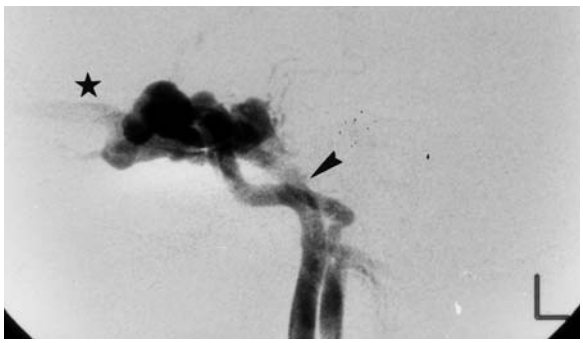

f

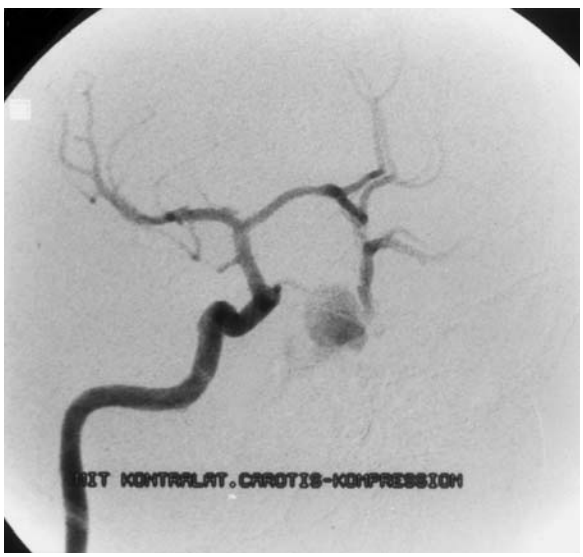

g

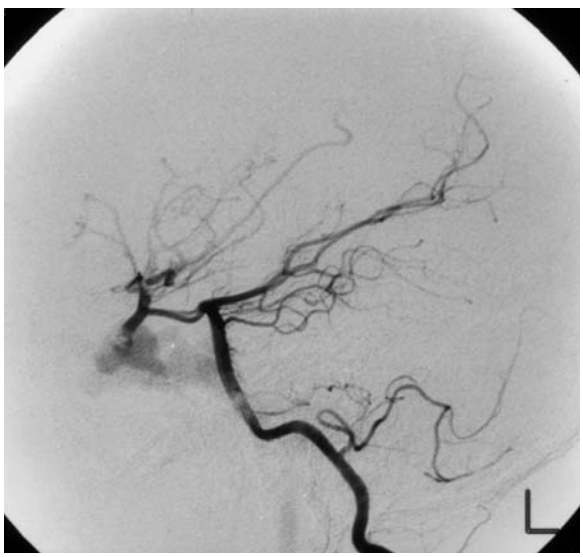

h

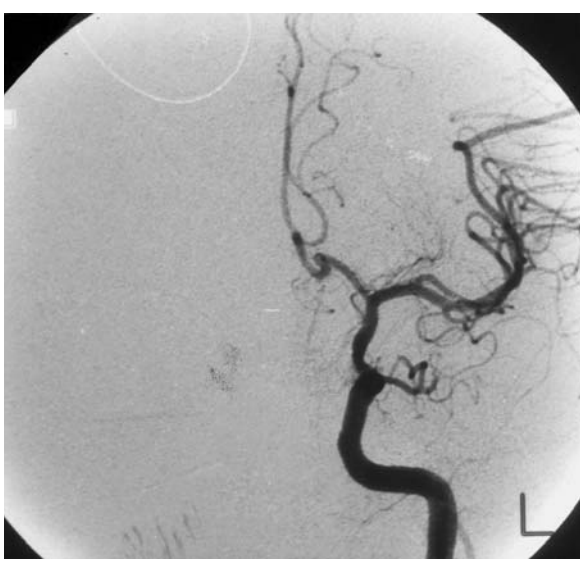

i

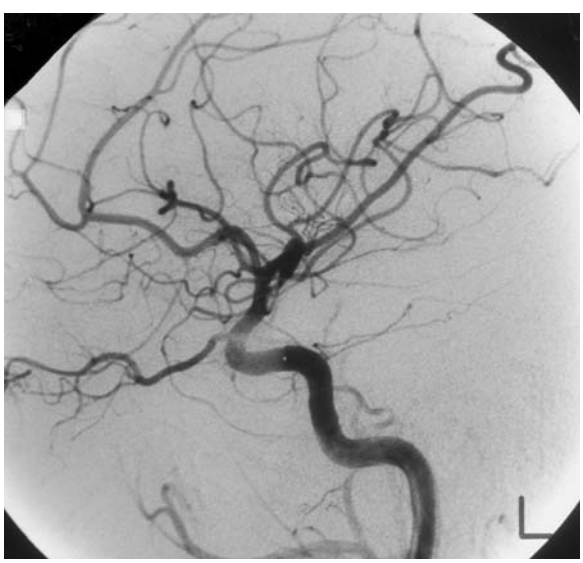

k

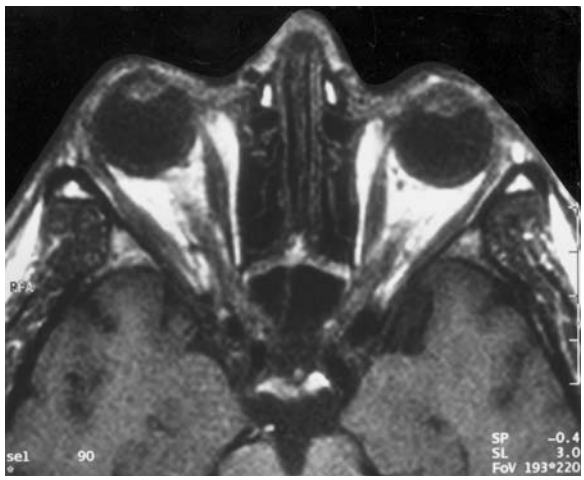

a

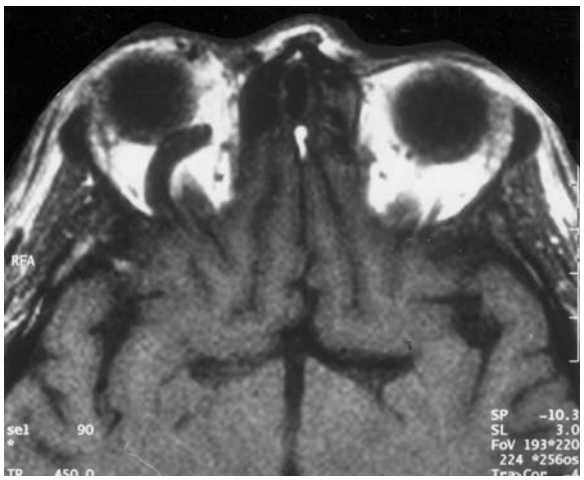

b

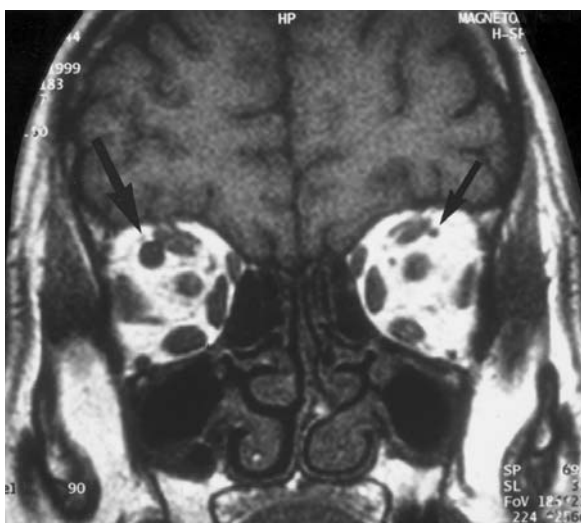

c

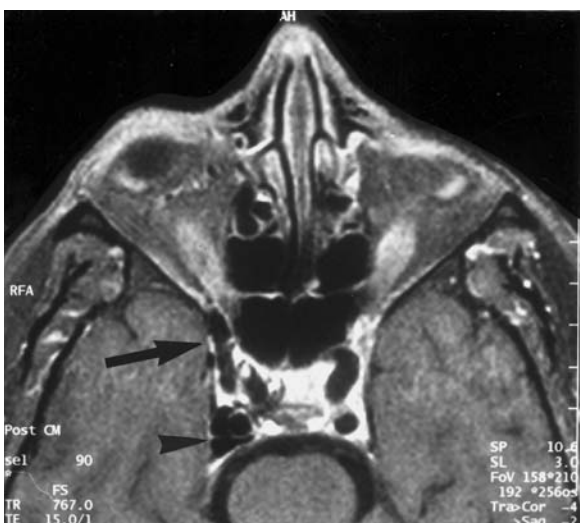

d

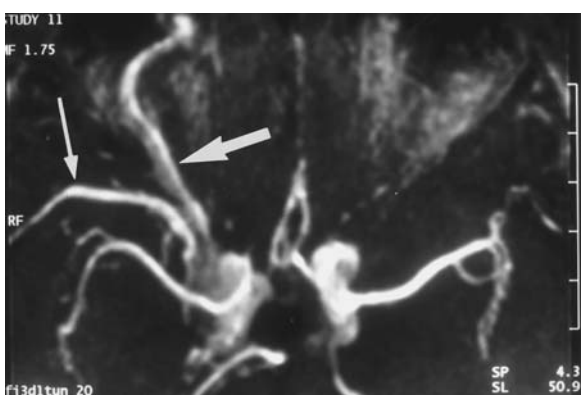

e

Fig. 6.62a–i. A 54-year-old man with spontaneous blurred vision and painless, but progressing proptosis of the right eye (5 mm in 4 weeks), in addition to chemosis, proptosis, and a (subjective and objective) pulsatile bruit over the right orbit. Diagnosis: high-flow CCF. MRI: **a** Axial T1-weighted native view at the level of the optic nerve, showing only mild proptosis, but initial enlargement of the right external muscles compared to the left. **b** Axial T1-weighted view of the upper orbit with extreme widening of the right superior ophthalmic vein. **c** Coronal T1-weighted view identifying the different lumen of the... ▷

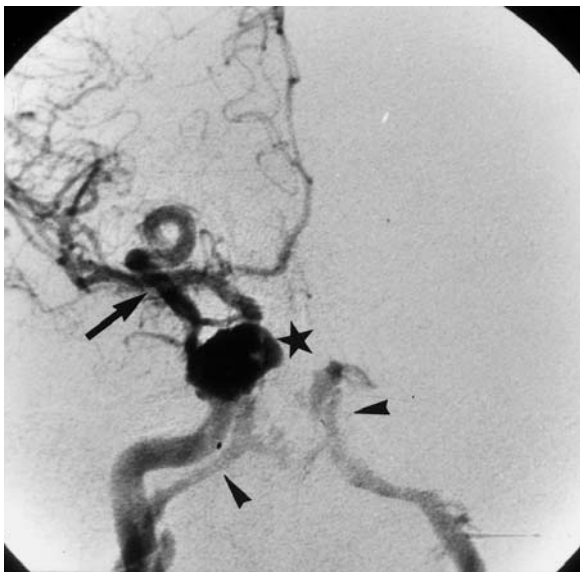

f

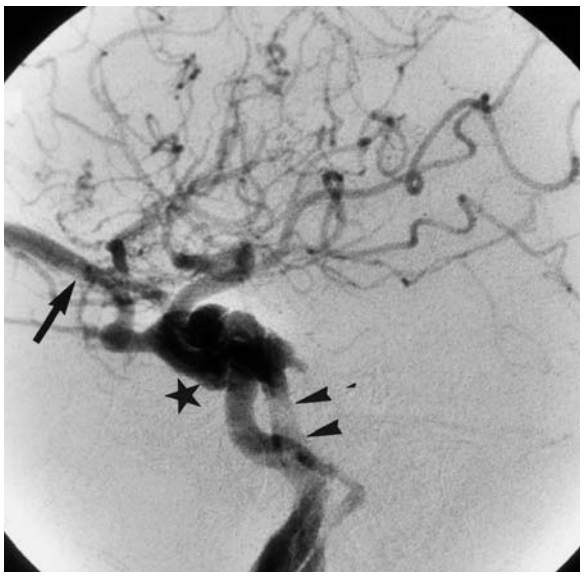

g

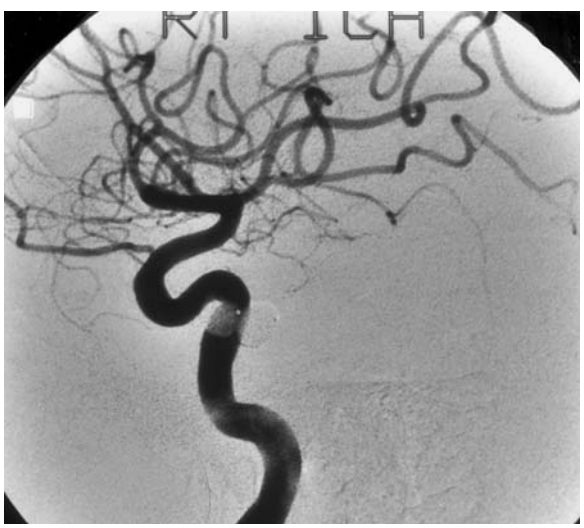

h

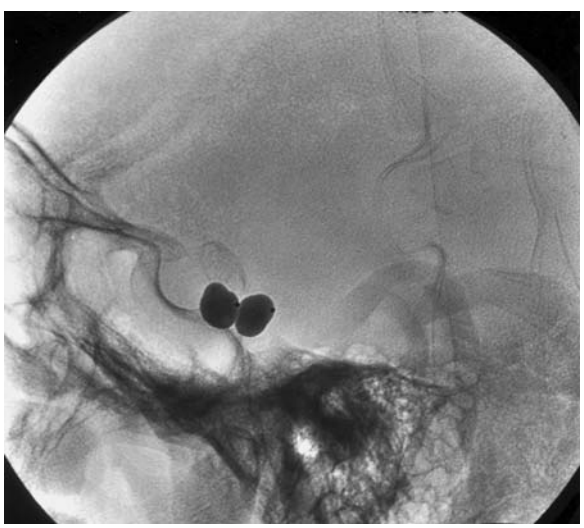

i

...right superior (*large arrow*) compared with the left superior ophthalmic vein (*small arrow*). **d** Axial, T1-weighted, contrast-enhanced (FS) view of the lower orbit, showing the junction of the widened superior ophthalmic vein (*arrow*) and the cavernous sinus in the superior orbital fissure, as well as the flow void of the arterialized right lateral part of the cavernous sinus (*arrowhead*). **e** MR-angiography (3D-TOF): axial view showing opacification of the right superior ophthalmic vein (*white arrow*), a smaller lumen of the right ICA, and a dilated sphenoparietal sinus (*small white arrow*) along the rostral circumference of the medial cranial fossa. **f** DSA: AP view of an early arterial phase of the right ICA with filling of the right cavernous sinus (*star*) and widening of the superior ophthalmic vein (*arrow*), projecting over the ipsilateral M1 segment. Opacification of the left and right basilar venous plexus (*arrowheads*). **g** Corresponding lateral view. **h** Lateral view after interventional therapy with placement of two detachable balloons in the cavernous sinus, demonstrating complete occlusion of the fistula with antegrade flow in the ICA. **i** Corresponding native view, showing the extension and placement of the inflated balloons

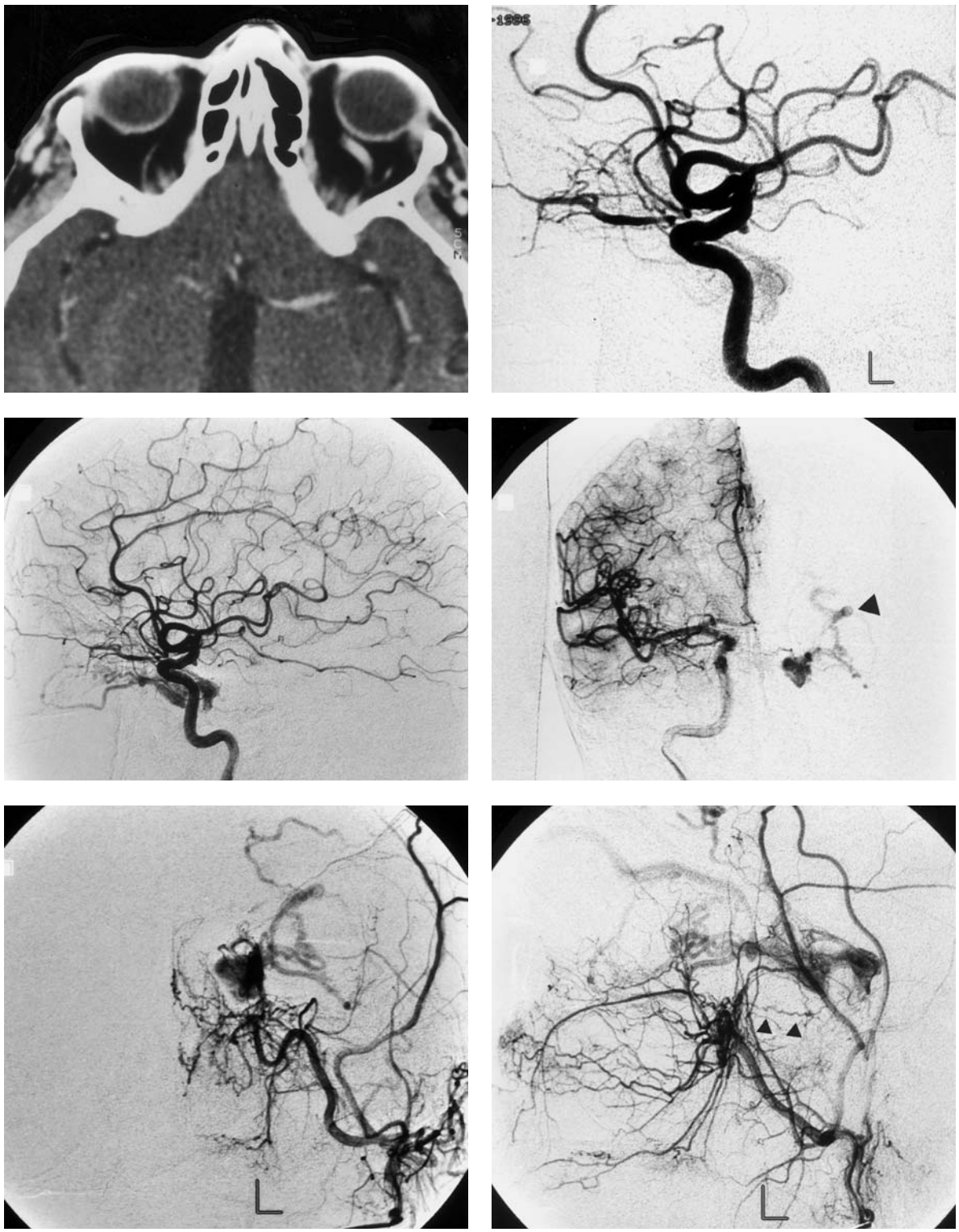

Fig. 6.63a–f. A 74-year-old woman with progressive vision loss and chemosis of the left eye. Diagnosis: carotid-cavernous sinus fistula (CCF), type B. CT: **a** Axial contrast-enhanced image with slight, but unequivocal enlargement of the left superior ophthalmic vein. DSA: **b** Lateral view of the left ICA, showing a slightly contrasted cavernous sinus. **c** Later phase of the lateral view of the left ICA with improved filling of the cavernous sinus. **d** AP view of the right ICA; comparable to the left side; small capillary-sized arteries of the inferolateral trunk can be identified and are suspected of feeding the low-flow shunt; antegrade filling of the cavernous sinus and the superior ophthalmic vein (*arrowhead*). **e** AP view of the left external carotid artery (ECA). **f** Lateral view of the left ECA with an additional shunt fed by the artery of the round foramen (*arrowheads*)

6.2.3 Inflammatory Lesions

6.2.3.1 Idiopathic Orbital Disorders ("Orbital Pseudotumor")

Since the commentary of Rootman (1998), the term orbital pseudotumor, previously used to classify a vast range of diseases of diverse character and etiology, should be discontinued. Since this term has contributed to diagnostic confusion both clinically and pathologically, it should be replaced by a more specific definition regarding the clinical and pathophysiological underlying patterns. Although the diversity of underlying disorders represents the most frequent pathologic processes of the orbit and, in particular, of the globe, and the third most common ophthalmologic disease after Graves' and lymphoproliferative diseases (Weber et al. 1996a; Zurlo et al. 1999), there are four major clinical processes that may affect any structure of the orbit. These include inflammatory, infiltrative, mass effect, and vascular changes that present with different but specific clinical symptoms. Following consideration of a specific finding on imaging study, the age of the patient, systemic evaluation, testing, and biopsy, the diagnosis can be made in an individual case (Rootman 1998). A biopsy is required upon the detection of a nonspecific, possibly granulomatous, benign orbital inflammation without evidence of specific local or systemic disease to exclude the possibility of other diseases. However, systemic steroid therapy without prior biopsy confirmation may be regarded as a pragmatic therapeutic strategy in the majority of cases. Care should be taken not to misinterpret the rapid improvement as being pathognomonic, since many tumors (especially lymphomas) are characterized by a similar presentation and may only be differentiated by biopsy (Mombaerts et al. 1996).

Inflammatory signs and symptoms consist of painful proptosis, warmth, loss of function including blurred vision, and mass effect (Harnsberger 1990; Casper et al. 1993; Rootman 1998). In an acute or subacute course, symptoms develop in days or weeks, while the chronic form may develop over a period of months, striking either sex at any age (Henderson 1994). Infiltrative changes are characterized by evidence of destruction, entrapment, or both, making the differential diagnosis from neoplasia or chronic infiltrative/inflammatory processes difficult. Mass effect consists of orbital structure displacement without or with signs of involvement of sensory or neuromuscular structures, while vascular changes show alterations in the character, size, or structural integrity of the vessels (Rootman 1998).

Histologically, cellular components are extremely variable (Mombaerts et al. 1996), consisting of mature lymphocytes, lymphoid follicles, plasma cells, neutrophil and eosinophil granulocytes, histiocytes, and macrophages (Rootman et al. 1988c, 1994), while vascular changes consist of capillary proliferation with lymphocytic infiltration (Henderson 1994).

Bilateral involvement is considered to be a manifestation of chronic, progressive, immune-mediated, generalized fibrosis, observed in patients with additional retroperitoneal fibrosis (Ormond disease) or in Erdheim–Chester disease (Fig. 6.69) (Levine et al. 1993; Flanders et al. 1989; Shields et al. 1991; McCarthy et al. 1993; Mombaerts et al. 1996; Valmaggia et al. 1997; Schaffler et al. 2000; Sheidow et al. 2000). The differential diagnosis of the latter two conditions is not readily achieved based on clinical symptoms and imaging findings, and a biopsy should be carried out.

The classification of idiopathic orbital disease varies, with some authors making a division on the basis of the temporal course into the clinical stages of acute or chronic (Bilaniuk et al. 1990), or according to the specific localization of the inflammatory process (Mafee 1996). We prefer a morphologic classification according to diffuse and local forms (Harnsberger 1990; De Potter et al. 1995; Casper et al. 1993). Though this classification dates from the time of the so-called "orbital pseudotumor", in our opinion a classification into diffuse or local involvement still remains useful in clinical terms. In diffuse idiopathic orbital inflammation, every orbital structure may be involved to a different degree, whereas in the localized form, only one of the different parts of the orbit, i.e., the globe, fat, or muscles, are affected (see scleritis 6.1.3.1, perineuritis 6.4.2.1).

Although nonspecific, the most frequently observed CT and MRI finding characteristic of idiopathic orbital inflammation is contrast enhancement, due to the high vascularity of the inflammatory process (Figs. 6.64, 6.65, 6.66), infiltration of the fat, proptosis, and an isolated or general, uni- or bilateral, extraocular muscle enlargement (Flanders et al. 1989). The MRI appearance of hypointensity on T2-weighted images relative to normal muscle signal intensity may differentiate idiopathic orbital inflammation from metastatic tumors or vascular congestion (Atlas and Galetta 1996). In the differential diagnosis from true orbital tumors (e.g., lymphomas), the abrupt, mostly painful clinical onset with blurred vision at an early stage

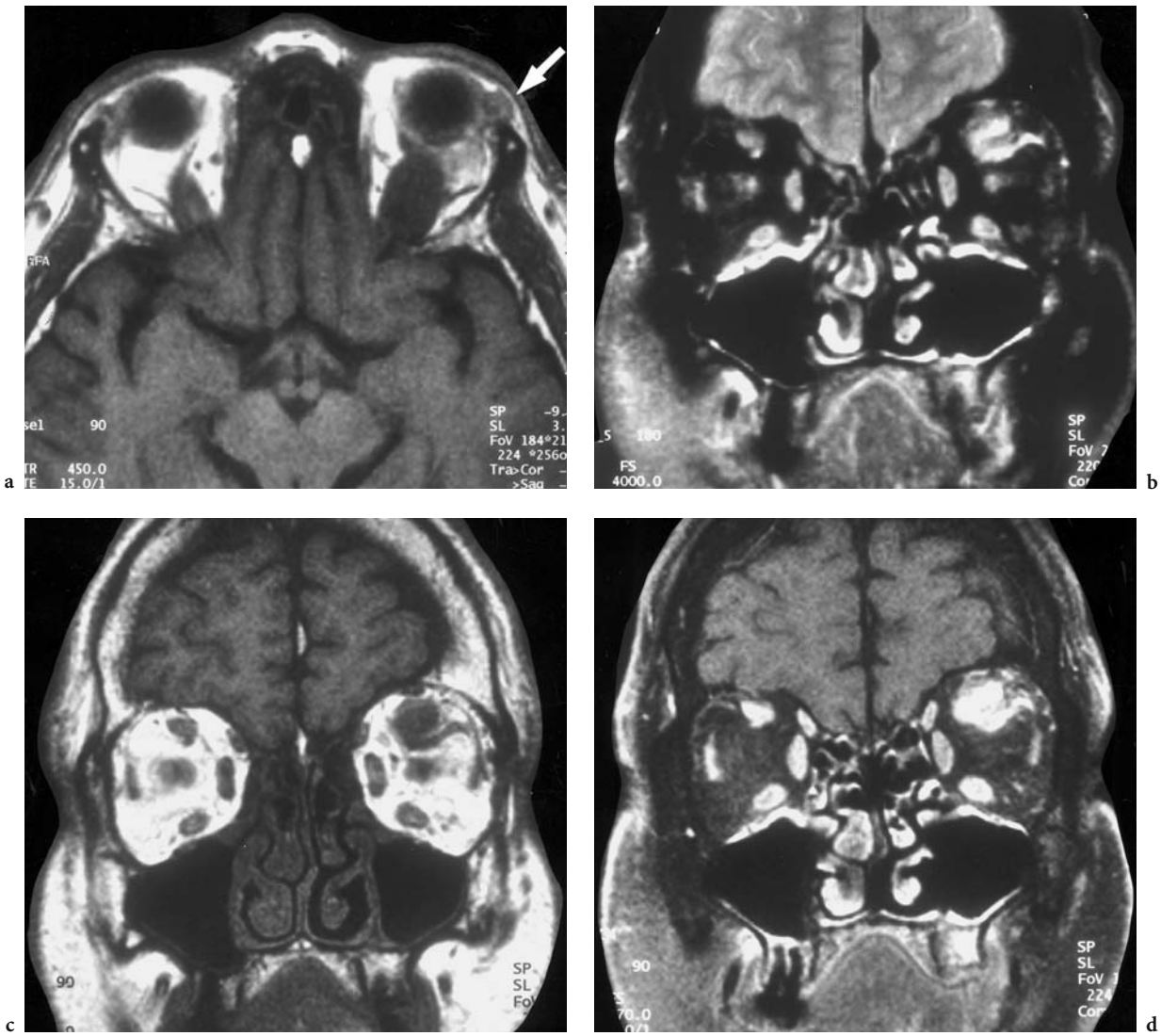

Fig. 6.64a–d. A 48-year-old man with slowly progressing, left exophthalmos suspicious for Graves' disease. Diagnosis: chronic granulomatous inflammation. MRI: **a** axial T1-weighted view with enlargement of the superior rectus muscle and neighboring lateral extraconal lesion, protruding towards the left lacrimal gland (*arrow*). **b** Coronal T2-weighted (FS) image with apparently edematous infiltration of the fascia, dividing the involved superior rectus and levator palpebrae muscle. **c** Corresponding T1-weighted native view. **d** Corresponding contrast-enhanced (FS), T1-weighted view where the signal enhancement of the infiltration is best seen between the superior rectus and levator palpebrae muscle

may also be suggestive (Mauriello and Flanagan 1989). The differential diagnosis may be difficult when imaging shows a lack of infiltration, distortion of the shape of the globe, or bony erosion, especially in the tumefactive type of idiopathic orbital inflammation (Flanders et al. 1989).

As mentioned above, idiopathic orbital inflammation may involve all orbital compartments and exhibit different patterns. Typical characteristics include painful, acute to subacute, mostly unilateral proptosis, combined with imaging findings of diffuse infiltration, swelling, and/or contrast enhancement of several intraorbital tissues (Figs. 6.65–6.67); it further may occur in a localized form in the intra- and extraconal compartment. Although usually confined to the orbital soft tissue, idiopathic orbital inflammation with or without mass effect can produce bone destruction and extraorbital extension (De Potter et al. 1995). In diffuse idiopathic orbital inflammation, CT and MRI show an infiltrative process of orbital fat with a

reticular pattern and variable contrast enhancement (Fig. 6.65). On MRI it is best seen on fat-suppressed T1-weighted images, where signal enhancement is marked in the acute form and minimal to moderate in the sclerosing and chronic type of idiopathic orbital inflammation (De Potter et al. 1995) (Fig. 6.64).

The differential diagnosis should comprise scars (Fig. 6.68), and in the presence of bilateral involvement, the possibility of xanthogranulomatous (lipoid) cell infiltration should be considered. In Erdheim-Chester disease (Fig. 6.69), a rare sporadic, systemic, histiocytic disorder of unknown etiology in adults, the patient presents with fibrosing xanthogranulomas, composed of xanthomatous histiocytes, fibrosis, and Touton giant cells. They are mainly found in the bone (Fig. 6.69), but may affect multiple organ systems, as lung involvement and retroperitoneal fibrosis are found (Egan et al. 1999). The histological features of foamy histiocytes may overlap with Langerhans' cell histiocytosis (see Sect. 6.3.1.4.3, 7.2.1.2.3, Fig. 5.19), but age and negative immunohistochemical staining with CD-1a and S100 should lead to the diagnosis of Erdheim-Chester disease (van der Lee et al. 1999). Corticosteroids might be efficacious, but the clinical course is potentially fatal. Orbital involvement is an uncommon manifestation, with usually bilateral xanthomatous infiltration of the anterior orbital fat, rarely the extraocular muscles and lacrimal gland (Shields et al. 1991; Jakobiec et al. 1993; Valmaggia et al. 1997; Wright et al. 1999). An extremely rare finding is the involvement of the entire orbit (Fig. 6.69), leading to compressive optic neuropathy and consecutive visual and eye movement deficits, but the combination with adjacent bone involvement like the sphenoid and sphenoid sinus may lead to a specific diagnosis.

Myositis is the local presentation of an idiopathic orbital inflammation with preferred involvement of only one external muscle. The combination of painful, acute proptosis with swelling of one affected muscle combined with impaired motility may be regarded as pathognomonic. Imaging demonstrates not only the enlarged muscle, but also inflammation of the tendon, a characteristic sign (Figs. 6.70–6.72). The most important differential diagnosis is that of Graves' disease, where the enlargement of the external muscle spares the tendon.

(Text continues on p. 213)

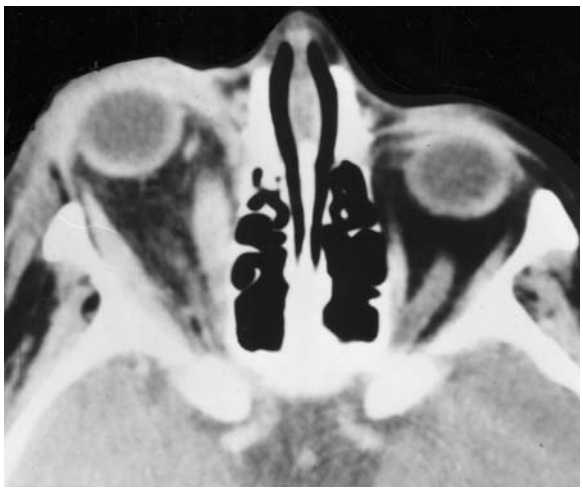

Fig. 6.65. A 4-year-old girl with progressing proptosis of the right eye and inflammatory constellation. Diagnosis: diffuse idiopathic orbital inflammation. The contrast-enhanced CT shows enhancement of all structures of the right orbit: the conjunctiva, sclera, rectus muscles, as well as the orbital fat

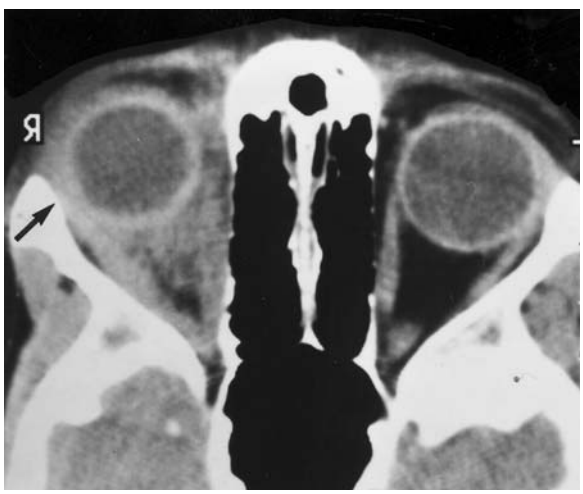

Fig. 6.66. Axial CT of a 10-year-old girl with painful, progressive exophthalmos of the right eye. Diagnosis: diffuse idiopathic orbital inflammation. Diffuse scleral thickening of the entire circumference, distinct, hazy hyperdensity of the retrobulbar fat, diffuse swelling of the lateral rectus muscle, including the tendinous insertion (*arrow*), but not affecting adjacent structures. (With permission of Müller-Forell and Lieb 1995b)

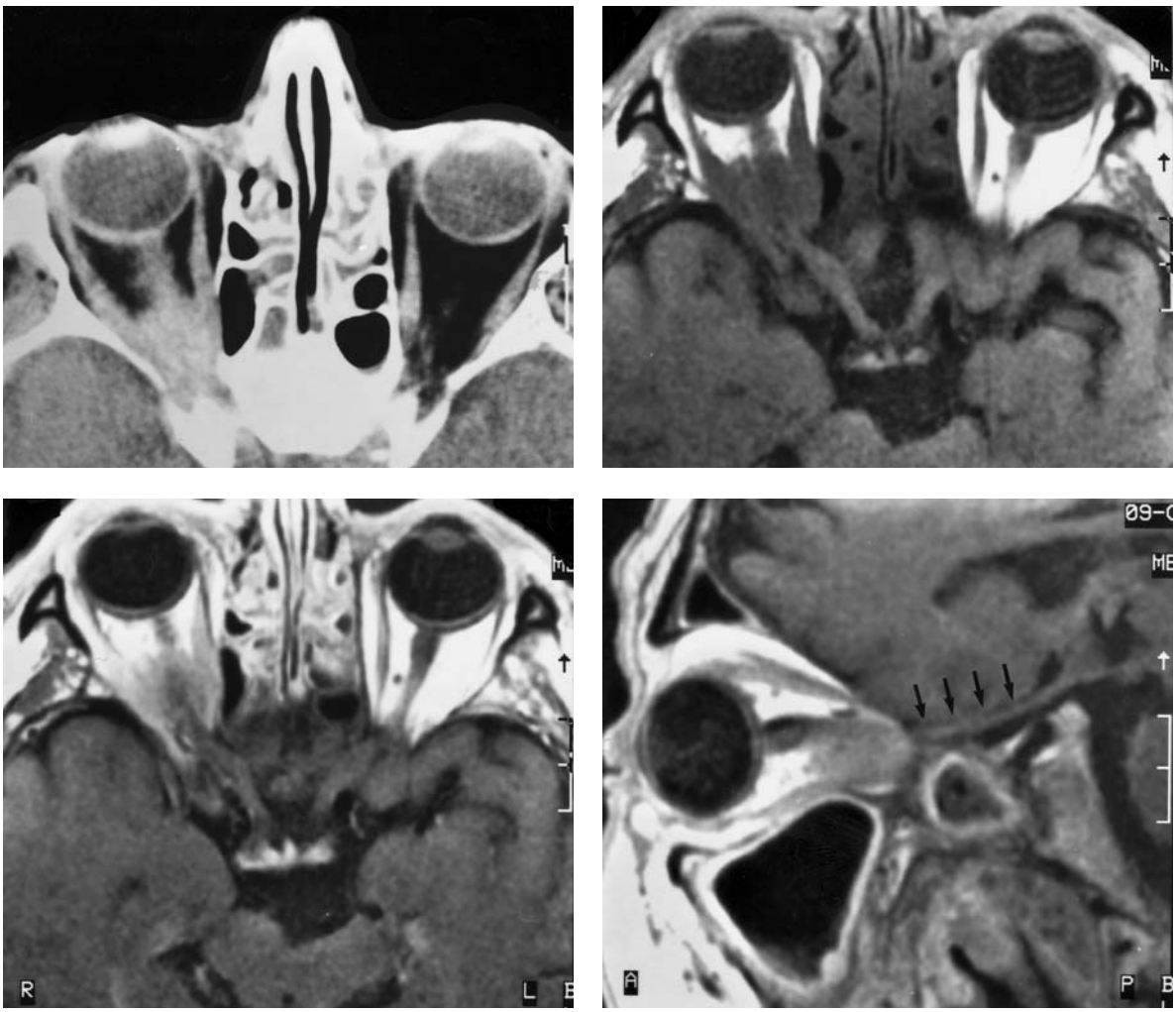

Fig. 6.67a–d. A 61-year-old man with a rapid, progressive visual deficit. Diagnosis: idiopathic orbital inflammatory mass. CT: **a** Axial contrast-enhanced image, showing an indistinct, space-occupying lesion in the right orbital apex. Apparent infiltration of the optic nerve is likely in view of the poor demarcation of the proximal part. MRI: **b** Corresponding axial T1-weighted native view with additional infiltration of the enlarged medial and lateral rectus muscles, compared with the left orbit. **c** Corresponding view after i.v. gadolinium, showing that the entire formation inclusive of the proximal optic sheath exhibits signal enhancement, confirming the inflammatory infiltration. **d** Parasagittal, T1-weighted, contrast-enhanced view showing the exclusive intraorbital location of the indistinct tumor-like lesion, and providing a overview of the intracanalicular optic nerve and optic tract. (With permission of Müller-Forell and Lieb 1995b)

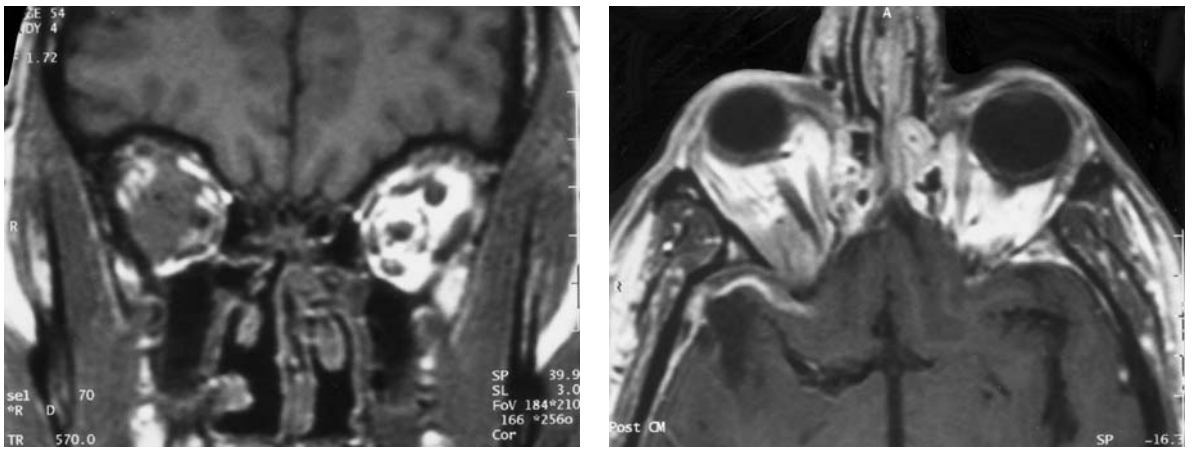

Fig. 6.68a,b. A 52-year-old man with slowly progressing, right-sided vision loss, ptosis of the right lid, double vision, right-sided temporo-orbital pain, and a history of severe head trauma several years prior to presentation. Diagnosis: scar tissue with chronic inflammatory infiltration after head trauma. MRI: **a** Coronal T1-weighted native view with intraconal, irregularly shaped formation in the right intraconal space, lateral of the optic nerve. **b** Axial, T1-weighted, contrast-enhanced image showing a space-occupying, slightly enhancing lesion of the right orbital apex. Note enhancement of the temporopolar dura and the defect of the temporopolar parenchyma. The histological assessment after orbitotomy did not identify a chronic inflammation, but confirmed the presence of chronic inflammatory infiltration

Fig. 6.69a–o. *(Continued on pp. 210+211)*

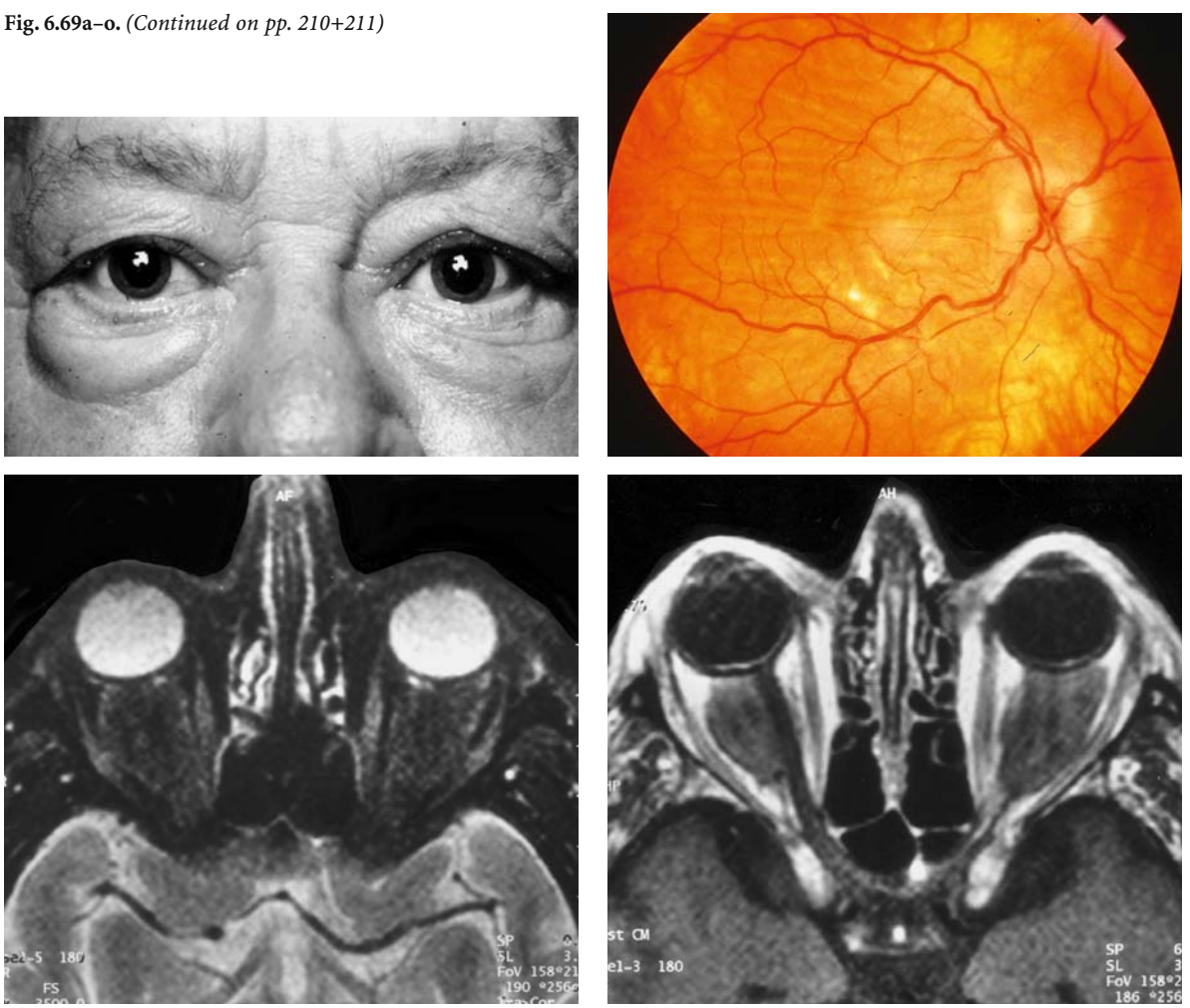

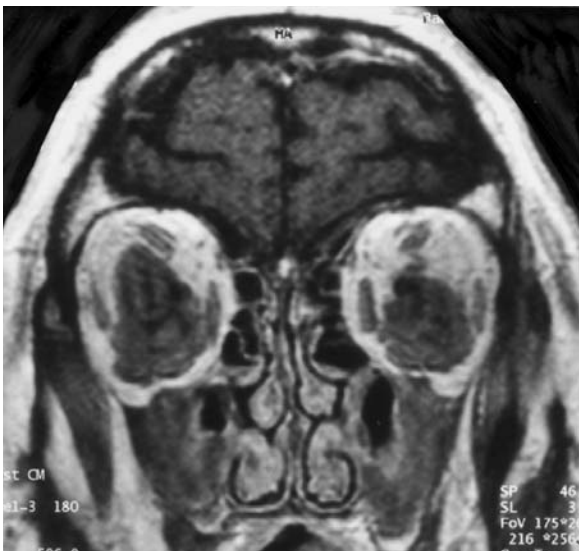
SP
SL
FoV 175*
216 *256

e

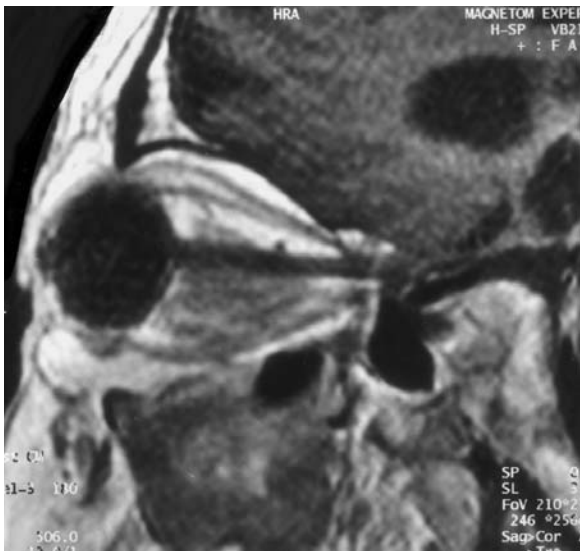
HRA
MAGNETOM EXPE
H-SP
SP
SL
FoV 210*
246 *25
Sag>Cor

f

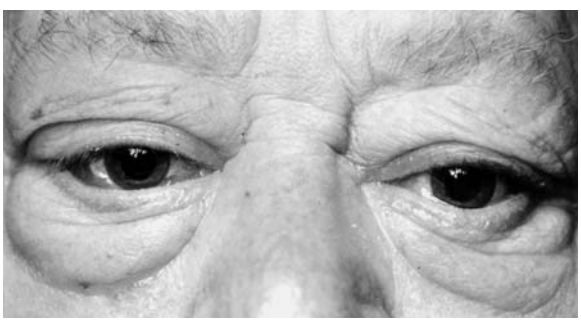

g

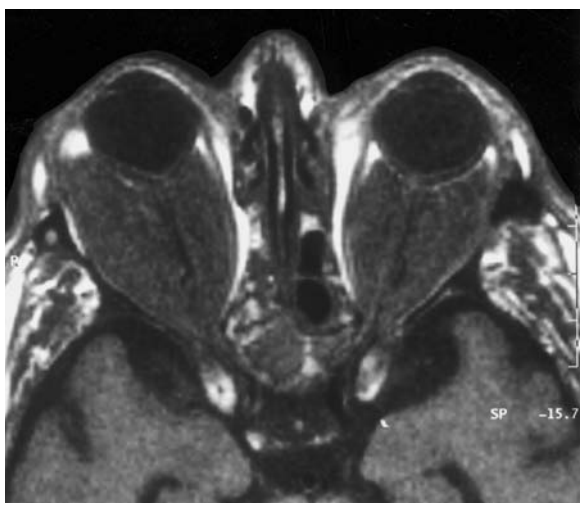
SP

h

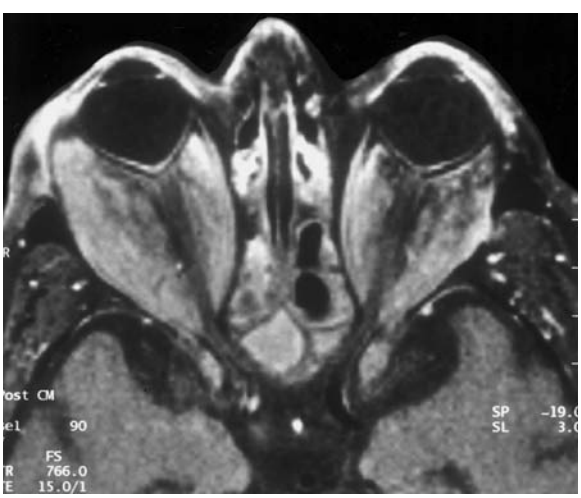
SP
SL
90
FS
766.0
15.0/1

i

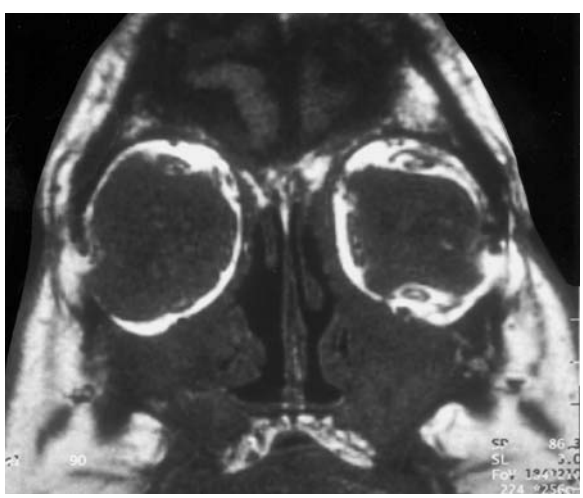
90

k ▷

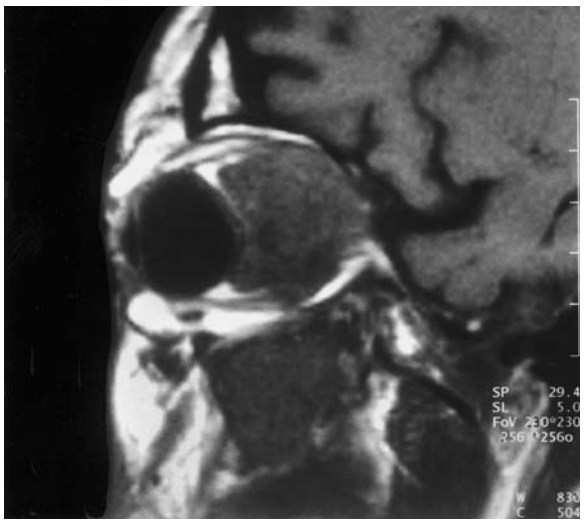

l

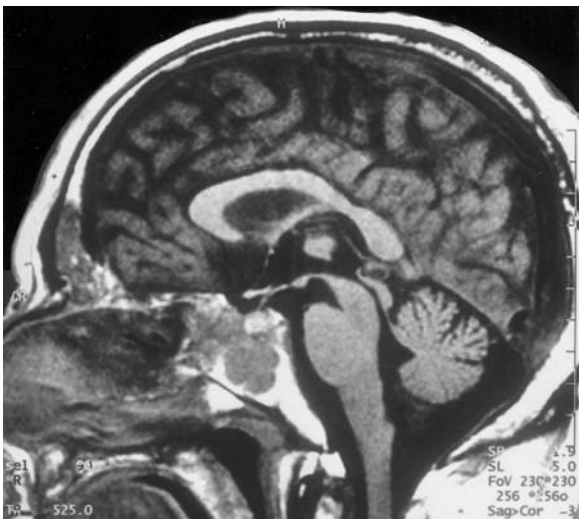

m

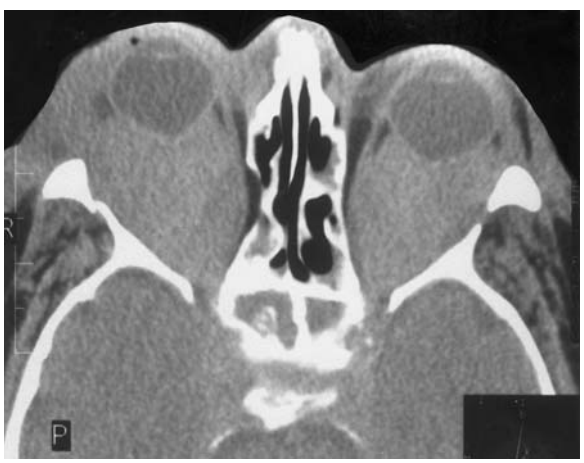

n

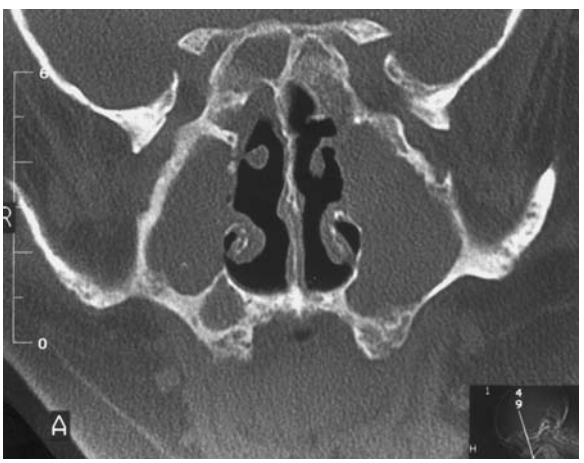

o

Fig. 6.69a–o. A 61-year-old man with slowly progressing, painless, bilateral protrusion. Diagnosis: bilateral idiopathic orbital mass associated with histologically proven retroperitoneal and epicardial fibrosis (Erdheim–Chester disease). **a** Portrait of the patient. **b** Fundus with choroidal folds and discrete blurring of the optic disc margin. MRI: **c** Axial T2-weighted view with bilateral, intraconal, solid, tumor-like structures with inhomogeneous and slightly hyperintense signal compared with the rectus muscles. **d** Axial, T1-weighted, contrast-enhanced view demonstrating a slight signal enhancement of the lesions (less than the external rectus muscles), but clear differentiation from the retrobulbar fat and the right optic nerve. **e** Coronal, T1-weighted, contrast-enhanced view, showing the infra-, para- and supraoptic expansion to be more extensive in the right orbit. Note the bilateral maxillary sinusitis. **f** Parasagittal, T1-weighted, contrast-enhanced view parallel to the left optic nerve with delineation of the impressed but not enlarged inferior rectus muscle. Course of the disease 5 years later with the patient suffering only from progressive visual deficit: **g** portrait of the patient with progression of proptosis. MRI: **h** Axial T1-weighted native view, demonstrating massive enlargement of the retrobulbar intraconal process, shaping the posterior parts of both globes, more extensively on the right than on the left side. Note the small, uninvolved external rectus muscles and compare with **d**. **i** Corresponding contrast-enhanced (FS) view where the signal enhancement is more pronounced than in **d**. **k** Coronal T1-weighted native view, showing the entire intraconal space occupied by the mass. Note the rest of retrobulbar intraconal fat in the left inferior orbit, divided by the inferior rectus muscle, and the compressed extraconal fat. **l** Sagittal paramedian T1-weighted view parallel to the left optic nerve (corresponding to **f**) with demonstration of additional supraoptic extension of the infiltrating tissue, now occupying the entire intraconal space. **m** Midsagittal view of the entire brain, showing infiltration of the frontal and sphenoid sinus as well as of the clivus. CT: **n** axial view. Note the spontaneous impression of the lamina papyracea, infiltration of the sphenoid sinus, and thickening of the walls, representing bone involvement of the granulomatous infiltration. **o** Coronal view in bone window, demonstrating chronic inflammatory disease with irregular thickening of all sinus walls

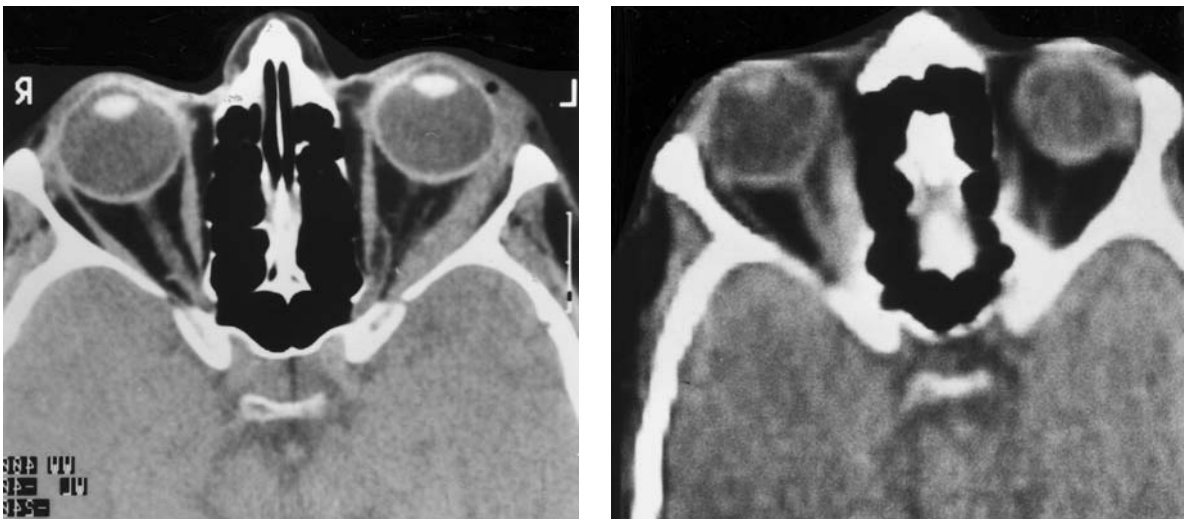

a b

Fig. 6.70a,b. A 56-year-old woman with painful proptosis of the left eye; the patient reported occurrence of the same symptoms on the contralateral side several years previously. Diagnosis: myositis of the left lateral rectus muscle. Axial CT: **a** thickening of the left lateral rectus muscle, including the tendon insertion. **b** CT done some years before, demonstrating inflammatory involvement of the contralateral medial rectus muscle. (With permission of Müller-Forell and Lieb 1995b)

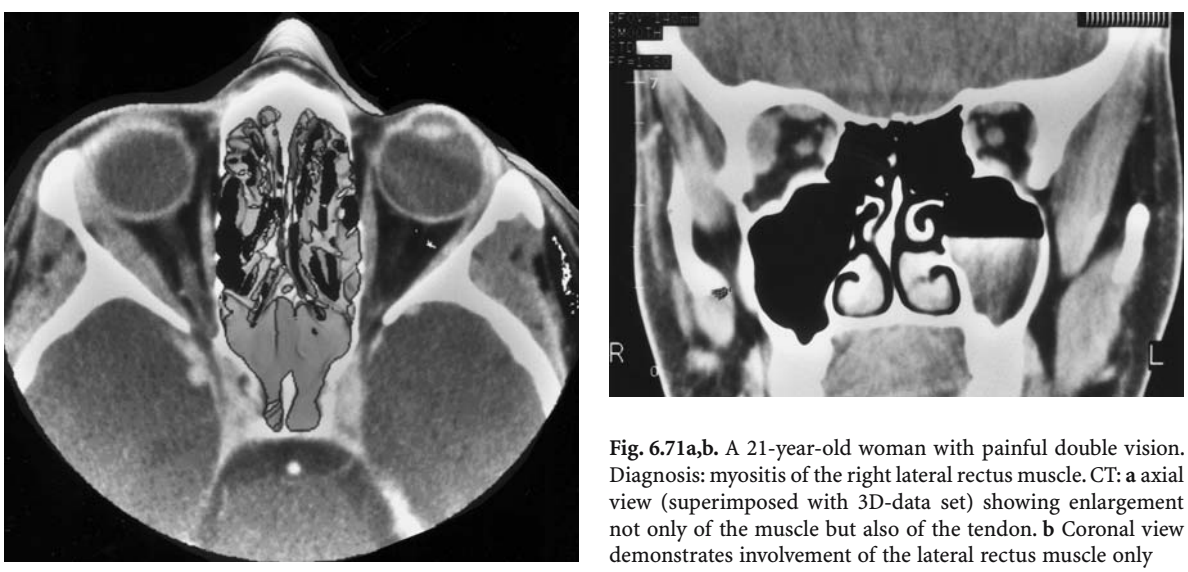

a b

Fig. 6.71a,b. A 21-year-old woman with painful double vision. Diagnosis: myositis of the right lateral rectus muscle. CT: **a** axial view (superimposed with 3D-data set) showing enlargement not only of the muscle but also of the tendon. **b** Coronal view demonstrates involvement of the lateral rectus muscle only

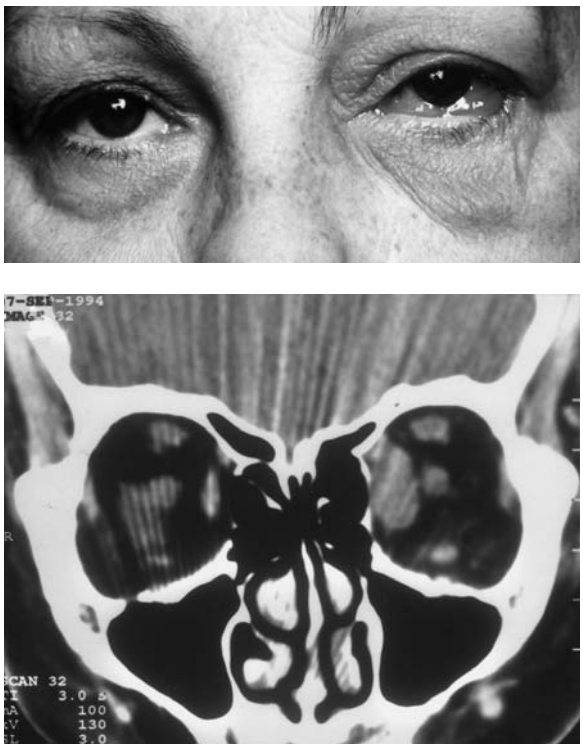

Fig. 6.72a–c. A 49-year-old woman with painful proptosis of the left eye, presenting with chemosis. Diagnosis: myositis of the left medial rectus muscle. **a** Portrait of the patient. CT: **b** Axial view, demonstrating thickening of the left medial rectus muscle, including the tendon. **c** Coronal view demonstrating the exclusive involvement of the medial rectus muscle

6.2.3.2 Endocrine Orbitopathy (Syn. Graves' Disease)

Dysthyroid endocrine orbitopathy is the most frequent cause of uni- or bilateral proptosis in adults. The clinical presentation of slowly progressing proptosis in this genetically determined autoimmune disease of the rectus muscles and the orbital connective tissue may be the first symptom in the course of autoimmune hyperthyroidism (morbus Basedow) or Graves' disease (Weetman and Hunt 1999; Pappa et al. 2000; Wiersinga and Prummel 2001). Apart from the classic clinical and ophthalmologic signs including conjunctival injection, lid retraction, and disturbance of motility, and endocrinological findings, imaging is indicated for the primary diagnosis as well as for follow-up examinations in the course of the disease. The extraocular muscles are the main targets with T-cell infiltration in the early stage of the disease and increased HLA-DR antigen expression on fibroblasts at all stages, suggesting an early immunosuppressive therapy in order to influence late fibrosis (Pappa et al. 2000). In addition to the extraocular muscles, lymphocyte inflammation, mucopolysaccharide and plasma cell infiltration leading to tissue edema involve all orbital structures (including the lacrimal gland). As bilateral involvement is more frequent than unilateral involvement (Char 1990; Kahaly et al. 1996), the preferred and primarily involved structures are the inferior and medial rectus muscles, followed by the superior and lateral orbital muscles (Fig. 6.73).

The most important morphological diagnostic criteria of endocrine orbitopathy include spindle-shaped spreading of the rectus muscles (>4 mm) without involvement of the tendon (Peyster and Hoover 1984) (Figs. 6.73, 6.74) and compression of the optic nerve in the orbital apex ("crowded orbital apex syndrome"; Neigel et al. 1988; Nugent et al. 1990) (Figs. 6.75, 6.76). An extended course of the disease may lead to a corresponding impression of the lamina papyracea – the normally parallel configured medial wall of the orbit – similar to spontaneous decompression (Fig. 6.75) (Nowinski and Flanagan 1986).

Volume measurements demonstrate an additional significant increase in retrobulbar fat (Fig. 6.77), predominantly in men, with a good correlation to the proptosis and duration of the disease (Müller-Forell et al. 1999). In more chronic stages, collagen deposition in the affected muscle results in fibrosis, and may be associated with fat accumulation (Fells

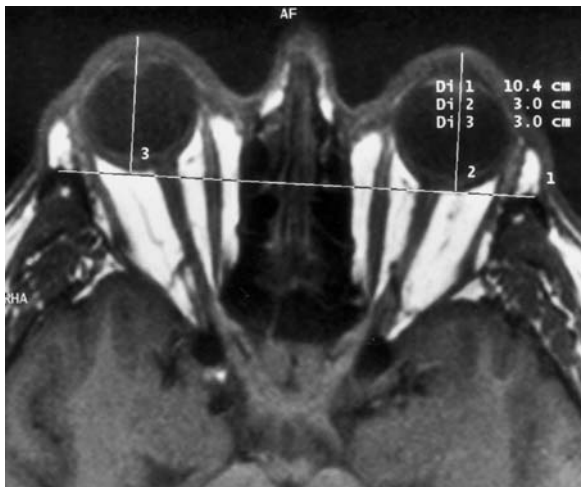

a

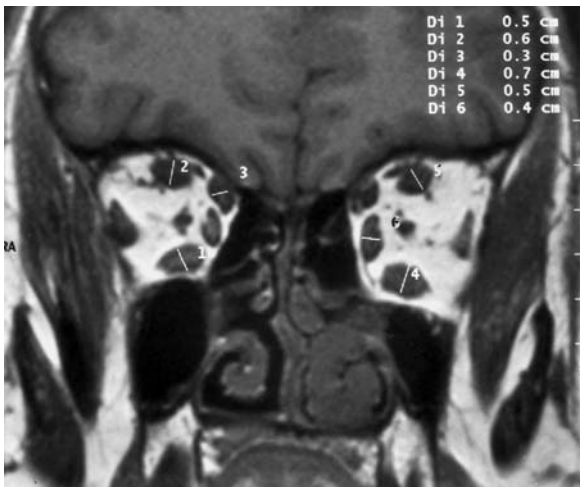

b

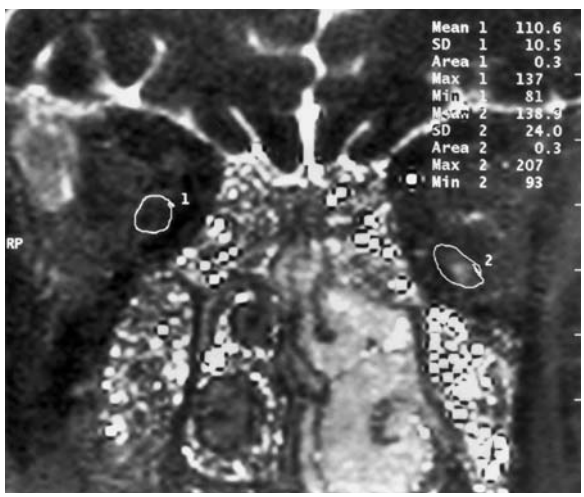

c

Fig. 6.73a–c. A 36-year-old woman with bilateral axial proptosis. Diagnosis: Graves' disease. MRI: **a** Axial T1-weighted view showing only minor muscle enlargement, while the measurement identifies a 30 mm bilateral ventral protrusion of the globe (D2, D3); the standard Hertel coefficient ranges at 23 mm. **b** Coronal T1-weighted view with measurement of muscle enlargement. **c** Coronal view with calculation of the T2 value, demonstrating acute inflammation of the left inferior rectus muscle at a T2 time of 138.9 compared with the corresponding right muscle (110.6). (With permission of Müller-Forell 1998)

et al. 1994), which is best seen on MRI. T1-weighted images show signal enhancement of the fatty degeneration, corresponding to hypointensity after i.v. gadolinium and fat suppression (Fig. 6.74).

In contrast to CT, where density measurements do not provide satisfactory answers to important questions regarding the acuteness of the disease, MRI offers the required additional information. On T2-weighted images, an increase in water content with a corresponding signal enhancement indicates the increased lymphocyte and mucopolysaccharide concentration of the involved inflamed muscle. Measurements of T2 relaxation time, using a T2-weighted multi-echo sequence, show lengthening of the affected muscles compared with the uninvolved ones, thus allowing the differentiation between an acute and chronic course of the disease (Hosten et al. 1989; Just et al. 1991). A prolongation of the calculated T2 relaxation time is seen in the presence of acute inflammation of the rectus muscle (Figs. 6.73, 6.76). A combination with fat-suppression techniques (STIR) further enables the detection of possible edema in the retrobulbar fat tissue (Hiromatsu et al. 1992; Pauleit et al. 1997). This differentiation is of the greatest interest with regard to the decision as to whether the patient may or may not benefit from immunosuppressive and/or radiation therapy (Utech et al. 1995; Pauleit et al. 1997). In rare cases where the evaluation of the acuity of Graves' disease is exceedingly difficult, an (expensive) extremely sensitive nuclear medical method is applied. Because in active Graves' disease activated lymphocytes express the somatostatin receptor

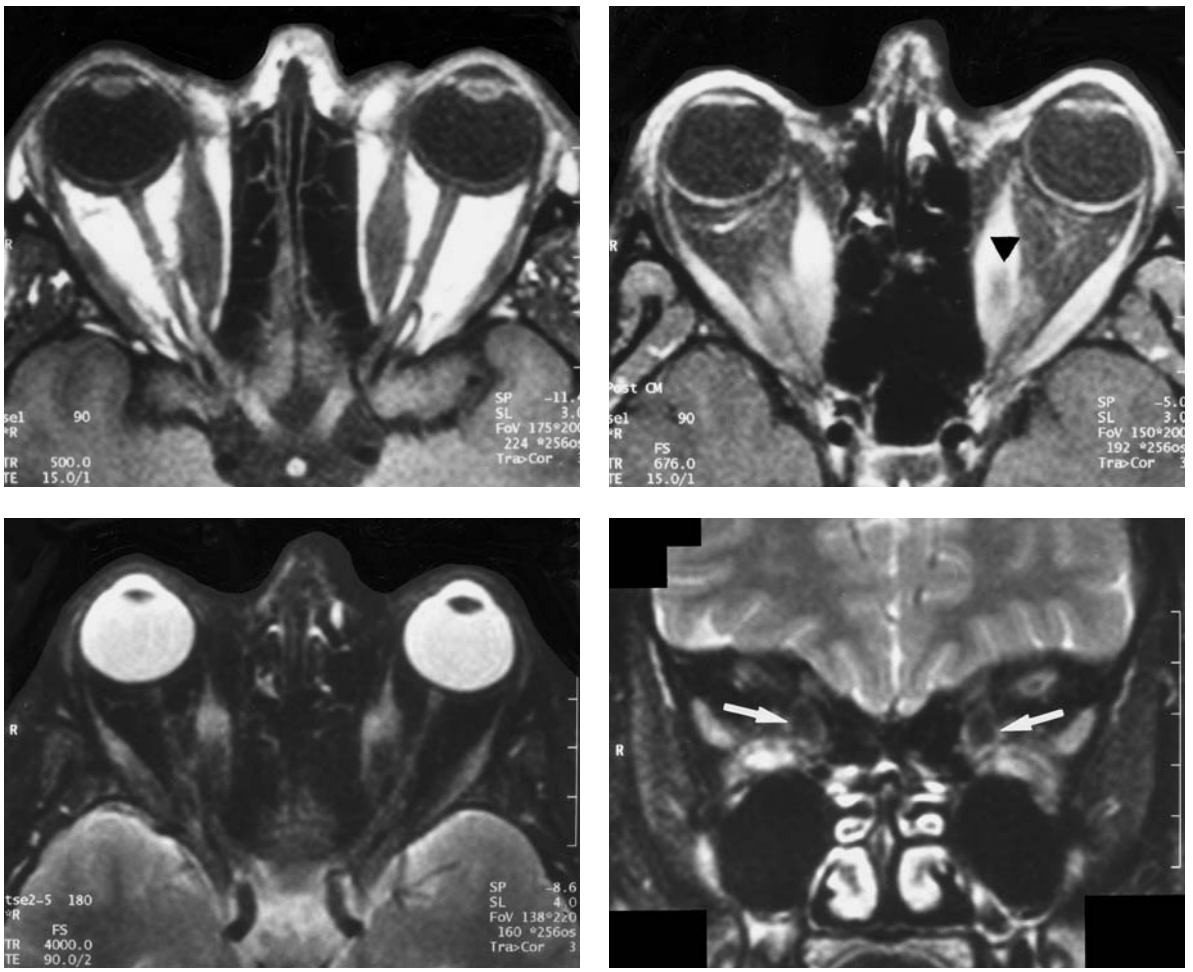

Fig. 6.74a–d. A 26-year-old woman with bilateral axial proptosis persisting for several years in the course of Graves' disease. Diagnosis: fatty degeneration in chronic Graves' disease. MRI: **a** Axial T1-weighted view, demonstrating a bilateral protrusion caused by the pouch-like, bilateral, symmetrical enlargement of the medial rectus muscles, sparing the tendons. **b** Corresponding T1-weighted, contrast-enhanced (FS) image showing a hypointense area in the left rectus muscle (*black arrowhead*), suspicions of fatty degeneration. **c** Corresponding T2-weighted (FS) acquisition confirming the presence of fatty degeneration by signal loss of the medial parts of both medial rectus muscles (*white arrows*). **d** Coronal T2-weighted view, signal loss of the areas of fatty degeneration is observed in the medial left as well as in both superior rectus muscles. (The hyperintensity of both inferior rectus muscles is due to susceptibility artifacts at the orbital floor)

octreotide, the local accumulation of octreotide in the orbital tissue can be demonstrated as a marked somatostatin receptor analogue that accumulates only in orbital tissue of high activity (Krenning et al. 1993; Kahaly et al. 1995) (Fig. 6.78).

In summary, we consider MRI to be the most effective tool in establishing the initial diagnosis of endocrine orbitopathy. Although the anatomic differentiation of orbital structures is similar for both CT and MRI, we prefer MRI for the primary diagnostic procedures not only because of the absence of invasiveness (radiation burden), but also due to its capability of differentiating between acute inflammatory and chronic stages of the disease.

The increase in orbital volume may lead to compression of the optic nerve in the orbital apex with corresponding venous congestion (the so-called "crowded orbital apex syndrome"; Neigel et al. 1988),

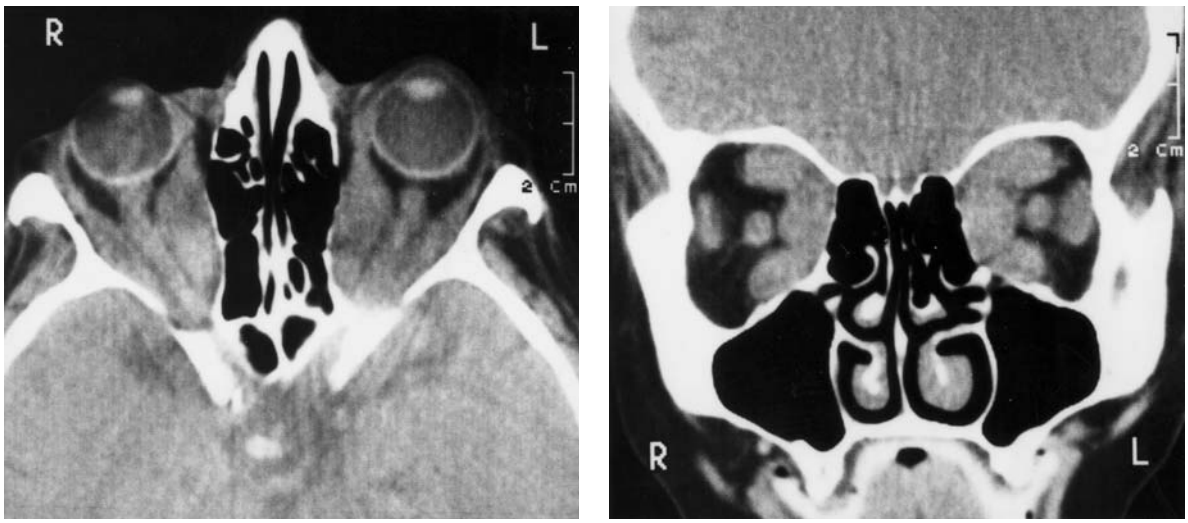

a b

Fig. 6.75a,b. A 73-year-old woman with bilateral exophthalmos. Diagnosis: Graves' disease. CT: **a** Axial view with severe thickening of all external rectus muscles, excluding the tendinous insertion. Note marked compression of both optic nerves at the apex and pressure exertion on the lamina papyracea responding to slight spontaneous decompression. **b** Coronal view. (With permission of Müller-Forell and Lieb 1995b)

which may lead to slowly progressing or acute visual deficit or loss. This finding, in addition to the presence of corneal ulcers due to massive proptosis, is a conclusive indicator for surgical intervention, while it is discretionary in the case of cosmetically disfiguring exophthalmos. Surgical decompression of the optic nerve with removal of different orbital walls is a therapy that provides space for the enlarged muscles and alleviates optic nerve compression (Fig. 6.79). In these cases, CT may be the method of choice, especially because it is capable of presenting the bony structures, and since postoperative complication with acute hemorrhage demands an emergency examination (Fig. 6.80).

The differential diagnosis of endocrine orbitopathy includes lymphoma, metastasis, diffuse or focal idiopathic orbital inflammation with mass effect (Fig. 6.64), any tumor of the nasal cavity and sinuses (Förster and Kahaly 1998), and vascular diseases like carotid sinus cavernous fistula (Ahmadi et al. 1983). The most important differential diagnosis of endocrine orbitopathy is myositis, the local form of idiopathic orbital inflammation (see Sect. 6.2.3.1), especially in unilateral involvement (Fig. 6.81). In addition to the different clinical presentations with painful, unilateral proptosis combined with double vision and diffuse orbital swelling, the most important differential imaging criterion, visualized by both CT and MRI, is the enlargement of the muscle, including the tendon (Figs. 6.71, 6.72). This pattern is characteristic of the inflammation of a single muscle, especially since the isolated idiopathic orbital inflammation shows no preference for a muscle group, i.e., the inferior or medial rectus muscles (Harnsberger 1990; Casper et al. 1993). Rare conditions such as unspecific, benign lymphoid hyperplasia may mimic the clinical findings of Graves disease, but present with different symptomatology and imaging morphology, as shown in Fig. 6.167.

(Text continues on p. 221)

a

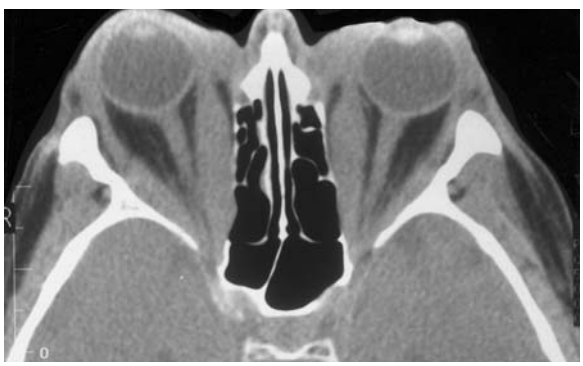

b

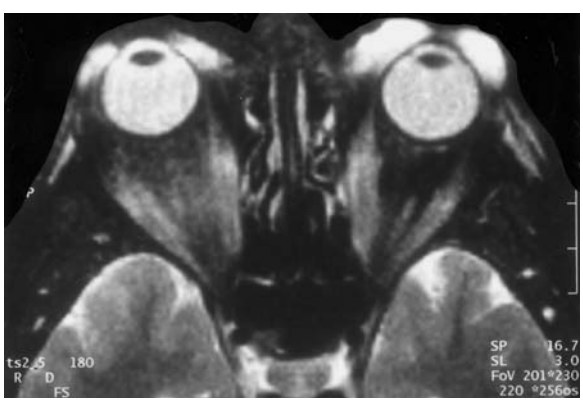

c

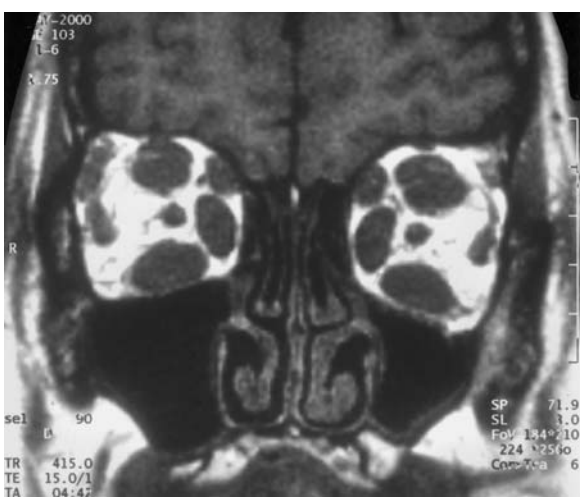

e

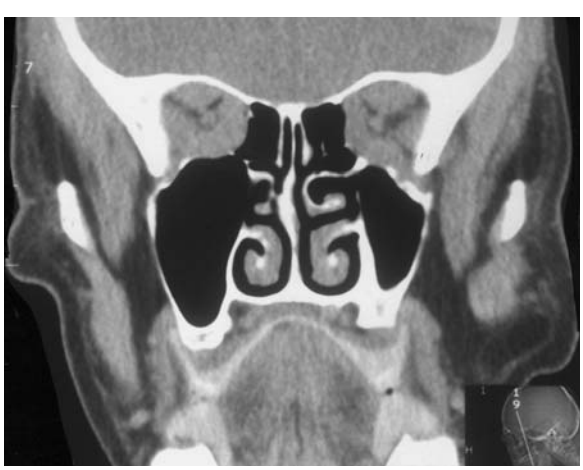

d

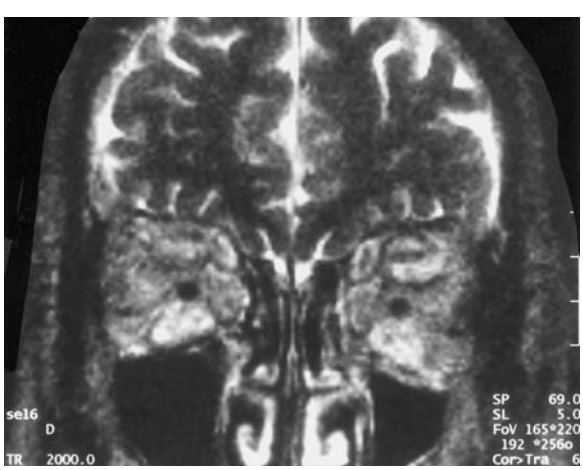

f

Fig. 6.76a–f. A 48-year-old man with acute, bilateral, symmetric proptosis, chemosis, reduced mobility of both eyes, and hyperthyreosis. Diagnosis: endocrine orbitopathy (Graves' disease). **a** Portrait of the patient, demonstrating chemosis and severe bilateral lid edema. **b** Axial CT, demonstrating bilateral proptosis (Hertel 25 mm), thickening of the medial and lateral rectus muscles, and slight pressure on the right lamina papyracea. Note thickening of both conjunctivas. **c** Corresponding T2-weighted (FS) MRI with signal enhancement not only of the enlarged rectus muscles, but also of the edema of the conjunctiva of both eyes. **d** Coronal CT with marked involvement of all external muscles, including both oblique and levator palpebrae muscles. **e** Coronal T1-weighted MRI. **f** Corresponding coronal T2-weighted image with the edema being primarily detectable in the inferior, superior, and oblique rectus muscles. Additional T2-time measurements (not shown) identified a difference of more than 100 ms in comparison with the non-inflammatory involved lateral muscles

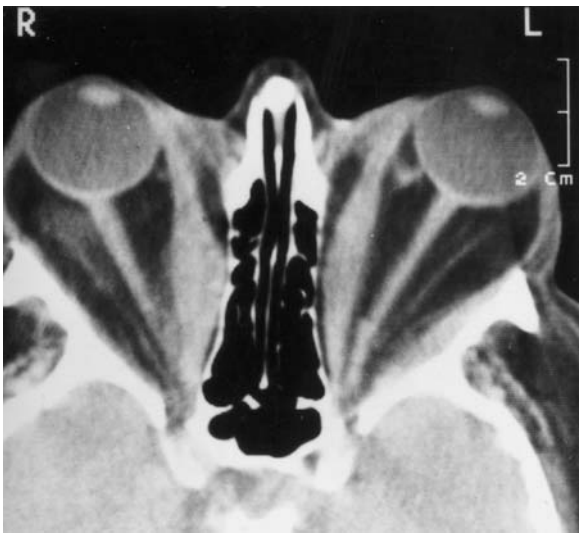

Fig. 6.77. A 49-year-old woman with persistent Graves' disease. Axial CT shows severe thickening of the medial rectus muscles, more pronounced on the right side, and marked bilateral pressure on the lamina papyracea. Note substantial hypertrophy of the orbital fat, responsible for extreme exophthalmos and stretching of both optic nerves. (With permission of Müller-Forell and Lieb 1995b)

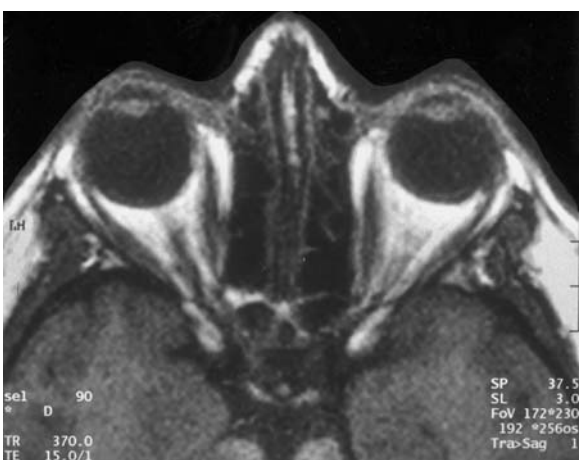

a

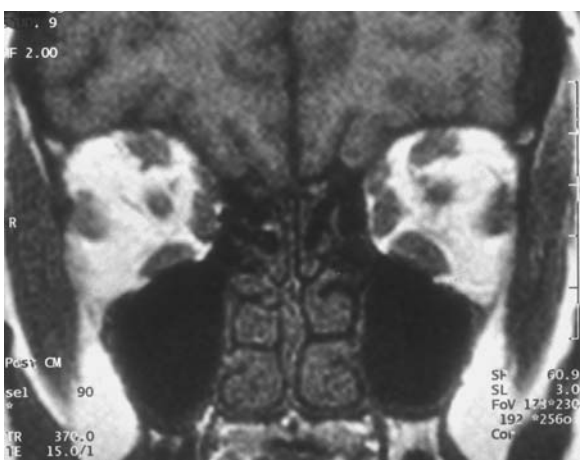

b

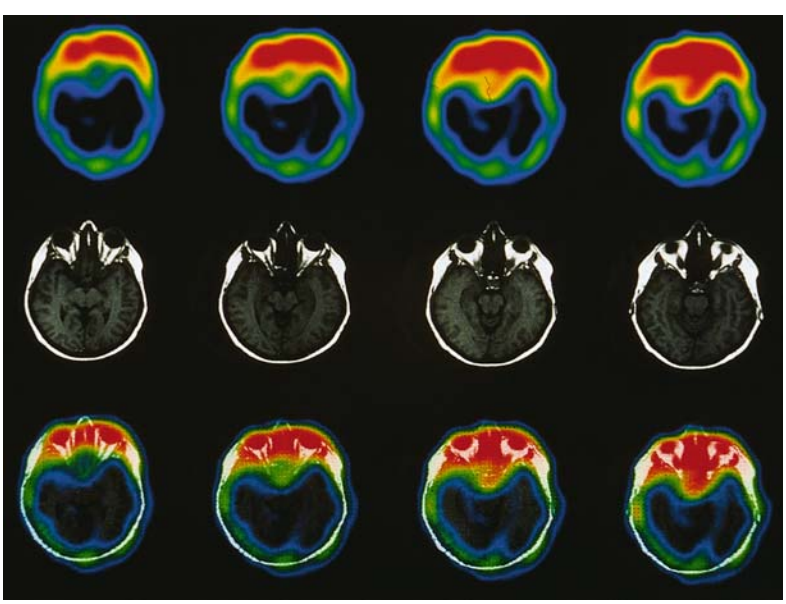

c

Fig. 6.78a–c. A 46-year-old woman with symptoms of recurrence of known Graves' disease. Diagnosis: acute Graves' disease. MRI: **a** Axial T1-weighted view without apparent evidence of enlarged rectus muscles. **b** Coronal T1-weighted view demonstrating moderate enlargement of all rectus muscles, but slight thickening of the left inferior rectus muscle. **c** Axial view of octreotide/MR-matching, demonstrating coating of both entire orbits with octreotide. *Above*: octreotide scan, *middle*: corresponding MR (3D) slices, *below*: matched slices. (**c** with the permission of Dr. Förster, Institute of Nuclear Medicine, Medical School, University of Mainz)

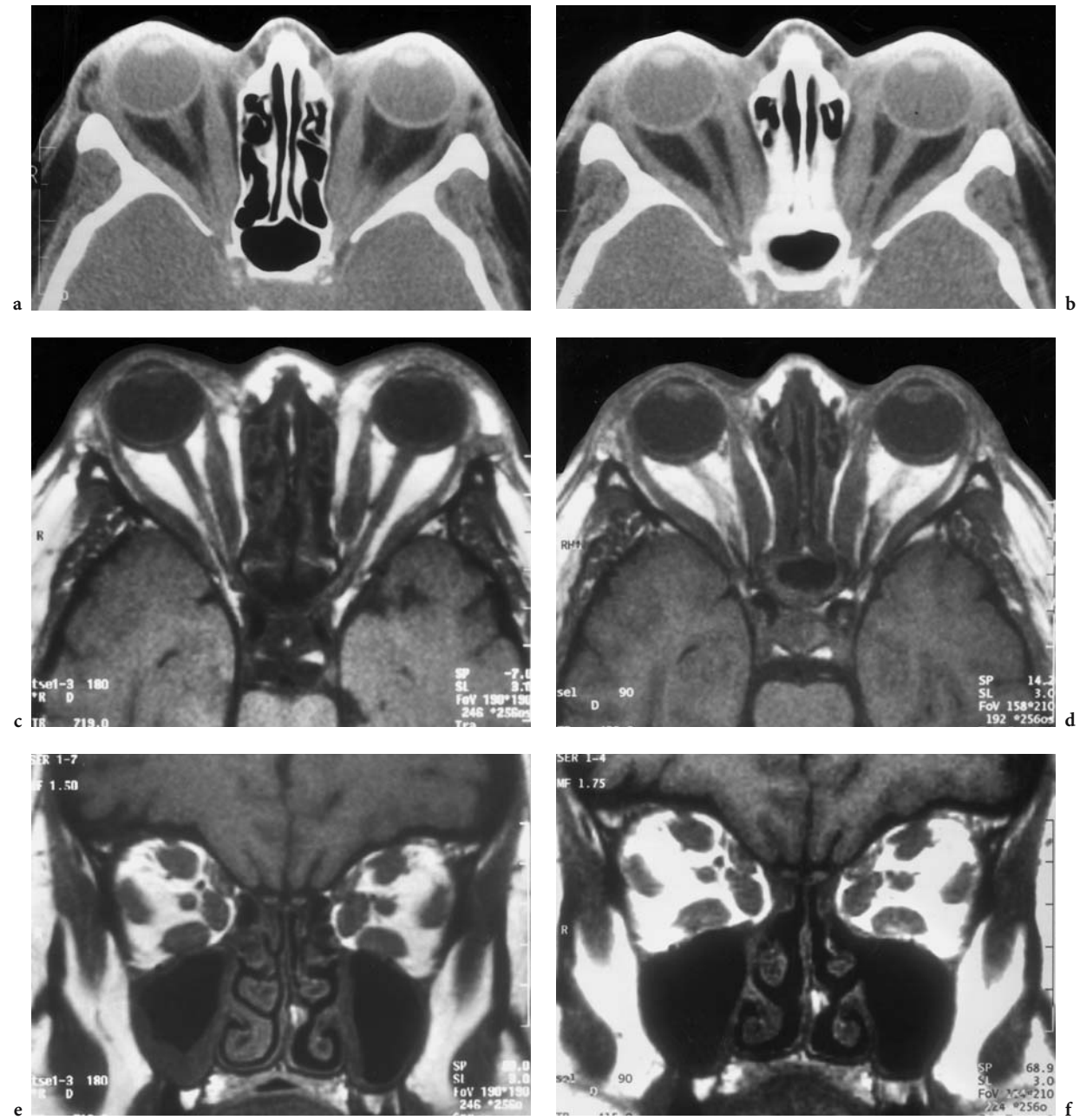

Fig. 6.79a–f. A 50-year-old woman with bilateral proptosis in the course of Graves' disease. Diagnosis: Graves' disease. CT: **a** Preoperative view with bilateral symmetric enlargement of the medial and (less marked) lateral rectus muscles. Note slight impression of the medial orbital wall as some spontaneous decompression. **b** Corresponding postoperative view with protrusion of the medial rectus muscles in the former ethmoidal cell area. MRI: **c** axial T1-weighted view, corresponding to **a. d** Corresponding postoperative image. Note that the enlargement of the muscles themselves remains unaffected. **e** Coronal T1-weighted preoperative view. **f** Corresponding postoperative image

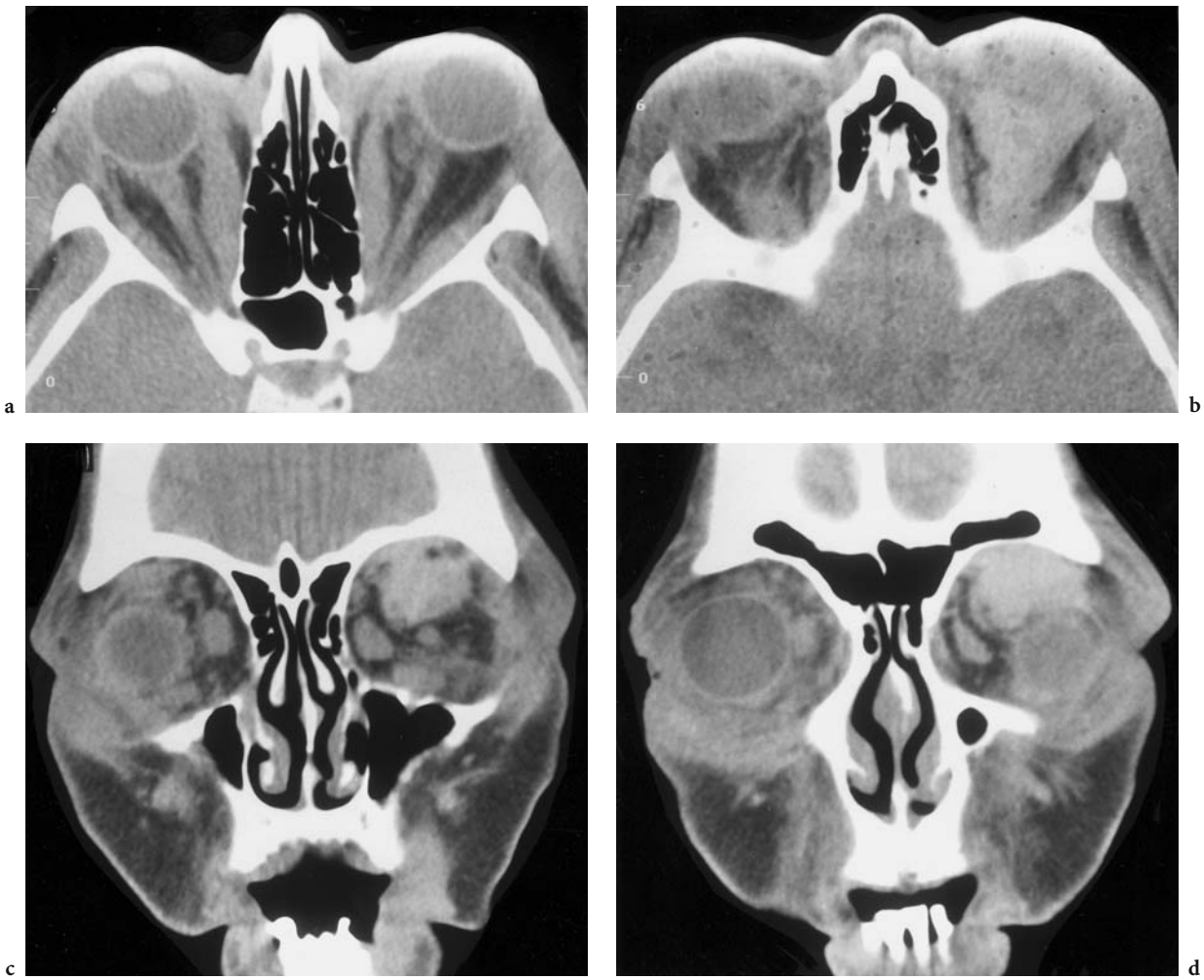

Fig. 6.80a–d. A 51-year-old woman with known Graves disease. One day after operative fat resection of the left eye, the patient developed acute deterioration of the severe proptosis (right: 29 mm, left 33 mm), but no visual deficit. Diagnosis: acute retrobulbar hemorrhage (as an operative complication). CT: **a** Axial, native view of the medial orbit, where demonstrating bilateral severe proptosis and inferior dislocation of the left globe. **b** Axial view of the upper orbit with hyperdense mass in the region of the left superior muscle complex. **c** Coronal view of the region of the posterior globe where the hyperdense hemorrhage is seen, apparently involving the superior rectus muscle. **d** Coronal view of the anterior orbit, demonstrating best an inferior dislocation of the protruded left globe by the space-occupying hemorrhage

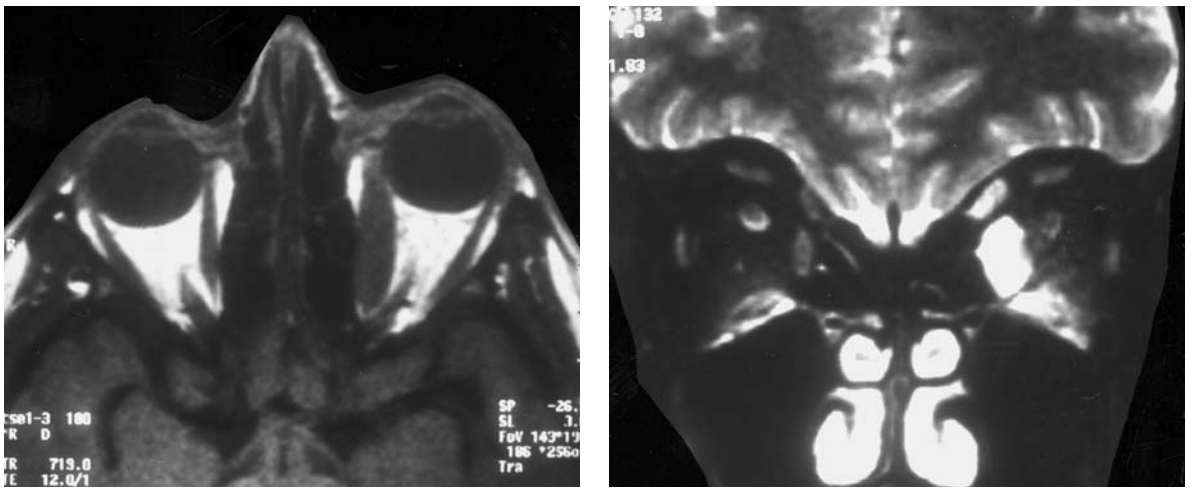

Fig. 6.81a,b. A 45-year-old woman with known hyperthyroidism, painless, left-sided proptosis, and incomplete abduction paralysis on the left side. Diagnosis: unilateral Graves' disease. MRI: **a** Axial T1-weighted view with enlargement of the left medial external muscle (although the tendon appears to be involved, Graves' disease was confirmed based on clinical symptoms and endocrinological findings; the patient profited from radiation therapy). **b** Coronal T2-weighted view with massive signal enhancement of the swollen inferior and medial left rectus muscles, representing intramuscular edema

6.2.4 Miscellaneous (Amyloidoma, Metastasis, Varia)

6.2.4.1 Amyloidoma

Amyloidoma of the orbit is a rare lesion (see Sect. 6.3.4.2.4) and may resemble multiple differential diagnoses, most frequently idiopathic orbital inflammation, but also inflammatory or tumorous lesions of other etiology (Mafee et al. 1999b). Clinical symptoms of painless proptosis and lack of other inflammatory signs, combined with an inhomogeneous intraorbital mass without significant signal enhancement after i.v. contrast administration, but calcification on CT, should enable an accurate diagnosis (Fig. 6.82).

6.2.4.2 Metastasis

Metastases represent the most common malignancy of the orbit and may thus involve any orbital area, with preference for the extraconal area, whereas substantial involvement of the intraconal space is rare. Enophthalmos may present as the first symptom in remote carcinoma. Solid or diffuse infiltration of the intraconal area, leading to secondary rectus muscle shortening and contraction, and in some instances to bone destruction, is seen in cirrhotic breast carcinoma metastasis (Fig. 6.83) (Reifler and Davison 1986; Ewald et al. 1994; Lagreze et al. 1997). Traumatic/posttraumatic conditions represent another, more common etiology of enophthalmos (Fig. 6.156).

An extremely rare condition is the intraorbital metastasis of a small-intestinal carcinoid (Fig. 6.84). The finding of an intramuscular mass may be of differential diagnostic value if additional specific examination with a positive octreotide scan is not available (Shields et al. 1987b; Guthoff et al. 2000).

6.2.4.3 Varia

Although located in the extraconal area, sphenoid bone dysplasia may exert a secondary influence on intraconal tissue (muscles). Exposure of the fan-shaped fibrillation of muscle fibers occurring as a secondary process to prolonged irregular strain on the rectus muscles may lead to deformity in persisting, thus far unknown disorders (Fig. 6.85), rendering, e.g., a strabismus operation impossible.

(Text continues on p. 226)

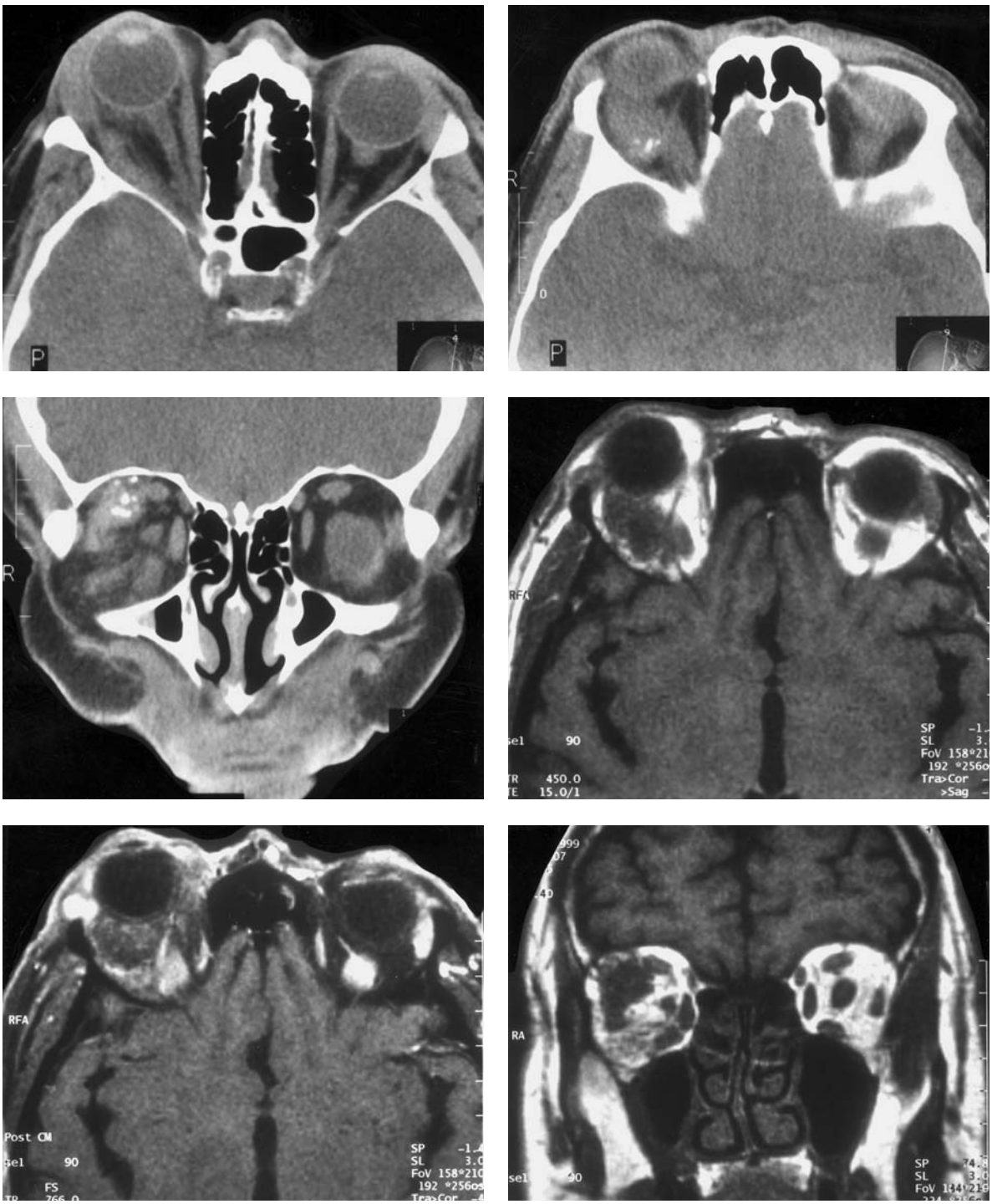

Fig. 6.82a–f. A 71-year-old man with persistent, slowly progressing, right-sided proptosis, but an acute history of ipsilateral painful chemosis. Diagnosis: orbital amyloidoma. CT: **a** Axial native view where medial of the orbit, in addition to exophthalmos of the right eye and extraconal location of the slightly enlarged lacrimal gland, an irregular contour of the lateral rectus muscle and adjacent bulbar fat can be identified. **b** Axial native view of the superior orbit which is characterized by an irregular, partly calcified mass. **c** Coronal view of the middle orbit, demonstrating the partly calcified intraconal mass between the lateral and superior rectus muscle. MRI: **d** Axial T1-weighted native view, corresponding to **b**. Note the small, normal superior ophthalmic vein in both images. **e** Corresponding contrast-enhanced (FS) view without marked contrast enhancement of the mass. **f** Coronal T1-weighted view (corresponding to **c**) with suspicion of additional extraconal involvement

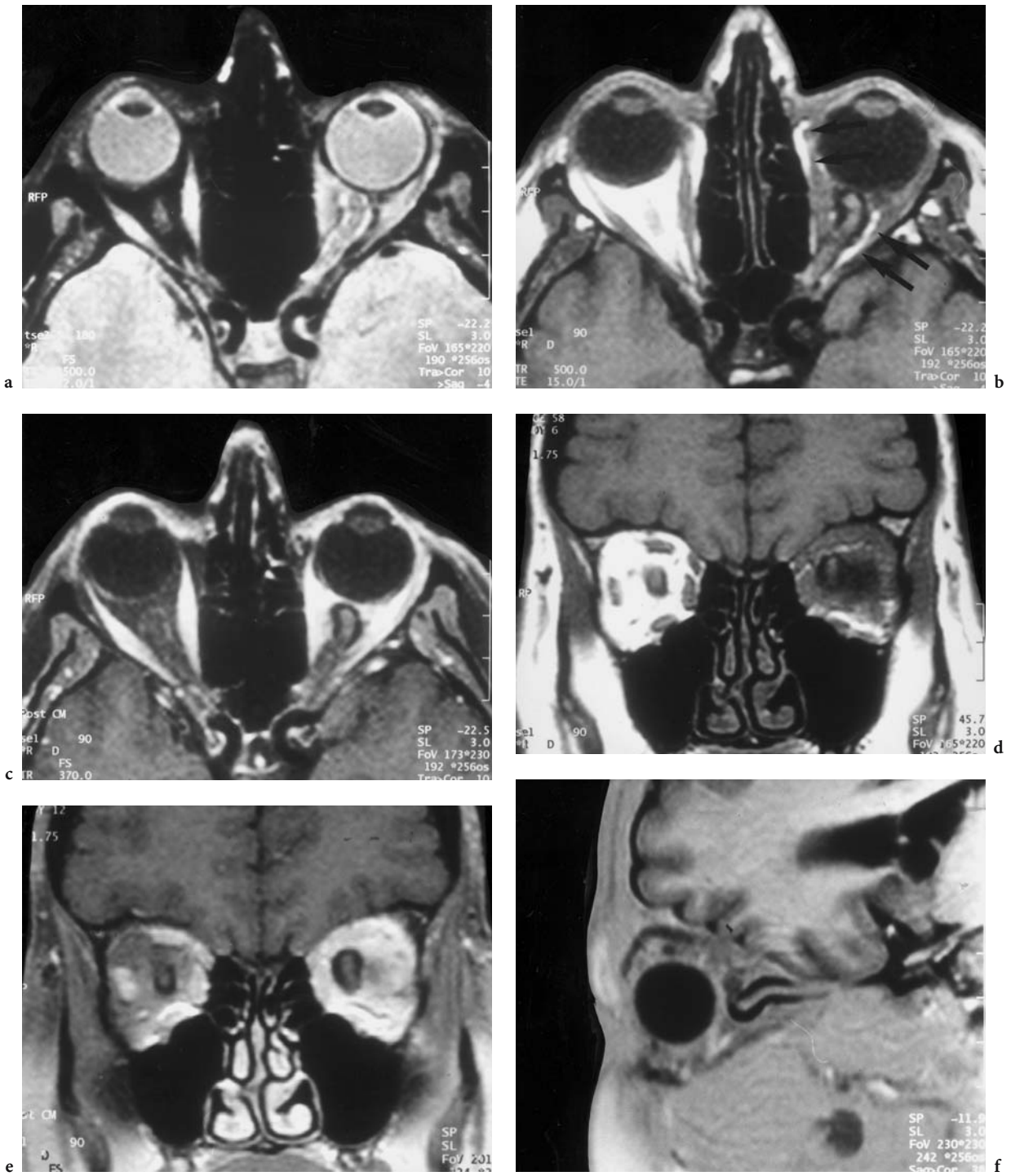

Fig. 6.83a–f. A 57-year-old woman with known NF 1, and enophthalmos for the past 6 weeks, combined with increasing double vision for all directions of the left eye. Diagnosis: (estrogen-receptor positive) metastasis of a cirrhotic breast carcinoma as initial symptom of the disease. MRI: **a** Axial proton density view of the orbit, demonstrating enophthalmos of the left eye, pathologic signal intensity of the retrobulbar space and widening of the CSF space of the left optic nerve. **b** Corresponding T1-weighted native view, distinguishing only little intra- and extraconal (medially) fat (*arrows*). **c** Corresponding T1-weighted, contrast-enhanced (FS) view, showing enhancement of the entire orbital tissue (compare with corresponding right side). **d** Coronal T1-weighted native view with similar signals of the rectus muscles and of the primarily intra- but also extraconal tumor. Remnants of orbital fat are seen as small hyperintense structures in the inferior left orbit. **e** Corresponding T1-weighted, contrast-enhanced (FS) view with complete tumor enhancement. **f** Parasagittal T1-weighted IR view, demonstrating compression of the optic nerve and widening of the CSF space in the optic nerve sheath (compare to **a**)

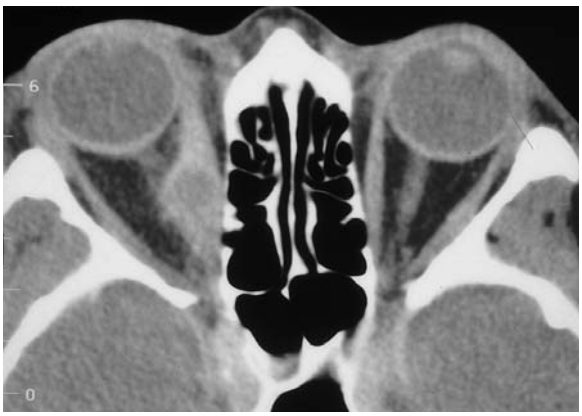

a

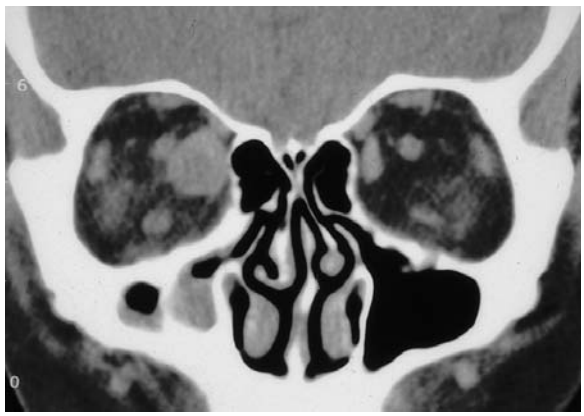

b

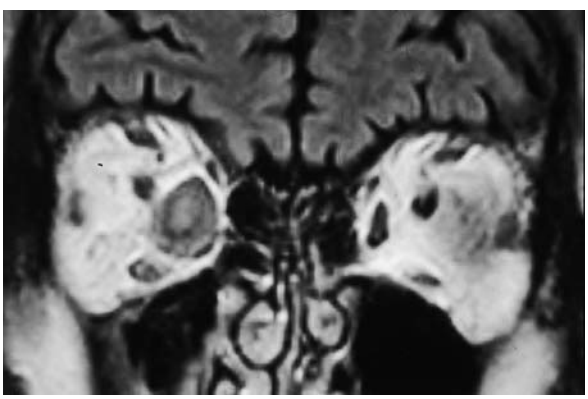

c

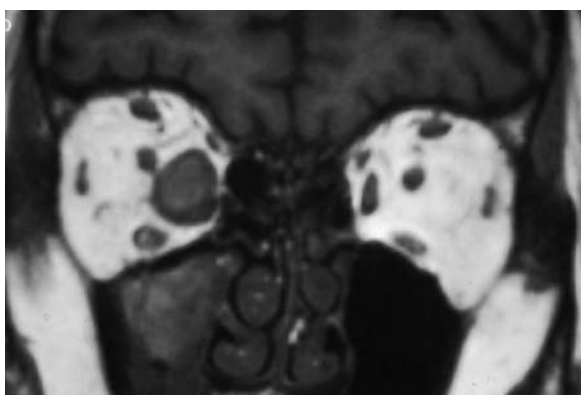

d

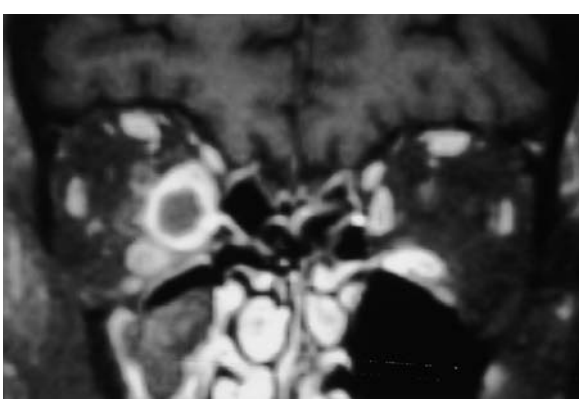

e

Fig. 6.84a–e. A 68-year-old woman with known enteric carcinoid for the past 3 years, presenting with acute onset of double vision. Diagnosis: Suspected metastasis of an enteric carcinoid (no histology, patient refused therapy). CT: **a** Axial, contrast-enhanced view with belly-like enlargement of the right medial rectus muscle due to a slightly ring-shaped enhancing intramuscular mass. **b** Corresponding coronal view. Coronal MRT: **c** T2-weighted (FLAIR) view where the target-like mass presents definitely intramuscularly. **d** Corresponding T1-weighted native view. **e** Corresponding T1-weighted, contrast-enhanced (FS) view with extensive signal enhancement of the outer rim of the lesion. Note the slight enlargement of the ipsilateral inferior rectus muscle

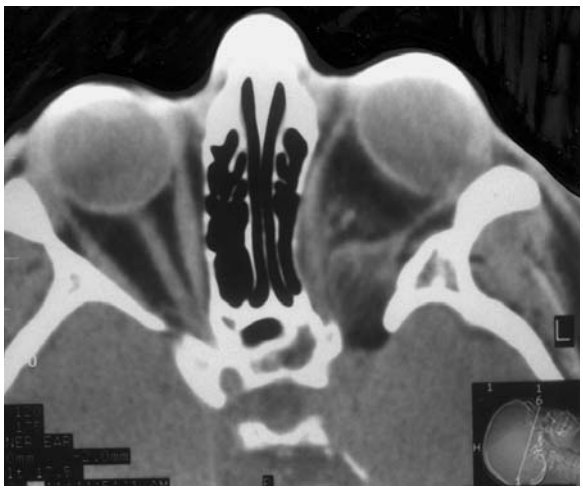

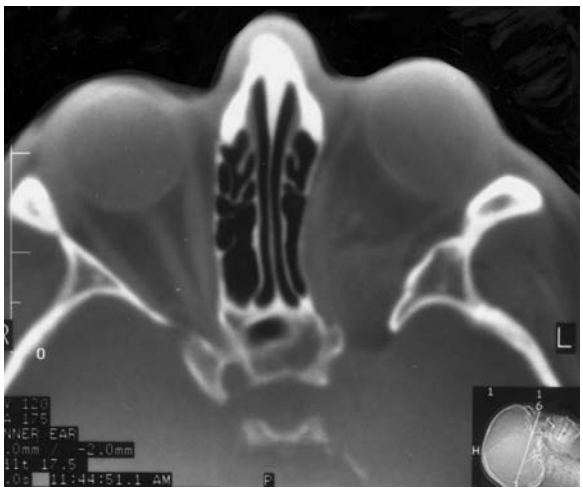

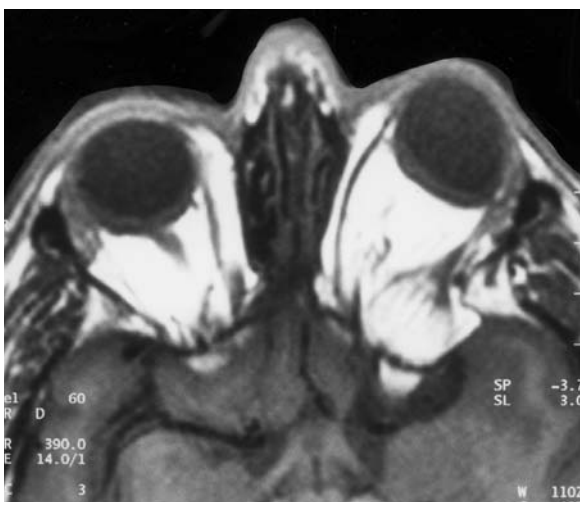

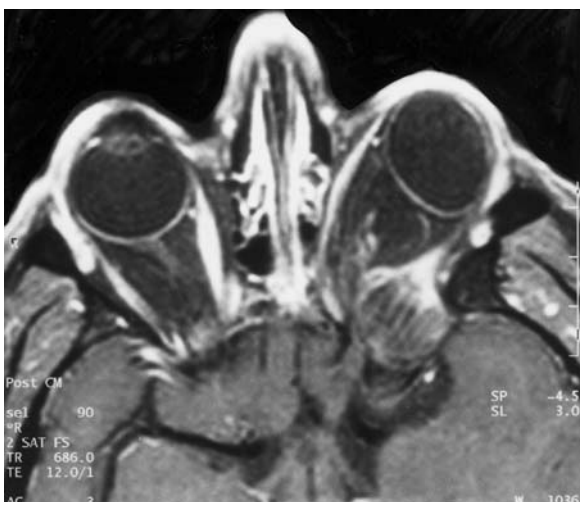

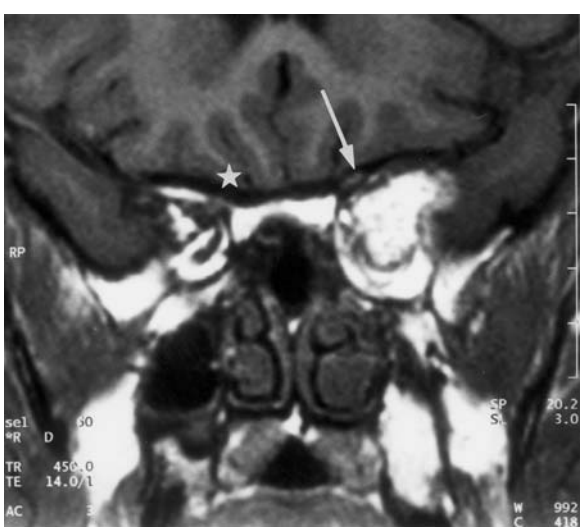

Fig. 6.85a–e. A 36-year-old man undergoing imaging prior to planned surgical correction of persistent divergent strabismus. Diagnosis: NF 1 with sphenoid wing dysplasia and subsequent muscle degeneration. CT: **a** Axial image with deformed left orbital content: deformed globe and lateral rectus muscle as well as bony pathology are more conclusively visualized in corresponding view in bone window (**b**). Impression of the lamina papyracea, thickening of the large wing of the sphenoid, and widening of the orbital fissure (normal optic canal – not shown), apparently due to the absence of the small wing of the sphenoid, findings leading to suspected NF 1. MRI: **c** Corresponding axial native T1-weighted view. Note the deformed left globe. **d** Corresponding contrast-enhanced (FS) image demonstrating the spread of single muscle fibers of the lateral rectus muscle, expanding intracranially and impinging on the temporal pole. **e** Coronal T1-weighted view at the level of the optic canal (*white star*: right, *white arrow*: left), showing extensive intracranial expansion of intraorbital tissue

6.3 Extraconal Area

Defined as the orbital space outside the muscle cone, the only "organs" of the extraconal space are fat and the lacrimal gland. However, this orbital compartment is the first section that orbital or extraorbital (nasal/paranasal) tumors and infections invade on their way to deeper orbital and even intracranial structures.

6.3.1 Tumors

6.3.1.1 Rhabdomyosarcoma

The orbit is the most common location in children, with 40% of all head and neck tumors appearing there (Barkovich 2000). The most common, malignant, soft-tissue tumor in childhood with up to 4%–8% of all pediatric (less than 15 years old) malignant tumors is rhabdomyosarcoma. The incidence of rhabdomyosarcoma ranges from 1% to 4% of all biopsied orbital lesions, with a slight predilection for boys over girls (5: 3); the average age at diagnosis is 7 to 8 years old (Jones et al. 1965; Ellenbogen and Lasky 1975; Grosfeld et al. 1983; Chin and Wei 1993; LeGall et al. 1994), but older patients may also be affected (Fig. 6.86). The tumor is mostly unilateral and, in some cases, may originate in the adjacent sinonasal region (Figs. 6.86, 6.87). Rhabdomyosarcoma may invade the skull base as well as the cavernous sinus and middle cranial fossa by growth along the orbital fissures (Sartor 1992; De Potter et al. 1995; Mafee 1996; Barkovich 2000). The characteristic clinical presentation of orbital rhabdomyosarcoma is rapidly progressing exophthalmos with dislocation of the eye, disturbance of motility, sometimes combined with unilateral ptosis (Fig. 6.88) (Gloor and Klaman 1992; Shields and Shields 1993). The tumors arise from primitive, undifferentiated mesenchymal cells and can be divided histopathologically into four different subgroups: (a) embryonal, (b) pleomorphic, (c) alveolar, and (d) botryoid rhabdomyosarcoma, with the alveolar tumor being the more malignant variant, characterized by anaplastic tumor cells spreading along soft-tissue septa or in the central cavity (Hogan and Wood 1972; Holbach et al. 1989). Conventional H&E staining as well as immunohistochemistry with detection of myoglobin and desmin support the diagnosis (Porterfield and Zimmerman 1962; Hirashima et al. 1986; Sun et al. 1990).

Rhabdomyosarcoma is frequently accompanied by conjunctival swelling and redness of the eye, suggesting an inflammatory rather than a neoplastic process (Sartor 1992). Delayed diagnosis may confront parents and physicians with an extremely rapidly growing tumor, and in rare cases with total destruction of the orbit. The majority of orbital rhabdomyosarcoma is found in the superior medial orbit (Fig. 6.89), mainly occupying the intra- and extraconal compartment. Since no lymph vessels exist in the orbit, lymphogenous spread in regional lymph nodes and/or lymphatic metastasis is rare, and only seen in cases of tumor invasion into the eyelid and the conjunctiva. Extraorbital metastasis, especially into the lung, occurs by hematogenous spread (Liebner 1976; Gehan et al. 1981; Adhikary and Fitzmaurice 1982; Wiener 1994; Sohaib et al. 1998).

While ultrasound and Doppler technology provide information on vascularization, they are, nevertheless, insufficient to establish the diagnosis. CT and (superior) MRI on the other hand give precise information about tumor size and the extent of tumor growth that may be both intraconal and extraconal, and possibly involve bone with destruction. On CT, the usually well-outlined tumor is isodense to the orbital muscles, showing significant contrast enhancement, because of its high vascularization (Fig. 6.90) (Wende et al. 1977; Gado and Smith 1978; Scotti and Nash 1982; Hopper et al. 1992). MRI shows long T1 and T2 characteristics with moderate to marked signal enhancement after i.v. gadolinium (Figs. 6.86–6.89, more prominent on fat-suppressed images (Figs. 6.86–6.89) (Sartor 1992; Cooper et al. 1994; Barkovich 2000; De Potter et al. 1995; Yang et al. 1997; Mafee et al.

(Text continues on p. 230)

Fig. 6.86a–g. A 36-year-old woman with pressure sensation and a reddish, swollen left eye; no double vision. Diagnosis: rhabdomyosarcoma of the left ethmoid. Axial CT: **a** View of the medial orbit with destruction of the medial orbital wall by a medially extending ethmoidal tumor. **b** Upper orbit with additional infiltration of the skull base at the site of the cribriform lamina. MRI: **c** axial T2-weighted image, corresponding to **a**, demonstrating left-sided proptosis. Tumor infiltration is seen in the lamina papyracea and the nasal bone, and (hyperintense) mucous retention in the ipsilateral region of the sphenoid sinus. **d** Corresponding T1-weighted native view, superior visualization of the extraconal intraorbital extension with suspected infiltration of the tendon of the left medial rectus muscle. **e** Corresponding T1-weighted, con-

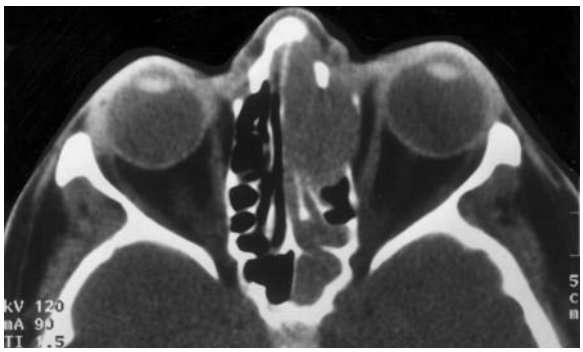

a

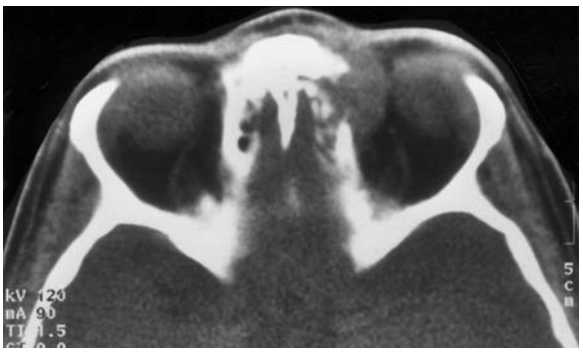

b

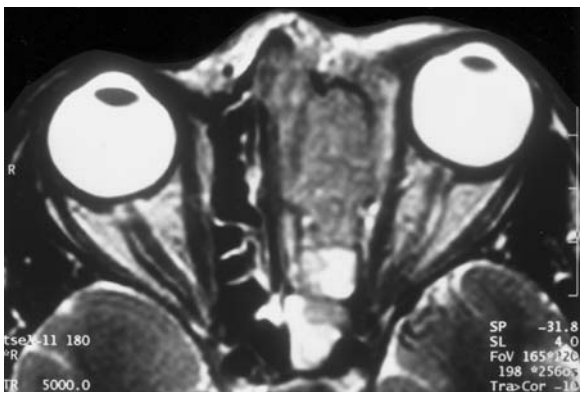

c

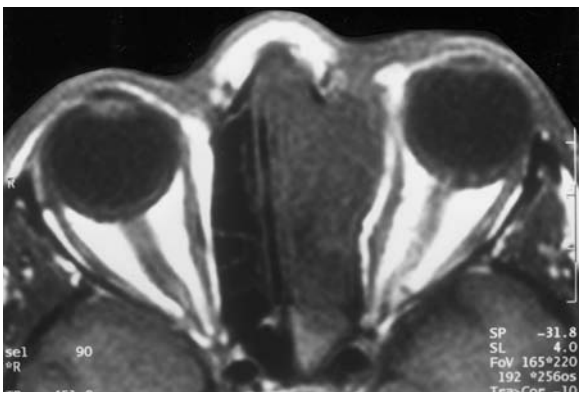

d

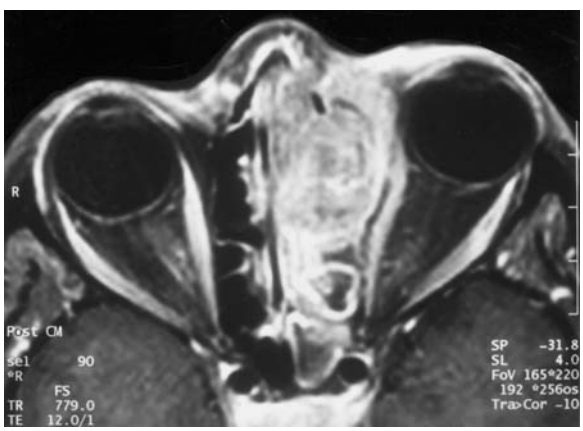

e

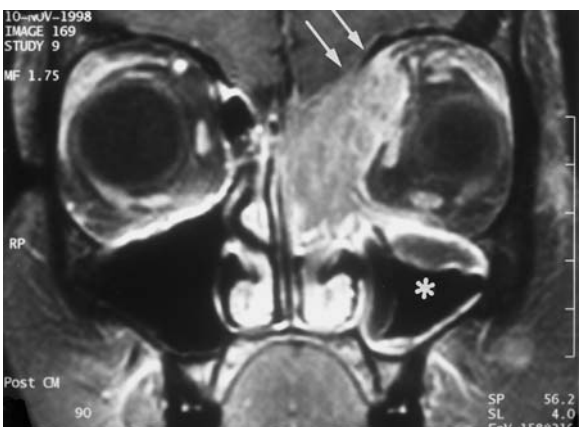

f

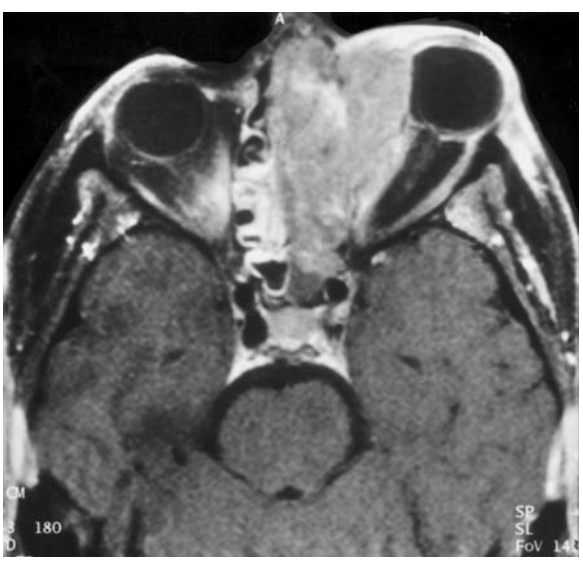

g

trast-enhanced (FS) view. **f** Coronal, T1-weighted, contrast-enhanced (FS) view with dislocation of the medial rectus muscle and inferior extra-axial dislocation of the left globe. Note the intracranial extension with slight dural enhancement (*white arrows*), representing corresponding infiltration, and mucous retention in the upper maxillary sinus (*white star*), due to tumor occlusion of the infundibulum. The patient presented with recurrent and exacerbated proptosis 2 weeks after immediate tumor surgery: **g** axial, T1-weighted, contrast-enhanced (FS) image (corresponding to **e**) demonstrating the recurrent tumor to be twice as large as preoperatively. Note the substantial intranasal and intraorbital infiltration, including the medial rectus muscle and causing massive proptosis

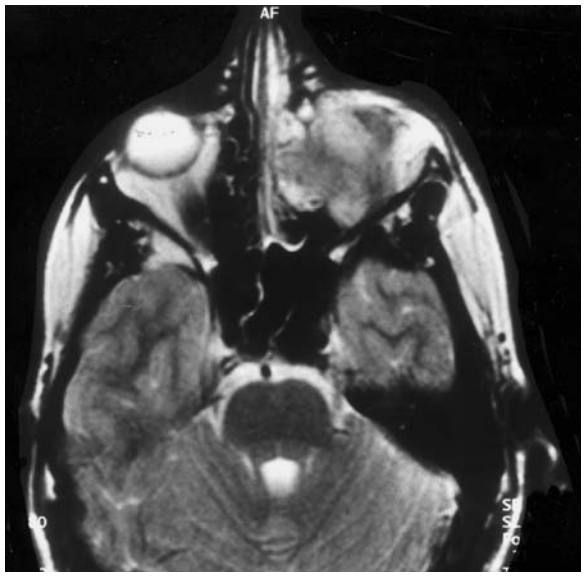

a

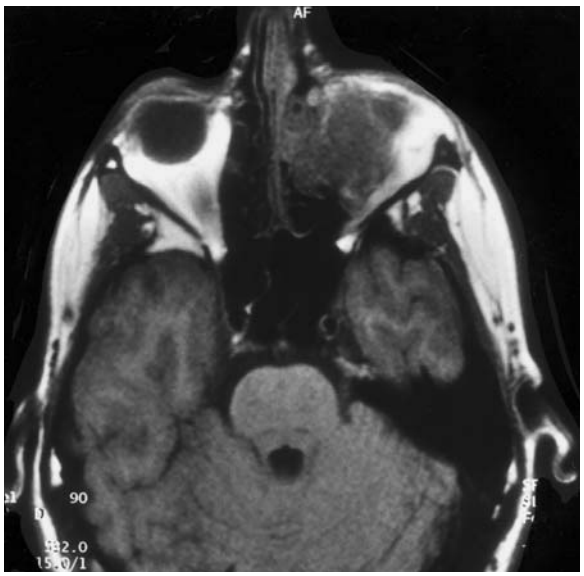

b

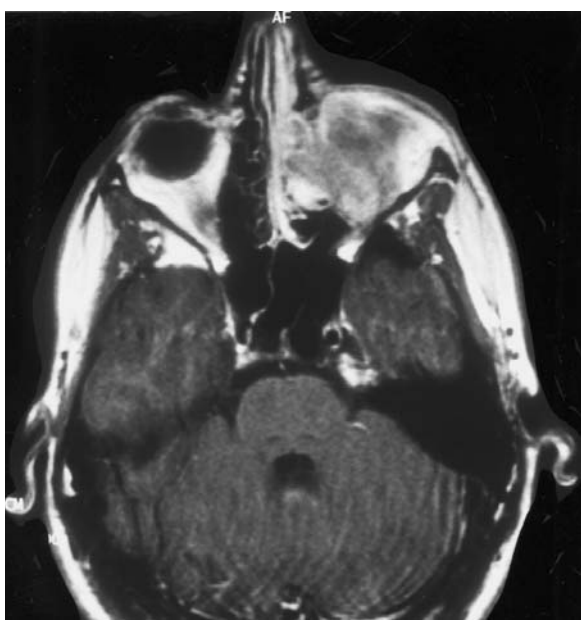

c

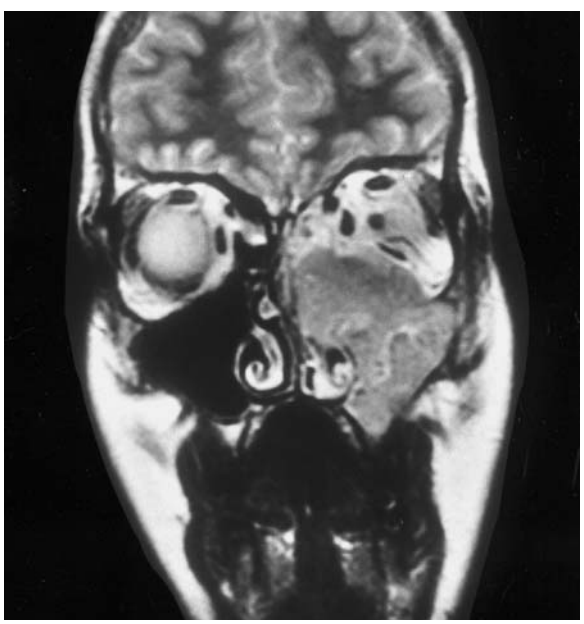

d

Fig. 6.87a–d. A 16-year-old man with swollen left lid and cheek. Diagnosis: rhabdomyosarcoma of the left maxillary sinus. MRI: **a** Axial T2-weighted view with inhomogeneous mass in the left nasal cavity and inferior orbit, displacing the inferior rectus muscle. **b** Corresponding T1-weighted native view. **c** Corresponding T1-weighted, contrast-enhanced view with moderate signal enhancement. **d** Coronal T2-weighted view showing the entire tumor. Inferior invasion of the left orbit, apparently without infiltration of the muscle cone

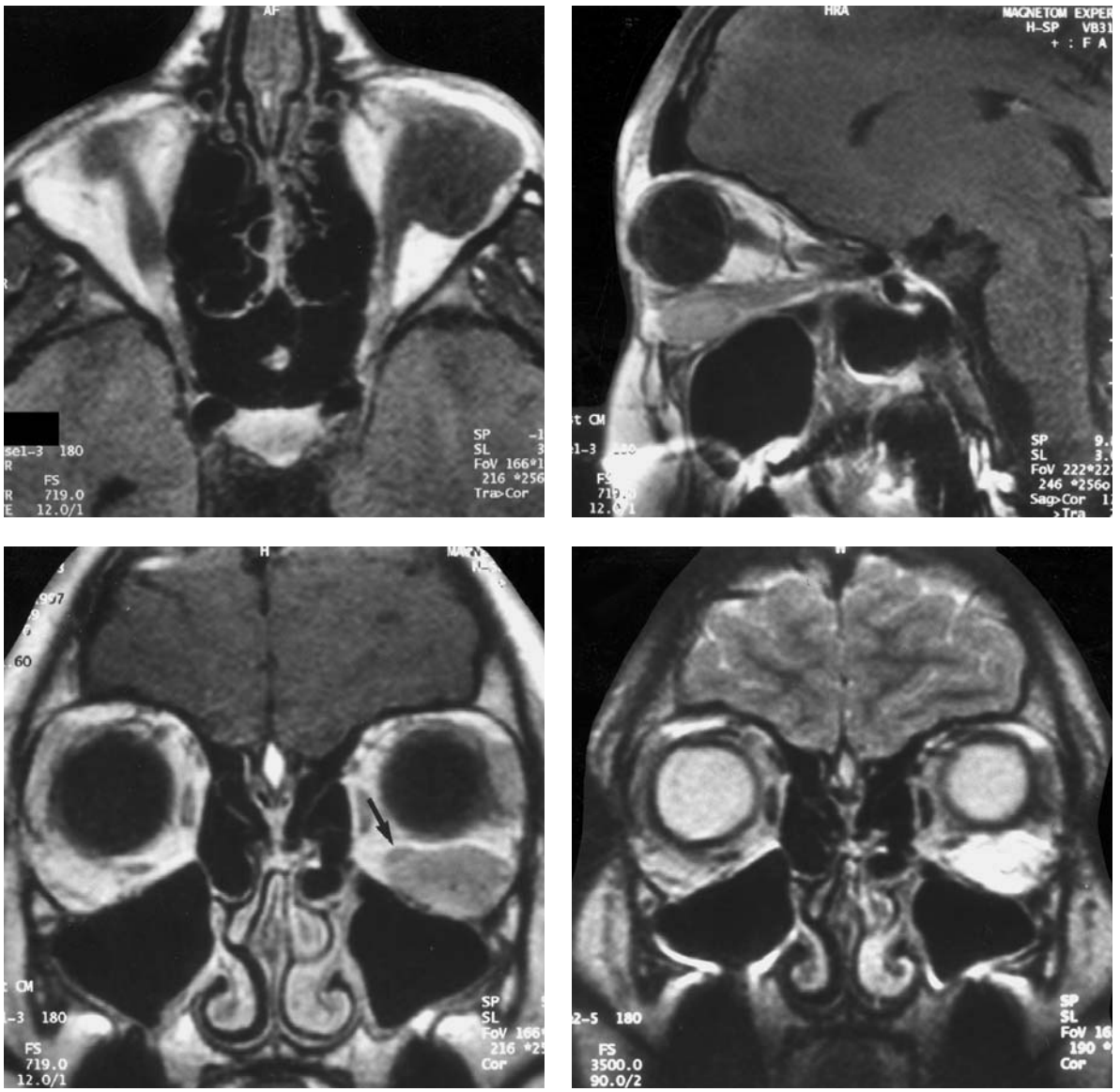

Fig. 6.88a–d. A 14-year-old boy with initial complaint of double vision followed by painless protrusion of the left eye after 1 week. Diagnosis: rhabdomyosarcoma. MRI: **a** Axial T1-weighted native view of the inferior region of the orbit, showing isointensity of the tumor lateral to the inferior rectus muscle. Differentiation from the muscle cannot be made. **b** Parasagittal, T1-weighted, contrast-enhanced (FS) view where the tumor appears to depress the inferior rectus muscle from caudal. **c** Coronal, T1-weighted, contrast-enhanced image where part of the inferior rectus muscle is demarcated medially (*small arrow*) by increased enhancement of the tumor compared with enhancement of the muscle. **d** Corresponding T2-weighted-image with demarcation of the tumor from the inferior rectus muscle, occupying the inferior, lateral region of the orbit

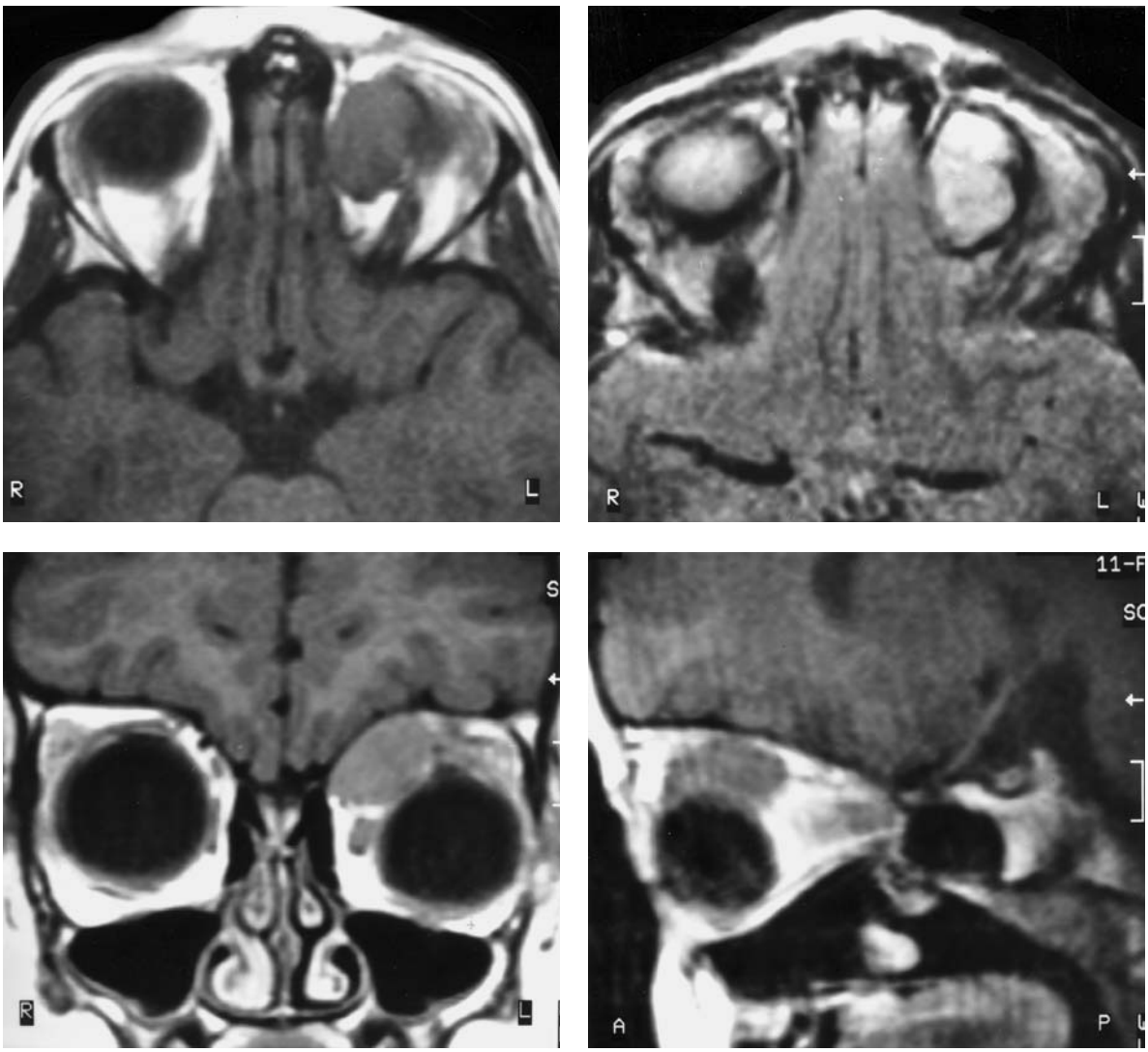

Fig. 6.89a–d. A 6-year-old girl with rapidly progressing, painless, unilateral, extra-axial proptosis of the left eye. Diagnosis: rhabdomyosarcoma. Triplanar MRI: **a** axial T1-weighted native view with slightly hyperintense, sharply defined lesion in the medial superior quadrant. **b** Corresponding T2-weighted image with hyperintensity of the tumor. **c** Coronal, T1-weighted, contrast-enhanced view showing similar enhancement. Caudal and lateral dislocation of the globe, corresponding to the location of the tumor in the anterior region of the superior oblique muscle. **d** Sagittal, T1-weighted, contrast-enhanced image with superior view of the AP expansion (slightly blurred image due to the young patient's movements). (With permission of Müller-Forell and Lieb 1995b)

1998). The differential diagnosis of rapidly growing capillary hemangioma is sometimes difficult (De Potter et al. 1995) and should include neuroblastoma, lymphoma, metastasis, as well as aggressive idiopathic orbital inflammation (Sartor 1992).

Surgical biopsy and histopathologic confirmation should be performed even under emergency conditions and are mandatory for the definite diagnosis and acute planning of therapy. The conventional regimen of surgical removal of the tumor followed by radiotherapy (30–60 Gy) has been substituted by chemotherapy (VAC – vincristine, actinomycin D, and cyclophosphamide), which was demonstrated to lead to successful remission and a survival rate of 93% (Rousseau et al. 1994). Radiotherapy harbors the risk of radiation-induced secondary tumors, leukoencephalopathy, cataract, retinopathy, and orbital deformation with enophthalmos (Van den Bogaert et al. 1992; Sagerman 1993; Regine et al. 1995).

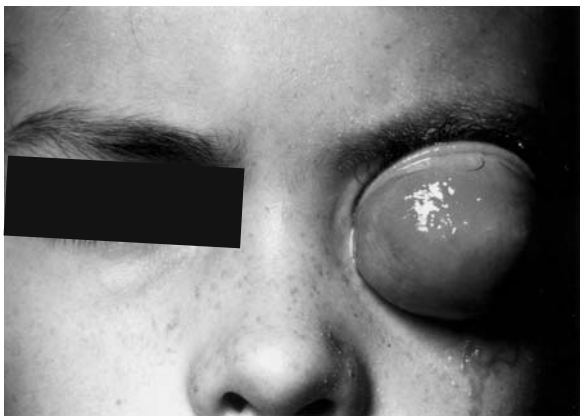

a

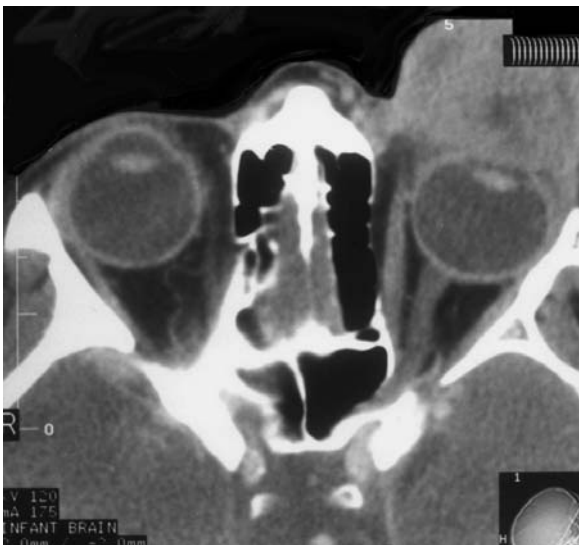

b

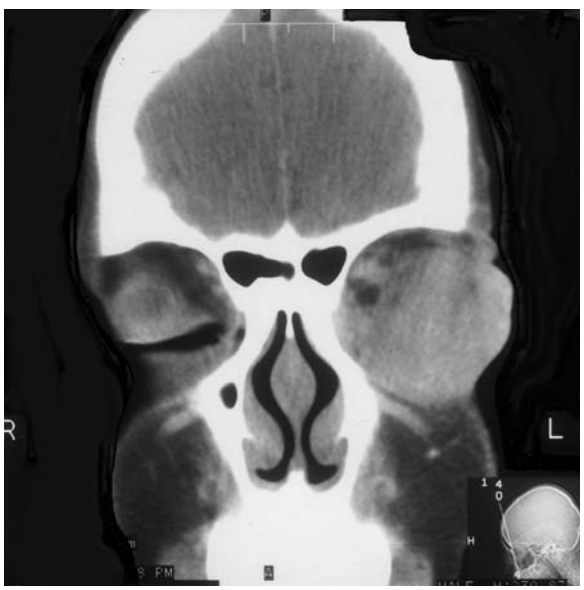

c

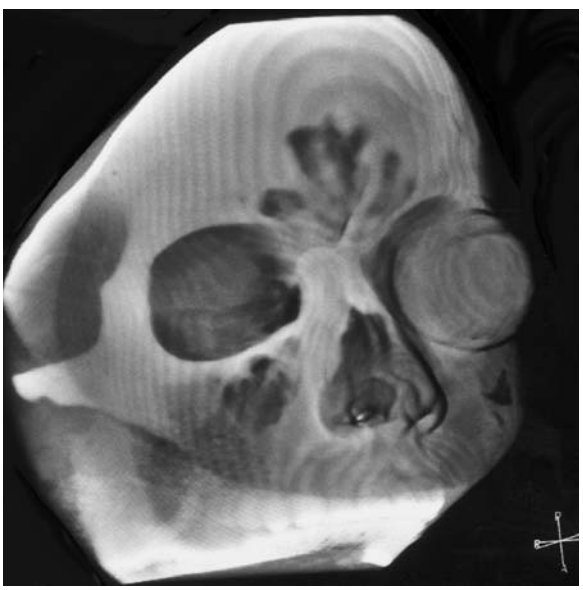

d

Fig. 6.90a–d. A 14-year-old boy with recurrent rhabdomyosarcoma of the left orbit. **a** Portrait of the patient. CT: **b** axial contrast enhancement view showing the huge recurrent tumor of the RMS, growing primarily in the superior orbit and occupying the entire frontal orbital surface. **c** Coronal view. **d** 3D reconstruction

6.3.1.2 Hemangiopericytoma

Hemangiopericytomas are rare, uncommon, ubiquitous, highly vascular tumors, originating from cells (Zimmermann's pericytes), which are arranged around capillaries and postcapillary venules (McMaster et al. 1975). Although the orbit is a rare location, hemangiopericytomas prefer the superior part of the orbit (Croxatto and Font 1982). They become clinically manifest as slowly progressing proptosis or lid swelling (Fig. 6.91). There is no gender predominance, the mean age of presentation is the 4th decade of life, and recurrences of the mostly (50%) benign tumor are known in about 30% of patients (McMaster et al. 1975; Henderson and Ferrow 1978). Histologically, hemangiopericytomas consist of numerous sinusoidal vascular spaces, lined with flat to ovoid endothelial cells and surrounded by proliferating pericytes (Karcioglu et al. 1997; Bilaniuk 1999). Because of

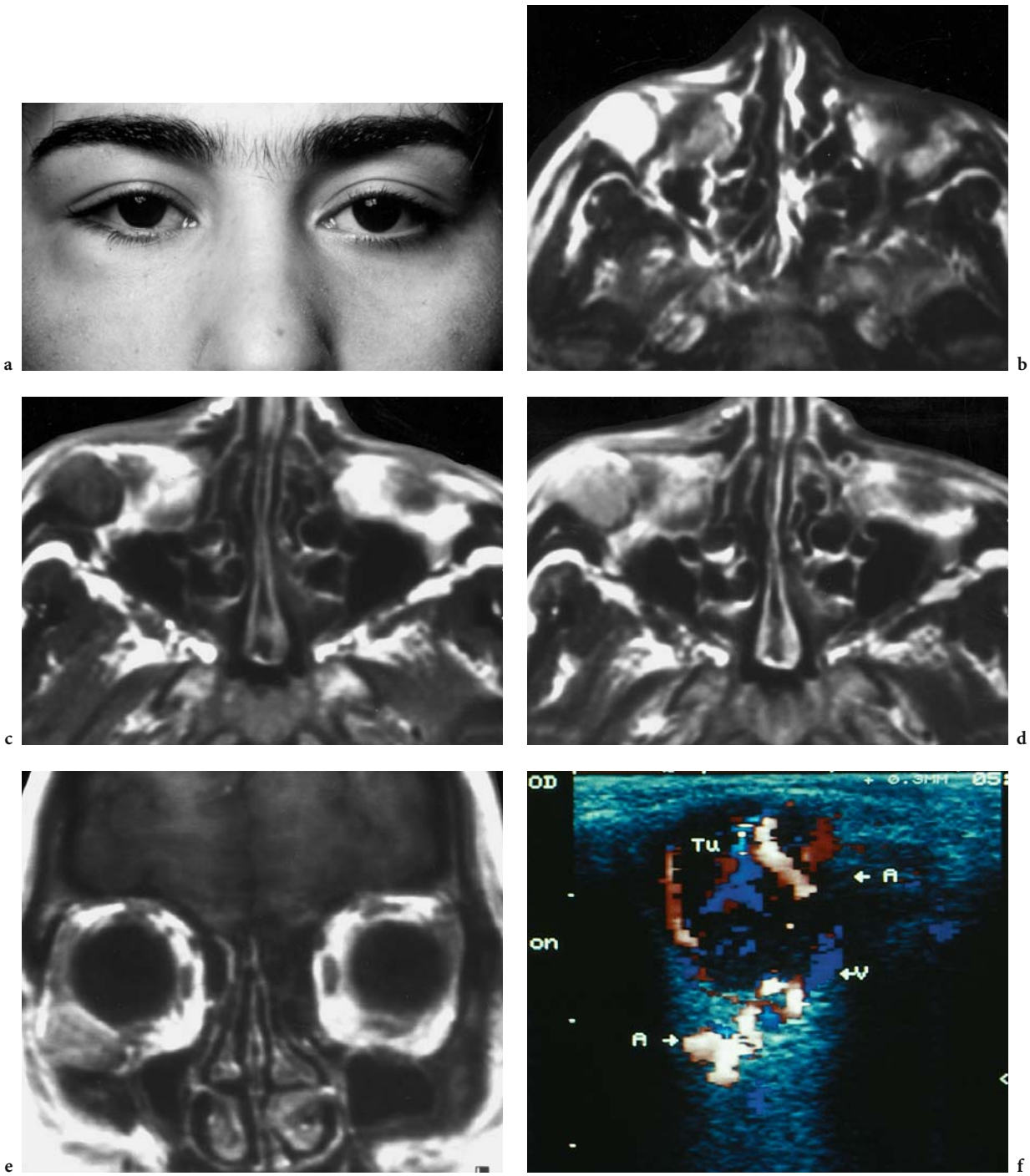

Fig. 6.91a–f. An 18-year-old woman with smooth swelling of the right lower eyelid. Diagnosis: benign hemangiopericytoma. a Portrait, showing the smooth subcutaneous tumor in the inferior lateral region of the right orbit. MRI: **b** Axial T2-weighted image with a signal-intense, sharply defined mass in the lateral inferior part of the right extraconal space. **c** Corresponding T1-weighted native image with an intermediate to hypointense signal. **d** Corresponding T1-weighted, contrast-enhanced image demonstrating distinct, homogeneous signal enhancement of the tumor, extending to the tendon of the inferior rectus muscle. **e** Coronal, T1-weighted, contrast-enhanced view identifying the inferior rectus muscle to be as small and tender as the contralateral one. **f** Color-coded Duplex ultrasound with a highly vascularized, sharply defined tumor (*Tu*) and conclusively identified vessel stalk. The macroscopically sharply defined, highly vascularized, noninfiltrating tumor was removed by anterior orbitotomy with confirmation of the sonographically identified vessel stalk (A = artery, V = vein). (**a, f** with permission of Rohrbach and Lieb 1998)

the frequent recurrence, but also metastasis of this usually benign tumor, complete surgical excision is recommended (Sullivan et al. 1992b; Karcioglu et al. 1997; Cascone et al. 1998).

Imaging demonstrates a soft-tissue, well-circumscribed, generally encapsulated and occasionally lobulated, markedly enhanced mass. An irregular margin is seen in tumors that infiltrate adjacent tissue, including muscles and bone (Fig. 6.92), and is best identified on CT. MRI best enables a complete delineation of the lesion, presenting isointense with slight contrast enhancement on T1-weighted images and with variable iso- to hyperintense signal on T2-weighted series (Fig. 6.91).

In addition to the extraconal location and isointensity on T2-weighted images, a dense tumor stain on angiography (if performed) is one of the most important differential diagnostic criteria of cavernous hemangioma. Cavernous hemangioma shows a high-intensity signal caused by its blood content, delayed contrast enhancement on MRI, but no contrast stain on angiography (Kikuchi et al. 1994a; Bilaniuk 1999). The differential diagnosis of hemangiopericytoma includes among others fibrous histiocytoma, mesenchymal chondrosarcoma, hemangioendothelioma, leiomyosarcoma, malignant schwannoma, and liposarcoma (Rootman 1988).

6.3.1.3 Neurinoma, Neurofibroma

Neurinoma, benign tumors of the peripheral nerve cells, may involve the orbit not only in the intraconal space (Figs. 6.40, 6.41), but also extend/involve the extraconal area, where they may present as encapsulated, well-defined lesions presenting with unspecific symptoms or cranial nerve palsy (Fig. 6.93). In the presence of sphenoid bone dysplasia, additional multiple, clustered masses, presenting with marked contrast enhancement, neurofibroma should be considered as a possible diagnosis, as in the case of a previously unknown neurofibromatosis type 1 without further clinical signs (Fig. 6.94).

6.3.1.4 Secondary Tumors (Sinus-Nasal Malignancies, Metastasis, Olfactory Neuroblastoma, Miscellaneous)

6.3.1.4.1 Sinus-Nasal Malignancies, Metastasis

Any sinus lesion that is inflammatory or neoplastic, may involve the orbit secondarily. Carcinoma of the maxillary sinus is the most common sinus neoplasm

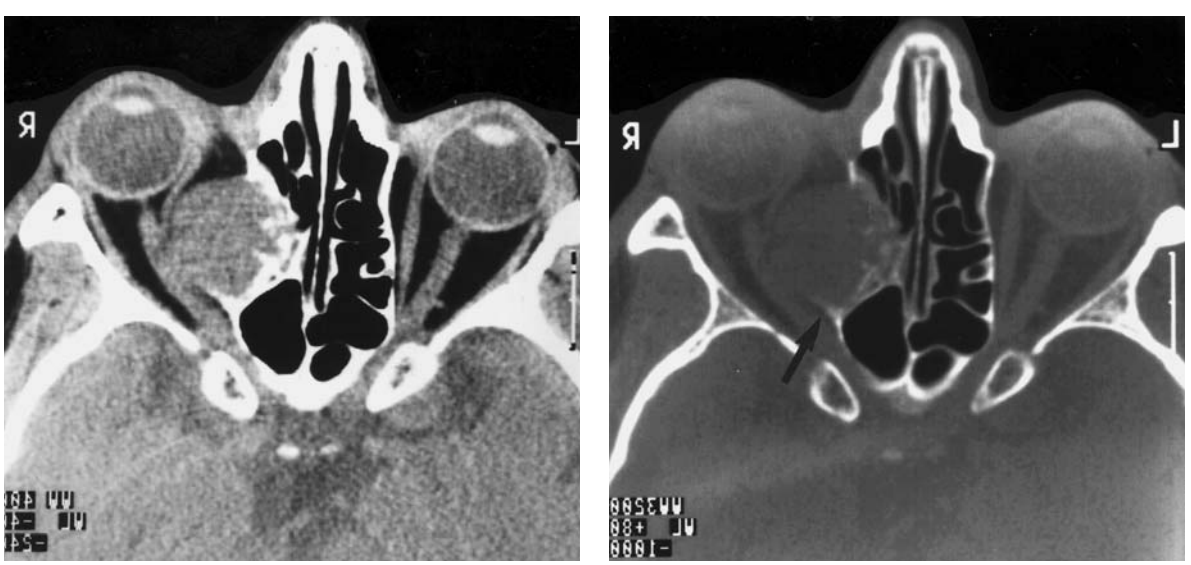

Fig. 6.92a,b. A 60-year-old man with extra-axial proptosis of the right eye. Diagnosis: hemangiopericytoma. Axial CT: **a** Spherical tumor of the right extraconal space, dislocating, but not infiltrating the medial rectus muscle up to the optic nerve. **b** Apparent destruction of the medial orbital wall is visualized in the corresponding bone window. The angular extension of the posterior lamina papyracea (*arrow*) represents the suspected origin of the growth. (With permission of Müller-Forell and Lieb 1995b)

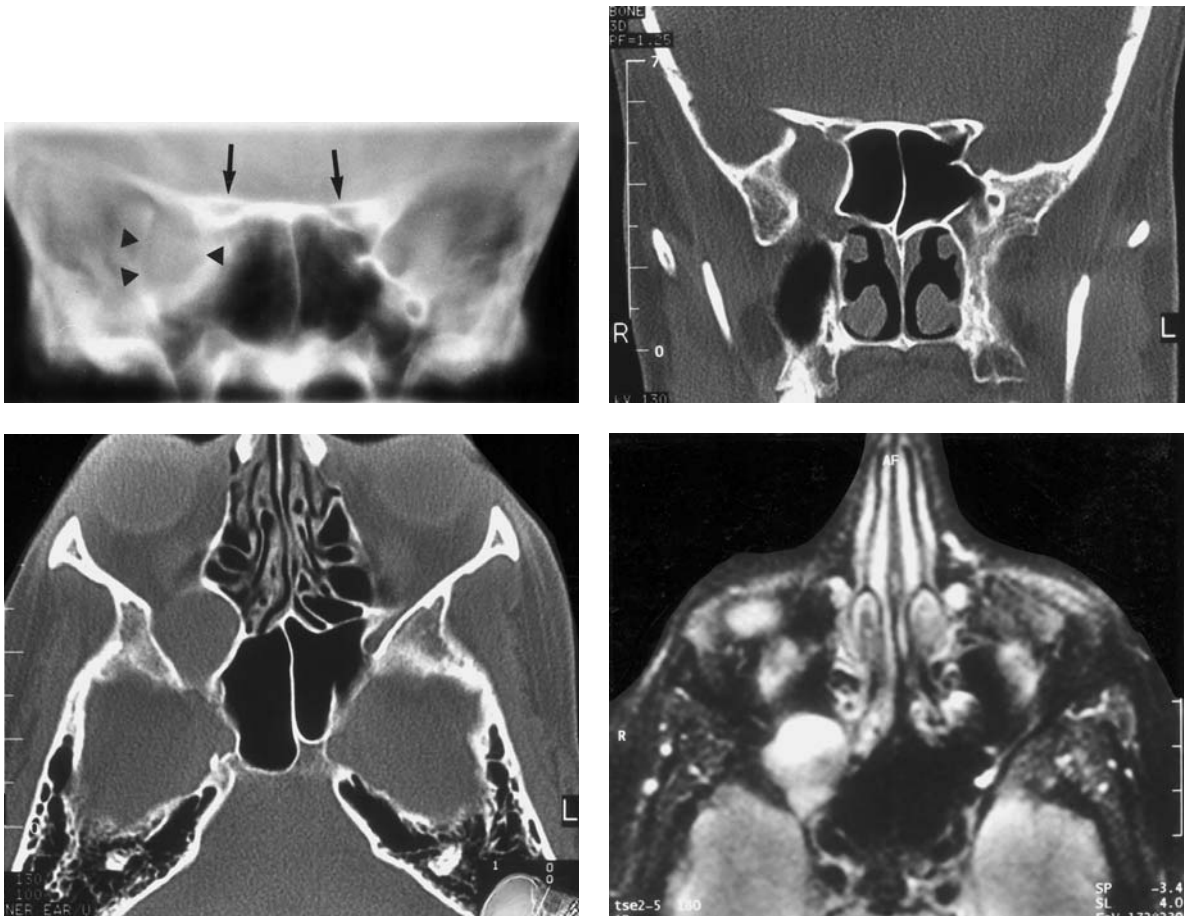

Fig. 6.93a–h. A 61-year-old woman with sudden vision loss 20 years ago, presenting for follow-up examination of the previously diagnosed mucocele. Diagnosis: suspected schwannoma of the superior orbital fissure. **a** Coronal conventional tomography (done 20 years ago) at the level of the optic canal (*arrows*) with biconvex widening of the superior orbital fissure (*triangles*). Current CT (bone window): **b** Corresponding coronal view to **a**, **c** Axial view, both demonstrating an extraconal, intraorbital mass located in the region of the superior orbital fissure, depressing the lateral wall of the (normally pneumatized) sphenoid sinus and causing widening of the lateral part of the sphenopalatine fossa. MR: **d** Axial T2-weighted view with a hyperintense

to invade the orbit (Fig. 6.95). These malignant tumors may not only infiltrate the orbit but also extend to the endocranium (Fig. 6.96). Metastatic involvement of the orbit is known to be the first manifestation of an occult primary malignant tumor in 30%–50% of cases, accounting for less than 5%–11% of all orbital tumors (Moss 1962; Rootman 1988). The most frequent primary tumors are breast (Fig. 6.97), lung, and prostate carcinoma (Fig. 6.98), while metastases of neuroblastoma (Fig. 6.99) or orbital infiltration of extraorbital melanoma (Fig. 6.100) are extremely rare (Zakka et al. 1980; Rootman 1988). As the ophthalmic presentation of metastatic disease is varied (including exophthalmos and enophthalmos, ptosis, motility disorders, and papilledema), clinical symptoms of pain and dysesthesia are highly suggestive of neoplastic lesions growing on a sensory nerve. If infiltrative tumor growth is combined with evidence

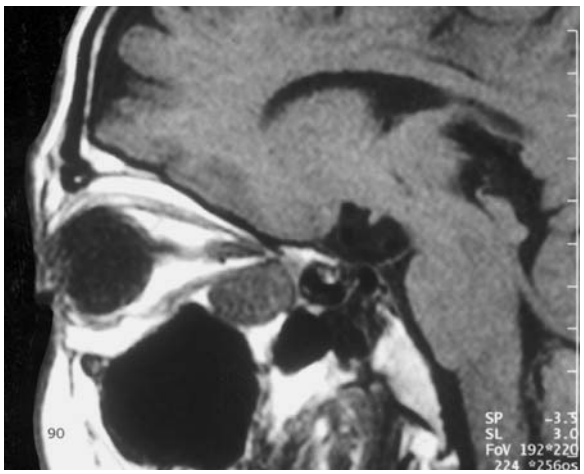

e

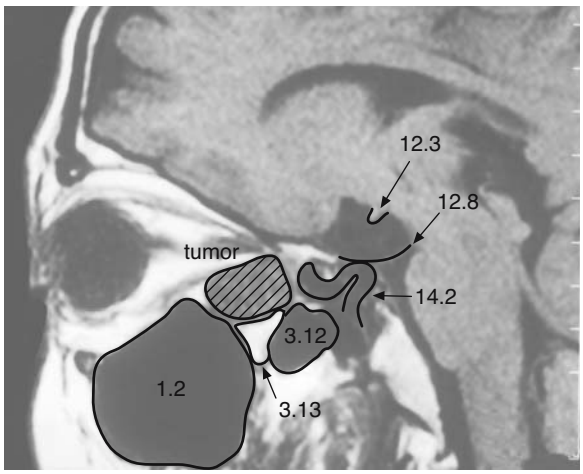

f

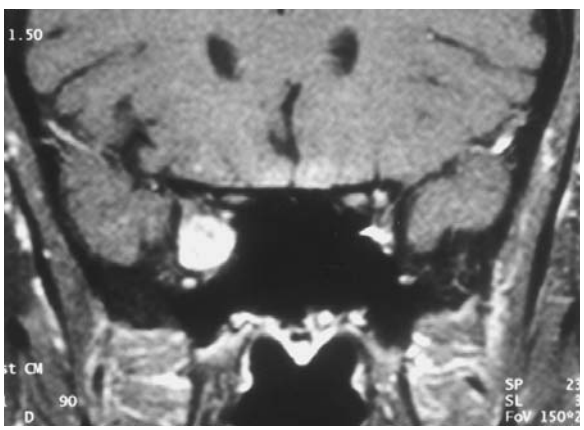

g

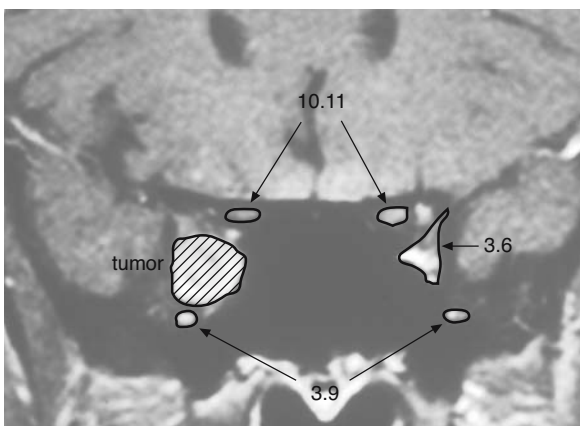

h

. . . mass in the inferior part of orbital apex. **e** Parasagittal (parallel to the optic nerve) T1-weighted native image showing the extraconal location in the inferior apex; note widening of the entrance of the pterygopalatine fossa **f** Corresponding diagram. 1.2 = maxillary sinus, 3.12 = sphenoid sinus, 3.13 = pterygopalatine fossa, 12.3 = optic tract, 12.8 = oculomotor nerve (N III), 14.2 = ICA. **g** Coronal, T1-weighted, contrast-enhanced (FS) view (corresponding to **a** and **b**) with clear signal enhancement, but slight central hypointensity of the encapsulated tumor, which is sharply differentiated from the adjacent structures. **h** Corresponding diagram. 3.6 = superior orbital fissure, 3.9 = round foramen, 10.11 = optic nerve

of irregular bony destruction, biopsy and systemic work-up are needed to make a definite diagnosis (Casper et al. 1993).

Neuroblastoma in childhood arises, as a rule, primarily in abdominal organs, but represents the second most frequent malignant orbital tumor after rhabdomyosarcoma in this patient group (Casper et al. 1993). Primary neuroblastoma originating in other locations as, e.g., in the maxillary bone (Fig. 6.101) is relatively rare. Clinical symptoms of acute, painful proptosis combined with unilateral ecchymotic swelling of the lid are guiding symptoms for the most frequently bilateral metastasis of neuroblastoma, which primarily involves the abdominal organs. The diffuse, in up to 40% bilateral tumor infiltration of the sphenoid wing and intracranial, pachymeningeal tumor involvement (Fig. 6.99) are characteristic for the orbital presentation of neuroblastoma (Casper et al. 1993).

(Text continues on p. 243)

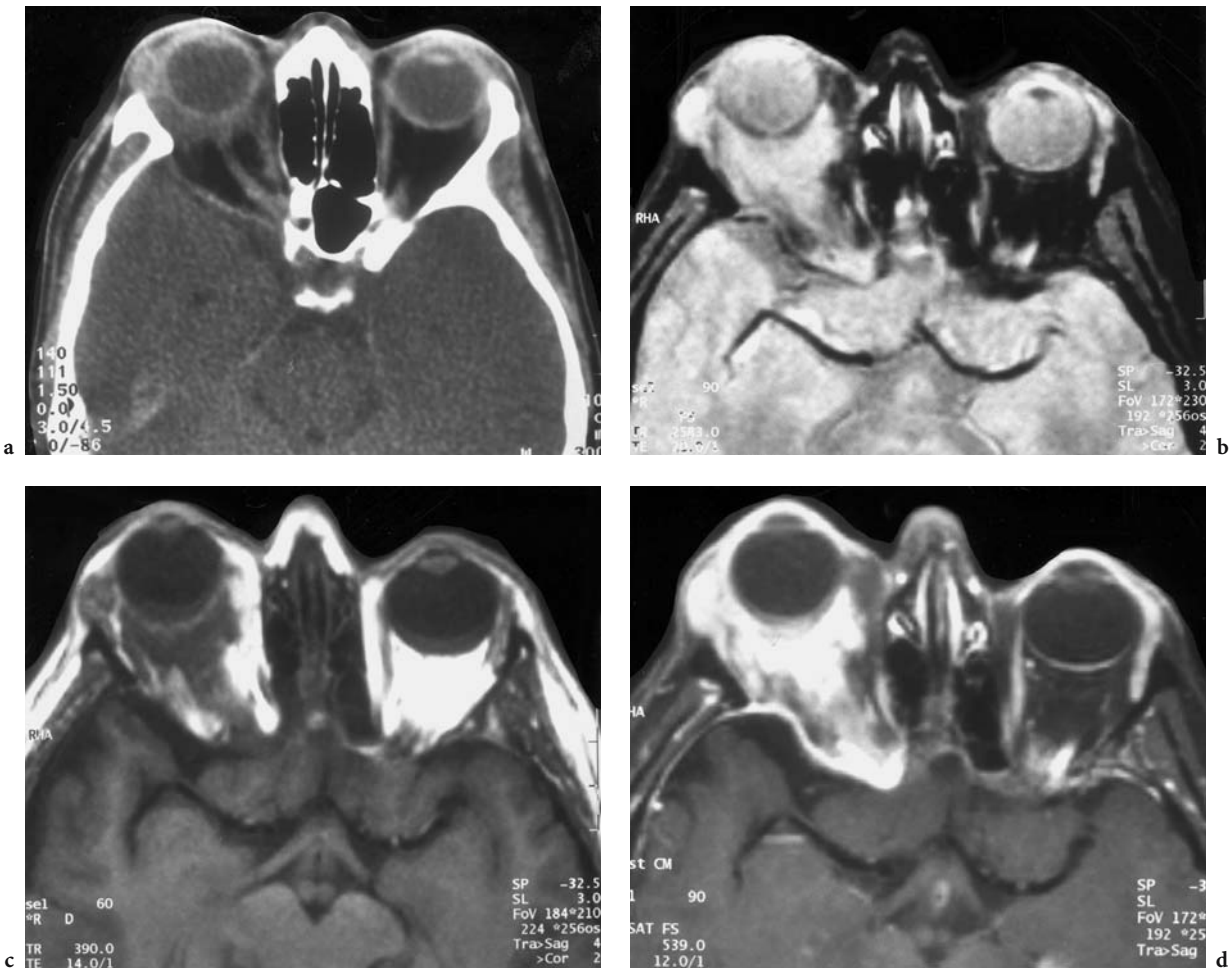

Fig. 6.94a–h. A 37-year-old woman with Graves' disease persisting for several years, currently presenting with proptosis of the right eye (31 mm), progressing slowly over the past few months. No other known history of diseases. Diagnosis: neurofibromatosis in (previously unknown) NF 1. CT: **a** Axial medial orbital view, where in addition to the inhomogeneous mass infiltrating the retrobulbar fat and the lacrimal gland, the right lateral sphenoid wing is missing. MR: **b** Axial proton density-weighted view, demonstrating the primarily intraconal but also extraconal mass. **c** Axial T1-weighted native view. **d** Corresponding T1-weighted, contrast-enhanced (FS) view with infiltration of the largest part of the retrobulbar fat by the irregularly shaped tumor. Note the bright enhancement of the temporopolar dura. **e** Coronal, T1-weighted, contrast-enhanced (FS) view where the entire tumor, sparing the external rectus muscles, is seen. Note the normal size of the conal muscles without any sign of

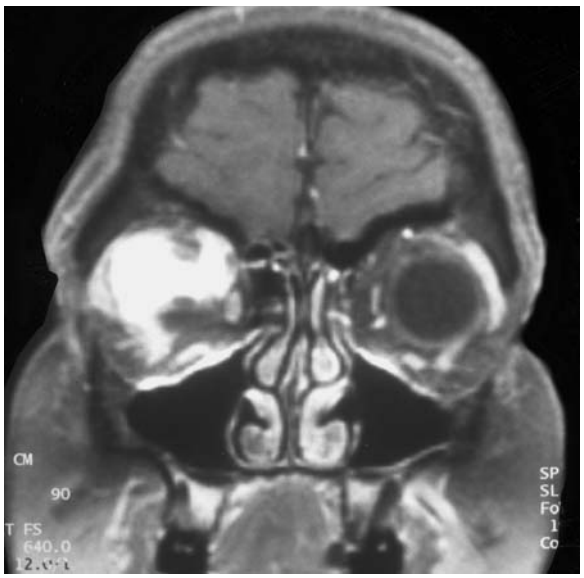

e

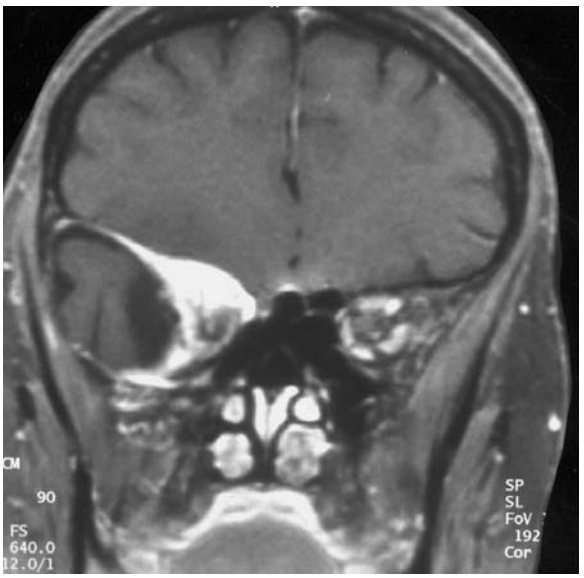

f

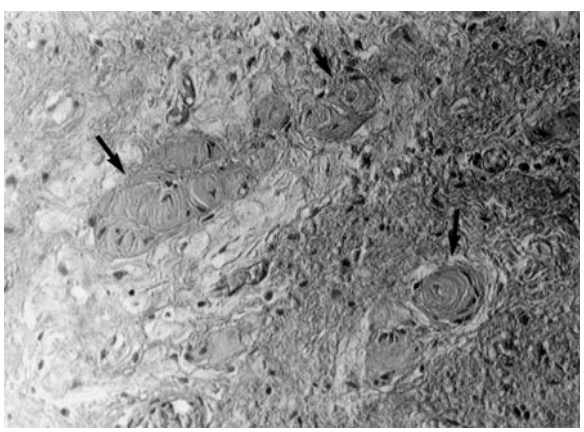

g

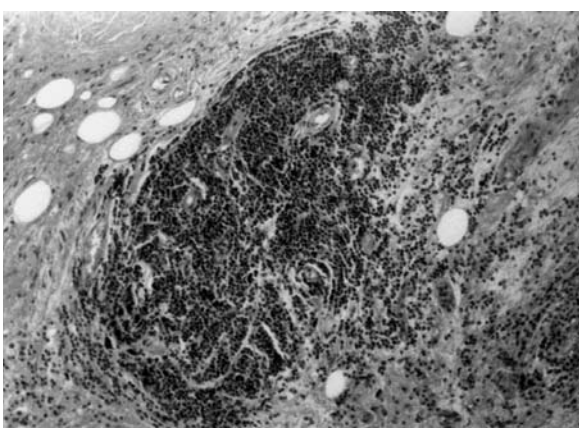

h

Graves'... ... disease. **f** Coronal, T1-weighted, contrast-enhanced (FS) of the orbital apex, demonstrating dural enhancement of the entire middle cranial fossa region. Note asymmetry of the middle cranial fossa as well as of the orbit. Histology: **g** (×280) several pseudomesserian corpuscles (*arrows*), surrounded by a dense fibrillary connective tissue, diffusely proliferating in the orbital tissue, confirm the diagnosis of neurofibroma. **h** (×140): focal lymphatic infiltration (corresponding to Graves' disease) in the neighborhood of some blood vessels surrounded by a dense fibromatous tissue. (CT image with permission of Radiologie Brüderkrankenhaus Trier, histology with permission of Dr. Bohl, Department of Neuropathology, Medical School, Mainz)

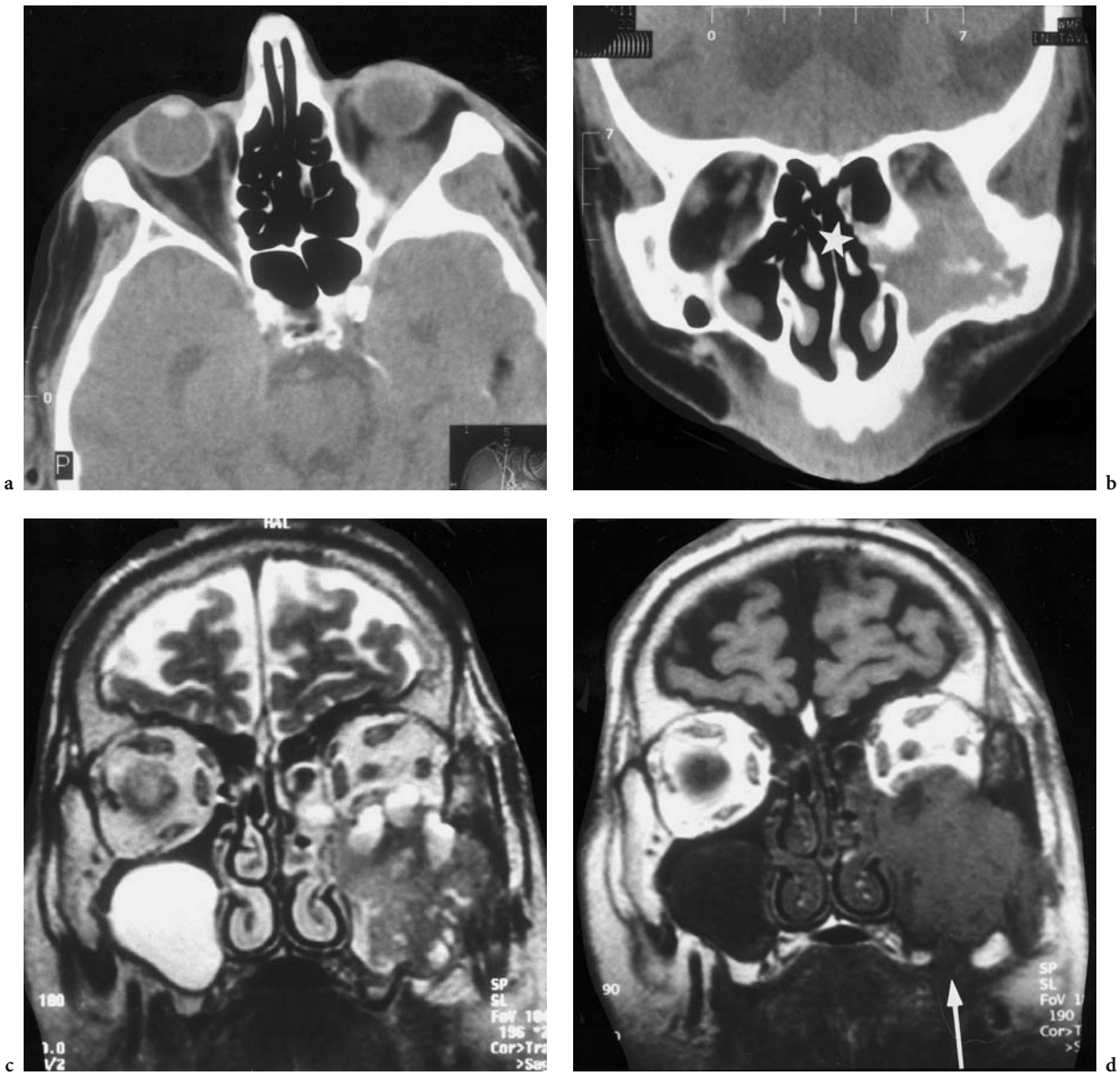

Fig. 6.95a–d. A 78-year-old man presenting with epistaxis and numbness of the left cheek. Diagnosis: carcinoma of the left maxillary sinus. CT: **a** Axial native view showing soft tissue in the inferior left orbit with poor distinction from the lateral rectus muscle. **b** Paracoronal native view, demonstrating the destruction of the maxillary sinus roof and medial wall leading to tumor invasion into the inferior orbit and nasal cavity (*white star*). MRI: **c** Coronal T2-weighted view with demarcation of necrotic tumor parts (high signal). Although destruction of the periorbital area might be expected, no infiltration of the inferior rectus muscle is seen. Note a maxillary sinus cyst (hyperintense) on the right side. **d** Corresponding T1-weighted native view identifying additional pronounced destruction of the maxillary sinus floor (*white arrow*) on comparison with **c**

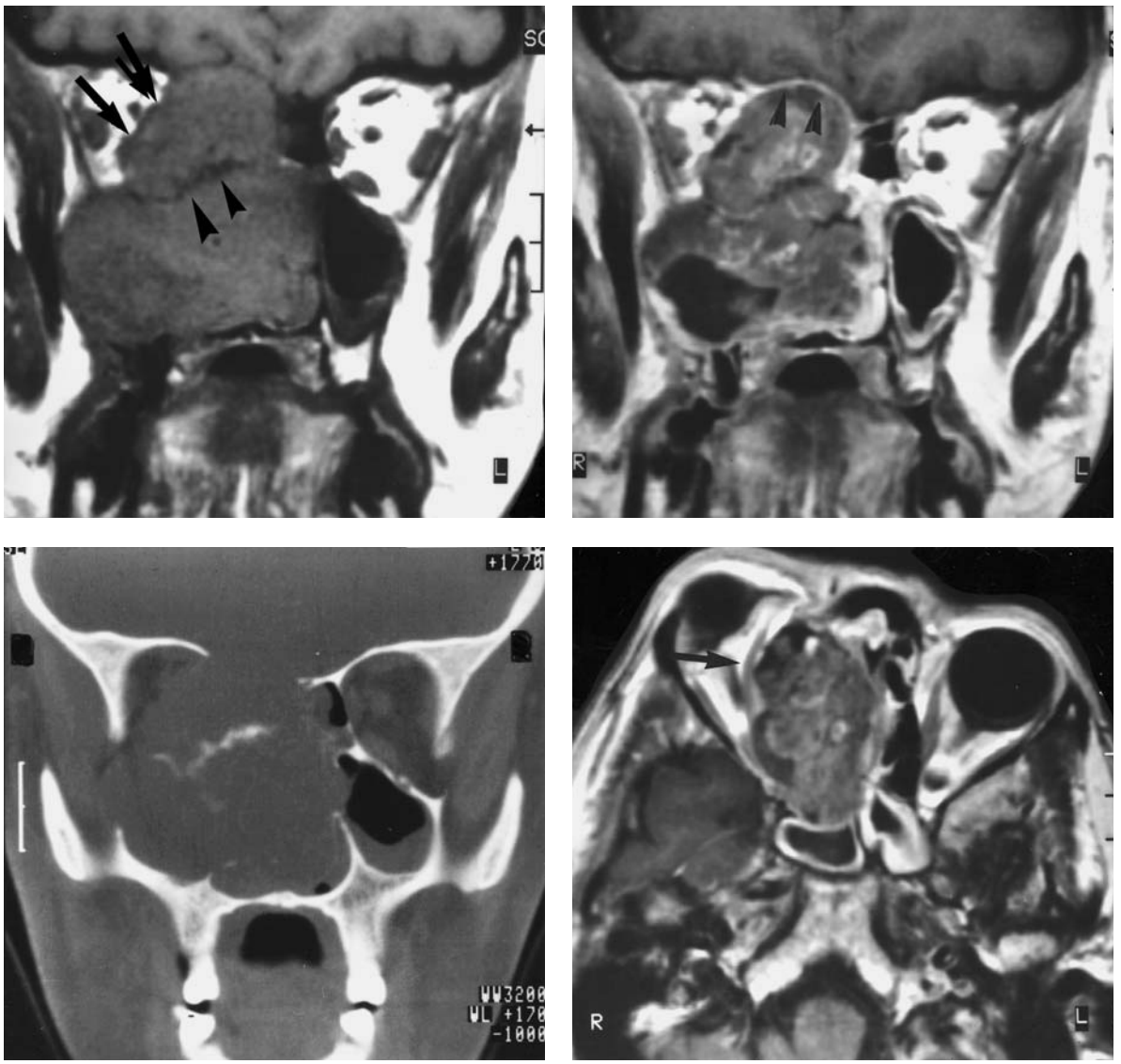

Fig. 6.96a–d. A 44-year-old woman with right exophthalmos associated with maxillary sinus carcinoma. Diagnosis: orbital and intracranial infiltration of an adenocarcinoma of the maxillary sinus. MRI: **a** Coronal T1-weighted native view where the complete extension of the tumor is seen not only in the maxillary, ethmoidal sinus, both nasal cavities and the orbit, but also in the anterior cranial fossa. The transverse hypointensity (*arrowheads*) demarcates the remaining orbital and ethmoidal floor (see **c**). Differentiation from the medial and inferior rectus muscles (*arrows*) is markedly better in the native view than in the corresponding contrast-enhanced view (**b**) due to normal signal enhancement of the muscles. While the frontobasal dura (*arrowheads*) appears to be intact, the rectus and medial orbital gyrus are compressed by tumor expansion. CT: **c** Coronal view (bone window) yielding superior visualization of the full extent of the bony destruction in addition to that of the right maxillary and orbital walls. The tumor crosses the midline, extending into the left ethmoidal cells and the left infundibulum. MR: **d** Axial, T1-weighted, contrast-enhanced image where the extraconal invasion of the right orbit with dislocation of the medial rectus muscle (*arrow*) is clearly visualized. Marginal swelling of the mucous membrane of the sphenoid sinus indicates retention of mucus caused by tumor occlusion of the ducts. (With permission of Müller-Forell and Lieb 1995b)

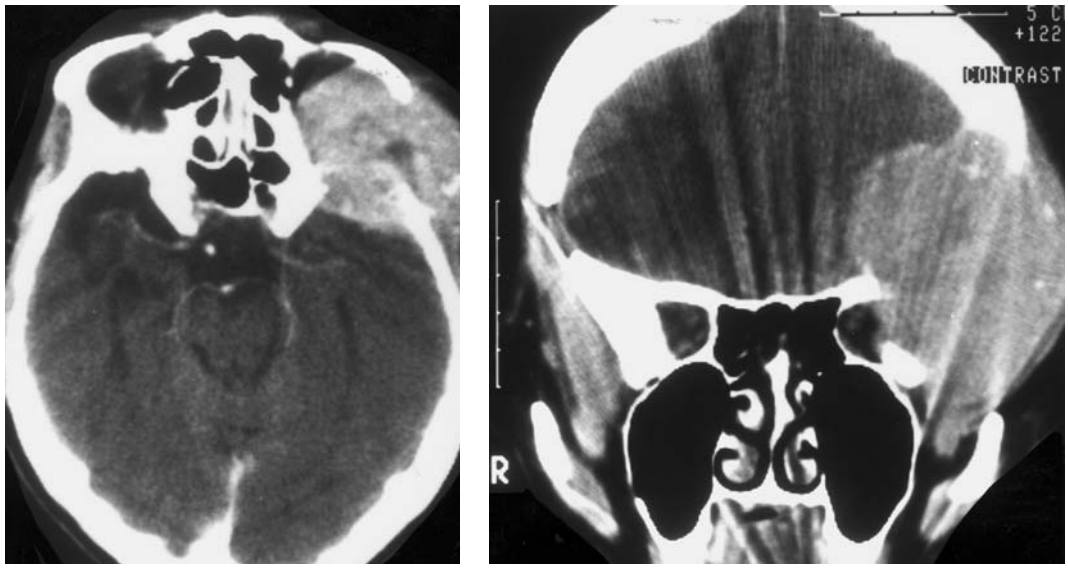

a b

Fig. 6.97a,b. A 68-year-old woman with painful swelling of the left periorbital region. Diagnosis: metastasis of breast carcinoma. CT: **a** Axial contrast-enhanced view with destruction of the frontal, sphenoid, and temporal bone as a result of intraorbital, intracranial, and infratemporal tumor expansion. **b** Coronal contrast-enhanced view, the defect of the right frontal bone corresponds to metastasis removal 12 months previously

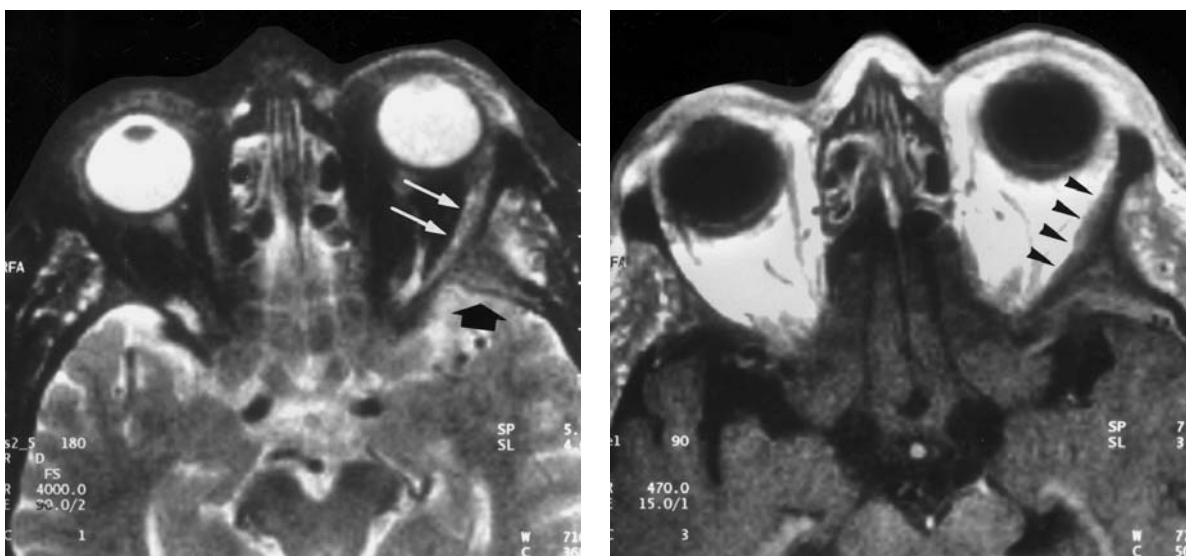

a b

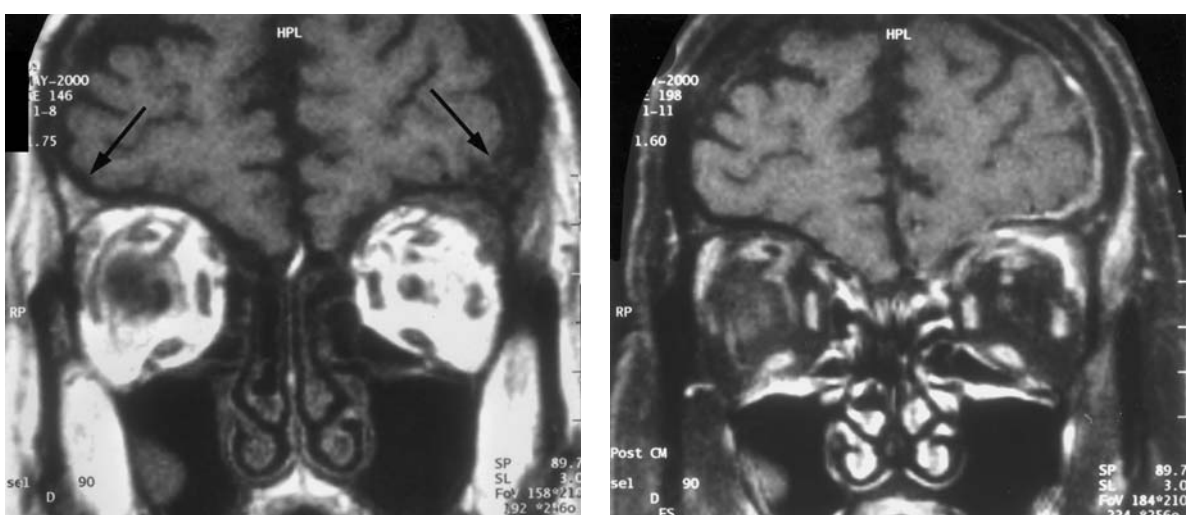

c d

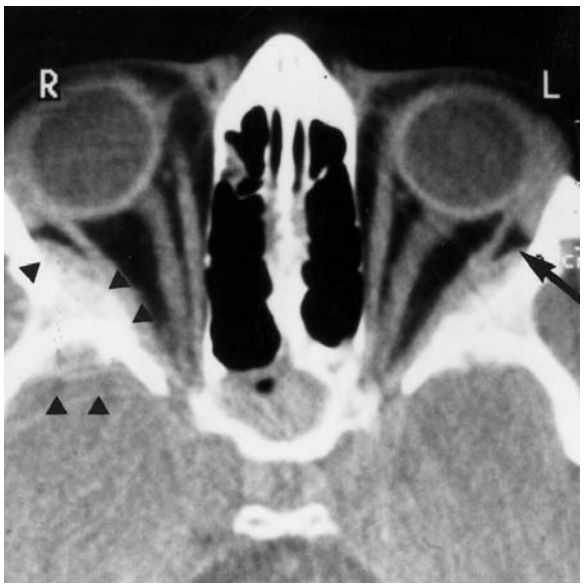

a

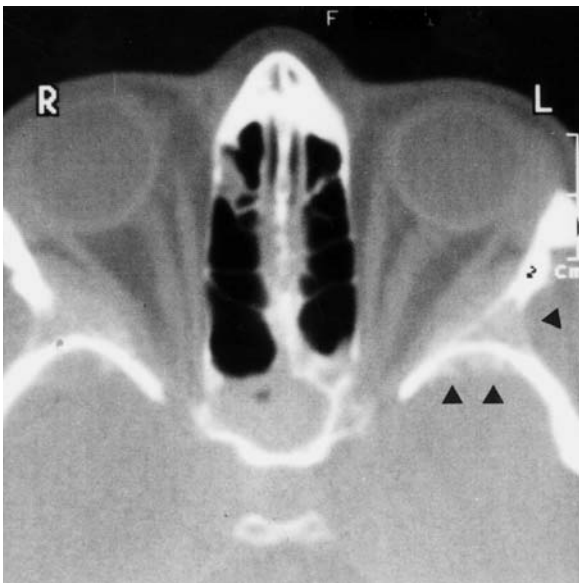

b

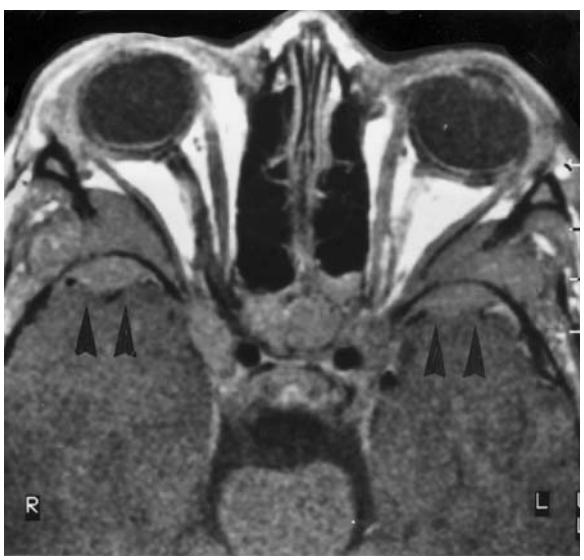

c

Fig. 6.99a–c. A 10-year-old girl with bilateral proptosis and bilateral ecchymotic swelling of the lids. Diagnosis: metastatic neuroblastoma. CT: **a** Axial native view with bilateral extraconal tumor mass and osteodestruction of the great sphenoid wing (*triangles*), dislocating the lateral rectus muscles with emphasis to the left (*arrow*). **b** Corresponding bone window yielding better visualization of the osseous destruction (*triangles*). MR: **c** Corresponding native T1-weighted image. The bilateral extraconal tumor extension with respect to the dislocated rectus muscles and the intracranial extraparenchymal tumor infiltration are more distinctly differentiated than on CT (**a**). MRI further enables the diagnosis of bony destruction based on the absence of both the characteristic signal loss of the bone cortex and the signal intensity of the bone marrow. (With permission of Müller-Forell and Lieb 1995b)

◁ **Fig. 6.98a–d.** A 59-year-old man with history of carcinoma of the prostate, no subjective symptoms, but nuclide concentration in the left orbital region in bone radionuclide scan. Diagnosis: metastasis of a prostate carcinoma in the left superolateral orbital wall. MR: **a** Axial T2-weighted image with enhancement of the lateral rectus muscle region (*white arrows*) and enlargement of the great sphenoid wing (*short black arrow*). **b** Corresponding T1-weighted native view with irregular soft-tissue infiltration of the lateral orbital wall (*arrowheads*) and temporopolar thickening of the dura. **c** Coronal T1-weighted native view where a soft extraconal tissue mass extending to the intermuscular septum is identified. Note the different signal of both lateral parts of the great wing of the sphenoid (*short black arrows*), indicating infiltration of the respective bone marrow fat. **d** Corresponding T1-weighted, contrast-enhanced (FS) view, demonstrating infiltration of the periorbit, the dura, and even the temporal muscle by metastasis

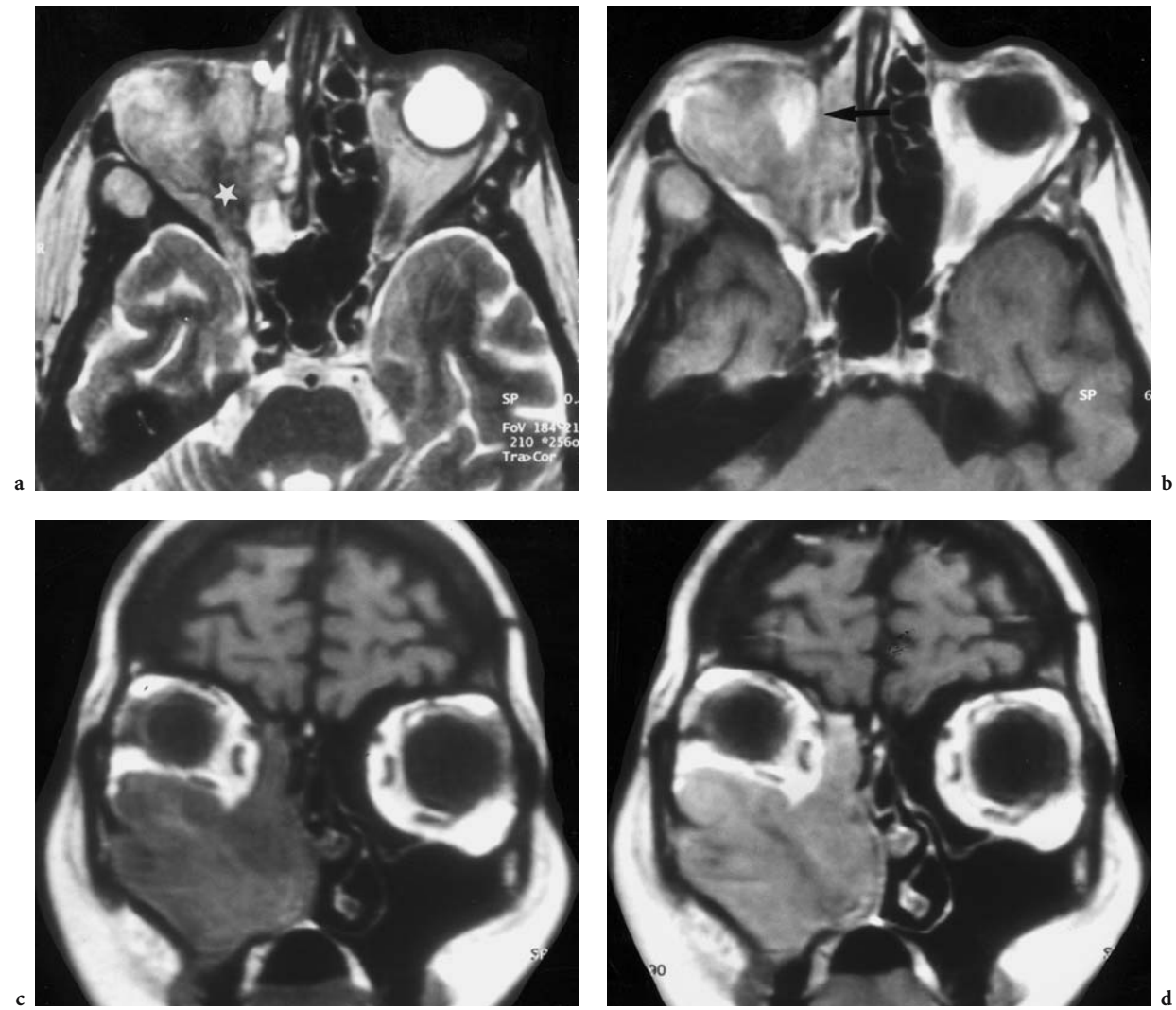

Fig. 6.100a–d. A 37-year-old woman with previously operated primary melanoma of the maxillary sinus, presenting with swelling of the right eye. Diagnosis: intraorbital expansion of the maxillary sinus melanoma. MR: **a** Axial T2-weighted view of the inferior orbit, filled with tumor on the right side leading to the suspicion of infiltration of the inferior rectus muscle (*white star*) and orbital fat. Note additional tumor invasion of the ipsilateral temporal fossa. The bright signal of the ethmoidal cells represents mucous retention. **b** Corresponding T1-weighted, contrast-enhanced view with slight, homogeneous enhancement of the tumor, but a nearly normal signal intensity for the fat (*arrow*) medial to the rectus muscle. **c** Coronal T1-weighted native view showing the entire tumor expansion in the right maxillary sinus, nasal cavity, and ethmoidal sinus, as well as inferior orbital invasion. Note the upward displacement without infiltration of the inferior rectus muscle and globe. **d** Corresponding T1-weighted, contrast-enhanced view showing nearly homogeneous enhancement

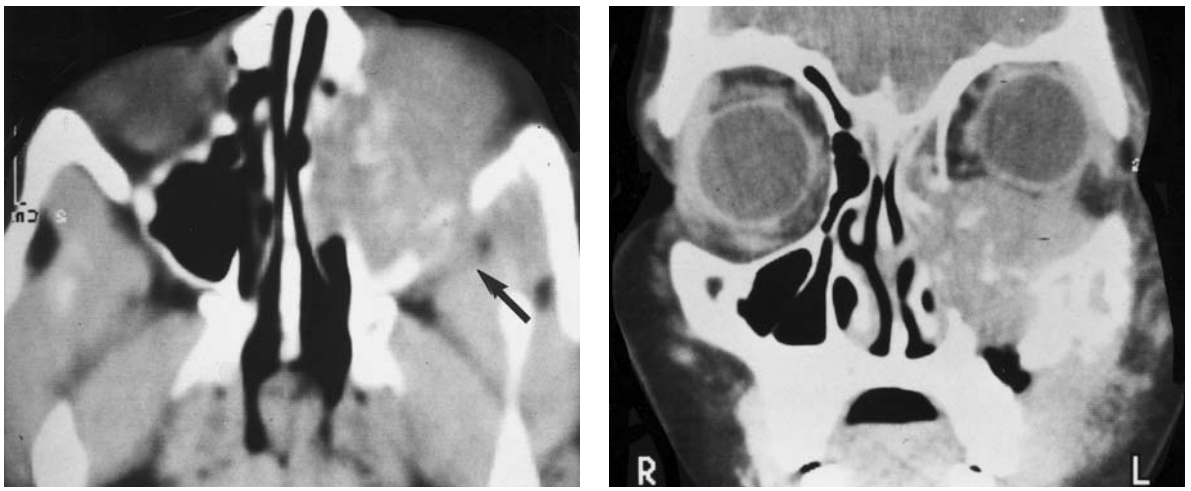

a b

Fig. 6.101a,b. A 10-year-old girl with persistent swelling of the left cheek. Diagnosis: neuroblastoma. CT: **a** axial image, showing tumor invasion of the left maxillary sinus, ipsilateral retromaxillary (*arrow*), and nasal space with bone destruction. **b** Coronal view with upper globe displacement due to intraorbital tumor expansion with suspected infiltration of the external inferior muscle. Tumor growth probably started in the left upper maxillary sinus roof, destroying the maxillary and nasal bone and also invading the ipsilateral ethmoid

6.3.1.4.2 Olfactory Neuroblastoma (Syn. Esthesioneuroblastoma)

The relatively uncommon olfactory neuroblastoma represents a malignant neuroectodermal tumor originating from bipolar olfactory receptor cells high in the mucosa of the nasal cavity, affecting both sexes with an approximately equal frequency (Finkelstein et al. 2000). This slowly growing tumor may occur at any age, with a cluster around 20 and 50 years, and is typically associated with long-standing symptoms of nasal obstruction, anosmia, and epistaxis. The involvement of the orbit and/or endocranium already represents an advanced stage (Kadish et al. 1976). Imaging discloses an upper nasal vault mass with focal bony destruction, presenting with mixed signal intensity on MRI and a moderate but inhomogeneous enhancement after contrast administration (Osborn 1994) (Figs. 6.102–6.104). In cases of difficult differential diagnosis concerning other tumors of the paranasal sinuses, the performance of ^{123}I-MIBG SPECT may be justified (Sasjima et al. 2000).

6.3.1.4.3 Langerhans-Cell Histiocytosis (LCH)

Histiocytosis X was first defined by Lichtenstein (1953) to include an inflammatory eosinophilic granuloma of the bone and the adjacent soft tissue. Involvement of a dendritic cell of bone marrow origin (Langerhans-type histiocyte) has been demonstrated as the common pathologic element and unique identifier, described as Langerhans-cell histiocytosis (Neselof et al. 1973; Chu et al. 1987; Tien et al. 1991). Langerhans-cell histiocytosis is a disease of unknown origin with variable clinical manifestations ranging from nonprogressive solitary eosinophilic granuloma of the bone to progressive, more aggressive, and often fatal multisystemic involvement (Howarth et al. 1999; Poe et al. 1994) (see also Sect. 7.2.1.2.3). A single system disease, found in about 70% of the patients, is most frequently seen as an isolated bone lesion, with preference for the skull and femur. Solitary or monostotic eosinophilic granuloma is the most common presentation of LCH in children, typically affecting the skull vault and presenting as a well-defined circumscribed mass (Fig. 6.105). On CT, the lesion is typically of similar density as the cortical gray matter, while on MRI a marked hypointensity on T2-weighted images appears to be characteristic and may be related to a severe fibrotic reaction of the involved meningeal tissue. After administration of contrast medium, a marked contrast enhancement is seen (Fig. 6.105c) (Barkovich 2000).

(Text continues on p. 248)

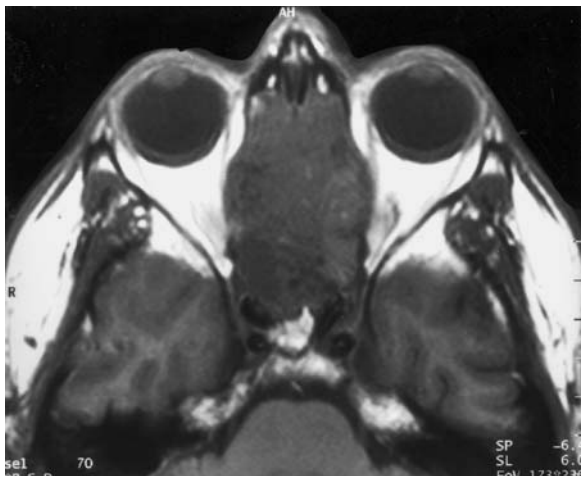

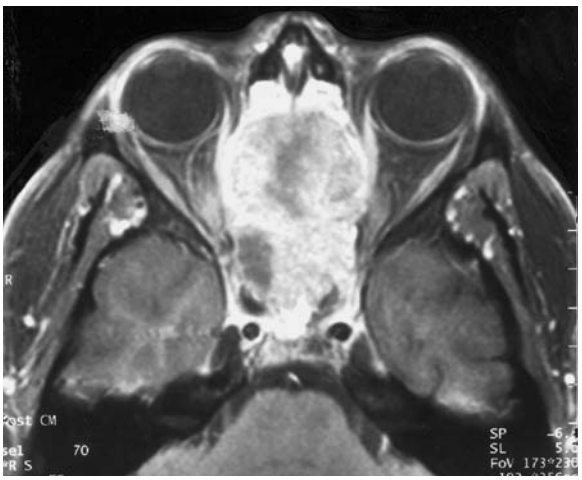

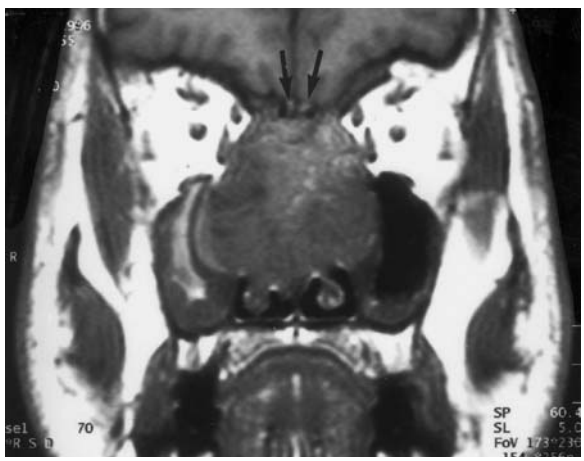

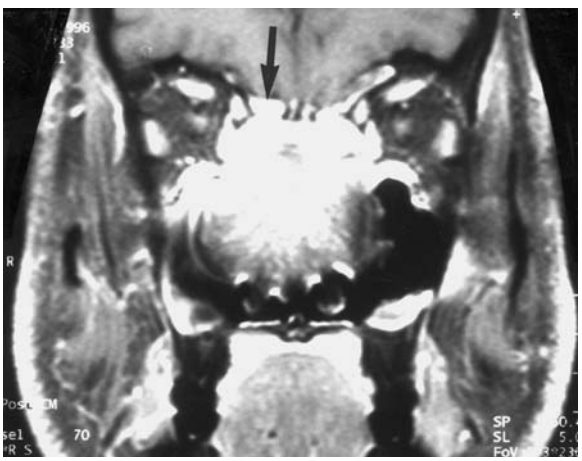

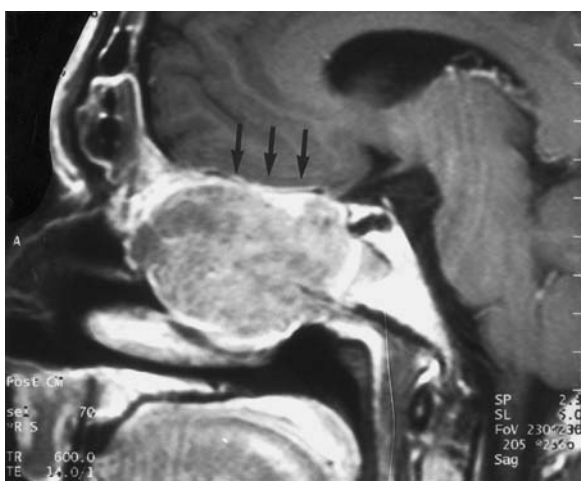

Fig. 6.102a–e. A 38-year-old man, presenting with persistent pressure on both eyes in addition to persistent nasal obstruction. Diagnosis: esthesioneuroblastoma. MRI: **a** Axial T1-weighted image, demonstrating complete tumor-like obstruction of the ethmoid and sphenoid sinuses with marked bilateral intraorbital extension in the region of the lamina papyracea. **b** Corresponding T1-weighted, contrast-enhanced (FS) image showing intraorbital tumor growth with slight impression of both medial rectus muscles but the presence of an apparently intact periorbit. Note the hypointensity at the center of the tumor, corresponding to necrotic areas. **c** Coronal T1-weighted native view demonstrating the intraorbital growth. Widening of the frontal groove may be responsible for the destruction of the frontal base and intracranial expansion. Note the olfactory bulbs (*small arrows*), located below the rectus gyri. **d** Corresponding T1-weighted, contrast-enhanced (FS) image with tumor invasion of the base of both supraorbital recesses and mucous retention, identified by homogeneous signal intensity enhancement (*arrow*), no conclusive dural enhancement. **e** Sagittal paramedian, T1-weighted, contrast-enhanced view showing dural enhancement along the entire sphenoid plane (*small arrows*). Note the AP and craniocaudal dimension of the tumor growth with destruction of the sphenoid bone and the bony palate

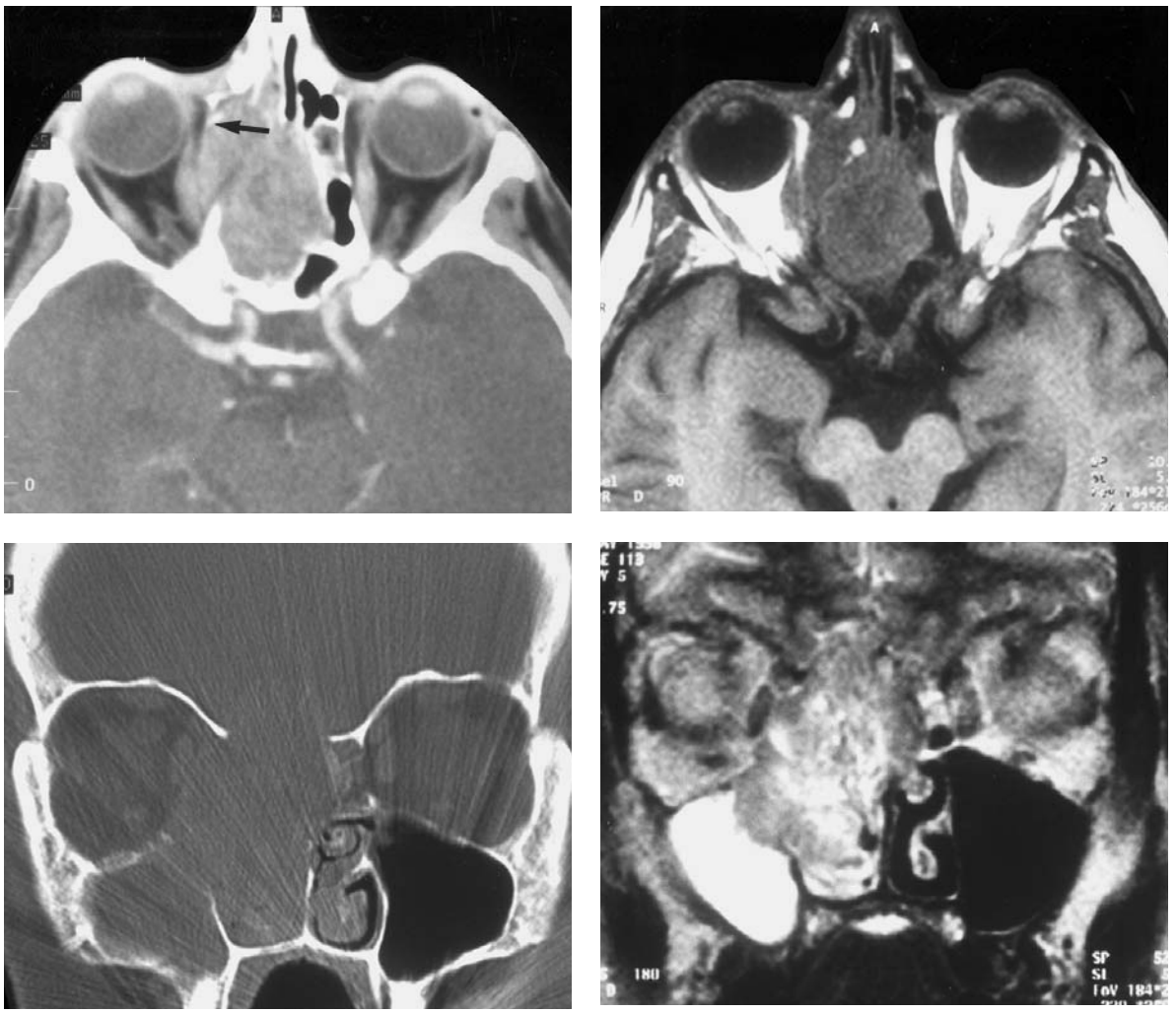

Fig. 6.103a–h. A 65-year-old woman, presenting with slight proptosis of the right eye, diffuse pressure in the orbital region, and difficulty in nasal breathing for a period of several months. Diagnosis: esthesioneuroblastoma. **a** Axial contrast-enhanced CT demonstrating a very large tumor occupying predominantly the right ethmoid and sphenoid sinuses and crossing the midline. Although the medial orbital wall is destroyed and intraorbital extraconal tumor expansion with medial dislocation of the medial rectus muscle is visualized, the presence of a small fat border (*arrow*) indicates sparing of the periorbit. **b** Corresponding T1-weighted native MRI, showing intraorbital expansion less conclusively, but providing a superior view of the periorbital growth. Note the expansion to the bony optic canal. **c** Coronal CT in the bone window, demonstrating additional destruction of the skull base and craniocaudal expansion of the tumor into the entire right nasal cavity. **d** Corresponding T2-weighted MRI with excellent differentiation between the mixed solid and necrotic tumor with slight high intensity and the bright signal of congestion due to maxillary mucus, but with only poor differentiation between tumor and brain parenchyma/gray matter. **e–h** see next page

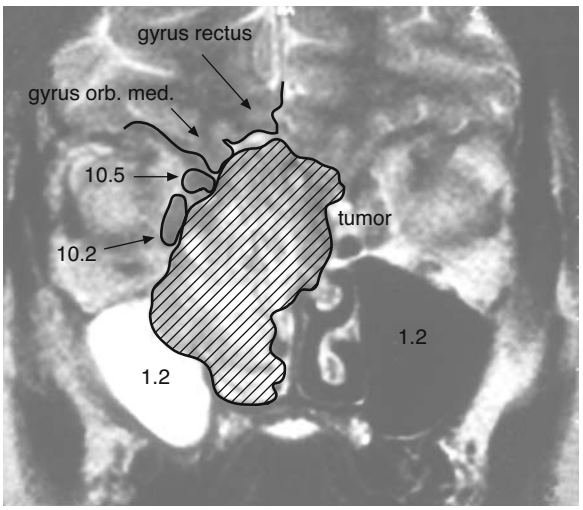

e

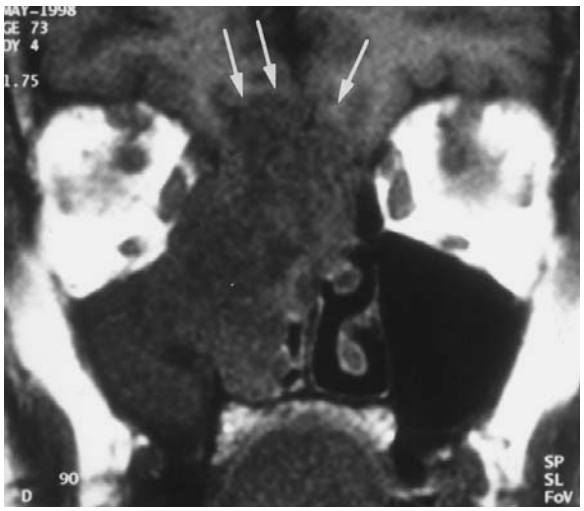

f

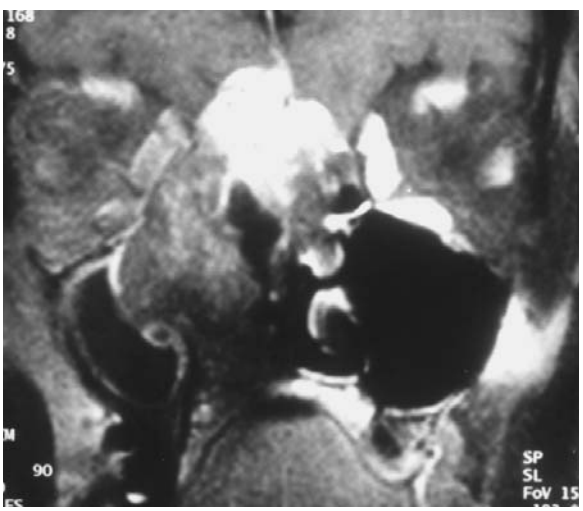

g

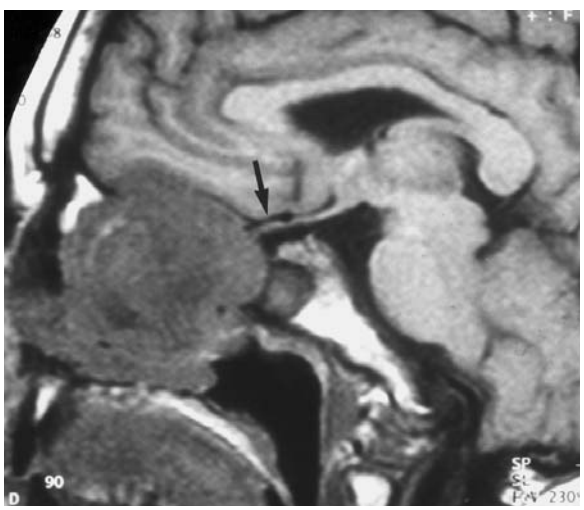

h

Fig. 6.103 *(continued)* **e** Corresponding diagram: 1.2 = maxillary sinus, 10.2 = medial rectus muscle, 10.5 = superior oblique muscle. **f** Coronal T1-weighted native view, demonstrating intracranial extradural expansion with bilateral (predominantly right) compression and dislocation of the rectus gyrus (*small white arrows*). Note the better differentiation of the cranial tumor region, in contrast to the inferior region and maxillary mucus, compared with **d**. **g** Corresponding T1-weighted, contrast-enhanced (FS) image with maximum signal enhancement in the intracranial, extradural tumor region. **h** Right paramedian, sagittal, T1-weighted native view, demonstrating the close vicinity of the tumor and the right optic nerve (*small arrow*) (compare with **b**)

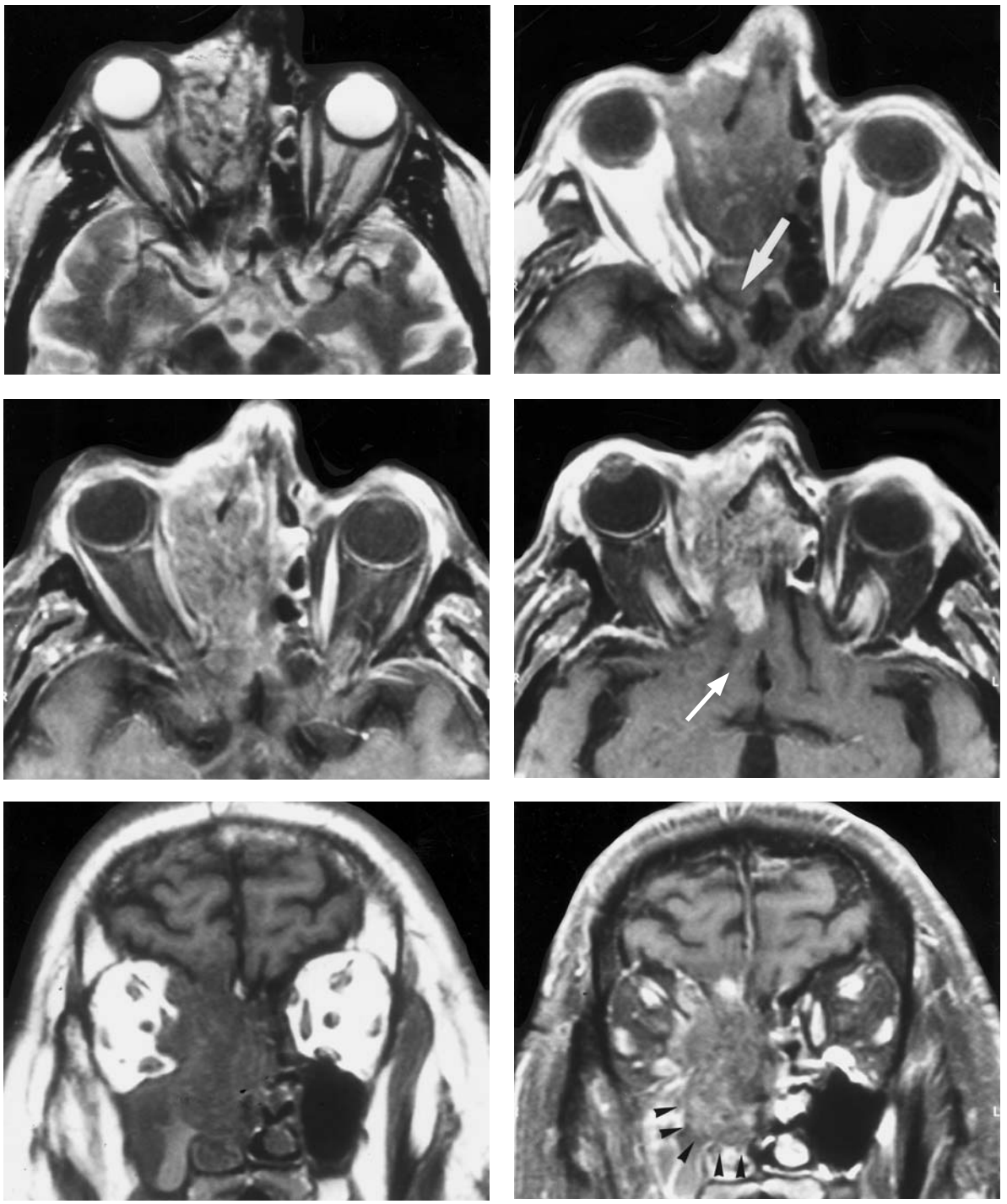

Fig. 6.104a–f. A 60-year-old man with a swollen right eye and history of nasal breathing disability. A nasal tumor was biopsied at an external hospital. Diagnosis: esthesioneuroblastoma. MRI: **a** Axial T2-weighted image of the medial orbit, demonstrating a tumor invasion of the right medial orbit (with dislocation of the medial rectus muscle), the medial lid, and nasal region by a tumor originating from the right nasal cavity. **b** Corresponding T1-weighted native view with apparent bony destruction of the entire right lamina papyracea. Note the invasion of the sphenoid sinus and region of the right optic canal (*white arrow*). **c** Corresponding T1-weighted, contrast-enhanced (FS) view with less marked delineation toward the optic nerve. **d** Axial, T1-weighted, contrast-enhanced (FS) slice of the upper orbit, demonstrating intracranial tumor invasion (*arrow*). **e** Coronal T1-weighted native view, showing the entire tumor expansion in the nasal cavity, orbit, and endocranium. Note the inaccurate delineation of orbital and intracranial structures from the tumor. **f** Corresponding T1-weighted, contrast-enhanced (FS) view, where mainly the intracranial tumor compartment with impression of the right rectus gyrus shows bright signal enhancement. Note the mucous retention in the ipsilateral maxillary sinus; compare with the native view (*arrowheads* demarcate the tumor border)

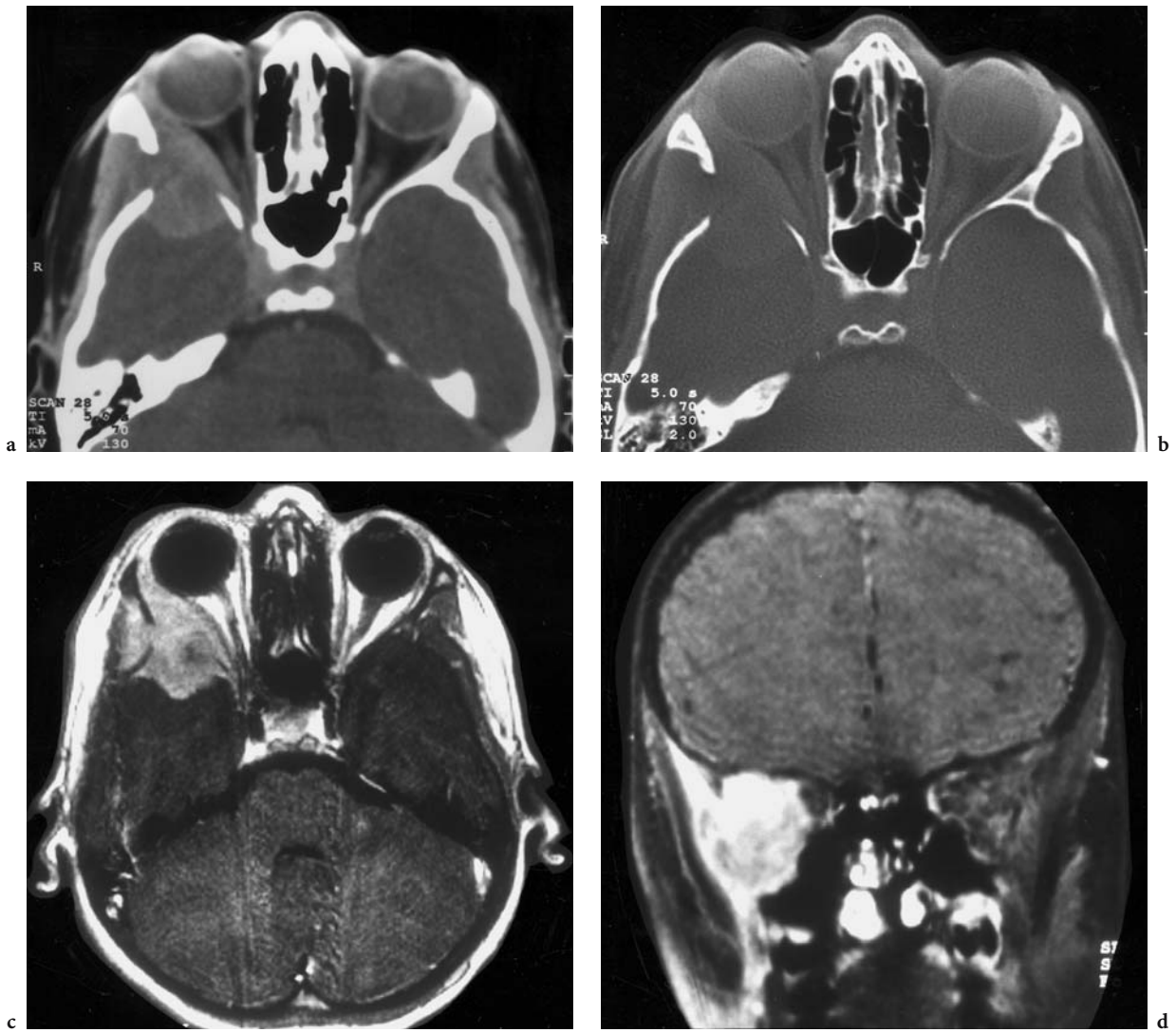

Fig. 6.105a–d. An 8-year-old boy with right orbital pain persisting for 2 months, followed by proptosis after 1 month; no neuro-ophthalmologic deficit. Diagnosis: Langerhans-cell histiocytosis. CT: **a** Axial contrast-enhanced view, demonstrating bony destruction of the large wing of the sphenoid bone, including parts of the zygomatic and temporal bone. A sharply defined, homogeneous lesion extending into the orbit is seen, with apparent dislocation of the lateral rectus muscle, and further extension to the posterior part of the lacrimal gland as well as subperiosteal in the direction of the optic canal. **b** Corresponding bone window. T1-weighted MRI: **c** Axial contrast-enhanced image, corresponding to **a** with distinct differentiation of the lateral rectus muscle from the tumor. Note superior identification of additional infiltration of the temporal fossa than on CT. **d** Coronal contrast-enhanced (FS) view, showing the craniocaudal dimension of the tumor with extension to the orbital roof. (MR images with permission of Drs Eberle, Krohn, Friedburg)

6.3.2 Tumor-like Lesions

6.3.2.1 Fibrous Dysplasia (Jaffé-Lichtenstein Syndrome)

Fibrous dysplasia is a benign, developmental disorder of the bone, characterized by replacement of normal medullary bone by fibrous connective tissue with immature bone trabeculae, primarily affecting the spongy bone substance, although in rare cases the cortex of the bone may also be affected (Lichtenstein and Jaffé 1942; Freyschmidt 1993; Jaffe et al. 1997; Wenig et al. 1998). It appears to represent an arrest in the maturation of primitive fibrous stroma in the woven bone stage, thus preventing the normal replacement of immature woven bone by lamellar bone, and is obviously caused by a specific mutation

of the G_s alpha gene (Marie et al. 1997; Wenig et al. 1998). Fibrous dysplasia may occur in a monostotic form in 70%, oligo- or polyostotic appearance is seen in 30% of cases, with the latter developing at an earlier age than the former. In rare cases, fibrous dysplasia occurs in combination with endocrine dysfunction and cutaneous hyperpigmentation (precocious puberty, hyperthyroidism), the McCune–Albright syndrome (MAS) (Albright et al. 1937; Freyschmidt 1993; Marie et al. 1997; Wenig et al. 1998). Craniofacial lesions occur in 50% of patients with oligo- or polyostotic fibrous dysplasia, and in nearly 100% of patients with a severe polyostotic form (Megerian et al. 1995). The most frequently affected bones of the craniofacial skeleton are the ethmoid, sphenoid, frontal (Fig. 6.106), and temporal bones (Mohammadi-Araghi and Haery 1993). Detection of fibrous dysplasia is mostly incidental, but if clinically symptomatic, it correlates with the involved region and the extent of the involvement (Katz and Nerad 1998). The typical age of presentation is late childhood or adolescence, because especially in monostotic forms (Fig. 6.107), the disease is self-limited with stability at the onset of puberty (Henry 1969; Jaffe et al. 1997; Wenig et al. 1998). Histologically, irregularly shaped trabeculae of osteoid and immature bone are seen arising metaplastically from the fibrous stroma, forming odd geometric patterns, resembling Chinese letters (Mohammadi-Araghi and Haery 1993). Surgical treatment is required in cases of progressive facial deformity (Fig. 6.106) or cranial, and particularly optic, nerve involvement (Fig. 6.188) (Papay et al. 1995; Katz and Nerad 1998). Radiation therapy is known to link directly to sarcomatous transformation of the lesions and should be avoided (Stanton and Montgomery 1996; Wenig et al. 1998; Freyschmidt 1993).

As histopathologic differentiation from ossifying fibroma may sometimes be difficult, the presence and consideration of radiological features are crucial for the definite diagnosis. CT has replaced plain film and represents the method of choice in the initial diagnosis and definition of the extent of fibrous dysplasia, especially with 3D-reformation for preoperative planning of esthetic surgery in patients with extensive facial involvement (facies leontina). In craniofacial lesions, three morphologically different types of radiologic features of fibrous dysplasia are known, depending on the stage of development and the degree of fibrous stroma replacement:

- the pagetoid pattern represents the most common form (56%), especially in polyostotic fibrous dysplasia, showing mixed density of the thickened external and internal table.
- involvement of the skull base, with preference of the sphenoid bone, often exhibits a sclerotic pattern (23%) with a diffuse, sometimes uniform homogeneous density of the spongy layer ("ground glass pattern") in the enlarged segment, and a wide margin to the unaffected bone.
- the cystic type (21%) is characterized by an expansion of the entire bone, with cortical thinning of the external (rarely the internal) tabula, mostly with a sharp sclerotic border to the unaffected bone (Freyschmidt 1993; Wenig et al. 1998) (Fig. 6.106).

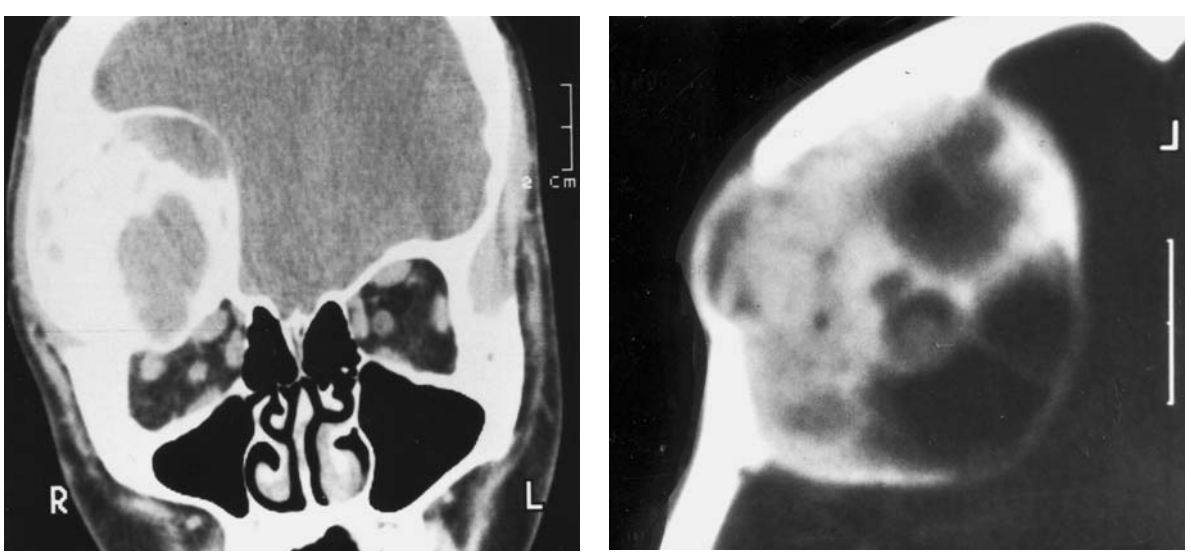

a b

Fig. 6.106a,b. A 14-year-old girl with slowly progressing, right-sided orbital protrusion and inferior dislocation of the globe developing over a period of several years. Diagnosis: aneurysmatic bone cyst associated with fibrous dysplasia (Jaffé–Lichtenstein disease). CT: **a** Coronal view with extracerebral intraosseous lesion of the right frontal bone, expanding to the orbital roof and to the orbit itself; a comparison with the left side confirms caudal dislocation. **b** Axial (sectioned) view in bone window, showing rare configured, chambered, snail-shell-shaped thickening of the diploë of the right frontal bone, consisting of a partly cystic, partly solid portion, causing superficial destruction of the external tabula

Normal segments of cortex between areas of expansion lead to a scalloped pattern, and the absence of sharp margins in focal thinning of bone cortex is characteristic for fibrous dysplasia (Stanton and Montgomery 1996; Jaffe et al. 1997).

MRI patterns of fibrous dysplasia show a nonhomogeneous low signal with a sharp margin on T1-weighted images, while on T2-weighted images areas of various signals represent the protein-rich or true cystic areas of fibrous dysplasia. Signal enhancement after contrast administration may be seen, representing the presence of vessels rather than cellular activity (Casselman et al. 1993).

In the differential diagnosis, the fact that the disease normally stabilizes in early adulthood should be emphasized, as the age of the patient at presentation is an important criterion contributing to an accurate assessment. Although homogeneous sclerosing of the sphenoid bone may suggest fibrous dysplasia, most adults older than 35 or 40 years and new asymmetry of the race and orbit as a rule harbor intraosseous meningioma of the sphenoid (Fig. 6.108, Fig. 7.32).

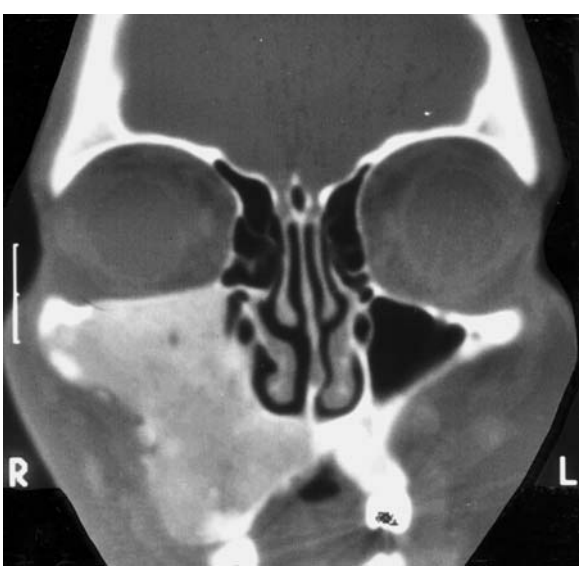

Fig. 6.107. A 15-year-old girl with facial deformation in the absence of visual problems. Diagnosis: fibrous dysplasia (Jaffé–Lichtenstein disease). Coronal CT, showing characteristic sclerosing of the entire maxillary bone, leading to deformation of the right orbital floor

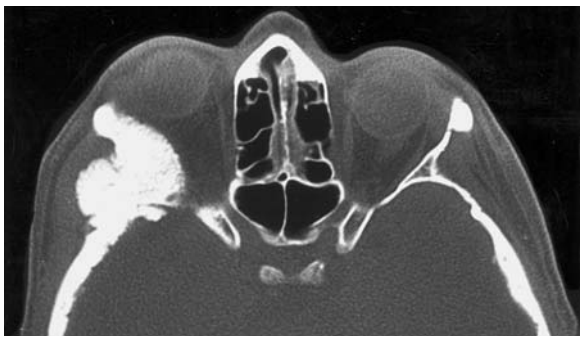

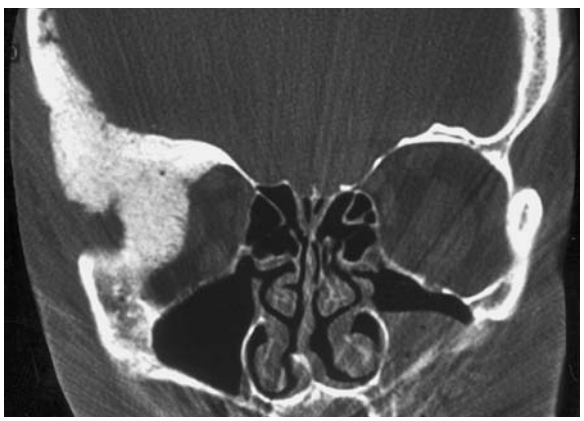

Fig. 6.108a–f. A 50-year-old woman with slowly progressing protrusion of the right eye persisting for the past 3 years, and concomitant nonlocalized headache, but without neurological symptoms. Diagnosis: meningioma of the right sphenoid wing. CT: **a** Axial HR image in bone window at the level of the optic canal. Compared with the left side, the lateral sphenoid wing, the zygomatic bone, and the rostral part of the temporal bone are characterized by irregular sclerosis of the entire bone, including the tabula interna, external, and diploë with exostotic growth into the temporal fossa. **b** Coronal HR-CT with irregular, knotty sclerosis and thickening of the right sphenoid, also invading the frontal and zygomatic bone. **c** Oblique coronal view of a 3D-CT reconstruction. MR: **d** Axial T1-weighted native view (corresponding to **a**). Note thickening of the temporopolar dura (*small arrows*). **e** After i.v. gadolinium, not only the invaded temporopolar dura shows signal enhancement, but some dotted, hazy signals are also seen in parts of the thickened bone. **f** Coronal T1-weighted native image (corresponding to **b**) with superior visualization of the space-occupying effect with compression of the posterior part of the upper orbit, compared to the left side

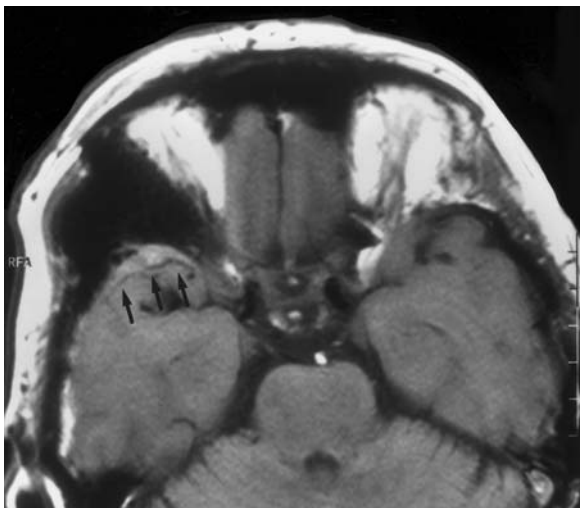

d

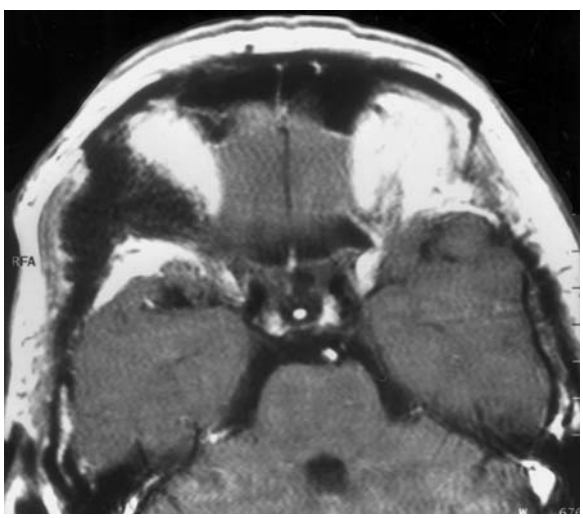

e

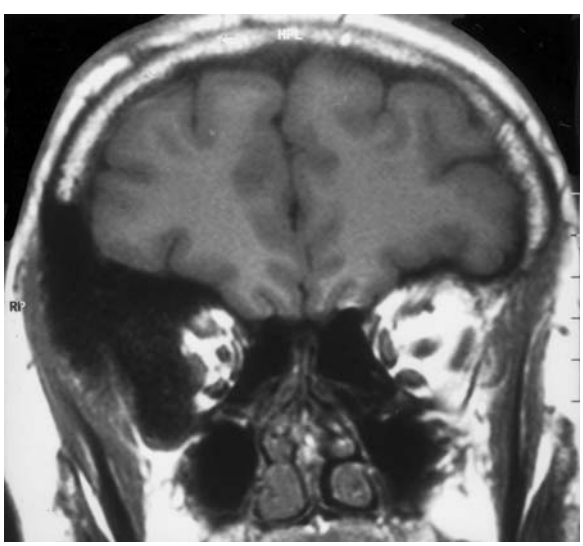

f

6.3.2.2 Ossifying Fibroma

Ossifying fibroma represents the second most common fibro-osseous lesion after fibrous dysplasia. This benign, indolent, fibro-osseous tumor of bone is found in the cranial region and occurs in almost all cases in a monostotic form. Often diagnosed incidentally in an older, predominantly female population, it may also be seen in children, where especially maxillary lesions can be extended, demanding a wide local excision (Marvel et al. 1991). Arising from the mesenchyme of the periodontal ligament, these tumors are composed of highly cellular fibrous stroma and islands of bone (Nemzek et al. 2000). On CT, they present as a large mass of heterogeneous density (Fig. 6.109) and may in some instances have a radiodense rim of different width. On MRI, ossifying fibromas usually show an intermediate signal with moderate contrast enhancement on T1-weighted, and a hypointense signal on T2-weighted images (Wenig et al. 1998).

6.3.2.3 Osteoma

Osteomas are benign, slowly growing tumors with a preference for the craniofacial region, occurring most commonly in the frontal and ethmoidal sinuses (Earwaker 1993). Histologically, osteomas are composed of irregular mature bony lamella and are sometimes rimmed by osteoblasts. Interosseous spaces may be loosely filled with highly vascularized, moderate cellular stroma of fibrous, fibrovascular, or fatty tissue, that may lead to a misinterpretation of a osteosarcoma (Wenig et al. 1998; Lang and Sulzbacher 2001). Osteomas are usually asymptomatic and found incidentally; patients may present with headache, facial deformity, or ocular disturbances. On native X-ray, osteomas are identified as sharply delineated, dense lesions protruding into or developing from a sinus. On CT, the origin of the osteoma is optimally delineated (Fig. 6.110). Additional contrast administration may provide additional information as to whether a secondary pathology, e.g., an additional inflammation (Fig. 6.111), is apparent; on MRI contrast material may define the interosseous tissue (Fig. 6.110).

The differential diagnosis should include not only ossifying fibroma (Fig. 6.109), fibrous dysplasia (Figs. 6.106, 6.107), but also calcified meningioma (Fig. 7.27).

a

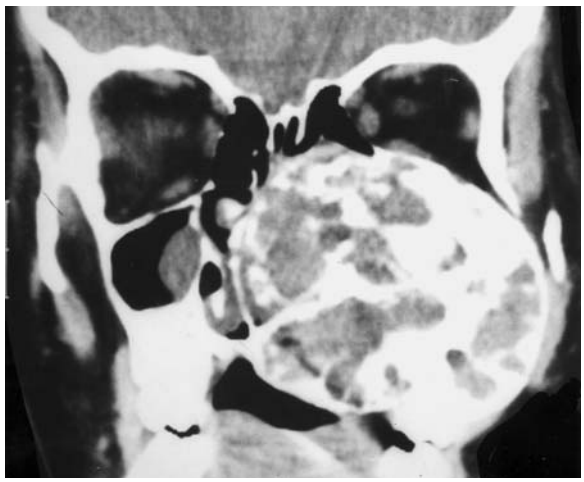

b

Fig. 6.109a,b. A 10-year-old girl with slowly progressing enlargement of the left maxillary region and secondary ptosis of the left eye. Diagnosis: ossifying fibroma of the left maxillary bone. **a** Portrait of the patient. Note narrowing of the palpebral fissure with secondary ptosis of the left eye due to a maxillary mass. **b** Coronal CT, demonstrating a sharply defined, sclerosing mass with osseous trabeculae, occupying and enlarging the entire left upper jawbone. Note the diminution of the left orbit with elevation of the orbital floor, dislocation of the nasal septum to the right, and that no left maxillary sinus nor distinct maxillary structures are seen. (With permission of Rohrbach and Lieb 1998)

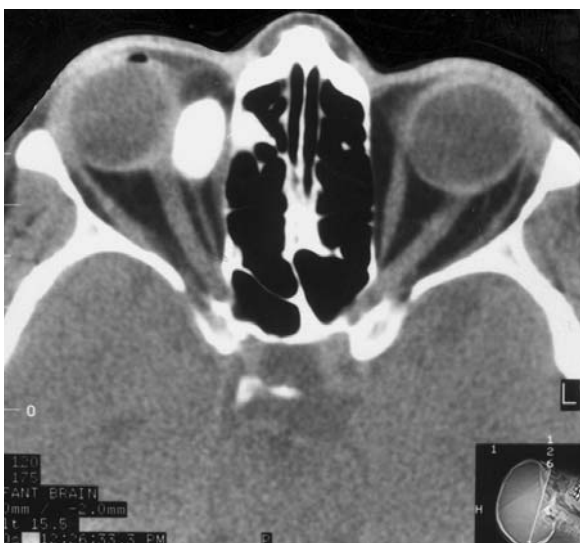

a

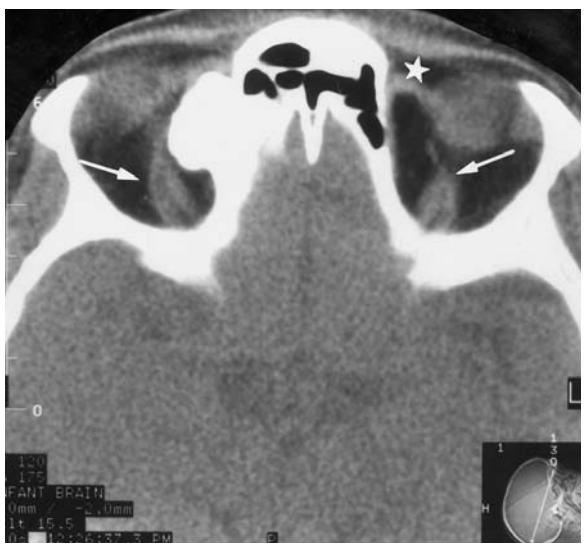

b

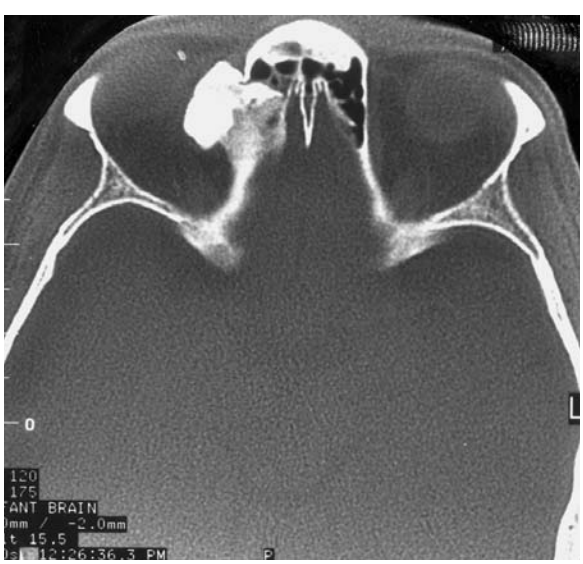

c

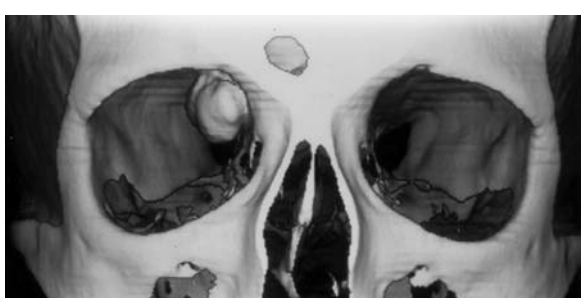

d ▷

Fig. 6.110a–g. A 50-year-old woman with ptosis and protrusion of the right eye. Diagnosis: osteoma of the right ethmoid bone. CT: **a** Axial view at the level of the optic nerves with the inferior section of a 1×1.5 cm large osteoma, causing substantial expansion of the medial rectus muscle medially with slight impression of the globe. **b** Axial view at the level of the superior ophthalmic veins (*white arrows*). In this area of complete and maximum intraorbital extension of the osteoma, the origin of the lesion in the superior ethmoid is identified. Note... ...the

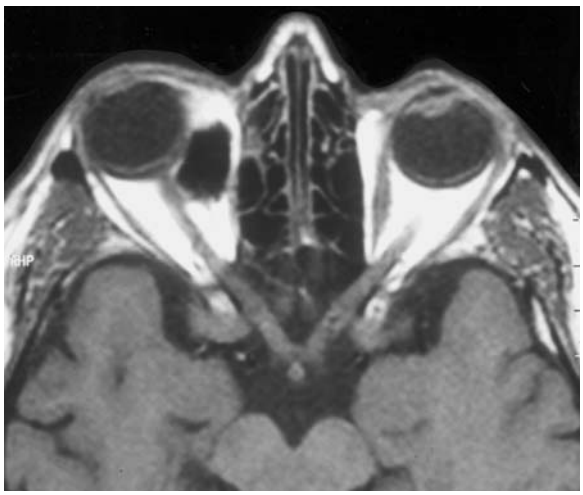

e

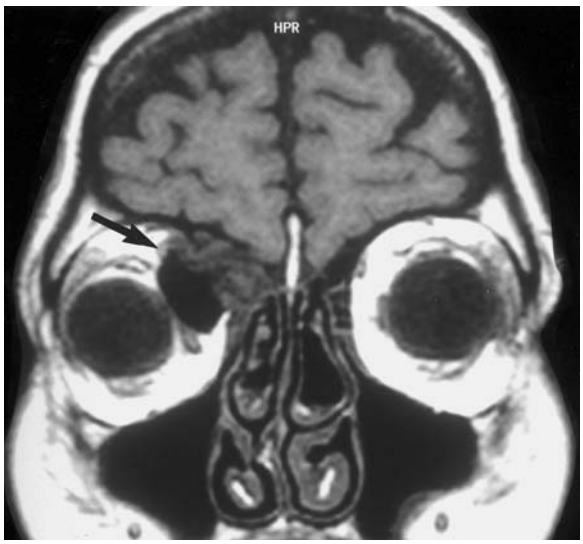

f

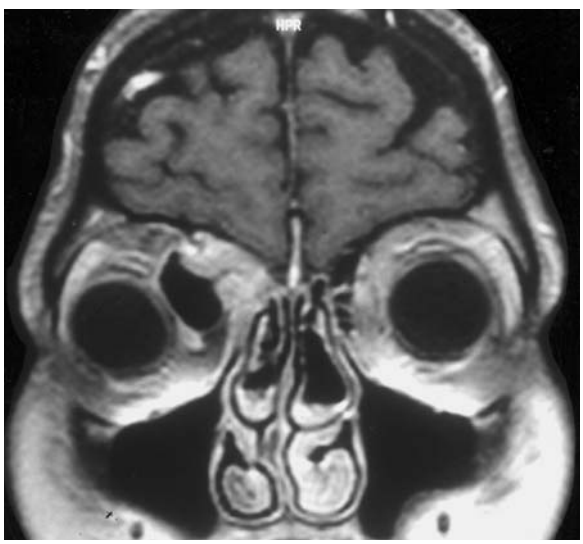

g

trochlea of the left superior oblique muscle (*star*). **c** Corresponding bone window. **d** Coronal 3D-reconstruction with better demonstration of the dimension of the space occupied by this benign bone tumor. MR: **e** Axial T1-weighted view, corresponding to **a**. **f** Coronal T1-weighted view visualizing the expansion of the osteoma between the caudally and medially depressed medial rectus muscle and the superior oblique muscle (*arrow*). **g** Corresponding T1-weighted, contrast-enhanced (FS) view. (**c**, **d** with permission of Müller-Forell 1998)

6.3.3 Inflammatory Lesions

6.3.3.1 Orbital Infections

Orbital complications of paranasal sinusitis are relatively common in children but uncommon in adults. On the basis of clinical and imaging criteria, they are classified as bacterial preseptal cellulitis, subperiostal abscess, orbital abscess, and cavernous sinus thrombosis (Chandler et al. 1970; Hershey and Roth 1997; Eustis et al. 1998).

Preseptal cellulitis, a bacterial inflammation of the skin and the subcutaneous tissue, represents the most common orbital complication of inflammatory paranasal processes, clinically presenting as erythema with severe pain, rarely as lid edema, chemosis, and proptosis, or even limited eye motility. The orbital septum as a reflection of the periorbita at the anterior margins of the orbit provides an effective barrier against intraorbital infection, as does the periorbita at the lamina papyracea (Eustis et al. 1998). This isolated disease normally does not require orbital imaging, but in case of a tentative diagnosis, CT may demonstrate radiographically normal tissue posterior to the orbital septum.

Inflammatory edema, clinically presenting with eyelid swelling and proptosis, is the first manifestation of orbital involvement of paranasal sinusitis, representing postseptal cellulitis, an affection of the proper orbit posterior to the orbital septum. Postcontrast studies demonstrate some enhancement of the extraconal fat adjacent to the involved sinus (Figs. 6.112–6.114). Orbital phlegmon is an advanced

stage of postseptal cellulitis, characterized by soft-tissue infiltration along the orbital wall with replacement of the peripheral fat and subperiosteal space by soft tissue (Figs. 6.115, 6.116) (Eustis et al. 1998).

The formation of a subperiostal abscess is due to the spread of the infection through the congenital dehiscences and foramina of the thin orbital bones as well as (less common) to thrombophlebitic spread (Eustis et al. 1998). In addition to chemosis, marked eyelid swelling and erythema of the lids, limited eye motility, or even visual loss, caused by a rapid increase of intraorbital pressure, may occur (Harris 1994; Eustis et al. 1998). Although some patients respond to conservative medical treatment, surgery is required in the majority of cases to prevent deterioration and visual loss. Imaging is thus required in emergency situations. On contrast-enhanced CT, a sharply defined, extraconal, space-occupying mass with marginal ring enhancement is seen, sometimes displacing the corresponding rectus muscle. The differentiation from spontaneous subperiosteal hematoma, especially in rare cases of chronic sinusitis (Griffeth et al. 1997), might be difficult (Fig. 6.117). On MRI, the subperiosteal abscess is characterized by an intermediate signal on T1-weighted and proton density images that appears hyperintense on T2-weighted images with rim enhancement of the capsule after contrast administration. Intracranial complications as, e.g., epidural or subdural abscesses, purulent meningitis, or cavernous sinus thrombosis, are major complications with a mortality rate of about 21% (Maniglia et al. 1989).

Because of modern antibiotic therapy the development of true orbital abscess secondary to paranasal sinusitis or dental infection is rather uncommon (Eustis et al. 1998).

Cavernous sinus thrombosis results from different causes, i.e., the spread of infection to sinonasal cavities, to the middle third face, or a paraneoplastic disorder (Fig. 6.59) (Dolan and Chowdhury 1995; Berenholz et al. 1998; Eustis et al. 1998). On CT and MRI, these severely ill patients with signs of meningitis and multiple, bilateral cranial nerve palsies present with filling defects in the engorged cavernous sinus combined with enlargement of the superior ophthalmic vein and extraocular muscles (Schuknecht et al. 1998). On MRI, the thrombosis of the superior ophthalmic vein presents as a hyperintense area within the lumen of the vein (Eustis et al. 1998).

Fungal orbital inflammations, caused with great frequency by mucormycosis and *Aspergillus*, are less common than bacterial infections. They are often found in patients with a history of uncontrolled diabetes mellitus, as well as in immunocompromised patients. The role of imaging is its clear demonstration of the relationship between the nasal sinus, orbit, and cranial disease (Eustis et al. 1998). On CT, a nonspecific thickening of the sinus mucosa, at times combined with bony erosion, is seen in mucormycosis infection, which is not always different in appearance from *Aspergillus* sinusitis. A nonspecific, but characteristic finding on T2-weighted MRI is the hypointensity of mycotic infection, and some calcification of the intrasinusoidal mass on CT (Eustis et al. 1998).

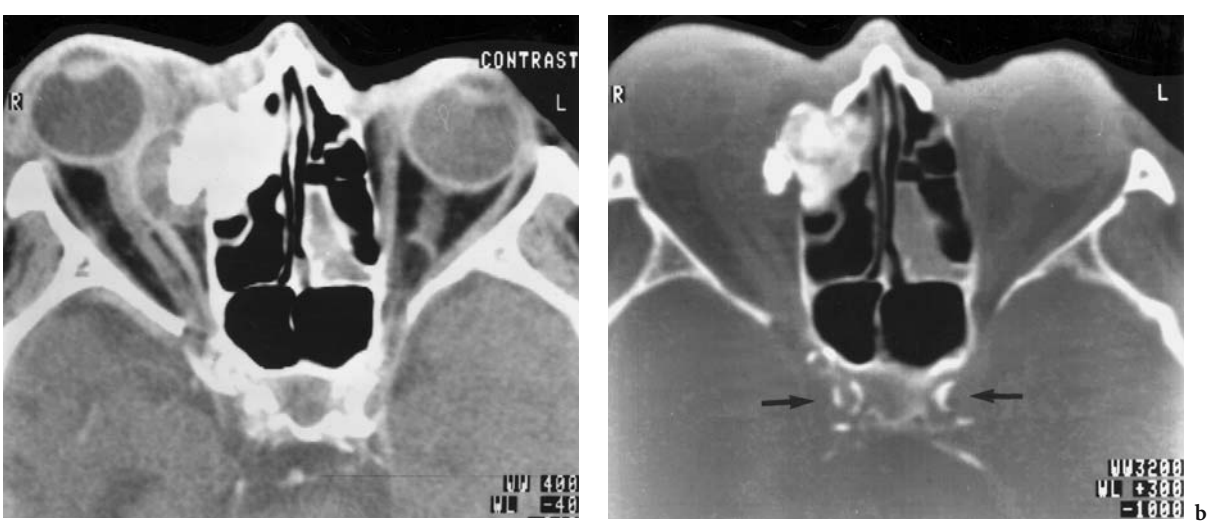

a b

Fig. 6.111a,b. A 73-year-old woman with progressive, painful orbital swelling and rubeosis of the right eye. Diagnosis: super infected osteoma of the lamina papyracea. Axial CT: **a** After i.v. contrast, visualization of a capsulated formation of mixed density originating from the surface of an ethmoid osteoma in the right extraconal space. Inflammation with pre- and postseptal extension, dislocating the medial rectus muscle up to the also dislocated optic nerve, representing the cause of extra-axial proptosis. **b** The bone window demonstrates the mixed density of the intraorbital osteoma of the frontal ethmoid. Note bilateral calcification of the cavernous part of the ICA (*arrows*). (With permission of Müller-Forell and Lieb 1995b)

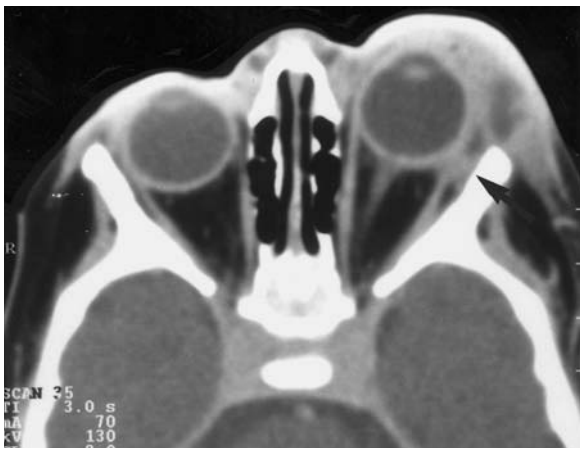

Fig. 6.112. A 9-month-old girl with swollen left lid and febrile state. Diagnosis: lid abscess. Axial contrast-enhanced CT with protrusion of the left globe, inflammatory infiltration of the left lid with necrosis rostral to the zygomatic process, and slight extraconal postseptal infiltration between the lateral orbit wall and the lateral rectus muscle (*arrow*)

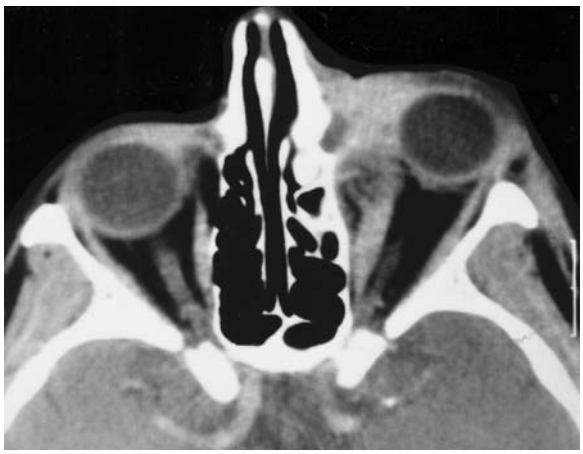

Fig. 6.114. A 60-year-old woman with painful, reddish swelling and proptosis of the left eye after neurosurgical operation for meningioma. Diagnosis: orbital phlegmon. Axial contrast-enhanced CT with irregular, contrast-enhancing, space-occupying lesion, showing both pre- and postseptal expansion as well as infiltration of the orbital fat and the medial rectus muscle. (With permission of Müller-Forell and Lieb 1995b)

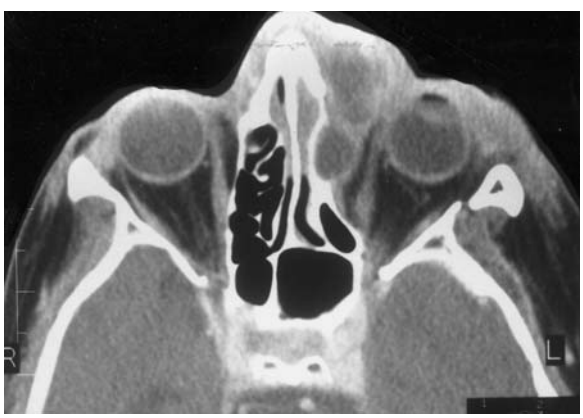

a

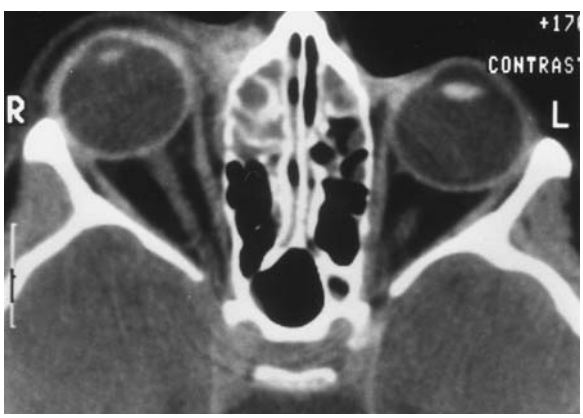

a

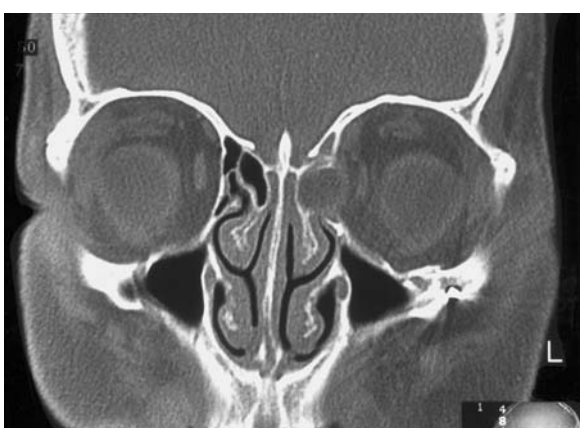

b

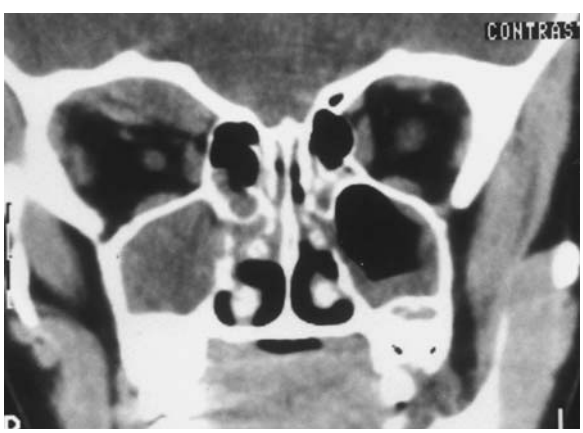

b

Fig. 6.113a,b. A 40-year-old man with reddish, swollen left lid and decreased motility of the left globe; state after an accident with orbital floor fracture 5 years previously. Diagnosis: ethmoid pyocele, cause of orbital phlegmon. CT: **a** Axial contrast-enhanced view with dilated, infected, medial ethmoid cell and preseptal subcutaneous infection of the medial orbital region. Note the presence of dehiscence from the left zygomatic bone and from the zygomatic process of the left temporal bone, representing a sequel of the accident. **b** Coronal view in bone window where the metallic artifacts after surgical therapy of the orbital floor fracture and the secondary low level of the left orbital floor are visualized

Fig. 6.115a,b. A 13-year-old girl with acute purulent pansinusitis and acute exophthalmos of the right eye. Diagnosis: subperiosteal abscess. CT: **a** Axial contrast-enhanced image with bilateral purulent ethmoidal cell infiltration and extraconal, pre- and postseptal abscess of the right orbit. **b** Coronal contrast-enhanced view, demonstrating an additional, sharply demarcated, subperiosteal formation, causing dislocation of the muscle cone

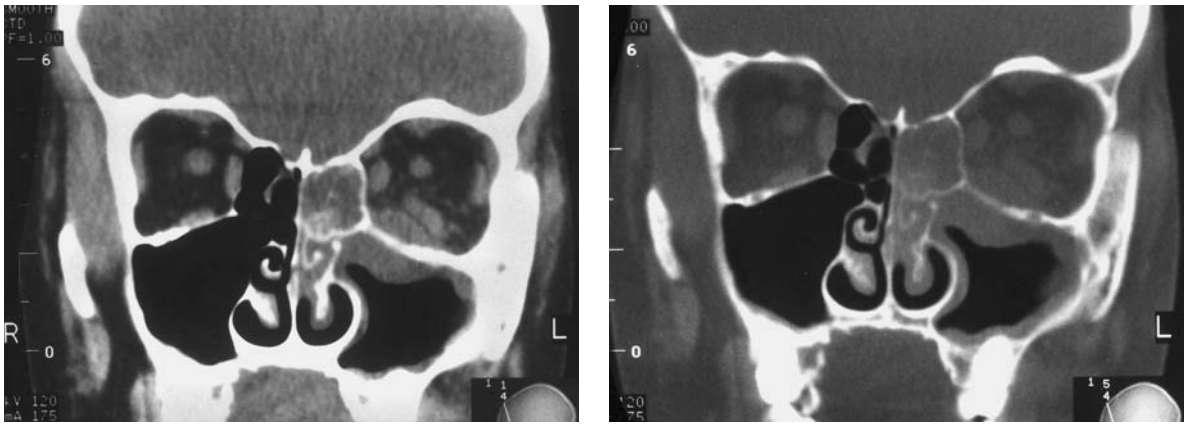

Fig. 6.116a,b. A 10-year-old girl with pansinusitis and reddish swelling of the left cheek, showing a hypomobility of the left eye and fever. Diagnosis: orbital complication of phlegmonous ethmoidal sinusitis. CT: **a** Coronal view showing subperiostal extension of the process and bone destruction to the left inferior orbit. **b** Corresponding bone window

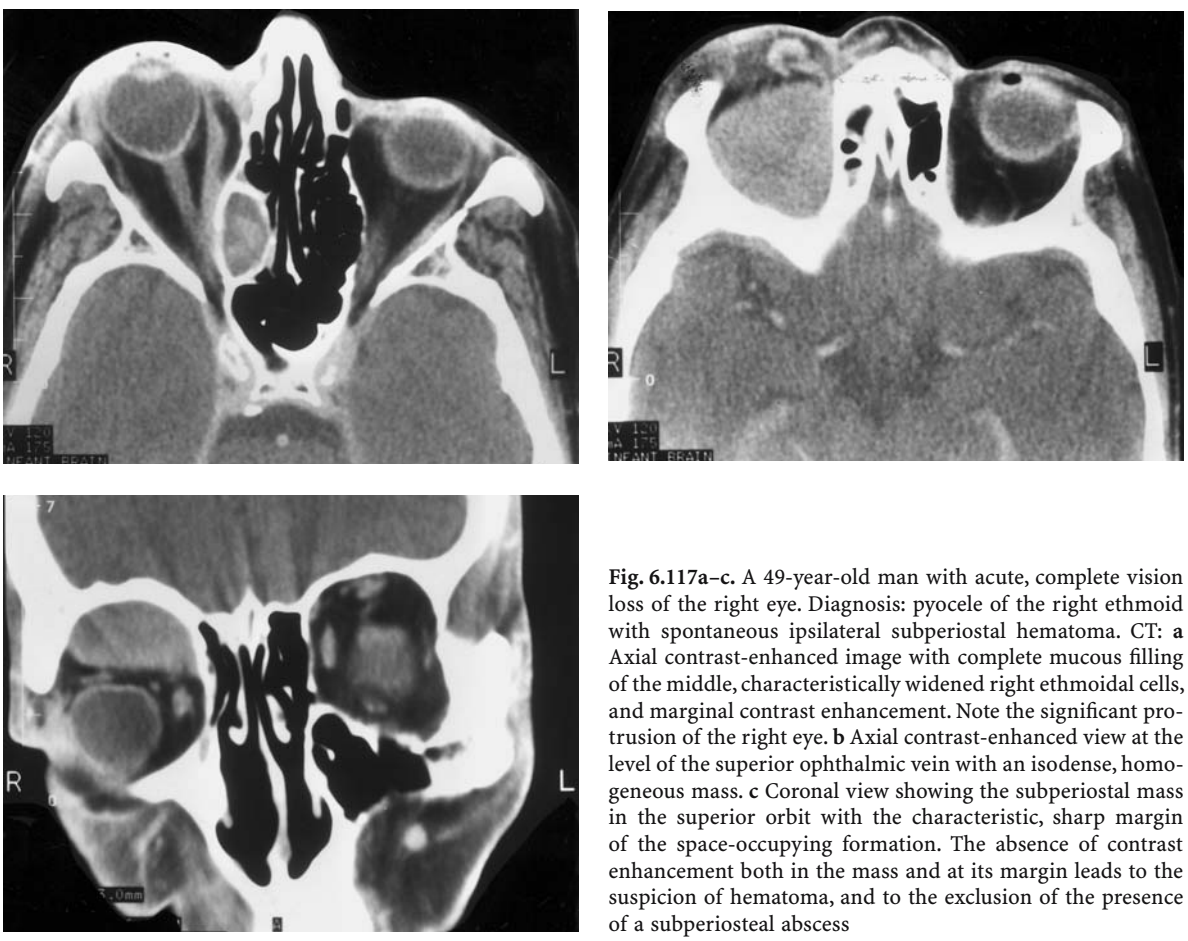

Fig. 6.117a–c. A 49-year-old man with acute, complete vision loss of the right eye. Diagnosis: pyocele of the right ethmoid with spontaneous ipsilateral subperiostal hematoma. CT: **a** Axial contrast-enhanced image with complete mucous filling of the middle, characteristically widened right ethmoidal cells, and marginal contrast enhancement. Note the significant protrusion of the right eye. **b** Axial contrast-enhanced view at the level of the superior ophthalmic vein with an isodense, homogeneous mass. **c** Coronal view showing the subperiostal mass in the superior orbit with the characteristic, sharp margin of the space-occupying formation. The absence of contrast enhancement both in the mass and at its margin leads to the suspicion of hematoma, and to the exclusion of the presence of a subperiosteal abscess

6.3.3.2
Abscess Secondary to Ethmoid/Sphenoid Sinusitis, Mucocele/Pyocele

An involvement of the extraconal space or the face in inflammatory disease of the paranasal sinuses is most commonly caused by mucoceles (Figs. 6.118, 6.119). Mucoceles contain a mucous sac lined by mucous membrane and most commonly result from inflammatory obstruction of the ostium of the affected sinus (primary mucocele). Secondary mucoceles are posttraumatic, postoperative, or are seen in neoplastic

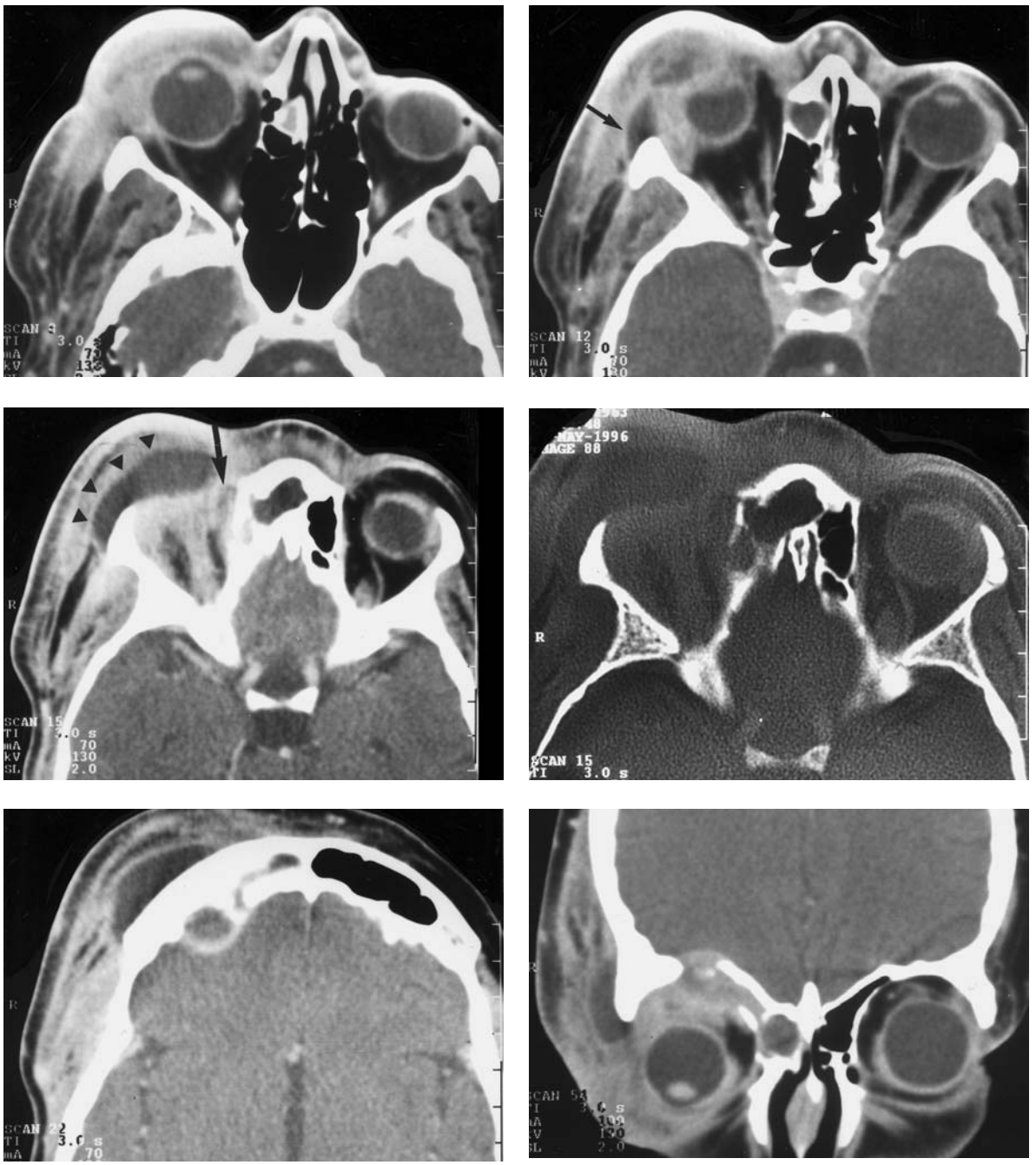

Fig. 6.118a–f. A 21-year-old woman with headache persisting for 2 weeks and swelling of right cheek and face, including the right eye; a physician was consulted for her continuous febrile state. Diagnosis: phlegmon of the right face with intracranial extension, caused by ethmoidal pyocele. CT: **a** Axial contrast-enhanced image of the inferior orbit with inferior globe dislocation and preseptal inflammation, expanding subcutaneously to the temporal fossa. Note that the paranasal sinuses are normal despite the presence of a small, ipsilateral, paramedial ethmoidal cell. **b** Axial contrast-enhanced view at the level of the optic nerve showing infiltration of the lacrimal gland, as well as a small subcutaneous necrotic area rostral to the zygomatic process (*small arrow*). Note widening of the paramedial ethmoidal cell with apparent necrotic content and destruction of the corresponding lamina papyracea. **c** Axial contrast-enhanced view at the level of the superior ophthalmic vein, identifying the largest necrotic area (*triangles*). Slight postseptal infiltration of the medial orbit is detectable in the region of the superior ethmoidal cells (*arrow*) and is characterized by an irregular formation. **d** Corresponding bone window demonstrating erosion and destruction of the ethmoidal cell septa, the apparent origin of the inflammatory process. **e** Axial contrast-enhanced view at the level of the frontal brain parenchyma reveals necrotic subgaleal swelling, intracranial, extradural inflammatory infiltration and inflammatory destruction of the frontal posterior sinus wall. **f** Coronal view demonstrating the pathological changes consisting of ethmoidal pyocele as the apparent origin, the extent of the inferior and rostral globe dislocation, the extent of the soft-tissue infiltration, the destruction of the frontal base, and the intracranial extradural extension

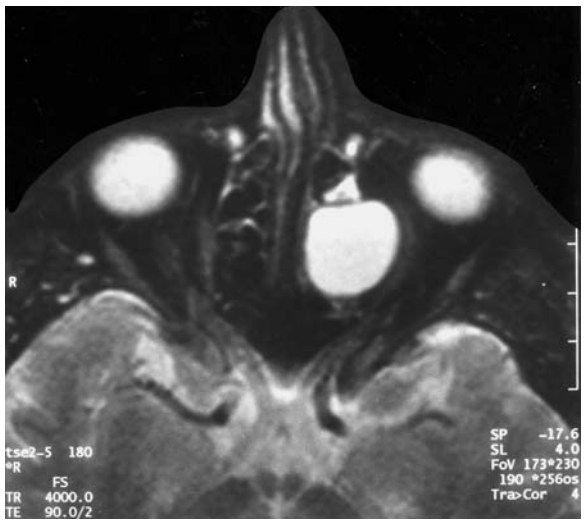

a

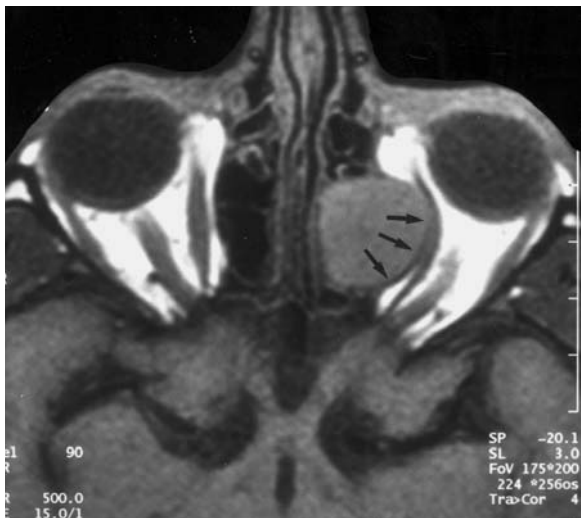

b

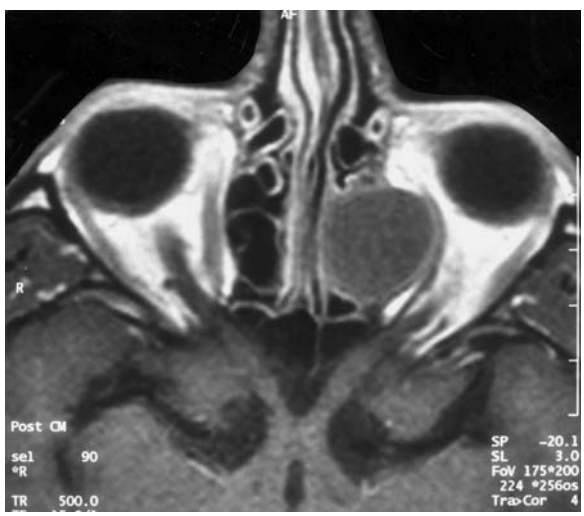

c

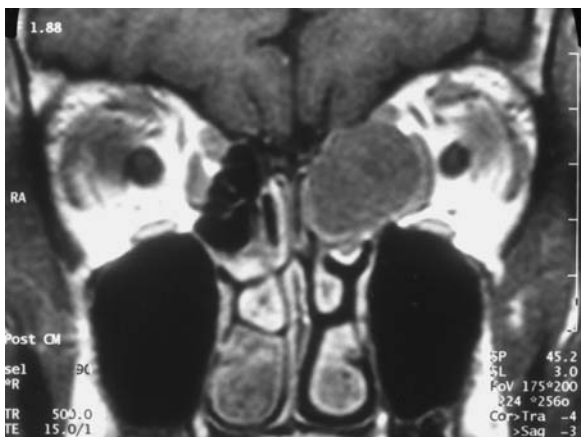

d

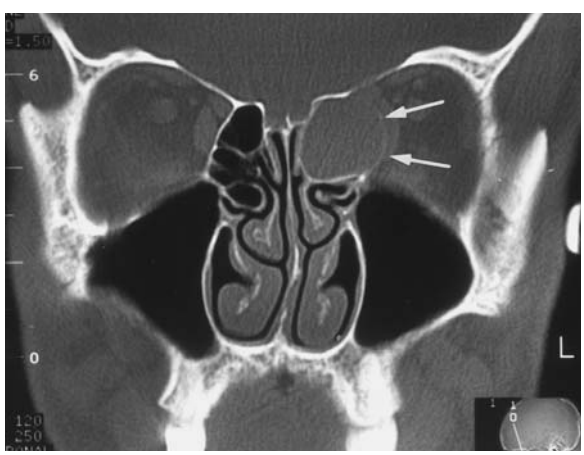

e

Fig. 6.119a–e. A 25-year-old man, presenting with unspecified pressure of the left orbit persisting for several months and a recent onset of double vision. Diagnosis: mucocele of the left ethmoid. MR: **a** Axial T2-weighted view with a hyperintense, well-delineated, cystic structure of the left middle ethmoid region. **b** Corresponding T1-weighted native image, demonstrating pressure exerted on the periorbit and an attenuated, impressed, and dislocated medial rectus muscle. Note the hypointense line of the bony cortex and periorbit (*small arrows*) medial to the extraconal orbital fat. **c** Corresponding T1-weighted, contrast-enhanced view with better visualization of the cystic structure. **d** Coronal, T1-weighted, contrast-enhanced view with intraorbital expansion and flattening of the medial rectus muscle. **e** Corresponding coronal CT with characteristic biconvex configuration of the ethmoid cell and thinned bony cortex (*small white arrows*)

disorders of the nasal sinuses. In case of superinfection, the described mucous retention is referred to as pyocele (Figs. 6.118, 6.120, 6.121) and presents as a marginal enhancement after contrast application (Harnsberger 1990). On CT, mucocele is defined as a hypointense, expanding mass, originating from a paranasal sinus (most frequently in the fronto-ethmoidal sinuses), characterized by a crescent-shaped, sharp, and thinned remodeling of the bony wall (Figs. 6.119, 6.122) (Harnsberger 1990; Friedman et al. 1993). Subperiosteal spread of superinfected sinusoidal mucous is a rare complication of paranasal pathology (Fig. 6.123). On MRI, mucocele may appear in differ-

(Text continues on p. 262)

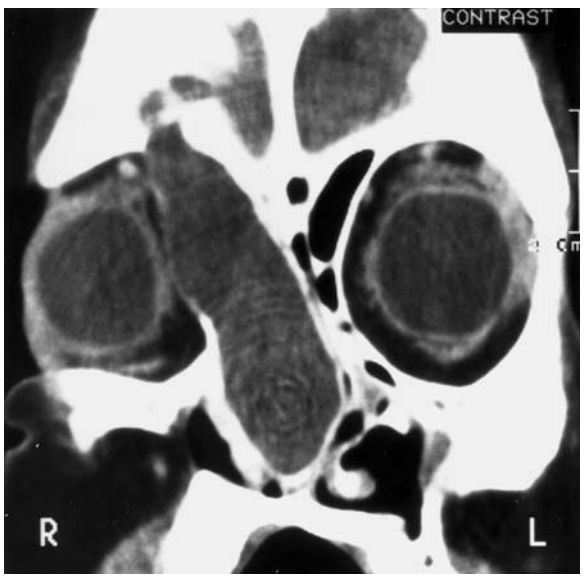

Fig. 6.120. A 61-year-old woman with febrile state and history of a head injury with frontal sinus involvement. Diagnosis: pyocele. Coronal contrast-enhanced CT: dislocation of orbital structures including the right globe by a very large cele of the supraorbital recess of the right frontal sinus, showing contrast enhancement at the margin, and occupying the entire nasal volume

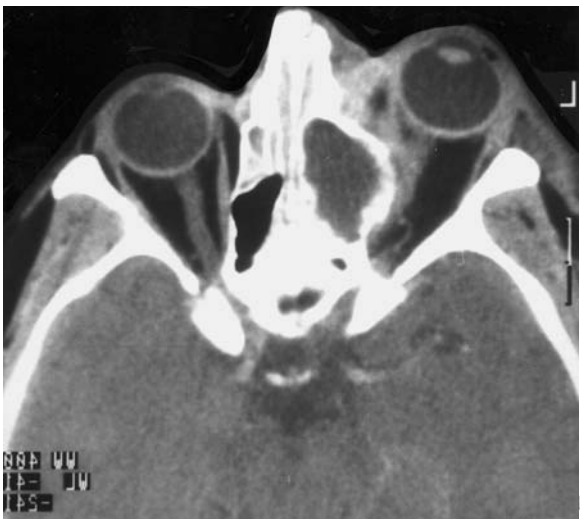

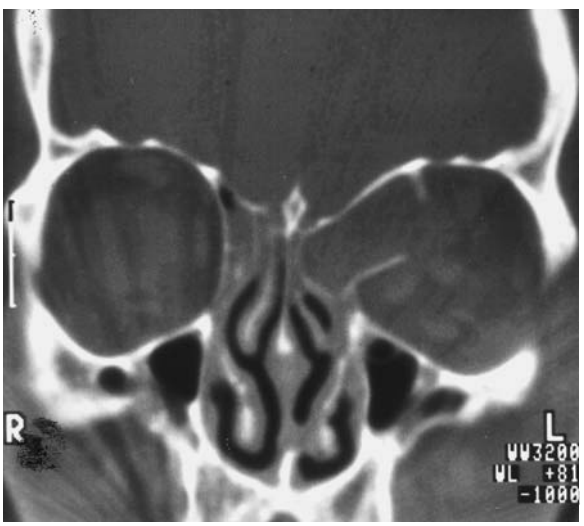

Fig. 6.121a,b. A 55-year-old man with subfebrile state and a prominent left orbital protrusion. Diagnosis: orbital complication due to pyocele of the ethmoid cells. Contrast-enhanced CT: **a** Axial view with intraorbital extension of the ethmoidal cell enlargement. Note marginal contrast enhancement and an intraorbital, postseptal formation, indicating intraorbital involvement of the inflammatory process. **b** Coronal bone window with a defect in the lateral wall of the enlarged, infected ethmoidal mucocele

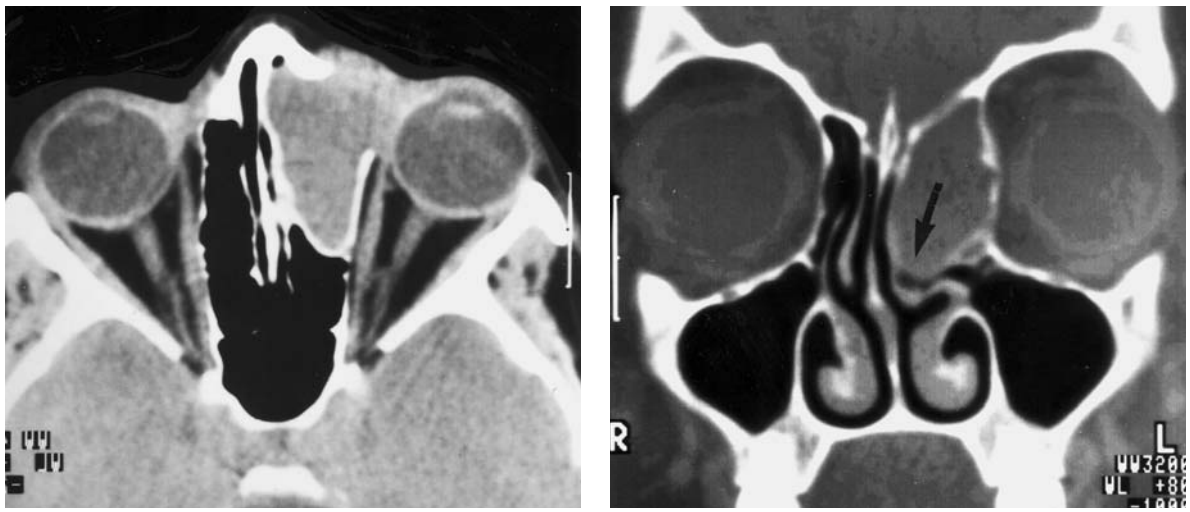

Fig. 6.122a,b. A 12-year-old girl with extra-axial proptosis of the left eye. Diagnosis: mucocele of the left frontal ethmoid. CT: **a** Axial view with homogeneous formation, arising from the medial ethmoidal cells and lateral expansion, and extending to the preseptal extraconal orbit. Note thickening of the left medial orbital wall as a sign of a chronic inflammatory process. **b** Coronal view (bone window) demonstrating characteristic crescent-shaped thinning of the bone (arrow), resulting from the slowly expanding, tumor-like growth of the secretory retention. Note the secondary dilation of the infundibulum of the left maxillary sinus and chronic inflammation of the left lamina papyracea. (With permission of Müller-Forell and Lieb 1995b)

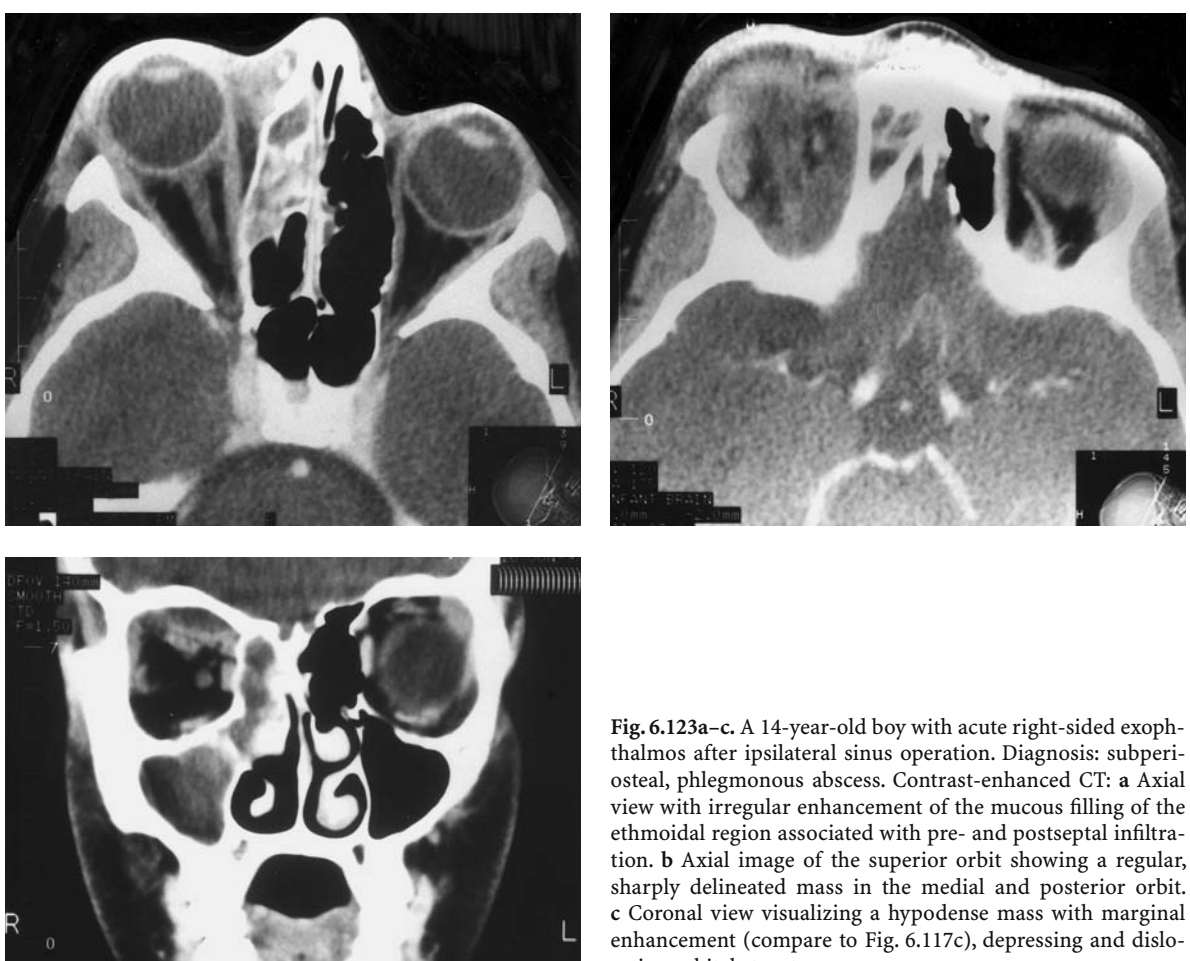

Fig. 6.123a–c. A 14-year-old boy with acute right-sided exophthalmos after ipsilateral sinus operation. Diagnosis: subperiosteal, phlegmonous abscess. Contrast-enhanced CT: **a** Axial view with irregular enhancement of the mucous filling of the ethmoidal region associated with pre- and postseptal infiltration. **b** Axial image of the superior orbit showing a regular, sharply delineated mass in the medial and posterior orbit. **c** Coronal view visualizing a hypodense mass with marginal enhancement (compare to Fig. 6.117c), depressing and dislocating orbital structures

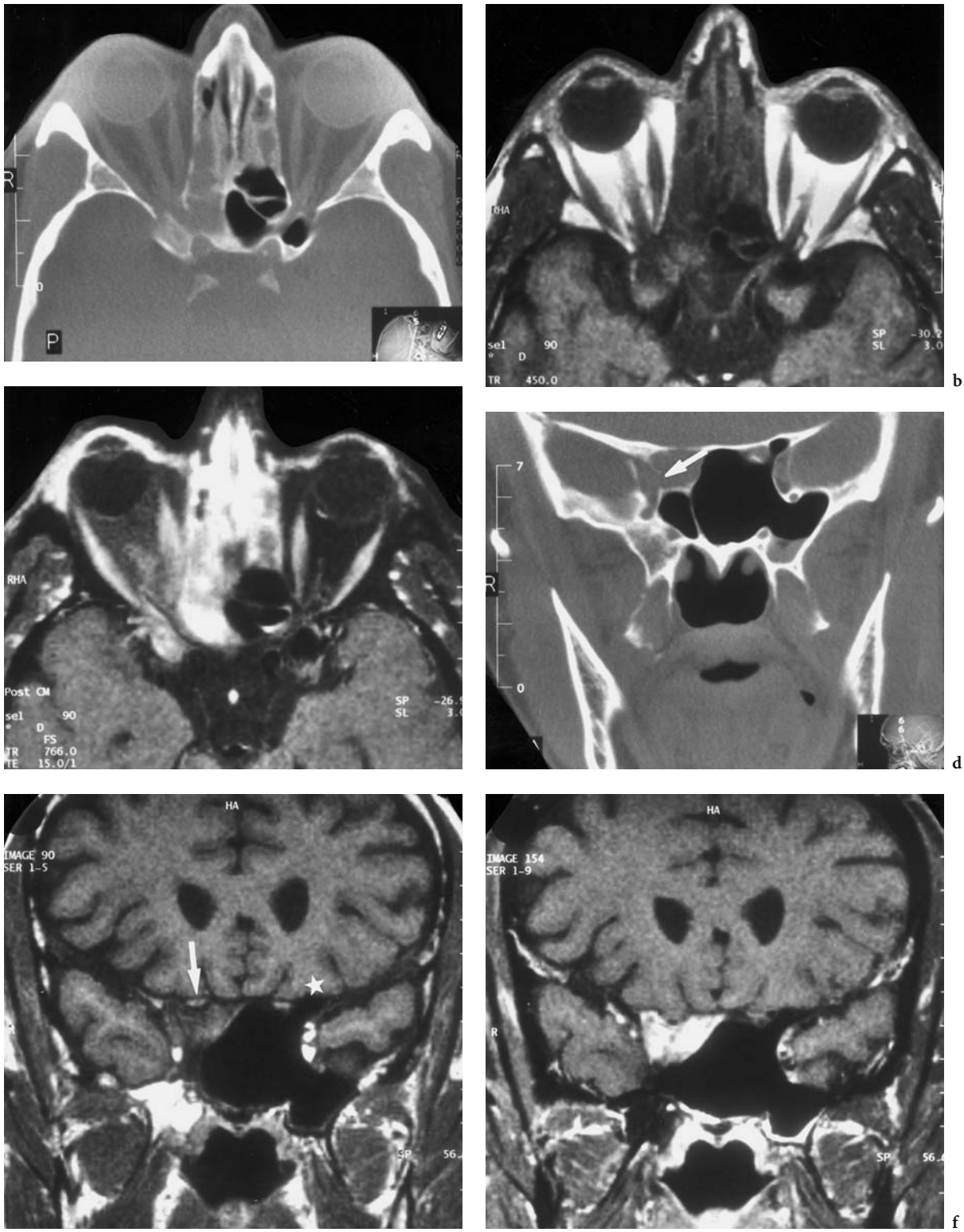

Fig. 6.124a–f. A 55-year-old man with diplopia of the right eye, N IV and N VI paresis, and a history of recently ethmoidal cell operation, in the absence of visual problems. Diagnosis: secondary orbital apex inflammation of an ethmoidal mucocele. **a** Axial CT in bone window of the orbital apex and optic canal, showing the irregular destruction of the medial wall of the right optic canal, originating from the ipsilateral, shadowed sphenoid sinus. **b** Corresponding T1-weighted native MRI. **c** Corresponding T1-weighted, contrast-enhanced (FS) view, showing signal enhancement of the intrasphenoidal mass. **d** Coronal CT showing the destruction of the medial wall of the superior orbital fissure (*white arrow*). **e** Corresponding T1-weighted native MRI with an isointense mass in the right lateral sphenoid sinus, inferior to the right optic nerve located in the nerve canal (*white arrow*). As a symmetric pneumatization might be expected of the right anterior clinoid process as compared with the left (*white star*), involvement of the described part of the sphenoid sinus is apparent (compare with **d**). **f** Corresponding T1-weighted, contrast-enhanced (FS) view

ent ways, depending on the extent of hydration of the sinus secretions. In the presence of high serous fluid (free water) content, the sinus appears hypointense on T1-weighted and hyperintense on T2-weighted images (Fig. 6.119). At increasing dehydration, hyperintense signals may be seen on both T1-weighted and T2-weighted images. When the secretions become inspissated, the signal intensities may decrease in both weightings, simulating a normal air content of the sinus. In order to avoid false-negative findings, CT should therefore be the method of choice in clinically suspected mucocele (Harnsberger 1990; Hasso and Lambert 1994).

The definition of postoperative complication after sinonasal surgery may sometimes be challenging for both surgeons and neuroradiologists. A subperiosteal abscess represents a rare complication of sinonasal pathology (Fig. 6.123), as well as a secondary infection with development of an orbital apex syndrome with cranial nerve palsies (Fig. 6.124).

6.3.3.3 Miscellaneous (Subperiosteal Hematoma, Osteomyelitis, Cholesterol Granuloma)

Postoperative subperiosteal hematoma is a rare, but severe complication after sinonasal operation (Fig. 6.125), demanding surgical decompression in emergencies. In contrast to a diffuse retrobulbar hematoma, the sudden onset of subperiosteal hematoma and its substantial mass can lead to complete vision loss.

Cranial osteomyelitis, primarily arising from complications of paranasal sinus infections and often resistant to medical therapy, represents a somewhat rare disorder, especially when a hematogenous etiology is suspected (Fig. 6.126). CT and MRI provide a precise delineation of soft and bony tissue, especially in combination with bone SPECT, a sensitive technique for the detection of osteomyelitis of the skull in patients without prior surgery (Seabold et al. 1995).

The differential diagnosis should take into consideration other rare lesions as, e.g., cholesterol granuloma (Kuroiwa et al. 2000). Although able to cause bone destruction, these nevertheless benign lesions with a strong male preponderance occur at a characteristic site immediately adjacent to the lacrimal fossa (Fig. 6.127) (Hill and Mosely 1992). Especially in nonpneumatized bone, the underlying pathology is thought to be posttraumatic, postsurgical, or postinflammatory, even in the absence of a history of trauma (Dobben et al. 1998).

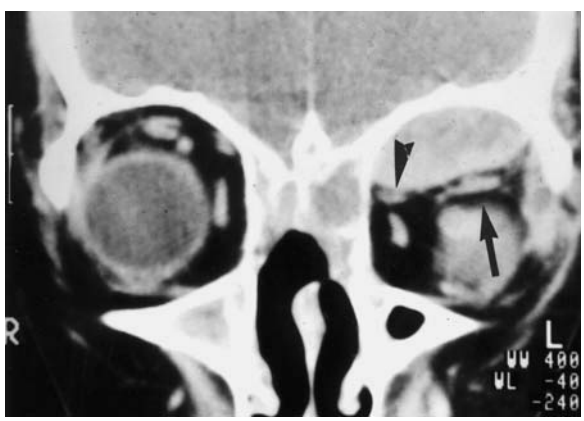

Fig. 6.125. A 35-year-old woman with acute exophthalmos developing a few hours after a nasal sinus operation. Diagnosis: subperiosteal hematoma. Coronal CT: sharply defined, biconvex, homogeneous, hyperdense, space-occupying lesion at the orbital roof with caudal dislocation and flattening of the superior rectus (*arrow*) and superior oblique (*arrowhead*) muscle, completely shaded ethmoidal cells. (With permission of Müller-Forell and Lieb 1995b)

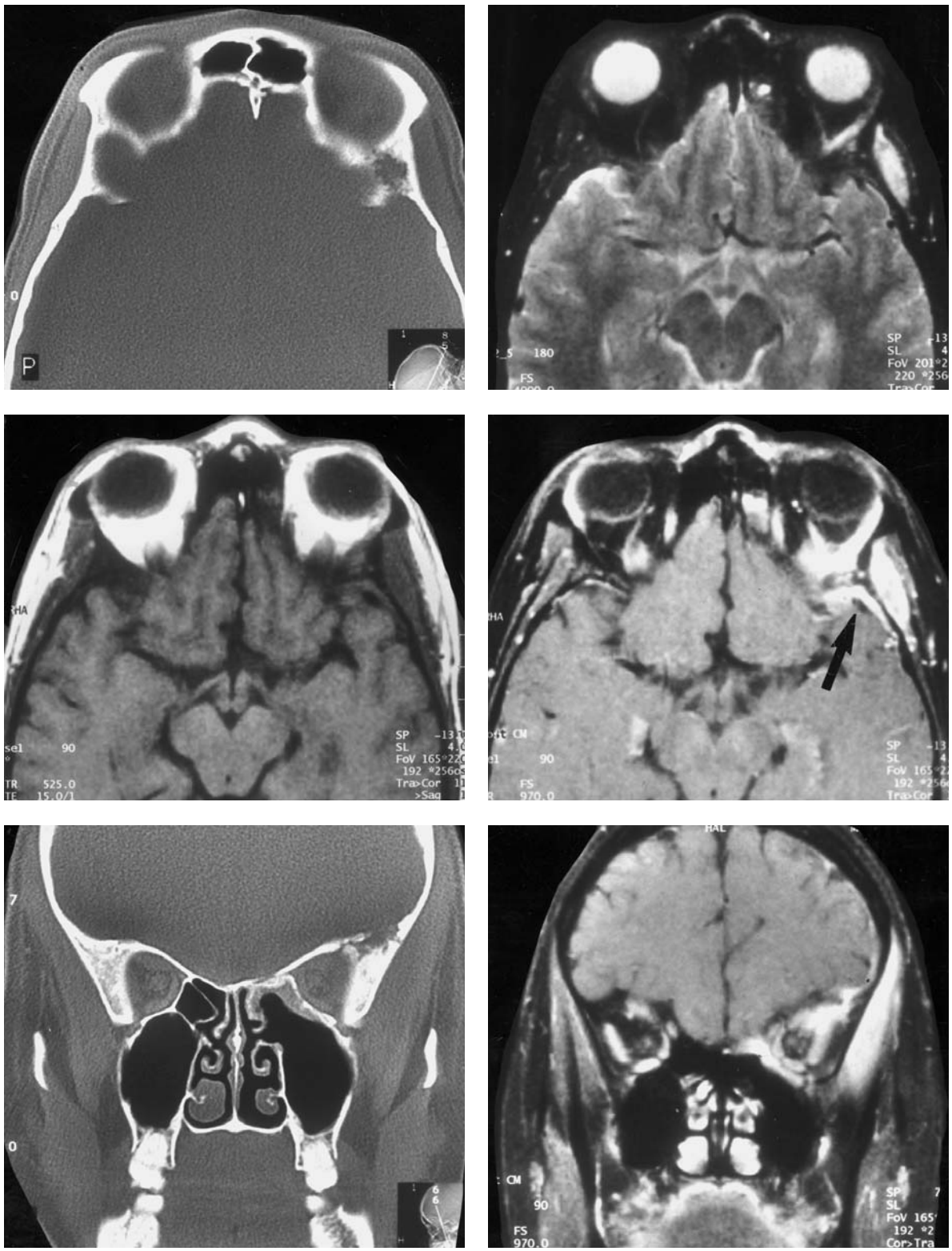

Fig. 6.126a–f. A 19-year-old woman with recurrent, generally painful proptosis, swollen upper lid, and chemosis of the left eye of still unknown etiology. Diagnosis: osteomyelitis of the left upper lateral orbital wall, involving the sphenoid and frontal bone and soft tissue of the upper orbit. **a** Axial CT (bone window) of the cranial orbital region with irregular destruction of the frontotemporal bone. **b** Corresponding T2-weighted MRI with hyperintense infiltration of the temporal muscle and the upper periorbital region of the left eye. **c** Corresponding T1-weighted native view. **d** Corresponding T1-weighted, contrast-enhanced (FS) view with bright enhancement of the involved tissue and the temporopolar dura (*arrow*). **e** Coronal CT (bone window) demonstrating apparent inflammatory infiltration. **f** Corresponding T1-weighted, contrast-enhanced (FS) MRI

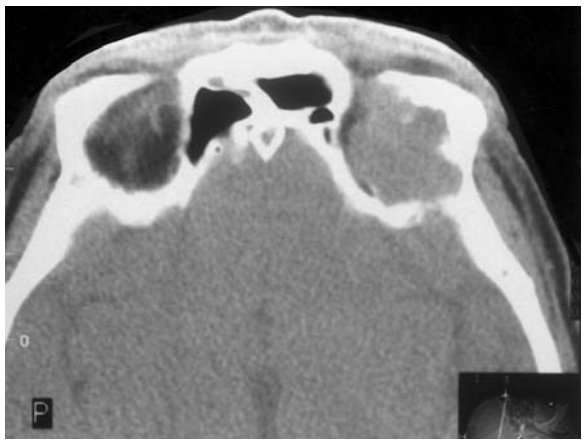

a

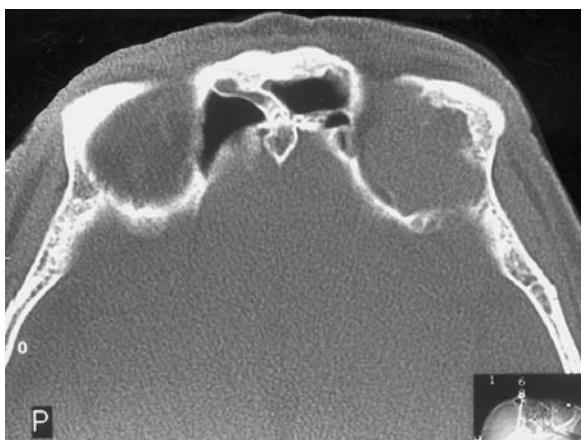

b

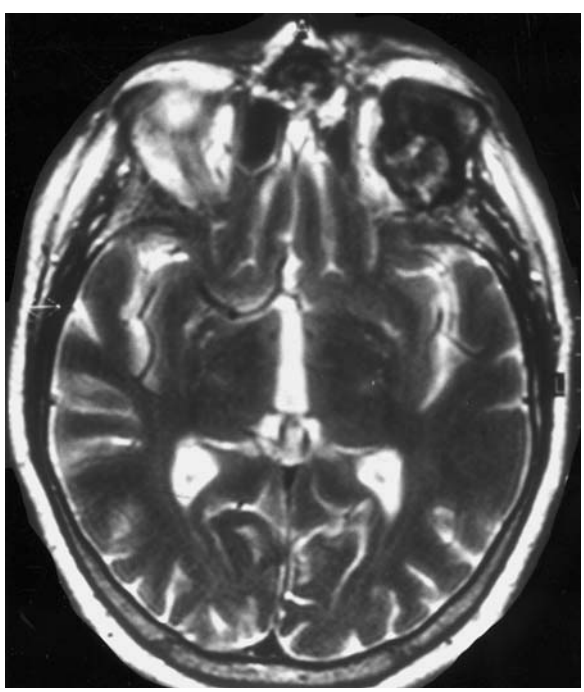

c

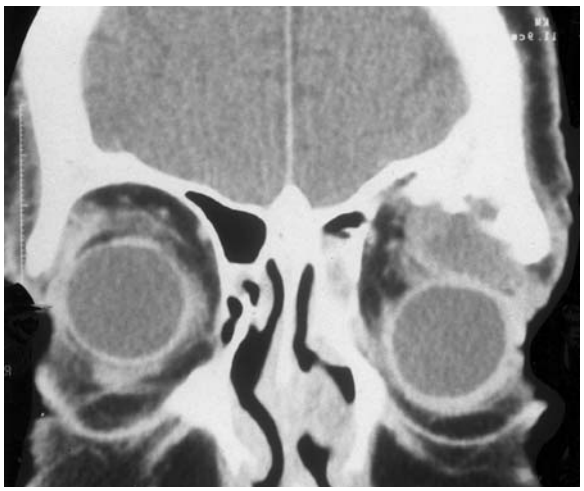

d

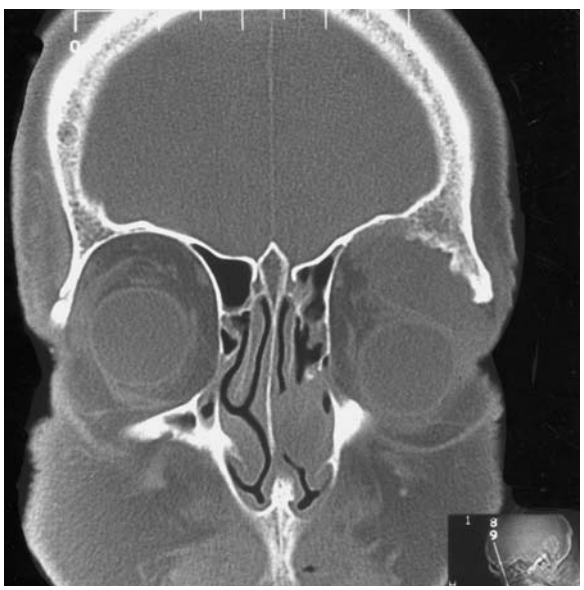

e

Fig. 6.127a–g. A 68-year-old man with slowly progressing extra-axial proptosis and dislocation of the lower left eye. Diagnosis: cholesterol granuloma. **a** Axial CT demonstrating a mass in the lateral upper orbit with destruction of the frontal and zygomatic bones. **b** Corresponding bone window where the sclerosing character of the destruction indicates a benign lesion. **c** Corresponding T2-weighted MRI, showing the low to intermediate signal of the intraosseous lesion. **d** Coronal CT demonstrating the extra-axial dislocation of the left globe. **e** Corresponding bone window. **f** Coronal T1-weighted MRI perpendicular to the axis of the left optic nerve, identifying the intraosseous extraconal location of the granuloma. Histology (×280): **g** many whetstone-shaped (hone-shaped) crystals are surrounded by a dense granulation tissue with multinucleated giant cells (foreign body cells) in close vicinity to the crystals. (MR images with permission of APP-Gem Neustadt, histology with permission of Dr. Bohl, Department of Neuropathology, Medical School, Mainz)

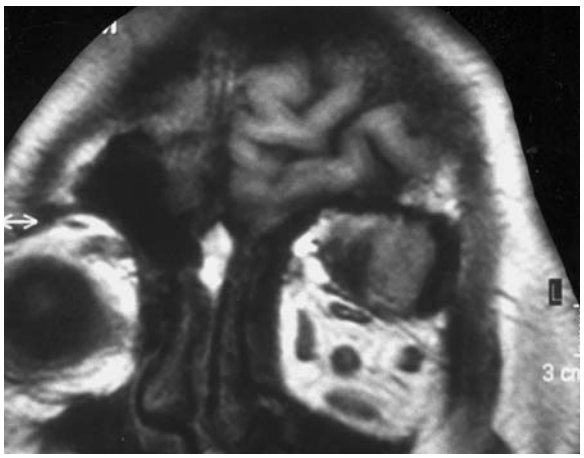

f

g

Fig. 6.127f,g

6.3.4 Lacrimal Gland

The spectrum of lacrimal gland pathology represents a challenge, because it poses special problems for the differential diagnosis and management, due to the superolateral, extraconal, intraorbital location of the gland and the respective surrounding structures. Lacrimal gland lesions, mainly presenting as an unspecific enlargement of the gland, can be classified both as epithelial and nonepithelial lesions, the former including largely neoplastic disorders, while the latter consist mostly of congenital, inflammatory, but also neoplastic conditions (Mafee et al. 1999b).

6.3.4.1 Congenital Lesions (Dermoid Cysts)

Dermoid cysts arise from epithelial remnants in embryonal epithelial tissue. They exhibit a tendency to develop along the bony structures of the orbit, especially along the suture. Their incidence varies depending on the definition, but they account for about one-quarter of all orbital biopsies. Superficial dermoid cysts occur primarily in the lateral aspects of the brow (Fig. 6.128) or the medial upper eyelid and are manifest already within the 1st year of life (Fig. 6.129). However, removal can be delayed unless the lesion is growing rapidly or causing recurrent bouts of inflammation. Dermoid cysts must be distinguished from deep orbital dermoids, which constitute 4%–6% of orbital tumors (Mortada 1971; Pear 1970; Pollard and Calhoun 1975; Reim et al. 1975; Hurwitz et al. 1982; Shields et al. 1986; Smirniotopoulos and Chiechi 1995).

Macroscopically, orbital dermoids are round to oval-shaped, encapsulated tumors, filled with various skin appendices and fatty material. Histologically, the typical dermoid is outlined by a keratinizing squamous epithelium with dermal appendices such as hair follicles and sebaceous glands (Dithmar et al. 1993).

In addition to the clinical examination, which is sufficient for most superficial orbital dermoids, ultrasound A- and B-scans are helpful, because these demonstrate a sharply outlined lesion with a capsule and low reflective contents, thus making CT or MRI rarely necessary (Ossoinig 1975; Rochels et al. 1986).

CT reveals a sharply delineated, cystic tumor of low, sometimes negative density, due to the presence of fatty components (Figs. 6.128, 6.129). Contrast enhancement may be seen in the capsule, and calcifications are occasionally detected and may be helpful in the differentiation from mucoceles. Shallow impression of the bone is a common feature (Fig. 6.128). In some (rare) cases, a bony defect along the frontozygomatic suture may cause a so-called dumbbell-shaped orbital dermoid with a small portion extending into the fossa temporalis (Wackenheim et al. 1977; Wende et al. 1977; Tadmor and New 1978; Grove 1979; Zilkha 1982; Samuelson et al. 1988; Sathananthan et al. 1993).

MRI demonstrates dermoids and epidermoids as sharply outlined lesions with a hypointense signal similar to the signal in the presence of water on T1-

(Text continues on p. 268)

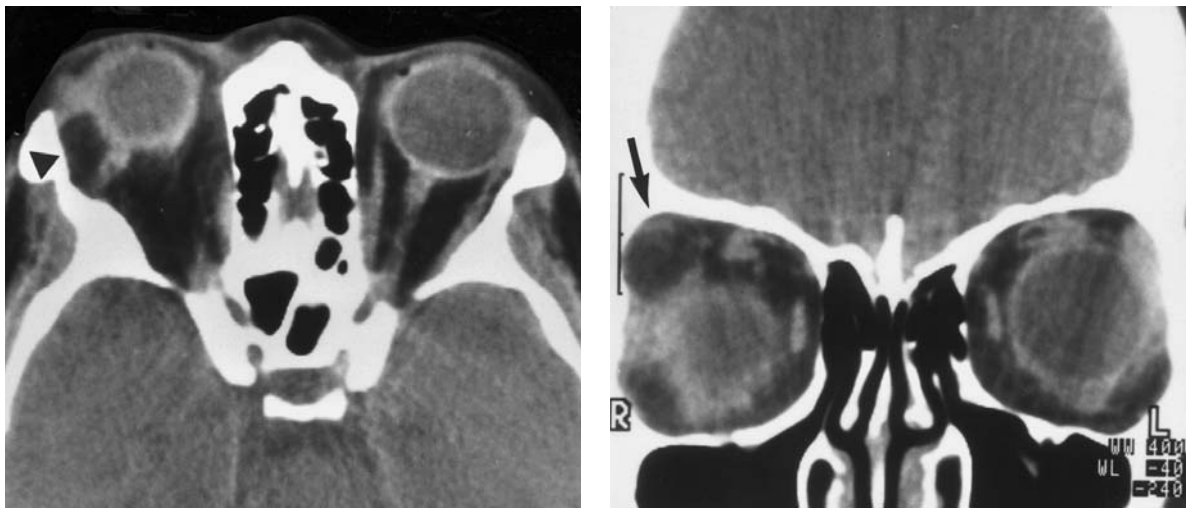

Fig. 6.128a,b. A 32-year-old woman with slowly progressing, painless, eccentric, inferior proptosis of the right eye. Diagnosis: epidermoid of the lacrimal gland. CT: **a** Axial view, with a hypodense (fatty) mass in the superior lateral orbit (*arrowhead*), displacing the globe inferiorly. Note the impression of the zygomatic bone. **b** Coronal view, demonstrating the communication with the upper lacrimal gland (*arrow*)

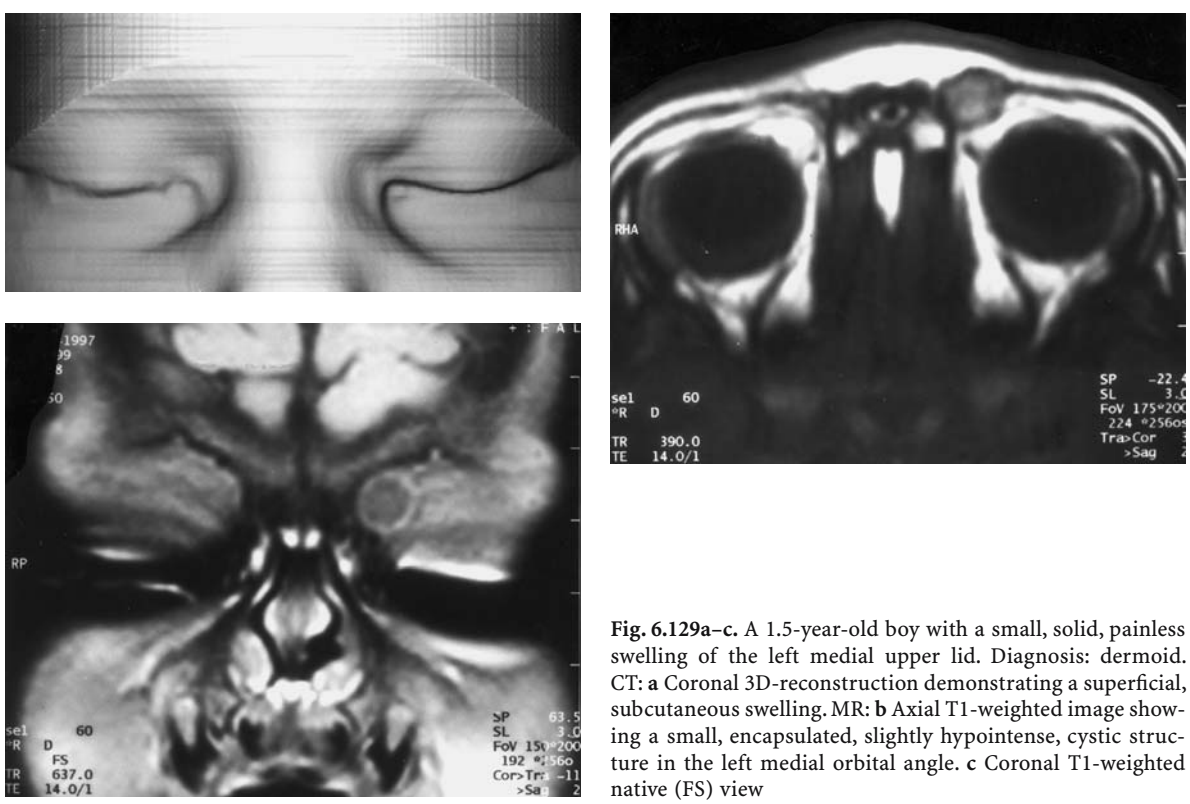

Fig. 6.129a–c. A 1.5-year-old boy with a small, solid, painless swelling of the left medial upper lid. Diagnosis: dermoid. CT: **a** Coronal 3D-reconstruction demonstrating a superficial, subcutaneous swelling. MR: **b** Axial T1-weighted image showing a small, encapsulated, slightly hypointense, cystic structure in the left medial orbital angle. **c** Coronal T1-weighted native (FS) view

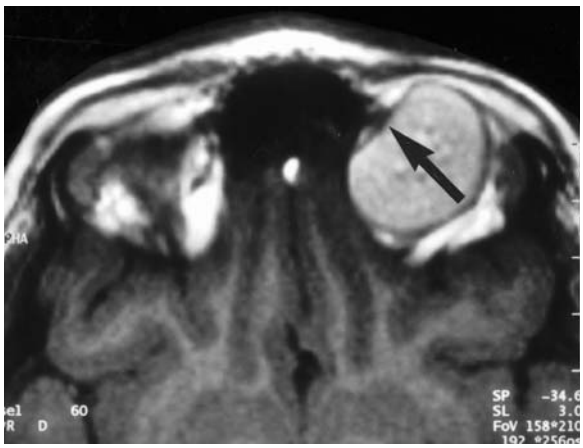

a

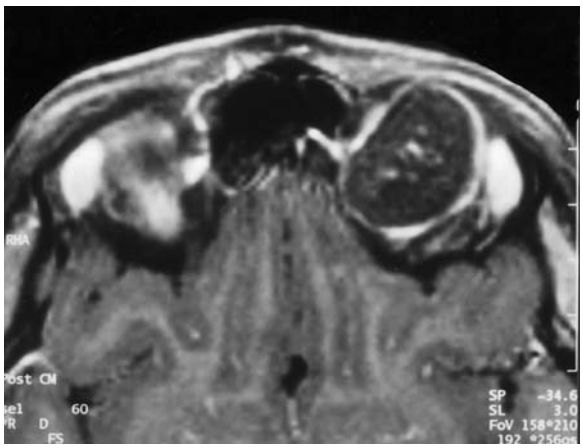

b

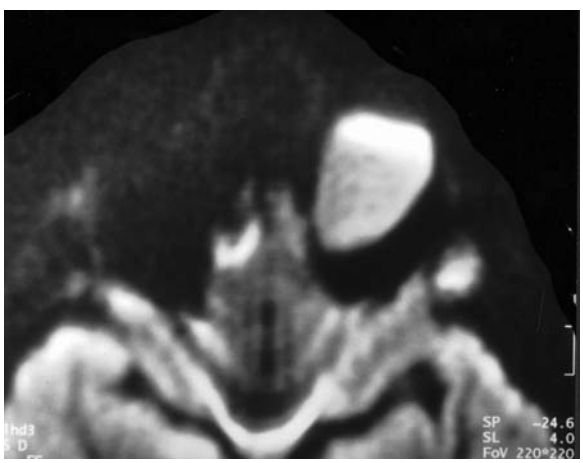

c

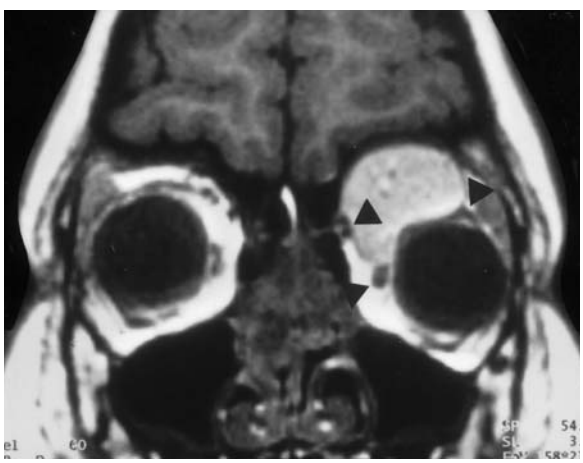

d

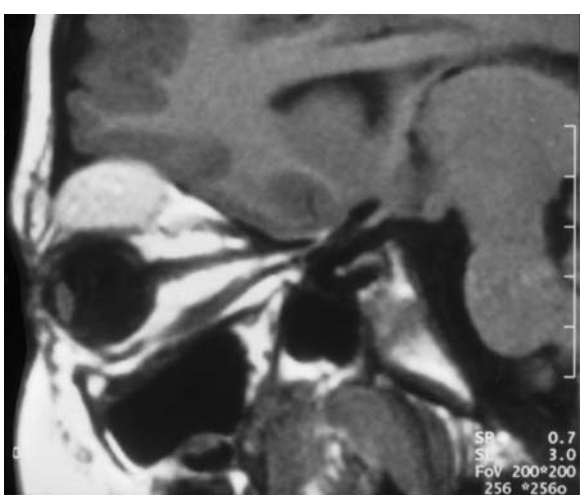

e

Fig. 6.130a–e. A 12-year-old girl with slowly progressing, eccentric exophthalmos and narrowing of the palpebral fissure of the left side. Diagnosis: dermoid. MR: **a** Axial native T1-weighted view of the upper orbit demonstrating an encapsulated, well-defined, homogeneous, high signal lesion of the medial left orbit. Note the dislocated superior oblique muscle at the level of the trochlea (*arrow*). **b** Corresponding contrast-enhanced (FS) image with enhancement of the capsule but hypointensity of the lesion (due to fat suppression). **c** Corresponding DW image, demonstrating characteristic signal enhancement of the tumor. **d** Coronal T1-weighted native view demonstrating both the eccentric downward dislocation of the left globe and the asymmetric widening of the entire left orbit (corresponding to a persisting benign process). Note the formative adaptation of the process to the globe and bone of the orbital roof, as well as the progressing dislocation of the external muscles (*triangles*). **e** Parasagittal T1-weighted native view with superior demonstration of the extraconal localization of the dermoid tumor

weighted and hyperintense on T2-weighted images (Fig. 6.130). Despite significant fat contents in dermoid cysts with a hyperintense signal both on T1-weighted and T2-weighted sequences, definite differentiation from fluid may be impossible. The problem is resolved when diffusion-weighted imaging (DWI) is used, enabling specific definition by signal enhancement (Fig. 6.130) (Guenalp and Guenduez 1996; Kaufmann et al. 1998; Dechambre et al. 1999).

Small dermoids do not require immediate therapy and are usually removed within the 2nd or 3rd year of life. Complete removal without rupturing is required in order to avoid inflammatory reactions or local recurrences. Larger orbital dermoids may cause severe effects, including exophthalmos and recurrent inflammations. These conditions require immediate, complete removal, in the majority of cases by lateral orbitotomy with bone resection.

6.3.4.2 Tumors

As discussed above, lacrimal gland lesions can be divided into epithelial and nonepithelial lesions. The classification of lacrimal gland epithelial tumors is similar to that of salivary gland ones and comprises 40%–50% of all lacrimal masses, one-half of which are benign mixed tumors, while the other half constitute malignant masses (Warner et al. 1996).

6.3.4.2.1 Pleomorphic Adenoma (Benign Mixed Tumor)

The most common benign tumor of the lacrimal gland is the benign mixed or pleomorphic adenoma of the lacrimal gland, which originates mainly, but not exclusively from the inner, orbital lobe (Mafee and Haik 1987; Rose and Wright 1992; Vangveeravong et al. 1996). Clinical signs include a painless, slow-growing mass in the lateral orbit, persisting for more than 12 months, leading in some cases, particularly in middle-aged patients (about 40–50 years of age; without any gender predilection), to proptosis and limited ocular motility (Rose and Wright 1992; Mafee et al. 1999b). The generally encapsulated tumor is characterized by irregular solid parts with myxoid, chondroid, or mucinous areas. Although benign, these tumors can undergo malignant transformation, primarily in cases where only a biopsy or incomplete excision were performed, both of which are associated with a high rate of recurrence (Stewart et al. 1979; Rose and Wright 1992; Mafee et al. 1999b).

Imaging features represent histologic conditions, and the tumors are defined as well circumscribed, encapsulated, round to oval-shaped masses, which might cause lacrimal fossa deformation. On CT, calcifications may be seen, while on MRI, a heterogeneous signal is identified, especially on T2-weighted images with low to moderate contrast enhancement (Fig. 6.131). Irregularity at the edge of the tumor or infiltration of the adjacent orbital tissue may be seen in malignant transformation (Mafee et al. 1999b).

6.3.4.2.2 Adenoid Cystic Carcinoma

Although an uncommon tumor, adenoid cystic carcinoma is the most frequent malignant tumor of the lacrimal gland, accounting for 29% of all epithelial lacrimal gland tumors (Henderson and Farrow 1980; Warner et al. 1996). In contrast to the older patient population with benign mixed tumors, adenoid cystic carcinoma occurs most frequently in the 4th decade of life, although young adults may also be affected (Tellado et al. 1997; Mafee et al. 1999b). Patients present with a hard mass in the upper lateral orbit, often associated with pain caused by the infiltrative perineural growth. Different long-term prognoses for patients suffering from adenoid cystic carcinoma have been reported, ranging from only 5 years in 40% of patients (Font et al. 1998) to an estimated survival rate of 15 years in 58% of patients (Tellado et al. 1997). Histologically, these tumors are characterized by the absence of a mesenchymal matrix, and can be divided into different histologic types according to the predominant cell type. The cell types include tubular, sclerosing, comedo carcinoma, basaloid, or cribriform patterns, the last-mentioned being composed of benign-appearing sheets of basaloid epithelial cells and surrounding spaces of varying shapes and sizes with the characteristic cribriform pattern of Swiss cheese (Tellado et al. 1997; Mafee et al. 1999b).

On CT or MRI, the appearance of a nodular and infiltrative tumor, combined with bone erosion (Fig. 6.132), suggests adenoid cystic carcinoma, especially in the presence of soft-tissue involvement. Although calcification is found in benign mixed tumors, it is more common in malignant lacrimal gland lesions (Mafee et al. 1999b).

6.3.4.2.3 Lymphoma of the Lacrimal Gland

Lymphomatous lesions of the lacrimal gland include a wide spectrum, ranging from reactive lymphoid

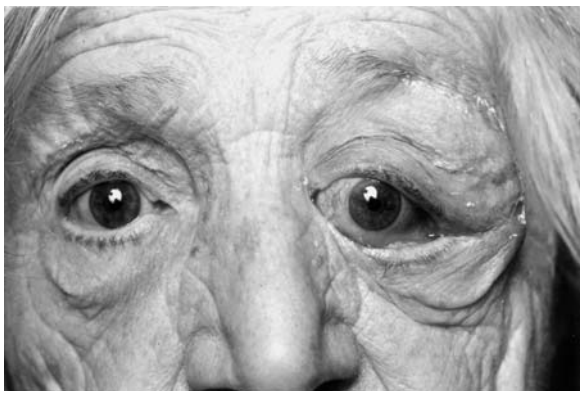

a

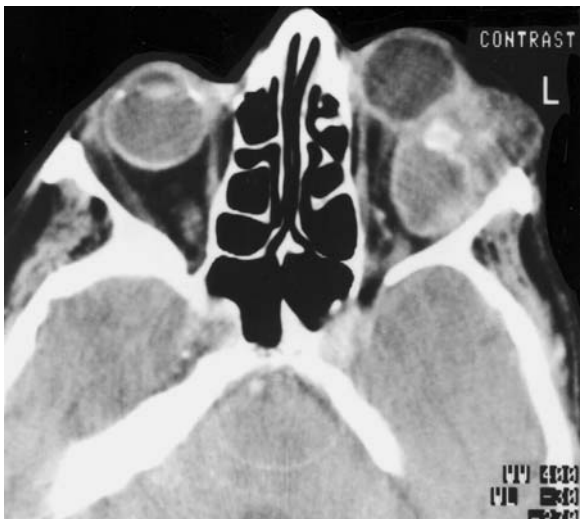

b

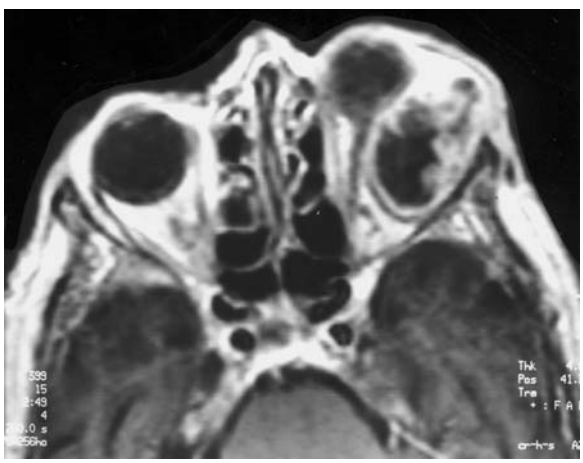

c

Fig. 6.131a–c. A 86-year-old woman with a long history of extra-axial proptosis of the left eye. Diagnosis: pleomorphic adenoma of the lacrimal gland. **a** Portrait of the patient, showing the proptosis of the left eye, caused by a superolateral space-occupying lesion. **b** Axial contrast-enhanced CT with a predominantly solid, partly calcified, partly cystic encapsulated tumor of the left extraconal space, and significant depression and flattening of the anterior dislocated globe. MRI: **c** Corresponding T1-weighted, contrast-enhanced view with more distinct differentiation of the capsule and the cystic tumor parts. (With permission of Müller-Forell and Lieb 1995b)

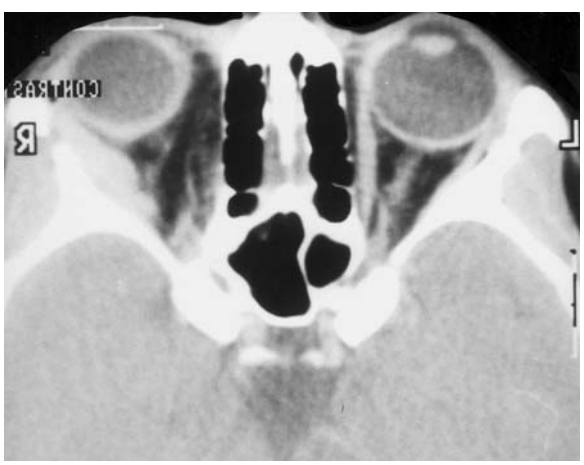

a

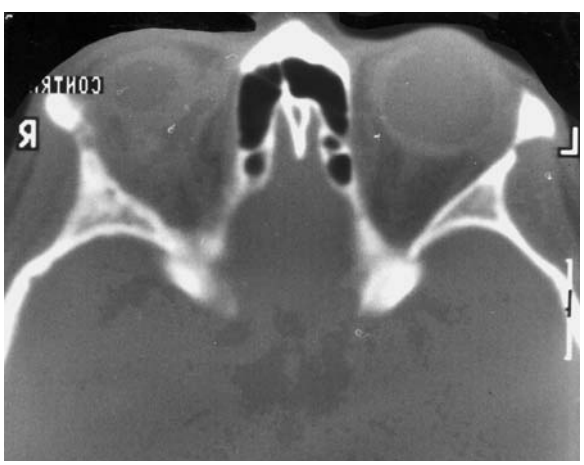

b

Fig. 6.132a,b. A 39-year-old woman presenting without clinical signs of pathology for routine check-up examination 2 years after operation for adenoid cystic carcinoma of the right lacrimal gland. Diagnosis: recurrent adenoid cystic carcinoma. CT: **a** Axial contrast-enhanced view with hyperdense formation in the mediolateral part of the superior right orbit. **b** Corresponding bone window identifying both osteolytic and sclerosing destruction of the zygomatic and sphenoid bone

hyperplasia, low-grade mucosa-associated lymphoid tissue (MALT) lymphomas, to malignant lymphomas of various types (Jakobiec et al. 1979; Agulnik et al. 2001). Although rare (Galieni et al. 1997), primary lymphomas without systemic involvement appear to be the most common nonepithelial tumor of the lacrimal gland (Rootman et al. 1988). Lymphomas of the lacrimal gland present in older patients as a painless, slowly growing, salmon-colored mass in the upper lateral orbit, in some cases combined with conjunctival redness (25%) or visual impairment (13%) (Polito et al. 1996; Mafee et al. 1999b). As radiotherapy and chemotherapy promise complete remission in most cases, an accurate histological or cytological diagnosis should be achieved by biopsy (Jeffrey et al. 1995; Galieni et al. 1997; Agulnik et al. 2001).

Although imaging of patients with lymphoproliferative disorders is characterized by nonspecific features, making the differential diagnosis with respect to acute or chronic idiopathic orbital inflammation, metastasis, capillary hemangioma, and plexiform neurofibroma difficult, specific features may lead to the diagnosis of lymphoma: Lymphoid tumors frequently have a superior orbital or retrobulbar component, show straight or angulated edges, as they grow along orbital fascial planes and muscles, and a striped profile on infiltrating retrobulbar orbital fat (Yeo et al. 1982). CT and MRI show one or more, lobulated or round, slightly isodense/isointense masses, molding adjacent structures without causing indentation (Figs. 6.44, 6.133–6.135). In addition, a wedge-shaped enlargement of the lacrimal gland causing a smooth impression of the orbital walls without bone erosion is apparent, while substantial destruction and invasion of the adjacent tissue, including bones and the brain, is seen in malignant variants (Figs. 6.136, 6.137) (Yeo et al. 1982; De Potter et al. 1995; Polito et al. 1996; Mafee et al. 1999b). Lymphomas are usually bulkier than idiopathic orbital masses; they may mold and drape onto the globe, with more frequent evidence of anterior or posterior extension (Mafee et al. 1999b) and symmetric, bilateral involvement (Fig. 6.138). An important diagnostic criterion on MRI is moderate to marked hyperintensity of the extraocular muscles and the orbital fat on T2-weighted images. On T1-weighted images, lymphomas exhibit hyperintensity in comparison with the extraocular muscles, hypointensity compared with the orbital fat, as well as moderate to marked enhancement in fat-suppressed, gadolinium-enhanced images. These factors make a reliable differentiation from the above-mentioned pathologies difficult (De Potter et al. 1995; Asao et al. 1998).

6.3.4.2.4 Miscellaneous (Amyloid Tumor, Extramedullary Plasmocytoma)

In contrast to diseases due to degeneration and amyloid deposits, focal amyloidosis is a very uncommon disorder that may present either as a mass or with diffuse infiltration. It may involve different orbital structures as, e.g., orbital fat (Fig. 6.82), external muscles (Okamato et al. 1998), or the lacrimal gland (Fig. 6.138) (Motta et al.

(Text continues on p. 174)

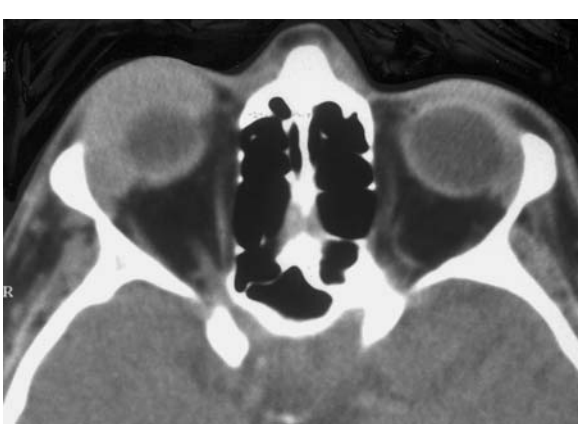

a

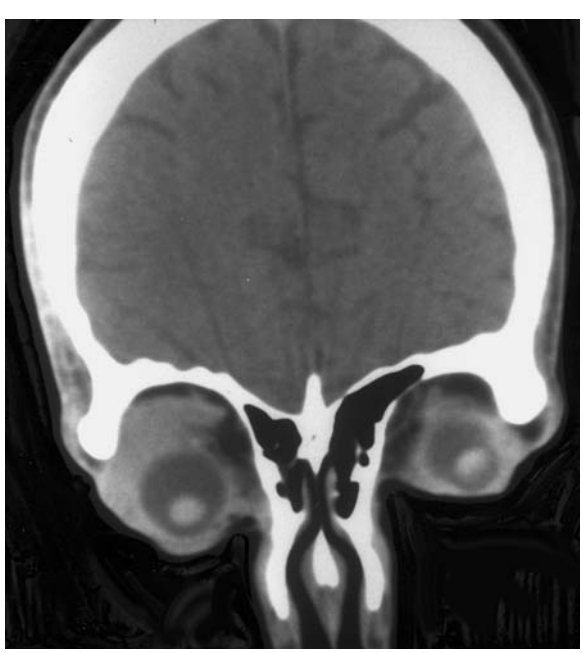

b

Fig. 6.133a,b. A 45-year-old man with progressive, extra-axial right eye protrusion. Diagnosis: lymphoma. CT: **a** Axial view of the upper orbit with homogeneous tumor-like enlargement of the right lacrimal gland, expanding over the entire lateral and superior globe, apparently depressing the globe. **b** Coronal view demonstrating shifting of the globe, although differentiation of the formation from normal lacrimal structures is not possible

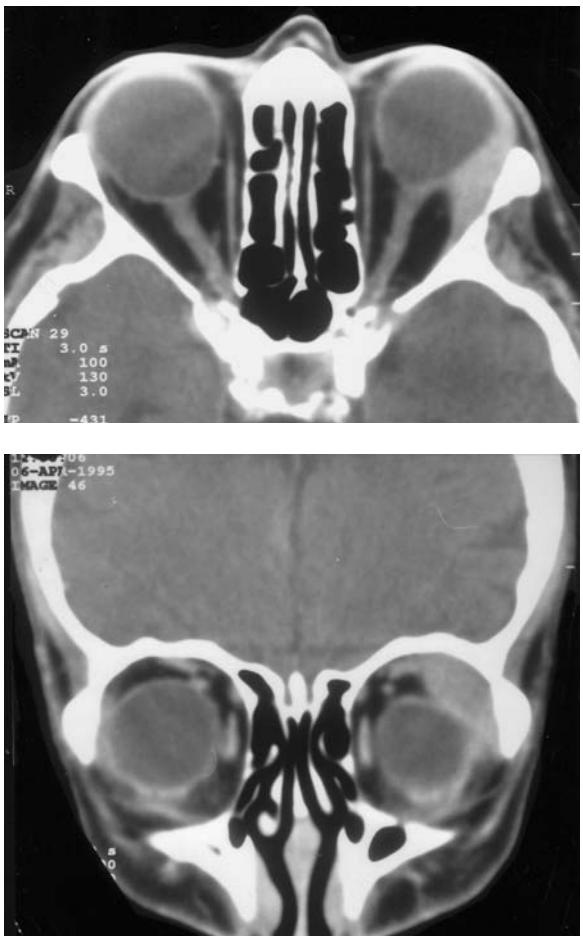

a

b

Fig. 6.134a,b. An 82-year-old woman with painless proptosis of the left eye persisting for 2 weeks. Diagnosis: non-Hodgkin lymphoma of the lacrimal gland. Contrast-enhanced CT: **a** Axial view with slightly enhancing mass of the left lacrimal gland, flattening the circumference of the left globe. **c** Corresponding coronal view where the extra-axial inferior dislocation of the bulb is more distinct than in **a**

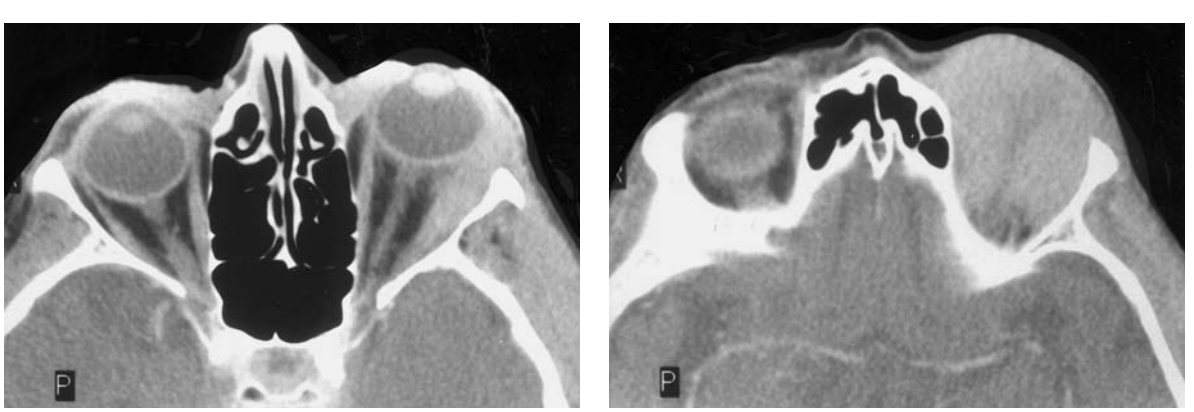

a

b

Fig. 6.135a,b. An 86-year-old woman with chronic blepharo-conjunctivitis of the left eye and known NHL for the past 9 years. Diagnosis: NHL lymphoma. CT: **A** axial view with preseptal and postseptal orbital involvement (infiltration of the lateral external muscle) and extraorbital infiltration of the temporal muscle. **b** Axial view of the upper orbit showing involvement of the lacrimal gland and the medial upper orbit. Note the slight hypodensity of the uninvolved, but bilaterally compressed superior rectus muscle

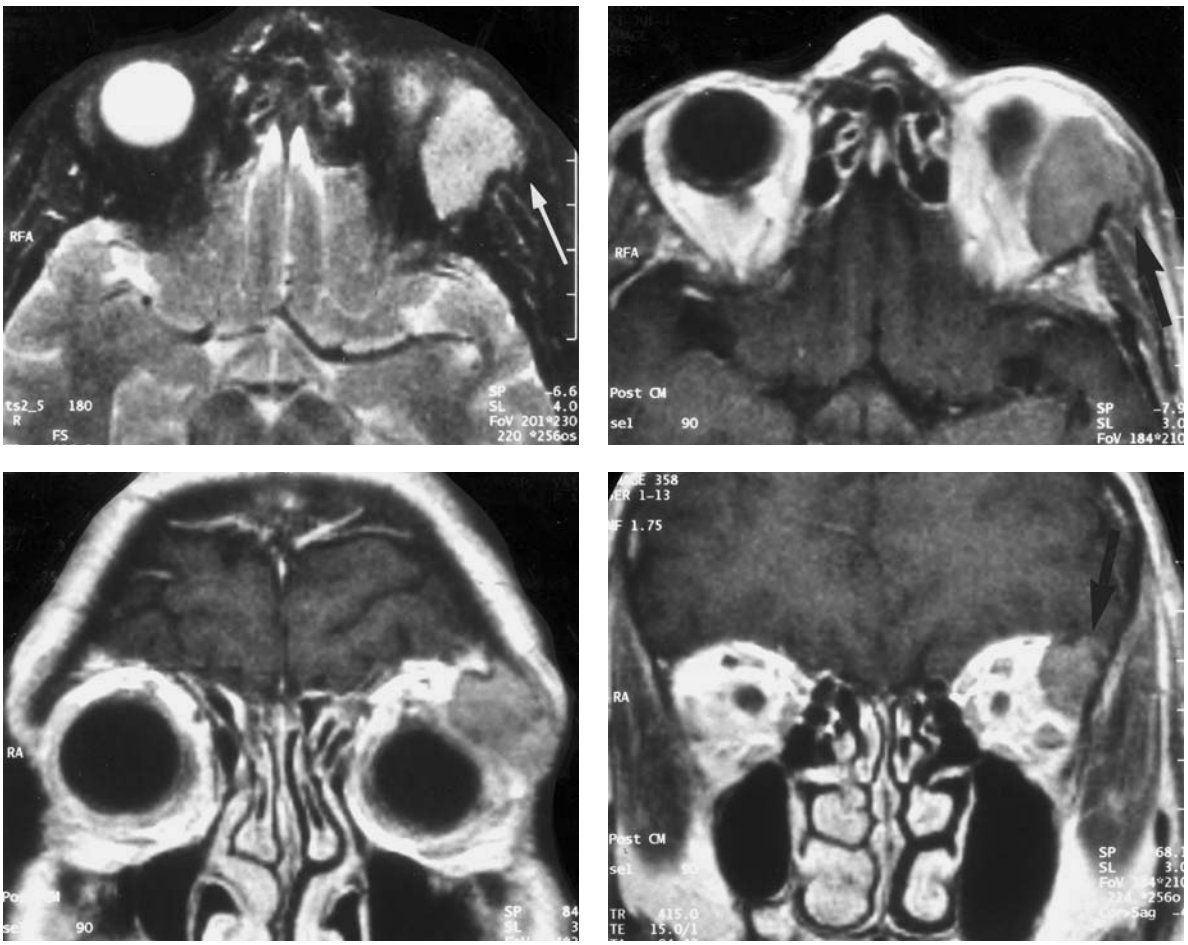

a b c d

Fig. 6.136a–d. A 59-year-old woman presenting with subacute, left, extra-axial proptosis and enlarged lacrimal gland. Diagnosis: malignant NHL (B-cell type). MR: **a** Axial T2-weighted image, a comparison with the right side clearly demonstrates both enlargement of the left lacrimal gland and destruction of the zygomatic bone (*white arrow*). **b** Corresponding T1-weighted, contrast-enhanced view showing the loss of cortical integrity of the upper lateral orbital wall with tumor extension to the subcutaneous fat (*arrow*). **c** Coronal T1-weighted, contrast-enhanced view with demonstration of the irregular tumor mass. Note the compression exerted by the tumor leading to inferior dislocation and flattening of the globe. **d** Corresponding image of the posterior part of the orbit, visualizing tumor destruction of the orbital roof and intracranial, but extradural extension (*arrow*)

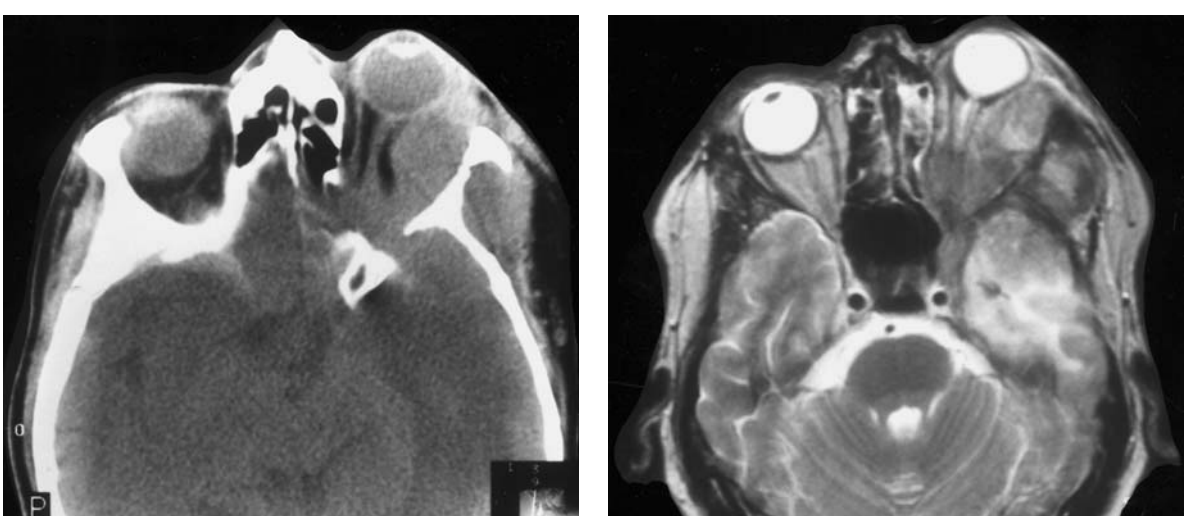

a b

Fig. 6.137a–h. A 44-year-old man after complete therapy for a T-cell lymphoma (chemotherapy and radiation), presenting with swollen and protruding left eye and suspected osteomyelitis of the upper jawbone. Diagnosis: T-cell lymphoma. **a** Axial CT of the upper orbital region where an intra- and extraorbital, intra- and extracranial mass is seen. **b** Corresponding T2-weighted MRI, demonstrating not only the extreme proptosis caused by the mass, but also a temporopolar mass with perifocal edema...

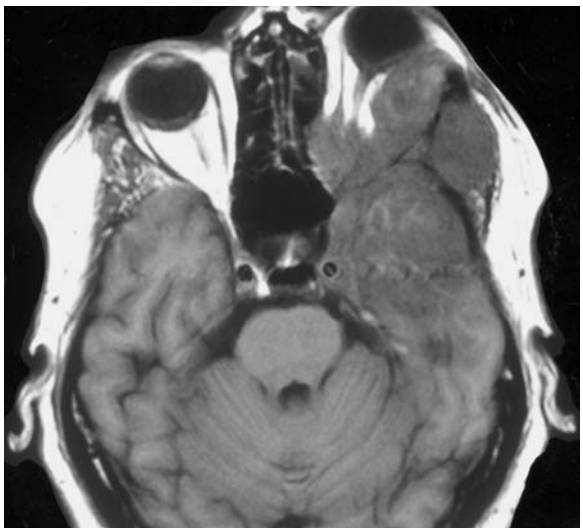

c

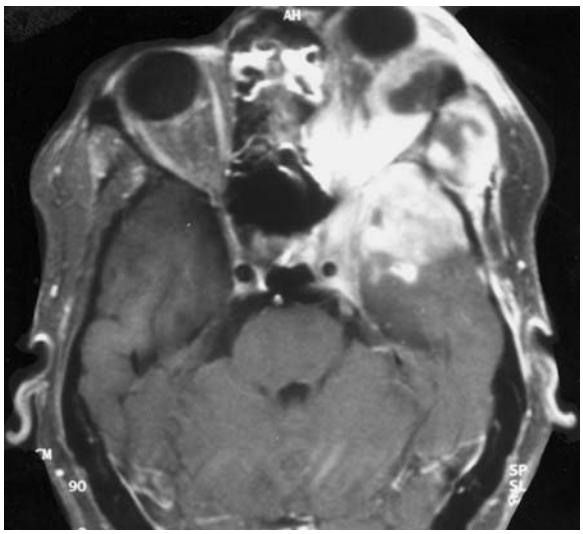

d

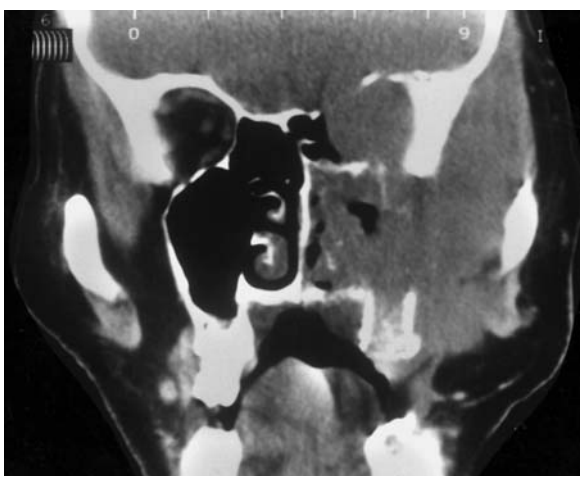

e

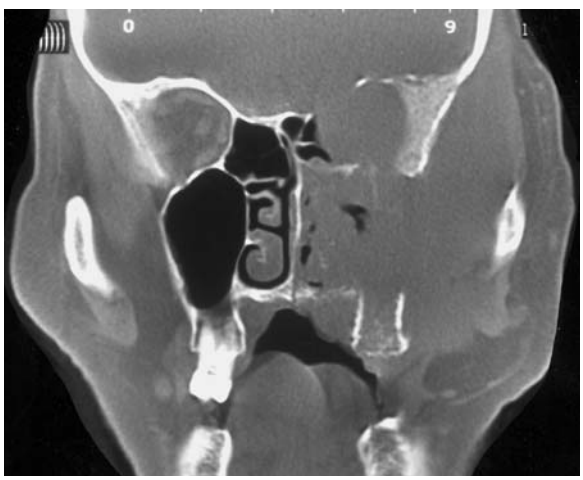

f

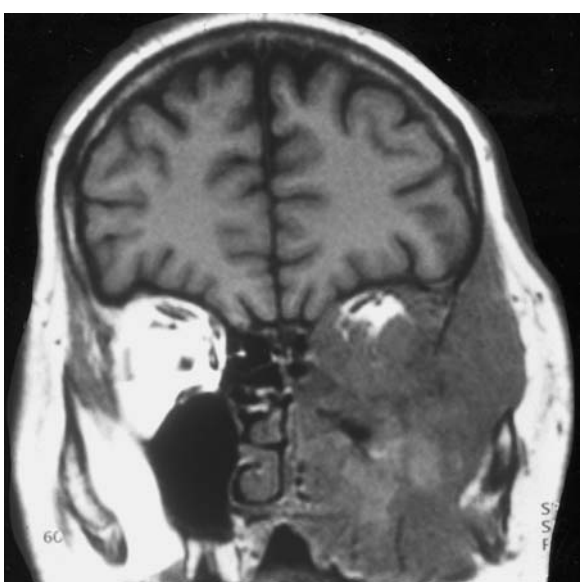

g

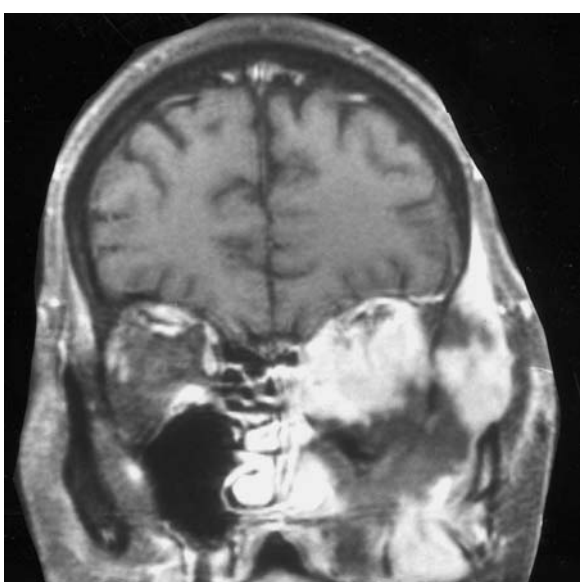

h

... **c** Corresponding T1-weighted native view, where the infiltration of all structures of the orbital apex is also seen. **d** Corresponding T1-weighted, contrast-enhanced (FS) view, showing enhancement of the entire mass and additional infiltration of the cavernous sinus. **e** Coronal native CT of the midorbital region, where the additional involvement of the maxillary sinus and bone is apparent. **f** Corresponding bone window. **g** Corresponding T1-weighted native MRI. **h** Corresponding T1-weighted, contrast-enhanced view

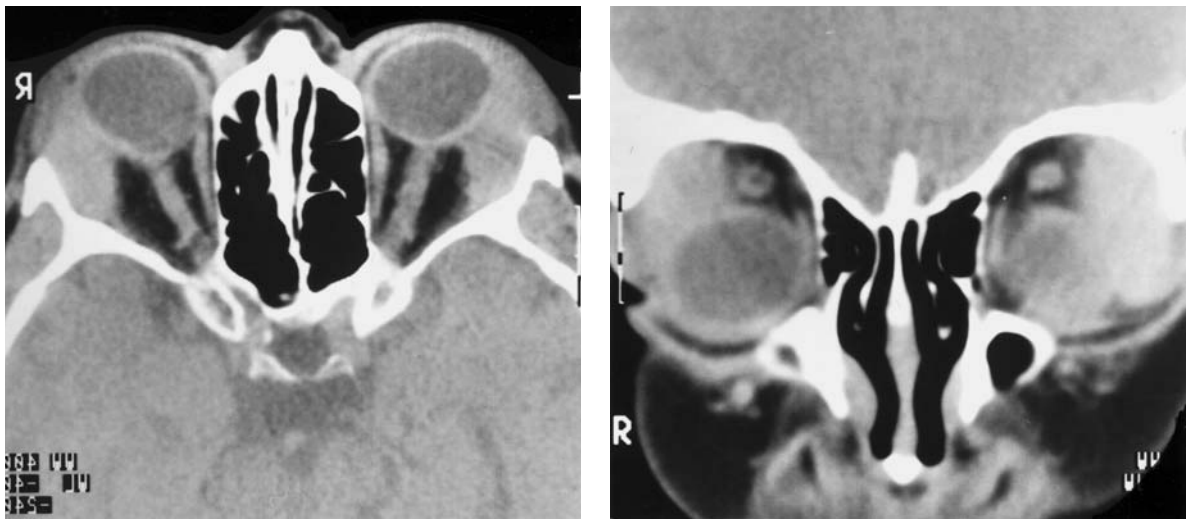

a b

Fig. 6.138a,b. A 69-year-old woman with symmetric, bilateral, extra-axial proptosis. Diagnosis: bilateral lymphoma of the lacrimal gland. CT: **a** Axial native view with significant enlargement of the lacrimal glands, depressing both globes and flattening the circumference of the globes. **b** Corresponding coronal view. (With permission of Müller-Forell and Lieb 1995b)

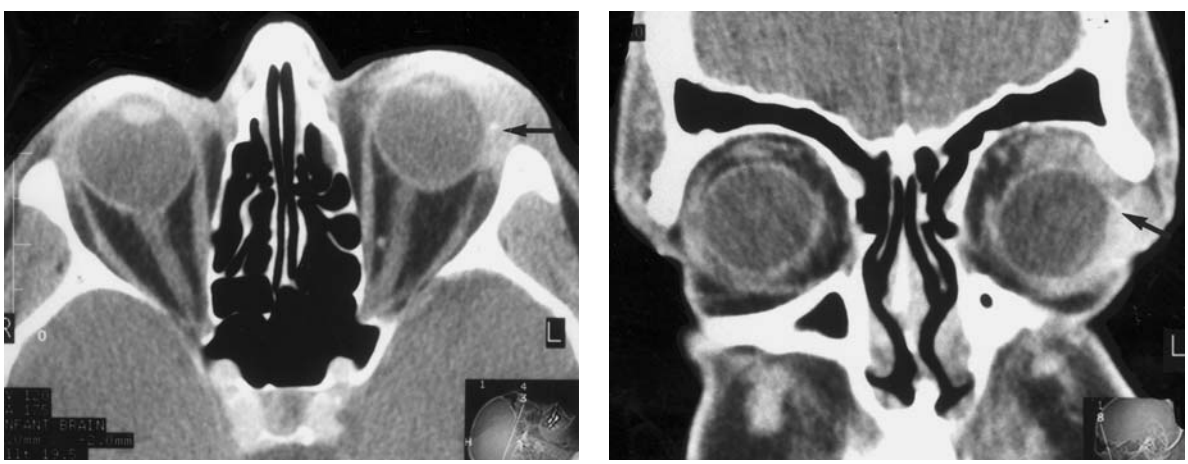

a b

Fig. 6.139a,b. A 66-year-old man with progressive protrusion and undefined pressure of the left eye. Diagnosis: amyloid tumor of the lacrimal gland. CT: **a** Axial view showing moderate enlargement of the lacrimal gland with a small calcification (*arrow*). **b** Coronal view identifying encasement of the superior circumference of the globe

1983; Levine and Buckman 1986; Conlon et al. 1991; Murdoch et al. 1996). Isolated involvement of the lacrimal gland may mimic inflammatory or even tumorous lesions (Mafee et al. 1999b). Clinically presenting with painless proptosis, amyloidoma of the lacrimal gland is associated with an enlarged gland, molding to adjacent orbital structures, and frequently with punctuate calcification (Fig. 6.139), resembling phleboliths, which is best identified with CT (Fig. 6.82) (Massry et al. 1996). With MRI, amyloid deposits show hypointensity on T2-weighted images (Fig. 6.82) (Mafee et al. 1999b). With both imaging modalities, they demonstrate virtually no contrast enhancement (Cohen and Lessell 1979; Okamoto et al. 1998).

As tumors of the lacrimal gland behave in a similar fashion to those of the salivary or parotid gland, extramedullary plasmocytoma may also be seen in the lacrimal gland, sometimes mimicking amyloid deposition (Ustun et al. 2001). A rare entity, belonging to the category of non-Hodgkin lymphoma, they represent up to 4% of all plasma cell tumors. Extramedullary plasmocytoma primarily involves the nasal cavity and the paranasal sinus (Alexiou et al. 1999; Liebross et al. 1999; Galieni et al. 2000), while orbital involvement is extremely rare (Fig. 6.140) (Uceda-Montanes et al. 2000). The tumors most fre-

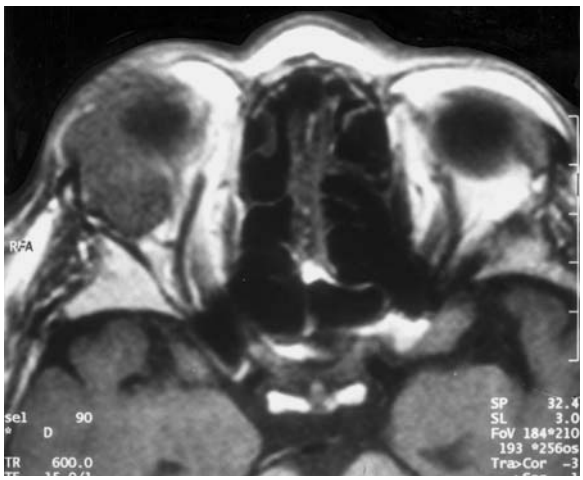

a

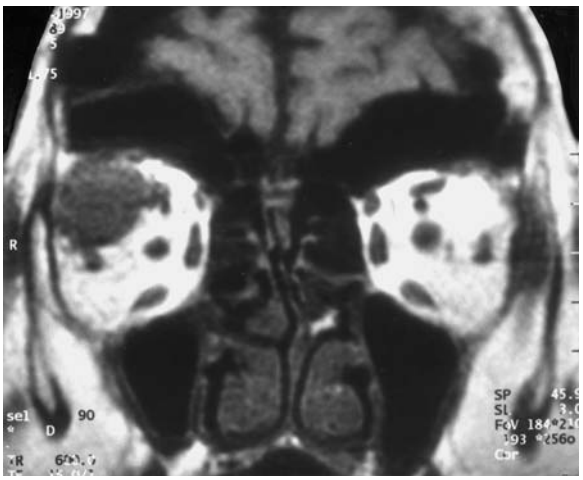

b

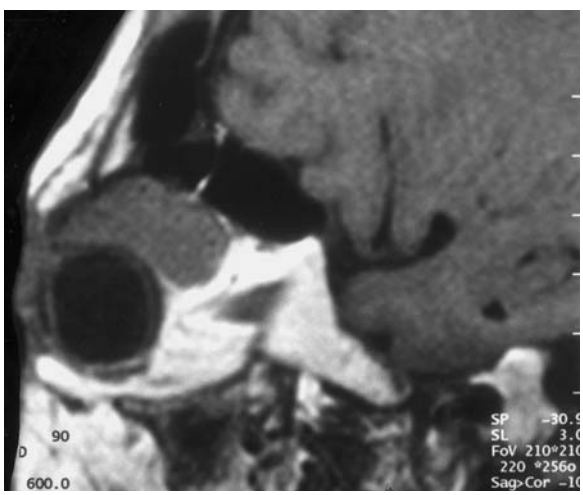

c

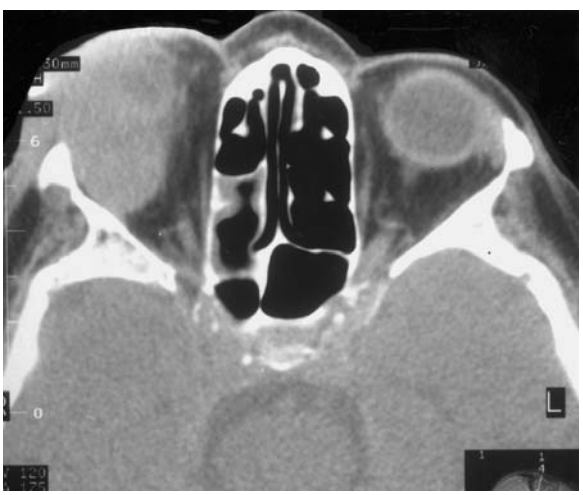

d

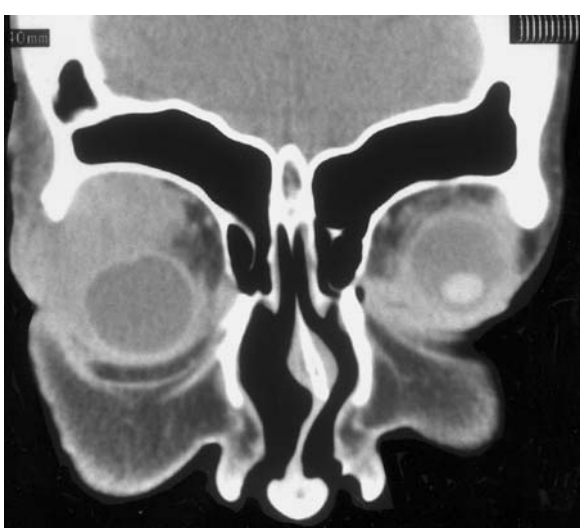

e

Fig. 6.140a–e. Follow-up of a 68-year-old woman with rapidly progressing protrusion of the right globe. Diagnosis: isolated, extramedullary plasmocytoma of the lacrimal gland. MR: **a** Axial T1-weighted native image with homogeneous enlargement of the right lacrimal gland and compression of the globe. **b** Coronal T1-weighted native view showing the sharply delineated tumor in the extraconal space. **c** Right parasagittal T1-weighted native view. CT check-up examination for progressing exophthalmos 10 days after biopsy: **d** Axial view corresponding to **a** with demonstration of extensive posterior growth of the tumor. **e** Coronal view. Thickening of the galea of the temporal fossa is shown to be caused by the biopsy, instead of being due to tumor invasion

quently affect patients in the 4th to 7th decade of life (Alexiou et al. 1999), and the diagnosis is based on the presence of a mass of clonal plasma cells, immunohistochemical stains for Kappa light chains and epithelial membrane antigen, distinct from bone and bone marrow, and without evidence of occult disease elsewhere (Liebross et al. 1999; Uceda-Montanes et al. 2000). Due to the fact that imaging shows a homogeneous mass in the region of the lacrimal gland (Fig. 6.140), confusion with lymphoma or idiopathic orbital inflammation may occur. The most effective therapeutic management with a high rate of complete remission consists of local radiation therapy, or combined surgery and radiation treatment (Alexiou et al. 1999; Liebross et al. 1999; Galieni et al. 2000).

6.3.4.3 Inflammatory Lesions

6.3.4.3.1 Idiopathic Inflammatory Disorder ("Pseudotumor") of the Lacrimal Gland

As previously described, idiopathic orbital inflammation may involve any intraorbital organ, and occur either diffuse or solitary. The lacrimal gland is the preferred organ for inflammation, but there are no definite imaging criteria in the differentiation of inflammatory from other, especially systemic tumorous lesions of the gland (Au Eong and Choo 1997; Eifrig et al. 2001) or epithelioid cell granuloma e.g. in a patient with sarcoidosis (Fig. 6.141). Involvement of the lacrimal gland leads to a presentation with acute or subacute dacryoadenitis, S-shaped upper lid deformity with tenderness and enlargement (Figs. 6.142, 6.143), palpable superotemporal mass and conjunctival injection (Mafee et al. 1999). A chronic course is not uncommon in the sclerosing type of "pseudotumor" of the lacrimal gland (Fig. 6.144). Imaging shows diffuse, at times massive enlargement of the gland with moderate to marked enhancement after contrast administration, occasionally in association with posterior scleritis (Fig. 6.145). In the majority of cases, imaging is not able to unequivocally differentiate idiopathic lacrimal gland inflammation from lymphoma of the lacrimal gland (Mafee et al. 1999b).

6.3.4.3.2 Sjögren Syndrome

Sjögren syndrome is an idiopathic autoimmune disorder characterized by dryness of the eyes and mouth, caused by chronic lymphocytic infiltrates of the lacrimal and salivary glands (Fox 1996a). In the primary form (sicca complex), there is only keratoconjunctivitis sicca and xerostomia, while the secondary form comprises an association with such connective tissue diseases as rheumatoid arthritis, scleroderma, polymyositis, or polyarteritis nodosa (Weber et al. 1999). Keratoconjunctivitis is caused by impaired function of the lacrimal and the accessory lacrimal glands of the conjunctiva. Focal lymphocytic infiltration with plasma cells, genetic and environmental factors (e.g., members of the herpes

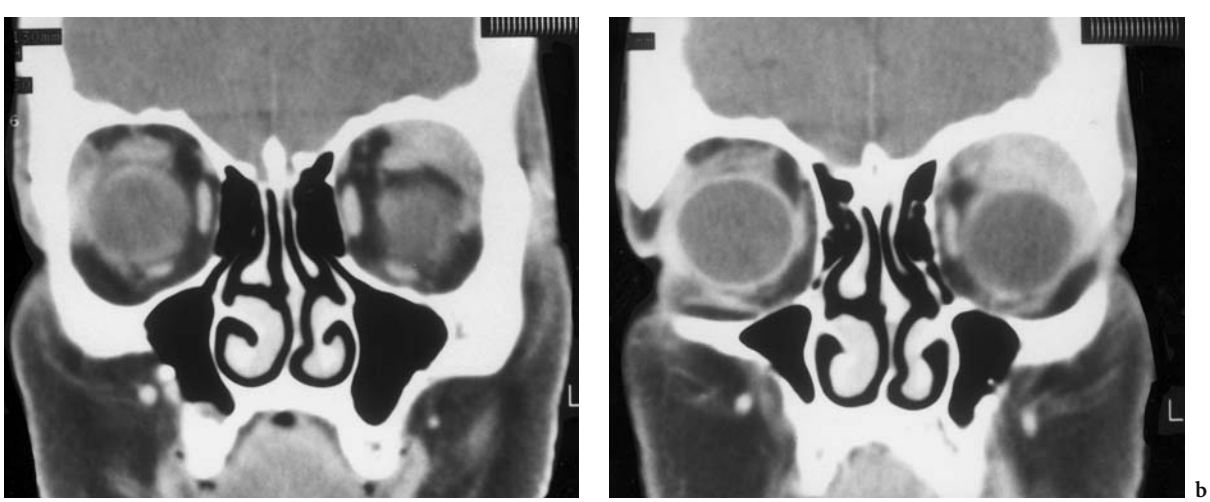

Fig. 6.141a,b. A 68-year-old woman with slowly progressing dislocation and protrusion of the left globe. Diagnosis: epithelioid-cell granuloma in the course of a sarcoidosis. CT: **a** Coronal view of the posterior globe, **b** Coronal view at the lacrimal fossa. Both images demonstrate the sharply defined, homogeneous, extraconal tumor with posterior expansion, covering and slightly depressing the globe

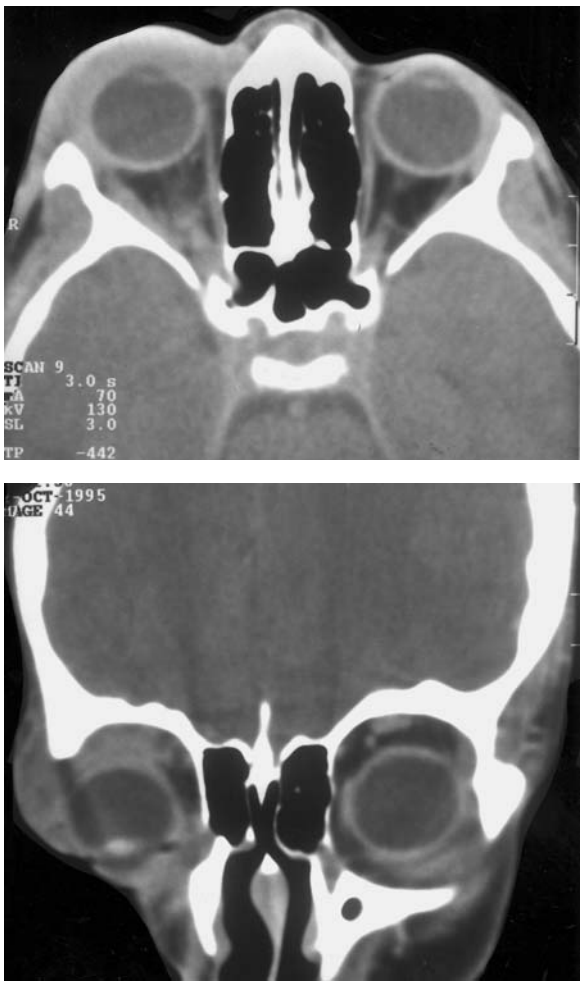

Fig. 6.142a,b. A 12-year-old boy with painful swelling of the right eye. Diagnosis: idiopathic orbital inflammation. CT: **a** axial view with swelling of the conjunctiva (preseptal infiltration medially) and lateral external muscle, including the lateral lacrimal gland of the right orbit. **b** Coronal view demonstrates additional infiltration of the superior external muscle complex

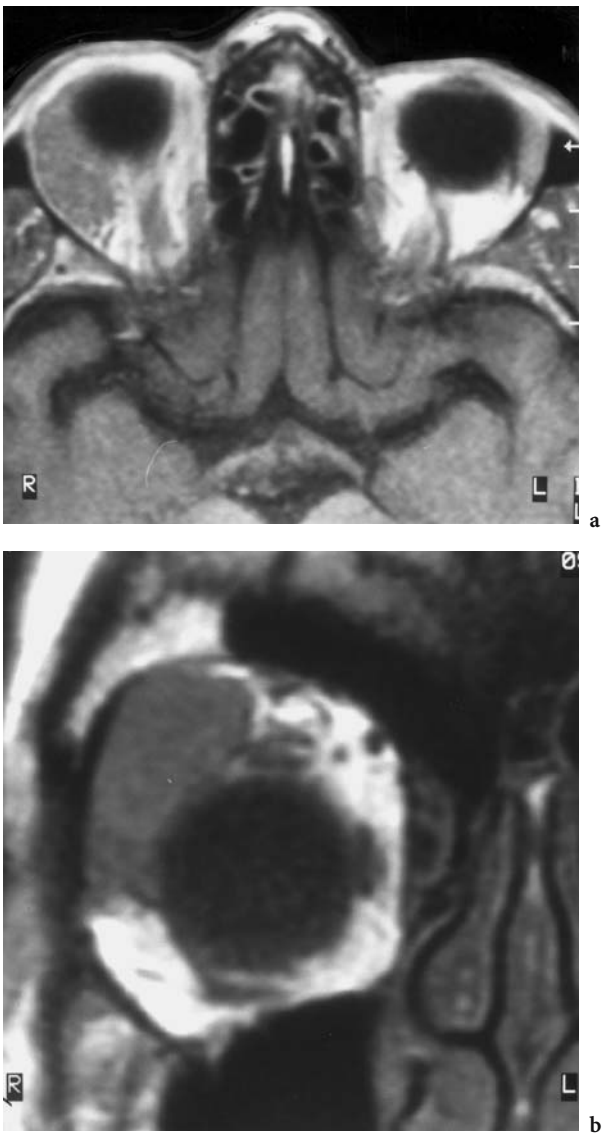

Fig. 6.143a,b. A 72-year-old woman with slowly progressing lid swelling and extra-axial proptosis of the right globe. Diagnosis: idiopathic orbital inflammation of the lacrimal gland. MRI: **a** axial contrast-enhanced view demonstrating slight signal enhancement of the enlarged right lacrimal gland. Note asymmetry of the globe, caused by inferior displacement of the right. **b** Coronal native view in the region of the posterior lacrimal fossa; the extraconal location of the space-occupying enlargement of the right lacrimal gland is visualized

virus or retroviral family) play a potentially important role in the initiation and perpetuation of the autoimmune process (Fox 1996a,b; Weber et al. 1999). Chronic dacryoadenitis, presenting with usually painless, slow lacrimal enlargement, is secondary to subacute infections like Sjögren or Mikulicz syndrome. Although imaging is not essential for the differential diagnosis, bilateral enlargement of the lacrimal (and parotid) glands due to infectious or neoplastic causes sometimes renders the differential diagnosis more difficult (Fig. 6.146) (Harnsberger 1990; Casper et al. 1993).

6.3.4.4 Lacrimal Pathway

Congenital disorders of the lacrimal system (gland and excretory channels) are rare but may be seen in children with facial anomalies (Older 1988).

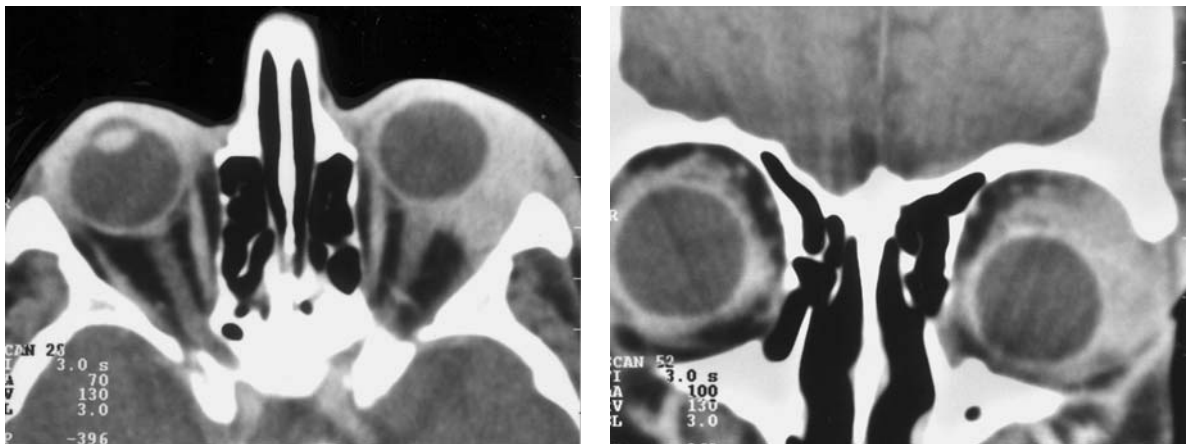

Fig. 6.144a,b. A 61-year-old man with slowly progressing protrusion of the intermittently infected left eye. Diagnosis: chronic sclerosing dacryoadenitis. Contrast-enhanced CT: **a** Axial view demonstrating global enlargement of the lacrimal gland, and indistinct differentiation in the absence of compression of the globe. **b** Coronal view with irregular encasement of the globe

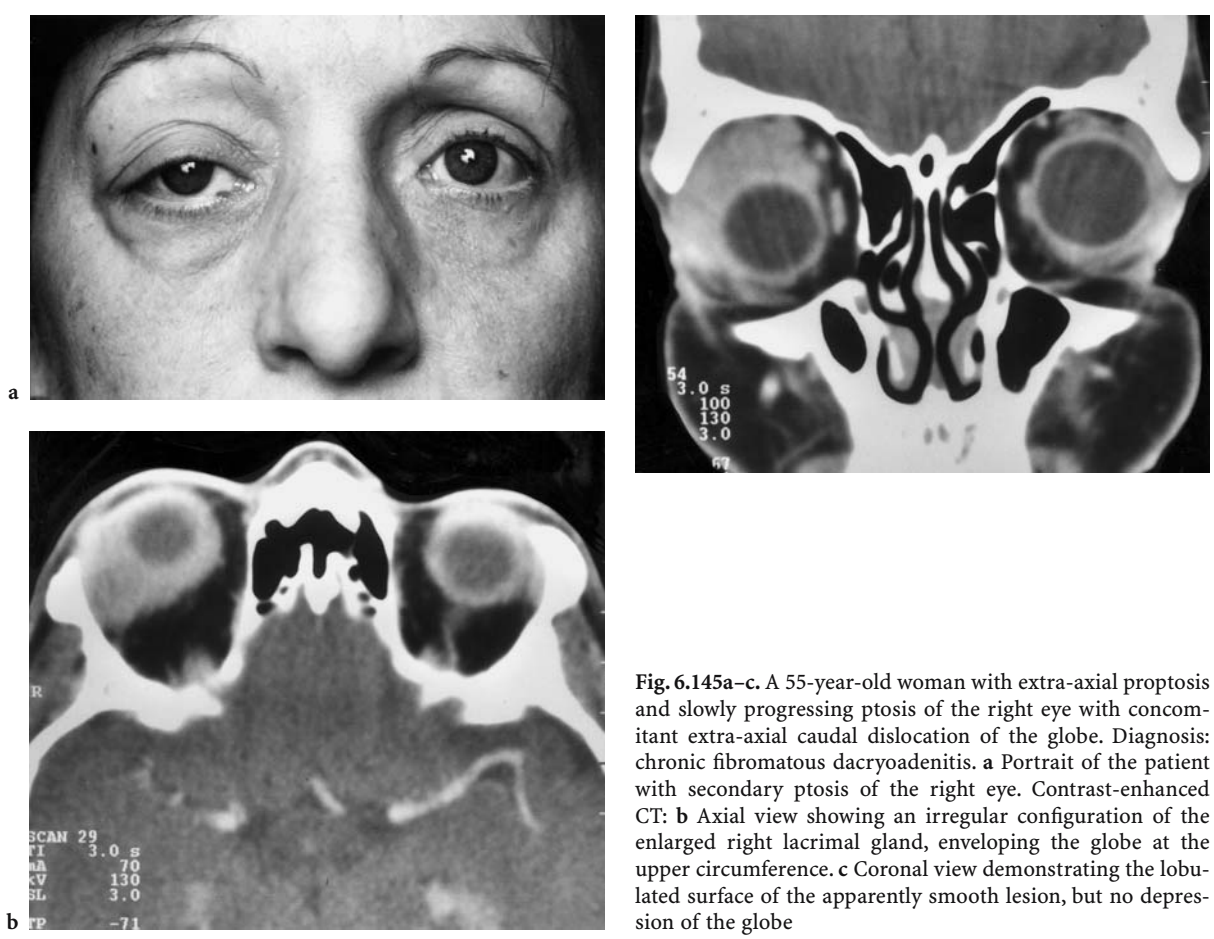

Fig. 6.145a–c. A 55-year-old woman with extra-axial proptosis and slowly progressing ptosis of the right eye with concomitant extra-axial caudal dislocation of the globe. Diagnosis: chronic fibromatous dacryoadenitis. **a** Portrait of the patient with secondary ptosis of the right eye. Contrast-enhanced CT: **b** Axial view showing an irregular configuration of the enlarged right lacrimal gland, enveloping the globe at the upper circumference. **c** Coronal view demonstrating the lobulated surface of the apparently smooth lesion, but no depression of the globe

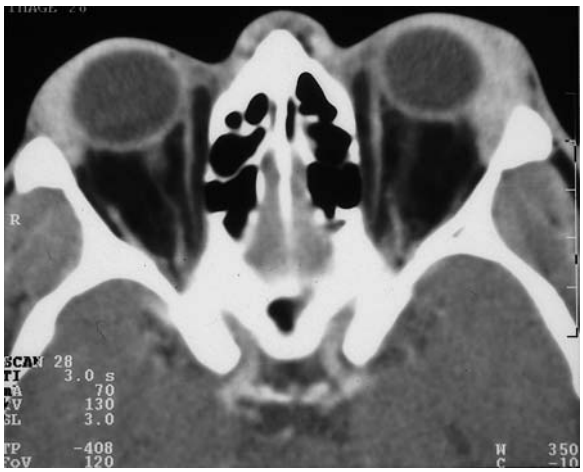

Fig. 6.146. A 36-year-old man with proptosis and enlargement of both lacrimal glands for the past 3 months. Diagnosis: Sjögren syndrome. Axial CT, demonstrating the bilateral lacrimal gland enlargement

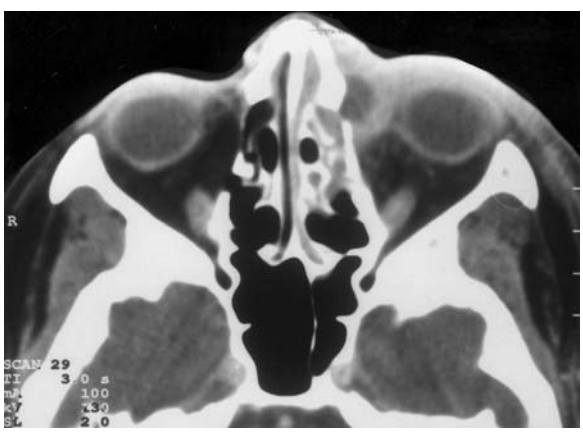

a

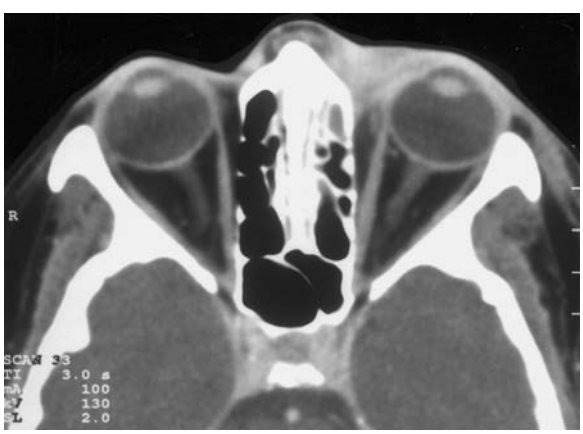

b

Fig. 6.147a,b. A 43-year-old woman with painful swelling and redness of the left medial orbital region, and known lacrimal duct stenosis. Diagnosis: abscess-forming dacryocystitis of the left eye. Axial contrast-enhanced CT: **a** necrotic cyst in the region of the lacrimal point. **b** Preseptal swelling of the medial orbital tissue with slight dislocation of the left globe

Although a relatively common, treatable disorder, an imperforate valve of Hasner may prevent tear drainage and lead to dacryostenosis (McCormick and Linberg 1988). Lacrimal gland cysts (which may arise from any lobe or remainder of ectopic lacrimal tissue) are rare lesions, becoming evident in adult life. They may develop into dacryops or ductal cysts as a result of chronic inflammation, infection, or trauma (Brownstein et al. 1984; Eifrig et al. 2001).

Since the term dacryoadenitis is used to describe all lacrimal gland inflammations, they can be characterized as acute or chronic diseases.

Dacryocystitis may also occur in an acute or chronic form and is generally caused by superinfection with normal conjunctival flora, resulting from stagnation of lacrimal drainage in the sac due to an obstruction (Figs. 6.147, 6.148) (Linberg 1983). In the case of untreated obstruction, dacryocystitis may progress or resolve by spontaneous fistula formation, either externally into the orbit or sinus, or back into the nasolacrimal duct distal to the obstruction (Fig. 6.149) (Casper et al. 1993).

Dacryocystography represents contrast filling of the lacrimal duct after cannulation of the inferior lacrimal punctum and is the method of choice in the diagnostic management of suspected stenosis or obstruction of the lacrimal drainage system (Fig. 6.149) (Pereira et al. 1997). Dacryocystography is identified in the presence of epiphora, suggesting a mechanical obstruction of the lacrimal drainage; it may be of traumatic, tumorous, or inflammatory origin (Becker 1986). Dacryocystography defines the level of any obstruction, whether complete or incomplete. As it is able to determine the cause of the obstruction, it guides the surgeon in managing the problem (Becker 1986; Kassel and Schatz 1996). In combination with CT, the relationship between the nasolacrimal drainage system and the surrounding soft-tissue and/or bony structures is better seen (Fig. 6.149), in addition to providing the possibility of three-dimensional imaging (Kirchhof et al. 2000). MRI has limited applications but is useful to differentiate fluid from solid masses within the lacrimal sac and to define tumor extension from the sac to the duct, as well as in anatomic regions outside them (Weber et al. 1996c). Acute or chronic inflammatory residues (Figs. 6.148, 6.149) account for the majority of lacrimal sac and/or duct obstructions, followed by posttraumatic lesions and tumors. In the majority of cases, the last mentioned constitute carcinoma of nasal sinus origin, but malignant tumors of the lacrimal drainage system in the form of transitional cell carcinoma may occur (Fig. 6.150).

(Text continues on p. 182)

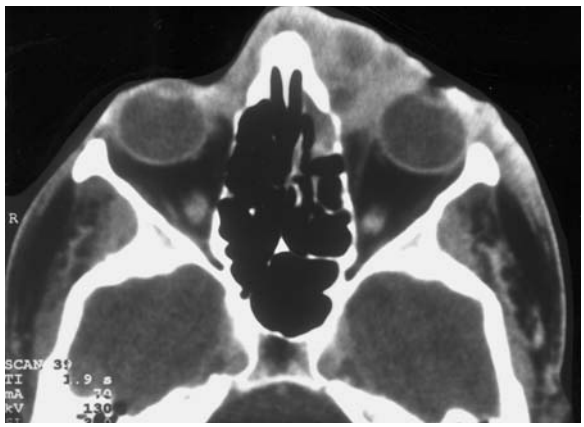

a

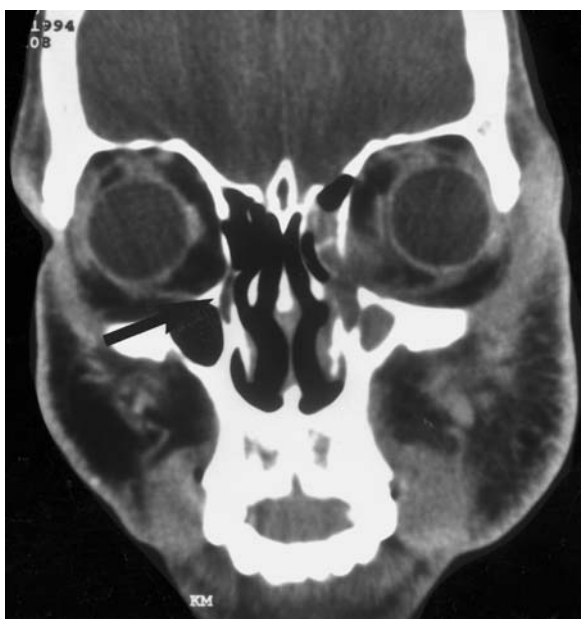

b

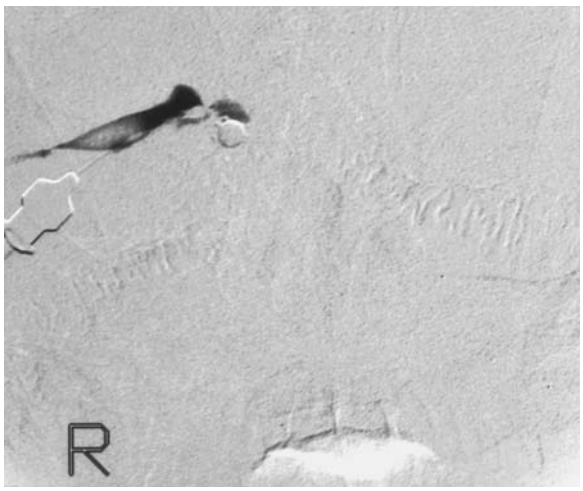

a

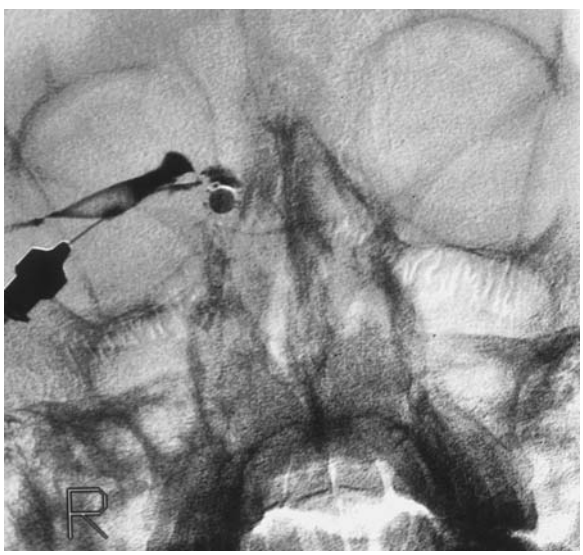

b

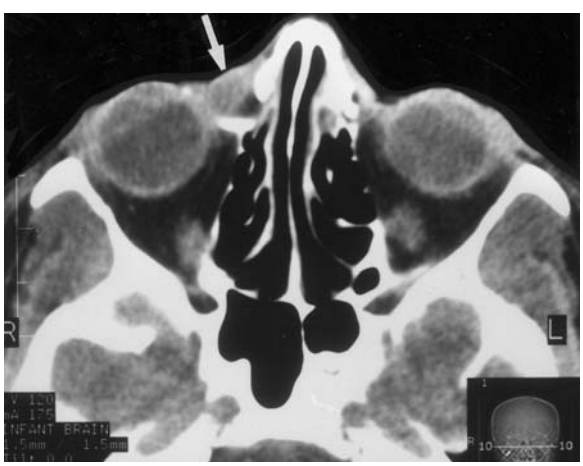

c

Fig. 6.148a,b. A 36-year-old man with acute inflammation of the left face, chronic dacryocystitis persisting for 3 months, and putrid exudation of the left lacrimal point. Diagnosis: chronic dacryocystitis with preseptal orbital and facial phlegmon. Contrast-enhanced CT: **a** axial view with inflammatory, partly necrotic infiltration of the inferior, medial, extraconal space in the region of the nasolacrimal duct. Note the presence of tissue in the rostral left ethmoid, but attenuated medial muscle and tendon. **b** Coronal view visualizing widening of the entrance and the left nasolacrimal duct (compared with the right [*arrow*]) due to inflammation, extending to the adjacent ethmoid cell. Note inflammation of the subcutaneous fat of the left cheek

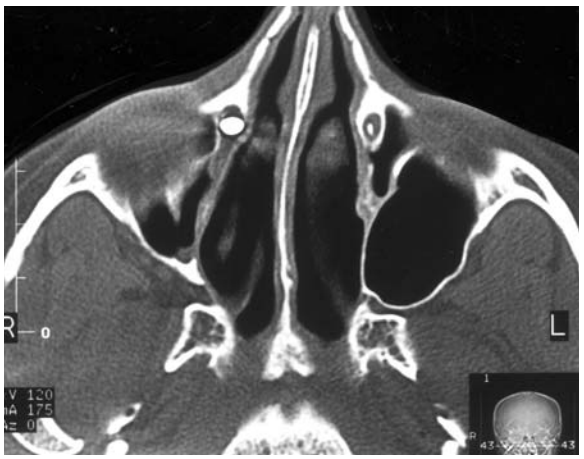

d

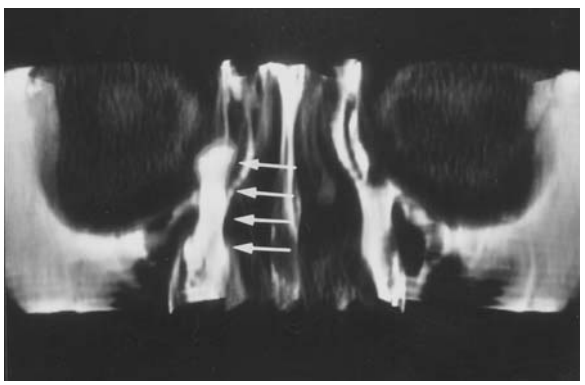

e

Fig. 6.149a–e. A 23-year-old woman with recurrent inflammation of the lacrimal point of the right eye and increased lacrimation. Diagnosis: blocking of the lacrimal sac by a mucosal fragment and chronic fibrosing inflammation. **a** Digital dacryoangiography of the right eye, demonstrating a contrast stop at the proximal lacrimal duct caused by a round X-ray-dense formation. **b** Corresponding view showing bone superposition, making the presence of a mucosal fragment with a dense structure more likely. **c** Postangiographic axial CT, demonstrating the mucosal fragment in the medial orbital angle at the level of the lacrimal point (*white arrow*), and a dorsal contrast level. **d** Axial CT at the level of the nasolacrimal duct, identifying contrast material in a poststenotic, dilated canal distal of the stenosis, and confirming the outlet function of the mucosal fragment. Compare with the normal diameter of the left lacrimal duct (dacryoangiography not shown).e 2D-reconstruction, showing poststenotic dilation of the right nasolacrimal duct (*small white arrows*)

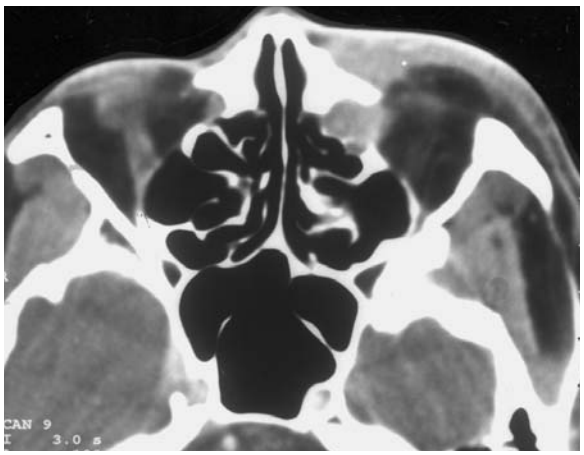

a

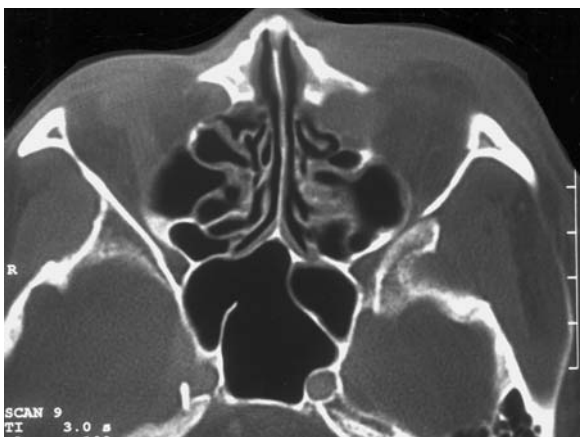

b

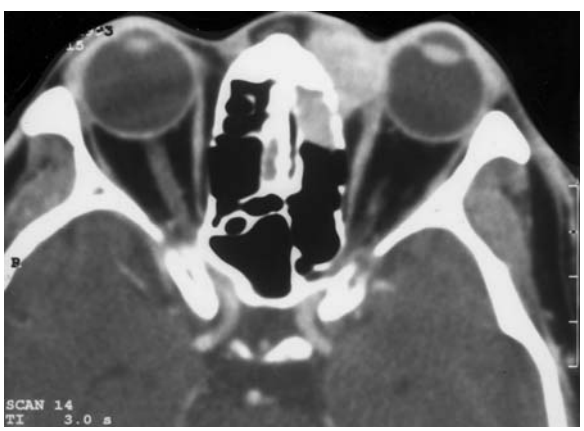

c

Fig. 6.150a–c. A 46-year-old man with chronic inflammation of the left lacrimal point. Diagnosis: lymphoepithelial tumor of the lacrimal duct. Axial contrast-enhanced CT: **a** View of the inferior orbit, where in addition to a subcutaneous, solid tumor of the medial inferior lid, widening of the left nasolacrimal canal, filled with solid tumor mass, is observed. **b** Corresponding bone window, demonstrating the difference in the diameter of the nasolacrimal canal and decalcification of the surrounding maxillary bone. **c** Axial view of the center of the orbit. The largest part of the tumor mass extends preseptally, compressing and dislocating the left globe; a definite differentiation of infiltration of the tendon of the left medial rectus muscle is not possible (not confirmed by surgery)

6.3.5 Traumatic Lesions

The variety of traumatic orbital lesions is manifold, but certain orbital fractures occur with greater frequency, i.e., fractures of the orbital floor and medial walls (lamina papyracea), than roof, lateral wall fractures or complex orbital rim fractures (Mauriello et al. 1999).

Biplanar high-resolution CT is the imaging modality of choice in the evaluation of orbital traumatic lesions (see also Sect. 6.1.4.2). As the medial and lateral walls are best seen in the axial plane, the orbital roof and floor are optimally visualized on coronal images. Spiral CT enables not only rapid examination, reducing motion artifacts in uncooperative patients, and avoiding slice-by-slice misregistration, but also secondary 2D- and 3D-reconstructions (Fig. 6.151) (Lakits et al. 1998; Mauriello et al. 1999). MRI is required in evaluating vessel injuries, to determine if soft-tissue injuries mandate operative correction, or if the differentiation of edema or hematoma is needed (Fig. 6.152). Furthermore, it is a useful method in the detection of nonmetallic foreign bodies (Rothman 1997; Kleinheinz et al. 1998; Mauriello et al. 1999).

Blow-out fractures represent isolated fractures of the orbital floor without involvement of the rim (Converse and Smith 1960). As a result of a sudden increase in intraorbital pressure from a traumatic impact to the orbital soft tissues, the thin orbital floor and the medial wall (the fragile lamina papyracea) expand and displace outward (Figs. 6.153, 6.154). A fine network of fibrous septa that functionally unites the periosteum of the orbital floor, the inferior fibrofatty tissues, and the sheaths of the inferior and oblique rectus muscles may be entrapped in a number of ways between these bone fragments, leading to restricted ocular motility (Fig. 6.152). In addition, ischemia, hemorrhage, and edema of the injured muscles present with diplopia, not always demanding surgical intervention (Koornneef 1979; Lyon and Newman 1989; Harris et al. 1998). The so-called "hanging drop" represents a small local hematoma at the fracture site (Figs. 6.152, 6.155). The inferior bony displacement causes a net increase in orbital space, resulting in enophthalmos (Fig. 6.156) (Casper et al. 1993; Mauriello et al. 1999).

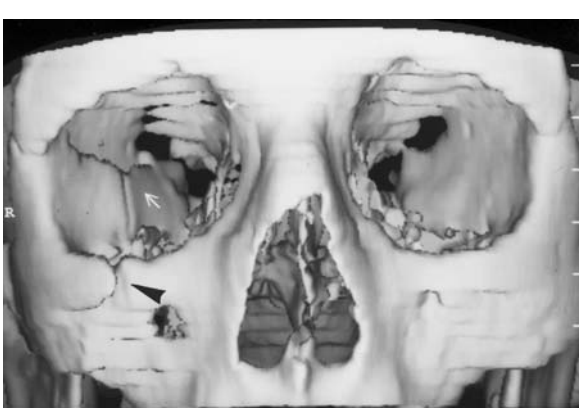

Fig. 6.151. A 54-year-old man with facial injury after a car accident. Diagnosis: orbital wall fracture. CT 3D-reconstruction: this image modality enables a lucid view of the fracture extending from the lateral right wall (white arrow) to the frontozygomatic suture and the orbital floor (*arrowhead*). (With permission of Müller-Forell and Lieb 1995b)

Isolated medial wall fractures of the lamina papyracea are less frequently identified, but may be diagnosed indirectly as orbital emphysema, since direct communication from the nasal sinuses to the orbital soft tissues may be present. The patients typically present with a sudden increase in lid swelling after sneezing or blowing the nose (Fig. 6.157) (Casper et al. 1993).

Orbital roof fractures account for only approximately 5% of all facial fractures (Flanagan et al. 1980). Although the roof itself is thin, the superior orbital rim is a strong, broad, and well-supported orbital wall that can only be fractured by severe blunt trauma with high impact (Casper et al. 1993). Frequently, the frontal sinus and/or frontal bone (Fig. 6.158) may be involved, with the possibility of the development of pneumocephalus and/or associated intracranial injuries with or without CSF leakage (McLaughlin et al. 1982; Messinger et al. 1989).

The lateral orbital wall rarely fractures alone. It is anatomically unique in that it is not only partially bordered by a sinus, but is composed of tough zygomatic bones that rarely fracture alone and are associated with Le Fort type injury (Casper et al. 1993; Mauriello et al. 1999). Combined fractures involve the zygomaticofrontal suture superiorly, the zygomatic arch laterally, and the zygomaticomaxillary suture inferomedially (Mauriello et al. 1999). As a consequence of blunt trauma, a ruptured vessel with subperiosteal hematoma may be responsible for acute vision loss (Fig. 6.159), demanding emergency surgical decompression, in order to restore visual acuity.

(Text continues on p. 287)

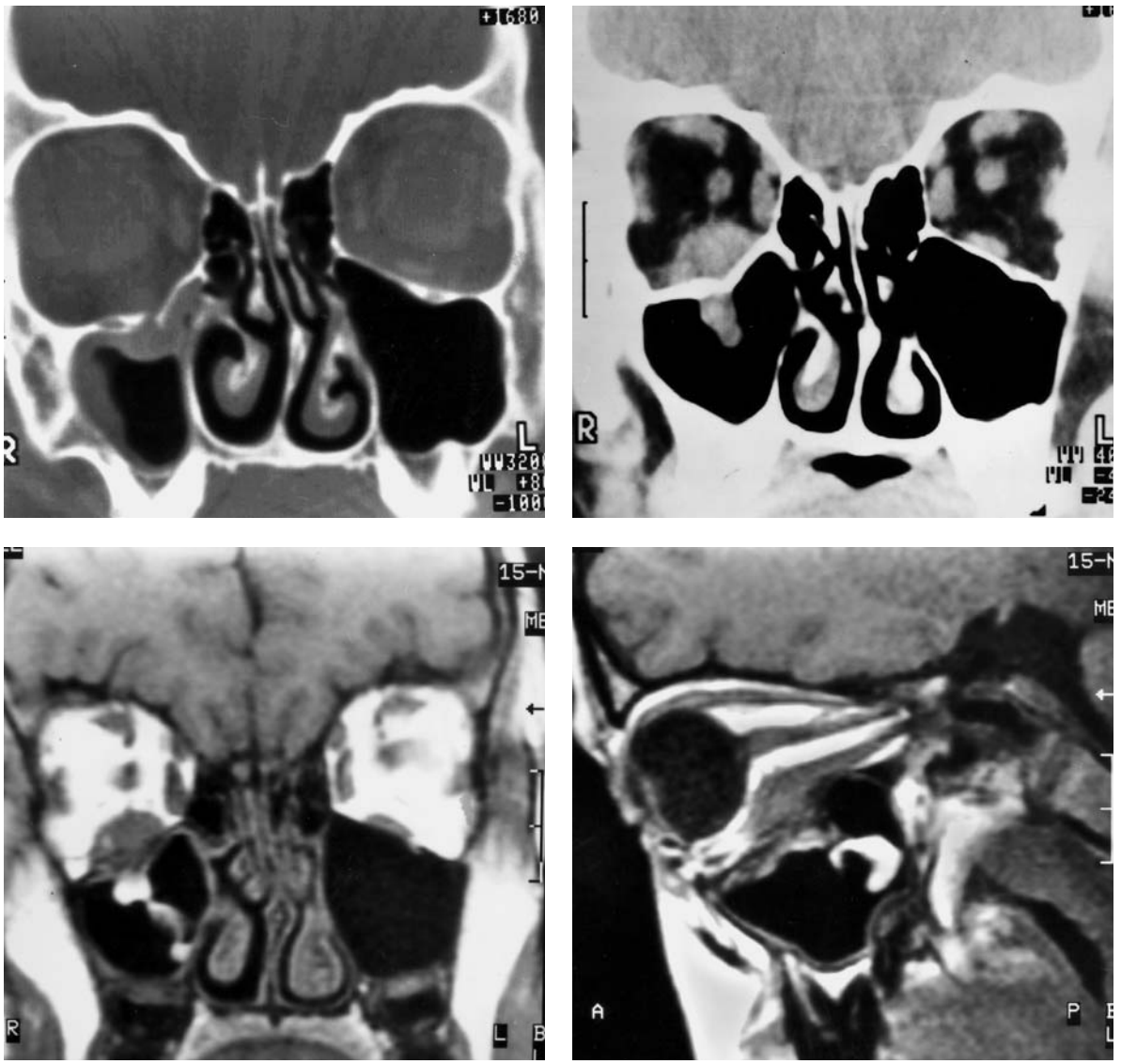

Fig. 6.152a–d. Follow-up of a 14-year-old boy with state after a bicycle accident. Diagnosis: fracture of the orbital floor. CT: **a** Coronal view in bone window with dislocated fragment medial to the infraorbital canal, typical sign of a "hanging drop", and accompanying hematosinus of the maxillary sinus. **b** The patient developed double vision when looking downward 2 days after operative reconstruction of the orbital floor. The corresponding CT does not yield differentiation between a postoperative intramuscular hematoma and edema in the thickened inferior rectus muscle. T1-weighted native MRI: **c** Corresponding image demonstrates normal signal intensity of the inferior rectus muscle, confirming the presence of intramuscular edema. Note the tissue differentiation of an additional hematoma with a bright signal seen at the orbital roof when compared with **b**. **d** Sagittal view demonstrates residual dislocation of the orbital floor with incarceration of the inferior rectus muscle. (With permission of Müller-Forell and Lieb 1995b)

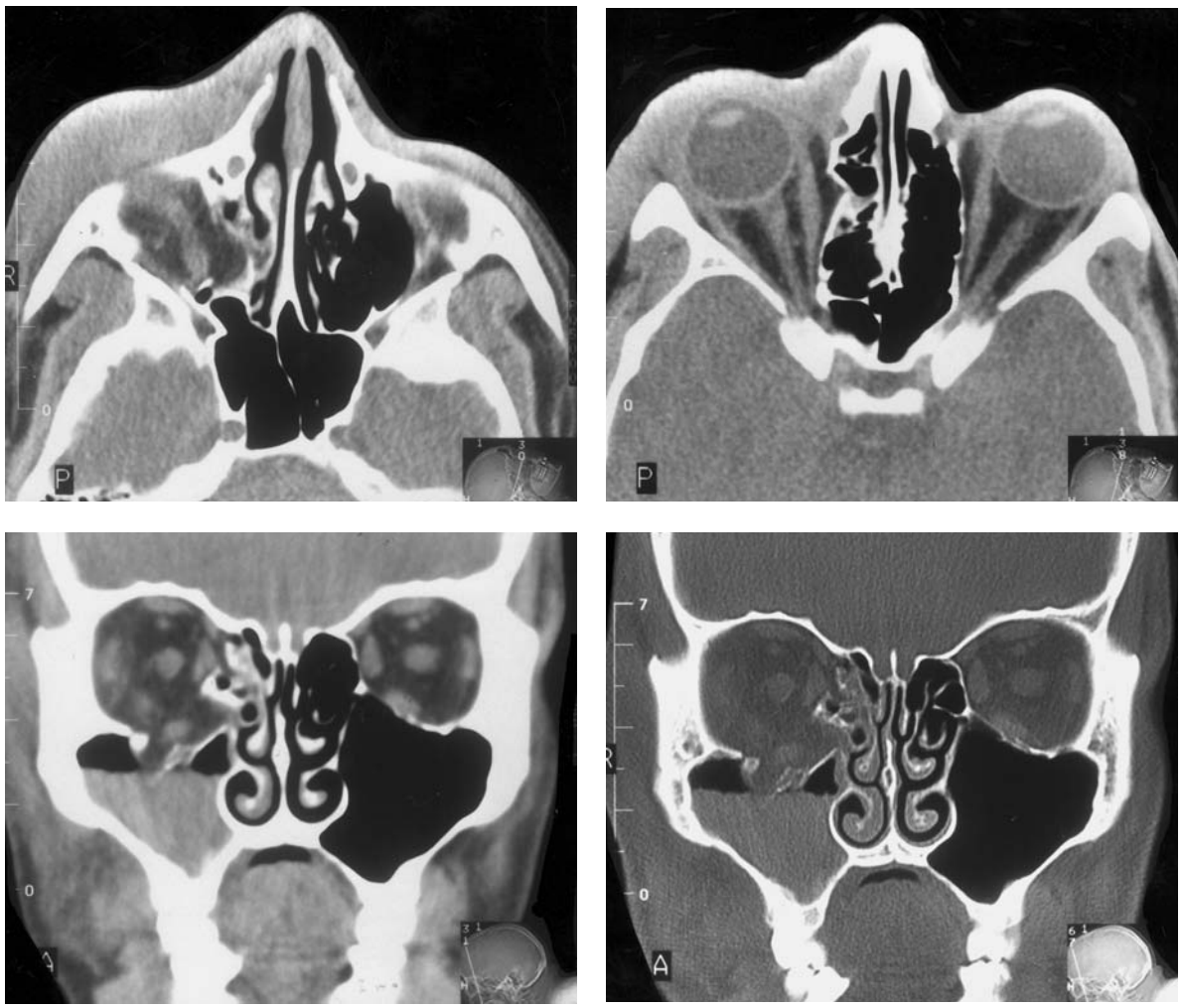

Fig. 6.153a–d. A 34-year-old man with monocle hematoma of the right eye and face after a fist fight. Diagnosis: fracture of the medial and inferior orbital wall. CT: **a** Axial view of the inferior orbit with cutaneous swelling and caudal dislocation of the inferior rectus muscle. Note the irregularity of the interior medial orbital wall. **b** Axial medial orbital view, demonstrating an intact orbital septum and retrobulbar space. Note the medial impression of the medial orbital wall. **c** Coronal view showing the fracture with dislocated fragments of both the orbital floor and the ethmoidal wall. Note the fluid level of the right maxillary sinus, corresponding to a hematoma. **d** Corresponding view in bone window

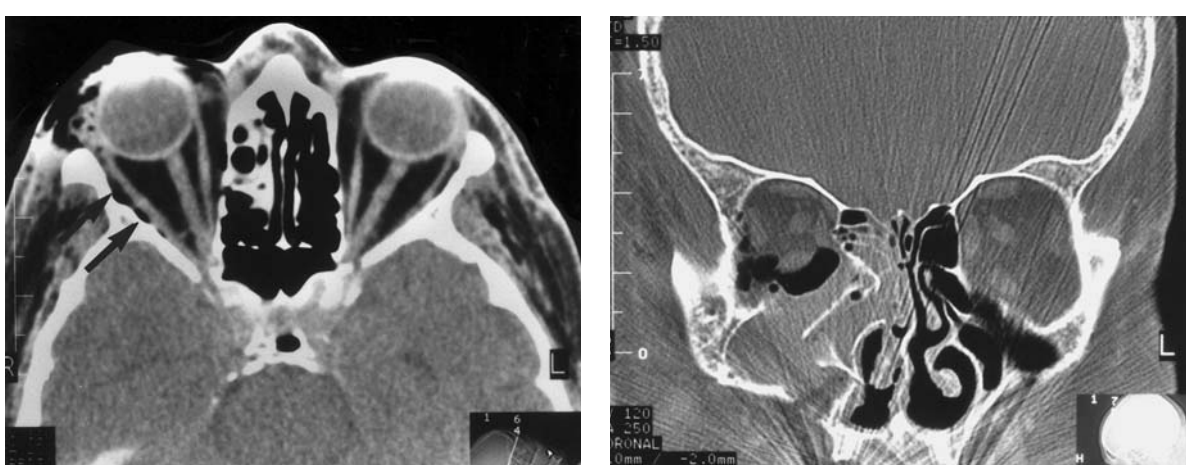

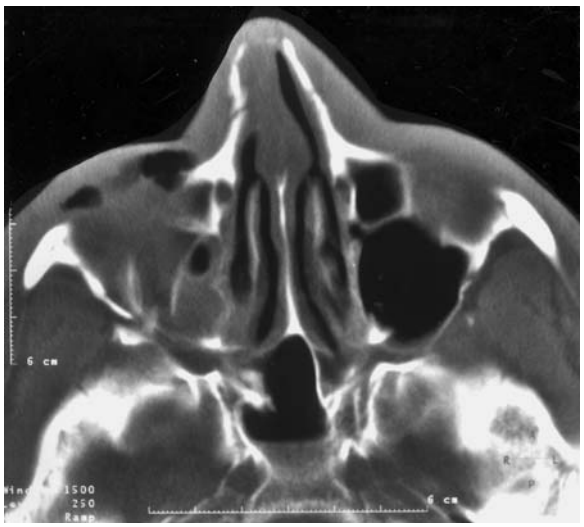

a

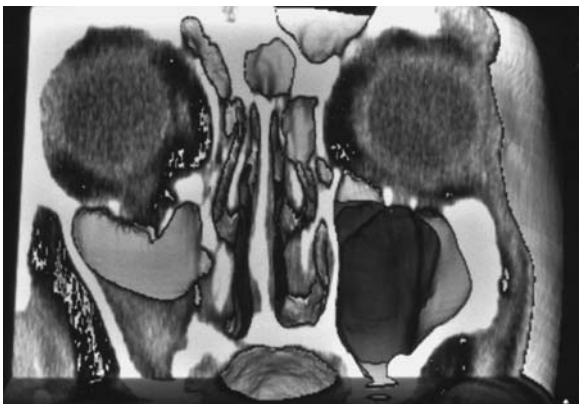

b

Fig. 6.155a,b. A 29-year-old unconscious man with head trauma after a car accident. Diagnosis: fracture of the orbital floor. CT: **a** Axial view in bone window at the inferior orbit with an irregular configuration of the right maxillo-orbital transition and subcutaneous air inclusion, in addition to a fractured ipsilateral nasal bone. **b** Corresponding 3D-reconstruction with superimposed soft tissue, demonstrating the extent of fragment dislocation

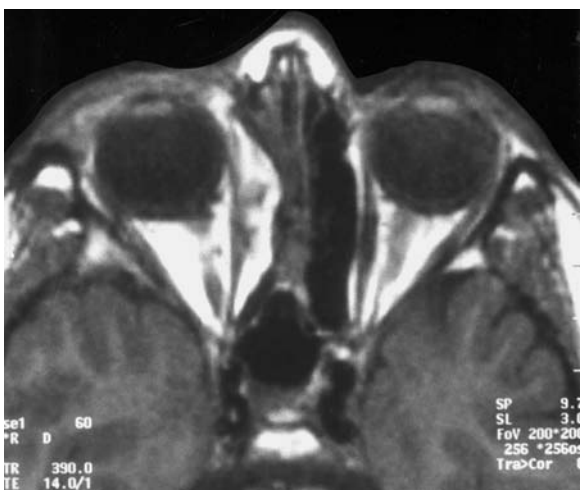

a

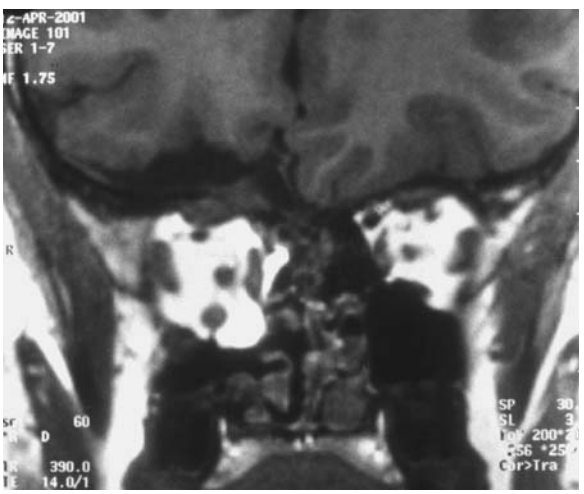

b

Fig. 6.156a,b. A 10-year-old boy with enophthalmos of the right eye, which developed several months after severe facial trauma. Diagnosis: state after orbital floor fracture with posttraumatic enophthalmos. T1-weighted native MRI: **a** Axial view with slight enophthalmos of the right globe and fat prolapse into the right ethmoidal cell, representing a posttraumatic residual. **b** Coronal view, demonstrating additional fat prolapsing into the maxillary sinus as a result of orbital floor dehiscence

◁ **Fig. 6.154a,b.** A 53-year-old man with complete vision loss of the right eye after a car accident. Diagnosis: orbital floor fracture and orbital emphysema. CT: **a** Axial view with some air inclusion in the lateral extraconal space (*arrows*) as well as in the pre- and postseptal region; no significant protrusion or lesion of the optic nerve. **b** Coronal view in bone window with superior visualization of air inclusions, especially in the inferior orbit. Further aspects identified include a fracture of the orbital floor with dislocation of a fragment into the maxillary sinus and extraconal emphysema caused by a fracture of the lamina papyracea; note an additional fracture of the maxillary sinus floor with superiorly dislocated fragment. (With permission of Müller-Forell 1998)

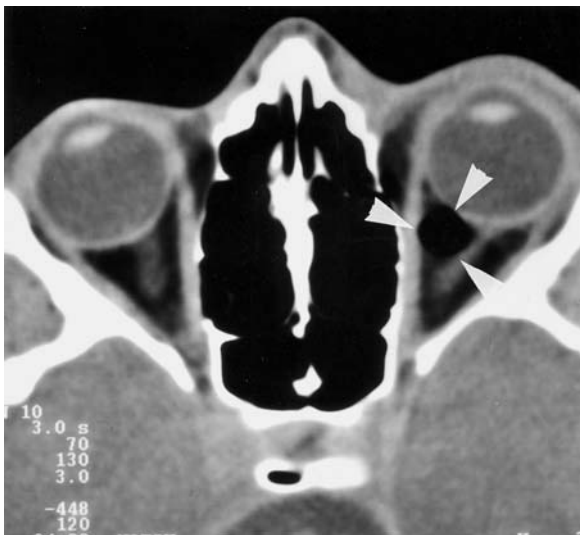

a

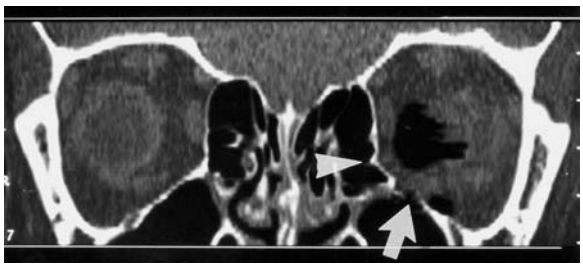

b

Fig. 6.157a,b. A 14-year-old boy after blunt orbital trauma. Diagnosis: blow-out fracture. HR-CT: **a** Axial view: despite the slightly swollen conjunctiva, a retrobulbar, intraconal emphysema is seen medial of the optic nerve (*white arrowheads*). **b** Coronal reconstruction demonstrating a small fracture of the medial orbital floor (*white arrow*) and a fracture of the lamina papyracea (*white arrowhead*), the cause of the orbital emphysema. (With permission of Müller-Forell 1998)

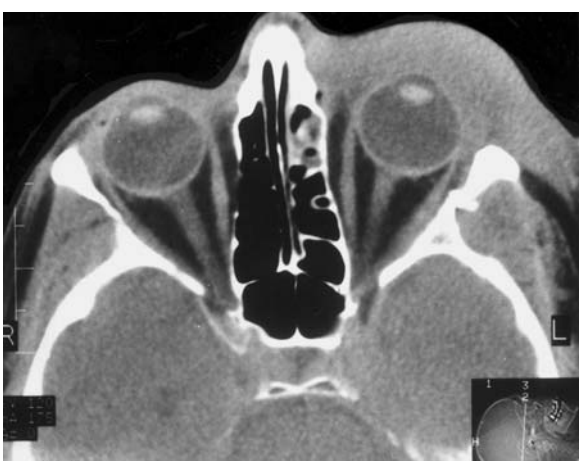

a

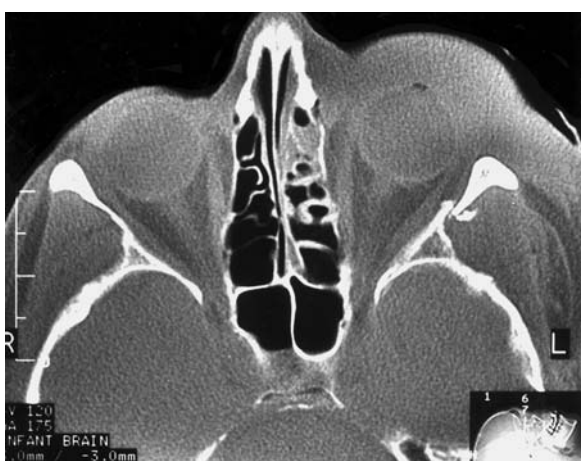

b

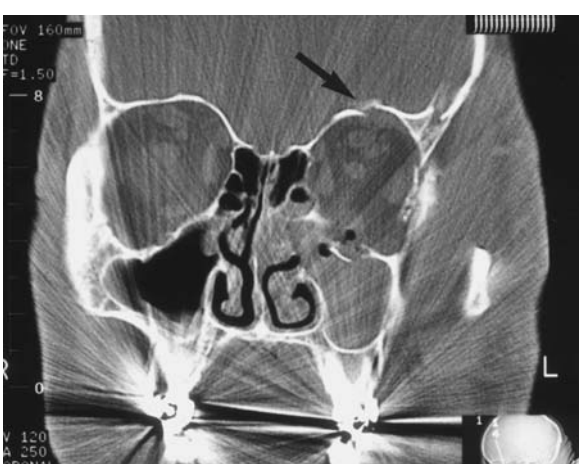

c

Fig. 6.158a–c. A 52-year-old man presenting with a swollen lid after a sudden fall; indication for CT was the exclusion of a retrobulbar hematoma. Diagnosis: fracture of all orbital walls, small superior subperiosteal hematoma. CT: **a** Axial view with extensive swelling of the lid and conjunctiva, no retrobulbar hematoma, irregularity of the lateral orbital wall at the spheno-zygomatic suture. **b** Corresponding bone window clearly demonstrating the dislocated, fragmented fracture. **c** Coronal view (bone window) showing fractures of all orbital walls (lateral, floor, lamina papyracea, and roof), and a small subperiosteal hematoma at the orbital roof (*arrow*)

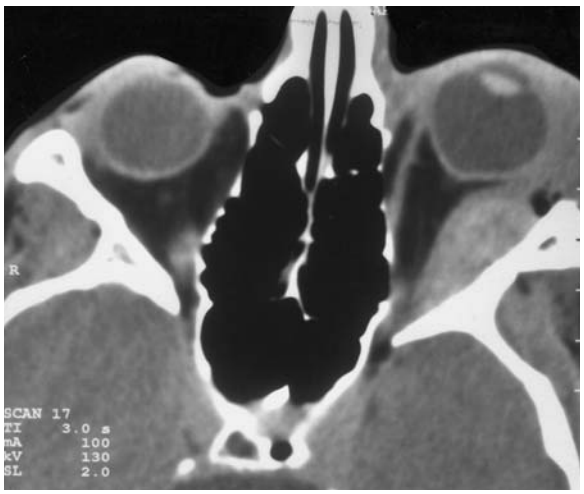

a

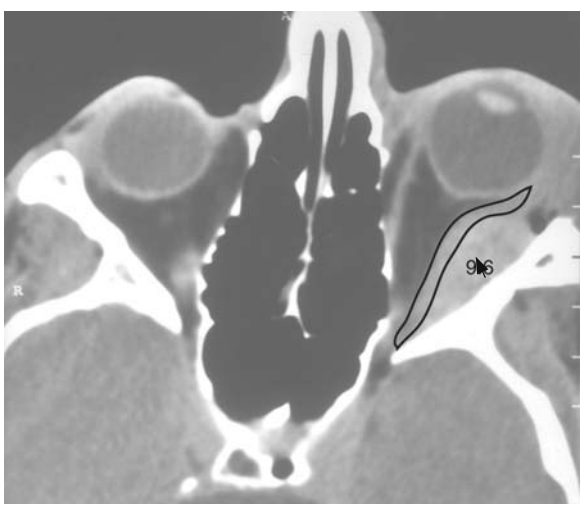

b

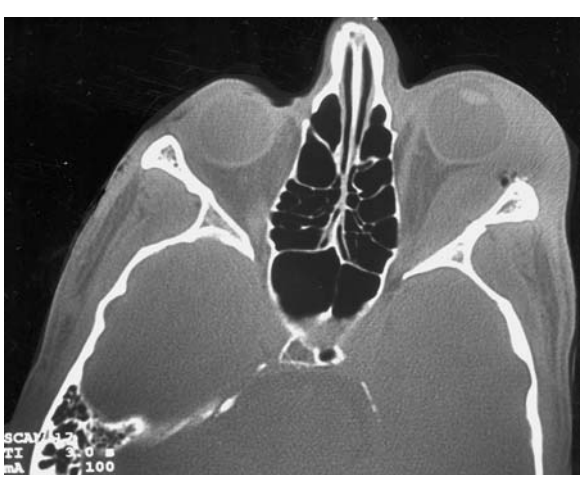

c

Fig. 6.159a–c. A 24-year-old man with acute vision loss of the left eye after a car accident (no seat belts!); vision loss did not resolve after emergency decompression (canthotomy). Diagnosis: extraconal retrobulbar hematoma. Axial CT: **a** slightly hyperdense mass (hematoma) in the left extraconal space with medial dislocation of the (hypointense compared with hematoma) lateral rectus muscle. **b** Corresponding diagram. 9.6 = lateral rectus muscle **c** Corresponding bone window (larger field of view, FOV) with superior visualization of air inclusions

6.3.6 Miscellaneous

6.3.6.1 Craniosynostosis (e.g., Crouzon Syndrome)

Craniosynostosis is divided into primary and secondary forms, with primary craniosynostosis referring to premature fusion of one or more cranial sutures due to a developmental error. Secondary synostosis refers to premature closure resulting from other causes, such as intrauterine compression, effects of teratogens, or lack of brain growth (Cohen 1987; Barkovich 2000). Another classification defines syndromic craniosynostosis as accounting for about 15% of cases and associated with other abnormalities of the body, and nonsyndromic forms in the remaining 85% (Chumas et al. 1997) of patients. Syndromic craniosynostosis includes a variety of inherited syndromes with abnormal development of the face and skull, often in conjunction with other anomalies of the brain and body. In some autosomal dominant craniosynostotic syndromes, the site of mutation of chromosome 10 in FGFR2 genes is found (Hollway et al. 1997). These include among others Apert syndrome (acrocephalosyndactyly) with syndactyly of hands and feet, Pfeiffer syndrome with a malformed enlarged thumb and big toe, soft-tissue syndactyly, and Crouzon syndrome. Craniofacial dysostosis – Crouzon syndrome – may serve as an example of these syndromes, where the early closure of variable synostosis in combination with maxillary hypoplasia and shallow orbits presents with proptosis, bifid uvula, or cleft palate (Casper et al. 1993; Barkovich 2000).

In most patients with craniosynostosis, only one suture is involved, but 20%–25% are cases of multisutural syndromes (Chumas et al. 1997). The most common fusions are coronal and sagittal, followed by the lambdoid suture, the latter leading to additional Chiari I malformation with a small posterior fossa (Barkovich 2000). In Crouzon syndrome, proptosis with prolapse of the globes in front of the eyelids is the result of flattened orbits, leading to compromised corneal coverage and damage to the optic nerve from excessive stretching (Fig. 6.160) that demands surgical management. Plain films show characteristic findings, but modern imaging should include not only MRI, which might demonstrate additional brain anomalies, but also three-dimensional CT (Fig. 6.160) in order to understand the pathological morphology and to define the surgical approach (Zonneveld et al. 1998).

(Text continues on p. 290)

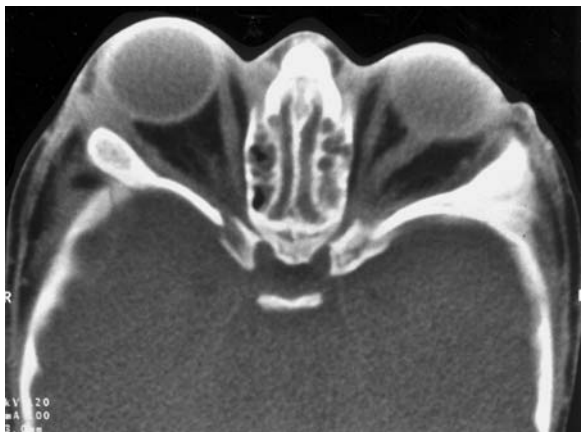

a

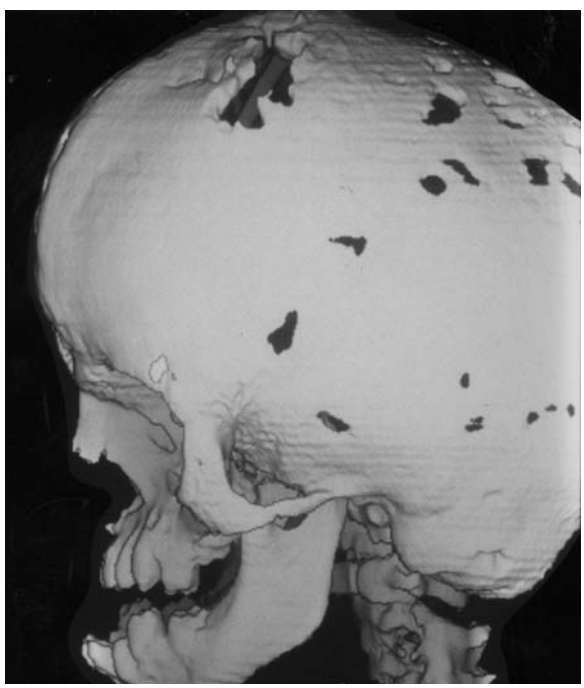

b

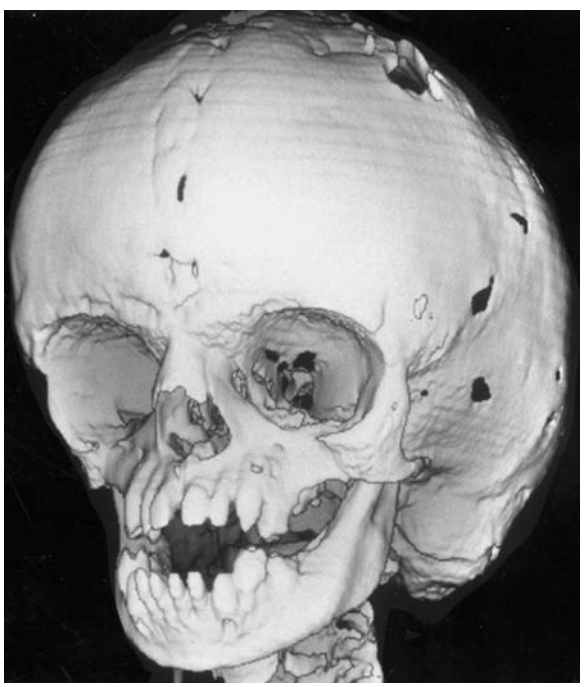

c

Fig. 6.160a–c. A 1.5-year-old girl with craniofacial dysostosis presenting with recurrent prolapse of both globes from the orbit (up to 30 times per day!). Diagnosis: Crouzon syndrome. CT: **a** Axial view, demonstrating bilateral proptosis caused by flattened orbits. **b** Lateral view of 3D-reconstruction, showing the absence of an orbital floor and extremely small maxillary bone/sinus. **c** Frontal view (3D) from the left

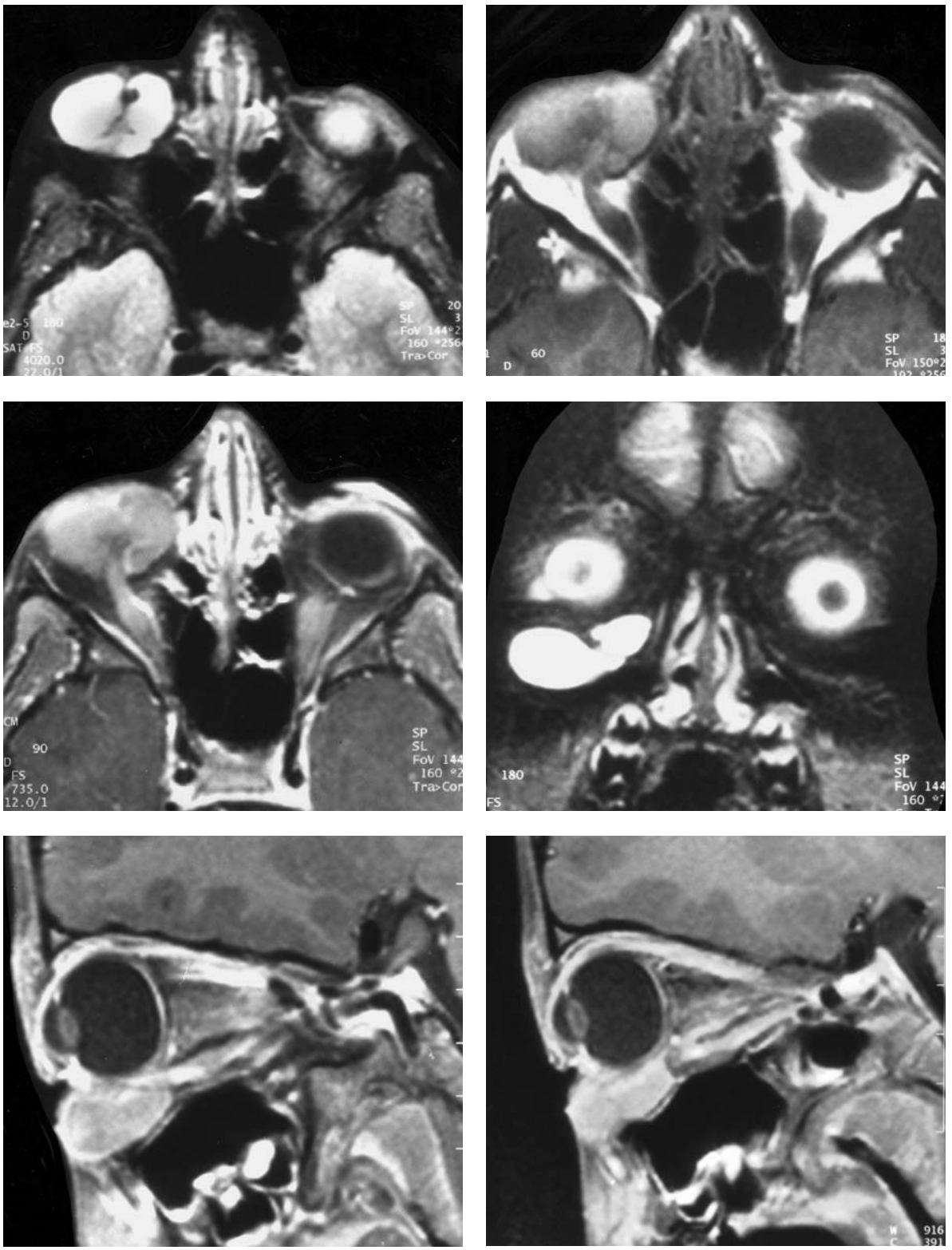

Fig. 6.161a–f. A 6-year-old boy with a livid, soft tumor of the inferior right lid. Diagnosis: hemangioma. MRI: **a** Axial T2-weighted image, showing a lobulated, hyperintense formation bilateral to the tendon of the right inferior rectus muscle. **b** Corresponding T1-weighted image, where the lesion presents with slightly hyperintense signal. **c** Corresponding contrast-enhanced (FS) image. **d** Coronal T2-weighted image demonstrating the fluid consistency of this formation. The septation is caused by the tendon of the inferior oblique muscle (confirmed by surgery). **e** Sagittal paramedian (lateral, **f** medial) T1-weighted, contrast-enhanced (FS) views with good differentiation of the malformation at the level of the inferior rectus muscle, but no definite delineation of the orbital septum

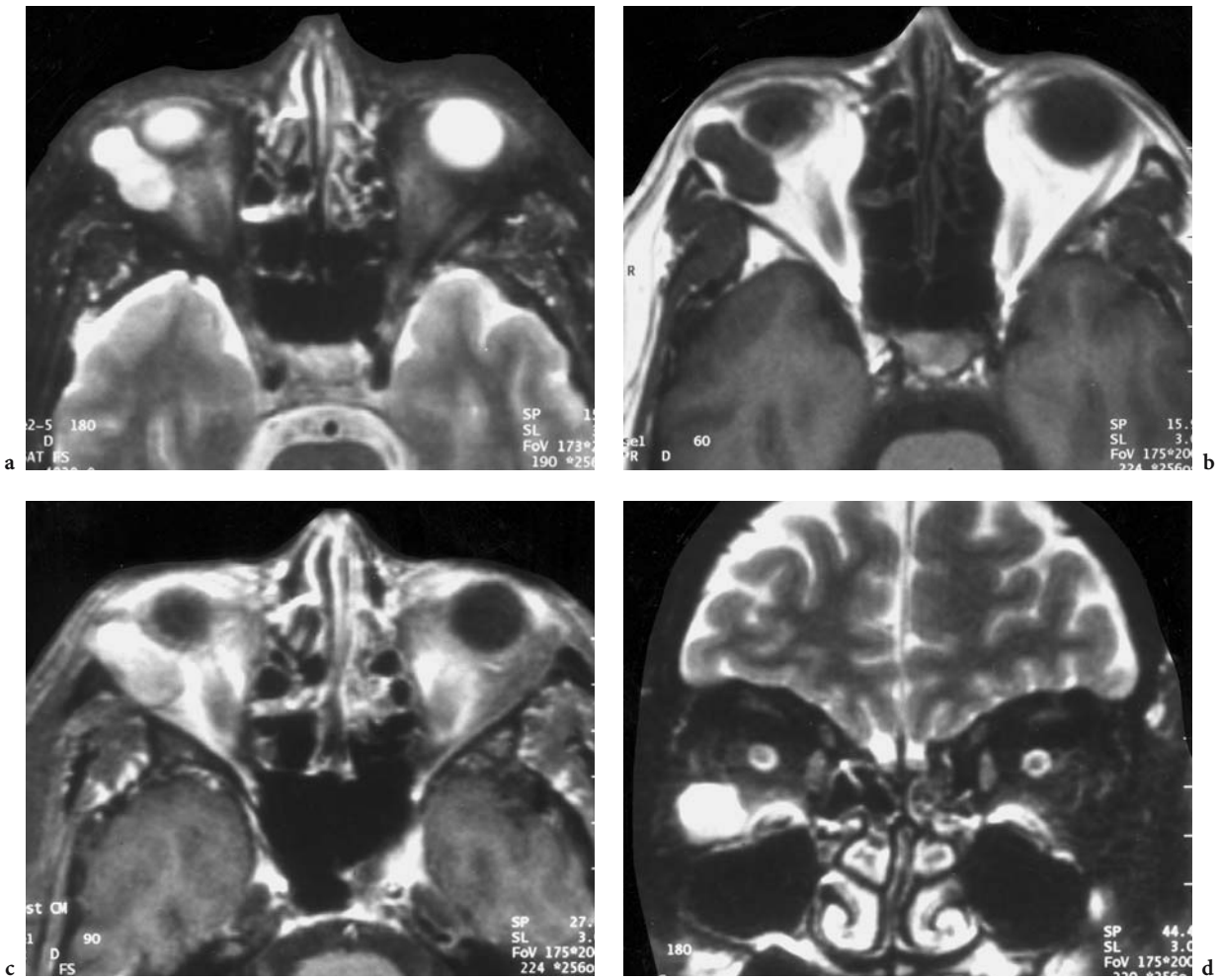

Fig. 6.162a–d. A 51-year-old woman with slowly progressing tumor of the right inferior lid. Diagnosis: hemangioma (primarily extraconal). MRI: **a** Axial T2-weighted view of the inferior orbit with sharply delineated hyperintense lesion of the inferior lateral orbit. **b** Axial T1-weighted native view of the inferior orbit with a dumb-bell-shaped, hypointense, well-defined formation lateral to the inferior rectus muscle and globe. **c** Corresponding T1-weighted (FS), contrast-enhanced view. **d** Coronal T2-weighted view visualizing the predominantly extraconal localization of the hyperintense tumor in the inferolateral orbit

6.3.6.2 Extraconal Vascular Lesions (Hemangioma)

In cases where a hemangioma occurs in the extraconal space, the capsule is not present, and the lesion extends in various ways along the orbital septum (Fig. 6.161), the lacrimal fossa (Fig. 6.162) or the lid (Fig. 6.163). Differential diagnosis for extraconal varices (Fig. 6.164) (see Sect. 6.2.2.4) or venous lymphatic malformation (Fig. 6.165) (see Sect. 6.2.2.3) might be difficult.

6.3.6.3 Rare Lesions

Orbital involvement with bony deformation/destruction in malignant sinonasal tumors is known, but extraconal deformation of the orbital apex and

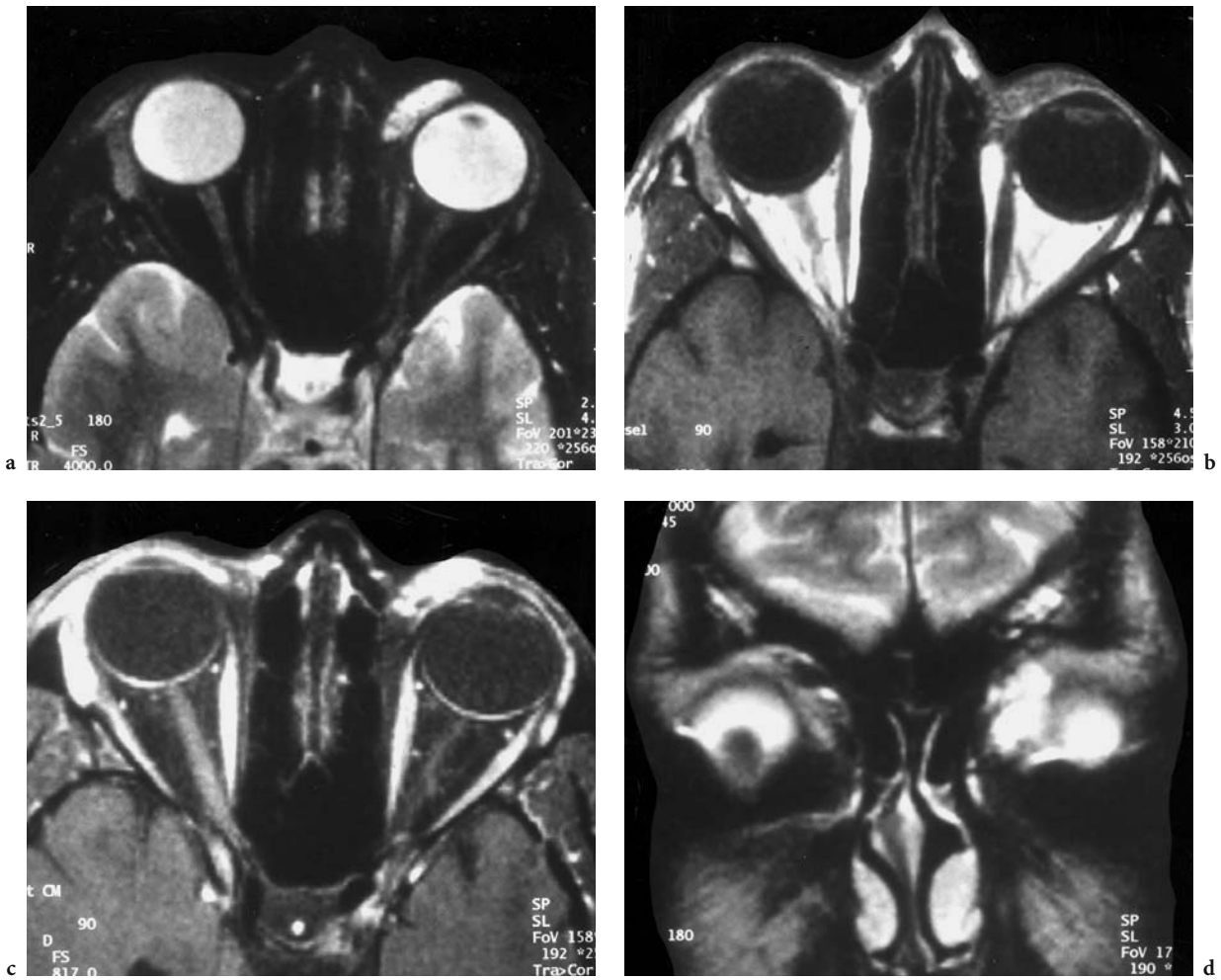

Fig. 6.163a–d. A 21-year-old woman with slowly progressing tumor of the right inferior lid. Diagnosis: hemangioma (primarily extraconal). MRI: **a** Axial T2-weighted view of the medial orbit showing a medially located hyperintense preseptal ovoid lesion. **b** Corresponding T1-weighted native view where a hypointense, well-defined formation in front of the medial rectus muscle and globe is seen. **c** Corresponding T1-weighted (FS), contrast-enhanced view with bright signal enhancement. **d** Coronal T2-weighted view with bright signal enhancement visualizing the predominantly extraconal localization of the hyperintense tumor in the superior medial orbit

nerve compression in the optic canal by an astrocytoma, a benign intracranial tumor represents an extremely rare entity (Fig. 6.166).

Another extremely rare lesion with a clinical presentation similar to Graves' disease, but with persisting proptosis and without clinical impairment, is the so-called benign lymphooid hyperplasia (Fig. 6.167), a disease mainly seen in dermatology (Gilliam and Wood 2000). Imaging demonstrates homogeneous tumors with a close relationship to the peripheral branches of the trigeminal nerve, resembling neurinoma.

(Text continues on p. 298)

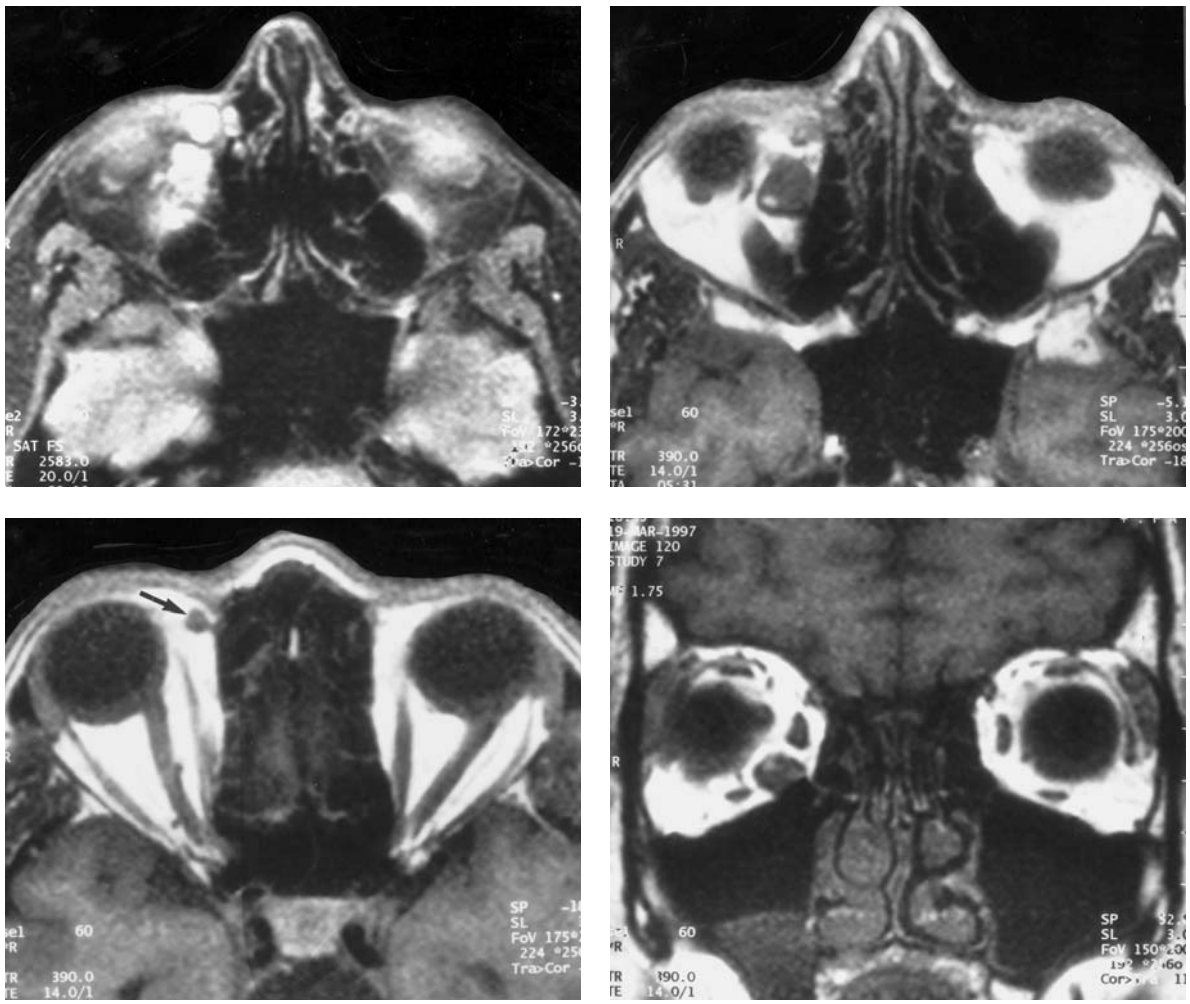

Fig. 6.164a–d. A 41-year-old woman with recurrent livid swelling in the right inferior periorbital to lid region. Diagnosis: pre- and postseptal varicosis. MRI: **a** Axial proton-weighted view of the inferior orbit with multilobulated, cystic formation in the right medial inferior orbit. **b** Axial T1-weighted view acquired a few millimeters above **a**. **c** Axial T1-weighted view at the level of the optic nerve identifying another small extraconal formation (*small arrow*). **d** Coronal view (pressure exerted) showing the most prominent of the venous enlargements on the tendinous parts of the muscle cone from inferomedial

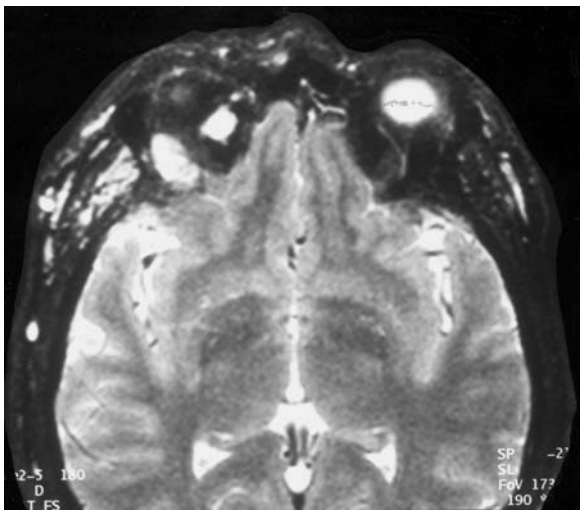

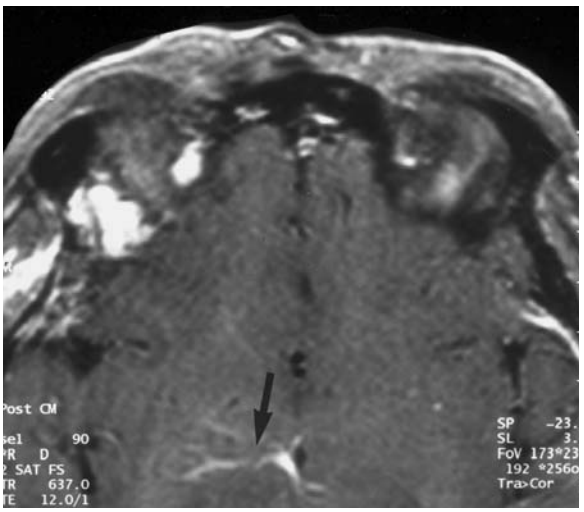

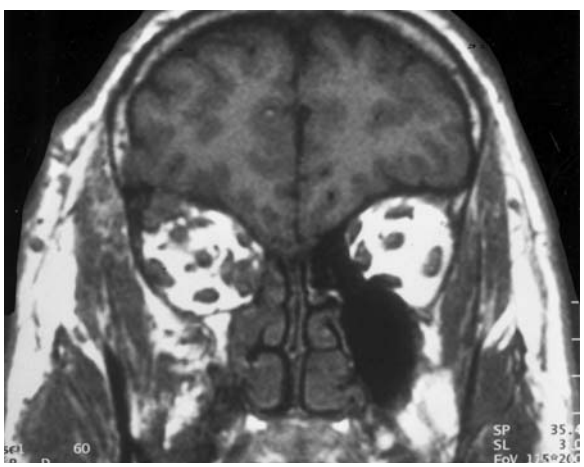

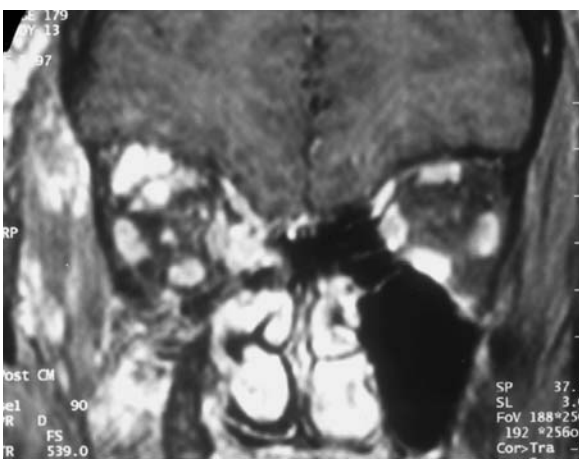

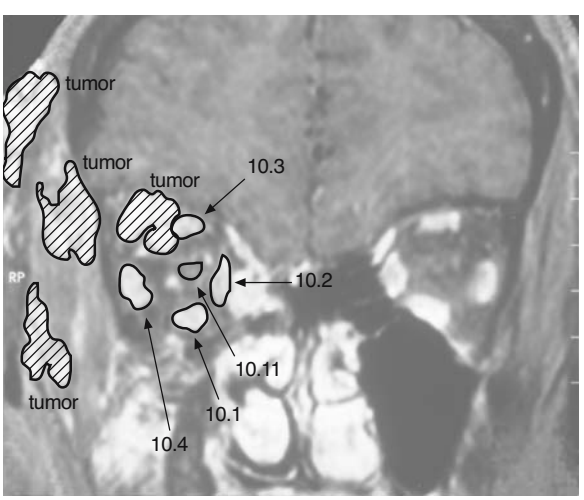

Fig. 6.165a–e. A 34-year-old man with progressing pressure and swelling of the right orbit, state after surgery for venous lymphatic malformation 15 years ago. Diagnosis: intra- and extraconal venous lymphatic malformation. MRI: **a** Axial T2-weighted view with hyperintense lesions medial and lateral of the superior rectus muscle as well as in the temporal fossa. **b** Corresponding, enlarged, T1-weighted, contrast-enhanced (FS) image. Note the intramedullary veins converging in the medial basal ganglia, corresponding to an additional DVA (*arrow*). **c** Coronal T1-weighted native image showing the lesions isointense to the muscles primarily in the extraconal space. This is observed not only in the superior but also in the medial orbit. **d** Coronal, T1-weighted, contrast-enhanced (FS), enlarged view with distinct signal enhancement of the vascular lesions also in the thickened muscles of the temporal fossa **e** Corresponding diagram. 10.1 = interior rectus muscle, 10.2 = medial rectus muscle, 10.3 = superior rectus muscle, 10.4 = lateral rectus muscle, 10.11 = optic nerve

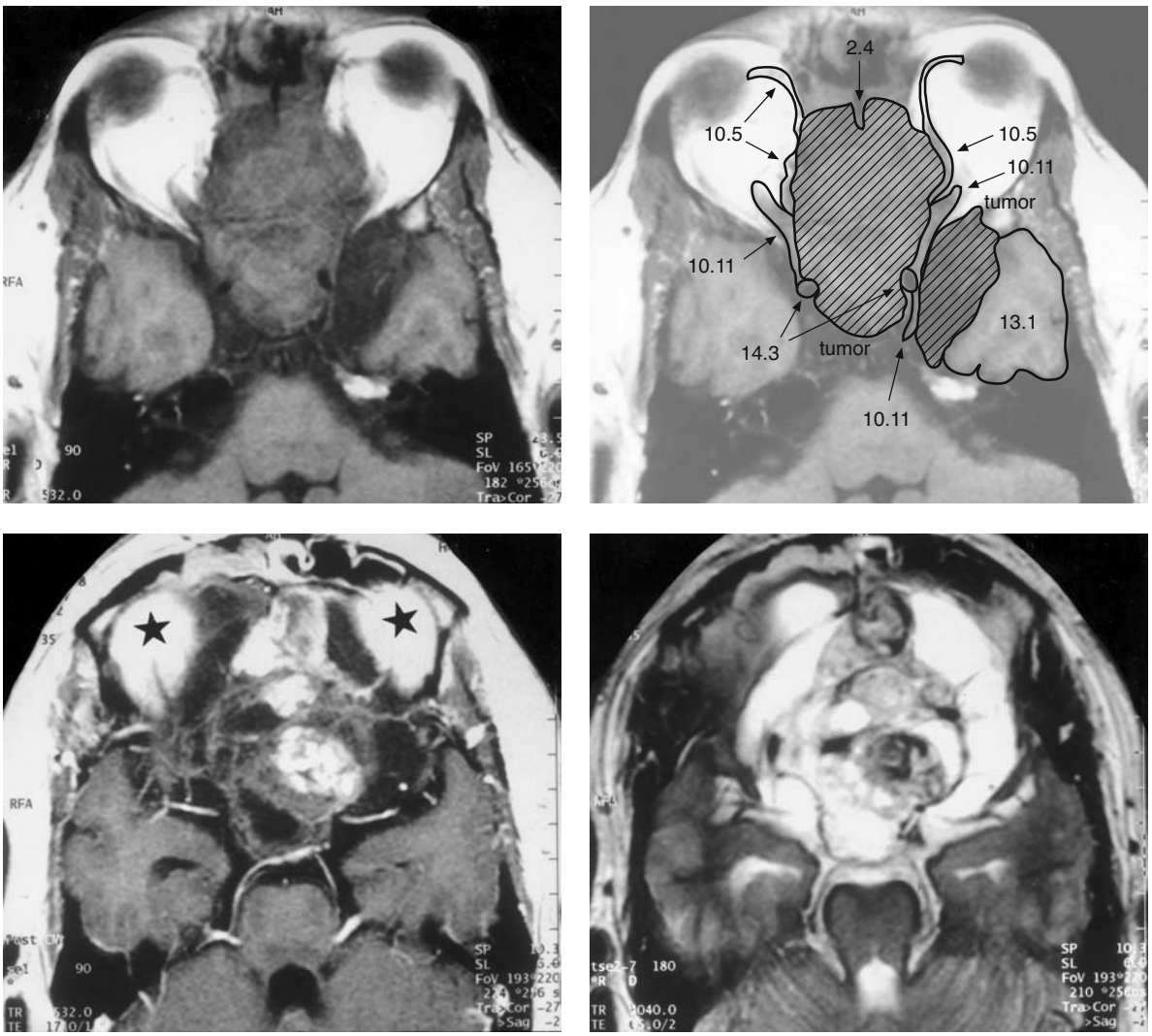

Fig. 6.166a–h. A 22-year-old man with untreated astrocytoma diagnosed when the patient was 5 years old. Known bilateral visual deficit exacerbated over 6 weeks prior to presentation, accompanied by onset of seizures. Diagnosis: astrocytoma WHO I. MRI: **a** Axial T1-weighted native view at the level of the optic canal, demonstrating an isointense solid lesion extending intrasellarly and invading both orbits with persistent pressure erosion of both laminae papyraceae. **b** Corresponding diagram. 2.4 = crista galli, 10.5 = superior oblique muscle, 10.11 = optic nerve, 13.1 = temporal lobe, 14.3 = siphon of ICA. **c** Axial, T1-weighted, contrast-enhanced view at a superior level, showing solid, enhancing tumor parts at the center surrounded by tumor cysts, occupying the entire anterior cranial fossa. Neither the optic nerve nor chiasm structures are distinguished (*stars* indicate fat in the superior orbit). **d** Corresponding axial T2-weighted image with superior demonstration of the cystiform tumor. Note the hypointense leptomeningeal layers of the brain surface, indicating the presence of chronic hemorrhage leading to superficial cerebral siderosis (without existing clinical symptomatology). **e** Midsagittal, T1-

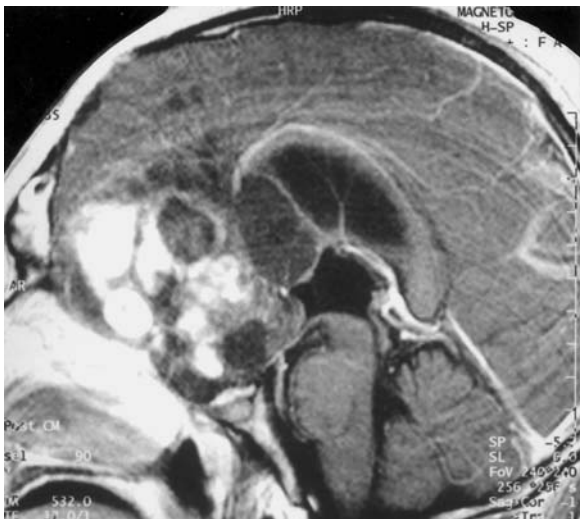

e

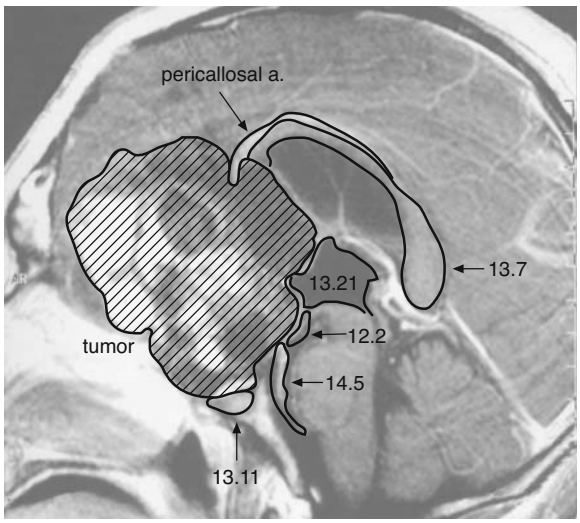

f

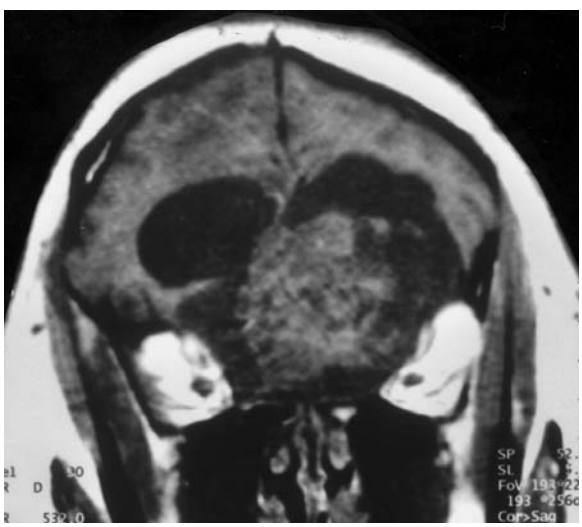

g

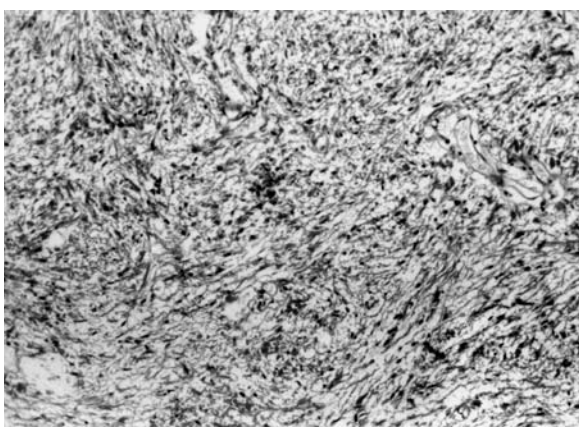

h

weighted, contrast-enhanced view, demonstrating the entire extension of the astrocytoma. The diminished chiasm can be identified by the location and configuration of the anterior recess of the third ventricle with the tumor flattened and depressed extremely along the attenuated pituitary stalk. Note the normal signal of the normal-sized pituitary gland, the depression and extension of the terminal lamina, and dislocation of the corpus callosum. **f** Corresponding diagram. 12.2 = chiasm, 13.7 = (posterior knee of the) corpus callosum, 13.11 = pituitary gland, 13.21 = third ventricle, 14.5 = (distal part of the) basilar artery. **g** Coronal T1-weighted native view with the most distinct visualization of the extraconal intraorbital extension and deformation of both orbits. Note the inferior extension of the tumor to the level of the orbital floor. **h** Histology (×280): small, uniform tumor cells with round or oval nuclei and long, fibrillary cytoplasmic processes build a loose network with only a few blood vessels. In some regions, there are many thick eosinophilic bundles (Rosenthal fibers). (Histology with permission of Dr. Bohl, Department of Neuropathology, Medical School, Mainz)

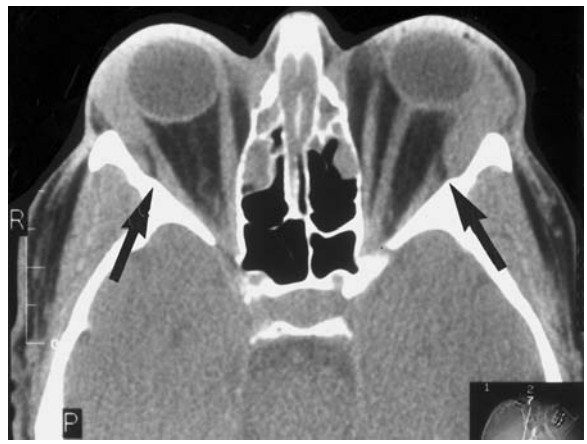

a

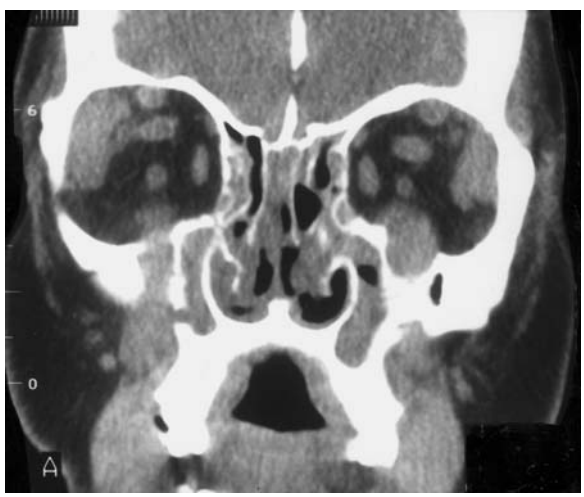

b

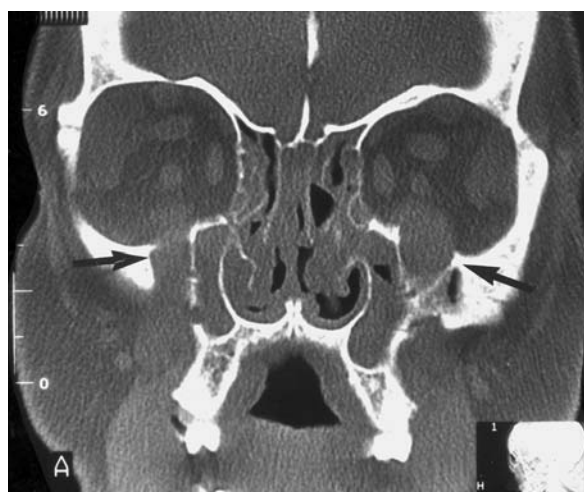

c

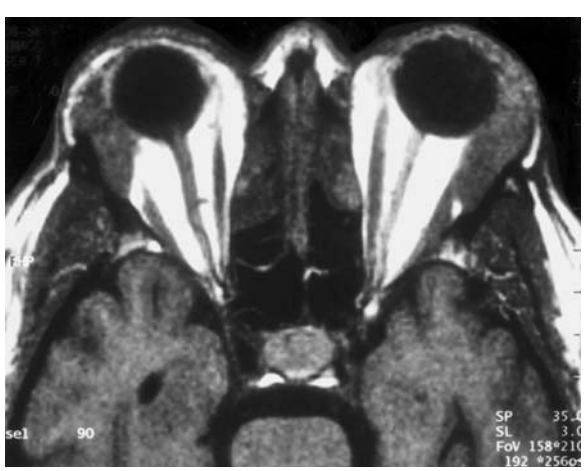

d

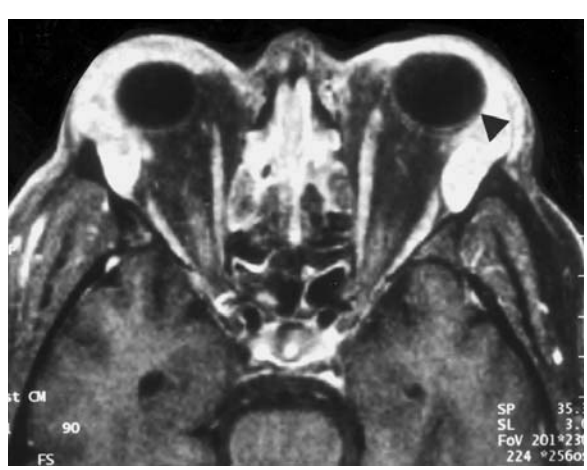

e

Fig. 6.167a–h. A 46-year-old woman with persisting bilateral exophthalmos (right: 26 mm, left: 31 mm) in the absence of other ophthalmological pathology, undergoing examination for suspected Graves' disease. Diagnosis: chronic benign lymphomatoid hyperplasia with infiltration of peripheral branches of both trigeminal nerves (*V1*: lacrimal, frontal nerve, *V3*: infraorbital nerve). CT: **a** Axial view, demonstrating the bilateral exophthalmos, and stretching of both optic nerves. Note the normal-sized external muscles and extraconal bilateral masses without distinct differentiation from the lacrimal gland; note also the small areas of intermediate extraconal fat (*arrows*). **b** Coronal view shows the extraconal location of the enlarged nerves, but no distinct differentiation of the inferior rectus muscles. **c** Corresponding bone window clearly demonstrates widening of both infraorbital foramina (*arrows*). MRI: **d** Axial T1-weighted native view, corresponding to **a**. **e** Corresponding contrast-enhanced (FS) image. The mass is characterized by homogeneous bright signal enhancement. Note the diminutive hypointense rim of the

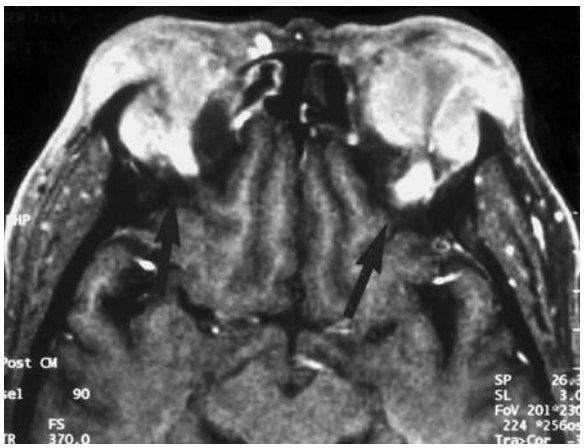

f

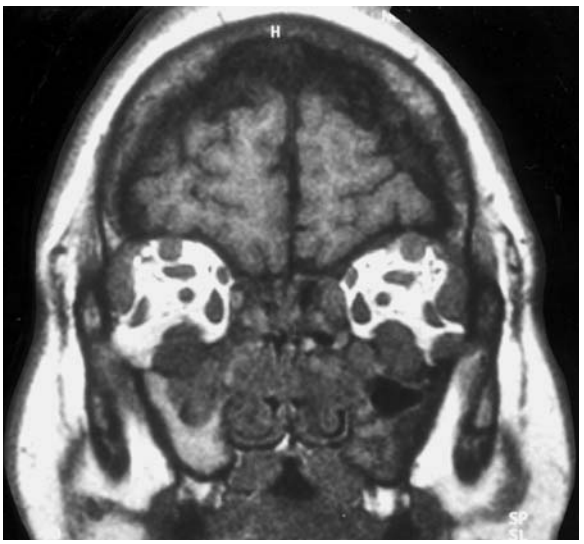

g

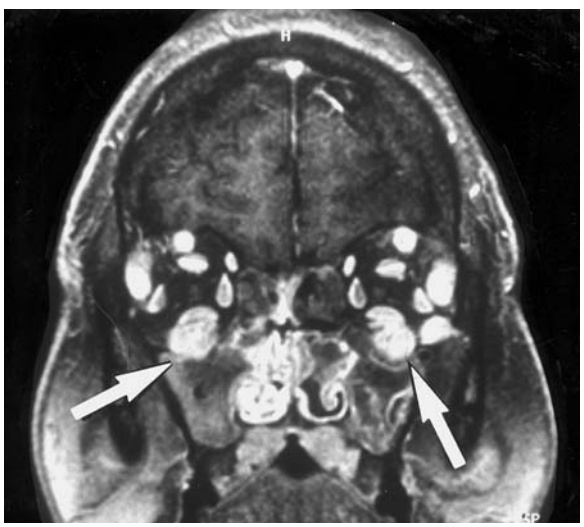

h

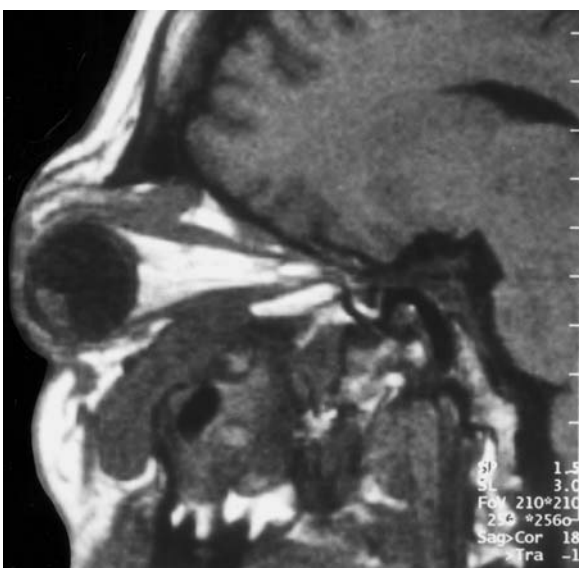

i

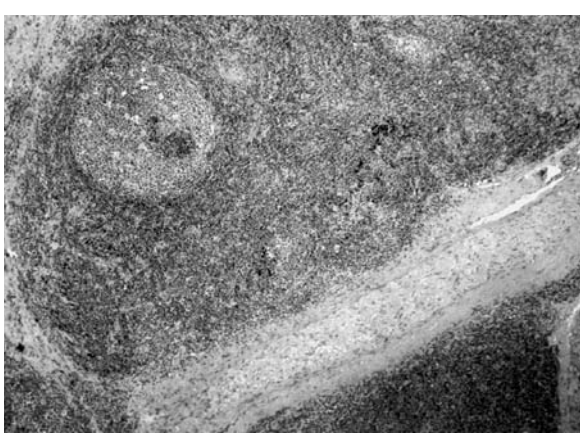

k

orbital septum, dividing the lesion from the flattened lacrimal gland (*triangle*). **f** Axial, T1-weighted, contrast-enhanced view of the upper orbit at the level of the superior rectus muscle (*arrows*) visualized behind the biconvex bilateral mass. **g** Coronal T1-weighted native view corresponding to **b** and **c**, confirming the extraconal localization. **h** Corresponding contrast-enhanced (FS) images. Note the round tumors of the infraorbital nerves (*white arrows*) located below the biconvex, normal-sized inferior rectus muscles. **i** Parasagittal T1-weighted native view of the left orbit with the entire intraorbital, intraforaminal, and extraorbital extension of the involvement of the infraorbital nerve, clearly differentiated from the inferior external muscle (part of the lacrimal nerve involvement is seen in the upper extraconal space). **k** Histology: regularly shaped lymphatic tissue with typical germ centers. A small peripheral nerve with an intact perineurium is seen crossing through the lymphatic tissue. (With permission of Dr. Bohl, Department of Neuropathology, Medical School, Mainz)

6.4 Optic Nerve

The optic nerve represents an approximately 45–50 mm long cerebral fiber tract with a diameter of 4–6 mm, covered by the three layers of the brain: the pia, arachnoidea, and dura (see Sect. 2.5). It is topographically divided into four parts. The intraocular part is located in the posterior part of the globe and does not contain a myelin sheath. Myelination starts at the lamina cribrosa, the beginning of the intraorbital segment, where the optic nerve is embedded in orbital fat. The optic nerve is surrounded by a muscular cone and tendons (Zinn's circlet) at the orbital apex and leaves the orbit proper at the optic canal, where the third part of the optic nerve begins. The optic canal represents the location of the transition of the optic nerve from its extracranial to the intracranial course. The optic canal and the dura-periosteum sheath of the optic nerve form a nonelastic osteofibrous canal where compression of traumatic or tumor origin, may cause an abrupt or slow decrease in the oxygen supply by the axons of the nerve itself, resulting in visual deficiency or complete visual loss. A differentiation of the fourth, the intracranial (prechiasmal) part of the optic nerve, is useful under conditions when pathologic lesions involve the optic nerve only in its intracranial course from the optic canal to the chiasm, which is primarily caused by adjacent tumors or by the optic nerve itself (Rauber and Kopsch 1987).

6.4.1 Tumors

6.4.1.1 Optic Nerve Glioma

Subclassified by their origin, gliomas of the optic nerve, histologically proven as (juvenile) pilocytic astrocytoma, are located intraocularly on the optic disc, intraorbital and intracranial, the latter with or without involvement of the chiasm (Hollander et al. 1999). Optic nerve gliomas are benign, slow-growing tumors of low radiation sensibility, accounting for 66% of all primary optic nerve tumors, and 4% of all orbital space-occupying lesions. They are more common than optic nerve sheath meningiomas (4:1) and have a female preponderance (Alvord and Lofton 1988; Hollander et al. 1999). Although solitary optic nerve gliomas are found, the incidence in NF1 is rather high, as 10%–38% of patients with optic nerve glioma have NF1, and approximately 50% of patients with NF1 harbor optic nerve glioma, a bilateral disease considered to be pathognomonic for NF1 (Alshail et al. 1977; De Potter et al. 1995; Hochstrasser et al. 1988; Brodsky 1993; von Deimling et al. 2000). In NF1, intraorbital tumor growth may be stable for years, but intracanalicular and intracranial growth with involvement of the chiasm, hypothalamus, and optic tracts is seen as well (Hollander et al. 1999; Barkovich 2000). Patients with NF1 may harbor additional cerebral astrocytoma, myelin vacuolization, dysplasia of the cerebral vasculature with stenosis, caused by intimal proliferation and sphenoid bone dysplasia (Aoki et al. 1989; Barkovich 2000) (see Sect. 5.4.1).

In children, the incidence of symptomatic optic pathway tumors is less than 7%, especially when the tumor is restricted to the optic nerve (Listernick et al. 1994; Barkovich 2000), but in recent studies ophthalmologic examination showed some degree of visual dysfunction in about 47% of patients (Balcer et al. 2001). It has further been observed that intracranial postchiasmal involvement was found more often in children with non-NF type 1 optic glioma than in children with NF1 (Listernick et al. 1995). Not only do those patients present symptoms earlier than those with intraorbital optic nerve glioma, they also present with a high incidence of hydrocephalus (Dutton 1994; Listernick et al. 1995). Visual impairment symptomatology includes afferent papillary defect caused by astrocytic proliferation and nerve fiber compression in about 75%, although various fibers persist over a long period of time, thus preserving vision in some cases (Goodman et al. 1975; Dutton 1994). Visual field loss is seen in 63% of patients, regardless of tumor location (Dutton 1994), while optic nerve atrophy is detected in about 59% of patients, regardless of age (Dutton 1994). Although the most prominent symptom in intraorbital optic nerve glioma is axial proptosis (94%), the discrepancy between the rather space-occupying orbital lesion and the rather discrete proptosis with only minimal motility impairment is pathognomonic (Dutton 1994).

Imaging techniques reveal an enlargement of the optic nerve without calcification but of different shapes, as it can present as tubular (Fig. 6.168), fusiform (Fig. 6.169), or lobulated, kinked, and buckled (Figs. 6.168, 6.170), the last mentioned probably due to an additional elongation (Jakobiec et al. 1984; De Potter et al. 1994). Thickening of the dura represents a perineural growth with tumor extension into the arachnoid space, highly characteristic of juvenile optic glioma (De Potter et al. 1994). Coronal CT shows the bony anatomy, the erosion and/or widening of the optic canal (Fig. 6.169), although superior contrast resolution and clear morphological demonstration of the lesion in axial, coronal, and parasagittal views makes MRI the method of choice

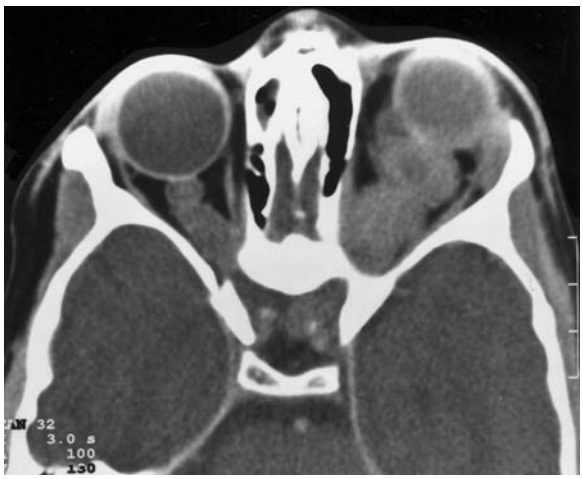

a

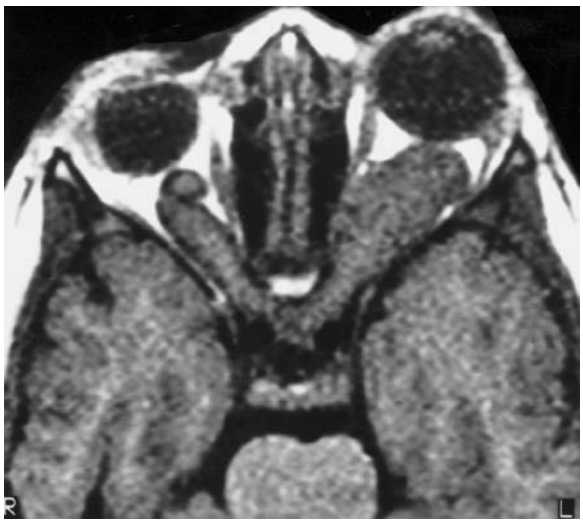

b

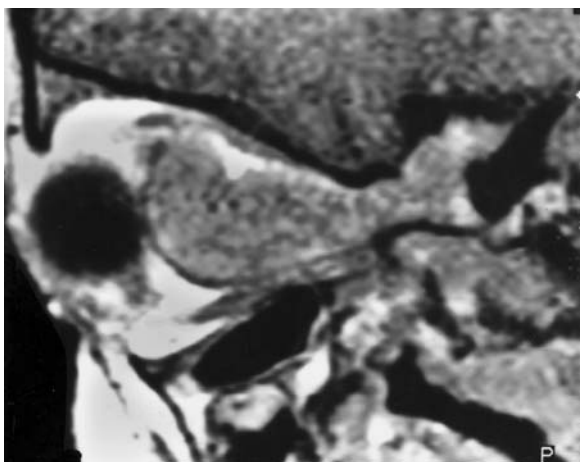

c

Fig. 6.168a–c. A 2-year-old boy with NF1. Diagnosis: bilateral optic nerve glioma. CT: **a** Axial contrast-enhanced image demonstrating bilateral tumor growth with emphasis to the left not only in the orbit, but also intracranially, distal to the dilated optic canal. MRI: **b** Corresponding T1-weighted native view. **c** Parasagittal view parallel to the course of the left optic nerve visualizing tumor growth also in the prechiasmal optic nerve. (With permission of Müller-Forell and Lieb 1995b)

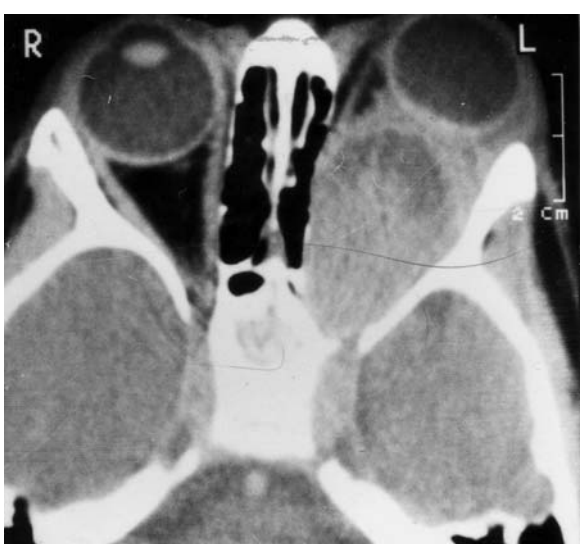

a

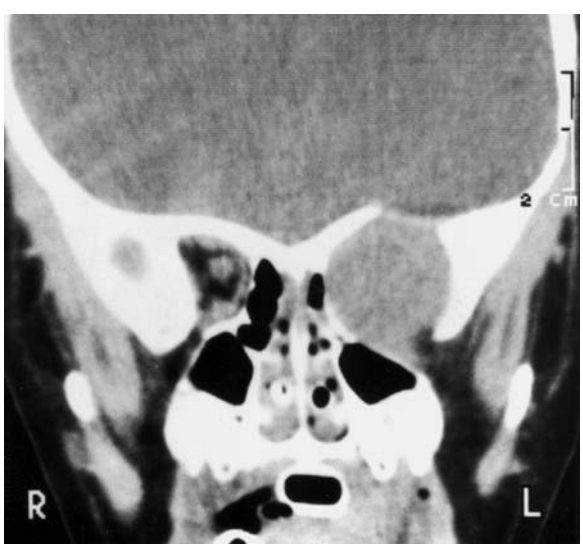

b

Fig. 6.169a,b. A 2-year-old girl with proptosis of the left eye. Diagnosis: left optic nerve glioma. CT: **a** Wide, sharply defined tumor occupying the entire orbit. Enlarged orbital diameter with depression of the left lamina papyracea and left lateral orbital wall (compared with right side), indicating slow tumor growth. **b** Coronal view showing the large diameter of the orbital apex and optic canal. The defect of the orbital roof is due to a previous operation. (With permission of Müller-Forell and Lieb 1995b)

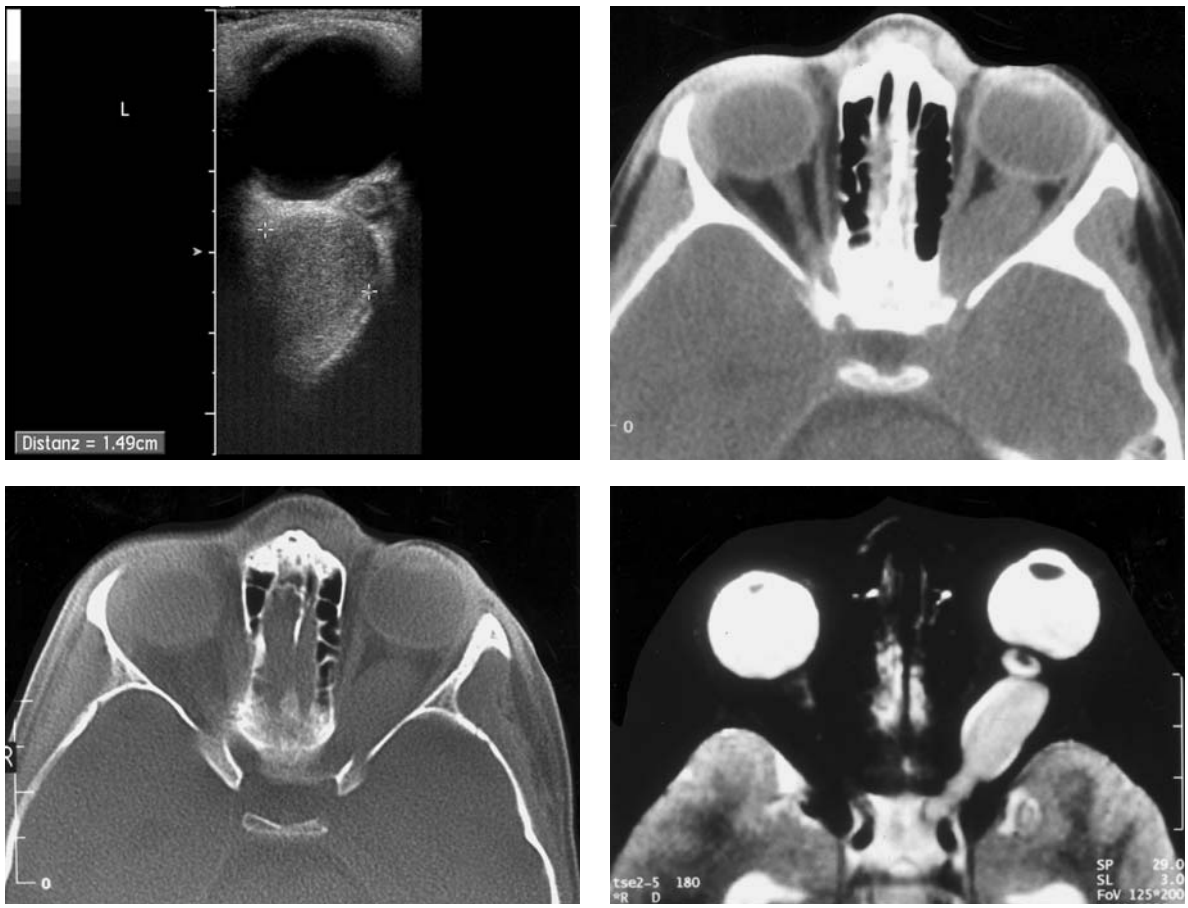

Fig. 6.170a–k. A 6-year-old boy with known NF1 and left-sided papilledema, detected on routine control of juvenile hypertonus. Diagnosis: left optic nerve glioma. **a** Ultrasound, demonstrating the thickening of the posterior part of the optic nerve (courtesy of Prof. Schumacher, Kinderklinik Mainz). Axial CT: **b** In the absence of left eye proptosis, a considerable widening of the left optic nerve sheath complex is seen. **c** Bone window at the level of the optic canal, showing its widening. MRI: **d** Axial T2-weighted view where a small hyperintense rim is seen that corresponds to the remaining arachnoid space around the optic nerve tumor, occupying the posterior two-thirds of the orbit (compare with **a**). **e** Axial, T1-weighted, contrast-enhanced view with enhancement of the tumor and demonstration of the remaining, slightly enlarged subarachnoid space (hypointensity). **f** Parasagittal, T1-weighted, contrast-enhanced view, where the extension of the glioma into the optic canal is seen (*arrow*). **g** Coronal T2-weighted view clearly showing the different diameters of the optic nerve. **h** Axial T2-weighted FLAIR view of the brain, demonstrating bilateral "hamartoma" of the basal ganglia region. Recurrence is suspected based on progressing proptosis of the left eye 6 months after initial surgery (prechiasmal amputation of the left optic nerve): **i** axial, T1-weighted, contrast-enhanced (FS) view, showing the pronounced proptosis and nearly unaffected left optic nerve glioma. **k** Coronal T1-weighted native view, demonstrating the extension of tumor into the defect of the roof of the optic canal, opened by previous surgery

in evaluating the intraorbital, the intracanalicular, and especially the intracranial extent of optic nerve glioma (Brown et al. 1987; Sartor 1992). T2-weighted images demonstrate homogeneous high signal intensity of the affected nerve in contrast to the low signal of the contralateral unaffected optic nerve (Fig. 6.170), characterizing the intraneural growth pattern with expansion of fibrovascular trabeculae by intra-axial astrocytic proliferation with little cystic degeneration (Seiff et al. 1987). The peripheral hyperintense portion surrounding the linear core of the isointense signal representing the compressed nerve characterizes the perineural growth of optic nerve glioma (Figs. 6.170, 6.171). It represents not only widening of the subarachnoid space by proliferating astrocytes (Stern et al. 1980), but also perineural arachnoidal gliomatosis, a myxoid proliferation of glial cells and blood vessels combined with arachnoidal hyperplasia, suggestive for patients with NF1 (Seiff et al. 1987; Brodsky 1993; De Potter et al. 1994). T1-weighted images should be obtained pre- and post-contrast injection, the latter with a fat suppression technique, as it best delineates subtle BBB disruption in the optic nerve itself (Figs. 6.170–6.172) and/or the chiasm (Fig. 6.171) and anterior visual pathway. The lack of

(Text continues on p. 304)

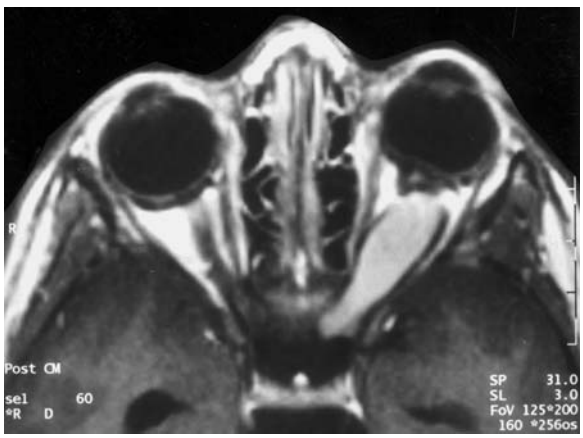
Post CM
sel 60
*R D
SP 31.0
SL 3.0
FoV 125*200
160 *256os

e

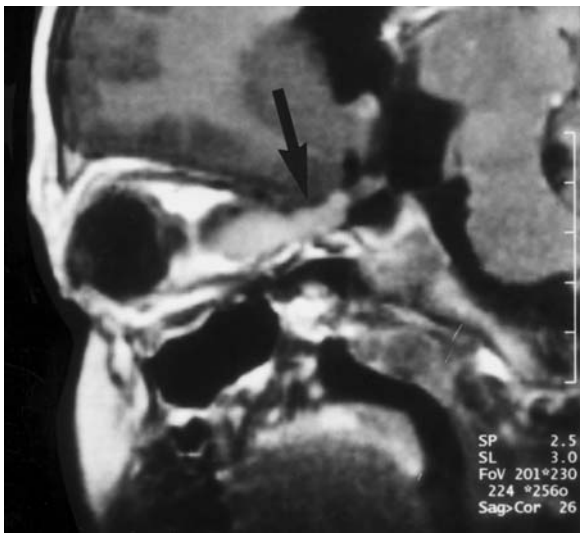
SP 2.5
SL 3.0
FoV 201*230
224 *256o
Sag Cor 26

f

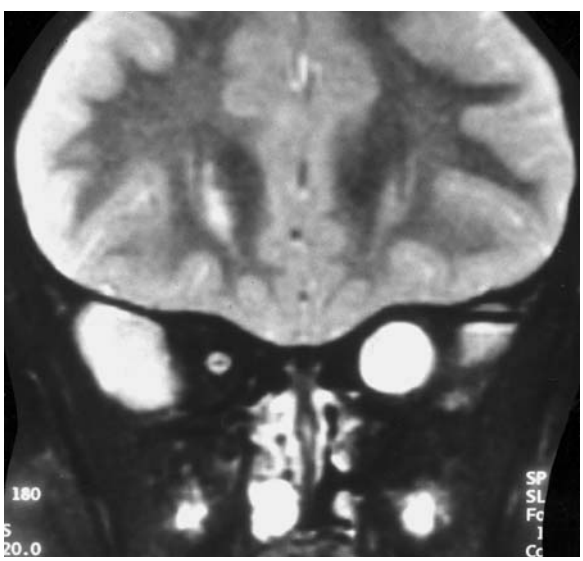
180
SP
SL

g

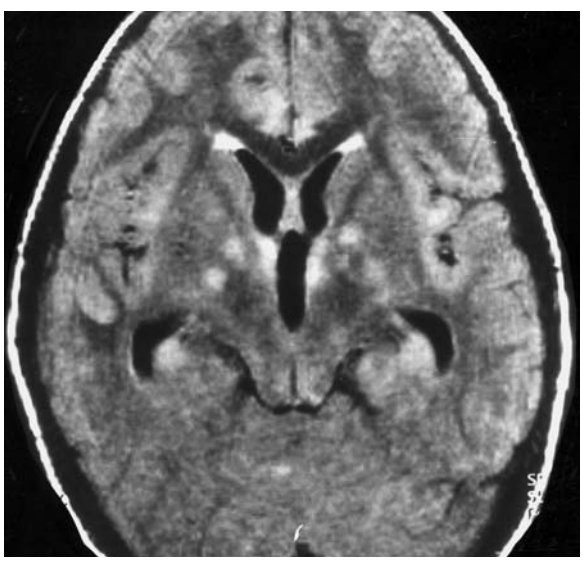

h

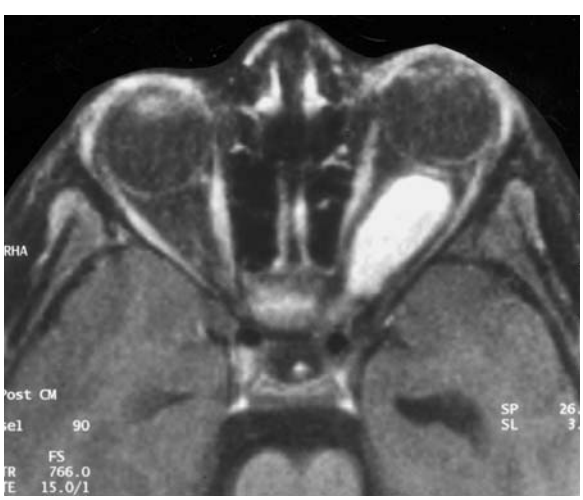
RHA
Post CM
sel 90
SP
SL
FS
TR 766.0
TE 15.0/1

i

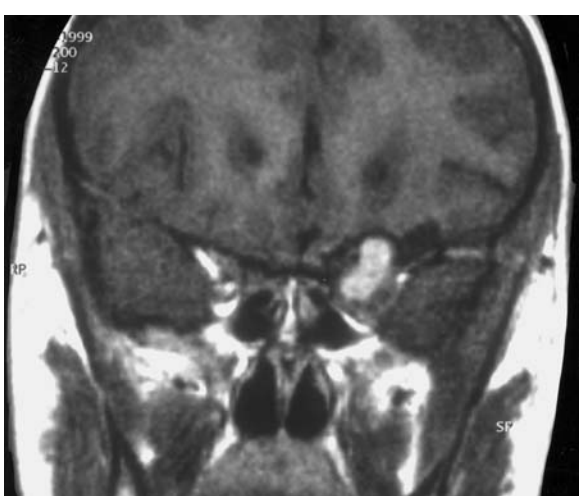
1999
200
12

k

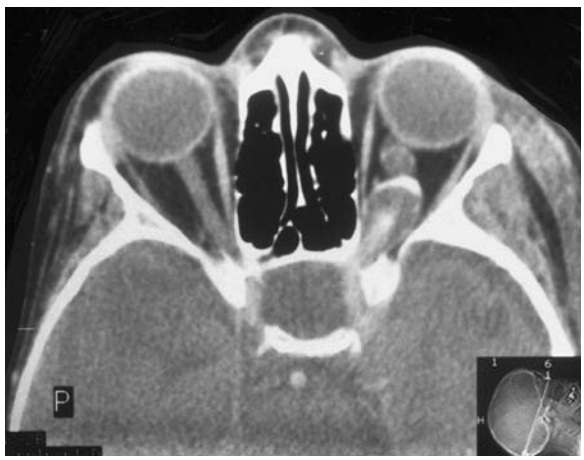

a

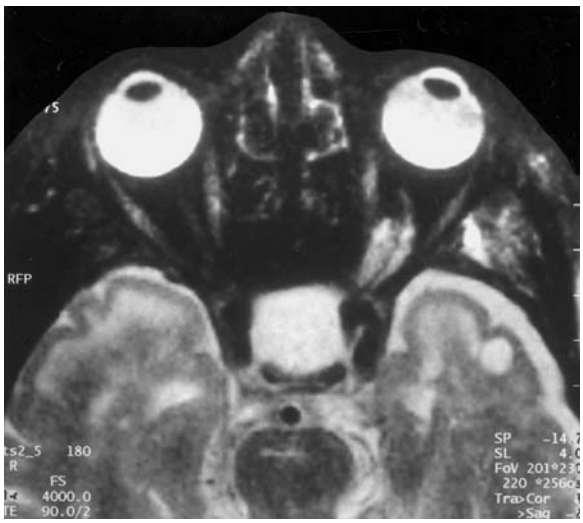

b

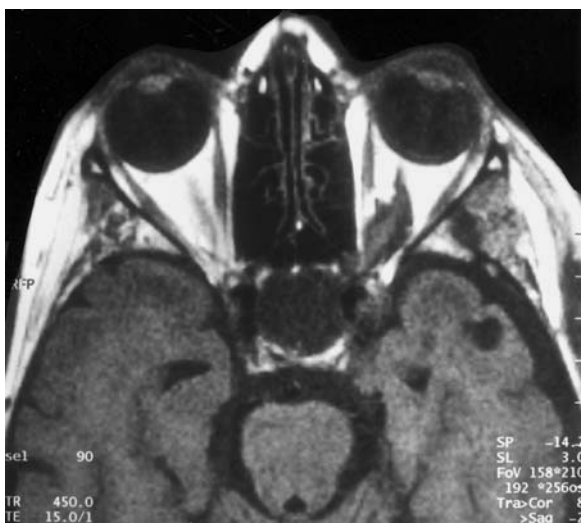

c

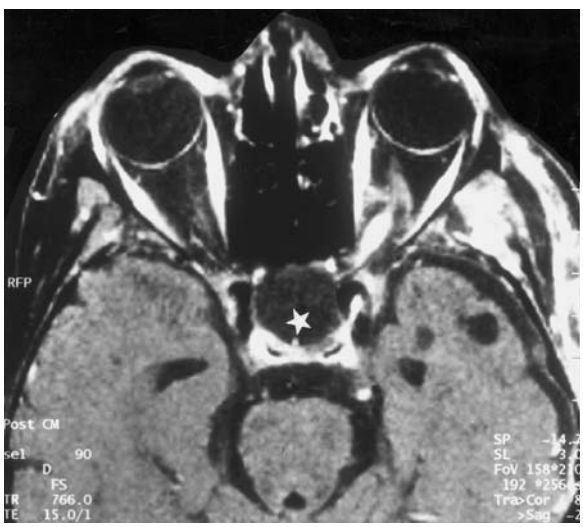

d

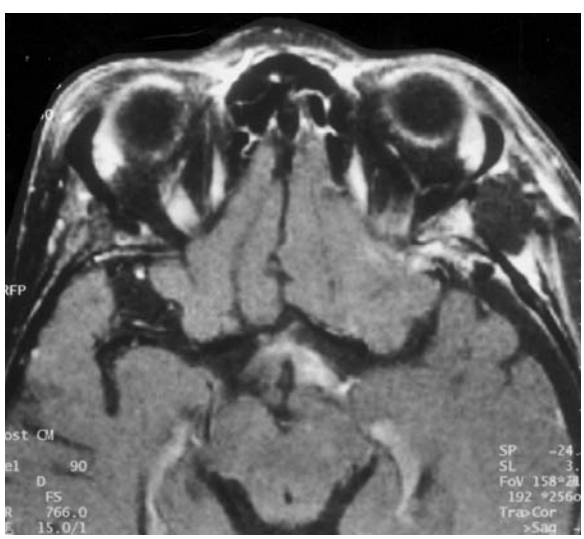

e

Fig. 6.171a–e. A 39-year-old woman with a history of loss of vision in the left eye and radiation therapy 30 years previously ("because of a glioma"). The patient underwent emergency surgery because of a huge left frontal meningioma (radiation-induced secondary tumor), imaging was performed postoperatively. Diagnosis: left optic nerve glioma. CT: **a** Axial contrast-enhanced view where an enhanced optic nerve is seen in a dilated left optic nerve sheath. Note the widened sella with CSF content, corresponding to an "empty sella", and the curved, elongated intraorbital optic nerve anterior to the tumor. MRI: **b** Corresponding T2-weighted view with widened subarachnoid space in the intraorbital area of the left optic nerve. Note the hyperintensity of the left temporal muscle, caused by operative residuals with seroma. **c** Corresponding T1-weighted native view. **d** Corresponding T1-weighted, contrast-enhanced (FS) view with bright signal enhancement of the optic nerve tumor. Note the small pituitary stalk (*white star*) pressed against the dorsum sellae. **e** Axial, T1-weighted, contrast-enhanced (FS) view at the level of the chiasm, demonstrating additional tumor invasion of the left chiasm and optic tract

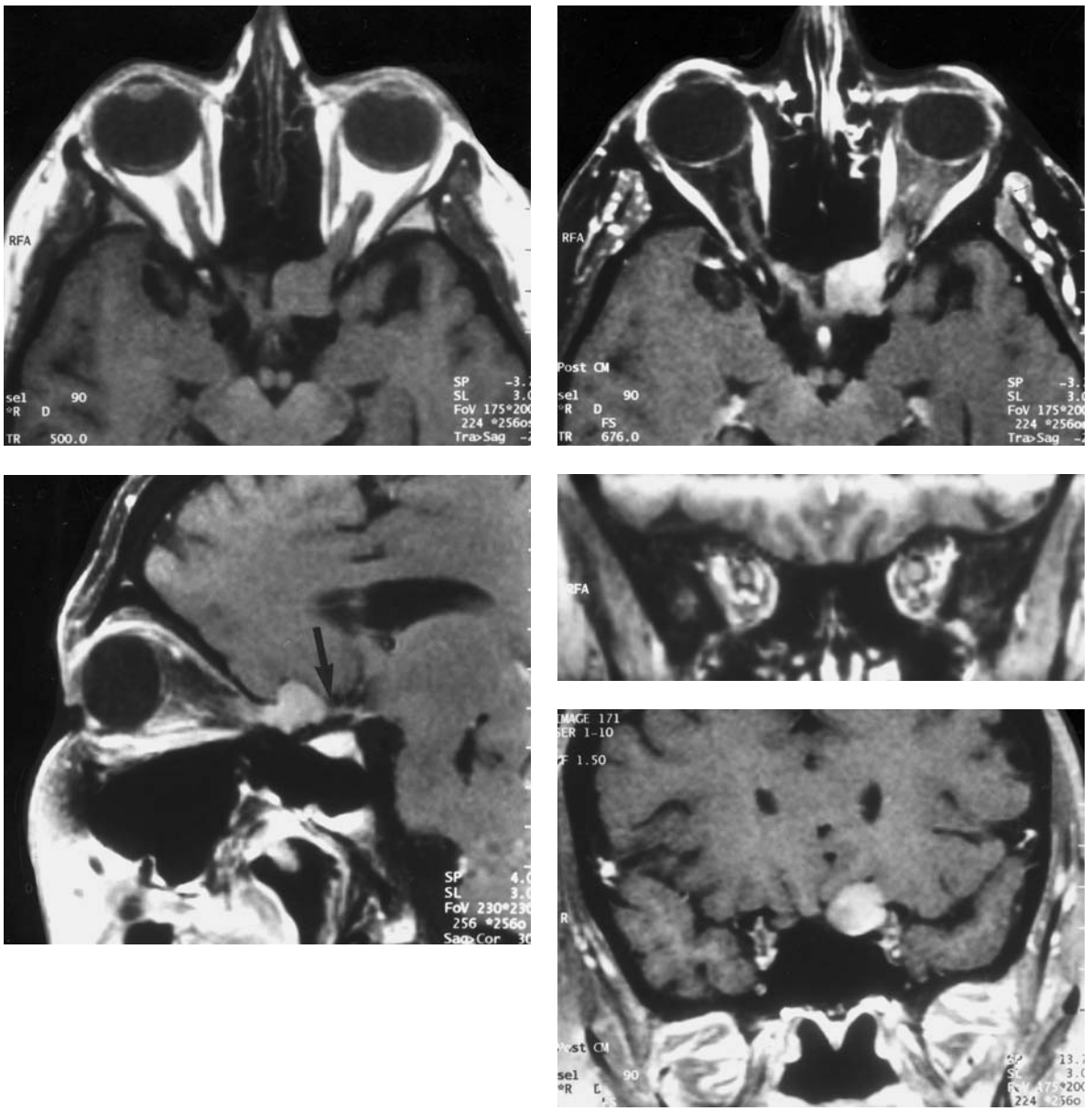

Fig. 6.172a–e. A 46-year-old woman with known left optic nerve atrophy persisting for more than 10 years (V 0.2). Diagnosis: suspected optic glioma of the left optic nerve (no histology). MRI: **a** Axial T1-weighted native image at the level of the optic canal, demonstrating dumb-bell-shaped widening of the intraorbital and intracranial left optic nerve, extending to but not invading the chiasm. **b** Corresponding T1-weighted, contrast-enhanced (FS) view with a slight homogeneous signal enhancement of the tumor. **c** Parasagittal (parallel to the optic nerve), T1-weighted, contrast-enhanced (FS) view with distinct demonstration of the normal configuration of the optic chiasm (*arrow*). **d** Coronal T1-weighted reconstruction of a 3D-data set, showing the asymmetric enlargement of the left optic nerve, while both meningeal sheaths exhibit a normal low signal. **e** Coronal, T1-weighted, contrast-enhanced (FS) view at the level of the optic canal, demonstrating additional impressive dislocation of the left rectus gyrus

signal enhancement in the periphery of the tumor may represent perineural arachnoid gliomatosis and/or an ectatic subarachnoid space around the affected nerve, but arachnoidal gliomatosis with reactive proliferation of the fibrovascular arachnoid trabeculae is characterized by enhancement (Fig. 6.171).

Additional intrinsic cerebral lesions seen in patients with optic nerve glioma in NF1 are astrocytomas, with a preferred location in the brainstem (Hochstrasser et al. 1988; Pollack et al. 1996). Other infra- and supratentorial white matter changes, seen only on T2-weighted images that are multiple, without any mass effect or contrast enhancement, correspond to regions of myelin vacuolization, areas of separation of the layers of the myelin sheath, as they spiral around the axon (DiPaolo et al. 1995). These lesions have characteristic locations (cerebellar white matter, pons, midbrain, internal capsule, splenium, and globus pallidum) and are seen in patients about 3 years old. The lesions increase in number and size until 10–12 years of age, with a subsequent decrease, becoming invisible in patients in their 20s, probably as a result of repair and remyelination (Sevick et al. 1992; Terada et al. 1996).

The differential diagnosis of optic nerve glioma should include optic nerve sheath meningioma (see Sect. 6.4.1.2), demyelinating optic neuritis (see Sect. 6.4.2.1), sarcoidosis, idiopathic inflammation of the optic nerve (Figs. 6.183, 6.184) (see also Sect. 6.4.2.2), lymphoma (Figs. 6.180, 6.181), medulloepithelioma, metastasis (Fig. 6.182) (Hollander et al. 1999), or involvement of the optic nerve in mucopolysaccharidosis (Fig. 6.179). Although optic nerve sheath meningiomas are found in children and young adults (Walsh 1975), the age of presentation and gender (preference for girls/women) should be considered in addition to imaging characteristics in the differentiation from optic glioma. While the described pathologic processes produce a thickened, enlarged, and enhancing optic nerve and sheath complex, consideration of additional clinical symptoms and findings may help in the accurate interpretation of the observed factors.

Management of these patients with optic nerve glioma is still being discussed controversially. A clear trend toward increased mortality in patients with intracranial extension, especially with hypothalamic involvement, is obvious (Dutton 1994). It is well-known that the long-term survival rate and prognosis are excellent when the tumor is confined to the optic nerve. Conservative management (Fig. 6.172) is to be established in view of the fact that only 21% of these patients show tumor progression (Dutton 1994). Surgery should be restricted to patients with severe proptosis, a blind painful eye, or when extension along the intracranial portion of the optic nerve threatens the chiasm (Albert and Puliafito 1979; Hoyt and Baghdassarian 1969; Dutton 1994). Radiotherapy does not appear to alter the ultimate prognosis even in cases where tumor involvement includes the hypothalamus and third ventricle (mortality rate: 28%), since CNS complications of radiotherapy, especially in very young children, might be severe (Dutton 1994).

6.4.1.2 Optic Nerve Sheath Meningioma

Meningiomas of the optic nerve sheath are primarily benign, slowly growing neoplasms that arise from the arachnoid cap cells within the optic nerve sheath complex, or from an intraorbital extension of sphenoid wing meningioma (Mafee et al. 1999a). Despite histological differences [most of them are meningotheliomatous (syncytial), fibroblastic, or transitional meningioma] (Marquardt and Zimmerman 1982; Mafee et al. 1999a), the most important clinical feature is their tendency to recur (Mafee et al. 1999a). Optic nerve sheath meningiomas account for 10%–33% of orbital meningiomas and show a female predominance (twice as often in women as in men), consistent with the presence of female hormonal receptors in most meningiomas (Grunberg et al. 1991; Block et al. 1996). Patients with optic nerve sheath meningioma (mean age: approx. 40 years) present with slowly progressive, painless visual loss and proptosis (Jakobiec et al. 1984; Mafee et al. 1999a). Transient visual obscuration is not uncommon as an initial symptom. Ophthalmoscopy may show optic disc pallor and/or disc swelling at the site of the lesion (Jacobiec et al. 1984; Pless and Lessell 1996), and opticociliary venous shunts (compensation of obstruction of the central retinal vein), highly suggestive of indolent optic nerve sheath or spheno-orbital meningioma (Mafee 1992). Visual impairment and proptosis depend on the location of the tumor, as visual impairment at an orbital apex location is more severe than at a more distal location, where proptosis leads to clinical symptomatology (Henderson 1973), although preservation of the central visual field may be stable for years.

A well-defined tubular thickening and/or calcification of the optic nerve complex is seen on CT (Figs. 6.173, 6.174) (Mafee et al. 1999a). Due to the high vascularization of meningiomas and the absence of a blood-brain barrier (BBB), marked contrast

enhancement is seen with both imaging techniques. Optic nerve sheath meningioma may present as diffuse or eccentric thickening of the nerve but the tramtrack sign (Fig. 6.173), originally called specific, may be seen also in optic nerve lymphoma or optic neuritis (Mafee 1992, 1996).

MRI is the method of choice in the diagnosis of optic nerve sheath meningioma, as it provides a high sensitivity and specificity, even though it is associated with a lower sensitivity for calcification. Especially in fat-suppressed, gadolinium-enhanced images, the presentation of an isointense signal of the often compressed optic nerve (Fig. 6.175), which is clearly differentiated from the homogeneous, marked, or moderate signal enhancement of the primarily isointense tumor, is significant (De Potter et al. 1995; Ortiz et al. 1996; Mafee et al. 1999a). Optic nerve sheath meningiomas present with three patterns (De Potter et al. 1995): as diffuse thickening of the optic nerve sheath complex (Figs. 6.175, 6.176), fusiform swelling (Fig. 6.177), or a globular eccentric tumor (Fig. 6.178). This gives rise to the question of whether ectopic intraorbital arachnoidal cells play a role in meningioma formation, since the differential diagnosis from neurofibroma or cavernous hemangioma is difficult in the presence of a marked dislocation of the optic nerve (Newman and Jane 1991; Mafee 1992). The great value of MRI is emphasized in cases of intracranial extension via the optic canal (Figs. 6.175, 6.176), where even small and thin en-plaque growth of the tumor matrix is distinctly visible, enabling bilateral involvement or optic chiasm affection to be ruled out.

6.4.1.3 Miscellaneous (MPS Type VI, Metastasis, Cerebral Pseudotumor, Fibrous Dysplasia)

6.4.1.3.1 Mucopolysaccharidosis Type VI

The mucopolysaccharidoses (MPS) are a family of six inherited, autosomal recessive disorders, dominated by the storage of glycosaminoglycan (previ-

(Text continues on p. 310)

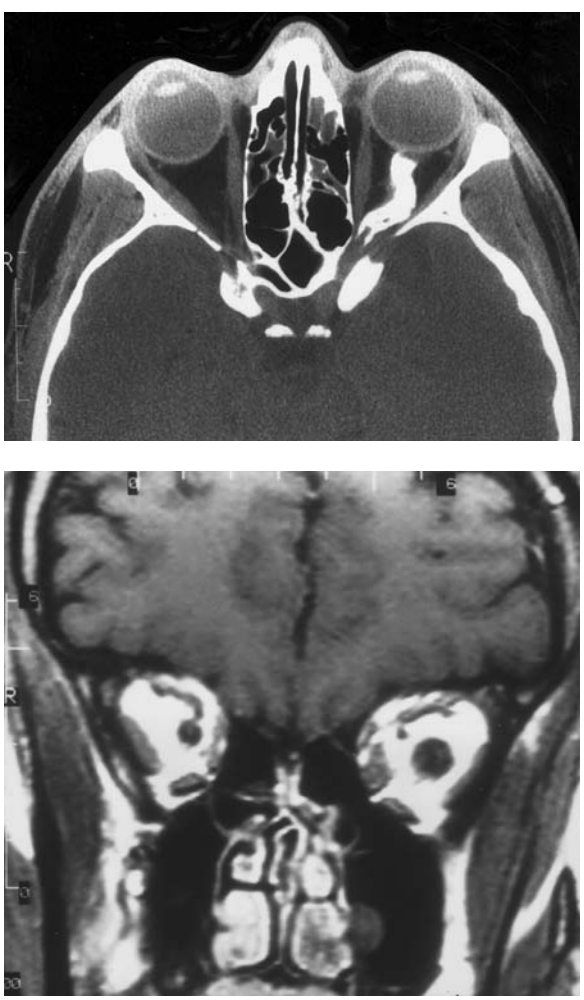

Fig. 6.173a–c. A 29-year-old man with slowly progressing and eventually complete loss of vision in the left eye. Diagnosis: calcified optic nerve sheath meningioma. CT: **a** Axial native image with symmetrical calcification (tramtrack sign) of the entire left intraorbital meningeal sheath. MRI: **b** Corresponding T1-weighted, contrast-enhanced axial view showing contrast enhancement only in the precanalicular orbital apex (*white arrow*). Note the thickening of the left optic nerve complex compared with the right side. **c** Coronal T1-weighted native view with enlargement of the left optic nerve sheath. (Courtesy of Prof. Sartor, Department of Neuroradiology, Heidelberg)

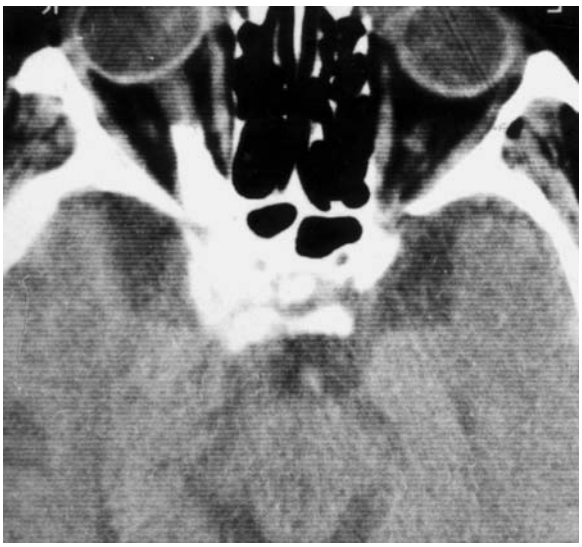

Fig. 6.174. A 66-year-old woman with complete visual deficit of the right eye. Diagnosis: calcified right sphenoid wing meningioma. Axial CT: Nearly complete calcification of the tumor, arising from the clinoid process with retrograde infiltration of the entire optic nerve sheath through the optic canal into the orbit, and antegrade infiltration of the ipsilateral cavernous sinus. (With permission of Müller-Forell and Lieb 1995)

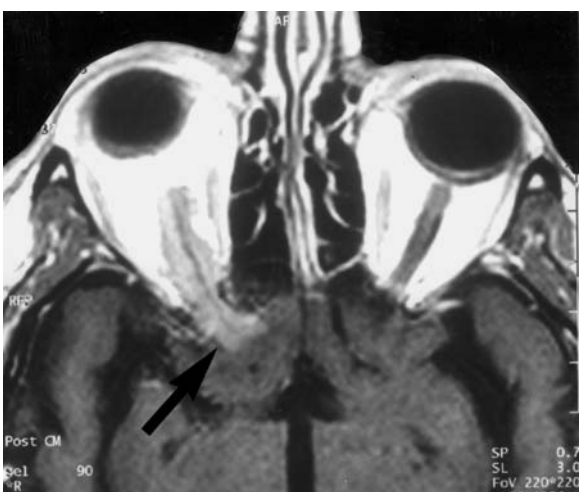

a

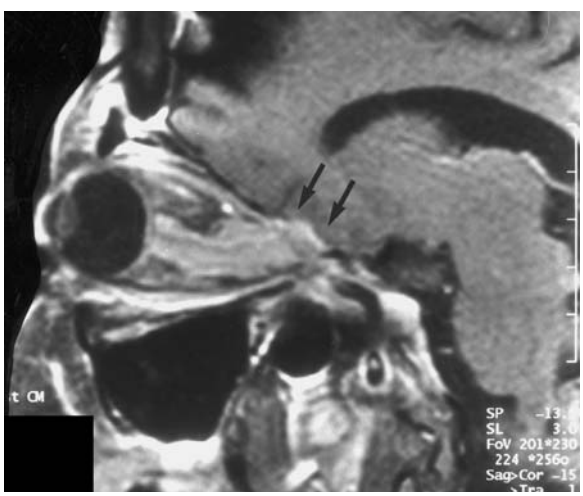

b

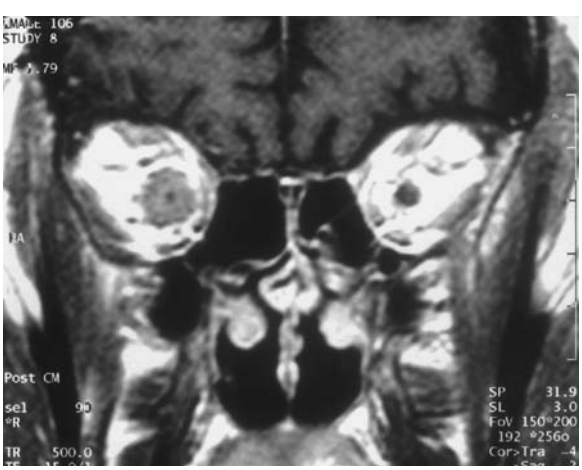

c

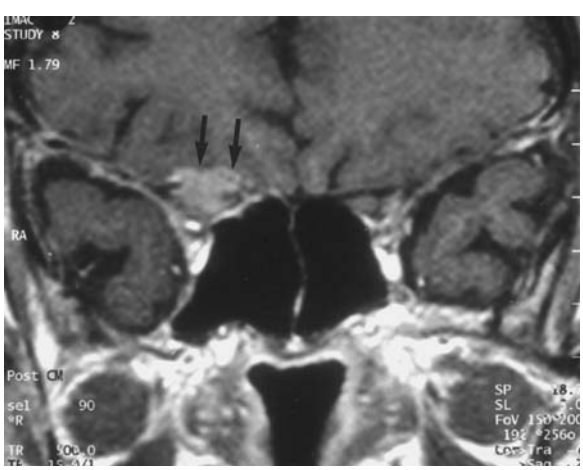

d

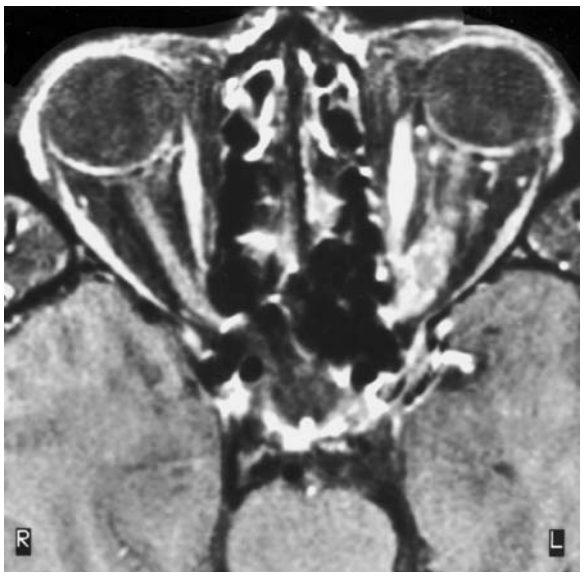

a

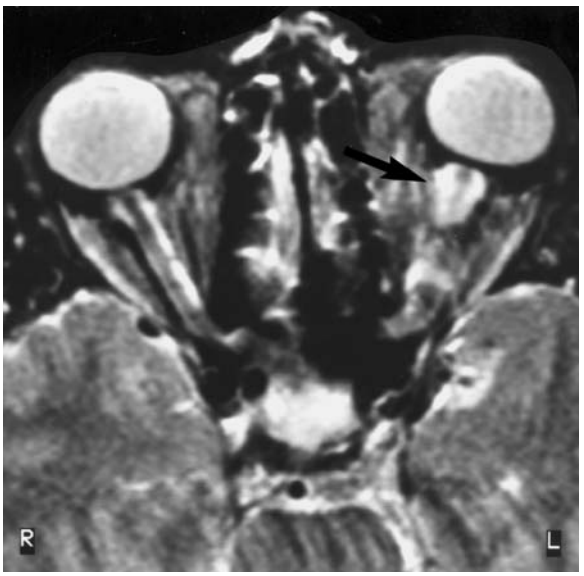

b

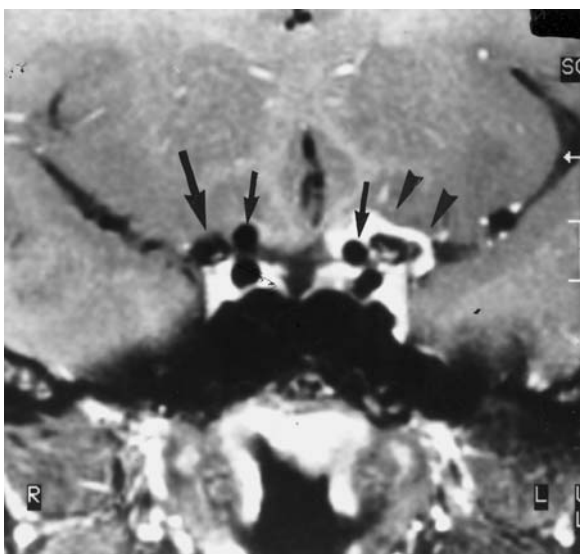

c

Fig. 6.176a–c. A 36-year-old woman with slowly progressing visual deficit of the left eye. Diagnosis: optic nerve sheath meningioma. MRI: **a** Axial, T1-weighted, contrast-enhanced (FS) view with signal intensity enhancement of the tumor in the posterior orbital apex. Thickening of the rectus muscles and dilation of intraorbital vessels (intermittent signal enhancement in the intraconal space) lead to the suspicion of venous congestion. **b** Corresponding T2-weighted image; comparison with the right optic nerve shows CSF block of the meningeal sheath demonstrated by retrobulbar widening of the subarachnoid space (*arrow*). **c** Coronal, T1-weighted, contrast-enhanced (FS) view at the site of the posterior optic canal, visualizing the spread of tumor growth (*arrowheads*) along the dura of the left clinoid process. Note the normal configuration of the contralateral right clinoid process (*arrow*), normal-sized diameter of both ICA (*small arrows*). (With permission of Müller-Forell and Lieb 1995b)

◁ **Fig. 6.175a–d.** A 49-year-old woman with complete loss of vision in the right eye. Diagnosis: optic nerve sheath meningioma with intracranial expansion. MRI: **a** Axial, T1-weighted, contrast-enhanced view with parallel thickening of the meningeal sheath, compression of the right optic nerve (medial hypointensity), widening of the optic canal, and intracranial infiltration (*arrow*) with expansion in the direction the optic chiasm. **b** Parasagittal, T1-weighted, contrast-enhanced (FS) view, demonstrating minor eccentric growth of the meningioma in the apical orbit, and flat extra-axial intracranial meningeal infiltration at the ipsilateral clinoid process (*arrows*). **c** Coronal, T1-weighted, contrast-enhanced view also demonstrating concentric compression of the medial part of the optic nerve. **d** Corresponding coronal view at the level of the optic canal, showing lateral widening of the canal, infiltration of the upper cortex of the clinoid process (*arrows*), and slight intracranial expansion, all associated with the tumor. Compare with normal configuration of the left side. (With permission of Müller-Forell 1998)

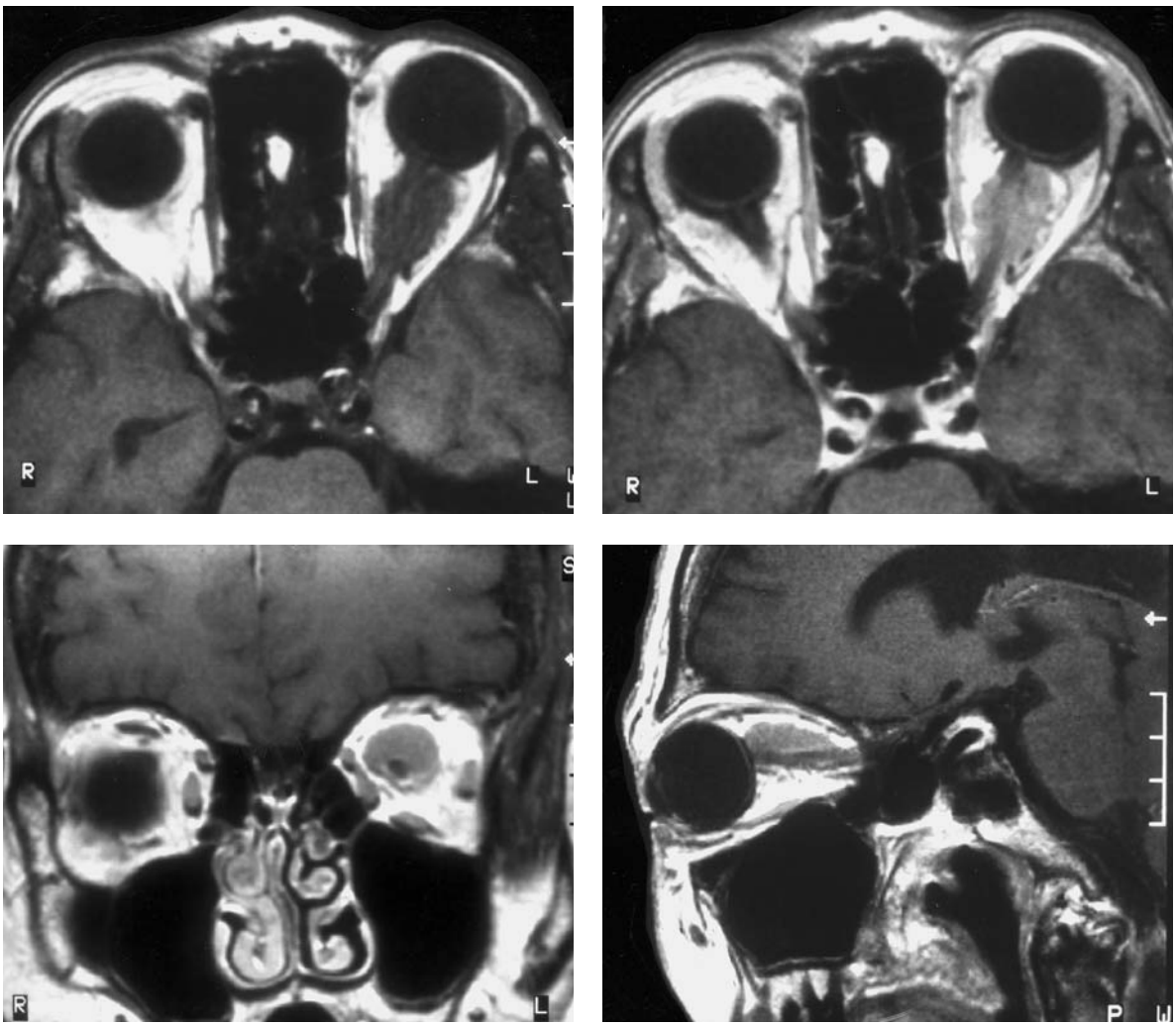

Fig. 6.177a–d. A 55-year-old woman with subsequent, slowly progressing loss of vision in the left eye. Diagnosis: eccentric optic nerve sheath meningioma. T1-weighted MRI: **a** Axial native view with slight proptosis of the left globe and a hyperintense lesion, enclosing the optic nerve. **b** Corresponding contrast-enhanced image demonstrating nearly homogeneous enhancement of the meningioma, sparing the isointense optic nerve. **c** Coronal contrast-enhanced view with superior visualization of the mostly supraoptic tumor extension. **d** Parasagittal contrast-enhanced view with demonstration of the supraoptic growth with neither intracanalicular nor intracranial extension

Fig. 6.178a–f. A 55-year-old woman with slowly progressing axial proptosis of the right eye, examined for possible endocrine ▷ orbitopathy. Diagnosis: eccentric meningioma of the optic nerve sheath. MRI: **a** Axial T2-weighted (FS) view with a well-defined intraconal mass. **b** Corresponding T1-weighted native view, demonstrating a homogeneous, apparently encapsulated mass. **c** Corresponding T1-weighted, contrast-enhanced (FS) view with homogeneous, but intermediate enhancement. **d** Coronal T1-weighted native view, where the supraoptic location with optic nerve compression and flattening by the mass is seen. **e** Corresponding T1-weighted, contrast-enhanced view with relatively low signal enhancement. **f** Parasagittal, T1-weighted, contrast-enhanced (FS) view, demonstrating the intraconal, supraoptic, immediately retrobulbar mass

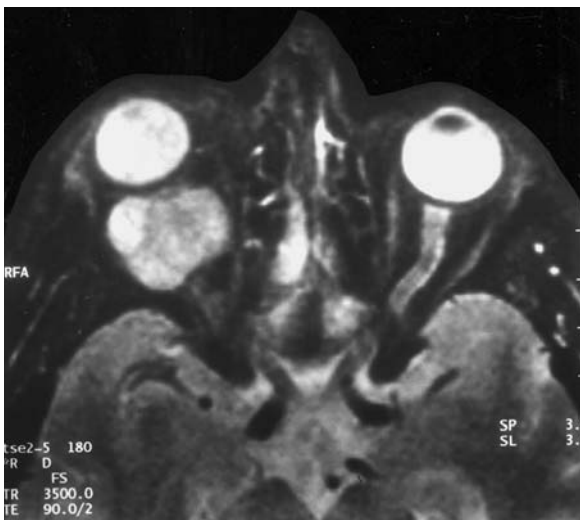

a

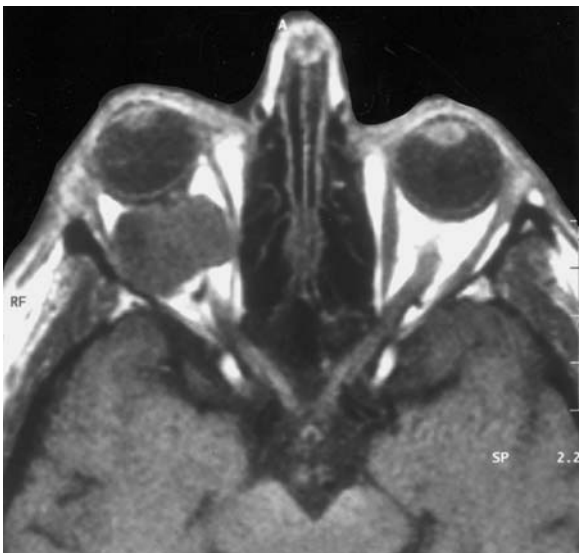

b

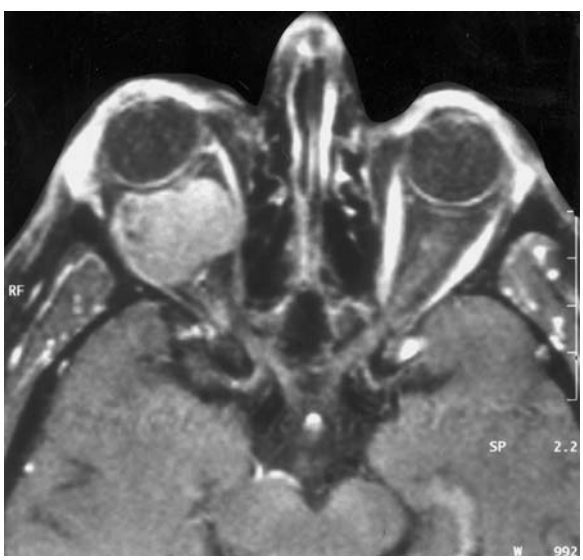

c

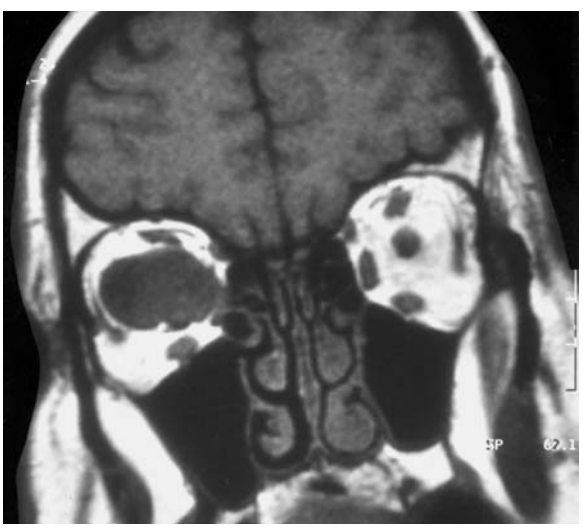

d

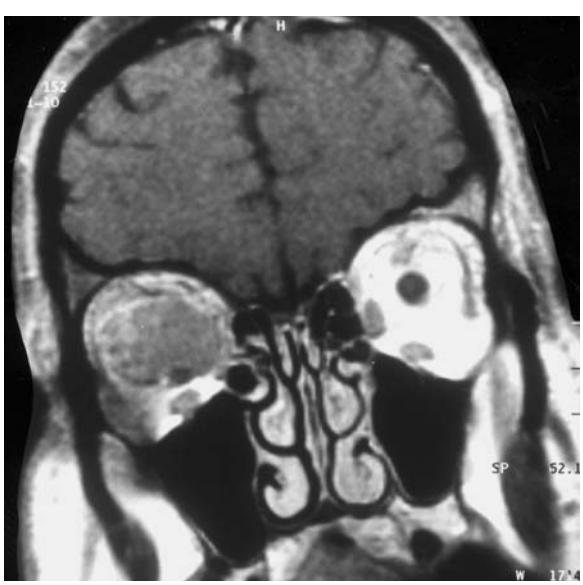

e

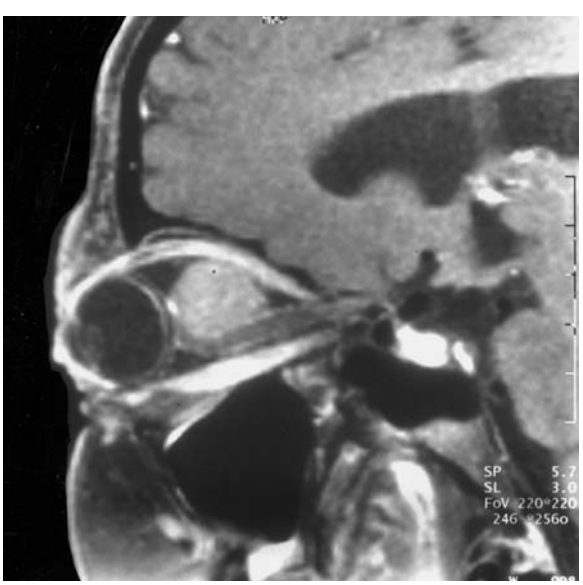

f

ously called mucopolysaccharides) within lysosomes of the cells of most tissues and organs (van der Knaap and Valk 1995; Lake 1997). Although there is some variation among the MPS types, they share a number of characteristic clinical features. In particular, patients with MPS type VI (Maroteaux–Lamy) (Fig. 6.179) clinically resemble, with the exception of normal intelligence (van der Knaap and Valk 1995), patients with MPS type I H (Hurler syndrome); the resemblance of imaging findings is therefore not unexpected. Apparent MRI findings may develop over a period of years and consist of small spot-like lesions in radial orientation to the cortex, caused by deposits of mucopolysaccharides in the perivascular Virchow-Robin spaces of the brain and variable ventricular enlargement (van der Knaap and Valk 1995; Lake 1997; Barkovich 2000). The hyperintensities on T2-weighted images may reflect demyelination and gliosis. Although ocular manifestations are seen in rare cases only (Kenyon 1976), optic nerve compression obviously caused by mucopolysaccharide deposits in the optic nerve sheath (Fig. 6.179) has yet not been described.

6.4.1.3.2 Metastasis

Although ocular involvement of central nervous system lymphoma is known (Akpek et al. 1999; Cassoux et al. 2000), leptomeningeal involvement of systemic or focal extracerebral malignancies in the optic nerve sheath is rare, and seen occasionally with only meningeal manifestation (Fig. 6.180). Patients usually become symptomatic with acute visual disturbances or vision loss (Müller et al. 1990). In HIV-related lymphoma, leptomeningeal involvement represents the most common central nervous system manifestation (Levine 1991), but is rarely observed in the optic nerve sheath. A particularly rare condition endemic to Africa, but sporadically occurring worldwide, is central nervous system and optic nerve sheath involvement in Burkitt lymphoma (Fig. 6.181), a high-grade undifferentiated lymphocytic neoplasm associated with the Epstein-Barr virus (Trese et al. 1980; Rootman et al. 1994; McCartney 1997; Spath-Schwalbe et al. 1999). Optic nerve sheath meningiosis is not restricted to lymphoma, but is also seen in other primary malignancies as, e.g., pancreatic carcinoma (Fig. 6.182). The differential diagnosis for idiopathic optic nerve inflammation in cases of known malignancy might be difficult and should not be based only on imaging criteria, but also on clinical symptoms and follow-up (Figs. 6.183, 6.184).

6.4.1.3.3 Cerebral Pseudotumor

Clinical symptoms of cerebral pseudotumor (syn. benign cerebral hypertension) include headache, visual impairment, and bilateral papilledema with or without visual impairment or loss of vision. Primary cerebral pseudotumor due to an intracranial space-occupying mass, sinus thrombosis, endocrine metabolic disorders (e.g., hyperparathyroidism, hypothyroidism, or hematological disorders) demand causal therapy (Reul 2001). Idiopathic intracranial hypertension most commonly occurs in middle-aged obese women (Weisberg 1985), but children or adolescents may also be affected (Phillips et al. 1998; Cinciripini et al. 1999). Although a large number of associated disorders as, e.g., chronic sinus thrombosis or intracranial dural fistula are known, the etiology remains unknown. However, an increase in CSF production or decreased resorption have been suggested (Donavan et al. 1998; Biondi et al. 1999; Friedman 1999). Clinical findings consist of increased intracranial pressure, but normal CSF composition (Manfre et al. 1995; Phillips et al. 1998; Suzuki et al. 2001). MRI shows normal to small ventricles and in some cases enlarged optic nerve sheaths, combined with a reversal of the optic head (Fig. 6.185) and/or signs of an empty sella. Venous MR-angiography may provide information about venous stenosis, but invasive cerebral venous angiography with manometry precisely defines the amount of venous hypertension (normally about 2–7 mmHg) in the superior sagittal sinus and proximal transverse sinus. The venous pressure increase may be caused by mild to significant narrowing of the distal transverse sinus, mostly of unknown etiology (Fig. 6.186) (King et al. 1995). Conservative therapy consists of medication with acetazolamide and/or prednisolone (Suzuki et al. 2001) in order to re-establish normal intracranial pressure with documented remission (Donovan et al. 1998; Suzuki et al. 2001). In chronic or refractory cases, optic sheath decompression should be performed to prevent a definite optic nerve defect with associated loss of vision (Fig. 6.187) (Horton et al. 1992; Spoor and McHenry 1995).

6.4.1.3.4 Fibrous Dysplasia

In active fibrous dysplasia, a visual deficit may occur when the process involves the optic canal (Fig. 6.188) (see also Sect. 6.3.2.1.).

(Text continues on p. 318)

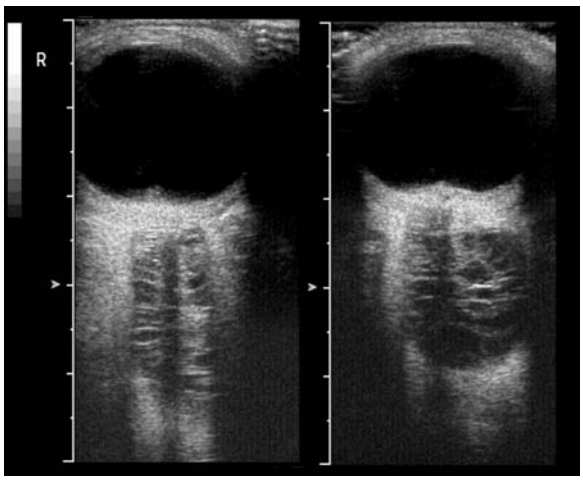

a

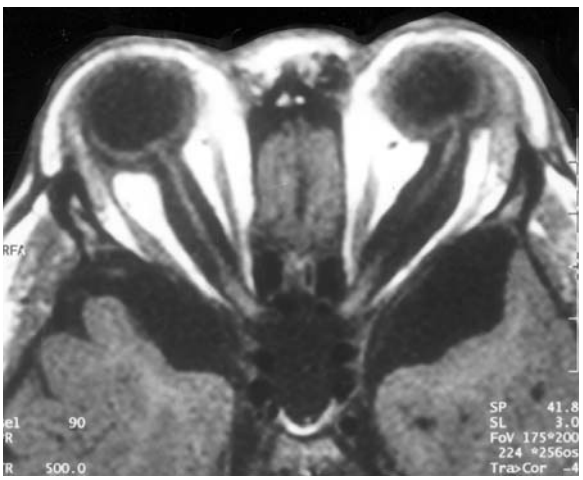

b

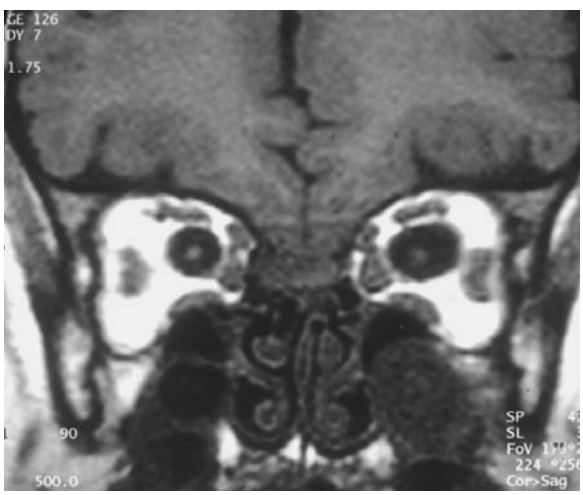

c

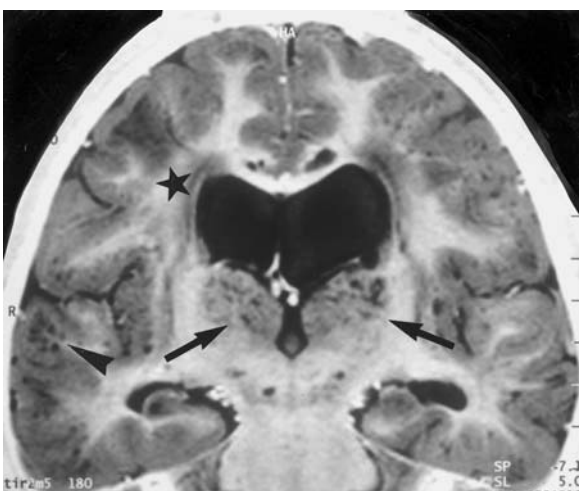

d

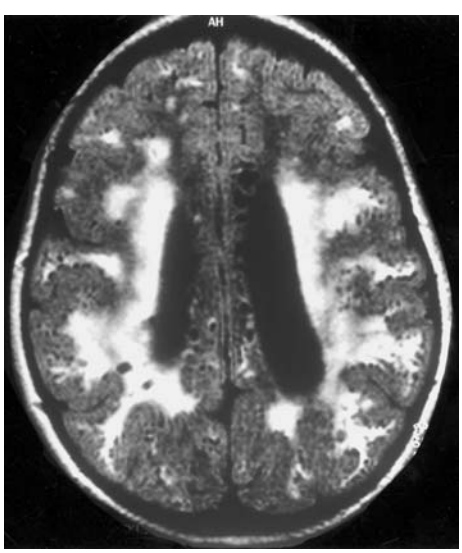

e

Fig. 6.179a–e. A 12-year-old girl with myopia persisting for several years, presenting for imaging follow-up of mucopolysaccharidosis type VI (Maroteaux–Lamy syndrome). Diagnosis: deposits of mucopolysaccharide in the optic sheath. **a** Ultrasound of the enlarged optic nerve complex (courtesy of Prof. Schumacher, Kinderklinik, Mainz). MRI (native): **b** Axial T1-weighted view of the orbit with extreme bilateral thickening of the optic nerve sheath shown to be more pronounced on the left. Both optic nerves are compressed in their orbital course, but exhibit a normal diameter (4 mm) in the optic canal. **c** Coronal T1-weighted view of the orbit. **d** Coronal T1-weighted IR view of the brain at the level of the basal ganglia, demonstrating characteristic hypointense perivascular spaces (filled with mucopolysaccharides) in the basal ganglia (*arrows*) and the subcortical vessels (*arrowhead*), in addition to atrophy of the white matter (*star*). **e** Axial T2-weighted FLAIR image at the level of the cella media of the ventricles. Substantial diffuse demyelination of the white matter and diffuse perivascular mucopolysaccharide deposits, isointense with CSF, are most distinctly visualized in the subcortical small vessels, presenting with hypointense signal

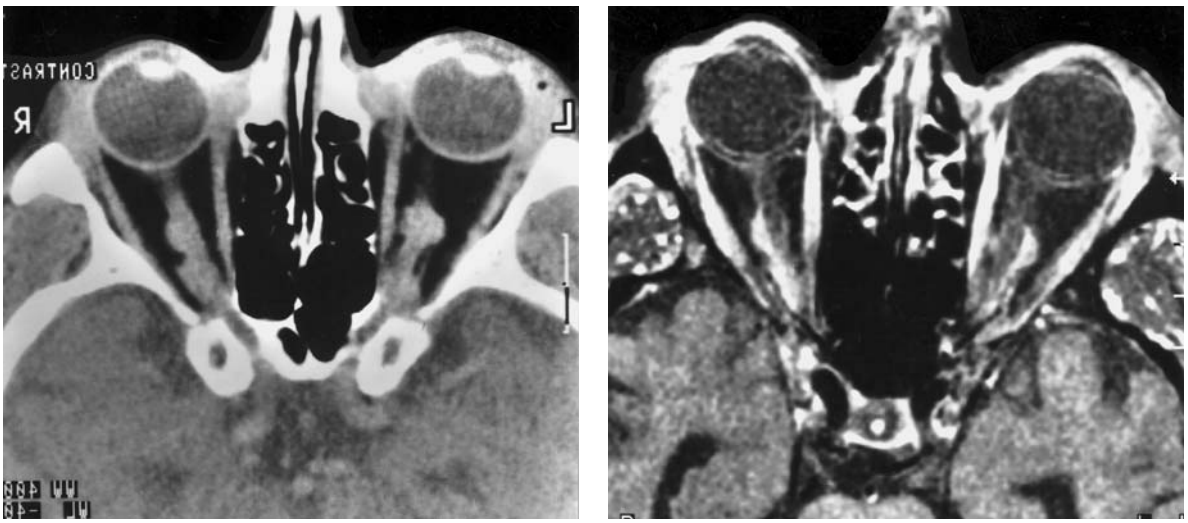

Fig. 6.180a,b. A 76-year-old man with systemic NH-lymphoma and acute visual disturbance. Diagnosis: meningeal metastasis of NH-lymphoma. CT: **a** Axial contrast-enhanced image with knotty, bulbar structures in the course of the optic nerve. MRI: **b** Corresponding axial, T1-weighted, contrast-enhanced (FS) image confirming the diagnosis of meningeal tumor spread with bilateral tumor seeding along the meningeal sheaths in the presence of regular signal and normal formation of both optic nerves. (With permission of Müller-Forell and Lieb 1995)

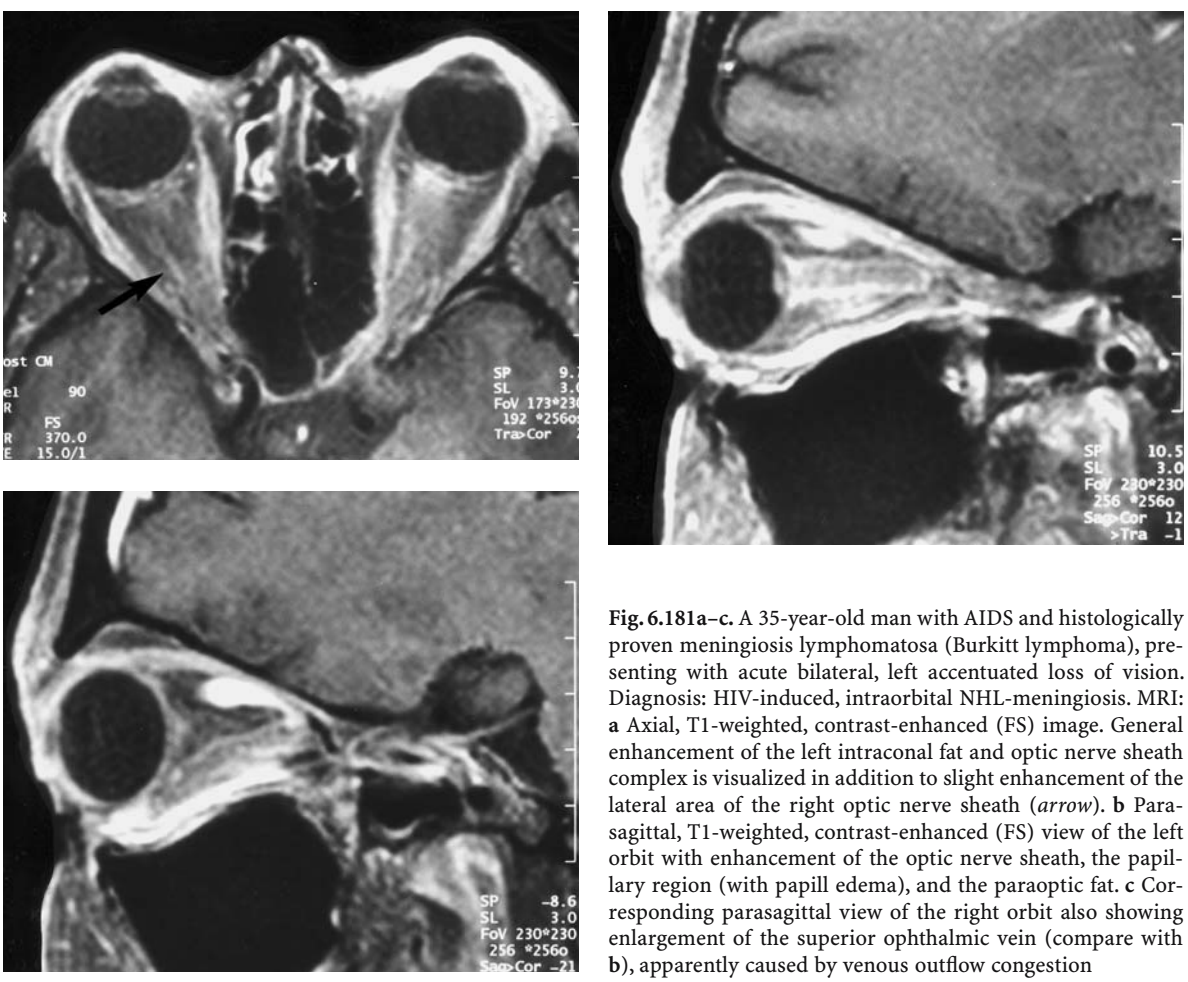

Fig. 6.181a–c. A 35-year-old man with AIDS and histologically proven meningiosis lymphomatosa (Burkitt lymphoma), presenting with acute bilateral, left accentuated loss of vision. Diagnosis: HIV-induced, intraorbital NHL-meningiosis. MRI: **a** Axial, T1-weighted, contrast-enhanced (FS) image. General enhancement of the left intraconal fat and optic nerve sheath complex is visualized in addition to slight enhancement of the lateral area of the right optic nerve sheath (*arrow*). **b** Parasagittal, T1-weighted, contrast-enhanced (FS) view of the left orbit with enhancement of the optic nerve sheath, the papillary region (with papill edema), and the paraoptic fat. **c** Corresponding parasagittal view of the right orbit also showing enlargement of the superior ophthalmic vein (compare with **b**), apparently caused by venous outflow congestion

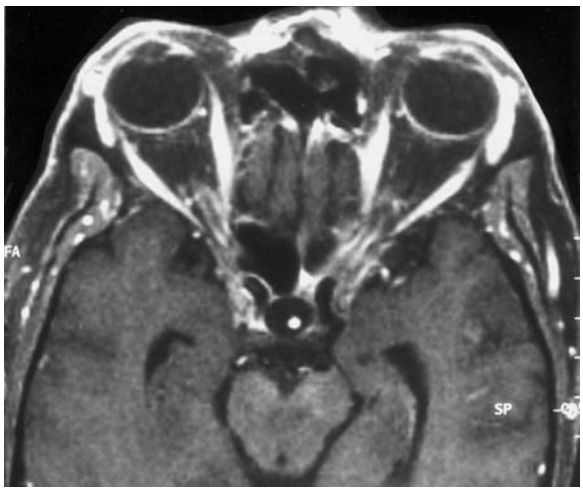

a

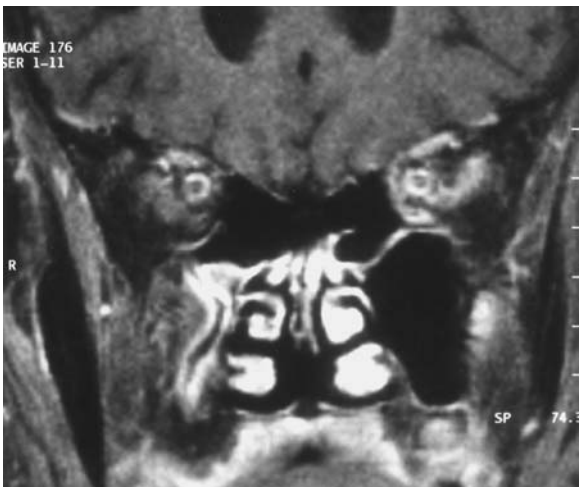

b

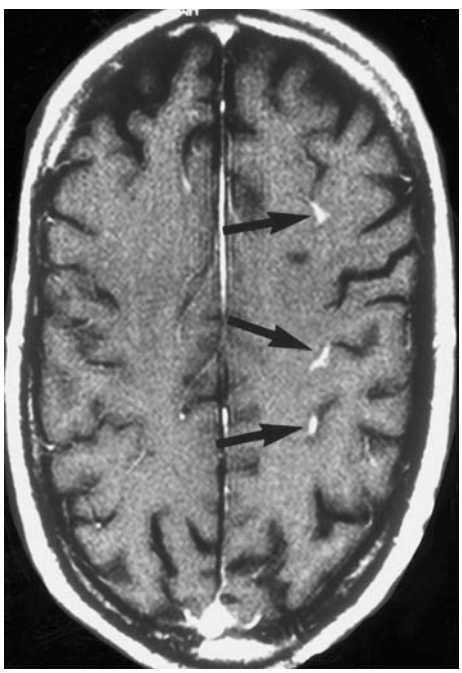

c

Fig. 6.182a–c. A 49-year-old man with metastatic spread of pancreatic carcinoma, presenting with bilateral papilledema and acutely decreasing visual loss. Diagnosis: leptomeningeal metastasis. MRI: **a** Axial, T1-weighted, contrast-enhanced (FS) view with bilateral enhancement of the subarachnoid space of the optic sheath, best seen at the optic canal. **b** Coronal, T1-weighted, contrast-enhanced (FS) view where both optic nerves are seen as hypointense structures, surrounded by hyperintense subarachnoid space. **c** Axial, T1-weighted, contrast-enhanced view of the brain, demonstrating leptomeningeal tumor infiltration at the depth of the left frontal sulci (*arrows*)

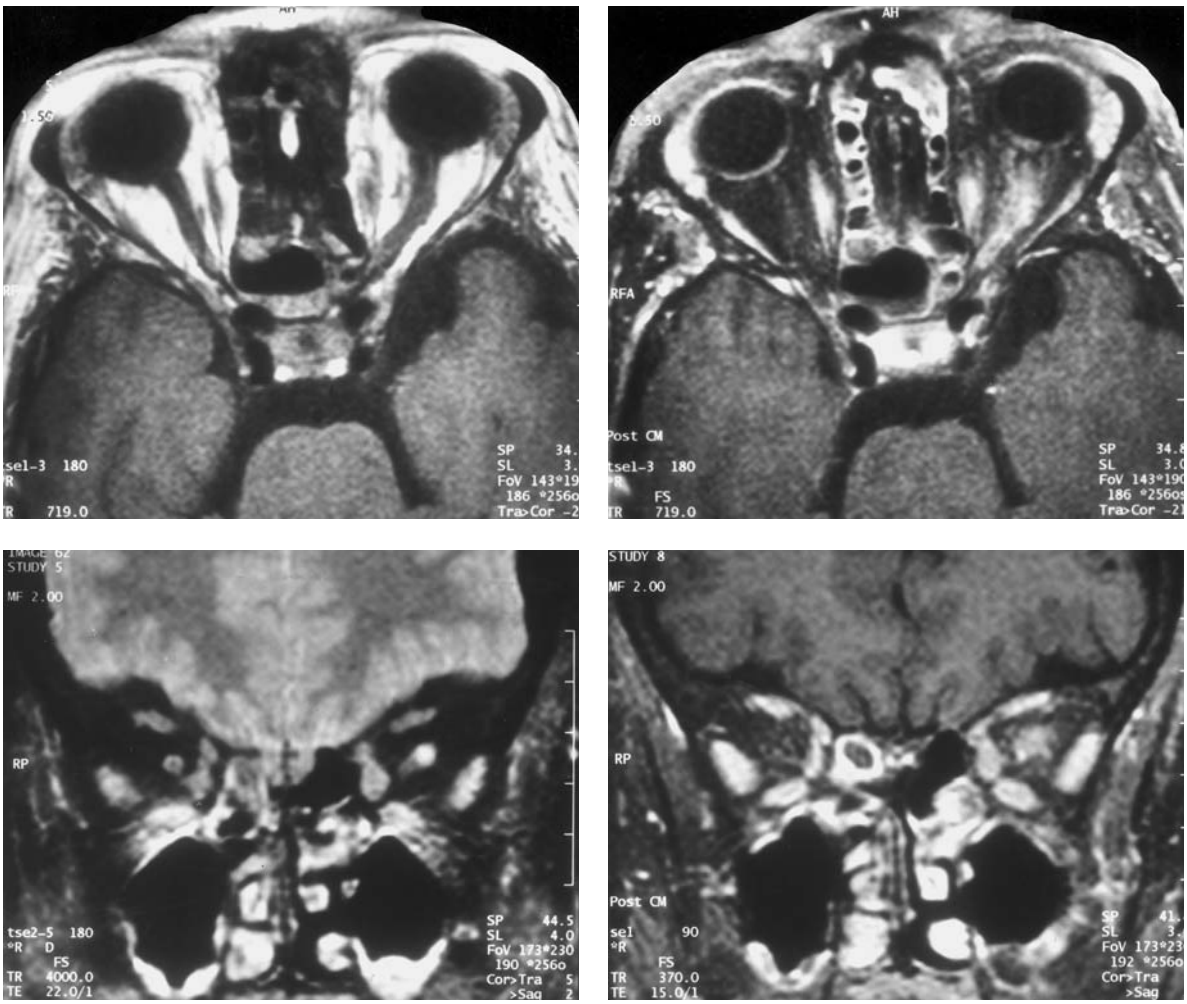

Fig. 6.183a–d. A 38-year-old woman with acute loss of vision in the left eye and a history of breast carcinoma. Cortisone therapy was successful, and nothing abnormal was detected on follow-up after 24 months; differential diagnosis of meningeal metastasis of the primary tumor is unlikely. Diagnosis: idiopathic inflammation of the left optic nerve. MRI: **a** Axial T1-weighted native view. **b** Corresponding contrast-enhanced (FS) image with irregular enhancement along the left optic nerve sheath complex. **c** Coronal T2-weighted view where the left optic nerve exhibits significant signal enhancement. **d** Corresponding T1-weighted, contrast-enhanced (FS) view with significant T1-time shortening of the left optic nerve

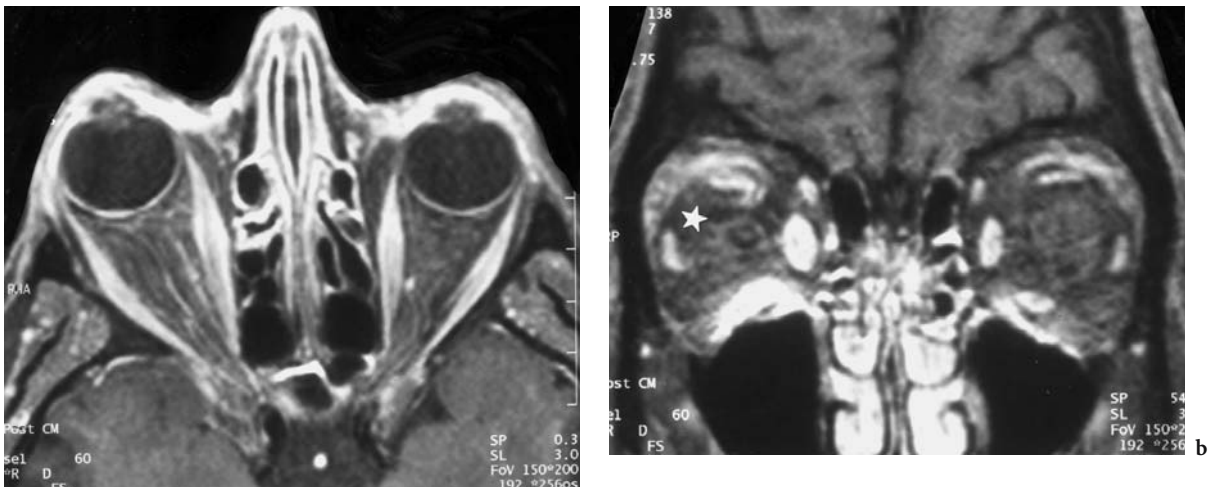

Fig. 6.184a,b. A 75-year-old woman with symptomatology of right-sided retrobulbar neuritis and a history of breast cancer. Diagnosis: idiopathic inflammation of the optic nerve sheath. MRI: **a** Axial, T1-weighted, contrast-enhanced (FS) view showing enhancement of the right optic nerve sheath. **b** Coronal view confirming additional infiltration of the paraoptic orbital fat (*white star*) suspected from another axial view (not shown). Differential diagnosis of meningeal metastasis was excluded on follow-up, which showed complete remission of the clinical symptoms after high-dose corticosteroid treatment, confirmed by neuroradiological imaging (not shown)

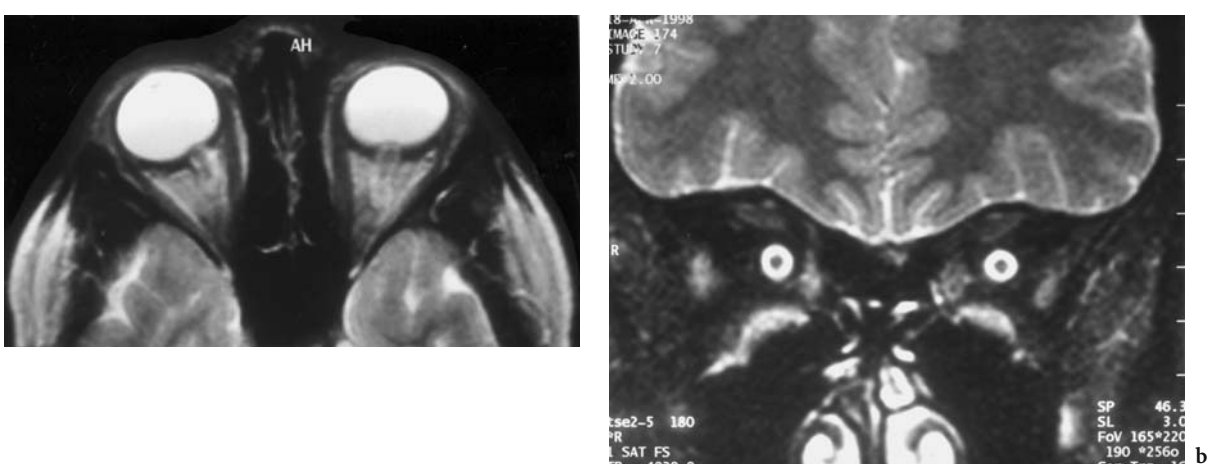

Fig. 6.185a,b. A 24-year-old woman with chronic papilledema. Diagnosis: cerebral pseudotumor. MRI: **a** Axial T2-weighted view demonstrating the impression of the papilla by the optic nerves. **b** Coronal T2-weighted view with enlargement of the subarachnoid space of the intraorbital optic nerve sheath

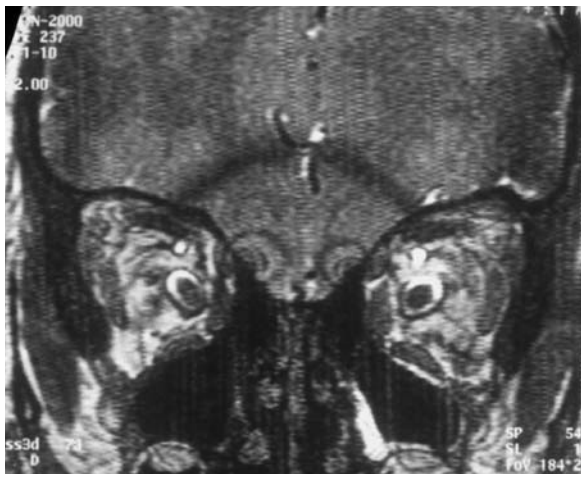

a

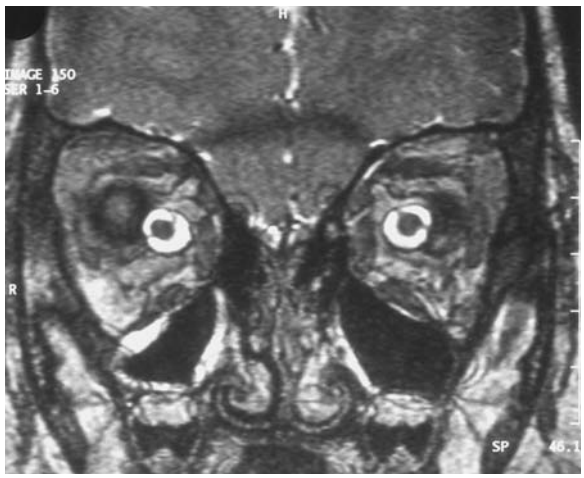

b

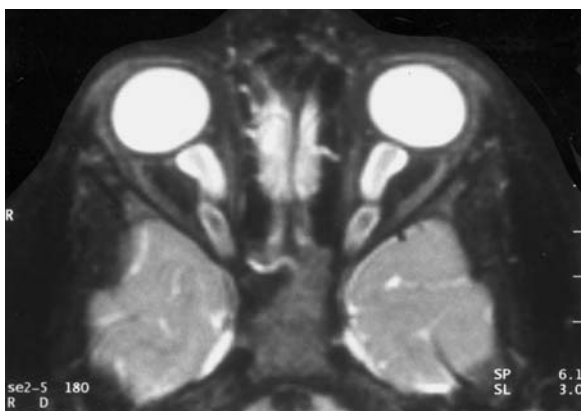

c

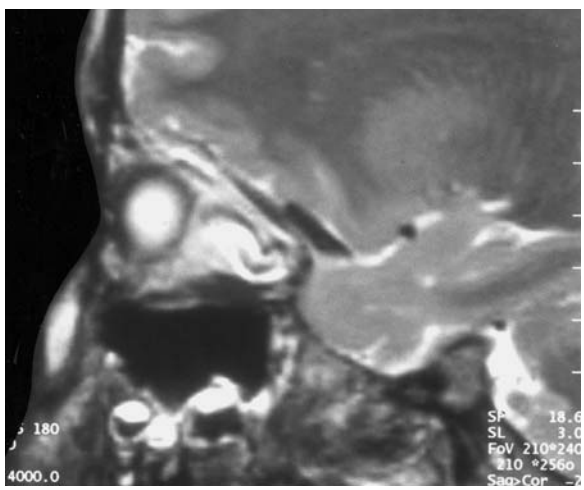

d

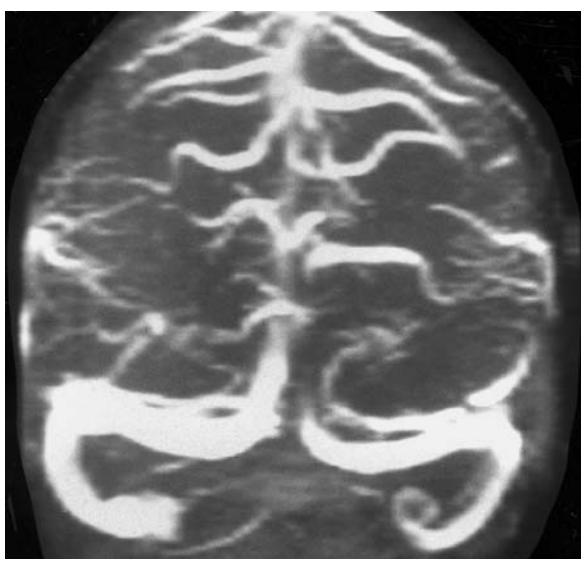

e

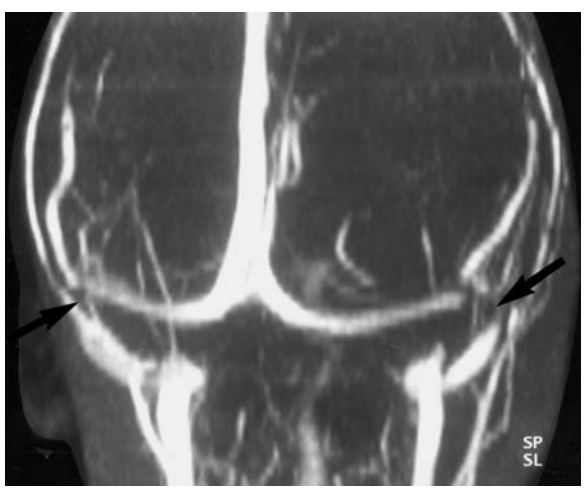

f

Fig. 6.186a–h. Course of a 3-year-old boy with papilledema, indicating the presence of a cerebral pseudotumor. Clinical normalization of the symptoms was observed after treatment with diamox. Diagnosis: cerebral pseudotumor. MRI: **a** Coronal T2-weighted HR view of the optic nerve with only slight dilation of the subarachnoid space. **b** Corresponding view 2 months after treatment, demonstrating a substantial enlargement. **c** Axial T2-weighted view taken at the same time, also showing enlargement of the optic nerve sheath and kinking of the nerve, better seen on the sagittal view. **d** Sagittal T2-weighted view of the right optic nerve. **e** MIP reconstruction of a TOF venous MR-angiography at the time of the onset of symptoms; no pathology is detectable. **f** Corresponding venous MRA 2 months later, showing apparent narrowing of both sigmoid sinus regions. DSA: **g** venous phase of the left ICA, confirming the findings of MRA by the presence of bilateral venous outflow stenosis (*arrows*). **h** Venous manometry showed a pressure gradient of 5 mmHg for the pre- and poststenotic (not shown) sinus area

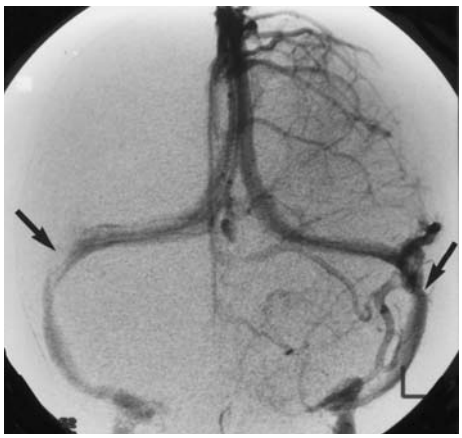

g

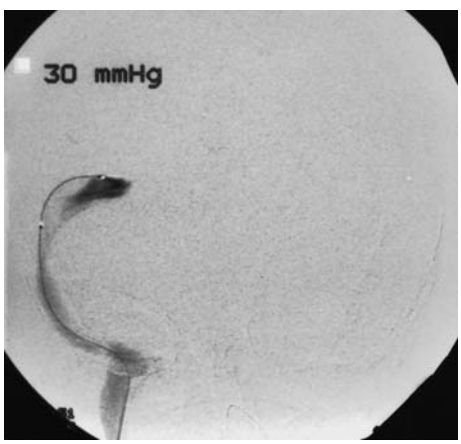

h

Fig. 6.187g,h

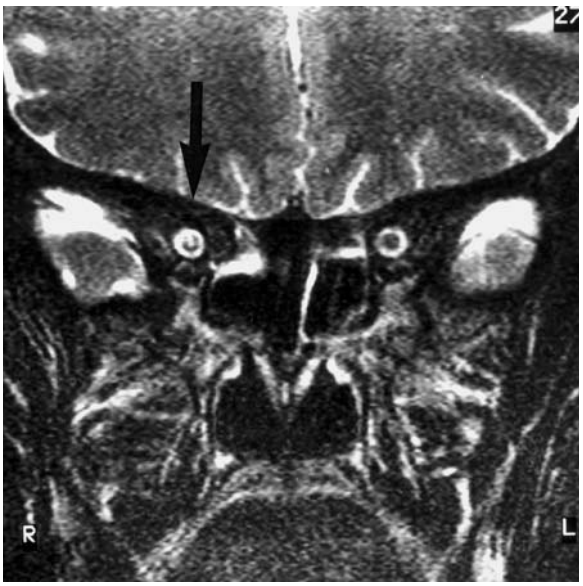

Fig. 6.187. A 50-year-old woman with persistent visual deficit and a history of chronic pseudotumor cerebri; postoperative state after optic sheath decompression. Diagnosis: postischemic defect of the right optic nerve. Coronal T2-weighted HR-MRI: high signal in the precanalicular part of the optic nerve. (With permission of Müller-Forell and Lieb 1995b)

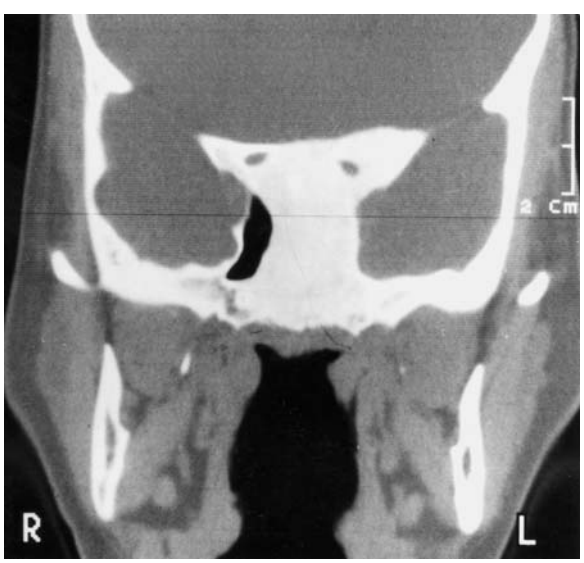

a

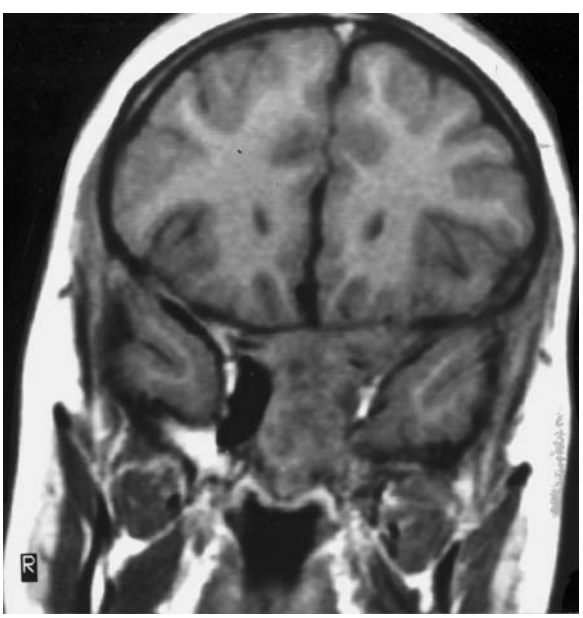

b

Fig. 6.188a,b. A 13-year-old boy with acute visual deficit. Diagnosis: fibrous dysplasia (Jaffé–Lichtenstein syndrome). CT (bone window): **a** Coronal view, showing homogeneous sclerosis of the small wings of the sphenoid bone with subsequent deformation and narrowing of both optic canals with emphasis to the left. T1-weighted MRI: **b** Corresponding view, where the optic nerves are not identified in the isointense signal of the pathologic sphenoid bone. (With permission of Müller-Forell and Lieb 1995b)

6.4.2 Inflammatory Lesion

6.4.2.1 Optic Neuritis (with or without Multiple Sclerosis)

Optic neuritis may be defined as an acute, unilateral or bilateral loss of central visual acuity, associated with central scotoma, loss of contrast sensitivity, color vision, stereopsis, and an afferent pupillary defect with or without associated retroocular pain on eye movement, as well as a reduced amplitude of the P100 component of the visual evoked potential (VEP) (Kakisu et al. 1991; Youl et al. 1991). The most common underlying pathologies are multiple sclerosis and acute disseminated encephalomyelitis (ADEM) (Fig. 6.189) (see also Sect 7.3.2.2.4.2). In 12%–30% of patients, acute optic neuritis is the first symptom of clinically not yet fully developed multiple sclerosis (Figs. 6.190, 6.191) (Christiansen et al. 1992; Frederiksen et al. 1992; Corona-Vasquez et al. 1997). Infections may also be responsible for

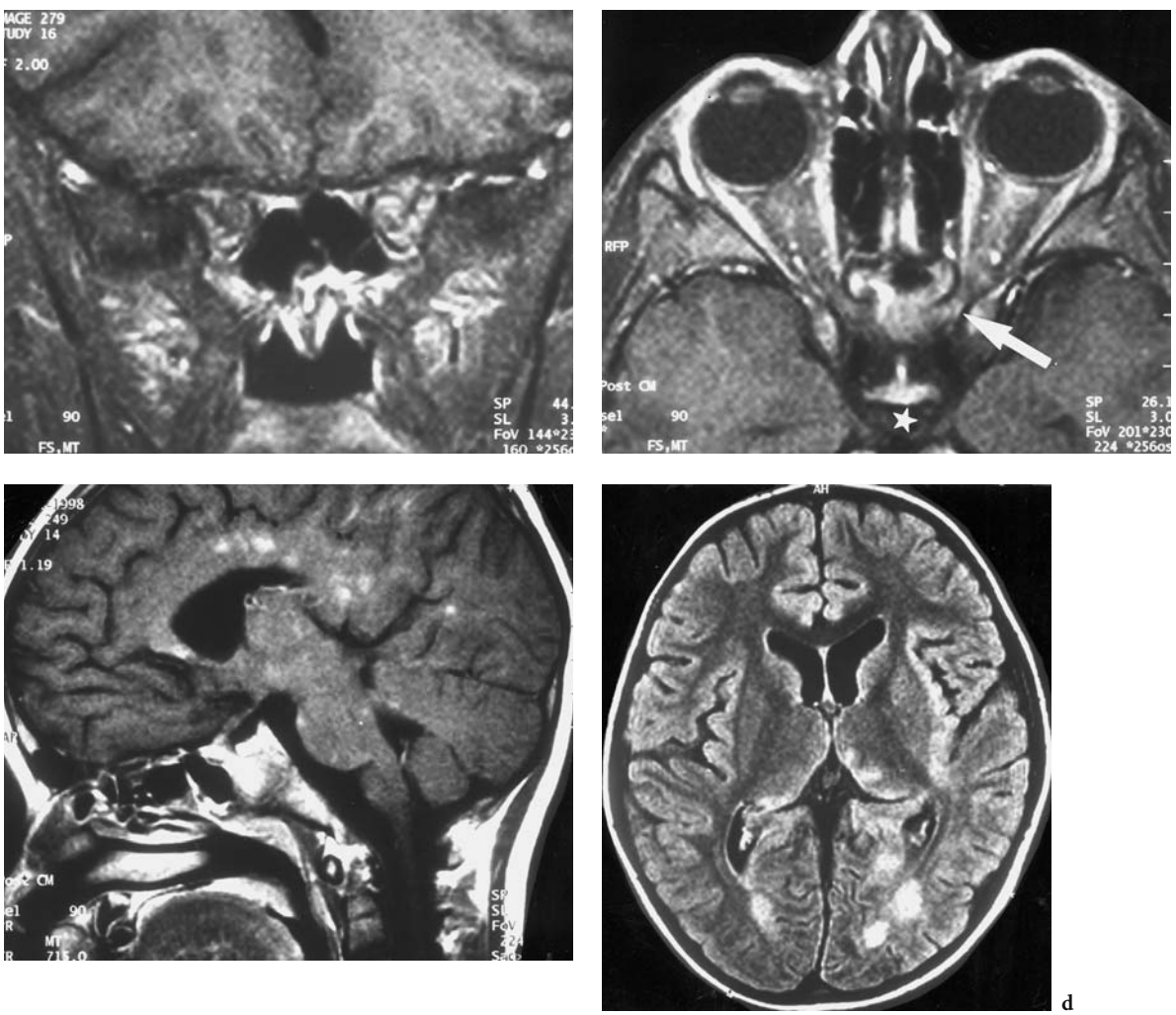

Fig. 6.189a–d. A 3-year-old boy with acute (not longer than 12 h) bilateral loss of vision (0.1) and acute, diffuse, disseminated pain in all parts of the body. Diagnosis: ADEM (acute disseminated encephalomyelitis). MRI: **a** Coronal T1-weighted (FS plus MT) native sequence demonstrating spontaneous signal enhancement of the left optic nerve in the optic canal. **b** Axial, T1-weighted, contrast-enhanced (FS) view, where the BBB disruption is accentuated after i.v. gadolinium (*white arrow*), including the chiasm (*white star*). **c** Left paramedian sagittal, T1-weighted, contrast-enhanced (plus MT) view, showing not only the high signal of the intracranial optic nerve, but also BBB disruption of multiple foci in the white matter of the cingulate gyrus, parietal and occipital lobe, and brainstem. **d** Axial T2-weighted FLAIR image where additional inflammatory lesions are seen in both occipital lobes, in the area of the left optic radiation, and in both thalami. Clinical tests failed to confirm the differential diagnosis of multiple sclerosis (MS); however, the patient showed complete clinical recovery with increasing vision (r: 0.3, l: 0.2) after steroid therapy

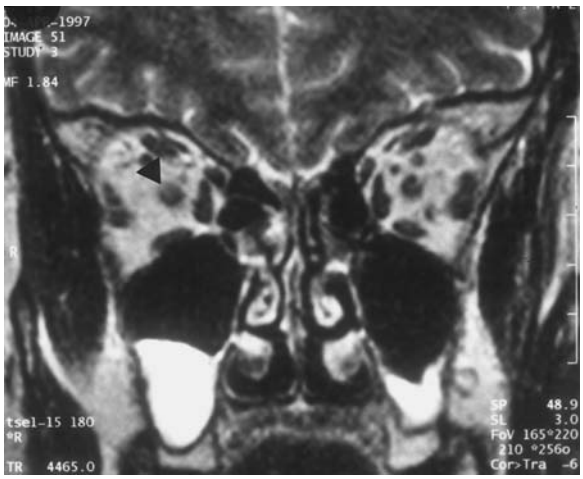

a

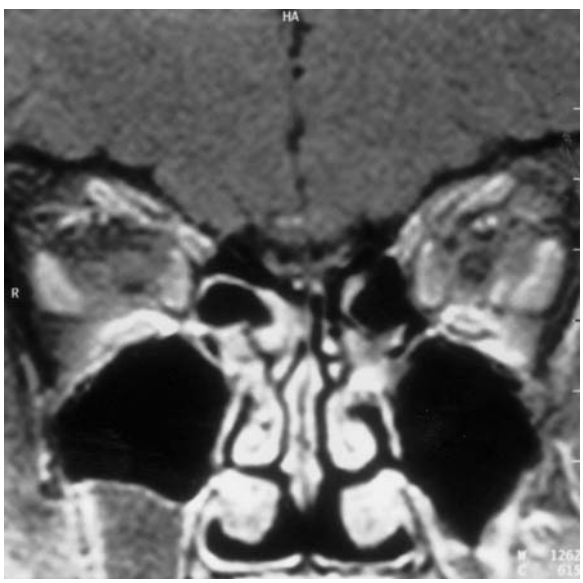

b

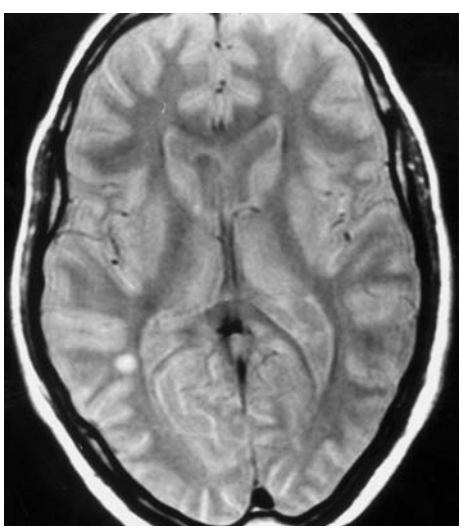

c

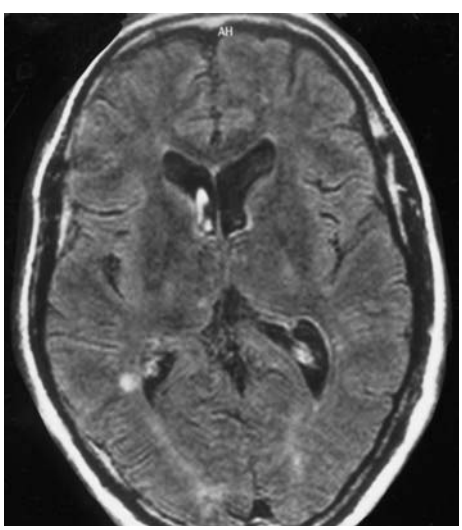

d

Fig. 6.190a–d. A 50-year-old man with first occurrence of right-sided loss of vision. Diagnosis: retrobulbar neuritis as the first manifestation of multiple sclerosis. MRI: **a** Coronal T2-weighted image with sharp signal enhancement of the right optic nerve (*triangle*). **b** Corresponding T1-weighted, contrast-enhanced (FS) image showing distinct enhancement of the right optic nerve. **c** Axial proton density intracranial view with demyelination in the region of right optic radiation. **d** Corresponding T2-weighted FLAIR image with typical paraventricular demyelination. (**a, b** with permission of Müller-Forell 1998)

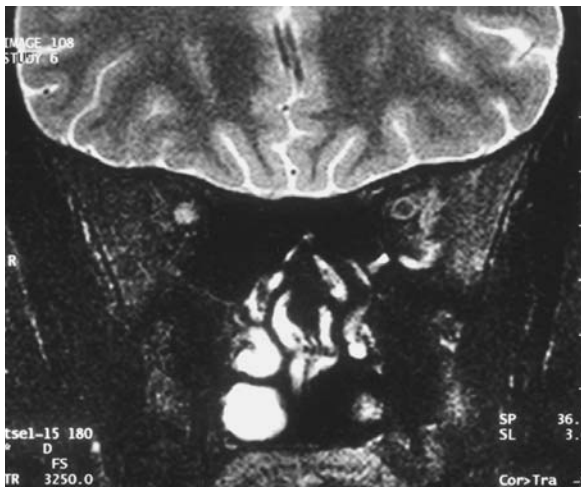

a

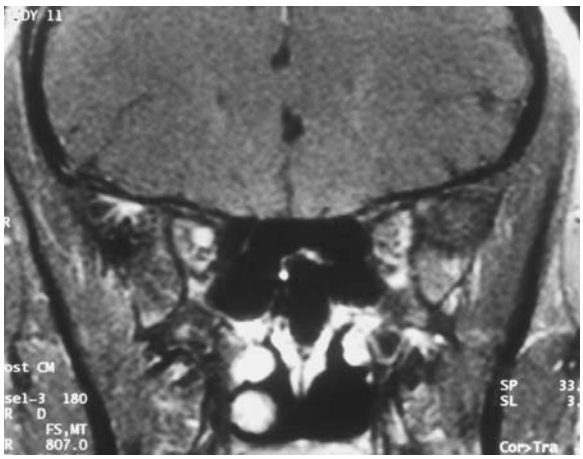

b

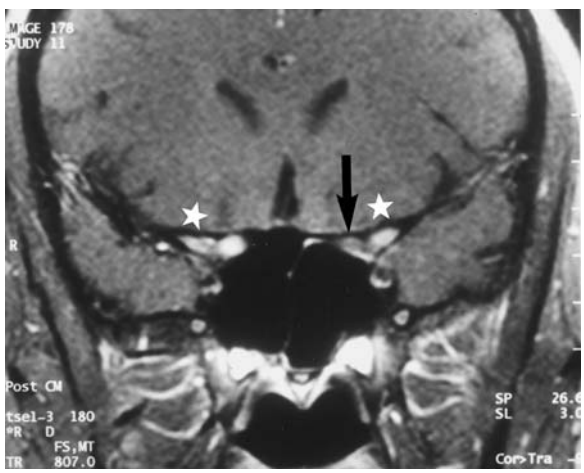

c

Fig. 6.191a–c. A 8-year-old girl with acute, nearly complete loss of vision in the right eye. Diagnosis: acute neuritis of the optic nerve of unknown origin. Neither symptoms nor clinical proof of multiple sclerosis or another inflammatory disorder were found. MRI: **a** Coronal T2-weighted (TSE) view with high signal intensity of the right intraorbital optic nerve. **b** Corresponding T1-weighted, contrast-enhanced (FS plus MT) sequence with apparent T1-shortening of the BBB disruption of the affected optic nerve. **c** Corresponding view at the level of the optic canal, where the swollen optic nerve appears thicker than the contralateral optic nerve (*arrow*). Note the high signal in the bone marrow of both clinoid process (*white stars*)

optic neuritis of different etiologies, which not only affect patients with human immunodeficiency virus (HIV) infection, where sporadic cases of various etiologies have been reported, but also immunocompetent patients. The various agents responsible for clinical symptoms include cytomegalovirus (causing retinitis and/or papillitis), varicella zoster, syphilis (leading to papillitis and perineuritis), mycosis, tuberculosis, and toxoplasmosis infections (Winward et al. 1989; McLeish et al. 1990; Gunduz and Ozdemir 1994; Nenning et al. 1994). Optic neuropathy is also known in patients suffering from autoimmune vasculitis and/or systemic lupus erythematosus (Dutton et al. 1982; Smith and Pinals 1982; Kira and Goto 1994), or paranasal infection (Sanborn et al. 1984). In rare cases, puerperal immune-mediated changes have been reported as responsible for activation of optic neuritis with relapsing multiple sclerosis (Leiba et al. 2000), and we saw optic neuritis in a patient with idiopathic inflammatory disease of the optic nerve and sheath (Fig. 6.183). However, in some cases, the triggering etiology remains unknown, despite extensive neurological and neurophysiological examination (Fig. 6.191).

Although secondary lesions of the optic nerve may be seen on CT, MRI is the imaging method of choice in the detection of intrinsic optic nerve lesions. The areas most frequently affected in optic neuritis are the intraorbital and intracanalicular portions of the optic nerve, while lesions of the chiasm (Fig. 7.10) or the papilla are rare (Kerty et al. 1991; Sartoretti-Schefer et al. 1997). In addition to an increased signal on T2-weighted and FLAIR images the majority of patients (81%) show contrast enhancement of the affected nerve as a sign of blood-optic-nerve barrier (BOB) disruption not only in acute but in even in persistent (more than 4 months) neuritis. Although it is no specific marker, as it is seen in a variety of inflammatory, ischemic, and tumorous disorders, multiple sclerosis is the most common underlying pathology in these cases (Sartoretti-Schefer

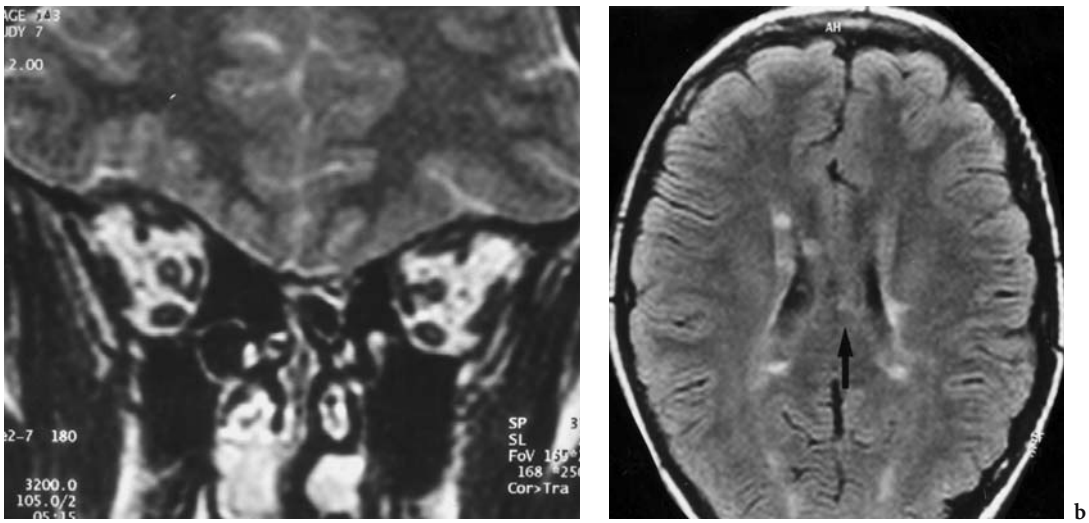

a b

Fig. 6.192a,b. A 13-year-old girl with first occurrence of acute right loss of vision with typical signs of retrobulbar neuritis. Diagnosis: multiple sclerosis. MRI: **a** Coronal T2-weighted image with distinct intraoptic signal enhancement of the right optic nerve. **b** Axial T2-weighted FLAIR-sequence of the intracranial parenchyma at the level of the cella media, demonstrating typical changes associated with multiple sclerosis as paraventricular and intracallosal (*arrow*) signal enhancement

et al. 1997). Focal thickening of the optic nerve or enhancement of the optic nerve sheath is less frequent, the latter occurring in perineuritis, a local variant of idiopathic orbital inflammation (Char et al. 1990), or in multiple sclerosis, preceding clinical symptomatology of optic neuritis (Beck et al. 1993; Sartoretti-Schefer et al. 1997). Focal contrast enhancement in acute demyelinating lesions is best demonstrated with fat-suppressed sequences (Guy et al. 1992; Sartoretti-Schefer et al. 1997). For differential diagnostic reasons, it is important to know that direct tumor infiltration of the optic nerve and sheath is known, especially in breast carcinoma and lymphoma (as leptomeningeal carcinomatosis), but with a nonspecific appearance, thus requiring consideration of the clinical history for a definite differential diagnosis (Char et al. 1990).

As mentioned elsewhere, optic neuritis may be the first symptom of multiple sclerosis, which is why a thorough evaluation of the brain should be performed (see Sect. 7.3.2.2.1). The finding of white matter lesions (3 mm or larger in diameter, at least one lesion periventricular or ovoid) allows us to determine whether or not these patients are at high risk for the development of clinically definite MS (Poser et al. 1984; Horowitz et al. 1989; Balcer 2001; Poser and Brinar 2001). Consequently, an effective treatment for optic nerve neuritis with intravenous methylprednisolone followed by oral prednisone and interferon-beta 1-a has been shown to reduce the development of clinically definite MS (Balcer 2001; Soderstrom 2001). In monosymptomatic optic neuritis, the visual deficit after 6 months is generally mild (Cleary et al. 1997). The prognosis of recovery is related to the MRI findings, as the location of acute optic neuritis in the intracanalicular portion of the optic nerve and a lesion greater than 17.5 mm are thought to lead to only incomplete or partial visual recovery (Dunker and Wiegand 1996).

6.4.2.2 Neuromyelitis Optica (Devic's Syndrome)

Neuromyelitis optica (Devic's syndrome), with the clinical syndrome of an acute and mostly simultaneously onset of (often bilateral) optic neuritis with total blindness and transverse myelitis of the cervical or upper thoracic spinal cord, is thought to be a disorder different from MS (van der Knaap and Valk 1995; Filippi et al. 1999; Wingerchuk et al. 1999). About 50% of patients die within several months of onset, mainly caused by respiratory failure as a consequence of cervical myelitis, another 15% of patients are reported to have a poor neurological outcome, while only about 35% of the patients are found to achieve a (nearly) complete recovery (van der Knaap and Valk 1995; Edwards-Brown and Bonin 1996; Margeaux et al. 1999; Wingerchuk et al. 1999). Along with optic nerve lesions and brain involvement, MRI shows single lesions of the cervi-

cal cord on T2-weighted images (Fig. 6.193), usually longer than two vertebral segments, and contrast-enhancing optic nerve lesions (Barkhof et al. 1991; Filippi et al. 1999; Wingerchuk et al. 1999).

6.4.2.3 Miscellaneous (Ectopic Pituitary Adenoma, Sphenoid Meningioma, Aneurysm)

Pituitary adenomas arising at a distance from the pituitary gland are rare. They develop as a result of defects in embryological migration and are found mostly in the sphenoid sinus or in the suprasellar region (Lloyd et al. 1986; Dyer et al. 1994; Hattori et al. 1994; Kikuchi et al. 1994b; Luk et al. 1996). In most cases, they manifest with pituitary dysfunction similar to findings in prolactinoma, Cushing disease, or acromegaly. To our knowledge, no case with hormone inactive ectopic pituitary adenoma in the clinoid process, presenting only with visual loss caused by optic nerve compression at the optic canal, has previously been reported (Fig. 6.194).

Despite a small diameter, the location of even small lesions in the vicinity of the optic canal may lead to optic nerve compression with residual visual deficit to loss of vision, whether the pathology arises from meningioma of the anterior clinoid process

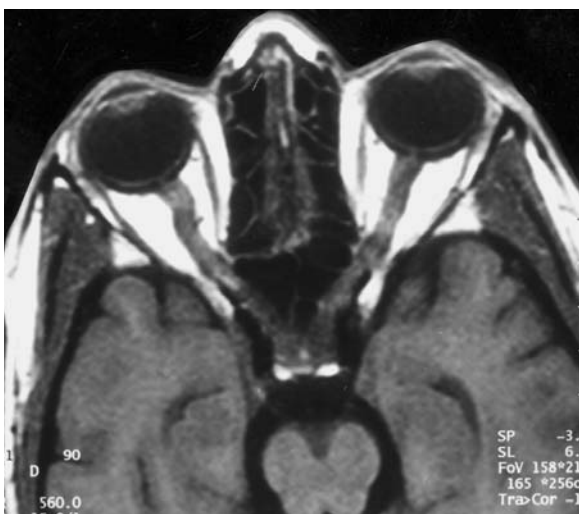

a

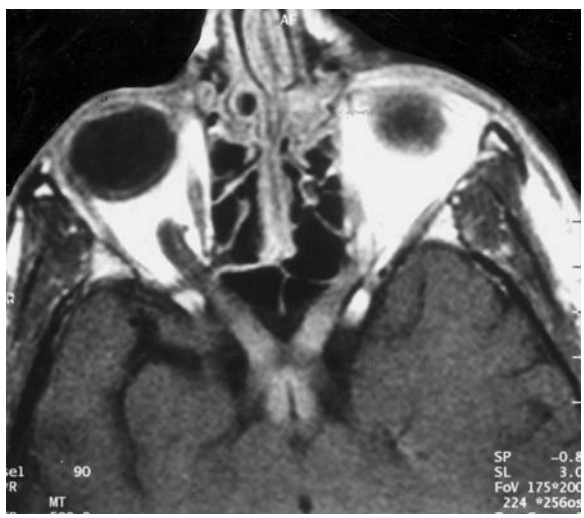

b

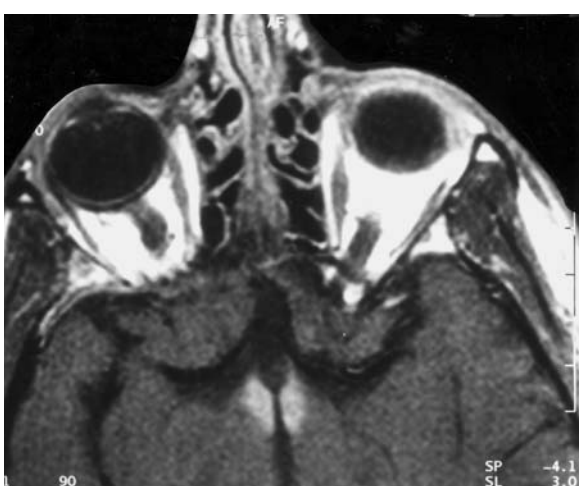

c

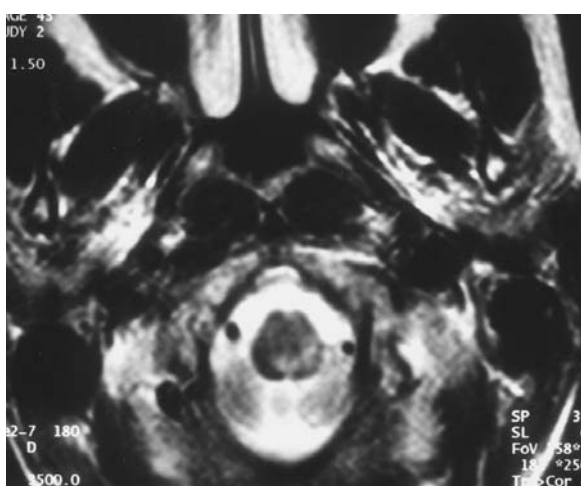

d

(Fig. 6.195) or an aneurysm of the internal carotid/ophthalmic artery (Fig. 6.196).

The diagnosis of optic nerve atrophy is usually made on clinical grounds. The typical clinical findings are relative afferent pupillary deficit, visual field loss, and optic disc swelling or atrophy. The vast majority are caused by ischemic or inflammatory processes, and the diagnosis may be adequately based on clinical findings and anamnestic data. However, the work-up may require imaging when compressive neuropathy is suspected (Burde et al. 1992). The hallmark of compressive disease, requiring a decision as to whether or not surgical therapy is needed, is painless, progressive loss of visual function (Fig. 6.197) (Lee and Brazis 1998).

6.4.3 Traumatic Lesions

In traumatic disorders of the face and orbit, the optic nerve may be one of the structures involved (Fig. 6.198), but single lesions of the optic nerve are rare. In cases where the extent of the injury is at variance with the clinical presentation, high-resolution CT may detect even small fractures as shown in Fig. 6.199.

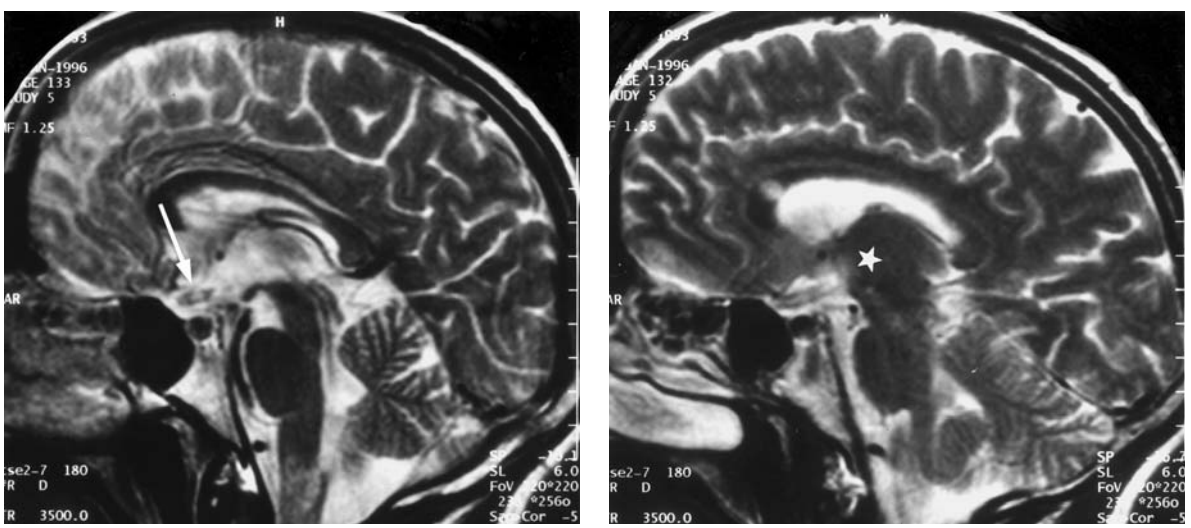

e **f**

Fig. 6.193a–f. A 42-year-old woman with acute symptomatology of retrobulbar neuritis, associated with tetraparesis. Diagnosis: neuromyelitis optica, type Device. MRI: **a** Axial T1-weighted view with a spontaneous slight enhancement of both optic nerves. **b** Axial T1-weighted native MT sequence demonstrating a primarily high signal of both intracranial optic nerves, the chiasm and the tuber cinereum. **c** Corresponding view above the level of the chiasm with primarily high signal of the tuber cinereum and some regions of the hypothalamus. **d** Axial T2-weighted image at the level of the foramen magnum visualizing the disseminated character of the demyelination as a high-signal area in the left region of the medulla of the craniocervical junction. **e** Corresponding sagittal view with high signal in the medulla oblongata and chiasm (*white arrow*). **f** Additional demyelination is demarcated in the genu of the corpus callosum. Note the demyelination of the hypothalamus (*white star*) and anterior part of the optic tract

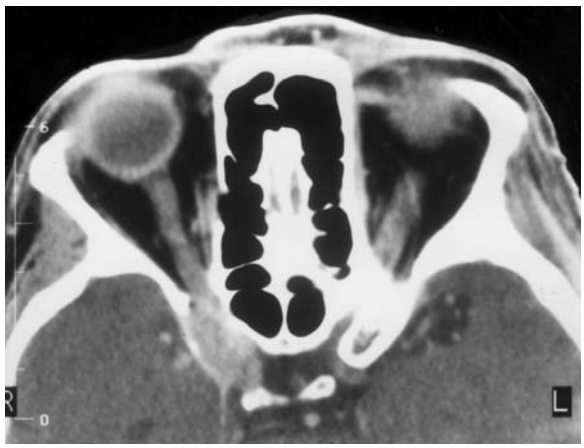
a

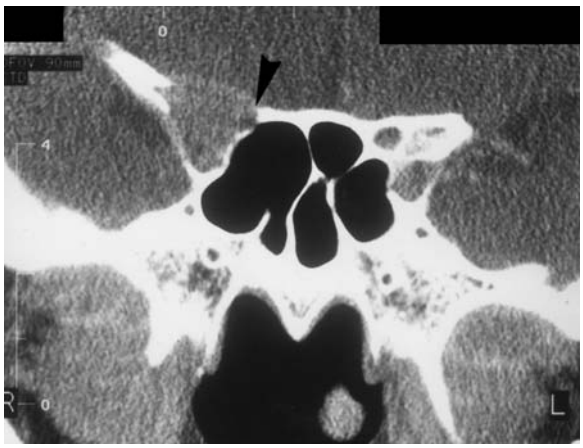
b

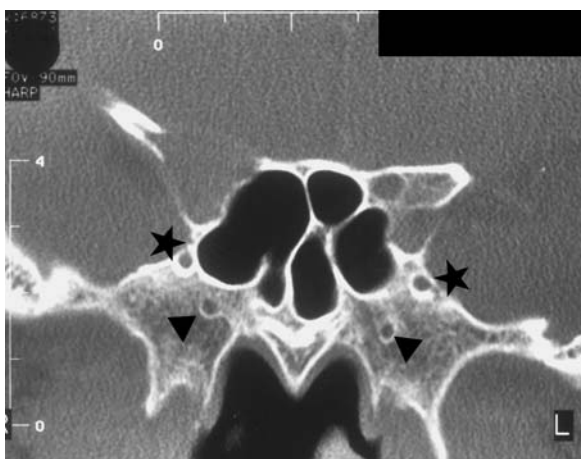
c

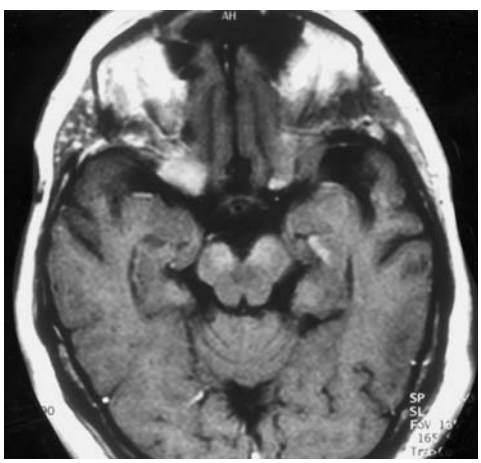
d

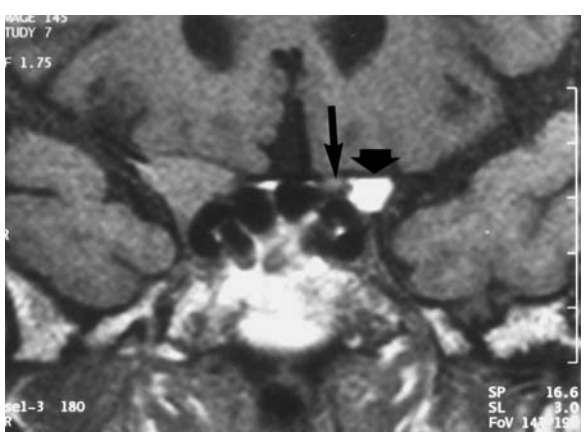
e

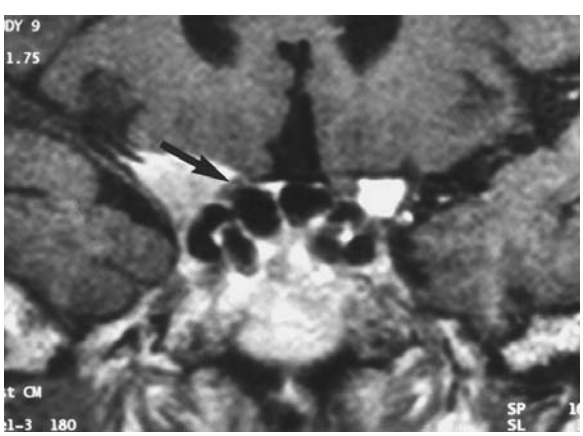
f

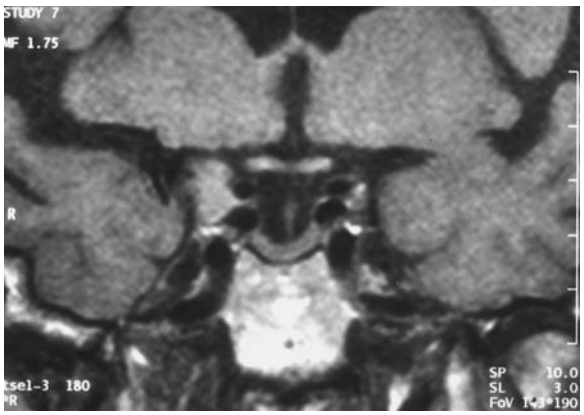

g

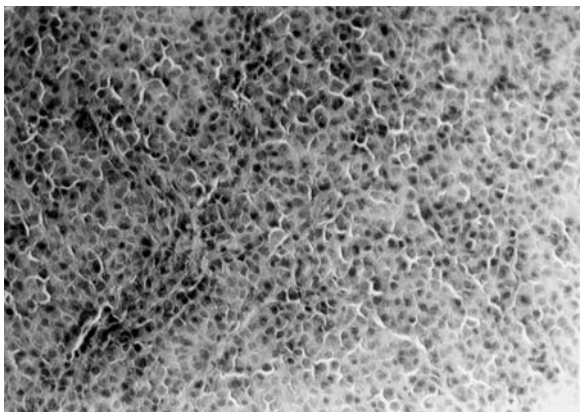

h

Fig. 6.194a–h. A 73-year-old woman with acute vision loss, suggesting internal optic atrophy (IOA). Diagnosis: extrasellar pituitary adenoma. CT: **a** Axial contrast-enhanced view at the level of the optic canal, demonstrating destruction of the anterior clinoid process with apparent compression of the optic nerve. **b** Coronal contrast-enhanced view. Despite its destructive character, the tumor is well-differentiated and clearly visualized. The small medial hypodensity (*arrowhead*) represents the optic nerve. **c** Corresponding bone window where the destruction of the walls of the optic canal, including the superior orbital fissure, is readily identified (*stars*: round foramen, *triangles*: vidian canal). MRI: **d** Axial, T1-weighted, contrast-enhanced view, a few millimeters superior to **a**. **e** Coronal T1-weighted native view (corresponding to **b** and **c**), demonstrating the strictly extradural location of the tumor with inferior extension along the cavernous sinus. Note the high signal of bone marrow fat in the left clinoid process (*short arrow*) left optic nerve (*arrow*). **f** Corresponding contrast-enhanced view with homogeneous signal enhancement of the tumor. Note flattening of the optic nerve (*arrow*) in its canalicular course. **g** Coronal T1-weighted native view at the level of the pituitary stalk, demonstrating the relationship to the uninvolved pituitary gland in an initially empty sella. **h** Histology (×280): polygonal epithelial tumor cells with round nuclei are forming a solid and uniform tissue, interrupted by only a few islets of connective tissue with some blood vessels. (With permission of Dr. Bohl, Department of Neuropathology, Medical School, Mainz)

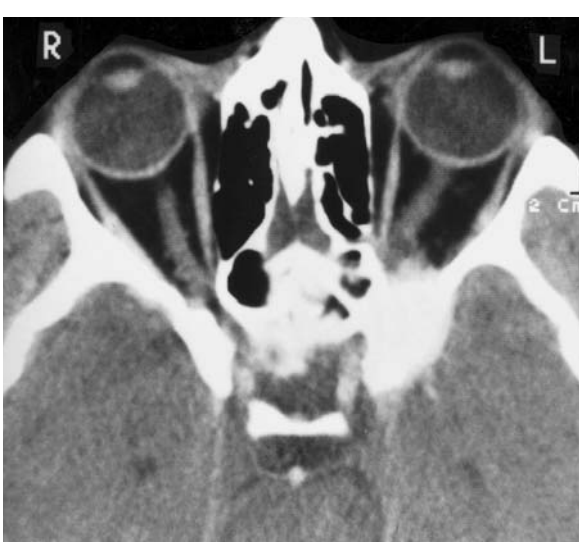

a

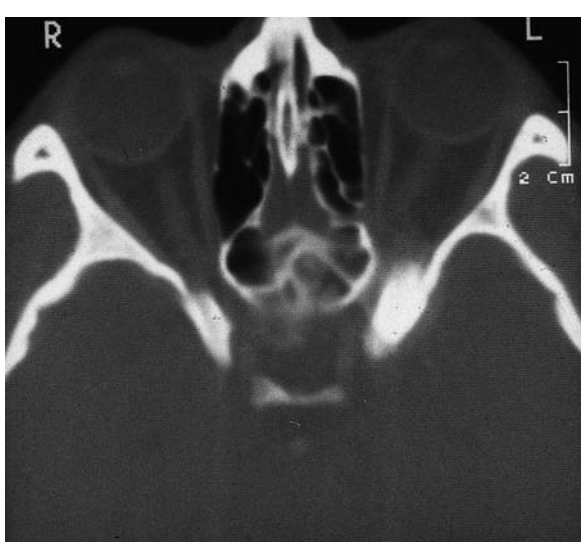

b

Fig. 6.195a,b. A 50-year-old woman with progressive visual deficit of the left eye. Diagnosis: left sphenoid wing meningioma of the clinoid process. Axial, contrast-enhanced CT: **a** Considerable thickening of the left sphenoid wing with emphasis on the clinoid process and constriction of the optic canal. **b** Corresponding image in bone window. (With permission of Müller-Forell and Lieb 1995)

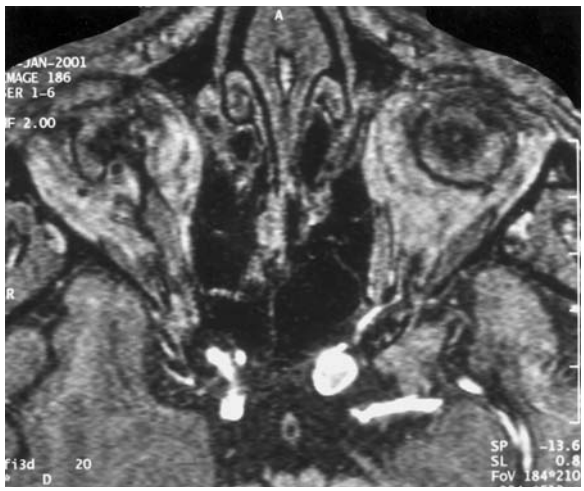

a

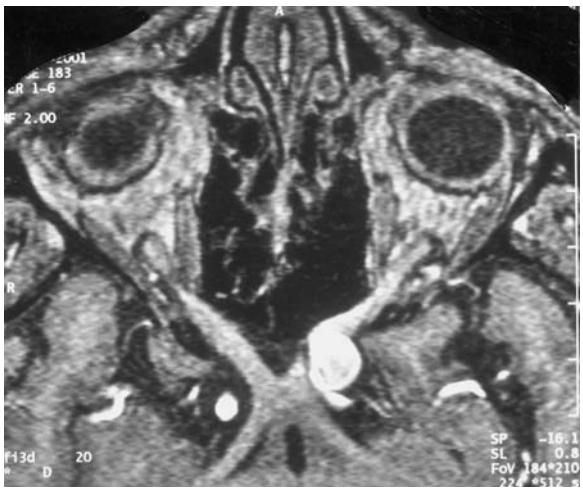

b

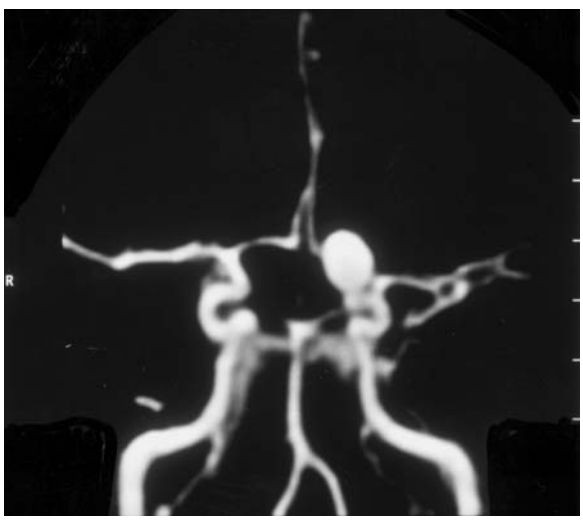

c

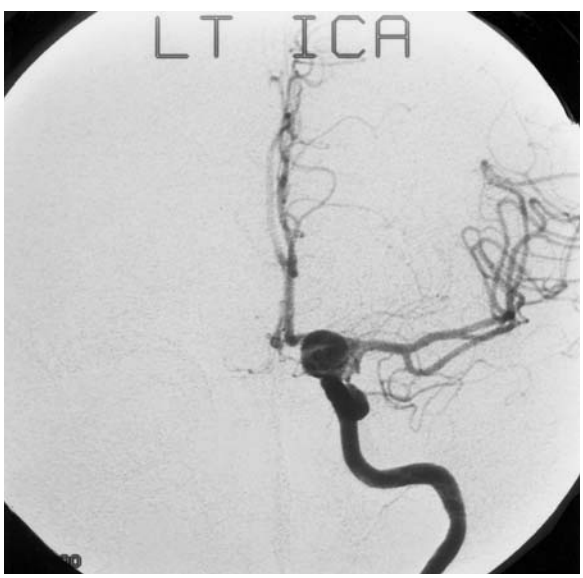

d

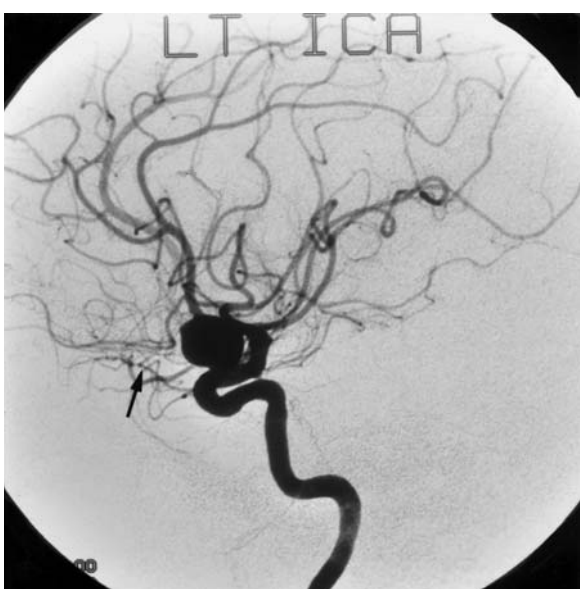

e

Fig. 6.196a–e. A 49-year-old woman presenting with chronic headache. No visual deficits were identified, but signs of left optic nerve compression were detected on Goldman visual field examination. Diagnosis: incidental ophthalmic aneurysm of the left internal carotid artery. MRI: **a** Axial T1-weighted HR view at the level of the ophthalmic artery, showing an aneurysm arising anteriorly at the origin. **b** At a level 2.5 mm above, the striking impression of the left optic nerve along the proximal intracranial course is seen. **c** MR-angiography (maximum intensity projection, MIP reconstruction) demonstrating extension of the lesion superiorly. DSA: **d** Corresponding AP view of the left carotid artery injection. **e** Lateral view, where the origin of the aneurysm at the origin of the ophthalmic artery (*arrow*) becomes apparent

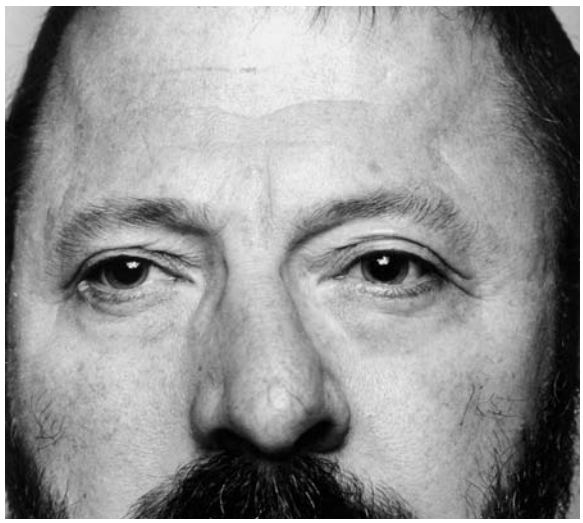

a

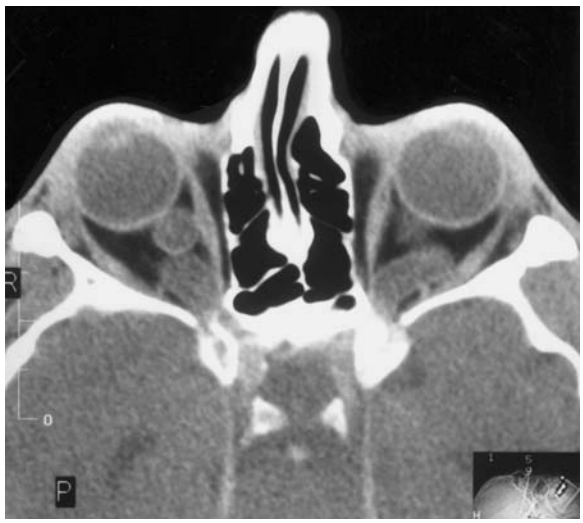

b

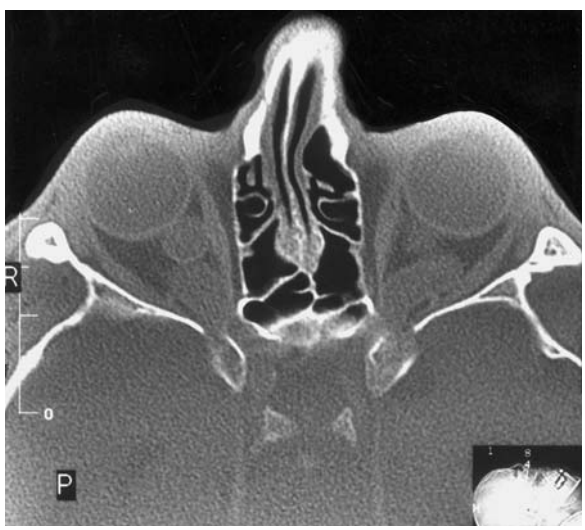

c

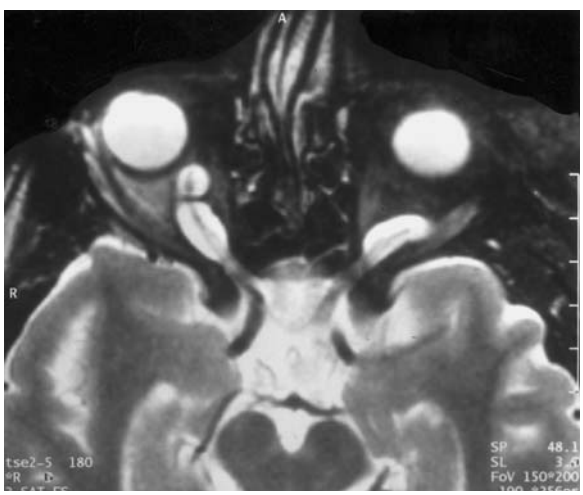

d

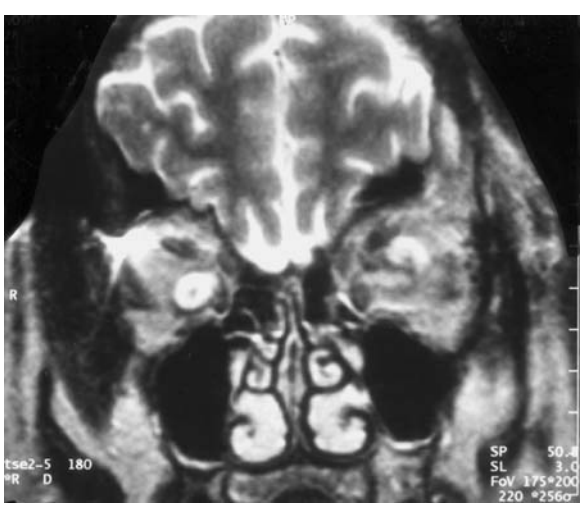

e

Fig. 6.197a–e. A 50-year-old man with optic nerve atrophy of the right eye (after trauma in childhood), presenting with a slowly progressing loss of vision (0.3) in the left eye (which improved after optic sheath decompression). Diagnosis: bilateral optic nerve atrophy, probably due to craniosynostosis (turricephaly). **a** Portrait of the patient. CT: **b** Axial view where bilateral dilation and kinking of the optic nerve sheath without narrowing of the optic canal are visualized. **c** Corresponding bone window. Note the flat angle of both orbits, due to skull deformity. T2-weighted MRI: **d** Axial view clearly demonstrating narrowed, small optic nerves in dilated subarachnoid space of both optic nerve sheaths. **e** Coronal view

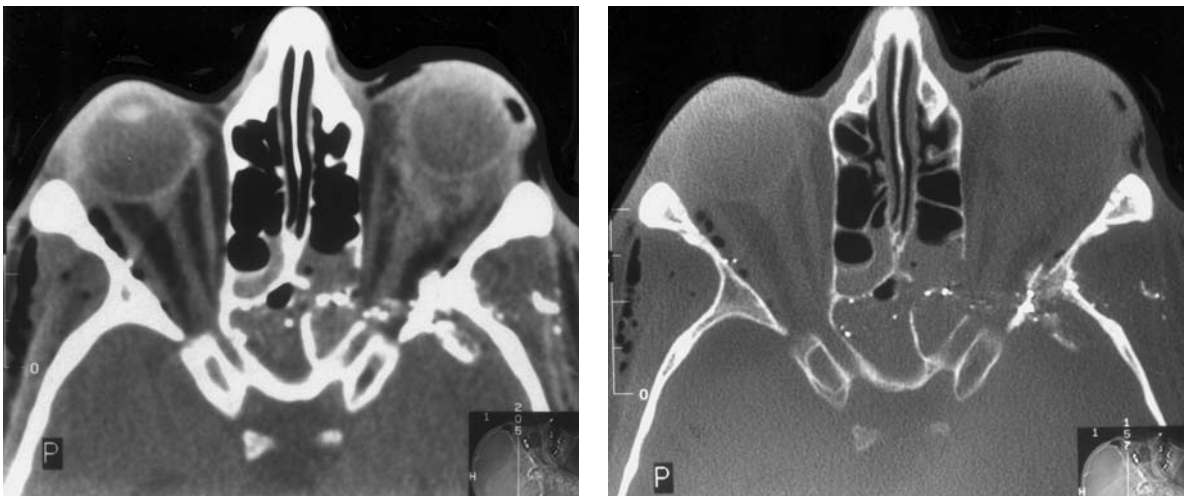

Fig. 6.198a,b. A 33-year-old man with bullet injury after suicide attempt. Diagnosis: rupture of the left optic nerve. CT: **a** axial view at the level of the optic nerve showing rupture of the optic nerve in the left orbital apex, bullet and bone fragments, as well as destruction of the lateral and medial orbital wall. Note the deformed globe, which ruptured as a result of the sudden, great pressure enhancement produced by the shot. The irregular hyperdensities of the retrobulbar space correspond to the presence of an additional retrobulbar hematoma. **b** Corresponding bone window with distinct differentiation of the different fragment materials. Note additional air bubbles in the right orbit and temporal fossa

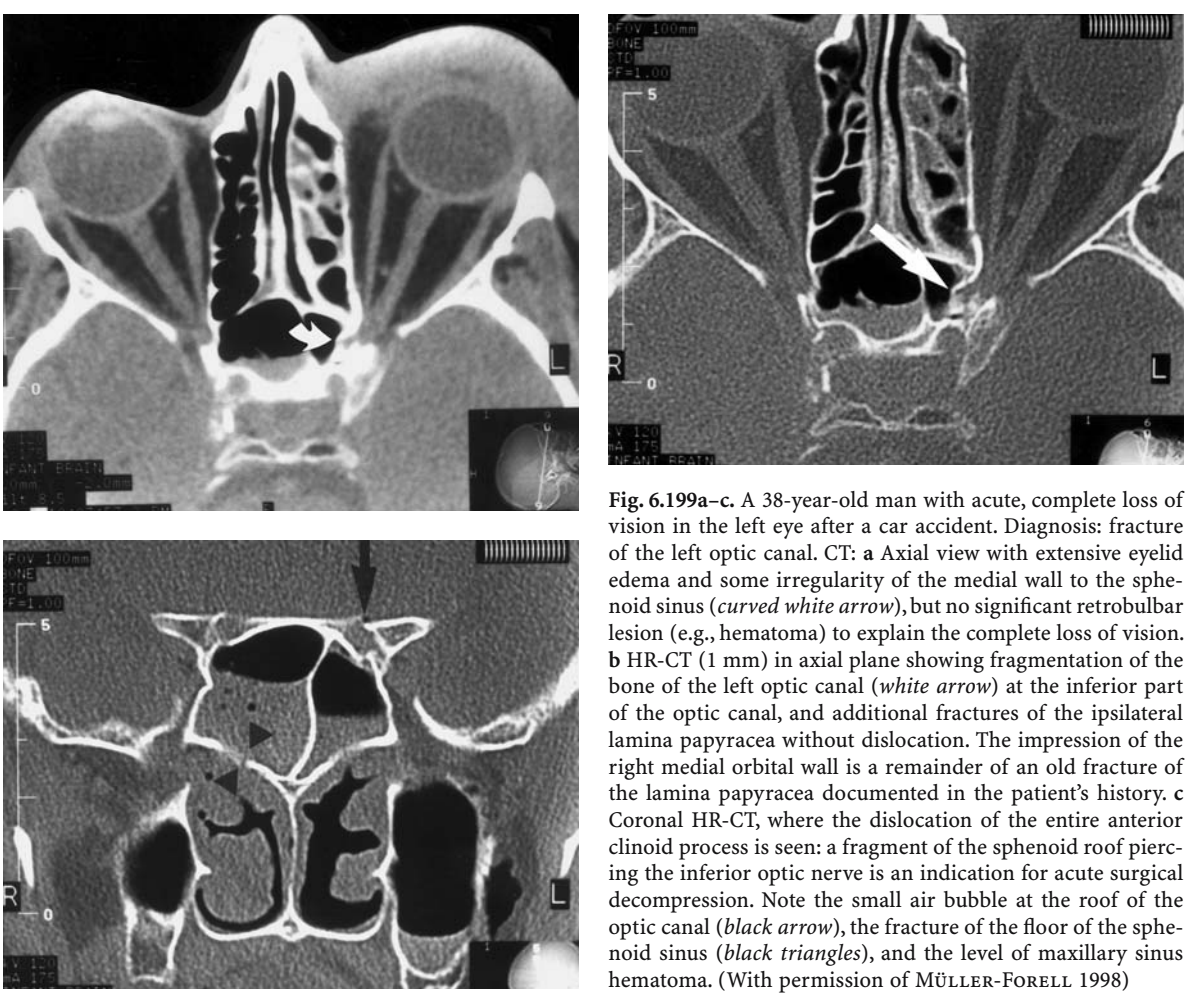

Fig. 6.199a–c. A 38-year-old man with acute, complete loss of vision in the left eye after a car accident. Diagnosis: fracture of the left optic canal. CT: **a** Axial view with extensive eyelid edema and some irregularity of the medial wall to the sphenoid sinus (*curved white arrow*), but no significant retrobulbar lesion (e.g., hematoma) to explain the complete loss of vision. **b** HR-CT (1 mm) in axial plane showing fragmentation of the bone of the left optic canal (*white arrow*) at the inferior part of the optic canal, and additional fractures of the ipsilateral lamina papyracea without dislocation. The impression of the right medial orbital wall is a remainder of an old fracture of the lamina papyracea documented in the patient's history. **c** Coronal HR-CT, where the dislocation of the entire anterior clinoid process is seen: a fragment of the sphenoid roof piercing the inferior optic nerve is an indication for acute surgical decompression. Note the small air bubble at the roof of the optic canal (*black arrow*), the fracture of the floor of the sphenoid sinus (*black triangles*), and the level of maxillary sinus hematoma. (With permission of Müller-Forell 1998)

References

Abe T, Kawamura N, Homma H, Sasaki K, Izumiyama H, Matsumoto K (2000) MRI of orbital schwannomas. Neuroradiology 42:466–468

Abramson DH, Ellsworth RM, Tretter P (1981) Treatment of bilateral groups I through III retinoblastoma with bilateral radiation. Arch Ophthalmol 99:1761–1762

Abramson DH (1982) Retinoblastoma: diagnostic management. Cancer J Clin 32:130– 140

Achauer BM, Vander Kam VM (1989) Capillary hemangioma (strawberry mark) of infancy: comparison of argon and Nd:YAG laser treatment. Plast Reconstr Surg 84:60–69

Adhikary H, Fitzmaurice DJ (1982) Presentation of orbital rhabdomyosarcoma. Clin Oncol 8:21–23

Agulnik M, Tsang R, Baker MA, Kazdan MS, Fernandes B (2001) Malignant lymphoma of mucosa-associated lymphoid tissue of the lacrimal gland: case report and review of the literature. Am J Clin Oncol 24:67–70

Ahmadi J, Teal JS, Segall HD, Zee CS, Han JS, Becker TS (1983) Computed tomography of carotid-cavernous fistula. AJNR Am J Neuroradiol 4:131–136

Akman-Demir G, Serdaroglu P, Tasci B (1999) Clinical patterns of neurological involvement in Behçet's disease: evaluation of 200 patients. The Neuro-Behçet Study Group. Brain 122:2171–2182

Akpek EK, Ahmed I, Hochberg FH, Soheilian M, Dryja TP, Jakobiec FA, Foster CS (1999) Intraocular-central nervous system lymphoma: clinical features, diagnosis, and outcome. Ophthalmology 106:1805–18110

Albert D, Puliafito C (1979) Foundations of ophthalmic pathology. Appleton-Century-Crofts, New York

Albright F, Butler AM, Hampton AO et al (1937) Syndrome characterized by osteitis fibrosa disseminata, areas of pigmentation and endocrine dysfunction with precocious puberty in females. N Engl J Med 216:727 (cited after Wenig et al. 1998)

Alexiou C, Kau RJ, Dietzfelbinger H, Kremer M; Spiess JC, Schratzenstaller B, Arnold W (1999) Extramedullary plasmocytoma: tumor occurrence and therapeutic concepts. Cancer 85:2305–2314

Alshail E, Rutka JT, Becker LE (1977) Optic chiasmatic-hypothalamic glioma. Brain Pathol 7:799–806

Alvord EC, Lofton S (1988) Gliomas of the optic nerve or chiasm: outcome by patient's age, tumor site and treatment. J Neurosurg 68:85–98

Anderson R, Panje W, Gross C (1982) Optic nerve blindness following blunt forehead trauma. Ophthalmology 89:445–455

Aoki S, Barkovich AJ, Nishimura K, Kjos BO, Machida T, Cogen P, Edwards M, Norman D (1989) Neurofibromatosis types 1 & 2: cranial MR findings. Radiology 172:527–534

Asao C, Korogi Y, Hotta A, Miyayama H, Negi A, Takahashi M (1998) Orbital lymphoproliterative diseases. Magnetic resonance imaging and pathological findings. Int J Neuroradiol 4:439–444

Atlas SW, Galetta SL (1996) The orbit and visual system. In: Atlas SW (ed) Magnetic resonance imaging of the brain and spine, 2nd edn. Lippincott-Raven, Philadelphia, pp 1007–1092

Atlas SW, Grossman RI, Hackney DB, Goldberg HI, Bilaniuk LT, Zimmerman RA (1988) STIR MR imaging of the orbit. Am J Roentgenol 151:1025–1030

Atmaca LS, Idil A; Batioglu F (1996) A descriptive study on Behçet's disease. Acta Ophthalmol Scand 74:403–406

Au Eong KG, Choo CT (1997) Burkitt lymphoma manifesting as acute proptosis. Am J Ophthalmol 123:856–858

Bachmann KD, Bartram CR, Chan-Claude J, Fonatsch C, Propping P (1998) Richtlinien zur Diagnostik der genetischen Disposition für Krebserkrankungen. Dtsch Ärztebl 95:A1396–A1403

Bader JL, Meadows AT, Zimmerman LE Rorke LB, Voute PA, Champion LA, Miller RW (1982) Bilateral retinoblastoma with ectopic intracranial retinoblastoma: trilateral retinoblastoma. Cancer Genet Cytogenet 5:203–213

Bairey O, Kremer I, Rakowsky E, Hadar H, Shaklai M (1994) Orbital and adnexal involvement in systemic non-Hodgkin´s lymphoma. Cancer 73:2395–2398

Balcer LJ (2001) Optic neuritis. Curr Treatment Opt Neurol 3:389–398

Balcer LJ, Liu GT, Heller G, Bilaniuk L, Volpe NJ, Galetti SL, Molloy PT, Phillips PC, Janss A, Vaughn S, Maguire M (2001) Visual loss in children with neurofibromatosis type 1 and optic pathway gliomas: relation to tumor location by magnetic resonance imaging. Am J Ophthalmol 131:442–445

Banna M, El-Ramahi K (1991) Neurologic involvement in Behçet disease: imaging findings in 16 patients. AJNR Am J Neuroradiol 12:791–796

Barkhof F, Scheltens P, Valk J, Waalewijn C, Uitdehaag BM, Polamn CH (1991) Serial quantitative MR assessment of optic neuritis in a case of neuromyelitis optica, using gadolinium-"enhanced" STIR imaging. Neuroradiology 33:70–71

Barkovich AJ (2000) Pediatric neuroimaging, 3rd edn. Raven, New York

Beck RW, Kupersmith MJ, Cleary PA, Katz B (1993) Fellow eye abnormalities in acute unilateral optic neuritis. Experience of the optic neuritis treatment trial. Ophthalmology 100:691–697

Becker MH (1986) The lacrimal drainage system. In: Gonzales CF, Becker MH, Flanagan JC (eds) Diagnostic imaging in ophthalmology. Springer, Berlin Heidelberg New York, pp 81–91

Behçet H (1937) Über rezidivierende, aphtöse, durch ein Virus verursachte Geschwüre am Mund, am Auge und an den Genitalien. Dermatol Wochenschr 105:1152–1157

Bellone G, Gallenga PE, Pasquarelli A (1974) Objective interpretation of eye and orbit tissue echograms. Ophthalmologica 169:290– 298

Berenholz L, Kessler A, Shlomkowitz N, Sarfati S, Segal S (1998) Superior ophthalmic vein thrombosis: complication of ethmoidal rhinosinusitis. Arch Ophthalmol Head Neck Surg 124:95–97

Berenstein A, Lasjaunias P (1992) Vein of Galen aneurysmal malformation. In: Berenstein A, Lasjaunias P (eds) Surgical neuroangiography, Vol 4. Endovascular treatment of cerebral lesions. Springer, Berlin Heidelberg New York, pp 267–317

Bettelheim H, Till P (1975) Diagnosis of orbital vascular disorders by ophthalmodynamography and echo-orbitography. Mod Probl Ophthalmol 14:299–304

Bilaniuk LT (1999) Orbital vascular lesions. Role of imaging. Radiol Clin North Am Imaging Ophthalmol II:169–183

Bilaniuk LT, Rappoport RJ (1994) Magnetic resonance imaging of the orbit. Top Magn Reson Imaging 6:167–181

Bilaniuk LT, Zimmerman A, Newton T (1990) Magnetic resonance imaging: orbital pathology. In: Newton T, Bilaniuk L (eds) Radiology of the eye and orbit. Raven, New York, pp 5.1–5.84

Biondi A, Casasco A, Houdart E, Gioino C, Sourour N, Vivas E, Dormont D, Marsault C (1999) Evolution of angiographic signs of venous hypertension and clinical signs of intracranial hypertension in intracranial dural arteriovenous fistula. J Neuroradiol 26:49–58

Block P, Carroll R, Zhang J (1996) The molecular biology of hormone and growth factor receptors in meningeoma. Acta Neurochir Suppl (Wien) 65:50–53

Brodsky MC (1993) The «pseudo-CSF» signal of orbital optic glioma on magnetic resonance imaging: a signature of neurofibromatosis. Surv Ophthalmol 38:213–218

Bron AJ, Tripathi RC, Tripathi BJ (1997) Wolff's anatomy of the eye and orbit, 8th edn. Chapman and Hall, London

Brown EW, Riccardi VM, Mawad M, Handel S, Goldman A, Bryan RN (1987) MR imaging of optic pathways in patients with neurofibromatosis. AJNR Am J Neuroradiol 8:1031–1036

Brownstein S, Belin MW, Krohel GB, Smith RS, Condon G, Codere F (1984) Orbital dacryops. Ophthalmology 91:1424–1428

Burde RM, Savino PJ, Trobe JD (1992) Clinical decisions in neuro-ophthalmology. Mosby Year Book, St Louis, pp 56–57

Byrne SR, Glaser JS (1983) Orbital tissue differentiation with standardized echography. Ophthalmology 90:1071–1090

Callender GR (1931) Malignant melanotic tumors of the eye: a study of histologic types in III cases. Trans Am Acad Ophthalmol Otolaryngol 36:131–142

Campbell R, Sobin LH (1998) Histologic typing of tumours of the eye and its adnexal. World Health Organization international histological classification of tumours. Springer, Berlin Heidelberg New York

Cappaert WE, Kiprov KE; Frank KE (1983) Sector B-scan ultrasonographic "hemangiomalike" pattern. Arch Ophthalmol 101:74–77

Carmody RF (2000) The orbit and visual system. In: Orrison WW Jr (ed) Neuroimaging. Saunders, Philadelphia, pp 1009–1069

Carmody RF, Mafee MF, Goodwin JA, Small K, Haery C (1994) Orbital and optic pathway sarcoidosis: MR findings. AJNR Am J Neuroradiol 15:775–783

Carroll GS, Haik BG, Fleming JC, Weiss RA, Mafee MF (1999) Peripheral nerve tumors of the orbit. Imaging in ophthalmology II. Radiol Clin North Am 37:195–202

Cascone P, Valentini V, Agrillo A (1998) Orbital hemangiopericytoma: case report of a long-term recurrency. J Craniofac Surg 9:55–59

Casper DS, Chi TL, Trokel SL (eds) (1993) Orbital disease, imaging and analysis. Thieme, Stuttgart

Casselman JE, DeJonge I, Neyt L, DeClerq D, D'Hont G (1993) MRI in craniofacial fibrous dysplasia. Neuroradiology 35:234–237

Cassier C, Kien P, Caillé JM (1986) CT images in constitutional abnormalities of the posterior pole of the eye: optic disc coloboma, posterior pole staphyloma. J Neuroradiology 13:11–21

Cassoux N, Merle-Beral H, Leblond V, Bodaghi B, Milea D, Gerber S, Fardeau C, Reux I, Xuan KH, Chan CC, LeHoang P (2000) Ocular and central nervous system lymphoma: clinical features and diagnosis. Ocul Immunol Inflamm 8:243–250

Castillo M, Wallace DK, Mukherji SK (1997) Persistent hyperplastic primary vitreous involving the anterior eye. AJNR Am J Neuroradiol 18:1526–1528

Cavanee WK, Murphree AL, Lingua RW (1986) Prediction of familial predisposition to retinoblastoma. N Engl J Med 314:1201–1207

Chajek T, Fainaru M (1975) Behçet's disease: report of 41 cases and a review of the literature. Medicine (Baltimore) 54:179–196

Chandler JR, Langenbrunner DJ, Stevens ER (1970) The pathogenesis of orbital complications in acute sinusitis. Laryngoscope 80:1414–1428

Chandra S, Vashisht S, Menon V, Berry M, Mukherji K (2000) Optic nerve cysticercosis: imaging findings. AJNR Am J Neuroradiol 21:198–200

Chang M, McLean IW, Merritt JC (1984) Coats' disease: a study of 62 histologically confirmed cases. J Pediatr Ophthalmol Strabismus 21:163–168

Char DH (1978) The management of small choroidal melanomas. Surv Ophthalmol 22:377–387

Char DH (1990) Thyroid eye disease, 2nd edn. Churchill Livingstone, New York

Char DH, Hedges TR, Norman D (1984) Retinoblastoma: CT diagnosis. Ophthalmology 92:1347–1350

Char DH, Unsöld R, Sobel DF, Salvolini U, Newton TH (1990) Computed tomography: ocular and orbital pathology. In: Newton TH, Bilaniuk LT (eds) Modern neuroradiology: radiology of the eye and orbit. Raven, New York, pp 9.1–9.64

Chin T, Wei CF (1993) Rhabdomyosarcoma in children: clinical analysis of 20 cases. J Formos Med Assoc 92:29–33

Christiansen P, Frederiksen JL, Henriksen O, Larsson HB (1992) Gd-DTPA-enhanced lesions in the brain of patients with acute optic neuritis. Acta Neurol Scand 85:141–146

Chu T, D'Angelo GJD, Favara B (1987) Histiocytosis syndromes in children. Lancet 1:208–209

Chumas PD, Cinalli G, Arnaud E, Marchac D, Renier D (1997) Classification of previously unclassified cases of craniosynostosis. J Neurosurg 86:177–181

Cinciripini GS, Donahue S, Borchert MS (1999) Idiopathic intracranial hypertension in prepubertal pediatric patients: characteristics, treatment and outcome. Am J Ophthalmol 127:178–182

Clark WC, Acker JD, Dohan FC (1985) Presentation of central nervous system sarcoidosis as intracranial tumors. J Neurosurg 63:851–856

Cleary PA, Beck RW, Bourque LB, Backlund JC, Miskala PH (1997) Visual symptoms after optic neuritis. Results from the optic neuritis treatment. J Neuroophthalmol 17:18–23

Coats G (1908) Forms of retinal disease with massive exudation. Royal London Ophthalmologic Hospital Reports17:440–525

Cohen MM, Lessell S (1979) Amyloid tumor of the orbit. Neuroradiology 18:157–159

Cohen MM Jr (1987) Craniosynostosis update 1987. Am J Med Genet Suppl 4:99–148

Cohen JA, Char DH, Norman D (1995) Bilateral orbital varices associated with habitual bending. Arch Ophthalmol 113:1360–1362

Coleman DJ, Jack RL, Franzen LA (1972) High resolution B-scan ultrasonography of the orbit. II. Hemangiomas of the orbit. Arch Ophthalmol 88:368–374

Collaborative Ocular Melanoma Study (COMS) (1998) Randomized trial of pre-enucleation radiation of large cho-

roidal melanoma. I. Characteristics of patients enrolled and not enrolled. (COMS report no 9) Am J Ophthalmol 125:767–778
Conlon MR, Chapman WB, Burt WL, Laroque BJ, Hearn SA (1991) Primary localized amyloidosis of the lacrimal glands. Ophthalmology 98:1556–1559
Convers J, Smith B (1960) Blowout fracture of the floor of the orbit. Trans Am Acad Ophthalmol Otolaryngol 64:676–688
Cooper S, Munk PL, Downey DB, Nicolle DA, Lee DH, Lin DT (1994) Findings of magnetic resonance and colour-flow Doppler imaging of orbital embryonal rhabdomyosarcoma. Can Assoc Radiol J 45:217–220
Corona-Vazquez T, Ruiz-Sandoval J, Arriada-Mendicoa N (1997) Optic neuritis progressing to multiple sclerosis. Acta Neurol Scand 95:85–89
Coskun O, Hamon M, Catroux G, Gosme L, Courthéoux P, Théron J (2000) Carotid-cavernous fistulas: diagnosis with spiral CT angiography. AJNR Am J Neuroradiol 21:712–716
Croxatto JO, Font RL (1982) Hemangiopericytoma of the orbit: a clinicopathologic study of 30 cases. Hum Pathol 13:210–218
Damadien R, Zaner K, Hor D (1973) Human tumors in MR. Physiol Chem Phys 5:381–402
Damato BE, Paul J, Foulds WS (1996a) Risk factors of residual and recurrent uveal melanoma after trans-scleral local resection. Br J Ophthalmol 80:102–108
Damato BE, Paul J, Foulds WS (1996b) Risk factors for metastatic uveal melanoma after trans-scleral local resection. Br J Ophthalmol 80:109–116
Davis KR, Hesselink JR, Dallow RL, Grove AJ (1980) CT and ultrasound in the diagnosis of cavernous hemangioma and lymphangioma of the orbit. J Comput Tomogr 4:98–104
Deans RM, Harris GJ, Kivlin JD (1992) Surgical dissection of capillary hemangiomas: an alternative to intralesional corticosteroids. Arch Ophthalmol 110:1743–1747
Debrun GM (1993) Endovascular management of carotid cavernous fistulas. In: Valavanis A (ed) Interventional neuroradiology. Springer, Berlin Heidelberg New York, pp 23–34
Dechambre S, Duprez T, Lecouvet F, Raftopoulos C, Gosnard G (1999) Diffusion-weighted MRI postoperative assessment of an epidermoid tumor in the cerebellopontine angle. Neuroradiology 41:829–831
De Potter P, Flanders AE, Shields JA, Shields CL, Gonzales CF, Rao VM (1994) The role of fat-suppression technique and gadopentate dimeglumine in magnetic resonance imaging evaluation of intraocular tumors and simulating lesions. Arch Ophthalmol 112:340–348
De Potter P, Shields JA, Shields CL (1995) MRI of the eye and orbit. Lippincott, Philadelphia
De Potter P, Shields CL, Shields JA Flanders AE (1996) The role of magnetic resonance imaging in children with intraocular tumors and simulating lesions. Ophthalmology 103:1774–1783
D'Hermies F, Elmaleh C, Mourier K, Berges O, Clay C, Cophignon J, Pouliquen Y (1993) Hemangiome caverneux de l'orbite. J Franc Ophthalmol 16:195–198
Dithmar S, Daus W, Voelcker HE (1993) Gedeckte Ruptur bei periokularen Dermoidzysten. Klinisch-histopathologische Studie. (Covered rupture of periocular dermoid cysts. Clinico-histologic study.) Klin Monatsbl Augenheilkd 203:403–407
DiPaolo DP, Zimmerman RA, Rorke LB, Zackai EH, Bilaniuk L, Yachnis AT (1995) Neurofibromatosis type 1: pathologic substrate of high-signal-intensity foci in the brain. Radiology 195:721–724
Dobben GD, Philip B, Mafee MF, Choi K, Belmont H, Dorodi S (1998) Orbital subperiostal hematoma, cholesterolgranuloma, and infection: evaluation with MR imaging and CT. Radiol Clin North Am 36:1185– 1200
Dolan RW, Chowdhury K (1995) Diagnosis and treatment of intracranial complications of paranasal sinus infections. J Oral Maxillofac Surg 53:1080–1087
Donovan JP, Schafer D, Shaw BW, Sorrel MF (1998) Cerebral oedema and increased intracranial pressure in chronic liver disease. Lancet 351:719–721
Dotan SA, Trobe SD, Gebarski SS (1991) Visual loss in tuberous sclerosis. Neurology 41:1915–1917
Duffin RM, Straatsma BR, Foos RY, Kerman BM (1981) Small malignant melanoma of the choroid with extraocular extension. Arch Ophthalmol 1827–1830
Dunker S, Wiegand W (1996) Prognostic value of magnetic resonance imaging in monosymptomatic optic neuritis. Ophthalmology 103:1768–1773
Dutton JJ (1994) Gliomas of the anterior visual pathway. Surv Ophthalmol 38:427–452
Dutton JJ, Burde RM, Klingele TG (1982) Autoimmune retrobulbar neuritis. Am J Ophthalmol 94:11–17
Dyer EH, Civit T, Abecassis JP, Derome PJ (1994) Functioning ectopic supradiaphragmatic pituitary adenoma. Neurosurgery 34:529–532
Dyer J, Atkinson L (1985) Cavernous hemangioma of the orbit. Aust N Z J Surgery 55:269–273
Earwaker J (1993) Paranasal sinus osteomas: a review of 46 cases. Skelatal Radiol 22:417–423
Edwards-Brown ME, Bonin JM (1996) White matter diseases. In: Atlas SW (ed) Magnetic resonance imaging of the brain and spine, 2nd edn. Lippincott Raven, New York, pp 649–706
Egan AJ, Boardman LA, Tazelaar HD, Swensen SJ, Jett JR, Yousem SA, Myers JL (1999) Erdheim-Chester disease: clinical, radiological, and histopathological findings in five patients with interstitial lung disease. Am J Surg Pathol 23:17–26
Egerer I, Tasman W, Tomer TL (1974) Coats' disease. Arch Ophthalmol 92:109–112
Eifrig CW, Chaudhry NA, Tse DT, Scott IU, Neff AG (2001) Lacrimal gland cyst abscess. Ophthal Plast Reconstr Surg 17:131–133
Ellenbogen E, Lasky MA (1975) Rhabdomyosarcoma of the orbit in the newborn. Am J Ophthalmol 80:1024–1027
Elston J (1997) Concomitant strabismus. In: Taylor D (ed) Pediatric ophthalmology, 2nd edn. Blackwell Science, Boston, pp 925–936
Enochs SW, Petherick P, Bogdanova A, Mohr U, Weissleder R (1997) Paramagnetic metal scavenging by melanin: MR imaging. Radiology 204:417–423
Eustis HS, Mafee MF, Walton C, Mondonca J (1998) MR imaging and CT of orbital infections and complications in acute rhinosinusitis. Radiol Clin North Am 36:1165–1183
Ewald H, Rochels R, Kimmig B (1994) Enophthalmus bei sekundärem Orbitatumor – ein kasuistischer Beitrag. Röntgenpraxis 47:275–276
Fells P, Kousoulides L, Pappa A, Murro P, Lawson J (1994) Extraocular muscle problems in thyroid eye disease. Eye 8:497–505

Filippi M, Rocca MA, Moiola L, Martinelli V, Grezzi A, Capra R, Salvi F, Comi G (1999) MRI and magnetization transfer imaging changes in the brain and cervical cord of patients with Devic's neuromyelitis optica. Neurology 53:1705–1710

Finkelstein SD, Hirose T, VandenBergh SR (2000) Olfactory neuroblastoma. In: Kleihues P, Cavenee WK (eds) Pathology and genetics. Tumors of the nervous system. IARC Press, Lyon, pp 150–152

Flanagan JC (1979) Vascular problems of the orbit. Ophthalmology 86:896–913

Flanagan JC, McLachlan D, Shannon GM (1980) Orbital roof fractures. Ophthalmology 87:325–329

Flanders AE, Mafee MF, Rao VM, Choi KH (1989) CT characteristics of orbital pseudotumors and other orbital inflammatory processes. J Comput Assist Tomogr 13:40–47

Flanders AE, De Potter P, Rao VM, Vinitski S, Tom BM, Shields JA, Shields CA (1996) Improved visibility of intraocular neoplasia using fat-suppressed, contrast enhanced MRI. Int J Neuroradiol 2:339–346

Font RL, Smith SL, Bryan RG (1998) Malignant epithelial tumors of the lacrimal gland: a clinicopathological study of 21 cases. Arch Ophthalmol 116:613–616

Förster G, Kahaly G (1998) Endokrine Orbitopathie 1998. Med Klin 93:65–73

Foster CS, Nguyen QD (2000) Adamantiades-Behçet disease. In: Albert DM, Jakobiec FA(eds) Principles and practice of ophthalmology, 2nd edn. Saunders, Philadelphia, pp 4596–4605

Foster CS, Baer JC, Raizman MB (1991) Therapeutic responses to systemic immunosuppressive chemotherapy agents in patients with Behçet syndrome affecting the eyes. In: O'Duffy JD, Kokman E (eds) Behçet disease: basic and clinical aspects. Dekker, New York, pp 581–588

Fox RI (1996a) Clinical features, pathogenesis, and treatment of Sjogren's syndrome. Curr Opin Rheumatol 8:438–445

Fox RI (1996b) Sjogren's syndrome: immunobiology of exocrine gland dysfunction. Adv Dent Res 10:35–40

Frederiksen JL, Larsson HBW, Olesen J (1992) Correlation of magnetic resonance imaging and CSF findings in patients with acute monosymptomatic optic neuritis. Acta Neurol Scand 86:317–322

Freyschmidt J (1993) Fibröse Dysplasie (Jaffé-Lichtenstein-Uehlinger). In: Freyschmidt J (ed) Skeletterkrankungen. Klinisch-radiologische Diagnose und Differentialdiagnose. Springer, Berlin Heidelberg New York, pp 522–537

Friedman DP, Rao VM, Flanders AE (1993) Lesions causing a mass in the medial canthus of the orbit: CT and MR features. Am J Roentgenol 160:1095–1099

Friedman DI (1999) Pseudotumor cerebroi. Neurosurg Clin North Am 10:609–621

Fukuyama H, Kamoyama M, Nabatame H, Takemura M, Nishimura K, Fujisawa I, Torizuka K (1987) Magnetic resonance images of neuro-Behçet syndrome shows precise brain stem lesions. Report of a case. Acta Neurol Scand 75:70–73

Gado MH, Smith ME (1978) Computerized tomography of the orbit. Int Ophthalmol Clin 18:151–156

Galieni P, Polito E, Leccisotti A, Marotta G, Lasi S, Bigazzi C, Bucalossi A, Frezza G, Latria F (1997) Localized orbital lymphoma. Haematologica 82:436–439

Galieni P, Cavo M, Pulsino A, Avvisati G, Bigazzi C, Neri S, Caliceti U, Benni M, Ronconi S, Lauria F (2000) Clinical outcome of extramedullary plasmocytoma. Haematologica 85:47–51

Gallie BL, Elsworth RM, Abramson DH, Phillips RA (1982) Retinoma: spontaneous regression of retinoblastoma or benign manifestation of the mutation. Br J Cancer 45:513–521

Gardner TW, Zaparackas ZG, Naidich TP (1984) Congenital optic nerve coloboma: CT demonstration. J Comput Assist Tomogr 8:95–102

Garner A (1988) Cavernous haemangioma of the orbit: a consideration of its origin and development. Orbit 7:149–152

Gehan EA, Glover FN, Maurer HM, Sutow WW, Hays DM, Lawrence W Jr, Newton WA Jr, Soule EH (1981) Prognostic factors of rhabdomyosarcoma. Natl Cancer Inst Monogr 56:83–92

Gerkowicz K, Probst M, Wawrzyniak M (1985) Experimental ocular siderosis after extrabulbar administration of iron. Br J Ophthalmol 69:149–153

Gilliam AC, Wood GS (2000) Cutaneous lymphoid hyperplasia. Semin Cutan Med Surg 19:133–141

Gloor B, Kalman A (1992) Neoplastische Raumverdrängung in der Orbita. I. Übersicht: Haemangiom, Lymphangiom, und embryonales Rhabdomyosarkom. Klin Monatsbl Augenheilkd 201:291–301

Goldberg MF, Mafee MF (1983) Computed tomography for diagnosis of persistent hyperplastic primary vitreous (PHPV). Ophthalmology 90:442– 451

Gomori JM, Grossman RI, Shields JA, Augsburger JJ, Joseph PM, DeSimeone D (1986) Choroidal melanomas. Correlation of NMR spectroscopy and MR imaging. Radiology 158:443– 445

Goodman SJ, Rosenbaum AL, Hasso A, Itabashi H (1975) Large optic nerve glioma with normal vision. Arch Ophthalmol 93:991–995

Graeb DA, Rootman J, Robertson WD, Lapointe JS, Nugent RA, Hay EJ (1990) Orbital lymphangiomas: clinical, radiological and pathologic characteristics. Radiology 175:417–421

Grant WM (1974) (ed) Toxicology of the eye, 2nd edn. Thomas, Springfield

Griffeth MT, Dailey RA, Ofner S (1997) Bilateral spontaneous subperiostal hematoma of the orbit: a case report. Arch Ophthalmol 115:679–680

Grosfeld J, Weber TR, Weetman RM, Baehner RL (1983) Rhabdomyosarcoma in childhood: analysis of survival in 98 cases. J Pediatr Surg 18:141–146

Grove AS Jr (1979) Giant dermoid cysts of the orbit. Ophthalmology 86:1513–1520

Grunberg SM, Weiss MH, Spitz IM (1991) Treatment of unresectable meningeomas with the antiprogesterone agent mifepristone. J Neurosurg 74:861–866

Guenalp I, Guenduez K (1995) Vascular tumors of the orbit. Doc Ophthalmol 89:337–345

Guenalp I, Guenduez K (1996) Cystic lesions of the orbit. Int Ophthalmol 20:273–277

Gunduz K, Ozdemir O (1994) Bilateral retrobulbar neuritis following unilateral herpes zoster ophthalmicus. Ophthalmologica 208:61–64

Guthoff R, Lieb WE, Rendl J, Reiners C (2000) Imaging of orbital metastasis of small-intestine carcinoid by octreotide scintigraphy. A critical evaluation of the methodology. Ophthalmology 97:272–275

Guy J, Mao J, Bidgood WD Jr, Manusco A, Quisling RG (1992) Enhancement and demyelination of the intraorbital optic

nerve. Fat suppression magnetic resonance imaging. Ophthalmology 99:713–719
Gyldenstedt C, Lester J, Fledelius H (1977) Computed tomography of the orbital lesions. A radiological study of 144 cases. Neuroradiology 13:141–150
Haik BG, Saint Louis L, Smith ME, Ellsworth RM, Abramson OH, Cahill P, Deck M, Coleman J (1985) Magnetic resonance imaging in the evaluation of leucocoria. Ophthalmology 92:1143–1152
Haik BG, Saint Louis L, Smith ME, Ellsworth RM, Deck M, Friedlander M (1987) Magnetic resonance imaging in choroidal tumors. Ann Ophthalmol 19:218–238
Harkin JC, Reed RJ (1969) Tumors of the peripheral nervous system. In: Atlas of tumor pathology, 2nd series, fasc 3. Armed Forces Institute of Pathology, Washington DC, pp 67–97
Harnsberger HR (1990) The orbit. (Handbook in radiology) Year Book Medical, Chicago, pp 329–376
Harris GJ, Jakobiec FA (1979) Cavernous hemangioma of the orbit. J Neurosurg 51:219–228
Harris GJ, Sakol PJ, Bonavolonta G, DeConcilis C (1990) An analysis of thirty cases of orbital lymphangioma. Pathophysiologic considerations and management recommendations. Ophthalmology 97:1583–1592
Harris GJ (1994) Subperiostal abscess of the orbit: age as a factor in the bacteriology and response to treatment. Ophthalmology 101:585–595
Harris GJ, Garcia GH, Logani SC, Murphy ML, Sheth BP, Seth AK (1998) Orbital blow-out fractures: correlation of perioperative computed tomography and postoperative ocular motility. Trans Am Ophthalmol Soc 96:329–347
Hasso AN, Lambert D (1994) Magnetic resonance imaging of the paranasal sinuses and nasal cavities. Top Magn Reson Imaging 6:209–223
Hattori N, Ishihara T, Saiwai S, Moridera K, Hino M, Ikekubo K, Kurahachi H (1994) Ectopic prolactinoma on MRI. J Comput Assist Tomogr 18:936–938
Hayes WS, Sherman JL, Stern BJ, Citrin CM, Pulaski PD (1987) MR and CT evaluation of intracranial sarcoidosis. AJNR Am J Neuroradiol 8:841–847
Henderson JW (1973) Meningioma. In: Henderson JW (ed) Orbital tumors. Saunders, Philadelphia, pp 527–554
Henderson JW (1994) Orbital tumors, 3rd edn. Raven, New York, pp 317–411
Henderson JW, Farrow GM (1978) Primary orbital haemangiopericytoma: an aggressive and potentially malignant neoplasm. Arch Ophthalmol 96:666–673
Henderson JW, Farrow GM (1980) Primary malignant mixed tumors of the lacrimal gland. Report of 10 cases. Ophthalmology 87:466–475
Henry A (1969) Monoostotic fibrous dysplasia. J Bone Joint Surg Br 51:300–306
Hershey BL, Roth TC (1997) Orbital infections. Semin Ultrasound CT MR 18:448–459
Hill CA, Moseley IF (1992) Imaging of orbitofrontal cholesterol granuloma. Clin Radiol 46:237–242
Hirashima S, Matsushita Y, Sameshima M (1986) Orbital rhabdomyosarcoma: case report with immunohistochemical detection of muscle cell type intermediate filament proteins. Jpn J Ophthalmol 30:461–471
Hiromatsu Y, Kojima K, Ishisaka N, Tanaka K, Sato M, Nonaka K, Nishimura H, Nishida H (1992) Role of magnetic resonance imaging in thyroid-associated ophthalmopathy: its predictive value for therapeutic outcome of immunosuppressive therapy. Thyroid 2:299–305
Ho VT, McGuckin JF Jr, Smergel EM (1996) Intraorbital foreign body: CT and MR appearance. AJNR Am J Neuroradiol 17:134–136
Hochstrasser H, Boltshauser E, Valavanis A (1988) Brain tumors in children with von Recklinghausen neurofibromatosis. Neurofibromatosis 1:233–239
Hogan M, Wood I (1972) Orbital rhabdomyosarcoma: an electron microscopic study. Trans Am Ophthalmol Soc 70:131–153
Holbach L, Beck JD, Ruprecht KW, Meythaler FH (1989) Zur immunzytochemischen Diagnose embryonaler Rhabdomyosarkome der Orbita. Klin Monatsbl Augenheilkd 195:190–195
Hollander MD, FitzPatrick M, O'Connor SG, Flanders AE, Tartaglino LM (1999) Optic gliomas. Radiol Clin North Am 37:59–71
Hollway GE, Suthers GK, Haan EA, Thompson E, David DJ, Gecz Mulley JC (1997) Mutation detection in FGFR2 craniosynostotic syndromes. Hum Genet 99:251–255
Hood CI (1970) Cavernous hemangioma of the orbit. A consideration of pathogenesis with an illustrative case. Arch Ophthalmol 83:49–53
Hopper KD, Sherman JL, Boal DK, Egli KD (1992) CT and MR imaging of the pediatric orbit. Radiographics 12:485–503
Horowitz AL, Kaplan RD, Grewe G, White RT, Salberg LM (1989) The ovoid lesion: a new MR observation in patients with multiple sclerosis. AJNR Am J Neuroradiol 10:303–305
Horton JC, Seiff SR, Pitts LH, Weinstein PR, Rosenblum ML, Hoyt WF (1992) Decompression of the optic nerve sheath for vision-threatening papilledema caused by dural sinus occlusion. Neurosurgery 31:203–211
Hosten N, Sander B, Cordes M, Schubert C, Schörner W, Felix R (1989) Graves ophthalmopathy: MR imaging of the orbits. Radiology 172:759–762
Housepian EM, Trokel SL, Jakobiec FO, Hilal SK (1982) Tumors of the orbit. In: Youmans JR (ed) Neurological surgery. Saunders, Philadelphia, pp 3024–3064
Howard GM, Ellsworth RM (1965) Differential diagnosis of retinoblastoma: a statistical survey of 500 children, part I. Relative frequency of the lesions which simulate retinoblastoma. Am J Ophthalmol 60:610–618
Howarth DM, Gilchrist GS, Mullan BP, Wiseman GA, Edmonson JH, Schomberg PJ (1999) Langerhans cell histiocytosis: diagnosis, natural history, management, and outcome. Cancer 85:2278–2290
Hoyt WF, Baghdassarian SA (1969) Optic gliomas of childhood: natural history and rationale for conservative management. Br J Ophthalmol 53:793–798
Humberclaude V, Vallee L, Sukno S, Vamecq J, Dhellemmes S, Pruvo JP, Nuyts JP (1993) Cerebral venous thrombosis disclosing Behcet disease. Arch Fr Pediatr 50:603–605
Hunter DG, Ellis FJ (1999) Prevalence of systemic and ocular disease in infantile exotropia: comparison with infantile esotropia. Ophthalmology 106:1951–1956
Hurwitz JJ, Rodgers J, Doucet TW (1982) Dermoid tumor involving the lacrimal drainage pathway: a case report. Ophthalmic Surg 13:377–379
Huss GP, Mattle H, Wessel K, Mumenthaler M (1992) Neuro-Behcet: Enzepahlitis und zerebrale venöse Thrombose – klinische und neuroradiologische Aspekte in 5 Fällen. Nervenarzt 63:352–358

Jacobs L, Kinkel W (1976) Computerized axial transverse tomography in the diagnosis of orbital tumors. Trans Am Acad Ophthalmol Otolaryngol 81:323–333

Jaffe T, Castillo M, Naidich TP, Armao DM, Byrd S, Bauer BA (1997) Facies to remember: fibrous dysplasia. Int J Neuroradiol 4:112–120

Jakobiec FA, Font RL (1986) Peripheral nerve sheath tumors. In: Spencer WH (ed) Ophthalmic pathology. An atlas and textbook. Saunders, Philadelphia, pp 2616– 2626

Jakobiec FA, Howard GM, Jones IS, Wolff M (1974) Hemangiopericytoma of the orbit. Am J Ophthalmol 78:816–834

Jakobiec FA, Tso MO, Zimmerman LE, Danis P (1977) Retinoblastoma and intracranial malignancy. Cancer 39:2048–2058

Jakobiec FA, McLean I, Font RL (1979) Clinical pathologic characteristics of orbital lymphoid hyperplasia. Ophthalmology 86:948–966

Jakobiec FA, Depot MJ; Kennerdell JS, Shults WT, Anderson RL, Alper ME, Citrin CM, Housepian EM, Trokel SL (1984) Combined clinical and computed tomographic diagnosis of orbital glioma and meningioma. Ophthalmology 91:137–155

Jakobiec FA, Mills MD, Hidayat AA, Dallow RL, Townsend DJ, Brinker EA, Charles NC (1993) Periocular xanthogranulomas associated with severe adult-onset asthma. Trans Am Ophthalmol Soc 91:99–125

Jeffrey PB, Cartwright D, Atwater SK, Char DH, Miller THR (1995) Lacrimal gland lymphoma: a cytomorphological and immunophenotypic study. Diagn Cytopathol 12:215–222

Johnston S (1975) The changing pattern of injury. Symposium on ocular trauma. Trans Ophthalmol Soc UK 95:307–310

Jones I, Reese AB, Kraut J (1965) Orbital rhabdomyosarcoma. An analysis of 62 cases. Trans Am Ophthalmol Soc 653:721–735

Just M, Kahaly G, Higer HP, Rösler HP, Kutzner J, Beyer J, Thelen M (1991) Graves ophthalmopathy: role of MR imaging in radiation therapy. Radiology 179:187–190

Kadish S, Goodman M, Wang CC (1976) Olfactory neuroblastoma. A clinical analysis of 17 cases. Cancer 37:1571–1576

Kahaly G, Diaz M, Just M, Beyer J, Lieb W (1995) Role of octreoscan and correlation with MR imaging in Graves' ophthalmopathy. Thyroid 5:107–111

Kahaly G, Förster G, Pitz S, Kutzner J, Eißner D, Müller-Forell W, Junginger T, Otto E, Hansen C, Beyer J, Mann W (1996) Endokrine Orbitopathie – eine interdisziplinäre Herausforderung. Ärzteblatt Rheinland-Pfalz July 1996, Fortbildungsbeitrag no. 230:212–219

Kakisu Y, Adachi-Usami E, Fujimoto N (1991) Pattern visually evoked cortical potential and magnetic resonance imaging in optic neuritis. J Clin Neuroophthalmol 7:1–5

Karcioglu ZA, Nasr AM, Haik BG (1997) Orbital hemangiopericytoma: clinical and morphologic features. Am J Ophthalmol 124:661–672

Kassel EE, Schatz CJ (1996) Lacrimal apparatus. In: Som PM, Curtin HD (eds) Head and neck imaging, Vol 3. Mosby, St. Louis, pp 1129–1183

Katz BJ, Nerad JA (1998) Ophthalmic manifestations of fibrous dysplasia: a disease of children and adults. Ophthalmology 105:2207–2215

Katz SE, Rootman J, Vangveeravong S, Graeb D (1998) Combined venous lymphatic malformations of the orbit (so-called lymphangiomas). Association with noncontiguous intracranial vascular anomalies. Ophthalmology 105:176–184

Kaufman LM, Villablanca JP, Mafee MF (1998) Diagnostic imaging of cystic lesions in the child's orbit. Radiol Clin North Am 36:1149–1163

Kawamoto K, Miyanaga Y (1997) Diagnosis of orbital lymphoma by molecular genetic analysis. Nippon Ganka Gakkai Zasshi 101:141–147

Kazim M, Kennerdell JS, Rothfus W, Marquardt M (1992) Orbital lymphangioma. Correlation of magnetic resonance images and intraoperative findings. Ophthalmology 99:1588–1594

Kenyon KR (1976) Ocular manifestations and pathology of systemic mucopolysaccharidosis. Birth Defects 12:133–153

Kerty E, Eide N, Nakstad P, Nyberg-Hansen R (1991) Chiasmal optic neuritis. Acta Ophthalmol 91:764–773

Kikuchi K, Kowada M, Sageshima M (1994a) Orbital haemangiopericytoma: CT, MR and angiographic findings. Comput Med Imaging Graph 18:217–222

Kikuchi K, Kowada M, Sasaki J, Sageshima M (1994b) Large pituitary adenoma of the sphenoid sinus and the nasopharynx: report of a case with ultrastructural evaluations. Surg Neurol 42:330– 334

King JO, Mitchell PJ, Thomson KR, Tress BM (1995) Cerebral venography and manometry in idiopathic intracranial hypertension. Neurology 45:2224–2228

Kira J, Goto I (1994) Recurrent opticomyelitis associated with anti-DNA antibody. J Neurol Neurosurg Psychiatry 57:1124–1125

Kirchhof K, Hahnel S, Jansen O, Zake S, Sartor K (2000) Gadolinium-enhanced magnetic resonance dacryocystography in patients with epiphora. J Comput Assist Tomogr 24:327–331

Kleinheinz J, Stamm T, Meier N, Wiesmann HP, Joos U (1998) MRI 3D imaging of the orbits in craniofacial abnormalities and injuries. Mund Kiefer Gesichtschir 2:S91–S93

Knudson AG Jr (1971) Mutation and cancer: a statistical study of retinoblastoma. Proc Natl Acad Sci USA 68:820–823

Knudson AG (1978) Retinoblastoma: a prototype hereditary neoplasm. Semin Oncol 5:57–60

Koornneef L (1979) Orbital septa: anatomy and function. Ophthalmology 86:876–880

Krenning EP, Kwekkeboom DJ, Bakker WH, Breeman WA, Kiji PP, Oei HY, van Hagen M, Postema PT, de Jong M, Reubi JC (1993) Somatostatin receptor scintigraphy with (111-IN-DTPA-D-Phe1)- and (123I –Tyr3)-octreotide: the Rotterdam experience with more than 1000 patients. Eur J Nucl Med 20:716–731

Kueker W, Ramaekers V (1999) Persistent hyperplastic primary vitreous: MRI. Neuroradiology 41:520–522

Kupersmith MJ (1993) Neurovascular neuroophthalmology. Springer, Berlin Heidelberg New York

Kuroiwa T, Ohta T, Tsutsumi A (2000) Xanthoma of the temporal bone: case report. Neurosurgery 46:996–998

Kyritsis AP, Tsokos M, Triche TJ, Chader GJ (1984) Retinoblastoma: origin from a primitive neuroectodermal cell? Nature 307:471–473

Lagreze WD, Wesenthal TA, Kommerell G (1997) Enophthalmus durch orbitale Metastase eines Mammkarzinoms. Klin Monatsbl Augenheilkd 211:68– 69

Lake B (1997) Lysosomal and peroxisomal disorders. In: Graham D, Lantos PL (eds) Greenfield's pathology. Arnold, London, pp 657–753

Lakits A, Steiner E, Scholda C, Kontrus M (1998) Evaluation of intraocular foreign bodies by spiral computed tomography and multiplanar reconstruction. Ophthalmology 105:307–312

Lang S, Sulzbacher I (2001) Differenzialdiagnostische Problematik bei der Befundung benigner Knochentumoren. Radiologe 41:533–539

Lasjaunias P (1997) Haemangiomas. In: Lasjaunias P (ed) Vascular diseases in neonates and children. Interventional neuroradiology management. Springer, Berlin Heidelberg New York, pp 565–591

Leatherbarrow B, Noble JL, Lloyd IC (1989) Cavernous hemangioma of the orbit. Eye 3:90–99

Lee AG, Brazis PW (1998) The diagnosis of optic neuropathies. In: Lee AG, Brazis PW (eds) Clinical pathways in neuroophthalmology. An evidence based approach. Thieme, New York, pp 1–24

LeGall F, Edan C, Toulemont PJ, Jouan H, Urvoy M, Ramee MP (1994) Rhabdomyosarcome orbitaire de l'enfant. A propos de 2 observations. J Fr Ophthalmol 17:67–73

Leiba H, Glaser JS, Schatz NJ, Siatkowski RM (2000) Postpartum optic neuritis: etiology and pathophysiologic considerations. J Neuroophthalmol 20:85–88

Levine AM (1991) Epidemiology, clinical characteristics and management of AIDS-related lymphoma. Hematol Oncol Clin North Am 5:331–342

Levine MR, Buckman G (1986) Primary localized orbital amyloidosis. Ann Ophthalmol 18:165–167

Levine MR, Kyae L, Mair S, Bates J (1993) Multifocal fibrosclerosis: report of a case of bilateral idiopathic sclerosing pseudotumor and retroperitoneal fibrosis. Arch Ophthalmol 111:841–843

Lexa FJ, Grossman RI (1994) MR of sarcoidosis in the head and spine: spectrum of manifestations and radiographic response to steroid therapy. AJNR Am J Neuroradiol 15:973–982

Lichtenstein L, Jaffé HL (1942) Fibrous dysplasia of bone. Arch Pathol 33:777–816

Lichtenstein C (1953) Histiocytosis X: integration of eosinophilic granuloma of the bone, "Letterer-Siwe disease" and "Schuller-Christian disease", as related manifestations of a single nosologic entity. Arch Pathol 56:84–102

Liebner E (1976) Embryonal rhabdomyosarcoma of head and neck in children. Correlation of stage, radiation dose, local control and survival. Cancer37:2777–2786

Liebross RH, Ha CS, Cox JD, Weber D, Delasalla K, Alexanian R (1999) Clinical course of solitary extramedullary plasmocytoma. Radiother Oncol 52:245–249

Linberg J (1983) Disorders of the lower excretory system. In: Milder B, Weil B (eds) The lacrimal system. Appleton-Century-Crofts, Norwalk, pp 133–144

Listernick R, Charrow J, Greenwald MJ, Mets M (1994) Natural history of optic pathway tumors in children with neurofibromatosis type I: a longitudinal study. J Pediatr 125:63–66

Listernick R, Darling C, Greenwald M; Strauss L, Charrow J (1995) Optic pathway tumors in children: the effect of neurofibromatosis type 1 on clinical manifestations and natural history. J Pediatr 127:718–722

Lloyd GA, Wright JE, Morgan G (1971) Venous malformations in the orbit. Br J Ophthalmol 55:505–508

Lloyd RV, Chandler WF, Kovacs K, Ryan N (1986) Ectopic pituitary adenomas with normal anterior pituitary glands. Am J Surg Pathol 10:546–552

Lohmann DR, Gerick M, Brandt B, Ölschläger U, Lorenz B, Passarge E, Horsthemke B (1997) Constitutional RB1-gene mutations in patients with isolated unilateral retinoblastoma. Am J Hum Genet 61:282–294

Luk IS, Chan JK, Chow SM, Leung S (1996) Pituitary adenoma presenting as sinonasal tumor: pitfalls in diagnosis. Hum Pathol 27:605– 609

Lyon DB, Newman SA (1989) Evidence of direct damage to extraocular muscles as a cause of diplopia following orbital trauma. Ophthalmol Plat Reconstr Surg 5:81–91

Mafee MF (1990) Magnetic resonance imaging: ocular pathology. In: Newton TH, Bilaniuk LT (eds) Radiology of the eye and orbit. Raven, New York, pp 3.1–3.45

Mafee MF (1992) Case 25: optic nerve sheath meningeoma. In: Siegel BA, Proto AV (eds) Head and neck disorders (fourth series) test and syllabus. Reston VA American College of Radiology, p 553

Mafee MF (1996) Eye and orbit. In: Som PM, Curtin HD (eds) Head and neck imaging, 3rd edn, Vol II. Mosby, St Louis, pp 1009–1128

Mafee MF (1998) Uveal melanoma, choroidal hemangiomas and simulating lesions. Radiol Clin North Am 36:1083–1099

Mafee MF, Haik BG (1987) Lacrimal fossa lesions: role of computed tomography. Radiol Clin North Am 25:767–779

Mafee MF, Peyman GA (1984) Choroidal detachment and ocular hypotony: CT evaluation. Radiology 153:697–703

Mafee MF, Peyman GA (1987) Retinal and choroidal detachment: role of MRI and CT. Radiol Clin North Am 25:487–507

Mafee MF, Peyman GA, McKusick MA (1985) Malignant uveal melanoma and similar lesions studied by computed tomography. Radiology 156:403–408

Mafee MF, Goldberg MF, Greenwald MJ, Schulman J, Malmed A, Flanders AE (1987a) Retinoblastoma and simulating lesions: role of CT and MR imaging. Radiol Clin North Am 25:667–681

Mafee MF, Miller MT, Tan W, Dobben GD (1987b) Dynamic computed tomography and its applications to ophthalmology. Radiol Clin North Am 25:715–731

Mafee MF, Linder B, Peyman GA, Langer BG, Choi KH, Capek V (1988) Choroidal hematoma and effusion: evaluation with MR-imaging. Radiology 168:781– 786

Mafee MF Goldberg MF, Cohen SB, Gotsis ED, Safran M, Chekuro L, Raofi B (1989) Magnetic resonance imaging versus computed tomography of leukocoric eyes and use of in vitro proton magnetic resonance spectroscopy of retinoblastoma. Ophthalmology 96:965–976

Mafee MF, Ainbinder DJ, Hidayat AA, Friedman SM (1995) Magnetic resonance imaging and computed tomography in the evaluation of choroidal hemangioma. Int J Neuroradiol 1:67–77

Mafee MF, Pai E, Philip B (1998) Rhabdomyosarcoma of the orbit. Evaluation of MR imaging and CT. Radiol Clin North Am 36:1215–1227

Mafee MF, Goodwin J, Dorodi S (1999a) Optic nerve sheath meningeoma. Radiol Clin North Am 37:37–58

Mafee MF, Edward DP, Koeller KK, Dorodi S (1999b) Lacrimal gland tumors and simulating lesions. Radiol Clin North Am 37:219–239

Manfre L, Lagalla R, Mangiameli A, Lupo F, Giuffre G, Ponte F, Cardinale AE (1995) Idiopathic intracranial hypertension: orbital MRI. Neuroradiology 37:459–461

Maniglia AJ, Goodwin WJ, Arnold JE, Ganz E (1989) Intracranial abscesses secondary to nasal, sinus, and orbital infections in adults and children. Head Neck Surg 115:1424–1429

Manschot WA (1958) Persistent hyperplastic primary vitreous. Arch Ophthalmol 59:188–203

Margaux J, Hayem G, Meyer O, Kahn MF (1999) Systemic lupus erythematosus with optic neuromyelitis (Devic's syndrome). A case with a 35-year follow-up. Rev Rhum Engl Ed 66:102–105

Margo CE, McLean IW (1984) Malignant melanoma of the choroid and ciliary body in black patients. Arch Ophthalmol 102:77–79

Margo CE, Mulla ZD (1998) Malignant tumors of the orbit. Analysis of the Florida Cancer Registry. Ophthalmology 105:185–190

Margo CE, Katz NN, Wertz FD, Dorwart RH (1983) Sclerosing endophthalmitis in children: computed tomography with histopathologic correlation. Ped Ophthalmol Strabism 20:180–184

Marie PJ, Pollack C de, Chanson P, Lomri A (1997) Increased proliferation of osteoblastic cells expressing the activating Gs alpha mutation in monostotic and polyostotic fibrous dysplasia. Am J Pathol 150:1059–1069

Marquardt MD, Zimmerman LE (1982) Histology of meningiomas and gliomas of the optic nerve. Hum Pathol 13:226–234

Mauriello JA, Lee HJ, Nguyen L (1999) CT of soft tissue injury and orbital fractures. Radiol Clin North Am 37:241–252

Mavel JB, Marsh MA, Catlin FI (1991) Ossifying fibroma of the midface and paranasal sinuses: diagnostic and therapeutic considerations. Otolaryngol Head Neck Surg 104:803–808

Massry GG, Harrison W, Hornblass A (1996) Clinical and computed tomographic characteristics of amyloid tumors of the lacrimal gland. Ophthalmology 103:1233–1236

Mauriello JA, Flanagan JC (1989) Pseudotumor and lymphoid tumor: distinct clinicopathologic entities. Surv Ophthalmol 34:142– 148

McCarthy JM, White VA, Harris G, Simons KB, Kennerdell J, Rootman J (1993) Idiopathic sclerosing inflammation of the orbit: immunohistologic analysis and comparison with retroperitoneal fibrosis. Mod Pathol 6:581–587

McCartney AC (1997) Regional neuropathology: optic nerve and orbit. In: Graham DI, Lantos PL (eds) Greenfield's neuropathology, 4th edn. Arnold, London, pp 973–1006

McCormick S, Linberg J (1988) Pathology of nasolacrimal duct obstruction: clinicopathologic correlates of lacrimal excretory system disease. In: Linberg J (ed) Lacrimal surgery. Churchill Livingstone, New York, pp 169–202

McLaughlin D, Flanagan J, Shannon G (1982) Complications of orbital roof fractures. Ophthalmology 89:1274–1278

McLean IW (1995) Prognostic features of uveal malignant melanoma. Ophthalmol Clin North Am 8:143–153

McLean IW (1996) Uveal nevi and malignant melanomas. In: Spencer WH (ed) Ophthalmic pathology, 4th edn. Saunders, Philadelphia, pp 2121–2217

McLean IW, Zimmerman LE, Evans RM (1978) Reappraisal of Calendar's spindle a type of malignant melanoma of choroidal and ciliary body. Am J Ophthalmol 86:557–564

McLeish WM, Pulido JS, Holland S, Culbertson WW, Winward K (1990) The ocular manifestations of syphilis in human immunodeficiency virus type 1-infected host. Ophthalmology 97:196–203

McMaster MJ, Soule EH, Ivins JC (1975) Haemangiopericytoma: a clinicopathologic study and long-term follow up of 60 patients. Cancer 36:2232–2244

McNab AA, Wright JE (1989) Cavernous haemangiomas of the orbit. Aust NZ J Ophthalmol 17:337–345

Medlock RD, Augsburger JJ, Wilkinson CP, Cox MS Jr, Gamel JW, Nicholl J (1991) Enlargement of circumscribed choroidal hemangiomas. Retina 11:385–388

Megerian CA, Sofferman RA, McKenna MJ, Eavey RD, Nadol JB Jr (1995) Fibrous dysplasia of the temporal bone: ten new cases demonstrating the spectrum of otologic sequelae. Am J Otol 16:408–419

Messinger A, Radkowski M, Greenwald MJ, Pensler JM (1989) Orbital roof fractures in the pediatric population. Plast Reconstr Surg 84:213–218

Michaelson IC, Campbell ACP (1940) The anatomy of the finer retinal vessels and some observations on their significance in certain retinal diseases. Trans Ophthalm Soc UK 60:71–76

Mohammadi-Araghi H, Haery C (1993) Fibro-osseous lesions of craniofacial bones: the role of imaging. Radiol Clin North Am 31:121–134

Mombaerts I, Goldschmeding R, Schlingemann R, Koornneef L (1996) What is orbital pseudotumor? Surv Ophthalmol 41:66–78

Mortada A (1971) Intra-orbital dermoid cyst. Bull Ophthalmol Soc Egyt 64:267–273

Moss H (1962) Expanding lesions of the orbit. A clinical study of 230 consecutive cases. Am J Ophthalmol 54:761–770

Motta AO, Han JS, Levine M, Benson JE (1983) Primary amyloid tumor of the lacrimal gland: CT findings. J Comput Assist Tomogr 7:1079–1080

Müller P, Schlimok G, Gerber H, Renner D (1990) Akuter einseitiger Visusverlust als initiales Symptom einer Meningeosis lymphomatosa. Klin Wochenschr 16:332–334

Müller-Forell W (1998) Erkrankungen der Orbita – Trauma, Entzündung, Tumor – aus der Sicht der Neuroradiologen. Verhandlungsbericht 1998: Interdisziplinäre Versorgung der Orbita – Trauma, Entzündung, Tumor. Dtsch Ges HNO Kopf Hals Chir Verh pp 23–37

Müller-Forell W, Lieb W (1995a) Neuroradiologie in der Ophthalmologie, part 1. Ophthalmologe 92:595–614

Müller-Forell W, Lieb W (1995b) Neuroradiologie in der Ophthalmologie, part 2. Ophthalmologe 92:757–784

Müller-Forell W, Pitz S, Mann W, Kahaly G (1999) Neuroradiological diagnosis in thyroid-associated orbitopathy. Exp Clin Endocrinol Diabetes 107 [Suppl 5]:177–183

Mukheriji SK, Tart RP, Fitzsimmons J, Belden C, McGorray S, Guy J Mancuso AA (1994) Fat-suppressed MR of the orbit and cavernous sinus: comparison of fast spin-echo and conventional spin-echo. AJNR Am J Neuroradiol 15:1707–1714

Mulliken JB, Glowacki J (1982) Hemangiomas and vascular malformations of infants and children: a classification based on endothelial characteristics. Plast Reconstr Surg 69:412–422

Mulliken JB, Young AE (1988) Vascular birthmarks: hemangiomas and malformations. Saunders, Philadelphia

Murdoch IE, Sullivan TJ, Moseley I, Hawkins PN, Pepys MB, Tan SY, Garner A, Wright JE (1996) Primary localized amyloidosis of the orbit. Br J Ophthalmol 80:1083–1086

Neigel JM, Rootman J, Belkin RI, Nugent RA, Drance SM, Beattie CW, Spinelli JA (1988) Dysthyroid optic neuropathy. The crowded orbital apex syndrome. Ophthalmology 95:1515–1521

Nemzek WR, Gandour-Edwards R, Westman DG (2000) The nasal cavity and paranasal sinuses. In: Orrison WW Jr (ed) Neuroimaging. Saunders, Philadelphia, pp 1070–1147

Nenning H, Meier P, Penk A, Kössling S (1994) Mykotische Retrobulbärneuritis. Klin Monatsbl Augenheilkd 204:244–247

Neselof C, Bassett F, Rousseau MF (1973) Histiocytosis X: histiogenetic arguments for a Langerhans cell origin. Biomedicine 18:365–37

Newman SA, Jane JA (1991) Meningiomas of the optic nerve, orbit and anterior visual pathways. In: Al-Mefty O (ed) Meningiomas. Raven, New York, pp 461–494

Nowinski TS, Flanagan JC (1986) Evaluation of exophthalmus and thyroid ophthalmopathy. In: Gonzales CF, Becker MH, Flanagan JC (eds) Diagnostic imaging in ophthalmopathy. Springer, Berlin Heidelberg New York, pp 189–199

Nugent RA, Belkin RI, Neigel JM, Rootman J, Robertson WD, Spinelli J, Graeb DA (1990) Graves orbitopathy: correlation of CT and clinical findings. Radiology 177:675–682

Numano F (2000) Vasa vasoritis, vasculitis and atherosclerosis. Int J Cardiol 75:S1–8

Ohbayashi M, Tomita K, Agawa S, Sichijo F, Shinno K, Matsumoto K (1988) Multiple cavernous hemangiomas of the orbits. Surg Neurol 29:32–34

Okamoto K, Ito J, Emura T, Kawasaki T, Furusawa T, Sakai K, Tokiguchi S (1998) Focal orbital amyloidosis presenting as rectus muscle enlargement: CT and MR findings. AJNR Am J Neuroradiol 19:1799–1801

Older J (1988) Congenital lacrimal disorders and management. In: Linberg J (ed) Lacrimal surgery. Churchill Livingstone, New York, pp 91–108

Orcutt J, Wulc A, Mills R, Smith C (1991) Asymptomatic orbital cavernous hemangiomas. Ophthalmology 98:1257–1260

Ortiz O, Schochet SS, Kotzan JM, Kostick D (1996) Radiologic-pathologic correlation. Meningioma of the optic nerve sheath. AJNR Am J Neuroradiol 17:901–906

Osborn AG (1994) Diagnostic neuroradiology. Mosby, St Louis

Ossoinig KC (1975) A-scan echography and orbital disease. Mod Probl Ophthalmol 14:203–235

Ossoinig KC, Keenan TP, Bigar F (1975) Cavernous hemangioma of the orbit. A differential diagnosis in clinical echography. Bibl Ophthalmol 83:236–244

Osterhuis JA, Journée- de Korver HG, Kakebeeke-Kemm HM, Bleeker JC (1995) Transpupillary thermotherapy in choroidal melanomas. Arch Ophthalmol 113:315–321

Papay FA, Morales L Jr, Flaharty P, Smith SJ, Anderson R, Walker JM, Hood RS, Hardy S (1995) Optic nerve decompression in cranial bas fibrous dysplasia. J Craniofac Surg 6:5–14

Pappa A, Lawson JMM, Calder V, Fells P, Lightman S (2000) T cells and fibroblasts in affected extraocular muscles in early and late thyroid associated ophthalmopathy. Br J Ophthalmol 84:517–522

Pauleit D, Schüller H, Textor J, Leutner C, Keller E, Sommer T, Träber F, Block W, Boldt I, Schild H (1997) Mr-Ralaxometriemessung mit und ohne frequenzselektive Fettunterdrückung (SPIR) bei endokriner Orbitopathie. Fortschr Röntgenstr 167:557–564

Pear BL (1970) Epidermoid and dermoid sequestration cysts. Am J Roentgenol Radium Ther Nucl Med 110:148–155

Pereira PL, Dammann F, Duda SH, Reinbold WD, Claussen CD (1997) Stellenwert der Dakryozystographie in der Lokalisationsdiagnostik der Tränenwegsstenosen. RöFo Fortschr Röntgenstr 166:498–501

Peyman GA, Juarez CP, Diamond DG, Raichand M (1984) Ten years experience with eye wall resection for uveal melanomas. Ophthalmology 91:1720–1725

Peyster RG, Hoover ED (1984) Graves' orbitopathy. In: Peyster RG, Hoover ED (eds) Computerized tomography in orbital diseases and neuro-ophthalmology. Year Book Medical Publisher, Chicago, pp 97–114

Phillips PH, Repka MX, Lambert SR (1998) Pseudotumor cerebri in children. J AAPOS 2:33–38

Pless M, Lessell S (1996) Spontaneous visual improvement in orbital apex tumors. Arch Ophthalmol 114:704–706

Poe LB, Dubowy RL, Hochhauser L, Collins GH, Crosley CJ, Kanzer MD, Oliphant M, Hodge CJ Jr (1994) Demyelinating and gliotic cerebellar lesions in Langerhans cell histiocytosis. AJNR Am J Neuroradiol 15:1921–1928

Polito E, Galieni P, Lecisotti A (1996) Clinical and radiological presentation of 95 orbital lymphoid tumors. Graefes Arch Clin Exp Ophthalmol 234:504–509

Pollack IF, Shultz B, Mulvihill JJ (1996) The management of brainstem gliomas in patients with neurofibromatosis I. Neurology 46:1652–1660

Pollard ZF, Calhoun J (1975) Deep orbital dermoid with draining sinus. Am J Ophthalmol 79:310–313

Popoff NA, Ellsworth RM (1971) The fine structure of retinoblastoma: in vivo and in vitro observations. Lab Invest 25:389–402

Porterfield JF, Zimmerman L (1962) Rhabdomyosarcoma of the orbit: a clinicopathologic study of 55 cases. Virchow Arch Pathol Anat 335:329–344

Poser CM, Brinar VV (2001) Diagnostic criteria for multiple sclerosis. Clin Neurol Neurosurg 103:1–11

Poser CM, Paty DW, Scheinberg L, McDonald WL, Davis FA, Ebers GC, Johnson KP, Sibley WA, Silberberg DH, Tourtelotte WW (1984) New diagnostic criteria for multiple sclerosis. Guidelines for research protocols. AJNR Am J Neurol 13:227–231

Proebstle TM, Schönfeldt C, Lüttke B, Weber L (1996) Morbus Behçet mit primärem Befall zerebraler Gefässe. Dtsch Med Wochenschr 121:16–20

Rauber, Kopsch (1987) Nervensystem und Sinnesorgane. In: Leonhardt H, Töndury G, Zilles K (eds) Anatomie des Menschen, Vol III. Thieme, Stuttgart

Regine WF, Fontanesi J, Kumar P, Ayers D, Bowman LC, Pappo AS, Coffey DH, Avery L, Rao BN, Kun LE (1995) Local tumor control in rhabdomyosarcoma following low-dose irradiation: comparison group II and select group III patients. Int J Rad Oncol Biol Physics 31:485–491

Reifler DM, Davison P (1986) Histochemical analysis of breast carcinoma metastasis. Ophthalmol 93:254–259

Reim M, Freund J, Wegel-Luessen L (1975) Giant dermoid cyst of the orbit causing disturbance of ocular motility. Mod Probl Ophthalmol 14:372–376

Reese AB (1955) Persistent hyperplastic primary vitreous. Am J Ophthalmol 40:317–331

Reul J (2001) Pseudotumor cerebri. In: Sartor K (ed) Neuroradiologie. Thieme, Stuttgart, pp 128–129

Rochels R, Nover A, Hackelbusch R (1986) Echographische Befunde und Differentialdiagnostik bei (peri-)orbitalen Dermoidzyste. (Echographic findings and differential diagnosis in (peri-) orbital dermoid cysts) Klin Monatsbl Augenheilkd 188:101–104

Rohrbach J, Lieb W (eds) (1998) Tumoren des Auges und seiner Adnexe. Schattauer, Stuttgart

Rootman J (1988) Frequency and differential diagnosis of orbital disease. In: Rootman J (ed) Diseases of the orbit. A multidisciplinary approach. Lippincott, Philadelphia, pp 119–139

Rootman J (1998) Why "orbital pseudotumor" is no longer a useful concept. Br J Ophthalmol 82:339–340

Rootman J, Graeb DA (1988) Vascular lesions. In: Rootman J (ed) Diseases of the orbit. Lippincott, New York, pp 525–568

Rootman J, Hay E, Graeb DA (1986) Orbital-adnexal lymphangiomas: a spectrum of hemodynamically isolated vascular hamartomas. Ophthalmology 93:1558–1570

Rootman J, Robertson W, Lapointe JS (1988) Inflammatory diseases. In: Rootman J (ed) Diseases of the orbit: a multidisciplinary approach. Lippincott, Philadelphia, pp 159–179

Rootman J, Kao SCS, Graeb DA (1992) Multidisciplinary approaches to complicated vascular lesions of the orbit. Ophthalmology 99:1440–1446

Rootmann J, McCarthy M, White V, Harris G, Kennerdell J (1994) Idiopathic sclerosing inflammation of the orbit. A distinct clinicopathologic entity. Ophthalmology 101:570–584

Rose GE, Wright JE (1992) Pleomorphic adenoma of the lacrimal gland. Br J Ophthalmol 76:395–400

Rothman M (1997) Orbital trauma. Semin Ultrasound CT MR 18:437–447

Rothova A (2000) Ocular involvement in sarcoidosis. Br J Ophthalmol 84:110–116

Rousseau P, Flamant F, Quintana E, Voute PA, Gentet JC (1994) Primary chemotherapy in rhabdomyosarcoma and other malignant mesenchymal tumors of the orbit: results of the International Society of Pediatric Oncology MMT 84 study. J Clin Oncol 12:516–521

Rubinstein LJ (1972) Digenetic syndromes (phakomatoses) associated tumors or tumor-like malformations of the nervous system. In: Rubinstein LJ (ed) Tumors of the central nervous system. Armed Forces Institute of Pathology, Washington DC, pp 300–311

Ruchman MC, Flanagan J (1983) Cavernous hemangioma of the orbit. Ophthalmol 90:1328–1336

Sagerman RH (1993) Orbital rhabdomyosarcoma: a paradigm for irradiation. Radiology187:605–607

Samuelson TW, Margo CE, Levy MH, Pusateri TJ (1988) Zygomaticofrontal suture defect associated with orbital dermoid cyst. Surv Ophthalmol 33:127–130

Sanborn GE, Kivlin JD, Stevens M (1984) Optic neuritis secondary to sinus diseases. Arch Ophthalmol 110:816–819

Sartor K (1992) MR imaging of the skull and brain. A correlative text-atlas. Springer, Berlin Heidelberg New York

Sartoretti-Schefer S, Wichmann W, Valavanis A (1997) Optic neuritis. Characteristic magnetic resonance imaging features and differential diagnosis. Int J Neuroradiol 3:417–427

Sasajima T, Kinouchi H, Tomura N, Watari J, Mizoi K (2000) High uptake of ^{123} I-metaiodobenzylguanidine related to olfactory neuroblastoma revealed by single-photon emission CT. AJNR Am J Neuroradiol 21:717–720

Sathananthan N, Moseley IF, Rose GE, Wright JE (1993) The frequency and clinical significance of bone involvement in outer canthus dermoid cysts. Br J Ophthalmol 77:789–794

Savoiardo M, Strada L, Passerini (1983) Cavernous hemangioma of the orbit: value of CT, angiography and phlebography. AJNR Am J Neuroradiol 4:741–744

Schaffler GJ, Simbrunner J, Lechner H, Langmann G, Stammberger H, Beham A, Ebner F (2000) Idiopathic sclerotic inflammation of the orbit with left optic nerve compression in a patient with multifocal fibrosclerosis. Am J Neuroradiol 21:194–197

Schuknecht B, Simmen D, Yuksel C, Valavanis A (1998) Tributary venosinus occlusion and septic cavernous sinus thrombosis: CT and MR findings. Am J Neuroradiol 19:617–626

Scotti G, Nash D (1982) Computed tomography of rhabdomyosarcomas of the skull base in children. J Comput Assist Tomogr 6:33–39

Seabold JE, Simonson TM, Weber PC, Thompson BH, Harris KG, Rezai K, Madsen MT, Hoffman HT (1995) Cranial osteomyelitis: diagnosis and follow-up with In-111 white blood cell and Tc-99 m methylene diphosphonate bone SPECT, CT, and MR imaging. Radiology 196:779–788

Seiff SR, Brodsky MC, MacDonald G, Berg BO, Howes EL, Hoyt WF (1987) Orbital optic glioma in neurofibromatosis. Magnetic resonance diagnosis of perineural arachnoidal gliomatosis. Arch Ophthalmol 105:1689–1692

Sevick R, Barkovich A, Edwards M, Koch T, Berg B, Lempert T (1992) Evolution of white matter lesions in neurofibromatosis type I: MR findings. AJR Am J Roentgenol 159:171–175

Sheidow TG, Nicolle DA, Heathcote JG (2000) Erdheim-Chester disease: two cases of orbital involvement. Eye 14:606–612

Sherman JL, McLean IW, Brallier DR (1983) Coats' disease. CT pathologic correlation in two cases. Radiology 146:77–78

Shields JA, Shields CL (1993) Rhabdomyosarcoma of the orbit. Int Ophthalmol Clin 33:201–210

Shields JA, Zimmerman LE (1973) Lesions simulating malignant melanoma of the posterior uvea. Arch Ophthalmol 89:466–471

Shields JA, Dolinskas C, Augsburger JJ, Shah HG, Shapiro ML (1984a) Demonstration of orbital varix with computed tomography and Valsalva maneuver. Am J Ophthalmol 97:109–109

Shields JA, Bakewell B, Augsberger JJ, Flanagan JC (1984b) Classification and incidence of space occupying lesions of the orbit: a survey of 645 biopsies. Arch Ophthalmol 102:1606–1611

Shields JA, Augsburger JJ, Donoso LA (1986) Orbital dermoid cyst of conjunctival origin. Am J Ophthalmol 101:726–729

Shields JA, Shields CL, Eagle RC (1987a) Cavernous hemangioma of the orbit. Arch Ophthalmol 105:853

Shields CL, Shields JA, Eagle RC Jr, Peyster RG, Conner BE, Green HA (1987b) Orbital metastasis from a carcinoid tumor. Computed tomography, magnetic resonance imaging, and electron microscopic findings. Arch Ophthalmol 105:968–971

Shields JA, Karcioglu ZA, Shields CL, Eagle RC, Wong S (1991) Orbital and eyelid involvement with Erdheim-Chester disease: a report of two cases. Arch Ophthalmol 109:850–854

Shields CL, Shields JA, Gross NE, Schwartz GP, Lally SE (1997) Survey of 520 eyes with uveal metastasis. Ophthalmology 104:1265–1276

Shields CL, Shields JA, Cater J, Lois, N, Edelstein C, Gündüz K, Mercado G (1998) Transpupillary thermotherapy for choroidal melanoma. Ophthalmology 105:581–590

Silodor SW, Augsburger JJ, Shields JA, Tasman W (1988) Natural history and management of advanced Coats' disease. Ophthalmic Surg 19:89–93

Smirniotopoulos JG, Chiechi MV (1995) Teratomas, dermoids and epidermoids of the head and neck. Radiographs 15:1437–1455
Smith CA, Pinals RS (1982) Optic neuritis in lupus erythematosus. Rheumatol 9:63–66
Soderstrom M (2001) Optic neuritis and multiple sclerosis. Acta Ophthalmol Scand 79:223–227
Sohaib SA, Moseley I, Wright JE (1998) Orbital rhabdomyosarcoma– the radiological characteristics. Clin Radiol 53:357–362
Sood S, Vashisht S, Betharia SM, Berry M (1992) CT evaluation of orbital osseous hemangioma. Aust Radiol 36:124–126
Spath-Schwalbe E, Genvresse I, Stein H, Gelderblom H, Lehmann R, Budach V, Possinger K (1999) Primary cerebral highly-malignant B-cell lymphoma of the Burkitt type. Dtsch Med Wochenschr 124:451–455
Specht CS, Laver NM (2000) Benign and malignant lymphoid tumors, leukemia, and histiocytic lesions. In: Albert DM, Jakobiec FA (eds) Principles and practice of ophthalmology, 2nd edn. Saunders, Philadelphia, pp 5146– 5168
Spoor TC, McHenry JG (1995) Optic nerve sheath decompression. American Academy of Ophthalmology. Academy Manual Lids Orbit III:48–59
Stanton RP, Montgomery BE (1996) Fibrous dysplasia. Orthopedics 19:679–685
Stern J, Jakobiec FA, Housepian EM (1980) The architecture of optic nerve gliomas with and without neurofibromatosis. Arch Ophthalmol 98:505–511
Stewart WB, Krohel, GB, Wright JE (1979) Lacrimal gland and fossa lesions: an approach to diagnosis and management. Ophthalmology 86:886–895
Stoffelns BM, Dick B (2000) Ziliarkörpermetastase als Ersthinweis auf ein kleinzelliges Bronchialkarzinom. Klin Monatsbl Augenheilkd 216:339–341
Stroszczynski C, Hosten N, Bornfeld N, Wiegel T, Schueler A, Foerster P, Lemke AJ, Hoffmann KT, Felix R (1998) Choroidal hemangioma: MR findings and differentiation from uveal melanoma. AJNR Am J Neuroradiol 19:1441–1447
Sullivan TJ, Aylward GW, Wright JE, Moseley IF, Garner A (1992a) Bilateral multiple cavernous haemangiomas of the orbit. Br J Ophthalmol 76:627–629
Sullivan TJ, Wright JE, Wule AE, Garner A, Moseley I, Sathananthan N (1992b) Haemangiopericytoma of the orbit. Aust NZ J Ophthalmol 20:325–332
Sun XL, Zheng BH, Li B, Li LQ, Soejima K, Kanda M (1990) Orbital rhabdomyosarcoma. Immunohistochemical studies of seven cases. Chin Med J 103:485–488
Suzuki H, Takanashi J, Kobayashi K, Nagasawa K, Tashima K, Kohno Y (2001) MR imaging of idiopathic intracranial hypertension. Am J Neuroradiol 22:196–199
Sweet C, Silbergleit R, Mehta B (1997) Primary intraosseous haemangiomas of the orbit: CT and MR appearance. Am J Neuroradiol 18:379–381
TadmorR R, New PF (1978) Computed tomography of the orbit with special emphasis on coronal sections, part II. Pathological anatomy. J Comput Assist Tomogr 2:35–44
Tan WS, Wilbur AC, Mafee MF (1987) The role of the neuroradiologist in vascular disorders involving the orbit. Radiol Clin North Am 25:849–861
Taylor D, Hoyt C (1997) Optic disc anomalies with midline defects. In: Taylor D, Hoyt C (eds) Practical paediatric ophthalmology. Blackwell Science, Boston, pp 158–161
Tellado MV, McLean IW, Specht CS, Varga J (1997) Adenoid cystic carcinomas of the lacrimal gland in childhood and adolescence. Ophthalmology 104:1622–1625
Terada H, Barkovich AJ, Edwards MSB, Ciricillo SF (1996) Evolution of high-intensity basal ganglia lesions on T1w MR in neurofibromatosis type I. AJNR Am J Neuroradiol 17:755–760
Teske S, Ohlrich SJ, Gole G, Spiro P, Miller M, Sullivan TJ (1994) Treatment of orbital capillary haemangioma with interferon. Aust NZ J Ophthalmol 22:13–17
Thorn KM, Arrue P, Delisle MB, Lacroix F, Lagarrigue J, Manelfe C (1999) Cavernous hemangioma of the orbit: MR imaging. J Neuroradiol 26:79–86
Tien R, Kucharczyk J, Kucharczyk W (1991) MR imaging of the brain in patients with diabetes insipidus. AJNR Am J Neuroradiol 12:533–542
Tohme A, Haddad F, Ghjayad E (1997) Neurologic manifestation in Behçet's disease. 16 cases in a cohort of 110 patients. Ann Med Interne (Paris) 148:118–124
Trese MT, Krohel GB, Hepler RS, Naeim F (1980) Burkitt's lymphoma with cranial nerve involvement. Arch Ophthalmol 98:2015–2017
Tso MOM (1980) Clues to the cells of origin of retinoblastoma. Int Ophthalmol Clin 20:191–210
Uceda-Montanes A, Blanco G, Saornil MA; Gonzalez C, Sarasa JL, Cuevas J (2000) Extramedullary plasmocytoma of the orbit. Acta Ophthalmol Scand 78:601–603
Ustun MO, Ekinci N, Payzin B (2001) Extramedullary plasmocytoma of the parotid gland. Report of a case with extensive amyloid deposition masking the cytology and histopathologic picture. Acta Cytol 45:449–453
Utech CI, Khatibnia U, Winter PF, Wulle KG (1995) MR T2 relaxation time for the assessment of retrobulbar inflammation in Graves' ophthalmopathy. Thyroid5:185–193
van der Knaap MS, Valk J (1995) Mucopolysaccharidoses. In: van der Knaap MS, Valk J (eds) Magnetic resonance of myelin, myelination, and myelin disorders, 2nd edn. Springer, Berlin Heidelberg New York, pp 97–105
van der Knaap MS, Valk J (1995) Multiple sclerosis. In: Knaap MS van der, Valk J (eds) Magnetic resonance of myelin, myelination, and myelin disorders, 2nd edn. Springer, Berlin Heidelberg New York, pp 296–313
van derLee I, Slee PH, Elbers JR (1999) A patient with diabetes insipidus and periorbital swellings: Erdheim-Chester disease. Neth J Med 55:76–79
von Deimling A, Foster R, Krone W (2000) Neurofibromatosis type I. In: Kleihues P, Cavenee WK (eds) Pathology and genetics. Tumors of the nervous system. IARC Press, Lyon, pp 216–218
Valmaggia C, Neuweiler J, Fretz C, Gottlob I (1997) A case of Erdheim-Chester disease with orbital involvement. Arch Ophthalmol 115:1467– 1468
Valvassori GE, Sabnis SS, Mafee RF, Brown MS, Putterman A (1999) Imaging of orbital lymphoproliferative disorders. Radiol Clin North Am 37:135–150
Van den Bogaert W, van Limbergen E, Dralands G, Drochmans A (1992) Curative irradiation of the entire orbit in rhabdomyosarcoma: a case report. Head and Neck 14:392– 394
Vangveeravong S, Katz SE, Rootman J, White V (1996) Tumors arising in the palpebral lobe of the lacrimal gland. Ophthalmology 103:1606–1612
Wackenheim A, van Damme W, Kosmann P, Bittighoffer B (1977) Computed tomography in ophthalmology. Density changes with orbital lesions. Neuroradiology 13:135–138

Walsh FB (1975) Meningeomas primary within the orbit and optic canal. In: Glaser JS, Smith JL (eds) Neuroophthalmology. Symposium of the University of Miami and Bascon Palmer Eye Institute. Mosby, St Louis

Watson PG (1982) Doyne memorial lecture. The nature and treatment of scleral inflammation. Trans Ophthalmol Soc UK 102:257–281

Warner MA, Weber AL, Jakobiec FA (1996) Benign and malignant tumors of the orbital cavity including the lacrimal gland. Neuroimaging Clin North Am 6:123–142

Weber AL (1992) Comparative assessment of diseases of the orbit using computed tomography and magnetic resonance imaging. Isr J Med Sci 28:153–160

Weber AL, Jakobiec FA, Sabates NR (1996a) Pseudotumor of the orbit. Neuroimaging Clin North Am 6:73–92

Weber AL, Jakobiec FA, Sabates NR (1996b) Lymphoproliterative disease of the orbit. Neuroimaging North Am 1:93–111

Weber AL, Rodriguez-De Velasquez A, Lucarelli MJ, Cheng HM (1996c) Normal anatomy and lesions of the lacrimal sac and duct: evaluated by dacryocystography, computed tomography, and MR imaging. Neuroimaging Clin North Am 6:199–217

Weber AL, Romo LV, Sabates NR (1999) Pseudotumor of the orbit: clinical, pathologic and radiologic evaluation. Radiol Clin North Am 37:151–168

Wechsler B, Gerber S, Vidailhet M, Dormont D (1999) Neurologic manifestation of Behçet's disease. Ann Med Interne (Paris) 150:555–561

Weetman AP, Hunt PJ (1999) The immunogenetics of thyroid-associated orbitopathy. Exp Clin Endocrinol Diabetes 107:S149–S151

Weisberg LA (1985) Computed tomography in benign intracranial hypertension. Neurology 35:1075–1078

Weiter JJ, Ernest JT (1974) Anatomy of the choroidal vasculature. Am J Ophthalmol 78:583–590

Wende S, Aulich A, Nover A, Lanksch W, Kazner E, Steinhoff H, Meese W, Lange S, Grumme T (1977) Computed tomography of orbital lesions. A comparative study of 210 cases. Neuroradiology 13:123–134

Wenig BM, Mafee MF, Ghosh L (1998) Fibro-osseous, osseous and cartilagenous lesions of the orbit and paraorbital region. In: Mafee (ed) The Radiologic Clinics of North America. Imaging Ophthalmol I:1241–1259

White VA, Gascoyne RD, McNeil BK, Chang WY, Brewer LV, Rootman J (1996) Histopathologic findings and frequency of clonality detected by the polymerase chain reaction in ocular adnexal lymphoproliterative lesions. Mod Pathol 9:1052–1061

Wiener ES (1994) Head and neck rhabdomyosarcoma. Semin Pediatr Surg 3:203–206

Wiersinga WM, Prummel MF (2001) Pathogenesis of Graves' ophthalmopathy – current understanding. J Clin Endocrinol Metab 86:501–503

Wing GL, Schepens CL, Trempe CL, Weiter JJ (1982) Serous choroidal detachment and the thickened-choroid sign detected by ultrasonography. Am J Ophthalmol 94:499–505

Wingerchuk DM, Hogancamp WF, O'Brien PC, Weinshenker BG (1999) The clinical course of neuromyelitis optica (Devic's syndrome). Neurology 53:1107–1114

Winward KE, Hamed LM, Glaser JS (1989) The spectrum of optic nerve disease in human immunodeficiency virus infection. Am J Ophthalmol 107:373–380

Woodruff JM (1996) Pathology of major peripheral nerve sheath tumors. In: Weiss SW, Brooks JSJ (eds) Soft tissue tumors (International Academy of Pathology Monograph). Williams and Wilkins, Baltimore, pp 129–161

Woodruff JM, Kourea HP, Louis DN, Scheithauer BW (2000) Schwannoma, Neurofibroma. In: Kleihues P, Cavenee WK (eds) Pathology and genetics. Tumors of the nervous system. IARC, Lyon, pp 163–168

Wright JE, Sullivan TJ, Garner A, Wulc AE, Moseley JF (1997) Orbital venous anomalies. Ophthalmology 104:905–913

Wright RA, Hermann RTC, Parisis JE (1999) Neurological manifestation of Erdheim-Chester disease. J Neurol Neurosurg Psychiatry 66:72–75

Yan XY, Edward DP, Mafee MF (1998) Ocular calcification. Radiologic-pathologic correlation and literature review. Int J Neuroradiol 4:81–86

Yang WT, Kwan WH, Li CK, Metreweli C (1997) Imaging of pediatric head and neck rhabdomyosarcomas with emphasis on magnetic resonance imaging and a review of the literature. Ped Hematol Oncol 14:243–257

Yanoff M, Fine BS (1975) Ocular pathology: a text and atlas. Harper and Row, Hagerstown Md, p 831

Yeo JH, Jakobiec FA, Abbott GF, Trokel SL (1982) Combined clinical and computed tomographic diagnosis of orbital lymphoid tumors. Am J Ophthalmol 94:235–245

Youl BD, Turano G, Miller DH, Towell AD, MacManus DG, Mooere SG, Jones SJ, Barret G, Kendall BE, Moseley IF et al (1991) The pathophysiology of acute optic neuritis. An association of gadolinium leakage with clinical and electrophysiological deficits. Brain 114:2437–2450

Zakka KA, Foos RY, Omphroy CA, Straatsma BR (1980) Malignant melanoma. Analysis of an autopsy population. Ophthalmology 87:549–556

Zhu X, Dunn JM, Goddard AD, Squire JA, Becker A, Philips RA, Gallie BL (1992) Mechanisms of loss of heterozygosity in retinoblastoma. Cytogenet Cell Genet 59:248–252

Zhu XP, Hutchinson CE, Chilvers PB, Morris GA, Hawnaur JM, Taylor CJ (1995) Off-resonance binominal composite pulses in2D and 3D fat/water imaging at 0.5 T. Br J Radiol 68:134–140

Zierhut M, Denk PO, Klein R, Berg PA, Erb C, Thiel HJ (1997) Autoantikörper – Merkmale bei Skleritis und Episkleritis. Ophthalmologe 94:157–160

Zilkha A (1982) Multiplanar reconstructions in computed tomography of the orbit. Comput Radiol 6:57–62

Zimmerman LE (1973) Problems in diagnosis of malignant melanomas of the choroid and ciliary body. Am J Ophthalmol 75:919–929

Zonneveld FW, Vaandrager JM, van der Meulen JHC, Koorneef L (1998) Three-dimensional imaging of congenital disorders involving the orbit. Radiol Clin North Am 36:1261–1279

Zurlo A, Sancesario G, Bernardi G, Loasses A (1999) Orbital pseudotumor: case report and literature review. Tumori 85:68–70

7 Intracranial Pathology of the Visual Pathway

W. Müller-Forell

CONTENTS

Ophthalmologic symptomatology caused by an intracranial lesion is characterized by a variety of contributing factors, depending on the site of the lesion (for a detailed discussion see chapter 3, Neuro-ophthalmology). The most common symptom of intracranial lesions involving the optic pathway is the progressive loss of visual acuity. Monocular visual disturbances occur in the presence of optic nerve involvement. In cases of acute visual loss, optic nerve neuritis has to be excluded, whereas with slowly progressing symptoms, a tumor of the clinoid or sellar/suprasellar region may be the causative factor. In daily clinical practice, we are repeatedly confronted with the unfortunate experience that in many patients imaging is performed only when decompensation of the visual system has become apparent. In the majority of these patients, a tumor originating from the pituitary gland or the skull base has already destroyed the surrounding neural substance. The most frequent clinical symptoms in these patients include persistent, slowly progressing, unilateral visual deficits that are frequently falsely attributed to aging or stress problems. In addition, although less frequently, these patients suffer from bitemporal hemianopia caused by inferior compression of the chiasm. In patients suffering from double vision or acute ptosis, the subjective disabling symptoms lead to both an earlier indication for imaging and the identification of clinical symptoms of homonymous defects of the visual field. In bitemporal hemianopia, a midline tumor (in most cases a pituitary adenoma) causes compression of the chiasm inferiorly at the crossing site of the nasal fibers. When the lesion involves the optic tract, this leads to the development of homonymous hemianopia to the contralateral visual field.

Although the high sensitivity of HR-CT for neoplastic changes in compact bone makes this technique an important tool in the preoperative diagnosis of intracranial pathology of the optic pathway, MRI should be the procedure of choice. Following the clinical definition of the neuro-ophthalmologic/neurologic deficit, MRI enables a focused examination of the entire visual pathway along its course from the inner aperture of the optic canal to the occipital pole.

7.1 Primary Brain Tumors

Although a comprehensive discussion of intracranial neoplasms is beyond the scope of this book, a brief overview of these lesions nevertheless appears to be requisite with regard to the patients presented.

By definition, primary brain tumors include neoplasms of the brain and the meninges as well as non-neoplastic intracranial cysts and tumor-like lesions that arise from adjacent structures, e.g., the skull base. These lesions affect the brain, either primarily or secondarily, and may occur at any age and at any intracranial location (Zülch 1983; Okazaki 1989; Burger et al. 1991; Osborn and Rauschning 1994). They therefore include both intrinsic (arising from cells covered by pia) and extrinsic (originating from cells outside the pia) space-occupying lesions, a definition important for both neuroradiological differential diagnosis and neurosurgical therapy (Yasargil 1994). As the

PD W. Müller-Forell, MD
Institute of Neuroradiology, Medical School University of Mainz, Langenbeckstrasse 1, 55101 Mainz, Germany

histology and topography of brain tumors differ essentially in adults and children, they should be considered separately. From 15% to 20% of all intracranial tumors occur in children younger than 15 years of age (Russell and Rubinstein 1989), 48% to 70% of these neoplasms are infratentorial, and most infantile intracranial neoplasms are astrocytomas. Roughly 70% of brain tumors in adults are located in the supratentorial compartment (Harwood-Nash 1991; Okazaki 1989). Brain tumors in adults occur at a similarly high rate as neoplasms of the hemopoietic type and lymphomas, ranking directly below the incidence of carcinoma of the stomach and lung (Zülch 1986). An universally accepted classification of brain tumors does not exist, although the current World Health Organization (WHO) classification of this multitude of different brain tumors is widely used. It takes into account not only the histological, cellular specificity but the biological behavior of the specific tumor and includes the following prognostic definitions: WHO grade I tumors, complete healing; WHO grade II tumors, mean survival rate of 3–5 years; WHO grade III tumors, 2–3 years; and WHO grade IV tumors with a mean survival rate of 6–9 months (Kleihues et al. 1993; Kleihues and Cavanee 2000).

There are many possibilities for the classification of brain tumors, however, for neuroradiologists, clinical information (especially of the age of the patient and length of history) and imaging data form the basis of the differential diagnosis of intracranial pathologic lesions. The use of modern imaging techniques provides instant information on the size, location, extension, shape, number of lesions, and secondary changes, enabling a conclusive differential diagnosis in more than 90% of cases (Yasargil 1994). General characteristics of brain tumors such as perifocal edema, midline shift, blood-brain-barrier disruption, and CSF-circulation disorders can be clearly identified with CT, the first imaging method to provide direct images of the brain. However, the high anatomic resolution in three (or more) planes and the high sensitivity of MRI for structural anatomic changes, especially for brain edema, make this technique the method of choice in the preoperative clinical diagnosis of brain tumors.

7.1.1 Intrinsic Lesions, Glioma in Adults

The term glioma stands for the corresponding three types of glial cells. The three major types of gliomas originate from: astrocytoma (see 7.2.1.5), oligodendroglioma and ependymoma (see 7.3.1.1), and the so-called mixed gliomas that contain two or more different cell types in varying proportions, most frequently primarily oligoastrocytoma (Okazaki 1989), whereas intraventricular choroid plexus papilloma and carcinoma are distinct from ependymoma (Kleihues and Cavanee 2000).

7.1.2 Extrinsic Tumors

Due to the fact that extrinsic (or extra-axial) tumors are frequently benign, the treatment and prognosis are based upon the correct diagnosis of suspected intracranial extrinsic masses. The use of MRI is mandatory for these tumors because it has the ability to differentiate the boundary between the brain parenchyma and the mass itself. The superior contrast resolution and multiplanar imaging capacity of MRI enable the identification of anatomic markers as cardinal features of an extra-axial lesion. Instead of the demonstration of the tissue contrast of extrinsic masses and brain parenchyma, the definition of boundary layers between the tumor and the brain surface permits the diagnosis of an extra-parenchymal intracranial lesion. The boundary layers represent cerebrospinal fluid (CSF), pial blood vessels, and/or the dura. CSF clefts are recognized as crescentic bands, frequently only over a portion of the tumor, with signal intensities similar to those of spinal fluid: low on T1-weighted, isointense on proton density-weighted, and high on T2-weighted images. In SE sequences, both normal anatomic and pathologic vessels are identified as rounded or curvilinear signal voids at specific locations of the lesion margin. The use of i.v. contrast agents enables the demonstration of the compartmentalization of extrinsic lesions, since a large number of tumors show a specific pattern, including extensive signal enhancement (meningioma, metastasis), while others show none (epidermoid and dermoid tumors) (Goldberg et al. 1996).

7.1.3 Metastasis

Intracranial metastasis or secondary brain tumors are defined as tumors involving the CNS and originate from, but are discontinuous with, primary systemic

neoplasms. They account for 15% to 30% of all intracranial tumors in pathologic series (Okazaki 1989; Nelson et al. 2000). The most frequent primary malignancies include lung carcinoma (40% metastasize to the brain), breast carcinoma (roughly 25% metastasize to the brain), hypernephroma, melanoma, and neuroblastoma, the latter occurring predominantly in children.

All areas of the brain may be affected, with preference for the corticomedullary junction as the starting point (Okazaki 1989), possibly due to greater capillarization of this region (Zülch 1986). The sellar region is the preferred location for hematogenous spread of primary carcinoma of extracranial origin. In addition to the convexity of the brain and/or cerebellum, leptomeningeal tumor cells deposit in the recess of the third ventricle but may also invade the parenchyma of the hypothalamus and/or chiasm (Figs. 7.1, 7.2).

7.2 Sellar Region

The sellar region represents one of the most complex areas of the endocranium, consisting of parenchymal structures, important vessels, and cranial nerves. The optic chiasm itself represents the center of the sellar region, bordered above by the hypothalamus and floor of the third ventricle, behind and below by the pituitary stalk and the pituitary itself, and surrounded by the important vessels and cranial nerves. On the arterial side, the vessels of Willis' circle include the distal parts of both internal carotid arteries (ICA), the A1-segments of both anterior cerebral arteries (ACA) and middle cerebral arteries (MCA), as well as the posterior communicating arteries (Pcomm) and the top of the basilar artery. The most important venous structure is the cavernous sinus, harboring the cranial nerves N III, N IV, N

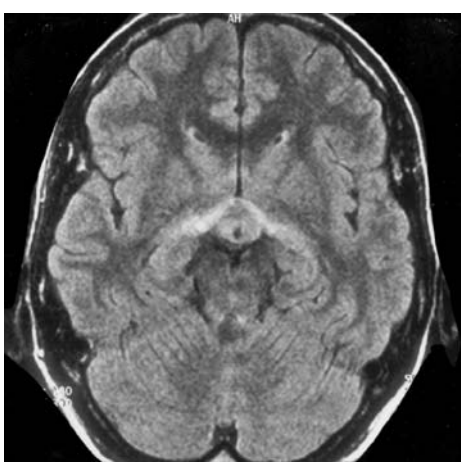

a

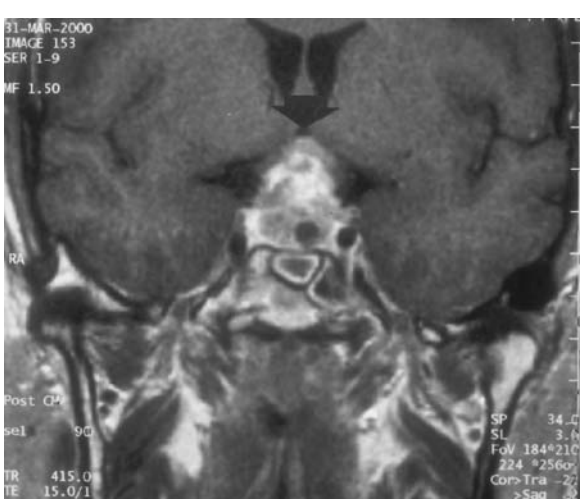

b

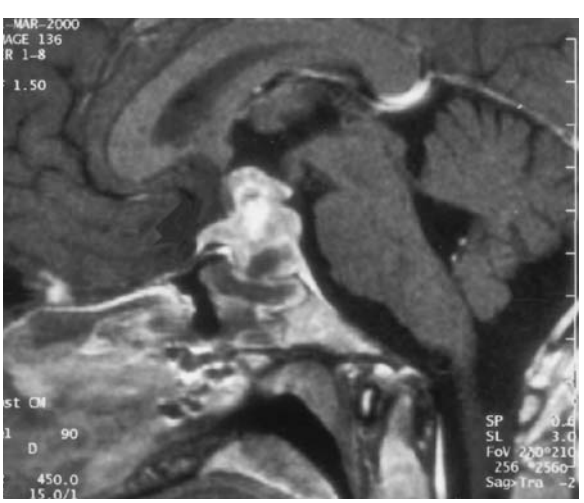

c

Fig. 7.1a–c. A 35-year-old woman with acute vision loss, predominantly of the right eye, and a history of breast carcinoma. Diagnosis: intra- and suprasellar metastasis. MRI: **a** Axial T2-weighted FLAIR sequence showing edema of the chiasm and both optic tracts. **b** Coronal, T1-weighted, contrast-enhanced view demonstrating tumor infiltration of the chiasm, confirmed during neurosurgery, where dissection of the optic fibers was impossible. **c** Paramedian sagittal, T1-weighted, contrast-enhanced view with hypothalamic infiltration, identified by flattening of the floor of the third ventricle. Note the loss of differentiation of the obviously infiltrated pituitary stalk and gland, dural infiltration of the sphenoid plane, and mucous filling of the sphenoid sinus

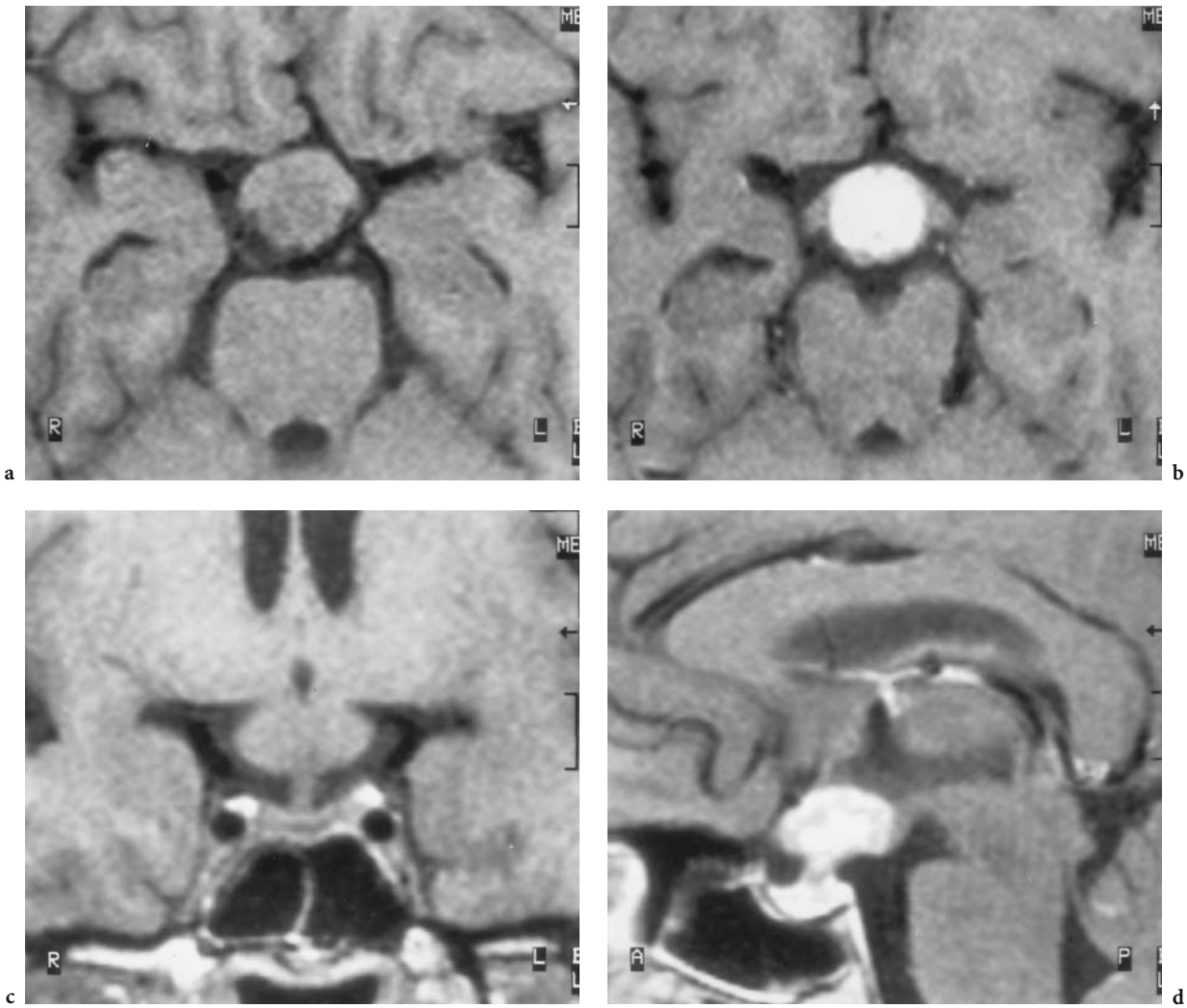

Fig. 7.2a–d. A 38-year-old woman with chiasm syndrome, diabetes insipidus, and a history of breast carcinoma. Diagnosis: hypothalamic and chiasmal metastasis of breast carcinoma. T1-weighted MRI: **a** Axial native view showing a slightly hypointense lesion dorsal to the chiasm with apparent invasion. **b** Corresponding contrast-enhanced view, identifying invasion of the chiasm and the proximal optic tracts. **c** Coronal native view. **d** Midsagittal contrast-enhanced view, demonstrating metastatic spread throughout the hypothalamus and pituitary stalk (**d** with permission of Müller-Forell 2001)

V1, N V2, and N VI (Rauber and Kopsch 1987; Kretschmann and Weinrich 1991; Leblanc 1992) (see Fig. 2.20).

Corresponding to the various tissues, a number of pathologic processes may occur. More than 30 different pathologic entities, primarily extrinsic lesions, involving and affecting structures of the sellar and juxtasellar region have been described (Osborn and Rauschning 1994). These tumors involve the brain parenchyma secondarily and are often cured completely without recurrences even if the lesion has reached a considerable size. Intrinsic brain tumors, which often show a recurrent clinical course even for benign tumors, develop less frequently in the sellar region. The cardinal clinical symptoms are as variable as the locations of the diseases of the sellar region. In addition to endocrinological disorders (pituitary, hypothalamus insufficiency) and complex focal episodes (temporal lobe), visual disturbances caused by chiasmal or optic nerve/tract compression and cranial nerve deficits (cavernous sinus) are the leading symptoms. In the presence of rare huge suprasellar processes, compression of Monro's foramen can cause occlusive hydrocephalus with

increased brain pressure. Occlusive hydrocephalus may result in additional clinical symptoms of headache, vomiting, and (in severe cases) loss of consciousness (Fig. 7.3). Extraparenchymal space-occupying lesions originating from the pituitary gland itself or from the frontobasal meningeal layers most frequently lead to the development of chiasmal compression syndrome.

7.2.1 Neoplasms and Tumor-like Lesions

7.2.1.1 Gliomas of the Chiasm

Gliomas of the anterior visual pathway, histologically defined as pilocytic astrocytoma (see also chapter 7.2.1.5), are uncommon lesions, but account for approximately 65% of intrinsic tumors of the optic nerve. As described in chapter 6.4.1.1, these lesions most frequently occur in children in the first decade of life (Dutton 1994), whereas only 10% present in patients older than 20 years (Wulc et al. 1989). As most of these gliomas are located in the intraorbital and intracranial part of the optic nerve, additional involvement of the chiasm is seen in about 75% of patients (Fig. 7.4). However, only 7% occur in the chiasm itself, and 46% involve both the chiasm and hypothalamus (Figs. 7.5–7.7), the latter increasing the mortality rate to over 50%, since no specific therapy alters the final outcome (Dutton 1994).

As already defined by Hoyt et al. (1973), chiasmal gliomas in adults represent a clinical entity distinct from the benign gliomas of childhood, due to the fact that they are malignant astrocytoma or glioblastoma, spreading subpially along the optic pathway, with hypothalamic and even temporal lobe infiltration (Figs. 7.8 and 7.9). They are not associated with NF 1 and uniformly show a fatal course of usually less than 1 year (Rush et al. 1982; Mason and Kandal 1991; Dutton 1994; Hollander et al. 1999). All patients report decreased vision in at least one eye, sometimes associated with retro-orbital pain. Primary ophthalmologic examination reveals disk edema (44%) and optic atrophy (31%) or macular edema (Dutton 1994), in addition to incongruous homonymous hemianopsia if the optic tract is involved and the homonymous sector is defect or, respectively, when the lateral geniculate nucleus is affected

(Text continues on p. 351)

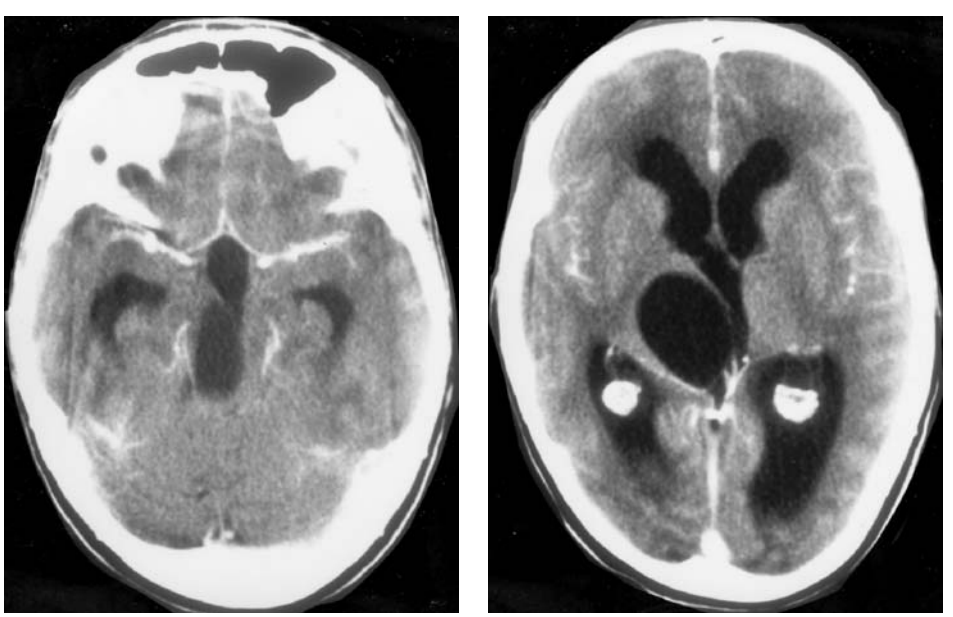

Fig. 7.3a,b. A 36-year-old woman with double vision in all directions, except the left, persisting for several weeks. The patient underwent emergency examination for acute loss of consciousness and bilateral papilledema. Diagnosis: intraparenchymal arachnoid cyst of unknown origin in the right thalamus and superior quadrigeminal plate causing an acute occlusive hydrocephalus. Axial contrast-enhanced CT: at the level of the quadrigeminal plate (**a**) and Monro's foramen (**b**), demonstrating isodensity of the CSF and the cystic content. The cyst extends to the thalamus, depressing the aqueduct (leading indirectly to a blockade of the left foramen of Monro, with asymmetrical widening of the posterior horn of the left ventricle) and dislocating the partially dilated third ventricle

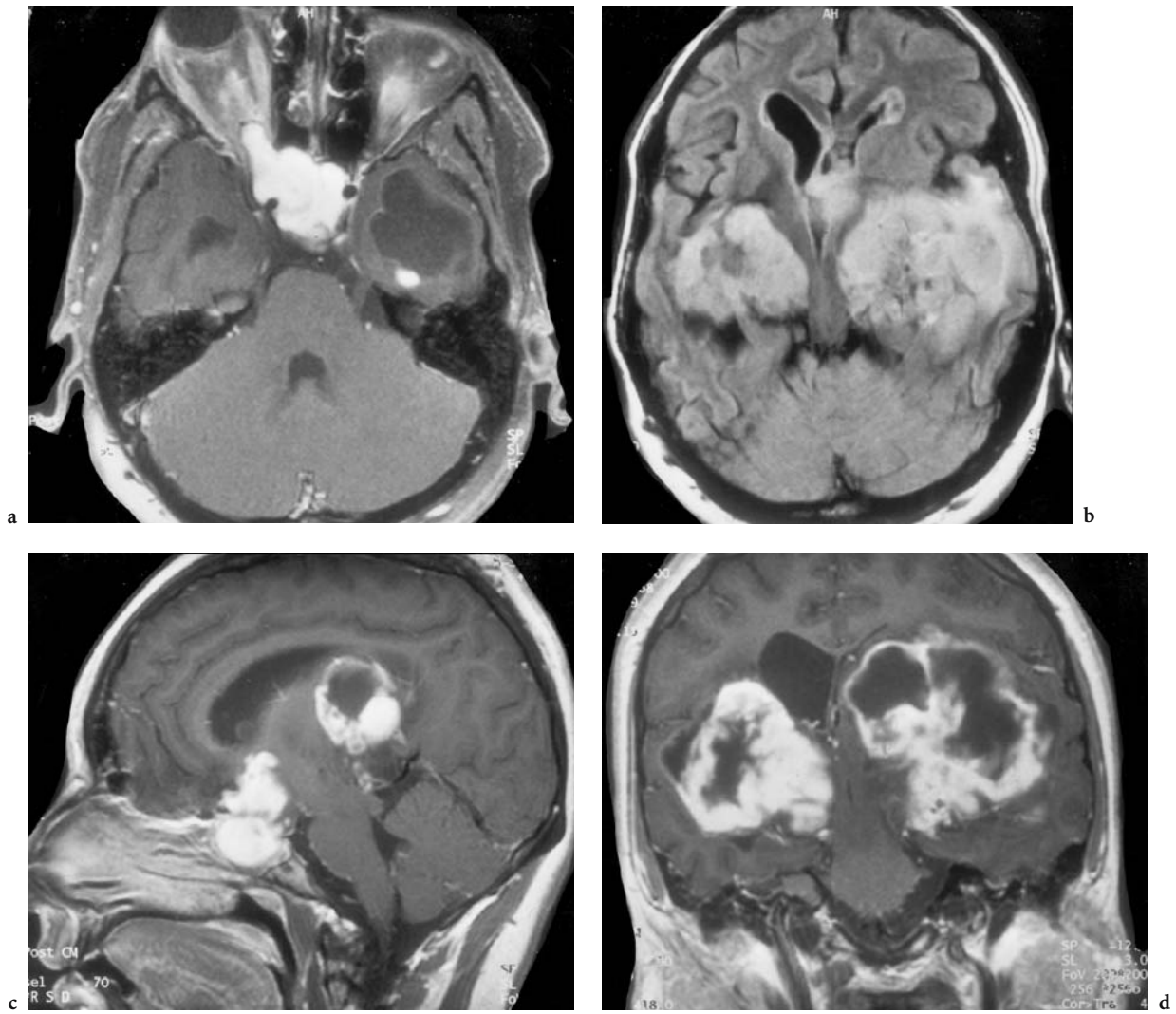

Fig. 7.4a–d. A 17 year old girl with complete blindness (and deafness) since childhood and a known neurofibromatosis. Diagnosis: astrocytoma WHO II. MRI: **a** Axial, T1-weighted, contrast-enhanced view at the level of the chiasm, showing the solid tumor in the entire suprasellar cistern, growing into the right optic nerve and canal with intraorbital expansion. Note a cystic tumor with a small, solid, contrast-enhancing tumor knot in the left temporal lobe. **b** Axial proton-weighted view, demonstrating the hypothalamic and bilateral thalamic infiltration, apparently arising from both optic tracts. **c** Sagittal, T1-weighted, contrast-enhanced view, in which not only the expansion into the sella with compression of the pituitary gland and hypothalamic infiltration is apparent, but another tumor part in the pulvinar of the thalamus is seen. **d** Coronal, T1-weighted, contrast-enhanced view showing the huge bilateral tumor expansion

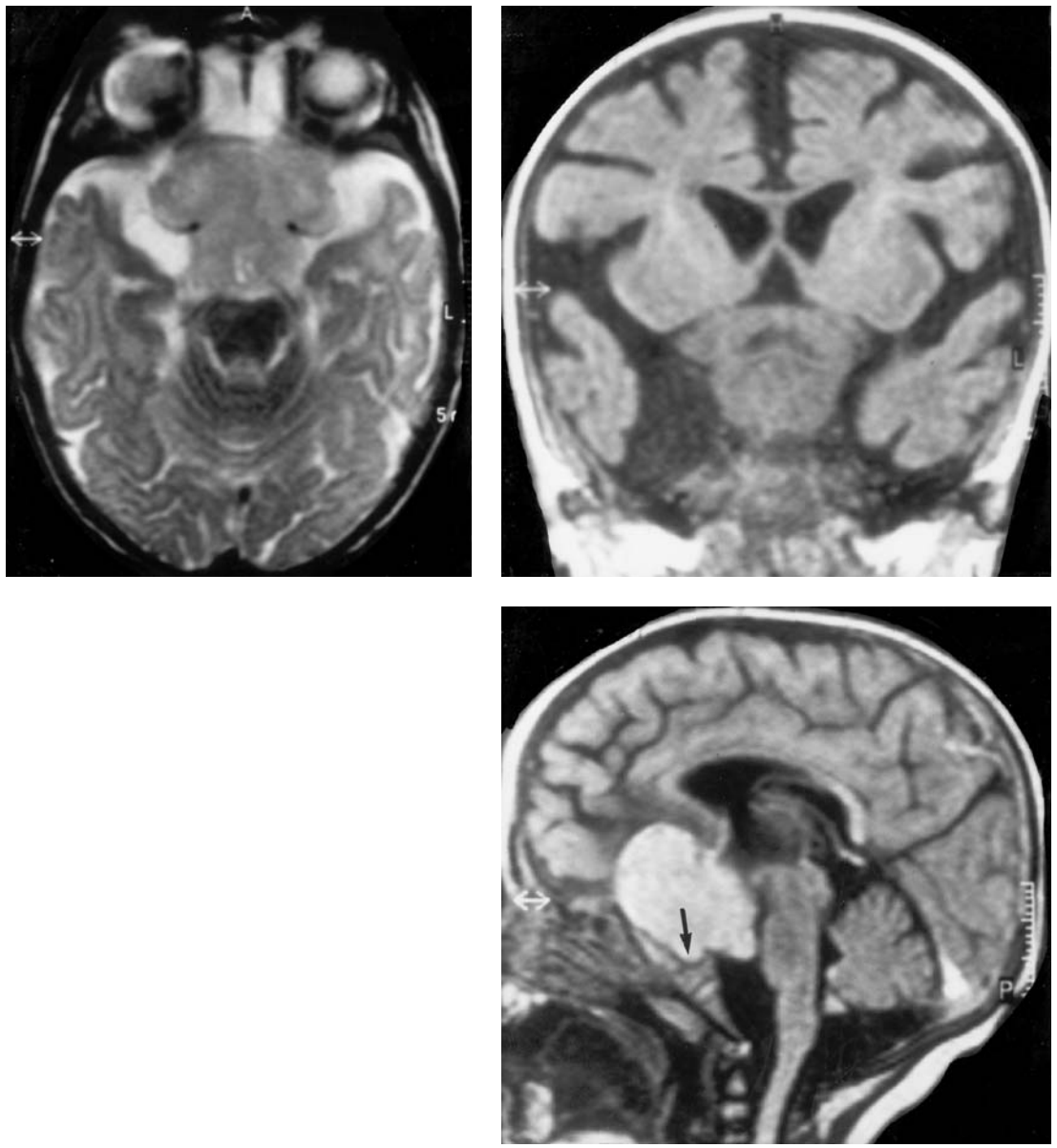

Fig. 7.5a–c. A 5-month-old girl with persisting vertical nystagmus, intermittent strabismus, and increased intracranial pressure. Diagnosis: astrocytoma (WHO II) of the chiasm with infiltration of the left optic nerve. MRI: **a** Axial T2-weighted view with a very large, space-occupying, isointense lesion located in a widened suprasellar cistern, depressing and spreading the basal vessels. **b** Coronal T1-weighted native view demonstrating pressure exertion on the widened third ventricle by the central hypointense (necrotic) tumor. **c** Midsagittal, T1-weighted, contrast-enhanced view with demarcation of the entire enhancing tumor, compressing and displacing the brainstem, and extending into the posterior fossa. Note widening of the entrance of the otherwise normally configured sella (*arrow*). (With permission of Dr. Klusemann, Radiologische Gemeinschaftspraxis, Bad Homburg)

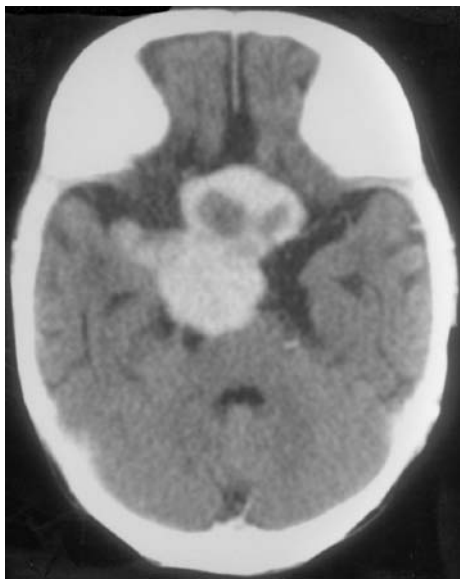

a

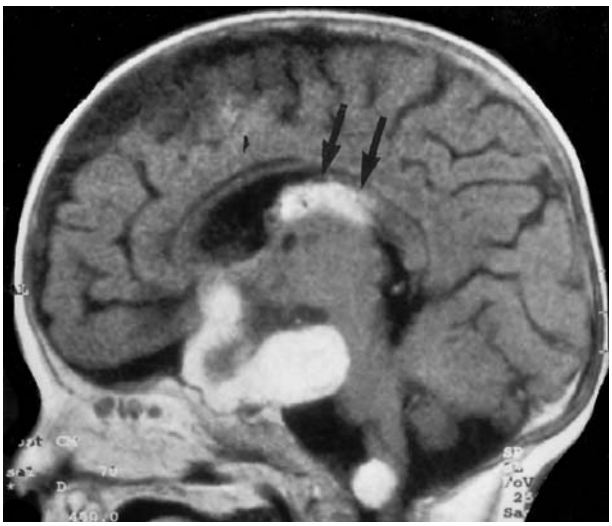

d

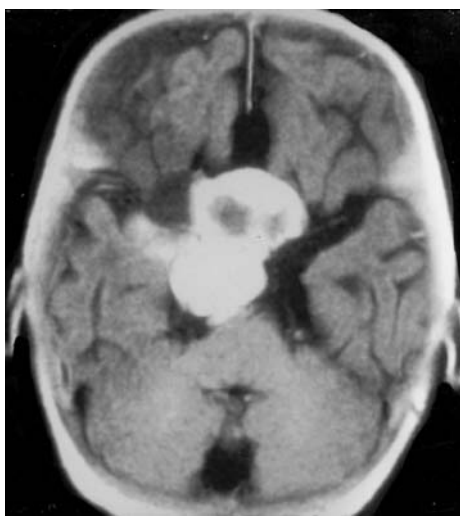

b

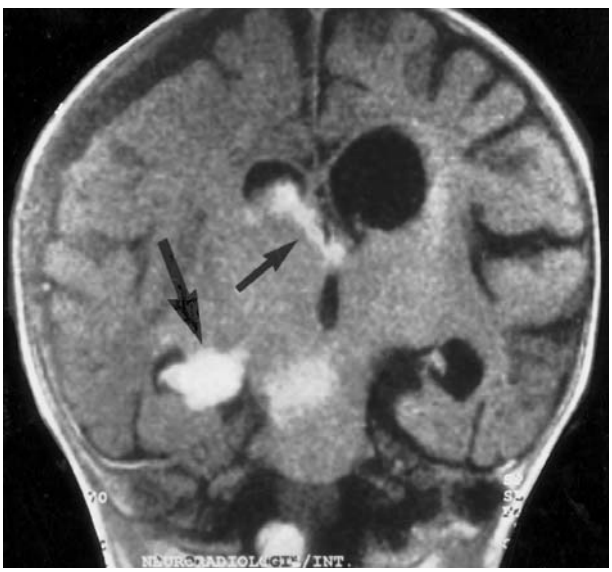

e

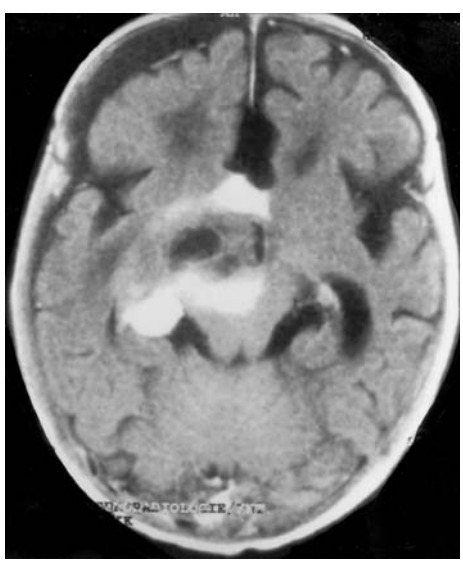

c

Fig. 7.6a–e. A 3-month-old girl with bilateral nystagmus and papilledema of the left eye. Diagnosis: juvenile pilocytic astrocytoma (WHO I–II) of the chiasm. CT: **a** Axial contrast-enhanced image, showing an extensive tumor with central necrosis in the suprasellar cistern. MRI: **b** Corresponding T1-weighted, contrast-enhanced view. **c** Axial, T1-weighted, contrast-enhanced view at the level of the cerebral peduncles with visualization of mixed intra- and extraparenchymal tumor, extending from the inferior third ventricle with infiltration of the right mesial temporal lobe and the ipsilateral cerebral peduncle. **d** Right paramedian, sagittal, T1-weighted, contrast-enhanced plane demonstrating the presence of hypothalamic infiltration, infiltration of the optic tract and fibers of the fornix (*arrows*), in addition to intracranial, CSF-induced metastasis at the craniocervical junction. **e** Coronal, T1-weighted, contrast-enhanced view with more distinct demonstration of infiltration of the optic tract (*large arrow*) extending towards the right lateral geniculate nucleus, as well as infiltration of the right fornix (*small arrow*) and the metastatic tumor at the right craniocervical junction

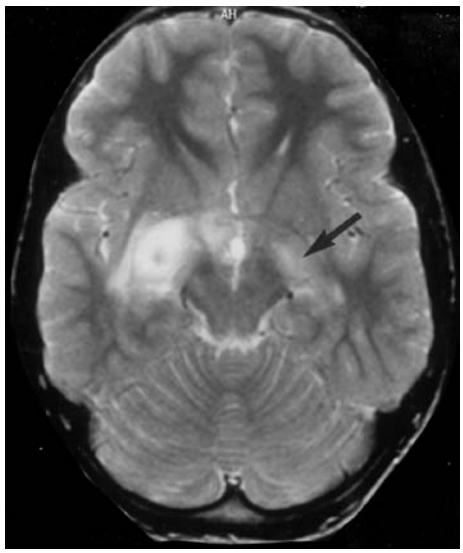

a

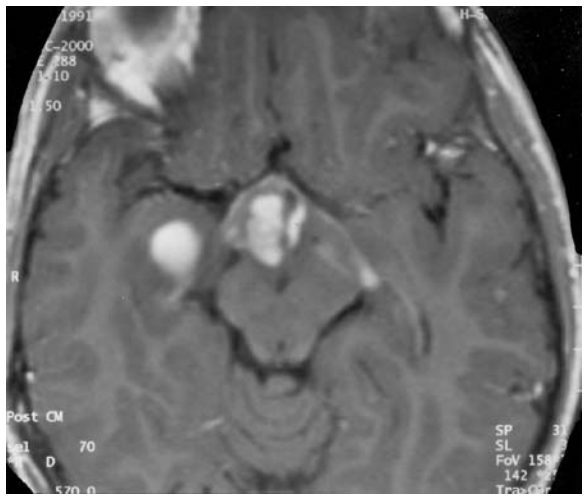

b

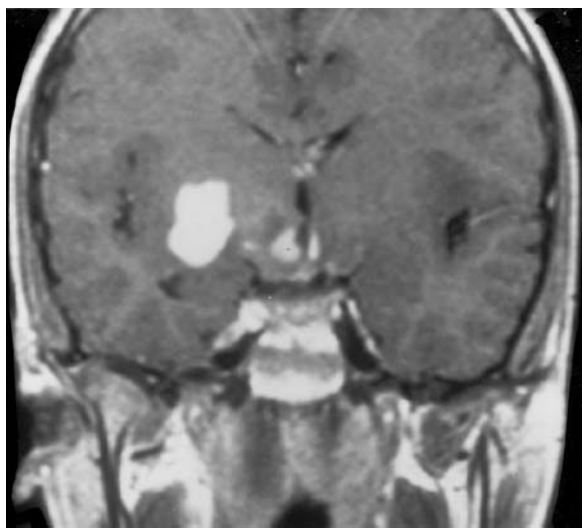

c

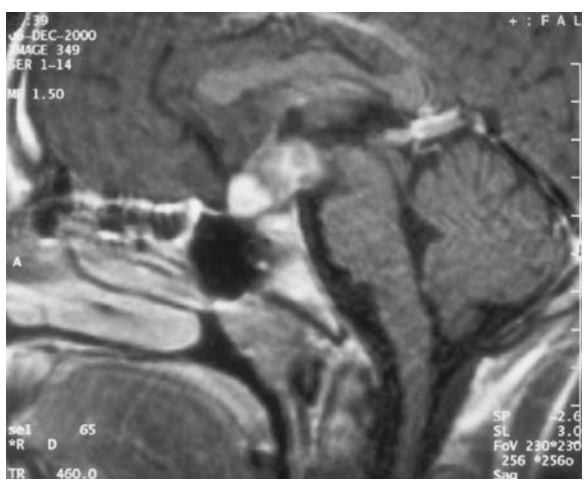

d

Fig. 7.7a–d. A 9-year-old boy with pubertas praecox. A bilateral optic nerve atrophy and visual deficit (right: 0.4, left: 0.6) were unknown, but found during ophthalmological examination. Diagnosis: optic glioma with hypothalamic involvement. MRI: **a** Axial T2-weighted view with right hypothalamic (posterior of the anterior commissure) and temporomesial tumor infiltration. Note the slight signal enhancement of the left optic tract (*arrow*), indicating an additional contralateral involvement. **b** Corresponding T1-weighted, contrast-enhanced view with BBB disruption of all tumor regions. **c** Coronal, T1-weighted, contrast-enhanced view, best demonstrating the basal ganglia and hypothalamic tumor spread with preference to the right side. **d** Midsagittal, T1-weighted, contrast-enhanced image without any delineation of the chiasm

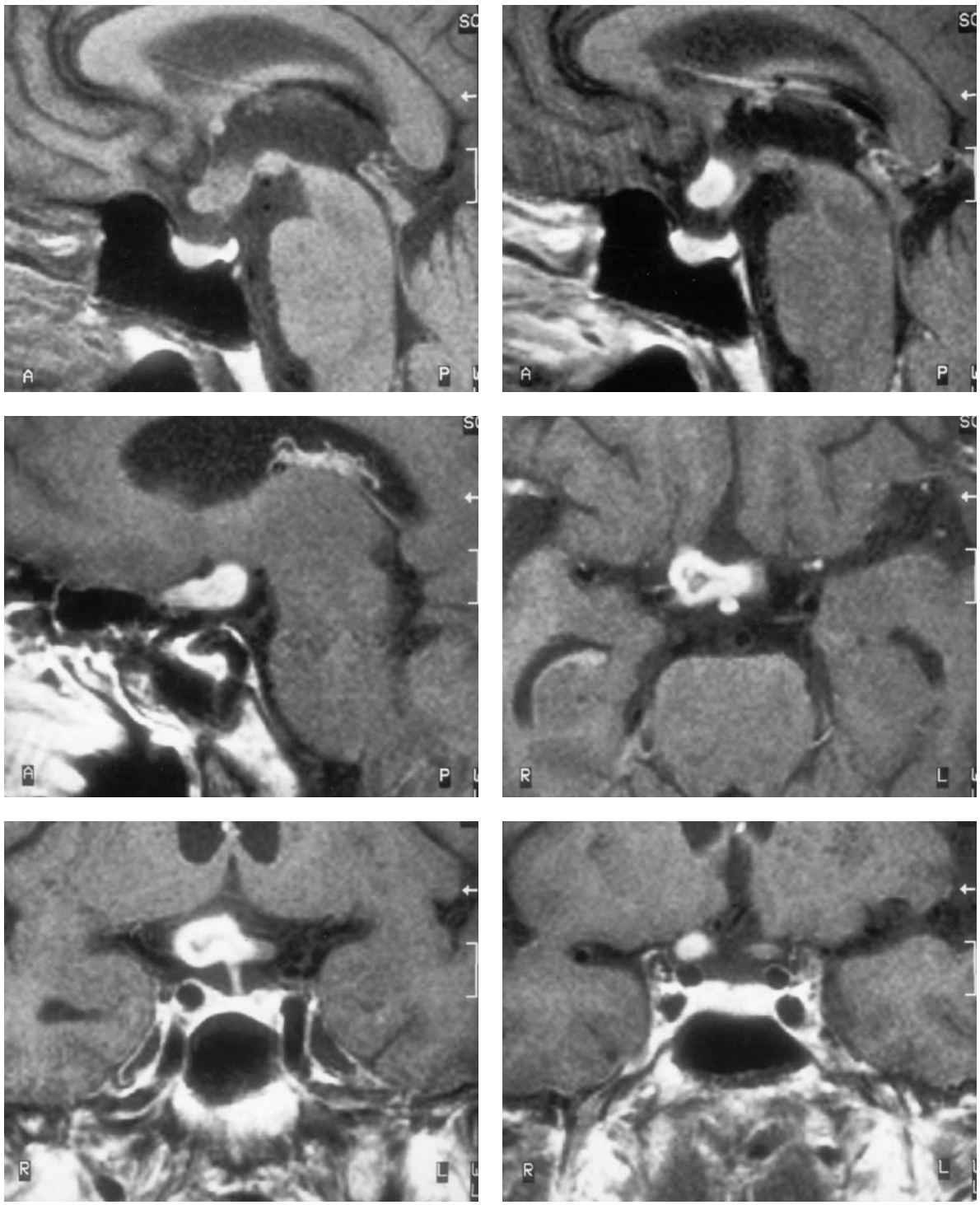

Fig. 7.8a–f. A 70-year-old woman with a visual deficit progressing to complete loss of vision in the right eye within 2 weeks, and subsequent loss of vision (0.1) in the left eye. Diagnosis: glioblastoma of the chiasm, intracranial optic nerve, and proximal optic tract. MRI: **a** Midsagittal T1-weighted native image with diffuse enlargement of the chiasm and hypothalamus. **b** Corresponding T1-weighted, contrast-enhanced image with brighter signal enhancement of the enlarged chiasm than of the pituitary stalk. **c** Right paramedian sagittal, T1-weighted, contrast-enhanced image showing tumor expansion along the proximal optic tract. **d** Axial, T1-weighted, contrast-enhanced view, demonstrating lateralization of the tumor growth to the right, as well as some necrosis at the center of the tumor. **e** Coronal, T1-weighted, contrast-enhanced image visualizing exclusive infiltration of the chiasm. **f** Coronal, T1-weighted, contrast-enhanced view, several millimeters anterior to **e** with tumor infiltration of the intracranial right optic nerve

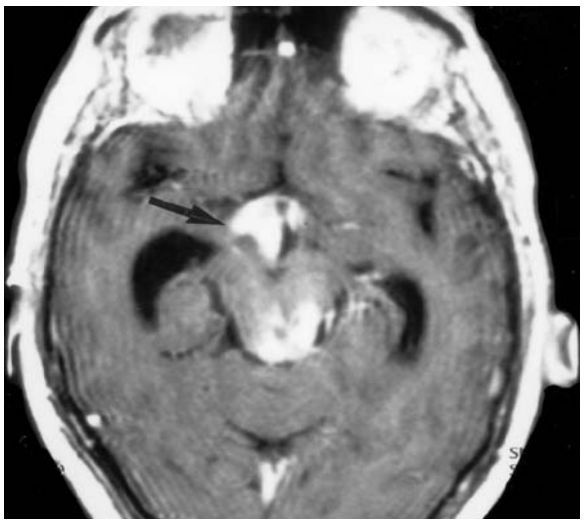

a

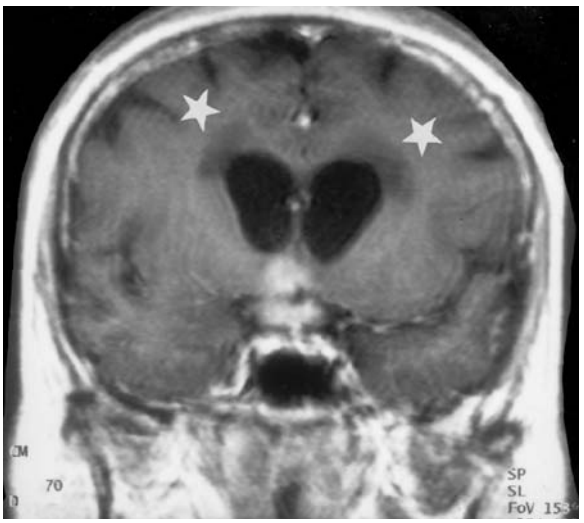

b

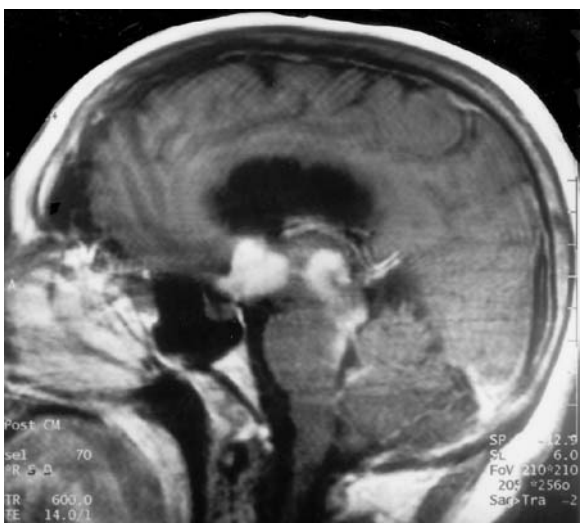

c

Fig. 7.9a–c. A 54-year-old woman with recurrent, exacerbating headache, N VI-paresis, and acute visual deficit in the right eye. Diagnosis: astrocytoma (WHO III). T1-weighted, contrast-enhanced MRI: **a** Axial image showing multilobulated, contrast-enhancing lesions at the chiasm (slightly asymmetric to the right), hypothalamus, and proximal part of the right optic tract (*arrow*), as well as at the quadrigeminal plate, with greater accentuation to the left side. Note widening of the temporal horns of the lateral ventricles as a sign of increased intracranial pressure exerted by an occlusive hydrocephalus, due to midbrain invasion with consecutive stenosis of the aqueduct. **b** Coronal view demonstrating invasion of both the chiasm and the right thalamus. Note periventricular signal diminution by transependymal CSF leakage (*white stars*) associated with the identified occlusive hydrocephalus. **c** Right paramedian sagittal image, showing complete tumor invasion of the chiasm, hypothalamus, rostral and posterior nuclei of the thalamus, the quadrigeminal plate, and the aqueduct, extending to the floor (rhombencephalon) and the roof of the fourth ventricle

(Walsh 1985). Visual impairment is dependent on the size and location of the mass, thus a significantly higher percentage of visual loss is seen in children with involvement of the postchiasmal visual pathway (Balcer et al. 2001).

Imaging should discriminate from non-neoplastic tumor-like lesions as in the patient with recurrent retro-bulbar neuritis (RBN) of unknown origin, that present with additional involvement and thickening of the chiasm (Fig. 7.10). If the chiasmal lesion demonstrates signs of malignancy like a necrotic area (Fig. 7.8), spread into the nearby brain parenchyma, or meningeal implants (Fig. 7.9) (Shapiro et al. 1982), the diagnosis of malignant glioma of the chiasm is likely.

7.2.1.2 Pituitary Lesions

7.2.1.2.1 Pituitary Adenoma

Although pituitary adenomas represent 10%–15% of all intracranial tumors (Kovacs et al. 1985; Okazaki 1989), the systematic of tumors of the "nervous system" (Kleihues and Cavanee 2000) consistently lacks the definition of pituitary adenomas, which most frequently manifest in adults. These benign, slowly growing, and dislocating tumors composed of cells of the adenohypophysis normally have a pseudocapsule, which enables good

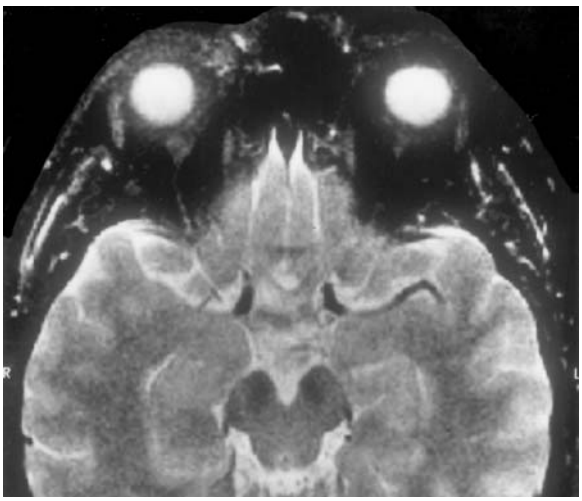

a

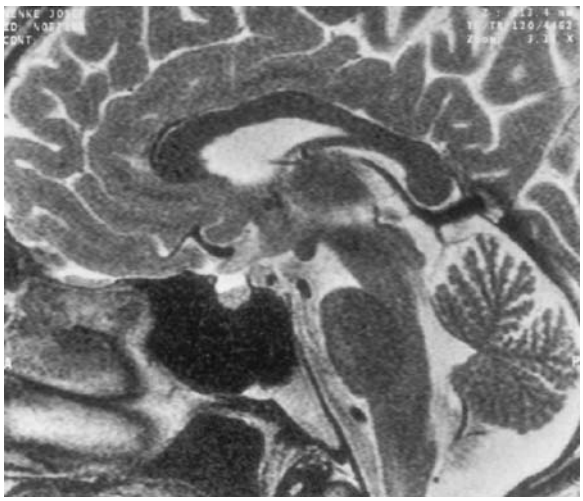

b

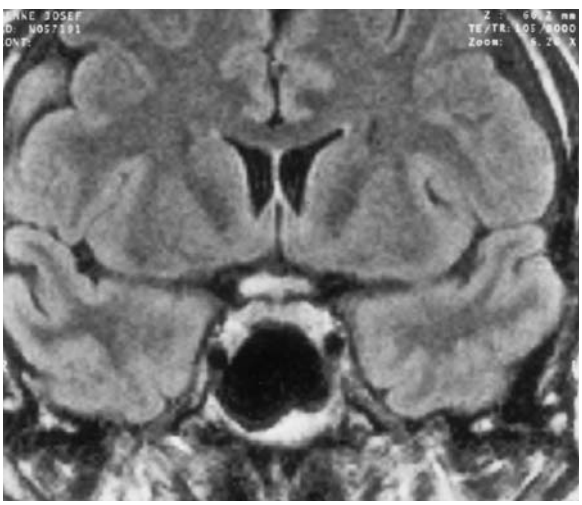

c

Fig. 7.10a–c. A 44-year-old man presenting with recurrent, alternating signs of bilateral retro-bulbar neuritis (RBN) with visual field defects and retardation on VEP without an afference defect; no pathologic findings on CSF and humoral immunology. Diagnosis: chiasmal edema of unknown origin. T2-weighted MRI: axial (**a**), sagittal (**b**), and coronal (**c**) (FLAIR) views demonstrating a thickening and high signal intensity of the entire chiasm with preference to the right. No systemic disorder could be found, but cortisone therapy diminished the subjective symptoms

demarcation from the neighboring structures. They frequently present as degenerative cysts with small necrotic areas and hemorrhages, sometimes leading to acute degeneration, i.e., adenoma apoplecticum (Figs. 7.11–7.13). This entity occurs as a result of sudden infarction or hemorrhage in the course of tumor growth. However, the clinical symptomatology of insufficiency of the adenohypophysis, presenting with headache, nausea, and vomiting, is not as frequent as presumed (Bonneville et al. 1986; Zülch 1986; Kucharczyk et al. 1996). In medical clinical symptomatology, pituitary adenomas present predominantly in the form of endocrinological disorders, depending on the activity of the pathological cells, which is why endocrinological active pituitary adenomas are most frequently found in the group of microadenomas (diameter <10 mm). Conversely, hormone-inactive tumors (belonging to our subject) fulfill the criteria of macroadenomas (diameter >10 mm) as they present with the characteristic clinical symptom of bitemporal visual field deficit, due to inferior compression of the

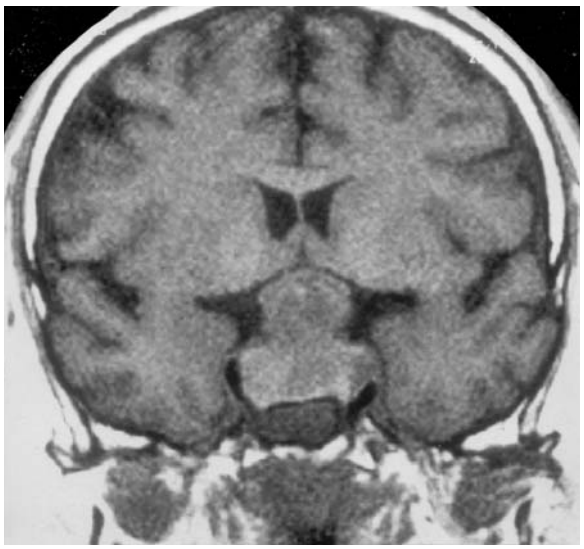

a

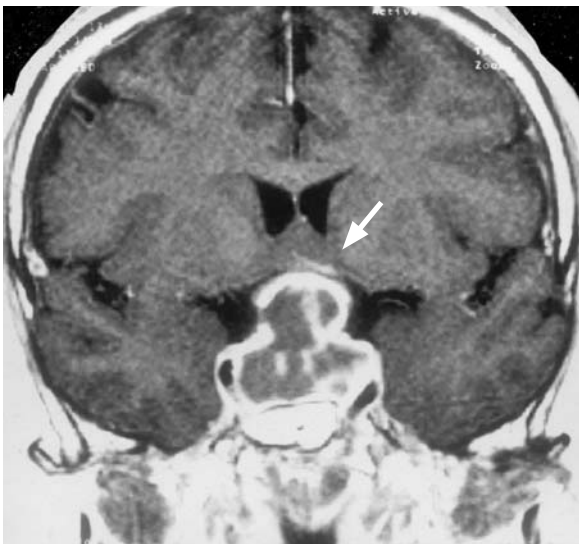

b

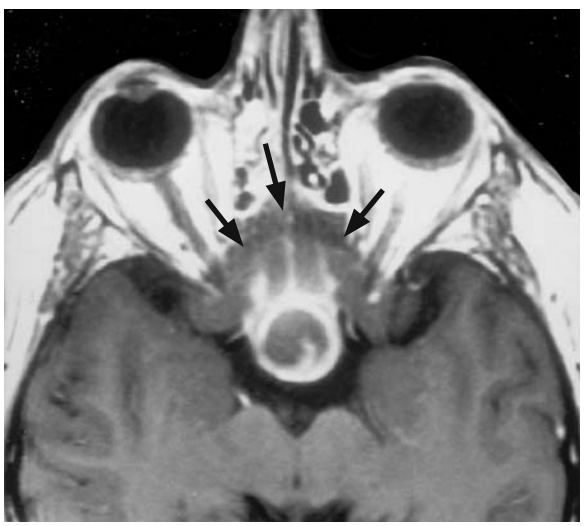

c

Fig. 7.11a–c. A 47-year-old man who presented in pituitary coma. After substitution, he complained of headache and variable visual deficits. Hemianopia to the left, visual deficit (right: 0.6, left: 0.2) was found, together with an inflammatory clinical constellation with fever and meningism. Diagnosis: abscess-forming pituitary adenoma with adjacent bacterial leptomeningitis. T1-weighted MRI: **a** Coronal native view with intra- and suprasellar lesion and inferior chiasmal compression. Note the slightly hypointense signal in the sphenoid sinus. **b** Corresponding contrast-enhanced view with inhomogeneous contrast enhancement of the intra-/suprasellar, apparently encapsulated lesion, but homogeneous enhancement in the sphenoid sinus. CORR = Sponding to sinus inflammation, note the small leptomeningeal enhancement at the base of the left frontal lobe (*arrow*). **c** Axial contrast-enhanced view with necrotizing, encapsulated tumor and leptomeningeal enhancement of the basal frontal sulci (*arrows*)

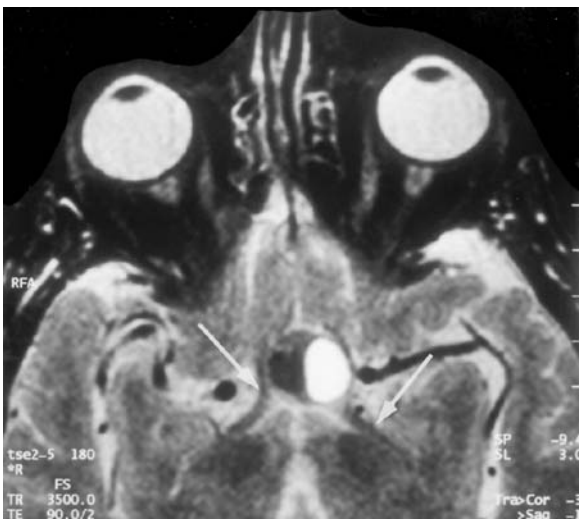

a

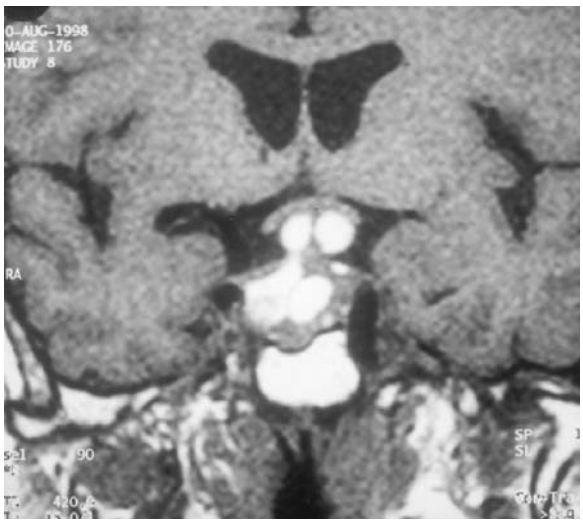

b

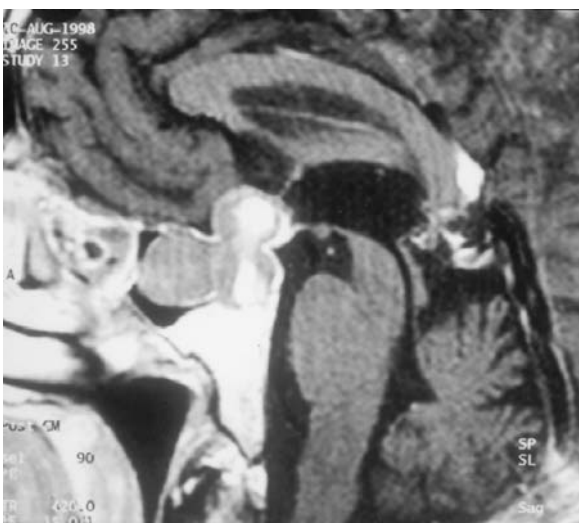

c

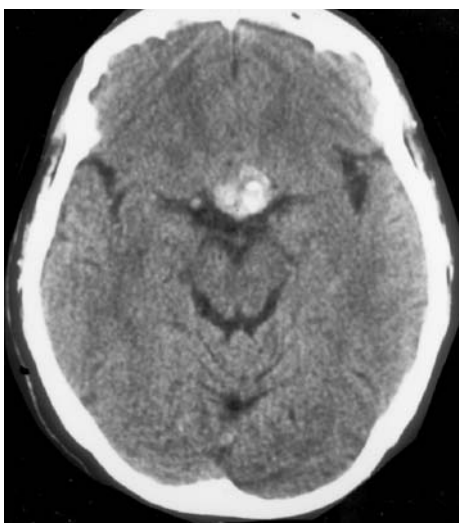

d

Fig. 7.12a–d. A 62-year-old man with slowly progressing visual deficit of the left eye persisting for 2 years. Diagnosis: pituitary adenoma with small colloidal cysts (proven by histology), not clearly differentiated from older hemorrhage (methemoglobin). MRI: **a** Axial T2-weighted view identifying different signals with high (*left*) and apparently low signal intensity (*right*) of the tumor of the suprasellar region, spreading to the proximal optic tracts (*white arrows*). **b** Coronal T1-weighted native image in which both intrasellar and suprasellar expansion with inferior impression of the chiasm is demonstrated. **c** Midsagittal, T1-weighted, contrast-enhanced view identifying slight signal enhancement of the solid tumor parts invading the sphenoid sinus. Note the hyperintense lesion superior to the posterior knee of the corpus callosum, representing a small lipoma. After 5 days, the patient developed acute, nearly complete loss of vision on the left side as well as severe, ipsilateral N VI paresis, together with an adynamic state: **d** axial native emergency CT shows acute hemorrhage into the pituitary adenoma, expanding superiorly, necessitating immediate decompression of the chiasm

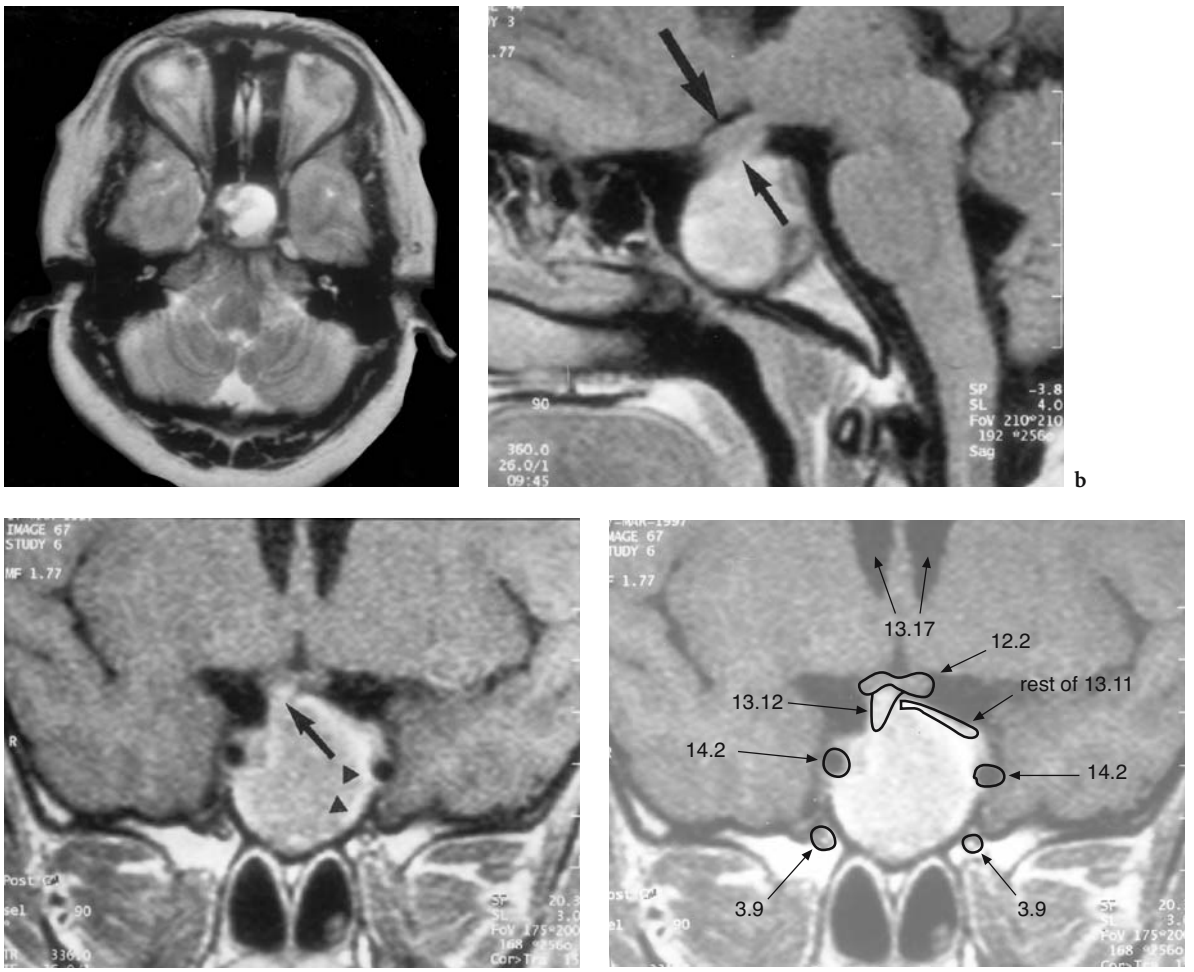

Fig. 7.13a–d. A 21-year-old man with hypogonadism and hypophyseal-hypothalamic insufficiency in the absence of ophthalmologic deficits. Diagnosis: prolactinoma with acute hemorrhage. MRI: **a** Axial T2-weighted view with irregular hyperintensity (methemoglobin) in the sphenoid sinus and enlarged sella. **b** Right paramedian, sagittal, T1-weighted native view demonstrating suprasellar tumor expansion, compression of the slightly hyperintense pituitary stalk (*small arrow*), and tumor extension to the right prechiasmal optic nerve (*large arrow*). **c** Coronal, T1-weighted, contrast-enhanced view with dislocation of the enhanced pituitary stalk (*arrow*) to the right. Note the thin layer on the left side of the tumor, representing the remaining pituitary gland (*arrowheads*). **d** Corresponding diagram: 3.9 = round foramen, 12.2 = chiasm, 13.11 = pituitary gland, 13.12 = pituitary stalk13.17 = ventricles, 14.2 = ICA

chiasm (Fig. 7.14) (Kucharczyk et al. 1996; Majos et al. 1998), but sometimes even only with unspecific visual deficits (Fig. 7.15).

Imaging Characteristics. MRI as the method of choice generally shows a lengthening of both T1 and T2 relaxation times. In macroadenomas, MRI enables a high anatomic resolution and definition of the neighboring tissue, i.e., intracranial optic nerves, chiasm, and cavernous sinus. In most cases, native, non-contrast-enhanced images allow accurate and conclusive differentiation of the tumor and deformed, compressed, flattened visual structures of the optic nerves, chiasm, and/or optic tracts (Figs. 7.11, 7.12, 7.15–7.19). Due to the lack of a solid barrier between the pituitary gland and the cavernous sinus in the presence of only a loose circumferential fibrous bed (Dietemann et al. 1998), even a careful analysis of the pre- and post-contrast images does not routinely enable the definite prediction of tumor invasion of the cavernous sinus. Only a carotid artery encasement or an extension lateral of the cavernous sinus towards the temporal lobe is a reliable indicator of cavernous sinus invasion (Scotti et al. 1988; Kucharczyk et al. 1996). In pre-contrast images, most adenomas show a homogeneous, isointense signal and a similarly

(Text continues on p. 360)

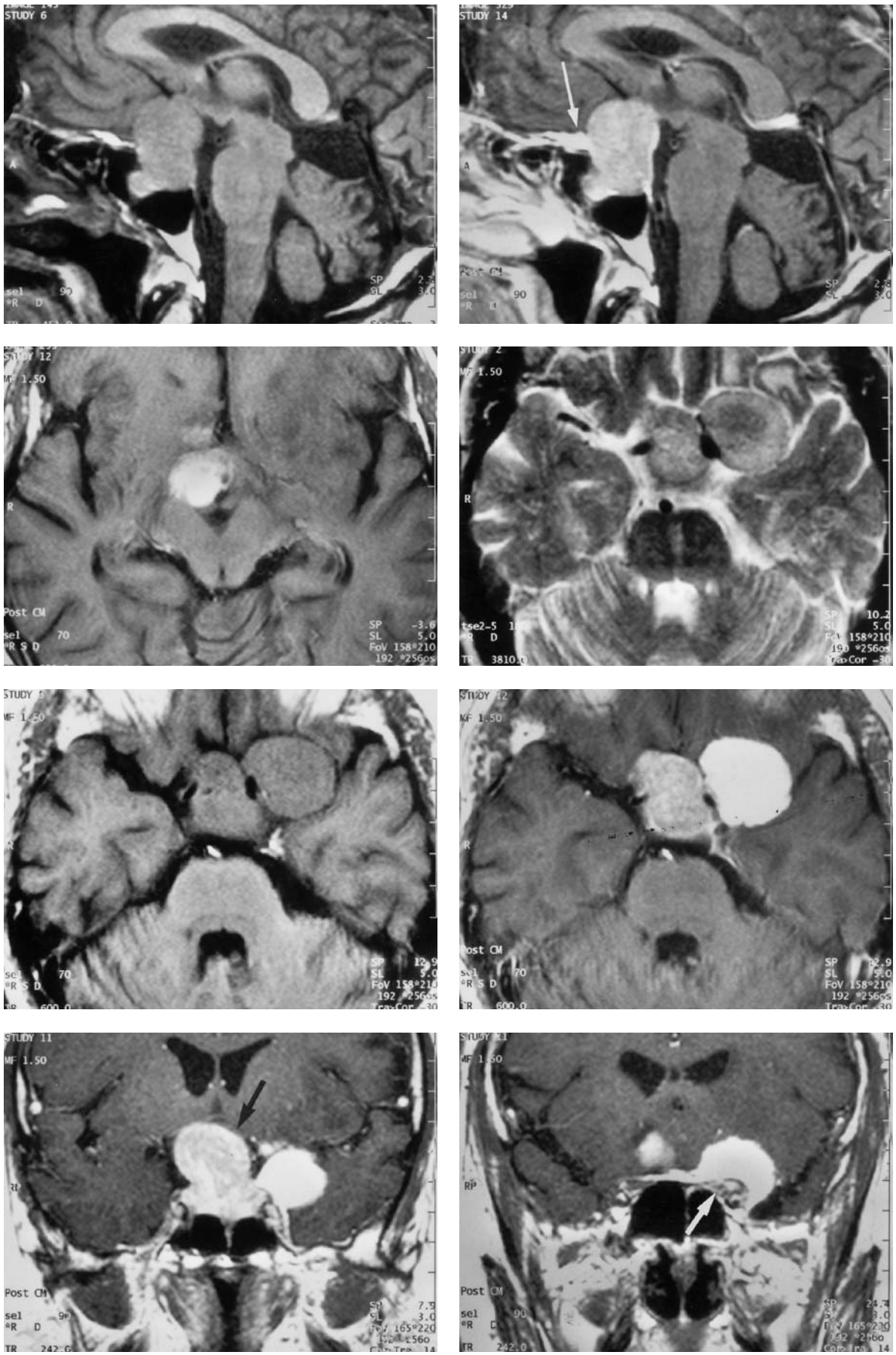
STUDY 6
STUDY 14
STUDY 12
Post CM
STUDY 11
a
b
c
d
e
f
g
h

◁ **Fig. 7.14a–h.** A 73-year-old man with slowly progressing consecutive bilateral loss of vision of 95%. Diagnosis: (1) pituitary adenoma, (2) left sphenoid wing meningioma. MRI: **a** Left paramedian, sagittal, T1-weighted native view showing a large intra- and suprasellar tumor with extension into the sphenoid sinus. Superior and posterior dislocation and depression of the chiasm. **b** Corresponding contrast-enhanced image with dural enhancement of the sphenoid plane region (*white arrow*). **c** Axial, T1-weighted, contrast-enhanced image demonstrating the superior extension of the tumor behind and between the right chiasm and the proximal optic tract. **d** Axial T2-weighted view at the level of the basal cistern where another tumor with intermediate signal is seen lateral to the left distal, slightly compressed ICA. Corresponding T1-weighted native (**e**) and contrast-enhanced (**f**) images exhibiting different signal intensities in the post-contrast images only; the intense and homogeneous enhancement of the left tumor leads to the diagnosis of meningioma. **g** Coronal, T1-weighted, contrast-enhanced view identifying, in addition to the indentation of the pituitary adenoma caused by the remainder of the sellar diaphragm, dislocation of the chiasm by the pituitary adenoma to the left side (*arrow*), as well as substantial lateral expansion of the meningioma. **h** Coronal, T1-weighted, contrast-enhanced view at the level of the optic canal with superior visualization of the meningioma with a characteristic dural tail in the sphenoid plane and thickening of the anterior clinoid process (as starting point of the meningioma). Note compression of the canalicular optic nerve (*white arrow*) caused by tumor infiltration of the optic canal

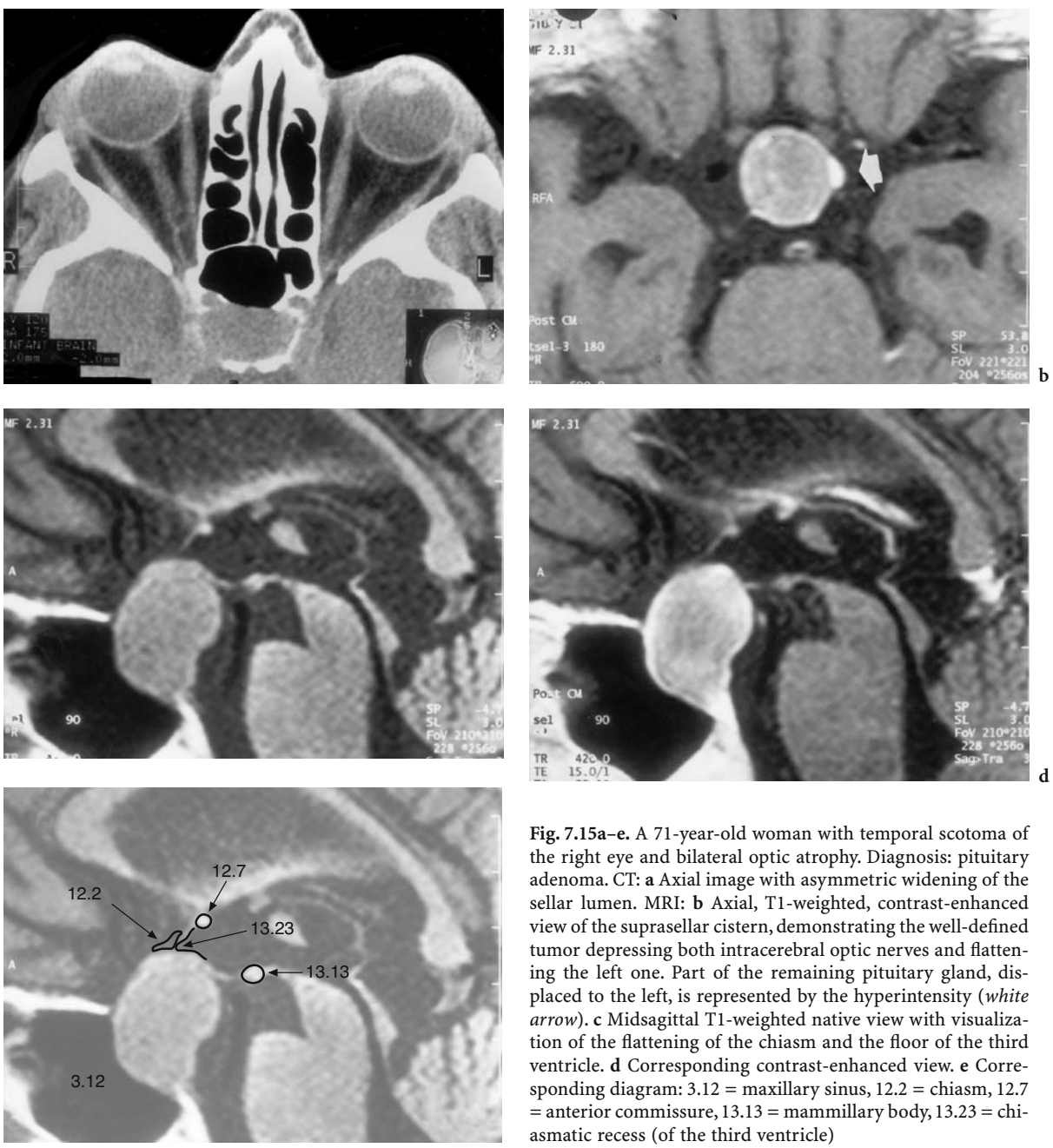

Fig. 7.15a–e. A 71-year-old woman with temporal scotoma of the right eye and bilateral optic atrophy. Diagnosis: pituitary adenoma. CT: **a** Axial image with asymmetric widening of the sellar lumen. MRI: **b** Axial, T1-weighted, contrast-enhanced view of the suprasellar cistern, demonstrating the well-defined tumor depressing both intracerebral optic nerves and flattening the left one. Part of the remaining pituitary gland, displaced to the left, is represented by the hyperintensity (*white arrow*). **c** Midsagittal T1-weighted native view with visualization of the flattening of the chiasm and the floor of the third ventricle. **d** Corresponding contrast-enhanced view. **e** Corresponding diagram: 3.12 = maxillary sinus, 12.2 = chiasm, 12.7 = anterior commissure, 13.13 = mammillary body, 13.23 = chiasmatic recess (of the third ventricle)

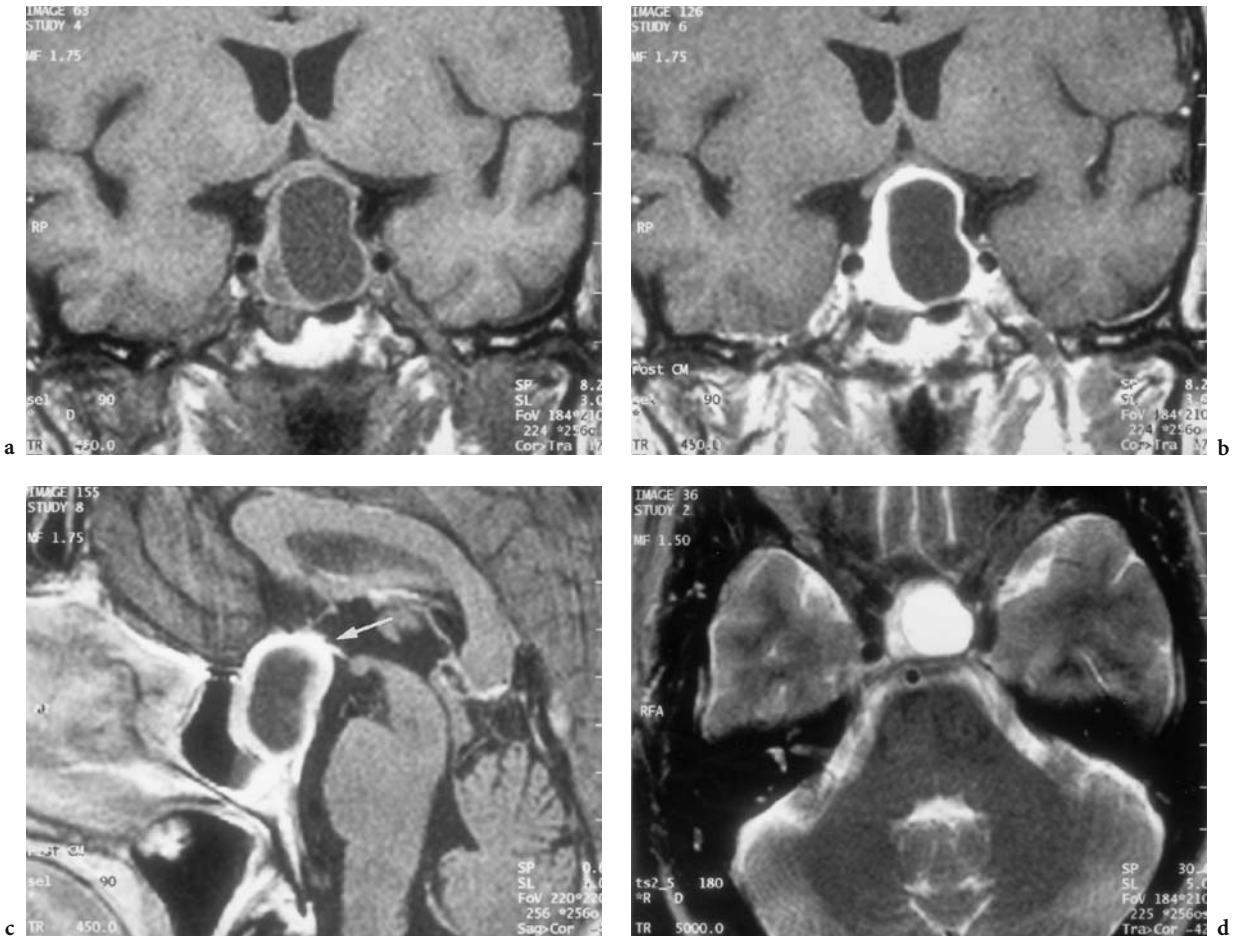

Fig. 7.16a–d. A 64-year-old woman with a bitemporal visual defect detected on ophthalmologic control examination. Diagnosis: cystic, degenerated, nonhormogenic pituitary adenoma. MRI: **a** Coronal T1-weighted native view, showing a predominantly hypointense tumor of the pituitary gland, associated with widening of the sellar lumen, and extension primarily into the suprasellar region, leading to caudal, left accentuated elevation and inferior compression of the chiasm. In addition, the remaining region of the pituitary gland, visualized in the right area of the image, appears hypointense. **b** Corresponding contrast-enhanced image demarcating the cystic tumor from the remaining pituitary gland. **c** Midsagittal T1-weighted image with posterior dislocation of the chiasm. The pituitary stalk is not identified, although the pointed infundibular recess of the third ventricle (*white arrow*) is seen in the posterior region of the cystic tumor. **d** Axial T2-weighted image confirming the fluid character of the cyst

Fig. 7.17a–c. A 55-year-old man with acute loss of vision and incomplete N III and N VI paresis of the left eye. Diagnosis: ▷ pituitary adenoma. T1-weighted MRI: **a** Coronal native view demonstrating depression of the medial chiasm by the abnormally horizontally oriented pituitary stalk (identified by central, target-like hypointensity, corresponding to the recess of the pituitary stalk of the third ventricle (*arrow*)). **b** Corresponding contrast-enhanced image, showing enhancement of the pituitary stalk. Note the uncommon configuration of the adenoma, spreading to both cavernous ICA in the previously infradiaphragmal area, while only a small indentation of the sellar diaphragm enables suprasellar expansion of the tumor. **c** Midsagittal contrast-enhanced view, visualizing both the predominantly prechiasmal expansion with inferior compression by the remaining caudally dislocated and depressed pituitary gland (*arrowheads*) and the approximately normal configuration of the third ventricle. Note the presence of substantial intrasellar tumor extension with erosion of the clivus

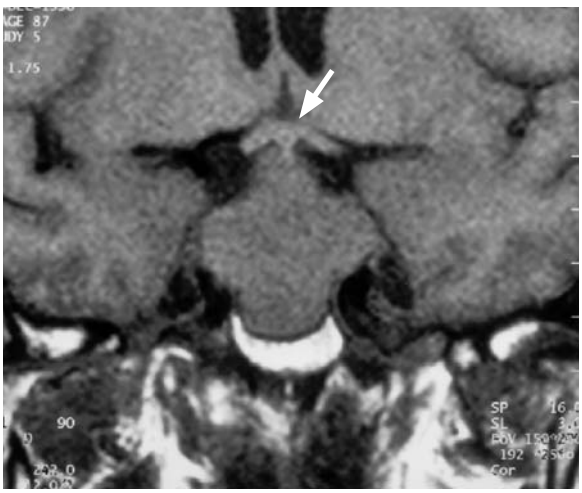

a

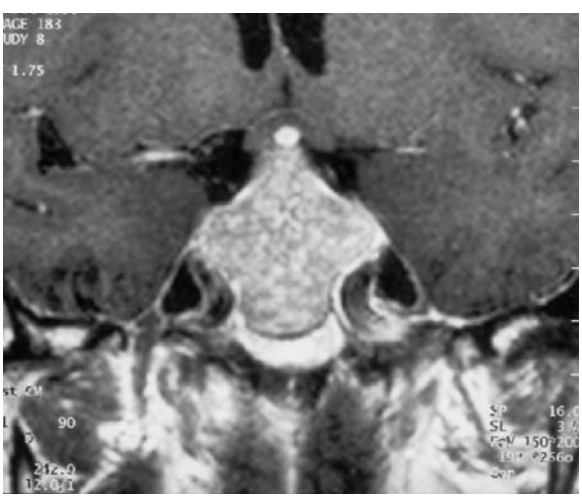

b

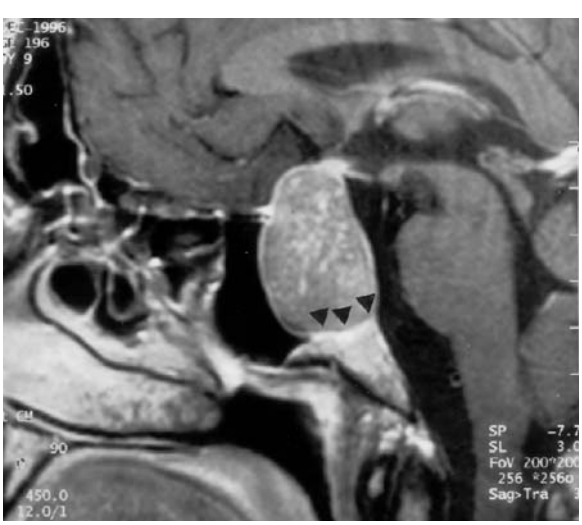

c

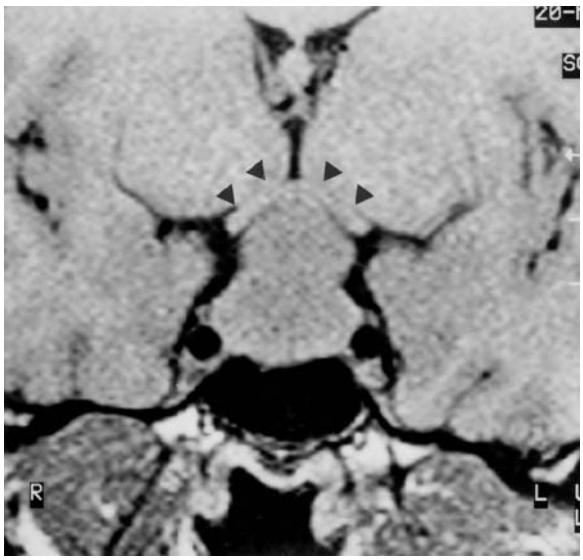

a

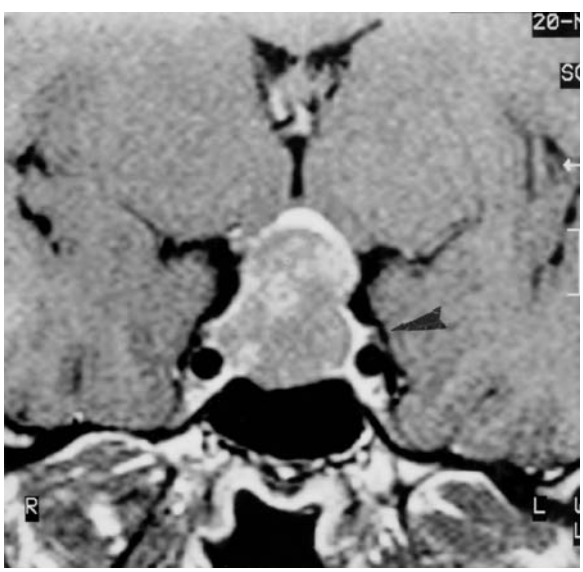

b

Fig. 7.18a,b. A 25-year-old woman with progressive visual deficit. Diagnosis: macroadenoma of the pituitary gland. T1-weighted MRI: **a** Coronal native view with distinct differentiation of the structure of the superiorly depressed chiasm (*arrowheads*) from the impressing macroadenoma. The indentation of the tumor is due to the remnant of the sellar diaphragm. **b** Corresponding, contrast-enhanced image demonstrating inhomogeneous enhancement of the tumor; the crescent-shaped signal enhancement corresponds to the cranially displaced and impressed remnant of the pituitary gland with normal enhancement. While the chiasm is less clearly differentiated than in **a**, the cranial nerves are visualized in the cavernous sinus (*arrowhead pointing N III*). (From Müller-Forell and Lieb 1995)

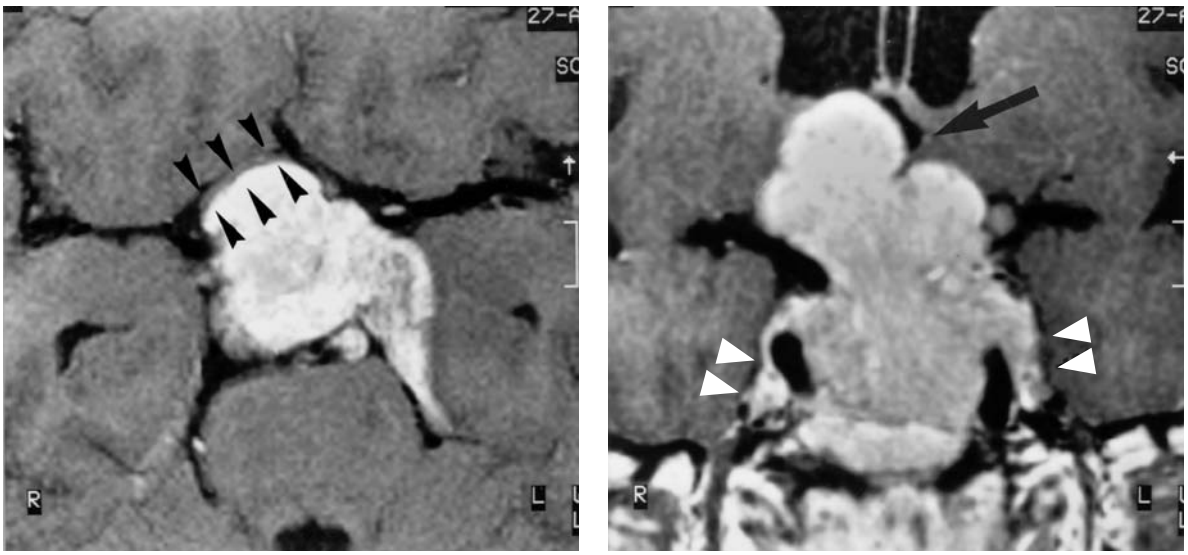

a b

Fig. 7.19a,b. A 39-year-old man with slowly progressing visual deficit. Diagnosis: macroadenoma of the pituitary gland. T1-weighted, contrast-enhanced MRI: **a** Axial view with anterior dislocation of the optic chiasm (*arrowheads*) and to the right, attenuated and extended by the tumor. **b** Coronal view demonstrating the entire craniocaudal extension with depression and dislocation of the floor of the third ventricle (*arrow*). The cavernous sinus is infiltrated by the tumor with preference to the left; the small, spheroid hypodensities correspond to cranial nerves V1, V2 (*arrowheads*) and VI medially. (From Müller-Forell and Lieb 1995)

homogeneous signal enhancement after contrast (Figs. 7.15, 7.18, 7.20). This applies in particular to medium-sized adenomas, while signal homogeneity in macroadenoma alters in relation to the number of regressive changes. These include cysts (Fig. 7.21), hemorrhages (Figs. 7.12, 7.13), and calcification, requiring not only T1-weighted but also T2-weighted and T2*weighted sequences. The differential diagnosis from other suprasellar lesions as, e.g., craniopharyngioma or cysts of Rathke's pouch may be difficult in purely cystic macroadenoma. Therapy with bromocriptine in prolactinoma is known to cause intratumoral hemorrhages that are frequently not identified clinically. In contrast to intracavernous meningiomas, the invasion of the cavernous sinus by macroadenomas normally does not lead to narrowing of the ICA, equivalent to a relatively slight impairment of cranial nerves III–VI. Sagittal images provide a superior demonstration of a subfrontal, retrosellar, or hypothalamic extension and/or compression of the third ventricle. The so-called invasive adenoma is a biologically benign, but aggressively growing lesion, capable of destroying the skull base with invasion of the bony sphenoid sinus and infiltration of the cavernous sinus. Primary sellar destruction caused by the very rare pituitary carcinoma may additionally lead to intracranial or intraspinal CSF metastasis (Sartor 1992; Engelbach et al. 1999).

The differential diagnosis of pituitary adenoma includes meningioma of the sellar region (see chapter 7.2.1.3), craniopharyngioma (see chapter 7.2.1.4), optic gliomas (see chapter 7.2.1.1), germ cell tumors (see chapter 7.2.1.7.1), terato-tumors, chordomas (see chapter 7.2.1.7.4), and even metastasis (Fig. 7.1).

7.2.1.2.2 Inflammatory Lesions, e.g., Pituitary Abscess

Infections of the pituitary gland are highly uncommon and usually become clinically manifest once an abscess has formed (Kucharczyk et al. 1996). The rare entity of pituitary abscesses, mostly caused by gram-positive cocci, is known to occur in the presence of other sellar masses or by contiguous spread from an infected sphenoid or cavernous sinus (Daningue and Wilson 1977; Kucharczyk et al. 1996). The clinical presentation with headache and visual loss is similar to that of other large intrasellar masses; septic fever is reported to be uncommon (Kucharczyk et al. 1996). The diagnosis should be based on the imaging presentation following i.v. contrast administration, showing rim enhancement around a hypointense center, representing the necrosis of the intrasellar tumor, and additional inflammatory infiltration of neighboring sinus and intracranial structures (Fig. 7.11).

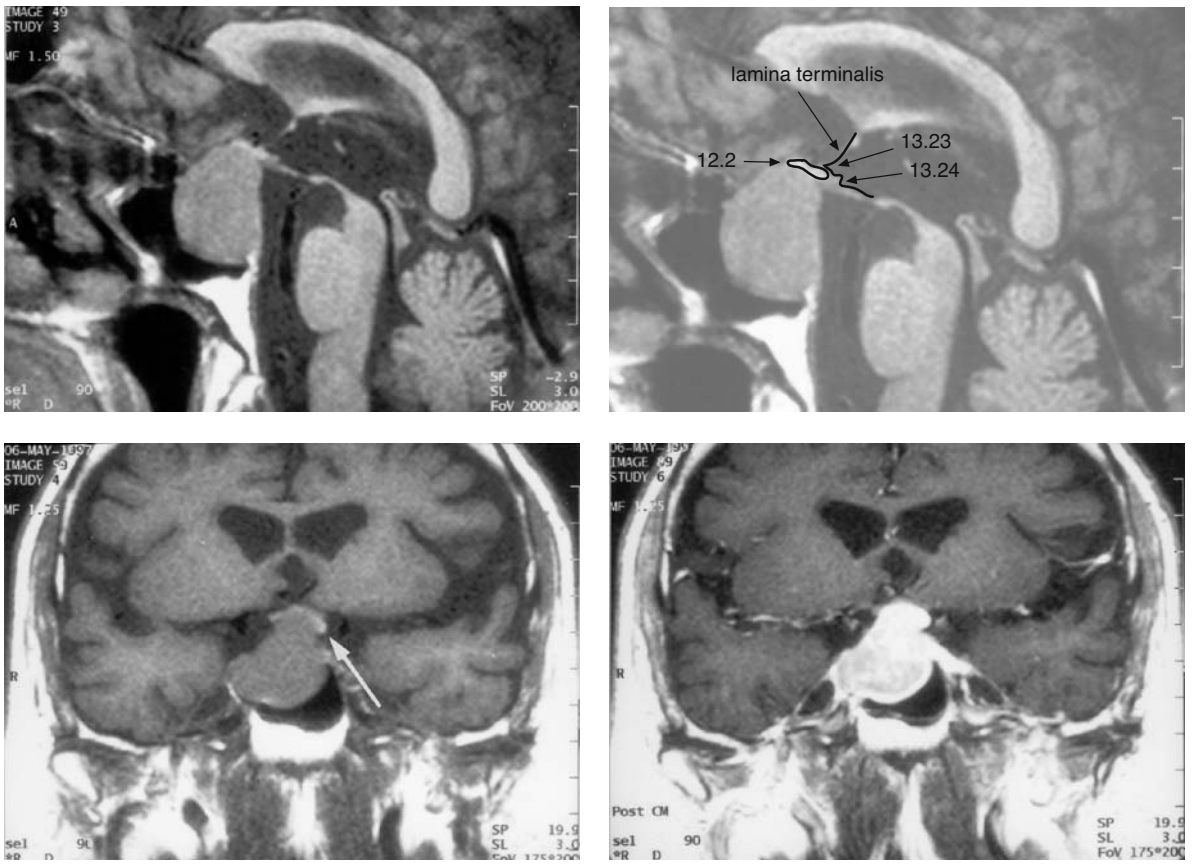

Fig. 7.20a–d. A 77-year-old man with acute bitemporal hemianopia. Diagnosis: hormone-inactive pituitary adenoma. MRI: **a** Midsagittal T1-weighted native image with large intra- and suprasellar tumor, displacing and depressing the chiasm from inferior and with asymmetric widening of the sellar floor. **b** Corresponding diagram: 12.2 = chiasm, 13.23 = chiasmatic recess (of the third ventricle), 13.24 = recess of the pituitary stalk (of the third ventricle). **c** Coronal T1-weighted native view, demonstrating the slightly asymmetric depression of the chiasm from inferior right. Note the slightly hyperintense signal of the remaining pituitary gland (*white arrow*) at the upper left between the tumor and the chiasm, seen as a slight structure with intermediate signal. **d** Corresponding contrast-enhanced view, the remaining pituitary gland showing normal (higher than the tumor) enhancement. Note the lace on the left, due to remaining sellar diaphragm

7.2.1.2.3
Pituitary Stalk Lesions (Langerhans Cell Histiocytosis)

As already considered in chapter 6.3.1.4.3, Langerhans cell histiocytosis (LCH) may occur as a multifocal systemic or single system disease (Howarth et al. 1999). In 25% of the patients with LCH, the classical clinical triad of Hand-Schüller-Christian syndrome develops, presenting with diabetes insipidus, exophthalmos, and bone lesions (Kucharczyk et al. 1996). As CNS involvement is not uncommon as a part of the systemic process, it is mainly seen in children and characterized by a proliferation of histiocytes (Kepes and Kepes 1969; Tien et al. 1990). The pituitary stalk, as the main target of CNS involvement demonstrates a thickening, with or without an associated hypothalamic mass, that show an intense contrast enhancement after intravenous administration of gadolinium (Fig. 7.22) (Rosenfield et al. 1990; Tien et al. 1990; Maghnie et al. 1992). The differential diagnosis should include germinoma, neurosarcoidosis, tuberculosis, infiltration of adjacent mass lesions such as craniopharyngioma, and metastasis (Tien et al. 1990).

7.2.1.2.4
Skull Base Disorders

Pathologic processes of the skull base like mucoceles or the even rare case of a cholesterol granuloma of the sphenoid sinus should be differentiated from

(Text continues on p. 364)

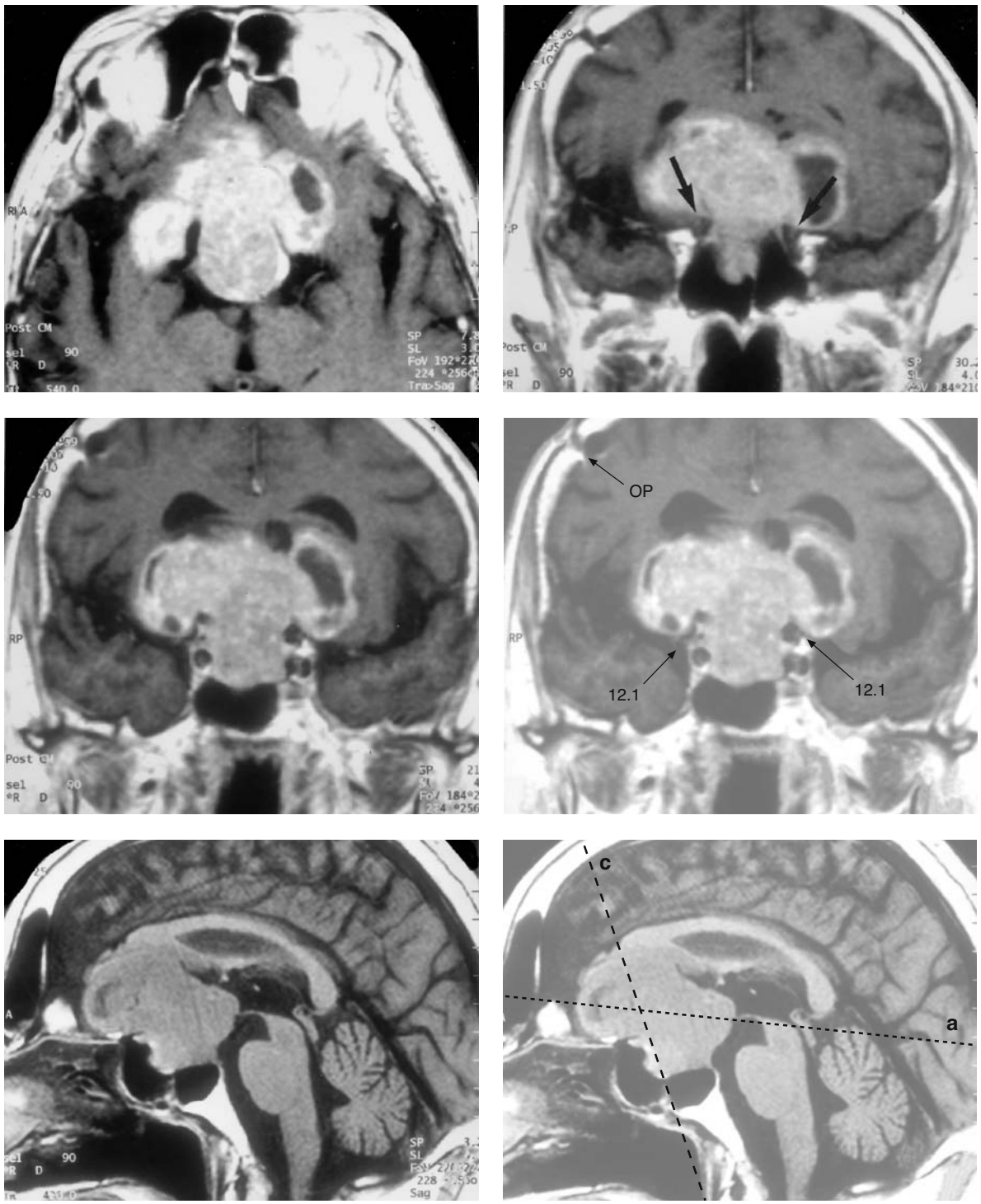

Fig. 7.21a–f. A 67-year-old man with a history of pituitary adenoma, operated on approximately 25 years ago, presenting with sudden onset of visual loss in the right eye. Diagnosis: recurrent pituitary adenoma (hormone inactive). T1-weighted MRI: **a** Axial contrast-enhanced view with a substantial, partly cystic tumor occupying the entire pentagon cistern, distorting the cerebral vessels, and developing into the right lateral fissure. **b** Coronal contrast-enhanced view at the level of the optic canal, showing both optic nerves (*arrows*), the left in the respective canal, while the roof of the right optic canal is partly eroded from the tumor. **c** Corresponding contrast-enhanced view at the suspected level of the chiasm. Both optic nerves are identified at the lateral indentation of the former sellar diaphragm. **d** Corresponding diagram: 12.1 = prechiasmatic optic nerve. Note the residual defect of the skull from the former operation. **e** Midsagittal native view demonstrating the correlation between the tumor, the chiasm, and the frontal brain. **f** Corresponding diagram with the planes of **a** and **c**

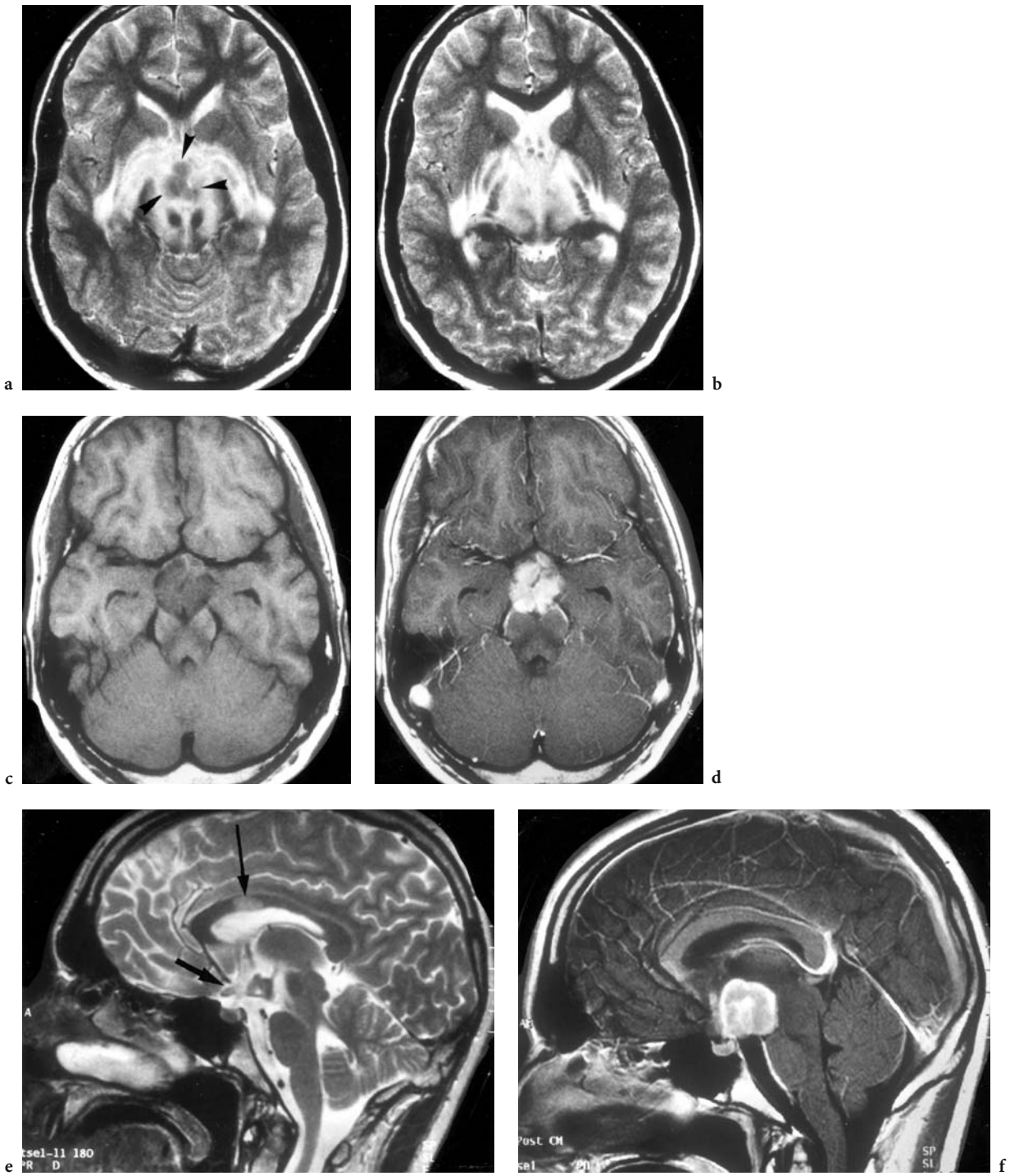

Fig. 7.22a–f. A 15 year old boy who presented with increasing weight, apathy, adynamia, and excessive memory defects, but no proven visual or additional hypothalamic disturbances (e.g., diabetes insipidus). Diagnosis: Langerhans cell granuloma. MRI: a Axial T2-weighted image at the level of the anterior commissure. In addition to an extensive edema along the anterior commissure and cerebral peduncle, an isointense, irregular, medially located mass is seen (*arrowheads*). **b** Axial T2-weighted view at the level of the interventricular foramen, demonstrating the widespread edema in both striate and thalami. **c** Axial T1-weighted native view at the level of the chiasm, which is seen compressed between the anterior cerebral arteries and the mass, extending through the entire interpeduncular cistern. **d** Corresponding contrast-enhanced view, demonstrating the extensive signal enhancement of the lesion. **e** Paramedian, sagittal, T2-weighted image, demonstrating the hypothalamic mass and slight swelling of the chiasm (*arrow*). Note another focus in the anterior part of the corpus callosum (*thin arrow*). **f** Midsagittal, T1-weighted, contrast-enhanced view, where the entire mass is apparent

intrasellar tumors. As unspecific clinical symptoms of headache will rarely indicate further examination, specific visual or diencephalic disturbances should lead to diagnostic imaging. Cholesterol granuloma are expansile cystic lesions, mainly arising in the temporal bone, which contain hemorrhage and cholesterol crystals and are not yet described in the sphenoid sinus. They present as hyperintense on both T1-weighted and T2-weighted MRI scans (Fig. 7.23) (Osborn and Rauschning 1994), while mucocele, equally sharply demarcated by expanded, remodeled bony structures, demonstrates quite variable signal intensities, depending on the composition of its protein content (Van Tessel et al. 1989).

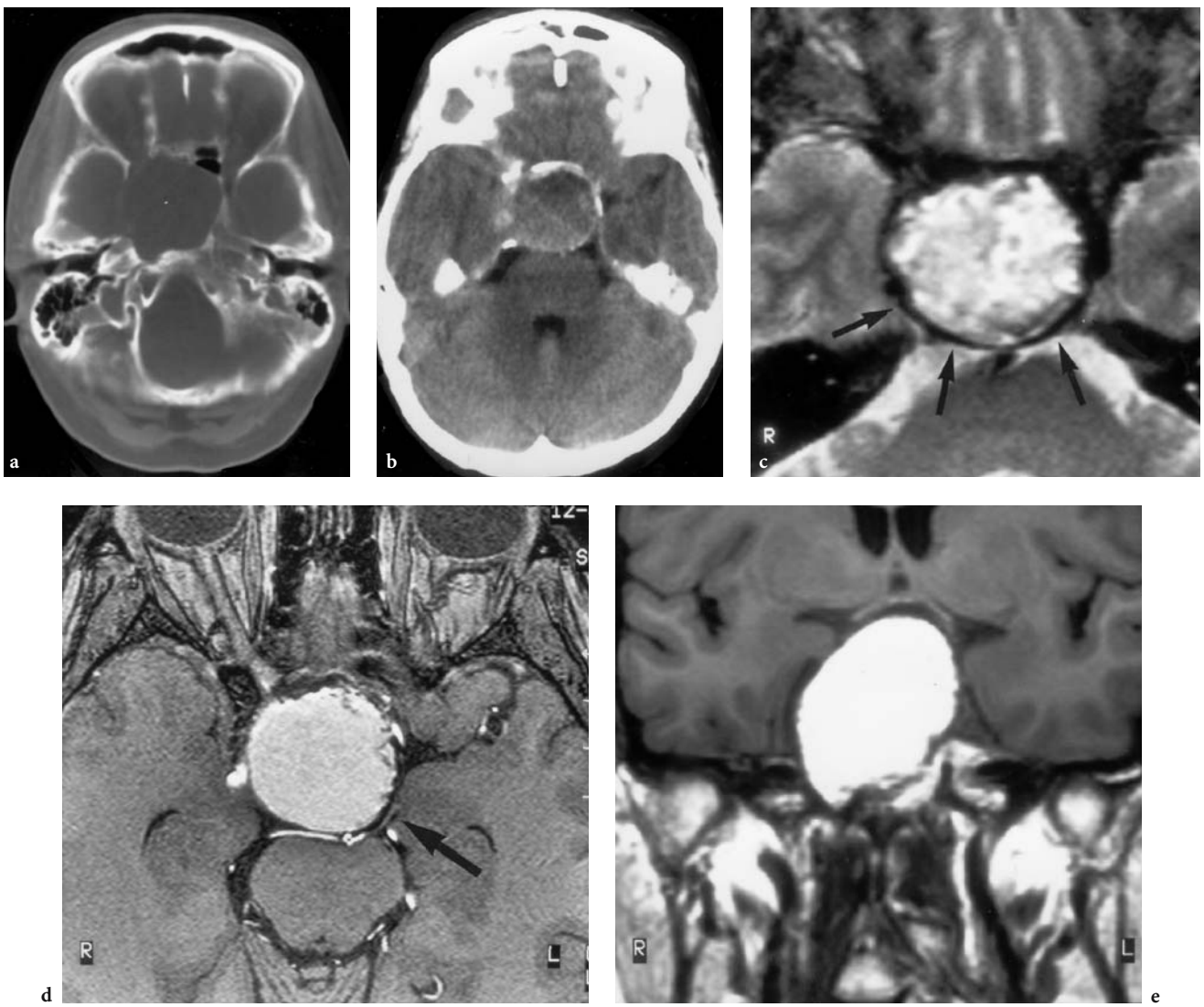

Fig. 7.23a–e. A 40-year-old woman with progressive visual deficit persisting for 15 months, as well as slowly progressing headache and dysmenorrhea, presenting with left temporal hemianopsia. Diagnosis: cholesterol granuloma of the sphenoid sinus. Axial CT: **a** Bone window at the skull base, demonstrating substantial widening with erosion (no destruction), especially of the right side of the sphenoid sinus, including the region of the right optic and reaching the carotid canal. **b** At the suprasellar level, an isodense, sharply circumscribed mass occupies the pentagon cistern. MRI: **c** Axial T2-weighted view showing an irregular hyperintense mass in the sphenoid sinus and sellar floor region, sparing the bony cortex of the clivus (hypointensity, *arrows*). **d** Axial T1-weighted native HR image at the level of the right optic canal, with homogeneous hyperintensity of the granuloma. Note slight compression of the brainstem with dislocation of the left oculomotor nerve (N III) (*arrow*). **e** Coronal T1-weighted image visualizing substantial craniocaudal extension of the mass with inferior compression of the chiasm

7.2.1.3 Meningioma

Meningiomas are WHO grade I–III tumors consisting of neoplastic meningothelial (arachnoidal) cells, occurring predominantly in middle-aged and elderly patients with a marked female bias of approximately 2:1. They constitute up to 26% of primary intracranial tumors and elicit neurologic signs and symptoms by compression of adjacent structures (Louis et al. 2000). Meningiomas associated with hereditary tumor syndrome such as schwannoma (i.e., in patients with NF2) (Woodruff et al. 2000) (Fig. 7.24) mainly occur in younger patients. Approximately 20% of meningiomas are located in the sellar region, with 50% arising from midline structures such as the sphenoid plane (Fig. 7.25), tuberculum sellae (Figs. 7.26–7.28), diaphragm sellae, or the dura of the cavernous sinus (Fig. 7.29). The remaining 50% consist of sphenoid wing meningiomas (Figs. 7.30, 7.32, 6.108) or meningiomas of the clinoid process (Figs. 7.14, 7.24, 7.31, 7,33, 6.174) (Sartor 1992). The characteristic hyperostosis associated with these tumors is due to their tendency to invade the Haversian canals (Zülch 1986). As a result of their slow, asymptomatic, and in some instances intraosseous growth, en plaque meningiomas of the middle cranial fossa, including parasellar and sphenoid wing meningiomas, may demonstrate substantial extension (Fig. 7.32). Globular meningiomas of the suprasellar or paraclinoid region may produce early ophthalmological symptoms because of optic nerve

(Text continues on p. 371)

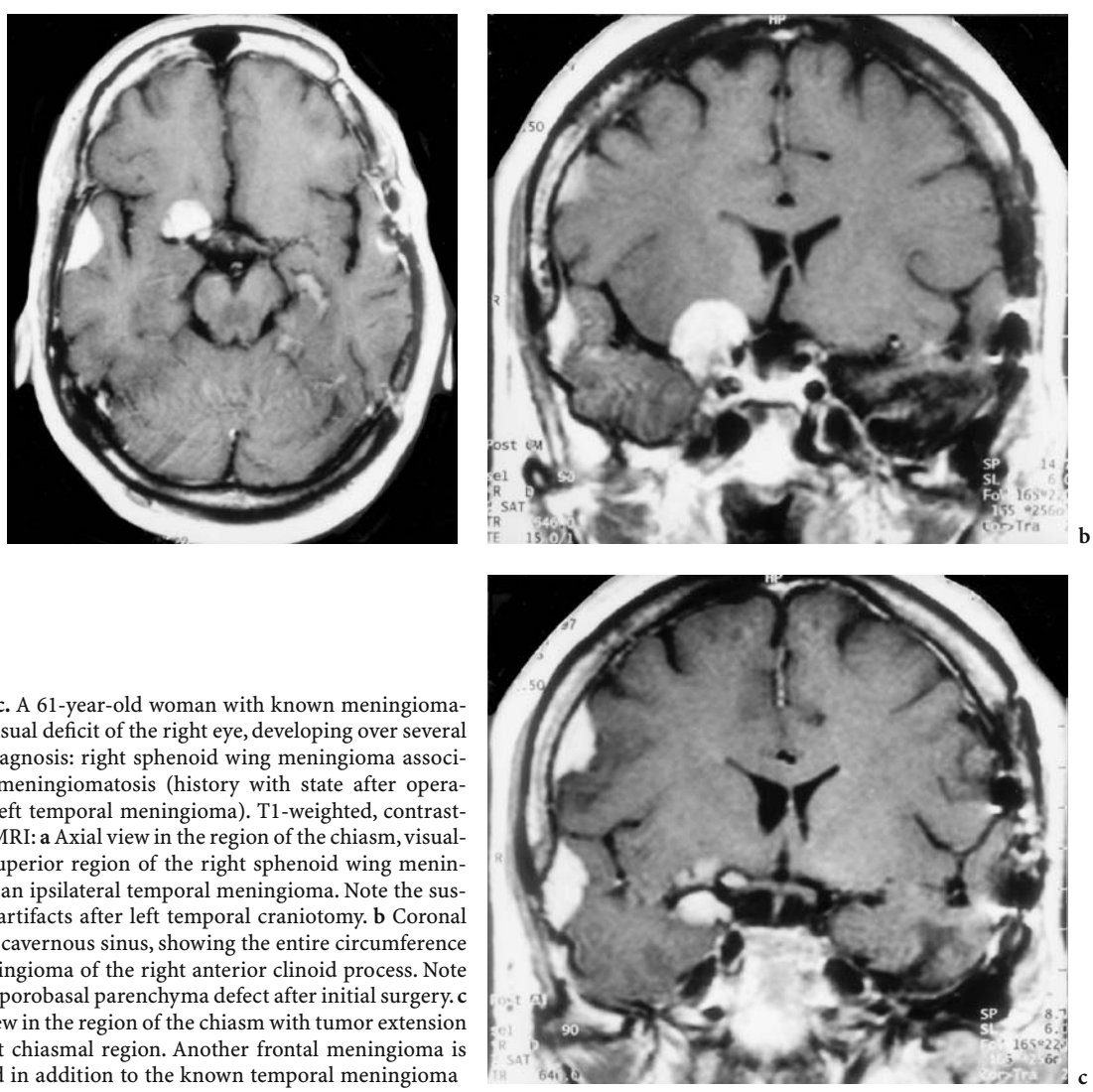

Fig. 7.24a–c. A 61-year-old woman with known meningiomatosis and visual deficit of the right eye, developing over several months. Diagnosis: right sphenoid wing meningioma associated with meningiomatosis (history with state after operation for a left temporal meningioma). T1-weighted, contrast-enhanced MRI: **a** Axial view in the region of the chiasm, visualizing the superior region of the right sphenoid wing meningioma and an ipsilateral temporal meningioma. Note the susceptibility artifacts after left temporal craniotomy. **b** Coronal view at the cavernous sinus, showing the entire circumference of the meningioma of the right anterior clinoid process. Note the left temporobasal parenchyma defect after initial surgery. **c** Coronal view in the region of the chiasm with tumor extension to the right chiasmal region. Another frontal meningioma is demarcated in addition to the known temporal meningioma

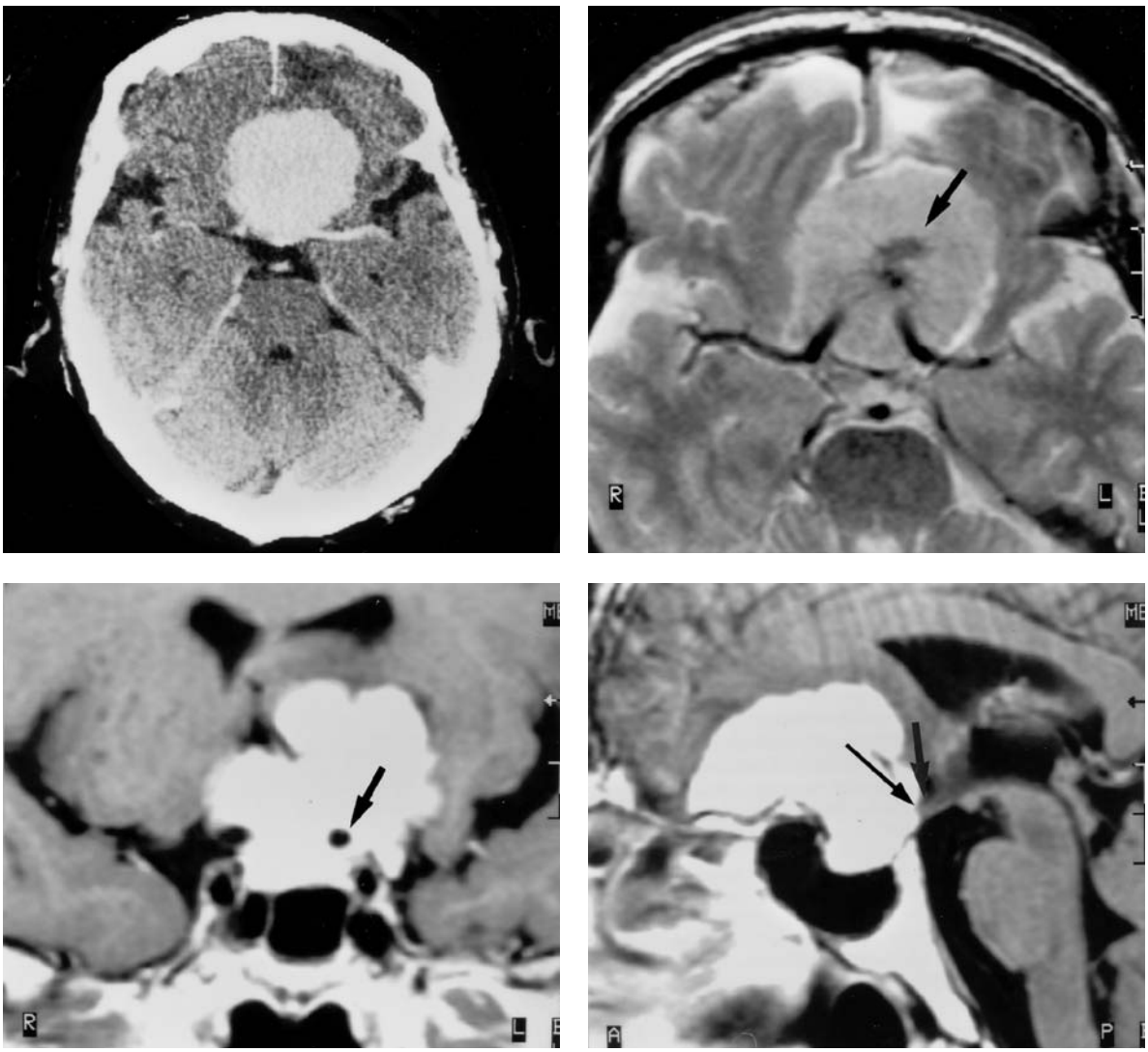

Fig. 7.25a–d. A 69-year-old man with slowly progressing bilateral visual deficit with emphasis to the left. Diagnosis: meningioma of the sphenoid plane. Axial, contrast-enhanced CT: **a** Homogeneous enhancement of a spherical tumor with emphasis to the left is seen at the posterior part of the frontal base. Note a slight perifocal edema in the left frontal white matter. MRI: **b** Corresponding T2-weighted view with displacing growth of the extraparenchymal tumor, indicative of the so-called tumor "belly" (*arrow*). Note hyperintensity of the left frontal white matter, due to perifocal edema (compare with **a**) **c** Coronal T1-weighted, contrast-enhanced view with clearly visible homogeneous tumor enhancement and a knotty tumor surface. Only slight narrowing of the left ICA (*arrow*), located in the medial region of the meningioma. **d** Midsagittal, T1-weighted, contrast-enhanced image where the origin of the meningioma is distinguished by thickening of the secondary curved sphenoid plane. Note intrasellar tumor expansion with compression of the pituitary stalk at the dorsum sellae (*arrows*). (From Müller-Forell and Lieb 1995)

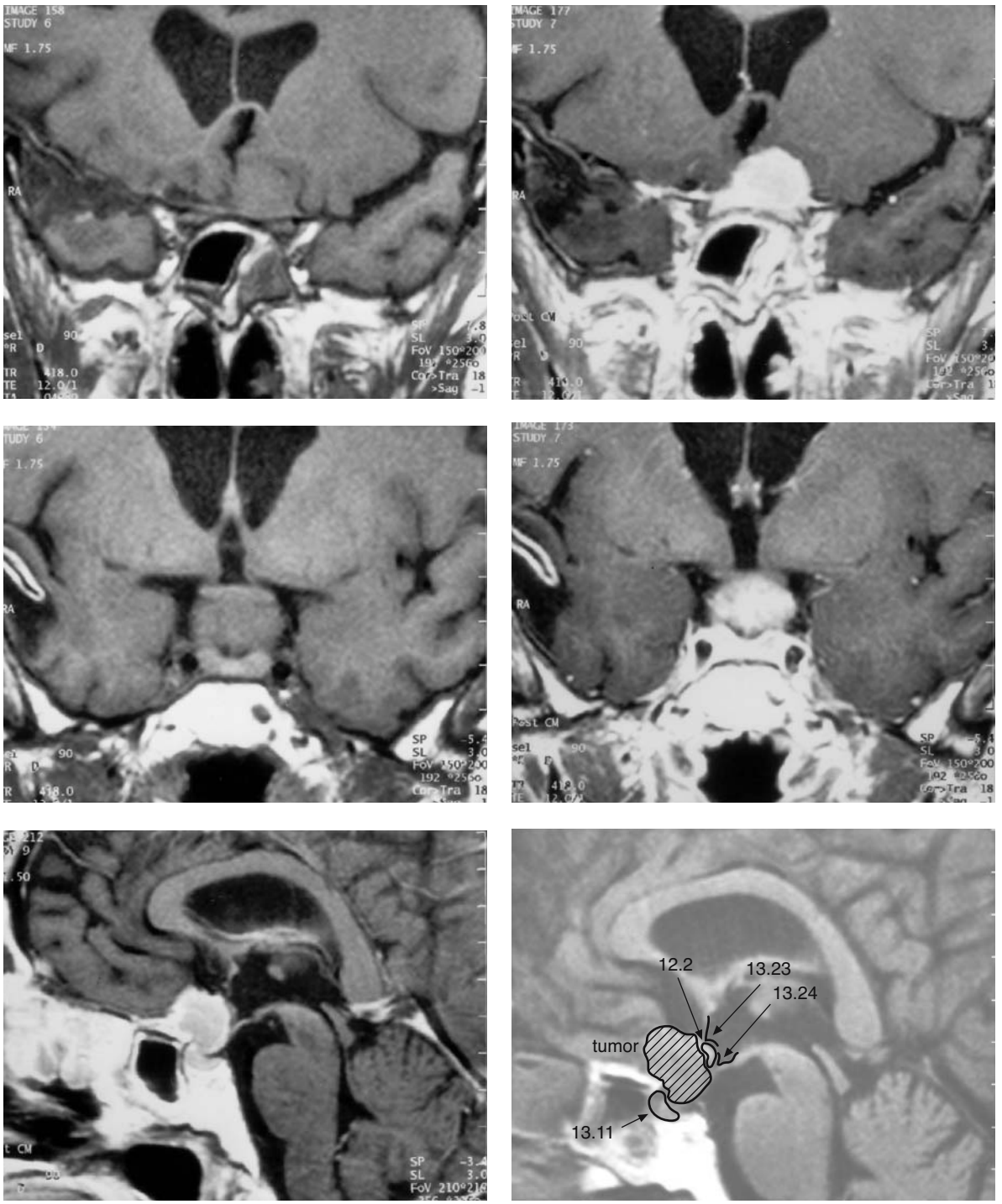

Fig. 7.26a–f. A 61-year-old man with acute loss of vision in the left eye. Diagnosis: meningioma of the tuberculum sellae. T1-weighted MRI: **a** Coronal native view at the level of the optic canal, showing an isointense formation with compression and elevation of the left rectus gyrus. **b** Corresponding contrast-enhanced view showing that the left optic nerve is flattened by tumor infiltration of the optic canal. **c** Coronal native view at the level of the chiasm, which appears to be slightly depressed from inferior. Note the normal configuration of the pituitary gland in a normal-sized sella and differentiation of the pituitary stalk in between. **d** Corresponding contrast-enhanced image. **e** Midsagittal, T1-weighted, contrast-enhanced image demonstrating the tumor growth at the tuberculum sellae and sphenoid plane and also the flattened chiasm at the posterior circumference of the meningioma. **f** Corresponding diagram: 12.2 = chiasm, 13.11 = pituitary gland, 13.23 = chiasmatic recess (of the third ventricle), 13.24 = recess of the pituitary stalk (of the third ventricle)

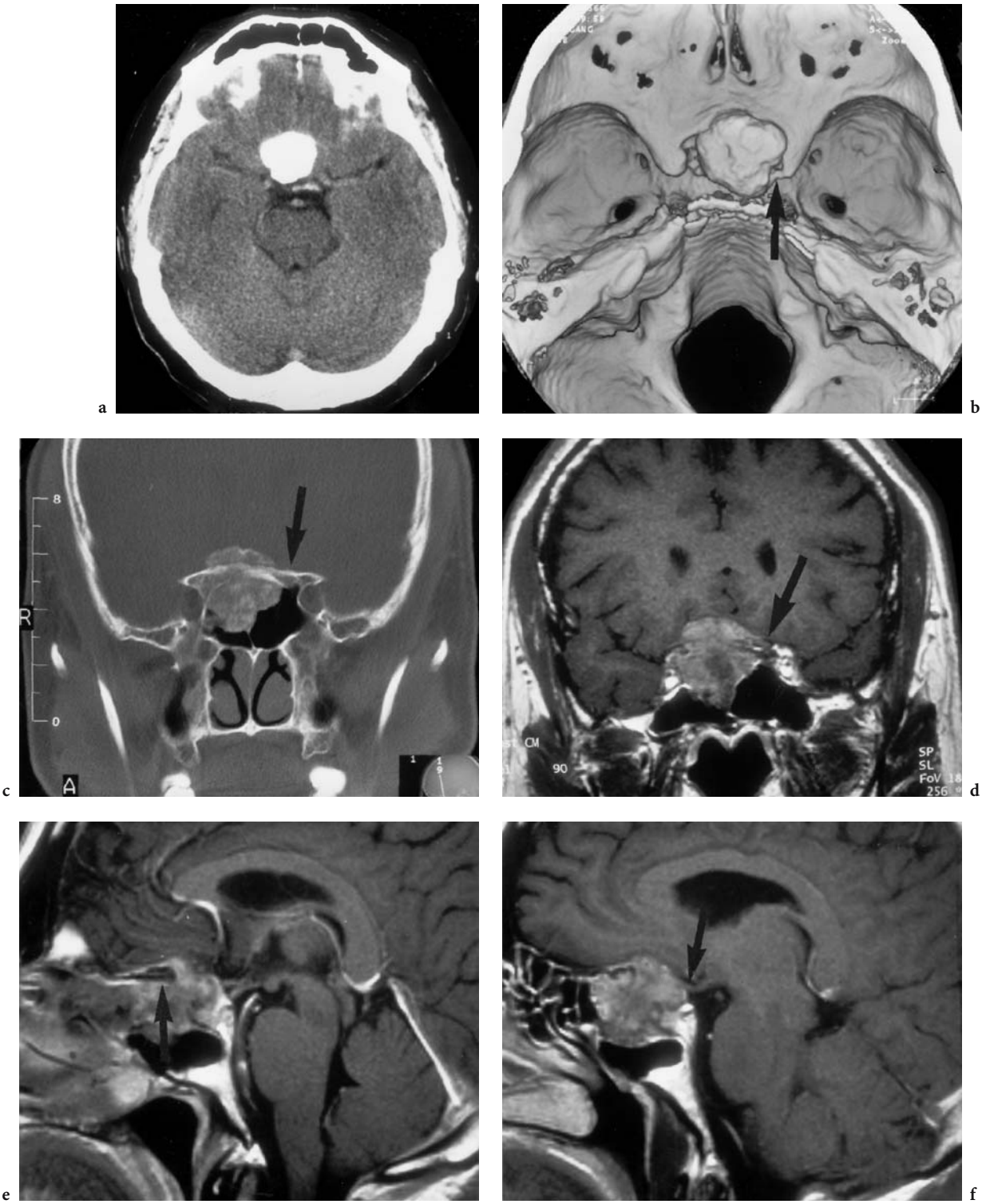

Fig. 7.27a–f. A 45-year-old man with slowly progressing visual deficit of the right eye. Diagnosis: intra- and extracranial sphenoid meningioma. CT: **a** Axial native view of the suprasellar region showing homogeneous calcification of the right posterior sphenoid plane, extending to the area of the dorsum sella. **b** 3D-reconstruction, view from above (right is left and vice versa) where the calcification occludes the distal right optic canal (*arrow*), while the left is seen to be almost free from calcification. **c** Coronal view in bone window, demonstrating occlusion of the right optic canal by the predominantly calcified tumor, showing expansion primarily in the sphenoid sinus and only some expansion at the sphenoid plane. The *arrow* indicates the left intact optic canal. T1-weighted, contrast-enhanced MRI: **d** Corresponding coronal view. While the left optic nerve is seen in the optic canal (*arrow*), the right optic nerve is not distinguishable in the tumor mass. **e** Midsagittal view, showing extension of the meningioma to the normal local chiasm as well as its growth along the sphenoid plane (so-called meningeal "tail") with hyperostosis of the origin (*arrow*). **f** Right paramedian, sagittal view where the right optic nerve is seen distal from the optic canal (*arrow*). (MR images with permission of Radiologische Abteilung Krankenhaus, Winnenden)

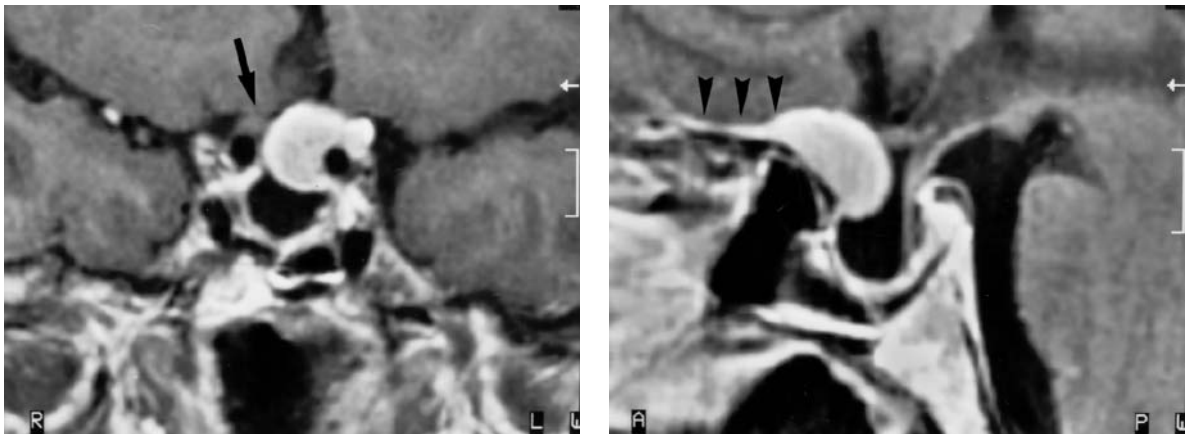

Fig. 7.28a,b. A 53-year-old woman with slowly progressing visual deficit. Diagnosis: meningioma of the tuberculum sella. T1-weighted, contrast-enhanced MRI: **a** Coronal view at the level of the optic canal showing a homogeneous, sharply defined tumor of the left tuberculum sellae, encasing the ipsilateral ICA, although without diminution of the ICA diameter. No differentiation of the left optic nerve is possible because the tumor crosses the midline and reaches the right optic canal (*arrow*). **b** Midsagittal view with the typical meningeal „tail" along the sphenoid plane (*arrowheads*). Empty sella as an incidental finding. (From Müller-Forell and Lieb 1995)

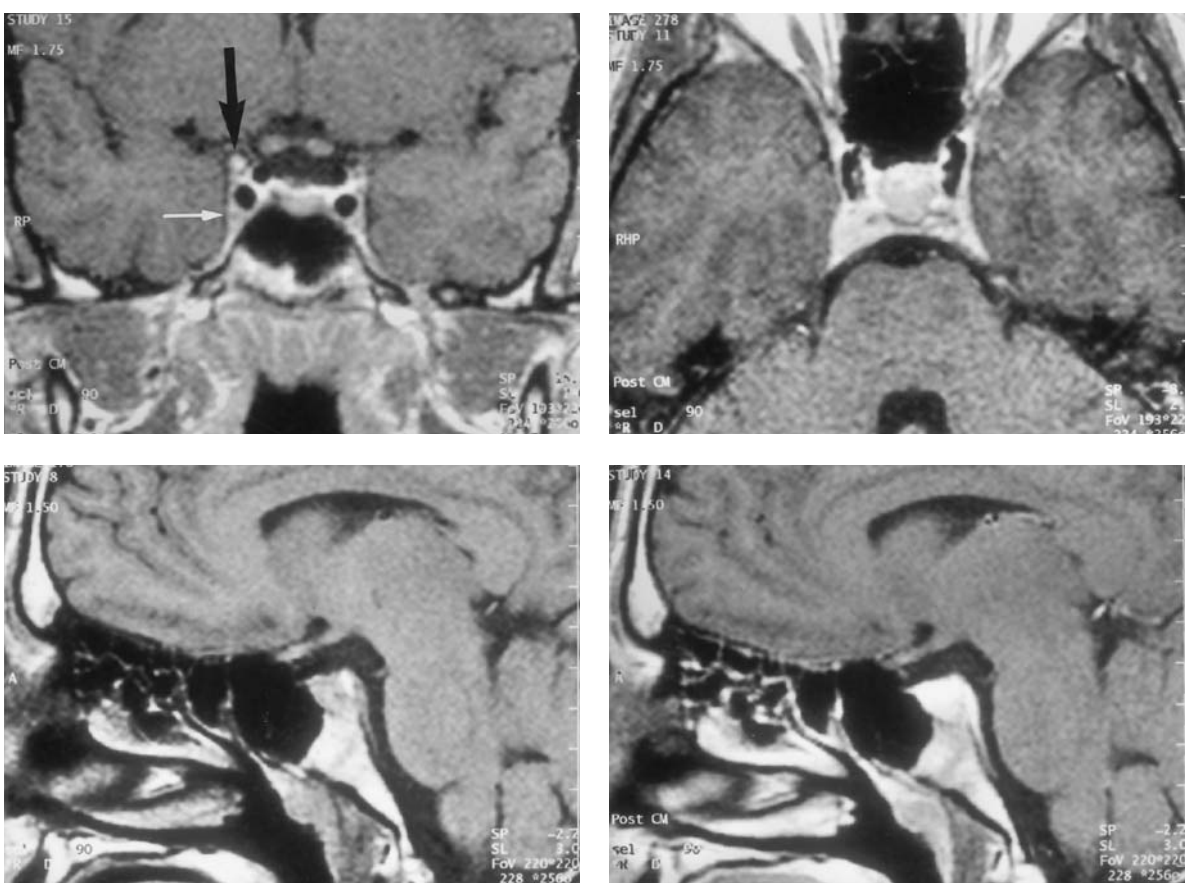

Fig. 7.29a–d. A 20-year-old man with acute right N VI paresis persisting for 14 days. Diagnosis: suspected meningioma of the right lateral clivus (including Dorell canal). T1-weighted MRI: **a** Coronal contrast-enhanced view of the cavernous sinus where the location of the right abducent nerve is distinguished in the cavernous sinus (*white arrow*). Note a small, round structure at the upper end of the right cavernous sinus (*black arrow*) corresponding to the upper end of the tumor. **b** Axial contrast-enhanced image demonstrating a slight asymmetry of the cavernous sinus configuration of the right side. **c** Right paramedian, sagittal native view, lateral to the pituitary gland with a slightly hyperintense mass and thickening of the dura. **d** Corresponding contrast-enhanced image, showing enhancement of both the mass and the dura of the clivus. The patient was transferred for stereotactic radiation but lost to follow-up

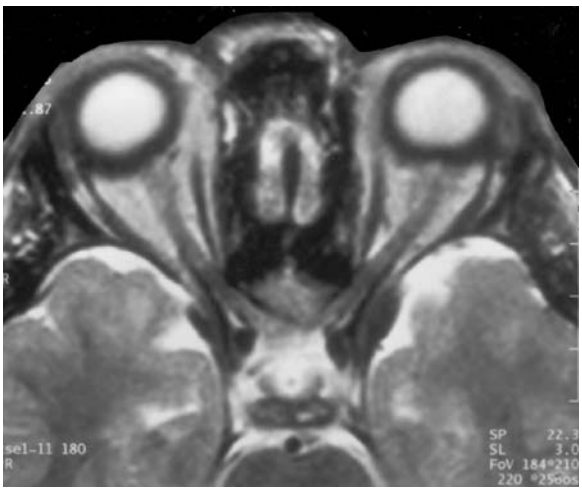

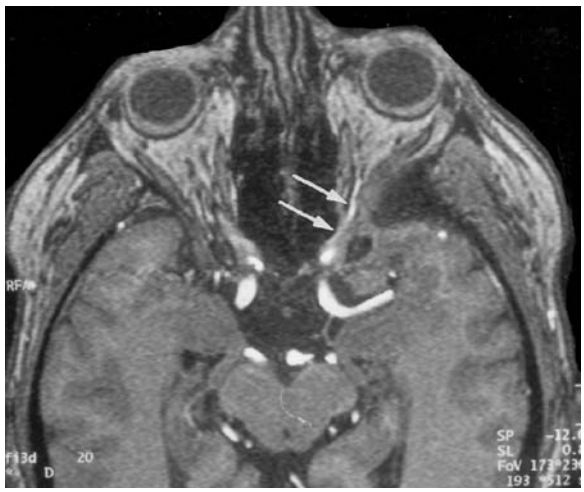

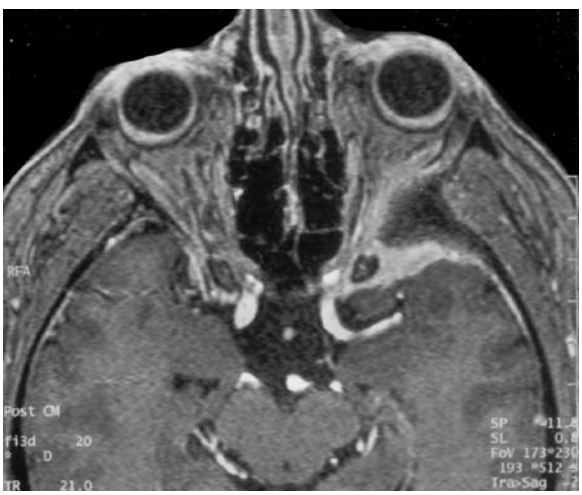

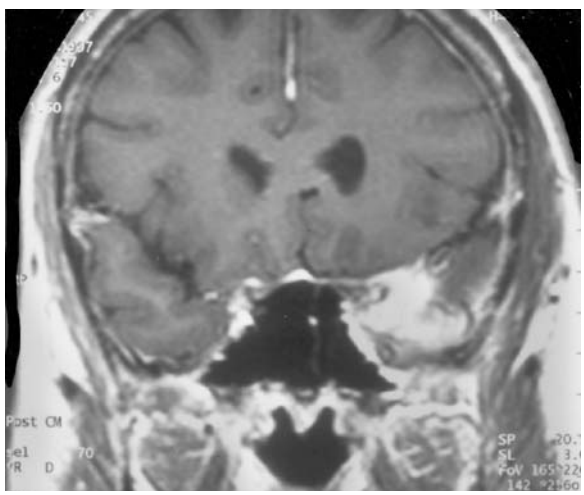

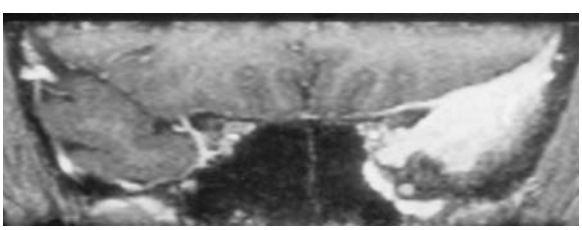

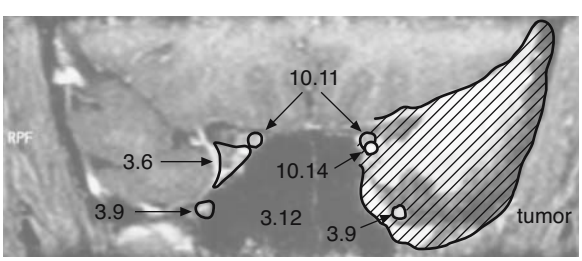

Fig. 7.30a–f. A 52-year-old woman with rapidly progressing visual field deficits of the left eye and ipsilateral proptosis. Diagnosis: meningioma of the inferior part of the left sphenoid wing. MRI: **a** Axial T2-weighted image at the level of the optic canal where only slight thickening of the left clinoid process is seen. **b** Axial T1-weighted native HR image (3D data set) at the level of the superior orbital fissure, showing thickening of the left sphenoid bone with depression of the lateral orbit and inferior optic nerve, identified by the high signal of the ophthalmic artery (*small white arrows*). **c** Corresponding contrast-enhanced image with identification of the intraorbital and temporal parts of the tumor. **d** Coronal, T1-weighted, contrast-enhanced view at the level of the optic canal where inferior expansion of the tumor becomes apparent, although a direct relationship to the optic nerve cannot be determined. **e** Coronal reconstruction of the contrast-enhanced 3D data with confirmation of the relationship to the left optic nerve, showing inferior compression of the ophthalmic artery, originating from the tumor growth through the superior orbital fissure. **f** Corresponding diagram: 3.6 = superior orbital fissure, 3.9 = round foramen, 3.12 = sphenoid sinus, 10.11 = optic nerve, 10.14 = ophthalmic artery

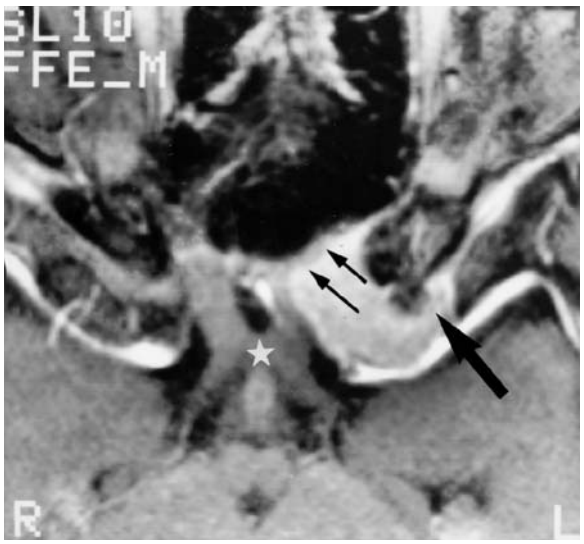

Fig. 7.31. A 51-year-old woman with progressive visual deficit of the left eye. Diagnosis: left sphenoid (small) wing meningioma. T1-weighted, contrast-enhanced HR-MRI: the tumor progresses from the distal area of the clinoid process (*arrow*) to the optic canal. Note the anterior dislocation of the prechiasmal part of the flattened, attenuated optic nerve (*small arrows*) to the lateral posterior wall of the sphenoid sinus, and the flattened, impressed, dorsal dislocation of the (hyperintense) ICA bifurcation area with proximal MCA (*white star*: chiasm). (From Müller-Forell and Lieb 1995)

or chiasmal compression (Figs. 7.28, 7.31, 7.33), and therefore do not normally exceed 2 cm in diameter (Sartor 1992).

Imaging Characteristics. Due to their high cell density and psammomatous calcification, meningiomas of the sellar region present on CT as isodense to hyperdense midline lesions. Diffuse hyperostosis is particularly apparent on CT images of en plaque meningioma (Figs. 6.195, 6.174). A perifocal edema is detected only in the rare cases where the cerebral cortex is destroyed by this tumor (Fig. 7.25). Apart from the differentiation of pituitary adenomas, where a transsphenoidal approach is the preferred operative procedure, the most important question for neurosurgeons is the possible invasion of the cavernous sinus and/or narrowing of the ICA, which is best addressed by MRI. The high-resolution, multidirectional imaging provided by this method enables an accurate, detailed description of anatomic and pathologic morphology. In view of the fact that meningiomas often show an isointense signal for gray matter, contrast administra-

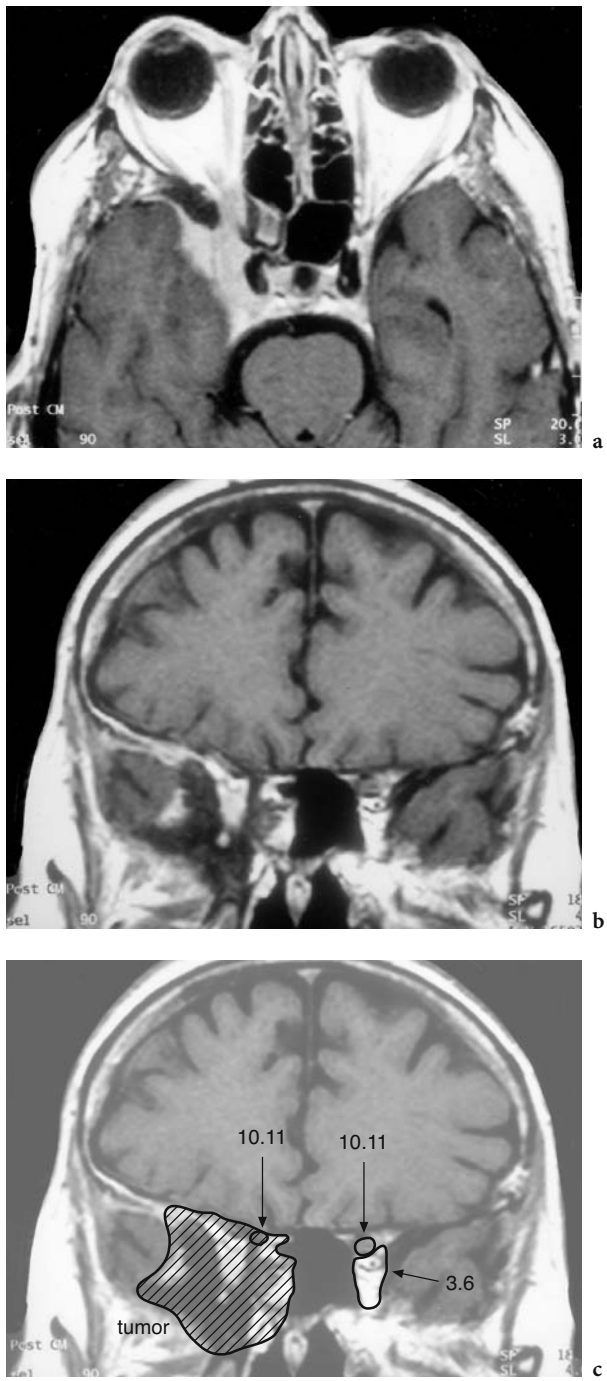

Fig. 7.32a–c. A 73-year-old man with slowly progressing visual deficit of the right eye. Diagnosis: sphenoid wing meningioma. T1-weighted, contrast-enhanced MRI: **a** Axial view with thickening of the large wing of the right sphenoid. The tumor occupies the temporal pole and the superior orbital fissure, extending to and invading the anterior part of the cavernous sinus without encasement or dislocation of the ipsilateral ICA. **b** Coronal view at the apex-orbital level visualizing tumor invasion extending to the base of the large sphenoid wing and to the superior orbital fissure. **c** Corresponding diagram: 3.6 = superior orbital fissure, 10.11 = optic nerve

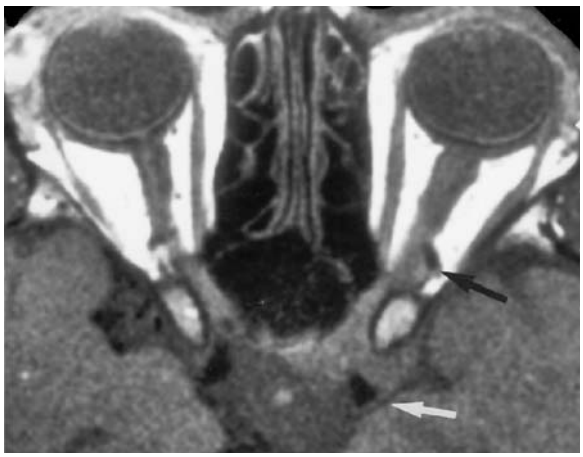

a

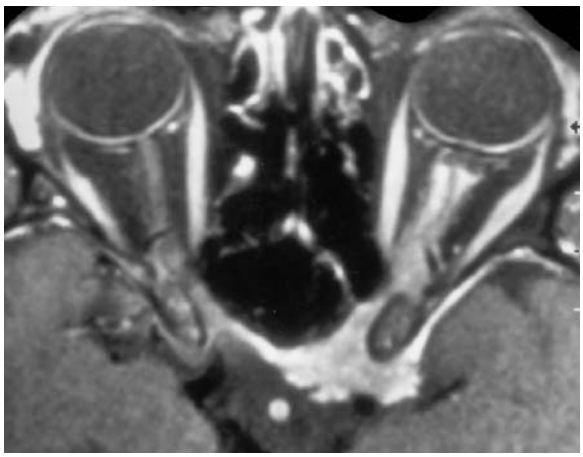

b

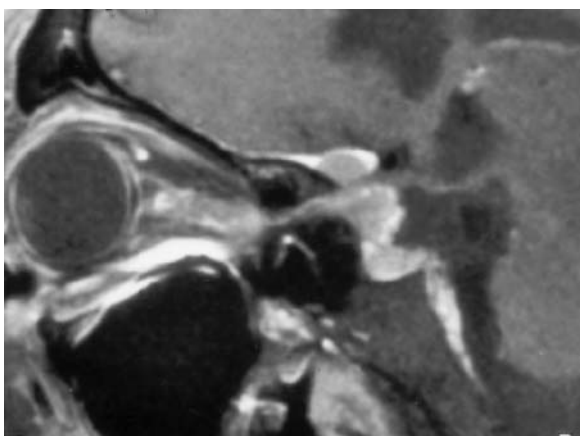

c

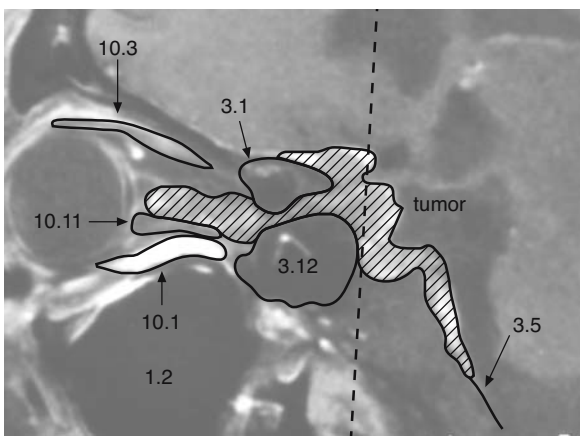
10.3
3.1
tumor
10.11
3.12
10.1
3.5
1.2

d

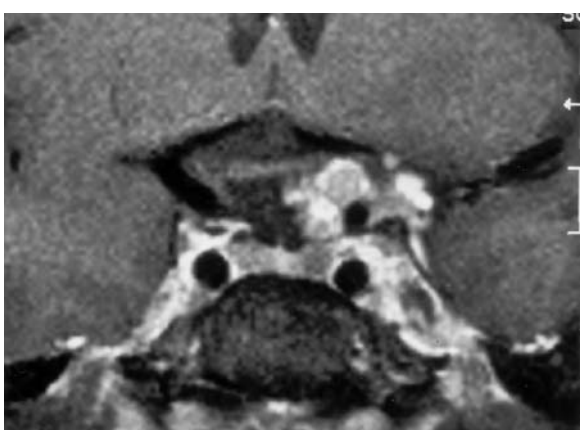

e

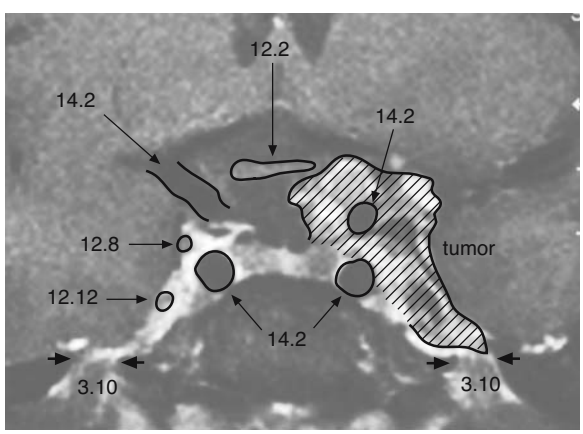
12.2
14.2
14.2
12.8
tumor
12.12
14.2
3.10
3.10

f

tion is absolutely indicated to detect even tumors or tumor parts in areas only millimeters in size (Figs. 7.30, 7.33). Homogeneous, intensive enhancement is detected in almost all cases after i.v.-iodinated contrast medium, due to the presence of high tumor vascularization. Knowledge of MRI anatomy including the location and shape of the basal cisterns and vessels is required to establish the accurate diagnosis, especially with en plaque meningiomas of the sphenoid wing. With regard to diagnostic evidence, sagittal and coronal views are superior to axial images even in thin slices, a factor of relevance for all lesions of the sellar region. Despite the low sensitivity for compact bone, MR demonstration of hyperostosis indicating the origin of the meningioma is in some cases superior to that provided by CT (Figs. 7.14, 7.25, 7.27, 7.31, 7.33) (Sartor 1992; Osborn 1994a).

The differential diagnosis for globular meningioma and partially thrombosed giant aneurysms (see chapter 7.2.1.6) of the ICA is facilitated by the high sensitivity of MRI for flow and thrombi. Other important lesions to be excluded include supra- and extrasellar pituitary adenoma, trigeminal schwannoma, metastasis, and inflammatory granu-loma. Differentiation between a suprasellar pituitary adenoma and a meningioma originating from the sellar diaphragm can be achieved based on the definition of a normal pituitary gland inferior to the lesion and the demonstration of the sellar diaphragm, especially on the coronal view (Fig. 7.34).

7.2.1.4 Craniopharyngioma

Craniopharyngiomas correspond to the WHO grade I tumor classification and are defined as benign, partly cystic, epithelial tumors of the sellar region, typically occurring in children and adolescents. They are assumed to arise from Rathke's pouch epithelium and account for 1.2%–4.6% of all intracranial tumors and thus represent the second most frequent tumors of the sellar region after pituitary adenomas. Craniopharyngiomas show no sex bias but a bimodal age distribution, with one peak involving children and adolescents and another one involving adults (Adamson et al. 1990; Crotty et al. 1995). A clinicopathologic distinction is made between adamantinous and papillary craniopharyngioma. Most adamantinomas are hormone-inactive lesions and present as solid tumors with a variable, at times predominantly cystic component, containing cholesterol-rich, thick, brownish-yellow fluid with the appearance of machine oil. Although craniopharyngiomas have a smooth surface, reactive fibrous tissue components are in some instances responsible for their firm attachment to adjacent brain structures (Figs. 7.35, 7.36), impeding complete neurosurgical removal. As described above, craniopharyngiomas can be divided into an adamantinous and a papillary type, with the cystic component being predominant in the majority of cases. The adamantinous type is seen more frequently in children and is often marked by calcification, with a crumbly consistency in the solid parts and a shell-like appear-

(Text continues on p.376)

◁ **Fig. 7.33a–f.** A 33-year-old man with known amaurosis of the left eye persisting for 2 years; presenting to the attending physician complaining of double vision for the previous 2 weeks. Diagnosis: sphenoid wing meningioma with secondary optic nerve sheath infiltration. T1-weighted MRI: **a** Axial native view at the level of the normal-sized optic canal. In addition to slight thickening of the optic nerve complex, a small solid mass is visualized in the area of the thickened left clinoid process with lateralisation of the slightly nidened ophthalmic artery (*black arrow*). Note posterior dislocation of the C1 segment of the ipsilateral ICA (*white arrow*). **b** Corresponding contrast-enhanced (FS) image. Although the identified mass is small, the pathologic process is delineated around the left clinoid process with the tumor mass extending from the middle cranial fossa to the right optic canal, to the ipsilateral intraorbital space, and to the region of the posterior fossa. **c** Paramedian, sagittal, contrast-enhanced (FS) view, showing the trapped intracranial optic nerve dividing the tumor of the enlarged clinoid process. Note the various compartments affected by tumor expansion, including the orbital space along the optic nerve sheath, the anterior cranial fossa at the clinoid process, the suprasellar region, and the posterior cranial fossa with tumor growth along the clivus. **d** Corresponding diagram: 1.2 = maxillary sinus, 3.1 = (thickened) anterior clinoid process, 3.5 = clivus, 3.12 = sphenoid sinus, 10.1 = inferior rectus muscle, 10.3 = superior rectus muscle, 10.11 = optic nerve. **e** Coronal, T1-weighted, contrast-enhanced view (at the level of the *dotted line* in **d**) demonstrating supraclinoid expansion of the bulbous tumor formation with elevation of the left chiasm. The enlargement of the cavernous sinus indicates tumor invasion, obviously responsible for eye movement disorders. **f** Corresponding diagram: 3.10 = oval foramen, 12.2 = chiasm, 12.8 = oculomotor nerve (N III), 12.12 = ophthalmic nerve (NV1), 14.2 = ICA

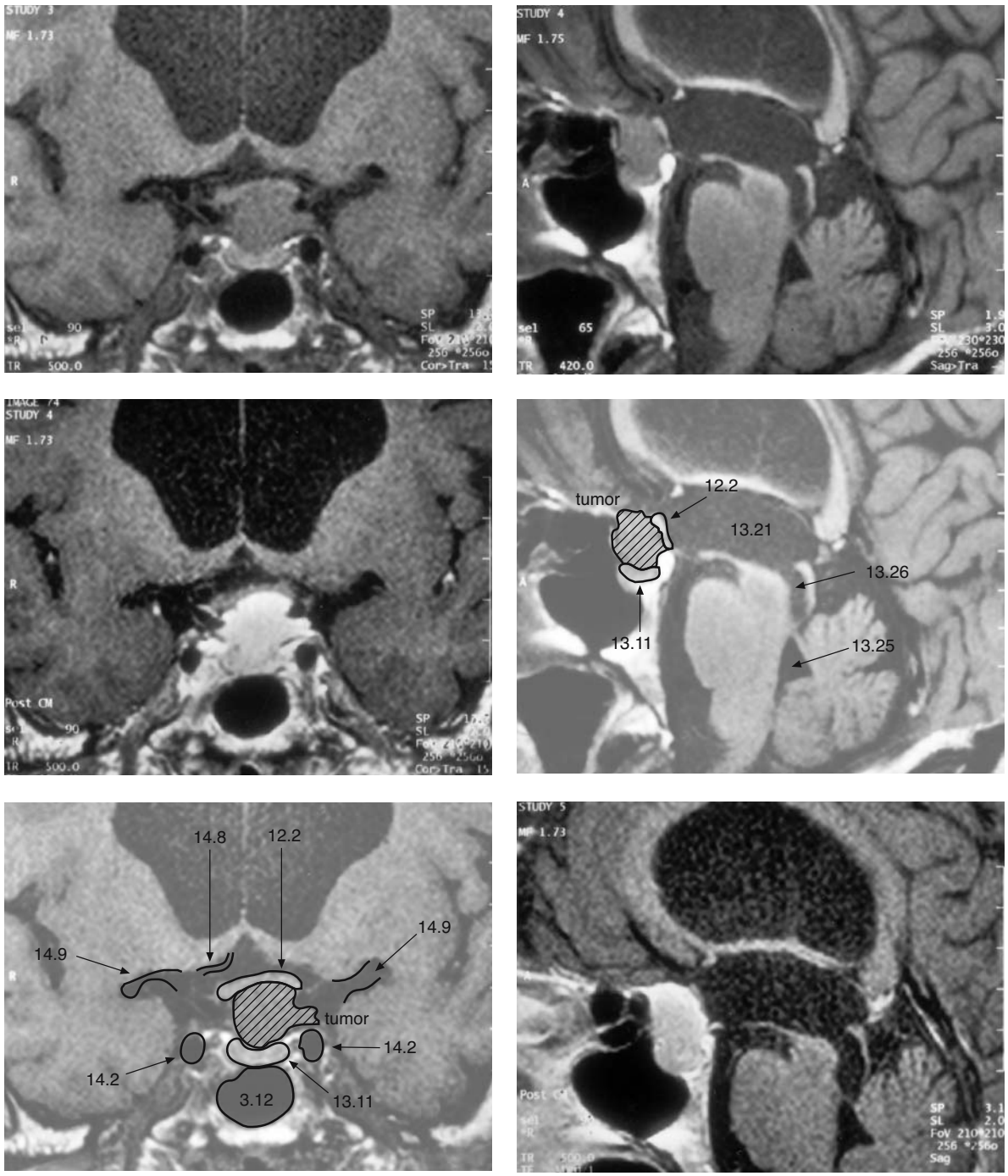

Fig. 7.34a–f. A 59-year-old man with progressing visual deficit of the left eye. Diagnosis: meningioma of the tuberculum sellae and a clinically compensated occlusive hydrocephalus. T1-weighted MRI: **a** Coronal native view, demonstrating a suprasellar mass with lower signal intensity than the pituitary gland, depressing the sellar diaphragm and compressing the left chiasm from inferior. **b** In the corresponding contrast-enhanced view, differentiation between the tumor and the gland is poorer after i.v. gadolinium. Note the lateral tumor expansion between the cavernous (inferior) and C1 part (superior) of the left ICA. **c** Corresponding diagram: 3.12 = sphenoid sinus, 12.2 = chiasm, 13.11 = pituitary gland, 14.2 = ICA, 14.8 = ACA, 14.9 = MCA. **d** Midsagittal T1-weighted native image demonstrating anterior compression of the chiasm. Note the different signal for the meningioma and the pituitary gland. **e** Corresponding diagram: 12.2 = chiasm, 13.11 = pituitary gland, 13.21 = third ventricle, 13.25 = fourth ventricle, 13.26 = aqueduct. **f** Corresponding contrast-enhanced view with superior visualization of the "tail" of the meningioma along the sphenoid floor. Note the enlarged supratentorial ventricles that are apparently due to compensated occlusion of the aqueduct (independent finding). (With permission of Radiologen am Brand, Mainz)

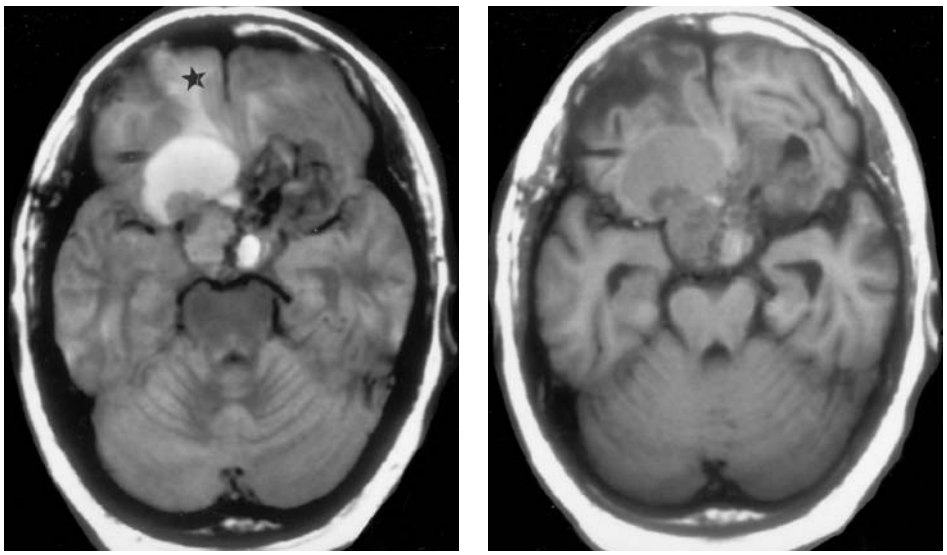

a b

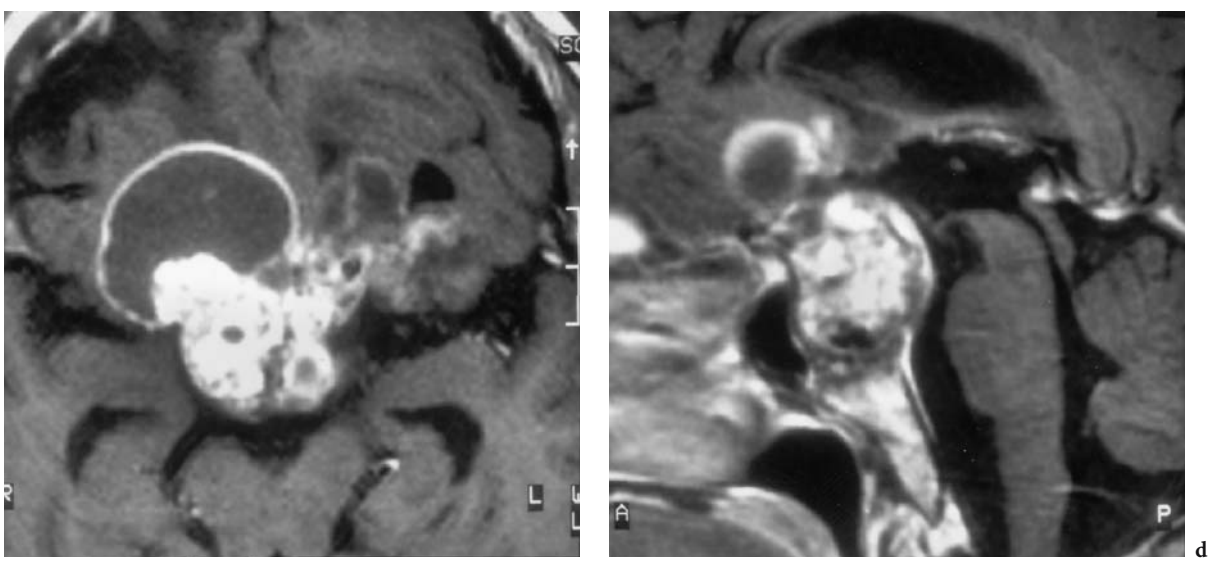

c d

Fig. 7.35a–d. MRI of a 20-year-old woman suffering from headache and visual deficit of both eyes, with dominance of the right side. Diagnosis: recurrent craniopharyngioma. MRI: **a** axial proton density view with inhomogeneous signal patterns of a bilateral, primarily median, frontal tumor. Note that the hyperintense cyst on the right side exhibits a more intense signal than the CSF of the right frontobasal parenchymal defect (*star*) after initial operation. **b** Corresponding T1-weighted native view demonstrating an intermediate signal of the cystic area, which is accounted for by the protein content of the cyst. **c** Enlarged corresponding T1-weighted, contrast-enhanced view where the cystic wall as well as the solid regions of the tumor exhibit strong signal enhancement. **d** Midsagittal, T1-weighted, contrast-enhanced T1-weightedview with widening of the sella and depression of the floor of the third ventricle and of the inferior frontal lobe by the tumor cyst. Neither chiasmal nor pituitary stalk structures can be differentiated

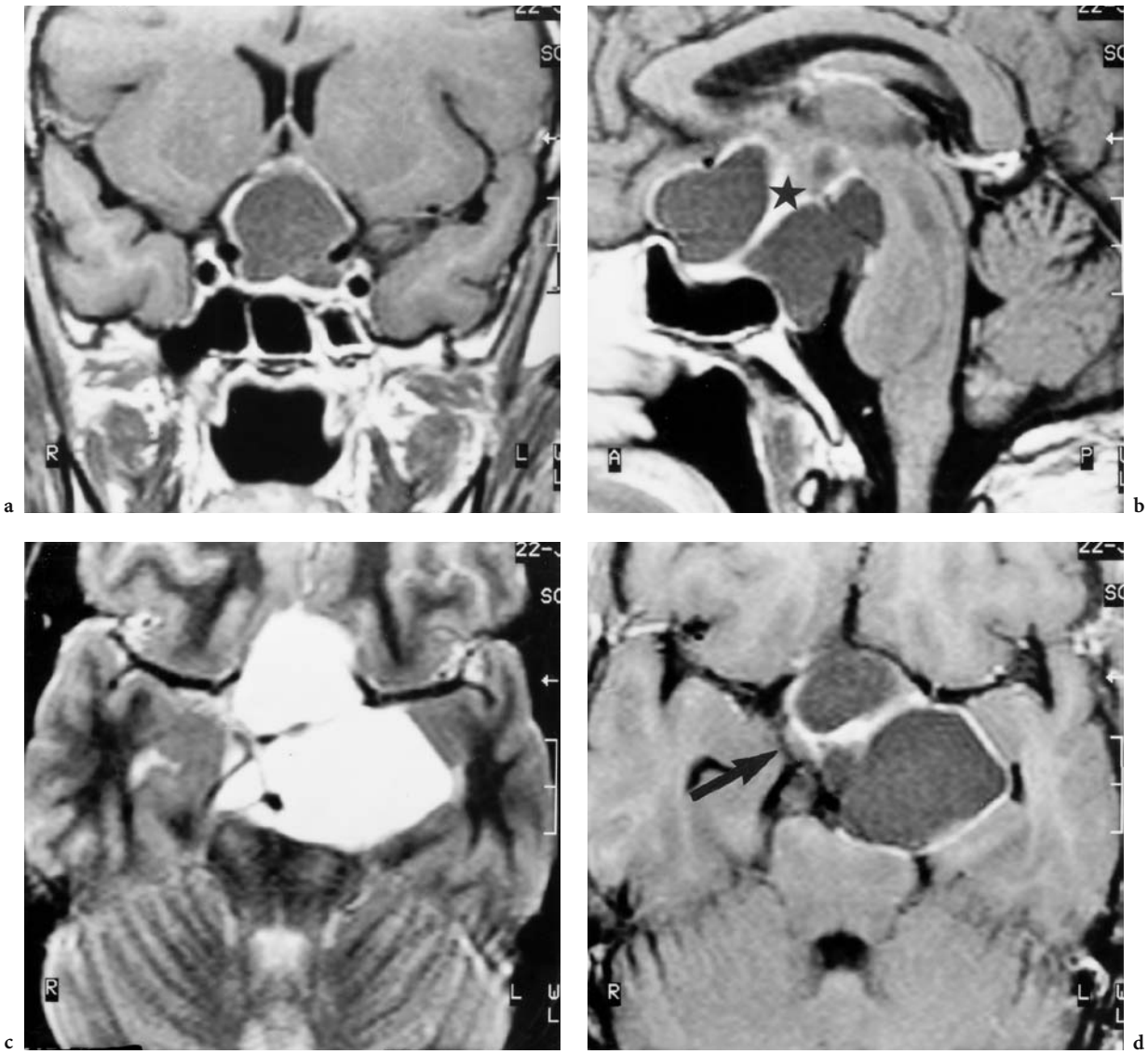

Fig. 7.36a–d. A 36-year-old man with visual deficit (finger counting) of the right eye, detected during routine control. Diagnosis: craniopharyngioma. MRI: **a** Coronal, T1-weighted, contrast-enhanced image with caudal depression of the third ventricle by the predominantly suprasellar, cystic tumor. The contrast-enhanced capsule is visualized, while the chiasm is not seen. **b** Midsagittal view with differentiation of the pituitary stalk (*star*). Note the depression, dislocation, and deformation of the brainstem. **c** Axial T2-weighted image demonstrating the high proton content (high signal) of the oily fluid content of the cystic tumor region. Note the deformed brainstem. **d** Corresponding T1-weighted, contrast-enhanced image where a remnant of the chiasm (confirmed on operation) is seen at the medial right tumor surface (*arrow*). (From Müller-Forell and Lieb 1995)

ance in the cyst walls (Fig. 7.37). Papillary craniopharyngiomas with more solid structures are found more frequently in adult patients (Zülch 1986; Kleihues et al. 1993; Giangaspero et al. 1997; Janzer et al. 2000; Sartoretti-Schefer et al. 1997).

The most frequent symptoms include headache, nausea, vomiting, and papilledema, as a result of blockage of the interventricular foramen and a subsequent increase in intracranial pressure due to occlusive hydrocephalus. The clinical symptomatology is characterized by endocrine deficiencies (diabetes insipidus, dwarfism, delayed puberty) in up to 87% of patients, predominantly in children. Visual disturbances following compression of the optic structures are more frequently in adults (Fig. 7.38) than in children, although they occur in up to 84% of patients, often with suprasellar extension (Kucharczyk et al. 1996; Sartoretti-Schefer et al. 1997).

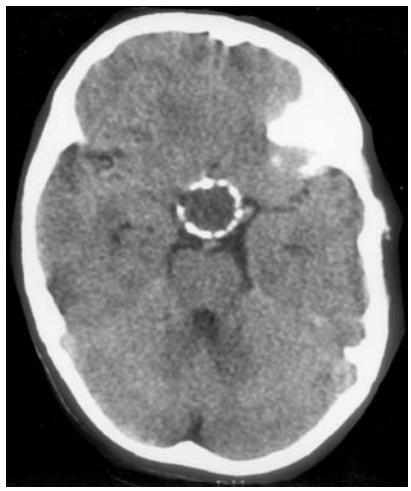

a

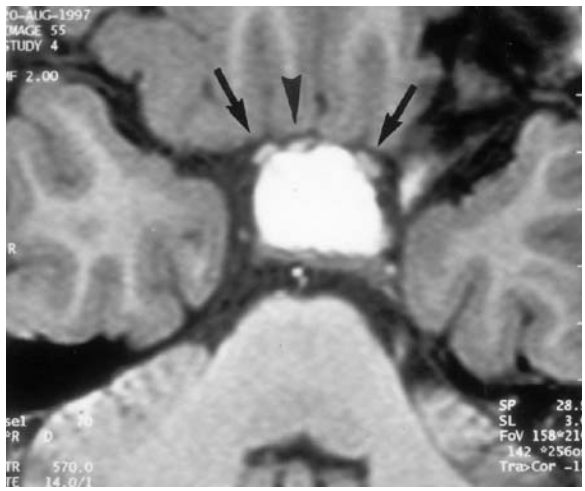

b

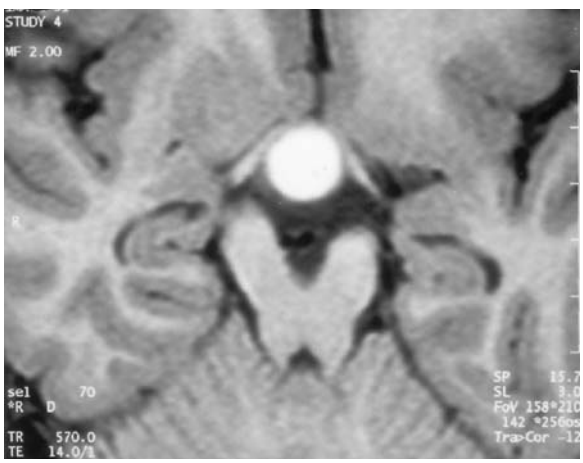

c

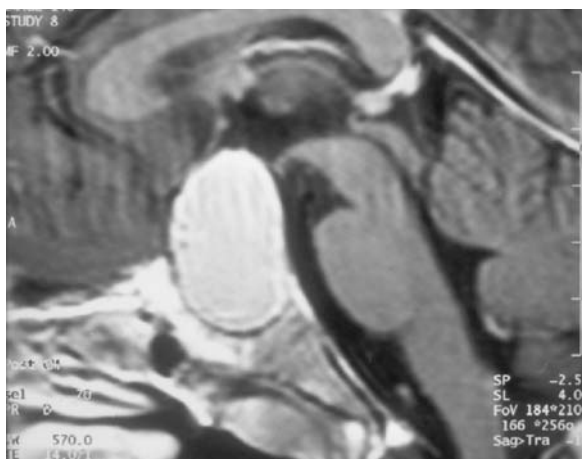

d

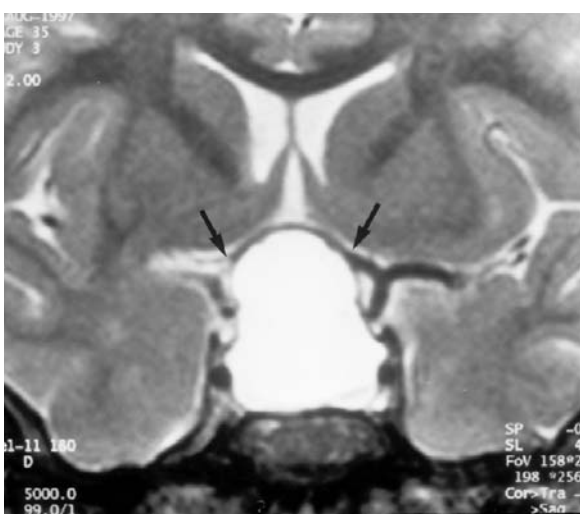

e

Fig. 7.37a–e. A 3-year-old boy with recurrent headache, leading to imaging, no neuro-ophthalmologic deficit. Diagnosis: craniopharyngioma. CT: **a** Axial native view with suprasellar mass armored by a ring-shaped calcification. MRI: **b** Corresponding T1-weighted native view showing a markedly homogeneous, hyperintense intrasellar mass. Both prechiasmal optic nerves (*arrows*) and the pituitary stalk (*arrowhead*) are identified at the anterior circumference of the tumor. **c** Axial T1-weighted native view at the level of the chiasm, which is expanded by the postchiasmal hyperintense upper tumor part. **d** Midsagittal, T1-weighted, contrast-enhanced view with demonstration of the entire (nonenhancing) retroinfundibular tumor, depressing the floor of the third ventricle. **e** Coronal T2-weighted view with depression of the chiasm, visualized as a thin structure at the top of the cystic tumor formation, less hypointense than the left A1 segment of the ACA (*arrows* indicate the width of the elongated chiasm). Note as well the higher signal of the cystic tumor compared with CSF. (CT image with permission of Dr. Brunier, Darmstadt)

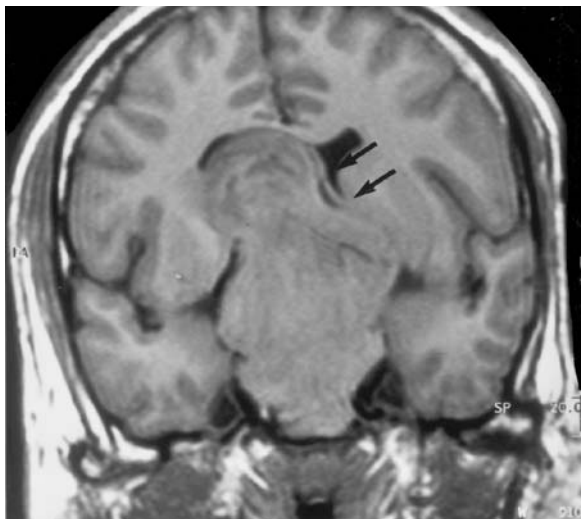

a

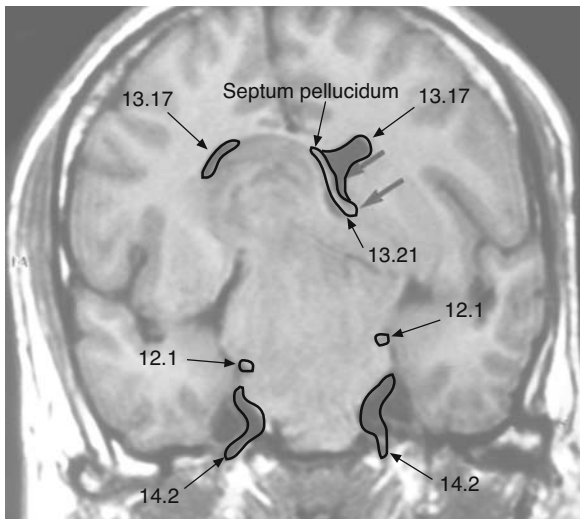

b

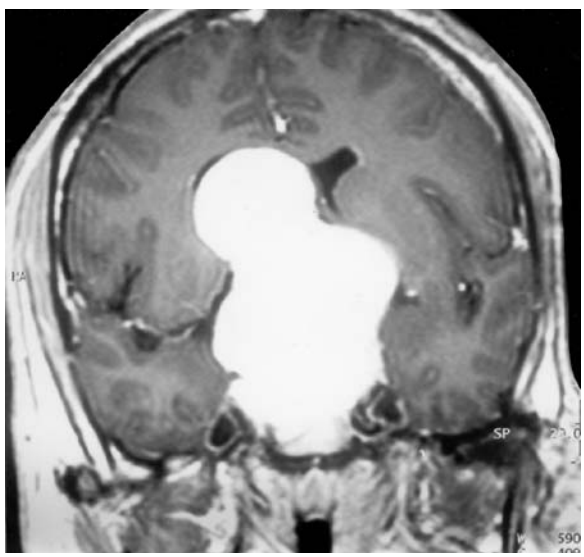

c

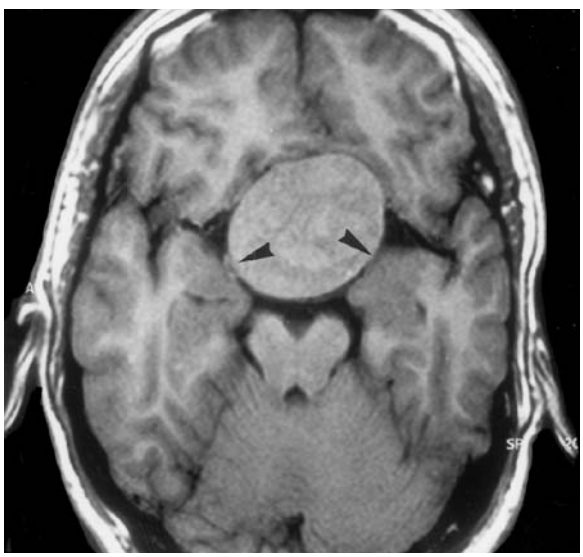

d ▷

Imaging Characteristics. CT in the axial and coronal views is still justified for the basic and differential diagnosis of craniopharyngiomas, in view of the characteristic calcification of parts of the tumor seen in 50%–70% of cases (Fig. 7.37). Even in the absence of calcification, the solid tumor parts appear hyperdense with prominent contrast enhancement, whereas the cysts seem isodense to CSF and may show enhancement of the wall (Holland et al. 1985; Kazner et al. 1989). MRI enables superior delineation of the tumor extent, especially on the coronal and sagittal views (Figs. 7.36, 7.38). Morphology and signal patterns are marked by great variety: adamantinous craniopharyngioma primarily shows a combination of T1-weighted hypointense and T2-weighted massive hyperintense signal character (Figs. 7.35, 7.37), whereas in papillary craniopharyn-gioma, a hyperintense signal on T1-weighted and hypointensities on T2-weighted sequences may dominate (Sartoretti-Schefer et al. 1997). The solid tumor parts of both types generally show a hyperintense signal on T1-weighted images and prominent enhancement of the tumor and cyst wall (Figs. 7.35, 7.36) (Kucharczyk et al. 1996).

The differential diagnosis should include cystic pituitary adenomas (Figs. 7.12, 7.16), gliomas of the optic chiasm or hypothalamus (Fig. 7.39), Rathke's pouch cyst, epidermoid and dermoid, germinomas of the third ventricle, and suprasellar meningiomas (Sartor 1992; Osborn 1994a).

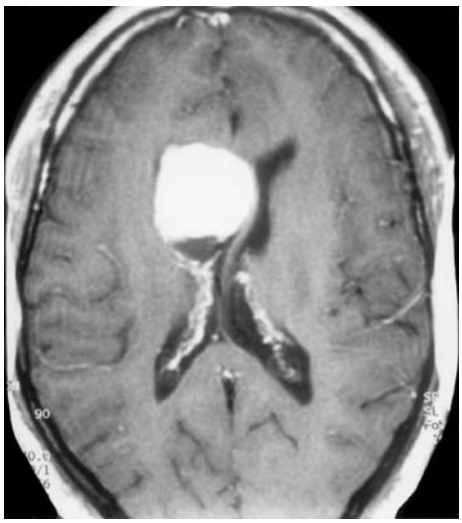

e

Fig. 7.38a–g. A 46-year-old North African man with total blindness persisting for several years. Diagnosis: suspected craniopharyngioma (patient refused operation). T1-weighted MRI: **a** Coronal native view demonstrating the extremely large suprasellar extension of a simultaneously intrasellar homogeneous tumor with dislocation of the right ventricle and extreme extension of the septum pellucidum (*small arrows*). **b** Corresponding diagram: 12.1 = prechiasmatic optic nerve, 13.17 = ventricles, 13.21 = third ventricle, 14.2 = ICA. **c** Corresponding contrast-enhanced view with homogeneous enhancement. **d** Axial native view at the level of the basal cisterns. Note the small structures (*arrowheads*) at the posterior lateral circumference of the tumor, possibly corresponding to the extended optic nerves. **e** Axial contrast-enhanced view at the level of the sella media, showing a small cystic part of the assumed intraventricular region of the tumor. **f** Midsagittal contrast-enhanced image where differentiation of an intact, but flattened sellar diaphragm supports the suspected diagnosis. Note the small, flattened, nonenhanced neural structure anterior to Monro's foramen, corresponding to the suspected, dislocated chiasm. **g** Corresponding diagram: 3.5 = clivus, 12.2 = chiasm,13.7 = corpus callosum, 13.11 = pituitary gland

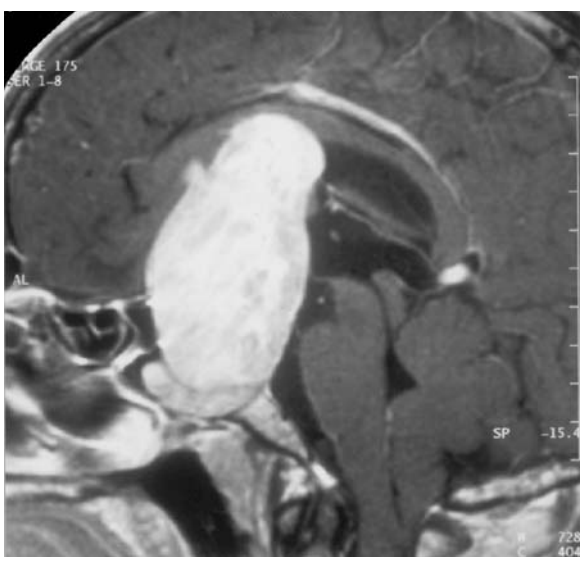

f

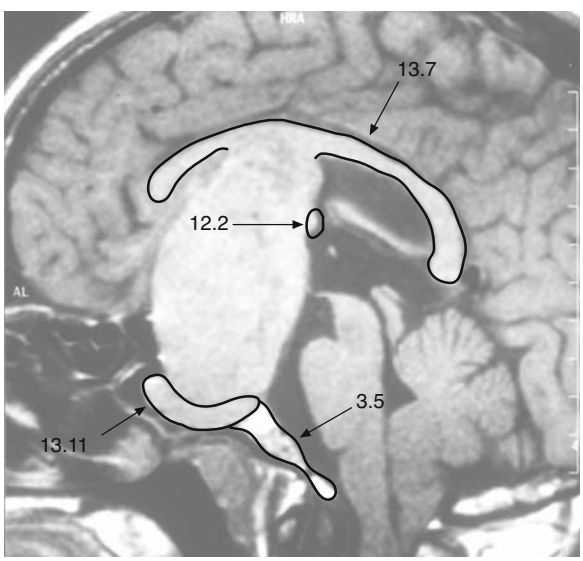

g

7.2.1.5 Astrocytomas

Astrocytic tumors, arising from differentiated, neoplastically transformed astrocytes, represent the most frequent entity of primary brain tumors with up to 60% of all intracranial neoplasms and comprise a wide range of age and gender distribution, growth potential, extent of invasiveness, morphological features, tendency for progression, and clinical course (Okazaki 1989; Cavanee et al. 2000). Astrocytomas primarily manifest in adults and may arise at any site of the CNS, exhibiting a wide range of histopathological features and biological behavior. Astrocytomas include, e.g., pilocytic and subependymal giant cell astrocytoma (both WHO I), diffuse low grade astrocytoma (WHO II), anaplastic astrocytoma (WHO III), and glioblastoma (WHO IV). These different entities reflect the type and sequences of genetic alterations acquired during the process of transformation, where the progression from low grade to anaplastic astrocytomas and glioblastomas is associated with the cumulative acquisition of multiple genetic alterations (Cavanee et al. 2000). All astrocytomas are characterized by more or less localized or diffuse infiltration of the adjacent or distant brain parenchyma and may have an inherent tendency for malignant progression, with glioblastoma as the most malignant phenotypic endpoint (Burger et al. 2000; Cavanee et al. 2000; Kleihues et al. 2000a,b).

Fig. 7.39a–g. A 5-year-old boy with known NF 1, presenting with cachexia in the absence of ophthalmological symptoms. Diagnosis: hypothalamic astrocytoma. MRI: **a** Axial T2-weighted view at the level of the chiasm with homogeneous signal enhancement of a well-defined suprasellar retrochiasmal tumor. **b** Axial, T1-weighted, contrast-enhanced view (different tilt) with distinct identification of the central cystic features of the tumor (*white arrows* indicate the optic tracts). **c** Corresponding diagram: 12.3 = optic tract, 13.19 = temporal horn, 14.8 = ACA. **d** Paramedian sagittal, T1-weighted, contrast-enhanced view showing the entire craniocaudal extension of the exclusively suprasellar, hypothalamic lesion. Note the small pituitary gland and pituitary stalk. **e** Corresponding diagram presenting the axis of the demonstrated figures **a**, **b**, **f**: 3.5 = clivus, 12.2 = chiasm, 13.11 = pituitary gland. **f** Coronal, T1-weighted, contrast-enhanced image at the level of the compressed pituitary stalk, demonstrating expansion of the astrocytoma between the proximal optic tracts (*white arrows*). **g** Corresponding diagram: 12.3 = optic tract, 13.11 = pituitary gland, 13.12 = pituitary stalk

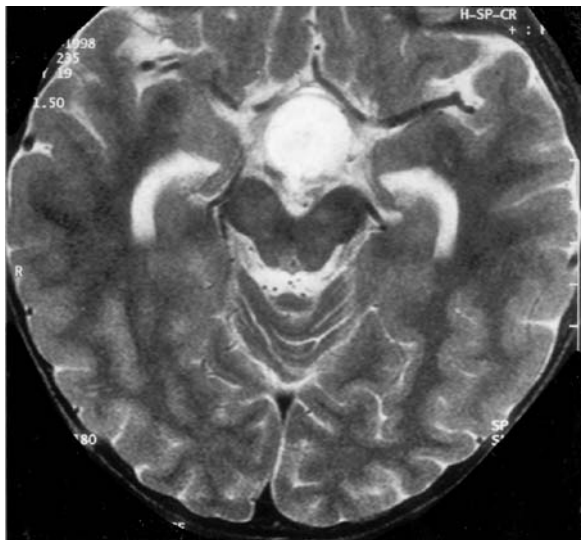

a

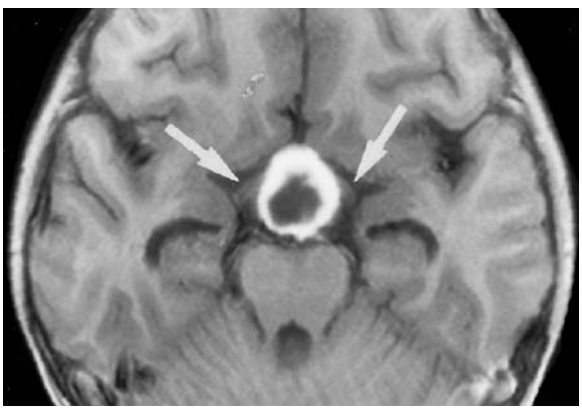

b

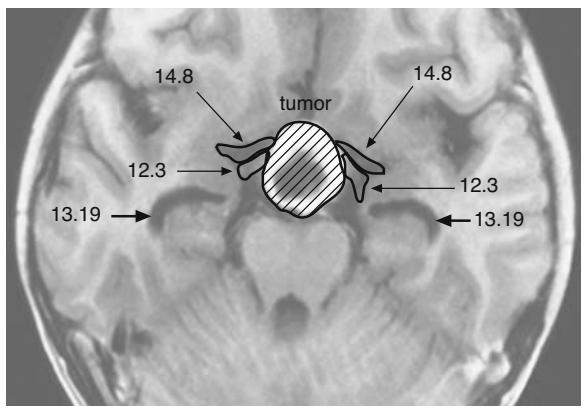

c

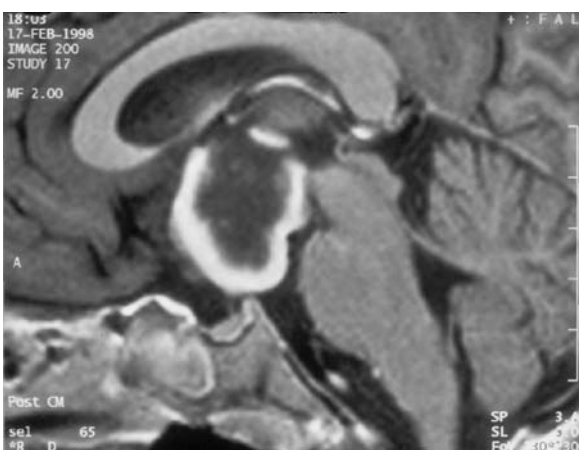

d

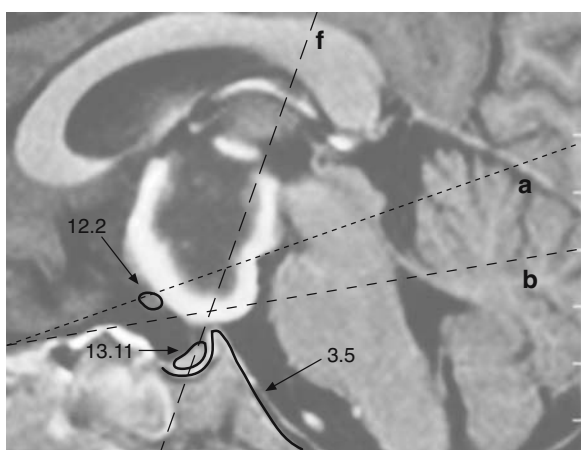

e

7.2.1.5.1
Pilocytic Astrocytoma (WHO I)

Pilocytic astrocytomas (WHO I) should be differentiated from diffuse growing astrocytomas as they are more circumscribed, slow-growing lesions with different location, morphology, genetic profile, and clinical behavior (Burger et al. 2000). Pilocytic astrocytoma typically presents in the first two decades with no clear gender predilection. Although they arise throughout the neuroaxis, the preferred sites are the optic nerve and chiasm (Fig. 7.40) and/or hypothalamus (Fig. 7.4), sometimes associated with clinical diagnosis of NF type 1 (Aoki et al. 1989) (Figs. 7.41). Tumors in the hypothalamic location do not readily allow the definition of the site of origin as they are often large entities with intraventricular extension (Hoyt and Baghdassarian 1969; Dutton 1994; Burger et al. 2000) and, although histologically benign, may show CSF seeding (Fig. 7.6), an unfavorable prediction (Perilongo et al. 1997). Clinical presentation of diencephalic pilocytic astrocytoma may be unassociated with visual symptoms in early cases, but in advanced cases hydrocephalus and hypothalamic dysfunction is apparent (Rodriguez et al. 1990; Perilongo et al. 1997; Burger et al. 2000).

7.2.1.5.2
Subependymal Giant Cell Astrocytoma (WHO I)

Subependymal giant cell astrocytoma (WHO I) are benign, slowly growing, often calcified tumors, typically arising from the wall of the lateral ventricles, composed of large ganglioid astrocytes and found only in patients suffering from tuberous sclerosis complex. Tuberous sclerosis complex is one disorder out of the group of phakomatosis (neurocutaneous syndromes) and comprises a group of autosomal dominant disorders characterized by hamartomas and benign neoplastic lesions, affecting the CNS as well as nonneural tissue organ systems with an approximate incidence of 1:10,000 (Elster 1992) with preference for the skin, where facial angiofibromas (adenoma sebaceum) (Wiestler et al. 2000b) allow a diagnosis at first glance.

Clinical presentation is characterized by a triad of tuberous facial nevus (adenoma sebaceum), seizures, and mental retardation (Gomez 1988). The CNS findings include cortical hamartomas (tubers), white matter lesions, subependymal nodules, and subependymal giant cell astrocytoma (Braffman et al. 1992). Cortical hamartomas are found in about 80% of the patients and tend to calcify with age (Kingsley et al. 1986); white matter lesions include among others straight to curvilinear bands that extend from the ventricle to the cortex and represent disorganized, dysplastic white matter foci (Iwazaki et al. 1990). Subependymal hamartomas, mostly near the caudate nucleus, are found in about 95% of patients with tuberous sclerosis, presenting calcified on CT and with variable signal character on MRI, where they appear as irregular nodules jutting into the CSF-filled ventricle (Fig. 7.42) (Osborn and Rauschning 1994). Subependymal giant cell astrocytomas, found in about 15% of patients with tuberous sclerosis, are often calcified, contrast-enhancing lesions adjacent to the foramen of Monro, often causing an associated obstructive hydrocephalus (Fig. 7.42) (Braffman et al. 1992; Osborn and Rauschning 1994).

7.2.1.5.3
High Grade Glioma

Diffuse astrocytoma (WHO II) is characterized by a high degree of cellular differentiation, slow growth, and diffuse infiltration of the adjacent brain

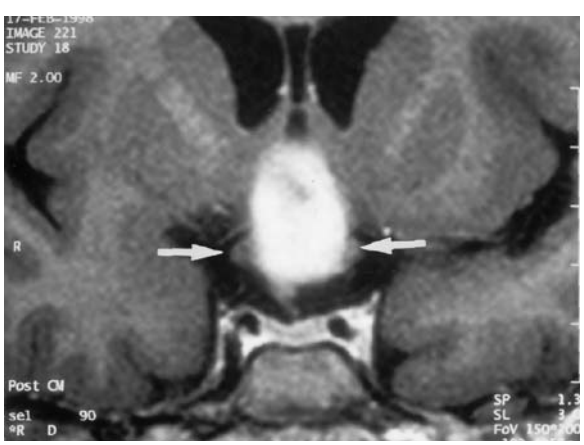

f

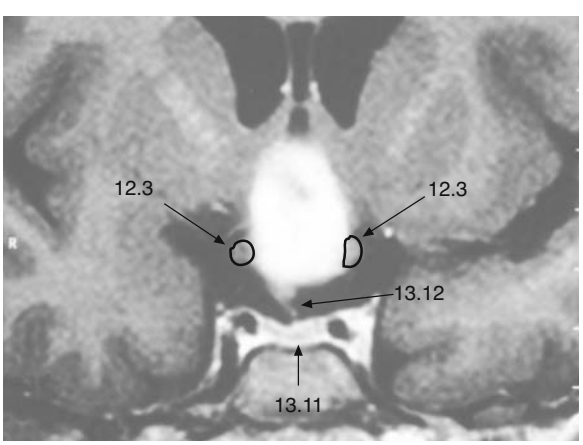

g

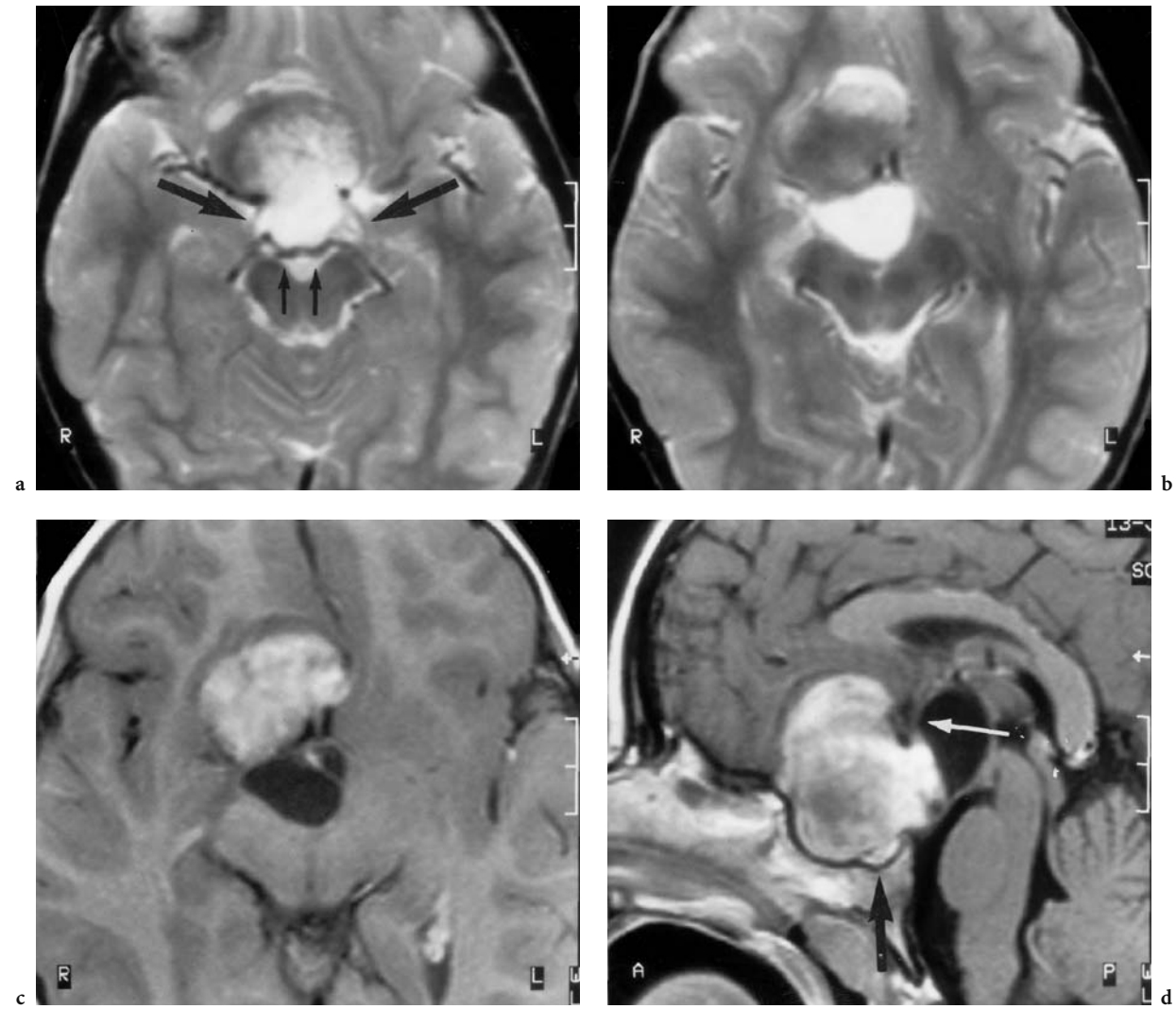

Fig. 7.40a–d. A 3-year-old boy with a visual deficit on the right side and initial right optic nerve atrophy (on ophthalmoscopy). Diagnosis: glioma (astrocytoma) of the optic chiasm. MRI: **a** Axial T2-weighted view at the level of the chiasm, demonstrating a dumbbell-shaped tumor with a predominantly high signal intensity, extending to the suprasellar cistern and expanding the vessels of Willis' circle and both optic tracts (*arrows*). Note the impression of both mammillary bodies (*small arrows*). **b** The next slice shows an additional dorsal tumor cyst. Note the absence of perifocal edema. **c** Corresponding T1-weighted, contrast-enhanced view, showing enhancement of the solid tumor part. **d** Midsagittal, T1-weighted, contrast-enhanced view demonstrating the cystic tumor region posterior and the solid tumor region anterior to the pituitary stalk (*white arrow*). Note substantial enlargement of the sellar configuration, but an intact diaphragm, and normal pituitary gland (*black arrow*)

Fig. 7.41a–d. A 9-year-old boy with known NF1, presenting with left N VI paresis and right-sided papilledema. Diagnosis: ▷ pilocystic astrocytoma of the hypothalamus. MRI: **a** Proton-weighted axial view visualizing a partly cystic, partly solid tumor in the left hypothalamic region. Note the sickle-shaped hypointensity at the right perifocal site (*arrowheads*), representing the remainder of the third ventricle, and the extremely widened temporal horns. **b** Corresponding T1-weighted, contrast-enhanced view with bright signal enhancement of the partly necrotic solid tumor part, and the cyst with CSF-like signal intensity. **c** Coronal view with right dislocated pituitary stalk (*arrow*) and flattened pituitary gland. **d** Midsagittal T1-weighted view demonstrating craniocaudal extension of the process. The chiasm (*arrow*) is seen ventral of the solid tumor. Note that the hypointensity cranial to the lesion represents the tumor cyst, but not CSF of the third ventricle, which is apparently completely occupied by the tumor (see **a**, **b**). (**c** with permission of Müller-Forell 2001)

structures. It has a tendency for malignant progression to anaplastic astrocytoma and, ulti-mately, glioblastoma (Kleihues et al. 2000c). Most of these patients are adults (Fig. 7.9), presenting with seizures and clinical symptoms, depending on the localization.

Glioblastoma presents with histopathologic features including cellular polymorphism, nuclear atypia, brisk mitotic activity, vascular thrombosis, microvascular proliferation, and necrosis. They may develop from diffuse astrocytoma WHO III or anaplastic astrocytoma, but may manifest de novo with a short history (just weeks) of clinical symptoms of neurological deficit, headache, and personality changes (Figs. 7.43, 7.44) (Kleihues et al. 2000b). Glioblastomas account for about 60% of all astrocytomas and up to 15% of all intracranial neoplasms, representing the most frequent malignant intracranial tumor. They may manifest at any age, with a peak incidence between 45 and 70 years. The affected sites are the cerebral hemispheres; in case of multifocal independent development (Fig. 7.44), variable histological features are known (Barnard and Geddes 1987; Kleihues et al. 2000b).

Imaging Characteristics. Comparable to the analysis of clinical and neuropathological features, imaging studies of astrocytomas show variable results. Although most glial tumors arise from a segment of only one gyrus (Yasargil 1994), the affected parenchyma (usually white matter, but an involvement of gray matter is often seen) demarcates an ill-defined area, hypodense on CT. On MRI, astrocytomas mostly present as mildly hypointense on T1-weighted and hyperintense on T2-weighted, due to the fact that they represent a degenerative microcystic formation, filled with clear fluid, and an irregular, not always clearly distinguished perifocal edema (Sartor 1992; Burger and Scheithauer 1994). As BBB disruption is rare in low grade astrocytoma, it may be a factor in tumor progression of WHO II astrocytomas (Figs. 7.39, 7.40, 7.45) and can

(Text continues on p. 388)

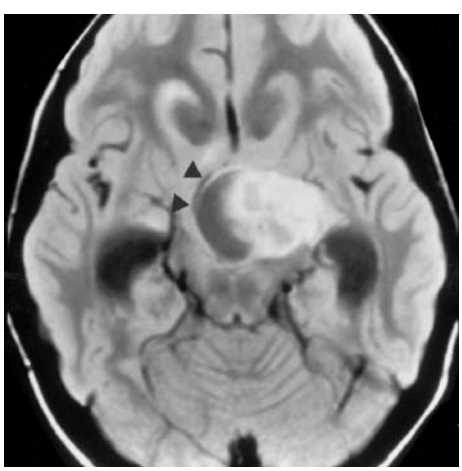

a

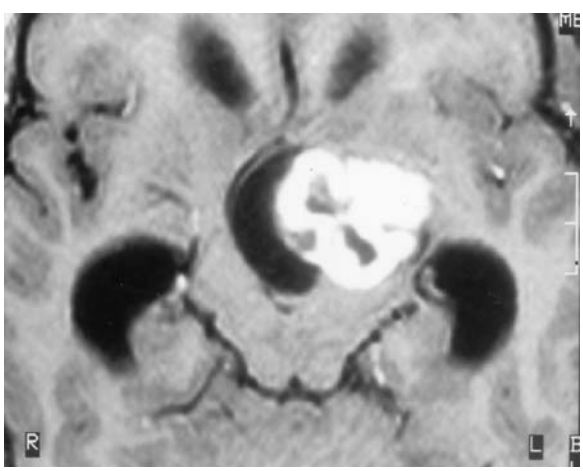

b

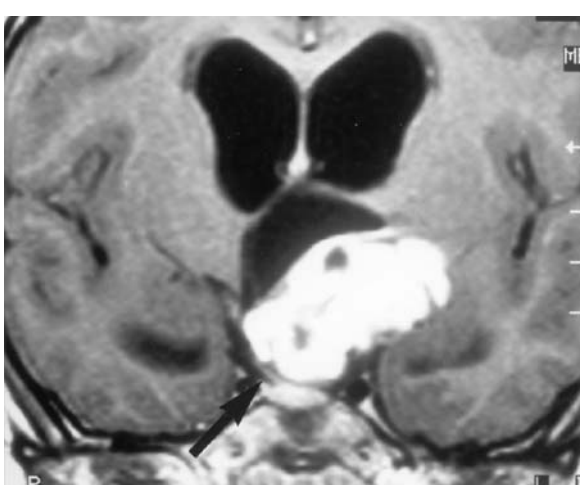

c

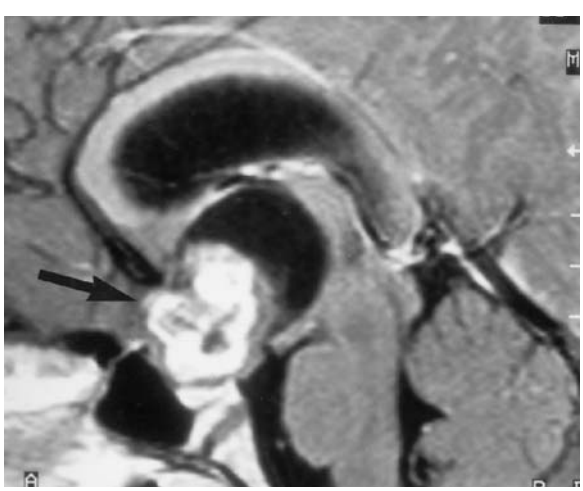

d

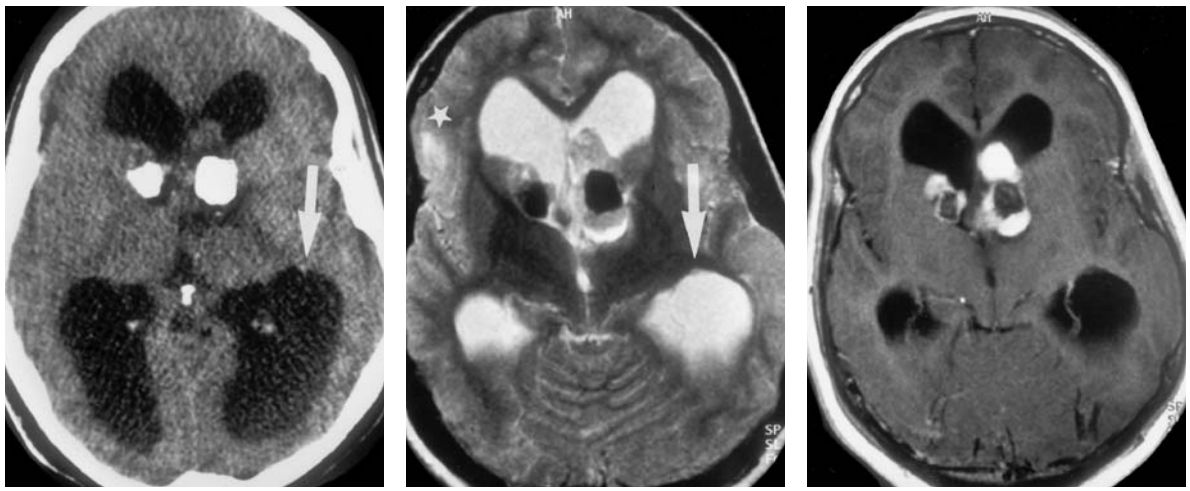

a,b c

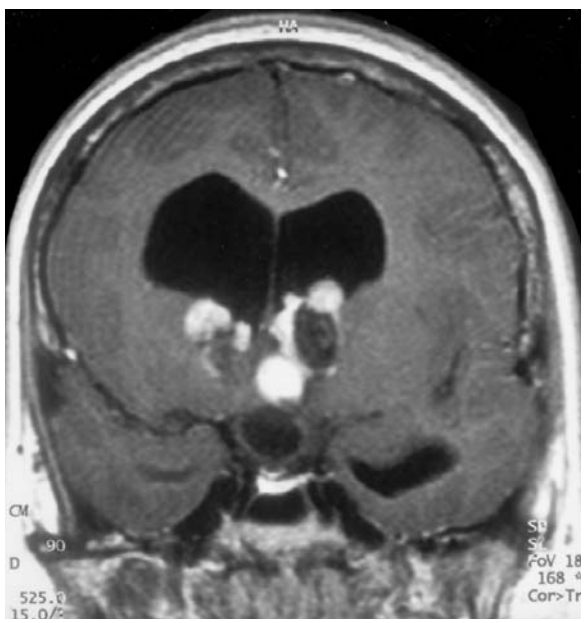

d

Fig. 7.42a–d. A 27-year-old hypophrenic woman with Bourneville's disease, who became conspicuous because of increasing clumsiness in her home environment, giving rise to suspicion of a visual deficit. Ophthalmologic examination demonstrated bilateral visual loss with only light and dark perception. Diagnosis: bilateral calcified giant-cell astrocytoma with chronic occlusive hydrocephalus associated with Bourneville's disease. CT: **a** Axial native view at the level of the intraventricular Monro's foramen, showing significant calcification of the bilateral intraforaminal tumors, occluding Monro's foramen and expanding into both frontal horns, with dominance on the left side. The *arrow* indicates a small, slightly calcified subependymal hamartoma (see also **b**). MRI: **b** Corresponding T2-weighted image where the calcification is seen as signal loss and the solid intraventricular tumor region as a slightly hyperintense mass. The *star* indicates another small (suspected) astrocytoma in the frontal (opercular) lobe. Note the small, compressed third ventricle. **c** Corresponding T1-weighted, contrast-enhanced image demonstrating increased signal enhancement of the noncalcified solid tumor regions. **d** Coronal, T1-weighted, contrast-enhanced view. No chiasm is identified (confirmed on surgery), while a cystic region of the tumor occupies the entire suprasellar cistern

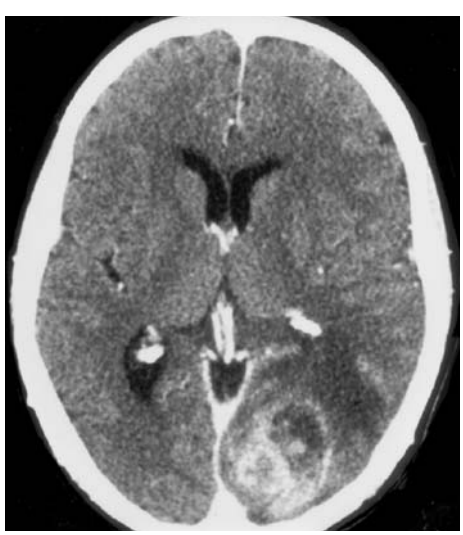

Fig. 7.43. Contrast-enhanced CT of a 62-year-old woman with nonspecific blurred vision and hemianopia to the right. Diagnosis: glioblastoma of the left occipital lobe

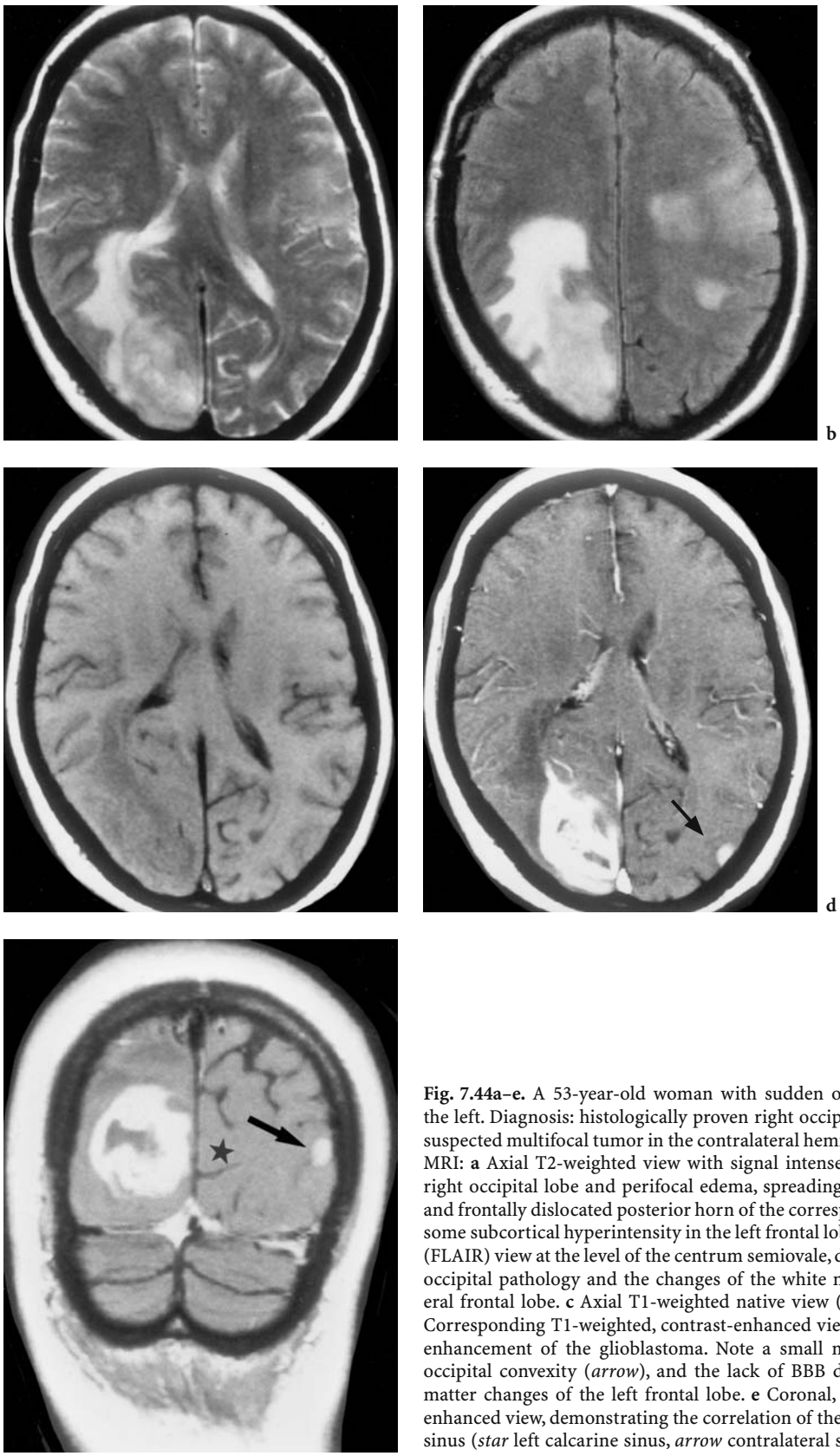

Fig. 7.44a–e. A 53-year-old woman with sudden onset of hemianopia to the left. Diagnosis: histologically proven right occipital glioblastoma [with suspected multifocal tumor in the contralateral hemisphere (no histology)]. MRI: **a** Axial T2-weighted view with signal intense solid structure in the right occipital lobe and perifocal edema, spreading along the compressed and frontally dislocated posterior horn of the corresponding ventricle. Note some subcortical hyperintensity in the left frontal lobe. **b** Axial T2-weighted (FLAIR) view at the level of the centrum semiovale, demonstrating the right occipital pathology and the changes of the white matter of the contralateral frontal lobe. **c** Axial T1-weighted native view (corresponding to **a**). **d** Corresponding T1-weighted, contrast-enhanced view with irregular signal enhancement of the glioblastoma. Note a small meningioma at the left occipital convexity (*arrow*), and the lack of BBB disruption in the white matter changes of the left frontal lobe. **e** Coronal, T1-weighted, contrast-enhanced view, demonstrating the correlation of the tumor to the calcarine sinus (*star* left calcarine sinus, *arrow* contralateral small meningioma)

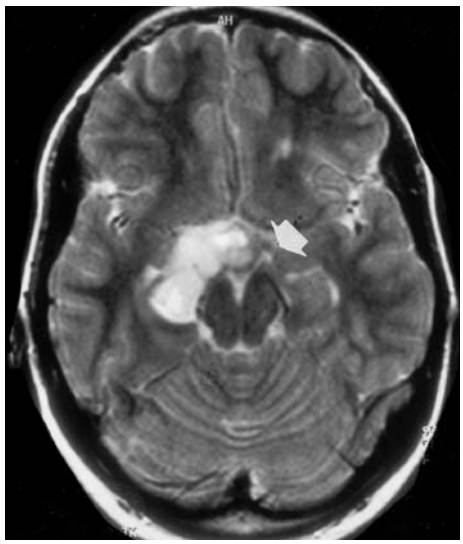
a

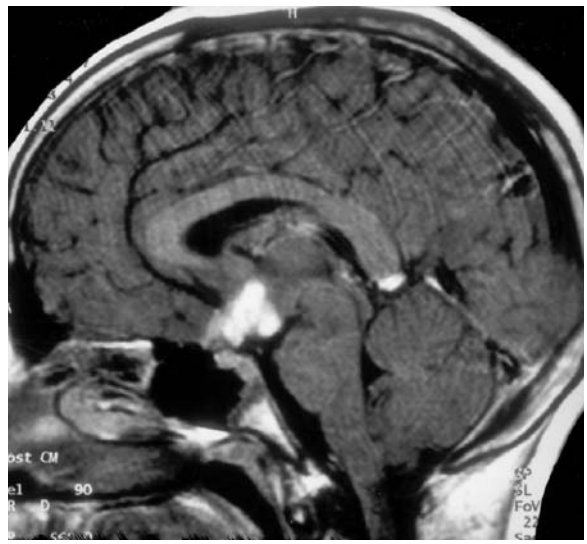
d

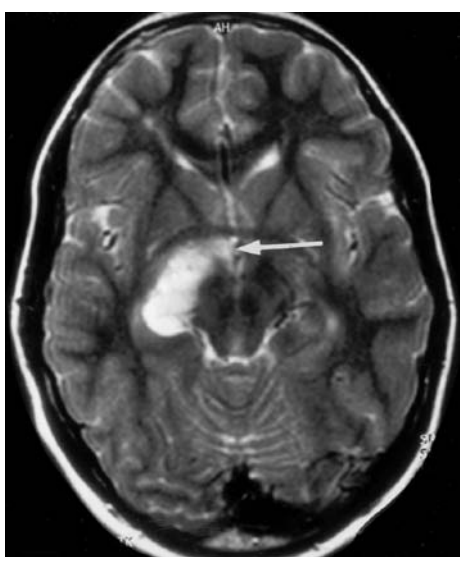
b

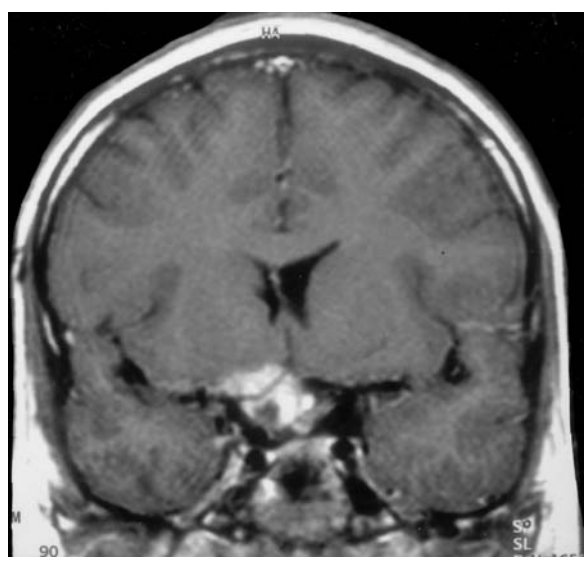
e

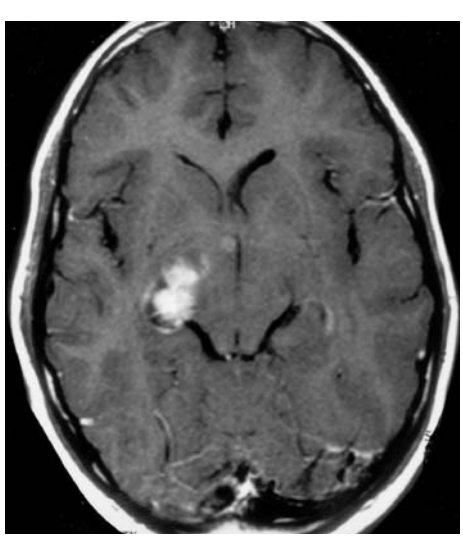
c

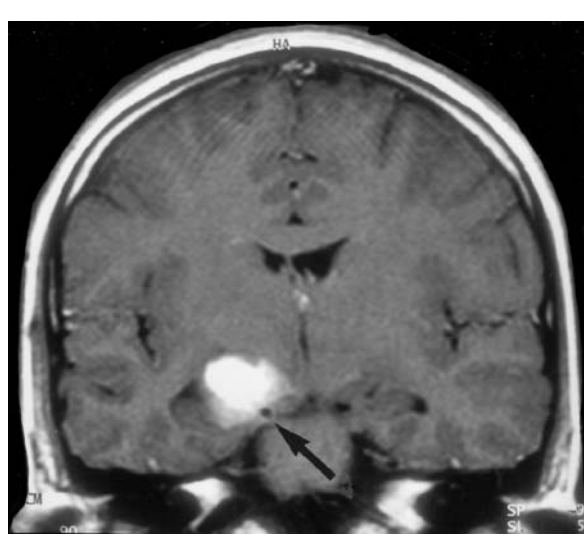
f ▷

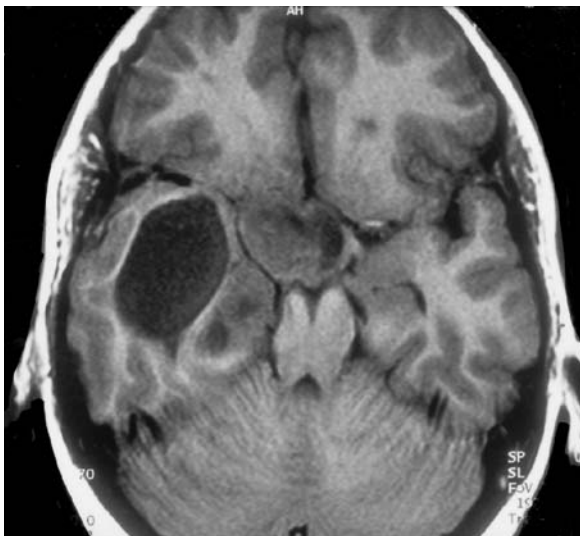

g

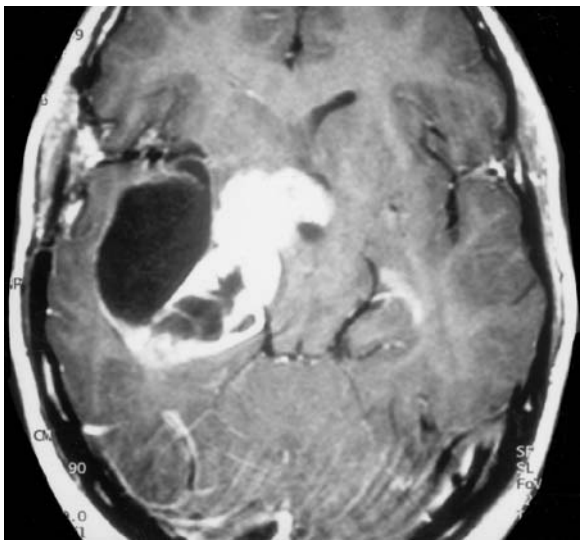

h

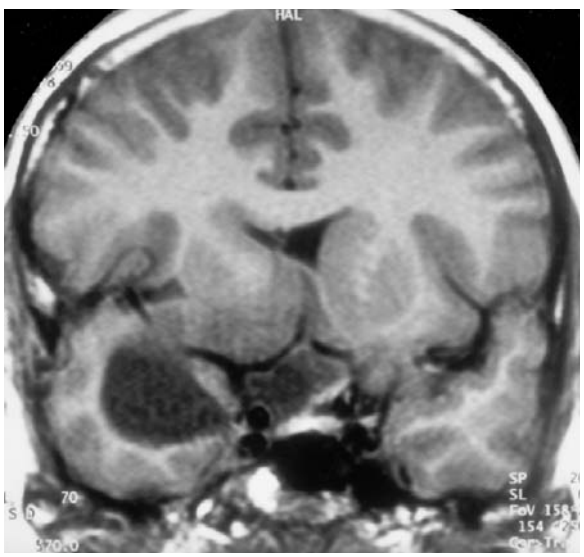

i

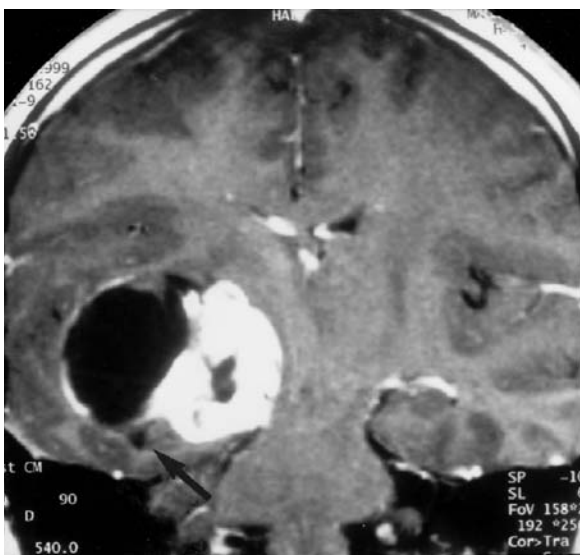

k

Fig. 7.45a–k. A 10-year-old boy with headache persisting for 6 weeks and double vision for 2 days; bitemporal hemianopia representing the only neurologic deficit. Diagnosis: astrocytoma (WHO II) of the optic tract, state after ventriculoperitoneal shunt. MRI: **a** Axial T2-weighted view, demonstrating tumor growth from the right chiasm and hypothalamus along the right optic tract to the lateral geniculate nucleus. Note the lack of infiltration of the left optic tract, visualized as a hypointense structure (*white arrow*). **b** Axial T2-weighted image at the level of the anterior commissure with distinct definition of the left optic tract on its way to the lateral geniculate nucleus. Note (as in **a**) compression of the right mesial temporal lobe as well as infiltration of the ipsilateral anterior thalamus (*white arrow*). **c** Axial, T1-weighted, contrast-enhanced image, corresponding image to **b**, showing signal enhancement in the distal part of the tumor as well as in the thalamus. **d** Midsagittal, T1-weighted, contrast-enhanced image demonstrating infiltration of the entire chiasm, hypothalamus, and the anterior part of the third ventricle (linea terminalis). **e** Coronal T1-weighted contrast-enhanced view at the level of the chiasm, demonstrating lateralization of the tumor growth. **f** Coronal T1-weighted view at the level of the optic tract. Note the compression of the right basal vein (*arrow*). The boy presented for imaging check-up 1.5 years after the initial investigation and additional surgery. Although he did not exhibit new deficits and reported feeling well, an extremely large tumor was visualized. MRI: **g** Axial T1-weighted native view at the level of the chiasm (compare with **a**) with distinct infiltration of the chiasm and the mesial temporal lobe, accompanied by a lateral tumor cyst. **h** Axial, T1-weighted, contrast-enhanced image (compare with **b**, **c**) showing the thalamic area of the tumor impinging on the tumor in the optic tract. Note the space-occupying effect with compression of the brainstem (see also **g**). **i** Coronal T1-weighted native view (compare with **e**) demonstrating progressing compression of the chiasm and inferior enlargement to the sellar diaphragm. **k** Coronal, T1-weighted, contrast-enhanced view at the level of the midbrain (compare with **f**) showing the entire extension of the recurrent tumor with compression of the temporal horn of the right ventricle (*arrow*) and an initial midline shift

be assumed in high grade glioblastoma (Figs. 7.8, 7.44) (Russell and Rubinstein 1989; Zülch 1986; Osborn and Rauschning 1994; Atlas 1996).

7.2.1.6 Aneurysms

The classification of intracranial aneurysms can be made morphologically into saccular and nonsaccular aneurysms. Another differentiation is based on a specific etiology as, e.g., congenital degenerative, traumatic, dissecting, infectious, or flow-related aneurysms (in the territory of feeding arteries in cerebral arteriovenous malformations, AVM) (Stehbens 1995; Byrne and Guglielmi 1998). Endothelial dysfunction as the underlying pathological instability has been recognized as the basic pathology (Stehbens 1972, 1995). The actual incidence of intracranial aneurysms is unknown, since published data vary according to the definition of an aneurysm and whether the study is based on autopsy findings, clinical data, or angiographic studies. The estimated incidence rates may thus be too low as a result of incomplete ascertainment caused by the failure to recognize the presence of an aneurysm (Osborn and Rauschning 1994; Byrne and Guglielmi 1998). The rupture of an intracranial aneurysm is the most common atraumatic cause of subarachnoid hemor-rhage (SAH), presenting with a sudden onset of headache, varying loss of consciousness, vomiting, seizure, confusion, and focal neurologic deficits (Fig. 7.46) (Yoshimoto et al. 1979; Adams et al. 1980; Juvela et al. 1993). In view of a high incidence of often life-threatening rebleeding (Winn et al. 1977; Kassel and Torner 1983) and/or delayed cerebral vasospasm (Weir et al. 1978; Wilkins 1988), this clinical event requires immediate, either neurosurgical or interventional neuroradiological therapy.

Saccular aneurysms are characterized by non-specific dysfunction of the arterial wall, while in fusiform aneurysms the pathologic lesion may be symmetric or asymmetric, depending on whether the respective arterial wall pathology is serpentine or tubular (Fig. 7.47). Aneurysms occur predominantly in patients older than 30 to 40 years and are associated with arteriosclerotic degeneration of the arterial wall (Hayes et al. 1967). They are characteristically located at Willis' circle or its major branches and develop at bifurcations or at the origins of branch arteries (Stehbens 1972, 1995). Some 10%–18% of unruptured aneurysms present with symptoms of mass effect (Figs. 7.47–7.51) (Raps et al. 1993; Khanna et al. 1996). Unruptured symptomatic intracranial aneurysm of the infraclinoid or supraclinoid ICA, the anterior cerebral artery, or (rarely) the basilar artery presents different clinical symptoms, depending on the site of compression of neighboring structures. Orbital, periorbital, or facial pain is the most common symptom of cavernous carotid aneurysms, followed by different types of cranial nerve palsy. Isolated N III palsy may lead to an aneurysm of the posterior communicating artery, while an aneurysm of the ICA is suspected in the presence of a combination of N VI or N IV palsy and a sensory deficit of the trigeminal nerve (Kupersmith 1993a). Neither the extent nor the clinical symptomatology of slowly progressing visual field deficits caused by aneurysms may be readily distinguished from those caused by neoplasms. Depiction of the extent of the visual deficit may fluctuate due to thrombosis and dilation of the aneurysm; in neoplasms, slowly progressive exacerbation, with the exception of hemorrhage or infarction, is typical in pituitary adenoma (Figs. 7.12, 7.13), while cyst expansion might be observed in craniopharyngioma, where acute deterioration of vision may occur (Kupersmith 1993a).

Depending on the origin and the direction of growth, compression of the optic pathway and resulting neuro-ophthalmologic symptoms are variable. Aneurysms of the ICA involving the visual pathway may be classified by their origin, arising from the cavernous (Fig. 7.49), ophthalmic (Figs. 7.46, 7.50), or distal carotid segment (Figs. 7.47, 7.48, 7.51) (Byrne and Guglielmi 1998).

1. Although only 3% of all intracranial aneurysms are found in the cavernous carotid artery segment (Krayenbühl 1973), they comprise approximately 15% of symptomatic unruptured aneu-

Fig. 7.46a–f. A 48-year-old woman with acute loss of vision in the left eye, accompanied by severe headache. Diagnosis: acute subarachnoid hemorrhage caused by an ophthalmic aneurysm of the left ICA. CT: **a** Axial image with acute subarachnoid hemorrhage of the basal cisterns and a circular target-shaped formation in the left subcallosal area. **b** 3D-CT-angiogram (left is right and vice verse) showing a lobulated aneurysm of the left ICA. DSA: **c** Lateral view of the left ICA reveals an upwardly directed, slightly lobulated aneurysm of the C5-part at the base of the ophthalmic artery origin (*arrow*). **d** Oblique view to the right. **e** Intraoperative view visualizing attenuation of the intracranial, prechiasmal region of the massively flattened left optic nerve, caused by the dome of the aneurysm. (With permission of Prof. Perneczky, Director of the Neurosurgical Clinic, University of Mainz). **f** Corresponding diagram

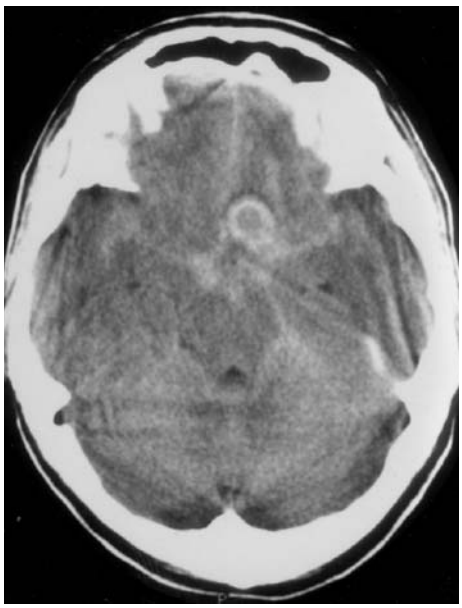

a

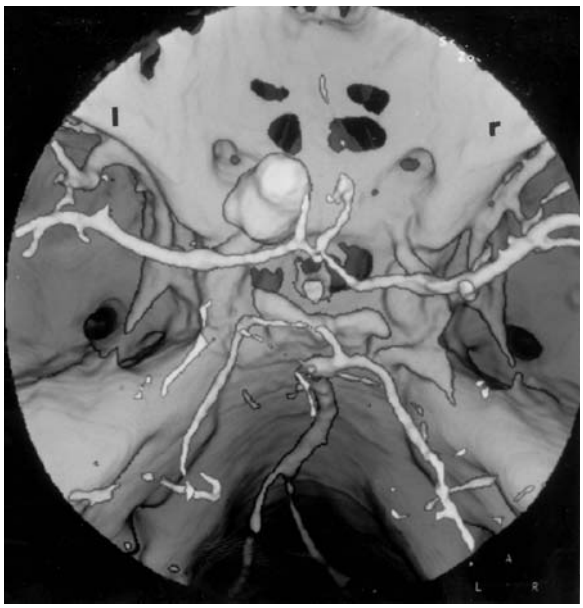

b

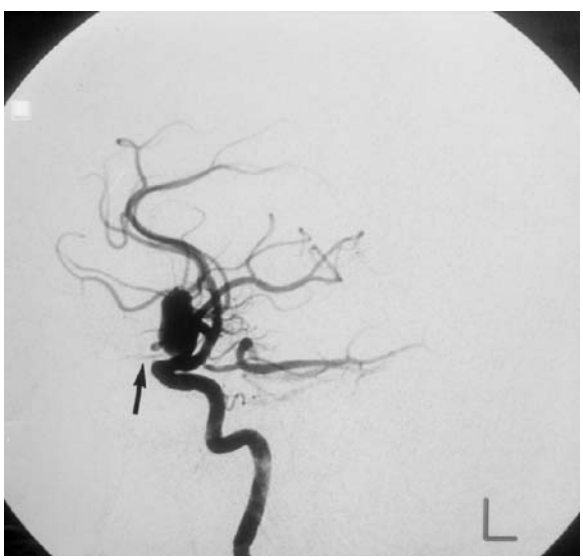

c

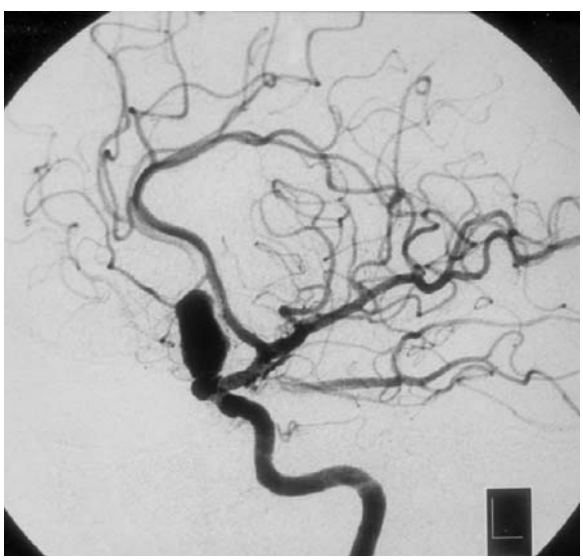

d

e

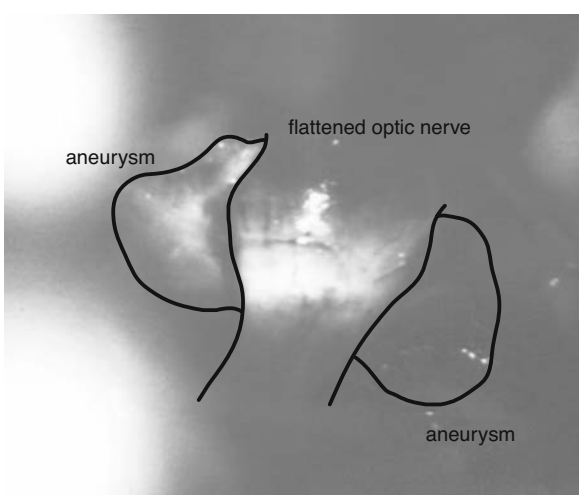

f

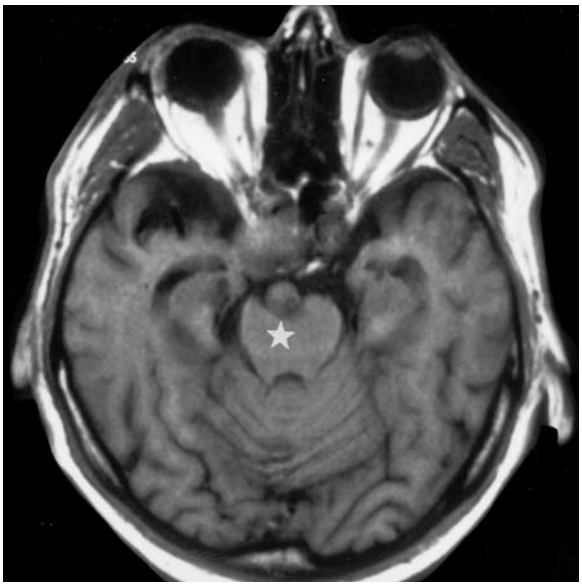

a

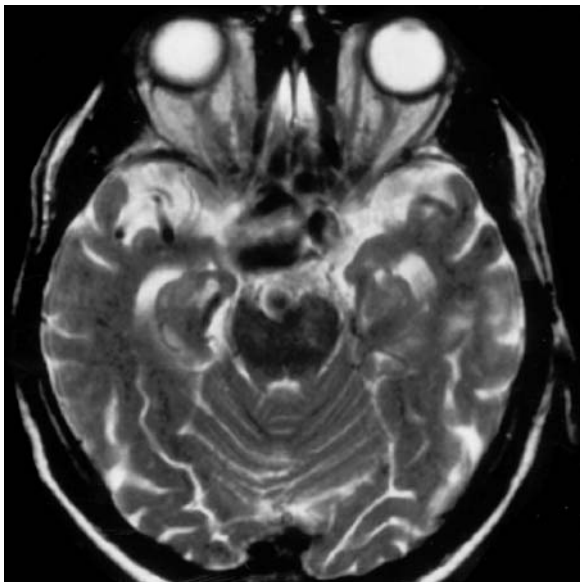

b

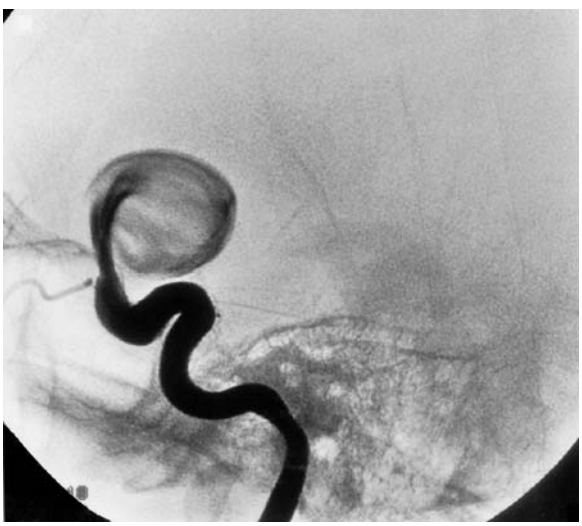

c

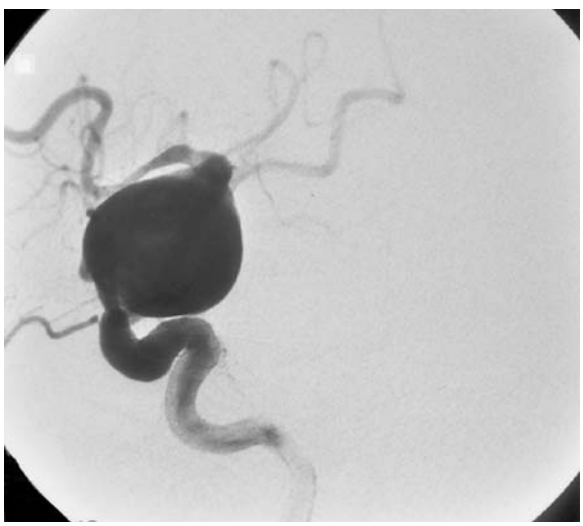

d

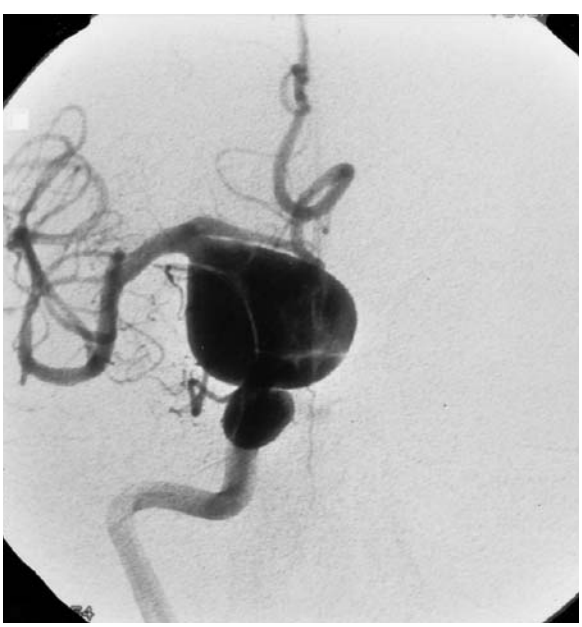

e

Fig. 7.47a–e. A 62-year-old man with progressive visual loss (amaurosis of the right, V 05.5 of the left eye), clinically not clearly apparent, because of residual aphasia and right hemiparesis after apoplexy of the left MCA 9 years previously. Diagnosis: giant aneurysm of the right ICA with a diffuse, fusiform, dilated, cerebral vascular system. MRI: **a** Axial T1-weighted native view at the level of the optic canal showing an isointense, well-defined space-occupying lesion at the right optic canal, extending to the midline. Note the isointense formation in the interpeduncular cistern corresponding to the dilated, enlarged basilar artery (*star*) with extremely slow flow (no signal void) and the right temporopolar defect, a residual of the MCA infarction. **b** Corresponding T2-weighted image with pronounced sensitivity of flow, resulting in a slight signal void of the ICA aneurysm and the basilar artery. DSA of the right ICA: **c** Lateral view demonstrating an early phase with superimposed bony structures. The supraclinoid area of the ICA opens to the inflow zone of the giant aneurysm distal to the ophthalmic artery. **d** The entire aneurysm and the ACA are opacified a few seconds later. **e** The AP view demonstrates the space-occupying effect of the aneurysm of the entire intracranial ICA with impression of the elongated A1 segment. (MRI images with permission of Drs Halbsguth and Lochner, Frankfurt/Main)

rysms (Henderson 1955) and are seen often in women over 40 years of age (Kupersmith 1993a). Because ICA aneurysms of the cavernous segment are located extradurally, subarachnoid or subdural hemorrhage is rare and seen only in intradural extension (Smith et al. 1994); however, pain and progressive unilateral cranial nerve palsy with diplopia, ptosis, blurred vision from accommodative paresis, and anesthesia of the forehead and cornea may lead to diagnostic imaging (Cogan and Mount 1963; Kupersmith et al. 1984). Signs of cavernous sinus dysfunction always precede visual loss due to extension of large aneurysms to the optic canal with optic nerve distortion. In addition, almost all patients have a complete ophthalmoplegia (Fig. 7.49) (Kupersmith 1993a).

2. Carotid ophthalmic aneurysms represent 1.5%–8% of all intracranial aneurysms (Sengupta et al. 1976; Yasargil et al. 1977), but 13% of symptomatic unruptured aneurysms (Locksley 1966). They are defined as intradural aneurysms arising from the ICA just at or above the origin of the ophthalmic artery (C5 or C6 segment), mostly from the superomedial or superior wall, and only rarely from its inferolateral or lateral wall (Drake et al. 1968; Bouthillier et al. 1996; Byrne and Guglielmi 1998; Osborn 1999). The proximity to the intracranial optic nerve is responsible for the most common clinical presentation of ipsilateral acute visual loss, whether in SAH after rupture or in unruptured aneurysms (Figs. 7.46, 7.51). Asymptomatic, even large aneurysms may be clinically tolerated for a long time, and the (sometimes unnoticed) visual loss, generally accompanied by optic nerve atrophy, is caused by chronic pulsatile compression (Fig. 7.50) (Kupersmith et al. 1984; Perneczky et al. 1999). The neuro-ophthalmological presentation of asymmetric (bilateral) visual deficits is caused by the involvement of the optic chiasm and crossing fiber compression (Ferguson and Drake 1981).
3. Distal internal carotid artery aneurysms are described according to the nearest branch artery. Aneurysms directly involving the visual pathway arise most likely from the superior hypophyseal artery with a clinical presentation similar to that of ophthalmic IAC aneurysms. As aneurysms of the PcoA predominantly cause N III palsy, large or giant aneurysms of the distal ICA at or close to the bifurcation may involve the intracranial optic nerve, the lateral chiasm, or optic tract together or individually. Accordingly, variable neuro-ophthalmological symptoms and deficits may occur from ipsilateral scotoma and quadrant-anopia (optic nerve), contralateral temporal quadrantanopia (chiasm), to homonymous hemi-anopia (optic tract).

Patients with aneurysms of the ICA bifurcation (Fig. 7.48), which have an incidence of only approximately 4% of all intracranial aneurysms, often present with headache, hemiparesis, and progressive vision loss as a result of the mass effect. Progressive optic nerve dysfunction with optic atrophy can develop from direct compression or displacement of the optic structures (Ley 1950; Kupersmith 1993a).

Imaging Characteristics. The role of CT and MRI as noninvasive methods is to confirm and define the clinical diagnosis of symptomatic aneurysms following rupture or compression symptoms, while intra-arterial angiography with digital subtraction technique (DSA) remains the preferred technique for cerebral vessels (Byrne and Guglielmi 1998). Without doubt, CT is the method of choice in acute subarachnoid hemorrhage (Fig. 7.46) and demonstrates not only the hemorrhage itself, but also the volume and distribution of the acute hemorrhage and its complication as acute CSF disturbance. As unruptured but symptomatic aneurysms are generally larger than ruptured aneurysms at the time of presentation, secondary changes, e.g., bony erosion of the sphenoid in aneurysms of the cavernous sinus or calcification in the wall (Figs. 7.49, 7.48) can be demonstrated. Partial thrombosis of the lumen may be visible, especially when comparing noncontrast CT images with those after intravenous contrast administration, where the patent portion of the lumen is distinctly hyperdense and the generally highly attenuated clot appears darker (Pinto et al. 1979). Helical scanning by CT-angiography (CTA) (Fig. 7.46) with a relatively high sensitivity for aneurysms larger than 3 mm in diameter during administration of contrast material and secondary 3D-reconstruction is a helpful tool in the acute phase (Schwartz et al. 1994).

MRI is the method of choice in visualizing the vicinity of the aneurysm and its relation to the optic pathway, due to its high sensitivity and spatial resolution, enabling the detection of flowing blood (flow void) and the multiplanar capability. In SE sequences, flowing blood appears dark on both T1- and T2-weighted images (Fig. 7.49), while aged blood (methemoglobin) in a thrombus is seen as a signal intense white area, which exhibits an onion-like, mul-

(Text continues on p. 395

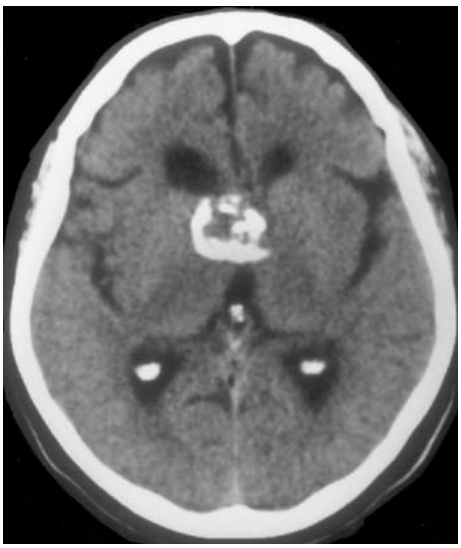

a

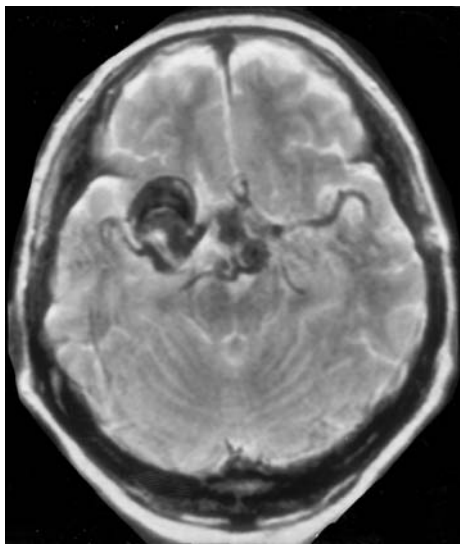

b

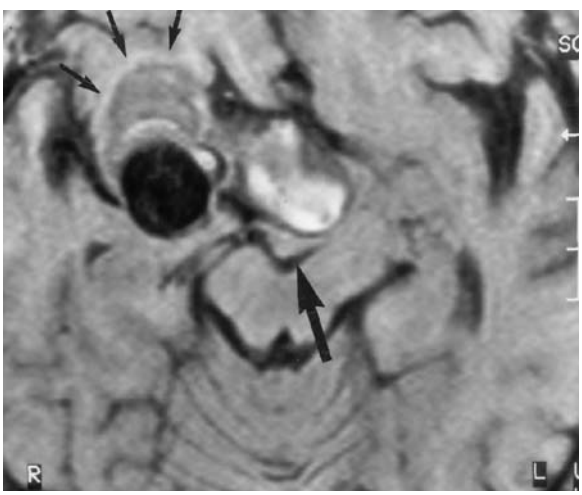

c

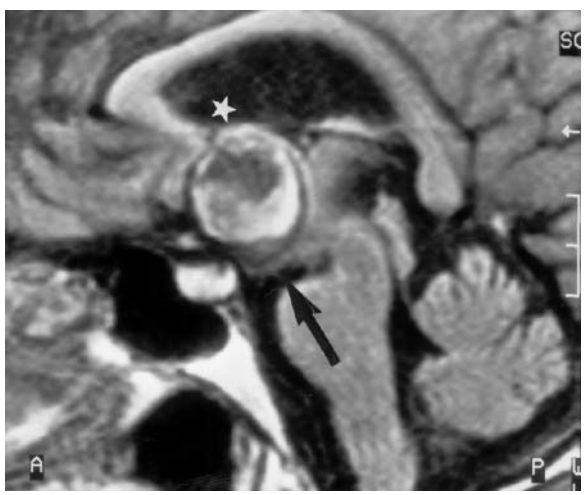

d

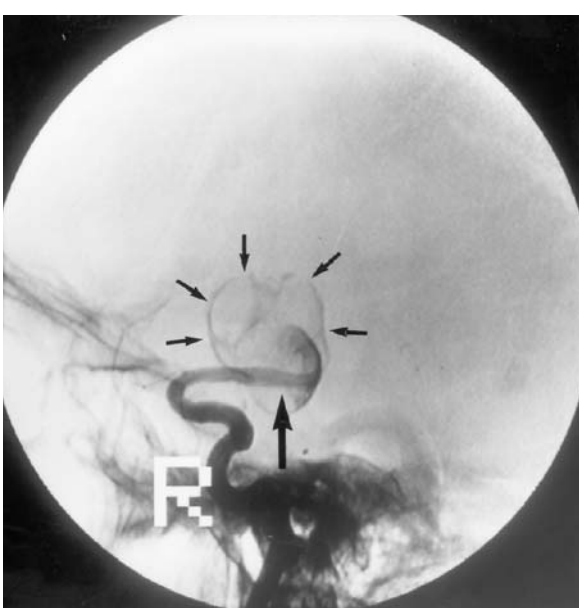

e

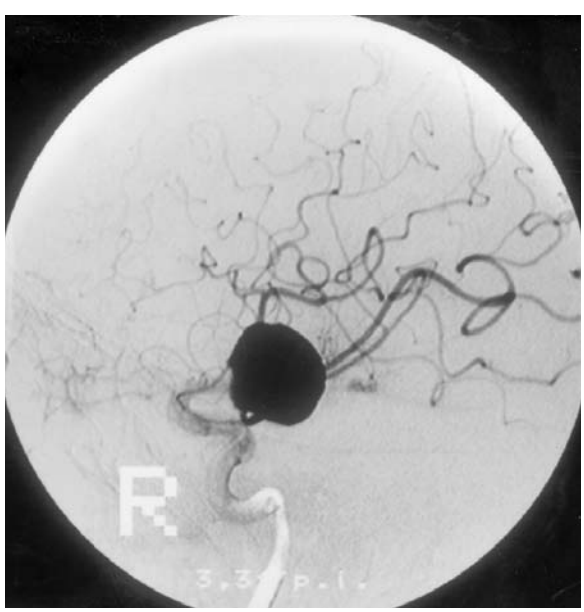

f

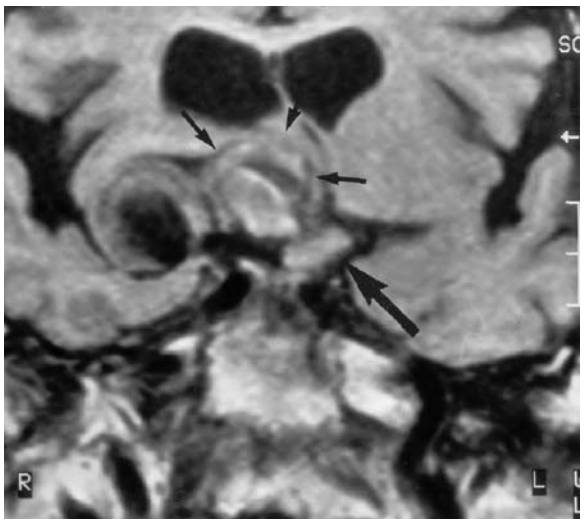

g

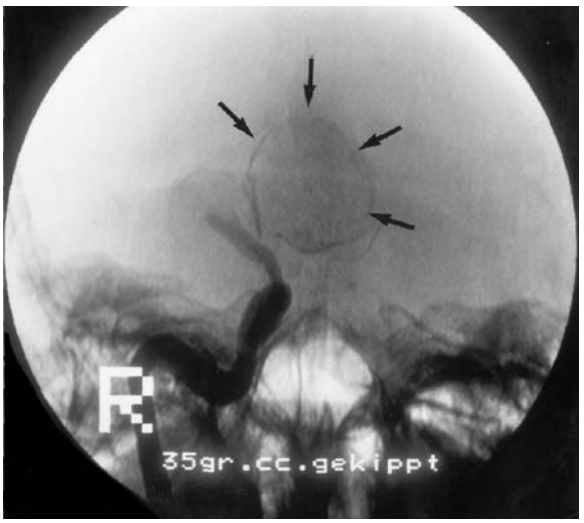

h

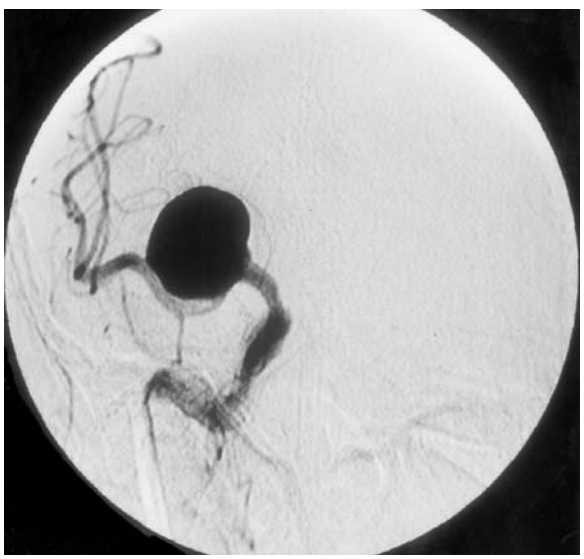

i

Fig. 7.48a–i. A 66-year-old woman with pressure sensation behind the right eye and slowly progressing visual deficit (bilateral 0.8), presenting with incomplete N III paresis of the right eye. Diagnosis: partly thrombosed (butterfly-shaped) aneurysm of the right ICA bifurcation. CT: **a** Axial native view at the suprasellar region, showing a ring-shaped coarse calcification in the right paramedian region of the basal ganglia and thalamus. MRI: **b** Axial T2-weighted view of the suprasellar region showing an irregular flow void lateral to the ICA bifurcation, as well as a hypointense structure in the interpeduncular cistern. **c** Corresponding (enlarged) T1-weighted view demonstrating the flow void of the open area of the aneurysm, in addition to an onion-shaped (older) thrombosed part frontal to the aneurysm (*small arrows*). The slightly hyperintense, sharply defined lesion in the midline compresses the chiasm (*arrow*) as well as the left cerebral peduncle, and represents another thrombosed area of the aneurysm. **d** Midsagittal T1-weighted native view, showing depression and dislocation superior to the chiasm (*arrow*) by the completely thrombosed and calcified suprasellar area of the aneurysm, extending to Monro's foramen (*white star*). DSA: **e** Lateral nonsubtracted view (early arterial phase) documenting the size of the calcification (*small arrows*, compare to **a**) as well as the inflow zone (*large arrow*) of the open area, representing a prolongation of the horizontal course of the distal ICA. **f** Late arterial phase, documenting first the very slow flow of the generally dilated arteries and demonstrating second the size of the open, not thrombosed area of the aneurysm. Note the lack of opacification of the ipsilateral ACA. **g** Coronal T1-weighted native MRI documenting the butterfly shape of the lesion: Note the (hypointense) flow void of the open aneurysm in the extension of the right ICA, surrounded by the onion-shaped thrombotic area (compare with **c**) and the completely thrombosed medial part with a distinct calcified wall (*small arrows*), depressing the basal ganglia and thalamus (compare with **a**); the *large arrow* indicates the distal part of the left ICA. DSA: **h** Early arterial phase in frontal projection (Towne), corresponding to **e** with labeled calcification (non-subtracted view). **i** Arterial phase (corresponding to **f, g**) where the entire open area is demonstrated as well as the origin of the aneurysm at the ICA bifurcation with location of the right M1 segment below. Note the lack of opacification of the ipsilateral ACA, which may be due to both compression and (by the thrombosed part) minor antegrade flow

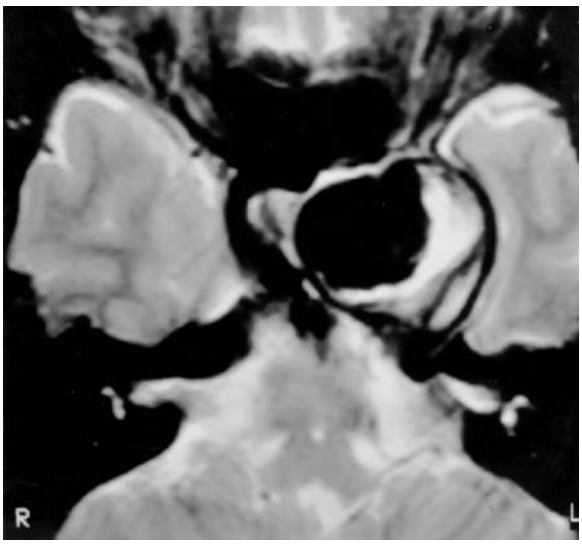

a

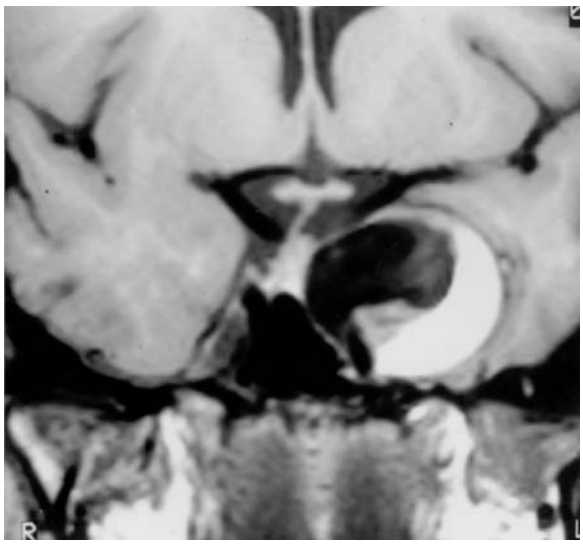

b

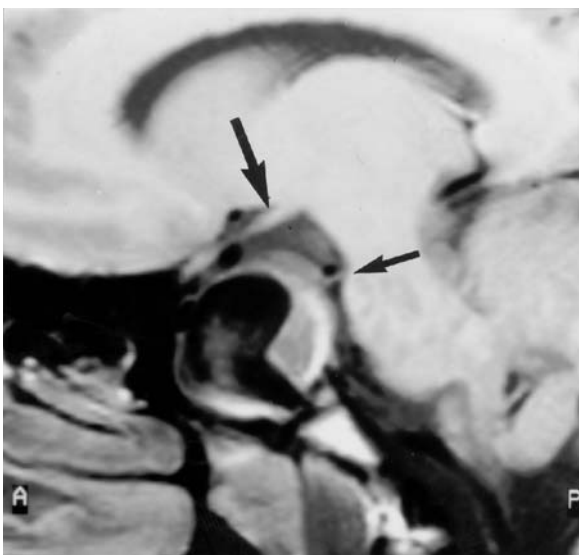

c

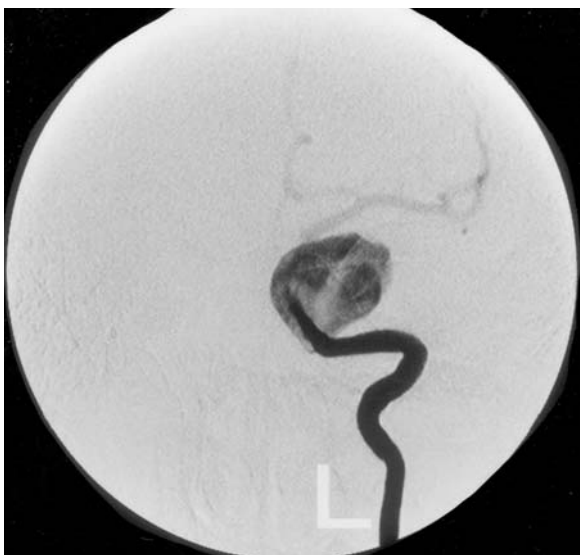

d

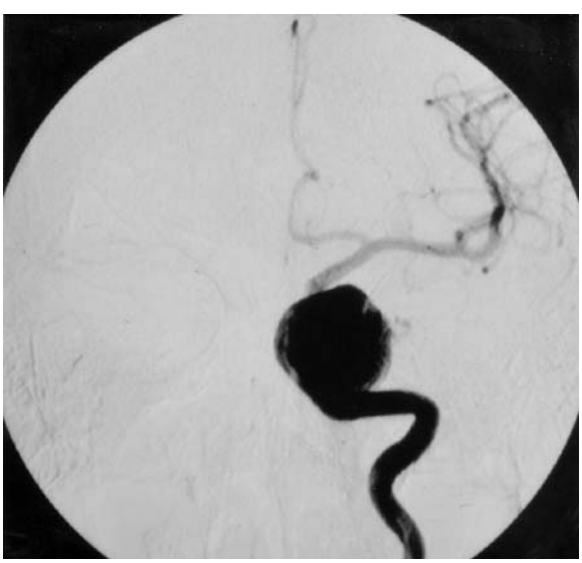

e

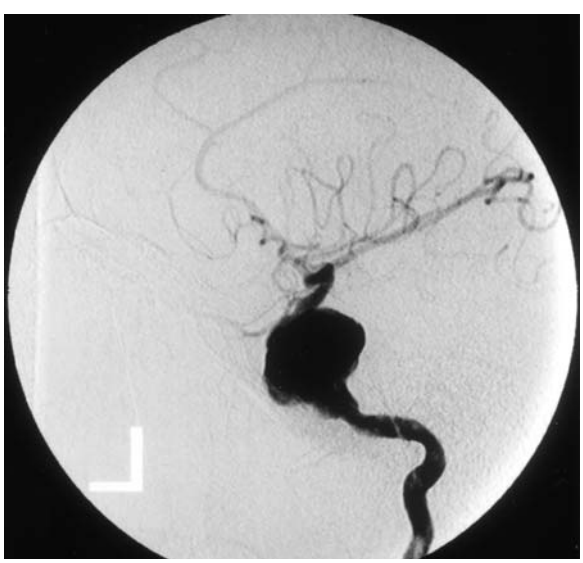

f

Fig. 7.49a–f. A 16-year-old boy with double vision to the left, headache, and slowly resolving ptosis of the left eye. Diagnosis: intracavernous aneurysm of the left ICA. MRI: **a** Axial T2-weighted view of the sellar region with excavation of the cavernous sinus by a primarily hypointense (flow void) lesion with hyperintense rim, representing the freshly thrombosed (methemoglobin) periphery of the aneurysm. **b** Coronal T1-weighted view showing substantial lateral expansion of the aneurysm: Beginning at the wall of the cavernous sinus, the mesial temporal lobe is apparently depressed and dislocated by both the open and the thrombosed part of the aneurysm. **c** Left paramedian sagittal T1-weighted image demonstrating the inflow zone of the aneurysm, whose proximal part is compressed by the thrombus. Note expansion to the brainstem with compression of N III (*small arrow*) located between the superior cerebellar (flow void below) and PCA (above), and additional compression of the left optic tract (*large arrow*) by distal ICA and proximal ACA. DSA: **d** Frontal view, early arterial phase where the configuration of the open part is comparable to the coronal MRI of **b**. **e** Frontal view, later arterial phase with relatively low opacification of the distal ICA, and bifurcation into the MCA and ACA. **f** Lateral view, compared with **c**, demonstrating only the open areas of the aneurysm, while the surrounding structures are not visualized

tilayered, laminated shape of the thrombosed part of the clot (Figs. 7.48, 7.50) (Schubiger et al. 1987). On combining the MRI images with 3D TOF or 3D phase contrast MRA (Fig. 7.51), the detection rate of aneurysms greater than 3 mm in diameter is approximately 100% (Ross et al. 1990; Wilcock et al. 1996).

Intra-arterial DSA of the cerebral vessels is still the gold standard in the detection or exclusion of intracranial aneurysms as it represents the most sensitive method available (Figs. 7.46–7.49, 7.51) (Caplan and Wolpert 1991). The method is applied with the aim to determine the anatomical relationship of the lesion, in particular with regard to the size of the ostium and open lumen, the relationship to adjacent arteries, the presence of vasospasm, collateral blood flow, and other vascular pathologies (Osborn 1994c; Byrne and Guglielmi 1998). The protocol includes the transfemoral catheterization of both carotid and vertebral arteries in at least four projections.

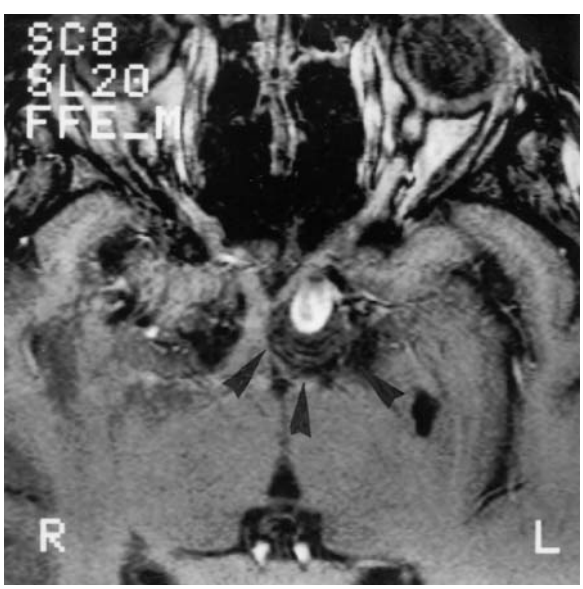

Fig. 7.50. A 58-year-old woman with slowly progressing blurred and double vision persisting for 2 months. Diagnosis: unruptured, partly thrombosed aneurysm of the left ICA. Axial HR-MR: the visualized spherical hyperintensity represents the sack of the aneurysm. In addition to the thrombus [crescent-shaped hypointensity (*arrowheads*)], the clinical symptoms are due to severe compression of the prechiasmal optic nerve and the chiasm by the aneurysm and aneurysmal pulsation. (From Müller-Forell and Lieb 1995)

7.2.1.7 Miscellaneous (Germ Cell Tumors, Metastasis, Cavernoma of the Cavernous Sinus, Chordoma, Tolosa-Hunt Syndrome, Cystic Lesions)

7.2.1.7.1 Germ Cell Tumors/Pineal Tumors

Germ cell tumors of the CNS constitute an unique class of rare tumors of different malignant character, affecting children and young adolescents. The histopathology and biological behavior of germ cell tumors is similar to homologous germ cell neoplasms arising in the gonads and other extragonadal sites. Even distinctive germ cell tumors are often characterized by overlapping features due to the fact that germinoma as mature teratoma with low mitotic activity (Fig. 7.57) with or without malignant transformation, yolk sac tumor with variable mitotic activity, embryonal carcinoma with high mitotic activity, and choriocarcinoma are included in this group of tumors (Rosenblum et al. 2000). Although germ cell tumors represent only 0.5% of all intracranial neoplasms, approximately 3% are detected in patients younger than 20 years of age. About 80% of CNS-germ cell tumors impinge on the midline with preference for the region of the pineal gland. Other preferred sites include supra- or intrasellar locations (Figs. 7.52, 7.53) that are involved simultaneously or sequentially if the tumor is multifocal, but intraventricular (mostly III ventricle), basal ganglionic, and thalamic variants may be encountered (Jennings et al. 1985; Matsutani et al. 1997; Rosenblum et al. 2000). The clinical features of germ cell tumors

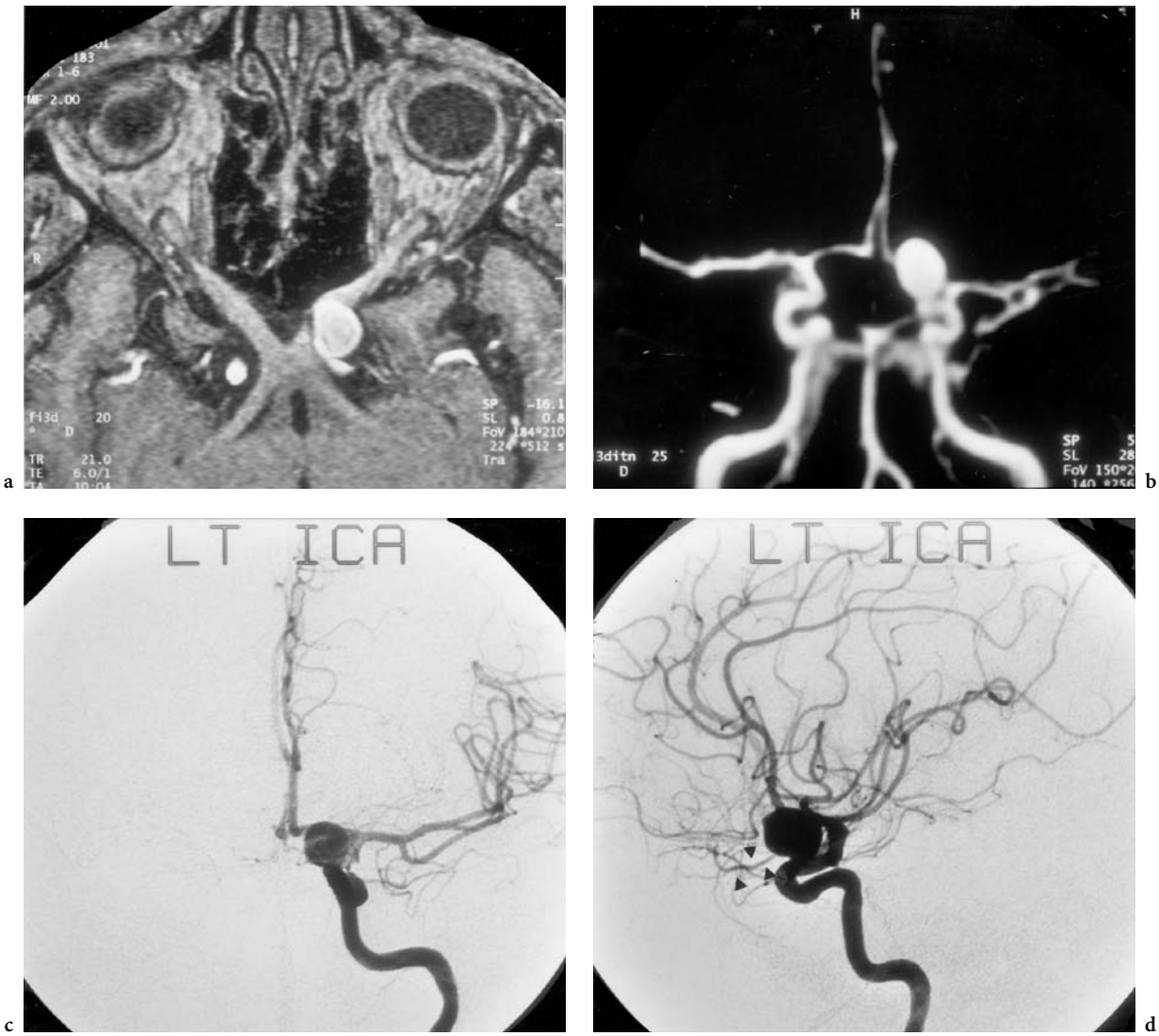

Fig. 7.51a–d. A 49-year-old woman with chronic headache, leading to imaging, no visual deficit, but signs of left optic nerve compression upon Goldman visual field examination. Diagnosis: incidental ophthalmic aneurysm of the left ICA. MRI: **a** Axial T1-weighted high resolution view (flash 3D) showing the impression of the left optic nerve at its proximal intracranial course by an anteriorly arising aneurysm at the origin of the ophthalmic artery. **b** MR-angiography (MIP reconstruction), demonstrating the superior extension of the lesion. DSA: **c** corresponding AP view of the left carotid artery injection. **d** Lateral view, where the origin of the aneurysm at the origin of the ophthalmic artery (*arrowheads*) is apparent

depend on their histological type and site. With respect to visual pathway disturbances, involvement of the pineal gland may lead to Parinaud's syndrome, which is characterized by paralysis of the upward gaze and convergence (Fig. 7.54), whereas a suprasellar growth typically impinges on the chiasm with resulting visual or cranial nerve problems (Figs. 7.53, 7.55). Hormonal disturbances may be an additional and in some cases the only clinical symptomatology (Fig. 7.52) caused by infiltration and disruption of the hypothalamic-hypophyseal axis with pituitary failure. These patients present with the clinical symptoms of diabetes insipidus, growth retardation (Figs. 7.53, 7.55), precocious puberty, or retarded sexual maturation (Kucharczyk et al. 1996; Rosenblum et al. 2000).

Pinealoblastomas are rare, malignant, poorly differ-entiated embryonal tumors of the pineal gland (WHO grade IV), accounting for about 45% of all pineal parenchymal tumors. They may arise in any age group, but with a dominance of the first two decades and a slight male preponderance (Mena et

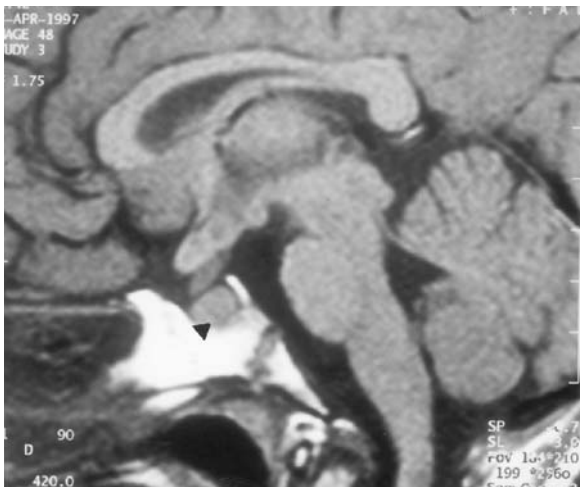

a

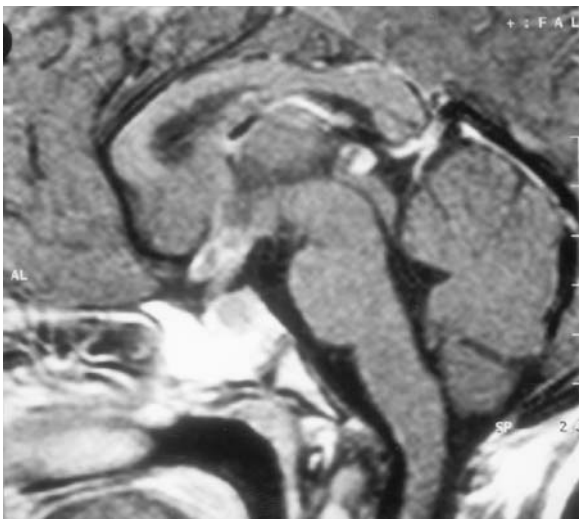

b

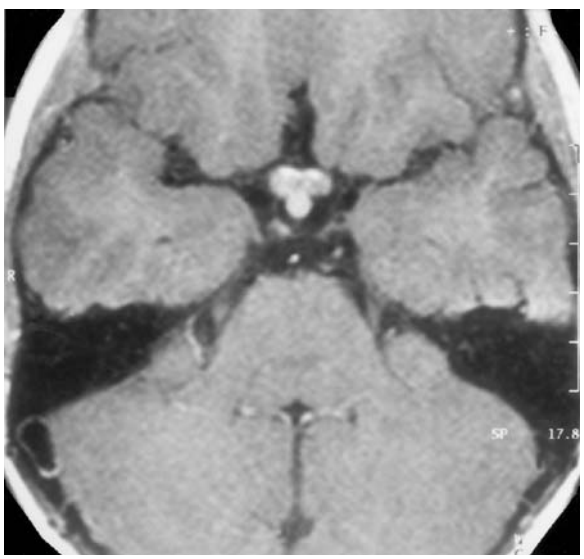

c

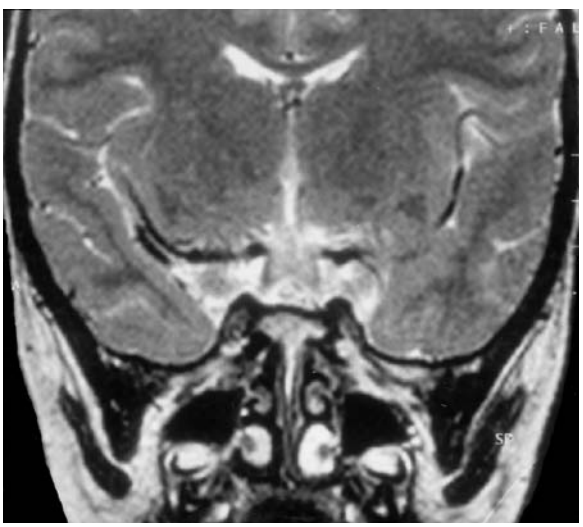

d

Fig. 7.52a–d. An 11-year-old girl with universal infantilism but no visual symptoms. Diagnosis: pituitary and hypothalamic germinoma. MRI: **a** Midsagittal T1-weighted view with enlargement of the optic chiasm and pituitary stalk. Note the round configuration of the pituitary gland and slight hypointensity of the posterior part (*arrowhead*). **b** Corresponding contrast-enhanced view with inhomogeneous signal enhancement of the chiasm, hypothalamus, and pituitary gland, the intraglandular tumor being unenhanced, corresponding to the primarily hypointense region in **a**. **c** Axial, T1-weighted, contrast-enhanced view with tumor enhancement of the chiasm and thickened pituitary stalk. **d** Coronal T2-weighted view demonstrating infiltration of the chiasm

al. 2000). They often infiltrate surrounding structures, including the meninges, responsible for common craniospinal dissemination. The clinical presentation is mostly unspecific with signs of increased intracranial pressure and neuro-ophthalmological deficits as, e.g., Parinaud's syndrome, similar to those found in other tumors of the pineal region (Fig. 7.56) (Sartor 1992).

Imaging Characteristics. As germinomas are composed of large polygonal germ cells and clusters of lymphocytes in a dense connective tissue stroma, they appear as a solid, homogeneous mass on imaging. In contrast to craniopharyngioma, they rarely include cystic parts. Suprasellar germinomas tend to infiltrate the hypothalamus, are not encapsulated, and, like pineal germ cell tumors, tend to spread into the subarachnoid space. Appearing hyperdense on CT, hyperintense on MRI (even unspecific) on T2-weighted views, and slightly hypointense in T1-weighted images, marked enhance-ment is seen after contrast administration with both imaging techniques (Figs. 7.52–7.55) (Osborn and Raus-

(Text continues on p. 403)

Fig. 7.53a–g. A 10-year-old girl with recurrent vomiting and severe weight loss. Ophthalmologic examination detected paleness of the optic papilla, but no deficit of the visual field. Diagnosis: malignant germinoma of the pituitary gland. MRI: **a** Axial T2-weighted view at the level of the optic chiasm where the partly cystic tumor occupies the entire pentagon cistern and causes spreading of the vessels of Willis' circle. Although the chiasm and the anterior part of the expanded left optic tract are visualized, the corresponding right structures are hidden by the tumor. **b** Corresponding T1-weighted, contrast-enhanced view. **c** Corresponding diagram: 12.2 = chiasm, 12.3 = optic tract. **d** Axial T2-weighted view at the level of the anterior commissure demonstrating the intraventricular (III ventricle) growth between the extended columns of the fornix (*arrowheads*). **e** Coronal, T1-weighted, contrast-enhanced view showing the lobulated configuration of the lesion with an interfornical tumor segment (*white arrow*). **f** Midsagittal, T1-weighted, contrast-enhanced image, demonstrating the caudocranial direction of the tumor growth arising from the widened sella, along the no longer identifiable pituitary stalk, dislocating the chiasm (*small white arrow*) anterior, invading the hypothalamus and third ventricle, and expanding superiorly to the level of the internal cerebral veins (*large white arrow*). **g** Corresponding diagram: 3.3 = sella turcica, 3.5 = clivus, 12.2 = chiasm, 15.2 = internal cerebral vein, 15.3 = vein of Galen

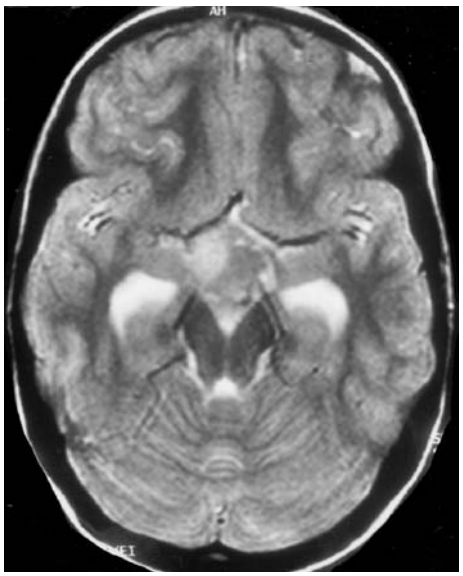
a

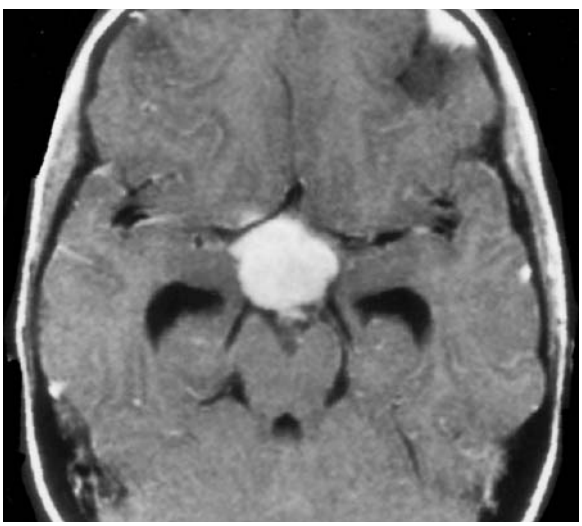
b

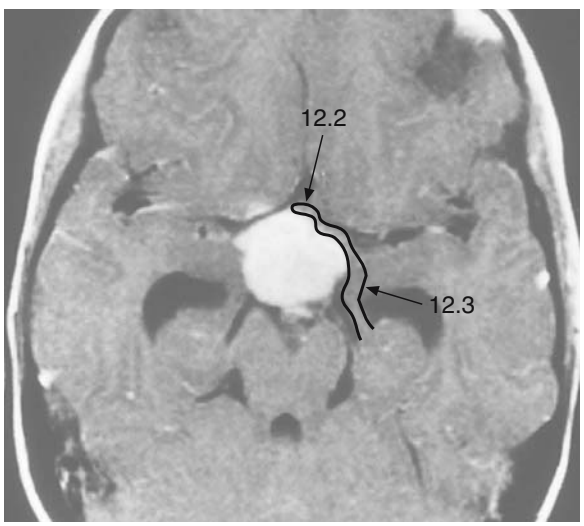

c

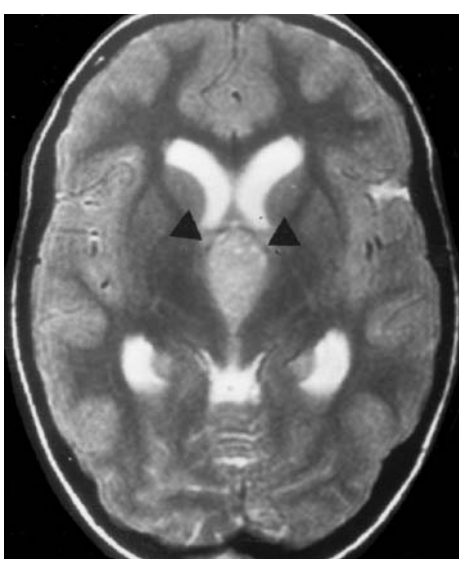
d

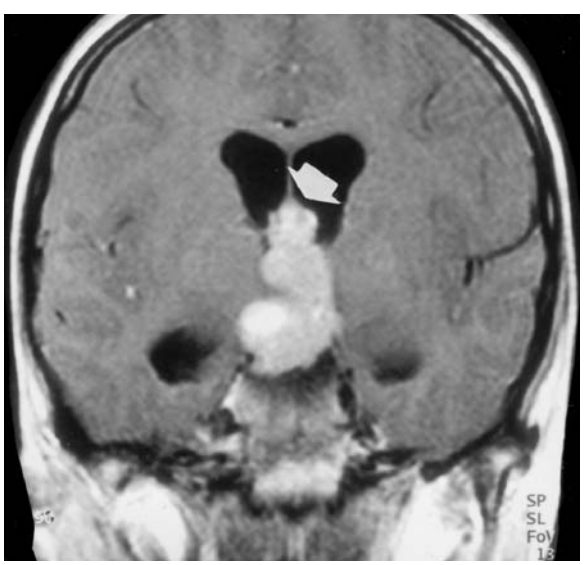
e

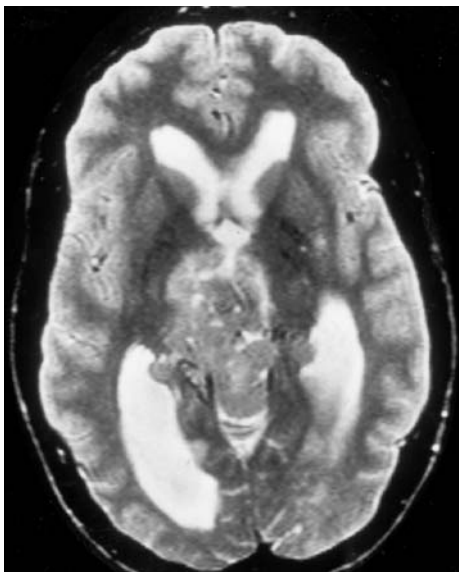

a

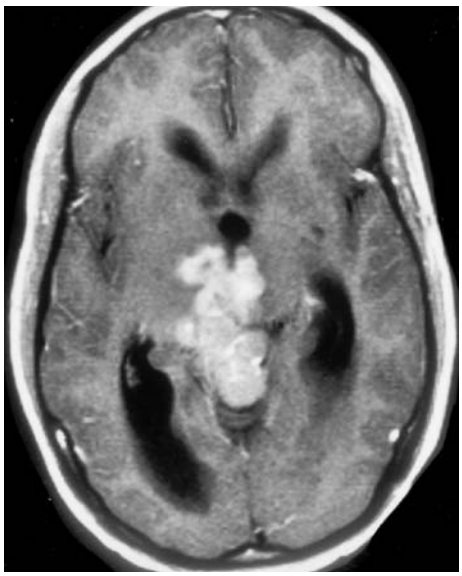

b

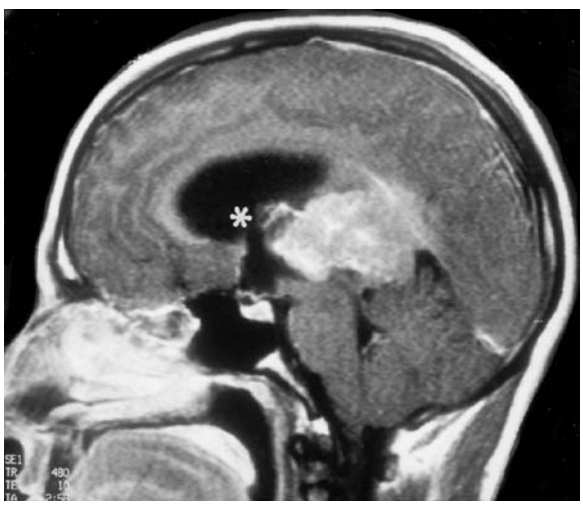

c

Fig. 7.54a–c. A 32-year-old man with severe headache and horizontal gaze palsy. Diagnosis: germinoma of the pineal gland. MRI: **a** Axial T2-weighted image with a primarily isointense, irregularly shaped tumor in the region of the pineal gland, associated with compression of the third ventricle and occlusive hydrocephalus. **b** Corresponding T1-weighted, contrast-enhanced view with homogeneous signal enhancement, leading to a suspicion of infiltration of the thalami. **c** Paramedian sagittal, T1-weighted, contrast-enhanced view with superior visualization of the AP extension of the pineal gland tumor. Note intraventricular tumor growth towards the proximal aqueduct, compression of the quadrigeminal plate in addition to the signs of occlusive hydrocephalus, including widening of Monro's foramen (*asterisk*), and flattening of the floor of the third ventricle. (With permission of Drs. Kemmer and Grebe, DKD, Wiesbaden)

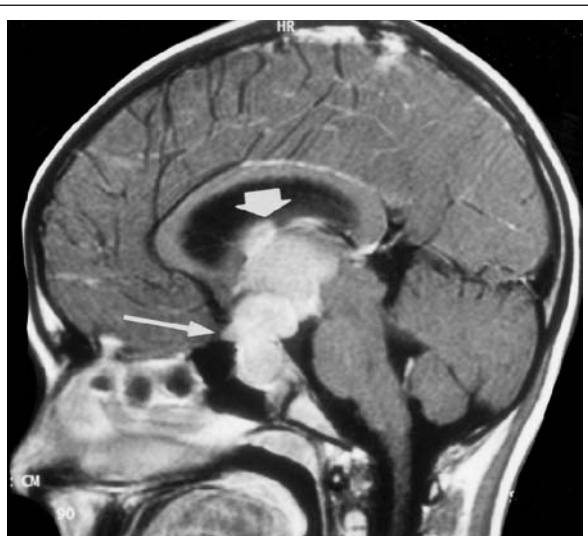

f

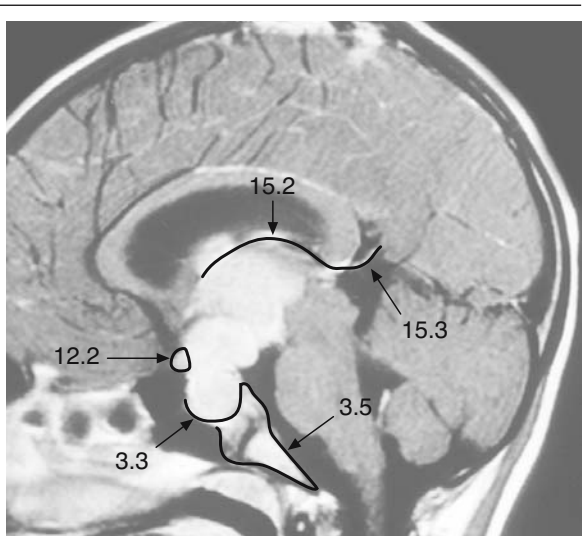

g

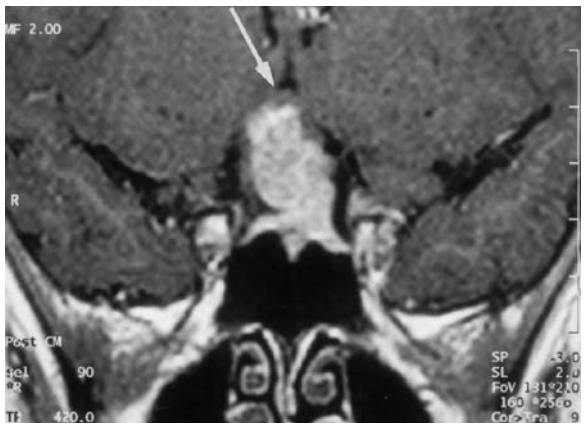

a

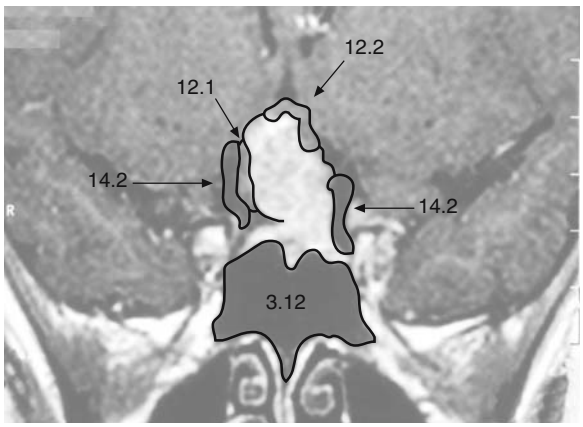

b

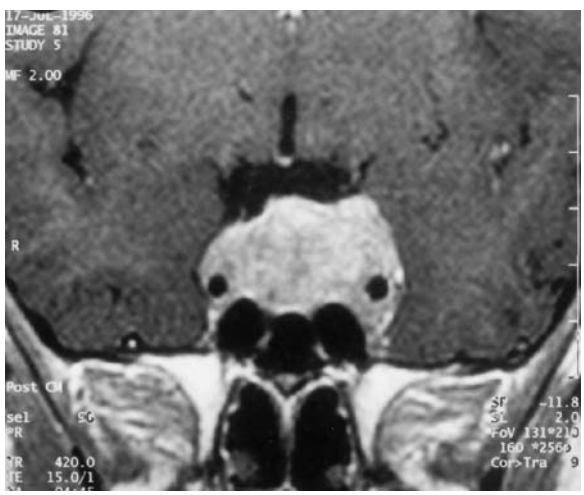

c

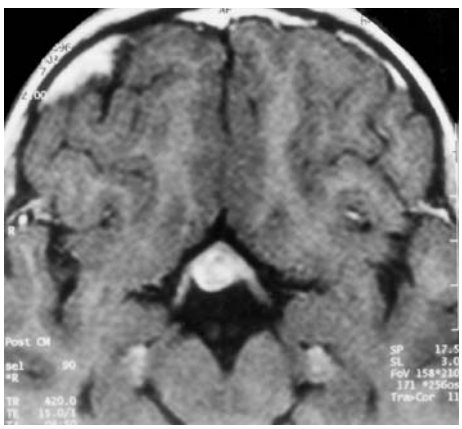

d

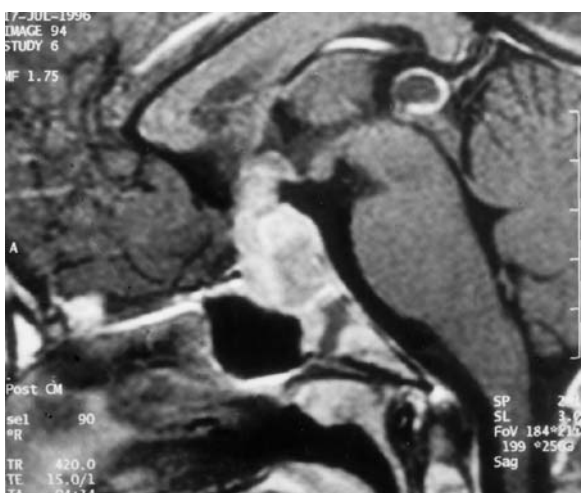

e

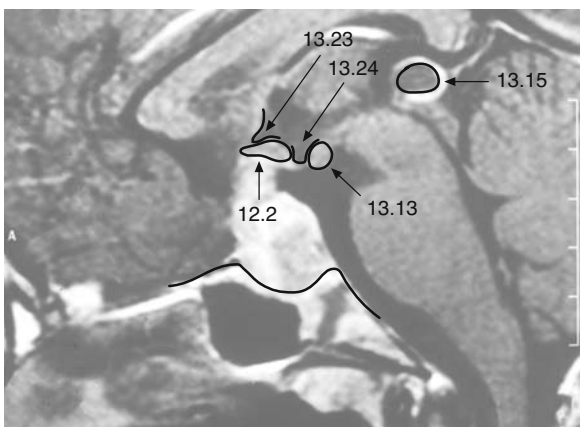

f

Fig. 7.55a–f. An 11-year-old girl with impaired growth, protrusion and ptosis of the left eye. Diagnosis: germinoma of the pituitary gland. T1-weighted, contrast-enhanced MRI: **a** Coronal view at the chiasm showing extreme elevation and inferior depression of the chiasm (*white arrow*) and third ventricle floor. Note the elongated, extended optic nerve between tumor and right ICA. **b** Corresponding diagram: 3.12 = sphenoid sinus, 12.1 = prechiasmatic optic nerve, 12.2 = chiasm, 14.2 = ICA. **c** Coronal view at the cavernous sinus, demonstrating the entire right-left extension with bilateral infiltration of the cavernous sinus and suprasellar tumor growth. **d** Axial view at the level of the suprasellar cistern where both the depression of the optic chiasm and the spreading of the anterior parts of both optic tracts are clearly visualized. **e** Midsagittal view demonstrating the craniocaudal extension with depression of the floor of the third ventricle. Note the small isointense formation, corresponding to the depressed chiasm, the widening of the configuration of the sella, and a cystic enlargement of the pineal gland (incidental finding without clinical symptoms). **f** Corresponding diagram: 12.2 = chiasm, 13.13 = mammillary body, 13.15 = pineal gland, 13.23 = chiasmatic recess (of the third ventricle), 13.24 = recess of the pituitary stalk (of the third ventricle).

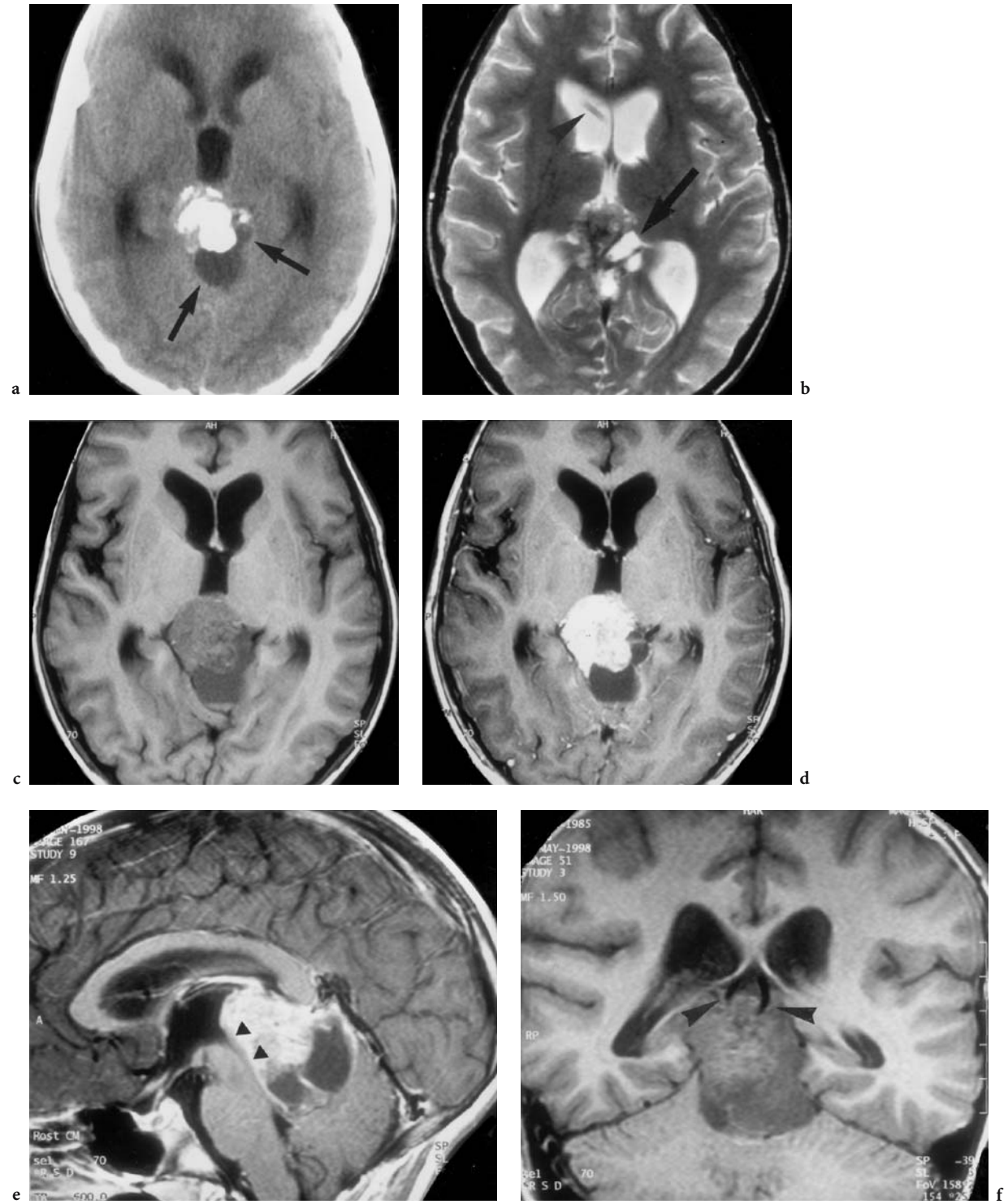

Fig. 7.56a–f. A 12-year-old boy with horizontal gaze paralysis (Parinaud's syndrome) and headache with drowsiness. Diagnosis: pinealoblastoma. CT: **a** Axial native view demonstrating occlusive hydrocephalus caused by a solid calcified tumor of the pineal region with cystic compartments (*arrows*); no significant contrast enhancement (not shown). MRI: **b** Corresponding T2-weighted image. The calcifications are identified by signal void, the cystic tumor region (*arrow*) is localized on the left, lateral to the expanded internal cerebral veins. Note normalization of ventricle lumen (best seen at the third ventricle) after emergency ventricular drainage (*arrowhead*). **c** Axial T1-weighted native view showing the relation of solid and cystic tumor part extending to the cistern of Galen's vein, the solid part depressing the posterior wall of the third ventricle and both pulvinar of the thalamus. **d** Corresponding contrast-enhanced image where, in contrast to CT, signal enhancement is bright. **e** Midsagittal, T1-weighted, contrast-enhanced view, impressively demonstrating the entire extension of the lesion. Note flattening of the quadrigeminal plate, seen as an isointense, small, post-aqueductal structure (*small arrowheads*), in addition to the infratentorial extension with depression of the upper vermis by the tumor cyst. **f** Coronal T1-weighted native image demonstrating the supra- and infratentorial growth with expansion of the internal cerebral veins (*arrowheads*) and lateral extension to the atrium of the right lateral ventricle

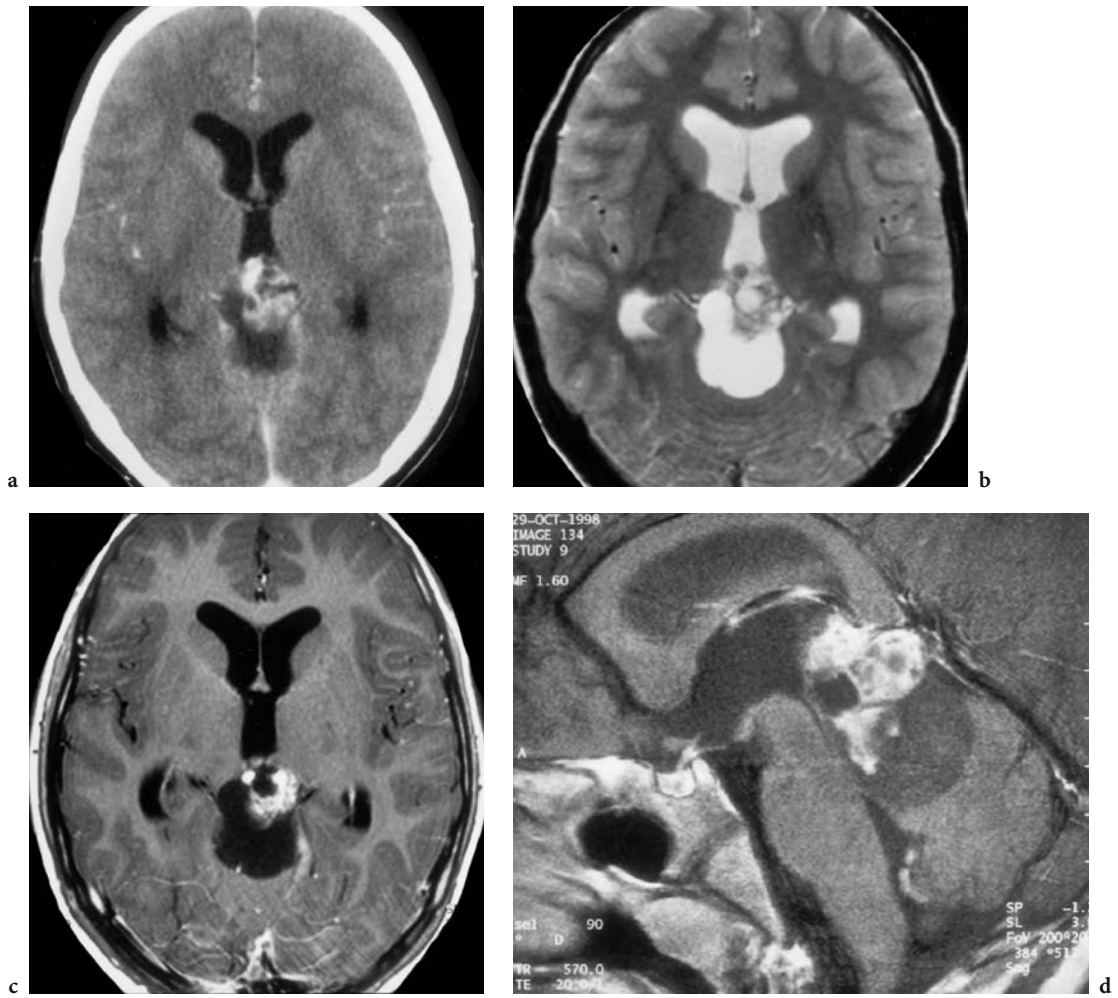

Fig. 7.57a–d. A 20-year-old man with headache and horizontal gaze palsy. Diagnosis: benign teratoma of the pineal gland. **a** Axial contrast-enhanced CT, demonstrating an inhomogeneous tumor of the pineal region with subsequent hydrocephalus of the supratentorial ventricles. MRI: **b** Corresponding axial T2-weighted image showing inhomogeneity of the tumor with a posterior cyst (with slightly higher signal intensity than CSF). **c** Corresponding T1-weighted, contrast-enhanced view. **d** Midsagittal, T1-weighted, contrast-enhanced view with superior visualization of the infratentorial extension, in particular of the tumor cyst with depression of the vermis

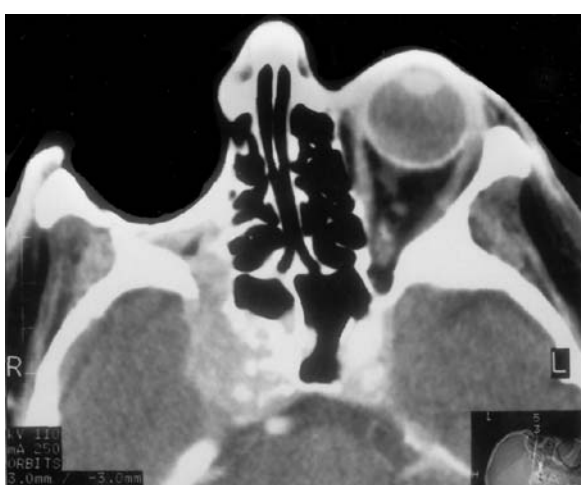

Fig. 7.58. A 76-year-old man with a history of exenteration of the right orbit for retinal melanoma; presenting with right N III paresis and severe orbital pain. Diagnosis: recurrent intra-orbital melanoma with intracranial expansion. Axial contrast-enhanced CT at the inferior region of the cavernous sinus, demonstrating local orbital tumor recurrence in the orbital apex and invasion of the cavernous sinus, identified by irregular, bulbous widening and enhancement of the right region of the cavernous sinus (compare with the left side)

chning 1994; Kucharczyk et al. 1996).

Pineoblastomas may already be quite large at the time of diagnosis (Fig. 7.56) and present as a lobulated, in some cases poorly demarcated homogeneous mass with heterogeneous contrast enhancement, depending on the portion of solid tumor tissue (Sartor 1992; Osborn and Rauschning 1994). The MRI appearance of teratoma is related to the respective tumor grade. Benign teratoma (Fig. 7.57) thus shows a heterogeneous composition of different tissues (generally including fat and/or calcifications with hypo- and hyperdense areas on CT, respectively) with a well demarcated lesion in the absence of invasion of the adjacent brain structures. In contrast, malignant teratoma shows no fat signal, but tumor infiltration of brain parenchyma with perifocal edema is usually present (Sartor 1992).

7.2.1.7.2 Metastasis

Secondary lesions should always be included in differential diagnostic considerations of extrinsic and even intrinsic tumors of the sellar region, particularly with a view to the capacity of some primarily extracranial tumors to involve the skull base (per continuitatem) or be hematogenous. Metastases involving the cavernous sinus predominantly arise from malignant tumors of the nasal cavity, growing perineurally or perivascu-larly via the basal foramina. They primarily become symptomatic because of cranial nerve deficits, e.g., double vision or ptosis. The leading entities of this tumor group consist of squamous cell carcinoma and adenoid cystic carcinoma of the epipharyngeal and nasal/paranasal region. A number of these reach the intracranial space with considerable destruction of the skull base, since the dura does not serve as a barrier over a prolonged period of time. The location of the metastasis determines the neurologic symptomatology (Fig. 7.58).

Imaging characteristics are nonspecific and similar to those encountered in more common tumors of the sellar region (Sartor 1992; Kucharczyk et al. 1996).

7.2.1.7.3 Cavernoma (Syn. Cavernous Hemangioma) of the Cavernous Sinus

Defined as the only venous vascular malformation consisting of thin-walled venous sinusoids without intervening neural tissue (Rosenblum et al. 1986), in neurologic patients, cavernoma are primarily localized in the brain parenchyma (Berenstein and Lasjaunias 1992). In rare instances of intracranial extraparenchymal location in adults, the cavernous sinus is involved in the majority of cases (Suss et al. 1984; Tannouri et al. 2001), representing the basis for a differential diagnosis from meningioma or neurinoma of the cavernous sinus. Cavernoma of the cavernous sinus obviously originate from the dural compartment (Willing et al. 1993) and present clinically with unspecific symptoms such as retro-orbital pain or ocular nerve disorders (Fig. 7.59). They present as well-defined tumorous lesions with a homogeneous, intermediate signal on T1-weighted views, a hyperintense signal on T2-weighted sequences, and homogeneous, massive enhancement after gadolinium administration (Fig. 7.59).

7.2.1.7.4 Chordoma

Arising from intraosseous vestigial remnants of the notochord, chordomas are extremely rare, with an incidence of less than 1% of all intracranial neoplasms. They are slow growing, osteodestructive, histologically benign, midline tumors with variable calcification and intratumoral hemorrhage (Zülch 1986; Okazaki 1989). They participate in ophthalmic disorders in only rare cases, i.e., when they arise from the clivus with an extension towards the chiasm (Fig. 7.60). On MRI, chordomas present with an intermediate signal on T1-weighted and a marked signal on T2-weighted images, but with only moderate enhancement after Gd-DTPA administration (Meyers et al. 1992). The differential diagnosis should include chondromas, chondro-sarcomas, metastasis, as well as destructive, hormone-inactive pituitary adenomas or skull base meningiomas (Meyers et al. 1992).

7.2.1.7.5 Tolosa-Hunt Syndrome

The Tolosa-Hunt syndrome (THS) is an inflammatory disease of unknown origin, limited to the superior orbital fissure and the cavernous sinus (Smith and Taxdal 1966). The presentation of cranial nerve paresis of one or several of the cranial nerves passing the cavernous sinus (N III, N IV, N VI, and N V1) may coincide with the onset of orbital pain or follow it within a period of up to 2 weeks. The pain must be relieved within 72 h after steroid therapy. Although high resolution CT or MRI can neither exclude nor confirm THS when a lesion compatible with an inflammatory process is visualized, other causative lesions as, e.g., a malignant tumor must be excluded

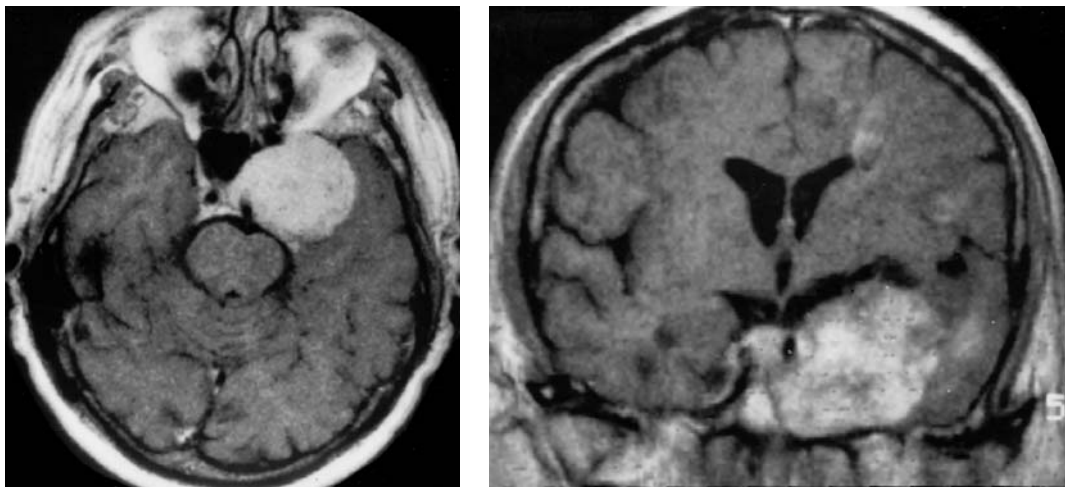

Fig. 7.59a,b. A 50-year-old man with left N VI paresis. Diagnosis: cavernous hemangioma. MRI: **a** Axial T1-weighted native view showing a huge, hyperintense, extra-axial, well-defined formation originating in the lateral region of the cavernous sinus. Note compression of the temporal parenchyma and the brainstem, as well as the sharply defined depression of the sphenoid sinus. **b** Coronal T1-weighted native view with distinct visualization of the expansion into the cavernous sinus and the clivus. (With permission of Drs Kemmer and Grebe, DKD, Wiesbaden)

(Forderreuther and Straube 1999). Clinical and neuroradiological follow-up must be done for at least 2 years, even in patients with negative findings on imaging at onset (Schramm and Hähnel 2001).

7.2.1.7.6 Cystic Lesions

In the differential diagnosis of suprasellar tumor-like lesions, arachnoid cyst and epidermoid cyst play some important role, along with Rathke's cleft cyst and hypothalamic hamartoma.

Rathke's cleft cyst, a benign epithelium-lined cyst arising from remnants of Rathke's pouch, may become symptomatic in the case of intra- and suprasellar extension, a rather rare condition (Rose et al. 1992). On MRI, signal intensities vary with cyst content from serous to mucoid (Osborn 1994b).

Arachnoid cysts account for about only 1% of all intracranial space-occupying lesions, but 10% arise in the suprasellar region (Armstrong et al. 1983). Arachnoidal cysts are filled with CSF; the etiology of these mainly congenital lesions remains poorly understood and controversial, but meningeal mal-development is preferred, so that minor aberrations of CSF flow through the loose, primitive, perimedullary mesenchyme are considered to result in a focal splitting of leptomeninges and the formation of a diverticulum or blind pocket within the arachnoid membrane (Schachenmayr and Friede 1979; Becker et al. 1991). As an arachnoid cyst is a well defined, sharply demarcated, extra-axial formation filled with CSF, MRI signal characteristics correspond with hypointense signal on T1-

Fig. 7.60a–f. A 61-year-old woman with slowly progressing visual deficit (only shadow vision) of the right eye. A left-sided amaurosis was a result of three-fold cataract operation. Diagnosis: chordoma. MRI: **a** Axial T2-weighted view with distinct delineation of the encapsulated tumor, which occupies the sphenoid sinus, invades both orbits from medial and inferior, and extends into the posterior fossa. **b** Axial T1-weighted native view (3 mm above **a**) showing only slight signal enhancement and invasion of the right cavernous sinus and gasserian ganglion (*arrow to the left*). **c** Coronal T1-weighted native view at the level of the optic canal, demonstrating bilateral destruction of the medial walls of the optic canal, expansion of the tumor in the entire sphenoid sinus, and destruction of the sphenoid plane. **d** Coronal T1 weighted native view at the chiasmal level, demonstrating elevation and inferior compression of the chiasm as well as invasion of the right cavernous sinus; the right ICA is completely incorporated into the tumor. **e** Midsagittal non-contrast-enhanced view where the entire extension of the chordoma with complete invasion of the skull base and hard palate, as well as compression of the brainstem, is distinctly visualized. (Note distinctly visualized tumor hemorrhage with T1-weighted hyperintense, T2-weighted hypointense areas of fresh to subacute hemorrhage in the other figures. as well.) **f** Corresponding diagram (presenting the axis of figs. **a**, **c**, **d**): 12.2 = chiasm, 13.13 = mammillary body

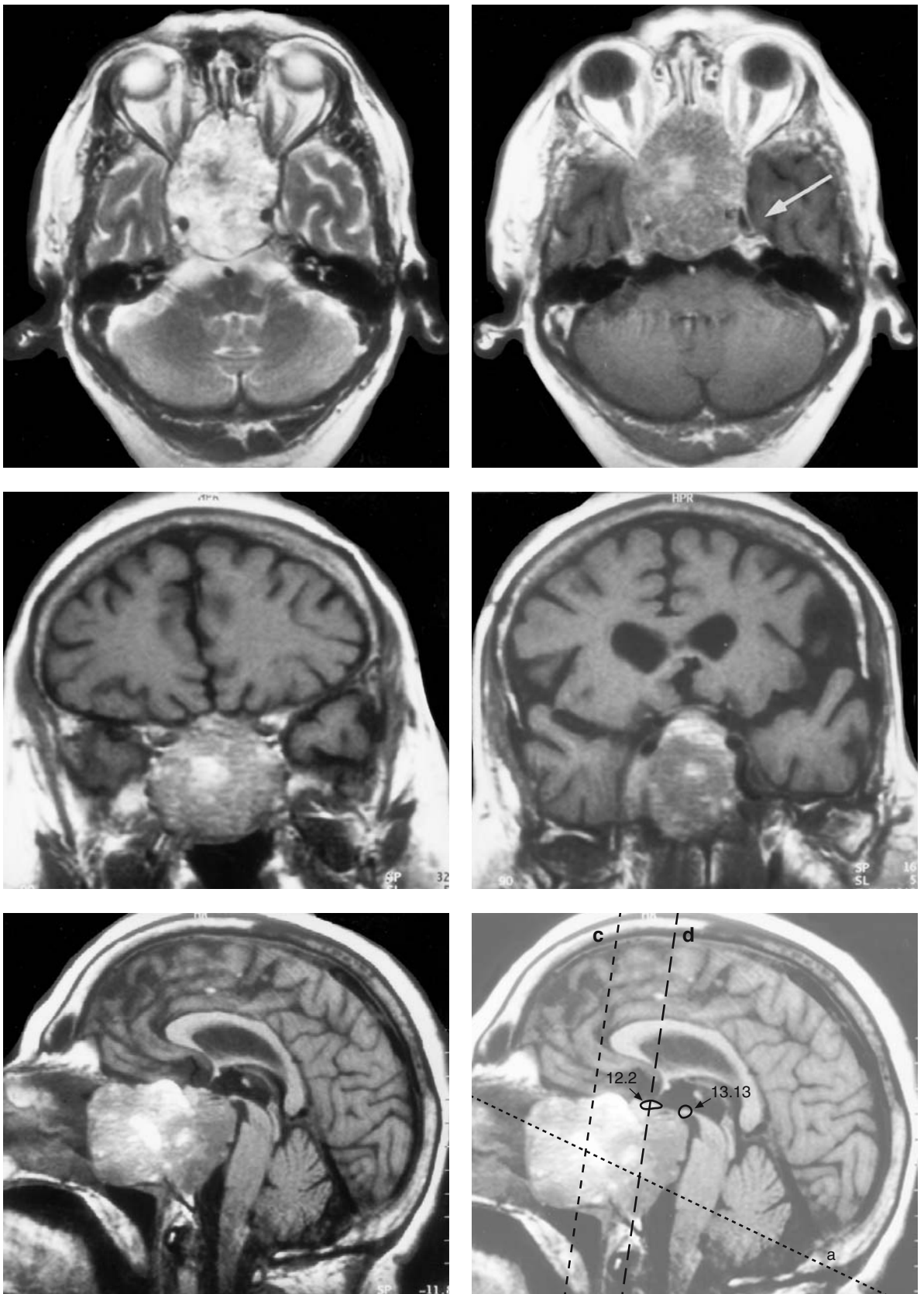
a
b
c
d
e
f
c
d
12.2
13.13
a

weighted and hyper-intensity on T2-weighted images (Figs. 7.61, 7.62). 3D-CISS sequence (Casselman et al. 1996) demonstrates a high sensitivity for even small structures, its application is helpful in the differential diagnosis, especially from suprasellar congenital epidermoid cysts (Osborn 1994b).

Epidermoid cysts probably arise from inclusion of ectodermal epithelial elements at the time of neural tube closure (Vion-Dury et al. 1987), accounting for 0.2%–1% of all primary intracranial tumors, 7% of them in the suprasellar region (Osborn 1994b). Imaging of these well-delineated, tumor-like cystic lesions is not always able to differentiate them from arachnoid cyst, especially since the MRI signal intensities are similar to CSF in every conventional sequence. However, the high resolution capability of a 3D-CISS sequence is able to define the irregular, lobulated surface ("cauliflower-like") of the lesion, and additional DWI confirms the diagnosis (Fig. 7.63) (Fitzek et al. 1998).

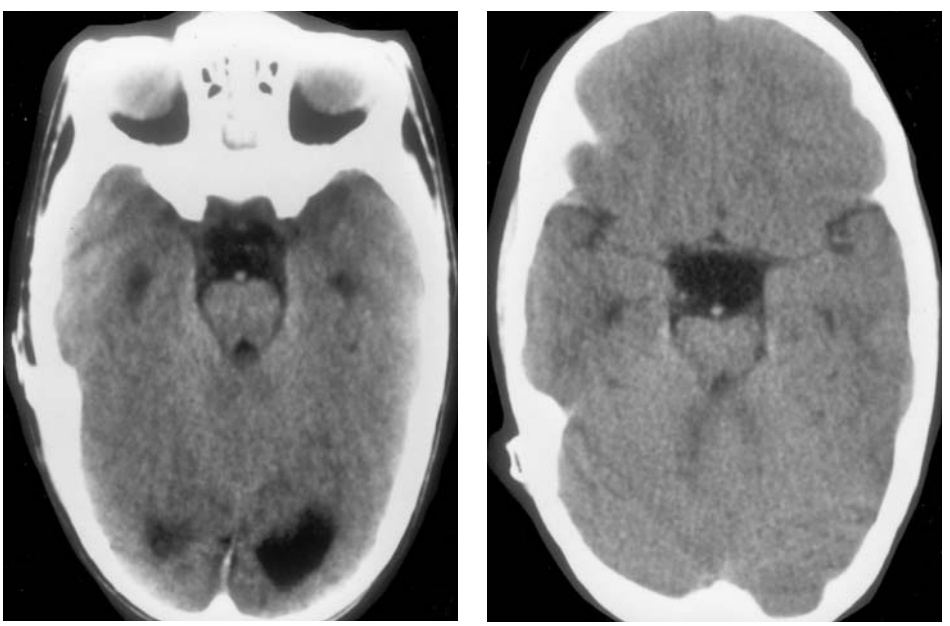

a b

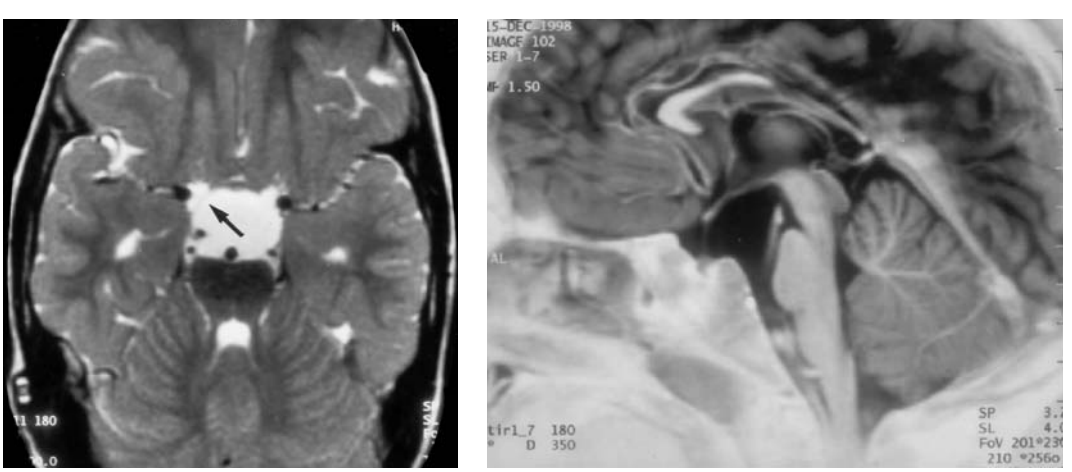

c d

Fig. 7.61a–d. A 4-year-old boy with connatal (shunted) hydrocephalus, presenting with progressive visual deficits. Diagnosis: suprasellar arachnoid cyst. CT: **a** Axial CT taken 2 years before the current presentation, showing a wide suprasellar cistern. **b** Corresponding CT at the time of visual deficits where the suprasellar cistern appears expanded and the brainstem flattened. MRI: **c** Corresponding axial T2-weighted image demonstrating a miniscule wall (*small arrow*). **d** Midsagittal T1-weighted IR view with extension of the pituitary stalk/chiasm complex, elevation of the floor of the third ventricle, and pressure exertion by the basilar artery against the flattened, deformed pons. (With permission of Müller-Forell 2001)

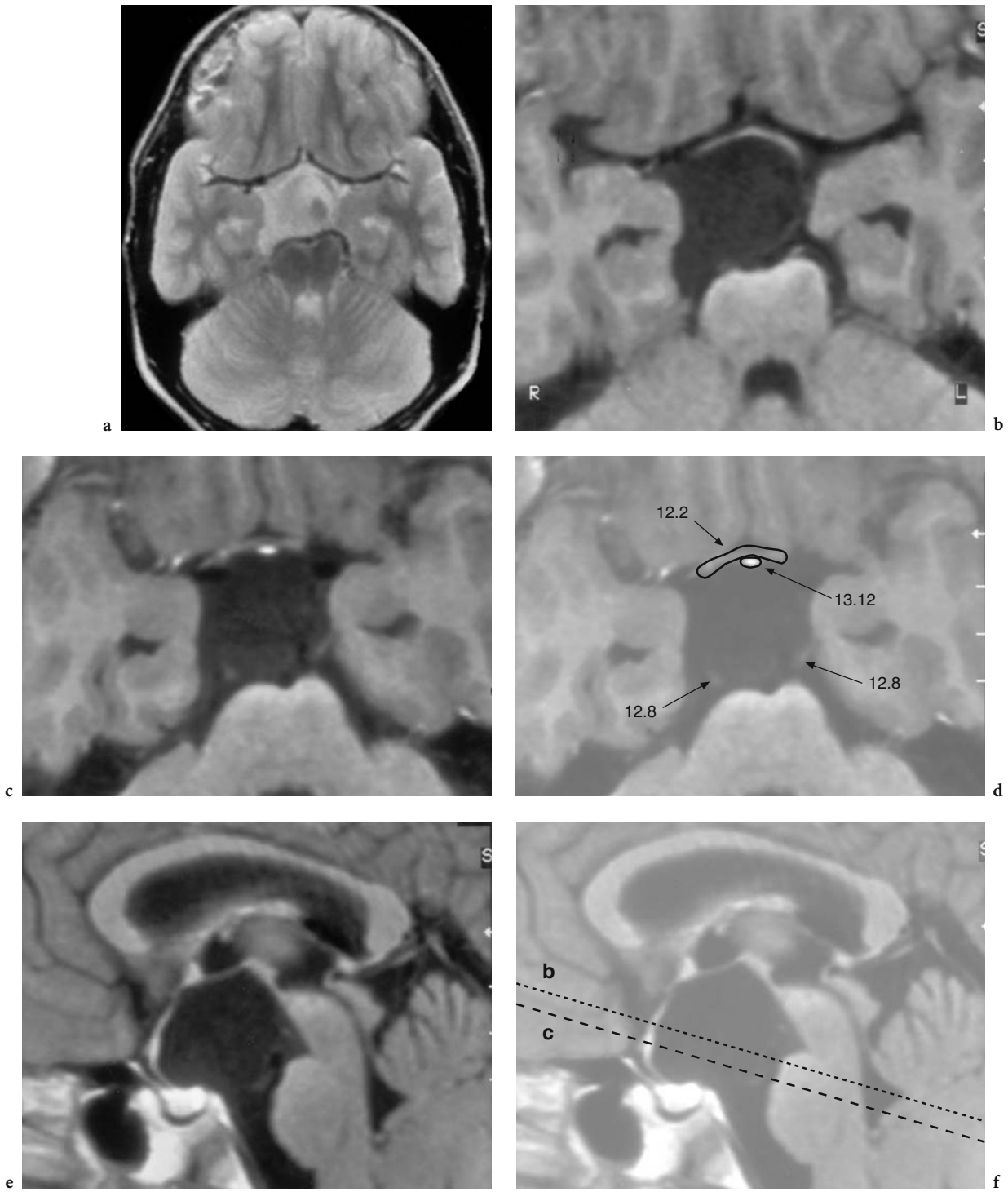

Fig. 7.62a–f. MRI of a 10-year-old boy with precocious puberty and pituitary dwarfism in the absence of ophthalmological deficits. Diagnosis: suprasellar arachnoid cyst. **a** Axial proton-weighted view with extreme expansion of the pentagon cistern, deformed flattening of the brainstem, and widening of Willis' circle. **b** Corresponding T1-weighted image (enlarged) with manifest flattening of the chiasm caused by the retrochiasmal cyst. **c** One slice below demonstrates the pituitary stalk (hyperintense) to be pressed against the chiasm. Note the neural structures at the posterior circumference of the cyst, corresponding to the flattened and extremely extended N III. **d** Corresponding diagram: 12.2 = chiasm, 12.8 = oculomotor nerve (N III), 13.12 = pituitary stalk. **e** Midsagittal T1-weighted view with superior visualization of the space-occupying effect, and identifying elevation and depression of the floor of the third ventricle. **f** Corresponding diagram with labeling of the axial images

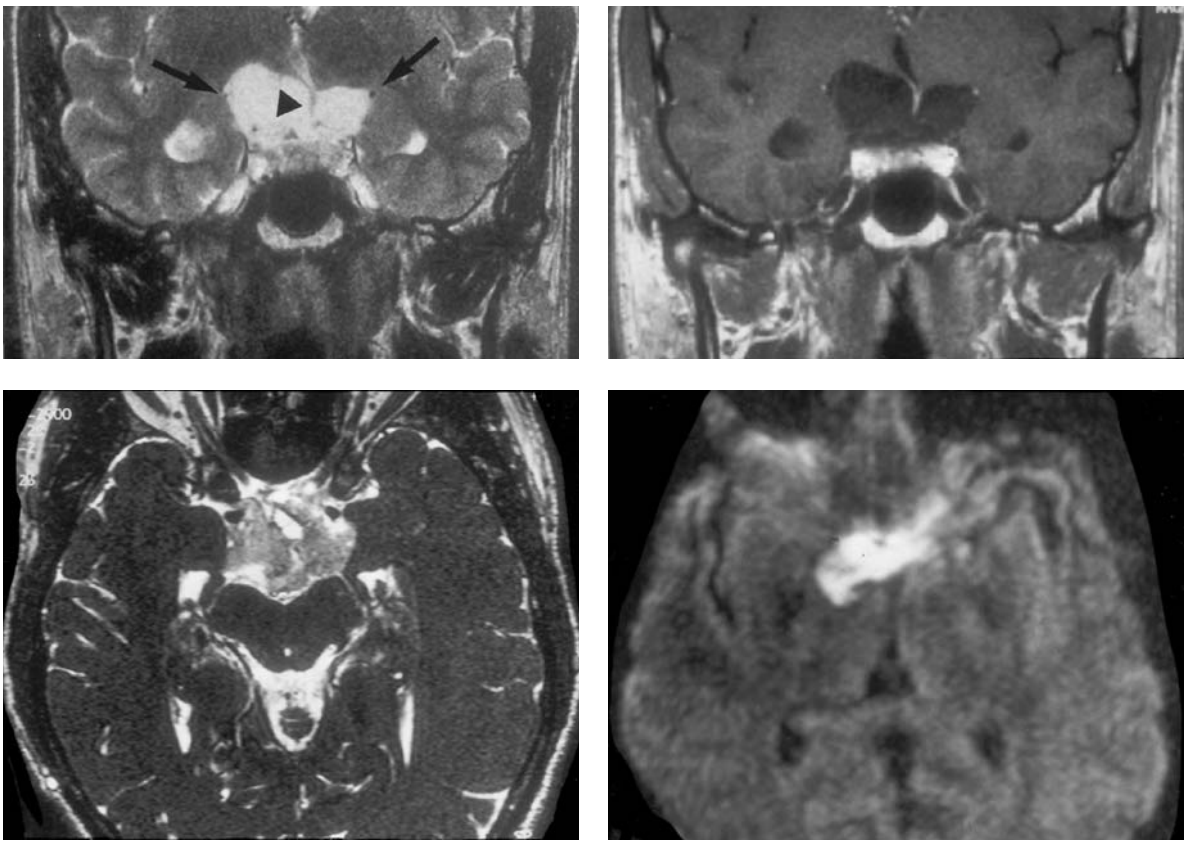

Fig. 7.63a–d. A 30-year-old man with atrophy of the right optic nerve and slowly progressing visual field deficit. Diagnosis: suprasellar epidermoid. MRI: **a** Coronal T2-weighted view demonstrating a hyperintense suprasellar mass, dislocating the vessels (*arrows*) and the pituitary stalk seen paramedian (*arrowhead*). **b** Corresponding T1-weighted, contrast-enhanced view, showing no enhancement of the lesion but the proximal pituitary stalk. **c** Axial T2-weighted view with intermediate signal enhancement of the irregular mass. **d** Axial diffusion-weighted image, the signal enhancement proves the suspected epidermoid. (**a**, **b** with permission of the colleagues of Radiologische Praxis, Alzey)

7.3 Optic Tract and Area

7.3.1 Neoplasms

7.3.1.1 Ependymoma

Intracranial ependymomas (WHO grade II) are slowly growing tumors, which exhibit variable morphologic features and biological behavior. They arise from the ependymal layers of the ventricles and include subependymoma, myxopapillary ependymoma (both WHO grade I), and anaplastic ependymoma (WHO grade III). Ependymomas account for 3%–9% of all neuroepithelial tumors (Wiestler et al. 2000a), with intracranial manifestation preferentially in children and young adults, most commonly in the infratentorial compartment, in contrast to a predominantly intraspinal involvement in adults (Mork and Loken 1977; Atlas 1996; Prayson 1999). These tumors occur at any site along the ventricular system with preference for the fourth but also the lateral ventricle. Supratentorial intraparenchymal ependymoma may occur particularly in children or young adults, originating from embryonic ependymal remnants (Naidich and Zimmerman 1984; Wiestler et al. 2000a). Although the histological grading of ependymoma is rather low (WHO II), the clinical outcome is poor in young children (below 3 years), incomplete tumor resection, and anaplastic histo-pathological features, whereas it is about 50% for supratentorial localization and appearance in young adults (Pollack et al. 1995; Horn et al. 1999).

Imaging Characteristics. On MRI, these quite distinctly circumscribed lesions present with heterogeneous signal intensities, low on T2-weighted and slightly hypointense on T1-weighted images reflecting the partly cystic, partly calcified, necrotic and hemorrhagic areas of the mass (Fig. 7.64) while solid tumor parts may show BBB disruption. Because of CSF dissemination, usually found in conjunction with recurrence at the primary site, MRI is the method of choice for the accurate determination of the relationship to adjacent structures along the CSF spaces (Burger and Scheithauer 1994; Atlas 1996).

7.3.1.2 Primary CNS Lymphoma (Malignant Lymphoma)

The incidence of primary CNS lymphoma has recently increased worldwide from 0.8%–1.5% to 6.6% of primary intracranial neoplasms, mainly thought to be a consequence of patients with acquired immune deficiency syndrome (AIDS) (Miller et al. 1994). Current studies report a decreasing incidence in these patients but an increase in the immunocompetent population (Nasir and DeAngelis 2000). Primary CNS lymphomas are defined as extranodal malignant

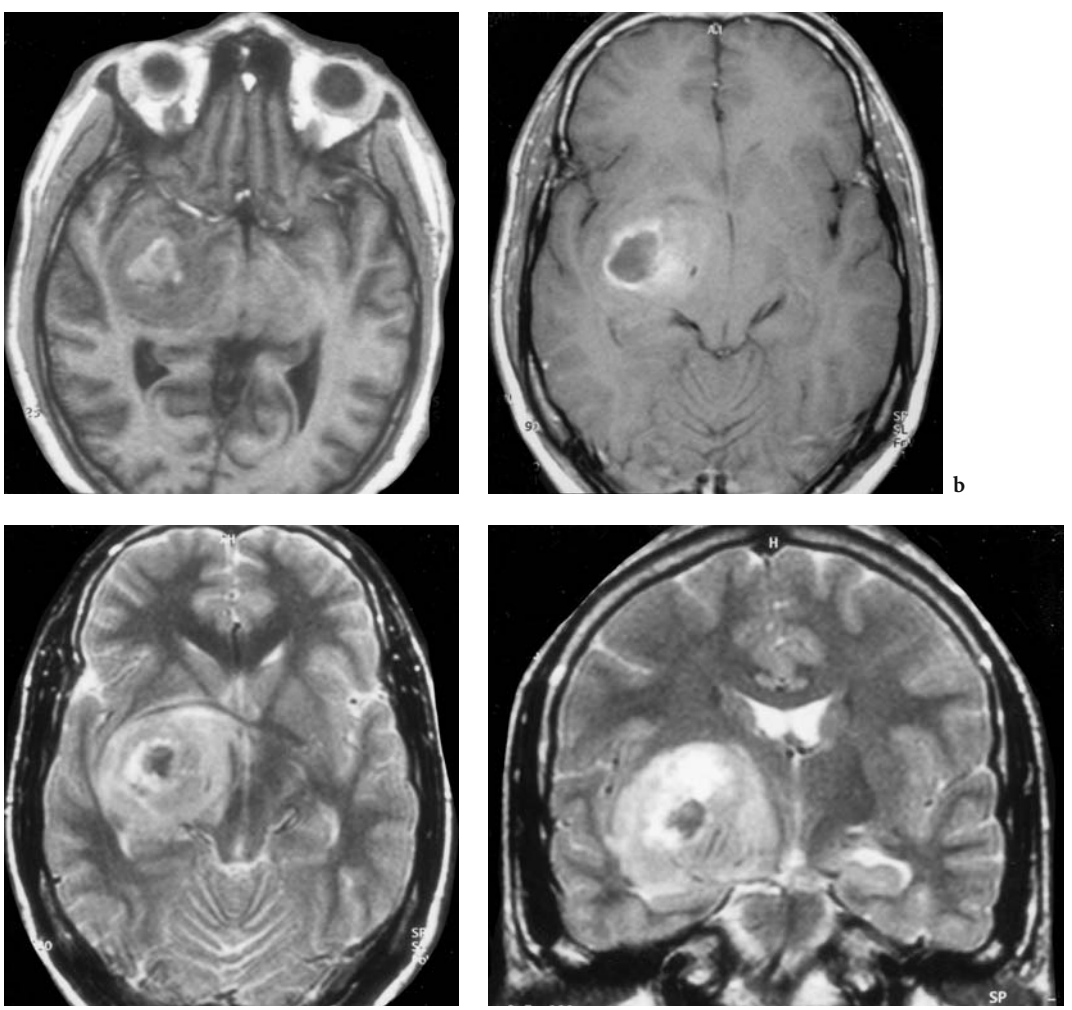

Fig. 7.64a–d. A 20-year-old man with left hemiparesis and hemianopia to the left. Diagnosis: ependymoma WHO II–III with spontaneous intratumoral hemorrhage. MRI: **a** Axial T1-weighted native view (3D-data set) showing a round, iso- to hypointense lesion with central cockade-shaped hyperintensity in the right basal ganglia, indicating the presence of subacute hemorrhage. **b** Axial, T1-weighted (tilted orbito-meatal), contrast-enhanced view with superior demonstration of the tumor location in the basal ganglia and BBB disruption of the solid tumor. **c** Corresponding T2-weighted image, with superior demonstration of the interruption of the fibers of the optic tract to the lateral geniculate nucleus, interrupted by the mass, which dislocates the anterior commissure. **d** Coronal T2-weighted view. Note, identical to **c**, the characteristic signal of acute (hypointense) to subacute (hyperintense) hemorrhage (also hyperintense on the T1-weighted image)

lymphomas arising in the CNS in the absence of obvious lymphoma outside the nervous system at the time of the diagnosis, and should be differentiated from secondary manifestation of systemic lymphoma (Paulus et al. 2000). The mean age of manifestation in immunocompetent patients is the sixth to seventh decade, whereas the median age of incidence in immunocompromised patients (organ transplant recipients, congenitally immunodeficient or HIV patients) ranges from 10 to 39 years (Paulus et al. 2000). The most common location is supratentorial; involvement of the occipital lobe is seen in only 3%. Although multiple locations are observed in up to 50%, primary leptomeningeal involvement is seen in only 8% of patients (Grove and Vyberg 1993). The clinical presentation is unspecific, with mostly focal neurological deficits or neuropsychiatric symptoms (Paulus et al. 2000). As an exquisite sensitivity to steroids exists, these drugs should be withheld until tissue is obtained for diagnosis by stereotactic biopsy (Nasir and DeAngelis 2000).

Imaging Characteristics. Classic imaging findings show multiple, sometimes solitary masses involving deep gray matter structures, periventricular regions, and the corpus callosum (Jack et al. 1988). Hyperdense on CT or isointense to gray matter on all MRI sequences, they present with moderate perifocal edema, generally less marked than in glioblastoma or metastasis, and a diffuse contrast enhancement (Figs. 7.65, 7.66). The detection of enhancement along perivascular, leptomeningeal spaces (Fig. 7.67) should put CNS lymphoma at the top of the differential diagnosis, together with sarcoidosis and toxoplasmosis (see Fig. 7.87). In rare cases of CNS lymphoma, an additional dural involvement of the skull base, cavernous sinus, and orbit is reported (Fig. 7.67) (Jaiswal et al. 2000). Biopsy is needed, as imaging characteristics of cerebral involvement especially in AIDS patients may mimic any pathological lesion, and even the serostatus may not discriminate CNS lymphoma from toxoplasmosis. One highly sensitive and specific finding for cerebral lymphoma is the detection of Epstein-Barr virus DNA in CSF (Atlas 1996; Miller et al. 1998).

7.3.2 Nonneoplastic Lesions

7.3.2.1 Vascular Lesions

Although cerebral vascular lesions, clinically presenting as stroke, often manifest in a similar manner as other acute functional disorders of the brain, the underlying pathology includes a heterogeneous group of cerebrovascular disorders. The four major types of stroke are cerebral infarction (80%) caused by arterial vessel occlusion or as a result of inflammatory vascular disease, spontaneous subarachnoid (5%) or intracerebral hemorrhage (15%), and venous occlusion (Bradac 1990; Hankey and Warlow 1991). It is beyond the scope of this book to discuss the different clinical presentations, pathology, etiology, prognosis, and treatment of these diseases in detail (and the reader is referred to special textbooks), but some of the most important pathophysiological and diagnostic imaging criteria with regard to the visual pathway will be briefly reviewed.

7.3.2.1.1 Cerebral Infarction

Most patients presenting with the clinical symptomatology of a stroke with the sudden onset of neurological deficit as hemiparesis or hemiplegia suffer from atherosclerosis, causing macroangiopathic vascular lesions (mostly of the carotid bifurcation) with infarction of a cerebral territory (Figs. 7.68–7.71). The main arterial supply of the optic tract and optic radiation arises from the territory of the posterior cerebral artery (PCA). The PCA gives rise to the medial and posterior choroidal arteries which are in hemodynamic balance with the anterior choroidal artery, arising from the ICA and supplying the optic tract. Although considerable variation exists, the PCA mainly supplies the inferior temporal lobe and the occipital lobe (van der Zwan et al. 1992). As in acute cerebral ischemia and infarction, the blood flow is significantly diminished, but the

(Text continues on p. 416)

Fig. 7.65a–f. A 55-year-old man suffering from recurrent blurred vision. Diagnosis: primary malignant CNS lymphoma. MRI: **a** Axial T2-weighted view identifying enhancement of the right occipital paraventricular gray matter with slight perifocal edema. **b** Corresponding T1-weighted native view. **c** Corresponding T1-weighted, contrast-enhanced view with intense, homogeneous signal enhancement in the region of the right calcarine sulcus with compression of the trigone of the ipsilateral ventricle. Note the sulcal location of the left calcarine vein (*arrow*) draining into the distal left internal cerebral vein. **d** Coronal T2-weighted (FLAIR) view, demonstrating the relation of the tumor (intermediate signal) and perifocal edema (bright signal) to the calcarine sulcus (*arrows*). **e** Corresponding T1-weighted, contrast-enhanced view. **f** Paramedian sagittal, T1-weighted, contrast-enhanced view demonstrating additional, exclusively intraparenchymal tumor infiltration of the cuneus, possibly as a result of growth along the parieto-occipital sulcus

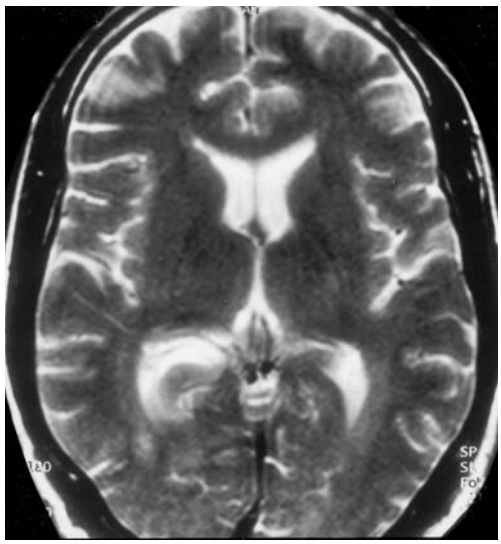

a

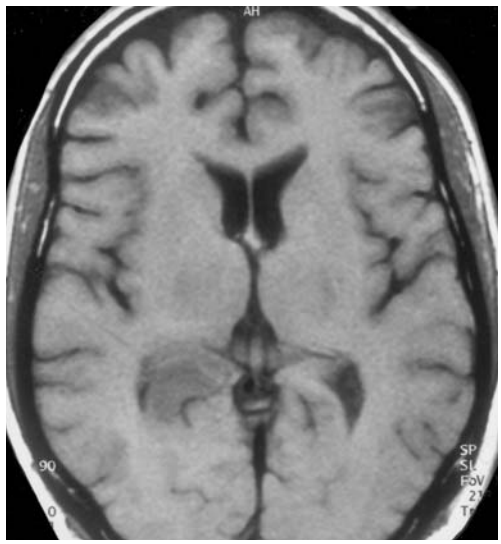

b

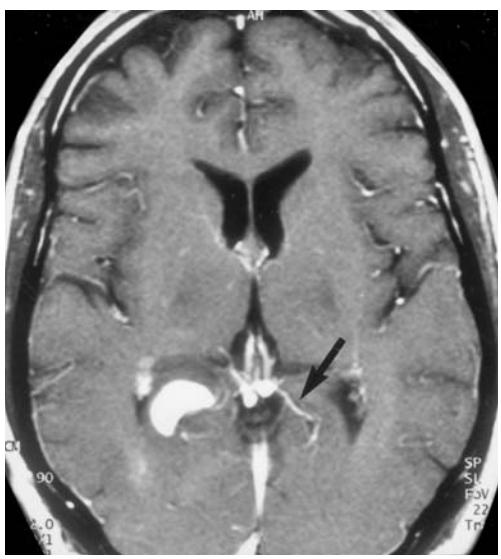

c

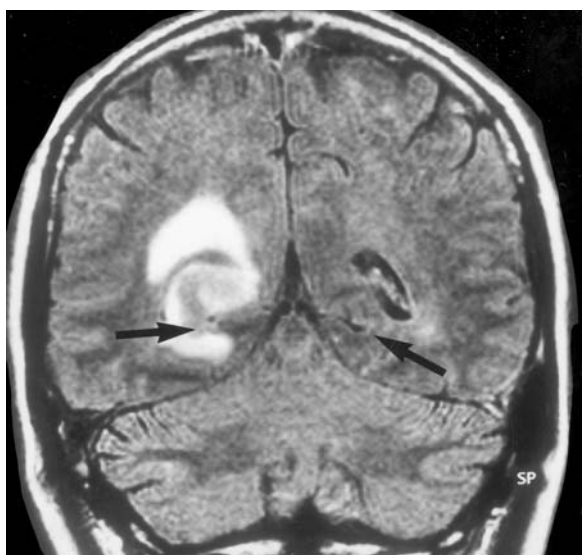

d

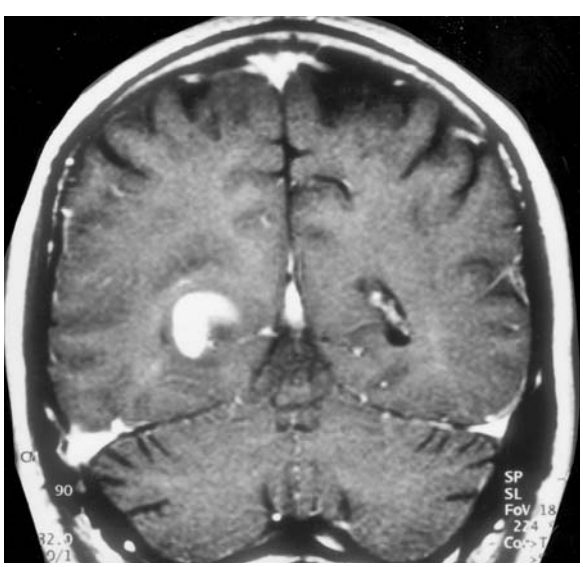

e

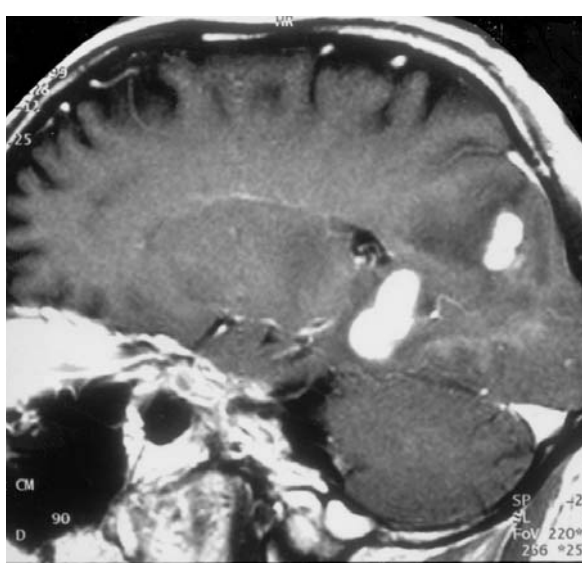

f

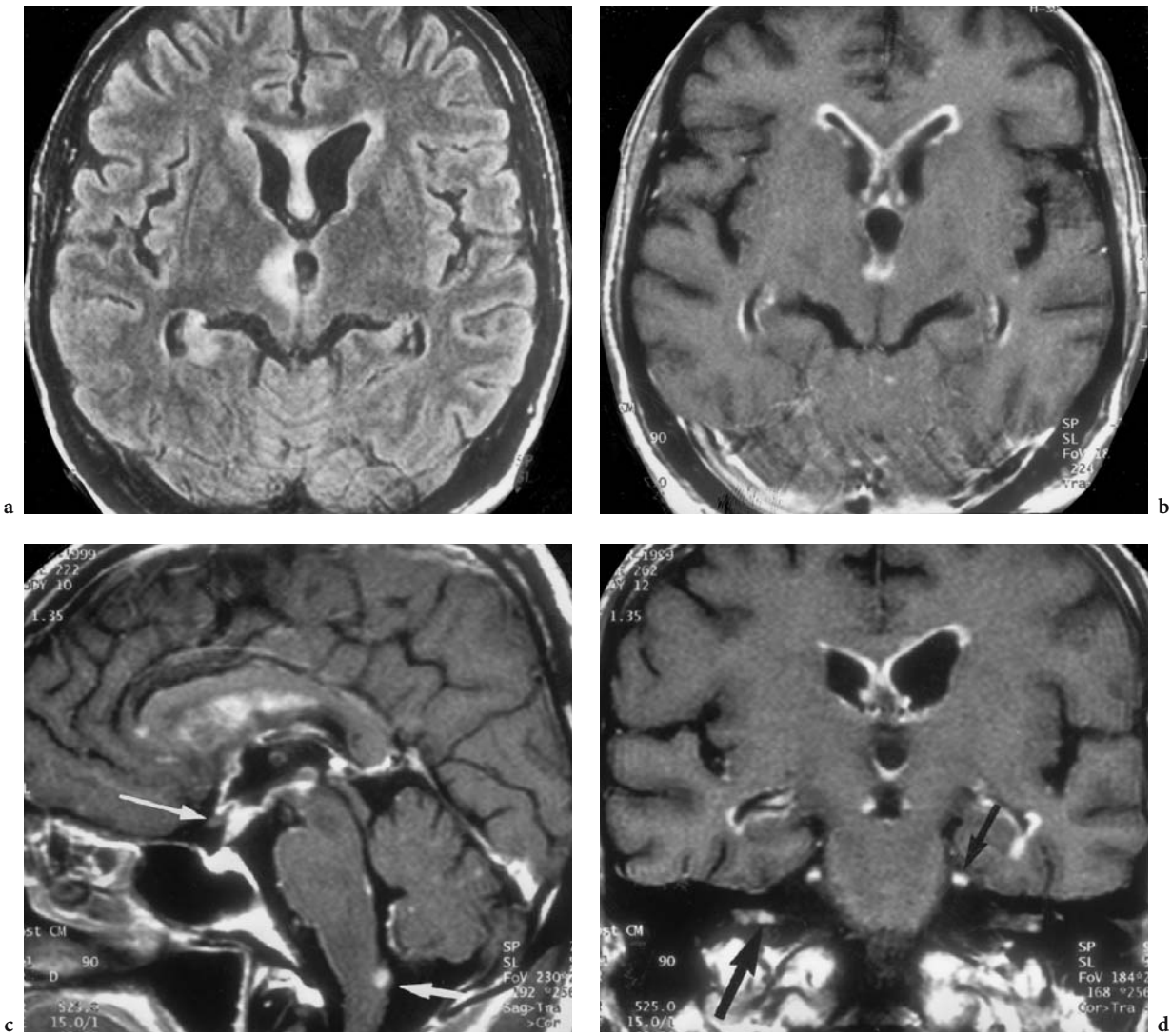

Fig. 7.66a–d. A 68-year-old man with known NHL VI a, suffering from an acute bilateral visual deficit associated with anacusis. Diagnosis: leptomeningeal NHL metastasis. MRI: **a** Axial T2-weighted FLAIR view with periventricular signal enhancement in the right thalamus and corpus callosum, indicating perifocal edema. **b** Corresponding T1-weighted, contrast-enhanced view with ependymal signal enhancement of the tumorous infiltration. **c** Midsagittal, T1-weighted, contrast-enhanced view with superior visualization of the cast of the infundibular and chiasmal recess of the third ventricle. Note signal enhancement of the ventricle ependyma, of the third and lateral ventricle, as well as meningeal metastasis at the obex (entrance of the central canal, *short white arrow*) but identification of the chiasm itself (*long white arrow*). **d** Coronal, T1-weighted, contrast-enhanced image demonstrating additional involvement of both trigeminal nerves in their cisternal course (*small arrow* indicating the left) and both vestibular nerves inside the internal auditory canal (*large arrow* on the right)

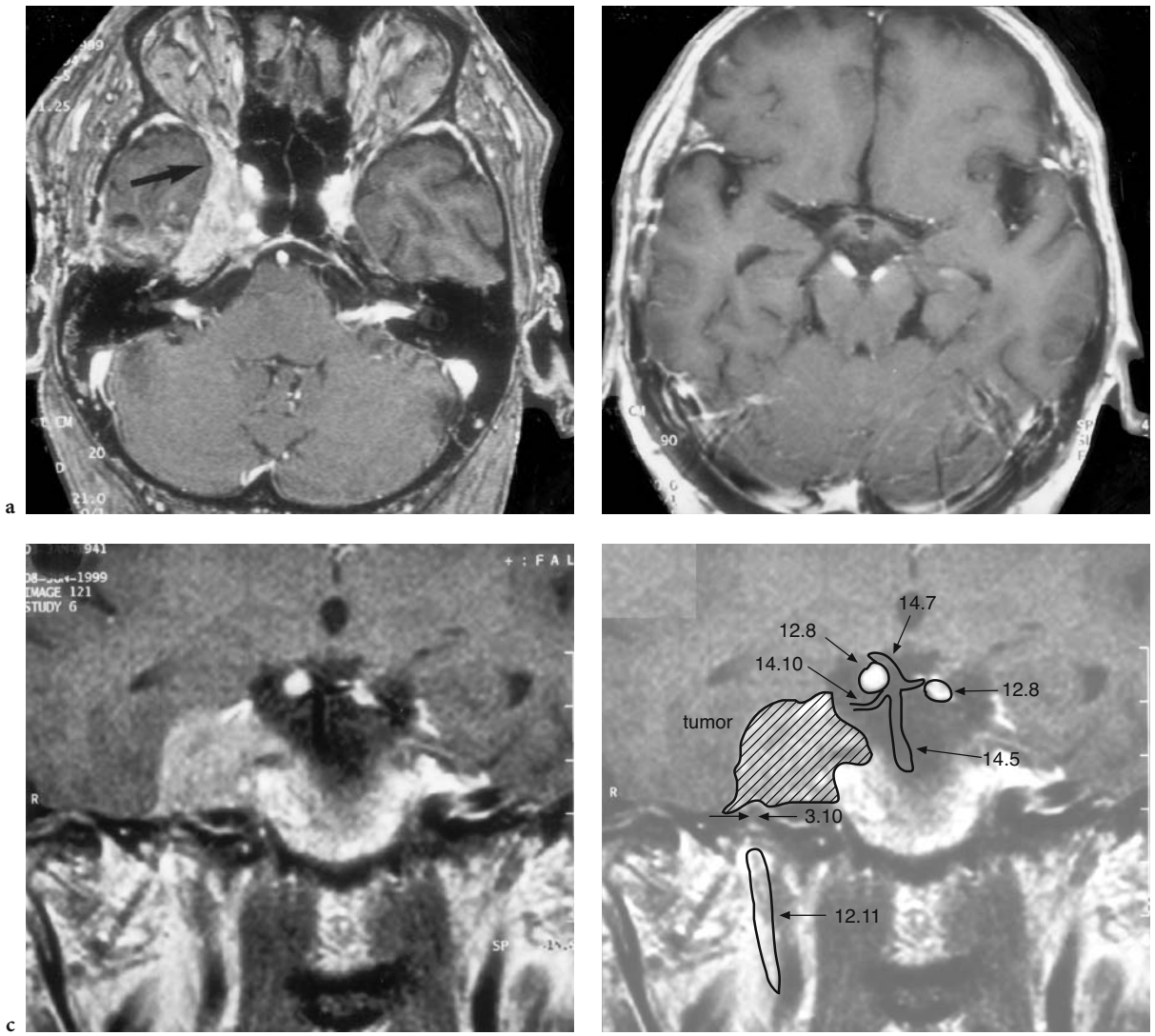

Fig. 7.67a–d. A 58-year-old man with acute ptosis of the right eye, deafness, and deficits of several cranial nerves. Diagnosis: primary CNS lymphoma. T1-weighted, contrast-enhanced MRI: **a** Axial view at the level of the internal auditory canal, demonstrating tumor involvement of both N VII/VIII nerve complexes, and a wide meningeal tumor in the right middle cranial fossa with expansion to the ipsilateral superior orbital fissure (*arrow*) and invasion of the inferior region of the ipsilateral cavernous sinus. **b** Axial view at the level of the chiasm showing significant signal enhancement of the leptomeningeal tumor-coating of both oculomotor nerves in their initial cisternal course. **c** Coronal view demonstrating both pathological findings. Note the course of the oculomotor nerves between the PCA and superior cerebellar artery. **d** Corresponding diagram: 3.10 = oval foramen, 12.8 = oculomotor nerve (N III), 12.11 = mandibular nerve (N V3), 14.5 = basilar artery, 14.7 = PCA, 14.10 = superior cerebellar artery

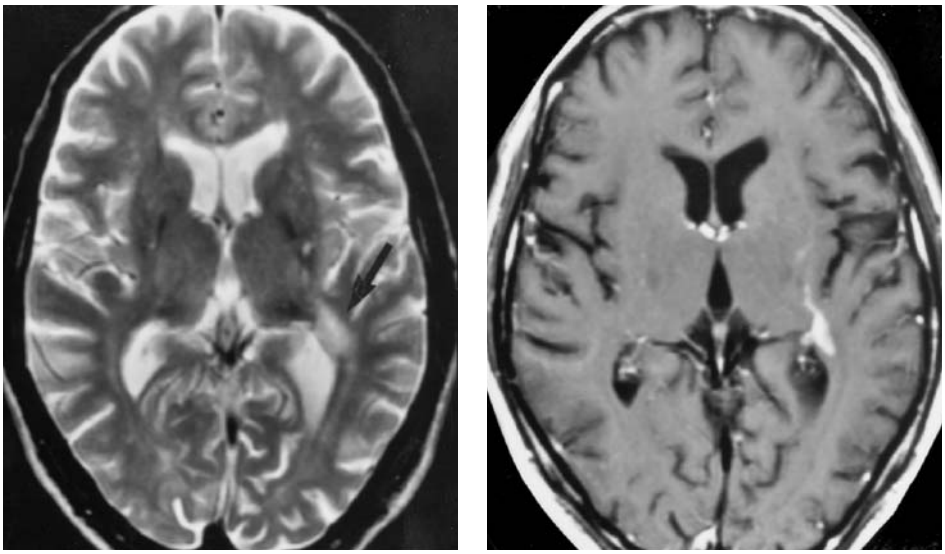

Fig. 7.68a,b. A 54-year-old man with acute hemianopia to the right and hemisymptomatology of the right lower limb. Diagnosis: isolated infarction of the anterior choroid artery. MRI: **a** Axial T2-weighted view with a hyperintense region, corresponding to the presence of infarction at the temporal horn of the left ventricle (optic radiation, *arrow*), spreading to the posterior part of the internal capsule. **b** Corresponding T1-weighted, contrast-enhanced image demonstrating BBB disruption with high signal intensity at the site of infarction. (From Müller-Forell and Lieb 1995)

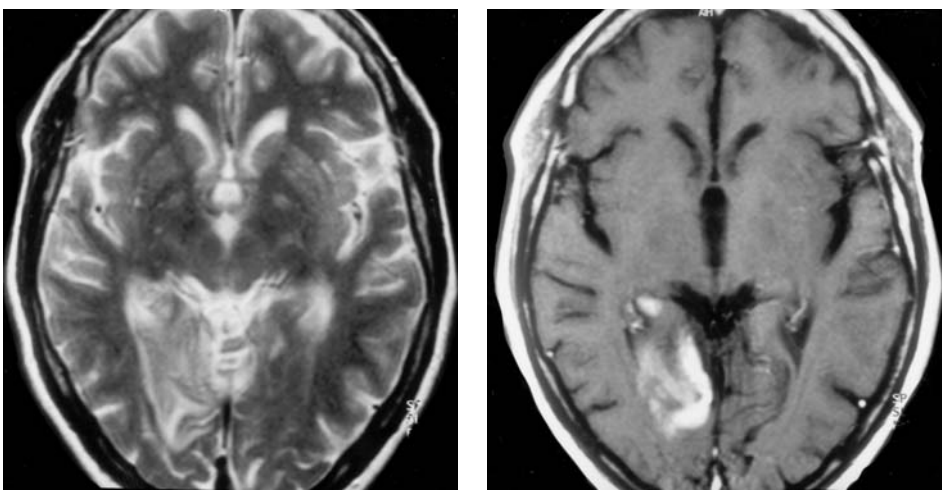

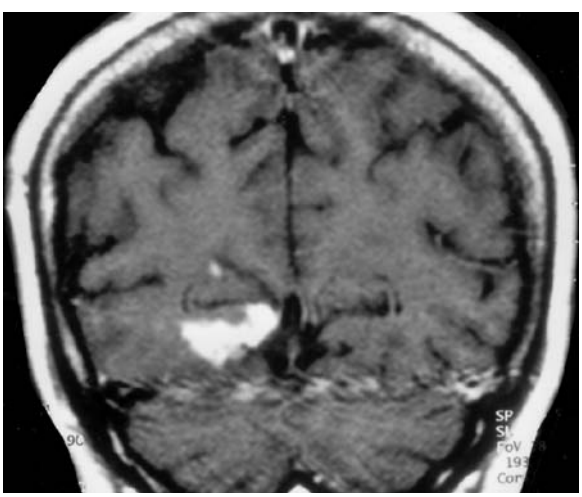

Fig. 7.69a–c. A 61-year-old woman presenting 10 days after developing symptomatology of acute left hemiparesis, without visual deficits like homonymous hemianopia. Diagnosis: infarction of the right posterior cerebral artery (PCA). MRI: **a** Axial T2-weighted view with high signal of the right rostral occipital lobe. **b** Corresponding T1-weighted, contrast-enhanced image showing the extension of the BBB disruption. **c** Coronal view visualizes sparing of the cortex of the calcarine sulcus, which explains the absence of visual deficits

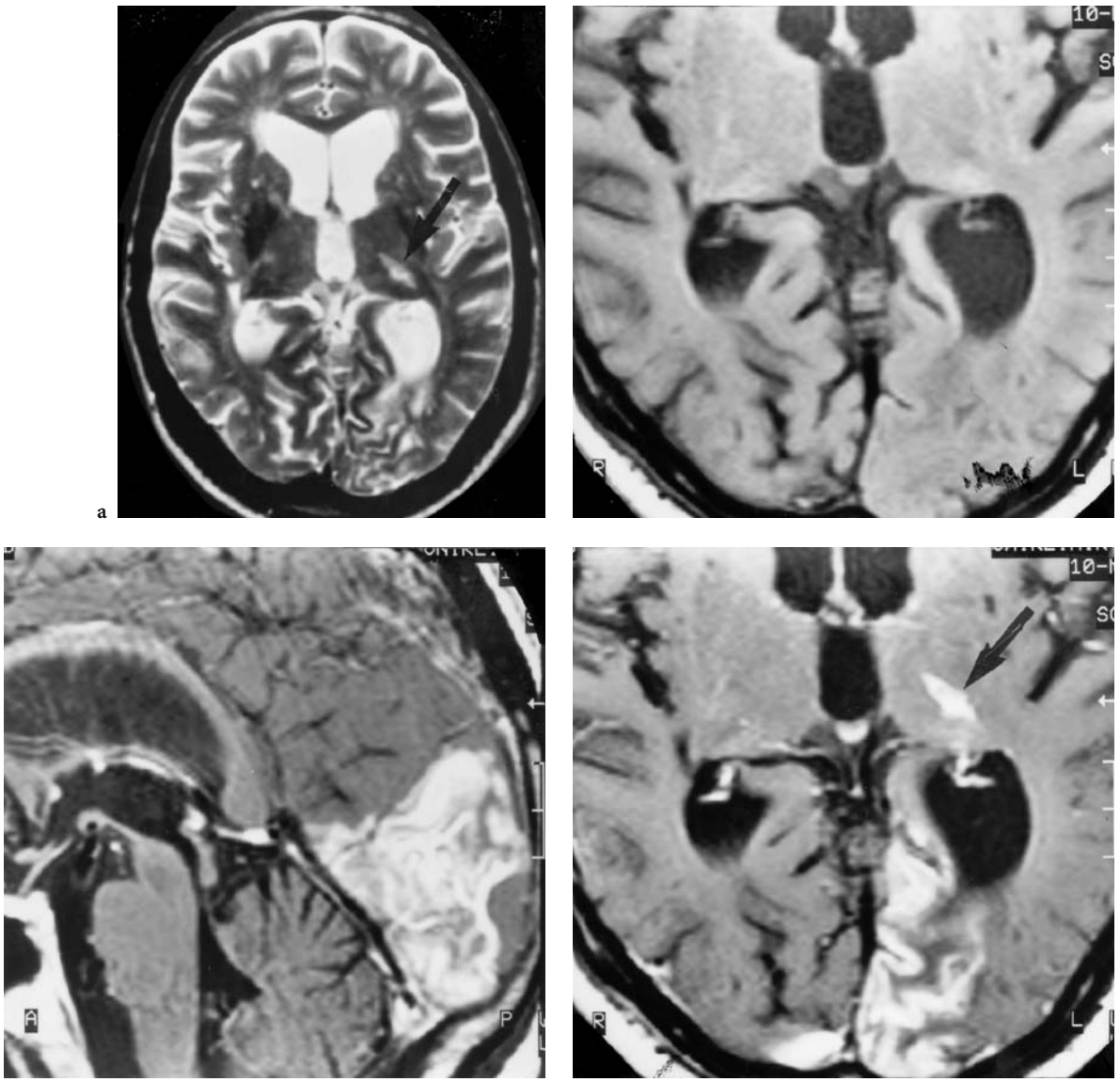

Fig. 7.70a–d. A 57-year-old man with acute homonymous hemianopia to the right. Diagnosis: infarction of the left PCA. MRI: **a** Axial T2-weighted view with slight hyperintensity in the left subcortical occipital parenchyma and lens-shaped hyperintensity in the left thalamus (*arrow*). The irregularities in the spheroid hyperintensities in the basal ganglia region correspond to pre-existent lacunar defects. **b** Corresponding T1-weighted native image showing a slight swelling of the occipital lobe and hypointense white matter. **c** Midsagittal, T1-weighted, contrast-enhanced view showing BBB disruption throughout the entire parenchyma of the occipital lobe. **d** Contrast-enhanced image (corresponding to **b**) with demarcation of the entire infarction of the occipital lobe and posterior left thalamus (*arrow*) by signal enhancement due to BBB disruption. (From Müller-Forell and Lieb 1995)

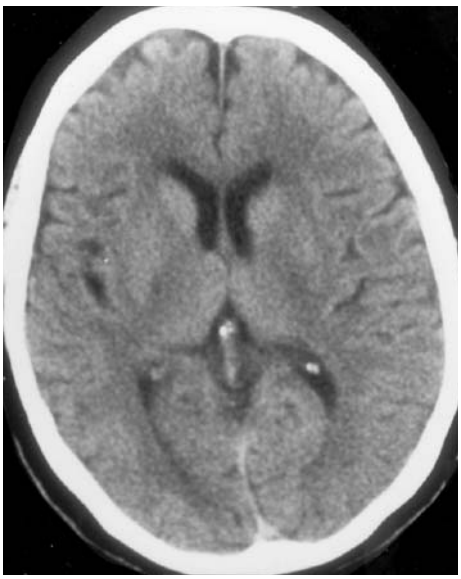

a

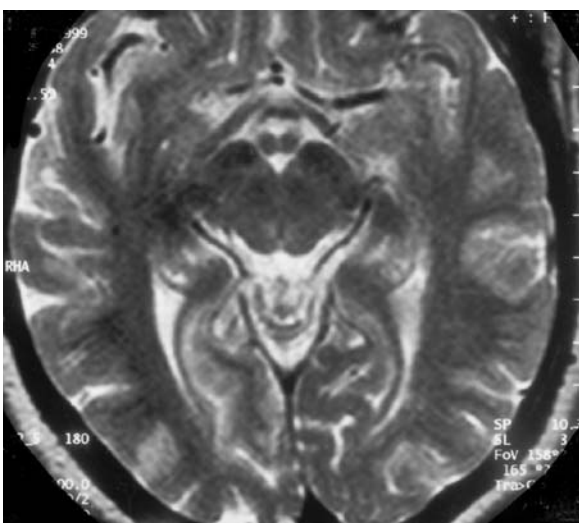

b

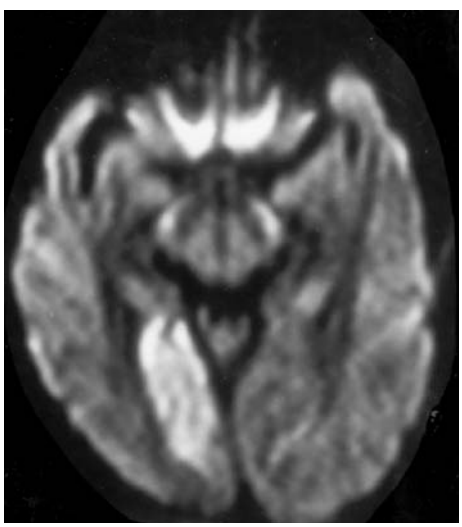

c

Fig. 7.71a–c. A 63-year-old woman presenting with acute hemianopia to the left. Diagnosis: infarction of the left PCA. CT: **a** Axial view 2 h after onset of symptomatology demonstrating only initial hypodensity of the right paramedian occipital lobe, compared with the left. MRI: **b** Corresponding T2-weighted view, acquired at the same time, showing slight subcortical signal enhancement of the right calcarine area. **c** Corresponding diffusion-weighted image, clearly delineating the involved area

damage to the affected brain depends on vulnerability, collateral supply, degree and duration of the cerebral ischemia (Osborn 1994d). This may result in some form of disproportion as even large ischemic areas or hemorrhagic infarction may only cause a little deficit and vice versa (Figs. 7.68, 7.71, 7.72–7.74). The complex tissue changes include loss of ion homeostasis, accumulation of Ca^{2+}, Na^{+}, and Cl^{-} along with osmotically required water, and anaerobic glycolysis with production of intracellular and extracellular metabolic acidosis (Siesjö 1992).

These alterations of cell membrane function and loss of cytoskeletal integrity with subsequent cell death are reflected in standard imaging studies (Hankey and Warlow 1991). In particular, MRI studies, including T2-weighted, DWI, PWI, and MRA sequences, identify the localization of the occlusion and also the area of brain damage earlier and more sensitively than with CT (Jansen and Brückmann 2001), but indirect signs, also known on CT, with subtle swelling of the affected gyri and compression of the sulci (Fig. 7.71) should not be disregarded. Additional FLAIR sequences enable the exclusion of intracerebral hemorrhage as sensitively as CT (Kueker et al. 2000; Lansberg et al. 2001). The acute accumulation of intra- and extracellular edema induces a prolongation of both T1 and T2, resulting in a high signal intensity on T2-weighted images. The early cytotoxic edema restricts the water diffusion, resulting in a high signal intensity of infarcted tissue compared with unaffected normal brain tissue, where Brown's molecular movement of protons is

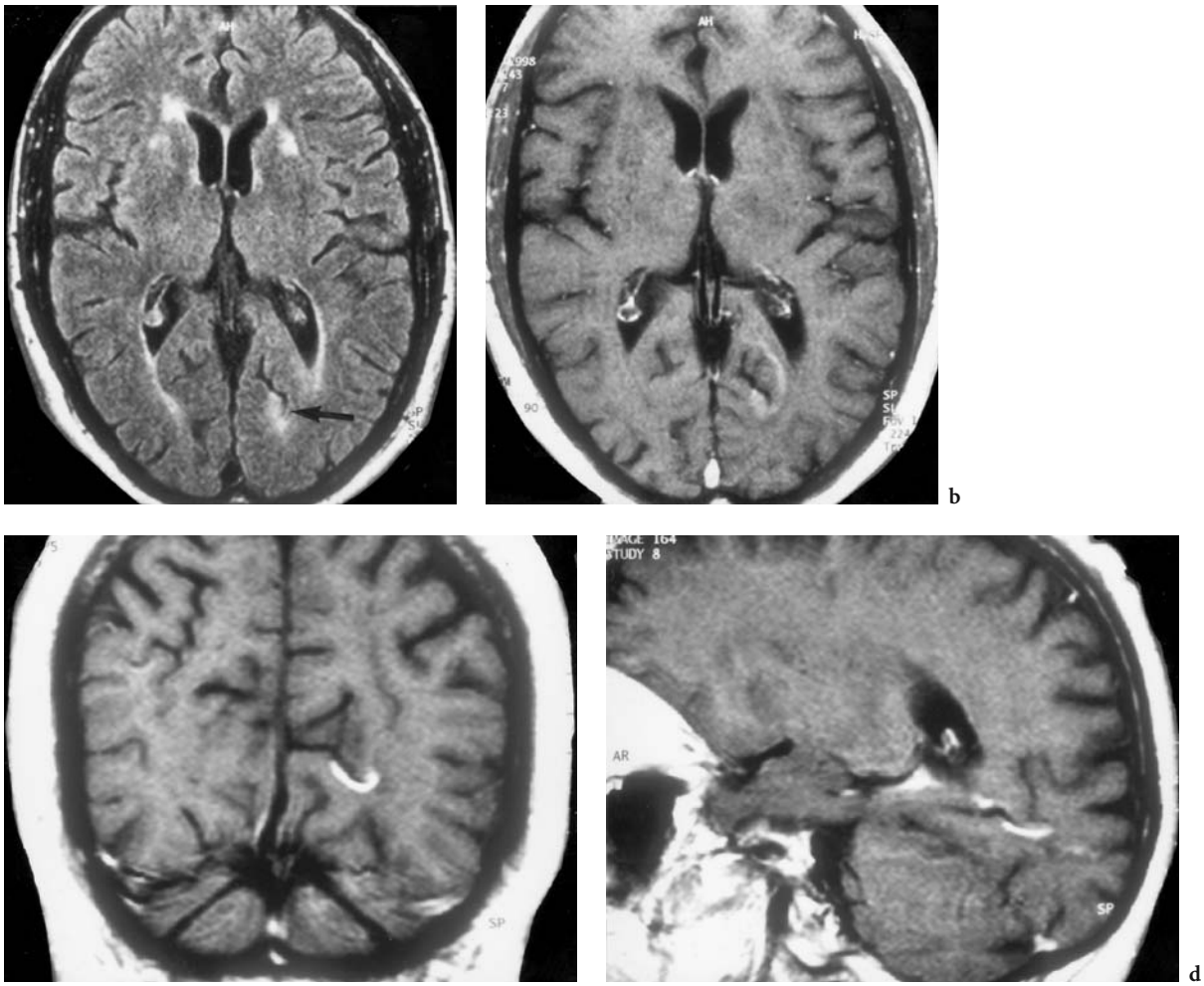

Fig. 7.72a–d. A 71-year-old man with an episode of vertigo accompanied by acute hemianopia to the superior right, 10 days previously. Diagnosis: partial PCA infarct. MRI: **a** Axial T2-weighted FLAIR sequence with a high signal in the gray matter of the left calcarine sulcus (*arrow*), in addition to older vascular lesions in the basal ganglia region. **b** Corresponding T1-weighted, contrast-enhanced view, exhibiting associated BBB disruption. Coronal (**c**) and sagittal (**d**) T1-weighted and contrast-enhanced view, respectively, demonstrating exclusive involvement of the gray matter in the depth of the calcarine sulcus

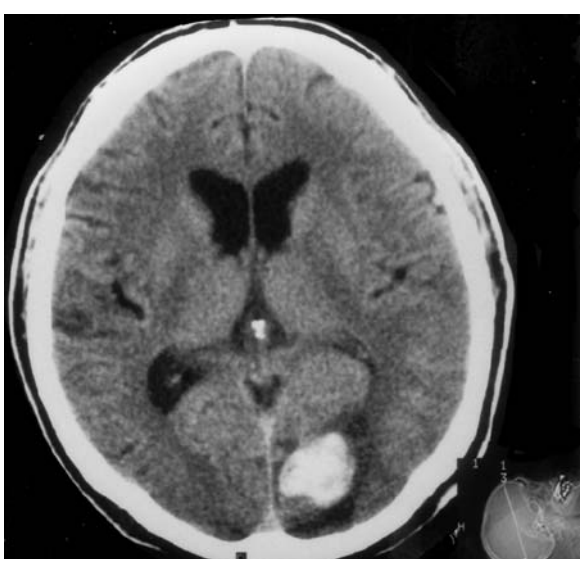

Fig. 7.73. CT of a 74-year-old man with acute hemianopia to the right side. Diagnosis: acute, spontaneous hemorrhage of the left occipital lobe

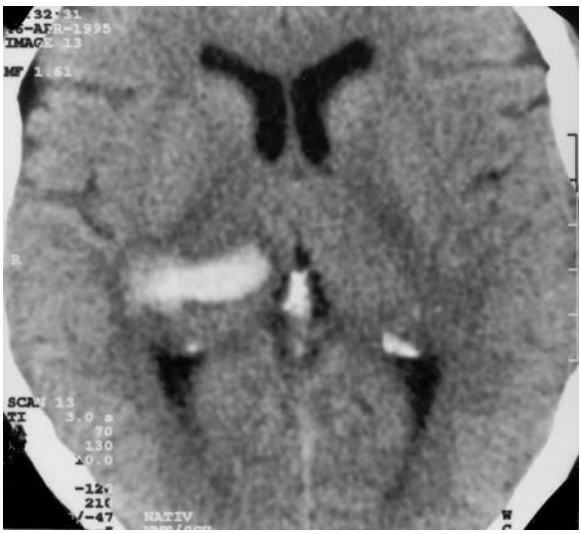

Fig. 7.74. CT of a 41-year-old woman with acute incomplete hemianopia to the left. Diagnosis: spontaneous intracranial hemorrhage of the right thalamus, extending to the proximal part of the right optic radiation. (From Müller-Forell and Lieb 1995)

unrestricted, apparent as normal low to intermediate signal intensity on DW images (Fig. 7.71, 7.75). In the course of the infarction, hemorrhagic transformation at the gray-white matter border may become evident within the first few days, while BBB disruption is identified best after the 10th day (Figs. 7.68–7.70, 7.76, 7.77) (Osborn 1994d).

7.3.2.1.2
Others (Vasculitis, Sturge-Weber)

7.3.2.1.2.1
Vasculitis

As only 5% of cerebral infarctions is caused by nonatheromatous occlusions (Hankey and Warlow 1991), vasculitis should be taken into consideration in the differential diagnosis especially in younger patients (Ferro 1998). Vasculitis is defined by its pathological findings of inflammation and necrosis of the blood vessel walls, with involvement of virtually any size or type of organ system (Fauci et al. 1978). CNS involvement is rather uncommon, classifications vary of primary (e.g., periarteritis nodosa, giant cell arteritis, Wegener's granulomatosis) or secondary in collagen vascular disease (e.g., systemic lupus erythematosus, rheumatoid arteritis), and infectious (e.g., bacterial, fungal) or noninfectious (e.g., immune/cell-mediated, chemical/drug-induced disorders, Behçet disease (Fig. 7.78), (see chapter 6.1.3.2.1) (Banna and El-Ramahi 1991; Huss et al. 1992; Osborn 1994d; Proebstle et al 1996; Ferro 1998; Wechsler et al. 1999), while isolated CNS vasculitis is a rather rare disorder (Block and Reith 2001). Multiple laboratory parameters [e.g., erythrocyte sedimentation rate (ESR), C-reactive protein (CRP), rheumatoid factor (CF), complement, cryoglobulin, and different antibodies] should rule out or prove a specific, systemic vasculitis, while CSF findings may be unspecific.

Clinical symptoms of patients suffering from cerebral vasculitis are variable and range from headache, meningeal irritation, and cranial nerve palsies to seizures or psychiatric syndromes and stroke, which may arise singly or in combination with the above. In case of additional neuropathy, myopathy and/or other organ involvement (liver, kidney), the clinical symptoms lead to the diagnosis of a systemic vasculitis (Block and Reith 2000).

As the pathologic process of perivascular inflammation may affect not only capillaries but also arterioles and arteries, MRI findings of patients with CNS vasculitis show various lesions (although not specific) with a simultaneous occurrence of microinfarctions, territorial and hemodynamic infarctions (Figs. 7.75, 7.76), and hemorrhages, but normal findings will not rule out a cerebral involvement (Block and Reith 2000). Cerebral angiography showing multiple arterial vessel irregularities with stenosis or vessel occlusion confirms the diagnosis (Fig. 7.75) (Osborn 1994d; Block and Reith 2000).

7.3.2.1.2.2
Sturge-Weber Syndrome

Sturge-Weber syndrome (synonym: encephalotrigeminal angiomatosis) is a sporadically occurring phacomatosis, one of the congenital disorders, that affects both the skin and the CNS. It is characterized by a "port wine" stain of the face (nevus flammeus) in the trigeminal nerve distribution, leptomeningeal venous angiomatosis, seizures, dementia, hemiplegia, hemianopia, buphthalmos, and glaucoma. Although the etiology is still unknown, it may be an isolated and sporadic vascular malformation with faulty development of cortical venous drainage (Elster and Chen 1990; Smirniotopoulos and Murphy 1996). The reddish-brown cutaneous stain, present at birth, is composed of abnormal, immature, small vessels with the histologic feature of both dilated capillaries as well as small veins (Enjolras et al. 1985). The intracranial involvement is always ipsilateral to the nevus flammeus of the face, affecting the occipital lobe preferentially, followed by the posterior temporal and the parietal lobe. With increasing demand of cerebral blood flow, the abnormalities of the venous drainage become

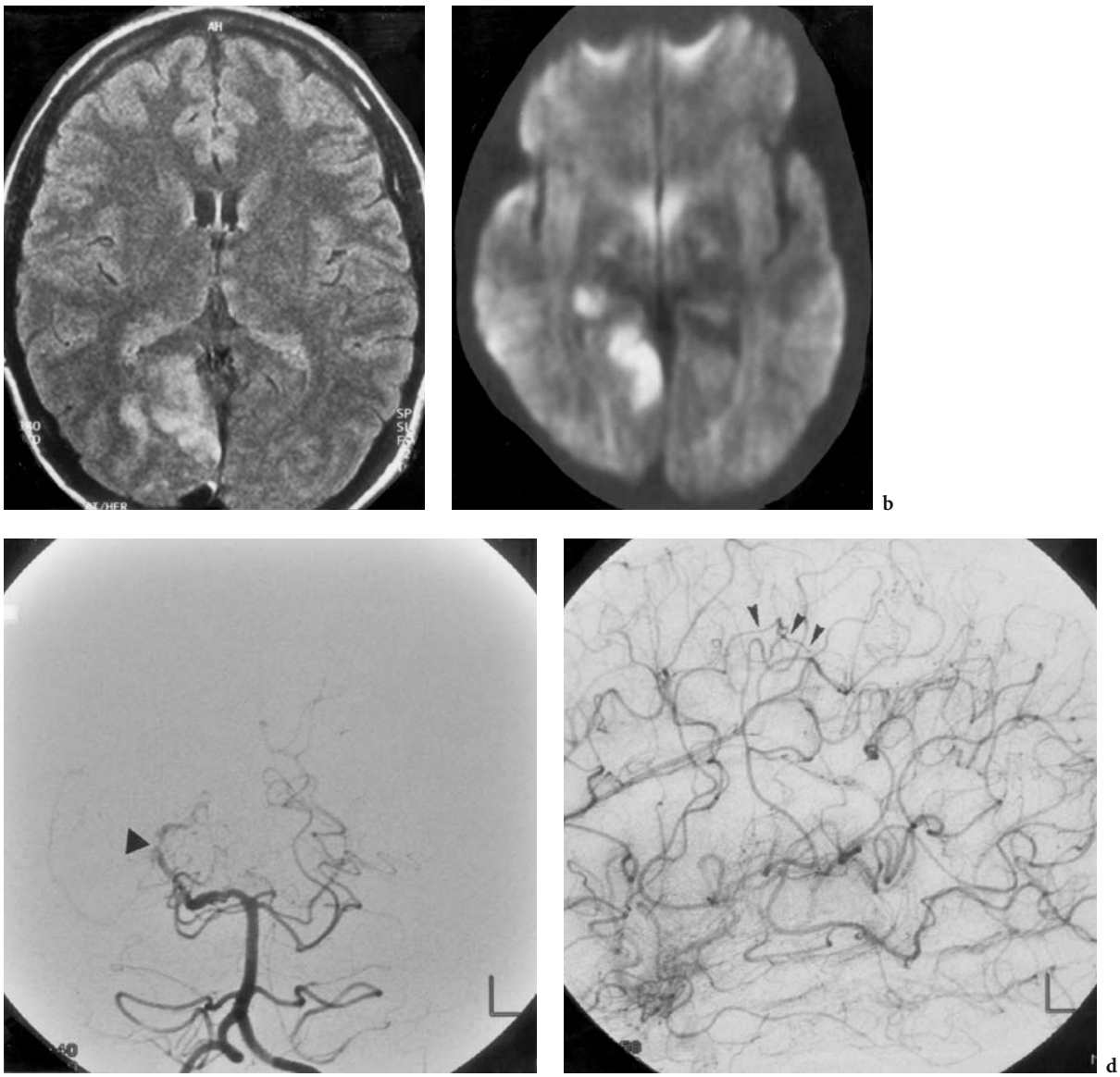

Fig. 7.75a–d. A 33-year-old woman with acute homonymous hemianopia to the left. Diagnosis: infarction of PCA associated with cerebral vasculitis. MRI: **a** Axial T2-weighted FLAIR image with an area of high signal intensity in the calcarine region. **b** Corresponding DW image with corresponding and additional signal enhancement in the right parahippocampal gyrus. Intra-arterial DSA: **c** Early arterial phase in AP (Town) view of the left VA with clearly apparent irregularity with narrowing (*arrowhead*) and fusiform widening of the right PCA in the entire distribution area. **d** Arterial phase of the left ICA in lateral view, confirming the diagnosis by segmental irregularity (*arrowheads*) of the distal branches of the MCA

significant, leading to secondary venous hypertension and thus reduced oxygen tension, leading to electrical instability of the cortex and ultimately to seizures. In the course of the disease, cellular death enables deposition of dystrophic calcification into the atrophic cortex (Fig. 7.79), which can be seen on plain skull films (Schmauser and Bittner 1990; Osborn 1994e).

MRI is more sensitive than CT in identifying the secondary changes of the affected areas, with cerebral cortical atrophy, (compensatory) ventricular and choroid plexus enlargement, and calvarial hemihypertrophy. The explanation for the superficial "gyriform" enhancement after application of gadolinium (Fig. 7.80) may be slowly flowing blood within the persistent plexus of the subarachnoid space and/or BBB loss within the cerebral cortex from chronic ischemia (Smirniotopoulos and Murphy 1996).

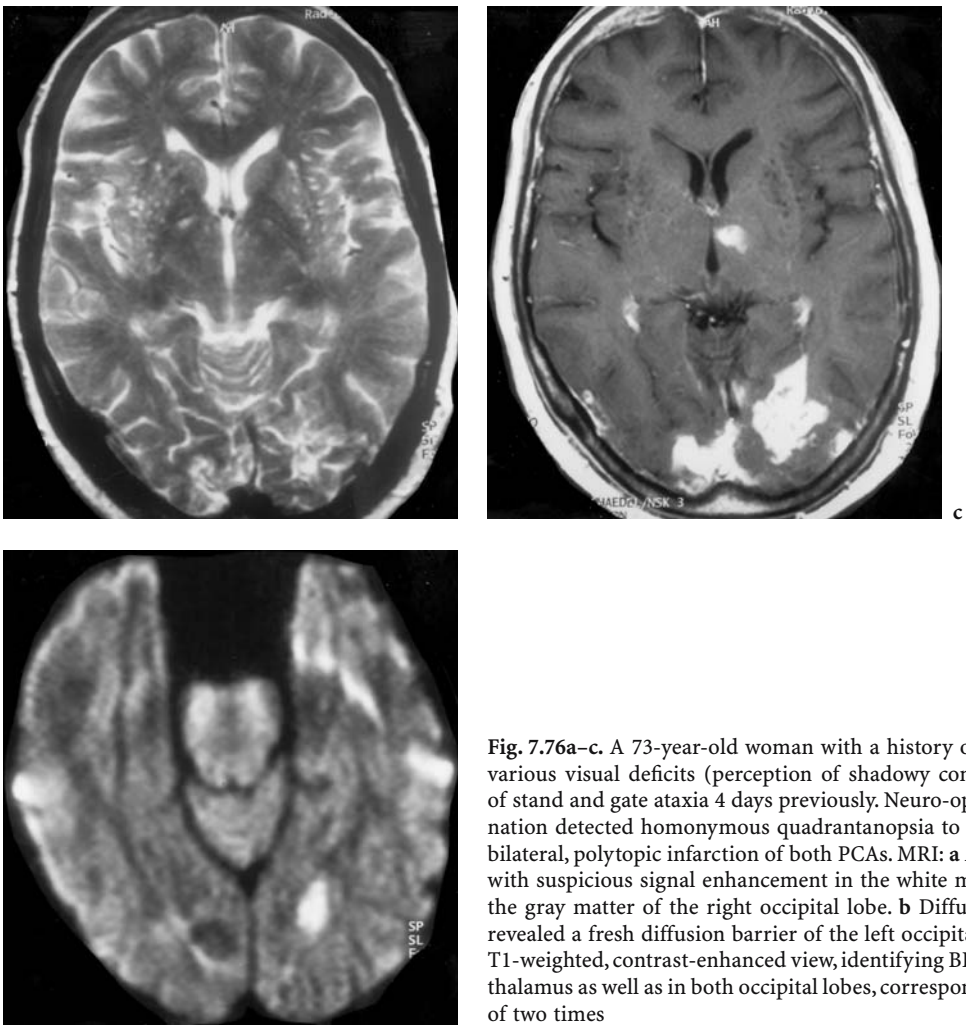

Fig. 7.76a–c. A 73-year-old woman with a history of rheumatoid arthritis, various visual deficits (perception of shadowy contours only), and onset of stand and gate ataxia 4 days previously. Neuro-ophthalmological examination detected homonymous quadrantanopsia to left inferior. Diagnosis: bilateral, polytopic infarction of both PCAs. MRI: **a** Axial T2-weighted view with suspicious signal enhancement in the white matter of the left and in the gray matter of the right occipital lobe. **b** Diffusion-weighted imaging revealed a fresh diffusion barrier of the left occipital white matter. **c** Axial, T1-weighted, contrast-enhanced view, identifying BBB disruption in the left thalamus as well as in both occipital lobes, corresponding to two infarctions of two times

7.3.2.1.2.3
Wyburn-Mason Syndrome

Another disease in the group of neurocutaneous disorders is Wyburn-Mason syndrome. This rare genetic disease without any sex predominance represents an arteriovenous malformation (AVM) that may involve parts of or even the entire visual pathway (Wyburn-Mason 1943; Lasjaunias 1997; Moussa et al. 2001). It is characterized by a diffuse nidus extending from the retina to the (mainly) ipsilateral visual pathway on its way to the calcarine fissure with involvement of the thalamus. The defect occurs early during embryogenesis, when the medial portion of the rostral and middle primitive vascular mesoderm develops, which should supply the prosencephalon and diencephalon with nasofrontal and maxillary arteries (Kupersmith 1993c; Patel and Gupta 1990; Couly et al. 1995; Lasjaunias 1997). Associated cutaneous, mainly facial abnormalities are infrequent, clinical symptomatology with progressive deficits and even retinal or intracranial hemorrhage develops over time. Visual or neurologic deficits depend on the site and extent of the malformation. CT and MRI show serpiginous vessels and alterations of the tissue in the vicinity of the lesion, cerebral angiography visualizes a typical network of small and/or large arterial feeders and draining veins supplying the AVM in the orbit, face, or brain (Kupersmith 1993c; Lasjaunias 1997).

7.3.2.2
White Matter Diseases and Inflammatory Lesions

White matter diseases include a broad spectrum of different disorders, associated with a wide range of diseases. The classification includes demyelinating disorders, characterized by a secondary loss of

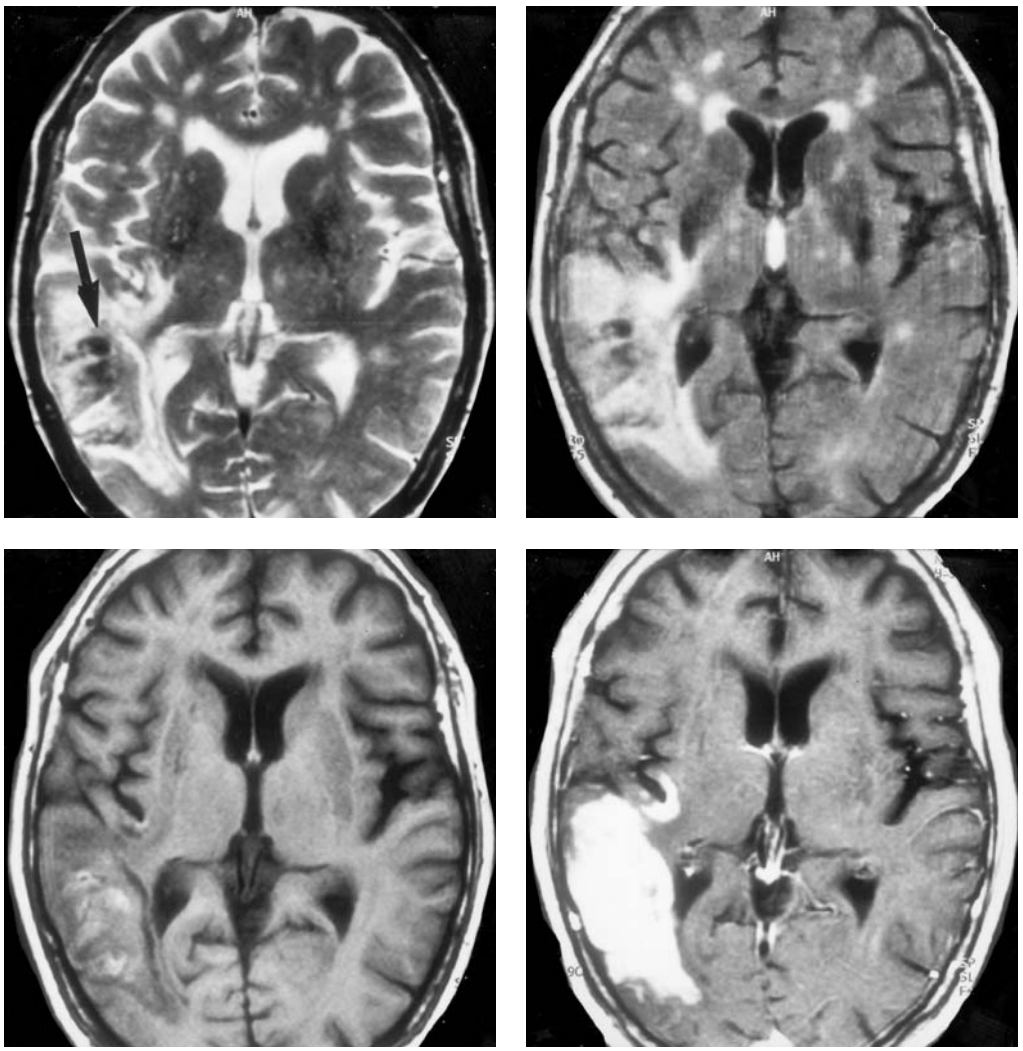

Fig. 7.77a–d. A 77-year-old woman with atrophy of both papillae and hemianopia to the left of unknown duration. Diagnosis: acute hemorrhagic infarction of the temporo-occipital right ACM territory in vascular encephalopathy. MRI: **a** axial T2-weighted view with bright signal enhancement of the right temporo-occipital parenchyma, in addition to several lacunar subcortical and thalamic infarctions. Note hypointensity (*arrow*) of the cortex and in the subcortical temporal region, corresponding to susceptibility disturbance caused by fresh to subacute blood. **b** Corresponding T2-weighted FLAIR image, where the infarction is more distinctly differentiated from the older lacunar defects. **c** T1-weighted native view with the hyperintense region (methemoglobin) of the hemorrhagic portion of the infarct area. **d** Corresponding T1-weighted, contrast-enhanced image with bright BBB disruption of the entire infarct area, corresponding to a 2- to 3-week-old infarction

myelin (e.g., multiple sclerosis) and dysmyelination, and conditions in which the process of myelination is disturbed, leading to abnormal, irregular myelination (e.g., damaged white matter after perinatal hypoxia or inherited metabolic disorders as leukodystrophy). Neurodegenerative diseases include cortical dementia among others and also primary degeneration of the deep gray matter (e.g., Wernicke's encephalopathy) (van der Knaap and Valk 1995d).

7.3.2.2.1 Multiple Sclerosis

The wide range of CNS diseases affecting the myelin sheath and largely sparing the axon (Okazaki 1989) include acute demyelinated encephalomyelitis (ADEM), demyelinating disorders associated with systemic diseases, and multiple sclerosis (MS) as the most common demyelinating disorder of the CNS.

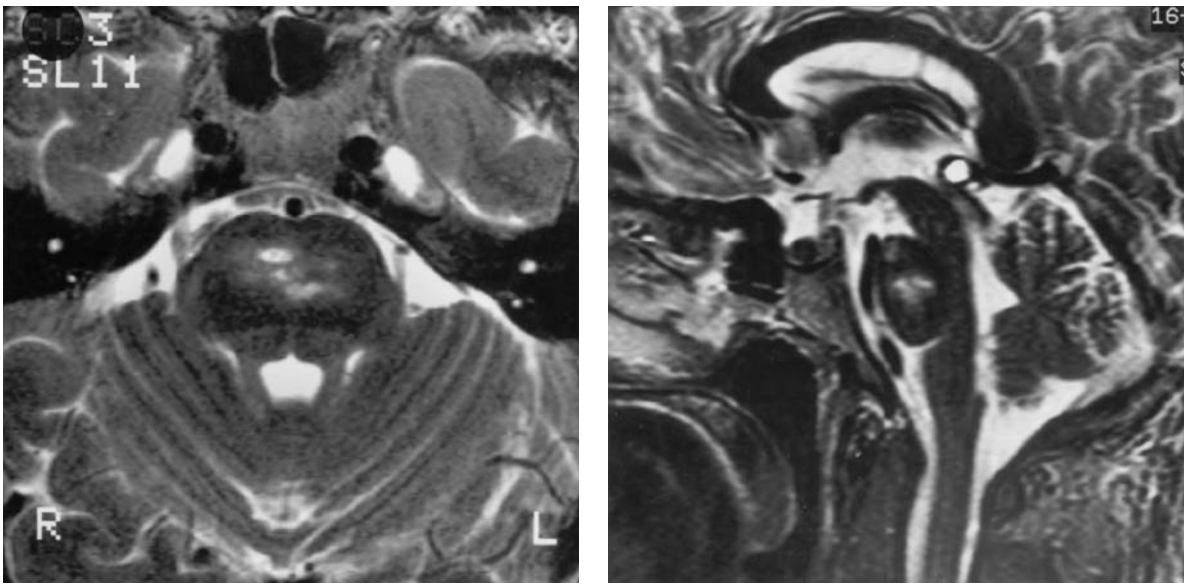

a b

Fig. 7.78a,b. A 40-year-old man with brainstem symptoms and known Behçet's disease (same patient as in Fig. 6.23, 4 years later). Diagnosis: brainstem infarction developed in the course of Behçet' disease. T2-weighted MRI: axial (**a**) and midsagittal (**b**) views showing hyperintensities in the pons, corresponding to infarctions, secondary to the perivascular inflammation (additional pineal cyst without pathognomonic relevance). (From Müller-Forell and Lieb 1995)

However, the etiology of MS is still poorly understood. Two main theories can be distinguished: one favors genetic factors, while the other advocates environmental factors. One might be influenced by the other, so that the expression of a susceptibility gene (or genes) depends on environmental factors. The chromosomal localization of the genetic material determining susceptibility for MS is probably in or near the HLA (human leukocyte antigen) region, or its expression depends on the action of certain HLA alleles (van der Knaap and Valk 1995a). The other most likely suggested pathomechanism is an autoimmune process in a genetically primed immune system assumed to produce an abnormal response, resulting in focal episodes of immune-mediated destruction of myelin sheaths (Prineas and McDonald 1997). In a vicious circle, exogenic factors may activate T-lymphocytes, which pass the BBB, express interferon-gamma and cytokines, and act as toxic agents for oligodendrocytes. Other toxic cytokines are liberated by activated macrophages, which again destroy oligodendrocytes. In the presence of additional BBB disruption, other immune cells, antibodies, and complements are involved in the inflammatory disease (Hickey 1991; Olson 1992; Arnason and Reder 1994).

The onset of MS usually occurs in patients aged from 20 to 40 years (15% before 20 years of age, 10% after 50 years) with a female predominance (Osborn 1994f; Edwards-Brown and Bonin 1996). Most often, the first and only clinical symptom consists of impaired vision, presenting as retro-bulbar neuritis (RBN) (see chapter 6.4.2.1), followed or combined with fluctuating periods of sensomotoric or gait disturbances. The clinical course of disease progression can be divided

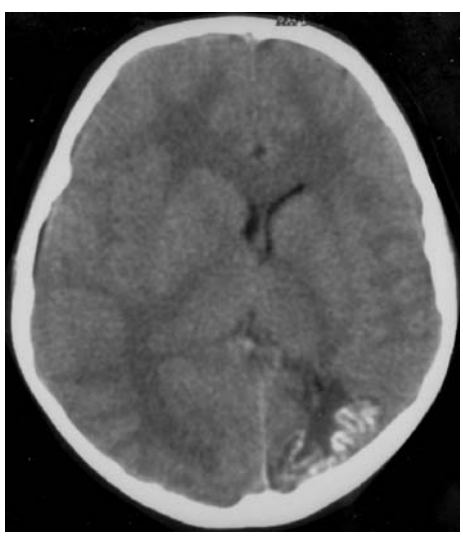

Fig. 7.79. A 7-year-old girl with occipital EEG flattening and nevus flammeus of the left face. Diagnosis: Sturge-Weber syndrome. Axial CT: gyral calcification and occipital lobe atrophy. Note the additional hemiatrophy of the left hemisphere

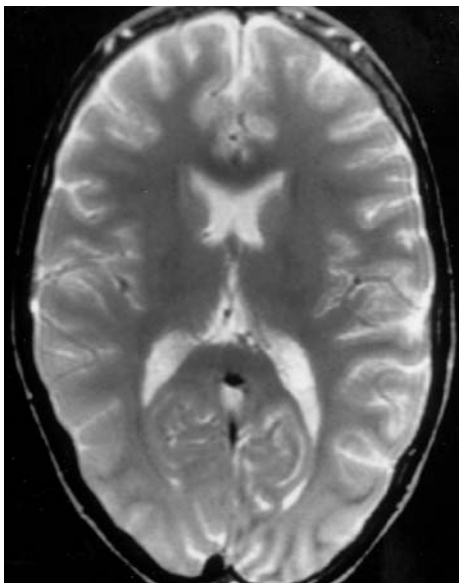

a

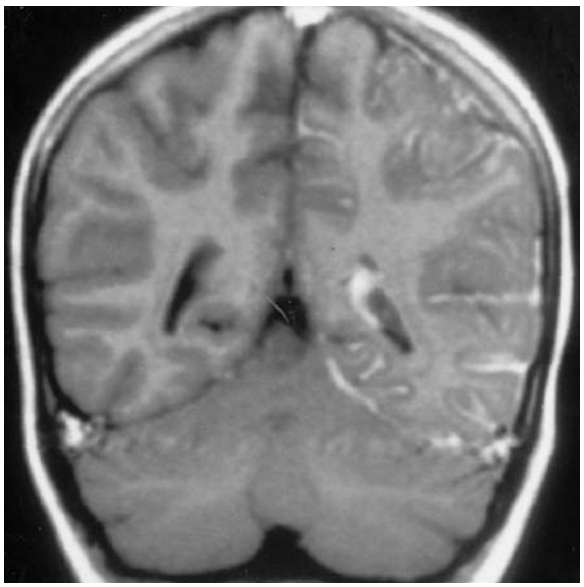

d

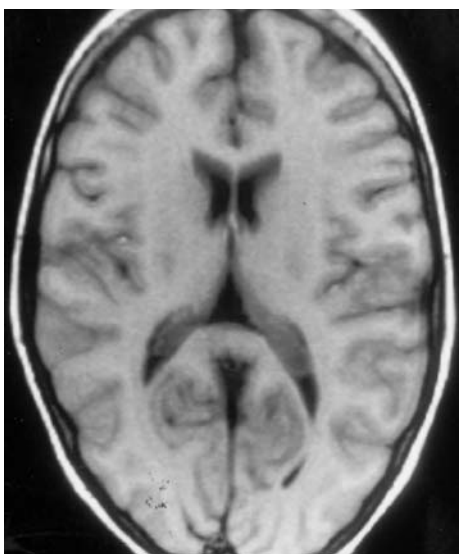

b

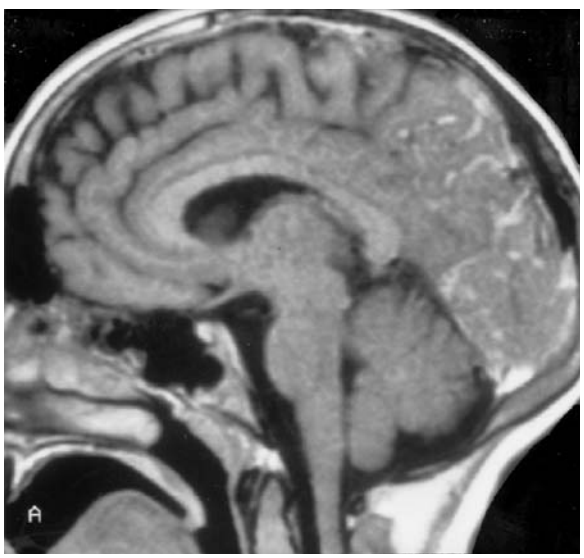

e

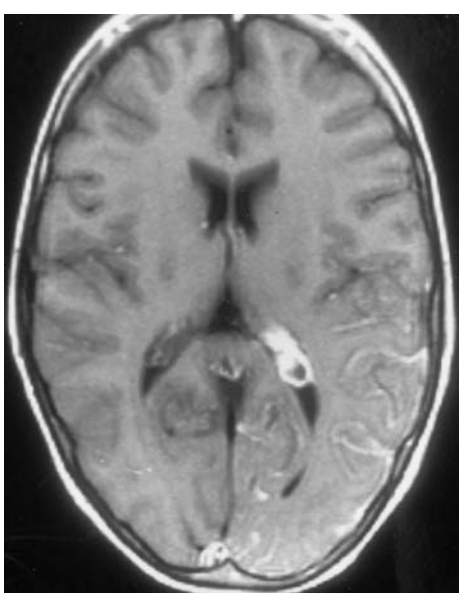

c

Fig. 7.80a–e. An 11-year-old girl with unexplained unconsciousness and known Sturge-Weber syndrome. Diagnosis: Sturge-Weber syndrome. MRI: **a** axial T2-weighted image without any evident abnormality. **b** Corresponding T1-weighted native view. **c** Corresponding T1-weighted, contrast-enhanced image, demonstrating leptomeningeal enhancement of the left temporo-occipital region as well as thickening and asymmetric enhancement of the ipsilateral choroid plexus. Coronal (**d**) and paramedian sagittal (**e**) views. Note the slight pachymeningeal enhancement at the tentorium and the convexity

into a relapsing-remitting and a chronic progressive form (Heaton et al. 1985). For the diagnosis of MS recently published new guidelines on diagnostic criteria of MS enable the physician to define the diagnosis for MS, possible MS or nor MS, replacing the diagnostic criteria of Poser et al from 1983 (McDonald et al. 2001). These guidelines include the evidence of dissemination in time and space of lesions typical for MS, objectively determined with clinical and imaging signs. The obtained imaging criteria for MS should require evidence of at least three of the four following findings:

1. one gadolinium enhancing lesion or nine T2-hyperintense lesions if there is no gadolinium enhancing lesion,
2. at least one infratentorial lesion,
3. at least one juxtacortical lesion,
4. at least three periventricular lesions.

Additional findings of CSF abnormalities with the presence of autochtone IgG production (oligoclonal bands) (McLean et al. 1990), lymphocytic pleocytosis, and abnormal VEP, typical for MS (delayed but with well preserved wave form) provide supplement information (Halliday 1993) to clinical finding of neurological disturbances typical for MS.

Imaging Characteristics. MRI is the imaging tool of choice in suspected demyelinating disorders (Sartor 1992; Osborn 1994f; van der Knaap and Valk 1995a; Edwards-Brown and Bonin 1996; McDonald et al. 2001). Although the sensitivity in detecting MS lesions is about 85% (Lee et al. 1991), the correlation of neurological symptoms and localization of imaging findings is generally poor as most foci are clinically silent (Barkhof et al. 1992), but in some cases a correlation of clinical and imaging findings is probable (Fig. 7.81). The imaging protocol should include axial and sagittal PD/T2-weighted and FLAIR sequences, where the demyelinated areas demonstrate a high signal (Filippi et al. 1999a; Reiche et al. 2000). The sagittal view is best in order to show the characteristic periventricular/pericallosal, ovoid lesions (so-called Dawson's finger), caused by the centripetal course of the medullary veins, representing the perivascular inflammation (Horowitz et al. 1989). T1-weighted native and contrast-enhanced sequences demonstrate acute or recurrent inflammatory lesions, which normally enhance contrast media, caused by BBB disruption (Paty 1997; Fazekas et al. 1999; Reiche et al. 2000).

7.3.2.2.2 Wernicke's Encephalopathy

Wernicke's encephalopathy (WE) is one of multiple exogenous toxic encephalopathies, the result of the interaction of a chemical compound with the brain, preferentially affecting the so-called topistic areas of selective vulnerability, such as e.g., basal ganglia, tectum, and tegmentum and/or the periaqueductal gray matter. As WE is caused by a nutritional deficiency of vitamin B (thiamine), it is as such not confined, but is mainly found in chronic alcoholics. The acute

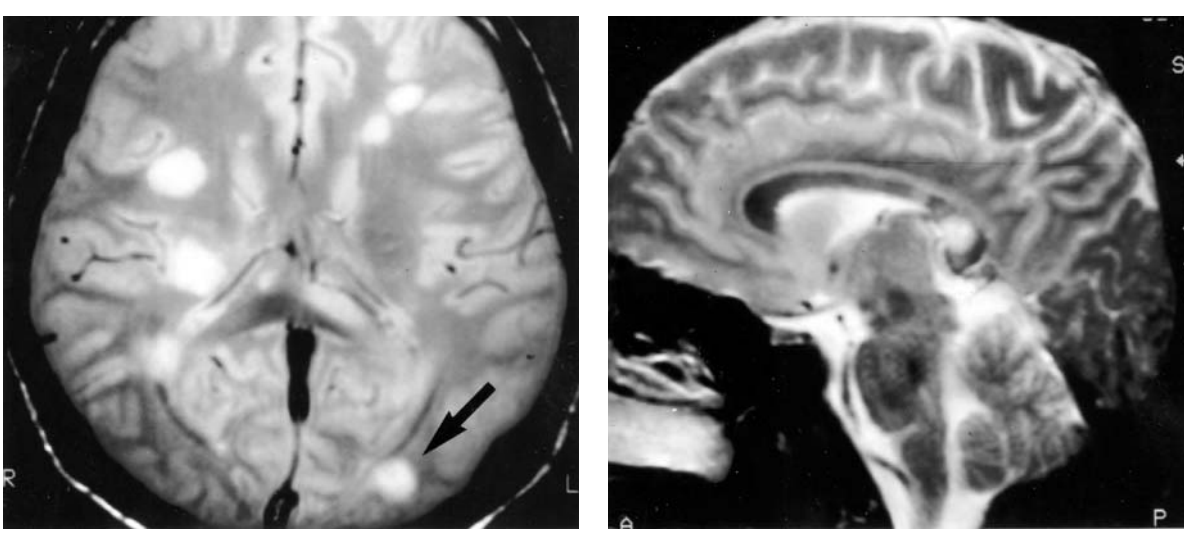

Fig. 7.81a,b. MRI of a 21-year-old man with known multiple sclerosis and an acute sensomotoric symptomatology, but no visual deficit. **a** Axial PD view, showing the disseminated inflammation areas with typical ovoid to spherical configuration in the periventricular white matter, in the area of distal left optic radiation (*arrow*), and in the posterior left splenium. **b** Sagittal T2-weighted view, where the demyelination of the posterior corpus callosum is visualized

onset of clinical symptoms consists of ophthalmoplegia, ataxia, and confusion, sometimes with additional peripheral neuropathy (Okazaki 1989; Galluci et al. 1990). The thiamine deficit results in a reduced function of excitable membranes, glucose metabolism, and neurotransmitter production, altogether resulting in a characteristically spongy degeneration of the neuropil, but relative preservation of nerve cell bodies, and a hypertrophy and hyperplasia of capillary and small vessels may show fresh petechial hemorrhage. The lesions are distributed symmetrically in the diencephalon along the brainstem, involving the mammillary bodies, the periaqueductal gray matter, and the thalami around the third ventricle (Witt 1985; Okazaki 1989; van der Knaap and Valk 1995c). The chronic stage of WE corresponds to Korsakoff disease, with consistent atrophy of the mammillary bodies and variable involvement of the dorsomedial nuclei of the thalamus (van der Knaap and Valk 1995c).

MRI reflects the pathological findings with hyperintensities on T2-weighted images at the periventricular nuclei of the thalami and mammillary bodies (Fig. 7.82); in acute stages, a contrast enhancement may be seen (Fig. 7.83) (Schroth et al. 1991).

7.3.2.2.3 Sarcoidosis

Sarcoidosis is a systemic granulomatous disease of unknown origin. With a slight predilection for women, most patients are younger than 40 years old and present with hilar adenopathy, anergy, hypercalcemia, uveitis, and a positive Kveim test. In up to 10% of the patients, neurologic involvement is evident, in rare cases as the only clinical manifestation (neurosarcoidosis) (Clark et al. 1985; Hayes et al. 1987; Zajicek et al. 1999). Histopathologic findings typically consist of noncaseating granulomas closely related to blood vessels in the leptomeninges, mostly around the base of the brain and in the posterior fossa. In some cases, an intraparenchymal extension via the Virchow-Robin spaces is seen, whereas cranial nerve

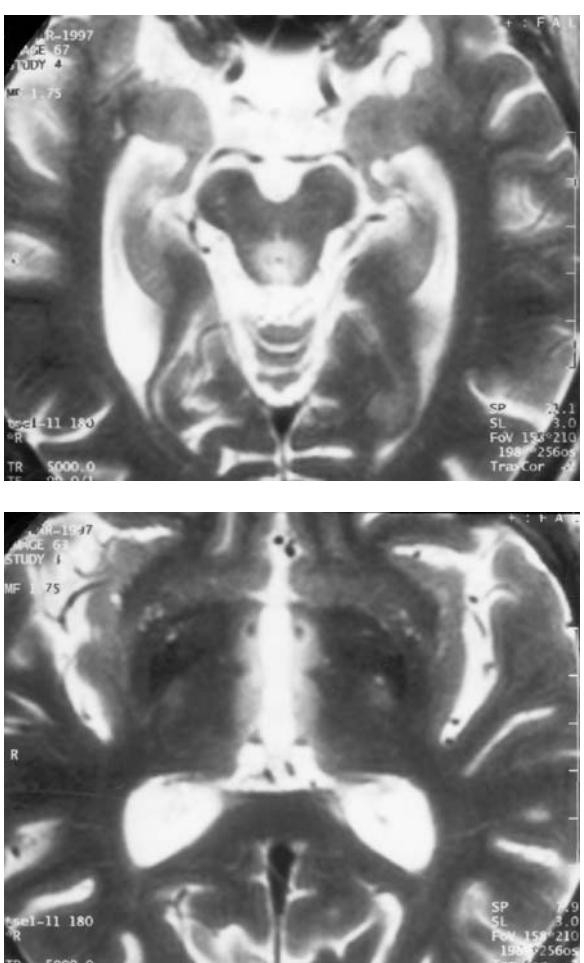

Fig. 7.82a–c. A 47-year-old woman alcoholic presenting with internuclear ophthalmoplegia (INO) and ataxia. Diagnosis: Wernicke's encephalopathy. Axial T2-weighted MRI: consecutive slices of the mesencephalon (**a** cerebral peduncles, **b** red nucleus, **c** thalamus) show characteristic signs of periaqueductal and periventricular demyelination but little involvement of the mammillary bodies (*arrows*). Neither T1-weighted abnormalities nor BBB disruption was detected

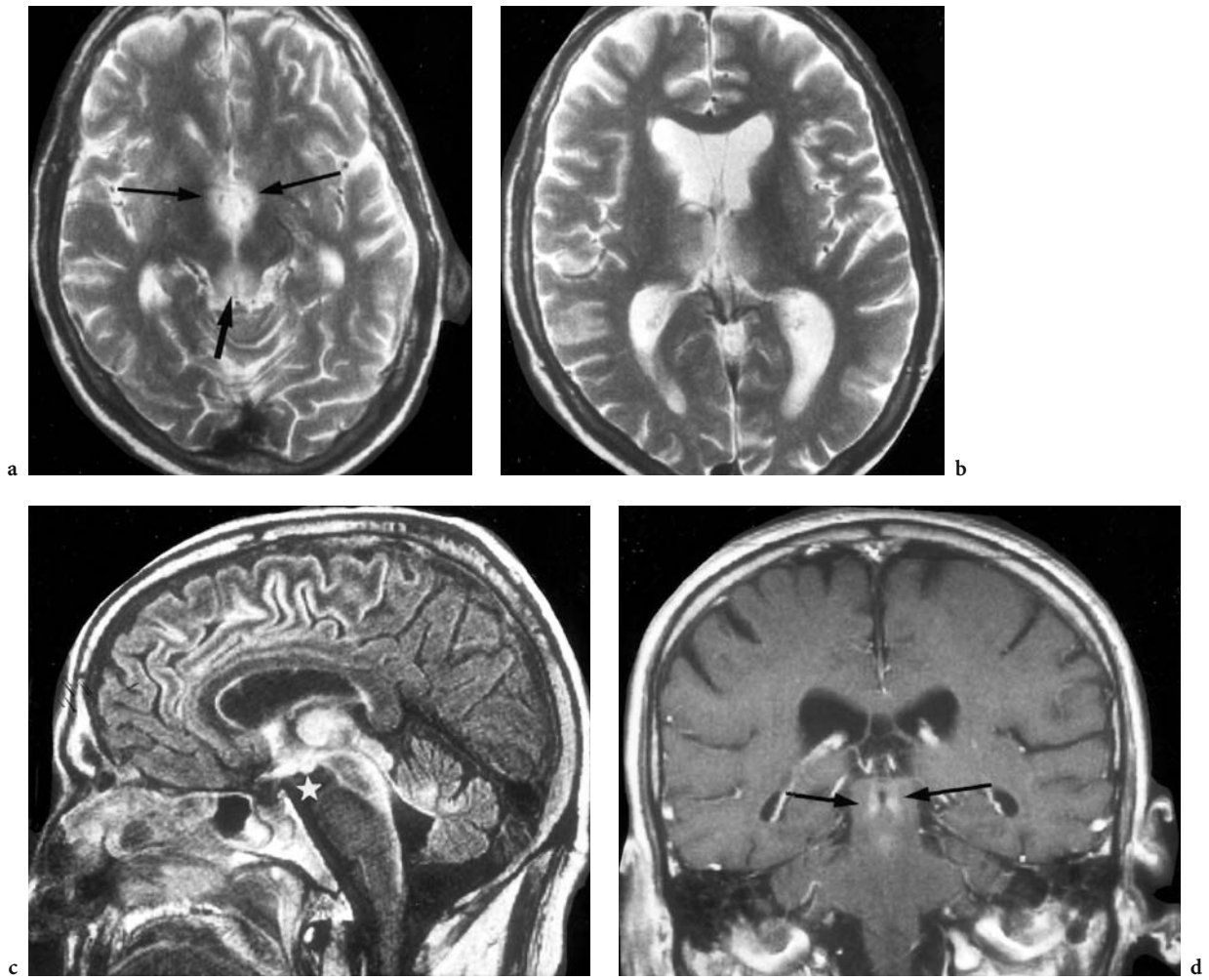

Fig. 7.83a–d. A 58-year-old man, known alcoholic, who needed resuscitation when he was found in an unconscious condition of unknown duration. MRI: **a** Axial T2-weighted view at the level of the anterior commissure, demonstrating a periaqueductal (*arrow*) and diencephalic (*thin arrows*) signal enhancement. **b** Axial T2-weighted view 10 mm above with hyperintensity of the periventricular (to the third ventricle) thalami. **c** Midsagittal T2-weighted (FLAIR) view which shows the entire lesion reaching from the hypothalamus, mammillary bodies (*white star*), thalamus, whole tegmentum, and floor and roof of the fourth ventricle. Note the cortical enhancement of the fontal brain parenchyma, residuals of hypoxemia (laminar necrosis). **d** Coronal, T1-weighted, contrast-enhanced view, where the periaqueductal BBB disruption (*thin arrows*) is apparent. (With permission of Dr. Lorenz, Radiology Department of St. Vincenz Hospital, Mainz)

involvement including the optic chiasm and nerves is the most common site of affection (Mirfakhraee et al. 1986; Okazaki 1989) (Figs. 7.84, 7.85).

Depending on the character of the lesions (solitary, multiple, or diffuse disseminating), imaging findings may resemble multiple sclerosis, systemic lupus erythematosus (SLE), non-Hodgkin lymphoma (NHL) or even inflammatory affections like tuberculous menengitis (Fig. 7.86) (Edwards-Brown and Bonin 1996; Woitalla et al. 2000). As periventricular signal intense lesions are seen in about 50% of the patients, the differential diagnosis from multiple sclerosis may be difficult, but a possible additional leptomeningeal involvement makes the diagnosis of sarcoidosis more likely (Hayes et al. 1987; Zajicek et al. 1999; Woitalla et al. 2000). In solitary or multiple lesions which often demonstrate a contrast enhancement and show a preference for the diencephalon (the floor of the third ventricle, hypothalamus) and suprasellar region, solid tumors of the suprasellar region should be taken into consideration in the differential diagnosis, along with multiple metastasis, NHL, or Langerhans cell histiocytosis (Fig. 7.22) (Woitalla et al. 2000). In up to

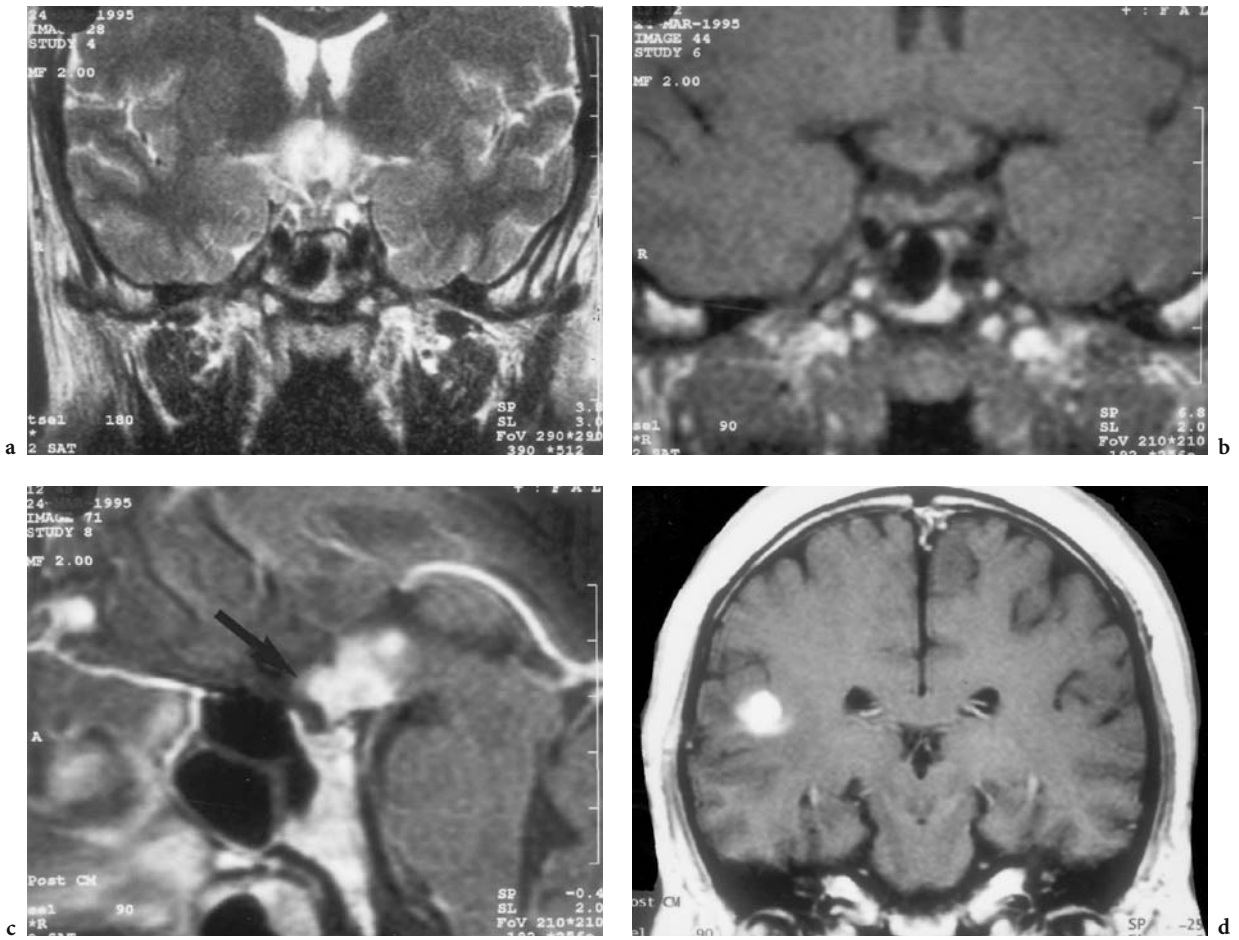

Fig. 7.84a–d. A 38-year-old man presenting with convulsions. Diagnosis on biopsy of a right temporal circumscribed focus: sarcoidosis. MRI: **a** Coronal T2-weighted view with hyperintensity of the chiasm and hypothalamic region. **b** Corresponding T1-weighted native image with undefined thickening of the chiasm. Note the small pituitary gland and short pituitary stalk. **c** Sagittal, T1-weighted, contrast-enhanced view showing localization of the enhancing granuloma in the hypothalamus and proximal pituitary stalk, reaching the largely unaffected chiasm (*arrow*) in the anterior part of the granuloma. **d** Coronal, T1-weighted, contrast-enhanced view, demonstrating the biopsied intracerebral granuloma in the posterior part of the superior temporal gyrus. (With permission of ZIR Klinikum, Ludwigshafen)

67% of patients with sarcoidosis, leptomeningeal and/or ependymal involvement is found (Herring and Urich 1969; Lexa and Grossman 1994) as part of intraparenchymal involvement with the possibility of the development of an occlusive hydrocephalus (Woitalla et al. 2000).

7.3.2.2.4
Miscellaneous Inflammations and Infections (Toxoplasmosis, Acute Disseminated Encephalomyelitis (ADEM))

In the wide range of inflammatory brain lesions, whether originating from viral, bacterial, parasitic, or fungal infection, we focus on only two but refer to comprehensive textbooks for detailed information (Osborn 1994g; Atlas 1996).

7.3.2.2.4.1
Toxoplasmosis

In immunodeficient patients, mainly those undergoing immunosuppressive therapy or patients with AIDS, the seropositivity for adults caused by an infection with the obligate intracellular protozoan *Toxoplasma gondii* is up to 70% (Levy et al. 1985). The most common opportunistic infection in these patients (20%–40%) involves *T. gondii*, which may lead to focal or diffuse necrotizing toxoplasma

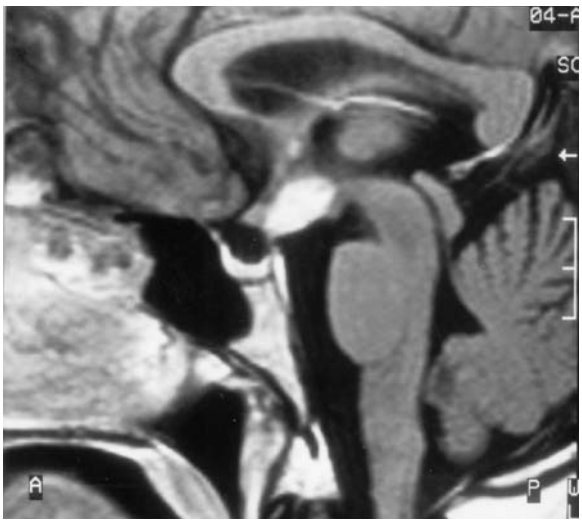

a

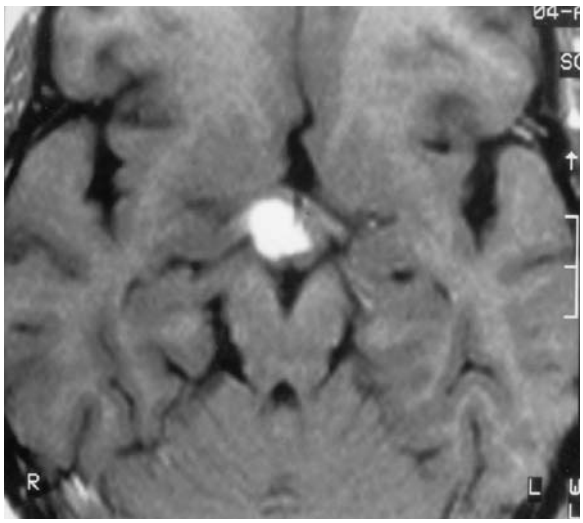

b

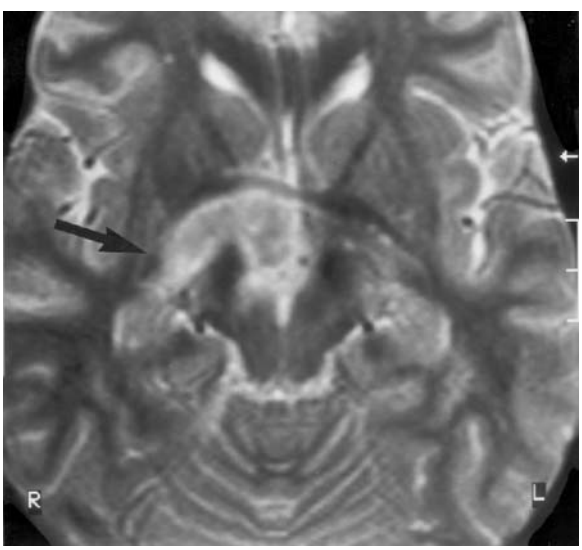

c

Fig. 7.85a–c. A 21-year-old woman with secondary dysmenorrhea, weight gain, and deregulation of temperature in the absence of ophthalmological deficits. Diagnosis: sarcoidosis. MRI: **a** midsagittal, T1-weighted, contrast-enhanced view with homogeneous lesion of the hypothalamus, located anterior of the mammillary bodies and apparently dislocating the chiasm, better seen in **b**. **b** Axial, T1-weighted, contrast-enhanced image showing substantial posterior depression and anterior dislocation, particularly on the right side, of the chiasm. **c** Axial T2-weighted image at the level of the anterior commissure, demonstrating dislocation of the anterior commissure as well as infiltration of the right optic tract (*arrow*). (**c** with permission of Müller-Forell 2001)

encephalitis, clinically presenting with altered mental status, fever, seizures, and/or focal neurologic deficit (Rovira et al. 1991; Whelan et al. 1983). Pathologically, toxoplasmotic cerebral lesions show three distinct zones but no capsule: (1) a central avascular zone that demonstrates coagulative necrosis but few organisms, (2) a hypervascular intermediate zone, containing numerous free extra- and intracellular tachyzoites but less necrosis, and (3) a peripheral zone, mostly composed of encysted organism (Rovira et al. 1991).

Corresponding to pathological changes, a "target" appearance of the solitary or multiple ring-enhancing masses with perifocal edema is common. Rim or focal nodular enhancement following contrast administration are seen on CT and also on MRI (Fig. 7.87) (Osborn 1994g). The most important, but sometimes hardly distinguishable differential diagnosis is from primary CNS lymphoma (Dina 1991). While a periventricular location and subependymal spread favor lymphoma, more than one lesion, preferentially adjacent to or in the region of the basal ganglia, make toxoplasmosis likely (Osborn 1994g).

7.3.2.2.4.2

Acute Disseminated Encephalomyelitis (ADEM)

In contrary to multiple sclerosis, ADEM is characterized by an acute monophasic disorder, predominantly occurring following a viral infection or vaccination with a mean latent period of 4–6 days or several weeks; sometimes it is seen without recognized antecedent. ADEM may occur at any age,

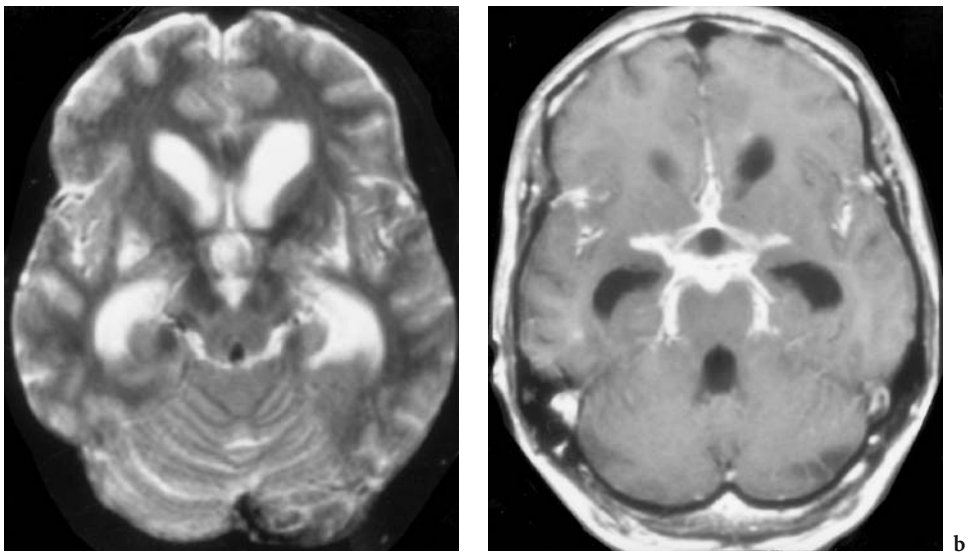

Fig. 7.86a–c. MRI of a 40-year-old man with a progressive visual deficit followed by loss of consciousness. Diagnosis: tuberculous meningitis. MRI: **a** Axial T2-weighted view at the level of the anterior commissure, demonstrating bilateral infarction of the basal ganglia in addition to enlargement of the supratentorial ventricles (indicating CSF disturbance). **b** Corresponding T1-weighted, contrast-enhanced view visualizing inflammatory infiltration of the entire basal cisterns. **c** Coronal, T1-weighted, contrast-enhanced view also showing complete casting of the basal cisterns with encasement of the chiasm and vessels

but shows a preference for children or young adults (van der Knaap and Valk 1995b; Osborn 1994g; Barkovich 2000). Consequently, the simultaneous occurrence of polytopic neurological symptoms such as hemi-, di- or tetraplegia, cerebellar ataxia or cranial nerve palsies, combined with optic neuritis and bladder dysfunction, may lead to the correct diagnosis. The patients may present with multifocal symptoms ranging from seizures and focal neurological deficit to coma and death (Rosemberg et al. 1992). The pathology consists of perivenous and perivenular inflammatory mononuclear cell infiltrates, associated with a zone of demyelination in the brain, brainstem, and spinal cord. The bilateral but slightly asymmetric lesions typically affect both the white and gray matter, with severer destruction in the white matter (Okazaki 1989; van der Knaap and Valk 1995b).

As in all demyelinating diseases, MRI shows best the mainly subcortical, confluent, bilateral but slightly asymmetric hyperintense foci on T2-weighted images (Fig. 6.189). Consequently, along with the monophasic clinical symptoms, if BBB disruption is apparent, a similar enhancement of the lesion is seen, in contrast to MS, where only acute foci show a T1 time shortening with signal enhancement (Osborn 1994g; Barkovich 2000; Schwarz and Gass 2001).

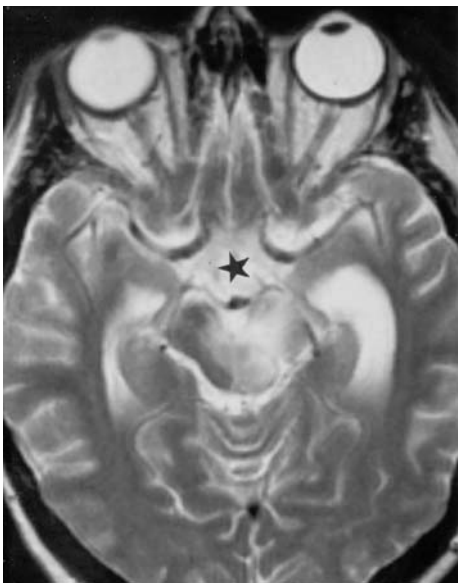

a

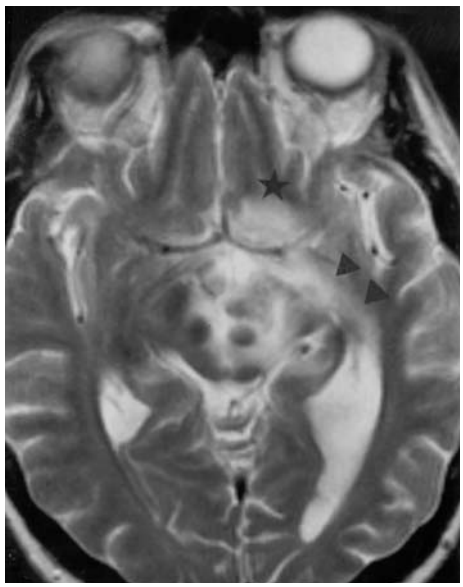

b

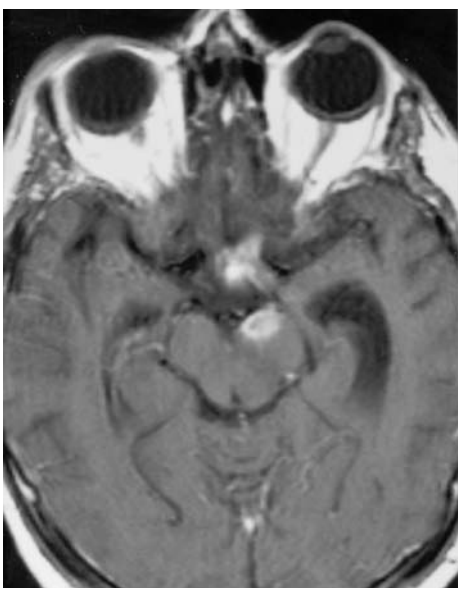

c

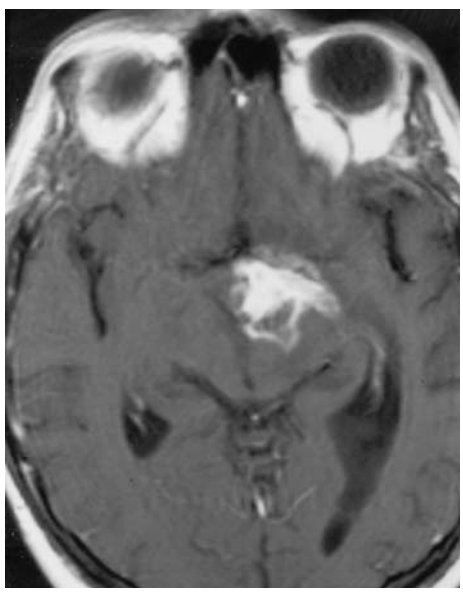

d

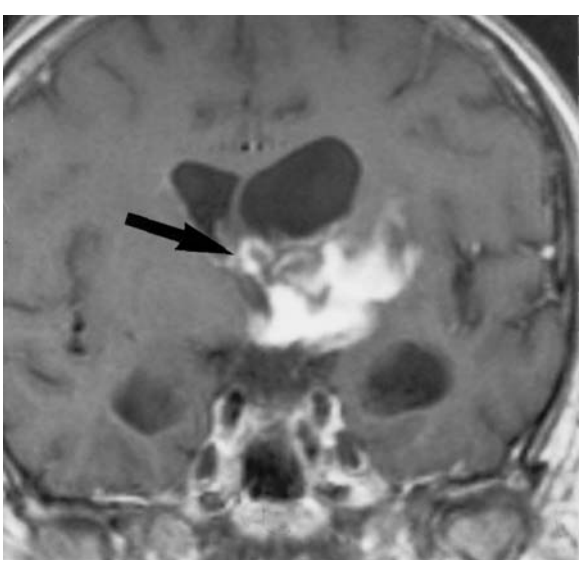

e

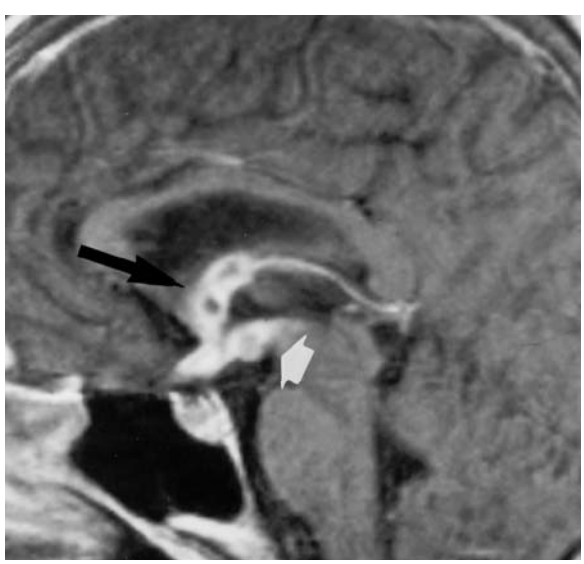

f

Fig. 7.87a–f. A 42-year-old man with a history of HIV infection, suffering from undefined visual deficits and indisposition. Diagnosis: cerebral toxoplasmosis. MRI: **a** Axial T2-weighted view showing irregular signal enhancement in the midbrain, favoring the left peduncle and inferior quadrigeminal plate, as well as involvement of the entire chiasm (*star*). **b** Additional T2 signal enhancement is seen in the basal part of the frontal lobe (subcallosal area) (*star*) and the left optic tract (*arrowheads*). Note sparing of the red nuclei in the edematous cerebral peduncle. **c** Axial, T1-weighted, contrast-enhanced image corresponding to **a** with BBB disruption of the chiasm and anterior left peduncle. **d** Corresponding image to **b** with infiltration of the hypothalamus, left cerebral peduncle and the left optic tract. **e** Coronal contrast-enhanced view identifying local toxoplasmotic inflammation of the basal ganglia as well as additional infiltration of the left fornix (*arrow*), better seen in **f** paramedian sagittal, T1-weighted, contrast-enhanced view with additional involvement of the mammillary bodies (*large white arrow*).(With permission of Dr. R. Gustorf-Aeckerle, Katharinen Hospital, Stuttgart)

References

Adams HP, Jergenson DD, Kassell NF, Sahs AL (1980) Pitfalls in the recognition of SAH. JAMA 244:794–796

Adamson TE, Wiestler OD, Kleihues P, Yasargil MG (1990) Correlation of clinical and pathological features in surgically treated craniopharyngiomas. J Neurosurg 73:12–17

Aoki S, Barkovich AJ, Nishimura K, Kjos BO, Macida T, Cogen P, Edwards M, Norman D (1989) Neurofibromatosis types 1 and 2: cranial MR findings. Radiology 172:527–534

Armstrong EA, Harwood-Nash DC, Hoffman H, Fitz CR, Chuang S, Petterson H (1983) Benign suprasellar cysts: the CT approach. AJNR Am J Neuroradiol 4:163–166

Arnason BGW, Reder AT (1994) Interferons and multiple sclerosis. Clin Neuropharmacol 17:495–547

Atlas SW (1996) Magnetic resonance imaging of the brain and spine, 2nd edn. Lippincott-Raven, Philadelphia

Balcer LJ, Liu GT, Heller G, Bilaniuk L, Volpe NJ, Galetta SL, Molloy PT, Phillips P, Janss AJ, Vaughn S, Maguire MG (2001) Visual loss in children with neurofibromatosis type 1 and optic pathway gliomas: relation to tumor location by magnetic resonance imaging. Am J Ophthalmol 131:442–445

Banna M, El-Ramahi K (1991) Neurologic involvement in Behçet disease: imaging findings in 16 patients. AJNR Am J Neuroradiol 12:791–796

Barkhof F, Scheltens P, Frequin ST, Nauta JJ, Tas Mw, Valk J, Hommes OR (1992) Relapsing-remitting multiple sclerosis: sequential enhanced MR imaging vs clinical findings in determining disease activity. AJR 159:1041–1047

Barkovich JA (2000) Pediatric neuroimaging, 2nd edn. Lippincott/Williams and Wilkins, Philadelphia

Barnard RO, Geddes JF (1987) The incidence of multifocal cerebral gliomas. A histological study of large hemisphere sections. Cancer 60:1519–1531

Becker T, Wagner M, Hofmann E, Warmuth-Metz M, Nadjmi M (1991) Do arachnoid cysts grow? A retrospective study. Neuroradiology 33:341–345

Berenstein A, Lasjaunias P (1992) Classification of brain arteriovenous malformations. In: Berenstein A, Lasjaunias P (eds) Endovascular treatment of cerebral lesions. Springer, Berlin Heidelberg New York, pp 1–88 (Surgical neuroangiography, vol 4)

Block F, Reith W (2001) Isolierte Vaskulitis des CNS. Radiologe 40:1090–1097

Bonneville J-F, Cattin F, Dietemann J-L (1986) Computed tomography of the pituitary gland. Springer, Berlin Heidelberg New York

Bouthillier A, van Loeveren HR, Keller JT (1996) Segments of the internal carotid artery: a new classification. Neurosurgery 38:425– 433

Bradac GB (1990) Angiography in cerebral ischemia. Riv Neuroradiol 3 [Suppl]:57–66

BraffmanBH, Bilaniuk LT, Naidich TP, Altman NR, Post MJ, Quencer RM, Zimmerman RA, Brody BA (1992) MR imaging of tuberous sclerosis: pathogenesis of this phakomatosis, use of gadopentate dimeglumine, and literature review. Radiology 183:227–238

Burger PC, Scheithauer BW (1994) Tumors of neuroglia and choroid plexus epithelium. In: Tumors of the central nervous system. Armed Forces Institute of Pathology, Washington DC, pp 25–161

Burger PC, Scheithauer BW, Vogel FS (1991) Brain tumors. In: Surgical pathology of the nervous system and its coverings, 3rd edn. Churchill Livingstone, New York, pp 193–437

Burger PC, Paulus W, Kleihues P (2000) Pilocytic astrocytomas. In: Kleihues O, Cavanee WK (eds) Pathology and genetics of tumors of the central nervous system. International Agency for Research on Cancer, Lyon, pp 45–51

Byrne JV, Guglielmi G (1998) Endovascular treatment of intracranial aneurysms. Springer, Berlin Heidelberg New York

Caplan LR, Wolpert SM (1991) Angiography in patients with occlusive cerebrovascular disease: views of a stroke neurologist and neuroradiologist. AJNR Am J Neuroradiol 12:593–601

Casselman JW, Kuhweide R, Ampe W, D'Hont G, Offeciers EF, Fa WK, Pattyn G (1996) Inner ear malformations in patients with sensorial hearing loss: detection with gradient-echo (3DFT-CISS) MRI. Neuroradiology 38:278–286

Cavenee WK, Furnari FB, Nagane M, Huang HJS, Newcomb EW, Bigner DD, Weller M, Berens ME, Plate KH, Israel MA, Noble MD, Kleihues P (2000) Diffusely infiltrating astrocytomas. In: Kleihues O, Cavanee WK (eds) Pathology and genetics of tumors of the central nervous system. IARC Press, Lyon, pp 10–21

Clark WC, Acker JD, Dohan FC (1985) Presentation of central nervous system sarcoidosis as intracranial tumors. J Neurosurg 63:851–856

Cogan D, Mount HT (1963) Intracranial aneurysms causing ophthalmoplegia. Arch Ophthalmol 70:757–771

Couly G, Coltey P, Eichmann A, LeDouarin NM (1995) The angiogenic potentials of the cephalic mesoderm and the origin of brain and head blood vessels. Mech Dev 52:1–16

Crotty TB, Scheithauer BW, Young WF Jr, David DH, Shaw EG, Miller GM, Burger PC (1995) Papillary craniopharyngioma: a clinical study of 48 cases. J Neurosurg 83:206–214

Daningue JN, Wilson CB (1977) Pituitary abscesses: report of 7 cases and review of the literature. J Neurosurg 46:601–608

Dietemann JL, Kehrli P, Maillot C, Diniz R, Reis M Jr,

Neugroschl C, Vinclair L (1998) Is there a dural wall between the cavernous sinus and the pituitary fossa? Anatomical and MRI findings. Neuroradiology 40:627–630
Dina TS (1991) Primary central nervous system lymphoma versus toxoplasmosis in AIDS. Radiology 179:823–838
Drake CG, Vanderlinden RG, Amacher AL (1968) Carotid-ophthalmic aneurysms. J Neurosurg 26:96–144
Dutton JJ (1994) Gliomas of the anterior visual pathway. Surv Ophthalmol 38:427–452
Edwards-Brown ME, Bonin JM (1996) White matter diseases. In: Atlas SW (ed) Magnetic resonance imaging of the brain and spine, 2nd edn. Lippincott-Raven, Philadelphia, pp 649–706
Elster AD (1992) Radiologic screening in the neurocutaneous syndromes. Strategies and controversies. AJNR Am J Neuroradiol 13:1078–1082
Elster AD, Chen MYM (1990) MR imaging of Sturge-Weber syndrome. AJNR Am J Neuroradiol 11:685–689
Engelbach M, Hey O, Thews DS, Bohl J, Müller-Forell W, Both S, Schneider S, Kunt T, Forst T, Pfützner A, Kann P, Beyer J (1999) TSH-producing hypophyseal carcinoma and prolactin-producing hypophyseal carcinoma: report of two different cases. Exp Clin Endocrinol Diabetes 107:184
Enjolras O, Rich MC, Merlan JJ (1985) Facial port-wine stains and Sturge-Weber syndrome. Pediatrics 76:48–51
Fauci AS, Haynes B, Katz P (1978) NIH conference. The spectrum of vasculitis: clinical, pathologic, immunologic, and therapeutic considerations. Ann Intern Med 89:660–676
Fazekas F, Barkhof F, Filippi M, Grossman RI, Li DK, McDonald WI, McFarland HF, Paty DW, Simon JH, Wolinsky JS, Miller DH (1999) The contribution of magnetic resoence imaging to the diagnosis of multiple sclerosis . Neurology 53:448–456
Ferguson G, Drake CG (1981) Carotid-ophthalmic aneurysm visual abnormalities in 32 patients and the results of treatment. Surg Neurol 16:1–8
Ferro JM (1998) Vasculitis of the cerebral nervous system. J Neurol 245:766–776
Filippi M, Rocca MA, Wiessmann M, Mennes S, Cercignani M, Yousri TA, Soriani MP (1999) A comparison of MR imaging with fast-FLAIR, HASTE-FLAIR, and EPI-FLAIR sequences in the assessment of patients with multiple sclerosis. AJNR Am J Neuroradiol 20:1931–1938
Fitzek C, Mewes J, Gawehn W, Mann W, Stoeter P (1998) Examination of cholesteatoma of the petrous bone with diffusion weighted echo planar imaging (DWI). Neuroradiology 40 [Suppl 1]:S62–S63
Forderreuther S, Straube A (1999) The criteria of the international headache society for Tolosa-Hunt syndrome need to be revised. J Neurol 246:371–377
Galluci M, Bozzao A, Splendiani A, Masciocchi C, Passariello R (1990) Wernicke encephalopathy: MR findings in five patients. AJNR Am J Neuroradiol 11:887–892
Giangaspero F, Burger PC, Osborne DR, Stein RB (1997) Suprasellar papillary squamous epithelioma („papillary craniopharyngioma"). Am J Surg Pathol 8:57–64
Goldberg HI, Lavi E, Atlas SW (1996) Extra-axial brain tumors. In: Atlas SW (ed) Magnetic resonance imaging of the brain and spine, 2nd edn. Lippincott-Raven, Philadelphia, pp 423– 487
Gomez MR (1988) Criteria for diagnosis in tuberous sclerosis. In: Gomez MR (ed) Tuberous sclerosis, 2nd edn. Raven, New York, pp 9–19
Grove A, Vyberg M (1993) Primary leptomeningeal T-cell lymphoma: a case and a review of primary T-cell lymphoma of the central nervous system. Neuropathology 12:7–12
Halliday AM (1993) Evoked potentials in clinical testing. 2nd edn. Churchill Livingston, London
Hankey GJ, Warlow CP (1991) The role of imaging in the management of cerebral and ocular ischemia. Neuroradiology 33:381–390
Harwood-Nash DC (1991) Primary neoplasms of the central nervous system in children. Cancer 67:1223–1228
Hayes WT, Bernhardt H, Young JM (1967) Fusiform arteriosclerotic aneurysms of the basilar artery. Five cases including two ruptures. Vasc Surg 1:171–178
Hayes WS, Sherman JL, Stern BJ, Citrin CM, Pulaski PD (1987) MR and CT evaluation of intracranial sarcoidosis. AJNR Am J Neuroradiol 8:841– 847
Heaton RK, Nelson LM, Thompson DS, Burks JS, Franklin GM (1985) Neuropsychiatric findings in relapsing-remitting and chronic-progressive multiple sclerosis. J Consult Clin Psychol 53:103–110
Henderson JW (1955) Intracranial arterial aneurysms. A study of 119 cases with special reference to ocular findings. Trans Am Ophthalmol Soc 53:349–462
Herring AB, Urich H (1969) Sarcoidosis of the central nervous system. J Neurol Sci 9:405–422
Hickey WF (1991) Migration of hematogenous cells through the blood brain barrier and the initiation of CNS inflammation. Brain Pathol 1:97–105
Holland BA, Kucharczyk W, Brant-Zawadzki M, Norman D, Haas DK, Harper PS (1985) MR imaging of calcified intracranial lesions. Radiology 157:353–356
Hollander MD, FitzPatrick M, O'Connor SG, Flanders AE, Tartaglino LM (1999) Optic gliomas. Radiol Clin North Am 37:59–71
Horn B, Heidemann R, Geyer R, Pollack L, Packer R, Goldwein J, Tomita T, Schomberg P, Ater J, Luchtman-Jones L, Rivlin K, Lamborn K, Prados M, Bollen A, Berger M, Dahl G, McNeil E, Patterson K, Shaw D, Kubalik M, Russo C (1999) A multinstitutional retrospective study of intracranial ependymoma in children: identification of risk factors. J Pediatr Hematol Oncol 21:203–211
Horowitz AL, Kaplan RD, Grewe G, White RT, Salberg LM (1989) The ovoid lesion: a new MR observation in patients with multiple sclerosis. AJNR Am J Neuroradiol 10:303–305
Howarth DM, Gilchrist GS, Mullan BP, Wiseman GA, Edmonson JH, Schomberg PJ (1999) Langerhans cell histiocytosis: diagnosis, natural history, management, and outcome. Cancer 85:2278–2290
Hoyt WF, Baghdassarian SA (1969) Optic glioma of childhood. Natural history and rationale for conservative management. Br J Ophthalmol 53:793–798
Hoyt WF, Meshel LG, Lessell S, Schatz NJ, Suckling RD (1973) Malignant optic glioma of adulthood. Brain 96:121–132
Huss GP, Mattle H, Wessel K, Mumenthaler M (1992) Neuro-Behçet syndrome: encephalitis and cerebral venous thrombosis: clinical aspects and neuroradiology of 5 cases. Nervenarzt 63:352–358
Iwazaki S, Nakagawa H, Kichikawa K, Fukusumi A, Watabe Y, Kitamura K, Otsuji H, Ohishi H, Uchida H (1990) MR and CT of tuberous sclerosis: linear abnormalities in the cerebral white matter. AJNR Am J Neuroradiol 11:1029–1034
Jack CR Jr, O'Neill BP, Banks PM, Reese DF (1988) Central nervous system lymphoma: histologic types and CT appearance. Radiology 167:21–215

Jaiswal AK, Tripathi M, Chandra PS, Sharma MC, Mahapatra AK (2000) An unusual case of primary lymphoma of the skull base extending from cerebello-pontine angle to cavernous sinus and orbit. A case report. J Neurosurg SCI 44:145–148

Jansen O, Brückmann H (2001) Ischämische Hirnerkrankungen. In: Sartor K (ed) Neuroradiologie, 2nd edn. Thieme, Stuttgart, pp 140–158

Janzer RC, Burger PC, Giangaspero F, Paulus W (2000) Craniopharyngioma. In: Kleihues P, Cavenee WK (eds) Pathology and genetics. Tumors of the nervous system. IARC Press, Lyon, pp 244–246

Jennings MT, Gelman R, Hochberg F (1985) Intracranial germ cell tumors: natural history and pathogenesis. J Neurosurg 63:155–167

Juvela S, Porras M, Heiskanen O (1993) Natural history of unruptured intracranial aneurysms: a long-term follow-up study. J Neurosurg 79:174–182

Kassel NF, Torner JC (1983) Aneurysmal rebleeding: a preliminary report from the Cooperative Aneurysm Study. Neurosurgery 13:479–481

Kazner E, Wende S, Grumme Th, Stochdorph O Felix R, Claussen C (eds) (1989) Computed tomography and magnetic resonance tomography of intracranial tumors. Springer, Berlin Heidelberg New York

Kepes JJ, Kepes M (1969) Predominantly cerebral forms of histiocytosis X: a reappraisal of "Gagel's hypothalamic granuloma", "granuloma infiltrans of the hypothalamus" and "Ayala's disease" with a report of four cases. Acta Neuropathol (Berl) 14:77–98

Khanna RK, Malik GM, Qureshi N (1996) Predicting outcome following surgical treatment of unruptured intracranial aneurysms: a proposed grading system. J Neurosurg 84:49–54

Kingsley D, Kendall B, Fitz C (1986) Tuberous sclerosis: a clinicoradiological evaluation of 110 cases with particular reference to atypical presentation. Neuroradiology 28:38–46

Kleihues O, Cavanee WK (eds) (2000) Pathology and genetics of tumors of the central nervous system. International Agency for Research on Cancer, Lyon

Kleihues O, Burger PC, Scheithauer BW (1993) Histological typing of tumors of the central nervous system. World Health Organization International Histological Classification of Tumors, 2nd edn. Springer, Berlin Heidelberg New York

Kleihues P, Davis RL, Ohgaki H, Cavanee WK (2000a) Astrocytic tumours. In: Kleihues O, Cavanee WK (eds) Pathology and genetics of tumors of the central nervous system. International Agency for Research on Cancer, Lyon, pp 9–54

Kleihues P, Burger PC, Collins VP, Newcomb EW, Ohgaki H, Cavanee WK (2000b) Glioblastoma. In: Kleihues O, Cavanee WK (eds) Pathology and genetics of tumors of the central nervous system. International Agency for Research on Cancer, Lyon, pp 29–39

Kleihues P, Davis RL, Ohgaki H, Burger PC, Westphal MM; Cavanee WK (2000c) Diffuse astrocytoma. In: Kleihues O, Cavanee WK (eds) Pathology and genetics of tumors of the central nervous system. International Agency for Research on Cancer, Lyon, pp 22–26

Kovacs K, Horvath E, Asa CL (1985) Classification and pathology of pituitary tumors. In: Wilkins RH, Rengachary SS (eds) Neurosurgery. McGraw-Hill, New York, 834–842

Krayenbühl H (1973) Klassifikation und klinische Symptomatologie der zerebralen Aneurysmen. Ophthalmo-logica 167:122–164

Kretschmann HJ, Weinrich W (1991) Klinische Neuroanatomie und kranielle Bilddiagnostik. Computertomographie und Magnetresonanztomographie, 2nd edn. Thieme, Stuttgart

Kucharczyk W, Montanera W, Becker LE (1996) The sella turcica and parasellar region. In: Atlas SW (ed) Magnetic resonance imaging of the brain and spine. Lippincott-Raven, Philadelphia, pp 871–930

Kueker W, Thiex R, Rohde I, Rohde V, Thron A (2000) Experimental acute intracerebral hemorrhage. Value of MR sequences for a safe diagnosis at 1.5 and 0.5 T. Acta Radiol 41:544–552

Kupersmith MJ (1993a) Aneurysms involving the motor and sensory visual pathway. In: Kupersmith MJ (ed) Neurovascular neuroophthalmology. Springer, Berlin Heidelberg New York, pp 239–299

Kupersmith MJ (1993b) Inflammatory vascular disorders of the brain and eye. In: Kupersmith MJ (ed) Neurovascular neuroophthalmology. Springer, Berlin Heidelberg New York, pp 413–439

Kupersmith MJ (1993c) Orbital vascular lesions. In: Kupersmith MJ (ed) Neurovascular neuroophthalmology. Springer, Berlin Heidelberg New York, pp 151–196

Kupersmith MJ, Berenstein A, Choi IS, Ransohoff J, Flamm ES (1984) Percutaneous transvascular treatment of giant carotid aneurysms: neuro-ophthalmological findings. Neurology 34:328–335

Lansberg MG, Thijs VN, O'Brien MW, Ali JO, de Crespigny AJ, Tong DC, Moseley ME, Albers GW (2001) Evaluation of apparent diffusion coefficient, diffusion-weighted, and T2-weighted signal intensity of acute stroke. AJNR Am J Neuroradiol 22:637–644

Lasjaunias P (1997) Pial arteriovenous malformation. In: Lasjaunias P (ed) Vascular diseases in neonates, infants and children. Springer, Berlin Heidelberg New York, pp 203–320

Leblanc A (1992) Anatomy and imaging of the cranial nerves. Springer, Berlin Heidelberg New York

Lee KH, Hashimoto SA, Hooge JP, Kastrukoff LF, Oger JJ, Li DK, Paty DW (1991) Magnetic resonance imaging of the head in the diagnosis of multiple sclerosis: a prospective 2-year follow-up with comparison of clinical evaluation, evoked potentials, oligoclonal banding, and CT. Neurology 41:657–660

Lexa FJ, Grossman RU (1994) MR of sarcoidosis in the head and spine: spectrum of manifestations and radiographic response to steroid therapy. AJNR Am J Neuroradiol 15:973–982

Levy RM, Bredesen DE, Rosenblum ML (1985) Neurological manifestation of the acquired immunodeficiency syndrome (AIDS): experience at USCF and review of the literature. J Neurosurg 62:475–495

Ley A (1950) Compression of the optic nerve by a fusiform aneurysm of the carotid artery. J Neurol Neurosurg Psychiatry 13:75–86

Locksley HB (1966) Report on the cooperative study of intracranial aneurysms and subarachnoid hemorrhage, section 5, part 1. Natural history of subarachnoid hemorrhage, intracranial aneurysms and arteriovenous malformation. J Neurosurg 25:219–239

Louis DN, Scheithauer BW, Budka H, von Deimling A, Kepes JJ (2000) Meningiomas. In: Kleihues P, Cavenee WK (eds) Pathology and genetics. Tumors of the nervous system.

International Agency for Research on Cancer, Lyon, pp 176–184
Maghnie M, Arico M, Villa A, Genovese E, Beluffi G, Severi F (1992) MR of hypothalamic-pituitary axis in Langerhans cell histiocytosis. AJNR Am J Neuroradiol 13:1365–1371
Majos C, Coll S, Aguilera C, Acebes JJ, Pons LC (1998) Imaging of giant pituitary adenomas. Neuroradiology 40:651–655
Mason C, Kandal ER (1991) Central visual pathways. In: Kandal ER, Schwartz JH, Jessell TM (eds) Principles of neural science, 3rd edn. Elsevier, New York, pp 420–439
Matsutani M, Sano K, Takura K, Fujimaki T, Nakamura O, Funata N, Seto T (1997) Primary intracranial germ cell tumors: a clinical analysis of 153 histologically verified cases. J Neurosurg 86:446–455
McDonald WI, Compston A, Edan G, Goodkin D, Hartung HP, Lublin FD, McFarland HF, Paty DW, Polman CH, Reingold SG, Sandberg-Wollheim M, Sibley W, Thompson A. van den Noort S, Weinhenker BY, Wolinski JS (2001) Recommended diagnostic criteria multiple sclerosis: Guidelines from the international panel on the diagnosis of multiple sclerosis. Ann Neorol 50:121–127
McLean BN, Luxton RW, Thompson EJ (1990) A study of immunoglobulin G in the cerebrospinal fluid of 1007 patients with suspected neurological disease using isoelectric focusing and the log IgG-index. Brain 113:1269–1289
Mena H, Nakazato Y, Jouvet A, Scheithauer BW (2000) Pinealoblastoma. In: Kleihues P, Cavenee WK (eds) Pathology and genetics. Tumors of the nervous system. IARC, Lyon, pp 116–121
Meyers SP, Hirsch WL, Curtin HD, Barnes L, Sekhar LN, Sen C (1992) Chordomas of the skull base: MR features. AJNR Am J Neuroradiol 13:1627–1636
Miller DC, Hochberg FH, Harris NL, Gruber ML, Louis DN, Cohen H (1994) Pathology with clinical correlations of primary central nervous system non-Hodgkin's lymphoma. The Massachusetts General Hospital experience 1958–1989. Cancer 74:1383–1397
Miller RF, Hall-Craggs MA, Costa DC, Brink NS, Scaravilli F, Luca SB, Wilkinson ID, Ell PJ, Kendall BE, Harrison MJ (1998) Magnetic resonance imaging, thallium-201 SPET scanning and laboratory analysis for discrimination of cerebral lymphoma and toxoplasmosis in AIDS. Sex Transm Infect 74:258–264
Mirfakhraee M, Crofford MJ, Guinto FC, Nauta HJW, Weedn VW (1986) Virchow-Robin space: a path of spread in neurosarcoidosis. Radiology 158:715–720
Mork SJ, Loken AC (1977) Ependymoma: a follow-up study of 101 cases. Cancer 40:907–915
Moussa RF, Wong JH, Awad IA (2001) Genetic factors related to intracranial arteriovenous malformations. Neurochirurgie 47:154–157
Müller-Forell W (2001) Tumoren der Sellaregion und der Schädelbasis. In: Sartor K (ed) Neuroradiologie. Thieme, Stuttgart, pp 109–128
Müller-Forell W, Lieb W (1995) Neuroradiologie in der Ophthalmologie, part 2. Ophthalmologe 92:757–784
Naidich TP, Zimmerman RA (1984) Primary brain tumors in children. Semin Roentgenol 19:100–114
Nasir S, DeAngelis LM (2000) Update on the management of primary CNS lymphoma. Oncology (Huntingt) 14:228–234
Nelson JS, von Deimling A, Petersen I, Janzer RC (2000) Metastatic tumors. In: Kleihues O, Cavanee WK (eds) Pathology and genetics of tumors of the central nervous system. IARC, Lyon, pp 250–253
Okazaki H (1989) Fundamentals of neuropathology. Morphologic basics of neurologic disorders. Igaku-Shoin, New York
Olson T (1992) Immunology of multiple sclerosis. Curr Opin Neurol Neurosurg 5:195–202
Osborn A (1994a) Meningiomas and other nonglial neoplasms. In: Osborn A (ed) Diagnostic neuroradiology. Mosby, St Louis, pp 579–625
Osborn A (1994b) Miscellaneous tumors, cysts and metastasis. In: Osborn A (ed) Diagnostic neuroradiology. Mosby, St Louis, pp 626–670
Osborn A (1994c) Intracranial aneurysms. In: Osborn A (ed) Diagnostic neuroradiology. Mosby, St Louis, pp 248–283
Osborn A (1994d) Stroke. In: Osborn A (ed) Diagnostic neuroradiology. Mosby, St Louis, pp 330– 398
Osborn A (1994e) Disorders of histogenesis: neurocutaneous syndromes. In: Osborn A (ed) Diagnostic neuroradiology. Mosby, St Louis, pp 72–113
Osborn A (1994f) Acquired metabolic, white matter, and degenerative diseases of the brain. In: Osborn A (ed) Diagnostic neuroradiology. Mosby, St Louis, pp 748–781
Osborn A (1994g) Infections of the brain and its linings. In: Osborn A (ed) Diagnostic neuroradiology. Mosby, St Louis, pp 673–715
Osborn A (1999) Diagnostic cerebral angiography, 2nd edn. Lippincott/Williams and Wilkins, Philadelphia
Osborn A, Rauschning W (1994) Brain tumors and tumorlike masses: classification and differential diagnosis. In: Osborn A (ed) Diagnostic neuroradiology. Mosby, St Louis, pp 401–528
Patel U, Gupta SC (1990) Wyburn-Mason syndrome. A case report and review of the literature. Neuroradiology 31:544–546
Paty DW (1997) MRI as a method to reveal in vivo pathology in MS. J Neural Transm [Suppl] 49:211–217
Paulus W, Jellinger K, Morgello S, Deckert-Schlüter M (2000) Malignant lymphomas. In: Kleihues P, Cavenee WK (eds) Pathology and genetics. Tumors of the nervous system. IARC, Lyon, pp 198–203
Perilongo G, Carollo C, Saviati L, Murgia A, Pillon M, Basso G, Gardiman M, Laverda AM (1997) Diencephalic syndrome and disseminated juvenile pilocytic astrocytoma of the hypothalamic-optic chiasm region. Cancer 80:142–146
Perneczky A, Müller-Forell W, van Lindert, Fries G (eds) (1999) Keyhole concept in neurosurgery with endoscopic-assisted microsurgery and case studies. Thieme, Stuttgart
Pinto RS, Kricheff II, Butler AR et al (1979) Correlation of computed tomographic, angiographic and neuropathological changes in giant cerebral aneurysms. Radiology 135:85–92
Pollack IF, Gerszten PC, Martinez AJ, Lo KH, Shultz B, Albright AL, Janosky J, Deutsch M (1995) Intracranial ependymoma of childhood: long-term outcome and prognostic factors. Neurosurgery 78:859–863
Poser CM, Paty DW, Scheinberg L, McDonald WI, Davis FA, Ebers GC, Johnson KP, Sibley WA, Silberberg DH, Tourtelotte WW (1983) New diagnostic criteria for multiple sclerosis: guidelines for research protocols. Ann Neurol 13:227–231
Prayson RA (1999) Clinicopathologic study of 61 patients with ependymoma including MIB-1 immunohistochemistry. Ann Diagn Pathol 3:11–18
Prineas JW, McDonald WI (1997) Demyelinisating diseases. In: Graham DI, Lantos PL (eds) Greenfield's neuropathology, 6th edn. Arnold, London, pp 813–896

Proebstle TM, Schonfeldt C, Luttke B, Weber L (1996) Morbus Behçet mit primärem Befall zerebraler Gefässe. Dtsch Med Wochenschr 121:16–20

Raps EC, Rogers JD, Galetta SL, Solomon RA Lennihan L, Klebanoff LM, Fink ME (1993) The clinical spectrum of unruptured intracranial aneurysms. Arch Neurol 50:265–268

Rauber z, Kopsch z (1987) Nervensystem, Sinnesorgane. In: Leonhardt H, Töndury G, Zilles K (eds) Anatomie des Menschen, Lehrbuch und Atlas, Vol III. Thieme, Stuttgart

Reiche W, Merkelbach S, Reith W (2000) Neuroradiologische Aspekte bei Encephalitis disseminata. Radiologe 40:1045–1056

Rodriguez LA, Edwards MS, Levin VA (1990) Management of hypothalamic gliomas in children: an analysis of 33 cases. Neurosurgery 26:242–246

Rose DA, Norman D, Wilson CB (1992) Radiologic characteristics and results of surgical management of Rathke's cysts in 43 patients. Neurosurgery 31:173–179

Rosemberg S, Amaral LC, Kleinmann SE, Arita FN (1992) Acute encephalopathy with bilateral striatal necrosis. A distinctive clinicopathological condition. Neuropediatrics 23:310–315

Rosenblum B, Rothman AS, Lanzieri C, Song S (1986) Cavernous sinus cavernous haemangioma. J Neurol Sci 36:233–238

Rosenblum MK, Matsutani M, Van Meir EG (2000) CNS germ cell tumors. In: Kleihues O, Cavanee WK (eds) Pathology and genetics of tumors of the central nervous system. IARC, Lyon, pp 208–214

RosenfieldNS, Abraham J, Komp D (1990) Brain MR in patients with Langerhans cell histiocytosis: findings and enhancement with Gd-DTPA. Pediatr Radiol 20:433–436

Ross JS, Masaryk TJ, Modic MT, Ruggieri PM, Haacke EM, Selman WR (1990) Intracranial aneurysms: evaluation by MR angiography. AJNR Am J Neuroradiol 11:449–456

Rovira MJ, Post MJD, Bowen BC (1991) Central nervous system infections in HIV-infected persons. Neuroimaging Clin North Am 1:179–200

Rush JA; Younge BR, Campbell RJ, MacCarty CS (1982) Optic glioma: long-term follow-up of 86 histopathologically verified cases. Ophthalmology 89:1213–1219

Russell DS, Rubinstein LJ (1989) Pathology of tumors of the central nervous system, 5th edn. Williams and Wilkins, Baltimore

Sartor K (1992) MR imaging of the skull and brain. A correlative text-atlas. Springer, Berlin Heidelberg New York

Sartoretti-Schefer S, Wichmann W, Aguzzi A, Valavanis A (1997) MR differentiation of adamantinous and squamous-capillary craniopharyngioma. AJNR Am J Neuroradiol 18:77–87

Schachenmayr W, Friede RL (1979) Fine structure of arachnoid cysts. J Neuropathol Exp Neurol 38:434–446

Schmauser I, Bittner R (1990) MR-imaging findings in children with Sturge-Weber syndrome. Neuropediatrics 21:146–152

Schramm P, Hähnel S (2001) Das Tolosa-Hunt-Syndrom – eine neuroradiologische Ausschlussdiagnose? Fortschr Röntgenstr 173:962–964

Schroth G, Wichmann W, Valavanis A (1991) Blood brain barrier disruption in acute Wernicke encephalopathy: MR findings. J Comput Assist Tomogr 15:1059–1061

Schubiger O, Valavanis A, Wichmann W (1987) Growth mechanism of giant intracranial aneurysms. Demonstration by CT and MR imaging. Neuroradiology 29:266–271

Schwartz RB, Tice HM, Hooten SM, et al (1994) Evaluation of cerebral aneurysms with helical CT: correlation with conventional angiography and MR angiography. Radiology 192:712–722

Schwarz A, Gass A (2001) Demyelinisierende Erkrankungen. In: Sartor K (ed) Neuroradiologie, 2nd edn. Thieme, Stuttgart, pp 217–231

Scotti G, Yu CY, Dillon WP, Norman C, Colombo N, Newton TH, De Groot J, Wilson CB (1988) MR imaging of cavernous sinus involvement by pituitary adenomas. AJR 151:799–806

Sengupta RP, Gryspeerdt GL, Hankinson J (1976) Carotid ophthalmic aneurysms. J Neurol Neurosurg Psychiatry 39:837–853

Shapiro SK, Shapiro J, Wirtschafter J, Mastri AR (1982) Malignant optic glioma in an adult: initial CT abnormality limited to the posterior orbit, leptomeningeal seeding of the tumor. Minn Med 65:155–159

Siesjö BK (1992) Pathophysiology and treatment of focal cerebral ischemia. J Neurosurg 77:169–184

Smirniotopoulos JG, Murphy FM (1996) Central nervous system manifestations of the phakomatoses and other inherited syndromes. In: Atlas SW (1996) Magnetic resonance imaging of the brain and spine, 2nd edn. Lippincott-Raven, Philadelphia, pp 773–802

Smith JL, Taxdal DS (1966) Painful ophthalmoplegia. The Tolosa-Hunt syndrome. Am J Ophthalmol 61:1466–1472

Smith RR, Zubkov YN, Tarassoli Y (1994) Cerebral aneurysms. Microvascular and endovascular management. Springer, Berlin Heidelberg New York, pp 90–104

Stehbens WE (1972) Intracranial arterial aneurysms. In: Stehbens WE (ed) Pathology of the cerebral blood vessels. Mosby, St Louis, pp 351–470

Stehbens WE (1995) Cerebrovascular disease. In: Stehbens WE, Lie JT (eds) Vascular pathology. Chapman and Hall, London, pp 437–488

Suss RA, Kumar AJ, Dorfman HD, Miller NR, Rosenbaum AE (1984) Capillary hemangioma of the sphenoid bone. Skeletal Radiol 11:102–107

Tannouri F, Divano L, Caucheteur V, Hacourt A, Pirotte B, Salmon I, Balériaux D (2001) Cavernous haemangioma in the cavernous sinus: case report and review of the literature. Neuroradiology 43:317–320

Tien RD, Newton TH, McDermott MW, Dillon MW, Kucharczyk J (1990) Thickened pituitary stalk on MR images in patients with diabetes insipidus and Langerhans cell histiocytosis. AJNR Am J Neuroradiol 11:703–708

van der Knaap MS, Valk J (1995a) Multiple sclerosis. In: van der Knaap MS, Valk J (eds) Magnetic resonance of myelin, myelination, and myelin disorders, 2nd edn. Springer, Berlin Heidelberg New York, pp 296–313

van der Knaap MS, Valk J (1995b) Acute disseminating encephalomyelitis and acute hemorrhagic encephalomyelitis. In: van der Knaap MS, Valk J (eds) Magnetic resonance of myelin, myelination, and myelin disorders, 2nd edn. Springer, Berlin Heidelberg New York pp 320–326

van der Knaap MS, Valk J (1995c) Toxic encephalopathy. In: van der Knaap MS, Valk J (eds) Magnetic resonance of myelin, myelination, and myelin disorders, 2nd edn. Springer, Berlin Heidelberg New York, pp 350–361

van der Knaap MS, Valk J (1995d) Myelin and white matter. In: van der Knaap MS, Valk J (eds) Magnetic resonance of myelin, myelination, and myelin disorders, 2nd edn. Springer, Berlin Heidelberg New York, pp 1–17

Van Tessel P, Lee YY, Jing BS, de Pena CA (1989) Mucoceles of the paranasal sinuses: MR imaging with CT correlation. AJNR Am J Neuroradiol 10:607–612

Vion-Dury J, Vincentelli F, Jiddane M, van Bunnen Y, Rumeau C, Grisoli F, Salamon G (1987) MR imaging of epidermoid cysts. Neuroradiology 29:333–338

Walsh TJ (1985) Neuro-ophthalmology: clinical signs and symptoms, 2nd edn. Lea and Febiger, Philadelphia

Wechsler B, Gerber S, Vidailhet M, Dormont D (1999) Neurologic manifestations of Behçet's disease. Ann Med Interne (Paris) 150:555–561

Weir B, Grace M, Hansen J, Rothberg C (1978) Time course of vasospasm in man. J Neurosurg 48:173–178

Whelan MA, Kricheff II, Handler M, Ho V, Crystal K, Gopinathan G, Laubenstein L (1983) Acquired immunodeficiency syndrome: cerebral computed tomography. Radiology 149:477–484

Wiestler OD, Schiffer D, Coons SW, Prayson RA, Rosenblum MK (2000a) Ependymoma. In: Kleihues O, Cavanee WK (eds) Pathology and genetics of tumors of the central nervous system. IARC, Lyon, pp 72–76

Wiestler OD, Lopes BS, Green AJ, Vinters HV (2000b) Tuberous sclerosis complex and subependymal giant cell astrocytoma. In: Kleihues O, Cavanee WK (eds) Pathology and genetics of tumors of the central nervous system. IARC, Lyon, pp 227–230

Wilkins RH (ed) (1988) Cerebral vasospasm. Proceedings of the 3rd international symposium in Charlottesville. Raven, New York

Wilcock D, Jaspan T, Holland I, Cherryman G, Worthington B (1996) Comparison of magnetic resonance angiography with conventional angiography in the detection of intracranial aneurysms in patients presenting with subarachnoid hemorrhage. Clin Radiol 51:330–334

Willing SJ, Faye-Petersen O, Aronin P, Faith S (1993) Capillary hemangioma of the meninges. AJNR Am J Neuroradiol 14:529–536

Winn HR, Richardson AE, Jane JA (1977) The long-term prognosis of untreated cerebral aneurysms. 1. Incidence of late hemorrhage in cerebral aneurysms: a 10 year evaluation of 364 patients. Ann Neurol 1:358–370

Witt ED (1985) Neuroanatomical consequences of thiamine deficiency: a comparative analysis. Alcohol Alcohol 2:201–221

Woitalla D, Henkes H, Felber S, Weber W, Jänisch W, Kühne D (2000) Klinik und bildgebende Diagnostik der Sarkoidose des Nervensystems. Radiologe 40:1064–1076

Woodruff JM, Kourea HP, Louis DN, Scheithauer BW (2000) Schwannoma. In: Kleihues O, Cavanee WK (eds) Pathology and genetics of tumors of the central nervous system. IARC, Lyon, pp 164–166

Wulc AE, Bergin DJ, Barnes D, Scaravilli F, Wright JE, McDonald WI (1989) Orbital optic nerve glioma in adult life. Arch Ophthalmol 107:1013–1016

Wyburn-Mason R (1943) Arteriovenous aneurysm of midbrain and retina, facial naevi and mental changes. Brain 66:163–209

Yasargil MG (1994) A CNS tumors: surgical anatomy, neuropathology, neuroradiology, neurophysiology, clinical considerations, operability, treatment options. Thieme, Stuttgart, pp 116–245 (Microneurosurgery, vol IV)

Yasargil MG, Gasser GJ, Hodosh RM, Rankin TY (1977) Carotid ophthalmic aneurysms: direct microsurgical approach. Surg Neurol 8:155–165

Yoshimoto T, Uchida K, Kaneko U, Kayama T, Suzuki J (1979) An analysis of follow-up results of 1000 intracranial saccular aneurysms with definite surgical treatment. J Neurosurg 50:152–157

Van der Zwan A, Hillen B, Tulleken CA, Dujovny M, Dragovic L (1992) Variability of the territories of the major cerebral arteries. J Neurosurg 77:927–940

Zajicek JP, Scolding NJ, Foster O, Rovaris M, Evanson J, Moseley IF, Scadding JW, Thompson EJ, Chamoun V, Miller DH, McDonald WI, Mitchell D (1999) Central nervous system sarcoidosis – diagnosis and management. QJM 92:103–117

Zülch KJ (1986) Brain tumors. Their biology and pathology. Springer, Berlin Heidelberg New York

Subject Index

Citation with pages in fat italics correspond to relevant figures

Anatomic Structures

Bones:

1 maxillary bone
1.1 infraorbital foramen / canal
1.2 maxillary sinus
1.3 nasolacrimal canal (duct)
1.4 lacrimal sac / fossa

2 ethmoid bone
2.1 nasal septum
2.2 lamina papyracea
2.3 cribriform plate (lamina cribrosa)
2.4 crista galli
2.5 ethmoid sinus
2.6 middle turbinate (concha)
2.7 inferior turbinate (concha)
2.8 vomer

3 sphenoid bone
3.1 anterior clinoid process
3.2 optic canal
3.3 sella turcica
3.4 dorsum sellae
3.5 clivus
3.6 superior orbital fissure
3.7 inferior orbital fissure
3.8 great wing
3.9 round foramen (foramen rotundum)
3.10 oval foramen (foramen ovale)
3.11 sphenoid plane
3.12 sphenoid sinus
3.13 pterygo-palatine fossa
3.14 pterygopalatine canal
3.15 pterygomaxillary fossa
3.16 sphenopalatine foramen

4 zygomatic bone
4.1 fronto-zygomatic suture
4.2 temporal fossa

5 lacrimal bone (os lacrimale)
5.1 fossa of the lacrimal sac
6 mandibular bone
7 frontal bone (os frontale)
7.1 orbital roof
7.2 frontal sinus
7.5 zygomatic process
7.6 olfactory groove

8 petrous bone

Soft tissue of the orbit:

9 globe
9.1 lens
9.2 ciliary body (corpus ciliare)
9.3 sclera
9.4 retina
9.5 choroid
9.6 macula
9.7 vitreous body

10 orbit
10.1 inferior rectus muscle
10.2 medial rectus muscle
10.3 superior rectus muscle
10.4 lateral rectus muscle
10.5 superior oblique muscle
10.6 inferior oblique muscle
10.7 levator palpebrae muscle
10.8 trochlea
10.9 orbital septum
10.10 orbital fat
10.11 optic nerve
10.12 optic nerve sheath
10.13 superior ophthalmic vein
10.14 ophthalmic artery
10.15 lacrimal gland
10.16 intermuscular septum

Intracranial anatomy:

11 cranial regions
11.1 anterior cranial fossa
11.2 middle cranial fossa
11.3 posterior cranial fossa
11.4 temporal bone
11.5 petrous bone

12 nerves and tracts
12.1 prechiasmatic optic nerve
12.2 chiasma
12.3 optic tract
12.4 medial geniculate nucleus
12.5 lateral geniculate nucleus
12.6 optic radiation
12.7 anterior commissure
12.8 oculomotor nerve (NIII)

12.9 abducens nerve (N VI)
12.10 maxillary nerve (N V2)
12.11 mandibular nerve (N V3)
12.12 ophthalmic nerve (N V1)
12.13 pontin part of the trigeminal nerve (N V)
12.14 trigeminal (Gasserian) ganglion

13 brain parenchyma
13.1 temporal lobe
13.2 frontal lobe
13.3 occipital lobe
13.4 calcarine sulcus
13.5 parietal lobe
13.6 pons
13.7 corpus callosum
13.8 genu (of the corpus callosum)
13.9 body (of the corptus callosum)
13.10 thalamus
13.11 pituitary gland
13.12 pituitary stalk
13.13 mammillary body
13.14 fornix
13.15 pineal gland
13.16 quadrigeminal plate
13.17 ventricles (left, right)
13.18 frontal horn
13.19 temporal horn
13.20 foramen of Monroi
13.21 third ventricle
13.22 septum pellucidum
13.23 chiasmatic recess (of the third ventricle)
13.24 recess of the pituitary stalk (of the third ventricle)
13.25 fourth venticle
13.26 aqueduct
13.27 mesencephalic cistern (ambient)

14 arteries
14.1 carotid canal
14.2 ICA (internal carotid artery)
14.3 siphon of ICA
14.4 ophthalmic artery
14.5 basilar artery
14.6 Pcomm (posterior communicating artery)
14.7 PCA (posterior cerebral artery)
14.8 ACA (anterior cerebral artery)
14.9 MCA (middle cerebral artery)
14.10 superior cerebellar artery

15 veins
15.1 cavernous sinus
15.2 internal cerebral vein
15.3 vein of Galen

List of Abbreviations

ACA	anterior cerebral artery
Acomm	anterior communicating artery
ADEM	acute disseminating encephalomyelitis
AIDS	acquired immuno deficiency syndrome
AIUM	American Institute of Ultrasound in Medicine
aoS	accessory optic system
AP	anterior-posterior
AVM	arteriovenous malformation
BA	Broca area
bf	binocularly seen part of the right rvhf
BBB	blood-brain-barrier
BG	burst-generator neuron
BOLD	blood-oxygen-level-dependant
BOMS	brainstem oculomotor system
BUN	build-up neuron
CBF	cerebral blood flow
cbl	cerebellum
CBV	cerebral blood volume
CCSF	carotid cavernous sinus fistula
CDI	color Doppler imaging
CISS	constructive interference in steady state
CNS	central nervous sytem
CRA	central retinal artery
CRV	central retinal vein
CS	cavernous sinus
CSF	cerebrospinal fluid
CT	Computer Tomography
CTA	CT-angiography
DLPC	dorsolateral prefrontal cortex (Brodmann area 46)
DLPN	dorsolateral pontine nucleus
DNA	desoxy-ribonuclein acid
DOG	difference-of-Gaussian
DSA	digital subtraction angiography
DVA	developmental venous anomaly
DVM	delayed visual maturation
DW	diffusion weighted
ECA	external carotid artery
EEG	electroencephalography
epS	extrapyramidal system
ER-fMRI	event related fMRI
F	fovea
FDA	Food and Drug Administration
FEF	frontal eye field
FLAIR	flow attenuated inversion recovery
FN	fixation neuron
fMRI	functional magnetic resonance imaging
FS	fat suppressed
FSE	fast spin echo
GABA	gamma-amino-butyric acid
GBM	glioblastoma multiforme
Gy	Gray (radiation dose unit)
HLA	human leukocyte antigen
HU	Hounsfield unit
HIV	human immunodeficiency virus
HR	high resolution
ICA	internal carotid artery
InC	interstitial nucleus of Cajal
INO	internuclear ophthalmoplegia
IOA	internal optic atrophy
ipl	inferior parietal lobe
IR	inversion recovery
IT	inferior temporal cortex/area
i.v.	intravenous
LCH	Langerhans cell histiocytosis
le	left eye
LGN	lateral geniculate nucleus
LIP	lateral intraparietal area
ln	lower nasal quadrant
LO	lateral occipitotemporal (cortex)
lt	low temporal quadrabt
mAS	milli Ampere second
MCA	medial cerebral artery
MEG	magnet encephalography
MELAS	mitochondrial encephalopathy, lactic acidosis, and stroke-like episodes
Mhz	mega Hertz
MIN	minimum intensity
MIP	multi intensity projection
MLF	medial longitudinal fasciculus
MPS	mucopolysaccharidosis
MR	Magnetic Resonance
MRA	MR-angiography
MRF	mesencephalic reticular formation
MRI	magnetic resonance imaging
MS	multiple sclerosis
MST	medial superior area
mSv	milli Sievert (effective radiation dosis unit)
MT	magnetization transfer (MRI)
MT	middle temporal (area) (chapter neuroophthalmology, chapter fMRI)
NHL	non Hodgkin lymphoma
NAA	N-acetyl aspartate

NF	neurofibromatosis
Nrtp	nucleus reticularis tegmentis pontis
NV	vestibular nucleus
OA	ophthalmic artery
OIS	ocular ischemic syndrome
OKR	optokinetic reflex/response
OP	omnipause neuron
OPG	optic pathway glioma
OTC	ornithine carbymal transferase
PC	phase contrast
PCA	posterior cerebral artery
PCA	posterior ciliary artery (in chapter 1)
Pcomm	posterior communicating artery
PDw	proton density weighted
PEF	parietal eye field
PET	positron emission tomography
PHPV	persistent hyperplastic vitreous
PIT	posterior inferior temporal area
PMD	Pelizaeus-Merzbacher disease
Pph	prepositus hypoglossi nucleus
ppm	parts per million
PPRF	paramedian pontine reticular formation
pvS	peripheral vestibular system
PVL	periventricular leukomalacia
pw	proton weighted
RB1	retinoblastoma–gene
RBN	retrobulbar neuritis
re	right eye
rf	receptive field
RiMLF	rostral interstitial nucleus of the MLF
ROP	retinopathy of the premature
RMS	rhabdomyosarcoma
rvhf	right visual hemifield
SAH	subarachnoid hemorrhage
SC	superior colliculi
SE	spin echo
sef	supplementary eye field
SLE	systemic lupus erythematosus
SNpr	substantia nigra pars reticularis
SNR	Signal to Noise Ratio
SOD	septo-optic dysplasia
SOV	superior ophthalmic vein
SP	smooth persuit
SPECT	single photon emission tomography
SPAI	spatial peak average intensity
spl	superior parietal lobe
STIR	short-tau-inversion-recovery
SPTA	situ peak temporal average
SSC	semicircular canal
T1w	T1 weighted
T2w	T2 weighted
THS	Tolosa-Hunt Syndrome
TOF	time of flight
TSE	turbo spin echo
TTT	transpupillary thermotherapy
UBO	unidentified bright object
un	upper nasal quadrant
ut	upper temporal quadrant
V1f	foveal representation in visual area 1
V1p	peripheral representation in visual area 1
VA	vertebral artery
VEP	visual evoked potential
vi	striate and extrastriate visual cortex/area
VOR	vestibulo-ocular reflex
Vv	vortex vein
vx	vestibular cortex
WE	Wernicke's encephalopathy

List of Contributors

Eugen Boltshauser, MD
Professor, Children's University Hospital
Steinwiesstrasse 75
8032 Zürich
Switzerland

PD Spyros S. Kollias, MD
Institute of Neuroradiology
University Hospital of Zurich (USZ)
Frauenklinikstrasse 10
8091 Zürich
Switzerland

Wolfgang Lieb, MD, PhD
Professor, Eyeclinic Medical School
University of Würzburg
Julius Maximilians-Universität
Josef-Schneider-Strasse 11
97080 Würzburg
Germany

Ernst Martin, MD
Professor, Children's University Hospital
Steinwiesstrasse 75
8032 Zürich
Switzerland

PD Wibke Müller-Forell, MD
Institute of Neuroradiology
Medical School University of Mainz
Langenbeckstraße 1
55101 Mainz
Germany

Susanne Pitz, MD
Department of Ophthalmology
Medical School University of Mainz
Langenbeckstraße 1
55101 Mainz
Germany

PD Urs Schwarz, MD
Department Neurology
University Hospital of Zürich
Frauenklinikstrasse 26
8091 Zürich
Switzerland

Werner Wichmann, MD, PhD
Professor, Institute of Neuroradiology and Radiology
Klinik im Park AG
Seestrasse 220
8027 Zürich
Switzerland